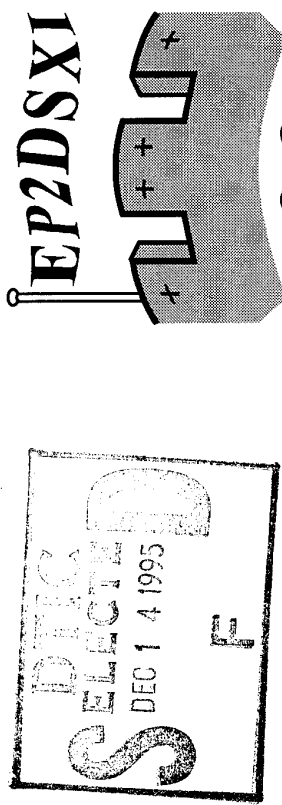


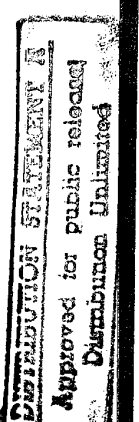
WORKBOOK & PROGRAMME

Eleventh International Conference on the *Electronic Properties of Two Dimensional Systems*



1995
Nottingham

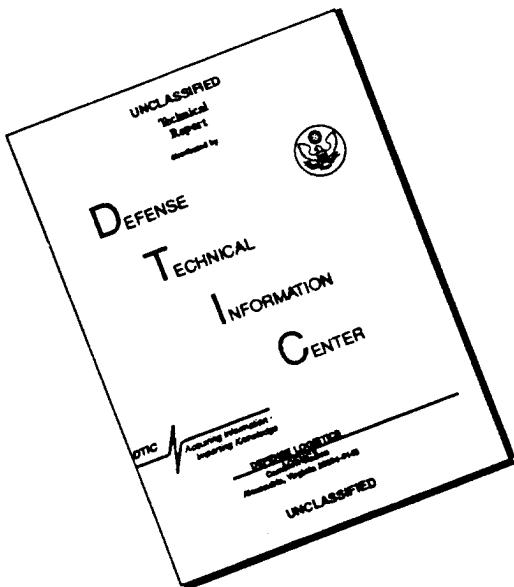
19951212 081



August 7-11, 1995
Nottingham
U.K.

DPLC 02/01/95 14:44:20 1

DISCLAIMER NOTICE



**THIS DOCUMENT IS BEST
QUALITY AVAILABLE. THE COPY
FURNISHED TO DTIC CONTAINED
A SIGNIFICANT NUMBER OF
PAGES WHICH DO NOT
REPRODUCE LEGIBLY.**

Preface

LOCAL ORGANIZING COMMITTEE (NOTTINGHAM)

L. Eaves • K.A. Benedict • B.L. Gallagher • A.J. Kent
P.C. Main • C.J. Mellor • F.W. Sheard

This Workbook contains the unrefereed manuscripts of contributions to be presented at the 11th International Conference on the Electronic Properties of Two-Dimensional Systems (EP2DS XI) to be held at the East Midlands Conference Centre, University of Nottingham, from August 7 1995 to August 11 1995. For those manuscripts which were not received in camera-ready format in time to be printed in the Workbook, abstracts are included. Manuscripts for the contributions contained in the Workbook will be refereed, and those accepted will be published in a special issue of Surface Science.

We are most grateful to the following companies and organisations for their generous financial support and sponsorship of this meeting. The list of sponsors to the date of publication of this workbook (14 July 1995) is:

Hitachi Ltd. (Japan)

Matsushita Electric Industrial Co. Ltd.(Japan)

Sharp Corporation (Japan)

Toshiba Corporation (Japan)

European Research Office of the U.S. Army

U.S. Office of Naval Research

Hitachi Cambridge Laboratory

Sharp Laboratories of Europe

Toshiba Cambridge Research Centre Ltd

Oxford Instruments (UK) Ltd.

Cryogenic Limited

The Engineering and Physical Sciences Research Council (UK)

International Union of Pure and Applied Physics

The Commission of The European Community

The University of Nottingham, Office of Professional and Industrial

Training

University of Nottingham, Department of Physics

By NQ200/4-95/-0630

Distribution /

Availability Codes

Dist	Avail and / G Special
A-1	

J. M. Worlock (Salt Lake City) • H. Z. Zheng (Beijing)

F. I. B. Williams (Saclay)

V. B. Timofeev (Chernogolovka)

PROGRAMME COMMITTEE

G. Abstreiter (Garching) • T. Ando (Tokyo)
C. W. J. Beenakker (Leiden)
L. J. Challis (Nottingham) • L. Eaves (Nottingham)
D. C. Glattli (Saclay) • R. J. Nicholas (Oxford)
M. Pepper (Cambridge) • M.S. Skolnick (Sheffield)
H. Störmer (Murray Hill),
V. B. Timofeev (Chernogolovka)

INTERNATIONAL ADVISORY COMMITTEE

E. Andrei (Piscataway) • G. Bauer (Linz)
P. N. Butcher (Warwick) • A. Chaplik (Novosibirsk)
R. G. Clark (Sydney) • A. Dahm (Cleveland)
M. Diorio (Ottawa) • L. Esaki (Tsukuba)
E. Gornik (Vienna) • C. Hamaguchi (Osaka)
P. Hawrylak (Ottawa) • M. Heiblum (Rehovot)
O. Hipólito (São Paulo) • S. Kawaji (Tokyo)
F. Koch (Garching) • J. P. Kotthaus (Munich)
G. Landwehr (Würzburg) • J. C. Maan (Nijmegen)
B. D. McCombe (Buffalo)
A. MacDonald (Bloomington) • J. J. Quinn (Knoxville)
M. Saitoh (Osaka) • B. Shanabrook (Washington DC)
J. Singleton (Oxford) • P. J. Stiles (Providence)
P. Středa (Prague) • C. Tejedor (Madrid)
D. C. Tsui (Princeton) • H. van Houten (Eindhoven)
K. von Klitzing (Stuttgart) • M. Voos (Paris)

EP2DS XI - SUMMARY PROGRAMME

Sunday, 6th August 1995

16.00-20.00 Conference Registration in Rutland Hall

19.00 Dinner and Informal Reception in Rutland Hall

Monday, 7th August 1995

09.00-09.15 Conference Opening

09.15-10.45 TRANSPORT A followed by coffee break

11.15-12.30 COMPOSITE FERMIONS & FQHE A

12.45-14.15 Lunch in Rutland Hall

14.15-15.45 WIGNER SOLIDS followed by tea break

16.15-17.45 OPTICAL SPECTROSCOPY

18.00 Dinner in Rutland Hall

19.30 Conference Reception

Tuesday, 8th August 1995

09.00-10.45 INTEGER QUANTUM HALL EFFECT followed by coffee break

11.15-12.45 HYBRID STRUCTURES

12.45-14.15 Lunch in Rutland Hall

14.15-15.30 QUANTUM DOTS followed by tea break

16.00-17.30 TRANSPORT B

18.00 Dinner in Rutland Hall

19.30-22.00 POSTER SESSION A

Wednesday, 9th August 1995

09.00-10.15 COMPOSITE FERMIONS & FQHE B

10.15-12.30 Coffee and POSTER SESSION B

13.00-18.00 Conference Excursion to Chatsworth House

19.00 Dinner in Rutland Hall

Thursday, 10th August 1995

09.00-10.45 OPTICAL NANOSTRUCTURES followed by coffee break

11.15-12.45 CHAOS AND FLUCTUATIONS

13.00-14.00 Lunch in Rutland Hall

14.15-15.15 ORGANIC CONDUCTORS

15.15-17.45 Tea and POSTER SESSION C

18.00 Dinner in Rutland Hall or Conference Banquet at Prestwold Hall

Friday, 11th August 1995

09.00-10.15 COMPOSITE FERMIONS & FQHE C followed by coffee break

10.45-12.15 NOVEL TECHNIQUES & MATERIALS

12.15-12.30 Closing Session

13.00 Lunch in Rutland Hall

Conference Ends

EP2DS XI - PROGRAMME

Sunday, 6th August 1995				10.45-11.15
Conference Registration in Rutland Hall				16.00-20.00
Dinner and Informal Reception in Rutland Hall				19.00
Monday, 7th August 1995				09.00-09.15
Conference Opening				09.15-10.45
Transport A		Chair: L. Esaki		p.19
B. J. Keay (Invited), S. J. Allen Jr., K. D. Maranowski, A. C. Gossard, U. Bhattacharya and M. J. M. Rodwell				p.1
09.15 <i>Multiphoton-assisted tunneling, dynamic localization and absolute negative conductance</i>				
TR1 F. F. Ouali, N. N. Zinov'ev, L. J. Challis, A. Akimov, D. N. Hill, F. W. Sheard and M. Henini				p.5
09.45 <i>Non-equilibrium acoustic phonon-assisted tunnelling in GaAs/(AlGa)As double barrier devices</i>				
12.45-14.15				
Lunch in Rutland Hall				
14.15-15.45				
Wigner Solids		Chair: L. J. Challis		p.21
I. Kono (invited) and K. Shirahama				p.23
14.15 <i>Sliding of the Wigner solid on liquid helium</i>				
I4 H. C. Manoharan (invited), Y. W. Suen, M. B. Santos and M. Shayegan				p.27
14.45 <i>Correlated insulating states of an interacting bilayer electron system</i>				
15.15				
WS1 T. Günzler, B. Bitnar, G. Mistura, S. Neser and P. Leiderer				p.31
15.15 <i>Evidence for quantum melting in the two-dimensional electron system on a thin helium film</i>				

WS2	R. J. Hyndman, T. Ihn, B. L. Gallagher, P. J. Rodgers, M. Henini, T. J. Foster and J. R. Middleton	p.33
15.30	<i>Observation of correlated $v = I$ quantum Hall and insulating states in strongly coupled p-type double quantum wells</i>	

Tuesday, 8th August 1995

Integer Quantum Hall Effect Chair: P. J. Stiles 09.00-10.45		
Tea		
	15.45-16.15	
	16.15-17.45	
Optical Spectroscopy	Chair: J. C. Maan	
I5	G. Finkelstein, H. Shtrikman and I. Bar-Joseph (invited)	
16.15	<i>Optical spectroscopy of neutral and charged excitons in GaAs/AlGaAs quantum wells in high magnetic fields</i>	p.35
OS1	S. R. Ryu, W-Y. Yu, L. P. Fu, Z. Jiang, A. Petrou and B. D. McCombe	
16.45	<i>Negatively charged exciton (X) and D triplet transitions in GaAs/Al_{0.3}Ga_{0.7}As multiple quantum wells</i>	p.39
OS2	K. Hirakawa, I. Wilke, K. Yamanaka, H. G. Roskos, M. Voßbürgen, F. Wolter, C. Waschke, H. Kurz, M. Grayson and D. C. Tsui	
17.00	<i>Coherent submillimeter-wave emission from non-equilibrium two-dimensional free carrier plasmas in AlGaAs/GaAs heterojunctions</i>	p.41
OS3	T. Mélin and F. Laruelle	
17.15	<i>Optical anisotropy of doped type I quantum wire arrays: from the zone center to the Fermi edge</i>	p.43
OS4	H. van der Meulen, J. Rubio, J. M. Calleja, H. Schweizer, F. Scholz, V. Härlie and R. Bergmann	
17.30	<i>Magnetic field dependence of many-body processes in quantum well luminescence</i>	p.45
Dinner in Rutland Hall		18.00-19.30
Conference Reception		19.30
Hybrid Structures Chair: D. K. Ferry 11.15-12.45		
I8	B. J. van Wees (invited)	
11.15	<i>Supercurrent and quasiparticle transport in a two-dimensional electron gas with superconducting electrodes</i>	p.61
HS1	H. Takayanagi, T. Akazaki and J. Nitta	
11.45	<i>Observation of the quantized critical current in a superconducting quantum point contact</i>	p.65
HS2	M. Leadbeater, N. R. Claughton, C. J. Lambert and V. N. Prigodin	
12.00	<i>Theory of Andreev resonances in quantum dots</i>	p.67

HS3	H. Drexler, J. Harris, E. L. Yuh, K. C. Wong, S. J. Allen, E. G. Gwinn, H. Kroemer and E. L. Hu	p.69	Transport B	Chair: C. Hamaguchi	16.00-17.30
12.15	<i>Superconductivity and the Josephson effect in a periodic array of Nb-InAs-Nb junctions</i>		TR5	V. B. Pevzner, V. L. Gurevich and G. J. Lafrate	
			16.00	<i>Electrophonon resonances and optical phonon generation in nanowires</i>	p.83
HS4	A. K. Geim, S. V. Dubonos, I. V. Grigorieva and S. J. Bending	p.71	TR6	L. I. Glazman and I. L. Aleiner	
12.30	<i>Size-scaling experiment in a two dimensional electron gas using inhomogeneous magnetic field due to a superconducting gate</i>		16.15	<i>Two-dimensional electron liquid in a weak magnetic field</i>	p.85
<hr/>					
Lunch in Rutland Hall					
<hr/>					
		12.45-14.15	TR7	Y. B. Lyanda-Geller	
			16.30	<i>Berry phase, conductance oscillations and phase breaking in mesoscopic transport</i>	
<hr/>					
Quantum Dots	Chair: M. Pepper	14.15-15.30	TR8	C. H. W. Barnes, D. R. Mace, G. Faini, D. Mailly, M. Y. Simmons, C. J. B. Ford and M. Pepper	p.89
QD1	I. P. Kouwenhoven, N. C. van der Vaart, Yu. V. Nazarov, S. Jauhar, D. Dixon, K. McCormick, J. Orenstein, P. L. McEuen, Y. Nagamune, J. Motohisa and H. Sakaki	p.73	16.45	<i>Detection of the oscillation of the Fermi energy of a 2DEG</i>	
14.15	<i>High-frequency transport through mesoscopic structures</i>		TR9	P. J. Richardson, A. Blackburn, K. Djerfi, M. I. Dykman, C. Fang-Yen, P. Forootani, A. Kristensen, M. J. Lea and A. Santrich-Badal	p.91
QD2	R. H. Blick, R. J. Haug, K. von Klitzing and K. Eberl	p.75	17.00	<i>Many-electron magnetoconductivity in 2D electrons on liquid helium</i>	
14.30	<i>Photon assisted tunneling through a double quantum dot</i>		TR10	T. Schlosser, K. Ensslin, J. P. Kotthaus and M. Holland	
			17.15	<i>Interplay of Landau band width and band separation in a square lateral superlattice</i>	
<hr/>					
			Dinner in Rutland Hall		
<hr/>					
		15.30-16.00			
			Tea		

Wednesday, 9th August 1995

Composite Fermions and FQHE B	Chair: G. Kirczenow	09.00-10.15
CF4	D. R. Leadley, M. van der Burgt, R. J. Nicholas, P. J. Gee, J. Singleton, J. J. Harris and C. T. Foxon	p.95
09.00	<i>The unifying role of effective field in the composite fermion model of the fractional quantum Hall effect</i>	
CF5	R. R. Du, A. S. Yeh, H. L. Stormer, D. C. Tsui, L. N. Pfeiffer and K. W. West	p.97
09.15	<i>Composite fermions around Landau level filling factor $\nu = 3/2$</i>	
CF6	F. Plentz, D. Heiman, A. Pinczuk, L. N. Pfeiffer and K. W. West	p.99
09.30	<i>Magnetoexciton luminescence at 1/3 Landau filling as a function of electron-hole separation</i>	
CF7	Z. F. Ezawa	p.101
09.45	<i>Josephson phenomena in bilayer quantum Hall systems</i>	
CF8	J. E. Digby, C. J. Mellor, A. J. Kent, K. A. Benedict, L. J. Challis, J. R. Middleton and T. Cheng	p.103
10.00	<i>Time-resolved phonon absorption in the fractional quantum Hall regime</i>	

Thursday, 10th August 1995

Optical Nanostructures	Chair: M. S. Skolnick	09.00-10.45
I10	A. Zrenner (invited)	p.105
09.00	<i>Optical spectroscopy of single quantum dots</i>	
ON1	K. Bollweg, T. Kurth, D. Heitmann, E. Vassiliadou, P. Grambow and K. Eberl	p.109
09.30	<i>Coupled modes and filling factor dependent edge potentials in double-layered antidot arrays</i>	
ON2	R. Heitz, M. Grundmann, N. N. Ledentsov, L. Eckey, M. Veit, D. Bimberg, V. M. Ustinov, A. Yu. Egorov, A. E. Zhukov, P. S. Kop'ev and Zh. I. Alferov	p.111
09.45	<i>Efficient exciton-relaxation in self-organised InAs/GaAs quantum dots</i>	
ON3	P. Hawrylak, A. Wojs, D. J. Lockwood, P. D. Wang, C. M. Sotomayor Torres, A. Pinczuk and B. S. Dennis	p.113
10.00	<i>Optical spectroscopies of electronic excitations in quantum dots</i>	
ON4	S. Fafard, S. Raymond, G. Wang, R. Leon, D. Leonard, S. Charbonneau, J. L. Merz, P. M. Petroff and J. E. Bowers	p.115
10.15	<i>Temperature effects on the radiative recombination in self-assembled quantum dots</i>	
ON5	G. Schedelbeck, E. Silveira, R. Strenz, U. Bockelmann, G. Abstreiter, G. Böhm and G. Weimann	p.117
10.30	<i>Resonant inelastic light scattering by electronic excitations in tunable quantum wire structures</i>	
	19.00	
	Coffee	
	Conference Excursion to Chatsworth House	
	Dinner in Rutland Hall	

Chaos and Fluctuations		Chair: J. Kotthaus	11.15-12.45
I2	B. Altshuler (invited)		p.119
11.15	<i>Chaos in quantum dots</i>		
CH1	P. B. Wilkinson, T. M. Fromhold, L. Eaves, F. W. Sheard, N. Miura and T. Takamatsu		
11.45	<i>Evidence for periodic 'scar' patterns in the wavefunctions of a chaotic quantum well</i>		
CH2	R. A. Jalabert, K. Richter and D. Ullmo		p.123
12.00	<i>Persistent currents in the ballistic regime</i>		
CH3	A. M. Chang, H. U. Baranger, L. N. Pfeiffer and K. W. West		p.125
12.15	<i>Weak localization in chaotic versus non-chaotic cavities: a striking difference in the lineshape</i>		
CH4	G. Kurdkar, C.-J. Chen, D. C. Tsui, J. P. Lu, M. Shayegan, S. Parikh and S. A. Lyon		p.127
12.30	<i>Experimental investigation of Pauli exclusion principle using noise in coherent electron transport</i>		
Lunch in Rutland Hall		13.00-14.00	
Organic Conductors		Chair: H. Kamimura	14.15-15.15
II1	J. Singleton (invited), A. House, N. A. Harrison, S. J. Blundell, J. A. A. J. Perenboom, A. Polisski, W. Hayes, M. Kurmoo and P. Day		p.129
14.15	<i>Magnetic field-dependent Fermi surfaces in quasi-2D organic conductors</i>		
OC1	R. H. McKenzie, J. S. Brooks, R. G. Clark, R. Newbury, R. P. Starrett, A. Skougarevsky, R. A. Lewis, S. Takasaki, J. Yamada, H. Anzai, Y. Tanaka, T. Kinoshita, N. Kinoshita, M. Tokumoto and M. Kartovsnik		p.133
14.45	<i>Magneto-oscillations and field-induced phase transitions in organic conductors</i>		
OC2	C. M. Fischer, M. Burghard, S. Roth and K. von Klitzing		p.135
15.00	<i>Novel tunneling experiments on organic heterostructures</i>		
Tea and Poster Session C		15.15-17.45	
Dinner in Rutland Hall or Conference Banquet at Prestwold Hall		18.00-19.00	
Buses leave at 18.30			
Friday, 11th August 1995			
Composite Fermions and FQHE C		Chair: R. J. Nicholas	09.00-10.15
II2	N. Read (invited)		
09.00	<i>Recent progress in the theory of composite fermions near even-denominator filling factors</i>		
CF9	R. L. Willett and N. Pfeiffer		
09.30	<i>Composite fermions examined with surface acoustic waves</i>		
CF10	A. Stern and B. I. Halperin		
09.45	<i>The physical significance of singularities in the Chern-Simons Fermi liquid description of a partially-filled Landau level</i>		
CF11	B. Tieke, U. Zeitler, R. Fletcher, S. A. J. Wiegers, A. K. Geim, J. C. Maan and M. Henini		
10.00	<i>Universal behaviour in the thermoelectric power of composite fermions</i>		
Coffee			
10.15-10.45			
Novel Techniques and Materials		Chair: H. Störmer	10.45-12.15
II13	M. F. Crommie (invited), C. P. Lutz, D. M. Eigler and E. J. Heller		
10.45	<i>Quantum interference in 2-d atomic-scale structures</i>		

PA14	G. Faini, C. Vieu, F. Laruelle, P. Krauz, E. Bedel and C. Fontaine <i>Quantum box energy spectroscopy by 3D-0D resonant tunnelling</i>	p.183	PA24	S. I. Shevchenko <i>An unusual superconductivity mechanism in the systems with pairing of spatially separated electrons and holes</i>	p.203
PA15	S. S. Makler, D. E. Tuyarot, E. V. Anda and M. I. Vasilevskyi <i>Ultra-high-frequency coherent sound generation in resonant tunneling</i>	p.185	PA25	M. Field, C. G. Smith, M. Pepper, K. M. Brown, E. H. Linfield, M. P. Grimshaw, D. A. Ritchie and G. A. C. Jones <i>Coulomb blockade as a non-invasive probe in double layer 2DEG systems</i>	p.205
PA16	P. K. H. Sommerfeld, A. M. C. Valkering, R. W. van der Heijden and A. T. A. M. de Waele <i>The effect of confining electric fields on new magnetoplasma excitations in a 2-D electron system</i>	p.187	PA27	A. S. Plaut, A. Pinczuk, B. S. Dennis, J. P. Eisenstein, L. N. Pfeiffer and K. W. West <i>Observation of many-body interactions of electrons in coupled double quantum wells</i>	p.207
PA17	P. L. Elliott, A. A. Levchenko, C. I. Pakes, L. Skrbek and W. F. Vinen <i>Shear modes in 2D ion crystals trapped below the surface of superfluid helium</i>	p.189	PA28	G. Goldoni, V. Schweigert and F. M. Peeters <i>Stability and dynamical properties of a bi-layer Wigner crystal in two dimensions</i>	p.209
PA18	Y. Berk, A. Kamenev, A. Palevski, H. Shtrikman and M. Slutsky <i>Single particle and electron-electron scattering rates in coupled quantum wells</i>	p.191	PA29	T. Jungwirth and A. H. MacDonald <i>Tunneling between parallel two-dimensional electron liquids</i>	p.211
PA19	L. Świertkowski, J. Szymański and Z. W. Gortel <i>Strong enhancement of Coulomb drag in double layer systems due to correlations among carriers</i>	p.193	PA30	T. S. Lay, S. P. Shukla, J. Jo, X. Ying and M. Shayegan <i>Magnetotransport of a low-disorder triple-layer electron system in perpendicular or parallel magnetic fields</i>	p.213
PA20	H. Rubel, E. H. Linfield, N. P. R. Hill, J. T. Nicholls, D. A. Ritchie, K. M. Brown, M. Pepper and G. A. C. Jones <i>Frictional drag between closely spaced two-dimensional electron gases</i>	p.195	PA31	A. L. Ivanov and H. Haug <i>Collective excitonic phase with spatial order in quantum wires</i>	p.215
PA21	J. E. Simmons, N. E. Harff, T. M. Eiles, S. K. Lyo and J. F. Klem <i>Tuning a double quantum well Fermi surface with in-plane magnetic fields</i>	p.197	PA32	T. Tsuchiya, S. Katayama and T. Ando <i>Phase of magnetic oscillation of luminescence energy in asymmetric quantum wells</i>	p.217
PA22	Y. Ohno and H. Sakaki <i>Effects of a floating channel on magnetotransport properties of two dimensional electron gases in a resonantly coupled double quantum well structure</i>	p.199	PA33	O. Mauritiz and U. Ekenberg <i>Strain-induced suppression of spin splitting in asymmetric p-type quantum wells</i>	p.219
PA23	Z. W. Gortel and L. Świertkowski <i>Superfluid ground state in electron-hole double layer systems</i>	p.201	PA34	J. Los and A. Fasolino <i>Dependence of the optical absorption on the in-plane light polarization of QW's grown on low symmetry (011), (012), (112) and (113) surfaces</i>	p.221

PA35	D. Bertram, H. T. Grahn, O. Kuhn, D. K. Maude, J. C. Portal, K. Ploog and K. von Klitzing <i>Magneto-oscillations in the electroluminescence intensity of excited subbands in resonantly coupled superlattices</i>	p.223	Yu. B. Vasilyev, S. V. Ivanov, B. Ya. Meltser, S. D. Suchalkin and P. Grambow <i>Cyclotron resonance in InAs quantum wells in tilted magnetic fields</i>	p.241
PA36	N. N. Zinov'ev, A. V. Andrianov, L. J. Challis, C. T. Foxon and J. J. Harris <i>Photoluminescence studies of current-induced non-equilibrium population in magnetically quantized two-dimensional electron gases</i>	p.225	A. C. Ferreira, A. V. Buyanov, P. O. Holtz, B. E. Sernelius, B. Monemar, O. Mauritz, U. Ekenberg, M. Sundaram, K. Campman, J. L. Merz and A. C. Gossard <i>Optical and transport studies of highly acceptor doped GaAs/AlGaAs quantum wells</i>	p.243
PA37	L. V. Butov, A. Zrenner, M. Hagn, G. Abstreiter, G. Böhm and G. Weimann <i>Anomalous transport of indirect excitons in coupled AlAs/GaAs quantum wells</i>	p.227	J. A. Brum, S. A. Brown, P. Hawrylak, J. F. Young and Z. Wasilewski <i>Mobile excitons and the Fermi edge singularity in an interacting 2D electron gas</i>	p.245
PA38	J. M. Shi, F. M. Peeters and J. T. Devreese <i>Resonant bound bipolarons in a superlattice in a high magnetic field</i>	p.229	P. D. Altukhov <i>Excitons in dense two-dimensional electron gas at a semiconductor surface</i>	p.247
PA39	I. A. Buyanova, W. M. Chen, A. Henry, W. X. Ni, G. V. Hansson and B. Monemar <i>Luminescence spectroscopy of two-dimensional hole gas in p-type modulation-doped SiGe quantum wells and Si epilayers</i>	p.231	P. D. Buckle and P. Dawson <i>High density, spatially separated electron/hole plasmas in mixed type I-type II GaAs/AlAs heterostructures</i>	p.249
PA40	K. Luo, H. Zheng, S. Xu and H. Zhou <i>Spatially direct-to-indirect transition of excitons in step quantum wells</i>	p.233	N. J. Traynor, M. J. Snelling, R. T. Harley, R. J. Warburton and M. Hopkinson <i>Investigation of g-factors, Zeeman splittings, exchange interactions and field-dependent spin relaxation in III-V quantum wells</i>	p.251
PA41	K. Unterrainer, J. N. Heyman, K. Craig, B. Galdrikian, M. S. Sherwin, H. Drexler, K. Campman, P. F. Hopkins and A. C. Gossard <i>Nonlinear resonant optical rectification in a coupled quantum well</i>	p.235	P. O. Holtz, Q. X. Zhao, B. Monemar, M. Willander, K. Campman, M. Sundaram, J. L. Merz and A. C. Gossard <i>The D⁻ bound exciton observed in GaAs/AlGaAs quantum wells</i>	p.253
PA42	T. Fukuda, K. Yamanaka, H. Momose, N. Mori, C. Hamaguchi, Y. Imanaka, Y. Shimamoto and N. Miura <i>Cyclotron resonance in short period (GaAs)_n/(AlAs)_n superlattices</i>	p.237	J. G. S. Lok, A. K. Geim, J. C. Maan, I. Marmorkos, F. M. Peeters, P. J. McDonnell, M. Henini, N. Mori, L. Eaves and P. C. Main <i>Resonant tunnelling through D⁻ states</i>	p.255
PA43	R. Winkler <i>Cyclotron resonance and subband-Landau-level coupling in 2D electron and hole gases</i>	p.239	A. Manassen, R. Harel, E. Cohen, Arza Ron E. Linder and L. N. Pfeiffer <i>Cooperative exciton-electron transitions in quantum wells</i>	p.257

PA53	H. Buhmann, P. H. Beton, L. Eaves and M. Henini <i>Creation and annihilation of positively and negatively charged excitons in GaAs quantum wells</i>	p.259	PB5	Y. Levinson <i>Electron-electron scattering in a two-dimensional electron gas in a strong magnetic field</i>	p.277
PA54	A. J. Shields, M. Pepper, M. Y. Simmons and D. A. Ritchie <i>Magneto-optical spectroscopy of neutral and negatively charged excitons in GaAs quantum wells</i>	p.261	PB6	M. E. Raikh and L. I. Glazman <i>Inelastic transport in a system of 2D electrons localized in a smooth potential: giant negative magnetoresistance</i>	p.279
PA55	C. M. Hu, E. Batke, K. Köhler and P. Ganser <i>Influence of the electron-electron and electron-phonon interaction on the cyclotron resonance of a 2DEG in GaAs</i>	p.263	PB7	T. V. Shahbazyan and M. E. Raikh <i>Weak levitation of delocalized states as a result of Landau level mixing</i>	p.281
PA56	J. X. Shen, W. Ossau, F. Fischer, A. Waag and G. Landwehr <i>Electron and hole g factor oscillations in CdTe-based modulation doped quantum wells</i>	p.265	PB8	T. Ogawa and H. Otani <i>Fermi-edge singularity of the Tomonaga-Luttinger liquids in a magnetic field</i>	p.283
PA57	B. E. Cole, S. O. Hill, Y. Imanaka, Y. Shimamoto, W. Batty, J. Singleton, J. M. Chamberlain, N. Miura, M. Henini and T. Cheng <i>Effective mass anisotropy and many body effects in 2D GaAs/AlGaAs hole gases observed in very high magnetic fields: comparison of theory and experiment</i>	p.267	PB9	M. Stopa and Y. Aoyagi <i>Ordering in the ionized donor layer of modulation doped heterostructures</i>	p.285
PA58	H. Sigg, P. van Son and K. Köhler <i>Photon drag saturation spectroscopy of a two-dimensional electron system</i>	p.269	PB11	J. H. Oh, K. J. Chang, G. Ihm and S. J. Lee <i>Electron density dependence of the effective g-factor in a 2-dimensional electron gas at strong magnetic fields</i>	p.287
PA59	C. Gauer, M. Hartung, A. Wixforth, J. P. Kotthaus, B. Brar and H. Kroemer <i>Zero-field spin-splitting in InAs/AlSb quantum wells</i>	p.271	PB12	R. N. Gurzhi, A. N. Kalinenko and A. I. Kopeliovich <i>Inefficiency of odd relaxation and propagation of electron beams in a two-dimensional electron system</i>	p.289
			PB13	D. A. Broido and T. L. Reinecke <i>Thermoelectric transport in superlattices</i>	p.291
			PB14	Y. Fu and M. Willander <i>Energy band diagrams of nano-size field-effect transistors</i>	p.293
			PB15	V. Gudmundsson and R. R. Gerhardts <i>The Hofstadter energy spectrum for an interacting 2DEG</i>	p.295
			PB16	L. Smrčka, P. Vášek, J. Koláček, T. Jungwirth and M. Čukr <i>Fermi contour of 2D electron layer at GaAs/Al_xGa_{1-x}As heterojunction subject to in-plane magnetic fields</i>	p.297
			PB3	H. A. Fertig and M. C. Cha <i>Phase transitions from disorder in two-dimensional solids</i>	p.273
			PB4	S. V. Iordanskii, Y. Levinson and S. Levit <i>Phonon assisted energy relaxation for 2D electrons at high magnetic field</i>	p.275
			POSTER SESSION B		
			10:45-12:45		
			Wednesday 9th August		

PB17	A. Manolescu, R. R. Gerhardts, M. Tornow, D. Weiss, K. von Klitzing and G. Weimann <i>Coulomb interaction effects on the magnetoconductivity of laterally modulated two-dimensional electron systems</i>	p.299	PB26	V. I. Kozub and A. M. Rudin <i>Shot noise in the mesoscopic 2D diffusive systems in the limit of strong electron-electron scattering</i>	p.319
PB18	I. A. Larkin and J. H. Davies <i>Edge of a two-dimensional electron gas in a gated heterostructure</i>	p.301	PB27	M. Reznikov, M. Heiblum, Hadas Shtrikman and D. Mahalu <i>Temporally correlated transport and shot noise suppression in a ballistic quantum point contact</i>	p.321
PB19	M. Boero and J. C. Inkson <i>Calculated I-V characteristics of low-dimensional structures</i>	p.303	PB28	J. P. Bird, K. Ishibashi, D. K. Ferry, R. Newbury, D. M. Olatana, Y. Ochiai, Y. Aoyagi and T. Sugano <i>Phase breaking in ballistic quantum dots: a correlation field analysis</i>	p.323
PB20	T. Okamoto, Y. Shinohara, S. Kawai and A. Yagi <i>Collapse of quantum Hall state by floating-up of extended-state bands with increasing disorder</i>	p.305	PB29	V. I. Fal'ko and K. B. Efetov <i>Multifractal statistics of eigenstates of 2D disordered conductors</i>	p.325
PB21	V. B. Shikin <i>I-V characteristic of a 2D electron channel with the filling factor close to integer</i>	p.307	PB30	M. V. Budantsev, Z. D. Kvon, A. G. Pogosov, N. T. Moshegov, A. I. Plotnikov and A. I. Toropov <i>Magnetotransport in one-dimensional electron Sinai billiards</i>	p.327
PB22	D. G. Polyakov and M. E. Raikh <i>Quantum Hall effect with strong spin-orbit mixing of Zeeman states</i>	p.309	PB31	G. S. Boebinger, G. Müller, H. Mathur, L. N. Pfeiffer and K. W. West <i>Stable orbit bifurcations in a quantum well in a tilted magnetic field</i>	p.329
PB22a	W. Dietsche, K. von Klitzing and K. Ploog <i>Potential drops across quantum Hall effect samples - in the bulk or near the edges?</i>	p.311	PB32	K. A. Matveev, L. I. Glazman and H. U. Baranger <i>Theory of Coulomb blockade of tunneling through a double quantum dot</i>	p.331
PB23	G. Lütjering, K. Richter, D. Weiss, J. Mao, R. H. Blick, K. von Klitzing and C. T. Foxon <i>Weak localisation in ballistic cavities filled with antidot arrays</i>	p.313	PB33	A. S. Sachrajda, C. Gould, Y. Feng, M. W. C. Dharma-wardana and P. T. Coleridge <i>Tunneling experiments through coupled zero-dimensional systems</i>	p.333
PB24	G. Edwards, A. Grincwajg and D. K. Ferry <i>Calculations of magneto-transport fluctuations in ballistic quantum dots</i>	p.315	PB34	C. H. Crouch, C. Livermore, F. R. Waugh, R. M. Westervelt, K. L. Campman and A. C. Gossard <i>Coulomb gap of coupled quantum dots with adjustable interdot tunneling</i>	p.335
PB25	J. Jaroszyński, J. Wróbel, M. Sawicki, T. Skośkiewicz, G. Karczewski, T. Wojtowicz, J. Kossut, T. Dietl, E. Kamińska, E. Papis and A. Piotrowska <i>Conductance fluctuations in nanostructures of doped CdTe and Cd_xMn_{1-x}Te epilayers</i>	p.317	PB35	D. Dixon, L. P. Kouwenhoven, P. L. McEuen, Y. Nagamune, J. Motohisa and H. Sakaki <i>Linear and non-linear transport through coupled quantum dots</i>	p.337

PB36	E. Hofmann, T. Heinzel, D. A. Wharam, J. P. Kotthaus, G. Böhm, W. Klein, G. Tränkle and G. Weimann <i>Coulomb blockade in coupled quantum dots</i>	p.339	PB46 L. Wendler and V. G. Grigoryan <i>The fine-structure of magnetoplasmons in quantum-well wires and their magneto-optical manifestation</i>	p.361
PB37	P. N. Butcher and J. A. McInnes <i>Wave function and conductance calculations for a quantum dot at resonant tunnelling peaks</i>	p.341	PB47 A. A. Bykov, L. V. Litvin and S. P. Moschenko <i>Coherent properties of in-plane gated InGaAs/AlGaAs submicron rings</i>	p.363
PB38	A. Nogaret, M. J. Gompertz, P. C. Main, L. Eaves, T. J. Foster, M. Henini, and S. P. Beaumont <i>Magneto-tunnelling spectroscopy of a quantum dot charged with a few electrons</i>	p.343	PB48 K. W. Park, S. J. Lee, M. Shin, E-H. Lee and H. C. Kwon <i>New h/e oscillations and electrostatic Aharonov-Bohm effect in a GaAs/AlGaAs-based mesoscopic ring</i>	p.365
PB39	L. D. Hallam, N. A. Bruce and P. A. Maksym <i>Ground states of 2D and 3D quantum dots</i>	p.345	PB49 Z. Borosofldi, I. A. Larkin, A. R. Long, M. Rahman, M. C. Holland, J. M. R. Weaver, J. H. Davies and J. G. Williamson <i>Spectroscopy of quantum dots in the few electron limit</i>	p.367
PB40	G. Pilling, D. H. Cobden, P. L. Euen, C. I. Duruöz and J. S. Harris Jr. <i>Intrinsic bistability in nonlinear transport through a submicron lateral barrier</i>	p.347	PB50 E. Yuh, J. G. E. Harris, T. Eckhouse, K. C. Wong, E. Gwinn, H. Kroemer and S. J. Allen <i>Far-infrared studies of induced superconductivity in quantum wells</i>	p.369
PB40a	C. I. Duruöz, C. M. Marcus and J. S. Harris Jr. <i>Conduction threshold, switching, and hysteresis in quantum dot arrays</i>	p.349	PB51 J. Nitta, B. J. van Wees, J. P. Heida, T. M. Klapwijk, A. Dimoulas, W. van de Graaf and G. Borghs <i>Transport through a 2DEG channel with superconducting boundaries</i>	p.371
PB41	J. C. Smith, C. Berven, M. N. Wybourne and S. M. Goodnick <i>Conductance instabilities in quantum point contacts</i>	p.351	PB52 D. A. Williams, A. M. Marsh and H. Ahmed <i>Transport through superconductor-semiconductor junctions in different scattering limits</i>	p.373
PB42	A. J. Naylor, K. R. Strickland, A. J. Kent and M. Henini <i>Phonoconductivity measurements of the electron-phonon interaction in quantum wire structures</i>	p.353	PB53 H. A. Carmona, A. Nogaret, A. K. Geim, P. C. Main, T. J. Foster, M. Henini, S. P. Beaumont, H. McLelland and M. G. Blamire <i>Two-dimensional electrons in a lateral magnetic superlattice</i>	p.375
PB43	L. Y. Gorelik, M. Jonson and R. I. Shekter <i>Microwave-induced resonant reflection and localization of ballistic electrons in quantum microchannels</i>	p.355	PB54 A. Endo, S.-I. Izawa, S. Katsumoto and Y. Iye <i>Magnetoresistance oscillation in a two-dimensional electron gas under periodic modulation of electric and magnetic fields</i>	p.377
PB44	G. R. Nash, S. J. Bending, Y. Kershaw, K. Eberl, P. Grambow and K. von Klitzing <i>Surface acoustic wave studies of quantum nanostructures</i>	p.357	PB55 P. D. Ye, D. Weiss, R. R. Gerhards, K. von Klitzing, K. Eberl and H. Nickel <i>Magnetotransport of electrons in arrays of wires in Si/Si_{0.7}Ge_{0.3} heterostructures</i>	p.379
PB45	M. Holzmann, D. Többen, P. Baumgartner, G. Abstreiter, A. Kriegl, H. Lorenz and F. Schäffer <i>Magnetotransport of electrons in arrays of wires in Si/Si_{0.7}Ge_{0.3} heterostructures</i>	p.359		

PB56	I. S. Ibrahim and F. M. Peeters <i>Electrons in a periodic magnetic field</i>	p.381	
PB57	E. Hofstetter, J. M. C. Taylor and A. MacKinnon <i>2-dimensional electron gas in a spatially varying magnetic field</i>	p.383	
PB58	L. T. Hansen, R. Taborowski, A. Smith, P. E. Lindelof and P. Hedegård <i>Magnetoresistance of a two-dimensional electron gas in random magnetic fields</i>	p.385	
PB59	L. Y. Gorelik, V. S. Shumeiko, R. I. Shekhter, G. Wendin and M. Jonson <i>Microwave-induced "somersault effect" in flow of Josephson current through a quantum constriction</i>	p.387	
PB60	P. Christ, W. Biberacher, A. G. M. Jansen, M. Kartsovnik, A. Kovalev, N. Kushch, E. Steep and K. Andtes <i>Comparative torque studies of α-(BEDT-TTF)₂MHg(SCN)₄ where $M = K, Tl, NH_4$</i>	p.389	
PB61	P. S. Sandhu, G. J. Athas, J. S. Brooks, E. Haanappel, J. D. Goettee, D. Rickel, M. Tokumoto, N. Kinoshita, T. Kinoshita and Y. Tanaka <i>High field Shubnikov-de Haas studies of the organic superconductor α-(BEDT-TTF)₂NH₄Hg(SCN)₄</i>	p.391	
PB62	S. Hill, M. Boonman, S. Uji, J. A. A. J. Perenboom, J. Singleton, A. Wittlin, J. S. Brooks, R. Kato, H. Sawa, S. Anouma, M. Kurnoo and P. Day <i>Millimetre wave magneto-optical studies of low-dimensional organic conductors</i>	p.393	
POSTER SESSION C		15.15-17.45	
Thursday 10th August			
PC1	V. Bayot, E. Grivei, X. Ying, H. C. Manoharan and M. Shayegan <i>Thermopower of composite fermions in 2D hole systems</i>	p.395	
PC2	P. A. Crump, B. Tieke, R. J. Barracough, B. L. Gallagher, R. Fletcher, J. C. Maan, T. M. Fromhold and M. Henini <i>Evidence for composite fermions from the magneto-thermopower of 2D holes</i>	p.399	
PC3	R. Meissels, I. Kulagć, G. Sundaram, F. Kuchari, B. D. McCombe, G. Weimann and W. Schlapp <i>Electron spin resonance in AlGaAs/GaAs in the regime of fractional filling</i>	p.401	
PC4	A. S. Sachrajda, Y. Feng, P. Coleridge, H. A. Carmona, A. K. Geim, P. C. Main, L. Eaves and C. T. Foxon <i>Mesoscopic transport properties of composite fermions</i>	p.403	
PC5	J. Herfert, Y. Takagaki, R. Hey, K.-J. Friedland, K. Ploog, D. K. Mandt, J. C. Portal, J. Takahara and K. Gamo <i>Transport properties of composite fermions in narrow cross junctions</i>	p.405	
PC6	A. V. Khaetskii, Yu. V. Nazarov and G. E. W. Bauer <i>Balistic conductance of composite fermions</i>	p.407	
PC7	C.-T. Liang, C. G. Smith, D. R. Mace, J. T. Nicholls, J. E. F. Frost, M. Y. Simmons, A. R. Hamilton, D. A. Ritchie and M. Pepper <i>Measurements on a composite fermion split-gate</i>	p.409	
PC9	B. Huckestein <i>Critical behavior in the fractional quantum Hall effect</i>	p.411	
PC10	D. B. Chklovskii and B. I. Halperin <i>Understanding the dynamics of fractional edge states with composite fermions</i>	p.413	
PC11	D. Shahar, L. W. Engel, D. C. Tsui, M. Shayegan, R. N. Bhatt and J. E. Cunningham <i>Liquid to insulator transition of composite particles</i>	p.415	
PC12	T. Nakajima and H. Aoki <i>Composite-fermion picture for the double-layer fractional quantum Hall effect</i>		

PC13	Song He and P. M. Platzman <i>Resonant Raman scattering and numerical study in the fractional quantum Hall regime</i>	p.417	PC24	R. Fletcher, P. T. Coleridge and Y. Feng <i>Oscillations in the low-field diffusion thermopower of a 2D electron gas</i>	p.439
PC14	N. d'Ambrumenil and R. Morf <i>Effective masses of composite fermions</i>	p.419	PC25	P. Štředa, P. Vašek and M. Culkr <i>Magnetoresistance anomaly of a two-dimensional electron gas in tilted magnetic fields</i>	p.441
PC15	T. Takamatsu, H. Dodo and N. Miura <i>Breakdown phenomena of integer and fractional quantum Hall effects under pulsed high magnetic fields</i>	p.421	PC26	A. Mittal, R. G. Wheeler, D. E. Prober and R. N. Sacks <i>Electron-phonon scattering rates in GaAs/AlGaAs 2DEG samples below 0.5K</i>	p.443
PC16	M. Shayegan and H. C. Manoharan <i>Bare and composite fermions in anisotropic two-dimensional metals</i>	p.423	PC27	P. Weitz, R. J. Haug, K. von Klitzing and F. Schäffler <i>Tilted magnetic field studies of spin- and valley-splitting in Si/Si_{1-x}Ge_x heterostructures</i>	p.445
PC17	I. V. Kukushkin, R. J. Haug, K. von Klitzing and K. Eberl <i>Influence of scattering processes on the electronic properties of composite fermions</i>	p.425	PC28	T. J. Thornton, A. Matsumura and J. Fernández <i>Negative magnetoresistance and electron-electron interaction in Si:SiGe quantum wells</i>	p.447
PC18	G. Ernst, N. B. Zhitenev, R. J. Haug, K. von Klitzing and K. Eberl <i>Pulse propagation in spin-polarized edge channel and at fractional filling factors</i>	p.427	PC29	R. B. Dunford, R. Newbury, V. A. Stadnik, F. F. Fang, R. G. Clark, R. H. McKenzie, R. P. Starrett, E. E. Mitchell, P. J. Wang, J. O. Chu, K. I. Ismail and B. S. Meyerson <i>Low temperature magneto-transport of 2D electron and hole systems in high mobility Si-Si_{1-x}Ge_x heterostructures</i>	p.449
PC19	A. F. W. van de Stadt, P. M. Koenraad, J. A. A. J. Perenboom and J. H. Wolter <i>X_z-X_{xy} crossover in a two dimensional electron gas in AlAs</i>	p.429	PC30	S. I. Dorozhkin, C. J. Emeleus, O. E. Mironov, T. E. Whall and G. Landwehr <i>Magnetotransport anomalies in dilute two-dimensional electron systems: an experiment and a model</i>	p.451
PC20	J. Oswald, G. Heigl, M. Pippan, G. Span, T. Stellburger, D. K. Maude and J. C. Portal <i>Magnetotransport in wide parabolic PbTe quantum wells</i>	p.431	PC31	M. DiIorio, D. Stewart, S. Deblais, D. Brown and J.-P. Noël <i>Re-entrant metal-insulator transitions in Si-SiGe-Si heterostructures</i>	p.453
PC21	F. A. P. Blom, F. M. Peeters, K. v. d. Zanden and M. van Hove <i>Magneto-oscillations of the gate current in a laterally modulated two-dimensional electron gas</i>	p.433	PC32	V. M. Pudalov, M. DiIorio and J. W. Campbell <i>Electric field induced non-Ohmic conduction in the 2D insulating phase</i>	p.455
PC22	G. Lütjering, D. Weiss, R. Tank, K. von Klitzing, A. Hülsmann, T. Jakobus and K. Köhler <i>Metal-non-metal transition at the crossover from antidots to quantum dots</i>	p.435	PC33	G. E. Pikus and F. G. Pikus <i>Conduction band spin splitting and negative magnetoresistance in A₃B₅ heterostructures</i>	p.457
PC23	Jennifer J. Quinn and John J. Quinn <i>Semimetal-semiconductor transition in InAs-GaSb heterostructures</i>	p.437			

PC34	P. T. Coleridge, M. Hayne, P. Zawadzki and A. S. Sachrajda <i>Effective masses in high mobility 2D electron gas structures</i>	p.459	PC44	Th. Ihn, C. Gauer, F. Koch and J. P. Kotthaus <i>Anisotropy of the conductivity in δ-doped multilayers</i>	p.479
PC35	F. W. Van Keuls, X. L. Hu, A. J. Dahm and H. W. Jiang <i>The Coulomb gap and the transition to Mott hopping</i>	p.461	PC44a	A. R. Alves, J. S. Cruz, P. S. S. Guimaraes, A. S. Chaves, R. P. Diniz, A. G. de Oliveira and M. Henini <i>Asymmetric magnetoresistance in GaAs/AlGaAs mesoscopic heterostructures</i>	p.481
PC36	S. V. Kravchenko, Whitney Mason, G. E. Bowker, J. E. Furneaux, V. M. Pudalov and M. D'lorio <i>Scaling of a metal/insulator transition in a 2D system at $B = 0$</i>	p.463	PC45	P. H. Beton, A. Dunn and P. Moriarty <i>Room temperature manipulation of C_{60} on a Si surface</i>	p.483
PC37	Whitney Mason, S. V. Kravchenko, G. E. Bowker and J. E. Furneaux <i>Experimental evidence of the Coulomb gap in high-mobility 2D electron system in silicon</i>	p.465	PC46	S. Yamada and M. Yamamoto <i>Coulomb blockade and dot size in split-gate wire with a small mesa or a hole made by scanning tunneling microscopy</i>	p.485
PC38	G. M. Gusev, U. Gennser, X. Kleber, D. K. Maude, J. C. Portal, D. I. Lubyshev, P. Basmaji, M. de P. A. Silva, J. C. Rossi and Yu. N. Nastaushev <i>Magnetoresistance oscillations in a dimpled two-dimensional electron gas</i>	p.467	PC47	M. L. Leadbeater, C. L. Foden, J. H. Burroughes, T. M. Burke, L. H. Wang, M. P. Grimshaw, D. A. Ritchie and M. Pepper <i>Electron transport in a non-planar 2DEG</i>	p.487
PC39	T. H. Sander, S. N. Holmes, J. J. Harris, D. K. Maude and J. C. Portal <i>Magnetoresistance oscillations due to intersubband scattering in a two-dimensional electron system</i>	p.469	PC48	L. Sfaxi, F. Petit, F. Lelarge, A. Cavanna and B. Etienne <i>From low to high field: magneto-transport properties of electron gases in lateral superlattices grown on GaAs vicinal surfaces</i>	p.489
PC40	A. K. Savchenko, V. V. Kuznetsov, A. Wolfe, D. R. Mace, M. Pepper, D. A. Ritchie and G. A. C. Jones <i>Resonant tunneling through two impurities in disordered barriers</i>	p.471	PC49	L. A. Kuzik, V. A. Yakovlev, F. A. Pudonin and G. Mattei <i>Quantum size effects in the optical conductivity of ultrathin metal films</i>	p.491
PC41	A. A. Verevkin, N. G. Ptitsina, G. M. Chulcova, G. N. Goltsman, E. M. Gershenson and K. S. Yngvesson <i>Direct measurements of energy relaxation time of electrons in AlGaAs/GaAs heterostructures under quasi-equilibrium conditions</i>	p.473	PC50	V. Ya. Prinz, V. A. Seleznev and A. K. Gutakovskiy <i>Novel technique for fabrication of one- and two-dimensional systems</i>	p.493
PC42	M. Hayne, A. Usher, J. J. Harris and C. T. Foxon <i>An elegant verification of the negative charge-state of the DX-centre from mobility measurements of 2D electrons</i>	p.475	PC51	P. Radojkovic, E. Hartmann, M. Schwartzkopff, E. Stefanov and F. Koch <i>Coulomb staircase with negative differential resistance at room temperature for a metal tip/metal dot/semiconductor double junction</i>	p.495
PC43	P. Wisniewski, T. Suski, E. Litwin-Staszewska, G. Brunthaler and K. Köhler <i>Mobility and quantum lifetime in GaAs/AlGaAs heterostructure. Tuning of the remote-charge correlations</i>	p.477	PC52	J. W. G. Wildoer, A. J. A. van Roy, C. Harms and H. van Kempen <i>Semiconductor band-switching induced by single-electrons on a metal island</i>	p.497

- PC53** Marcos R. S. Tavares and C. Tejedor
Magneto-optical spectra in a doped 2-dimensional system with periodic lateral modulation p.499
- PC54** S. Huant and B. Etienne
Magneto-optical studies of laterally modulated nanostructures grown on GaAs vicinal substrates p.501
- PC55** G. Biese, S. Schüller, T. Kurth, D. Heitmann, P. Grambow and K. Eberl
Combined 1D-2D intersubband excitations and 1D single-particle spectrum in narrow quantum wires p.503
- PC56** G. W. Bryant, P. S. Julienne and Y. B. Band
Excitons in complex quantum nanostructures p.505
- PC57** R. Steffen, Th. Koch, J. Oshinowo, F. Faller and A. Forchel
Exciton interaction effects in the emission spectra of single free-standing InGaAs/GaAs quantum dots p.507
- PC58** M. V. Marquezini, M. J. S. P. Brasil, J. A. Brum, P. Poole, S. Charbonneau and M. C. Tamargo
Radiative and non-radiative recombination times in a single quantum well with self-assembled islands p.509
- PC59** D. Gammon, E. S. Snow and D. S. Katzer
Spectroscopy of single naturally-formed GaAs quantum dots p.511
- PC60** P. A. Knipp, S. W. Pierson and T. L. Reinecke
Effects of collective modes on single particle electronic excitations of semiconductor quantum wells and quantum dots p.513
- PC61** T. A. Fisher, A. M. Afshar, D. M. Whittaker, M. S. Skolnick, J. S. Roberts, G. Hill and M. A. Pate
Magnetic field effects on the vacuum Rabi coupling in semiconductor quantum microcavity structures p.515

Multiphoton-Assisted Tunneling, Dynamic Localization and Absolute Negative Conductance

B.J. Keay, S.J. Allen Jr.
Center for Free-electron Laser Studies
UCSB, Santa Barbara, CA 93106

K.D. Maranowski, A.C. Gossard
Materials Department
UCSB, Santa Barbara, CA 93106

U. Bhattacharya, M.J.W. Rodwell
Department of Electrical and Computer Engineering
UCSB, Santa Barbara, CA 93106

Abstract

We report the observation of Absolute Negative Conductance (ANC), multiphoton stimulated emission and dynamical localization in sequential resonant tunneling semiconductor superlattices driven by intense terahertz electric fields. With increasing terahertz field strength the conductance near zero DC bias decreases towards zero and then becomes negative. This is accompanied by new steps and plateaus that are attributed to multiphoton-assisted resonant tunneling between ground states of neighboring quantum wells accompanied by the stimulated emission of a photon.

Introduction

We report the observation of dynamic localization, absolute negative conductance (ANC) and electric field domains driven by photon assisted tunneling (PAT) in multi-quantum well superlattices. Theories predicting dynamic localization and absolute negative conductance in semiconductor superlattices subjected to AC electric fields have existed for twenty years [1], but have not been verified experimentally. These theories are based upon semiclassical models of electron motion in superlattices in the miniband or coherent tunneling regime. An essential feature of these models is Bloch oscillation in the presence of intense high frequency electric fields, high frequency fields sufficient to drive carriers beyond the mini-band zone boundary, into a region of k-space with negative velocity [1]. However, in this report we are concerned with sequential resonant tunneling, distinguished from the former by incoherent tunneling and a loss of phase memory after tunneling into a neighboring well. There has been little discussion about this case, discouraged perhaps by the notion that a ladder of levels, the ground states of superlattice quantum wells in an applied electric field, are all equally populated and therefore offer no net coupling to the photon field [2].

At the outset we wish to distinguish the observation of ANC from rectification in asymmetric structures like solar cells, p-n junctions and Schottky diodes. In the work reported here, we have an essentially symmetric structure and no current flows at zero applied DC bias with or without intense terahertz electric fields. The phenomenon is more closely related to absolute negative conductance in resonant tunneling diodes [3] and in bulk GaAs driven with strong microwave fields at GHz frequencies [4]. Here, in a combined DC and AC electric field the average current can be negative at a positive DC bias because the current on negative swings of the microwave field can be greater than the current on positive swings of the oscillating field. This is a purely classical, circuit effect but analogous to the aforementioned theoretical predictions of absolute negative conductance caused by large k-space excursions in the strongly driven Bloch oscillator [1]. We believe the observations made here are beyond simple rectification in asymmetric structures or the classical absolute negative resistance produced by driving a symmetric device into its differential negative resistance regime with a strong AC field. PAT is a well established phenomenon describing quasi-particle tunneling in superconducting electronics in the presence of high frequency radiation [5]. Only recently has it emerged in high frequency transport in semiconductor multi-quantum well superlattices [6-9] and nanostructures [10, 11]. The recent development of an intersubband laser is thought to rely, under some conditions, on photon assisted tunneling [12].

Experiment

The sequential resonant tunneling superlattice used in these experiments consisted of 300 nm of GaAs doped at $n^+ = 2 \times 10^{18} \text{ cm}^{-3}$, followed by a 50nm GaAs spacer layer and ten 15 nm GaAs quantum wells and eleven 5 nm GaAs/Al₃₀Ga₇₀As barriers and capped by another 50nm GaAs spacer layer and 300nm of $n^+ = 2 \times 10^{18} \text{ cm}^{-3}$ Si doped GaAs. The substrate is semi-insulating and the superlattice and spacer layers were n doped to $3 \times 10^{15} \text{ cm}^{-3}$ with Si. These experiments were facilitated by integrating the superlattice into broad band bow-tie antennas. The devices were then glued onto a high resistivity hemispherical silicon lens and gold wires were bonded to the two gold bows. The experiments were performed over a temperature range of 8-15 K with the sample mounted in a temperature controlled flow-type cryostat with Z-cut quartz windows. Radiation was incident on the curved surface of the silicon lens with the polarization parallel to the axis connecting the two gold lobes of the bow-tie.

Dynamic Localization, Multiphoton Emission and NAC

In Fig. 1 we show the DC current-voltage (I-V) characteristics measured without radiation and with terahertz radiation at three different laser powers. The I-V without laser radiation (E_{AC} = 0) shows an ohmic region characteristic of miniband transport followed by saw tooth oscillations associated with sequential resonant tunneling and electric field domains [13]. At low bias, the current through the sample occurs via ground state to ground state tunneling. As the bias

is increased, the current approaches a "critical current", the maximum current that the ground state to ground tunneling can support, and a quantum well breaks off forming a high field domain. The high field domain is characterized by the alignment of the ground state in one well with the excited state in the "down hill" well. As the bias is increased still further one well after another breaks off into the high field domain, indicated by the saw tooth NDR structure, until the entire sample is encompassed by the high field domain. In this work we are concerned only with the behavior near zero bias, where the transport occurs via ground state to ground state tunneling. In the presence of a terahertz electric field the conductance at zero bias is first suppressed. That is to say, the terahertz electric field tends to localize the electrons, a manifestation of dynamic localization. However as the DC bias is increased the one-photon emission channel is brought into resonance with the ground state in the neighboring well and the current increases resulting in the formation of a step in the I-V characteristic. (Note that the voltage where this occurs is approximately $N\hbar\omega/e$, where N is the number of quantum wells, $N=10$ here. The relation is not exact due to voltage drop in the set back regions between the n^+ contacts and the superlattice.).

At the next higher power shown in Fig. 1, the conductance near the origin actually becomes negative. When this happens the electrons use the absorbed energy from the laser field to tunnel against the applied DC bias. While localization and near zero conductance is predicted absolute negative conductance is not.

At this level of terahertz excitation, as the DC bias voltage is increased beyond the absolute negative conductance region, the one-photon emission step is encountered in the I-V characteristic (Fig. 1). The current becomes positive and the electrons are driven down the superlattice accompanied by the stimulated emission of a photon [14]. Remarkably, a two-photon emission step is also seen at the appropriate voltage. Finally, at the highest power shown in Fig. 1, the one-photon emission step is substantially diminished, the current at the two photon step has decreased by a factor of two and the formation of the three-photon emission step is clearly seen at the appropriate bias voltage.

It is clear (Fig. 1) that the transport through the various emission channels, as well as the zero bias conductance, is strongly dependent on the laser field strength. In Fig. 2 we show the step height for the one, two and three photon emission steps and zero bias conductance as a function of terahertz field strength. For the one, two and three photon processes these steps are defined as the height along the current axis from the base of the step to the upper edge of the step. For each, the step at negative and positive bias has been averaged. The zero bias conductance has been defined as the difference in current measured from the beginning of the ohmic region at negative bias through the origin to the end of the ohmic region, measured at positive bias, divided by the voltage difference.

We can project these results on the model of Tien and Gordon in the following way. We assume that the basic transport mechanism is the sequential tunneling from one quantum well to

its neighbor. Then following Tien and Gordon [5] we expect that in the presence of a laser field the transition probability to virtual states separated from the ground state by $\pm\hbar\omega$ is proportional to $J_n^2(edE_{AC}/\hbar\omega)$. In particular, $J_0^2(edE_{AC}/\hbar\omega)$ describes the suppression of the conductance at zero bias, i.e. dynamic localization, and we expect the conductance to be driven to zero when the argument, $edE_{AC}/\hbar\omega$, equals the zero of the Bessel function. Likewise, we expect the new channels, that appear as steps at the appropriate bias voltage, to develop in a non-monotonic way as $J_n^2(edE_{AC}/\hbar\omega)$.

This is essentially what is observed in Fig. 2. In fact, we can scale the horizontal axis so that

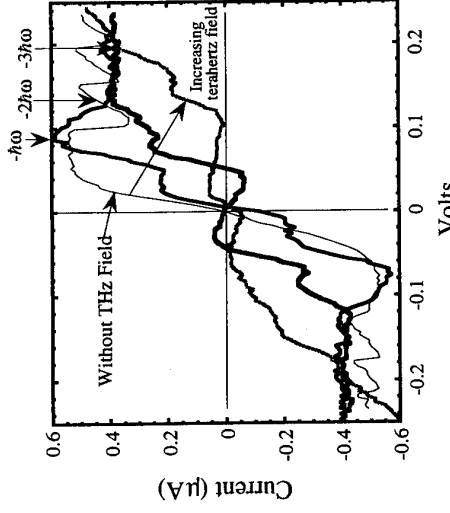


Figure 1. Current - Voltage characteristics measured without radiation and with 1.30 THz radiation at three different laser field strengths.

While the dynamic localization is expected, the absolute negative conductivity does not arise in a straight forward way from this model and requires some consideration of level width, temperature and electron distribution. In Figs. 3 a, b we schematically show a broadened level in one well coupled to the neighboring well by the laser field. For the purposes of this discussion we assume that the electrons in these wells are distributed thermally with more at the bottom of the broadened levels than at the top. It is important to realize that near the first minimum of $J_0^2(edE_{AC}/\hbar\omega)$ transport will be dominated by the photon-assisted channels. In Fig. 3a the applied DC field is less than $\hbar\omega/ed$ and the one photon emission channel is blocked by filled

final states, but the absorption channel can proceed and the current will flow to the left or against the applied DC bias. As soon as the DC bias exceeds $\hbar\omega_0 / e\delta$, Fig. 3b, the picture is reversed and current will flow from left to right, in the direction of the applied DC bias.

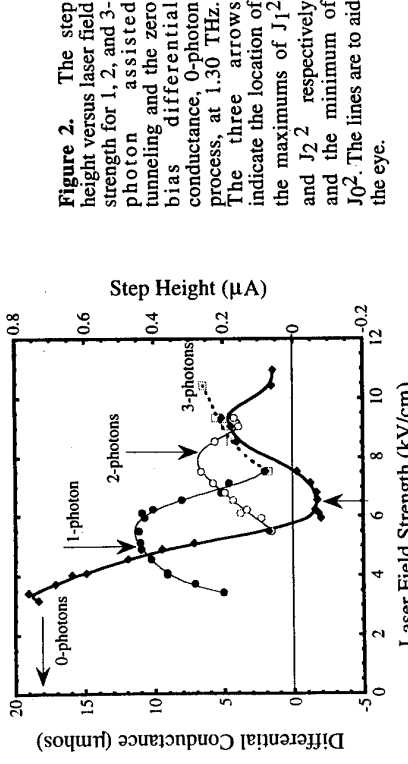
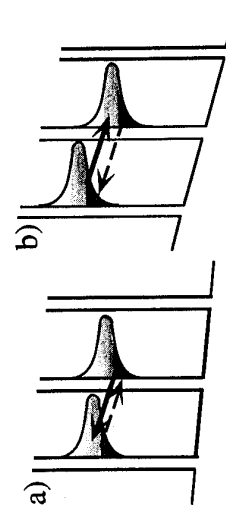


Figure 2. The step height versus laser field strength for 1, 2, and 3-photon assisted tunneling and the zero bias differential conductance, 0-photon process, at 1.30 THz. The three arrows indicate the location of the maximums of $J_{1/2}$ and $J_{2/2}$ respectively and the minimum of 10^2 . The lines are to aid the eye.

In this picture the range of DC voltages over which this scenario takes place is intimately related to the level broadening. For very narrow well defined levels, this dispersive behavior of the current flow, first against the applied bias, then with it, will occur over a very narrow voltage range. The strength of this discontinuity while obviously related to the strength of the terahertz electric field will may also depend on temperature in an interesting way. At high temperature, where $kT \gg \Delta E$ and (ΔE) is a measure of level broadening, there will be little strength in this discontinuity [14]. Furthermore, it would appear that the occurrence of negative current flow for small positive bias requires a level broadening that is sufficient to cause the tails of the energy levels to extend to within reach of the photon assisted channel but not so broad that it will completely "wash out" the effect.

Figure 3. a) Broadened levels in the presence of radiation at low bias, emission channels are inhibited while the absorption channels are enhanced. b) At higher bias the absorption channels are inhibited while the emission channels are not. The arrows represent fixed photon energy and represent the inhibited process (dashed arrow) and enhanced process (solid arrow).



It seems likely that the photon assisted channels which correspond to stimulated emission of as many as three terahertz photons are critically related to level broadening as well. Under DC bias the ladder of quantum well ground states will all be equally occupied and, at first blush, net stimulated absorption or emission of a photon should be absent. But it is apparent that net gain (stimulated emission) can occur on the low frequency side of the Stark ladder splittings and net loss (stimulated absorption) can occur on the high frequency side. This view relieves the apparent contradiction with Bastard et al. [2].

In conclusion, we have observed dynamic localization and negative absolute conductance in a multi-quantum well superlattice in the sequential tunneling limit. The dynamic localization and NAC are accompanied by the appearance of photon assisted channels that correspond to the stimulated emission of as many as three terahertz photons.

Acknowledgments. We would like to thank help of the staff at the Center for Free-Electron Laser Studies, J.R. Allen, D. Enyeart, G. Raman and D. White. Funding for the Center for Free-Electron Laser Studies is provided by the Office of Naval Research. Additional funding was provided by the Army Research Office, the NSF, and the Air Force Office of Scientific Research.

References.

- [1] V.V. Pavlovich and E.M. Epshtain, *Sov. Phys. Semicond.*, **10**, 1196 (1976).
- [2] G. Bastard, I.A. Brown, R. Ferreira, *Solid State Physics: Semiconductor Heterostructures and Nanostructures*, Vol. **44**, 325, Eds. H. Ehrenreich, D. Turnbull, (Academic Press, San Diego, 1994).
- [3] Solner et al., *Physics of Quantum Electron Devices*, Federico Capasso, ed., Berlin ; New York : (Springer-Verlag, 1990).
- [4] Juris Pochela, *Plasma and Current Instabilities in Semiconductors*, Oxford; New York, (Pergamon, 1981).
- [5] F.K Tien and J.P. Gordon, *Phys. Rev.* **129**, 647 (1963).
- [6] P.S.S. Guimaraes, B.J. Keay, J.P. Kaminski, S.J. Allen Jr., P.F. Hopkins, A.C. Gossard, L.T. Florez, J.P. Harbison, *Phys. Rev. Lett.* **70**, 3792 (1993).
- [7] B.J. Keay, P.S.S. Guimaraes, J.P. Kaminski, S.J. Allen Jr., P.F. Hopkins, A.C. Gossard, L.T. Florez, J.P. Harbison, *Surface Science* **305**, 385 (1994).
- [8] B.J. Keay, S.J. Allen Jr., J.P. Kaminski, K.L. Campman, A.C. Gossard, U. Bhattacharya, M.J.W. Rodwell, J. Galán, *The Physics of Semiconductors: Proceedings of the 22nd International Conference*, vol **2**, 1055, D.J. Lockwood ed., Vancouver, Canada (World Scientific, 1995).
- [9] B.J. Keay, S.J. Allen Jr., J.P. Kaminski, J. Galán, K.L. Campman, A.C. Gossard, U. Bhattacharya, M.J.W. Rodwell, (submitted to Physical Review Letters).
- [10] S. Vergheze, R.A. Wyss, Th. Schäpers, A. Förster, M.J. Roots, Q. Hu, (submitted to Physical Review Letters).
- [11] L.P. Kouwenhoven, S. Jauhar, J. Orenstein, P.L. McEuen, *Phys. Rev. Lett.* **73**, 3443 (1994).
- [12] J. Faist, F. Capasso, D.L. Sivco, C. Sirtori, A.L. Hutchinson, A.Y. Cho, *Science* **264**, 553 (1994).
- [13] K.K. Choi, B.F. Levine, R.J. Malik, J. Walker, and C.G. Bethea, *Phys. Rev. B* **35**, 4172 (1987).
- [14] R.F. Kazarinov and R.A. Suris, *Sov. Phys. Semicond.*, **5**, 707 (1971).

Non-equilibrium Acoustic Phonon-Assisted Tunnelling in GaAs/(AlGa)As Double Barrier devices

F F Ouali*, N N Zinov'ev†, L J Challis*, A V Akimov†, D N Hill*,
F W Sheard* and M Hemini*

* Department of Physics, University of Nottingham, NG7 2RD, UK
† Ioffe Physical Technical Institute, 194021 St, Petersburg, Russia

Abstract: We report measurements of assisted tunnelling induced by non-equilibrium phonons in double barrier tunnelling devices in GaAs. The phonon signal has a peak at a bias voltage which depends linearly on phonon energy.

There has been a great deal of interest in the physics of resonant double barrier devices and their potential for device applications [1]. Since the observation of a broad satellite peak above the main peak in the current-voltage ($I(V)$) characteristic [2] caused by assisted tunnelling via the emission of longitudinal optic (LO) phonons, it has been clear that phonon-assisted processes can have an important role [3]. In this work, we report measurements of assisted tunnelling induced by non-equilibrium acoustic phonons.

The samples are GaAs/(Al_{0.4}Ga_{0.6})As double barrier resonant tunnelling devices (DBRTDs), consisting of two 5.5 nm barriers separated by a 5 nm thick well, grown on a (100) Si substrate. The barriers are separated from the n⁺ doped contacts by a 2.5 nm undoped spacer (details of the structure are given elsewhere [4]). Separate experiments were made on three samples A, B and C with corresponding areas of 3 × 80 μm^2 , 50 μm diameter and 3 × 20 μm^2 . The back of the 0.4 mm thick substrate was polished and a 60 × 600 μm^2 constantan 2 μm thick heater was evaporated opposite the mesa for samples A and B and opposite but displaced 2 mm for sample C. Non-equilibrium phonons are generated by applying electrical pulses to the heater (duration 0.2–30 μs , repetition rate 0.1–1 kHz). The heater temperature during the pulse T_h is determined from the input power to the heater using mismatch theory [5]. The change in tunnel current induced by the phonons $\Delta I_i(V)$ is measured as a function of the applied bias to the device. This report focusses largely on measurements on samples with 2DEG emitters (A and C) and work on a 3DEG emitter (B) will be reported later.

The characteristics $I(V)$ and dI/dV for sample A are shown in fig 1. The small shoulder at 0.415V (more clearly seen in dI/dV) is attributable to electron tunnelling into Si donor states of energy ~10–15 meV below the main peak [6,7]; the donors originate from Si diffusion from the n⁺ doped regions to the well during growth [8]. The donor wavefunction is confined in the plane of the layers to within a length of a_0 ($a_0 \sim 10$ nm is the Bohr radius in GaAs). This relaxes the constraints of conservation of in-plane momentum $k_{||}$ for tunnelling from a 2DEG emitter to $\Delta k_{||} \lesssim 1/a_0$ and since $k_F > 1/a_0$, tunnelling occurs within an energy range $\sim \hbar^2/2m^* a_0^2 \sim 6$ meV above the emitter ground state. Charge build up in the well results in bistability in the main resonance of the DBRTD, which complicates the response of the device to non-equilibrium phonons. To avoid this, we focus our measurements on tunnelling into the impurity donor level $I_i(V)$. A resonance in $I_i(V)$ occurs when $eV_b = E_0$ (V_b is the potential drop across the first barrier and E_0 is the energy of the donor state relative

to that of an emitter with $k_{||} \sim 1/a_0$).

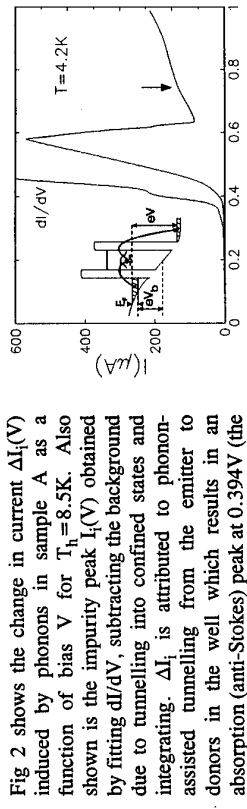


Fig. 1 shows the change in current $\Delta I_i(V)$ induced by phonons in sample A as a function of bias V for $T_h=8.5$ K. Also shown is the impurity peak $I_i(V)$ obtained by fitting dI/dV , subtracting the background due to tunnelling into confined states and integrating. ΔI_i is attributed to phonon-assisted tunnelling from the emitter to donors in the well which results in an absorption (anti-Stokes) peak at 0.394V (the process is illustrated in the inset to fig 1) and a broad peak at 0.45V which seems attributable to stimulated emission (Stokes); this is more apparent in the data in fig 4.

For monoenergetic phonons of energy $\hbar\omega$ incident normally on the emitter ($q_{||}=0$) energy conservation leads to maxima in $\Delta I_i(V)$ when $eV_b \pm \hbar\omega = E_0$ which are displaced from that in $I_i(V)$ by $e\delta V_b = \pm \hbar\omega$. (This neglects effects due to charge storage in the well). For the range of T_h used, emitted phonons travel ballistically across the ~0.4mm substrate (confirmed by time of flight measurements on sample B) and have a planckian spectrum with a maximum number of phonons at $\hbar\omega \sim 2k_B T_h$. However, for deformation potential coupling, the maximum for the phonons assisting tunnelling is shifted to $\hbar\omega \sim 3k_B T_h$ if screening is neglected (this would be at lower energies for piezoelectric coupling). Hence the phonon peaks should be displaced from the impurity peak by $\pm 3k_B T_h$ and δV_b should vary linearly with T_h . The linearity is confirmed by measurements of the absorption peak shown in fig 3; the emission peak is too broad to provide precise data. The slope $dV/dT_h \sim 9.3V_b/e$ shows that $dV_b/dV \sim 1/3.1$ which is broadly consistent with estimates based on electrostatics. The phonon distribution has a half width of ~1meV which is much less than that of $I_i(V)$ which accounts for the similar width of $\Delta I_i(V)$ and $I_i(V)$. We also note that the probability of a phonon producing assisted tunnelling, estimated from the size of ΔI_i to be $\sim 3 \times 10^{-6}$, is much smaller than the probability that a phonon is absorbed in the emitter ($\sim 10^{-2}$) [9]. However, since the electron-electron scattering rate is much faster than the tunnelling rate, the higher energy electrons resulting from the absorption should all be thermalised before tunnelling and the rise in electron temperature, estimated to be ≤ 1.5 mK, seems far too small to produce a significant signal.

Although δV_b varies linearly with T_h with approximately the expected slope, the relationship $e\delta V_b \sim 3k_B T_h$ is not obeyed since the position of the peak in ΔI_i (fig 3) has an extrapolated value at $T_h=0$ K which is ~15 mV smaller than that of the impurity peak $I_i(V)$. We attribute this to charge storage in the well caused by non-assisted tunnelling. Initially [4], since $I > I_i$, we assumed this would be predominantly associated with the charge stored as mobile electrons in the confined states in the well and attributed the shift to the screening they produce of the impurity charge. The density of donors in the well n_d is estimated to be $\sim 4 \times 10^{10} \text{ cm}^{-2}$ and, for the bias at which $\Delta I_i(V)$ occurs when $eV_b = E_0$ (V_b is the tunnelling time into the collector) is estimated to $\sim 3 \times 10^9 \text{ cm}^{-2}$. This

is smaller than n_d , so it seems likely that the phonon-assisted tunnelling will take place largely into donors with unscreened impurity potentials. However, for the bias at which $I_t(V)$ peaks, $n_d \sim 6 \times 10^9 \text{ cm}^{-2}$ is larger than n_d so that all the donors are screened. Hence the unassisted tunnelling takes place through states of higher energy than the phonon-assisted tunnelling. To account for the observed difference, an increase in donor energy by $\sim 5 \text{ meV}$ ($dV_g/dV \sim 1/3$) is needed, corresponding to an impurity charge Ze reduced by $\sim 10\%$ (the ionization energy $\propto Z^4$). While this model might explain the shift in the absorption peak, it could not account for the roughly similar shift that occurs in the higher voltage (emission) peak since the donors would presumably then have similar energies to their values at the peak of $I_t(V)$. It seems more likely therefore that both shifts are due to the charge stored on the donors as a result of the resonant tunnelling current I_t . The phonon-assisted current $\Delta I_t(V)$ is proportional to the tunnelling probability into an empty donor multiplied by the number of empty donors. Now, for absorption, the probability of assisted tunnelling into one donor has a maximum at the peak of $I_t(V) \hbar \omega/e$ but since the number of empty donors has a minimum near to this peak, the maximum in $\Delta I_t(V)$ should lie somewhere on the edge of the $I_t(V)$ peak as observed. Further details will be given elsewhere.

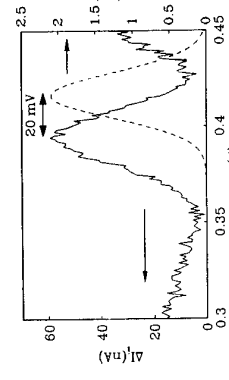


Fig. 2: The change in current $\Delta I_t(V)$ produced by non-equilibrium phonons at $T_h = 8.5\text{K}$. The dashed line shows the impurity peak $I_t(V)$ obtained from fig 1

Measurements have also been made of the phonon-assisted tunnelling at $T_h = 8.5\text{K}$. The dashed line in a substrate at temperature T . Since the incident phonon flux absorbed $\propto T^4$, the current due to phonon-assisted tunnelling should rise rapidly with T and the size of the contribution at T can be obtained by subtracting from it $I_t(V)$ measured at a temperature $\ll T$. The phonon-assisted component at 4.2K obtained in this way is shown in Fig. 4 which is a plot of $\Delta I = I_{4.2} - I_{1.3}$. As can be seen by slight extrapolation of Fig. 3, this phonon peak occurs at the

same bias, to within experimental error, as the absorption peak from a pulsed heater at 4.2K with a substrate at 1K . Since the phonon intensity on the DBRTD from the pulsed heater at T is estimated to be ~ 60 times smaller than when the whole substrate is at T the position of the peak is shown to be independent of phonon intensity and to depend solely on phonon frequency in analogy with the photoelectric effect. Measurements on sample C show that the phonon peak in $\Delta I(V)$ obtained from equilibrium measurements also shifts linearly with substrate temperature as expected. However the slope, $dV/dT \sim 3.8k_B/e$, is only 0.4 that in non-equilibrium experiments. The reason for this may be that, in equilibrium, the phonon flux is incident at all angles so most of the absorbed phonons have significant in-plane momentum. This would reduce the slope particularly if the probability of producing assisted tunnelling increases with angle. Measurements are planned to investigate this angular dependence.

We conclude that the change in the tunnel current produced by non-equilibrium phonons at normal incidence is due to phonon-assisted tunnelling. The variation in the position of the peak with phonon frequency shows that a DBRTD can be used as a phonon spectrometer. The resolution is rather modest but should improve if we are able to tunnel into the main bound state.

REFERENCES:

- [1] F. Capasso, S. Sen, F. Beltram and Y.Y. Cho, in *Physics of Quantum Electron Devices* (Ed F Capasso) Springer Series in Electronics and Photonics **28** (1990) 181
- [2] V.J. Goldman, D.C. Tsui and J.E. Cunningham, Phys. Rev. **B36** (1987) 7635
- [3] F. Chevoir and B. Vinter, Appl. Phys. Lett. **55**, 1859 (1989) and C. H. Grein, E. Runge and H. Ehrenreich, Phys. Rev. **B47** (1993) 12590
- [4] F.F. Quali, N.N. Zinov'ev, L.J. Challis, F.W. Sheard, M. Henini, D.P. Steenson and K.R. Strickland, Phys. Rev. Lett. in press
- [5] W. Kappus and O. Weiss, J. Appl. Phys. **44** (1973) 1947
- [6] J.W. Sakai, T.M. Fromhold, P.H. Beton, L. Eaves, M. Henini, P.C. Main and F.W. Sheard, Phys. Rev. **B48** (1993) 5664
- [7] G. Bastard, *Wave Mechanics Applied to Semiconductor Heterostructures*, Chapter IV, Les Editions de Physique, Paris (1990).
- [8] M. Henini, J.W. Sakai, P.H. Beton, L. Eaves and P.C. Main, J. Vac. Sci. Technol. **B11** (1993) 958
- [9] P.J. Price, Physica **B134** (1985) 164

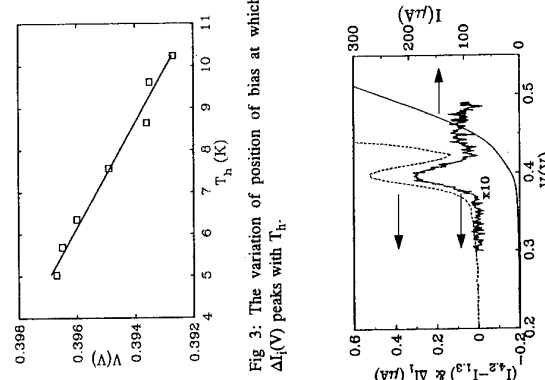


Fig. 3: The variation of position of bias at which $\Delta I_t(V)$ peaks with T_h

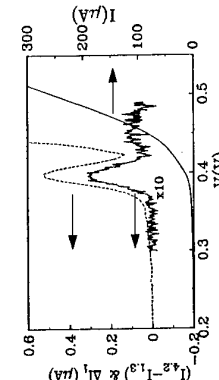


Fig. 4: The broken curve $\Delta I = I_{4.2} - I_{1.3}$ and the two solid lines show $\Delta I(V)$ produced by a phonon pulse at 5.0K and the $I(V)$ characteristic.

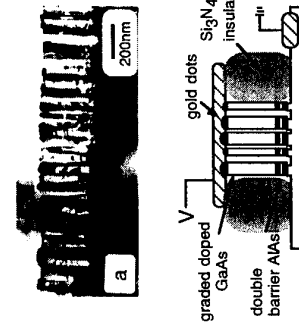
Field enhanced blockade of the confined energy levels in nanometer scale pillar arrays

B.W. Alphenaar, Z.A.K. Durrani, and M. Wagner,
Hitachi Cambridge Laboratory and University of Cambridge Microelectronics Research Centre,
Cavendish Laboratory, Madingley Road, Cambridge CB3 0HE, UK

K. Köhler
Fraunhofer-Institut für Angewandte Festkörperforschung, Tullastraße 72, D-79108 Freiburg,
Germany

Abstract

We report observations of dramatic hysteretic switching behavior in nanometer scale pillar arrays. Using a new technique, we fabricate arrays of closely packed pillars 20–50 nm in diameter from a GaAs/AlAs resonant tunneling diode heterostructure. The array resistance switches between two stable states with a current peak to valley ratio of 500:1. Scanning tunneling microscope characterization of individual pillars suggests that the pillars trap charge to block the flow of current through the quantum confined states.



Electron transport through laterally confined resonant tunneling diodes [1] (RTDs) can be influenced by both Coulomb charging [2,3] and low-dimensional quantum size effects [4]. In a laterally confined RTD, a quantum dot is formed by etching a double barrier heterostructure into a submicron diameter pillar. In principle, charging and quantum confinement energies can be increased by simply reducing the pillar dimensions. In practice, there has been a limit to the minimum device diameter due to the presence of surface states which deplete the electron channel, and block current flow [5].

We have characterized arrays of nanometer scale RTD pillars and observe behavior which suggests that surface charge trapping can be used controllably, to gate current flow. Measurements of more than 10³ RTD pillars in parallel reveal that the array resistance switches between two stable states with a current peak to valley ratio of 500:1. Scanning tunneling microscope characterization shows that an individual pillar traps charge to change the position of the quantum confined states with respect to the conduction band. These results imply that in the array, the resistance switches due to the simultaneous charging of the individual pillars.

The nanoscale pillar arrays are made using a ‘natural’ lithographic technique [6]. First, we evaporate a thin gold film onto the semiconductor surface. It is well documented that for film thicknesses less than around 10 nm, gold forms a granular layer composed of disconnected islands [7]. The gold islands partially mask the underlying material so that plasma etching in a SiCl₄/Ar

environment selectively removes the material between the islands and produces an array of semiconductor pillars. Figure 1(a) shows a transmission electron micrograph of a typical sample after etching. The pillars are densely packed with diameters ranging from 20–50 nm and with an etch depth of approximately 320 nm. The dark bands visible in the micrograph show the strain caused by the etching process which leaves the pillars bent about 5° off normal.

Our device is drawn schematically in Fig. 1(b) [8]. An RTD pillar array is formed by etching a double barrier AlAs/GaAs heterostructure in the manner described above. In our structure, a 5.6 nm thick GaAs well is isolated between 2 nm thick AlAs barriers. The GaAs leads are Si doped n-type, with a concentration graded from 5×10^{18} cm⁻³ at the contacts to 2×10^{17} cm⁻³ near the barriers. Contact is made to the top of the pillars by evaporating a 30×30 micron gold pad. The gold pad does not fill the gaps between the pillars because the gold grain size is approximately the same as the pillar spacing. A Si₃N₄ insulating layer is used to support the wire bond. The back contact is AuGeNi annealed at 400°C for 10 s.

Figure 2 shows the result of a typical hysteresis measurement. Starting at zero bias, the device is initially in a high resistance state. Moving to negative bias, the current jumps sharply to a low resistance state at ~ 2.4 V. The device stays in the low resistance state until the bias crosses zero and increases to $+1.4$ V. Here the device switches back to the high resistance state with a current peak to valley ratio of 500:1. Further measurements show that the high resistance state remains stable at zero bias for an unlimited period of time while the low resistance state is stable for at least one hour before eventually switching to the high resistance state. In comparison, measurements of a standard 10 micron diameter RTD made from the same material showed a room temperature peak to valley ratio of only 3:1 and no hysteretic switching behavior [9]. Switching was observed in pillar arrays fabricated from two double barrier wafers which were obtained from separate growth facilities. However, no switching was observed in a similarly grown single barrier sample. This demonstrates that quantum well confinement is necessary for the switching effect. Because the pillars are small and closely packed, it is impossible to contact a single device by conventional means. However, using a scanning tunneling microscope (STM), we are able to locate and contact isolated pillars. Our measurements are done using a tungsten tip W.A. Technology STM operating at room temperature in air. We first locate an individual pillar by measuring the tunnel gap required to provide constant current while scanning the tip along the sample surface. Once a pillar is located, the gap is reduced bringing the tip in light contact with the sample. If we retract the tip, our original scan can be reproduced, demonstrating that the surface is not damaged by the process. A number of pillars giving similar results were measured in this way.

Figure 3(a) shows the current voltage characteristics of a 40 nm diameter RTD pillar measured with an STM tip contact. The trace is hysteretic: negative differential resistance (NDR) is observed when the bias starts at zero and is swept to a higher positive or negative value; NDR is not observed in the opposite sweep direction. Reproducible results are obtained for a constant sweep rate, but the peak to valley ratio decreases as the sweep rate is decreased. To explain these results, we propose that trapped charge modifies the position of the quantized states in the well [5]. One possible mechanism is seen in Fig. 4. On the surface of the pillar, a large density of localized states exist due to dangling bonds and strain. In equilibrium, (Fig. 4(a)), the Fermi energy

FIG. 2. Current versus source-drain bias for a typical resonant tunneling diode pillar array device. The peak to valley ratio is 500:1. The inset shows the current as a function of time as the device switches between the low and the high resistance state.

E_F is pinned within these surface states. This depletes the electron density in the center of the pillar and forms a large barrier in the central lightly doped region. When a large bias is placed on the device, (Fig. 4(b)), electrons are forced out of the surface states, creating a net positive charge Q . This positive charge acts as a gate to reduce the level of the central barrier and thus also the relative energies of the electron states confined in the well. Experimentally, NDR occurs in the forward sweep direction as the conduction band energy E_c moves above the well resonance, with increasing bias. But as the bias is swept back to zero, electrons have not yet repopulated the surface states and the resonance level stays pinned below E_c .

The charge gating effect can be observed more directly by monitoring the current as a function of time while the pillar recharges. The results of this experiment are shown in Fig. 3b. The device is biased at -15 V for 10 seconds (Fig. 4(b)), after which the current is plotted as a function of time while the device recharges at $+1.9$ V. A strong peak is observed on top of a slow decay in the current. As seen in Fig. 4(c), when the bias is switched to the recharging voltage, the quantum well resonance initially lies below E_c . As the surface states slowly return to their equilibrium value, the resonance state rises, and moves through E_c (Fig. 4(d)). This appears as a peak in Fig. 3(b). If we change the bias, we expect this will influence the recharging time, and thus move the peak position. In the inset, the peak is observed to occur sooner for larger biases, as would be expected for a faster recharging time.

We now consider the influence of charge gating on the large area device. Here, a sharp transition is observed between the high resistance and the low resistance state (Fig. 2). In the high resistance state, (Fig. 4(a)), current is blocked by the depletion region, which forms around the double barrier structure due to the negatively charged surface states. Upon application of reverse bias, electron charge is forced from the surface states, lowering the depletion region barrier (Fig. 4(b)). A sharp switch to the low resistance state eventually occurs when E_c in the depletion region is pulled below E_F .

In the low resistance state, the surface states are positively charged, and remain trapped below E_c in a quasi-stable situation. If positive bias is applied, the quantum well resonance eventually passes E_c . This switches the device off, and induces the surface states to return to the equilibrium level. Evidence for this resonant induced mechanism is provided by time dependent measurements of the large area device as it switches from the low to the high resistance state. As shown in the inset to Fig. 2, the switch occurs in less than 10^{-7} seconds, and is followed by a slow rise and then decay in the current. We attribute the initial switch to the confined level in the quantum well, while the slow rise and decay (as also seen in Fig. 3(b)) is due to the charging of the surface states.

Admittedly, this model does not completely describe the behavior of the large area device. It is still unclear why the positively charged state remains stable for so long, and why the resonance switch causes simultaneous repopulation of the trapped states. This

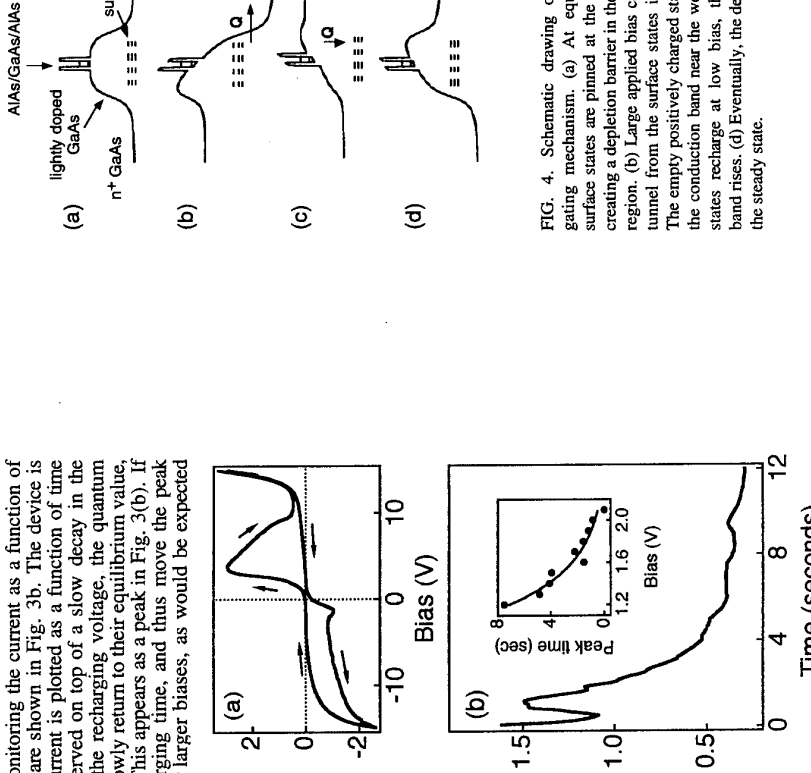


FIG. 3. Current-voltage characteristic of a 40 nm diameter RTD pillar measured with an STM tip contact. The sweep rate is 200 mV/sec. (b) Current as a function of time as the pillar recharges. The inset shows the position of the main peak for different recharging biases (see text). The solid line is a guide to the eye.

is in contrast to the single pillar, where more gradual charging is observed. A more detailed analysis is needed which perhaps takes into account interactions among the pillars. In conclusion, we have observed dramatic hysteretic switching behavior at room temperature in resonant tunneling pillar arrays. STM measurements of individual pillars suggest that this effect is caused by the charging and de-charging of trap states which influence the energy of the confined levels. We hope that further experiments will lead to a more complete theory to describe the observed behavior.

References

- [1] For a recent review of resonant tunneling diodes and their applications see F. Capasso, S. Sen and F. Beltram in *High-Speed Semiconductor Devices* edited by S.M. Sze, John Wiley & Sons, New York, 1990.
- [2] Atanas Groshev, Phys. Rev. B **42**, 5895 (1990).
- [3] B. Su, V.J. Goldman, and J.E. Cunningham, Science **255**, 313 (1992); Phys. Rev. B **46**, 7644 (1992); M. Tewordt, L. Martin-Moreno, J.T. Nichols, M. Popper, M.J. Kelley, V.J. Law, D.A. Ritchie, J.E.F. Frost, and G.A.C. Jones, Phys. Rev. B **45**, 14407 (1992).
- [4] M.A. Reed, J.N. Randall, R.J. Aggarwal, R.J. Matyi, T.M. Moore, and A.E. Weissel, Phys. Rev. Lett. **60**, 535 (1988).
- [5] M.A. Reed, J.N. Randall, J.H. Luscombe, W.R. Frensel, R.J. Aggarwal, R.J. Matyi, T.M. Moore, and A.E. Weissel, Festkörperprobleme **29**, 267 (1989).
- [6] There have been many recent publications demonstrating similar natural lithographic techniques. See for example: K. Hiruma, T. Katayama, K. Ogawa, M. Koguchi, H. Kakabayashi, and G.P. Morgan, Appl. Phys. Lett. **59**, 431 (1991); C. Schönenberger, H. van Houten, and H.C. Doonkersloot, Europhys. Lett. **20**, 249 (1992); M. Green, M. Garcia-Parajo, F. Khaleque and R. Murray, Appl. Phys. Lett. **66**, 1234 (1995).
- [7] For a review describing granular metal films see B. Abeles, Appl. Solid. Sci. **6**, 1 (1976).
- [8] B.W. Alphenaar, Z.A.K. Durran, A.P. Heberle, and M. Wagner, Appl. Phys. Lett. **66**, 1234 (1995).
- [9] C. J. Goodings, Ph.D. Thesis, University of Cambridge (1993).

and their applications see F. Capasso, S. Sen and F. Beltram in *High-Speed Semiconductor Devices* edited by S.M. Sze, John Wiley & Sons, New York, 1990.

[2] Atanas Groshev, Phys. Rev. B **42**, 5895 (1990).

[3] B. Su, V.J. Goldman, and J.E. Cunningham, Science **255**, 313 (1992); Phys. Rev. B **46**, 7644 (1992); M. Tewordt, L. Martin-Moreno, J.T. Nichols, M. Popper, M.J. Kelley, V.J. Law, D.A. Ritchie, J.E.F. Frost, and G.A.C. Jones, Phys. Rev. B **45**, 14407 (1992).

[4] M.A. Reed, J.N. Randall, R.J. Aggarwal, R.J. Matyi, T.M. Moore, and A.E. Weissel, Phys. Rev. Lett. **60**, 535 (1988).

[5] M.A. Reed, J.N. Randall, J.H. Luscombe, W.R. Frensel, R.J. Aggarwal, R.J. Matyi, T.M. Moore, and A.E. Weissel, Festkörperprobleme **29**, 267 (1989).

[6] There have been many recent publications demonstrating similar natural lithographic techniques. See for example: K. Hiruma, T. Katayama, K. Ogawa, M. Koguchi, H. Kakabayashi, and G.P. Morgan, Appl. Phys. Lett. **59**, 431 (1991); C. Schönenberger, H. van Houten, and H.C. Doonkersloot, Europhys. Lett. **20**, 249 (1992); M. Green, M. Garcia-Parajo, F. Khaleque and R. Murray, Appl. Phys. Lett. **66**, 1234 (1995).

[7] For a review describing granular metal films see B. Abeles, Appl. Solid. Sci. **6**, 1 (1976).

[8] B.W. Alphenaar, Z.A.K. Durran, A.P. Heberle, and M. Wagner, Appl. Phys. Lett. **66**, 1234 (1995).

[9] C. J. Goodings, Ph.D. Thesis, University of Cambridge (1993).

The Chemical Potential of a Charged Fermion Layer at High r_s Values

S. Shapira,^a U. Sivan,^a P. M. Solomon,^b E. Buchstab,^a M. Tischler^b, and G. Ben Yoseph^a

^a Solid State Inst. and Physics Dept., Technion - Israel Inst. of Technology, Haifa 32000, Israel.
^b IBM, T. J. Watson Research Center, Yorktown Heights, NY 10598, USA.

Abstract

We report the measurement of the chemical potential of a two dimensional hole layer in wide temperature and density ranges. The heavy hole mass allows the first detailed study of 2D degenerate fermions in a regime where the ratio of coulomb to kinetic energies approaches the theoretical value, $r_s = 37$, expected for Wigner crystallization. The measured low temperature chemical potential and compressibility are negative and agree well with theory that takes exchange and correlations into account. As the temperature is raised, the compressibility turns less negative and reverses sign at $T \approx 40K$. An ideal classical gas behavior is attained only at temperatures higher than interaction energy which is more than an order of magnitude larger than the Fermi energy. Conditions for a possible interaction-induced charge instability are discussed.

The phase diagram of a two dimensional charged fermion system, in the absence of magnetic fields, is governed by the interplay between the Fermi energy, E_F , the Coulomb interaction energy, $U = (e^2/4\pi\epsilon_0) \times \sqrt{np}$, and the temperature, $k_B T$ (κ is the dielectric constant and p is the carrier density). The relative importance of these energies is commonly characterized by two dimensionless parameters, the average interparticle distance measured in Bohr radii, $r_s = U/E_F$, and the classical plasma parameter, $\Gamma = U/k_B T$. The theoretically expected phases, neglecting possible spin polarization effects, are schematically indicated in fig. 1.

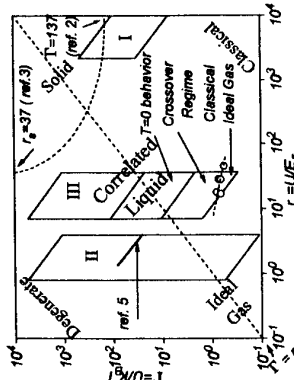


Fig. 1: Schematic phase diagram for 2D charged fermions. Circles- experimental points marking the transition to an ideal classical gas.

The extreme classical case, $r_s > \Gamma$, was extensively studied using 2D electrons on liquid helium[1] (marked I in fig. 1) and a classical liquid-solid transition was observed[2] at $\Gamma = 137$, $r_s = 3.6 \times 10^3 - 6.1 \times 10^3$. The degenerate regime was primarily investigated utilizing silicon inversion layers and in recent years, GaAs/AlGaAs heterostructures. The portion of phase space accessible with electrons in GaAs/AlGaAs heterostructures, assuming $n \geq 2 \times 10^{10} \text{ cm}^{-2}$, is marked II in fig. 1. Due to the light electronic mass it is limited to $r_s \leq 34$. One way to overcome this difficulty is by application of strong magnetic fields that quench the kinetic degree of freedom and hence lead to the fractional quantum Hall effect and Wigner crystallization in certain filling factors. Being interested in the zero magnetic field case, we adopt an alternative approach, namely, suppressing the kinetic energy by using heavy holes rather than electrons. Consequently, r_s numbers which are close to the theoretical value,[3] $r_s = 37$, for crystallization are attained. Moreover, the heavy hole mass allows the probing of the full crossover from a degenerate, strongly correlated liquid to an ideal gas in the same sample. The accessible range in phase space for $p \geq 2 \times 10^{10} \text{ cm}^{-2}$ is marked III in fig. 1.

The thermodynamics of the 2D hole layer is characterized by its chemical potential, $\mu = \frac{\partial (p \times F_{2D})}{\partial p}|_T$, where F_{2D} is the free energy per particle associated with inplane motion, excluding Hartree terms (see eq. 1). The chemical potential is measured using a structure similar to that described in ref. 4. It may be envisaged (inset of fig. 2) as a four plate capacitor, the two middle plates being parallel electron and hole layers whose densities are controlled by a top metal gate and a substrate, respectively. The spacing between the electron and hole layers is 14nm and the sample is processed in a Hall bar shape, thus allowing the determination of both mobilities and carrier concentrations by a low field (usually 0.4T) Hall effect.

The experimental technique[5] consists of a simultaneous measurement of n and p as the holes are continuously depleted by V_{sub} at a constant V_{pn} and V_{gn} . Due to the finite screening $(\partial \mu / \partial p \neq 0)$ of the hole layer, the electronic concentration, n , is also modified. The hole chemical potential is then extracted from the variation of n with p using the following procedure. The total free energy of the three plate system (inset of fig. 2) consisting of the electron and hole layers and the substrate, coupled to two batteries V_{pn} , V_{sub} , is given by

$$F = (F_{2D} + T_z + E_g)p - \epsilon p V_{pn} - e(n-p)V_{sub} + U_e, \quad (1)$$

where E_g is the GaAs band gap, T_z is the hole kinetic energy perpendicular to the plane, and U_e is the system's Hartree energy. Using the self consistent wavefunctions of ref [6] for the holes, F is expressed in terms of p , n , and the wavefunction inverse width b . The total free energy is then minimized with respect to these parameters yielding $\mu(p,T)$ in terms of n .

Typical data for p and n vs. V_{sub} at $T = 1.44 \text{ K}$ are depicted in fig. 2. The hole capacitance with respect to the substrate agrees with the calculated value down to $p \approx 1 \times 10^{11} \text{ cm}^{-2}$. At lower densities, the measured hole concentration depends on the magnetic field polarity, probably due to inhomogeneous carrier distribution. Since the distance from the substrate to the hole layer is large compared with s , the total charge, $e(p-n)$ varies linearly with V_{sub} . The average hole concentration can hence be deduced, even at low densities, from the known total capacitance of

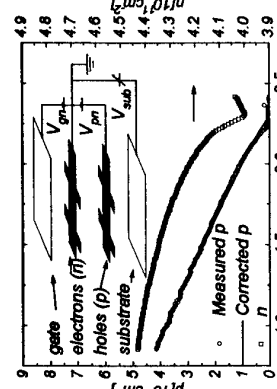


Fig. 2: Hole and electron concentrations vs. V_{sub} at a constant V_{pn} . Solid line- corrected p (see text). Inset- The system as a four plate capacitor.

the electron and hole layers with respect to the substrate, and an accurate measurement of n . The result of such an analysis is depicted by the solid line. The interesting physics rests with the dependence of n upon V_{sub} . Counterintuitively, n decreases as holes are depleted, indicating a negative screening or compressibility of the hole layer. Such an effect results from the large exchange and correlation interactions and reflects the large r_s numbers attained.

The hole chemical potential deduced from the data in fig. 2, using the above procedure, is depicted in fig. 3. It is negative for all densities. Both the magnitude and the trend are consistent with the numerical calculations of Tanatar and Ceperley[3] depicted for $m_h = 0.38m_0$ and $0.6m_0$ by the dashed and dotted-dashed lines, respectively. For comparison, the positive chemical potential of an ideal degenerate gas is depicted by the dotted line for $m_h = 0.6m_0$. The above mass values are based on cyclotron resonance measurements[7] done on a 2DHG with similar parameters. Note the large r_s values attained (top x-axis).

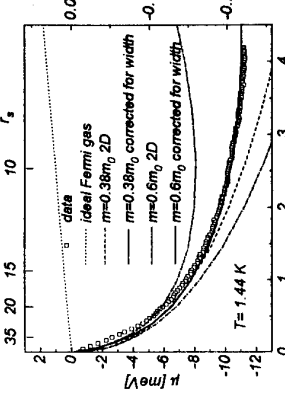


Fig. 3: Hole chemical potential vs. p. Top axis: r_s for $m_h = 0.6m_0$. Right axis: chemical potential in Rydbergs.

While theory[3] refers to an isolated, infinitely narrow layer, the actual hole layer has a finite thickness and is placed in proximity to a conducting electron layer. Due to the finite layer thickness, the absolute magnitude of the exchange interaction is reduced[8]. Using the result of ref. 8 and taking the correlation energy to be identically modified, we obtain the corrected theory described by the double dotted and solid lines for $m_h = 0.38m_0$ and $0.6m_0$, respectively. We find very good agreement with theory for $m_h = 0.6m_0$, particularly for $p \geq 1 \times 10^{11} \text{ cm}^{-2}$ where the 2DHG is homogeneous. No adjustable parameters are used. Despite the small separation between the electrons and the holes, measurements at various electron concentrations ($\geq 2.8 \times 10^{11} \text{ cm}^{-2}$) reveal independence of μ upon n ($p = 0$).

The chemical potential was measured for temperatures up to 94K. The resulting $\partial\mu(T, p)/\partial p$ is presented in fig. 4. At temperatures lower than $\approx 10 - 15$ K, the data are practically temperature independent for *all* hole concentrations and are properly described by a zero temperature theory[3,8]. In the absence of theory for the temperature dependent chemical potential in that regime, we are unable to explain this independence of $\mu(p)$ upon T . The corresponding range in

phase space is marked in fig. 1. As the temperature is raised above 15K, $\partial\mu/\partial p$ gradually turns less negative and reverses sign at low densities around $T \approx 40. The variation of $\partial\mu/\partial p$ in that range is linear in T for various densities. We attribute the gradual reduction in $\partial\mu/\partial p$ to weakening of the exchange and quantum correlation effects with T . Classical correlations, on the other hand, are expected to persist up to $T \approx 1$. Indeed, we find an experimental crossover to an ideal classical gas at $T = 0.6 - 0.8$ ($T = 45 - 94$ K for $p = 1.2 - 7.5 \times 10^{10} \text{ cm}^{-2}$). The corresponding transition line is marked in fig 1. It is interesting that the point $\partial\mu/\partial p = 0$, where correlations are exactly canceled against the kinetic terms, occurs at $T \approx 40 for all hole densities.$$

Generally, negative compressibility leads to a thermodynamic instability. It is hence emphasized that the chemical potential measured is derived from F_{2D} which is only a *part* of the total free energy, F , of the system (cf. eq. 1). The latter includes positive Hartree terms which stabilize the system for the experimental concentrations. Using the measured low temperature chemical potential (fig. 3), eq. 1 predicts, however, a charge instability at $p \leq 5 \times 10^9 \text{ cm}^{-2}$. In summary, the chemical potential of a two dimensional hole layer was measured in wide temperature $1.44 \text{ K} \leq T \leq 94 \text{ K}$ and concentration $0 \leq p \leq 4 \times 10^{11} \text{ cm}^{-2}$ ranges. Due to the heavy hole mass, r_s values larger than 35 were attained and the chemical potential was observed to be interaction dominated. At low temperatures, the measured μ and $\partial\mu/\partial p$ are negative and in good, quantitative agreement with theory[3,8]. The chemical potential is temperature independent for $T \leq 10 - 15$ K. As the temperature is increased, $\partial\mu/\partial p$ becomes less negative and reverses sign at $T = 40. A classical ideal gas behavior is observed only at temperatures higher than the interaction energy ($T \leq 0.6 - 0.8$).$

We acknowledge useful discussions with L. Pitaevskii, J. Eisenstein, and A. MacDonald. The research was supported by the US-Israel BSF and the Technion grant for the promotion of research.

References

- ¹ P. Liederer, *J. Low Temp Phys.* **87**, 247 (1992) and references therein.
- ² C.C. Grimes and G. Adams, *Phys. Rev. Lett.* **42**, 795 (1979).
- ³ B. Tanatar and D.M. Ceperley, *Phys. Rev. B* **37**, 8179 (1988).
- ⁴ U. Sivan, P.M. Solomon, H. Shtrikman *Phys. Rev. Lett.* **68**, 1196 (1992).
- ⁵ J. Eisenstein, L. Pfeiffer, K. West, *Phys. Rev. Lett.* **68**, 674 (1992).
- ⁶ F. F. Fang and W. E. Howard, *Phys. Rev. Lett.* **16**, 797 (1966).
- ⁷ H.L. Stormer, Z. Schlesinger, A. Chang, D.C. Tsui, A.C. Gossard, and W. Wiegmann, *Phys. Rev. Lett.* **51**, 126 (1983).
- ⁸ F. Stern, *Jap. J. Appl. Phys. Suppl. 2 Pt. 2*, 323 (1974).

Observation of the Zero Hall Resistance state in a Semimetallic Superlattice

M.S. Daly*, K.S.H. Dalton*, M. Lakrimi*, N.J. Mason*, D.K. Maude*, R.J. Nicholas*, J.C. Portal*, D.M. Symons*, M. van der Burg*, and P.J. Walker*.

* Physics Dept., Oxford University, Clarendon Lab., Parks Rd, Oxford, OX1 3PU, U.K.
+ LCM-CNRS, 25 Ave des Martyrs, BP166, 38042 Grenoble Cedex, France.

The quantum Hall effect has been measured in intrinsic semimetallic superlattices with almost equal electron and hole densities. Giant oscillations are seen in the Hall resistivity, and at high fields and hydrostatic pressures a zero resistance state is observed where the Hall resistivity goes to zero due to compensation of the Hall fields of the two carrier types. This behaviour is interpreted in terms of the limiting properties of σ_{xx} and σ_{xy} .

We report a new example of the quantum Hall effect in a semimetallic system with almost equal numbers of electrons and holes. The Hall resistivity shows giant oscillations and approaches zero for specific ranges of magnetic fields where there are equal numbers of electron and hole Landau levels occupied. The structures which we study are semimetallic InAs/GaSb superlattices with very closely matched electron and hole densities (typically $n_e = 1.01n_h$). The conduction band edge of the InAs falls below the valence band edge of the GaSb [1,2], leading to intrinsic charge transfer in either single heterojunctions or long period superlattices. Perfect structures would therefore be expected to have equal numbers of electrons and holes present.

Previous studies in single well structures, in which a significant amount of residual extrinsic charge was present, showed a compensated quantum Hall effect [3]. The Hall plateaux were given by the finite difference in the numbers of electron and hole Landau levels occupied, and so $\rho_{xy} = h[e^2(v_e - v_h)]$, where v_e and v_h are the (integer) number of filled electron and hole Landau levels respectively. At the same time the resistivity ρ_{xx} showed pronounced minima and this behaviour has been interpreted as due to a Fermi level which lies simultaneously within the localised states of both the electrons and holes. In superlattices with more closely matched electron and hole concentrations [4,5] the Hall resistivity shows large oscillations. We now have structures in which the localised states of both electrons and holes can be made to overlap for equal numbers of Landau levels. This generates qualitatively new behaviour, in which a zero Hall resistance state appears, accompanied by a divergence of the diagonal resistivity, ρ_{xx} .

The classical Hall effect for a two carrier system is dominated by the highest mobility carriers at low fields, while at high fields it measures the total net charge, with the Hall coefficient R_H given by $1/(n_e n_h)e$, where n_e and n_h are the electron and hole densities respectively [6]. For an intrinsic semimetal the Hall resistivity would therefore be expected to diverge when $n_e = n_h$.

The Hall conductivity is given by $\sigma_{xy} = \sigma_{xy}^e - |\sigma_{xy}^h|$ and for a 2-D system, when the Fermi level lies within the localised states, quantised Hall steps occur for both carrier types. Thus

$\sigma_{xy} = (v_e - v_h)(e^2/h)$, and for $v_e = v_h$ the Hall conductivity will be zero. The quantum limit behaviour of the Hall resistivity will depend on the limiting behaviour of the conductivity components as they tend to zero so that if there is a finite σ_{xx} which tends to zero less quickly

than σ_{xy} , a zero Hall resistance state will occur as a special condition of the quantum Hall effect. The samples used were long period superlattices of 20 (or 80) layers of 220 Å InAs and 21 (or 81) layers of 190 Å GaSb, with the superlattice terminated at each end with either bulk GaSb or a short period (30 Å InAs/30 Å GaSb) superlattice, designed to have a semiconducting energy gap and hence contain no intrinsic charge carriers at low temperatures. The samples are grown by MOVPE [7] onto a GaAs substrate, with a buffer layer of 2 μm of GaSb. They have very low levels of extrinsic charge, so that the short period superlattices are insulating at low temperatures, and the majority of the carriers in the long period superlattice arise due to charge transfer from the GaSb to the InAs. The interfaces are grown with a gas switching sequence which produces well defined interface monolayers of InSb, as demonstrated by Raman scattering [8]. The experiments use high pulsed magnetic fields (48 T pulses over 15 msec) down to 600 mK, high steady fields (28 T) down to 340 mK and high pressures in a dilution refrigerator.

Fig. 1 shows the resistivity and conductivity components at 340 mK for an 80 period superlattice terminated with GaSb. Fitting the low field data to a classical two carrier formula [6] gives electron and hole densities of 5.8 and $5.7 \times 10^{14} \text{ cm}^{-2}$, and mobilities 115,000 and 8,000 $\text{cm}^2 \text{V}^{-1} \text{s}^{-1}$. These values indicate that all 80 layers within the structure are active, and are consistent with the assumption that the overwhelming majority of the carriers present arise due to charge transfer from the GaSb to the InAs layers. Strong oscillatory features occur at high fields in both the conductivity components and in particular a very flat minimum appears in σ_{xy} in the region from 15 to 22 T, corresponding to two conductance quanta. Evidence from pressure measurements suggests that this may be due to the presence of residual 2-D layers at the end of the superlattice, which are not equivalent to the rest of the layers within the structure. We therefore move to "sandwich" structures which include a short period superlattice at each end, where this problem is eliminated. Fig. 2 shows the conductivity components at high field for a 20 period "sandwich" structure where the electron and hole densities are again very close. There are two strong minima in σ_{xy} in the regions around 16 and 44 T, which now approach zero. Previous experimental and theoretical studies of the Landau levels in this system [3,5] suggest that these features correspond to magnetic fields at which the Fermi level lies in the gaps between both hole and electron Landau levels such that either both (16T) or one (44T) of the spin states of the lowest Landau levels of each carrier is occupied. At fields above these points the levels cross each other, corresponding to a Fermi energy lying in the extended states, and divergent peaks occur in the Hall resistivity. It is expected theoretically [5-11] that mixing of the conduction and valence bands will occur, leading to level repulsion. This mixing will be relatively small in longer period structures, and at present there is no clear evidence of any influence of this mixing phenomenon.

To investigate more precisely the features where the Hall voltage approaches zero at low temperatures we apply hydrostatic pressure to the system, which reduces the band overlap [12,13], and hence moves the strong features down in magnetic field proportional to the decrease in separation of the hole and electron levels. This allows the use of D.C. fields and dilution refrigerator temperatures. Fig. 3 shows the resistivity components ρ_{xx} and ρ_{xy} of the "sandwich" structure at 8.6 kbar and 70 mK. The overlap of the conduction and valence band edges at zero field is now reduced to ~ 60 meV, giving electron and hole densities of $\sim 2.8 \times 10^{14} \text{ cm}^{-2}$ per layer, and low field fits of the Hall coefficient again show that all 20 layers are active. The large oscillatory features now occur at lower magnetic fields, so that by 8 T only one Landau level each of the electrons and holes are occupied for each layer. At this point the Fermi level lies within the localised states for both electrons and holes, and the Hall effect from both carriers is quantised

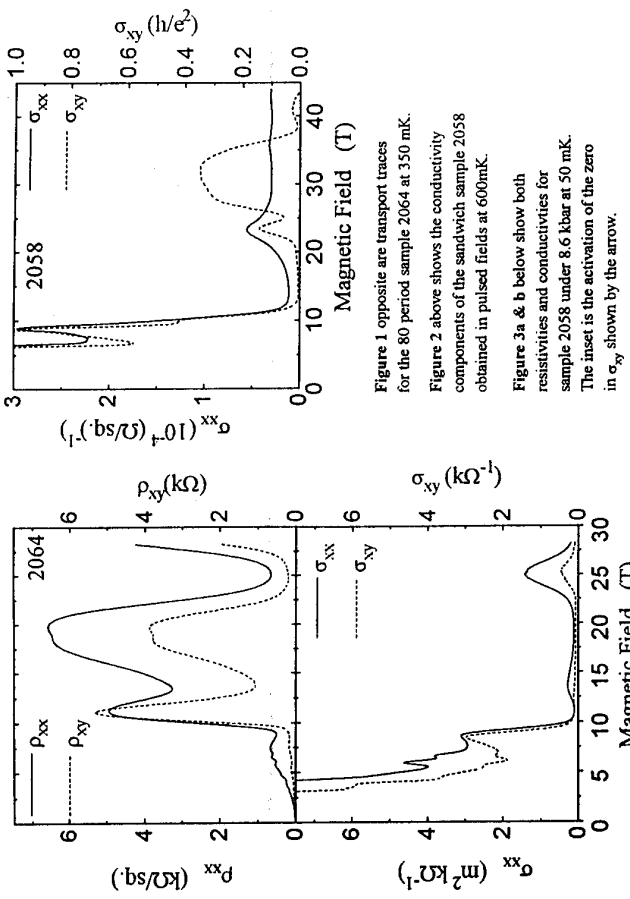


Figure 1 opposite are transport traces for the 80 period sample 2064 at 350 mK.

Figure 2 above shows the conductivity components of the sandwich sample 2038 obtained in pulsed fields at 600mK.

Figure 3a & b below show both resistivities and conductivities for sample 2058 under 8.6 kbar at 30mK. The inset is the activation of the zero in σ_{xy} shown by the arrow.

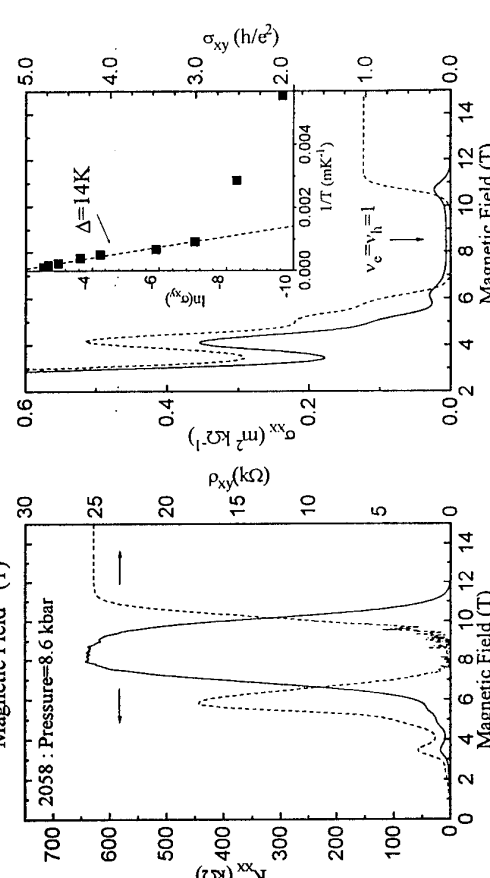


Figure 2 above shows the conductivity components of the sandwich sample 2038 obtained in pulsed fields at 600mK.

Figure 3a & b below show both resistivities and conductivities for sample 2058 under 8.6 kbar at 30mK.

The inset is the activation of the zero in σ_{xy} shown by the arrow.

with equal magnitude and opposite sign. The Hall voltage disappears, and ρ_{xx} diverges. The corresponding traces for σ_{xy} and σ_{xx} both show minima at this point (fig. 3), but some finite σ_{xx} remains. At slightly lower fields the extended states of the electrons and holes overlap, leading to a classical divergence of the Hall resistance, with $R_H = 1/(n_e n_h)e$, and $(n_e n_h) \ll n_c$. For higher fields the levels begin to uncross, and a conventional quantum Hall plateau is observed at a resistivity of h/e^2 . This is thought to arise due to the small number of residual electrons in the superlattice becoming confined in only a single layer.

The magnitude of the gap between the extended states responsible for the appearance of the zero in the Hall resistance can be estimated from an activation plot of the σ_{xy} minimum, shown in fig. 3, which gives a value of 14K. This is comparable to the expected spin splitting of the lowest hole Landau level of a few tens of K [14], and the measured activation energy will be reduced from this value by level broadening which is estimated to be of order 15K, using the low field Hall mobility of the holes.

The observation of a zero Hall resistance state is crucially dependent on the limiting behaviour of σ_{xy} and σ_{xx} since $\rho_{xy} = \sigma_{xy}/(\sigma_{xy}^2 + \sigma_{xx}^2)$, in a region where both conductivity components are tending to zero. In studies on localised systems it has been shown [15,16] that a finite, essentially classical, value of ρ_{xy} occurs at the same time as ρ_{xx} diverges in the quantum limit for a single carrier system, known as the Hall insulator. This implies $\sigma_{xy} \approx \sigma_{xx}^2 / n_e$. Using a Landau level attachment transformation [16] suggests that deviations from exact quantization of integer units of the Hall conductivity will take place with $\Delta\sigma_{xy} \propto \sigma_{xx}^2/n_e$, suggesting that for a compensated Hall plateau, one might expect a finite value of ρ_{xy} . However, for an intrinsic semimetallic system the deviations from exact quantization of the Hall voltage about the centre of the plateau will balance, since equal numbers of electrons and holes will contribute to σ_{xy} by equal and opposite amounts, whereas both will contribute positively to σ_{xx} . Thus $(\Delta\sigma_{xy} - |\Delta\sigma_{xy}^h|) \ll (\sigma_{xx}^2 + \sigma_{xy}^2)/n_e$ leading to the opposite result of a zero Hall resistance state.

In conclusion, we have observed a new special condition of the quantum Hall effect, in which the contributions from electrons and holes exactly balances, leading to zero Hall resistance.

References

- [1] H. Sakaki et al, Solid State Commun. **26** 589 (1978)
- [2] R.J. Nicholas et al, Physica B **184** 268 (1993)
- [3] E.E. Mendez, L. Esaki and L.L. Chang, Phys. Rev. Lett. **55** 2216 (1985)
- [4] K.S.H. Dalton et al, Surf. Sci. **305** 156 (1994)
- [5] R.J. Nicholas et al, Physica B **201** 271 (1994)
- [6] R.A. Smith, *Semiconductors* (C.U.P., Cambridge, 1961) p107
- [7] G.R. Booker et al, J. Cryst. Growth, **145** 778 (1994); ibid **146** 495 (1995)
- [8] S.G. Lyapin, P.C. Klipstein, N.J. Mason and P.J. Walker, Phys. Rev. Lett. **74** 3285 (1995)
- [9] D.J. Barnes et al, Phys. Rev. **B49** 10474 (1994)
- [10] A. Fasolino, and M. Altarelli, Surf. Sci. **142** 322 (1984)
- [11] M. Altarelli, J.C. Maan, L.L. Chang and L. Esaki, Phys. Rev. **B35** 9867 (1987)
- [12] J. Beers et al , Phys. Rev. **B35** 3039 (1987); *ibid* **B36** 4742 (1987)
- [13] D.M. Symons et al, Phys. Rev. **B49** 16614 (1994)
- [14] R.W. Martin et al, Phys. Rev. **B42** 9237 (1990)
- [15] O. Viefweger and K.B. Efetov, J. Phys.: Condens. Matter **2** 7049 (1990)
- [16] S. Kivelson, D.H. Lee, and S.C. Zhang, Phys. Rev. **46** 2223 (1992)

Resonant Tunneling in Quantum Hall Regime: Measurement of Fractional Charge

Vladimir J. Goldman
Department of Physics, State University of New York, Stony Brook, NY 11794-3800, U. S. A.

In experiments on resonant tunneling through a quantum antidot in the QH regime periodic conductance peaks are observed both as a function of magnetic field and back gate voltage. A combination of the two periods constitutes a measurement of the charge of the tunneling particles and implies that charge deficiency on the antidot is quantized in units of the charge of quasiparticles of the surrounding quantum Hall condensate. The experiment yields values of the electron charge 1.57×10^{-19} C = $(0.93 \pm 0.03)e$ for $v = 1$ and 2 integer QH and the quasiparticle charge 5.20×10^{-20} C = $(0.325 \pm 0.01)e$ for $v = 1/3$ fractional QH effect.

Laughlin explained [1] the exactness of the Hall conductance quantization in the IQHE [2] as a consequence of the gauge invariance of electromagnetic field combined with the quantization of charge of current carriers, the electrons. He considered a gedanken experiment where a two-dimensional electron system (2DES) forms a finite length cylinder with magnetic field B normal to its surface and additional magnetic flux Φ threaded through the cylinder parallel to its axis. Laughlin showed that if (i) disorder is sufficiently small as not to destroy the Landau quantization, (ii) the chemical potential μ lies in the mobility gap between two Landau levels, and (iii) temperature T is small compared to cyclotron energy, then adiabatic change of Φ by ϕ_0 , the flux quantum, is strictly equivalent to transfer of one electron per Landau level from one edge of the cylinder to the other. This implies that the Hall conductance of such 2DES sample is quantized exactly to $i\epsilon^2/h$, where i is the number of Landau levels below μ . This gedanken experiment was adapted to Corbino geometry and elaborated by Halperin [3]. In a seminal work [4] Laughlin related FQHE [5] at Landau level filling $v=1/(2k+1)$ (k is integer) to fractional quantization of charge of elementary charged excitations (quasiparticles) of that state in units of $e^2=i\epsilon/(2k+1)$. Halperin and Haldane [6,7] recognized that the quasiparticles can be described by fractional statistics. It has been argued [8] that fractional quantization of Hall conductance implies fractional charge of quasiparticles; however, it was subsequently recognized that quantization of Hall conductance is a property of the condensate; for example, FQHE can be understood within the composite fermion theory,[9] without explicit consideration of quasiparticles at all. Several experiments have attempted to determine the charge of quasi-particles,[10] however, their interpretation is either ambiguous or the measurement can be related to the quantization of Hall conductance. Several theoretical works considered resonant tunneling (RT) in the QHE regime,[11,12] which is, in some sense, a microscopic implementation of Laughlin's gedanken experiment. Experimental work was reported on RT in confined quantum dots and antidots in IQHE,[13,14] and more recently in FQHE [15,16]. Here we review experiments [15] on RT through states magnetically bound on a lithographically defined potential hill ('quantum antidot') in the integer and fractional QHE regime. We observed periodic RT conductance peaks both as a function of B and back gate voltage V_{BG} . We find that a combination of these two measurements for a given v QHE state constitutes a direct measurement of the charge of the tunneling particles. Our results also imply that the charge deficiency on the antidot is quantized in units of charge of the quasiparticles of surrounding QHE condensate. Using this technique we have measured the electron charge at $v=1$ and $v=2$, and the quasiparticle charge at $v=1/3$.

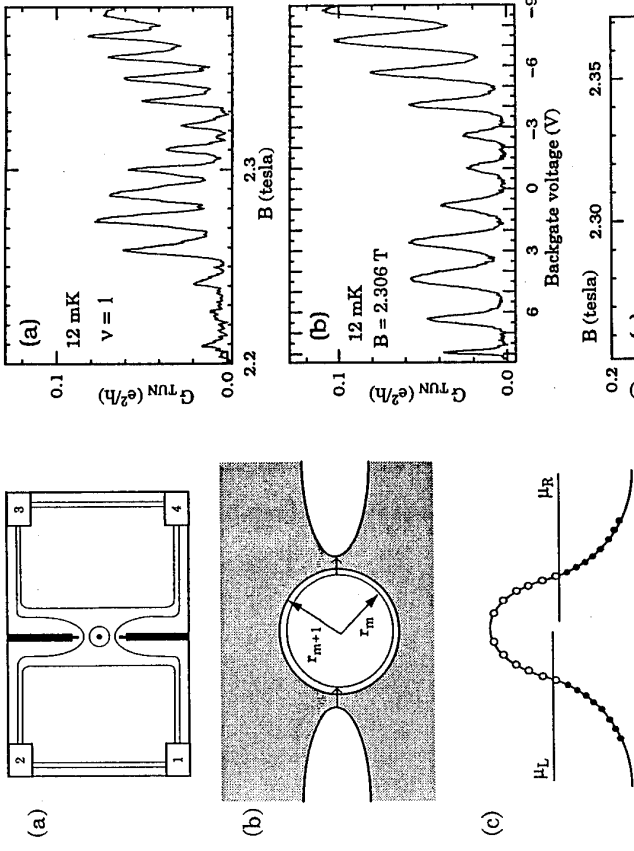


Fig. 1. (a) Illustration of the sample; numbered rectangles are ohmic contacts, black areas are front gates in etch trenches, lines are edge channels. (b) Near the antidot (potential hill) quasiparticle states are quantized; only two are shown: the highest occupied $(m+1)$ -st and the lowest unoccupied m -th. The dotted area represents QH condensate at v , two solid lines are the edge channels around the front gates. (c) Potential profile near the antidot; open circles are unoccupied states, closed circles are occupied.

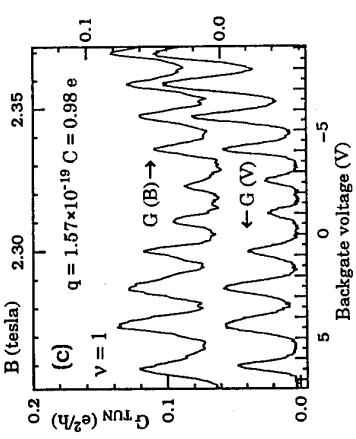


Fig. 2. Resonant tunneling conductance of electrons at $v=1$ (in the bulk). (a) $V_{BG}=2$. By combining the periods from the two data sets (a) and (b) we obtain the electron charge as discussed in the text. (c) illustrates correspondence between RT peaks vs B and V_{BG} .

Samples were fabricated from very-low disorder GaAs heterostructure material described previously [17]. The antidot-in-a-constriction geometry was defined by standard electron-beam lithography on a pre-etched mesa with ohmic contacts (Fig. 1). Sample was then chemically etched and Ag front gates were deposited in the etched trenches; samples were mounted on substrates with In, which serves as the back gate. 2DES with $n \approx 1 \times 10^{11} \text{ cm}^{-2}$ and $\mu \approx 2 \times 10^6 \text{ cm}^2/\text{Vs}$ were prepared by exposure to red light. Experiments were performed in a dilution refrigerator with sample probe wires filtered at mK T , so that total electromagnetic background at sample's contacts is $< 2 \mu\text{V}$ rms. Four-terminal magnetoresistance of the samples $R_{(2,3;1,4)}$ was measured with a lock-in amplifier with excitation $\sim 2 \mu\text{V}$.

The etched front gates and the antidot create depletion potential hills in the sample and, in quantizing B , the QHE edge channels are formed following equipotentials where the self-consistent electron density corresponds to integer or fractional v near the periphery of the undepleted 2DES, as illustrated in Fig. 1(a). In these low density, thick spacer samples it is necessary to apply considerable negative front gate voltage (-1 V) to bring the edges between the front gates and the antidot within a distance small enough so that RT conductance is measurable. This results in v between the front gates being smaller than v_B in the bulk of the sample, far from the front gates (the two front gates are biased to give the same v on either side of the antidot). Thus Fig. 1(a) illustrates $v=1$, $v_B=2$ for IQHE, or $v=1/3$, $v_B=2/5$ for FQHE. This situation (if no RT occurs) is identical to a single front gate biased to give v under it, when the rest of the sample has v_B [18]; the resistance is then given by $R_{(2,3;1,4)} = (h/e^2)(1/v - 1/v_B)$. Indeed, we do obtain these values of $R_{(2,3;1,4)}$ and use them to ascertain v . We checked v by also measuring the Hall resistance $R_{(2,4;1,3)}$ directly.

Figures 2 - 4 give the tunneling conductance G_{TUN} vs B and V_{BG} for $v=1$ and $v=1/3$. G_{TUN} was calculated from the directly measured $R_{(2,3;1,4)}$ with the quantized $(1/v - 1/v_B)$ contribution subtracted; the low B side of the $v_B=3/5$ plateau is seen in Fig. 3(a) for $B < 7.6 \text{ T}$. Both G_{TUN} vs B and G_{TUN} vs V_{BG} data display intervals of periodic RT peaks conjoined by a "phase slip". For example, phase slips are seen at 2.267 T in Fig. 2(a), at $V_{\text{BG}} \approx 0 \text{ V}$ in Fig. 2(b), at 7.62 T in Fig. 3(a), at -3.5 V in Fig. 3(b), and at 10.697 T in Fig. 4(a). Most of these phase slips are reproducible; their origin will be discussed later. The RT peaks in the G_{TUN} vs B data correspond to peaks in the G_{TUN} vs V_{BG} data, as illustrated in Figs. 2(c) and 3(c). RT peaks nearly wash out at 150 mK (50 mK) and when the ac excitation is raised to $30 \mu\text{V}$ rms ($10 \mu\text{V}$ rms) for $v=1$ ($v=1/3$); these values yield the energy quantization of quasiparticle states bound on the antidot $\sim 30 \mu\text{eV}$ for $v=1$ and $\sim 10 \mu\text{eV}$ for $v=1/3$ [19].

Figure 1(b) shows the detail of the edge states near the antidot. There are two edge channels corresponding to v going around each of the front gates; their energy spectrum is continuous where they intercept the chemical potential μ so that there is no gap for charged excitations at these edges. The states of the v edge channel around the antidot are quantized by the condition that the Aharonov-Bohm and statistical phase of the particle taken around the antidot be an integer multiple of 2π : $BS_m = m\phi_0 + \sum n_j \phi_j$ [12], where S_m is the area enclosed by m -th state and term $(\sum n_j \phi_j)/\phi_0$ represents (schematically) statistical phase due to n_j quasiparticles of species j within S_m (neglecting change in Coulomb interaction). In Fig. 1(c) we illustrate that the RT conductance measured with sufficiently small Hall voltage $\mu_L - \mu_R$ reflects tunneling of a particle from within kT of μ_L of the left edge to the lowest unoccupied quantized state on the antidot, and then to the right edge.

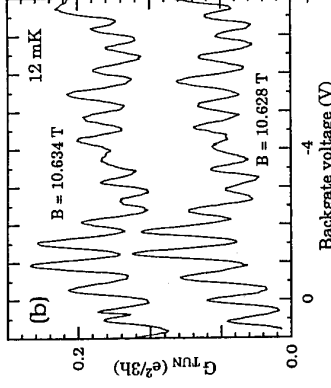
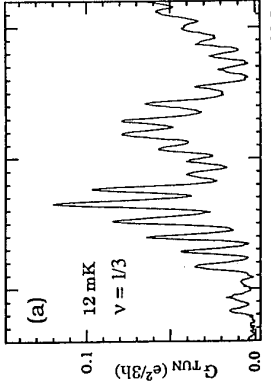
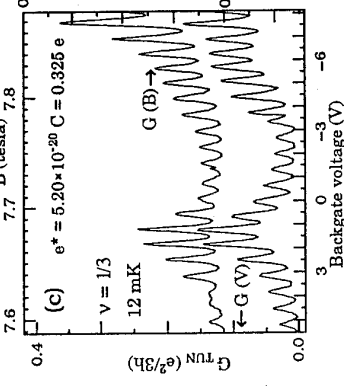
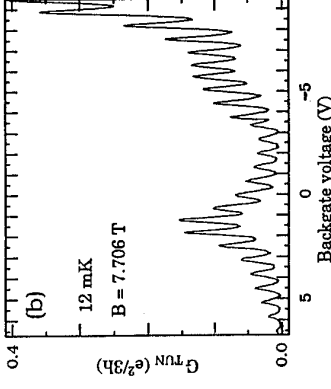
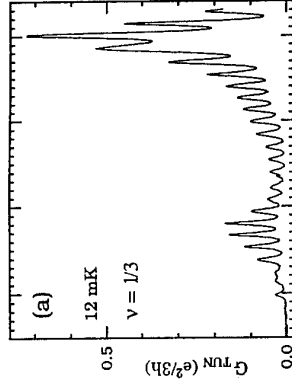


Fig. 4. Resonant tunneling conductance of quasi-electrons at $v=1/3$ ($v_B=3/5$). By combining the upper trace in (b) has conductance minimum at $V_{\text{BG}}=0$ (offset vertically by $0.08 \text{ e}^2/3\hbar$), the lower trace has conductance maximum at $V_{\text{BG}}=0$.



←
Fig. 3. Resonant tunneling conductance of quasi-electrons at $v=1/3$ ($v_B=3/5$). By combining the two data (a) and (b) we obtain the quasielectron charge as discussed in the text. (c) illustrates correspondence between RT peaks vs B and V_{BG} . $V_{\text{BG}} = 0$ in (a).

Suppose at some conditions (B^m , V_{BG}^m , front gate voltage) the lowest unoccupied quasiparticle state is aligned with μ ; then RT is possible and we observe a peak of the tunneling conductance G_{TUN} . At a fixed V_{BG} , as B is increased gradually, S_m decreases so that the product $BS_m = \phi_0$, $m+1$ -st state moves just above μ and becomes the lowest unoccupied state; satisfy $\Delta BS_m = \phi_0$. Thus ΔB is enough to move higher in energy and out of resonance. When B is raised by $\Delta B = B^{m+1} - B^m$ enough to now RT though this state becomes possible and we observe the next peak. This corresponds to addition of one ϕ_0 to within the area of the lowest unoccupied quasiparticle state S_m , as the number of quasiholes within this state increments by one, similar to the Laughlin's gettakken experiment. The area S_m is largely determined by selfconsistent electrostatics at B and front gate voltage corresponding to v ; for a small variation of B the area oscillates with amplitude $(\Delta B)S_m$. However, once every several periods, in order to minimize the selfconsistent Coulomb potential, a charged particle is added to within S_m so that the charge within S_m changes without corresponding change in flux; this results in a phase slip of the RT period. Σn_{ϕ_j} can change only by a multiple of ϕ_0 [12], and therefore change in statistical interaction does not result in a phase slip.

Similarly, when V_{BG} is decreased at a fixed B , peaks in G_{TUN} occur periodically when a quasielectron is removed from the m -th state, that is, every $\Delta V_{BG} = q/CS_m$, [20] where q is the charge of the quasiparticle and $C = \epsilon_0 A / d_{BG}$ is the capacitance per unit area between the compressible 2DES and the back gate separated by $d_{BG} = 428 \pm 5 \mu\text{m}$ of GaAs ($\epsilon = 13.1$). Here we say "compressible 2DES" since the quasiparticle is removed from an edge, where there is no gap and the action of the remote back gate on the bulk 2DES is very accurately described by a parallel plate capacitor model, even in the QHE regime. This is so because the QHE gap in the bulk is a mobility gap, so that there is nonzero density of localized states, and the occupation of these localized states can change, as required by electrostatics, under adiabatic change of the back gate voltage [21]. We can combine the above expressions for ΔB and ΔV_{BG} to obtain the unit of quantization of the charge in the QHE state at v :

$$q = (\epsilon_0 \phi_0 \Delta V_{BG}) / (q \nu d_{BG} \Delta B), \quad (1)$$

q is an integer giving the number of quasiparticles transferred from the antidot per added flux quantum at v ; for example, $p_v = 1$ for $v = 1, 1/3$ and $1/5$, $p_v = 2$ for $v = 2, 2/5$ and $2/9$, and so on. [22] Thus determined quasiparticle charges for several integer and fractional QHE states are: $1.55 \times 10^{-19} \text{ C} = (0.97 \pm 0.04)\phi_0$ at $v = 2$, $1.57 \times 10^{-19} \text{ C} = (0.98 \pm 0.03)\phi_0$ at $v = 1$, $5.20 \times 10^{-20} \text{ C} = (0.325 \pm 0.01)\phi_0$ at $v = 1/3$ (Fig. 3), and $5.3 \times 10^{-20} \text{ C} = (0.33 \pm 0.02)\phi_0$ at $v = 1/5$ (Fig. 4). All values are reasonably close to the expected values, however there appears to be a systematic error: experimental values are smaller than expected by $\sim 2\%$. In conclusion we would like to point out that even without reference to precise value of the capacitive coupling to the back gate, these experiments still measure the quasiparticle charge at $v = 1/3$ in units of the electron charge at $v = 1$: $e^* = (\Delta B^{(1)} \Delta V_{BG}^{(1)}) / (\Delta B^{(1/3)} \Delta V_{BG}^{(1)}) = 0.331 \pm 0.006$ from the data of Figs. 2 and 3. Also note that the data of Figs. 3 and 4 yield the same (within the experimental uncertainty) quasiparticle charge for significantly different $B \sim 8 \text{ T}$ and $\sim 11 \text{ T}$.

We are grateful to Bo Su for assistance in electron beam lithography and experiments, to M. Shayegan for MBE material and to A. S. Goldhaber, J. K. Jain, S. A. Kivelson, and K. K. Likharev for interesting discussions. This work was supported in part by NSF under Grant No. DMR-9318749 and by ONR under Grant No. N0014-93-1-1090.

References and Notes:

1. R. B. Laughlin, Phys. Rev. B **23**, 5632 (1981).
2. K. von Klitzing, G. Dorda, and M. Pepper, Phys. Rev. Lett. **45**, 494 (1980).
3. B. I. Halperin, Phys. Rev. B **25**, 2185 (1982).
4. R. B. Laughlin, Phys. Rev. Lett. **50**, 1395 (1983).
5. D. C. Tsui, H. L. Stormer, and A. C. Gossard, Phys. Rev. Lett. **48**, 1559 (1982).
6. B. I. Halperin, Phys. Rev. Lett. **52**, 1583 (1984).
7. F. D. M. Haldane, Phys. Rev. Lett. **51**, 605 (1983).
8. See, e.g., R. B. Laughlin, Int. J. Mod. Phys. B **5**, 1507 (1991).
9. J. K. Jain, Phys. Rev. Lett. **63**, 199 (1989); Science **266**, 1199 (1994).
10. R. G. Clark *et al.*, Phys. Rev. Lett. **60**, 1747 (1988); J. A. Simmons *et al.*, *ibid* **63**, 1731 (1989); A. M. Chang and J. E. Cunningham, Surf. Sci. **229**, 216 (1990).
11. J. K. Jain and S. A. Kivelson, Phys. Rev. Lett. **60**, 1542 (1988); S. A. Kivelson and V. L. Pokrovsky, Phys. Rev. B **40**, 1373 (1989); S. A. Kivelson, Phys. Rev. Lett. **65**, 3369 (1990); S. Feng and S. C. Zhang, Phys. Rev. Lett. **71**, 3533 (1993).
12. J. K. Jain, S. A. Kivelson, and D. J. Thouless, Phys. Rev. Lett. **71**, 3003 (1993).
13. B. J. van Wees *et al.*, Phys. Rev. Lett. **62**, 2523 (1989).
14. J. A. Simmons *et al.*, Phys. Rev. B **44**, 12 933 (1991); P. J. Simpson *et al.*, Surf. Sci. **305**, 453 (1994). We note that there is no Coulomb blockade for RT through an antidot since there is no isolated region that is being charged.
15. V. J. Goldman and B. Su, Science **267**, 1010 (1995).
16. C. J. B. Ford *et al.*, J. Phys. Cond. Matter **6**, L725 (1994).
17. V. J. Goldman, J. K. Jain, and M. Shayegan, Phys. Rev. Lett. **65**, 907 (1990).
18. R. J. Haug, A. H. MacDonald, P. Streda, and K. von Klitzing, Phys. Rev. Lett. **61**, 2797 (1988); S. Washburn, A. B. Fowler, H. Schmid, and D. Kern, *ibid* **61**, 2801 (1988); X.G. Wen, Int. J. Mod. Phys. B **6**, 1711 (1992).
19. The energy spacing of states bound on the antidot depends sensitively on the selfconsist-ent confining potential; therefore, the fact that the ratio of energy spacings is $\sim 3:1$ appears to be fortuitous. For our device $m \approx 500$, $r_m \approx 300 \text{ nm}$, $r_m + r_m \approx 0.3 \text{ nm}$, $E_m \approx 10^5 \text{ V/m}$.
20. For parallel plate capacitor formed by the 2DES and the back gate the charge induced per unit area is $Q = q \delta n = CV_{BG}$, where δn is the induced change in particle concentration in 2DES. The charge deficiency within the area of the antidot S_m is equal to QS_m ; this result for charge deficiency is exact in classical electrostatics model problems of either a circular hole or a narrow slit in a conducting plane in uniform external field (L.D. Landau and E.M. Lifshitz, "Electrodynamics of Continuous Media"). Thus, $q \delta n S_m = CV_{BG} S_m$, and for ΔV_{BG} corresponding to one particle within the area of antidot ($\delta n S_m = 1$) we obtain $\Delta V_{BG} = q/CS_m$.
21. $V_{BG} = 1 \text{ V}$ is a small perturbation, it takes $V_{BG} = 500 \text{ V}$ to deplete the 2DES.
22. For hierarchy of QHE states, J.K.Jain and V.J.Goldman, Phys. Rev. B **45**, 1255 (1992).

Composite Fermion Mean Field Theory and Fractionally Quantized Hall Conductances

George Kirczenow and Brad L. Johnson
Department of Physics, Simon Fraser University, Burnaby, B.C., Canada, V5A 1S6.

Abstract

We present a mean field theory of composite fermion edge channel transport in the fractional and integer quantum Hall regimes. An expression relating the electro-chemical potentials of composite fermions at the edges of a sample to those of the corresponding electrons is obtained and a plausible form is assumed for the composite fermion Landau level energies near the edges. The theory yields the observed fractionally quantized Hall conductances and also explains other experimental results. We also discuss briefly some experiments that are relevant to the question whether fractional edge states in real devices should be described as Fermi or Luttinger liquids.

Introduction

The composite fermion theory introduced by Jain [1] and developed further by Lopez and Fradkin [2], and by Halperin, Lee and Read [3] has been remarkably successful in explaining and predicting many interesting phenomena that occur in two-dimensional electronic systems at high magnetic fields. It has provided a unified explanation [1] of the integer [4] and fractional [5] quantum Hall effects, and a systematic understanding of the relative stabilities of the fractional quantum Hall phases [1] that are observed experimentally. It also explains [1] the scaling with magnetic field of the energy gaps that are observed [6] in the fractional quantum Hall regime. Another remarkable result [2] of the composite fermion theory is that at the Landau level filling factor $\nu = 1/2$, where the effective magnetic field experienced by the composite fermions vanishes, the lowest spin-polarized electron Landau level has many features in common with systems of electrons at zero magnetic field. For $\nu = 1/2$ it behaves somewhat like a system of quasi-classical electrons at very low magnetic fields. These predictions have been confirmed experimentally. [7]

Since the fractional quantum Hall effect can be viewed as an integer quantum Hall effect of composite fermions, [1] an important question has been whether it is possible to construct a transport theory of the fractional quantum Hall effect based on composite fermion edge states, and thus to generalize the very successful edge state theories of the integer quantum Hall effect [8] to the fractional quantum Hall regime. Such a theory of composite fermion edge states has recently been developed at the level of mean field theory and the main ideas are outlined in this talk.

Composite Fermion Mean Field Theory and Fractionally Quantized Hall Conductances

In the Chern-Simons version of the composite fermion theory, a singular gauge transformation is performed which has the effect of attaching a tube of fictitious gauge flux carrying an even number of flux quanta to each electron. [1]-[3] The composite particles thus formed obey fermi statistics and are referred to as "composite fermions." [1] Many of the predictions of composite fermion theory can be understood within a mean field description in which the interactions between composite fermions that are due to the vector potentials associated with the tubes of gauge flux attached to the electrons, are replaced by interactions with a fictitious average magnetic field and a

fictitious electric field. The fictitious magnetic field [1]-[3] is given by $\mathbf{B}_g = -mn\hat{\mathbf{B}}h/e = -mv\mathbf{B}$ where m is the (even) number of quanta of gauge flux carried by each composite fermion, n is the two-dimensional electron density, $v = nh/(eB)$ is the Landau level filling parameter, and $\hat{\mathbf{B}}$ is the unit vector in the direction of the true magnetic field \mathbf{B} . Thus the composite fermions interact with a total effective magnetic field $\mathbf{B}_{\text{eff}} = \mathbf{B} + \mathbf{B}_g$. The fictitious electric field [9] is given by $\mathbf{E}_g = -(J \times \hat{\mathbf{B}})mh/e^2$, where J is the two-dimensional electric current density.

We assume that the electron density is slowly varying with position and that, for v in the vicinity of $1/m$, the composite fermion Landau level energies behave qualitatively like

$$\varepsilon_{m,r} = \left(r + \frac{1}{2}\right)\hbar|B_{\text{eff}}|/m^* + W. \quad (1)$$

Here $r = 0, 1, 2, \dots$ and W is the position-dependent composite fermion effective potential energy, m^* is the composite fermion effective mass. Equation (1) is believed to be a good description of the composite fermion Landau level structure in uniform systems [1] and yields edge states that propagate in the direction consistent with experiment [10]. The assumed behavior of the composite fermion Landau levels near an edge is shown schematically in Fig. 1 for two cases of interest.

The composite fermion charge density is equal everywhere to the electron charge density because the transformation to composite fermions is a gauge transformation. Therefore the electric field felt by the composite fermions is the same as that felt by electrons except for an additional term E_g that does not occur in the ordinary electron picture. This term contributes to the difference between the effective electrochemical potentials μ^* of composite fermions at different edges of a current-carrying Hall bar but not to the corresponding electron electrochemical potentials μ . Thus

$$\mu_i^* - \mu_j^* = \mu_i - \mu_j + \int_j e\mathbf{E}_g \cdot d\mathbf{r} = \mu_i - \mu_j - \int_j (mh/e) \mathbf{J} \cdot \hat{\mathbf{B}} \times d\mathbf{r}, \quad (2)$$

where i and j label different edges of the Hall bar. Since the charge of a composite fermion is $-e$, the electric current carried through a Hall bar at zero temperature by a particular composite fermion Landau level (m,r) can be written

$$I_{m,r} = -\frac{e}{h} \int \frac{\partial \varepsilon_{m,r}}{\partial k} dk = -\frac{e}{h} \int d\varepsilon_{m,r} = -\frac{e}{h} \Delta \varepsilon_{m,r}, \quad (3)$$

as in edge state theories of the integer quantum Hall effect. [8] The integrals are over occupied states. For the type I edge states shown in Fig. 1, this means that $I_{m,r} = -e(\mu^* W_m)/h$. But since $(\mu^* W_m)$ is the local "Fermi energy," it is plausible that at fixed \mathbf{B} it should depend only on the local density where $\mathbf{B}_{\text{eff}} = 0$, which is independent of μ^* since $\mathbf{B}_{\text{eff}} = 0$ where $v = 1/m$. Thus $\mu^* W_m$

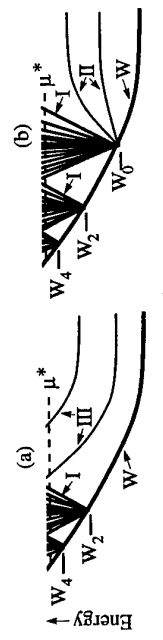


Fig.1 Schematic drawing of composite fermion Landau level structure near the edge for \mathbf{B}_{eff} in the bulk parallel (case (a)) and antiparallel (case (b)) to \mathbf{B} . The apex of each "fan" of energy levels occurs where $v = 1/m$, and there $\epsilon_{m,r} = W = W_H$. The three different types of composite fermion edge modes are labelled I, II and III. $R_H = 2e^2/h$ and $2e^2/(3h)$ in cases (a) and (b) respectively.

(and hence $I_{m,r}$) is independent of μ^* . This means that the current carried by a type I mode does not change when the edge electrochemical potential changes. That is, type I modes at edges with well-defined composite fermion electrochemical potentials are "silent."

Now consider a sample with \mathbf{B}_{eff} parallel to \mathbf{B} in the bulk. The Landau levels present are of types I and II, as is illustrated in Fig. 1(a). From equation (3), the current carried by a type III Landau level is $I_{m,r} = -e\Delta\mu^*/h$ where $\Delta\mu^*$ is the difference in composite fermion electrochemical potential between the sample. Since type I modes are silent, the net current through the sample is thus $I = -ep\Delta\mu^*/h$, where p is the number of composite fermion Landau levels that are occupied in the bulk. To compare this result with experiments one must eliminate the composite fermion electrochemical potential difference $\Delta\mu^*$ in terms of the corresponding electron electrochemical potential difference $\Delta\mu$, since the latter quantity is the difference between the electrochemical potentials of the electron reservoirs attached to the sample that is actually measured. Using equation (2) which takes the form $\Delta\mu^* = \Delta\mu + mh/e$, where m is the number of quanta of gauge flux per composite fermion in the bulk, this yields $I = -e\Delta\mu/(mp+1)h$, or a Hall conductance $G_H = -eh/\Delta\mu = e^2p/(mp+1)h$. Notice that the fractional (as opposed to integer) quantized value of the Hall conductance arises from the fact that the effective electrochemical potentials of composite fermions differ from those of electrons. The case where \mathbf{B}_{eff} is antiparallel to \mathbf{B} in the bulk is analyzed similarly (using the above result that $\mu^* - W_m$ is independent of μ^*) to yield $G_H = e^2p/(mp-1)h$.

The values $G_H = e^2p/(mp\pm 1)h$ of the Hall conductances thus obtained are just those that are found experimentally for the Landau level filling fractions $v=p/(mp\pm 1)$ that correspond to p filled composite fermion Landau levels in the bulk. That is, these results agree with experiments.

Are Fermi or Luttinger Liquids Present at the Edges of Fractional Quantum Hall Devices?

An important question that needs to be resolved experimentally is whether the edge states in real fractional quantum Hall devices constitute a Fermi liquid, as is suggested by the present mean field theory, or a chiral Luttinger liquid as has frequently been assumed in the literature. [1]

Experiments on selective population and detection of fractional edge channels [12] indicate that more than one conducting mode is present at the edge in $v = 1$ bulk systems, in contrast to the prediction of the chiral Luttinger liquid formalism that there should be only one mode present. These experiments are, however, in agreement with the present composite fermion mean field theory. [10] Also the observation of intermediate fractional plateaus (between $G = ve^2/h$ and $G = 0$, where v is the Landau level filling fraction in the bulk) in the two-terminal conductance G of point contacts [13] has not been explained by the Luttinger liquid theories, but has been explained by the composite fermion mean field theory. [10] However, these experiments did not probe the nature of the quasi-particles at the edge directly.

Measurements of the temperature dependence of the conductance of a point contact can be a direct probe, and experiments on disordered point contacts [14] have yielded results consistent with the predictions of chiral Luttinger liquid theory. For example, the off-resonance two-terminal conductance of a point contact was observed to decrease with decreasing temperature as a power of the temperature. However, these experiments do not rule out the possibility that the fractional edge states may be a Fermi liquid because the observed behavior of the conductance may have been due to the internal electronic structure of the point contact and not to exotic physics of the fractional edge states. For example, conduction via a pinned one-dimensional Wigner crystal,[15] or via one or more Coulomb-blockaded quantum dots[16] (either of which can plausibly be present in a disordered point contact at low electron densities) can also result in the conductance decreasing at low

temperatures as a power of the temperature. Thus in order to establish definitively whether fractional edge states are Fermi or Luttinger liquids, further experiments are clearly needed. It would be particularly interesting to know the temperature dependence of the Aharonov-Bohm conductance resonances of a ballistic nanoscale constriction containing an antidot in the fractional regime. These resonances have already been observed. [13] Their physical origin implies that their temperature dependence will reflect the nature of the quasi-particles in the fractional edge states. A composite fermion mean field theory of them and related phenomena will be presented elsewhere. [17] Preliminary measurements of their temperature dependence [18] appear to be consistent with a Fermi liquid picture of fractional edge states, but further experimental work is needed to determine how they behave at the lowest temperatures.

We wish to thank C. J. B. Ford, A. S. Sachrajda, A. M. Chang, J. Frost, D. Loss and M. P. A. Fisher for interesting discussions.

References:

- [1] J. K. Jain, Phys. Rev. Lett. **63**, 199 (1989); Science **266**, 1199 (1994).
- [2] A. Lopez and E. Fradkin, Phys. Rev. B**44**, 5246 (1991).
- [3] B. I. Halperin, P. A. Lee and N. Read, Phys. Rev. B**47**, 7312 (1993).
- [4] K. von Klitzing, G. Dorda and M. Pepper, Phys. Rev. Lett. **45**, 494 (1980).
- [5] D. C. Tsui, H. L. Störmer and A. C. Gossard, Phys. Rev. Lett. **48**, 1559 (1982).
- [6] R. R. Du *et al.*, Phys. Rev. Lett. **70**, 2944 (1993); I. V. Kukushkin *et al.*, Phys. Rev. Lett. **72**, 736 (1994); H. C. Manoharan *et al.*, Phys. Rev. Lett. **73**, 3270 (1994); D. R. Leadley *et al.*, Phys. Rev. Lett. **72**, 1906 (1994).
- [7] R. L. Willett *et al.*, Phys. Rev. Lett. **71**, 3846 (1993); W. Kang *et al.*, Phys. Rev. Lett. **71**, 3850 (1993); V. J. Goldman *et al.*, Phys. Rev. Lett. **72**, 2065 (1994).
- [8] B. I. Halperin, Phys. Rev. B**25**, 2185 (1982); P. Streda, J. Kucera and A. H. MacDonald, Phys. Rev. Lett. **59**, 1973 (1987); J. K. Jain and S. A. Kivelson, Phys. Rev. Lett. **60**, 1542 (1988); M. Büttiker, Phys. Rev. B**38**, 9375 (1988).
- [9] S. C. Zhang, H. Hansson and S. A. Kivelson, Phys. Rev. Lett. **62**, 82 (1989); S. C. Zhang, Int. J. Mod. Phys. B, **6**, 25 (1992); B. Rejaei and C. W. J. Beenakker, Phys. Rev. B**43**, 11392 (1991), Phys. Rev. B**46**, 15566 (1992); A. S. Goldhaber and J. K. Jain, Phys. Lett. A**199**, 267 (1995).
- [10] G. Kirczenow and B. L. Johnson, paper cond-mat 950238, www site http://xxx.lanl.gov/
- [11] See C. L. Kane and M. P. A. Fisher, Phys. Rev. B**51**, 3449 (1995) and references therein.
- [12] L. P. Kouwenhoven, *et al.*, Phys. Rev. Lett. **64**, 685 (1990); A. M. Chang and J. F. Cunningham, Phys. Rev. Lett. **69**, 2114 (1992).
- [13] C. J. B. Ford, *et al.*, J. of Phys. Condensed Matter **6**, L725 (1994); V. J. Goldman and B. Su, Science **267**, 1010 (1995).
- [14] F. P. Milliken, C. P. Umbach and R. A. Webb, Physics Today Vol. **47**, No 6, p. 21 (1994).
- [15] L.I.Giazmann, I. M. Ruzin and B. I. Shklovskii, Phys. Rev. B**55**, 8454 (1992).
- [16] K.A.Mateev, L.I.Giazmann and H.U.Baranger; A. Furusaki and K. A. Matveev, preprints.
- [17] G. Kirczenow, unpublished.
- [18] C. J. B. Ford, private communication.

THE AHARONOV-BOHM EFFECT IN THE INTERACTIONAL QUANTUM HALL REGIME

J.D.F. Franklin, I. Zaller, C.J.B. Ford, P.J. Simpson, J.E.F. Frost, D.A. Ritchie, M.Y. Simmons and M. Pepper
Concordia Laboratory, University of Cambridge Madingley Road, Cambridge, CB3 0HE, UK

We have investigated experimentally resonant tunnelling through single-particle states formed around an antidot by a magnetic field, in the fractional quantum Hall regime. For $1/3$ filling factor around the antidot, Aharonov-Bohm oscillations are observed with the same magnetic field period as in the integer quantum Hall regime. All our measurements are consistent with our quasiparticles of fractional charge $e^*/3$. However, the results are also consistent with particles of any charge $(\mathbb{Z} e^*)$ as the system must rearrange every time the flux enclosed increases by \hbar/e .

The Fractional Quantum Hall Effect (FQHE) is a much-studied many-body effect [1]. Complex electron-electron interactions give rise to a quantized Hall resistance, and to oscillations in the longitudinal resistance of a high-mobility two-dimensional electron gas (2DEG). For particular fractional values $p/(2p+1)$ of the filling factor ν (the ratio of the number of conduction electrons to magnetic flux quanta \hbar/e), where p is an integer, we can change the basis set of the quasi-particles, having fractional charge $e^* = e/(2p+1)$ [2-4]. For example

states constructed to quench the Coulomb interaction

$p = 1$ implies quasiparticles of charge $e^* = e/3$. Observation of fractional Hall plateaux is not, however, direct evidence for the existence of such quasiparticles [5-7]. It was suggested [5] that the Aharonov-Bohm (AB) effect might be used to determine e^* , since the single particle (SP) states around an antidot might be expected to enclose multiples of a flux quantum \hbar/e instead of \hbar/e . At first this appeared to be experimentally supported [8], but then it was pointed out that gauge invariance enforces a maximum period of \hbar/e [6,9]. Thus current theories predict an \hbar/e period in resonant tunnelling through an SP state in the FQHE regime for fractionally charged quasiparticles. A period of \hbar/e would be inconsistent with AB of electrons in a single-particle picture.

Further, Coulomb blockade of fractionally charged quasiparticles localized around the antidot might be expected to have an energy scale e^2/C_d , C_d being the capacitance of the antidot states to everything else [9]. Alternatively the SP energy spacing should scale as $E_r e^2/B$ where E_r is the slope of the potential at the SP state. The h/e^2 periodicity might obtain only if gauge invariance could be broken by particle picture.

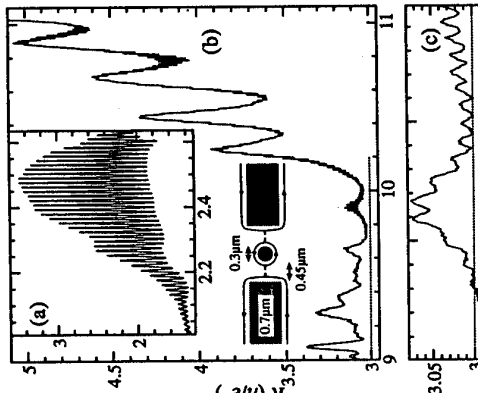
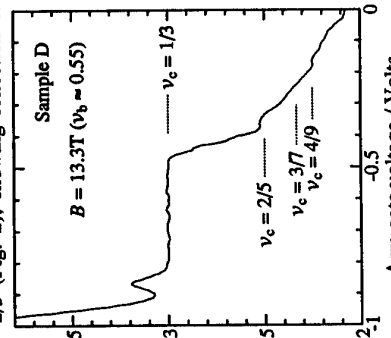


Figure 1. Aharonov-Bohm oscillations in the (a) integer and fractional (b) QHE regimes. (c) shows an enlargement of the $3\hbar/e^2$ plateau region similar to that in (b). Dotted lines indicate the plateau (Sample A).

shifting the system sufficiently adiabatically on a timescale apparently unobtainably short [6]. In this paper we present measurements of the period of AB oscillations in the integer and fractional regimes. We show that the period in magnetic field is the same in both regimes for four different devices. This period is consistent with being \hbar/e from the defined size of the antidots. We have also studied the period in gate voltage in the two regimes [10], and deduced single-particle energy-level spacings from temperature dependences and DC bias measurements. Our device consists of a patterned 2DEG formed in a GaAs/Al_xGa_{1-x}As heterostructure. An antidot (potential hump) is formed by a central 0.3 μm diameter gate, contacted separately using a special technique [11]. The macroscopic edge states are brought close enough to tunnel to the central states at two constrictions, the widths of which are determined by side-gate biases and magnetic depopulation (inset Fig. 1). Thus resonant tunnelling can take place through the ladder of SF states, each enclosing an integer number of \hbar/e magnetic flux quanta, allowing backscattering from one edge to the other and giving rise to oscillations in the resistance (Fig. 1) [11].

The carrier concentration n_s after illumination of the wafers used was $1-2 \times 10^{15} \text{ m}^{-2}$ with mobilities $150-300 \text{ m}^2 \text{ V}^{-1} \text{ s}^{-1}$. The depth to the 2DEG was 100 nm (devices A and B), 300 nm (device C) and 170 nm (device D). Four-terminal measurements were made using standard ac techniques in a dilution refrigerator, at a base electron temperature of about 30mK (verified by a substantial temperature dependence down to base). A constant current of 1nA (0.03nA) in the integer (fractional) regime was used, low enough to avoid electron heating.

We have compared the AB oscillations in the FQHE and IQHE regimes (Fig. 1). In the fractional regime, the filling factor in the bulk, $\nu_b = 2/3$, and that in the constrictions, $\nu_c = 1/3$. We can calculate the number of edge states propagating through the wider constriction in the IQHE from $\nu_c = \hbar/e^2R$, where R is the two-terminal longitudinal resistance [12], and the result is also found to hold in the FQHE. The oscillations can be seen to be rising off, and associated with, a well-defined $\nu_c = 1/3$ plateau indicating resonant reflection through a $\nu = 1/3$ state encircling the antidot. We can also, in some cases, see well-defined plateaux at other values, corresponding to $\nu_c = 2/5$ and higher while keeping $\nu_b = 2/3$ (Fig. 2), showing reflection of fractional edge states [13]. Two other processes can also take place: resonant transmission through inter-edge state scattering, presumably suppressed, and transmission through intra-edge state scattering. Each, however, probes SP resonant tunnelling via a magnetically bound state at the Fermi energy.



If v_c is an integer, there is one electron per state. Figure 2. Plateaux due to reflection of fractional edge states, for one constriction.

its predecessor. From counting electrons, we get $\Delta V_g = N/eC_g$, where C_g is the capacitance of one state to the metallised dot, and N is the number of Landau levels affected by the dot. From counting states we get $\Delta V_g = n_e \Delta A e/C_g$, which is equivalent in the integer regime. From $B\Delta A = h/e$ we get $\Delta V_g \propto V_b$, and by modelling of the electrostatics, even without self-consistency, one arrives at a figure within 1.5% of the experimental value. More accuracy is not expected due to uncertainties in the lithography. Counting states is no longer equivalent to counting electrons in the fractional regime however: one might expect CB of an integer number of electrons around the dot, leading to a difference between state-counting and electron-counting arguments. However, in this case the Fermi sea is connected and interacting, so normal CB arguments do not apply. As an aid to visualisation we present a qualitative interacting-electron picture (Fig. 4). Let us populate one in three of the available SP states ($v_c = 1/3$) with electrons. Self-consistent interaction processes force them to have a complicated many-body wavefunction, which we represent as a particular pattern of occupation relative to the applied potential. Smoothly changing the conditions such that the system moves by one single-particle state causes the electrons to rearrange themselves self-consistently to recover the original pattern of occupation on an ultra-short timescale [6], since this is the lowest energy state. Thus the periodicity is that of states, one-third of that expected from electron-counting, and the h/e period is regained.

One can thus describe the observed phenomena in three ways. The most convenient basis set is that of charge e^* quasiparticles with fractional statistics [3]. The formalism expressed in terms of charge e^* composite fermions will of course also give the same results [3,4]. From our simple picture one can see that *any* (quasi-)particles of charge $> e^*$ will give the same results, and therefore it is impossible to differentiate between formalisms with such experiments.

The SP energy-level spacing ΔE should vary as $V_b \propto 1/B$. Temperature dependence and DC bias results agree that ΔE is reduced by a factor of ~ 3 between integer and fractional regimes.

DC biasing in the integer (fractional) regime gave $\Delta E = 148 \mu\text{eV}$ ($46 \mu\text{eV}$). The temperature at which the amplitude of the oscillations (as calculated from the amplitude under the h/e Fourier peak) died to half its base value was $250 \pm 10 \text{ mK}$ ($60 \pm 10 \text{ mK}$); the magnetic field had changed by a factor of 3.1. The discrepancy may be due to the difficulty in calibrating the low electron temperatures. There is a good fit if A is a stable configuration then so is B, but not C.

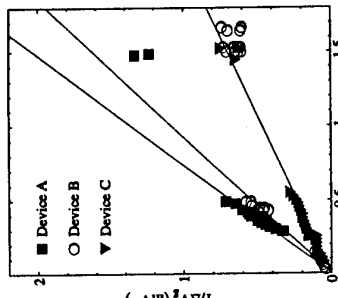


Figure 3. $1/\Delta V_g$ versus $1/V_b$ for three devices. The straight lines are fits through zero to the low-field data. Self-consistent interaction processes force them to have a complicated many-body wavefunction, which we represent as a particular pattern of occupation relative to the applied potential. Smoothly changing the conditions such that the system moves by one single-particle state causes the electrons to rearrange themselves self-consistently to recover the original pattern of occupation on an ultra-short timescale [6], since this is the lowest energy state. Thus the periodicity is that of states, one-third of that expected from electron-counting, and the h/e period is regained.

One can thus describe the observed phenomena in three ways. The most convenient basis set is that of charge e^* quasiparticles with fractional statistics [3]. The formalism expressed in terms of charge e^* composite fermions will of course also give the same results [3,4]. From our simple picture one can see that *any* (quasi-)particles of charge $> e^*$ will give the same results, and therefore it is impossible to differentiate between formalisms with such experiments.

The SP energy-level spacing ΔE should vary as $V_b \propto 1/B$. Temperature dependence and DC bias results agree that ΔE is reduced by a factor of ~ 3 between integer and fractional regimes. DC biasing in the integer (fractional) regime gave $\Delta E = 148 \mu\text{eV}$ ($46 \mu\text{eV}$). The temperature at which the amplitude of the oscillations (as calculated from the amplitude under the h/e Fourier peak) died to half its base value was $250 \pm 10 \text{ mK}$ ($60 \pm 10 \text{ mK}$); the magnetic field had changed by a factor of 3.1. The discrepancy may be due to the difficulty in calibrating the low electron temperatures. There is a good fit if A is a stable configuration then so is B, but not C.

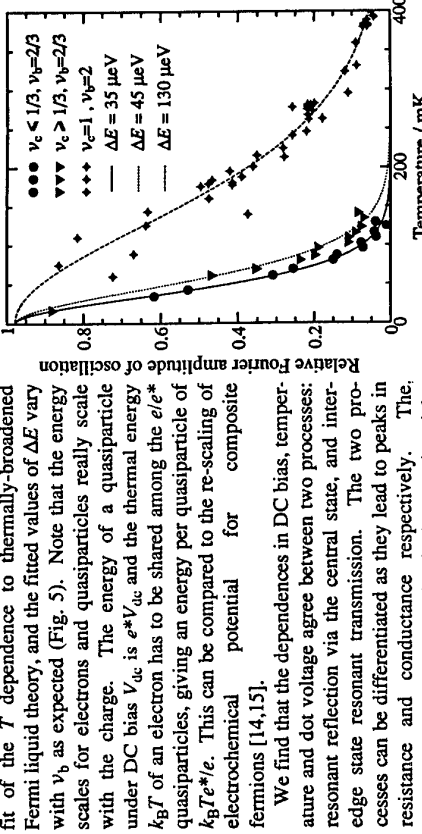


Figure 5. Temperature dependence of the relative Fourier amplitude of oscillations. The curves are labeled with symbols corresponding to the legend in the top right: $v_c < 1/3$, $v_c > 1/3$, $v_c = 1/3$, $v_c = 2/3$, $v_c = 1$, $v_c = 2$, $\Delta E = 35 \mu\text{eV}$, $\Delta E = 45 \mu\text{eV}$, and $\Delta E = 130 \mu\text{eV}$. We find that the dependences in DC bias, temperature and dot voltage agree between two processes: resonant reflection via the central state, and inter-edge state resonant transmission. The two processes can be differentiated as they lead to peaks in resistance and conductance respectively. The, perhaps surprising, conclusion is that quasiparticles can tunnel through a barrier in the latter case, perhaps because the quasiparticle state is no longer completely localised, and hence the charge on it is no longer absolutely quantized in units of e .

We note that after completion of this work Goldman and Su published similar results [16] that complement ours, based on calculating e^* from the known capacitance to a back-gate. We have now confirmed their results. This method allows one to add single electrons or quasiparticles to the region where $v = v_c$. However, as soon as the charge has changed by e^* , the system relaxes again as discussed above. Thus even this technique, which appears to measure e^* , only measures the filling factor of the region to which particles are added. We thank M. Büttiker, B.I. Halperin, G. Kirczenow, D.R. Mace, C.H.W. Barnes and M. Yosefin for helpful discussions, and acknowledge support from the UK EPSRC and Trinity College (I2).

References

- [1] D.C. Tsui, H.L. Stormer and A.C. Gossard, Phys. Rev. Lett. **48**, 1559 (1982).
- [2] R.B. Laughlin, Phys. Rev. Lett. **50**, 1395 (1983); B.I. Halperin, Phys. Rev. Lett. **52**, 1583 (1984).
- [3] J.K. Jain, Adv. in Phys. **41**, 105 (1992).
- [4] B.I. Halperin, P.A. Lee and N. Read, Phys. Rev. **B47**, 7312 (1993).
- [5] S.A. Kivelson and V.L. Pokrovsky, Phys. Rev. **B40**, 1373 (1989).
- [6] D.J. Thouless and Y. Gefen, Phys. Rev. Lett. **66**, 806 (1991).
- [7] J.K. Jain, Phys. Rev. Lett. **63**, 199 (1989).
- [8] J.A. Simmonds *et al.*, Phys. Rev. Lett. **63**, 1731 (1989).
- [9] P.A. Lee, Phys. Rev. Lett. **65**, 2206 (1990).
- [10] C.J.B. Ford *et al.*, J. Phys.: Condens. Matter **6**, 1725 (1994).
- [11] P.J. Simpson *et al.*, Appl. Phys. Lett. **63**, 3191 (1993); C.J.B. Ford *et al.*, Phys. Rev. **B49**, 17456 (1994).
- [12] M. Büttiker, Phys. Rev. **B38**, 9375 (1988).
- [13] L.P. Kouwenhoven *et al.*, Phys. Rev. Lett. **64**, 685 (1990).
- [14] G. Kirczenow and B.L. Johnson (Phys. Rev. B, to be published).
- [15] A.S. Goldhaber and J.K. Jain, 1995, paper cond-mat/9501080 at e-print archive cond-mat@xxx.lanl.gov.
- [16] V.J. Goldman and B. Su, Science **267**, 1010 (1995).

Roton in Gap Excitations of the
 $\nu=1/3$ Fractional Quantum Hall State

A. Pinczuk, B.S. Dennis, Song He, L.L. Sohn,
 L.N. Pfeiffer and K.W. West
 AT&T Bell Laboratories
 Murray Hill, NJ 07974 U.S.A.

Resonant inelastic light scattering experiments in the regime of the fractional quantum Hall state at $\nu=1/3$ have revealed a very sharp low energy (~ 1 meV) line that was interpreted as a $q=0$ excitation of the incompressible fluid [1]. The modes are constructed from intra-Landau level excitations and represent gaps associated with the FQHE. Such measurement gives evidence that the light scattering method could access the low energy excitations that emerge from the 2D electron gas when it condenses into highly correlated many-body ground states.

In the resonant light scattering experiments at $\nu=1/3$ reported here we have achieved a much greater contrast between the light scattering signal and the luminescence background. In these results we find, in addition to $q=0$ modes around $\Delta(0)$, another band at lower energy ($\sim 1/2 \Delta(0)$). The peak intensity of this band displays the temperature and field dependence that characterize the FQHE. We interpret this band as the critical point in the density of states of gap excitations due to the well-known roton (or magnetoroton) minimum predicted by theories of the FQHE. In this interpretation, the roton at $q \sim 1/\ell_0$ is made active by breakdown of wavevector conservation in resonant light scattering processes. The implied loss of translational invariance is explained by enhanced residual-disorder and localization in the FQHE state.

To gain further insight we calculated gap excitations of finite systems with up to 10 electrons. We found excellent agreement with measured energies when the finite width of the electron layer is taken into account. The calculations also indicate that $q=0$ excitations observed can be regarded as two-roton bound states. Such results lead us to proposals for the new resonant light scattering processes by gap excitations of the FQHE in terms of one- and two-dipole-like roton excitations.

[1] A. Pinczuk, B.S. Dennis, L.N. Pfeiffer, and K.W. West, Phys. Rev. Lett. **70**, 3983 (1993).

Sliding of the Wigner Solid on Liquid Helium

Kimitoshi Kono and Keiya Shirahama
*Institute for Solid State Physics, University of Tokyo,
 Roppongi 7-22-1, Tokyo 106, Japan*

Abstract

We have studied strongly nonlinear transport phenomena in the Wigner solid (WS) on liquid ^4He . The Corbino conductivity σ_{xx} exhibited an abrupt jump, which separates two states of the WS; in one state the WS is registered from the surface deformation, whereas in the other state the WS is decoupled from the deformation. The boundary between these two states is empirically described in terms of the input voltage V_{in} , the magnetic field B perpendicular to the surface, measuring frequency ω , electron density n_s , and pressing electric field E_\perp as $V_{in}\omega n_s^{-1.5}B^{0.8}E_\perp^{-1} \sim$ constant. A sliding model is described to account for the empirical relation, the collective sliding of the electrons out of the periodic deformation of the He surface. Anomalous behaviors of the conductivity of the WS are crucial to interpret the phenomenon.

Keywords: Models of non-linear phenomena, Electrical transport measurement, Electrical Transport (conductivity, resistivity, mobility, etc.), Noble gases, Liquid Surface.

Introduction

Surface state electrons (SSE) on the surface of bulk liquid helium have provided a nearly ideal tool for the study of electronic transport properties of non-degenerate two-dimensional system. Strong correlation between electrons is one of the characteristics of this system, which eventually results in the formation of the Wigner solid [1,2]. Several peculiar phenomena have been found in the collective transport properties of the Wigner solid (WS) [3-6]. Although several theoretical models have been proposed for the transport properties of the WS on the bulk-liquid-helium surface [7-9], the applicability of the theories has not been proved satisfactorily yet. The strong coupling between the WS and ripples makes the analysis difficult, where rippling is a quantized surface wave of liquid helium.

When the WS is formed, the diffusion of the SSE is suppressed and each electron begins to localize about its lattice site. The local pressure because of each electron gives rise to a surface deformation; each electron of the WS is accompanied by a small dimple at each lattice site [10]. The surface deformation acts as a massive object for the electron. Hence the dynamical properties of the WS change drastically; the dispersion relation of plasmons is renormalized and manifests several new branches, the phenomena which are known as the coupled plasmon-ripple (CPR) modes [2,11]. We refer to the state of the WS accompanied by the surface deformation as a CPR state. This state is analogous to charge density waves (CDW), which are accompanied by lattice deformations.

Transport properties of the CDW have attracted considerable interest [12]. The fascinating transport properties of the CDW are characterized by pinning and sliding. If the wave vector of the CDW is incommensurate to the underlying crystal lattice and the crystal is perfect, the total energy of the system is independent of the phase of the CDW. In the

presence of this translational symmetry, the CDW can move without friction, as argued by Fröhlich [13]. In practice, however, real crystals contain a certain amount of impurities or imperfections, which destroy the translational symmetry to pin the CDW. The pinning of the CDW makes the system insulating. By applying an electric field which is strong enough for the CDW to overcome the pinning force, the system may recover conductivity. Following this scenario, the CDW exhibit intriguing nonlinear transport phenomena. Phenomena similar to the sliding CDW have been found in the WS, in this case, not on bulk helium but on a helium film [14,15].

Sliding of the “pinned” WS on the surface of bulk superfluid helium. However, the similar phenomenon has been suggested by Fisher, Halperin, and Paltzman [14]. By driving the WS faster than the rippling phase velocity, the WS may leave the surface deformation. This is a transition from the CPR state to the free state of the WS and can be regarded as a new type of sliding phenomenon. Although this supine idea has not attracted much attention, we believe that the phenomenon itself has already been observed, that is, an abrupt “jump of σ_{xx} ” with changing the magnetic field, observed by Wilen and Giannetta [16]. It was originally assigned to the shear-induced melting. We have elucidated, recently, that the phenomenon is more appropriately interpreted by a sliding model [17].

We describe here how the sliding model explains the σ_{xx} jump. It is pointed out that the anomalous transport properties of the CPR-state Wigner solid, which have not been investigated extensively, play a crucial role to interpret the phenomenon.

Experimental Results

We have used a concentric copper electrode pair, which is known as the Corbino disk, to measure σ_{xx} under magnetic field B perpendicular to the SSE. The details of the experimental method have been written elsewhere [17]. The electrodes are biased at a positive voltage V_{de} , and the saturated electron density n_s is determined by $n_s = eV_{de}/4\pi cd$, where e is the dielectric constant of liquid ^4He , and d the depth of the liquid. For the saturated electron density, the electric field which presses the SSE perpendicular to the liquid surface is $2\pi cn_s$. An ac voltage V_{in} is superimposed to the inner electrode in order to measure σ_{xx} . An abrupt jump of σ_{xx} was then observed, for example, with increasing the amplitude of the driving voltage V_{in} [17]. The jump occurs stochastically and a hysteresis was observed between sweeping up and down of V_{in} . The σ_{xx} jump separates two distinct states of the WS on liquid helium, of which we assign one to the CPR state and the other to the sliding state. The transition between the states is observed by changing not only V_{in} , but also such quantities as B , driving frequency ω , pressing electric field E_\perp , electron density n_s , and temperature T . We show a typical behavior of the transition in Fig. 1 as a function of pressing electric field E_\perp . We have searched the boundary which separates two states by changing all the quantities mentioned above. In Fig. 2, we show the boundary on a $V_{in}\omega - \omega$ plane. The boundary is described by $V_{in}\omega \sim$ constant except for the high frequency region. Similar systematic behavior has been observed with respect to the other quantities, B , E_\perp , and n_s . The observation is summarized empirically as follows:

$$V_{in}\omega n_s^{-1.5}B^{0.8}E_\perp^{-1} \sim \text{constant}. \quad (1)$$

The details of temperature dependence is discussed elsewhere [17,18].

Discussion

In static equilibrium, the electrons are positioned at each bottom of the periodic deformation of the liquid helium surface [10,11]. In the presence of the electron-ripple interaction, the deformation causes a spatial corrugation of the potential energy for the electrons. The

corrugation has almost the same profile as the deformation. In the σ_{xx} measurement, the ac field drives the electrons together with the surface deformation. This field tilts the corrugating potential as a whole. For the electric field at which the local potential minima disappear and the potential becomes a monotonous function of radial coordinate, the electrons can move beyond the extrema which once existed between the local potential minima. In the presence of strong magnetic fields, the electrons drift along contours of equipotential. The condition for the disappearance of the local potential minima is equivalent to the condition that all the contours open and the electrons can move outside the minima. Regardless of whether the magnetic field exists or not, if the minima of the corrugating potential disappears, electrons start to leave the lattice sites and are decoupled from the surface deformation. We might consider this phenomena as a sort of sliding.

Regardless of whether the magnetic field exists or not, if the minima of the corrugating potential disappears, electrons start to leave the lattice sites and are decoupled from the surface deformation. We might consider this phenomena as a sort of sliding.

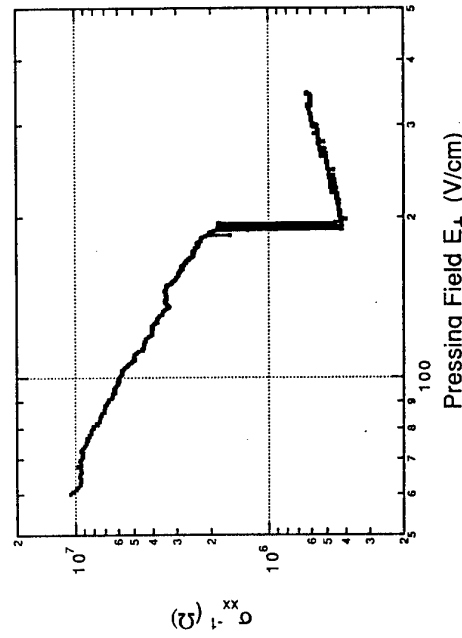


Fig. 1.
Pressing electric field E_1 dependence of σ_{xx}^{-1} . The other experimental conditions are: $n_s = 7.0 \times 10^{14} \text{ cm}^{-2}$, $T = 80 \text{ mK}$, $V_{in} = 200 \text{ mV}_{pp}$, $B = 145 \text{ G}$, and $\omega/2\pi = 100 \text{ kHz}$.

Along with the sliding model discussed above, we consider the sliding criterion. For the present experimental conditions, σ_{xx} of the WS is still so large that the total electric current flowing through the WS is limited by the capacitance between the SSE and the Corbino disk, and V_{in} . Providing the capacitance per unit area C ($\approx 0.9 \text{ pF/cm}^2$), the current is given by $i\omega C\pi r^2 V_{in}$ roughly, where r (= 10 mm) is the radius of the inner electrode of the Corbino disk. According to Ohm's law, the electric field $E_{||}$ parallel to the surface is given by

$$E_{||} \approx \frac{i\omega Cr}{2\sigma_{xx}} V_{in}. \quad (2)$$

The profile of the corrugating potential because of the surface deformation has been known well [11,19]. The amplitude of the potential corrugation is less than 1 mK. The critical electric field E_c at which the minima disappear is given by,

$$E_c \approx \frac{en_s E_{||}^2}{\alpha G_1} n_{G_1}, \quad (3)$$

where α is the surface tension of liquid helium, G_1 the shortest reciprocal lattice vector of the WS, and n_{G_1} is the form factor of the WS associated with G_1 . Here, a small contribution from the polarization term in the electron-ripple interaction was neglected, and only the dominant contribution associated with the shortest reciprocal lattice vector G_1 was taken into account. By equating Eq. (2) to Eq. (3), the following expression for the sliding criterion emerges [17],

$$V_{in} \omega n_s^{-1} G_1 \sigma_{xx}^{-1} E_{||}^{-2} n_{G_1}^{-2} \approx \frac{2e}{\alpha C r}. \quad (4)$$

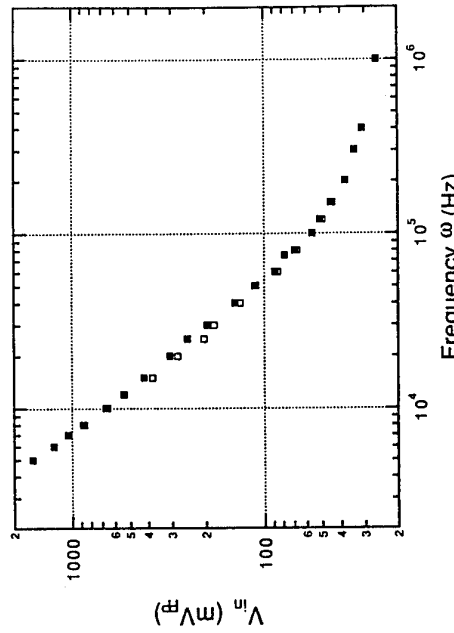


Fig. 2.

The phase boundary between the CPR state Wigner solid and the sliding state on the $V_{in} - \omega$ plane. Upper right region is the sliding state. The solid squares denote the boundary obtained with increasing V_{in} , while the open squares with decreasing V_{in} . The other conditions are: $n_s = 1.1 \times 10^{14} \text{ cm}^{-2}$, $B = 724 \text{ G}$, $E_{||} = 92.5 \text{ V/cm}$, and $T = 20 \text{ mK}$.

Comparing Eq. (4) with Eq. (1), we find immediately that the present sliding model gives the proper ω dependence unless σ_{xx} has a frequency dependence. At least for the condition where the conductivity jump takes place, σ_{xx} of the WS do not have significant dependence by

on ω . This ω dependence implies an important underlying physics. In the present model we assume that it is the electric field parallel to the WS that has an intrinsic critical value at which σ_{xx} jump occurs. The electric field E_{\parallel} is equivalent to the current flowing in the WS, since it is related to E_{\parallel} via conductivity tensor. If we attempt assuming a critical value for strain as considered by Wilen and Giannetta [16], we must integrate the current once with respect to time in order to have the strain. This cancels the ω dependence which appeared in Eq. (4). Therefore it is essential to assume a critical value for the electric field or current. As for the electron density, with keeping in mind that $\sigma_{xx} \propto n_s$ and $G_1 \propto 1/\sqrt{n_s}$, Eq. (4) results in the dependence $V_{\text{tr}} n_s^{-1.5} \sim \text{constant}$. This also accords with the experimental trend Eq. (1).

From Eq. (4) it is not obvious how B and E_{\perp} dependences arise. In Fig. 1 E_{\perp} dependence of σ_{xx}^{-1} is shown. In the small E_{\perp} region the WS is in the sliding state. With increasing E_{\perp} , σ_{xx}^{-1} decreases, roughly proportional to E_{\perp}^{-1} . Since in the fluid phase $E_{\perp}^{x=2}$ dependence is expected, the trend is similar to that of the fluid phase. With increasing E_{\perp} further, σ_{xx}^{-1} drops abruptly, signaling the transition to the CPR state, where the WS is accompanied by the surface deformation. In this region $\sigma_{xx}^{-1} \propto E_{\perp}^2$ for the sliding region, that is, $\sigma_{xx}^{-1} \propto E_{\perp}$. Substituting the relation $V_{\text{tr}} E_{\perp}^{-1} \sim \text{constant}$, consistent with Eq. (1), expression Eq. (4), we obtain the dependence $V_{\text{tr}} E_{\perp}^{-1} \sim \text{constant}$, consistent with Eq. (1). As for the B dependence, we have the similar situation. The magnetoresistance of the WS is found different from the Drude formula which predicts $\sigma_{xx} \propto B^{-2}$; σ_{xx} is inversely proportional to B , roughly speaking. Kovdya et al. reported the similar magnetic field dependence previously [6]. The relation $\sigma_{xx} \propto B^{-1}$ with Eq. (4) accounts for the observed trend Eq. (1) except for the quantitative difference in the exponent between -0.8 and 1 . Finally, it is noted that in addition to the proper functional dependence the expression Eq. (4) gives critical values of the same order of magnitude as what is observed.

In Eq. (3) the form factor n_G appears, which is finite in the solid phase decreasing gradually with increasing temperature and eventually disappears at the melting temperature. This behavior is consistent with the experimentally observed temperature dependence of the σ_{xx} jump [17,18].

Future Prospects

As discussed so far, the nonlinear conductivity jump can be interpreted very well in terms of the sliding model cooperated with the anomalous conduction properties of the CPR-state Wigner solid, namely anomalous B and E_{\perp} dependences. Nonetheless, several aspects are still left to be studied further. The sliding considered here occurs while the WS is moving. The disappearance of the minima of the corrugating potential occurs in the dynamical equilibrium, not in the static equilibrium as in the conventional case of the CDW. The velocity of the WS just below the sliding threshold becomes comparable or even exceeding the phase velocity of free ripples with the wave vector of G_1 . The dynamics of such waves is thought extremely nonlinear. The shape of the surface deformation may well be quite different from that considered in the linear frame.

It is interesting to argue if the collective quantum tunneling of the electrons have to tunnel is long of the WS. Although the path length through which the electrons have to tunnel is long $\sim n_s^{-1/2}$, some hundred nano meter, the height of the potential barrier is small < 1 mK. These two will cancel with each other and we may have a chance to observe such tunneling process.

What is the sliding state of the WS? Does it still keep the long range ordering? We are accumulating evidences that the sliding state is different from the fluid phase. Direct detection of the shear wave of the sliding WS is one of the crucial experiments.

The response of the WS to the pulse electric field is interesting. We observed the transition from the CPR state to the sliding state also by applying the pulse voltage. Recovering

time to the CPR state after the sliding is observable by this method. We can know a dynamical response of the liquid helium surface from such a measurement. What is the origin of the anomalous transport properties of the CPR-state Wigner solid? In this regard, a measurement on liquid ^3He is pedagogic, because the dynamical properties of the CPR state Wigner solid are strongly influenced by the underlying liquid. As known well, ^3He is a Fermion and does not undergo the phase transition to the superfluid phase in the conventional temperature range (> 1 mK) [20].

Acknowledgments

We are grateful to S. Ito and H. Suto for experimental help. One of the authors (KS) is supported by Grant-in-Aid from the Ministry of Education, Science and Culture of Japan.

References

- [1] E. Wigner, Trans. Faraday Soc. 34 (1938) 678.
- [2] C. C. Grimes and G. Adams, Phys. Rev. Lett. 42, 795 (1979).
- [3] A. S. Rybalko, B. N. Esel'son, and Yu. Z. Kovdya, Sov. J. Low Temp. Phys. 5 (1979) 450.
- [4] D. Martz, J. Pointernaud, and F. I. B. Williams, J. Phys. Lett. 41 (1980) L311.
- [5] R. Mehrotra, B. M. Guenin, and A. J. Dahn, Phys. Rev. Lett. 48 (1982) 641.
- [6] Yu. Z. Kovdya, V. A. Nikolayenko, O. I. Kirichek, S. S. Sokolov, and V. N. Grigor'ev, J. Low Temp. Phys. 91 (1993) 371.
- [7] Yu. P. Monarkha, Sov. J. Low Temp. Phys. 5 (1979) 451.
- [8] A. J. Dahn and R. Mehrotra, J. Low Temp. Phys. 50 (1983) 201.
- [9] M. Saitoh, J. Phys. Soc. Jpn. 55 (1986) 1311; M. Saitoh, *ibid.* 56 (1987) 706.
- [10] Yu. P. Monarkha and V. B. Shikin, Sov. Phys. JETP. 41 (1975) 710.
- [11] D. S. Fisher, B. I. Halperin and P. M. Platzman, Phys. Rev. Lett. 42 (1979) 798.
- [12] G. Grüner, Rev. Mod. Phys. 60 (1988) 1129.
- [13] H. Fröhlich, Proc. R. Soc. London Ser. A 223 (1954) 296.
- [14] K. Kajita, Jpn. J. Appl. Phys. Suppl. 26-3 (1987) 1943; K. Kajita, Surf. Sci. 196 (1988) 29.
- [15] H. W. Jiang and A. J. Dahn, Phys. Rev. Lett. 62 (1989) 1396.
- [16] L. Wilen and R. Giannetta, Jpn. J. Appl. Phys. Suppl. 26-3 (1987) 2105; R. Giannetta and L. Wilen, Solid State Comm. 78, (1991) 199.
- [17] K. Shirahama and K. Kono, Phys. Rev. Lett. 74 (1995) 781.
- [18] K. Shirahama, S. Ito, H. Suto, and K. Kono, submitted to Symposium on Quantum Fluids and Solids-1995, 12-17 June 1995, Ithaca, USA, to appear in J. Low Temp. Phys.
- [19] A.-M. Tremblay and V. Ambegaokar, Phys. Rev. B 20, 2190 (1979).
- [20] K. Shirahama, S. Ito, H. Suto, and K. Kono, submitted to Symposium on Quantum Fluids and Solids-1995, 12-17 June 1995, Ithaca, USA, to appear in J. Low Temp. Phys.

Correlated Insulating States of an Interacting Bilayer Electron System

H. C. Manoharan,^{*} Y. W. Suen,[†] M. B. Santos,[‡] and M. Shayegan

Department of Electrical Engineering, Princeton University, Princeton, New Jersey 08544, USA

In a two-dimensional electron system confined in a wide quantum well, we observe an insulating phase that manifests a dramatic evolution as the electron distribution is tuned from single-layer-like to an interacting bilayer system. The data strongly suggest that interlayer interactions play a dominant role and are able to stabilize a correlated *bilayer* Wigner crystal at total filling factor ν as large as 0.54 ($\nu > \frac{1}{4}$ in each layer).

It is possible to fundamentally alter the many-body ground states of a two-dimensional electron system (2DES) at high magnetic fields through the introduction of an additional quantum degree of freedom. For example, the addition of a spin degree of freedom enables the formation of particular spin-unpolarized fractional quantum Hall (FQH) states observed at lower fields [1,2], while radically increasing the perpendicular spatial degree of freedom leads to a weakening and eventual collapse of the FQH effect [3,4]. Here we report magnetotransport measurements on an interacting *bilayer* electron system confined in a wide quantum well. In this system, the additional layer degree of freedom stabilizes new FQH states such as the even-denominator incompressible liquids at Landau level filling factors $\nu = \frac{1}{2}$ [5–7] and $\nu = \frac{3}{2}$ [6], which have no counterpart in standard single-layer 2DESs. Our data reveal an intriguing interplay between the FQH effect and an insulating phase (IP) that displays behavior profoundly different from any observed in a standard 2DES. In this paper we focus on this IP, which we associate with a pinned, *bilayer* Wigner crystal (WC) in which intralayer and *interlayer* correlations are equally significant.

The sample, grown by molecular beam epitaxy, consists of a 750 Å GaAs quantum well surrounded on both sides by Al_{0.3}Ge_{0.6}As spacers and Si δ -doped layers. When cooled to low temperature in a dilution refrigerator, this sample has typical dark density $n \simeq 1 \times 10^{11}$ cm⁻² and mobility $\mu \simeq 1 \times 10^8$ cm²/Vs. Both n and the charge distribution symmetry are controlled via front- and back-side gates [5,6,8]. Here we concentrate primarily on data taken as n was varied with the gates tuned in such a fashion as to preserve symmetric charge distributions, i.e. “balanced” states. In the density range spanned by our experiments, $3.7 \times 10^{10} < n < 19.0 \times 10^{10}$ cm⁻², at most two subbands are occupied. For $n \lesssim 5 \times 10^{10}$ cm⁻², the Fermi energy drops below the second subband and only the lowest subband is populated. As electrons are added to the wide quantum well, their electrostatic repulsion causes them to pile up near the sides of the well, and the resulting electron distribution appears increasingly bilayer-like as n grows [8], as shown in Fig. 1. A relevant parameter that quantifies this evolution is the energy difference between the two lowest subbands which, for a symmetric charge distribution, corresponds to the symmetric-to-antisymmetric energy gap Δ_{SAS} ; this splitting is a measure of the coupling between the two layers. Also relevant is the interlayer distance, defined by the parameter d as shown in Fig. 1. A crucial property of the electron system in a wide quantum well is that, for a given well width, both Δ_{SAS} and d depend on n : increasing n makes d larger and Δ_{SAS} smaller so that the system can essentially be tuned from a bilayer electron system at high n to a (thick) single-layer-like system by decreasing n (Fig. 1). This evolution with density plays a decisive role in the properties of the correlated electron states.

Experimentally, Δ_{SAS} is deduced from Fourier transforms of the low-field magnetoresistance at various n .

We then perform self-consistent Hartree-Fock calculations at zero magnetic field B , with the well width as a single fitting parameter, to match the calculated Δ_{SAS} with the measured values. As shown in Fig. 1, the agreement between the calculated and measured Δ_{SAS} is excellent, and d may then be reliably deduced from the calculated wavefunctions and probability densities [9].

The evolution of the system is summarized in Fig. 2, where the diagonal resistivity ρ_{xx} at base temperature ($T \simeq 25$ mK) is plotted vs ν^{-1} or B for several representative n . At the lowest n the data exhibit the usual FQH effect at odd-denominator fillings, while at the highest n the strongest FQH states are those with *even numerators*, as expected for a system of two 2D layers in parallel. For intermediate n , an *even-denominator* FQH state at $\nu = \frac{1}{2}$ is observed. Concurrent with the evolution of the FQH states, we observe an IP which moves to *higher* ν as n is increased. Experimentally, this IP is identified by a resistivity that is both large ($\rho_{xx} > h/e^2 \simeq 26$ kΩ/◻, the quantum unit of resistance) as well as strongly T -dependent. For very low n , the IP appears near $\nu = \frac{1}{5}$, while at the highest n there is an IP for $\nu \lesssim \frac{1}{2}$. The IP observed in the intermediate density range ($10.4 \times 10^{10} < n < 14.2 \times 10^{10}$ cm⁻²) is most remarkable as it very quickly moves to larger ν with small increases in n (see, e.g., traces B, C, and D in Fig. 2); along the way, it also shows *reentrant* behavior around well-developed FQH states at $\nu = \frac{2}{7}$ (trace B) [10], $\nu = \frac{1}{3}$ (traces C and D), and $\nu = \frac{1}{2}$ (bold trace E). Then, as n increases past this point, the IP begins to move in the opposite direction to lower ν (trace F). The data shown in Fig. 2 for $n = 12.6 \times 10^{10}$ cm⁻² bear a striking resemblance to the IP observed reentrant around $\nu = \frac{1}{5}$ in low-disorder, single-layer 2DESs, generally interpreted as a pinned Wigner solid [11]; here, however, the IP is reentrant around the bilayer $\nu = \frac{1}{2}$ FQH state, with the reentrant peak reaching the prominently high filling of $\nu = 0.54$. For contrast, note that in an ideal 2DES a WC ground state is expected for a critical $\nu \lesssim 1/6.5 \simeq 0.15$ at low temperature [12]. Presumably, non-zero values of r_s [where $r_s \equiv (\pi n)^{-1/2}/a_B^2$ is the average interparticle separation in units of the effective Bohr radius $a_B^2 \equiv \hbar^2/m^*e^2$, and is $\simeq 3$ for typical 2DESs] increase the WC transition to $\nu \simeq \frac{1}{5} = 0.2$ for experimentally-realizable systems. In this bilayer system, the observed critical ν for insulating behavior far surpasses $\nu \simeq 0.4$, which one might expect for a system consisting of two high-quality 2DESs in parallel crossing the IP transition at filling $\simeq 1/5$ in each layer. Since r_s for our system is unchanged from typical single-layer 2DESs, there is clearly additional physics behind our observations.

The IPs presented in Fig. 2 cannot be explained by single-particle localization. First, in

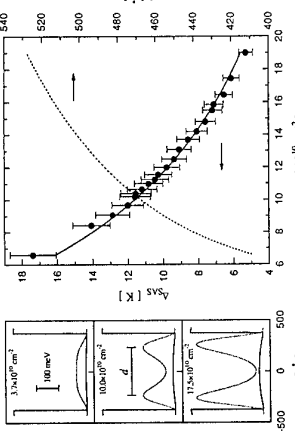


Fig. 1. Measured Δ_{SAS} (closed circles) as a function of total electron density n . The solid curve shows calculated Δ_{SAS} from Hartree-Fock simulations for a 747 Å well, from which self-consistent conduction band potentials (left, solid curves), electron densities (left, dotted curves), and layer separations d (right, dashed curve) are computed.

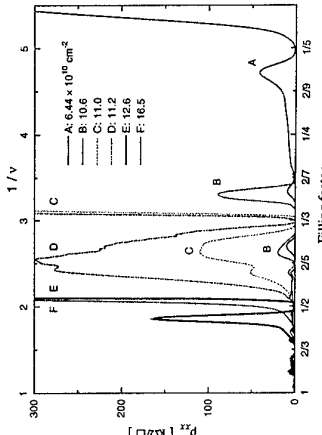
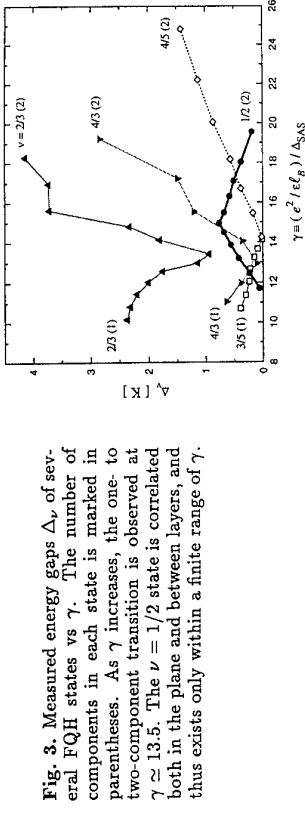


Fig. 2. Evolution of the IP at $T \approx 25$ mK. As n is increased, the IP moves quickly in to higher ν , becoming reentrant around several FQH states along the way, until it stabilizes around the $\nu = 1/2$ bilayer state (bold trace E). As n is further increased from this point, the IP reverses direction and begins to move out toward lower ν .

In the case of standard, single-layer 2DESs it is well known that as n is lowered, the quality of the 2DES deteriorates and the sample shows a disorder-induced IP at progressively larger ν [13]. This is opposite the behavior observed here: as n decreases from 19.0×10^{10} to 3.7×10^{10} cm^{-2} , the quality worsens as expected (e.g. mobility decreases monotonically from 1.4×10^6 to 5.3×10^5 cm^2/Vs) but the IP moves to smaller ν . Second, the observation of IPs which are reentrant around correlated FQH states, and particularly around the very fragile $\nu = \frac{1}{2}$ [6], strongly suggests that electron interactions are also important in stabilizing the IP. To illustrate that the behavior of this IP is indeed consistent with the WC picture, it is instructive to first discuss the evolution of FQH states in an electron system confined in a wide quantum well. This evolution has been studied in detail recently [6], and can be understood by examining the competition between (1) Δ_{SAS} , (2) the in-plane correlation energy $C e^2 / \ell_B$ [where C is a constant ~ 0.1 and $\ell_B \equiv (h/eB)^{1/2}$ is the magnetic length], and (3) the interlayer Coulomb interaction ($\sim e^2 / cd$). To quantify behavior it is useful to construct the ratios $\gamma \equiv (e^2 / \ell_B) / \Delta_{\text{SAS}}$ and $(e^2 / \ell_B) / (e^2 / cd) = d / \ell_B$. As n is increased, γ increases since both Δ_{SAS} and ℓ_B (for a FQH state at a given ν) decrease, and d / ℓ_B increases as discussed before. Experiments show that when γ is small, the system exhibits only “one-component” FQH states (standard single-layer odd-denominator states) constructed from only the symmetric subband, while for large γ the in-plane Coulomb energy becomes sufficiently strong to allow the antisymmetric subband to mix into the correlated ground state to lower its energy and a “two-component” state ensues. These two-component states, constructed out of the now nearly degenerate symmetric and antisymmetric basis states, come in two classes. For large d / ℓ_B , the system behaves as two independent layers in parallel, each with density $n/2$ (FQH states in this regime therefore have even numerator and odd denominator). For small enough d / ℓ_B , the interlayer interaction can become comparable to the in-plane interaction and a fundamentally new kind of FQH state becomes possible. Such a state has strong interlayer correlation and can be at even-denominator ν . A special example is the Ψ_{331} state associated with the $\nu = \frac{1}{2}$ FQH state observed in bilayer electron systems with appropriate parameters [5–7].

We have determined the quasiparticle excitation gaps of several FQH states in the current system for several n via thermal activation measurements, and have plotted the energy gaps vs γ in Fig. 3. As expected, we observe that increasing γ suppresses one-component states and enhances two-component states. Two states, $\nu = \frac{2}{3}$ and $\nu = \frac{4}{3}$, undergo a one-to

Fig. 3. Measured energy gaps Δ_ν of several FQH states vs γ . The number of components in each state is marked in parentheses. As γ increases, the one- to two-component transition is observed at $\gamma \approx 13.5$. The $\nu = 1/2$ state is correlated both in the plane and between layers, and thus exists only within a finite range of γ .



two-component phase transition as γ is increased [6]. The critical point for this transition, $\gamma \approx 13.5$, matches the point where the energy gaps of other one- and two-component states emerge from zero. Surrounding this point is a region where the $\nu = \frac{1}{2}$ FQH liquid stabilizes. Note that since this is the only two-component state observed which also possesses interlayer correlation (the two-component $\nu = \frac{2}{3}$ and $\frac{4}{3}$ states are simply $\frac{1}{3}$ and $\frac{2}{3}$ states in parallel layers), it exists only within a finite range of γ . The relevance of this plot to the IP is immediately highlighted by examining the three main reentrant peaks in Fig. 2 (from traces B, D, and E), which appear at $\nu = 0.30, 0.39$, and 0.54 for the IPs surrounding the $\nu = \frac{1}{2}$, $\frac{1}{3}$, and $\frac{2}{3}$ FQH states, respectively. The values of γ at these reentrant peaks are respectively $16.9, 16.3$, and 16.5 . The peak positions span a large region of ν , and yet the associated γ are remarkably similar. Moreover, at this value of $\gamma \approx 16.5$, interlayer interactions are clearly important as this point is straddled by the two-component $\frac{1}{2}$ state in Fig. 3.

The construction of a phase diagram for the observed insulating states facilitates a clear correlation between the IP evolution, the one- to two-component transition, and the development of the $\nu = \frac{1}{2}$ liquid. We have examined the T -dependence of ρ_{xx} at many n over the entire measurement range described earlier. We observe T -independent critical points, where $d\rho_{xx}/dT$ changes sign, in the high- B ($\nu < \frac{2}{3}$) regime when ρ_{xx} becomes large. The B fields of these critical points may be used to demarcate the boundary between the IP and non-insulating states. At low n , the critical point has a value very close to h/e^2 at the transition from the $\nu = \frac{1}{2}$ liquid to the IP. At higher n , the critical points shift to lower resistivities. As there is now experimental evidence that the quantum Hall liquid to insulator transition occurs at a universal resistivity value h/e^2 [14], and since in our sample whenever $\rho_{xx} > h/e^2$, the derivative $d\rho_{xx}/dT < 0$ (and usually $\ll 0$), we take $\rho_{xx} = h/e^2$ as a threshold point for the IP. At each n , these threshold points have been converted to critical ν for the onset of insulating behavior and are plotted in Fig. 4(a) vs the experimentally-determined γ [15]. The line connecting the points separates non-insulating from insulating states, and the resulting plot is therefore a phase diagram for the observed IP [16].

The first obvious feature of the phase diagram is the wrinkling in the phase boundary. This is caused by the reentrance of the IP around several FQH states as discussed earlier. The limiting critical ν at low n is close to $\frac{1}{5}$, consistent with a low-disorder single-layer 2DES, while for the highest density, where the system is effectively two layers in parallel, the IP is present for $\nu \lesssim \frac{1}{2}$, i.e. $\nu \lesssim \frac{1}{4}$ in each layer. This is reasonable considering that even at the largest n , interlayer interactions are present in this system as evidenced by the observation of a correlated $\nu = 1$ quantum Hall state at high n in the same well [17]. Such

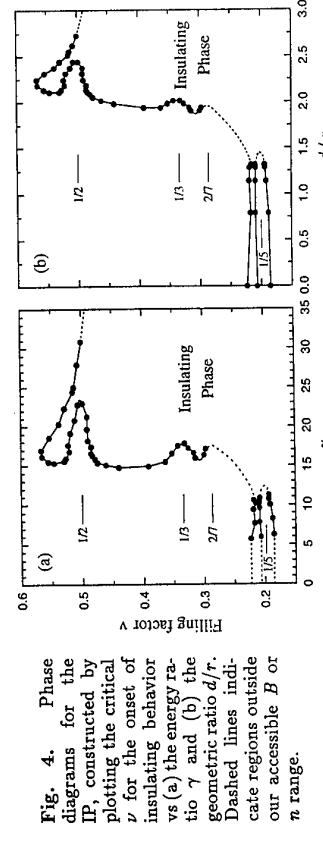


Fig. 4. Phase diagrams for the IP constructed by plotting the critical ν for the onset of insulating behavior vs (a) the energy ratio γ and (b) the geometric ratio d/r . Dashed lines indicate insulating regions outside our accessible B or n range.

interactions can move the WC ground state to $\nu \approx \frac{1}{4}$ (for each layer), somewhat larger than $\frac{1}{5}$ expected if there are no interlayer interactions (see below). We note, however, that our measurements on other wide quantum well samples indicate that in the high- n limit, the onset of the IP indeed approaches $\nu \approx \frac{2}{5}$, consistent with two high quality parallel layers becoming insulating near $\frac{1}{5}$ filling in each layer in the absence of interlayer interactions. It appears that this regime is outside the density limits of our current sample.

We now examine in more detail the evolution of the IP as depicted in the phase diagram of Fig. 4(a) by making comparisons to Fig. 3. In the intermediate n range, as γ increases, the IP first remains close to $\nu = \frac{1}{5}$ but then begins to move to higher ν in the range $12 < \gamma < 15$. This range is precisely bisected by $\gamma \approx 13.5$ (Fig. 3) where the one- to two-component transition occurs. Then the IP moves very quickly to $\nu \approx \frac{1}{2}$ as evidenced by the nearly vertical phase boundary at $\gamma \approx 16$. As discussed earlier and as evident from Fig. 3, this γ is centrally located in the parameter range necessary for the $\frac{1}{2}$ state.

Further support of the bilayer WC conjecture comes from replotted the critical ν for the IP vs d/r [Fig. 4(b)] to obtain a related phase diagram involving the relevant length scales in place of the energy scales. Here $r \equiv (2/\pi n)^{1/2}$ is the average interelectron spacing *within each layer*. Clearly from this diagram, the dramatic change in critical ν occurs at $d/r \approx 2$. Lack of theoretical models prevents us from making any further quantitative comparison, but we feel that $d/r \approx 2$ is a reasonable geometric parameter for a bilayer WC.

Finally, we note that it is plausible that interlayer interactions can modify the ground state energies so that for appropriate parameters a crossing of the liquid and solid states occurs at the large fillings we identify (e.g., $\nu = 0.54$, i.e. $\nu > \frac{1}{4}$ in each layer). Calculations [18] indicate that the effect of interlayer coupling can be particularly strong near the magnetron minimum and lead to the vanishing of the FQH liquid gap. This vanishing can be associated with an instability toward a ground state in which each of the layers condenses into a 2D WC [18].

In summary, our data clearly indicates that the IP we observe in this bilayer electron system for $\gamma \gtrsim 13$ is a product of the same electron-electron interactions (both within the layers and between them) that give rise to the one- to two-component FQH transition as well as the bilayer correlated $\nu = \frac{1}{2}$ state, evincing that the IP is indeed a correlated two-component state with comparable inter- and intralayer correlations, and very likely a bilayer correlated Wigner solid-like state.

We thank X. Ying, D. Shahar, and L. W. Engel for technical assistance. H. C. Manoharan is grateful to the Fannie and John Hertz Foundation for fellowship support. This work was supported by the NSF.

* E-mail address: hari@princeton.edu

[†] Present address: Department of Physics, National Chung Hsing University, Taichung, Taiwan, R.O.C.

Oklahoma 73019

[1] R. Willett, J. P. Eisenstein, D. C. Tsui, A. C. Gossard, and J. H. English, Phys. Rev. Lett. **59**, 1776 (1987).

[2] R. G. Clark, S. R. Haynes, A. M. Stucking, J. R. Mallett, P. A. Wright, J. J. Harris, and C. T. Foxon, Phys. Rev. Lett. **62**, 1536 (1989); J. P. Eisenstein, H. L. Stormer, L. Pfeiffer, and K. West, *ibid.*, 1540 (1989).

[3] M. Shayegan, J. Jo, Y. W. Suen, M. B. Santos, and V. J. Goldman, Phys. Rev. Lett. **65**, 2916 (1990).

[4] S. He, F. C. Zhang, X. C. Xie, and S. Das Sarma, Phys. Rev. B **42**, 11376 (1990).

[5] Y. W. Suen, L. W. Engel, M. B. Santos, M. Shayegan, and D. C. Tsui, Phys. Rev. Lett. **68**, 1379 (1992); Y. W. Suen, M. B. Santos, and M. Shayegan, *ibid.* **69**, 3551 (1992).

[6] Y. W. Suen, H. C. Manoharan, X. Ying, M. B. Santos, and M. Shayegan, Phys. Rev. Lett. **72**, 3405 (1994).

[7] The $\nu = \frac{1}{5}$ FQH state is also observed in bilayer electron systems in double quantum wells. [J. P. Eisenstein, G. S. Boebinger, L. N. Pfeiffer, K. W. West, and S. He, Phys. Rev. Lett. **68**, 1383 (1992)].

[8] Y. W. Suen, J. Jo, M. Santos, L. W. Engel, S. W. Hwang, and M. Shayegan, Phys. Rev. B **44**, 5947 (1991).

[9] Both Δ_{SAS} and d are expected to change in field, but the amount of change is difficult to determine. We believe that the zero field parameters are nevertheless instrumental in quantifying the high-field behavior.

[10] The IP on the high-field side of $\nu = \frac{2}{5}$ is incomplete because of problems with ohmic contacts above this field for this n .

[11] See, e.g., T. Sajoto, Y. P. Li, L. W. Engel, D. C. Tsui, and M. Shayegan, Phys. Rev. Lett. **70**, 2329 (1993), and references therein.

[12] Y. E. Lozovik and V. I. Yudson, JETP Lett. **22**, 11 (1975); P. K. Lam and S. M. Girvin, Phys. Rev. B **30**, 473 (1984).

[13] T. Sajoto, Y. W. Suen, L. W. Engel, M. B. Santos, and M. Shayegan, Phys. Rev. B **41**, 8449 (1990).

[14] D. Shahar, D. C. Tsui, M. Shayegan, R. N. Bhatt, and J. E. Cunningham, Phys. Rev. Lett. **74**, 4511 (1995).

[15] For $n < 6.5 \times 10^{10} \text{ cm}^{-2}$ (the four lowest n examined) we use the calculated Δ_{SAS} because we are unable to measure Δ_{SAS} directly from the Fourier transforms at very low n .

[16] The exact value of the threshold we choose does not alter the topology of the phase diagram and hence any of our conclusions.

[17] T. S. Lay, Y. W. Suen, H. C. Manoharan, X. Ying, M. B. Santos, and M. Shayegan, Phys. Rev. B **50**, 17725 (1994).

[18] H. C. Oji, A. H. MacDonald, and S. M. Girvin, Phys. Rev. Lett. **58**, 824 (1987).

Evidence for Quantum Melting in the Two-Dimensional Electron System on a Thin Helium Film

T. GÜNZLER, B. BITNAR, G. MISTURA, S. NESER and P. LEIDERER

Fakultät für Physik, University of Konstanz, P.O. Box 5550 M 634, D-7846 Konstanz

Abstract

The real and imaginary parts of the dielectric response of surface state electrons (SSE) on helium films adsorbed on oxidized Si platelets have been measured with a microwave cavity at 10 GHz. Preliminary measurements taken at $T=1.2\text{ K}$ show an abrupt increase of the SSE mobility at electron densities near 10^{11} cm^{-2} , which is suggestive of quantum melting of the Wigner solid. Reproducibility of this effect on different Si wafers will be discussed.

The phase diagram of the two-dimensional electron system (2DES) at low temperature T is characterized by a freezing of the Coulomb gas to a Wigner solid at low electron density n , where electrons behave classically, and, more interestingly, by a quantum melting of the Wigner solid to a degenerate Fermi liquid at high n . The classical part of the 2DES phase diagram, in particular the Wigner crystallization, has been investigated using SSE on the surface of liquid helium, an almost ideal substrate owing to its pure and predictable experimental conditions[1]. However, an instability of the charged surface limits the accessible range of electron density to $n = 2 \times 10^9\text{ cm}^{-2}$. A thin helium film is instead additionally stabilized by van der Waals forces which allow to reach higher n and thus to study the influence of the Fermi energy and possibly the quantum melting [2]. So far only the reverse transition – from a degenerate Fermi gas to a Wigner solid – has been observed in semiconductor heterostructures using extremely high magnetic fields.

On an helium film, the direct Coulomb repulsion is weakened by the screening due to the substrate which leads to a shrinking of the solid phase in the (n, T) phase diagram. In particular, the quantum region of the phase diagram is pushed to lower electron densities [2]. This reduction is larger as the film thickness becomes smaller. Etz et al. [3] demonstrated that it is possible to charge helium films to electron densities up to $n \approx 10^{11}\text{ cm}^{-2}$ and found that at such n the film thickness is greatly reduced and is essentially determined by the large electrostatic pressure. The reduction of the film thickness during charging (at $n \geq 10^{10}\text{ cm}^{-2}$) has the effect of increasing the probability of the SSE to tunnel through the film at some rough spot on the surface. On an insulating substrate those electrons which pass through the helium film stick to the surface, prevent other electrons from tunneling and become scattering and pinning centers for the movement of the SSE on the film. Furthermore, as the film gets thinner the lateral movement of the SSE becomes increasingly perturbed by the roughness of the underlying substrate and by the presence of surface impurities. This is the cause of the progressive disappearance of the signal in low frequency conductivity measurements as the electron density approaches 10^{11} cm^{-2} .

To avoid this complication, we have measured the response of the SSE at microwave frequencies. The experimental setup consists of a cylindrical cavity, 19.5 mm in diameter and 20 mm in length, forming a microwave resonator which is excited in the fundamental TM₀₁₀ mode at a frequency $f \approx 10\text{ GHz}$. A rectangular ($30 \times 10\text{ mm}$), oxidized silicon platelet, which serves as a substrate for the helium film, is placed along the axis of the cavity, parallel to the high frequency electric field of this mode. The cavity is inserted in a closed copper cell immersed in the liquid helium of a glass dewar. During the measurements high-purity helium gas is condensed into the sample cell at 1.2 K . The level of liquid helium inside the cavity with respect to the top face of the SiO₂ can be adjusted by using the frequency shift of the cavity itself as a level meter. The helium film is charged by firing a small filament mounted at the top of the cavity every $\approx 3\text{ sec}$ and by increasing very slowly the clamping voltage U , applied between the isolated Si-platelet and the grounded cavity, in order to guarantee a saturated charging of the film. During the charging, the resonance frequency f of the cavity and the transmitted power P are recorded by a computer. From P and f we then calculate the dimensionless relative absorption α and the effective susceptibility χ of the SSE, which represent the imaginary and real components, respectively, of the dielectric function $\tilde{\epsilon}(\omega, k)$ of the SSE at fixed ω and k .

So far, as substrates for the helium films we have studied platelets cut from thermally oxidized p-Si wafers with SiO₂ thicknesses d_s of 2600 Å and 4900 Å (SiI), and from a sputtered p-Si wafer $d_s \approx 5000\text{ \AA}$ (SiII). Figure 1 shows the results taken on SiI plated with an helium film, 400 Å thick, plotted against U . Assuming that the film is charged at saturation, $n = \epsilon_s \epsilon_0 U / d_s e$, where $\epsilon_s \approx 4$ is the permittivity of SiO₂. For the data presented here $n \approx 4 \times 10^{10}\text{ cm}^{-2}$ for $U = 1\text{ V}$. As the electron density n is increased from $n = 0$, we find three prominent structures appearing in both α and χ . First of all, at low n , α and χ are seen to vary linearly with n , although with slopes of opposite sign. This is the expected behavior for non-interacting electrons. Secondly, around $U=0.3\text{ V}$ both curves bend over to a region with a much smaller slope, implying a reduction in the SSE mobility. We interpret this kink as the transition from the classical Coulomb gas to a Wigner solid pinned to the surface. Its location ($n \approx 1.3 \times 10^{10}\text{ cm}^{-2}$) is much higher than the value of $\approx 2.5 \times 10^9\text{ cm}^{-2}$ obtained by extrapolating the experimental phase diagram on bulk helium to 1.2 K. This is due to shielding effects caused by the finite polarizability of the SiO₂ layer and Fermi energy corrections. The rounding of this transition is probably related to inhomogeneities of the SiO₂ surface. Similar behavior has been found in low frequency conductivity measurements of SSE on different substrates [4]. Finally, at U around 1 V, α and χ display a second step, such that the SSE mobility appears to increase again. Note that the signals after the step even assume values close to the linear extrapolation of the data at low U . This together with the fact that the feature occurs at a value of n which is expected from theoretical arguments [2] is suggestive of a quantum melting of the electron system from a Wigner solid to a degenerate Fermi gas.

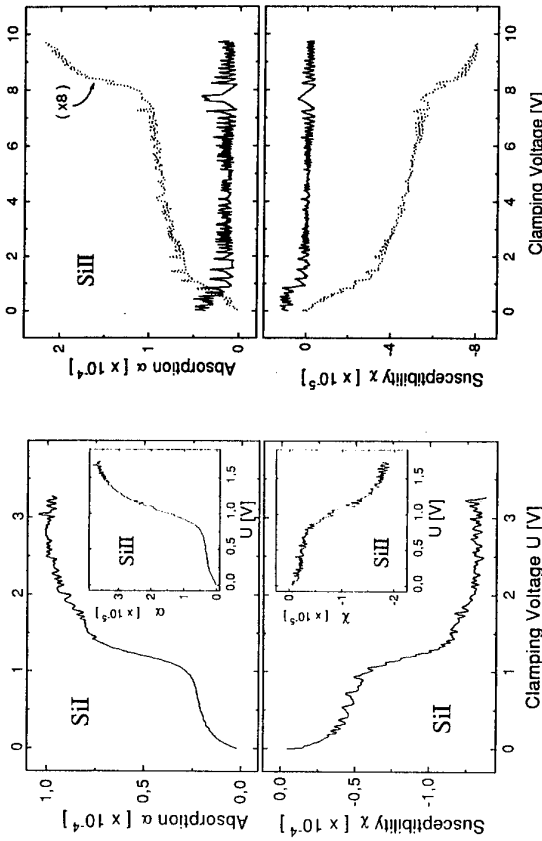


Fig. 1: Absorption α (top) and susceptibility χ (bottom) of the SSE taken on SiI and on SiII (insert) as functions of the clamping voltage. Initial helium film thickness $\approx 400 \text{ \AA}$. See text.

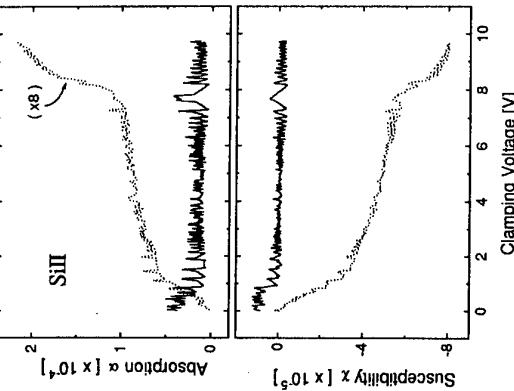


Fig. 2: Absorption α (top) and susceptibility χ (bottom) of the SSE measured on a "dry" SiO_2 surface (continuous line) and on an helium film 400 \AA thick, right after the "dry" charging (dotted line).

This result cannot be explained as a plasmon resonance of the free SSE because for our cavity it is expected to occur at a density $n \approx 3 \times 10^{13} \text{ cm}^{-2}$, 700 times more than we observe. Furthermore, this step cannot be due to charge carriers inside the Si substrate. The p-Si together with the SiO_2 layer forms a MOSFET-like structure with the electrons on top of the He film as the gate electrode. Owing to the strong clamping field, a 2D hole gas (2DHG) develops in the lowest sublevel of the inversion layer at the interface between Si and SiO_2 . This 2DHG, of the same density as the 2DEG on top of the He film, gives rise to microwave absorption, too. However, in the range of U values used in our measurements, the contribution of the 2DHG, as well as that of the charge carriers in the bulk silicon, is quite small. To prove that this is indeed the case, we evacuated the sample cell so that only a few monolayers of He covered the Si platelet, and repeated the charging procedure. The result is displayed in Fig. 2. The larger noise is due to temperature fluctuations in the cavity after each firing of the filament, which are now much larger than before due to the absence of a superfluid film. Both curves, α and χ , are straight lines parallel to the

horizontal axis up to $U = 10 \text{ V}$. This means that neither the electrons which are strongly bound to the SiO_2 surface, nor more importantly the charge carriers inside the Si give rise to any appreciable contribution to the microwave signal in our measurements. After this dry charging, we repeated the measurements with a saturated helium film (see Fig. 2). The new curves are similar to those of Fig. 1, but with two important differences. The voltage scale is shifted to higher values to overcome the repulsive potential due to the electrons pinned to the SiO_2 , and the overall change in α is much smaller implying a lower mobility of the SSE probably caused by scattering with an increased number of surface defects.

Figure 1 also shows curves taken on SiII of similar shapes to those on SiI. It is interesting to point out that compared to SiI the change in α and χ is about 2 times and 8 times smaller, respectively. These differences can be explained in terms of a lower mobility on SiII, an expected result due to the surface of the sputtered Si which is obviously not as smooth as that of SiI. Besides this, the second step occurs at a different voltage. Similar shifts have also been found with the same sample after several charging runs or after thermal cycling to room temperature. In other words, the quantitative reproducibility of the data so far seems to depend very much on the "history" of the sample. Systematic measurements are now in progress to better understand these effects. The next goal is to map out the phase diagram.

This research has been partially supported by the HCM-network of the European Community, contract No.: ERBCHRXCT930374. Some of the Si samples used have been kindly provided by Prof. Jutzi.

References

- [1] See e.g. F. I. B. Williams, *Surf. Sci.* **113**, 371 (1982) and references therein.
- [2] F. M. Peeters and P. M. Platzman, *Phys. Rev. Lett.* **50**, 2021 (1983); F. M. Peeters, *Phys. Rev. B* **30**, 159 (1984); M. Saitoh, *Surf. Sci.* **229**, 356 (1990).
- [3] H. Etz, W. Gombert, W. Idstein and P. Leiderer, *Phys. Rev. Lett.* **53**, 2567 (1984).
- [4] K. Kajita, *J. Phys. Soc. Jap.* **54**, 4092 (1985); H. W. Jiang and A. J. Dalm, *Phys. Rev. Lett.* **62**, 1396 (1989); F. Mugale, U. Albrecht, P. Leiderer and K. Kono, *J. Low Temp. Phys.* **89**, 743 (1992).

OBSERVATION OF CORRELATED $\nu=1$ QUANTUM HALL AND INSULATING STATES IN STRONGLY COUPLED P-TYPE DOUBLE QUANTUM WELLS

Hyndman R.J., Ihn T., Gallagher B.L., Rodgers P.J., Hennini M., Foster T.J. and Middleton J.R.

Department of Physics, University of Nottingham, Nottingham, NG7 2RD, U.K.

Abstract

We present magnetotransport results for strongly coupled p-type double quantum wells which demonstrate the existence of a correlated $\nu = 1$ quantum Hall state in the limit of weak tunnelling. Our results are in good agreement with the finite temperature phase transition predicted for this state. We also observe an activated insulating behaviour for $\nu < 1$ which may be evidence of a correlated bi-layer Wigner state.

In single layer two dimensional, 2D, conductors the integer quantum Hall effect (IQHE) arises when the Fermi energy lies in the region of localised states between Landau levels. The fractional quantum Hall effect (FQHE) arises from the intra-layer Coulombic interaction which leads to transitions into correlated liquid-like ground states when the Landau level filling factor, ν , has particular odd denominator fractional values. In these cases, there exists a finite gap separating the many-body ground state from the lowest-lying excited state. When two such 2D layers are in close proximity, the inter-layer Coulombic interaction can lead to further new correlated states. In particular new FQHE states are possible when the filling factor in each layer is an even denominator fraction.

In a double layer system the quantum Hall effect at a total Landau level filling factor $\nu = 1$ (i.e., $\nu = \frac{1}{2}$ in each layer) can arise in two ways. If tunnelling is strong a normal single particle state can occur in which the energy gap is that separating the lowest symmetric and antisymmetric states of the system (Δ_{SAS}). A new many body $\nu = 1$ state is also predicted to occur for sufficiently strong inter-layer Coulombic interaction even in the absence of tunnelling [1]. In n-type GaAs/GaAlAs double layer systems at small layer separation, when the inter-layer Coulombic energy is large, tunnelling also tends to be strong due to the small electron effective mass. This makes the unambiguous identification of the nature of the state difficult. $\nu = 1$ states consistent with the expected behaviour of the correlated state have been observed in a series of n-type double quantum wells which have Δ_{SAS} values as low as 0.8 K [2]. However in these samples tunnelling still plays an important role as is shown in tilted field experiments [2]. Complex behaviour has also been observed in very wide quantum wells which have some bi-layer character, but which also have very large Δ_{SAS} [3]. It is clear from these studies that inter-layer correlations are important in stabilising the observed $\nu = 1$ states. However the prediction of a $\nu = 1$ state in the limit of small Δ_{SAS} has still not been directly demonstrated experimentally.

In this paper we will concentrate on results for high mobility p-type double quantum wells for samples from one MBE grown wafer (NU1174), though the $\nu = 1$ state is observed in samples with appropriate densities from several wafers. Each quantum well is 100Å wide and they are separated a 30Å AlAs barrier as is shown in the insert of figure 1. The total carrier density and the relative densities in the two wells can be controlled using front and back gates and accurately determined from the Fourier transform of the low field Shubnikov-de Haas oscillations. As grown the carrier density in each well for NU1174 samples is within 5% of $1.1 \times 10^{15} \text{ m}^{-2}$ and the average mobility is $400,000 \text{ cm}^2 \cdot \text{V}^{-1} \cdot \text{s}^{-1}$. The mobility is found to be a very weak function of carrier density as is the case for p-type heterostructures [4]. The high hole mass leads to weak tunnelling even at small layer separation. The potential and density distribution for this structure, shown in figure (1), was obtained by solving the Poisson equation and the one-electron Schrödinger equation self-consistently. A parabolic dispersion with a mass of $0.45 m_0$ was used and many - body effects were included in the local - density approximation. This yields a weakly hole density dependent Δ_{SAS} of $\sim 70\text{mK}$.

Figure (1) shows the typical behaviour of the longitudinal resistance, R_{xx} , and the Hall resistance, R_{xy} when the hole number densities in the two wells are balanced. Figure (2) shows the temperature dependence of R_{xx} at $\nu = 1$ for a series of total densities with equal hole densities in each well. As can be seen strong $\nu = 1$ quantum Hall states are observed which have activation energies of up fifty times Δ_{SAS} . The states at $\nu = 3, 5, 7, \dots$ are all absent as expected for weak tunnelling. This is direct unambiguous proof of the existence of the correlated $\nu = 1$ state in the limit of weak tunnelling.

It is predicted that the correlated state should only be present when the ratio of the inter-layer Coulombic energy to the intra-layer Coulombic energy is sufficiently large. A measure of this is the ratio of the layer separation, d_1 , to the magnetic length, l_B . Recent theoretical calculations find that the state should only be present for $d/l_B < 1.6$ [1]. We find that the state systematically weakens with increasing total carrier density, as is shown in figure 2. This is in complete contrast with all the single layer IQHE and normal FQHE states which all strengthen with increasing density. It is however in agreement with the prediction that the correlated state will weaken with increasing l_B since the increased density moves the $\nu = 1$ state to higher B . We find that the state is destroyed as d/l_B approaches ~ 1.7 , in agreement with theory. Previous results on 180Å wide n-type double wells [2] indicate a critical value of ~ 2 . We attribute our better agreement with theory to the smaller finite thickness corrections for our 100Å quantum wells and the smaller values of Δ_{SAS} . In fact, as the insert to figure 1, shows there are two effects which can be thought to modify the Coulombic interactions and lead to a new effective (d/l_B) . Firstly, repulsion between the holes in the wells moves the peaks in the probability densities apart increasing the effective layer separation d_{eff} . Secondly the finite thickness softens both the intra-well and inter-well coulombic interaction. One can estimate this second effect by replacing d_{eff} by $(d_{eff} + \lambda^2)^{1/2}$ and l_B by $(l_B^2 + \lambda^2)^{1/2}$ where λ is the layer thickness. The latter increase is the larger and so the effect of the finite thickness is to reduce the effective (d/l_B) . Taken together these two effects tend to cancel as is apparent from figure (3). This goes some way to account for the remarkably good agreement between our measurements and theory.

The correlated $\nu = 1$ state is of particular interest since it is predicted that a finite-temperature Kosterlitz-Thouless transition may occur [1]. Evidence for such a transition has been recently found in wide parabolic quantum wells [5]. We find qualitatively similar behaviour in our samples but are also able to make direct comparison with theory since we are in the limit of small Δ_{SAS} . As figure (2) shows, the state shows activated behaviour at low enough temperatures but is unobservable above a critical temperature T^* . This temperature is considerably less than the activation temperature and so the behaviour is consistent with the predicted finite temperature phase transition in which the activation gap disappears at T^* . As figure 3 shows T^* tends to zero as d/l_B approaches ~ 1.7 in agreement with the theoretical prediction [1].

At the lowest densities a direct transition from the $\nu = 1$ quantum Hall state into an activated insulating state occurs followed by a re-entrance of the fractional quantum Hall state at $\nu = 2/3$ ($1/3$ filling factor in each well) as is shown in figure (4). In single layer electron gases insulating behaviour for $\nu < 2/9$ followed by a re-entrance of the $1/5$ state has been shown to be consistent with Wigner crystallisation [6]. For single layer hole gases similar behaviour around for $\nu < 2/5$ and re-entrance of the $1/3$ state has been taken on evidence of stabilisation of the Wigner state by Landau level mixing [7]. The observed behaviour is consistent with a correlated bi-layer Wigner solid in which the additional inter-layer Coulombic interaction stabilises the solid state. The strength of the insulating state correlates well with that of the $\nu = 1$ state supporting the idea that it is also stabilised by bi-layer correlations.

References

- [1] K. Moon et al (1995) Phys. Rev. B **51**, 5138 and references there in.
- [2] S.Q. Murphy et al. (1994) Phys. Rev. Lett. **72**, 728
- [3] Y.W. Suen et al. (1994) Phys. Rev. Lett. **72**, 3405
- [4] M. Henini, P.J. Rodgers, P.A. Crump, B.L. Gallagher and G. Hill (1994) AppdPhys. Lett. **65**, 2034.
- [5] T.S. Lay, Y.W. Suen, H.C. Manoharan, X. Ying, M.B. Santoz and M. Shayegan (1994) Phys. Rev. B **50**, 17725.
- [6] H.W. Jiang, R.L. Willet, H.L. Störmer, D.C. Tsui, L.N. Pfeiffer and K.W. West (1990) Phys. Rev. Lett. **65**, 633.
- [7] H.C. Manoharan and M. Shayegan(1994) Phys. Rev. B **50**, 17662, B.L. Gallagher et al. (1995) Physica B **211**, 417, and references there in

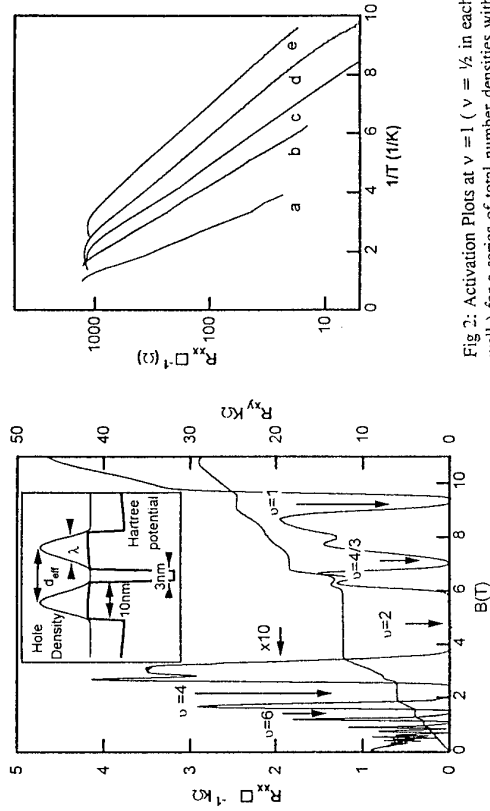


Fig. 1: Typical RxX and RxY results (at 60mK) for equal hole densities of $1.1 \times 10^{11} \text{ cm}^{-2}$ in each well. The inset shows the calculated potential profile and hole density distribution.

Fig. 2: Activation Plots at $v = 1$ ($v = 1/2$ in each well) for a series of total number densities with activation energy, ΔE in Kelvin given in braces. (a) $1.61 \times 10^{11} \text{ cm}^{-2}$ (2.9K), (b) $2.08 \times 10^{11} \text{ cm}^{-2}$ (1.9K), (c) $2.23 \times 10^{11} \text{ cm}^{-2}$ (1.7K), (d) $2.28 \times 10^{11} \text{ cm}^{-2}$ (1.4K), (e) $2.33 \times 10^{11} \text{ cm}^{-2}$ (1.3K).

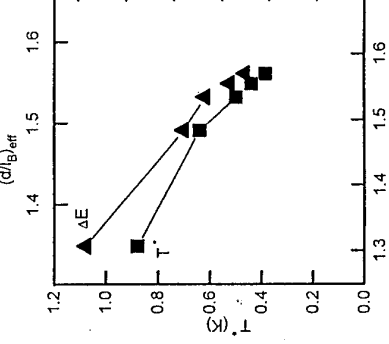


Fig. 3: Behaviour of the energy gap ΔE and critical temperature T^* with d/l_B (lower scale) and $(d/l_B)_{\text{eff}} = [(d_{\text{eff}}^2 + \lambda^2)^{1/2} / (l^2 + \lambda^2)^{1/2}]$ (upper scale). T^* is defined as the point of intersection of the extrapolated activation line and the horizontal at the saturation resistance at a single density.

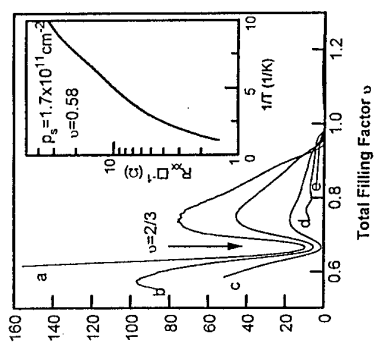


Fig. 4: Evolution of the insulating region at 80 mK for total number density of (a) $1.49 \times 10^{11} \text{ cm}^{-2}$, (b) $1.59 \times 10^{11} \text{ cm}^{-2}$, (c) $1.65 \times 10^{11} \text{ cm}^{-2}$, (d) $1.69 \times 10^{11} \text{ cm}^{-2}$, (e) $1.71 \times 10^{11} \text{ cm}^{-2}$. The insert shows activated behaviour of the insulator at a single density.

Optical Spectroscopy of Neutral and Charged Excitons in GaAs/AlGaAs Quantum Wells in High Magnetic Fields

Gleb Finkelstein, Hadas Shtrikman and Israel Bar-Joseph

Department of Physics, The Weizmann Institute of Science, Rehovot 76100, Israel

Abstract

We implement optical spectroscopy to study charged excitons in modulation doped GaAs/AlGaAs quantum wells. We report the first observation of the positively charged exciton and of the triplet state of the negatively charged exciton. Applying a gate voltage at high magnetic fields we investigate the transition between metallic to insulating states. We find that while the photoluminescence line of the metallic two dimensional electron gas smoothly transforms into X-, the Zeeman splitting of this line exhibits an abrupt change at the metal-insulator transition.

I. Introduction

Charged excitons are the semiconductor analog of the H⁻ and H₂⁺ hydrogen ions. Their existence was first discussed nearly 40 years ago,[1] yet their first observation was only recently reported.[2] It is clear that a large density of electrons (holes), which could bind to the photo-excited electron-hole pairs, is needed for the negatively (positively) charged exciton to be observed. However, a dense electron or hole gas might screen the Coulomb interaction and lead to unbinding of the charge exciton. These considerations led to the choice of a two dimensional electron gas (2DEG) near the metal-insulator transition as the appropriate system for the observation of the negatively charged exciton, X-. Indeed, we have recently shown that under these conditions a new line appears in the optical emission and excitation spectra of a high quality modulation doped GaAs/AlGaAs quantum well (QW).[3] We associated this line, which is ~1.2 meV below the exciton line, with an X-. A similar lineshape was observed in a resonant tunneling structure, when a low density of electrons is accumulated in the well.[4] In this work we use optical spectroscopy to study the properties of two dimensional electron and hole gases at magnetic fields from 0 to 9T. By applying a gate voltage we are able to investigate the transition from the metallic to the insulating state using the same sample.

II. The Negatively Charged Exciton X-

Figure 1 describes the evolution of the PL and PLE spectra of a 2DEG sample(500 Å spacer and 200 Å QW) with gate voltage. The PL spectrum at zero gate voltage shows a step-like behavior, typical for absorption in presence of a 2DEG. The PL spectrum is Stokes shifted, due to the relatively large 2DEG density, of ~ $2 \times 10^{11} \text{ cm}^{-2}$ (Burstein - Moss shift). At -1.5 V two broad peaks, corresponding to the onset of the heavy and light hole transitions, are seen. As the gate voltage approaches the metal - insulator transition the optical spectra change drastically. The Stokes shift decreases and both the PL and PLE peaks narrow to form a sharp resonance, denoted as X_{hh}⁻, at the band edge. At -1.6 V three broad features (X_{hh}⁻, X_{lh}⁻ and X_{hh}) are seen above this sharp resonance. As the gate voltage is further decreased the X_{hh} evolves into the heavy-hole exciton and the X_{lh} into

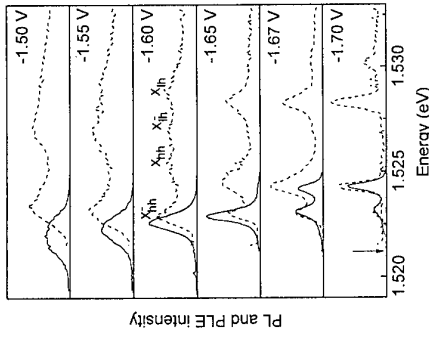


FIG. 1: Evolution of the PL (solid line) and PLE (dotted line) spectra of 500 Å spacer 2DEG with the gate voltage. The arrow represents the PLE detection energy (1.5212 eV)

When depleting the 2DHG (500 Å spacer 200 Å QW) we observe a change in the PL, which is very similar to that observed in the n-type samples. The PL line shifts to higher energies and at a certain critical density a neutral exciton line appears at an energy 1.25 meV above. We associate the low energy line with X⁺. This behavior was observed in 3 different samples, with different doping levels, and in different pieces of the wafers.

To substantiate the assignment of the PL peaks let us examine the expected polarization of the emitted light from a charged exciton as compared to that of a neutral exciton. Consider a resonant excitation at the light-hole exciton energy with a circularly polarized light. We get electrons with a spin projection along the growth direction $s_z^{\text{el}} = +1/2$ and light-holes with a total angular momentum projection $s_z^{\text{lh}} = +1/2$. Within a few tens of picoseconds the holes population relaxes into the heavy-hole states and is equally distributed between the $s_z^{\text{lh}} = \pm 3/2$ states. On the other hand, the electron spin relaxation is relatively slow and a substantial number of electrons preserve their spin projection until they recombine. These different relaxation rates for holes and electrons determine the polarization of the emitted light. Since only the $s_z^{\text{el}} = +1/2$ electron, the neutral exciton emission is predominantly counter-polarized relative to the incident light. The same behavior is expected in X⁺ since its electron is polarized and can recombine with only one of the heavy-hole states. On the other hand,

the two electrons in X^- are in a singlet state with opposite s_z^{el} and can recombine with both heavy-holes states. Consequently, the X -emission should be unpolarized.

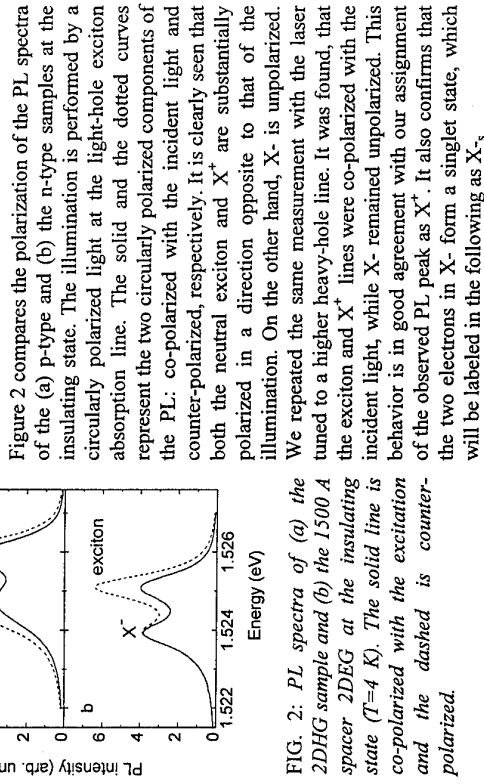


Figure 2 compares the polarization of the PL spectra of the (a) p-type and (b) n-type samples at the insulating state. The illumination is performed by a circularly polarized light at the light-hole exciton absorption line. The solid and the dotted curves represent the two circularly polarized components of the PL: co-polarized with the incident light and counter-polarized, respectively. It is clearly seen that both the neutral exciton and X^+ are substantially polarized in a direction opposite to that of the illumination. On the other hand, X^- is unpolarized. We repeated the same measurement with the laser tuned to a higher heavy-hole line. It was found, that the exciton and X^+ lines were co-polarized with the incident light, while X^- remained unpolarized. This behavior is in good agreement with our assignment of the observed PL peak as X^+ . It also confirms that the two electrons in X form a singlet state, which will be labeled in the following as X_s .

IV. The Triplet X_t

Figure 3 describes the evolution of the PL spectra of a 2DEG in the insulating state from 0 to 9 T. At $B > 4$ T a new peak, denoted as X_t , appears between the exciton and X_s . Approximately at the same range of fields the X_s line starts to reveal a clear Zeeman splitting. We attribute the X_t line to X^- with its two electrons forming a triplet state. This state is not expected to be bound at zero magnetic field, but could become bound at high magnetic field, due to the quenching of the kinetic energy. This should occur when the magnetic length becomes comparable with the exciton diameter, at ~ 4 T.

To prove the assignment of the X_t peak we examine the PL spectra at high magnetic fields and low temperatures, when the electron gas is spin polarized, $s_z^{\text{el}} = +1/2$. Figure 4 shows the PL spectra in the two circular polarization at 7 T and 2 K. We observed that the X_t peak exhibits a strong circular polarization. It is co-polarized with the lower energy component of X_s . This behavior is consistent with the assignment of the X_t line to a negatively charged exciton, in which the electrons are paired in $s_z^{\text{el}} = 1$ triplet state. The strong polarization of the X_t line is then due to the fact that the only possible recombination process of the $s_z^{\text{el}} = 1/2$ electron is with $s_{\text{hh}}^{\text{el}} = -3/2$ heavy-hole.

To further substantiate this assignment we studied the PLE spectra of a spin polarized 2DEG. Under this condition a photo-excited electron can pair with a host electron to form either a singlet or a triplet state, depending on its polarization: $s_z^{\text{el}} = +1/2$ electron will

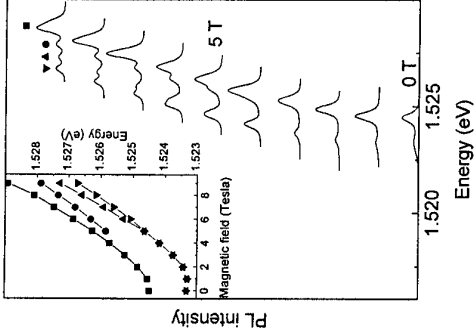


FIG. 3: PL spectra of the 500 Å spacer 2DEG in the insulating state, from 0 to 9 Tesla, ($T=4$ K). Inset: the peak positions as a function of the magnetic field. The squares denote excitons, circles - X_s , and triangles - X^- .

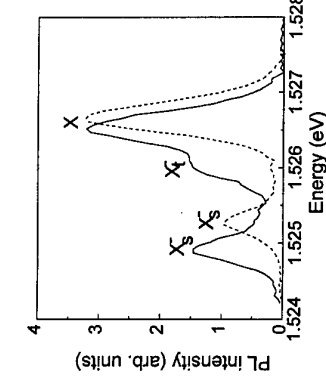


FIG. 4: The PL spectra of the 500 Å spacer 2DEG in the insulating state at 7 Tesla ($T=2$ K). The solid and the dotted line represent two circular polarizations.

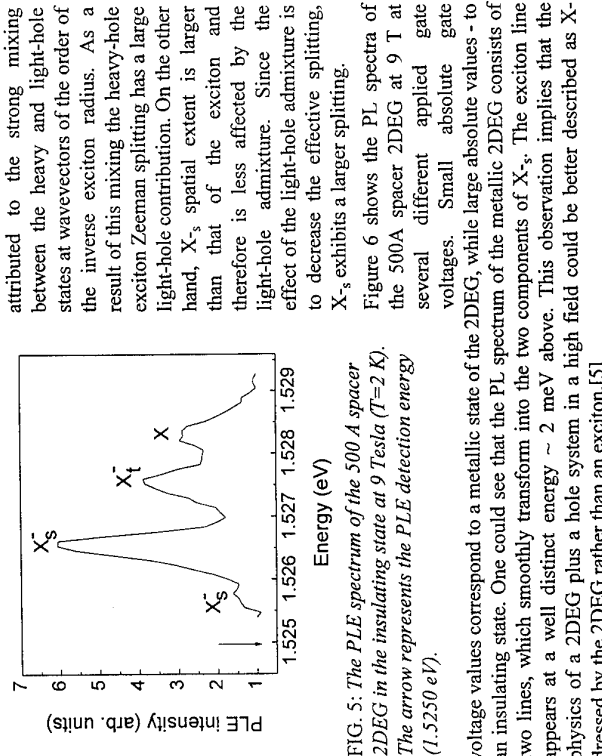
form X_t ($s_z^{\text{el}} = 1$) while $s_z^{\text{el}} = -1/2$ electron can form X^- . In the first case we get absorption at the X_t energy and in the second, we get absorption at the high energy component of the Zeeman split X_s .

This behavior is indeed observed in Fig. 5, which shows the PLE spectrum at 9 T and 2 K. The X_t peak is clearly visible and it is seen that the high energy component of the X_s doublet is much stronger than the low energy one. Similar arguments were used by Kheng *et al.* to prove the assignment of the peak in the PL and absorption of CdTe/CdZnTe QW with a negatively charged exciton.[2]

We note that as we apply a gate voltage beyond the metal - insulator transition the relative strength of the X_s and X_t lines vary with respect to the neutral exciton, but they keep the same relative strength among themselves. This indicates that the X_s and X_t lines indeed have a similar origin and their intensity scales with the density of electrons in the sample. The second triplet state, with $s_z^{\text{el}} = 0$, is not observed. A possible explanation is that it rapidly transforms into the singlet state, due to interaction of the total electron spin with the spin of the hole. We also do not observe the X_t with $s_z^{\text{el}} = -1$ state. Clearly, it can not be formed in a spin polarized $s_z^{\text{el}} = +1/2$ 2DEG.

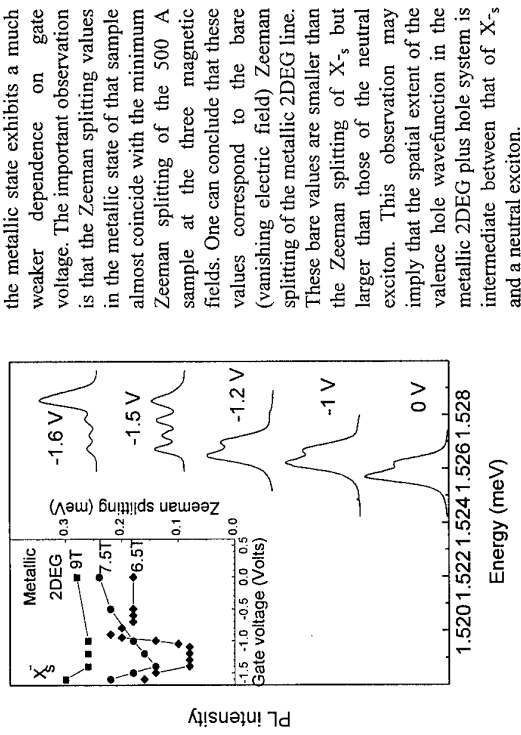
VI. The Zeeman splitting and the Metal - Insulator Transition

The Zeeman splitting of the X_s peak is significantly (~50 %) larger than that of the neutral exciton. The origin of this difference can be



An examination of X_s and the metallic 2DEG PL lines (Fig. 6) shows that their Zeeman splitting varies with gate voltage. This behavior is summarized in the inset, which shows the change of the Zeeman splitting as we go all the way from a metallic to an insulating state. Data for lower magnetic fields is also shown. It can be seen that the Zeeman splitting of the metallic 2DEG line decreases with gate voltage and reaches a minimum at ~ -1.4 V. This behavior is more pronounced at the lower magnetic fields. Beyond this voltage the Zeeman splitting jumps to X_s 's value. Thus, the measurement of the Zeeman splitting tells us where does the crossover between X_s and a metallic 2DEG recombination occurs in the smoothly transforming PL line. Notice, that at the same range of gate voltage the neutral exciton first appears in the PL spectra (Fig. 6). Transport measurements show that this transition voltage coincides with that of the metal - insulator transition. [3]

It was shown that an electric field in the growth direction lifts the spin degeneracy of the heavy-hole state and produces an effective Zeeman splitting at zero magnetic field.[6] This mechanism gives the dominant contribution to the Zeeman splitting in heterojunctions at magnetic fields < 10 T.[6] Indeed, a very large built-in electric field is present in our single-side modulation-doped QW samples at zero gate voltage. Applying negative gate voltages this electric field decreases, which results in a reduction of Zeeman splitting. This interpretation is supported by the behavior of the 1500 Å spacer 2DEG. In this sample the built-in electric field is much smaller and indeed the Zeeman splitting of



References

1. M.A. Lampert, Phys. Rev. Lett. **1**, 450, (1950).
2. K. Kheng *et al.*, Phys. Rev. Lett. **71**, 1752 (1993).
3. G. Finkelstein, H. Shtrikman and I. Bar-Joseph, Phys. Rev. Lett. **74**, 976 (1995).
4. H. Buhmann *et al.*, Phys. Rev. **B51**, 7969 (1995).
5. A.H. MacDonald, E.H. Rezayi and D. Keller, Phys. Rev. Lett. **68**, 1939 (1992); V.M. Apalkov and E.I. Rashba, Phys. Rev. **B46**, 1628 (1992).
6. D. A. Broido and L.J. Sham, Phys. Rev. **B31**, 888 (1985).

the metallic state exhibits a much weaker dependence on gate voltage. The important observation is that the Zeeman splitting values in the metallic state of that sample almost coincide with the minimum Zeeman splitting of the 500 Å sample at the three magnetic fields. One can conclude that these values correspond to the bare (vanishing electric field) Zeeman splitting of the metallic 2DEG line. These bare values are smaller than the Zeeman splitting of X_s , but larger than those of the neutral exciton. This observation may imply that the spatial extent of the valence hole wavefunction in the metallic 2DEG plus hole system is intermediate between that of X_s and a neutral exciton.

Negatively Charged Excitons (X^-) and D $^+$ Triplet Transitions in GaAs/Al_{0.3}Ga_{0.7}As Multiple Quantum Wells

S.R. Ryu, W.-Y. Yu, L.P. Fu, Z. Jiang, A. Petrou, and B. D. McCombe
 Physics Dept., SUNY at Buffalo, Buffalo, NY 14260, USA
 Emory University, Physics Dept., Atlanta, GA 30322, USA

W. Schaff
 School of Electrical Engineering, Cornell University, Ithaca, NY 14853, USA

ABSTRACT

From a combination of low temperature photoluminescence (PL) and far infrared magnetospectroscopy on several GaAs/AlGaAs multiple-quantum-well samples with different donor doping (well only, barrier only, both well and barrier) we have identified a recombination line due to negatively charged excitons (X^-). We have also studied the effects of excess free electrons in the wells on the X recombination. Magnetoo-PL for low density barrier-only-doped samples shows at values of field studied both free exciton and X^- recombination lines. However, for a more heavily doped sample ($3.2 \times 10^{11} \text{ cm}^{-2}$) the behavior is very different. As magnetic field is increased three distinct features evolve from the broad free carrier recombination lines. At low fields all three features are Landau level recombination lines. At a field corresponding to filling factor $v=2$ the lowest energy line undergoes a discontinuous change in slope and above this field it evolves into the X^- line. In related studies we have made a clear identification of one of the predicted negative donor ion (D^-) triplet transitions by far infrared magnetospectroscopy.

1. Introduction

In the past few years considerable theoretical and experimental work has been carried out on negative donor ions (D^-) in quasi-two-dimensional structures. The D $^-$ singlet transition has been observed for Si donors in a variety of GaAs/AlGaAs Multiple-Quantum-Well (MQW) samples [1, 2, 3]. However, negatively charged exciton (X^-), the excitonic analog of D $^-$, has only recently been observed in quasi-2D system [4, 5]. The binding energies of X^- in bulk semiconductors [6] and in the strict 2D limit [7] have been calculated for various electron/hole mass ratios. The identification of X^- was initially made in the CdTe/CdZnTe system [4], and very recently in modulation doped GaAs/AlGaAs structures [5]. However systematic investigations of different sample structures with different doping placement (wells, barriers, wells and barriers) and careful comparisons of various PL features have not been reported for the GaAs/AlGaAs system. In this work, we report results of such a study which substantiate the existence of strong X^- recombination lines in appropriate samples. In related work on some of the same samples, we have clearly identified one of the predicted D $^+$ triplet transitions [8, 9], the experimental observation of which has been the subject of some controversy [10, 11].

2. Sample and Experiments

We have performed reflectivity measurements at zero magnetic field, photoluminescence (PL) measurements in zero field and as a function of magnetic field, and far infrared magneto-transmission and photoconductivity measurements on a wide variety of GaAs / AlGaAs MQW samples [Table 1]. The PL was excited with the 488nm line of an Ar $^+$ ion laser and analyzed with a 3/4 meter double

monochromator / photomultiplier combination. Zero field measurements were performed at low temperature (1.5K to 15K) in a supervirtanemp optical cryostat and at temperatures between 10K and 70K in the optical tail of a Helium refrigerator. Measurements of the field dependence were carried out in a variable temperature optical superconducting magnet cryostat capable of 8T at temperatures between 5K and 50K. The far infrared magnetotransmission and photoconductivity studies were made with a Fourier transform spectrometer and an optically pumped far infrared laser system in conjunction with light-pipe, condensing cone optics and a 9T variable temperature superconducting magnet system.

The MQW samples with Al_{0.3}Ga_{0.7}As barriers were grown by MBE. Samples 1 - 4 are 0-doped with Si donors at the centers of the wells or the centers of the barriers (or both). The wide barriers of samples 1, 2 and 4 avoid complications due to the possibility of electronic bound states in the wells associated with the barrier impurities. Samples 5 - 7 were doped with Si donors over the central 1/3 of the barriers only.

3. Results and Discussion

Samples 1 - 4 were chosen for a systematic PL and FIR magnetospectroscopy study of the possibility of X $^-$ recombination. Sample 1 (doped in the barriers only) shows two PL features at low temperatures separated by 10cm $^{-1}$; the lower energy feature is labeled Y and the heavy hole free excitation is labeled X in Fig. 1a. The intensity of feature Y, which dominates at 10K, decreases rapidly with increasing temperature, while X remains and shifts down in energy as the gap narrows. At 30K, X is dominant, and Y is discernable as a low energy shoulder. Sample 2 (doped in the wells only), also shows two dominant features (with a low energy tail), but these are separated by 16cm $^{-1}$; the higher energy feature (X), is again the heavy hole free exciton, while we identify the low energy feature as the neutral-donor-bound exciton D 0 -X. FIR magnetospectroscopy of these samples shows no indications of impurities located at other than their nominal doping positions, i.e., sample 1 shows only a sharp cyclotron resonance of electrons in the wells, and sample 2 shows only transitions associated with neutral donors in the wells at low temperatures. The temperature dependence of D 0 -X is characteristic of a (weakly) bound state (the binding energy is about 2meV). Sample 3, which is doped in both the barriers and the wells, exhibits four distinct features in the PL spectrum labeled A, D 0 -X, Y and X in Fig. 1c. The separation between X and D 0 -X is 16cm $^{-1}$ and that between X and Y is 10cm $^{-1}$, identical to samples 2 and 1, respectively. It is likely that feature A is due to neutral-donor-valence band recombination (as is the low frequency tail in sample 2) [12]. Note that both D 0 -X and Y decrease rapidly with increasing temperature; with the integrated intensity of Y (obtained from Lorentzian fits) decreasing somewhat more rapidly than that of D 0 -X, consistent with a smaller binding energy for Y. In sample 4, which is nominally identical to sample 3 except for a higher barrier doping density, a spectrum very similar to that of sample 1 is observed (Fig. 1d); the only clear features are the Y line and the heavy-hole free exciton (X). Just as in sample 1, feature Y dominates at low temperature, rapidly decreasing in intensity with increasing temperature. Note that D 0 -X is

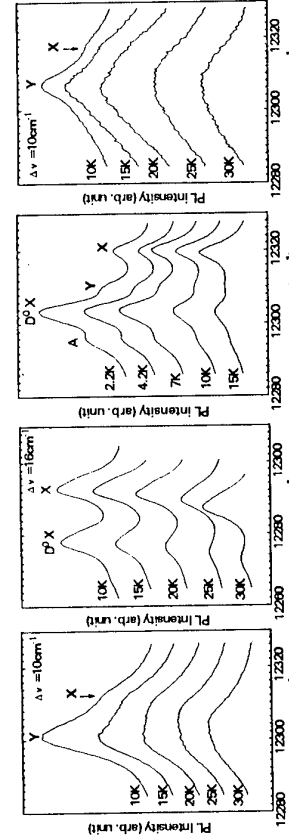


Fig. 1. Temperature Dependence of PL at $B=0$: (a) sample #1, (b) sample #2, (c) sample #3, (d) sample #4.

not observed in this sample, indicative of a very low density of neutral donors. This is confirmed by far infrared magnetospectroscopy, which showed only free electron cyclotron resonance and D° transitions in sample 4, but both D° and D' transitions in sample 3.

Feature Y cannot be associated with donor impurities (of any charge state) in the wells. It is not observed in sample 2 but is dominant in sample 1 (which has no observable donors in the wells). It is also strong in sample 4, which has a significant density of excess electrons in the wells and shows free carrier cyclotron resonance and D' ion transitions in far infrared magnetospectroscopy. In the sample (#3) that shows both neutral donor transitions and D° transitions, as well as a weak free carrier cyclotron resonance in FIR spectroscopy, both D°-X and feature Y are seen, with Y much weaker than D°-X. The studies of temperature dependence of the intensities of the various features show that Y is associated with a bound state and has a binding energy that is smaller than D°-X. These facts combined with the measured shift of Y from the heavy hole free exciton, and magneto-PL measurements that demonstrate that it is excitonic lead to our identification of this feature as the X-exciton. The binding energy of the second electron is 1.2 meV, consistent with observations in the GaAs/AlGaAs system [5] and also consistent with scaled value from CdTe/CdZnTe system [4].

We have also studied systematically the effect of excess electrons in the wells on X in sample 5 - 7, which are doped in the barriers only. Magneto-PL spectra taken on samples $5 (2 \times 10^{10} \text{ cm}^{-2})$ and $6 (8 \times 10^{10} \text{ cm}^{-2})$ show both X and X'. However, the behavior of Sample 7 is dramatically different, as shown in Fig. 2. Three distinct features evolve with increasing magnetic field from the broad free electron gas recombination at zero magnetic field. At low fields all three features are conduction - valence band Landau level transitions, which extrapolate to an effective gap smaller than the bare e-h-hl level transitions due to band gap renormalization. The lowest energy feature, which at low field is due to recombination between the lowest electron Landau level (0_e) and the highest heavy hole Landau level (0_h) undergoes a discontinuous slope change near filling factor $v = 2$, and then follows very closely the energy and field dependence of X observed in the other two samples [Fig. 2]. Similar behavior has been reported in absorption for the

CdTe/CdZnTe system [4].

In related work on some of the same samples (1-4) we have made a careful search for predicted D° triplet transitions. In addition to the singlet transition, two strong triplet transitions are allowed for D° ions [8,9]. We have observed two distinct transitions on the low energy (high field) side of cyclotron resonance in both Fourier Transform Spectroscopy and laser magneto-spectroscopy. Some of the results obtained in photoconductivity with the FIR laser are shown in Fig. 3; the two features are labeled A and B. Extensive studies of the temperature and carrier density dependence of these transitions have led us to conclude that feature A (12.5 cm^{-1} below CR) is the low energy D° triplet transition and feature B (8.9 cm^{-1} below CR) is a D° intra-excited-state transition, $2p-2s$ (in the low field hydrogenic notation). We have also observed two new quasi-2D features in the laser magneto-photoconductivity spectra (C and D in Fig. 3). Feature C appears between CR and the D° singlet transition, is more prominent in samples with higher barrier doping (it is not observed in the well-only-doped sample), and decreases in strength with increasing temperature. It is likely that this is the predicted high frequency triplet transition, but we are unable to make a more conclusive statement at this time. Feature D lies between the D° singlet transition and the D° 1s-2p° transition; this line increases in strength with increasing temperature, and is assigned to a transition between D° excited states. Detailed results, including FTIR and laser magneto-transmission data, and a statistical model of the occupancy of the various states will be published elsewhere.

This work was supported in part by ONR and the ONRMFEL program.

References

- [1] S. Huant, S.P. Najda and B. Etienne, Phys. Rev. Lett. **65**, 1486 (1990)
- [2] S. Holmes, J.-P. Cheng, B.D. McCombe and W. Schaff, Phys. Rev. Lett. **70**, 489 (1993)
- [3] E.R. Mueller, D.M. Larsen, J. Waldman and W.D. Goodhue, Phys. Rev. Lett. **68**, 2204 (1992)
- [4] K. Kheng *et al.*, Phys. Rev. Lett. **71**, 1752 (1993)
- [5] G. Finkelstein, H. Shtrikman, and I. Bar-Joseph, Phys. Status Solidi (b) **64**, 213 (1974)
- [6] G. Munschy and B. Stébé, Phys. Status Solidi (b) **105**, 545 (1989)
- [7] B. Stébé and A. Ainane, Superlattices and Microstruct. **5**, 545 (1989)
- [8] A.H. MacDonald, Solid State Comm. **84**, 109 (1992)
- [9] A.B. Dzyubenko, Sov. Phys. Solid State **34**, 1732 (1992)
- [10] W.J. Li, J.L. Wang, B.D. McCombe, J.-P. Cheng, and W. Schaff, Surf. Sci. **305**, 215 (1994)
- [11] A.B. Dzyubenko *et al.*, Phys. Rev. B **50**, 4687 (1994)
- [12] X. Liu, A. Petrou, B.D. McCombe, J. Ralston and G. Wickes, Phys. Rev. B **38**, 8522 (1988)

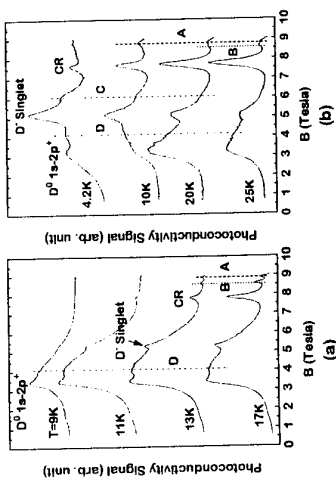


Fig. 2. Magneto-PL of sample #7. Lines for sample #5 for comparison; dotted line for X, solid line for X'.

Coherent Submillimeter-Wave Emission from Non-Equilibrium Two-Dimensional Free Carrier Plasmas in AlGaAs/GaAs Heterojunctions

K. Hirakawa, I. Wilke, and K. Yamanaka
Institute of Industrial Science, University of Tokyo, 7-22-1 Roppongi, Minato-ku, Tokyo 106, Japan

H. G. Roskos, M. Voßbürger, F. Wolter, C. Wachisse, and H. Kurz
Institut für Halbleitertechnik II, RWTH Aachen, Sommerfeldstrasse 24, D-52056 Aachen, Germany

M. Grayson and D. C. Tsui
Department of Electrical Engineering, Princeton University, Princeton, NJ 08544, U.S.A.

Abstract

We have investigated the coherent submillimeter-wave radiation from non-equilibrium plasma oscillations in AlGaAs/GaAs heterojunctions by time-resolved terahertz (THz) emission spectroscopy. The observed decay rate of optically excited plasma oscillations is found to be much shorter than the momentum relaxation time, suggesting that non-equilibrium hot two-dimensional (2D) plasmon modes relax via strong carrier-carrier interactions.

Introduction

The radiative decay of grating-coupled two-dimensional (2D) plasmons in semiconductor heterostructures is one of the most promising candidates for tunable solid-state far infrared (FIR) sources. Intensive studies have been done on plasmon emission from selectively doped Al_{0.3}Ga_{0.7}As/GaAs heterostructures [1,2] as well as Si metal-oxide-semiconductor field-effect transistors (MOSFETs) [3,4]. In spite of its potential, a detailed study of the emission properties of 2D plasmons has not been done because of the difficulties in performing spectroscopic analysis on weak FIR radiation from such structures.

In this work, the excitation of 2D plasmons in AlGaAs/GaAs heterostructures has been investigated by time-resolved THz emission spectroscopy [5]. Coherent submillimeter-wave emission from nonequilibrium free-carrier plasma oscillations generated by femtosecond laser pulse illumination has been observed for the first time. The observed spectral linewidths are found to be much broader than those observed in a quasi-static THz emission experiment [6] as well as those expected from the equilibrium dc electron mobility. Thus, the relaxation is much faster than the momentum relaxation, suggesting that non-equilibrium hot 2D plasmon modes relax presumably via strong carrier-carrier interactions.

Time-Resolved Plasmon Emission Experiments

The sample used in this experiment was a selectively doped AlGaAs/GaAs single-interface heterojunction. The electron density and the low-field mobility of the sample were $5.4 \times 10^{11} \text{ cm}^{-2}$ and $4 \times 10^5 \text{ cm}^2/\text{V}\cdot\text{s}$, respectively. In order to couple the 2D plasmons with electromagnetic radiation, an Al grating coupler with period Λ of $3 \mu\text{m}$ was fabricated on the sample surface by standard photolithographic technique. The metal-stripe/gap ratio of the grating was approximately 3/1. The thickness of the Al_{0.3}Ga_{0.7}As layer, d , which separates the Al grating coupler and the 2D electron system was 62 nm.

A non-equilibrium plasmon distribution was impulsively created by shining 100 fs-long laser pulses (20 meV FWHM bandwidth) from a mode-locked Ti:Al₂O₃ laser through the opaque Al grating stripes. The incident-beam angle was set to be 45°. The time-averaged laser beam power was 120 mW. The coherent electromagnetic transient emitted from the sample in the direction of the zeroth-order-reflected optical beam was detected by a micro-dipole antenna gated with delayed probe laser pulses, as schematically shown in Fig. 1. The laser wavelength was varied over a range from 768 nm to 817 nm, and the sample temperature was changed from 10 K to 200 K. The detail of the time-resolved THz emission spectroscopy is reported elsewhere [5].

Figure 2 (a) shows the results of THz emission measurements performed at various temperatures, T . The laser wavelength was set at 774 nm. From room temperature down to 200 K, the THz waveform consists of a single-cycle oscillation. With decreasing T , additional features appear in the trailing part of the main pulse and gradually become more pronounced. The small peak at 5.5 ps after the main pulse is the reflection of the main pulse at the backside of the wafer. Figure 2 (b) shows the Fourier transforms of the time-domain data. When $T < 150$ K, two FIR emission peaks are clearly seen at 0.45 THz and 0.9 THz. The frequencies of the two FIR emission peaks are in good agreement with the calculated first- and second-order plasmon frequencies [7] as well as those observed in the cw FIR emission experiment [6]. This fact clearly indicates that these coherent THz radiation peaks are due to radiative decay of 2D plasmons.

With decreasing T from 200 K to 70 K, the emission linewidth decreases from 0.27 THz ($\tau = 1.2$ ps) down to 0.15 THz ($\tau = 2.2$ ps) due to the reduction of the LO phonon scattering rate. Below 70 K, the emission spectra are almost unchanged and the linewidth saturates at around 0.11 THz ($\tau = 3$ ps). The plasmon decay rate will be discussed in more detail later.

Excitation of 2D Plasmons by Femtosecond Laser Pulses

In order to obtain information on the mechanism of excitation of the plasmons, we performed low-temperature THz emission experiments with variable photon energy of the pump beam. Figure 3 shows the Fourier transforms of the detected THz transients (not corrected for the spectral characteristics of the detection system). The reflection from the wafer backside is removed numerically by temporal windowing, which limits the spectral resolution of the Fourier transforms. The average power of the pump beam was kept to be 120 mW, while the wavelength was varied. Except for the shortest wavelength of 768 nm, the shape of the Fourier spectra in Fig. 3 does not vary significantly with the wavelength of the pump pulse, while the amplitude of the THz signal shows a strong dependence. THz emission sets in at 817 nm, which corresponds to the low-temperature bandgap of GaAs. The emission is initially weak but increases continuously in amplitude as the laser wavelength decreases to 768 nm.

The wavelength dependence is rather typical for THz emission from semiconductors upon valence-to-conduction-band excitation [8]. The onset of the THz signal is, however, much better explained by assuming an absorption edge at about 800 nm. This is consistent with optical transitions from the valence band maximum to the lowest quantized subband in the conduction band [9], rather than with the bandgap of bulk GaAs. This observation strongly suggests that only carriers excited in or very close to the accumulation layer contribute to the excitation of coherent plasma oscillations.

Periodic carrier-density variations by the optical excitation through the opaque Al grating provide an explanation for the mechanism of the generation of plasma oscillations. The periodic lateral density variations are expected to drive plasmons by inducing local currents with the lateral periodicity of the grating, which are caused by the following mechanisms: (i) The addition of electrons to the accumulation layer leads to a rise of the electron quasi-Fermi level, E_F . This effect will induce a lateral electron surge from the unmasked regions into the masked regions where E_F is lower. Assuming a $\delta(t)$ -like time dependence of the excitation, one estimates that the addition of 1×10^{10} electrons per cm^2 in the accumulation channel raises E_F by 0.36 meV at low temperatures.

(ii) The optically generated electron/hole pairs are instantaneously polarized in the dopant-induced static electrical field across the heterojunction [5,8]. The polarized photoexcited carriers partly screen the static confinement field, resulting in a reduction of the energies of the quantized electronic states. As the confinement potential becomes shallower, the subband energy changes with respect to that in the unilluminated regions, inducing a lateral electron surge.

Whatever the details of the excitation mechanism, the fact that our measurement technique is only sensitive to coherent THz radiation implies that the emission originates from plasmons which are initially all in phase with each other. In contrast, the radiation detected in the current-mediated FIR measurements stems from random plasma oscillations. Also, note that only the plasmon modes with wavevector $q = 2\pi i/\Lambda$ ($i = 1, 2, 3 \dots$) are excited by the femtosecond laser pulses.

Decaying Rate of Non-equilibrium 2D Plasmons

We finally discuss the decay time constant τ of the plasmons. At sample temperatures above 10 K, τ is limited by scattering with optical phonons. For temperatures below 10 K, however, τ approaches a value of 3 ps. This decay time constant is significantly shorter than that inferred from the cw FIR emission experiment [6], where it was concluded that the experimentally deduced time constant is well explained by the momentum scattering time of 16 ps.

The faster decay in the present experiment may be a consequence of a nonequilibrium nature of the excited coherent plasmon modes. In current-mediated cw THz plasmon emission experiments, all the electronic excitation modes are equally excited by joule heating and resulting rise in electron temperature [6]. Therefore, the 2D plasmon modes which participate in the THz emission are in quasi-equilibrium with other plasmon modes as well as single-particle excitation modes. On the contrary, in the present time-resolved THz emission experiment, only the plasmon modes which are commensurate with the period of the Al grating are excited by femtosecond laser pulses and other plasmon modes stay cold. Consequently, the optically excited nonequilibrium plasmon modes may quickly decay due to efficient carrier-carrier interactions with other cold modes, leading to a much shorter decay time constant.

Summary

We have investigated the coherent submillimeter-wave radiation from non-equilibrium plasma oscillations in AlGaAs/GaAs heterojunctions by time-resolved terahertz (THz) emission spectroscopy. The observed decay rate of optically excited plasma oscillations is found to be much shorter than the momentum relaxation time, suggesting that non-equilibrium hot 2D plasmon modes relax via strong carrier-carrier interactions.

Acknowledgements

This work was supported by the Grant-in-Aid from the Ministry of Education, Science, and Culture and also by the Industry-University Joint Research Program "Quantum Nanoelectronics (Q-NANO)". The work at RWTH Aachen was supported by the Deutsche Forschungsgemeinschaft and the Friedrich Krupp Foundation, and the work at Princeton was supported by the Army Research Office (DAHA0493G0071).

References

- [1] R. Höpfel, G. Lindemann, E. Gornik, G. Stangl, A. C. Gossard, and W. Wiegmann, *Surf. Sci.* **113** (1982) 118.
- [2] N. Ohtsu, Y. Sanbo, and T. Kobayashi, *Appl. Phys. Lett.* **48** (1986) 776.
- [3] D. C. Tsui, E. Gornik, and R. A. Logan, *Solid State Commun.* **35** (1980) 875.

- [4] R. A. Höpfel, E. Vass, and E. Gornik, *Phys. Rev. Lett.* **49** (1982) 1667.
- [5] H. G. Roskos, M. C. Nuss, J. Shah, K. Leo, D. A. B. Miller, A. M. Fox, S. Schmitt-Rink, and K. Kohler, *Phys. Rev. Lett.* **68** (1992) 14.
- [6] K. Hirakawa, K. Yamamoto, M. Grayson, and D. C. Tsui, submitted to *Appl. Phys. Lett.*
- [7] L. Zheng, W. I. Schach, and A. H. MacDonald, *Phys. Rev. B* **41** (1990) 8493.
- [8] P. C. M. Planken, M. C. Nuss, I. Brener, K. W. Goossen, M. S. C. Luo, S. L. Chuang, and L. Pfeiffer, *Phys. Rev. Lett.* **69** (1992) 3800.
- [9] T. Ando, *J. Phys. Soc. Jpn.* **51** (1982) 3893.

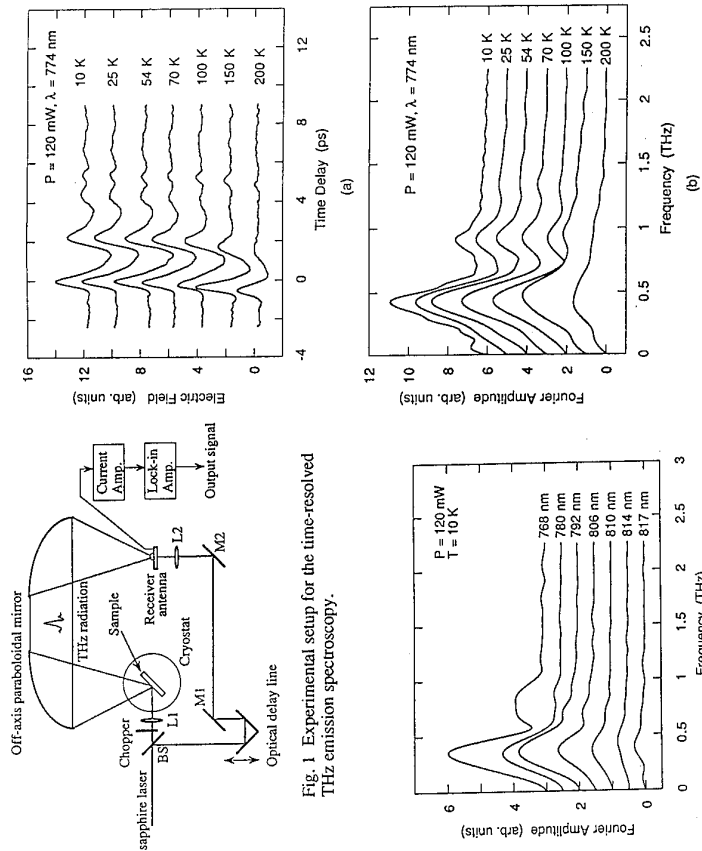


Fig. 1 Experimental setup for the time-resolved THz emission spectroscopy.

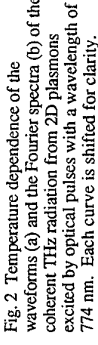


Fig. 2 Temperature dependence of the (a) waveforms and the Fourier spectra (b) of the coherent THz radiation from 2D plasmons excited by optical pulses with a wavelength of 774 nm. Each curve is shifted for clarity.

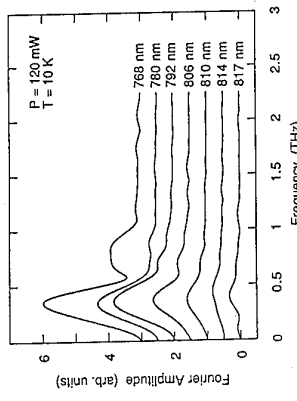


Fig. 3 Fourier transforms of the detected THz radiation for various wavelengths of the optical excitation pulses. Each curve is shifted for clarity.

**Optical Anisotropy of Doped Type I Quantum Wire Arrays :
From The Zone Center To The Fermi Edge**

T. Mélin and E. Laroche,
Laboratoire de Microstructures et de Microélectronique, C.N.R.S.,
B.P. 107, 92225 Bagneux Cedex, France.

Abstract

The photoluminescence spectrum of modulation doped tilted lateral superlattices is shown to exhibit a systematic enhancement at the Fermi edge. This is explained by considering the nature of the lateral potential which localizes the hole in a 1D potential for vertical lateral superlattices or couples the first two electric subbands in tilted lateral superlattices.

1. Introduction

The Fermi edge of the optical spectrum of a degenerate Electron System (ES) is singular due to the many-body interaction of electrons with the photocreated hole [1]. The singularity is weakened by the dynamical response of the Fermi sea [2, 3]. For ES embedded in semiconductors, the photocreated hole is free to move in the valence band leading to a smearing of the singularity due to the hole recoil induced by the Coulomb interaction [4, 5]. Therefore Fermi edge singularities have been clearly identified with two dimensional (2D) ES confined in III-V semiconductors in which alloy disorder provides the suitable hole localization that prevents the hole recoil [6]. When the second electric subband of the 2D ES is brought into resonance with the Fermi level, this leads also to pronounced Fermi edge singularities [7]. Our purpose is to demonstrate that a one-dimensional (1D) ES located in a tilted Lateral Superlattice (LSL) formed on a semiconductor vicinal surface [8] exhibit a systematic enhancement of the optical intensity at the Fermi edge. This is directly connected with the lateral potential symmetry. The hole phase space scattering reduction [9] in vertical LSLs and the coupling with the second electric subband in tilted LSLs are responsible for the observed Fermi edge enhancement.

2. Theory

A LSL on a vicinal surface with a terrace periodicity L_x consists in the stacking of N fractional monolayers (ML). Each LSL layer is made of GaAs and AlAs which are laterally intermixed so that the lateral Al concentration is best described as a cosine function with a L_x periodicity. This layer covers a fraction $1+\epsilon$ of the surface as depicted in fig.1. From one LSL layer to the other the cosine potential undergo a phase change of $2\pi\epsilon$ so that the LSL is vertical for $\epsilon=0$ and tilted otherwise. The resulting lateral potential can be written as :

$$V_\epsilon(x, z) = V_0 \left[1 + \lambda \cos\left(2\pi\frac{x}{L_x} + 2\pi\epsilon\frac{z}{a}\right) \right] \quad (1)$$

where V_0 is proportional the average Al content and to the band offset and a is the ML thickness.

λ describes the lateral growth ordering of GaAs and AlAs (it is typically 0.15–0.25). Due to the relative band offset between both materials we have : $V_0^{\text{conduction}} - 2V_0^{\text{valence}}$ so that the potential modulation is of type I. To eliminate the z dependence in Eq. 1 in case of an imperfect coverage ($\epsilon \neq 0$), we compute matrix elements between states of an infinitely deep quantum well Ψ_n

$$\Psi_n(z) = \sqrt{\frac{2}{Na}} \sin\left(\frac{n\pi z}{Na}\right), \quad (2)$$

in which a LSL potential is inserted. We get :

$$\begin{aligned} V_\epsilon^{m,n}(x) &= -\frac{V_0}{\pi} A_\epsilon^{m,n} \left\{ \cos\left[\pi N\epsilon + (m+n)\frac{\pi}{2}\right] \cos\left[\frac{2\pi x}{L_x}\right] - \sin\left[\pi N\epsilon + (m+n)\frac{\pi}{2}\right] \sin\left[\frac{2\pi x}{L_x}\right] \right\}, \\ A_\epsilon^{m,n} &= \frac{16 mn N\epsilon}{[(m-n)^2 - 4N^2\epsilon^2][(m+n)^2 - 4N^2\epsilon^2]} \sin[\pi N\epsilon + (m+n)\frac{\pi}{2}]. \end{aligned} \quad (3)$$

Fig. 2 displays the amplitude $A_\epsilon^{m,n}$ for $\{m,n\}=\{1,2\}$ as a function of $N\epsilon$. It can be noticed that the LSL tilt weakens the lateral potential for $m=n$ with an additional resonance in the case of $m=n=2$ when $N\epsilon \approx 1.8$. More striking is the coupling induced by a tilted LSL between the first and second subbands which is maximum when $N\epsilon=1$. In that case, the second subband does not feel any lateral potential since $A_{1,2}^{1,2}=0$. This reveals the peculiar nature of lateral potentials induced by tilted LSLs grown on vicinal surfaces.

3. Experiments

Samples were grown by molecular beam epitaxy (MBE) on GaAs vicinal substrates with a 32 nm terrace periodicity (0.5° miscut). The average LSL Al content is 7% and N is nominally 71 ML (20.1 nm) in sample A and 55 ML (15.6 nm) in sample B. Both LSLs are confined between two $\text{Ga}_{0.67}\text{Al}_{0.33}\text{As}$ barriers. The top barrier is remotely doped with a silicon sheet located 9 nm away from the LSL upper interface to provide an electron sheet density in the range of $7.8 \times 10^{11} \text{ cm}^{-2}$ under illumination. Samples are grown without substrate rotation in front of the MBE crucibles so that the spatial inhomogeneity of Ga and Al fluxes produces a continuous set of coverages on the wafer. Flux spatial variations are recorded in two reference quantum wells which allow their absolute determination from photoluminescence (PL) spectroscopy [10]. ϵ is therefore known with a high accuracy. Optical spectroscopy is performed in superfluid He at 1.8 K by scanning a 40 μm spot on the sample so that ϵ is defined with an 1×10^{-4} accuracy. The measurement spacing on the sample is 250 μm . Optical excitation is provided by a tunable Ti:Sa laser with a typical power of 300 μW . PL is analyzed with a double monochromator and with a GaAs photomultiplier connected to a gated photon counter which is synchronized with a photoelastic modulator in order to measure either PL or PL excitation (PLE) linear polarization [11].

4. Results and discussion

Fig. 3 displays PL and PLE spectra of samples A and B for various coverages ϵ . Both samples have very similar Fermi energies ($\approx 25 \text{ meV}$) as obtained from the width of the PL line up to the PL Fermi edge shown by an arrow. For such an Al content (7%), random alloy fluctuations are strong enough to localize holes so that PL can be observed up to the Fermi energy. Since PL spectrum is dominated by the low energy peak, the hole localization is not sufficient to prevent the hole recoil as observed in $\text{In}_{0.47}\text{Ga}_{0.53}\text{As}$ quantum wells where the PL line is dominated by recombination at

7. References

- the Fermi edge singularity [6]. Note the closer proximity to the Fermi level of the second subband edge in sample A because of a thicker LSL : the E₂-H₁ excitonic peak lies in the vicinity of the Fermi edge in PL and PLE spectra.
- In both samples the Fermi edge intensity systematically increases as ϵ goes to zero with an absolute maximum for non zero ϵ and a relative minimum for $\epsilon=0$. To evidence this effect, we plot the Fermi edge intensity normalized by the low energy peak intensity as a function of ϵ in fig. 4. We attribute the additional Fermi edge intensity for non zero ϵ values to the coupling with the second electric subband. The resonance of the Fermi level with the second subband edge E₂ is known to give rise to a strong Fermi edge singularity [7]. Here, E₂ lies above the Fermi level at some finite energy in both samples (6.5 meV in sample A, 21 meV in sample B). The E₁-E₂ coupling is provided by the tilted LSL so that the resonance is no longer required to produce the Fermi edge enhancement. Moreover the Fermi wavevector k_F ($2.2 \times 10^6 \text{ cm}^{-1}$) is very close to $2\pi/L_x$ ($2 \times 10^6 \text{ cm}^{-1}$) so that Fermi electrons are very efficiently coupled to the second subband at the zone center by the LSL potential. The absolute maxima lie for $|\epsilon|=0.013 \pm 0.002$ in sample A, and $|\epsilon|=0.023 \pm 0.001$ in sample B. Since the coupling between the first two subbands is maximum for $\epsilon=1/N$, these values of ϵ are in good agreement with the LSL thickness : $1/\epsilon=68 \pm 9$ in sample A ($N=71$) and $1/\epsilon=43 \pm 2$ in sample B ($N=55$).

Following the two level model of ref. 7, we compute the E₂ contribution to the Fermi edge intensity. The fit requires the knowledge of the V_{01} term in the conduction band in Eq. 3 which we determine to be 8.2 meV in sample A and 9.6 meV in sample B by fitting the PL linear polarization for $\epsilon=0$ (14.2% parallel to the wires in both samples). The oscillator strength M₁ and M₂ of the two coupled transitions is adjusted to fit the Fermi edge enhancement for $\epsilon=1/N$. The M₂/M₁ ratio is found to be 29 in sample A and 22 in sample B. These values are more than twice smaller than the ratio obtained from the resonant situation : 66 [7]. To produce the theoretical curves in fig. 4, we use the values of N determined above. We notice the systematic discrepancy of our fit with experimental data for $|\epsilon|$ larger than $2/N$. This might originates in our treatment that neglects the hole subband coupling by the tilted LSL which also increases the overlap with electrons.

The enhanced Fermi edge intensity for $\epsilon=0$, can be fully attributed to the 1D nature of the ES [9] because the coupling with the second subband is ineffective. Alternatively for $\epsilon=0$, the hole mass is heavier along x than along y due to the LSL potential. This hole mass enhancement may also explain the greater intensity at the Fermi edge [5].

5. Conclusion

We have shown here theoretically as well as experimentally the effect of LSL on the optical properties of modulated ES in a type I configuration. The systematic enhancement of the PL intensity at the Fermi edge is shown to originate from the E₁-E₂ coupling in tilted LSLs and from the 1D nature of holes for vertical LSLs. Our analysis shows that the relative oscillator strength of the second subband transition is a factor of two smaller than determined from a resonant situation.

6. Acknowledgments

We acknowledge fruitful and stimulating discussions with B. Etienne, C. Tanguy, F. Lelarge, L. Sfaxi, F. Petit and wish to thank A. Cavanna for technical support in the growth of the samples.

Figures

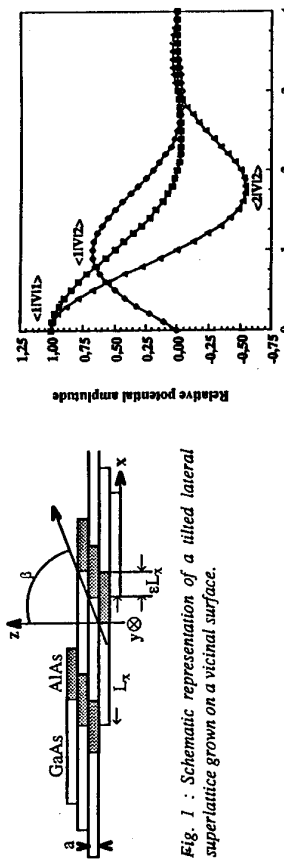


Fig. 1 : Schematic representation of a tilted lateral superlattice grown on a vicinal surface.

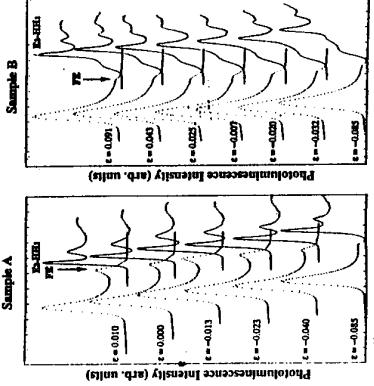


Fig. 2 : Plot of $A^{m,n}_\epsilon$ as a function of the dimensionless parameter $N\epsilon$ for $(m,n)=(1,2)$.

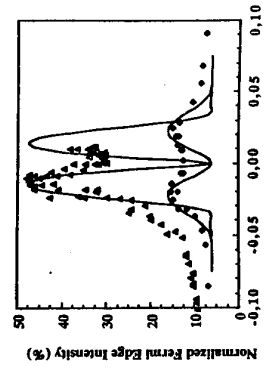


Fig. 4 : Normalized Fermi edge intensity for sample A (Δ) and B (●) as a function of ϵ . Continuous lines are fits to the experimental data as described in the text.

Fig. 3 : PL (dotted line) and PLE (continuous line) spectra for various values of ϵ for both samples.

Magnetic Field Dependence of Many-Body Processes in Quantum Well Luminescence

H.P. van der Meulen, J. Rubio and J.M. Calleja
 Instituto Nicolas Cabrera. Universidad Autónoma de Madrid
 Cantoblanco, Madrid 28049, Spain.

H. Schweizer, F. Scholz, V. Härlé and R. Bergmann
 Physikalisches Institut der Universität Stuttgart
 Pfaffenwaldring 57, 70550 Stuttgart, Germany.

Abstract

The effect of electron-electron interactions on the optical properties of a two-dimensional electron gas under magnetic fields is studied in a modulation-doped single quantum well of InGaAs. Optical singularities at the Fermi level and shakeup sidebands are observed at low temperatures. Their intensities and lineshapes undergo drastic changes which are periodic in the filling factor. The results are interpreted in terms of the magnetic field-dependent screening properties of the two dimensional electron gas.

Introduction

The optical properties of a degenerate electron gas are largely influenced by electron-electron interactions [1]. In semiconductor quantum wells the optical spectra of the two-dimensional electron gas (2DEG) display specific features due to many-body processes, such as a strong emission at the Fermi level (optical Fermi-edge singularity or FES) [1-4] and low-energy tails or sidebands in the emission spectra due to Auger-like processes (shakeup emission or SU) [4-6]. Both phenomena are determined by many-body processes in the Coulomb interaction between the electron gas and the photocreated hole. Their study can therefore give valuable information on electron-electron interactions and screening in a 2DEG, which are also relevant in transport phenomena like integer and fractional quantum Hall effect.

In this work we study the effect of a magnetic field on the emission spectra of a 2DEG in a single quantum well of InGaAs. Both FES and SU are observed at low temperatures. For increasing magnetic field, their intensities and lineshapes undergo drastic changes, which are periodic in the filling factor. Our results are interpreted in terms of the variable screening properties of the 2DEG, as it goes through compressible and incompressible states.

Experiment

The sample used is a 8 nm thick single quantum well of $\text{In}_{0.53}\text{Ga}_{0.47}\text{As}$ grown on a (100) InP substrate by low-pressure metalorganic vapor-phase epitaxy. The well is modulation-doped with 10 nm layers of InP containing 1.7×10^{13} S atoms per cm^3 in both barriers, separated from the well by 15 nm thick spacer layers. The electron density measured by Shubnikov-de Haas oscillations is around $8 \times 10^{11} \text{ cm}^{-2}$, in good agreement with the Fermi energy obtained from the

optical emission spectra. The mobility at 4.2 K is about $175,000 \text{ cm}^2/\text{Vs}$. Photoluminescence (PL) spectra were excited by the blue-green lines of an Argon laser using 1 mW power and linear or circular polarization. A double spectrometer and a Ge photodiode were used for detection. The spectrometer was purged with nitrogen to reduce water absorption in the spectral region of interest. The measurements were performed at 2.2 K in a superconducting magnet reaching up to 12 Tesla.

Both FES and SU are observed in the PL spectra for a wide range of magnetic fields, some of which are shown in Fig. 1. The FES appears as the intensity enhancement of the highest occupied LL, which disappears when the samples are heated above 40K [2,4]. The

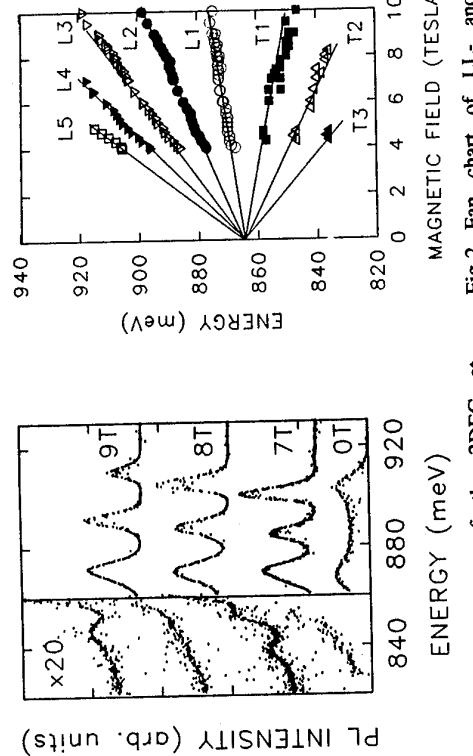


Fig.1 PL spectra of the 2DEG at different values of the magnetic field. The magnified low-energy region shows the field-dependent shakeup peaks.
 Fig.2 Fan chart of LL- and SU transitions. The interband energies are different, as explained in the text.

magnified low-energy region of Fig. 1 shows strong SU peaks [5] whose energies and intensities are field-dependent. The fan plot of both LL and SU peaks is given in Fig.2. It is very similar to that reported in ref. [5] except for the fact that the higher electron density of our sample allows the observation of 5 LL's in the PL spectra. The energy difference between adjacent SU peaks ($\text{m}^* = 0.046 \text{ m}_0$) is also slightly higher than that between LL's ($\text{m}^* = 0.053 \text{ m}_0$). Phonon sidebands have been observed in samples with lower electron density ($4 \times 10^{11} \text{ cm}^{-2}$). The Zeeman splitting of the different LL's (not shown in Fig.2) has been measured as the energy difference between PL signals for σ^+ and σ circular polarizations. It corresponds to an effective g factor

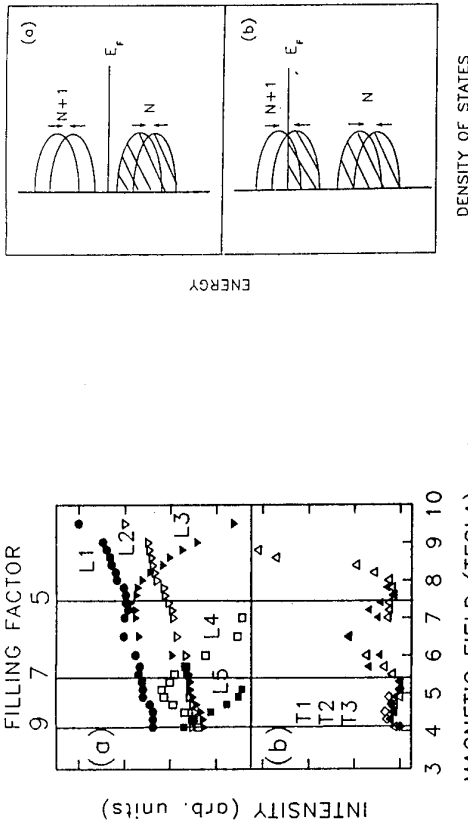


Fig. 3 (a) Peak intensities of the LL transitions versus magnetic field.
 (b) Peak-to-background ratio of the SU transitions versus magnetic field.

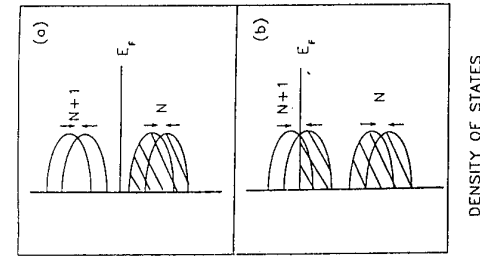


Fig.4 Schematic diagram indicating the alternance of compressible and incompressible states of the electron gas for (a) even and (b) odd filling factors.

The present results can be qualitatively understood as a consequence of the alternating compressible and incompressible character of the 2DEG as the field increases. For even filling factors the Fermi level lies between well separated LL's, as shown in the diagram of Fig. 4, and the 2DEG is essentially incompressible. The density of states (DOS) at the Fermi level is low and consequently the FES is weak [1]. In this situation the electronic excitations of lowest energy are inter-LL ones. Therefore SU transitions appear as well defined peaks at the cyclotron energy, with an effective mass close to the bare value (0.041 m_e [8]). The inter-LL spacing is slightly lower due probably to many-body effects. The SU peaks are strong because the poor screening of the electron-hole Coulomb interaction in the incompressible state [4].

The situation is contrary for odd filling factors, because the Zeeman splitting of our sample is smaller (around 3 meV at 12 T) than the inhomogeneous width of the LL transitions (6-7 meV). In this case the electron gas is a mixture of two (spin-up and spin-down) compressible systems, the DOS at the Fermi level is high and screening of the electron-hole interaction is efficient. Consequently low energy excitations across the Fermi level exist, which enhance the FES strength and smear the SU peaks into a continuous background. This behavior could not be observed in ref. [5], because the lower electron density of their sample resulted in filling factors lower than 2 for magnetic fields where SU peaks appear.

Conclusions

In conclusion the PL spectra of the 2DEG in a magnetic field presented here show that both the shape and the intensity of SU and FES change periodically with the filling factor. This behavior is the consequence of the changing values of the DOS at the Fermi level and the screening properties of the electron gas, as it goes through compressible and incompressible states.

Acknowledgements: This work has been supported by the ESPRIT-BRA contract No.6719 (NANOPT) of the E.U. and the project MAT94-0982-C02-01 of the spanish CICYT. Thanks are due to C. Tejedor, L. Brey and A. McDonald for helpful discussions.

References

- [1] G.D. Mahan, Many Particle Physics (Plenum, New York, 1990).
- [2] M.S. Skolnick, M. Ronison, K.J. Nash, D.J. Mowbray, P.R. Tapster, S.J. Bass and A.D. Pitt, Phys. Rev. Lett. **58** (1987) 2130.
- [3] P. Hawrylak, Phys. Rev. B **44** (1991) 11236.
- [4] T. Uenoyama and L.J. Sham, Phys. Rev. Lett. **65** (1990) 1048.
- [5] K.J. Nash, M.S. Skolnick, M.K. Saker and S.J. Bass, Phys. Rev. Lett. **70**, (1993) 3115.
- [6] P. Hawrylak, N. Pulsford and K. Ploog, Phys. Rev. B **46** (1992) 15193.
- [7] E.H. Perca, E.E. Mendez and C.G. Fonstad, Appl. Phys. Lett. **36**, (1980) 978.
- [8] O. Barolo, J.C. Woolley and J.A. van Vechten, Phys. Rev. B **8**, (1973) 3794.

Activated Conductivity in the Quantum Hall Effect

M. M. Fogler, D. G. Polyakov^(c) and B. I. Shklovskii
Theoretical Physics Institute, School of Physics and Astronomy,
University of Minnesota, 116 Church St. Southeast,
Minneapolis, MN 55455, U.S.A.

Abstract

Activated dissipative conductivity $\sigma_{xx}^* = \sigma_{xx}^* \exp(-\Delta/T)$ and the activated deviation of the Hall conductivity $\delta\sigma_{xy}^* = \sigma_{xy}^* \exp(-\Delta/T)$ from the precise quantization $\delta\sigma_{xy} = \sigma_{xy} - ie^2/h = \sigma_{xy}^* \exp(-\Delta/T)$ are studied in a plateau range of the quantum Hall effect. The prefactors σ_{xx}^* and σ_{xy}^* are calculated for the case of a long-range random potential in the framework of a classical theory. There is a range of temperatures $T_1 \ll T \ll T_2$, where $\sigma_{xx}^* = e^2/h$. In this range $\sigma_{xy}^* \sim (e^2/h)(T/T_2)^{80/21} \ll \sigma_{xy}^*$. At large $T \gg T_2$, on the contrary, $\sigma_{xy}^* = e^2/h$ and $\sigma_{xx}^* = (e^2/h)(T_2/T)^{10/13} \ll \sigma_{xy}^*$. Similar results are valid for a fractional plateau near the filling factor p/q if charge e is replaced by e/q .

The temperature dependence of the activated dissipative conductivity is widely used to study energy gaps in the quantum Hall effect. When the Fermi level lies in the middle between two Landau levels σ_{xx} has a form [1, 2, 3, 4]

$$\sigma_{xx} = \sigma_{xx}^* \exp(-\Delta/T), \quad (1)$$

provided the temperature T is not too low. The prefactor σ_{xx}^* has attracted a great deal of interest since σ_{xx}^* was claimed [2] to be equal to e^2/h independently of the Landau level number. This puzzling universality was observed in the fractional quantum Hall effect as well: at filling $\nu = p/q$ the prefactor $\sigma_{xx}^* = (e/q)^2/h$ [2]. On the other hand, both the numerical value of the prefactor [4] and the very independence of σ_{xx}^* on T have been questioned [3].

There have been several interesting attempts to calculate the prefactor universally, for any type of disorder, using the idea that at $T = 0$ an extended state exists at only one energy and phase-breaking processes are responsible for the delocalization of electrons within a narrow band of states near the Landau level center [2, 3, 5, 6, 7, 8]. Nevertheless, it has not been shown in these works that a range of temperatures exists where $\sigma_{xx}^* = e^2/h$. Two of us (PS) suggested a more specific approach and considered separately the cases of a short and a long-range random potential [9, 10]. In Ref. [9] they evaluated explicitly two major contributions to the conductivity for the case of a white noise potential: (i) from a narrow band of delocalized states which appear near the Landau level center at finite temperatures and (ii) from the variable range hopping between localized states in the tail of the density of states. It was shown that, in agreement with the conjecture made in Ref. [8], the interplay of these contributions is responsible for the inflection point in the dependence of $\ln \sigma_{xx}$ on $1/T$. PS demonstrated that in the vicinity of the inflection point σ_{xx} is a very slow function of the rate of phase breaking processes, and being fitted to the activation form [Eq. (1)] gives σ_{xx}^* somewhat smaller than e^2/h . So PS concluded that, strictly speaking,

no universality can be obtained for the case of a short range potential. In Ref. [10] PS calculated the prefactor σ_{xx}^* in the case of a long-range random potential $\epsilon(r)$, which exists in high-mobility heterojunctions. In this case, tunneling is suppressed and at not too low T the conductivity may be described by a completely classical theory. It was shown that there is a range of temperatures, where the prefactor is constant and universal. PS obtained $\sigma_{xx}^* = e^2/h$ for the contribution of a single Landau level to the conductivity in this range. The Plank constant appears in this expression only through the density of states at the Landau level.

Thermally activated electrons are also responsible for the deviation $\delta\sigma_{xy}$ from the precise quantization. At $T = 0$ the magnitude of σ_{xy} on each plateau is ie^2/h , where i is an integer. At finite temperatures the deviation $\delta\sigma_{xy} = \sigma_{xy} - ie^2/h$ from the precise quantization appears. This deviation is the second subject of this paper. First of all, we note that directly at the center of the plateau $\delta\sigma_{xy}$ must vanish due to electron-hole symmetry. Therefore, we consider the case when, say, the electron contribution to σ_{xy} dominates. This occurs when the Fermi energy is in the gap between two Landau levels but is closer to the upper one by at least several T . If the temperature is not too low so that variable range hopping can be neglected, then $\delta\sigma_{xy}$ determined by electrons thermally activated to the extended state at the classical percolation level $\epsilon = 0$ at the upper Landau level. One would expect

$$\delta\sigma_{xy} = \sigma_{xy}^* \exp(-\Delta/T), \quad (2)$$

where the activation energy Δ is the separation between the Fermi energy and the percolation level. The prefactor σ_{xy}^* was calculated in Ref. [11]. Below we will repeat the derivation of prefactors σ_{xy}^* and σ_{xx}^* and discuss the relation between them.

Let the correlation length d of the disorder potential be much larger than the magnetic length l_B . One can think of d as the setback distance of the nearby doping layer with charged impurities in a high-mobility heterostructure. The concentration of the activated electrons $n = (1/2\pi l_B^2) \exp[-(\Delta + \epsilon)/T]$ is exponentially small and we neglect the interaction between them. In the absence of inelastic scattering, guiding centers of electron orbits drift along the contours of constant ϵ , all of which for the exception of the one at $\epsilon = 0$ are closed loops. In this semiclassical picture the tunneling between two loops at the same energy ϵ is neglected. The tunneling occurs in the vicinity of saddle points where the loops come close to each other. However, the probability of such tunneling falls off with increasing barrier height V as $\exp(-V/T_1)$, where $T_1 \sim W(l_B/d)^2$ [12] with W being the standard deviation of $\epsilon(r)$. Below we consider the wide temperature range $T_1 \ll T \ll W$, and completely neglect the tunneling. Another important element of the model are inelastic electron-phonon processes. Due to them electrons can hop from one closed loop to another and thus travel across the entire sample. We assume that these inelastic processes are frequent enough, namely, that their rate τ_{ph}^{-1} is much higher than the characteristic frequency of drift motion. This inequality also implies that quantum coherence is completely destroyed by the inelastic collisions and together with the fact that quantum-mechanical tunneling is suppressed it means that in our model the motion of electrons is purely classical.

Typical hops occur between two contours a distance l_B from each other and so the characteristic phonon energy is $T_{ph} = WL_B/d$. The scattering rate can be readily evaluated using Fermi's golden rule to be $\hbar/\tau_{ph} = \alpha T$ for $T \gg T_{ph}$. For $T \ll T_{ph}$ one has to replace

α by $(eT_{\text{ph}})/(\sqrt{2\pi}T)$. Here $\alpha = \Xi^2/\rho h s^3 l_B^2$ is the electron-phonon coupling constant, and Ξ and ρ are the deformation potential constant and the crystal mass density, respectively. For GaAs $\alpha \simeq 0.03(100\text{\AA}/l_B)^2$ and this is the small parameter in this problem. Within this model we obtained

$$\sigma_{\text{xx}}^* = \frac{e^2}{h} \begin{cases} (1 + \alpha^2)^{1/2} & T_1 \ll T \ll T_2 \\ c_1(T_2/T)^{10/13} + O(\alpha^2), & T \gg T_2. \end{cases} \quad (3)$$

$$\sigma_{\text{xy}}^* = \frac{e^2}{h} \begin{cases} c_2(T/T_2)^{8/3}(T_{\text{ph}}/T_2)^{8/7}, & T_1 \ll T \ll T_{\text{ph}} \\ c_3(T/T_2)^{80/21}, & T_{\text{ph}} \ll T \ll T_2 \\ 1, & T \gg T_2, \end{cases} \quad (4)$$

where T_2 is defined as $\alpha^{10}W$. For σ_{xy}^* we got

$$\sigma_{\text{xy}}^* = \frac{e^2}{h} \begin{cases} (1 + \alpha^2)^{1/2} & T_1 \ll T \ll T_2 \\ c_4(T_2/T)^{10/13} + O(\alpha^2), & T \gg T_2. \end{cases}$$

Here c_i 's are numerical factors of order unity and we assume that $T_1 \ll T_{\text{ph}} \ll T_2$, which is equivalent to $d \gg \alpha^{-3/10}l_B$. The predicted relation between $\delta\sigma_{\text{xy}}$ and σ_{xx} is more complicated than a power law. However, the main T -dependence comes from the $\exp(-\Delta/T)$ factors and therefore, one can say that the temperature-driven dependence $\delta\sigma_{\text{xy}}(\sigma_{\text{xx}})$ is nearly linear. We would like also to note a “complementary” behavior of the prefactors σ_{xx}^* and σ_{xy}^* . At $T \gg T_2$, $\sigma_{\text{xy}}^* = e^2/h$ and $\sigma_{\text{xx}}^* \ll \sigma_{\text{xy}}^*$, while at lower temperatures $\sigma_{\text{xx}}^* = e^2/h$ but $\sigma_{\text{xy}}^* \ll \sigma_{\text{xx}}^*$.

We now turn to explanations of our results. The electron-phonon scattering gives rise to the diffusion with the diffusion coefficient $D \sim l_B^2/r_{\text{ph}}$ and therefore, the local dissipative conductivity $\sigma_{\text{xx}} = \sigma_{\text{yy}} = e^2 n D/T$. We will consider explicitly only the case $T \gg T_{\text{ph}}$ and then transfer the results onto lower temperatures $T \ll T_{\text{ph}}$ replacing α by $\alpha T_{\text{ph}}/T$ everywhere. For $T \gg T_{\text{ph}}$ the diagonal component of the conductivity tensor is $\sigma_{\text{xx}} = \frac{e^2}{h} \alpha \exp[-(\Delta + \epsilon)/T]$. As for the off-diagonal components, they are given by $\sigma_{\text{xy}} = -\sigma_{\text{yx}} = \frac{e^2}{h} \alpha \exp[-(\Delta + \epsilon)/T]$. Suppose the system is in a uniform external electric field E , then the current satisfies the equations

$$\mathbf{j} = \frac{1}{e} \{ \sigma_{\text{xx}} \nabla \mu + \sigma_{\text{xy}} [\hat{z} \times \nabla \mu] \}, \quad \mathbf{j} = [\hat{z} \times \nabla \psi], \quad (5)$$

where $\mu(\mathbf{r})$ is the electrochemical potential and $\psi(\mathbf{r})$ is the stream function. With the appropriate boundary conditions and the condition that the spatial average of $\nabla \mu$ is equal to eE , Eq. (5) fully determines $\mathbf{j}(\mathbf{r})$. For this system there exists a remarkable exact relation [13]

$$(\sigma_{\text{xx}}^*)^2 + (\sigma_{\text{xy}}^*)^2 = (e^2/h)^2 (1 + \alpha^2). \quad (6)$$

Unfortunately, it does not shed light on the individual behavior of σ_{xx}^* and σ_{xy}^* . This individual behavior is the subject of the present paper.

We begin by examining a chess-board geometry where $\epsilon = W \sin \left[\frac{\pi(x+y)}{\sqrt{2}d} \right] \left[\frac{\pi(x-y)}{\sqrt{2}d} \right]$ with the average electric field in the \hat{y} -direction (Fig. 1). The regions $\epsilon(\mathbf{r}) \gtrsim T$ (hills) have very low conductance, and hence, the current avoids them. It flows mainly in the valleys where $\epsilon(\mathbf{r}) < 0$ and crosses from one valley to another via the saddle points (where $\epsilon = 0$). Once the current passes the saddle point it flows along the slope of the valley gradually deviating from the contour $\epsilon = 0$ towards the more conductive bottom. The current distribution can be inferred from studying two basic elements of the chess-board: a saddle point and

a slope. Consider an isolated saddle point $\epsilon(\mathbf{r}) = W(\pi^2/2d^2)(x^2 - y^2)$ first. We choose the boundary conditions $\mu(x, -\infty) = 0$, $\mu(x, \infty) = eU$ and look for the solution that has the full symmetry of the problem: $\mu(x, y) + \mu(-x, -y) = eU$. The desired solution is [14] $\psi = (GU/2)\text{erfc}[(x + \beta y)/\sqrt{2}d]$, $\mu = (U/2)\text{erfc}[(x - \beta y)/\sqrt{2}d]$, where $\beta = \alpha + \sqrt{1 + \alpha^2}$, $\delta^2 = 2(d/\pi)^2 \alpha \beta T/W$. The quantity $G = \frac{e^2}{h} \sqrt{1 + \alpha^2} \exp(-\Delta/T)$ can be identified as the conductance of the saddle point. One observes from this solution that the current flows through the saddle point in a thin stream of width δ (Fig. 1). The stream deviates by a small angle $\alpha/2$ from the contour $\epsilon = 0$ towards the bottom of the valley. With E in the \hat{y} -direction, the current through saddle point A (Fig. 1) determines σ_{xx}^* and the current through saddle point B gives σ_{xy}^* . Our solution for an isolated saddle point is of use if the deviation of the current stream upon traveling the distance $AB = d$ exceeds the width of the stream δ . In this case only an exponentially small fraction of the current, which enters through saddle point A, leaves the valley through saddle point B.

The equivalent circuit of the chess-board is a square network of identical conductances $\frac{e^2}{h} \sqrt{1 + \alpha^2} \exp(-\Delta/T)$ (saddle points) connecting the reservoirs σ_{xx}^* . The current through saddle point A is GU , where $U = eEd/2$ is the voltage drop across this saddle point. Similarly, the current through B is almost zero since there is no voltage drop across this saddle point. Therefore,

$$\sigma_{\text{xy}}^* = 0, \quad \sigma_{\text{xx}}^* = \frac{e^2}{h} \sqrt{1 + \alpha^2}. \quad (7)$$

To examine the range of validity of Eq. (7), we need to know how a thin stream of current propagates along the slope of the chess-board.

For simplicity consider a uniform slope $\epsilon(X, Y) = -WX/d$. The Eqs. (5) may be written as $-D\nabla^2\psi + \frac{e^2}{h}\nabla\psi = 0$, where $v_Y = (l_B^2/h)(W/d)$ and $v_X = \alpha v_Y$. This equation is identical to the one describing the diffusion of a tracer in a hydrodynamic flow of constant velocity \mathbf{v} [15]. This analogy suggests that the current flows in a thin stream; the stream is directed along \mathbf{v} , thus making only a small angle with respect to the contour of constant ϵ ; as the current passes B, it enters the valley through saddle points A, then deviates from the perimeter of the valley spiraling counter-clockwise towards the interior. It then spirals back out clockwise to exit the valley using saddle point C. This clockwise part of the spiral can be interpreted as to a given point. Correspondingly, if the stream originates at (0, 0) then the fraction of current that reaches the stream of holes injected through saddle point C, which spiral counterclockwise to the interior where the holes recombine with the electrons injected through saddle point A. Applying this consideration to

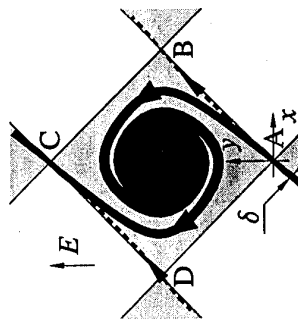


FIG. 1.

The picture illustrating our analytical solution of Eq. (5) for a chess-board of valleys (dark) and hills (blank).

The currents through saddle points A and B determine σ_{xx}^* and σ_{xy}^* , respectively. The latter current (shown by the dashed line with arrow) is exponentially small.

point A.

The main current (the black arrow) by-passes B. It enters the valley through saddle points A, then deviates from the perimeter of the valley spiraling counter-clockwise towards the interior. It then spirals back out clockwise to exit the valley using saddle point C. This clockwise part of the spiral can be interpreted as to a given point. Correspondingly, if the stream originates at (0, 0) then the fraction of current that reaches the stream of holes injected through saddle point C, which spiral counterclockwise to the interior where the holes recombine with the electrons injected through saddle point A. Applying this consideration to

the slope between saddle points A and B (Fig. 1), we find that Eq. (7) is valid if the temperature is low enough: $T \ll T_2^{\text{ch}}$, where $T_2^{\text{ch}} = \alpha W$. In fact, we understand now that in this regime a non-zero σ_{xy}^* appears only due to the fraction of current propagating along the path AB.

Our calculation gives $\sigma_{\text{xy}}^* = \frac{e^2}{h} \sqrt{8T/\pi T_2^{\text{ch}}} \exp(-T_2^{\text{ch}}/2T)$. Similarly, σ_{xx}^* differs from the value given by Eq. (7) due to the current propagating along the twice longer path ABC (Fig. 1). Correspondingly, the correction to σ_{xx}^* is of the order of $(\sigma_{\text{xy}}^*)^2$ (both in units of e^2/h) in agreement with Eq. (6).

Let us return to the random system. In this case reservoirs are not single valleys but collections of many of them with the typical diameter $\xi = d(W/T)^\nu$ and perimeter (or hull) $p = d(\xi/d)^{d_H}$, where $\nu = 4/3$ and $d_H = 7/4$ is the fractal dimension of the hull [15]. In the spirit of our analysis of the chess-board, we can say that the fraction $\exp(-p/L)$ of the current entered through a saddle point of the type A can exit through the neighboring saddle point of the type B. This fraction is exponentially small if $T \ll T_2$, where $T_2 = \alpha^{3/10}W$. It means that, as in the case of a chess-board, the equivalent circuit is the network of independent conductances. It has been proven [10] that for this network σ_{xx}^* is still given by Eq. (7). But the conclusion that σ_{xy}^* is also exponentially small would be incorrect. The reason is that in a random system the distance p along the perimeter between two critical saddle points might be as small as L , i.e., much less than a typical one. Such an event gives rise to a "Hall generator" contributing $\sim e^2/h$ to σ_{xy}^* . The Hall conductivity of the sample will then be proportional to the probability of finding such a rare generator in a square with the sides of length ξ [16]. The estimate of this probability [11] leads to the result $\sigma_{\text{xy}}^* = \frac{e^2}{h} (T/T_2)^{80/21}$ [Eq. (4)]. As explained above the results for the case $T_1 \ll T \ll T_{\text{ph}}$ are obtained by replacing α by $\alpha T_{\text{ph}}/T$, which changes the exponent from 80/21 to 8/3 [Eq. (4)].

Until now we have considered the situation when the Fermi level is far enough from the percolation level so that $\exp(-\Delta/T) \ll (T/T_2)^{80/21}$. Consider now the opposite case where almost all the area of each valley is covered by the "lake" of totally occupied states and the spiral in Fig. 1 reaches the line DB already inside the lake. It means that almost all the current I flows through the lake and therefore induces a Hall voltage lh/e^2 across the lake in the direction DB. Due to the periodicity of the chess-board the voltage of the same magnitude is applied to the saddle point B producing the current Glh/e^2 in the \hat{y} -direction. Using $G = \sigma_{\text{xx}}$ and $I = \sigma_{\text{xy}}^* U$ we obtain $\delta\sigma_{\text{xy}} = (h/e^2)\sigma_{\text{xx}}^*$ [17] in agreement with Refs. [14, 18]. Thus with decreasing Δ crossover from the linear dependence $\delta\sigma_{\text{xy}} = f(T)\sigma_{\text{xx}}$ to $\delta\sigma_{\text{xy}} \propto \sigma_{\text{xx}}^2$ is predicted. Note that in the latter regime the activation energy for $\delta\sigma_{\text{xy}}$ is twice larger than in Eq. (2).

Finally, we briefly discuss the transport at temperatures away from the range $T_1 \ll T \ll T_2$.

If $T \lesssim T_1$ tunneling and variable range hopping become important. The calculation of the Hall conductivity in this regime remains an unsolved problem. In the opposite limit

$T \gg T_2$, σ_{xy} approaches e^2/h . Indeed, at these temperatures the deviation of the current

stream from the contour $\epsilon = 0$ is much smaller than the width of the stream, i.e., $\alpha p \ll b$.

The current flows mainly within the strip of width δ centered around the contour $\epsilon = 0$.

It may be verified that within this strip $|\epsilon| \ll T$ and, therefore, the Hall conductivity

$\sigma_{\text{xy}} = \frac{e^2}{h} \exp[-(\Delta + \epsilon)/T]$ is approximately constant. In this case the sample averaging of

σ_{xy} necessary for calculating of σ_{xy}^* trivially gives $\sigma_{\text{xy}}^* = e^2/h$. As for σ_{xx}^* , it can be found

from the prefactor ρ_{xx}^* of the diagonal resistivity $\rho_{\text{xx}} = \rho_{\text{xx}}^* \exp(-\Delta/T)$ with the help of the relation $\sigma_{\text{xx}}^* = \rho_{\text{xx}}^* (\sigma_{\text{xy}}^*)^2$. Now ρ_{xx}^* can be estimated as the resistance of a wire of the width δ , the length p , and the resistivity ah/e^2 , which yields $\sigma_{\text{xx}}^* = (e^2/h)(T_2/T)^{10/13}$ in agreement with Refs. [10, 15].

In conclusion we would like to say a few words about related experimental data. Unfortunately, in high-mobility samples the temperature dependence of only σ_{xx} and only at its minima was studied. We propose to investigate the temperature dependence of both $\delta\sigma_{\text{xy}}$ and σ_{xx} away from the very minima of σ_{xx} to verify the predictions of Eqs. (3, 4) and the relationship between them given by Eq. (6).

When the Fermi level is exactly in the middle between two Landau levels in the minima of σ_{xx} , the absolute values of contributions of electrons and holes to σ_{xx} and σ_{xy} should be equal and we arrive at $\sigma_{\text{xx}}^* = 2e^2/h$ and $\sigma_{\text{xy}}^* = 0$. Our result for σ_{xx}^* differs by the factor of two from the values claimed in Ref. [2]. Note, however, that larger values of σ_{xx}^* were reported by another group [4]. Moreover, recently σ_{xx}^* has been found to be proportional to $1/T$ [3]. We do not know how to resolve these contradictions. It seems that more experimental evidence is needed here.

Useful discussions with I. L. Aleiner, V. I. Perel, and I. M. Ruzin are greatly appreciated. This work was supported by NSF under Grant No. DMR-9321417..

References

- [a)] Present address: Institut für Theoretische Physik, Universität zu Köln, 50937 Köln, Germany.
- [1] E. Stahl, D. Weiss, G. Weimann, K. von Klitzing, and K. Ploog, J. Phys. C **18**, L783 (1985).
- [2] R. G. Clark, J. R. Mallett, S. R. Haynes, J. J. Harris, and C. T. Foxon, Phys. Rev. Lett. **60**, 1747 (1988). R. G. Clark, Phys. Scr. T **39**, 45 (1991).
- [3] Y. Katayama, D. C. Tsui, and M. Shayegan, Phys. Rev. B **49**, 740 (1994).
- [4] A. Usher, R. J. Nicholas, J. J. Harris, C. T. Foxon, Phys. Rev. B **41**, 1129 (1990).
- [5] D.-H. Lee, S. Kivelson, and S.-C. Zhang, Phys. Rev. Lett. **68**, 2386 (1992).
- [6] S. Das Sarma and D. Liu, Phys. Rev. B **48**, 9166 (1993).
- [7] D.-H. Lee, S. Kivelson, and S.-C. Zhang, Phys. Rev. Lett. **71**, 2679 (1993).
- [8] R. N. Bhatt, N. Read, and B. Huckestein, Phys. Rev. Lett. **71**, 2678 (1993).
- [9] D. G. Polyakov and B. I. Shklovskii, Phys. Rev. Lett. **73**, 1150 (1994).
- [10] D. G. Polyakov and B. I. Shklovskii, Phys. Rev. Lett. **74**, 150 (1995).
- [11] M. M. Fogler and B. I. Shklovskii, Solid State Commun. **94**, 503 (1995).
- [12] H. A. Fertig and B. I. Halperin, Phys. Rev. B **36**, 7969 (1987).
- [13] S. H. Simon and B. I. Halperin, Phys. Rev. Lett. **73**, 3278 (1994).
- [14] N. R. Cooper and J. T. Chalker, Phys. Rev. B **48**, 4530 (1993).
- [15] M. B. Isichenko, Rev. Mod. Phys. **64**, 961 (1992) and references therein.
- [16] V. G. Karпов, A. Ya. Shik, and B. I. Shklovskii, Fiz. Poluprovodn. **16**, 1406 (1982) [Sov. Phys. Semicond. **16**, 901 (1982)].
- [17] M. M. Fogler and B. I. Shklovskii, unpublished.
- [18] A. M. Dykhne and I. M. Ruzin, Phys. Rev. B **50**, 2369 (1993).

Optically Pumped NMR Measurement of the Spin Magnetization and Spin Dynamics in the Quantum Hall Regimes

S. E. Barrett*,†, G. Dabbagh, L. N. Pfeiffer, K. W. West, and R. Tycko *‡,
AT&T Bell Laboratories, 600 Mountain Avenue, Murray Hill, New Jersey 07974.

Abstract-We review our recent measurements of the Knight shift ($K_S(v, T)$) and spin-lattice relaxation time ($T_1(v, T)$) of the ^{71}Ga nuclei located in n-doped GaAs quantum wells using Optically Pumped NMR, for Landau level filling $0.66 < v < 1.76$ and temperature $1.55 \text{ K} < T < 20 \text{ K}$. $K_S(v)$ (\approx the electron spin polarization $\langle S_z(v) \rangle$) drops precipitously on either side of $v=1$, which is evidence that the charged excitations of the $v=1$ ground state are finite-size skyrmions. For $v < 1$, the data are consistent with a many-body ground state which is not fully spin-polarized, with a very small spin-excitation gap that increases as $v \rightarrow 2/3$.

Electron-electron Coulomb interactions are known to significantly affect the physics of two-dimensional electron systems (2DES) in strong magnetic fields, resulting in novel collective phenomena such as the fractional quantum Hall effect [1]. Halperin [2] was the first to point out that these interactions may also lead to significant spin-reversal in the many-body ground state and low-lying excited states of 2DES, since for typical experimental conditions (e.g., $B=10$ Tesla) in GaAs, the Coulomb energy ($E_C = \frac{e^2}{k_L c} = 13.7$ meV) is much larger than the Zeeman energy ($E_Z = g^* \mu B = 0.3$ meV). Subsequent numerical calculations [3,4] and transport measurements [5-7] support this possibility.

In this paper, we will review our recent optically pumped nuclear magnetic resonance (OPNMR) [8] measurements of the Knight shift K_S [9] and spin-lattice relaxation time T_1 [10] of ^{71}Ga nuclei in an electron-doped multiple quantum well (MQW) structure as a function of Landau level filling factor v and temperature. These measurements provide the first experimental support for the recent predictions that the ground state at $v=1 \pm \varepsilon$ contains finite-size skyrmions [11,12], with an effective spin which reflects the competition between the Coulomb energy and the Zeeman energy. We conclude that OPNMR studies of the electronic spin degree of freedom are an important new probe of the many-body ground state and low-lying excited states in 2DES.

The MQW sample used in these measurements contains forty 300 \AA wide GaAs wells separated by 1800 \AA $\text{Al}_{0.1}\text{Ga}_{0.9}\text{As}$ barriers. Si delta-doping spikes are located in the center of each barrier. Characterization of this wafer by low-field transport measurements at 4.2 K yielded the electron density $n = (1.41 \pm 0.14) \times 10^{11} \text{ cm}^{-2}$ in each well, with mobility $\mu = 1.44 \times 10^6 \text{ cm}^2/\text{V s}$. Using home-built NMR probes, the growth axis of the MQW sample was tilted by an angle θ ($0^\circ < \theta < 60^\circ$),

0.5°) away from the constant field B , thereby varying the filling factor ($v = \frac{\pi \hbar c}{eB \cos(\theta)}$) *in situ*.

The OPNMR measurements described below utilized the timing sequence SAT - τ_L - τ_D - DET, where SAT represents an rf pulse train that saturates (destroys) the nuclear polarization, τ_L is a period of illumination by the laser (σ^+ light, $\lambda=806 \text{ nm}$, $10 - 300 \text{ mW/cm}^2$), τ_D is a period of no illumination ($\tau_D \geq 1 \text{ sec}$), and DET represents the direct detection of the NMR free induction decay (FID) signals following a single $\pi/2$ pulse [8]. During τ_L , optical pumping of interband transitions generates electrons and holes in the GaAs wells with non-equilibrium spin-polarizations, which then polarize the nuclei in the well through the contact hyperfine coupling. The electronic system quickly equilibrates at the beginning of τ_D , but the enhanced nuclear polarization persists until the DET period, since $T_1 \gg 1 \text{ sec}$. In practice, an NMR signal enhancement of ~ 100 has been obtained using this technique, which makes the study of quantum wells possible.

Figure 1 shows the ^{71}Ga NMR spectra acquired as a function of τ_L ($\tau_D = 1 \text{ sec}$) in a 7.05 Tesla field at $T=1.55 \text{ K}$ with $\theta = 0^\circ$ [9]. The broad, asymmetric resonance

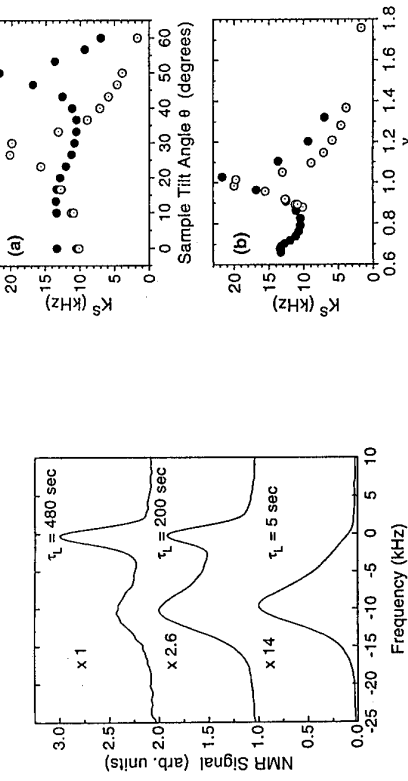


Fig. 1: ^{71}Ga NMR spectra of the GaAs/AlGaAs MQW acquired in the dark ($\tau_D=1 \text{ s}$) for various optical pumping times τ_L , with $B=7.05 \text{ T}$, $\theta=0^\circ$, and $T=1.55 \text{ K}$. For ease of comparison, the signals are scaled by the indicated factors, and are offset for clarity. (Adapted from Ref. [9]).

Fig. 2: (a) Dependence of ^{71}Ga Knight shift K_S on the sample's tilt angle θ for $B=7.05 \text{ T}$ (open circles) and $B=9.39 \text{ T}$ (filled circles) at 1.55 K . (b) Dependence of K_S on filling factor v for $B=7.05 \text{ T}$ (open circles) and $B=9.39 \text{ T}$ (filled circles) at 1.55 K . The conversion from θ to v used $n=1.50 \times 10^{11} \text{ cm}^{-2}$. (Adapted from Ref. [9]).

observed for $\tau_L = 5$ sec is due to the 71Ga nuclei in the GaAs wells, where the non-equilibrium nuclear spin polarization is photogenerated. As τ_L is increased, polarization diffuses into the barriers via the nuclear spin-spin coupling [8,10]. The narrow, symmetric resonance which dominates the spectrum for $\tau_L = 480$ sec is due to the 71Ga nuclei in the $\text{Al}_{0.1}\text{Ga}_{0.9}\text{As}$ barriers. The electrons confined in the wells produce an extra hyperfine field which shifts the well resonance below the barrier resonance, as expected for the Fermi contact interaction with $g^* < 0$ [13]. The variation of the lowest sub-band electron wavefunction along the growth direction leads to the asymmetry of the well resonance [10]. We define the Knight shift to be the peak-to-peak frequency splitting between the well and barrier resonance lines, so $K_S(v,T) = A_{zz} \langle S_z(v,T) \rangle$ for $\vec{B} \parallel \vec{z}$, where A_{zz} is the hyperfine coupling constant for nuclei in the center of the well [14].

Figure 2(a) shows the dependence of the 71Ga Knight shift K_S on the tilt angle θ for $B=7.05$ T and $B=9.39$ T, at $T=1.55$ K [9]. Assuming that the maximum K_S observed at $\theta=28.5^\circ$ for $B=7.05$ T corresponds to $v=1$, we infer an electron density $n=1.50 \times 10^{11} \text{ cm}^{-2}$. This density is used to convert the sample tilt angle θ to the Landau level filling factor v . Figure 2(b) is a plot of K_S versus v for $B=7.05$ T and $B=9.39$ T. The collapse of the two data sets onto one another in Fig. 2(b) suggests that the hyperfine coupling constant is isotropic, and therefore the Knight shift directly reflects the electron spin polarization, i.e., $K_S(v,\theta) = A \langle S_z(v,\theta) \rangle$. Clearly, $\langle S_z(v) \rangle$ drops precipitously both above and below $v=1$.

In Figure 3, two fits to the $K_S(v)$ data for $B=7.05$ T at $T=1.55$ K are shown [9].

The functional form of these fits is obtained by "generalizing" the $T \approx 0$ independent electron model for the spin polarization assuming fixed electron density, which parametrizes the effect of interactions near $v=1$. The underlying assumption is that each quasiparticle (or quasihole) added to the fully polarized $v=1$ ground state results in S (or $\mathcal{A}-1$) flipped spins. In this case:

$$K_S(v) = \frac{A}{2} \left(\Theta(1-v) \left(\frac{2}{v} (1-\mathcal{A}) - (1-2\mathcal{A}) \right) + \Theta(v-1) \left(\frac{2S}{v} + (1-2S) \right) \right), \quad (1)$$

where $\Theta(x) = 1$ for $x > 0$, and $\Theta(x) = 0$ for $x < 0$. Earlier estimates of the hyperfine coupling imply $A \sim 27$ kHz for three-dimensional electrons [13], or $A \sim 54$ kHz for nuclei in center of the 300 \AA GaAs well. $A = 44$ kHz is used for the fits in Fig. 3, a value consistent with the largest shift measured in either field at $T=1.55$ K. The solid line in Fig. 3, which assumes $\mathcal{A} = S = 1$ (i.e., non-interacting electrons), fails to fit the data. The dashed line is an excellent fit to the data for $0.9 < v < 1.1$, with $\mathcal{A} = 3.6 \pm 0.3$. Apparently, the charged excitations of the $v=1$ ground state have an effective spin of $\left(\frac{3.6 \pm 0.3}{2}\right)$.

These results are in good agreement with the recent predictions that the lowest energy charged excitations of the $v=1$ ground state are finite-size skyrmions,

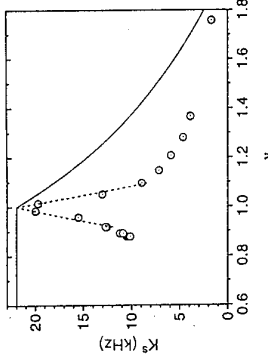


Fig. 3: Dependence of K_S on filling factor v for $B=7.05$ T. (open circles) at $T=1.55$ K. As explained in the text, both fits are given by Eqn. (1), but the solid line has $\mathcal{A} = S = 1$ (non-interacting electrons), while the dashed line has $\mathcal{A} = S = 3.6$ (finite-size skyrmions). (Adapted from Ref. [9].)

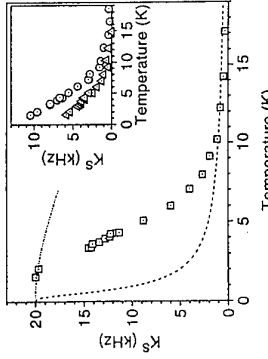


Fig. 4: Dependence of K_S on temperature, for $v=0.98$ and $B=7.05$ T (open squares). As explained in the text, the dashed line is a calculation of $K_S(T)$ assuming non-interacting electrons, and the dash-dot-dot line is a calculation of $K_S(T)$ assuming that the low-lying excitations are spin-waves. Inset: Dependence of K_S on temperature, for $v=0.98$ (open circles) and $v=1.2$ (open triangles), at $B=7.05$ T. (Adapted from Ref. [9].)

with a calculated effective spin of $\left(\frac{7}{2}\right)$ [12] (or $\left(\frac{4.8}{2}\right)$ [15]) at $\left(\frac{E_z}{E_c} \sim 0.015\right)$. Qualitatively, at $v=1+\epsilon$, a finite-size skyrmion is cylindrically symmetric with the boundary conditions of a down-spin at $r=0$ and an up-spin at $r=D$, with a particular radial transition between those two states that maximizes the alignment of nearest neighbor spins, leaving up-spins for $D < r < \infty$. The length scale D is set by the competition between the Coulomb and Zeeman energy, which increase and decrease D , respectively. The effective spin is $>1/2$, since all electrons within $0 < r < D$ are distorted. For brevity, we will refer to this object as a skyrmion [16]. By analogy, the $v=1-\epsilon$ ground state is an antiskyrmion, and skyrmion-antiskyrmion pairs are neutral excitations of the $v=1$ ground state. Although skyrmions may occur around other filling factors with incompressible many-body ground states (e.g. $v=1/3$) [11,17], they are not expected to be the relevant quasiparticles for $v=3.5, \dots$ [18]. Recent tilted-field magneto-transport measurements at odd filling factors [19] support these counterintuitive predictions. While there is good agreement between the number of flipped spins per quasiparticle-quasihole pair as determined by transport ($s=7$) [19] and OPNMR ($s = S + \mathcal{A} - 1 = 6.2 \pm 0.6$) [9] at $v=1$ and $\left(\frac{E_z}{E_c} \sim 0.015\right)$, both the magnitude of s and its dependence on $\frac{E_z}{E_c}$ are expected to be somewhat larger based upon Hartree-Fock calculations [12,15]. Additional theoretical investigations have

recently considered a skyrmion crystal [20] and the relationship between skyrmion condensation and certain spin-singlet quantum Hall states [21].

The temperature dependence of the Knight shift probes low-lying excited states, since $K_S(T) \propto \langle S_Z(T) \rangle$, and

$$\langle S_Z(T) \rangle = \frac{1}{Z} \langle 0 | S_Z(0) \rangle + \sum \frac{1}{Z} e^{\beta E_i/kT} \langle i | S_Z | i \rangle$$

where $|0\rangle$ is the many-body ground state, Z is the partition function, and the summation is over all excited states $|i\rangle$ with energy Δ_i . Figure 4 (main figure) shows the dependence of K_S on the temperature for $v=0.98$ in the 7.05 T field [9]. The shift saturates at ~ 20 kHz for T below ~ 2 K, which validates our comparison in Fig. 3 of the $T=1.55$ K shift data near $v=1$ with the $T=0$ skyrmion model.

A simple model for $\langle S_Z(T) \rangle$ at $v=1$ assumes non-interacting electrons which obey Fermi-Dirac statistics, with the chemical potential in the middle of the Zeeman gap. This leads to the dashed line in Fig. 4 ($K_S(T) = K(0) \tanh\left(\frac{E_Z}{4kT}\right)$, with $K(0)=20$ kHz and $E_Z/k = 2.08$ K), which clearly does not fit the data. Treating E_Z as an adjustable parameter in order to fit the saturated region implies an "exchange enhancement" of the Zeeman splitting by a factor of ~ 10 , a result consistent with other measurements [22]. A more realistic model for $\langle S_Z(T) \rangle$ at $v=1$ includes interactions, so that spin-wave modes (corresponding to reversed spins) are the low-lying excited states, with the Bose-Einstein distribution function determining the occupancy of each mode [23]. The dash-dot-dot line shown in Fig. 4 is a calculation [17] of $K_S(T)$ using the $T \approx 0$ two-dimensional spin-wave dispersion spectrum [24], and it is obvious that this model does not fit the data either. For T above ~ 2 K, $K_S(T)$ drops off more rapidly than the spin-wave fit, which qualitatively suggests a collapse of the exchange energy as the polarization is reduced. Recently, more sophisticated calculations, which either stress the similarity to an itinerant electron ferromagnet [25] or use a continuum quantum field theory of a ferromagnet [26], have achieved improved fits to the $\langle S_Z(T, v=1) \rangle$ data. $K_S(T)$ may also be measured at arbitrary v using OPNMR. The inset of Figure 4 shows the data for $v=0.88$ and $v=1.2$, which do not saturate by $T \sim 2$ K, demonstrating the dependence of the many-body states and energy spectrum on the filling factor.

OPNMR also enables measurement of the nuclear spin-lattice relaxation rate

$1/T_1$, which probes electron spin dynamics [27,28]. Figure 5 shows the dependence of $1/T_1$ on filling factor v at $T=2.1$ K for $B=7.05$ T and $B=9.39$ T [10]. The rate $1/T_1$ is determined by inverting the well resonance for $\tau_L=5$ sec, and monitoring its recovery during τ_D . The $1/T_1$ data are strongly dependent upon v , but nearly independent of total field, which suggests that the Fermi contact interaction dominates. Since the relaxation involves electron-nucleus flip-flop transitions between nearly degenerate initial and final electron states, a slow (fast) $1/T_1$ implies a large (small) gap to spin-flip excitations [14,23]. Although the slow rate at $v=1$ is consistent with either interacting or independent electrons, the rapid $1/T_1$ at $v \sim 0.85$

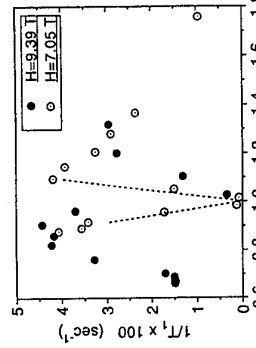


Fig. 5: Dependence of 71Ga nuclear spin-lattice relaxation rate $1/T_1$ on filling factor v at $T=2.1$ K, for $B=7.05$ T (open circles) and $B=9.39$ T (filled circles). The dashed line is directly proportional to $\langle K_S(v=1) \rangle K_S(v) \rangle$, where $K_S(v)$ is given by Eqn. (1), with $A = S = 3.6$ (see Fig. 3). (Adapted from Ref. [10]).

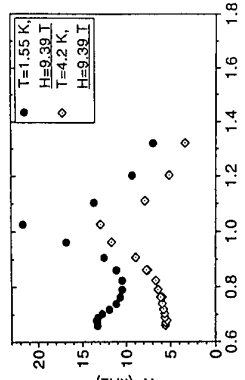


Fig. 6: Dependence of K_S on filling factor v for $T=1.55$ K (open diamonds) and $T=4.2$ K, $B=9.39$ T, at $T=2.1$ K, (filled circles). (Adapted from Ref. [9]).

can only be explained if interactions induce nearly gapless low-lying spin-flip excitations. The dashed line in Figure 5 shows that $\frac{1}{T_1(v)} \propto (K_S(v=1) - K_S(v))$ for $0.9 < v < 1.1$, where $K_S(v)$ is the dashed line in Figure 3. This suggests that low-lying spin-flip excitations near $v=1$ are related to the number of skyrmions in the ground state.

Clear signatures of the fractional quantum Hall regime [3-5] are also evident in the OPNMR data. First, Fig. 5 shows that $1/T_1(1.55 \text{ K}, v)$ has a local minimum near $v=2/3$, one of the fundamental FQHE states. Second, $K_S(1.55 \text{ K}, v)$ has a local maximum near $v=2/3$, as is seen in Fig. 6 [9]. The fact that $K_S(1.55 \text{ K}, v=2/3) \ll K_S(1.55 \text{ K}, v=1)$ suggests that the $v=2/3$ FQHE ground state may not be fully polarized [3,5] for $B=9.39$ T, but these measurements need to be repeated at lower temperatures to ensure that $\langle S_z(T, v=2/3) \rangle \equiv \langle S_z(0, v=2/3) \rangle$. Qualitatively, the temperature dependence of $K_S(v)$ shown in Fig. 6 suggests that the energy gap to spin-flip excitations is large, medium, and small for $v=1, 2/3$, and ~ 0.9 , respectively. This assignment is consistent with our measurements the 71Ga T_1 , since its temperature dependence is a strong function of v , as is seen in Table 1 [9].

We have shown that OPNMR is a powerful local probe of 2DES. Many interesting features of the above results remain to be understood theoretically. In future work, we will extend these measurements to other filling factors, lower temperatures, and higher fields. We thank J. P. Eisenstein, S. M. Girvin, M. Kasner, A. H. MacDonald, N. Read, S. Sachdev, and S. L. Sondhi for helpful discussions, and B. I. Greene and T. D. Harris for experimental assistance.

Table 1. ^{71}Ga nuclear spin-lattice relaxation time T_1 as a function of temperature and Landau level filling factor v . (Adapted from Ref. [9].)

	$v=1.01$	$v=0.88$	$v=0.66$
$T_1(T=4\text{ K})$ (s)	122	24	43
$T_1(T=2.1\text{ K})$ (s)	1280	20	68

*To whom correspondence should be addressed.

[†]Present Address: Department of Physics, Yale University, P.O. Box 208120, New Haven, CT 06520-8120, USA.

[‡]Present Address: National Institutes of Health, Bldg. 5, Rm. 112, Bethesda, MD 20892, USA.

- [1] D. C. Tsui, H. L. Störmer, and A. C. Gossard, Phys. Rev. Lett. **48**, 1559 (1982).
- [2] B. I. Halperin, Helv. Phys. Acta **56**, 75 (1983).
- [3] T. Chakraborty and P. Pietiläinen, "The Fractional Quantum Hall Effect", (Springer, Berlin, 1988).
- [4] "The Quantum Hall Effect", 2nd ed., R. E. Prange and S. M. Girvin, eds., (Springer, New York, 1990).
- [5] J. P. Eisenstein and H. L. Störmer, Science **248**, 1510 (1990).
- [6] R. L. Willett, J. P. Eisenstein, H. L. Störmer, D. C. Tsui, A. C. Gossard, and J. H. English, Phys. Rev. Lett. **59**, 1776 (1987).
- [7] R. G. Clark, S. R. Haynes, A. M. Suckling, J. R. Malliet, P. A. Wright, J. J. Harris, and C. T. Foxon, Phys. Rev. Lett. **62**, 1536 (1989); J. P. Eisenstein, H. L. Störmer, L. N. Pfeiffer, and K. W. West, Phys. Rev. Lett. **62**, 1540 (1989); J. E. Furneaux, D. A. Syphers, and A. G. Swanson, Phys. Rev. Lett. **63**, 1098 (1989).
- [8] S. E. Barrett, R. Tycko, L. N. Pfeiffer, and K. W. West, Phys. Rev. Lett. **72**, 1368 (1994).
- [9] S. E. Barrett, G. Dabbagh, L. N. Pfeiffer, K. W. West and R. Tycko, Phys. Rev. Lett. **74**, 5112 (1995).
- [10] R. Tycko, S. E. Barrett, G. Dabbagh, L. N. Pfeiffer, and K. W. West, Science **268**, 1460 (1995).
- [11] S. L. Sondhi, A. Karlheede, S. A. Kivelson, and E. H. Rezayi, Phys. Rev. B **47**, 16419 (1993).
- [12] H. A. Fertig, L. Brey, R. Côté, and A. H. MacDonald, Phys. Rev. B **50**, 11018 (1994).
- [13] D. Pojet, G. Lampel, B. Sapoval, and V. I. Safarov, Phys. Rev. B **15**, 5780 (1977).
- [14] C. P. Slichter, "Principles of Magnetic Resonance" (Springer, New York, 1990), 3rd ed.
- [15] A. Karlheede and S. L. Sondhi, unpubl. communication.
- [16] D.-H. Lee and C. L. Kane, Phys. Rev. Lett. **64**, 1313 (1990); R. Rajaraman, "Solitons and Instantons" (North-Holland, Amsterdam, 1989); R. Ladbury, Physics Today, July 1995, pg. 19.
- [17] A. H. MacDonald, private communication.
- [18] J. K. Jain and X.-G. Wu, Phys. Rev. B **49**, 5085 (1994); X.-G. Wu and S. L. Sondhi, Phys. Rev. B **51**, 14725 (1995).
- [19] A. Schmeller, J. P. Eisenstein, L. N. Pfeiffer, and K. W. West, Preprint, LANL cond-mat/9506133.
- [20] L. Brey, H. A. Fertig, R. Côté, and A. H. MacDonald, preprint, LANL cond-mat/9505154.
- [21] C. Nayak and F. Wilczek, Preprint, LANL cond-mat/9501052.
- [22] A. Usher, R. J. Nicholas, J. J. Harris, and C. T. Foxon, Phys. Rev. B **41**, 1129 (1990).
- [23] A. Narath, Chapter 7, "Hyperfine Interactions", A. J. Freeman and R. B. Frankel, eds., (Academic Press, New York, 1967).
- [24] Y. A. Bychkov, S. V. Iordanskii, and G. M. Eliashberg, JETP Lett. **33**, 143 (1981); C. Kallin and B. I. Halperin, Phys. Rev. B **30**, 5655 (1984).
- [25] M. Kasner and A. H. MacDonald, preprint.
- [26] N. Read and S. Sachdev, preprint.
- [27] A. Berg, M. Dober, R. R. Gerhardts, and K. v. Klitzing, Phys. Rev. Lett. **64**, 2563 (1990).
- [28] I. D. Wagner and Tsofar Maniv, Phys. Rev. Lett. **61**, 1400 (1988).

Imaging of Edge Channels in the Integer Quantum Hall Regime by the Lateral Photo-Electric Effect

R.J.F. van Haren, F.A.P. Blom, W. de Lange, J.H. Wolter
 COBRA Interuniversity Research Institute, Department of Physics,
 Eindhoven University of Technology, P.O. Box 513,
 5600 MB Eindhoven, The Netherlands

Abstract

By using a low-mobility two-dimensional hole gas in between the GaAs substrate and the two-dimensional electron gas as an interior gate, the edge channels in the quantum Hall regime can be made macroscopically wide. The location and width of the channels are detected by means of the lateral photo-electric effect. Two-dimensional images displayed in grey tones made across large areas of a Hall bar clearly show the positions of the channels.

Introduction

The electrical transport properties of a two-dimensional electron gas (2DEG) in the integer quantum Hall (QH) regime have been successfully analysed on the basis of the Büttiker model applied to quasi-one-dimensional edge channels [1]. The total width of the edge channels is predicted to be much larger than the magnetic length and the cyclotron radius [2]. Experimental evidence of a finite width of the edge channels has been given by studies of the breakdown of the integer and fractional QH effect [3], by edge magnetoplasmam experiments [4], and by magneto-capacitance measurements [5]. Spatially resolved measurements, such as those by the electro-optic technique [6,7], the fountain effect of superfluid helium [8], and phono-conductivity [9], are consistent with the edge channel model. However, the spatial resolution of these techniques is not high enough to resolve the separation and width of the individual channels. We succeeded in making the channels and their separations macroscopically wide [10,11]. A low-mobility two-dimensional hole gas (2DHG) in between the GaAs substrate and the 2DEG serves as an interior gate by which both the electron concentration and the electron concentration gradient can be varied. This p-i-n structure shows a pronounced lateral photo-electric effect when illuminated nonuniformly. By scanning a light spot across the width of a Hall bar the widened edge channels can be nicely imaged.

Results and discussion

Consider the geometry of the compressible (conducting) and incompressible strips as schematically shown in Fig. 1a. If an incompressible strip forms an infinitely high resistive barrier between the upwards and downwards going conducting-channels (no backscattering), V_{12} remains constant when the spot is moved from the left-hand side to the incompressible region separating 5 from 5'. The voltage is expected to fall off very rapidly to its negative value as the barrier between 5 and 5' is crossed. Fig. 1b presents a typical experimental result for V_{12} as function of position in the y-direction. The voltage is not constant between $y = -1000 \mu\text{m}$ and $+600 \mu\text{m}$, but steps on top of a gradually decreasing signal are observed. Apparently the backscattering is not completely suppressed. Just the fact that backscattering is not completely suppressed makes it possible to detect the transitions between the channels 4 and 5. The position of the steps corresponds to the transition from an incompressible to a compressible region. In Fig. 2 we present measurements of the differential lateral photo-effect as a function of position but here the laser spot has been scanned across a large area of the sample. The data obtained are stored in a 512×512 array and displayed as grey tones. The gradient in the electron concentration and the magnetic field are kept constant ($V_{G2} = 4 \text{ V}$, $B = 3.14 \text{ T}$) while the electron concentration is decreased from the bottom to the top of the figure. Most striking are the equidistant strips which move from the left-hand to the right-hand sample edge when the overall electron concentration decreases. Theoretically, the width of a strip (compressible plus incompressible region) is given by $w = n_L (\text{dn}/\text{dy})^{-1}$ where n_L is the degeneracy of a spin-split Landau level and dn/dy is the gradient in electron concentration. By substituting $B = 3.14 \text{ T}$ and $\text{dn}/\text{dy} = 1 \times 10^{11} \text{ cm}^2/\text{nm}$ one finds a width of about $750 \mu\text{m}$ which is in very good agreement with the width shown in Fig. 2. The white dots connected by the white lines indicate the positions in the bulk of the sample where the local filling factor is an integer. It is very clearly seen that when V_{G1} decreases, the edge channels near the low-concentration-side of the sample start to broaden, move across the width of the Hall bar, and finally disappear on the high-concentration-side. This process is repeated until the electron gas near the high-concentration-side is fully depleted. From these measurements we conclude that backscattering can only occur on the high-concentration-side as long as the width of an individual channel is smaller than the width of the Hall bar. The same conclusion was drawn from transport measurements on a

An MBE-grown GaAs/AlGaAs layer structure contains a δ -doped layer of Be atoms acting as a 2DHG at a distance of $0.72 \mu\text{m}$ below the 2DEG. The Hall bar

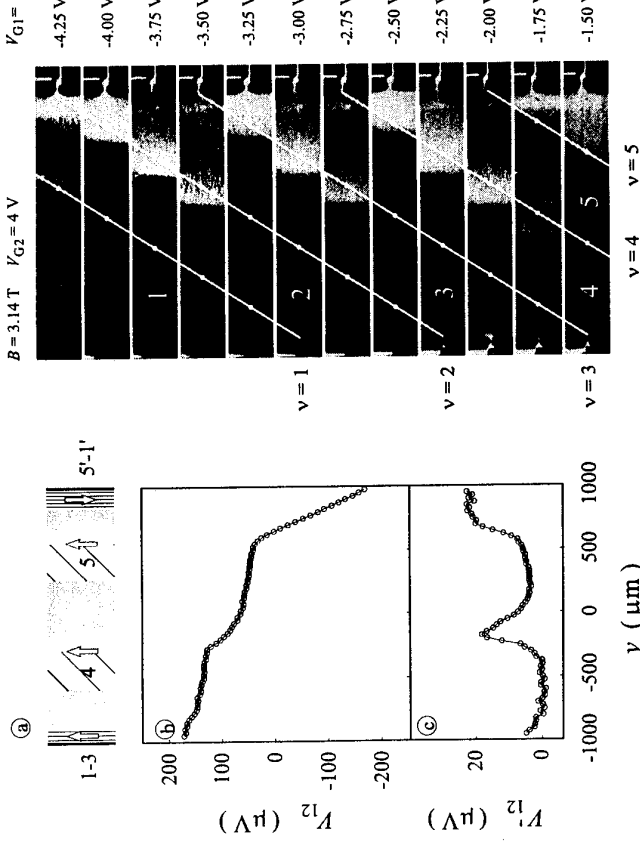


Fig.1 a) Illustration of positions of compressible and incompressible strips.
The lateral photo-voltage V_{12}' at $B = 3.14 \text{ T}$ as function of position in the Hall direction
Differential photo-voltage $V_{12}' = dV_{12}/dy$.

b)

c)

References

- [1] For reviews of the edge channel model, see M. Büttiker, in Nanostructure Systems, ed. M. Reed, Semicond. and Semimetals, Vol. 35 (Academic Press, Inc., San Diego, 1992), p. 191, and R.J. Haug, Semicond. Sci. Technol. **8**, 131 (1993).
- [2] D.B. Chlokovskii, B.I. Shklovskii, and L.I. Glazman, Phys. Rev. B**46**, 4026 (1992).
- [3] S.W. Hwang, D.C. Tsui, and M. Shayegan, Phys. Rev. B**48**, 8161 (1993).
- [4] N.B. Zhitenev, R.J. Haug, K. von Klitzing, and K. Eberl, Phys. Rev. Lett. **71**, 2292 (1993).
- [5] S. Takaoka, K. Oto, H. Kurimoto, K. Gamo, and S. Nishi, Phys. Rev. Lett. **72**, 3080 (1994).
- [6] P.F. Fontein, J.A. Kleinen, P. Hendriks, F.A.P. Blom, J.H. Wolter, H.G.M. Lochs, F. Driessens, L.J. Giling, and C.W.J. Beenakker, Phys. Rev. B**43**, 12090 (1991).
- [7] R. Knott, W. Dietsche, K. von Klitzing, K. Eberl, and K. Ploog, Semicond. Sci. Technol. **10**, 117 (1995).
- [8] U. Klass, W. Dietsche, K. von Klitzing, and K. Ploog, Physica B**169**, 363 (1991).
- [9] A.J. Kent, D.J. McKitterick, L.J. Challis, P. Hawker, C.J. Mellor, and M. Henini, Phys. Rev. Lett. **69**, 1684 (1992); D.J. McKitterick, A. Shik, A.J. Kent, and M. Henini, Phys. Rev. B**49**, 2585 (1994).
- [10] R.J.F. van Haren, R.T.H. Maessen, F.A.P. Blom, and J.H. Wolter, Phys. Rev. B**48**, 17897 (1993).
- [11] R.J.F. van Haren, F.A.P. Blom, and J.H. Wolter, Phys. Rev. Lett. **74**, 1198 (1995).

similar sample where Shubnikov-de Haas oscillations were found only on the high-concentration-side [10].

In conclusion we have shown that edge channels in the QH-regime can be made macroscopically wide and pushed into the bulk of the sample, where they can be imaged by means of the lateral photo-electric effect.

Voltage Distribution and Phase Breaking Scattering in Quantum Hall Regime

Tsumaya ANDO

Institute for Solid State Physics, University of Tokyo
7-22-1 Roppongi, Minato-ku, Tokyo 106, Japan

Numerical simulation is performed to study effects of inelastic scattering in the quantum Hall regime. The voltage distribution exhibits a clear crossover between the quantum case where the edge current picture is valid and the classical case where the bulk current picture is more appropriate.

1. Introduction

Two different pictures have been proposed for the explanation of the integer quantum Hall effect. In the bulk-current picture, the Hall electric field is essential and the current is carried by extended states existing in the vicinity of the center of each broadened bulk Landau level. In the edge-current picture, on the other hand, the current is carried by edge states localized along system boundaries and the Hall field is not required. The relationship between these two pictures remains still unclear. The purpose of the present paper is to demonstrate the crossover between the edge-current and bulk-current regimes through calculations of the voltage distribution in the presence of inelastic scattering. In Sec. 2 the model and the method of the calculation are described. Inelastic scattering is introduced through attachment at each lattice point of a one-dimensional wire which is connected to a reservoir. In Sec. 3 some examples of numerical results are presented and a crossover from edge transport to classical transport based on local conductivities is demonstrated. A summary and conclusion are given in Sec. 4.

2. Voltage Distribution

We consider a wire with width W in the y direction and length L in the x direction, connected to an infinitely long ideal wire which is eventually connected to a reservoir. The wire is replaced by a square lattice and scatterers are introduced by a random fluctuation of local site energies characterized by broadening Γ of the Landau level [1]. At each lattice point, a wire with a single current channel is attached and the wire is connected to a reservoir at ∞ [2, 3]. The reservoir voltage is determined by the condition that the net current passing through the wire vanishes. This voltage probe introduces inelastic scattering which can be adjusted freely by the change in the coupling of the wire to the system. The coupling is characterized by the imaginary part $-i\hbar/2\tau_\phi$ in the diagonal site energy with τ_ϕ being the inelastic scattering time. The phase coherence length L_ϕ is related to τ_ϕ through $L_\phi = \sqrt{2\tau_\phi D^*}$ with D^* being the diffusion coefficient given by $i^2\Gamma/\hbar$ [4], where i is the magnetic length.

3. Results

Numerical calculations are performed for the lowest Landau level and for $\Gamma/\hbar\omega_c = 0.2$ with ω_c being the cyclotron frequency. The voltage distribution is calculated by taking an average of results of 1000 samples typically. Figure 1 shows some examples of the results for $L/l = W/l = 500$ and $L_\phi/l = 20$ and $L_\phi/l = 500$ and Fig. 2 shows those for $L_\phi/l = 5$. In the former case the phase coherence length is larger than the system size, while it is smaller in the latter case.

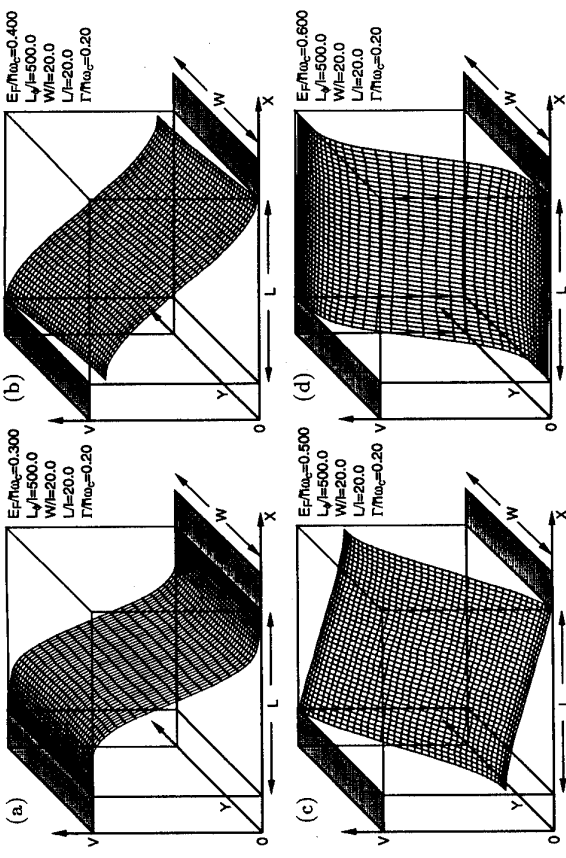


Fig. 1 Calculated voltage distribution in the case of weak inelastic scattering.

When the energy E lies near the center of the Landau level, i.e., (c) and (d) in Figs. 1 and 2, the voltage distribution is independent of the strength of inelastic scattering. The voltage distribution is approximated well by a flat plane determined classically by the local conductivity tensor σ_{xx} and σ_{xy} except in the region close to the system boundaries ($LE_x + WE_y = V$ and $|\sigma_{xy}|E_x + \sigma_{xx}E_y = 0$ where V is the voltage drop between left and right reservoirs and E_x and E_y are fields in the x and y directions, respectively).

The situation changes drastically when the Fermi level moves away from the center. When E lies in the region corresponding to the high-energy tail of the broadened Landau level, (d) in Figs. 1 and 2, the voltage exhibits a step-function-like change in the y direction for $L_\phi \gg L, W$, while the voltage decays linearly in the y direction for $L_\phi \ll L, W$. The same is applicable in the case that E lies in the region of the low-energy tail, i.e., (a) in Figs. 1 and 2, except that the voltage change now occurs in the x direction.

Figure 3 shows the effective field at the center ($L/2, W/2$) of the system for different values of L_ϕ/l . At the center of the broadened Landau level, $E/\hbar\omega_c \sim 0.46$ (shifted from $(1/2)\hbar\omega_c$ to the low energy side due to the nonparabolicity of the lattice model and due to level repulsion from higher Landau levels), the field in the x and y directions becomes independent of the strength of inelastic scattering. This again shows that the field distribution at the Landau-level center is the same as that determined classically by the local conductivity tensor σ_{xx} and σ_{xy} . Note that the sum $E_x + E_y$ is slightly larger than the classical value V/L in the present $L=W$ case.

Effects of inelastic scattering on the voltage distribution become stronger for states

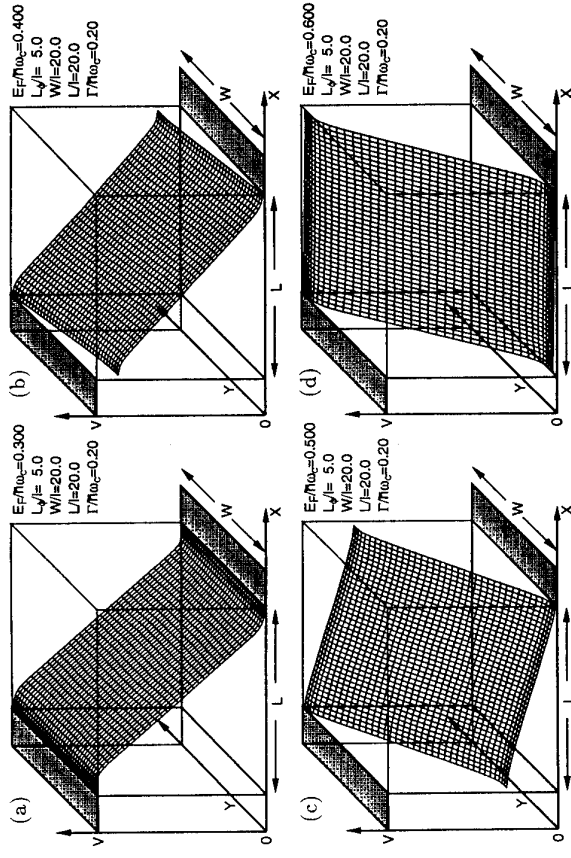


Fig. 2 Calculated voltage distribution in the case of strong inelastic scattering.

with energy away from the center. Furthermore, they become more appreciable with increasing system size even for a fixed value of L_ϕ as shown in Fig. 4. In this figure the decrease of the field for states with energy away from the center is quite prominent, while that of the field for states near the Landau-level center of the wire is roughly explained by the classical field. It is expected that the sum $E_x + E_y$ approaches that of the classical field independent of energy with increasing system size for a fixed L_ϕ .

A simple consideration reveals that the width of the region where the voltage distribution changes is determined by the localization length in the absence of inelastic scattering. When inelastic scattering is introduced, the voltage distribution in the central region becomes linear. The distance from the boundary where the distribution starts to deviate from this linear dependence is determined by the condition that the escape rate of an electron through boundaries becomes comparable to τ_ϕ^{-1} . Therefore, the width of this "boundary region" is determined only by the localization length and τ_ϕ . The crossover occurs when the system width exceeds the width of the "boundary region."

Note that the localization length determined from Fig. 3 by an extrapolation $L_\phi/l \rightarrow \infty$ is larger than the known localization length in two dimensions [5-7]. Although the localization length of a two-dimensional system without boundaries is a single relevant length scale [1], the actual localization length can be modified in the presence of confinement potential leading to edge states.

4. Summary and Conclusion

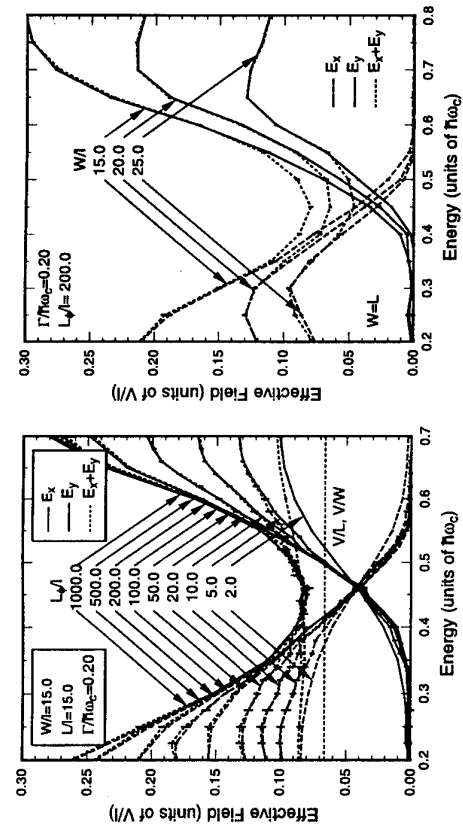


Fig. 3 Calculated effective field at the center of the wire. $W/l = L_\phi/l = 15$.

Fig. 4 Calculated effective field at the center of the wire. $L_\phi/l = 200$.

In this paper effects of inelastic scattering have been studied in two-dimensional systems in the quantum Hall regime. The voltage distribution shows a clear crossover between the quantum case where inelastic scattering is neglected and the classical case where the conventional description based on local σ_{xx} and σ_{xy} is valid. It is quite sensitive to small inelastic scattering and rapidly approaches the classical result corresponding to a constant Hall field with increasing system size for a fixed strength of inelastic scattering. It can be concluded that a simple edge current picture without inelastic scattering is valid only in the case of narrow quantum wires.

Acknowledgments

This work is supported in part by Grant-in-Aid for Scientific Research on Priority Area "Quantum Coherent Electronics: Physics and Technology" from Ministry of Education, Science and Culture, Japan. The numerical calculation has been performed using the facilities of Supercomputer Center at Institute for Solid State Physics, University of Tokyo.

References

1. T. Ando, Phys. Rev. B **49**, 4679 (1994).
2. M. Büttiker, Phys. Rev. B **32**, 1846 (1985); **33**, 3020 (1986); IBM J. Res. Develop. **32**, 63 (1988).
3. J.L. D'Amato and H.M. Pastawski, Phys. Rev. B **41**, 7411 (1990).
4. T. Ando and Y. Uemura, J. Phys. Soc. Jpn. **36**, 959 (1974).
5. T. Ando, J. Phys. Soc. Jpn. **52**, 1893 (1983); **53**, 310 and 3126 (1983); Phys. Rev. B **40**, 9965 (1989).
6. T. Ando and H. Aoki, J. Phys. Soc. Jpn. **54**, 2238 (1985).
7. B. Huckestein and B. Kramer, Phys. Rev. Lett. **64**, 1437 (1990); Solid State Commun. **71**, 445 (1989).

The 2D Electron Gas near $\nu = 1$ as a Skyrme Crystal

L. Brey¹, H.A. Fertig², R. Côté³, and A.H. MacDonald⁴

¹ Institut de Ciencia de Materiales CSIC, Universidad Autónoma de Madrid, 28049 Madrid, Spain

² Department of Physics and Astronomy, University of Kentucky, Lexington, Kentucky 40506-0055

³ Département de Physique, Université de Sherbrooke, Sherbrooke, Québec, Canada J1K 2R1

⁴ Department of Physics, Indiana University, Bloomington, Indiana 47405

ABSTRACT

The ground state of a two-dimensional electron gas at Landau level filling factors near $\nu = 1$ is studied within the Hartree-Fock approximation. It is found that a crystal state of skyrmions, with long range order in both the positions and the spin orientations, is lowest in energy. The favored structure is a square lattice, with opposing postures for the radial spin component of the skyrmions on opposite sublattices. The filling factor dependence of the electron spin-polarization in this state is in excellent agreement with recent experiments.

A two-dimensional electron gas (2DEG) in a strong magnetic field exhibits very interesting properties as the filling factor ν changes. (Here $\nu = 2\pi e^2 n_0$, where $e = \sqrt{\hbar c/eB}$ is the magnetic length and n_0 is the two-dimensional electron density). Recently it has been shown that at $\nu = 1$ the groundstate of this system is ferromagnetic, even in the limit of zero Zeeman coupling [1, 2]. Using a mapping of this system to the non-linear σ ($NL\sigma$) model, it has been demonstrated that the charged excitations of this system [1, 2] are skyrmions. Skyrmions are the lowest energy spin texture excitations of the $NL\sigma$ model, with unit topological charge. A skyrmion is characterized by the sign of its topological charge, its size, and the orientation of the component of the spin density perpendicular to the polarization of the groundstate. In the $NL\sigma$ model, the energy of an isolated skyrmion depends *only* on its topological charge. Recently [3], we have developed a microscopic approach using the Hartree-Fock approximation that allows quantitative studies of the skyrmion properties, particularly the effects of Zeeman coupling and realistic (i.e., Coulomb) electron-electron interactions.

In this work, we report on the results of Hartree-Fock studies of the quantum Hall ferromagnetic system for fillings around $\nu = 1$. It is found that the lowest energy state of this system is a Skyrme crystal, with lattice parameter that is proportional to $|1 - \nu|^{-1/2}$. Over a wide range of filling factors, the spin textures of the individual skyrmions are strongly coupled, favoring a state in which nearest neighbor sites have opposing orientations. (For a magnetic field in the \hat{z} direction, we define the orientation of a skyrmion as the angle formed by the $X - Y$ projection of the spin at some reference point near the skyrmion center, and the vector connecting that point to the skyrmion center.) Analogous states have been studied [4] in nuclear physics in the context of low energy hadron systems, for which certain effective field theory approaches contain chiral soliton solutions analogous to those of the $NL\sigma$ model.

Examples of our spin textures are illustrated in Fig. 1. For extremely low skyrmion densities [Fig. 1(a)], a triangular lattice is favored, consistent with calculations of classical

and the interactions $V_{i,j}$ by

$$V_{i,i} = H_0(q) <\rho_{1,1}(-\vec{q})> + <\rho_{2,2}(-\vec{q})> - X_0(q) <\rho_{1,1}(-\vec{q})>, \quad (3)$$

$$V_{i,j} = -X_0(q) <\rho_{j,i}(-\vec{q})>, \quad i \neq j. \quad (4)$$

In equations (3) and (4)

$$H_0 = \frac{e^2 r^2}{q\ell} \quad \text{and} \quad X_0 = \int_0^\infty dx J_0(q\ell x) e^{-\frac{x^2}{2}}.$$

In order to obtain the HFA solutions we solve self-consistently equations (1)-(4) by using the one electron Green's function equation of motion approach [6]. The Hamiltonian (1) has a number of different solutions corresponding to different states of the electron gas. Each one of these solutions is characterized by a set of order parameters $<\rho_{i,j}(\vec{q})>$. To find the HFA ground state we have to find the minimum energy solution. In this work we consider three different physically interesting solutions and compare their energies and spin polarizations. These are the following: i) A triangular Wigner crystal with no associated spin texture, ii) a triangular lattice with one skyrmion per unit cell (TLF), and iii) a square lattice with two skyrmions per unit cell (SLA). In the structure (ii) all the skyrmions have the same orientation, while in (iii) the two skyrmions in each unit cell can become mutually rotated.

Because we are studying lattice states, the different order parameters are related by symmetry operations; we can use this fact to decrease the number of order parameters needed in the actual computation. Specifically, we assume in the solution to the HFA $<\rho_{i,i}(\vec{G})> = <\rho_{i,i}(\mathbf{R}\vec{G})>$, where \mathbf{R} are the (rotational) symmetry operators of the corresponding lattice. To obtain skyrmion states, we assume in analogy with Ref. [3] that the interspin order parameter has a vorticity: $<\rho_{1,2}(\mathbf{R}\vec{G})> = e^{\pm i\theta} <\rho_{1,2}(\vec{G})>$, where θ is the angle formed by $\mathbf{R}\vec{G}$ and \vec{G} . The sign in the exponent depends on the topological (or, equivalently, electrical) charge of the skyrmions. Using a reduced set of order parameters based on these symmetries, Eqs. (1)-(4) are solved self-consistently, and it is found for most values of ν and experimentally realistic Zeeman couplings that structure (iii) above is lowest in energy, and has a spin polarization in quantitative agreement with experiment.

In conclusion, we have computed the energy, spin texture, and spin polarization of skyrmion lattices near $\nu = 1$, and have found that a square lattice with strongly coupled spin textures is the relevant structure for realistic Zeeman couplings. The spin polarization of this state is in excellent agreement with experiment.

REFERENCES

- K. Moon, H. Mori, Kun Yang, S.M. Girvin, A.H. MacDonald, L. Zheng, D. Yoshioka, and Shou-Cheng Zhang, Phys. Rev. B **51**, 5138 (1995).

2. S.L.Sonhdi, A.Karlhede, S.A.Kivelson, and E.H.Rezayi, Phys.Rev.B **47**, 16419 (1993); D.H.Lee and C.L.Kane, Phys.Rev.Lett. **64**, 1313 (1990); E.H.Rezayi, Phys.Rev.B **36**, 5454 (1987); **43**, 5944 (1991).
3. H.A.Fertig, L.Brey, R.Côté and A.H.MacDonald, Phys. Rev. B **50**, 11018 (1994).
4. I.Klebanov, Nucl.Phys. B **262**, 133 (1985); L.Castillejo *et al.*, Nucl.Phys. A **501**, 801 (1989); M.Kugler *et al.*, Phys.Rev.D **40**, 3421 (1989).
5. S.E.Barrett, G.Dabbagh, L.N.Pfeiffer, K.West and R.Tycko, unpublished.
6. R.Côté and A.H.MacDonald, Phys. Rev. B **44**, 8759 (1991); R.Côté, L.Brey and A.H.MacDonald, Phys. Rev. B **10**, 10239 (1992).

Coulomb particles. However, for experimentally relevant parameters, the system undergoes a phase transition to the square lattice illustrated in Fig. 1(b) at very small values of $|\nu - 1|$. As can be seen, the $X - Y$ spin component changes very little along nearest neighbor bonds, allowing a particularly small energy cost associated with gradients in the spin texture. By contrast, the triangular lattice is inherently frustrated, so that such favorable spin textures cannot be realized with this symmetry. The increased gradient energy for the triangular lattice effectively introduces a repulsion between the skyrmions that causes them to shrink in size compared to the square lattice case. It is interesting to note that in the pure NL σ model, skyrmions do not interact; presumably the coupling effects we have found in this work require higher order corrections [1,2] to describe the physics we have found in this approach. Indeed, in the analogous hadron systems [4], fourth order derivative terms – introduced to prevent the skyrmions from collapsing to zero size – are responsible for the effective interskyrmion interaction.

At larger densities, we expect that quantum fluctuations will melt the crystal. It is interesting to speculate that the typical coordination number of the charges in the resulting liquid state will be four, in order to minimize the gradient energy of the local spin texture.

Our results show remarkably good agreement with experiment. Recently, the Knight shift of the ^{71}Ga nuclei located in n-doped GaAs quantum wells for $0.66 < \nu < 1.76$ has been measured [5], using specialized NMR techniques. This quantity is proportional to the spin polarization, P , of the electron gas confined in the well. It was found that P drops very quickly on either side of $\nu = 1$, showing that the charged excitations of the $\nu = 1$ state carry large spins, consistent with our earlier calculations [3]. Figure 2 illustrates the experimental spin polarization, as well as that obtained for the square and triangular skyrmion lattices, at different values of the Zeeman coupling. In addition, results for independent electrons – which gives precisely the same polarization as a Wigner crystal without a spin texture – are shown, to illustrate the dramatic lowering of the spin polarization due to the skyrmion spin texture. The agreement between experiment and our square lattice results are remarkably good in the range $0.8 < \nu < 1.2$.

We now outline our method for obtaining these results within the Hartree-Fock approximation (HFA). Since we are essentially dealing with a strong field phenomenon, and we are interested in states for which the Zeeman splitting is much smaller than the cyclotron gap, we will only consider states in the lowest Landau level. In the Landau gauge the single particle states are given by $\psi_{X,j}(\vec{r}) = \frac{1}{\sqrt{L_y \ell \pi^{1/2}}} e^{i X y / \ell^2} e^{-(x-X)^2 / 2 \ell^2} \chi_j$. Here X is the electron guiding center, j is the spin variable ($j=1/2$ corresponds to spin \uparrow (1)), and χ_j is the corresponding spinor. In the HFA the Hamiltonian is, up to an additive constant,

$$H_{HF} = -\frac{\tilde{g}}{2} (\rho_{1,1}(0) - \rho_{2,2}(0)) + g \frac{e^2}{\ell} \sum_{\vec{q},i,j} V_{i,j}(\vec{q}) \rho_{i,j}(\vec{q}). \quad (1)$$

In this equation $g = \frac{L_x L_y}{2 \pi \ell^2}$, $\tilde{g} = g^* \mu_B B = g_I e^2 / \ell \ell$, where g^* the Landé factor and μ_B is the Bohr magneton. The operators $\rho_{i,j}$ are given by

$$\rho_{j,j'}(\vec{q}) = \frac{1}{g} \sum_{X,X'} e^{-\frac{i}{2} q_x (X+X')} \delta_{X,X'-q_y \ell^2} C_{X,j}^\dagger C_{X',j'} \quad (2)$$

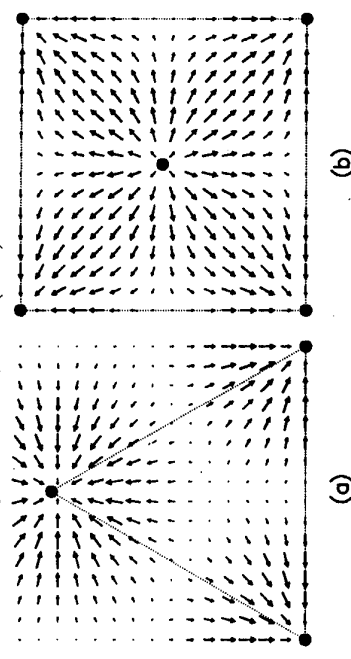


Fig. 1. Two-dimensional vector representation of the $x - y$ components of the spin density of a crystal of skyrmions as obtained in the HFA. (a) Triangular lattice state at $\nu = 1.1$ and $g^* = 0.015$; (b) Square lattice state at $\nu = 1.1$ and $g^* = 0.015$.

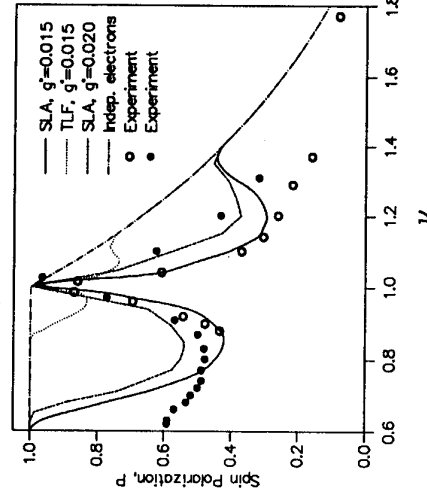


Fig. 2. Variation of the spin polarization, P , as a function of ν , for square (SLA) and triangular (TLF) Skyrmion crystal states and for different values of $g^* \equiv g \mu_B B / (e^2 \ell)$. The open circles are experimental data obtained for g^* near 0.016, while the filled circles show data obtained for g^* near 0.021.

Supercurrent and quasiparticle transport in a two-dimensional electron gas with superconducting electrodes.

B.J. van Wees*

Department of Applied Physics and Materials Science Centre

Nijenborgh 4, 13

University of Groningen

9747 AG Groningen, The Netherlands

We have investigated supercurrent and quasiparticle transport in the 2DEG present in InAs/Al(Ga)Sb quantum wells. The physics of these systems will be discussed with two examples: supercurrent transport in Nb/InAs/Nb junctions and phase dependent resistance in a superconductor-2DEG quasiparticle interferometer.

I. INTRODUCTION

Recent years have seen a revival of the research on transport in hybrid superconducting structures, where superconductors are coupled by either a normal metal or a semiconductor (for a review see [1]). In particular the possibility to couple superconductors to a (ballistic) two-dimensional electron gas (2DEG) has triggered a range of theoretical predictions [2], most of which have not yet or only partially been observed experimentally.

Experiments on quantum ballistic transport in a 2DEG show that the first order description of electron transport is in terms of non-interacting particles or waves [3]. The electron-electron and electron-phonon interaction lead to inelastic scattering and therefore induce phase breaking. However, at low temperatures the associated length scales for these processes can greatly exceed the sample dimensions.

Similar to the case of normal transport we therefore assume that the transport through a 2DEG coupled to superconductors can also be described in terms of non-interacting particles. A finite pair potential Δ is present in the superconducting electrodes, whereas we assume $\Delta=0$ in the 2DEG itself. With these assumptions the superconductor only affects the transport by means of *coherent Andreev reflection*. An electron from the 2DEG with energy E (relative to the Fermi energy) $< \Delta$ cannot enter the superconductor and will be reflected as a hole, provided that no potential barrier is present at the interface. A crucial aspect here is that, in the absence of a magnetic field and for $E=0$, the wave functions of the electron and Andreev reflected hole are phase conjugated. This phase conjugation has led to a range of theoretical predictions [4-7], some of which have been observed experimentally [8-10].

A second aspect is that in the Andreev reflection process the phase of the particle wave function changes with ϕ_1 when the electron is converted into a hole at the first superconductor, and $-\phi_2$ when the hole is converted back into an electron at the second superconductor. As a result bound electron-hole states are formed in the 2DEG and it can be shown (e.g. for quantum point contacts in refs. [11,12]) that a supercurrent can flow when the energy of these bound states depends on the superconducting phase difference $\Delta\phi = \phi_2 - \phi_1$. As we will show in section 4, the superconducting phase difference can not only determine the supercurrent, but can also affect the normal transport properties. In this paper

we will illustrate the physics of a superconductor coupled 2DEG with two examples: supercurrent transport in superconductor-2DEG/superconductor junctions and phase dependent resistance in a superconductor-2DEG quasiparticle interferometer.

II. DEVICE DESCRIPTION.

Our devices are based on the closely lattice matched InAs/Al(Ga)Sb III/V compound system. A 2DEG is created in an InAs quantum well by confining the electrons in between AlSb or GaSb barriers. A special feature of this system is that it is not intrinsically doped. Due to the relatively deep InAs well, and the pinning of the Fermi energy at the surface, the carrier density is about $1.0\text{--}1.5 \times 10^{16}/\text{m}^2$. The mobility is typically in the range $50.000\text{--}100.000 \text{ cm}^2/\text{Vs}$, resulting in an elastic mean free path $l_e \approx 1\mu\text{m}$. An additional feature of the InAs/GaSb system is that due to the special band alignment this system not only contains a 2D electron gas, but may also support a 2D hole gas. However, due to its higher effective mass and lower mobility we expect that the latter contribution to the (super) current can be ignored.

A similar system is employed by Nguyen et al. [13]. Note however that in their case the electron density is higher due to intentional doping, and more than one 2D subband may be occupied. Due to the relatively low electron density our systems are strictly two-dimensional. Superconducting contacts are made by first removing the top GaSb cap and AlSb barrier layers, using a selective wet etchant which exposes the InAs surface. The special property of InAs is that the Fermi energy of the exposed surface is pinned about 150 meV above the conduction band edge. As a result no Schottky barrier is formed when metal is deposited on top. Before the Nb deposition however, the oxide layer on the InAs surface is removed by Kaufmann Ar etching. This is required since the probability of Andreev reflection is severely degraded by the presence of a tunnel barrier at the superconductor-semiconductor interface [14].

III. SUPERCURRENT TRANSPORT IN NB/INAS/NB SYSTEMS.

Supercurrent transport through a 2DEG has been studied by several groups [13,15-18]. In these cases the 2DEG is formed either due to surface inversion on a p-type InAs substrate, or is present in an In(Ga)As quantum well. No conclusive evidence has been obtained yet for supercurrent transport in GaAs/AlGaAs heterojunctions [19-22]. A cross section of the devices we employ for supercurrent transport is given in fig. 1.



Fig. 1 Cross section of the device, illustrating Nb electrodes connected to the InAs/GaSb quantum well (thicknesses in nanometers).

The two superconducting electrodes are $0.25 \mu\text{m}$ apart. Due to the fabrication process the top barrier layer is also removed. Measurements show that this leads to a reduction of the elastic mean free path to a value $l_e \approx 0.25 \mu\text{m}$. Fig. 2(a) shows the differential resistance of the sample, measured as a function of voltage bias [24]. For $V \gg 2\Delta$, with the superconducting energy gap of Nb given by $\Delta \approx 1.5\text{meV}$, the normal state resistance R_n is measured. After correction for parallel conductance (due to the absence of a mesa etch), we find that the resistance is about 1.5 times the Sharvin resistance of the 2DEG [3], thus indicating some residual scattering. The decrease in resistance below $V=3\text{mV}$ clearly illustrates the onset of Andreev reflection. The structure at $V \approx 1.5\text{mV}$ can be related to multiple Andreev reflection [23].

Relevant for the magnitude of the supercurrent is that the electrode spacing is shorter than the superconducting coherence length $\xi_0 = \hbar v_F / \Delta$ (evaluated for the ballistic case). This implies that the junction is in the short-limit case [25]. Also at $T=130\text{ mK}$ the thermal coherence length $\xi_n = \hbar v_F / kT$ exceeds the junction length. This implies that the $I_c R_n$ product should be given by $\pi \Delta / e$ [25] $\approx 3\text{mV}$.

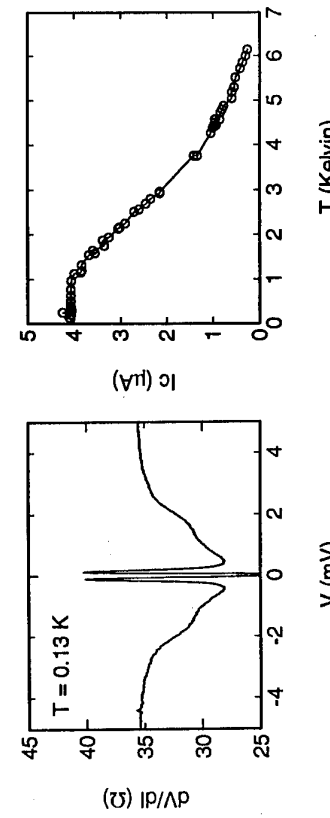


Figure 2 (a) Differential resistance for a $0.25 \mu\text{m}$ device, measured at 130 mK . (b) Temperature dependence of the critical current of a $0.25 \mu\text{m}$ gap device.

The temperature dependence of the supercurrent is given in fig. 2(b). The zero temperature critical current is much less than expected from theory. Also the temperature dependence is different from that expected for a short and clean junction [25]. Part of the results may be due to the fact that the 2DEG is not fully ballistic. Another aspect is that, since the contacts are fabricated on top of the InAs, the electrons can penetrate a finite distance underneath the superconductor before being Andreev reflected. The transport in such a *superconducting quantum well*(SQW) was studied theoretically by Volkov et al. [26]. However, we think that the (lack of) ballistic transport underneath the contacts plays an even more important role in degrading the supercurrent. This is supported by recent investigations on the effect of Kaufmann Ar cleaning on the 2DEG electron density and mobility [27].

IV. PHASE DEPENDENT RESISTANCE IN A SUPERCONDUCTOR-TWO-DIMENSIONAL ELECTRON GAS QUASIPARTICLE INTERFEROMETER.

As discussed in section 1 phase coherent Andreev reflection can reveal itself as a phase dependent normal resistance. An example is the phase dependent resistance in a superconductor-2DEG quasiparticle interferometer [28]. Several schemes for these so-called quasiparticle interferometers have been proposed [5,29-38]. Normal metal-superconductor interferometers have been studied experimentally, using either tunnel junctions [39], or clean contacts [40,41].

We have fabricated and studied an interferometer in the quasiballistic regime, with high transparency interfaces between the superconductor and the 2DEG. The geometry is shown in fig. 3(a).

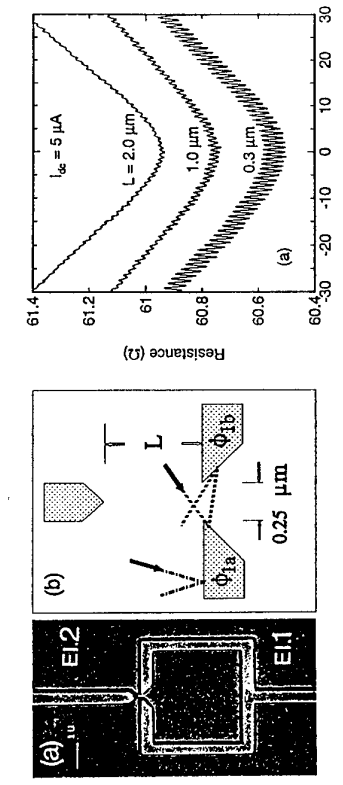


Fig. 3. SEM micrograph (a) and schematic view (b) of the electrodes of the superconductor-2DEG quasiparticle interferometer. (c) Phase dependent resistance of the device at three different spacings between injector and ring electrode, obtained at $5\mu\text{A}$ DC bias.

A ring shaped electrode (EL1) is defined on top of an InAs layer. Near the $0.25 \mu\text{m}$ gap in this electrode a second electrode (EL2) is located, at a distance of 0.3 , 1.0 , or $2.0 \mu\text{m}$. In the experiment the (differential) resistance between the electrodes 1 and 2 is measured as a function of the magnetic flux Φ through the ring.

Electrode 1 injects electrons into the 2DEG. A fraction of these electrons will end up in the narrow gap in electrode 2, and will sense the phase difference $\Delta\phi = 2\pi\Phi/\Phi_0$, with $\Phi_0 = h/2e$ the superconducting flux quantum. Due to the all-niobium nature of the electrodes the first order description is in terms of a SQUID, due to the Josephson coupling between electrodes 2 and 1a, and 2 and 1b respectively. This behaviour is observed in the measurements of the differential resistance at zero current bias I_{c0} . For $L=0.3 \mu\text{m}$, the resistance is modulated with a period $h/2e$, and reaches the zero voltage state, whenever the critical current ($I_c \approx 500\text{nA}$) has a maxima at $\Phi = n\Phi_0$. When L is increased, the Josephson coupling becomes

weaker ($I_c \approx 40\text{nA}$ at $L=1.0\mu\text{m}$) until it cannot be detected anymore at $L=2.0\mu\text{m}$. An alternative way to reduce the effect of the Josephson coupling is to apply a DC current bias I_{DC} . Fig. 3(c) shows the measurement of the differential resistance at $I_{DC} = 5\mu\text{A}$, a value much higher than the estimated critical currents. Well defined oscillations are visible, which are attributed to quasiparticle interference. They distinguish themselves from the SQUID type oscillation by their different period, temperature dependence and dependence on injector spacing L [28]. The oscillations show a resistance minimum at $\Delta\phi=0$, however at low voltages and energies a resistance maximum is observed [28]. This behaviour is not yet understood.

Recently we have observed similar oscillations in a T-shaped interferometer [42]. Due to the lack of parallel conducting paths in the latter system, the amplitude of the oscillations is typically 1% of the total resistance, which should be compared to the 0.05% modulation in the system described above.

In summary we have given two examples of (phase coherent) Andreev reflection in superconductor coupled 2DEG systems. These show that the fundamental effects predicted by theory are indeed observed in the experimental systems. However, their manifestation is different, either quantitatively or qualitatively. We believe that by improving the device geometry, in particular the 2DEG region near or underneath the superconducting contacts, the comparison with theory can be tightened. Work in this direction is in progress.

*The research described in this paper has been performed in a collaboration between A. Dimoulas (current address: Dep. of Chemical Engineering, Caltech, Pasadena CA, USA), P.H.C. Magnee, J.P. Heida, S. den Hartog, B.J. van Wees, and T.M. Klapwijk from Groningen University, and W.v.d. Graaf and G. Borghs from IMEC VZW Leuven, Belgium. This work was supported by the Netherlands Organization for Scientific Research (NWO) through the Foundation for Fundamental Research on Matter (FOM). A.D. acknowledges support from the European Human Capital & Mobility Program, and B.J. v. Wees from the Dutch Royal Academy of Sciences. We thank A.F. Volkov and A.V. Zaitsev for valuable discussions.

- [9] S.J.M. Bakker, E. van der Drift, T.M. Klapwijk, H.M. Jaeger, S. Radelaar, Phys. Rev. B49, 13275 (1994).
- [10] P.H.C. Magnee, N. van der Post, P.H.M. Kooistra, B.J. van Wees, and T.M. Klapwijk, Phys. Rev. B50, 4594 (1994).
- [11] C.W.J. Beenakker and H. van Houten, Phys. Rev. Lett. 66, 3056 (1991).
- [12] A. Furusaki, H. Takayanagi, and M. Tsukada, Phys. Rev. Lett. 67, 132 (1991).
- [13] C. Ngyuen, H. Kroemer, and E.L. Hu, Phys. Rev. Lett. 69 2847 (1992).
- [14] G.E. Blonder, M. Tinkham, and T.M. Klapwijk, Phys. Rev. B25, 4515 (1982).
- [15] H. Takayanagi and H. Kawakami, Phys. Rev. Lett. 54, 2449 (1985).
- [16] H. Takayanagi and T. Akazaki, submitted to Phys. Rev. B, see also this volume.
- [17] L. Mur et al., unpublished.
- [18] T. Matsuyama, in Quantum dynamics of Submicron Structures, ed. H.A. Cerdeira, B. Kramer, and G. Schon, Kluwer Academic Publishers, pag. 503 (1995)
- [19] K.M.H. Lenssen et al., IEEE Trans. Appl. Supercond. 3, 1961 (1993).
- [20] J.R. Gao et al., Appl. Phys. Lett. 63, 334 (1993).
- [21] A.M. Marsh et al., to be published.
- [22] Z. Ivanov, T. Claeson, and T. Anderson, Jpn. J. Appl. Phys. 26, Suppl. 26-3 (1987).
- [23] T.M. Klapwijk et al., PhysicaB&C 109-110, 1657 (1982); M. Octavio et al., Phys. Rev. B27, 6739 (1983).
- [24] J.P. Heida et al., to be published.
- [25] I.O. Kulik, and A.N. Omal'yanchuk, Sov.J.Low.Temp.Phys.3,459 (1977)
- [26] A.F. Volkov et al., Physica C242, 261 (1995)
- [27] P.H.C. Magnee, S.G. den Hartog, B.J. van Wees, T.M. Klapwijk, W. van de Graaf, and G. Borghs, submitted to Phys. Rev. B.
- [28] A.D. Dimoulas, J.P. Heida, B.J. van Wees, T.M. Klapwijk, W. v.d. Graaf and G. Borghs, Phys. Rev. Lett. 74, 602 (1995).
- [29] B.L. Alt'schuler and D.B.Z. Spivak, Sov. Phys. JETP 65, 343 (1987).
- [30] B.Z. Spivak and D.E. Khmel'nitskii, JETP Lett. 35, 413 (1982).
- [31] H. Nakano and H. Takayanagi, Solid State Commun. 80, 997 (1991).
- [32] Yu. V. Nazarov, Phys. Rev. Lett. 73, 1420 (1994).
- [33] Y. Takane, and H. Ebisawa, J. Phys. Soc. Jap. 60, 3130 (1991).
- [34] Y. Takane, and H. Otani, J. Phys. Soc. Jap. 63, 3361 (1994).
- [35] C.J. Lambert, J.Phys.Cond. Matter 5, 707 (1993).
- [36] A.F. Volkov and A.V. Zaitsev, to be published in Phys. Rev. B
- [37] A.Kadigrobov, A. Zagostin, R.I. Shekter, and M. Jonson, to be published.
- [38] P.M. Cook, V.C. Hui, and C.J. Lambert, Europhys. Lett. 30, 355 (1995)
- [39] H. Poithier, S. Gueron, D. Esteve, and M.H. Devoret, Phys. Rev. Lett. 73, 2488 (1994).
- [40] V.T. Petrushov, V.N. Antonov, P. Delsing, and T. Claeson, JETP Lett. 60, 607 (1994).
- [41] P.G.N. de Vegvar et al., Phys. Rev. Lett. 73, 1416 (1994).
- [42] S.G. den Hartog et al., to be published.

Observation of the quantized critical current in a superconducting quantum point contact

Hideaki Takayanagi, Tatsushi Akazaki, and Junsaku Nitta

3-1, Morinozato-Wakamiya, Atsugi-Shi, Kanagawa 243-01 Japan

E-mail: takayan@will.nitt.brj.jp Fax: +81 462 40 4722

Abstract

The quantization of the critical current has been confirmed in a superconducting quantum point contact consisting of a split-gated superconductor-(two-dimensional electron gas)-superconductor junction. Both the critical current and the conductance show a step-wise change as a function of the gate voltage.

1. Introduction

Along with recent progress in nano-fabrication technology, interest is increasing in the quantum transport of superconducting structures coupled with mesoscopic-scale normal-metals or semiconductors [1]. Quantization of the maximum supercurrent (the critical current I_c) was theoretically predicted in a superconducting quantum point contact (SQPC) [2-4] by analogy of a quantum point contact. This letter reports on the quantization of the I_c in an SQPC consisting of a split-gated superconductor(S)-normal metal(N)-super-conductor(S) junction using the two-dimensional electron gas (2DEG) in the semiconductor heterostructure as the normal metal.

2. Sample

The SQPC is made from a semiconductor $\text{In}_{0.52}\text{Al}_{0.48}\text{As}/\text{In}_{0.53}\text{Ga}_{0.47}\text{As}$ heterostructure grown by molecular beam epitaxy on a Fe-doped semi-insulating InP substrate. Figure 1(a) is a schematic of the fabricated SQPC. The details of the fabrication process are reported elsewhere [5]. The 2DEG is confined in the inserted 4-nm InAs layer and has a high mobility and a high carrier density [6]. Two superconducting Nb electrodes are coupled with the 2DEG, and a supercurrent as well as a normal current flow through the 2DEG. The distance L between the two Nb electrodes is 0.2-0.6 μm and the width W of the electrodes is 10 μm . As shown in the figure, the junction has a HEMT-type split gate with a very short gate length L_g of less than 0.1 μm . This gate configuration makes it possible to vary the carrier density and mobility of the 2DEG underneath the gate by changing the gate voltage, and this results in changes in both the superconducting critical current I_c and the normal resistance R_N of the junction.

The carrier density N_s , the mobility μ , and the effective mass m^* of the 2DEG were respectively determined to be $2.3 \times 10^{12} \text{ cm}^{-2}$, 111,000 cm^2/Vs , and $0.045m_e$, at 4.2 K by Shubnikov-de Haas measurement. Here, m_e is the free electron mass. From these values, the coherence length $\xi_N = \hbar v_F/2\pi k_B T$ (where v_F is the Fermi velocity) in the clean limit and the mean free path ℓ were calculated to be 0.28 μm at 4.2 K and 2.8 μm , respectively. Therefore, the junction belongs to the clean limit regime ($\ell > \xi_N$) with ballistic transport ($\ell > L$).

3. Experimental results

The critical current is measured as a function of the gate voltage V_g at a low temperature of about 10 mK. When the absolute value of gate voltage is small ($V_g > -0.8$ V), I_c oscillates due to the Fabry-Pérot interference of quasiparticles [7, 8]. When the absolute value of gate voltage is large ($V_g < -1$ V), the 2DEG underneath the gate electrode is pinched off and as the absolute value of gate voltage is increased the constriction width L_w is reduced gradually by the depletion regions. When L_w becomes comparable to the Fermi wavelength of the 2DEG, $\lambda_F \approx 16$ nm, one-dimensional (1-D) subbands are generated in the constriction and both the normal and the superconducting current flow through them. The number of subbands is given by $2L_w/\lambda_F$ and may be changed one by one by the gate voltage. For a quantum point contact this gate control provides the so-called quantized conductance in units of $2e^2/h$ [9, 10]. For an SQPC it should also give rise to quantization of the critical current [2-4].

Figure 2 shows the measured critical current and conductance of an SQPC with $L = 0.3 \mu\text{m}$ as a function of gate voltage at a temperature of about 10 mK. It is clear that both the critical current and the conductance undergo step-wise changes as a function of gate voltage and that the behavior of the critical current is similar to that of the conductance. These data prove that -as predicted by theory- the critical current flowing through an SQPC is quantized in magnitude by the number of 1-D subbands in the constriction. The step height is not universal but depends on junction parameters such as L and the Andreev reflection probability at the S-2DEG interface [3]. The step height for the sample in Fig. 2 was about 5 nA, which is much smaller than the theoretical value of about 50 nA. However, the ratio of the step height to the critical current for $V_g = 0$ was calculated to be 3.3×10^{-3} in the experiment and this value agrees with the theoretical value of 2×10^{-3} . Moreover, it also agrees qualitatively with the theory that the step height decreases from about 6 nA to 4 nA as the step-order increases from the 1st to the 7th.

In Fig. 2 conductance steps do not appear at the expected quantized value of $n \cdot 2e^2/h$ ($n = 1, 2, 3 \dots$) and the step height is a little bit larger than $2e^2/h$. This is due to single and multiple Andreev reflections between the two S-2DEG interfaces. It was theoretically shown that the conductance of the quantum point contact that faces an S-N interface is quantized in units of $4e^2/h$ (i.e., the doubling of the conductance step) [11]. In the theory the Andreev reflection probability

of one is assumed at the S-N interface. But this behavior of the conductance is not yet well understood, since there is no theory for conductance in an SQPC which consists of two S-N interfaces.

There are resonance structures at the edge of some steps, e.g., at the 2nd and the 4th current steps and the 7th and the 8th conductance steps. These structures can be explained by the interference of electrons and holes which traverse the 2DEG many times due to normal reflections at the S-2DEG interfaces [3].

Finally, it is noteworthy that the order of the critical-current step is different from that of the corresponding conductance step. The difference between them is three, and the same kind of difference was also observed in other samples. This suggests that several lower-order subbands do not contribute to the critical current. The present theory predicts an agreement between the order of the two kinds of steps. Further theoretical work along with more experimental data are required before the origin of this phenomenon can be clarified.

4. Conclusions

The critical current as well as the conductance in a split-gated semiconductor-coupled Josephson junction showed step-wise changes as a function of gate voltage. This result is evidence that the critical value of dc Josephson current is quantized in magnitude by the number of 1-D subbands in the quantum point contact. The behavior of ac Josephson current is very interesting and will be studied in the junction shown in this letter.

Acknowledgements

We thank Dr. A. Furusaki for discussions of transport in a superconducting quantum point contact, Dr. Y. Ishii, Dr. K. Arai and Dr. T. Enoki for discussions on the electron transport in the heterostructure, and T. Ishikawa for the MBE growth. We also thank Dr. T. Ikegami and Dr. N. Matsumoto for encouragement throughout this work.

References

- [1] T. M. Klapwijk, *Physica B* **197**, 481 (1994).
- [2] A. Furusaki, H. Takayanagi, and M. Tsukada, *Phys. Rev. Lett.* **67**, 132 (1991).
- [3] A. Furusaki, H. Takayanagi, and M. Tsukada, *Phys. Rev. B* **45**, 10563 (1992).
- [4] C. W. J. Beenakker and H. van Houten, *Phys. Rev. Lett.* **66**, 3056 (1991).
- [5] H. Takayanagi and T. Akazaki, to be published in *Jpn. J. Appl. Phys.*
- [6] T. Akazaki, J. Nitta, H. Takayanagi, T. Enoki, and K. Arai, *Appl. Phys. Lett.* **65**, 1263 (1994).
- [7] H. Takayanagi, T. Akazaki, and J. Nitta, *Phys. Rev. B* **51**, 1374 (1995).

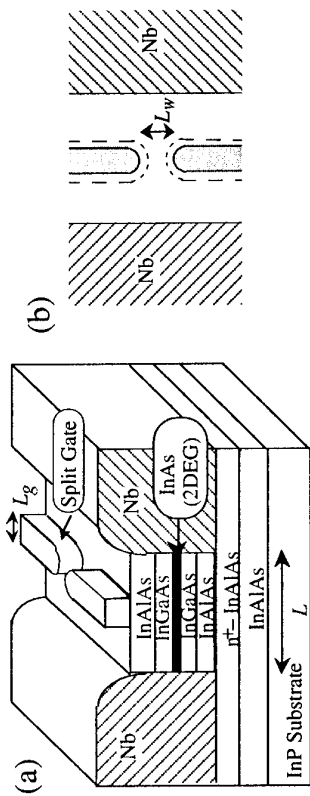


FIG. 1. (a) Cross-sectional view of the fabricated superconducting quantum point contact. The supercurrent flows through the split when the 2DEG underneath the gate becomes pinched-off by the gate voltage. (b) Top view of the sample. The depletion layer (shown by the dashed lines) defines the constriction in the 2DEG.

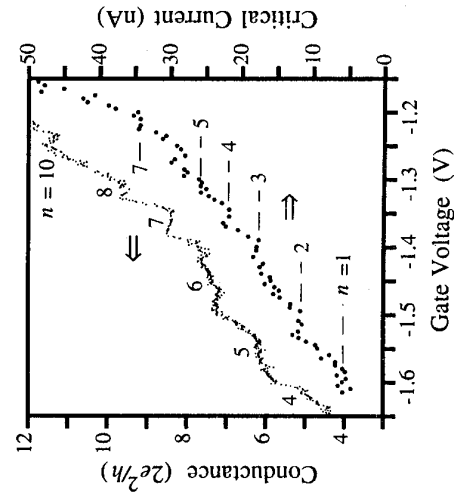


FIG. 2. The critical current and the conductance as a function of the gate voltage.

THEORY OF ANDREEV RESONANCES IN QUANTUM DOTS.

M. Leadbeater, N.R. Claughton, C.J. Lambert and V.N. Prigodin[†]
 School of Physics and Chemistry, Lancaster University,
 Lancaster, LA1 4YB, U.K.

[†]Max Planck Institute, Stuttgart, Germany

Abstract.

We present theoretical results for the electrical conductance G of a quantum dot in the presence of superconductivity. After deriving a generalization of the well-known Breit-Wigner formula, valid in the presence of superconducting leads, results for the distribution of conductance resonances are derived. For a normal (N) contact - normal dot (NDOT) - superconducting (S) contact, as the order parameter Δ of the S contact tends to zero, recent predictions for the resonant structure of a normal chaotic dot are reproduced. When Δ increases from zero, for finite applied voltage, resonances are destroyed.

1. Introduction. During the past few years resonant transport in mesoscopic systems has received a great deal of attention. Transport through normal resonant structures is well described by the standard Breit-Wigner formula[1]. The aim of this paper is to examine in detail the effect of superconductivity on conductance resonances through quantum dots. In section 2, a general formula for transport through phase coherent structures is introduced and in section 3, a Breit-Wigner formula for a normal lead - normal dot - superconducting lead structure is derived which extends the results of Beenakker[2] to the case of finite applied voltages. We predict that at finite energies transport resonances in such a structure are destroyed by the switching on of superconductivity.

2. Analysis of phase coherent, resonant transport. We are interested in a quantum structure connected to external leads labelled $L = 1, 2, \dots$ and therefore begin by considering two vector spaces A and B, spanned by a countable set of basis functions. In what follows, the sub-space B will represent the structure of interest and sub-space A the external leads. The coupling between A and B will be an operator of the form

$$\mathbf{H}_1 = \begin{pmatrix} 0 & \mathbf{W} \\ \mathbf{W}^\dagger & 0 \end{pmatrix} \quad (2.1)$$

and we therefore write the Green's function \mathbf{G} for the combined space $A \oplus B$ in the form

$$\mathbf{G} = \begin{pmatrix} \mathbf{G}_{AA} & \mathbf{G}_{AB} \\ \mathbf{G}_{BA} & \mathbf{G}_{BB} \end{pmatrix} \quad (2.2)$$

One can derive[3] a very general result for the transmission coefficient $T_{nn'}$ between two scattering channels n, n' of the leads (with $n \neq n'$), which underpins various analogues of Breit-Wigner formulae. The result is

$$T_{nn'} = 4 \operatorname{Trace} \left[\Gamma(n) \mathbf{G}_{BB} \Gamma(n') \mathbf{G}_{BB}^\dagger \right] \quad (2.3),$$

where $\mathbf{G}_{BB}^{-1} = \mathbf{g}_{BB}^{-1} - \sigma' - \sigma + i\Gamma$. In these expressions σ, σ' are Hermitian self-energy matrices, $\Gamma = \sum_n \Gamma(n)$, where $\Gamma(n)$ is a Hermitian matrix of inverse lifetimes, and \mathbf{g}_{BB} the Green's function of the dot when $\mathbf{H}_1 = 0$ which is given by

$$\mathbf{g}_{BB} = \sum_{\nu=1}^{N_0} \frac{|f_\nu\rangle \langle f_\nu|}{E - \epsilon_\nu} \quad (2.4).$$

Equation (2.3) immediately yields general expressions for the electrical conductance in the presence of an arbitrary number of external leads. In the presence of a superconducting reservoir (with no open quasi-particle channels) and a single normal lead (with $n_p = 1, 2, \dots, N_p$ denoting the N_p open channels of the normal lead, for quasi-particles of type p ($p = +$ for particles and $p = -$ for holes)), then the electrical conductance reduces to twice the Andreev reflection coefficient[4] and takes the form

$$G = 8 \operatorname{Trace} \left[\Gamma_+ \mathbf{G}_{BB} \Gamma_- \mathbf{G}_{BB}^\dagger \right] \quad (2.5),$$

where $\Gamma_\pm = \sum_{n_\pm=1}^{N_\pm} \Gamma(n_\pm)$ and $\mathbf{G}_{BB}^{-1} = \mathbf{g}_{BB}^{-1} - \Sigma + i(\Gamma_+ + \Gamma_-)$.

For structures where transport is dominated by resonances, only those levels with $\epsilon_\nu \approx E$, where E is the quasiparticle energy, are important and therefore a good approximation is obtained by restricting the sums on the right hand side of equation (2.4) to a small number of states.

3. Breit-Wigner Formula For A Normal lead - Normal dot - Superconducting Lead Structure. In this case it is necessary to make a two level approximation in which both a particle ν and a hole ν' level are retained in the approximate form \mathbf{g}_{BB} . Keeping two terms in the sum of equation (2.4) yields

$$\mathbf{G}_{BB}^{-1} = \begin{pmatrix} E - \epsilon_\nu - \Sigma_{\nu\nu} + i\Gamma_{\nu\nu} & -\Sigma_{\nu\nu'} + i\Gamma_{\nu\nu'} \\ -\Sigma_{\nu'\nu} + i\Gamma_{\nu'\nu} & E - \epsilon_{\nu'} - \Sigma_{\nu'\nu'} + i\Gamma_{\nu'\nu'} \end{pmatrix} \quad (3.1).$$

Since system A comprises one normal lead with N_+ (-) open particle(hole) channels and a superconducting lead with order parameter $\Delta_0 e^{i\phi}$, we find $\Gamma_{\nu\nu'} = \Gamma_{\nu'\nu} = 0$, $\Sigma_{\nu\nu'} = \sigma'_{\nu\nu}, \Sigma_{\nu'\nu} = \sigma'_{\nu'\nu}$ and $\sigma'_{\nu'\nu} = (\sigma_{\nu\nu})^*$ giving

$$\mathbf{G}_{BB} = \frac{1}{d} \begin{pmatrix} E - \epsilon_{\nu'} - \Sigma_{\nu'\nu'} + i\Gamma_{\nu'\nu'} & \sigma'_{\nu\nu'} \\ \sigma'_{\nu\nu'} & E - \epsilon_\nu - \Sigma_{\nu\nu} + i\Gamma_{\nu\nu} \end{pmatrix} \quad (3.2),$$

where

$$d = (E - \epsilon_\nu - \Sigma_{\nu\nu} + i\Gamma_{\nu\nu})(E - \epsilon_{\nu'} - \Sigma_{\nu'\nu'} + i\Gamma_{\nu'\nu'}) - \sigma'_{\nu\nu'} \sigma'_{\nu'\nu} \quad (3.3).$$

We are interested in the probability $T_{nn'}$ of a particle incident in channel n in lead 1 being Andreev reflected into an outgoing hole in channel n' in lead 1. In this case equation (2.3) becomes $T_{nn'} = 4\Gamma_{\nu\nu'}(n)(\mathbf{G}_{BB})_{\nu\nu'}|2\Gamma_{\nu'\nu'}(n')|^2$ and, since $(\mathbf{G}_{BB})_{\nu\nu'} = \sigma'_{\nu'\nu} = (\sigma'_{\nu\nu})^*$, this gives for the total conductance (2.5)

$$G(E) = 2R_a(E) = 2 \sum_n \sum_{n'}^N T_{nn'} = 8 \frac{\Gamma_{\nu\nu'} \Gamma_{\nu'\nu'} \sigma'_{\nu\nu'} \sigma'_{\nu'\nu}}{|d|^2} \quad (3.4)$$

where \mathcal{I} is defined in equation(3.3). In this expression, $\Gamma_{\nu\nu}$ and $\Gamma'_{\nu\nu}$ are proportional to the strength of coupling to the normal lead and $\sigma_{\nu\nu}'$ and $\sigma'_{\nu\nu}$ are proportional to the couplings to the superconducting lead. In the limit of zero applied voltage, where particle and hole levels are degenerate, we reproduced the formula obtained in [2]. However, for finite energy we can see that due to the breaking of the particle hole degeneracy at $E \neq 0$ the probability of finding a resonance is very small. Any resonances that do occur will be due to accidental overlapping of particle and hole levels.

To illustrate this we obtained numerical solutions for a tight binding form of the Bogoliubov – de Gennes equation for the structure in figure 1 using techniques outlined in [5]. The dot is M sites wide and M' sites long. The connection to the left lead is via hopping elements V_L to M_R sites of a superconducting region of length M'_S . For the other sites at the contacts the hopping elements are set to zero. The Fermi energy is given by $4\gamma - \epsilon_0$, where ϵ_0 is the diagonal element of the Hamiltonian in the leads and γ is the nearest neighbour hopping element in the leads. Within the dot, the diagonal element is uniformly distributed over the range $\epsilon \pm W$. Results for the N-NDOT-N system are obtained by setting $\Delta_0 = 0$ in the superconducting region and evaluating the conductance using the standard Landauer formula[6]. For the N-NDOT-S system, Δ_0 is set to a finite value. To ensure negligible transmission through the superconductor, Δ_0 and M'_S are chosen so that $M'_S \gg \xi$, where ξ is the superconducting coherence length. We then calculate the probability of a quasiparticle of energy E incident from the left Andreev reflecting from the system.

Figures 2 and 3 illustrate how the number of resonances changes as we go from zero to non zero energy. These show the results for normal transmission for $\Delta_0 = 0$ (upper curves) and Andreev reflection for finite Δ_0 (lower curves) as a function of ϵ . This quantity is varied to cover the whole band with $E = 0$ in figure 2, and $E = 0.027E_F$ in figure 3. The results presented in figures 2 and 3 are for a system with $M = 11$, $M' = 20$, $M'_S = 10$ and $M_L = M_R = 1$ with $V_L = V_R = 0.2\gamma$. For the superconducting system Δ_0 was set to a value of $0.54E_F$. This value was chosen so that for small systems many quasiparticle levels in the dot would exist below the energy gap of the superconducting lead. The dot was disordered with $W = 1.5$. It can be seen from figure 2 that for zero energy the probability of finding a resonance for the N-NDOT-S structure is approximately the same as finding one for the completely normal system although the relative heights and shapes of the resonance may be different. However, at finite energies, it is seen in figure 3 that we have virtually no difference in the probability of finding a resonance in the normal state transmission (the levels are only shifted) but for the N-NDOT-S system nearly all resonances are destroyed due to the breaking of particle-hole degeneracy.

4. Conclusions We have obtained a formula for resonant transport in a N-NDOT-S system which clearly predicts that at finite applied voltage, the probability of finding a resonance is small compared to that of a N-NDOT-N structure. To illustrate this we have carried out extensive numerical studies, the results of which are in agreement with the prediction.

Acknowledgements. This work is supported by the SERC, the EC HCM programme, the MOD and NATO.

References.

1. G. Breit and E. P. Wigner, Phys. Rev. **49** 519 (1936).
2. C.W.J. Beenakker, cond-mat preprint (to appear in Mesoscopic Quantum Physics, E. Alkermans, G.Montambaux and J.-L. Richard, eds (North Holland, Amsterdam.)
3. N.R. Claughton, M. Leadbeater, C.J. Lambert and V.N. Prigodin *to be published*.
4. G.E. Blonder, M. Tinkham and T.M. Klapwijk, Phys. Rev. B. **25** 4515 (1982).
5. C.J. Lambert, V.C. Hui and S.J. Robinson, J.Phys.: Condens. Matter, **5** 4187 (1993).
6. R. Landauer, Phil. Mag. **21** 863 (1970).

Figure Captions.

Figure 1. The tight binding, two-dimensional structure used for N-NDOT-S calculations. The shaded region denotes a superconducting region with on-site order parameter Δ_0 . The superconductor is then coupled to M_R sites on the dot by hopping elements V_R . The right lead is attached to the superconductor with hopping elements identical to those in the leads. The left lead is attached to M_L sites on the dot by hopping elements V_L . The dot is disordered, with disorder width $2W$.

Figure 2. Graphs of normal transmission (top) with $\Delta_0 = 0$ and Andreev reflection coefficient (bottom) with $\Delta_0 = 0.54E_F$ for quasiparticles of $E = 0$ as a function of the mean diagonal element ϵ for the dot.

Figure 3. Graphs of normal transmission (top) with $\Delta_0 = 0$ and Andreev reflection coefficient (bottom) with $\Delta_0 = 0.54E_F$ for quasiparticles of $E = 0.027E_F$ as a function of the mean diagonal element ϵ for the dot clearly showing the destruction of resonances.

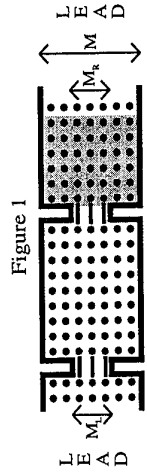


Figure 1

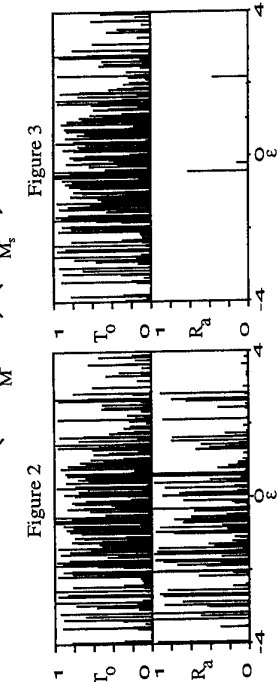


Figure 2

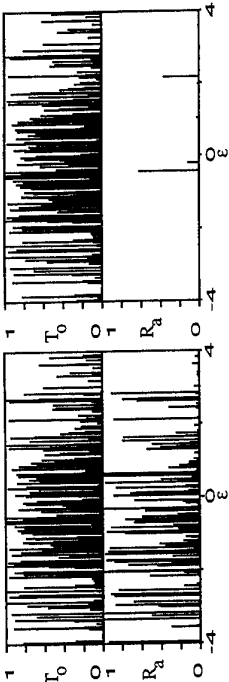


Figure 3

Superconductivity and the Josephson effect in a periodic array of Nb-InAs-Nb junctions

H. Drexler¹, J.G.E. Harris¹, E.L. Yuh¹, K.C Wong¹, S.J. Allen¹, E.G. Gwinn¹, H. Kroemer², E.I. Hu²

¹ Department of Physics and Center for Free-Electron Laser Studies

² Department of Electrical and Computer Engineering

University of California, Santa Barbara, CA 93106, USA

We have applied high-frequency radiation to a one-dimensional array of superconducting-normal-superconducting junctions, comprised of Nb-2D InAs-Nb, and observed Shapiro steps in the I-V curve which are dominated by a step at $V = h\nu/4e$, half the voltage of the usual AC Josephson effect. This result is discussed in view of a coupling between the Nb stripes that differs from the usual $\sin\Phi$ form. The zero-bias resistance of the sample is finite and increases exponentially with temperature. The Shapiro steps, however, persist up to the Nb transition temperature. These results imply that the finite resistance of the sample originates from excitations in the superconducting state.

In the past several years, a considerable amount of theoretical and experimental effort has been focused on understanding the various physical processes in superconductor-semiconductor (SSm) junctions [1,2]. Many experiments have shown that Andreev reflection at the superconductor-semiconductor interface determine the quasiparticle transport in these devices [3], particularly in samples with mesoscopic dimensions [4]. While the importance of Andreev reflections for the quasiparticle transport is well understood, the question whether Andreev reflections also contribute to the superconductivity often observed in SSmS junction is not yet answered. However, there are several theoretical models that predict such an influence [5,6].

In this study we employ the AC Josephson effect to study the superconducting state of a two-dimensional electron gas located between Nb electrodes. The sample is an array of SSmS junctions fabricated by placing a Nb grating onto InAs. We have found that a supercurrent in the InAs phase couples the superconductors up to the transition temperature of the Nb grating although it exhibits a finite zero-bias resistance. The AC Josephson effect is dominated by a Shapiro step at voltage $Nh\nu/4e$ and not by a step at $Nh\nu/2e$ as in the usual Josephson effect. Our experiments indicate that the coupling of the Nb stripes mediated by the two-dimensional electron gas differs from the usual $\sin\Phi$ form. This observation is consistent with a supercurrent due to multiple Andreev reflection of quasiparticles in the two-dimensional electron gas at the superconductor interfaces. The inset shows the crosssection of our sample. The period of the Nb grating is $a = 1\mu m$.

Fig. 1: Differential resistance of the sample as a function of applied voltage recorded at a temperature $T = 5.8K$ and zero magnetic field. The arrows highlight the structures which are due to multiple Andreev reflection of quasiparticles in the two-dimensional electron gas at the superconductor interfaces. However, this theory cannot explain all the observed features in a natural way.

The crosssection of the sample we use for the experiments is shown in the inset of Fig. 1. The heterostructure is a 150\AA thick InAs quantum well between n-doped AlSb barriers grown on a GaAs substrate crystal. The mobility of the as-grown quantum well is $\mu = 90,000 \text{ cm}^2/\text{Vs}$ and the charge densities of the two occupied subbands are $4 \cdot 10^{12}\text{cm}^{-2}$ and $3 \cdot 10^{12}\text{cm}^{-2}$. A holographic defined photoresist grating with a $1\mu m$ period is used as a mask to etch periodically the upper AlSb barrier and deposit Nb stripes directly onto the exposed InAs. Fermi level pinning in the InAs conduction band allows a Schottky barrier free interface. The spacing between the Nb stripes is $0.3\mu m$ and the width of the stripes is $0.7\mu m$. The sample geometry is defined by a $80\mu m$ wide Hall bar with about 300 Nb/InAs junctions between the voltage probes. So in the experiments a series connection of $N = 300$ junction is measured.

For the experiments the sample is placed in a temperature controlled flow-type cryostat with Zr -cut quartz windows. The sample temperature is read with a carbon-glass resistor that is in direct contact with the sample. Since the sample properties are very sensitive to even weak magnetic fields the component of the earth magnet field perpendicular to the sample is zeroed by a small buckling coil.

Fig. 1 shows the differential resistance of the sample as a function of voltage applied across the 300 junctions. The curve exhibits a rich sub-harmonic gap structure (highlighted by arrows) indicating multiple Andreev reflections between the SSm interfaces [7]. The strength of this structure indicates that the probability that a quasiparticle is Andreev reflected at the superconducting electrodes is significant in our sample. This proves the high quality of the SSm junctions.

In addition, a strong conductance enhancement near zero bias is found. The high frequency experiments discussed later demonstrate that the InAs is in a superconducting state for temperatures up to about $8K$, which is the transition temperature of the Nb stripes. Fig. 2 shows the zero-bias resistance of our sample as a function of temperature. The resistance is measured in the low-current limit, using a measuring current of $1\mu A$. Below the transition temperature of the Nb stripes the resistance of the sample decreases continuously with decreasing temperature. The inset shows the same curve on a logarithmic scale as a function of $1/T$. An exponential function $R \propto \exp(-\Delta E/kT)$ with $\Delta E = 3.5\text{meV}$ fits the data well over a large range of temperatures and resistances. This behavior suggests that the resistance is proportional to the number of thermally activated excitations with an energy of $\Delta E = 3.5\text{meV}$. A similar behavior is known from thin superconducting films [8]. In such films vortices and antivortices are present when the sample is superconducting. An applied current exerts a force on a vortex perpendicular to the current flow which leads to energy dissipation. Further experiments are needed to decide whether vortices are also the origin of the finite resistance in our sample and whether the activation energy of $\Delta E = 3.5\text{meV}$ is the pinning potential or the energy of these excitations.

In order to investigate the AC Josephson effect in the sample we measure the change of the I-V characteristic by illumination the sample with high frequency radiation in the range between 120GHz and 360GHz as a function of temperature, far-infrared power and magnetic field. In Fig. 3 curves recorded at different temperatures and with a frequency $v = 300\text{GHz}$ are shown. The features seen in the plot correspond to Shapiro steps in the irradiated I-V curves located at the indicated voltage positions. N -times the voltage of a single junction. The Shapiro step size can be estimated by dividing the height of the features with the differential resistance of the sample, at this voltage. So the height of the feature at $Nh\nu/4e$ of 2mV at a temperature $T = 2.2K$ corresponds to a Shapiro step size of about $2\text{mV}/60\Omega = 33\mu A$.

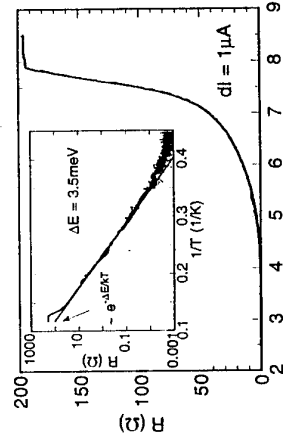


Fig. 1: Differential resistance of the sample as a function of

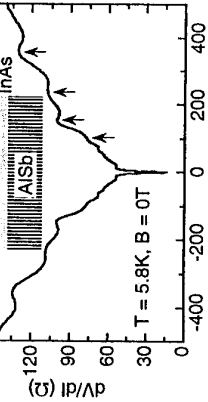


Fig. 2: Zero bias resistance of the sample versus temperature recorded with a measuring current of $dI = 1\mu A$.

The inset shows the same curve on a logarithmic scale as a function of $1/T$. The solid line is a fit to the data. The resistance is proportional to the number of thermally activated excitations with an energy of $\Delta E = 3.5\text{meV}$. A similar behavior is known from thin superconducting films [8]. In such films vortices and antivortices are present when the sample is superconducting. An applied current exerts a force on a vortex perpendicular to the current flow which leads to energy dissipation. Further experiments are needed to decide whether vortices are also the origin of the finite resistance in our sample and whether the activation energy of $\Delta E = 3.5\text{meV}$ is the pinning potential or the energy of these excitations.

In order to investigate the AC Josephson effect in the sample we measure the change of the I-V characteristic by illumination the sample with high frequency radiation in the range between 120GHz and 360GHz as a function of temperature, far-infrared power and magnetic field. In Fig. 3 curves recorded at different temperatures and with a frequency $v = 300\text{GHz}$ are shown. The features seen in the plot correspond to Shapiro steps in the irradiated I-V curves located at the indicated voltage positions. N -times the voltage of a single junction. The Shapiro step size can be estimated by dividing the height of the features with the differential resistance of the sample, at this voltage. So the height of the feature at $Nh\nu/4e$ of 2mV at a temperature $T = 2.2K$ corresponds to a Shapiro step size of about $2\text{mV}/60\Omega = 33\mu A$.

At the lowest temperature of $T = 2.2\text{K}$ two pronounced features at voltages $N \text{ hv}/4e$ and $N \text{ hv}/2e$ are observed. In addition, small features located at $N/m \text{ hv}/2e$ ($m = 3, 4, 5$) and a peak around zero bias are found. The peak near zero bias corresponds to biasing the sample at the knee of the I-V curve where the sample is most sensitive to far-infrared radiation. With increasing temperatures all peaks disappear, except the feature at $N \text{ hv}/4e$. This distinguishes this feature from all the other steps. In the following we will discuss this surprising result.

The sample resistance under the bias conditions where the Shapiro steps appear is about $20\Omega/\text{square}$ which is much lower than the impedance of free space ($377\Omega/\text{square}$). This means that the junctions are AC-current biased. The capacitance between two Nb stripes of about 10fF gives an impedance of 80Ω at a typical frequency of 200GHz , which is much higher than the resistance between two stripes of about 0.2Ω . So the junction can be considered as resistively shunted. In resistively shunted junctions where the coupling between the superconducting stripes can be described by $\text{Jsin}\Phi$ with $\Phi = 2eV/\hbar$, the integer Shapiro steps located at voltages $n\text{hv}/2e$ with $n = 1, 2, 3, \dots$, should be most pronounced and only very weak structures at voltage positions $n\text{m hv}/2e$ with $m = 2, 3, 4, \dots$ so-called subharmonic steps should appear [9]. This is in contrast to our experimental results.

Fig. 3: Change of the I-V characteristic of our device as a function of voltage when illuminated with $v = 300\text{GHz}$ radiation at different temperatures and zero magnetic field. The curves recorded at $T = 6.2\text{K}$ and $T = 6.8\text{K}$ are multiplied by a factor of 3 and 5, respectively. The vertical axis is increased only the feature at $N \text{ hv}/2e$ remains. The arrows indicate features at $V = N\text{m hv}/2e$ with $n = 3, 4$ and 5.

Very pronounced Shapiro steps at fractions n/m of $N \text{ hv}/2e$ where $n = 1, 2, 3, \dots$ and m fixed have been found in experiments on two-dimensional arrays of Josephson junctions [10]. Here the results are explained within a model of a flux superlattice that moves under illumination with high frequency radiation. The period of the superlattice is determined by the flux Φ_0/m per unit cell, where $\Phi_0 = h/e$. Fractions n/m show up in the $I-V$ when a flux Φ_0/m is applied. In Fig. 4 traces recorded at $v = 180\text{GHz}$ and a temperature $T = 7.2\text{K}$ are shown for different magnetic fields. It can be seen that the feature at $N \text{ hv}/4e$ disappears at magnetic fields of about $36\mu\text{T}$ and no other features appear. At lower temperatures, where more Shapiro steps are seen all features disappear with increasing magnetic field with relative heights that stay approximately constant. Therefore we do not believe that the observed resonances are associated with a flux superlattice in our sample.

With decreasing power the relative height of the $N \text{ hv}/4e$ compared to the $N \text{ hv}/2e$ feature increases. At the lowest power the $N \text{ hv}/2e$ has disappeared whereas the feature at $N \text{ hv}/4e$ is still clearly seen. All these experiments give strong evidence that the feature at $N \text{ hv}/4e$ is not a subharmonic but an integer step that corresponds to a coupling mechanism between the Nb stripes which has a 2Φ phase dependence, $\text{Jsin}2\Phi$ instead of $\text{Jsin}\Phi$, as in the usual Josephson effect [11, 12]. Indeed, such a coupling is predicted by Altshuler et al. [5] for superconductors which are coupled by a metal and interfaces with high Andreev reflection probability.

In this paper, Altshuler, Spivak and Khmel'nitskii [5] showed that interference of closed time-reversed path which include two Andreev reflections modulate the contribution of the electron-electron interaction in the normal metal to the free energy of the junction. This correction to the free energy gives rise to a supercurrent of the form $\text{Jsin}2\Phi$. However, the model of an Altshuler like supercurrent cannot explain all the observed features in a natural way in particular the odd- n subharmonics. Our data suggest that the coupling between the Nb stripes includes terms that depend on multiples of the phase difference between adjacent superconductors, namely $\text{sin}2\Phi$, $\text{sin}3\Phi$ etc.

Schussler and Kummel [6] predict that the supercurrent of Andreev coupled superconductors at low temperatures contains terms which depend on multiples of Φ , but the $\text{sin}\Phi$ component should still be the overwhelming dominant part of the coupling at $T > 0.5T_c$.

Acknowledgements: The authors would like to thank Nathan Argaman for many helpful discussions and the staff at the Center for Free-Electron Laser studies J.R. Allen, D. Enyeart, G. Ramian and D. White. Funding for the Center for Free-Electron Laser studies is provided by the Office of Naval Research. This research is also supported by the NSF Science and Technology Center for Quantized Electronic Structures, Grant No. DMR 91-20007.

References

- [1] H. Kroemer, C. Nguyen, E.L. Hu, E.I. Yuh, M. Thomas, K.C. Wong, Physica B **203**, 298 (1994).
- [2] T.M. Klapwijk, Physica B **197**, 481 (1994).
- [3] A.W. Kleinsasser, T.N. Jackson, D. McInturff, F. Rammo, G.D. Pettit, J.M. Woodall, Phys. Lett. **57**, 1811 (1990).
- [4] P.G.N de Vegaar, T.A. Fulton, W.H. Mallison, R.E. Miller, Phys. Rev. Lett. **73**, 1416 (1994).
- [5] B.L. Altshuler, D.E. Khmel'nitskii, B.Z. Spivak, Sov. State Comm. **48**, 841 (1983).
- [6] U. Schussler, R. Kümmel, Phys. Rev. B **47**, 2754 (1993).
- [7] M. Octavio, M. Tinkham, G.E. Blonder, T.M. Klapwijk, Phys. Rev. B **27**, 6739 (1983).
- [8] A.M. Kadin, K. Epstein, A.M. Goldman, Phys. Rev. B **27**, 6691 (1983).
- [9] C.A. Hamilton, E.G. Johnson, Jr., Physics Letters **41a**, 393 (1972).
- [10] S.P. Benz, M.S. Rzchowski, M. Tinkham, C.J. Lobb, Phys. Rev. Lett. **64**, 693 (1990).
- [11] W.M. van Huffelen, T.M. Klapwijk, D.R. Heisinga, M.J. deBoer, N. van der Post, Phys. Rev. B **47**, 5170 (1993).
- [12] M. Kuhlmann, U. Zimmetmann, D. Dikin, S. Abens, K. Keck, V.M. Dmitriev, Z. Phys. B **96**, 13 (1994).

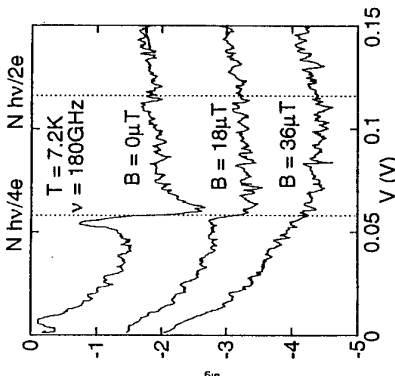


Fig. 4: Magnetic-field dependence of the high-frequency ($v = 180\text{GHz}$) irradiated current-voltage characteristic recorded at a temperature of $T = 7.2\text{K}$. The magnetic field component perpendicular to the two-dimensional electron gas is $B = 0\mu\text{T}$, $18\mu\text{T}$ and $36\mu\text{T}$ for the different curves. The vertical scale refers to the upper trace.

SIZE-SCALING EXPERIMENT IN A TWO DIMENSIONAL ELECTRON GAS USING INHOMOGENEOUS MAGNETIC FIELD DUE TO A SUPERCONDUCTING GATE

A.K.Geim¹, S.V.Dubonos², I.V.Grigorieva¹ and S.J.Bending³

¹⁾ High Field Magnet Laboratory, University of Nijmegen, 6500 GL Nijmegen, The Netherlands

²⁾ Institute of Microelectronics Technology, 142432 Chernogolovka, Russia

³⁾ School of Physics, University of Bath, Bath BA2 7AY, England

We have used a superconducting gate on the top of a two-dimensional electron gas (2DEG) to partition an external magnetic field into a distribution of submicron flux tubes (vortices) and measure the weak localisation contribution to the 2DEG conductance versus spatial separation of the vortices. It is found that the effect of a vortex extends far beyond its actual size. The experiment is discussed in terms of size scaling of the quantum conductance. The measured minimum size of an independent region of a 2DEG is in agreement with the phase-breaking length of electrons deduced from the weak localisation magnetoresistance.

There has been a growing interest in a hybrid superconductor-two-dimensional-electron-gas (2DEG) system in which an extremely inhomogeneous magnetic field created by a type-II superconducting gate is projected down onto a 2DEG below. An applied magnetic field is segregated within and near the superconductor into a distribution of magnetic-flux tubes (vortices) with the characteristic diameter d of just $\sim 0.2\mu\text{m}$ (see Figure 1). A number of novel phenomena have been reported for this system including nonlocal weak localisation [1], conductance fluctuations due to a single vortex in a mesoscopic conductor [2] and diffraction of 2D electron waves at vortices [3]. A point of fundamental interest here is the fact that characteristic relaxation lengths in a 2DEG can be much longer than the size of vortices, in which case the transport is essentially nonlocal.

In this work, the superconducting vortices have been employed to study the size scaling in zero-field resistivity of a 2DEG. For a vortex concentration $N = L^{-2}$, each $L \times L$ square of the 2DEG is "ear-marked" by a vortex ($d \ll L$) which changes slightly the resistance of this square.

As the vortex concentration increases, the 2DEG becomes effectively divided into smaller and smaller squares. Up to a certain concentration of vortices, the total resistance of the 2DEG is found to be proportional to the number of vortices. However, as the concentration is increased further, the linear dependence breaks down indicating that we have reached the minimum size L_{\min} ($> d$) below which the simple scaling is violated. In other words, it's impossible to put a vortex inside the 2DEG (or do anything else with

the 2DEG) without changing the properties of the entire region $L_{\min} \times L_{\min}$. We have measured the size of the minimum square for a number of 2DEG's and compared L_{\min} with the phase-breaking length of electrons L_0 extracted from fitting the curves for weak localisation magnetoresistance in uniform field. It is found that $L_{\min} \approx 2L_0$. We note that our experiment appears to be a very close implementation of the well-known gedanken experiment where a conducting plane is divided into squares of sequentially decreasing sizes. Instead of cutting a macroscopic sample into pieces as the size scaling experiment infers, we have effectively divided the 2DEG by tagging its parts with vortices. Thus, we have been able to give a concrete physical significance to L_0 in terms of our vortex mesh size in stark contrast to all previous work where L_0 only enters as a fitting parameter in theoretical models.

Our experimental system is shown schematically in Figure 1. A lead superconducting film ($\sim 0.1\mu\text{m}$ in thickness) has been deposited on the top of GaAlAs/GaAs heterostructures with a 2DEG at distances 60-80nm from the surface. Lead films of these thicknesses are type-II superconductors and have a very small value of the magnetic-field penetration depth $\lambda \sim 60\text{nm}$ at 1.3K. Taking into account spatial broadening of vortices when they emerge from the superconductor, we estimate $d \sim 0.2\mu\text{m}$ [1-3]. The vortex concentration in the 2DEG is controlled by the external magnetic field B as $N = B/\phi_0$ where $\phi_0 = h/2e$ is the superconducting flux quantum. Vortices in the 2DEG remain well separated in applied magnetic fields up to 100G. At larger fields the distance between individual vortices, $L(\mu\text{m}) = (\phi_0/B)^{1/2} \sim 5[B(\text{G})]^{-1/2}$, decreases to a value comparable with the vortex diameter and magnetic fields due to adjacent vortices overlap strongly. Consequently, the field inhomogeneity rapidly smears out, even though the lead gate remains superconducting up to $\sim 1\text{K}$. In this paper we discuss results for three heterostructures with electron concentrations of about $5 \times 10^{15}\text{ m}^{-2}$ and mobilities $3, 3.7$ and $5.9 \text{ m}^2 \text{ V}^{-1} \text{ s}^{-1}$ and the electron $V^{-1} \text{ s}^{-1}$. The relatively low mobility of the 2DEG has been chosen intentionally to avoid ballistic effects discussed in ref. [3]. These effects give rise to an extra vortex magnetoresistance in low fields.

Figure 2. Magnetoconductivity of the 2DEG in uniform magnetic field (solid curves) and in the distribution of vortices (crosses) at temperatures of (a) 4.2K and (b) 1.3K.

The electron mobility is $3 \text{ m}^2 \text{ V}^{-1} \text{ s}^{-1}$ and the electron concentration is $5.3 \times 10^{15} \text{ m}^{-2}$. The short-dash curves are the best fit to the Kawabata theory of weak localisation in the homogeneous field. The long-dash lines indicate the linear resistivity due to scattering of electrons at the vortices but this contribution is negligibly small for all data presented below. For further experimental details we refer to [1-3].

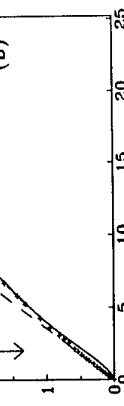


Figure 1. The 2DEG-superconductor hybrid system.

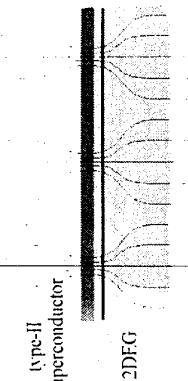


Figure 2. Magnetoconductivity of the 2DEG in uniform magnetic field (solid curves) and in the distribution of vortices (crosses) at temperatures of (a) 4.2K and (b) 1.3K. The electron mobility is $3 \text{ m}^2 \text{ V}^{-1} \text{ s}^{-1}$ and the electron concentration is $5.3 \times 10^{15} \text{ m}^{-2}$. The short-dash curves are the best fit to the Kawabata theory of weak localisation in the homogeneous field. The long-dash lines indicate the linear resistivity due to scattering of electrons at the vortices but this contribution is negligibly small for all data presented below. For further experimental details we refer to [1-3].

Figure 2(a,b) shows the magnetoresistance of one of the samples in magnetic fields below 25G at temperatures 1.3 and 4.2K. For brevity, the experimental data are presented directly in terms of 2DEG conductivity $\Delta\sigma$ and in units of the conductance quantum e^2/h . In the uniform magnetic field (solid curve) the sample exhibits a conventional negative magnetoresistance due to suppression of the time-reversal contribution to electron interference [4-6]. This magnetoresistance is well described by the Kawabata theory of weak localisation (dashed curve) which is applicable for our samples with a relatively long ballistic mean free path $l=0.5\mu\text{m}$ comparable with L_ϕ [4]. The fit allows us to find L_ϕ . We note that the Hikami-Larkin-Nagaoka theory [5], valid for $k \ll L_\phi$, gives us a slightly worse fit and yields somewhat smaller values of L_ϕ (typically 20% smaller). The symbols in Fig.2 correspond to the case of the non-uniform field created by the superconductor. The initial linear increase in conductivity of the 2DEG is due to the linear increase in vortex concentration when B increases. Note that the same field B influences the 2DEG much more strongly when the magnetic flux is segregated into a distribution of submicron tubes. This enhancement of the magnitude of the weak localisation magnetoresistance has been reported earlier [1] and discussed in detail in refs. [6].

Below, we will concentrate on another striking feature in the additional resistivity due to the presence of vortices in the 2DEG. For the plotted interval of vortex concentrations in Fig.2, magnetic fields due to adjacent vortices do not overlap. Nevertheless, the curves for the uniform magnetic field and the inhomogeneous field of vortices converge when the vortices are as far as several microns apart. At lower temperatures the difference between the two cases disappears at even lower fields, i.e. for larger vortex separations (see Fig.2). The observed behaviour indicates that a vortex suppresses the weak localisation in the 2DEG at distances far beyond the region where its magnetic field is present. When the extended regions of the 2DEG affected by adjacent vortices overlap, the dependence $\Delta\sigma \propto N$ breaks down. We define N_{\min} as the vortex concentration when deviations from the linear dependence exceed a level of the scatter in the experimental data. In Fig.2 such concentrations are shown by arrow marks. The value of N_{\min} yields the size of an independent unit of the 2DEG as $L_{\min} = N_{\min}^{-1/2}$. Figure 3 plots L_{\min} versus L_ϕ using data for all three 2DEG's at temperatures 1.3 and 4.2K. We have also included here the results from ref. [1] for nonlocal weak localisation in thin Bi films. The dotted line in Fig.3 shows the best linear fit to the experimental data which yields $L_{\min} \approx 2L_\phi + d$. This dependence shows that the influence of vortices extends over the distance $\sim L_\phi$ outside the region of the magnetic field, in agreement with the nature of the effect.

We note that the observed spatial enhancement of the effect of vortices is not due to the vector potential which of course extends outside the region of the magnetic field. Weak localisation is due to the constructive interference on time-reversal trajectories and the superconducting flux quantum $h/2e$ cannot destroy it since the acquired phase shift is equal to

2π [4-6]. Therefore, only those trajectories which pass through the region of the magnetic field and, hence, envelope a part of the superconducting flux quantum are influenced by vortices. The origin of the observed spatial enhancement lies in the statistics of diffusion in two dimensions where a diffusive electron trajectory circles any point in space an infinite number of times. Although in reality this divergence is suppressed due to the finite phase coherence length, the statistics dictates that every trajectory within a phase-coherent sample can pass through a vortex located inside [6]. The influence of vortices becomes non-additive (adjacent vortices begin to "feel" the presence of each other) when the phase-coherent trajectories pass through more than one vortex.

Finally, we note that several features in the observed behaviour remain to be explained. First, it is not clear whether the coefficient 2 in the empirical expression for L_{\min} is meaningful or relates to our definition of N_{\min} . We speculate that electrons with the highest probability of interacting with two vortices will have their origins midway between them. Thus the scaling behaviour would be expected to start to break down when such an electron has its origin at the distance L_ϕ from two adjacent vortices, or when the centre-to-centre vortex spacing is $2L_\phi + d$. The second surprising feature is a very small interval between N_{\min} and the vortex concentration where the curves for the uniform and non-uniform fields converge completely (see Figure 2). It is also worth mentioning that we have not seen the spatial extension of the effect of vortices for the case of ballistic scattering of 2D electrons at vortices [3]. In that experiment, the vortex resistivity disappeared only when the field inhomogeneity smeared out.

In conclusion, we have realised the size-scaling gedanken experiment for the case of weak localisation. Placing a number of vortices inside a macroscopic 2DEG we effectively divide it into a number of smaller samples, each ear-marked by a single vortex. As the vortex separation is decreased, a distinctive change in the effect of vortices on the 2DEG is observed indicating the size of the minimum independent region in the 2DEG. This size is found to be of the order of the phase-breaking length of electrons L_ϕ deduced from the weak localisation magnetoresistance. Although the importance of this scale has followed from the theory and experiments on weak localisation and mesoscopics, the gedanken experiment has never been realised, primarily because of the problem of electrical contacts to small, quantum devices.

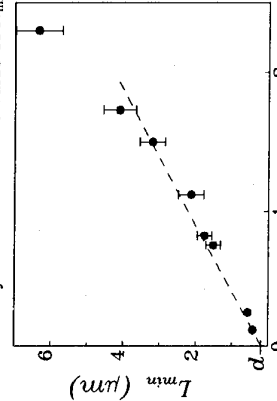


Figure 3. Dependence of the size of a 2DEG region affected by a vortex (L_{\min}) on the phase-breaking length of electrons (L_ϕ) deduced from the weak localisation magnetoresistance in the uniform field.

- [1]. A.K. Geim, JETP Lett. 50 (1989) 389; S.J.Bending, K.v.Klitzing, and K.Ploog, Phys.Rev.Lett. 65 (1990) 1060.
- [2]. A.K. Geim, V.I.Falko, S.V.Dubonos and I.V.Grigorieva, Solid State Commun. 82 (1992) 831.
- [3]. A.K. Geim, S.J.Bending and I.V.Grigorieva, Phys.Rev. Lett. 69 (1992) 2252; A.K. Geim, S.J.Bending, I.V.Grigorieva and M.G.Biamore, Phys. Rev. B 49 (1994) 5749.
- [4]. A.Kawabata, J. Phys.Soc.Jpn. 53 (1984) 3540.
- [5]. S.Hikami, A.I.Larkin and Y.Nagaoka, Prog.Theor.Phys. 63 (1980) 707.
- [6]. J.Rammer and A.L.Shelankov, Phys.Rev. B 36 (1987) 3135; S.J.Bending and A.K.Geim, Phys.Rev.B 46 (1992) 14912.

HIGH-FREQUENCY TRANSPORT THROUGH MESOSCOPIC STRUCTURES

L.P. Kouwenhoven, N.C. van der Vaart, and Yu.V. Nazarov
*Department of Applied Physics, Delft University of Technology,
P.O.Box 5046, 2600 GA Delft, The Netherlands.*
S. Jauhar, D. Dixon, K. McCormick, J. Orenstein, and P.L. McEuen,
University of California Lawrence Berkeley Laboratory, Berkeley, CA 94720, U.S.A.
Y. Nagamune, J. Motohisa, and H. Sakaki,
*Research Center for Advanced Science and Technology, University of Tokyo, 4-6-1 Komaba,
Meguro-ku, Tokyo 153, Japan*

Abstract We have measured dc transport through a GaAs/AlGaAs quantum dot in the presence of a microwave signal of frequency f . We find features related to the photon energy $\hbar f$ whose positions in gate voltage are independent of the microwave power but vary linearly with frequency. The measurements demonstrate photon-assisted tunneling in the mesoscopic regime.

Introduction

We have studied single electron tunneling in the time/frequency-dependent regime where the photon energy $\hbar f$ of a microwave signal exceeds the thermal energy $k_B T$. The main idea is that electron tunneling can be accompanied with absorption or emission of quanta (i.e. photons) from the external high-frequency signal [1]. The measurements on our dots, which are defined with metallic gates in the 2DEG of a GaAs/AlGaAs heterostructure, are performed at an effective electron temperature of about 100 mK [2,3]. We find that electrons can overcome the Coulomb gap in the quantum dot when discrete photons of energy $\hbar f$ are absorbed from the applied microwaves. These measurements agree well with our model calculations based on Coulomb blockade theory with the inclusion of Tien and Gordon's theory [1] for time-dependent tunneling.

Time Scales and Regimes of Operation

Transport processes through quantum dots encompass a variety of time scales. A listing of these energy/frequency scales is given in Table 1. The single-particle level spacing ΔE is 0.02 - 0.2 meV for typical dots and the charging energy e^2/C is usually 0.2 - 2 meV. The effects of thermal broadening of the electron energies ($\sim 4k_B T$) determine the observability of these two energy scales.

Other characteristic times of the dot are transport times. Γ is the typical time required to tunnel on or off the dot. This time is set by the transmission coefficient $|t|^2$ of the barriers and by the larger of ΔE or the source-drain voltage V_{sd} . It can be arbitrarily small for opaque tunnel barriers. The final time scale is the tunneling time; i.e. the actual time spent during tunneling through the barrier. This time is quite fast (~ 2 ps) for typical barriers (calculated, e.g., within the Büttiker-Landauer framework [4]).

Quantity	Equivalent frequency	Typical parameters
Thermal broadening	$\sim 4k_B T/\hbar$	10 GHz (at $T = 125$ mK)
Tunneling rate on/off the dot	$\Gamma \sim (\Delta E \text{ or } eV)/\hbar t ^2$	0 - 10 GHz
Level spacing (transit time)	$\Delta E / \hbar$	4 GHz - 40 GHz
Charging energy	$(e^2/C) / \hbar$	40 GHz - 400 GHz
Tunneling time	$1/\tau_{\text{tunnel}}$	200 GHz - 1 THz

Table 1. A list of the important energy/frequency scales for transport through quantum dots.

To access these time scales, AC signals can be applied to the dot, and the effects on the DC transport can be measured. In the experiments reported to date [2,3,5] the frequencies of the applied signals have varied from the RF ($f \sim 1$ MHz) to the microwave ($f \sim 40$ GHz). In these experiments, the level spacing of the dots was not an important parameter (i.e. $\Delta E \ll 4k_B T$), and it will be neglected here.

Another transport division is shown in Table 2. If $f \ll \Gamma$ the electrons see an essentially static potential and we are in the *adiabatic regime*. If $f \gg \Gamma$ the electron experiences many cycles of the AC signal while it is on the dot; i.e. the *non-adiabatic regime*. The second issue is whether the photon energy $\hbar f$ is greater or less than the thermal smearing of $4k_B T$. If $\hbar f < 4k_B T$, single photon processes are masked by thermal fluctuations, and a classical description is appropriate. If $\hbar f > 4k_B T$, single-photon processes should be observable. We refer to this as the quantum or time-dependent regime. To describe this quantum regime one needs to solve the time-dependent Schrödinger equation for the tunneling electron.

Classical ($\hbar f \ll k_B T$)	Adiabatic ($f \ll \Gamma$) (1) Classical Adiabatic wiggle (2) Turn stile	Non-Adiabatic ($f \gg \Gamma$) (3) Photon-Assisted Tunneling
Quantum or Time-dependent ($\hbar f \gg k_B T$)		

Table 2. Overview of different AC transport regimes.

Classical, Time-Independent Regime.

In the classical adiabatic regime the device behavior can be understood entirely in the context of the DC characteristics. Fig. 1 shows Coulomb blockade oscillations where, in addition to the DC voltages, an AC gate voltage of $f = 10$ MHz was applied to one of the gates [3]. The different curves correspond to different amplitudes of the AC signal. To understand these results we note that the AC voltage simply modulates the electrostatic potential of the dot sinusoidally. The result is a Coulomb peak that is, in effect wiggled back and forth by an amount proportional

to the amplitude of the AC signal. The expected current, obtained by convolving the DC $I-V_g$ characteristic with a sinusoidal AC signal is in good agreement with the data. Note that the amplitude of the current at any given V_g is proportional to the time that the oscillating gate voltage spends at that value of V_g . Since a sine wave spends most of its time near its extrema, the result is a broadened current peak that is maximal at its edges.

If the barrier height, and hence the tunneling rate Γ , is made to oscillate by the AC signal, the device can cross over from the adiabatic to the non-adiabatic regime *within* a given cycle of the AC potential. This is the basis for the quantum dot turnstile [5], a device that moves one electron through the dot per AC cycle and thus produces a current of $I = ef$. Note that turnstile and pump devices do produce frequency dependent currents [5,6]. However, the photon energy $\hbar f$ at MHz frequencies is much too small to be energetically of importance. Therefore, these devices operate in the classical, time-independent regime.

Photon-Assisted Tunneling

At higher frequencies, the photon energy becomes important and we move into the quantum regime. In this regime the effect of the AC potential on electron tunneling can be described in terms of the absorption and emission of photons [1]. For example, an electron may be able to tunnel onto the dot by the absorption of a photon, as is shown in Fig. 2. These photon-assisted tunneling (PAT) processes strongly affect the DC currents in a quantum dot. Fig. 3(a) shows the effect of microwave photons on the Coulomb oscillations. The current without microwaves, (dotted) is displayed along with the current in the presence of microwaves at various powers. Results for three different frequencies are shown. The most notable feature is the presence of a shoulder on the left-hand side of the Coulomb-blockade peak. Fig. 3(b) shows the derivative, dI/dV_g , of the data in 3(a). The shoulder in 3(a) results in a peak in dI/dV_g in 3(b), as indicated by the arrows. In contrast to the classical data of Fig. 1, we see that the position of this peak is independent of the microwave power, but shifts with photon frequency. This shoulder/peak is due to PAT onto the dot, as is schematically illustrated in Fig. 2. An electron absorbs a photon when tunneling onto the dot, producing extra current up to $\hbar f$ away from the Coulomb-blockade peak. The fact that the position of this shoulder is independent of the microwave amplitude, but linear in the frequency, is a direct proof of the single-photon origin.

In conclusion, we have reported experiments on mesoscopic structures in the time-dependent regime. The observed microwave induced features in the current can be described quantitatively with a model based on the orthodox Coulomb blockade theory with the inclusion of the Tien-Gordon model (see for details and more references Ref. 2).

This work was supported by the Office of Naval Research, the Packard Foundation and the Royal Netherlands Academy of Arts and Sciences (L.P.K.).

References

- [1] P.K. Tien, and J.R. Gordon, Phys. Rev. **129**, 647 (1963).
- [2] L.P. Kouwenhoven et al., Phys. Rev. B **50**, 2019 (1994); Phys. Rev. Lett. **73**, 3443 (1994).
- [3] S. Janhár, et al., unpublished.
- [4] See, e.g. R. Landauer and Th. Martin, Rev. Mod. Phys. **66**, 217 (1994).
- [5] L.P. Kouwenhoven et al., Phys. Rev. Lett. **67**, 1626 (1991).
- [6] L.J. Geerligs et al., Phys. Rev. Lett. **64**, 2691 (1990).

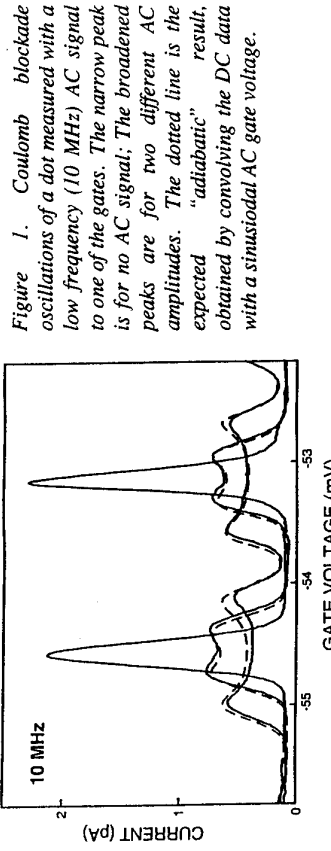


Figure 1. Coulomb blockade oscillations of a dot measured with a low frequency (10 MHz) AC signal to one of the gates. The narrow peak is for no AC signal; The broadened peaks are for two different AC amplitudes. The dotted line is the expected "adiabatic" result, obtained by convolving the DC data with a sinusoidal AC gate voltage.

Figure 2. Energy level diagram for a quantum dot illustrating photon-assisted tunneling (PAT). Solid lines are occupied levels, while dotted lines are unoccupied. Shown is the configuration just before a peak in G versus V_g . In the presence of microwaves an electron can overcome the Coulomb gap and tunnel onto the dot via the absorption of a photon. This leads to a shoulder in the Coulomb peak.

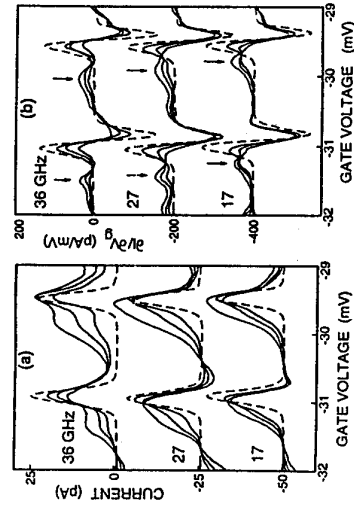


Figure 3. Current versus gate voltage V_g for a quantum dot irradiated by microwaves at three different frequencies. The dashed curves are without microwaves and the solid lines are for increasing power. A photon-induced shoulder is observed whose position is independent of power but linearly dependent upon frequency. (b) Derivatives dI/dV_g of the data in (a). The arrows indicate the photon induced features.

Photon-assisted tunneling through a Double Quantum Dot

R.H. Blick, R.J. Haug, K.v. Klitzing, and K. Eberl
Max-Planck-Institut für Festkörperforschung, Heisenbergstr. 1, 70569 Stuttgart, Germany

Transport measurements on a double quantum dot are performed under the influence of microwave radiation. It is shown that the radiation effectively couples to the micro-structure, inducing a photo-current with a clear frequency dependence. This process of photon-assisted tunneling through the double dot can be employed for microwave spectroscopy on this artificial molecule.

Recent experiments on quantum dots have established microwave spectroscopy of these artificial atoms as a new experimental method [1, 2] in addition to common transport spectroscopy. The physical mechanism involved is photon-assisted tunneling (PAT), which up to now is theoretically investigated only for single quantum dots [3]. Here we present transport measurements on a double quantum dot system coupled in series under the influence of high frequency microwave radiation. The radiation is coupled optically into the micro-structure, allowing a broad range of frequencies to be applied. The effect of the radiation on transport is detected in the induced photo-current through the system.

The double dot systems (DDS) consists of dots of different size, which are coupled by a tunneling barrier (see inset in Fig. 1a). The energies characterizing electronic transport through the DDS are the charging energies E_C of the individual dots. The energy necessary for tunneling through the DDS can be supplied either by the difference in the electro-chemical potentials of the reservoirs or by the application of microwave radiation.

For the definition of the quantum dots we employed metallic split-gates, as shown schematically in the left inset of Fig. 1a. The split-gates were fabricated by a micro-structure written with electron-beam lithography and depositing a 100 nm Au-layer on top of the 2DEG. The 2DEG in the AlGaAs/GaAs-heterostructure has a density of $2.2 \times 10^{11} \text{ m}^{-2}$ and a mobility of $81 \text{ m}^2/\text{Vs}$. The two quantum dots investigated are of different size, which is realized by an asymmetry of the gate structure and by biasing the split-gates differently (see inset in Fig. 1a). By varying the gate voltage (V_g) the number of electrons in the DDS is changed. Transport through the quantum dots is measured in a two-terminal setup with an ac-excitation voltage of $V_{ds}^{ac} = 5 \mu\text{V}$ at a frequency of 13 Hz (source and drain reservoirs are marked by S and D). As depicted in the right inset of Fig. 1a, transport through the coupled quantum dots is possible only if the energy levels in both quantum dots are in resonance with the electro-chemical potential $\mu_{1/2}$ of the reservoirs. By varying the gate voltage V_g this resonance condition is obtained for adjacent numbers of electrons in the DDS, leading to the Coulomb blockade (CB) oscillations in Fig. 1a. The different charging energies of the individual dots can be identified by the two periods of conductance resonances. We determine the charging energy for the small quantum dot A to be $E_C^A \approx 3 \text{ meV}$ and for the large quantum dot B to be $E_C^B \approx 1.2 \text{ meV}$. Due to the electrostatic coupling between the quantum dots these charging energies vary slightly, as is seen in the variation of the periodicities of the oscillations [4].

A finite drain-source voltage, $-eV_{ds} = \mu_l - \mu_r$, applied to the DDS opens an energetic window for tunneling electrons. Measuring the differential conductance in dependence on the gate voltage V_g and the drain-source voltage V_{ds} , a complex topology of resonances is found. For a single dot a simple trapezoidal pattern is observed [5], representing its charging energy. The complex topology can be understood as a superposition of two different trapezoidal patterns, corresponding to the charging energies of dot A and dot B (see Fig. 1b). This representation allows transport spectroscopy of the DDS, although the excited states are not resolved on the scale presented.

An alternative method for studying the excitations of quantum systems is microwave

spectroscopy. In the following, we investigate the microwave induced photo-current through the DDS. For our experiments we designed the gate structure to form an antenna which effectively enhances the coupling of the microwave radiation to the quantum dots (see Fig. 2) [2]. The frequencies we can apply to the micro-structure range from 30 to 400 GHz, corresponding to an energy range of 0.13 meV to 1.65 meV, comparable to the charging energies of our dots.

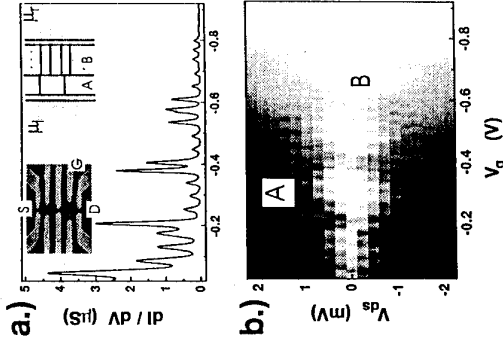


Figure 1: Plots of the differential conductance through the double dot system: a) The common Coulomb blockade oscillations at $V_{gs} = 0$. The left inset shows an SEM micrograph of the quantum dots used. The right inset shows schematically the energy levels of the system. 'A' refers to the small quantum dot and 'B' refers to the large one. b) A gray-scale plot of the conductance at finite drain-source voltage. A two-fold trapezoidal pattern is found; the corresponding charging regime are marked.

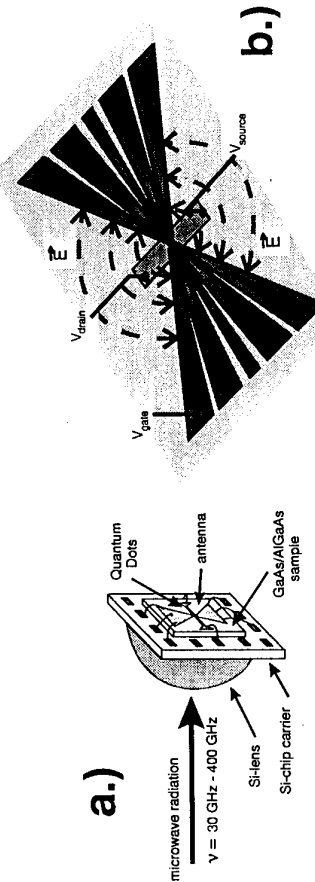


Figure 2: a.) Experimental configuration of the quantum dot structure with an on-chip antenna to effectively couple radiation to the dot. Radiation is sent through a focussing lens on the back-side of the chip-carrier.

b.) Image of the 'bow-tie' antenna, additionally serving as gate-contacts. Dashed lines represent the high-frequency electric field (\vec{E}) with transversal and longitudinal components.

The measurements are performed in a $^3\text{He}/^4\text{He}$ dilution refrigerator equipped with a special sample holder allowing direct irradiation of the sample. Best performance is achieved by placing the Si-chip carrier in front of a Si-lens, which focuses the radiation and serves as an impedance matching (see Fig. 2a). The antenna depicted in Fig. 2b is a modified 'bow-tie' antenna, which couples radiation most effectively to the micro-structure. The sample is mounted at the end of the wave-guide in the mixing chamber in direct contact with the superfluid ^4He , which ensures effective cooling of the sample. The heating of the 2DEG and of the electrons in the dots can be directly determined by analyzing the line shape of the CB oscillations. The ratio $\gamma = \hbar\nu/k_B T$ is an estimation of how far from thermal equilibrium the electrons are excited. Applying the experimental parameters, $\nu = 150$ GHz and $T = 200$ mK, we obtain a value of $\gamma = 36$, indicating a strong non-equilibrium situation.

In the measurements under irradiation only the dc-current is measured, which requires a preferential direction of the current. This is usually achieved by either biasing the quantum dots or by defining an asymmetric system, i.e. barriers of different thickness. Here we used a small bias voltage of $V_{ds} = 20$ μV and quantum dots of different size, which introduces the necessary asymmetry. The dc-current flowing through the DDS in the absence of radiation, is shown by the dotted curve in Fig. 3a. The solid lines in this figure show the current at two different microwave power levels applied to the sample. Obviously, additional resonances are induced, their positions marked by arrows. Clearly, the amplitude of the photo-current is enhanced when the microwave power is increased, but the resonance positions do not shift. In comparison to measurements performed on a single quantum dot [2], the resolution of the measurements presented in the present setup is strongly enhanced.

By applying radiation at *different* frequencies we find a shift of the position of the induced resonances. Fig. 3b, shows the shift of the resonances dependent on the applied frequencies. Obviously the shift is proportional to the frequency. This is in accordance with the ordinary picture of P.A.T. In the level diagram on the right hand side of Fig. 3 the two general possible mechanisms of photon-induced transport are indicated by '1' and '2'. In the first case, '1', the photon with the energy $\hbar\nu$ is absorbed in the quantum dot by an electron which then tunnels out of the system. An additional electron from the right lead is able to tunnel into the dot in order to fill the vacancy. The second possible case, '2', allows the absorption of a photon with the energy $\hbar\nu$ in the (right) lead. The electron thus overcomes the CB and tunnels through the dot. The state used for tunneling may either be a ground or an excited state. Hence, we may specify process '1' being the inner photo-effect and process '2', being the outer photo-effect. The outer photo-effect corresponds to the photo-effect described by Einstein for a metal [6]. Referring to the linear dependence of the energy absorbed it is more likely to assume an excitation in the leads. The offset at $\nu \rightarrow 0$ is not yet understood, but might be an artifact due to the limited resolution. The energetic window in which P.A.T. resonances can be observed is restricted by a charging energy E_C^* , as is indicated in Fig. 3a.

For further measurements we applied a finite magnetic field of $B = 2.4$ T perpendicular to the plane of the 2DEG, which leads to the formation of well separated Landau levels in the reservoirs with an energy separation of $\hbar\nu_c$. Therefore, the energy distribution of the electrons contributing to the current through the DDS is very sharp in comparison to a broad band of excited electrons without a magnetic field applied. (At $B = 0$ electrons from below the Fermi energy might also be excited.) Since the photon energy we applied is smaller than the cyclotron frequency $\nu < \nu_c$ and due to the strongly reduced density of states in the reservoirs at the energies, electrons excited by the radiation tunnel with a higher probability into the DDS. Furthermore, it is important to note that the relaxation of electrons has to occur on a longer time-scale than the time given by the excitation frequency [7].

Regarding the sensitivity of the DDS, it is obvious that such a quantum device is pre-

dicted for millimeter and sub millimeter wave radiation detection. The easiest approach is bolometric detection, since the conductance resonances are strongly temperature dependent. As we have seen in Fig. 3b, the induced resonances obey the linear relation $\Delta E = \hbar\nu$, thus the measurements show the possibility of frequency dependent detection.

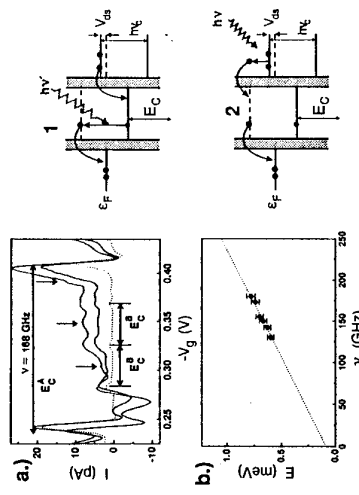


Figure 3: a) The induced photocurrent at a microwave frequency of $\nu = 168$ GHz at different power levels and a small bias voltage $V_{ds} = 20$ μV . The lowest line (dashed) is taken without irradiation. b): Dependence of the energy on the frequency. The dashed line is a linear regression for the data points. The level diagrams on the right hand side show the two principal mechanisms of photon absorption.

Furthermore, it is interesting to note that such a millimeter wave detector can be used as a mixing element. The combination with the process of single-electron tunneling then opens the possibility to study the process of mixing depending on the tunneling of a single particle [8]. Finally it should be noted that the experiment setup described can in principle be regarded as a new method for the determination of the quantity e^2/h and thus of the fine-structure constant α , as it was performed earlier on superconductor junctions [9]. This obviously shows the connection of single-electron tunneling and P.A.T. to quantum electrodynamics (QED).

In summary we have defined a double quantum dot system, which is electrostatically coupled. We have shown that high-frequency radiation is effectively coupled into the microstructured devices. Photon-assisted transport through the double quantum dot in the high-frequency regime is demonstrated. This proves the possibility of microwave spectroscopy on quantum dot systems. Furthermore, the measurements present the principle of operation of a quantum dot as a highly sensitive millimeter wave detector.

We like to thank D. Pfannkuche, D.W. van der Weide and J. Weis for numerous discussions. We like to thank V. Gudmundsson and Y. Kershaw for a critical reading of the manuscript. We would also like to acknowledge the technical help of M. Riek and F. Schartner. This work was funded in part by the Bundesministerium für Bildung, Wissenschaft, Forschung und Technologie (BMBF).

References

- [1] L. Kouwenhoven *et al.*, Phys. Rev. Lett. **73**, 3443 (1994).
- [2] R. Blick *et al.*, Appl. Phys. Lett. submitted (1995).
- [3] C. Bruder and H. Schoeller, Phys. Rev. Lett. **1076** (1994).
- [4] R. Blick *et al.*, submitted (1994).
- [5] J. Weis, R. J. Haug, K. v. Klitzing, and K. Ploog, Phys. Rev. Lett. **71**, 4019 (1993).
- [6] A. Einstein, Ann. d. Phys. **17**, 132 (1905).
- [7] K. Yakubo, S. Feng, and Q. Hu, submitted (1995).
- [8] J. Tucker, IEEE Journ. of Quant. Elec. **QE 15**, 1234 (1979).
- [9] W. Parker, B. Taylor, and D. Langenberg, Phys. Rev. Lett. **18**, 287 (1967).

Time-resolved single electron tunnelling between Landau states in a quantum dot

N.C. van der Vaart, M.P. de Ruyter van Steveninck, F. Cochius, L.P. Kouwenhoven, A.T. Johnson *

Y.V. Nazarov and C. Harmans

Department of Applied Physics and DMEES, Delft University of Technology, P.O.B. 5046, 2600 GA Delft, Netherlands

C.T. Foxon

Department of Physics, University of Nottingham, Nottingham, NG7 2RD, Great Britain

Abstract

In a quantum dot with two confined Landau levels the Coulomb blockade oscillations develop a distinct structure at zero bias, showing peak splitting and conductance switching in time. It is shown that both phenomena result from single electron tunnelling between the two confined Landau levels within the dot. The typical dwell time between switching events is found to depend very strongly on the magnetic field, reaching values on the order of 100 s at large fields.

In a 2-dimensional electron gas (2DEG) subject to a large magnetic field the transport in the integer QH regime takes place via extended edge states which develop from Landau levels at the boundary of the system. In this regime the scattering probability of electrons is strongly suppressed, allowing electrons in a particular edge state to travel over large distances (up to mm's) before being scattered into an adjacent edge state (1-3). Although the existence of edge states can be visualised in the simple independent particle picture, their properties are largely determined by the self-consistent arrangement of the charge near the edge (5,6). This results in strips of compressible (i.e. metallic) states at the Fermi energy, spatially separated by incompressible states. The scattering of an electron between adjacent edge states will be determined by the quantum properties of the compressible initial and final states as well as the incompressible state acting as the barrier.

Confining the 2DEG to a small area or quantum dot will not fundamentally affect this picture, provided the number of electrons enclosed in the dot is not too small. The strips will develop into closed-orbit states. However, in addition the Coulomb interaction leads to a finite energy required to add a single electron to the dot: the charging energy (6). If the dot is weakly coupled to two leads, this finite energy in general results in a Coulomb blockade (CB) for the exchange of particles between the dot and the leads, suppressing the conductance through the lead-dot-lead structure. Only whenever the total energy of the system does not change upon the addition of the single electron, -i.e. the two states are degenerate in energy-, the CB is suppressed. Note that this condition is equivalent to the alignment of the electrochemical potentials of the 2DEG reservoirs and of the electron system in the dot. This results in the famous Coulomb blockade oscillations.

In this paper we will present experiments to study the tunnelling between edge states confined inside a quantum dot. We will employ the sensitivity of the Coulomb blockade on the total electrostatic energy of the system via the specific distribution of the charge within the dot. The experiments are performed in quantum dots (figure 1) defined by metallic gates on top of a GaAs/AlGaAs heterostructure with the 2DEG 100 nm below the surface, with an electron density of $\sim 1.9 \times 10^{15} \text{ m}^{-2}$ and a mobility of $\sim 2 \times 10^6 \text{ cm}^2/\text{Vs}$. A dot is formed at the application of negative voltages to the four gates 1, 2, F and C. Two dots are investigated, with typical dimensions of 600 nm (I) and 400 nm (II). The weak coupling to the leads is obtained via the tunnel barriers induced by the gates 1-F and 2-F respectively. The number of electrons is varied by the potential V_C of gate C. Experiments are done in a dilution refrigerator with 10 mK base temperature; the leads

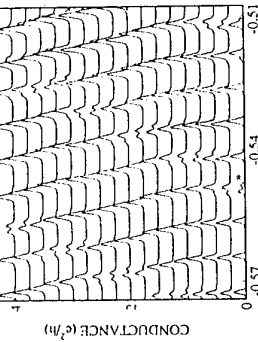


Figure 1. Schematic diagram of the gate geometry (hatched areas) and the edge states (1 or ring (R); and 2 or core (C))

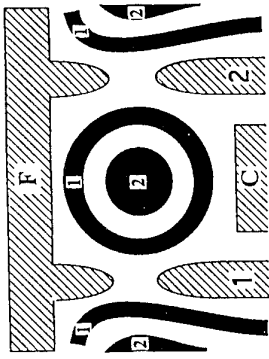


Figure 2. Coulomb blockade oscillations versus V_C of dot I, from $B=4.00 \text{ T}$ (bottom) to 4.632 T (top) in increments of 2 mT .

connecting to the sample are carefully filtered at room temperature as well as at the temperature of the mixing chamber. The magnetic field is taken such that only the lowest Landau level (LL) is occupied, forming the two spin-split states LL1 and LL2. The two resulting edge states are represented in figure 1 by the black areas denoted 1 and 2.

On the application of a magnetic field to dot I (and II as well) the regular CB oscillation pattern in dependence of V_C (6) becomes modified, with some of the CB peaks developing a splitted shape (figure 2). The splitted peaks show a well-defined behaviour versus the magnetic field. On increasing the magnetic field the nature of the splitting becomes more clear. Figure 3 is obtained on dot I at $B=5.2 \text{ T}$, with 3a showing the conductance versus gate voltage. Clearly one regular and two split peaks are seen. More specifically, with each black dot representing one individual measurement, the split structure is seen to be composed of two regular CB peaks, with one peak being displaced relative to the other in gate voltage. With the measurement progressing in time at a typical rate of once per second, the conductance follows either one of the two branches, randomly switching between the two. This switching is directly shown in figure 3b. Now at fixed V_C (indicated by the arrow in figure 3a) the conductance versus time is measured, showing a switching behaviour between two discrete levels, with a typical dwell time between switching events of approximately 10 s. Increasing the magnetic field strongly increases this time, and a value of ~ 200 s

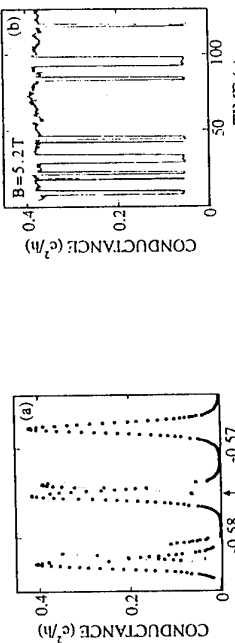


Figure 3. Conductance of dot I in dependence of (a) the gate voltage V_C at a fixed field $B=5.2 \text{ T}$ measured with a time constant of 150 ms, and (b) versus time at fixed B and V_C (arrow in (a)).

is found at $\sim 6\text{ T}$ (7). By the same token a smaller field increases the rate strongly. This is exactly what is seen in figure 2, where the rate is so large that individual switching events can no longer be resolve due to the rather long averaging time ($\sim 150\text{ ms}$) in the measurement. This results in a smearing between the two individual branches, yielding a continuous split-peak trace.

As discussed before the Coulomb blockade is controlled by the electrostatic energy of the system. Any rearrangement of the charge, either near to or inside the dot, leads to a change in this energy, and so it will affect the CB (4). We attribute the switching of the conductance to the tunnelling of a single electron between states in the two Landau levels 1 and 2 shown in figure 1. Inside the dot two compressible strips (RI) of states associated with LL1 and a disc-shaped core (CO) of states derived from LL2, separated by a ring-shaped tunnel barrier of incompressible states. Given the small scattering rate between CO and RI, and the large distance of CO from the entrance and exit tunnel barriers induced by the gates 1-F and 2-F, we assume that electron transport from entrance to exit *only* occurs via the ring states. Note however that the transport through RI is affected by the charge residing on CO.

With the decomposition of the electron system in the dot into two "isolated" areas (RI or 1, and CO or 2) containing N_1 and N_2 electrons respectively, three charging energies become of importance. In addition the weak coupling implies the assignment of individual electrochemical potentials to the ring (μ_2) and the core (μ_1), each depending on N_1 and N_2 , and on the external parameters V_C and B . Now two tunnelling processes have to be distinguished. First, the intra-dot tunnelling of the exchange of one electron between RI and CO, governed by internal charging with $N=N_1+N_2$ constant, depends on the difference $\delta=4/(N_1+N_2-1)-\nu_2(N_1-1,\nu_2)$. The actual tunnel rate depends on the properties of the RI- and CO-states and on the barrier. At non-zero temperature the rate may become thermally assisted to overcome the energy difference δ . Secondly, the transport through (the ring states of) the dot depends on the alignment of the electrochemical potentials of the ring (μ_1) and the reservoirs (μ_{res}). As μ_1 depends directly on N_1 and N_2 , it will shift upon the exchange of a particle between RI and CO. More specifically, if the external parameters are chosen such that initially $\mu_{\text{res}}=\mu_1(N_1-1,N_2)$ (yielding a maximum in the conductance), the tunnelling of an electron from core to ring will shift the electrochemical potential of RI to $\mu_1(N_1,N_2-1)$, i.e. away from the resonance condition with respect to μ_{res} . This will result in a switch of the conductance from "high" to "low". In this way the conductance through the ring states of Landau level 1 can be used as a probe to detect a tunnel event between the two confined Landau levels (8). Note that the system actually forms a fully controllable Two Level Fluctuator.

The occupation of the core and ring Landau states is determined by the gate voltage as well as the magnetic field. Increasing the magnetic field increases the Landau level degeneracy. As a result each time approximately one flux quantum is added to the dot, LL1 can accommodate one additional electron which is gained from the core region of LL2. In terms of energy this can be understood to result from the increase of the electrostatic energy accompanying the increased Landau level degeneracy (4). This will increase μ_2 relative to μ_1 , a process which continues until it becomes energetically more favourable to transfer one electron from LL2 to LL1, i.e. whenever $\delta=0$. Once the electron has tunneled to LL1 μ_2 drops relative to μ_1 . So the addition of successive flux quanta results in an approximately periodic saw-tooth shaped behaviour of μ_1 and μ_2 . Note that during this process the total number of electrons N in the dot is constant, and so only internal charging occurs.

If the gate voltage is adjusted such that μ_1 approximately lines up with μ_{res} the conductance will

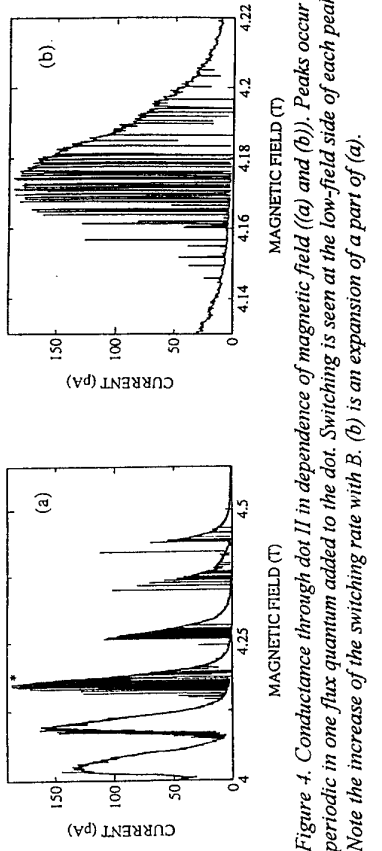


Figure 4. Conductance through dot II in dependence of magnetic field ((a) and (b)). Peaks occur periodic in one flux quantum added to the dot. Switching is seen at the low-field side of each peak. Note the increase of the switching rate with B. (b) is an expansion of a part of (a).

be non-zero with a value determined by the difference between μ_{res} and μ_1 . Figure 4a shows the conductance of dot II in dependence of the magnetic field, showing a strong asymmetry in the peak shape, demonstrating the saw-tooth behaviour of μ_1 . In addition strong switching is seen in all peaks. The detailed field dependent behaviour of the two-level switching can be seen more clearly by expanding one of these peaks (figure 4b). From $B\sim 4.15\text{ T}$ to $\sim 4.20\text{ T}$ a gradual transition occurs from preferentially "low" to "high" conductance. At $B\sim 4.17\text{ T}$ the up-down and down-up rates are equal, marking the condition $\delta=0$. From figure 4a two important observations can be made. First, the occurrence of switching is indeed found to be approximately periodic in a single flux quantum threading the dot, as anticipated from the behaviour of μ_2 relative to μ_1 . Second, from the "raggedness" of the low-field side of each peak we clearly see a strong increase of the typical dwell time (at $\delta=0$) at increasing magnetic field, rising from $\sim 0.1\text{ s}$ at $B\sim 4.10\text{ T}$ (second peak) to $\sim 3\text{ s}$ at $\sim 4.42\text{ T}$ (sixth peak). As mentioned before values of $>100\text{ s}$ are found in dot I at $B\sim 6\text{ T}$.

To explain this tunnel rate behaviour one needs to consider the properties of the incompressible strip and the density-of-states of the two Landau levels, including the effect of many-body interactions. In the simple single-particle approximation the transmission probability depends exponentially on the width of the incompressible strip. Since this width increases linearly with magnetic field (5) this may lead to an exponentially strong suppression of the tunnelling with the field, which is not incompatible with our experimental results. Further work, including the temperature dependence of the switching, is in progress to obtain a more quantitative description.

References

- (1) B.J. van Wees *et al.*, Phys. Rev. B39, 806 (1989)
- (2) S. Komiyama *et al.*, Phys. Rev. B40, 1256 (1989)
- (3) B.W. Alphenaar *et al.*, Phys. Rev. Lett. 64, 677 (1990)
- (4) P.J. McEuen *et al.*, Phys. Rev. B45, 11419 (1992); Physica B189, 70 (1993)
- (5) D.B. Chklovsky, B.I. Shklovsky and L.I. Glazman, Phys. Rev. B46, 4026 (1992)
- (6) "Single Charge Tunneling", ed. H. Grabert and M.H. Devoret (Plenum, New York, 1991)
- (7) N.C. van der Vaart *et al.*, Phys. Rev. Lett. 73, 320 (1994)
- (8) N.C. van der Vaart *et al.*, in: Proceedings of "Submicron Quantum Dynamics", NATO-ASI, Trieste, Italy (1994)

SCALING OF THE COULOMB BLOCKADE

L.W. Molenkamp^(a) and K. Flensberg^(b)

(a) 2. Physikalisches Institut, RWTH-Aachen, D-52056 Aachen, Germany*

(b) Mikroelektronik Centret, DTU, DK-2800 Lyngby, Denmark

When the conductance G_{bar} of the barriers that connect a quantum dot with the outside approaches $2 \times e^2/h$, the number of electrons N is no longer fixed at an integer value, leading to a breakdown of Coulomb-blockade-regulated transport.

This breakdown is a sensitive probe of the electron-electron interactions in the barriers themselves, which have been the subject of several recent theoretical studies applying Luttinger-liquid and Tomonaga-type scaling theories to describe the transport in low dimensional systems[1, 2]. These theories predict a scaling (power-law) dependence of the charging energy U on G_{bar} .

In this contribution, we describe two experiments on a double quantum dot structure that were designed to verify this scaling behavior, and thus the validity of these theories. The device is defined by means of eight gates in a two-dimensional electron gas for a convenient adjustment of the quantum-point-contact barriers.

(i) In one experiment, we use the device in an *electrometer* configuration[3], in which one dot measures the charging energy of its neighbor. Using this technique, we find that U scales quadratically with barrier reflectivity, in excellent agreement with a previous prediction[2] from scaling theory.

(ii) In a second experiment, we study the transition from single- to double- quantum dot behavior as a function of the conductance of the point-contact barrier that connects the two dots. For this experiment, we find that the relevant charging energy scales linear with barrier reflectivity, again in agreement with the predictions of Ref. [2].

For the interpretation of our experiments, we have developed a modelling of the transport behaviour of a quantum dot in the presence of quantum fluctuations in the electron number. This modelling is based on the conventional rate-equation approach, but replacing the appropriate Coulomb energies by their scaled counterparts. Our theory excellently reproduces the experimental data.

- [1] C. L. Kane and M. P. A. Fisher, *Phys. Rev. Lett.* **68**, 1220 (1992); K. A. Matveev and L. I. Glazman, *Phys. Rev. Lett.* **70**, 990 (1993).
- [2] K. Flensberg, *Phys. Rev. B* **48**, 11156 (1993).
- [3] P. Lafarge, H. Pothier, E. R. Williams, D. Esteve, C. Urbina, and M. Devoret, *Z. Phys. B* **85**, 327 (1991).

*Experiments performed at Philips Research Labs., 5656 AA Eindhoven, the Netherlands

Coherence and Phase Sensitive Measurements in a Quantum Dot

A. Yacoby, M. Heiblum, D. Mahalu and Hadas Shtrikman

Braun Center for Submicron Research, Dept. of Condensed Matter Physics
Weizmann Institute of Science, Rehovot 76100, Israel

Abstract

Via a novel interference experiment, which measures magnitude and phase of the transmission coefficient through a quantum dot in the Coulomb regime, we prove directly, for the first time, that transport through the dot has a coherent component. We find the same phase of the transmission coefficient at successive Coulomb peaks, each representing a different number of electrons in the dot, however, as we scan through a single Coulomb peak we find an abrupt phase change of π . The observed behavior of the phase can be understood in the framework of a 1D model of a dot strongly coupled to the ring.

The subject of ‘coherent’ versus ‘sequential’ resonant tunnelling (RT) process’ has been controversial for a long time. As is already known, straight forward conductance or optical measurements are not conclusive in establishing the nature of this process. We developed a novel interference experiment which determines conclusively the nature of transport through a submicron RT structure - a quantum dot (QD) in the Coulomb regime [1].

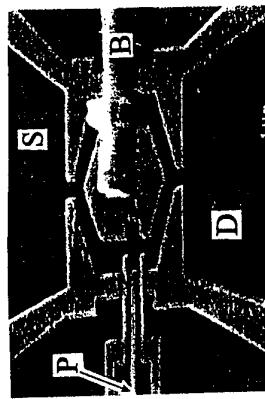


Figure 1. A SEM picture of the modified AB ring. The AB ring and QD are induced electrostatically by the respective metallic gates. The plunger gate (P) varies the number of electrons in the dot. The metal bridge (B) supplies the voltage that depletes the center part of the ring and is created using a special electron beam lithography process.

Our experiments were performed with a selectively doped GaAs - AlGaAs heterostructure supporting a two dimensional electron gas (2DEG) residing some 70 nm from the surface. The 4.2 K electron concentration and mobility are $2.2 \cdot 10^{11} \text{ cm}^{-2}$ ($E_F \approx 8 \text{ meV}$) and $5 \cdot 10^6 \text{ cm}^2/\text{V sec}$, respectively, leading to an elastic mean free path of order 10 μm . The modified AB ring was formed by depositing submicron metal gates on the surface of the

heterostructure and subsequently biasing them negatively in order to deplete the electrons underneath (see Fig. 1). The QD (0.4 μm wide and 0.5 μm long) is inserted in the left side arm, and its area, hence the number of electrons in it, is controlled by biasing the plunger gate, P. The coupling of the QD to the ring’s arm is controlled by the two gates surrounding the plunger gate, making the QD’s resistance considerably larger than the resistance of each arm. The AB ring, in turn, is coupled to the large 2DEG reservoir via two point contacts with resistance larger than that of the arms. This configuration enables a continuous variation of the QD’s resistance without affecting the two terminal resistance of the modified ring and the excitation voltage across the QD. Since each of the ring’s arms usually contains a few 1D channels and the estimated thermal smearing length is comparable to the ring’s size, the AB interference contrast of the bare ring (without an embedded QD) is typically around 10 % at 100 mK. The bare QD exhibits conductance resonances as the number of electrons increases one by one [2]. The bare AB ring, in turn, exhibits AB conductance oscillations when a magnetic flux is threaded through the ring’s interior with a periodicity of the flux quantum, h/e . As the dot is formed within one of the ring’s arms we find that the AB conductance oscillations persists even when the dot reaches the Coulomb blockade regime proving unambiguously, for the first time, that transport through a RT - QD has a substantial coherent component (see Fig. 2). Moreover, as the coupling of the QD to the ring’s arm is made weaker (the resistance of the QD increases) the contrast of the AB oscillations remains almost constant suggesting that the degree of coherence is maintained even when the estimated dwell times in the dot reach several nano seconds (see inset of Fig. 2).

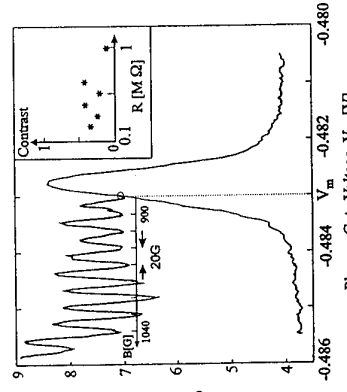


Figure 2. The ring’s current exhibiting the Coulomb peak of the quantum dot (the large background due to the non interfering current of the other arm had been subtracted). For a particular plunger gate voltage (V_p) the AB oscillations in the current are observed. Note that the contrast is defined relative to the peak height. Inset: Contrast of oscillations on the dot’s resistance.

After showing that transport has a coherent component we move on to study the dependence of the accumulated phase through the QD on its occupation. Considering only the coherent part and $k_B T < \Gamma_e$ (Γ_e is the intrinsic width of the resonant level), it can be shown that the phase of the

transmission coefficient deduced from a Breit - Wigner type resonance is expected to be almost constant away from the resonance and to undergo a smooth change of π as the energy scans the resonant peak [3]. Similarly, for $k_B T > \Gamma_e$, it can be easily shown that the phase is expected to change smoothly over a scale of $k_B T$ rather than Γ_e . An exact solution of a simple 1D RT model suggests that the phase of each resonance (or every other one when spin degeneracy is lifted) is out of phase with its predecessor. However, this might not be necessarily the case in other dimensions where it is even not clear theoretically whether a systematic behavior of the phase of the transmission coefficient with the number of electrons is expected. Note that since the number of electrons in the QD is around 200, the bare level average spacing is $\approx E_r / 200 = 40 \mu eV$ which is evidently larger than $k_B T$ ($\approx 9 \mu eV$). This suggests that each Coulomb peak results from tunnelling through a single resonant level.

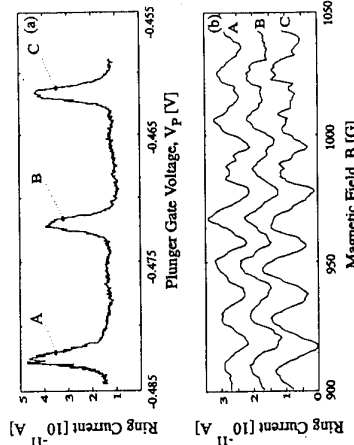


Fig. 3. (a) A series of Coulomb peaks (b) and the corresponding interference current oscillations taken at the marked points A, B, and C in successive peaks of the ring's current. All oscillations are seen to be in phase. The large current of the right arm is subtracted.

Experimentally we follow the phase evolution of the transmission coefficient through the QD by comparing AB interference patterns measured along a single Coulomb peak as well as at different Coulomb peaks. Figure 3 (b) shows the AB oscillations for three typical successive peaks (shown in Fig. 3 (a)), chosen out of a series of twelve measured successive peaks, with all oscillations taken at similar locations on the peaks (denoted by A, B, and C). It is clearly seen that the oscillations have the same phase at the three peaks, suggesting the same absolute phase of the transmission coefficient at each peak. However, the behavior of the phase along a single Coulomb peak is quite striking. Figure 4 (a) presents the expected line shapes for $k_B T \ll \Gamma_e$, for $k_B T > \Gamma_e$ and that of a measured Coulomb peak. Four different interference patterns, taken at the specified points on the Coulomb peak shown in Figs. 4 (a), are represented in Fig. 4 (b). The patterns indeed show a π phase change which takes place rather abruptly between points #2 and #3. We find that the phase change occurs on a scale of $\approx \frac{k_B T}{10}$, in direct contradiction with the expected change on the scale of the temperature. It is important to mention that the conductance

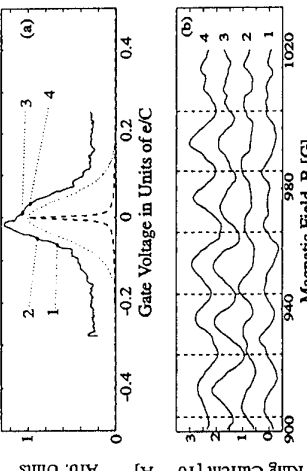


Fig. 4. The evolution of the phase along one conductance peak. (a) Level broadening, Γ , at $T=0$ (broken line) and for $k_B T > \Gamma_e$ (solid line), and the experimentally measured peak (shifted up solid line). (b) A series of interference patterns taken at the specified points on a peak. Note the phase jump between patterns #2 and #3.

References

- [1] A. Yacoby, M. Heiblum, D. Mahalu, and Hadas Shtrikman, Phys. Rev. Lett. **74**, 4047 (1995).
- [2] H. van Houten, C. W. J. Beenakker, and A. A. M. Staring, in Single Charge Tunneling, Edited by H. Grabert and M. H. Devoret, Plenum Press, New York and London, (1991).
- [3] G. Breit and E. Wigner, Phys. Rev. **49**, 519 (1936).
- [4] Y. Gefen, Y. Imry, and M. Ya. Azbel, Phys. Rev. Lett. **52**, 129 (1984).
- [5] A. Yacoby et al., to be published

Electronphonon Resonances and Optical Phonon Generation in Nanowires

V. B. Pevzner, V. L. Gurevich[†], and G. J. Iafrate[§]

[†]Electrical Engineering Department, North Carolina State University, Raleigh, NC USA

[‡]A.F.Ioffe Institute, Solid State Physics Division, Saint Petersburg, Russia

[§]Army Research Office, Research Triangle Park, NC USA

Abstract

We investigate the influence of optical phonons on the 1D hot electron ballistic transport in spatially uniform nanowires and predict a new type of resonance.

A new type of resonant behavior is predicted for the 1D hot electron transport in nanowires. The resonances occur at low temperatures provided that the electron transport is almost ballistic. By this we mean that, apart from non-Ohmic ballistic current, $J^{(0)}$, there is also a contribution, ΔJ , antiparallel to $J^{(0)}$, that is due to the electron-phonon interaction[1]. This part is assumed to be relatively small. Resonances occur whenever (i) a distance between a pair of levels of transverse quantization equals the energy of an optical phonon $\hbar\omega_0$, namely, when $\hbar\omega_0 = \epsilon_m(0) - \epsilon_n(0)$ and (ii) the condition for generation of optical phonons $eV > \hbar\omega_0$ is met where V is voltage bias. Resonances are manifested by a sharp drop of the total current, $J = J^{(0)} + \Delta J$ (see Fig. 1) and are accompanied by significant increase in the rate of optical phonon generation (see Fig. 2). We have calculated ΔJ as well as the rate of energy transfer from the phonons to the electrons in such a generation process. A surge in energy transfer rate is associated with each resonant increase in the resistance. The resonances are particularly pronounced at sufficiently low temperatures.

The physics of this phenomenon is a consequence of confinement and of a special form of the density of states in 1D case (which is absent in 2D and 3D situations). The same kind of singularity is also typical for 3D electron spectrum in a magnetic field. Hence there is a resemblance between this phenomenon and the magnetophonon resonance[2].

Even in the absence of collisions with phonons, a substantial deviation of current from the Ohmic value may be expected if the ratio eV/μ is not small — cf. with Ref. 1. The functional dependence of collisionless ballistic current $J^{(0)}(V)$ may be rather peculiar, so that the differential conductance $g_0 = dJ^{(0)}(V)/dV$ may have an oscillatory like behavior as a function of the bias voltage V provided $eV \geq k_B T$ (see for instance Refs. [3, 4, 5, 6, 7]). For this reason the structure implicit to g_0 must be carefully taken into account when examining

the total current J and the total differential conductance g experimentally. We emphasize that for $eV \ll k_B T$ the dependence $J^{(0)}$ on V is purely Ohmic, with an exponential accuracy.

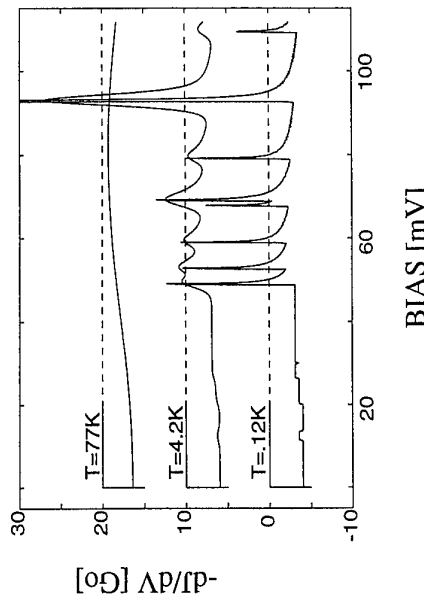


FIG. 1 Differential conductance as a function of bias voltage for various temperatures ($L_y=100\text{nm}$).

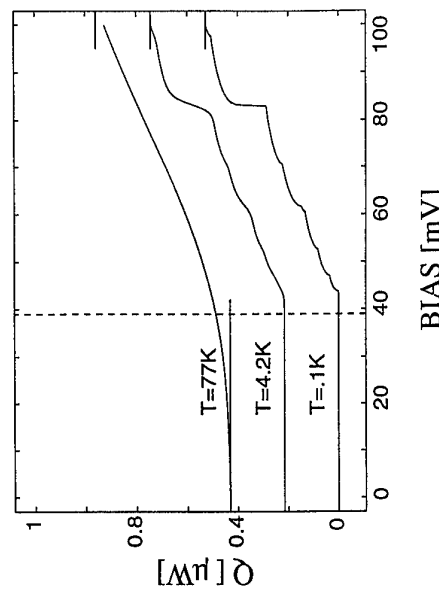


FIG. 2 Energy transfer rate Q as a function of voltage bias V for $T = 1, 4.2$ and 77K ($L_y=100\text{nm}$).

To calculate a negative change of current due to the electron-phonon scattering ΔJ , we apply a theory developed by Gurevich et al.[8, 9, 10] to treat transport in a two-terminal nanostructure consisting of a spatially uniform conductor[11] which is connected to large reservoirs, each in thermal equilibrium with itself. We have investigated resonant oscillations in the resistance as a function of applied voltage bias.

We believe that this effect can be used as an experimental probe for the investigation of various physical aspects of nanostructure systems. To name a few, for instance, one can investigate the character of the actual interactions between the electrons and optical phonons, or the details of the electron band structure and the actual positions of the levels of transverse quantization, or the role of nonequilibrium phonons in the transport phenomena. We also encourage experimentalists to think of a physical situation where a blockage of a single channel due to the electrophonon resonances may play a crucial role so that one can separate a one-channel contribution experimentally. We anticipate a possibility of a stimulated emission of coherent phonons with an application of a voltage across nanostructures. Hence, it is important to look for, both theoretically and experimentally, the ways to preserve the phase coherence of the emitted phonons as well as a possibility of the microwave generation in nanostructures and examine possible practical applications of these phenomena.

V. L. G. wishes to thank the European Office of the US Army for travel support and also Russian National Fund of Fundamental Research and NATO Linkage Grant. V. P. was supported by the Army Research Office and the National Research Council.

References

- [8] V. L. Gurevich, V. B. Pevzner and K. Hess, J. Phys.: Condens. Matter **6**, 8363 (1994); Phys. Rev. B **51**, 5219 (1995);
- [9] V. L. Gurevich, V. B. Pevzner and E. W. Fenton, Phys. Rev. B **51**, (15) 9465 (1995).
- [10] V. L. Gurevich, V. B. Pevzner and G. J. Iafrate, accepted by Phys. Rev. Lett. (to appear in August 1995 issue).
- [11] In nonhomogeneous wires, the optical phonon generation is most likely to start in the section that meets EPR condition (1) first.
- [12] Dekorsy et al., Phys. Rev. Lett. **74**(5), 738 (1995).

Two-dimensional Electron Liquid in a Weak Magnetic Field

L. I. Glazman and I. L. Aleiner

Theoretical Physics Institute, University of Minnesota, 116 Church St. SE, Minneapolis, MN 55455

Abstract

We present a theory describing the low-energy properties of an interacting 2D electron gas in a magnetic field at large non-integer filling factors $\nu \gg 1$. For a moderate interaction strength, $r_s < 1$, we find two energy scales controlling the electron dynamics at energies less than $\hbar\omega_c$. The first energy scale, $(\hbar\omega_c/\nu) \ln(\nu r_s)$, appears in the one electron spectral density as the width of a pseudogap. The second and larger scale, $r_s \hbar\omega_c$, characterizes the exchange-enhanced spin splitting and the thermodynamic density of states.

Since the discovery of the fractional quantum Hall effect [1], the properties of two-dimensional (2D) interacting electron systems in a strong magnetic field have been attracting persistent attention. Historically, almost all the efforts were directed towards the study of the strong magnetic field case when only the lowest Landau level is occupied, and the energy of the electron-electron interaction is much smaller than the spacing between Landau levels, $e^2/(\kappa\ell) \ll \hbar\omega_c$, where ℓ and κ are the magnetic length and the background dielectric constant respectively.

In a weak magnetic field, the bare Coulomb interaction leads to energies exceeding $\hbar\omega_c$. In this case, one can start from the Fermi liquid theory in zero magnetic field. The concept of Fermi liquid usually enables one to neglect the interactions between quasiparticles when determining their energy spectrum in the vicinity of the Fermi level. This concept is based, first, on the screening of Coulomb interaction, and, second, on the constraint on the phase space allowed for a scattering event. Landau quantization of the non-interacting quasiparticles in two dimensions creates a system of discrete levels. Obviously, the existence of the energy gap between the filled and empty levels affects adversely the screening. In addition, if the Fermi level coincides with a Landau level, the system of non-interacting quasiparticles becomes infinitely degenerate, and even a weak interaction lifts this degeneracy. This results in a non-trivial fine structure of the partially filled Landau level (PFLL), which is the subject of the present paper.

Our theory is based on the observation, that even though the electrons of the completely filled Landau levels can not screen the electric field because of energy gaps $\hbar\omega_c$, these electrons contribute significantly to the polarizability of the 2D system. As a result, the interaction between electrons of the PFLL is reduced, and the corresponding *renormalized* characteristic energy is smaller than $\hbar\omega_c$ even in a weak magnetic field. This observation enables us to obtain the effective Hamiltonian \hat{H}_{eff} that acts in the Fock space of the PFLL only, by tracing out all the other degrees of freedom:

$$\hat{H}_{eff} = - \lim_{\beta_0 \rightarrow \infty} \frac{1}{\beta_0} \ln T'_N \left\{ e^{-\beta_0 \hat{H}} \right\}. \quad (1)$$

Here \hat{H} is the full Hamiltonian of the two-dimensional electron system in a magnetic field, and T'_N means trace over Fock space of all the Landau levels *except* the PFLL. Hamiltonian (1) adequately describes all the excitations with energies smaller than $\hbar\omega_c$. Performing the trace [2], we find:

$$\hat{H}_{eff} = -\mu^* \int d^2r \hat{\rho}_N(r) + \frac{1}{2} \int d^2r_1 d^2r_2 U(r_1 - r_2) : \hat{\rho}_N(r_1) \hat{\rho}_N(r_2) :, \quad (2)$$

where $\hat{\rho}_N(r)$ is the projection of the density operator on N th Landau level, and $: \dots :$ means the normal ordering. Similar to the strong magnetic field case, $\nu < 1$, the Hamiltonian is just the energy of interaction between the electrons restricted to a single, partially filled Landau level. The main difference is that the PFLL has a high index, $N \gg 1$, and the interaction potential $U(r)$ is much smaller than bare Coulomb potential:

$$U(r) = \int \frac{d^2q}{(2\pi)^2} \frac{2\pi e^2}{\kappa q} \frac{1}{\varepsilon(q)} e^{iqr}, \quad \varepsilon(q) = 1 + \frac{2}{qa_B} [1 - \mathcal{J}_0^2(qR_c)]. \quad (3)$$

The static dielectric function $\varepsilon(q)$ describes the mentioned renormalization of the bare Coulomb potential; $a_B = \hbar^2 k/mc^2$ is the Bohr radius, $R_c = \lambda\sqrt{2N+1}$ is the cyclotron radius, and $\mathcal{J}_0(x)$ is the zeroth order Bessel function. The coordinate dependence of the pair interaction (3) is shown in Fig. 1.

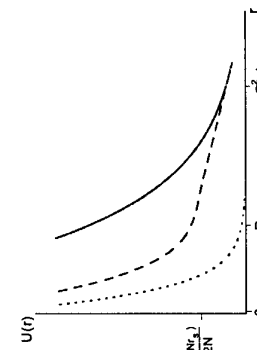


FIG. 1. The renormalized pair interaction $U(r)$ given by Eq. (3) as the function of the inter-electron distance (solid line). Dashed line is the bare Coulomb potential and the dotted line is the screened interaction in 2D metal.

The Hamiltonian (2) enables us to estimate the characteristic energy scales which control the low-energy dynamics of the 2D system. In order to make these estimates, we employ the Hartree-Fock trial function, based on the one-electron coherent states of the N -th Landau level [4]. At small filling factors of the PFLL, $\Delta\nu = \nu - 2N \ll N^{-1}$, the separation between electrons on this level exceeds the size of the wave function R_c . In this case the system under consideration is equivalent to a classical crystal of point charges interacting via potential (3). Due to the polarization effect, there is a wide region of electron densities in the weak field regime, $N^{-3}r_s^2 \lesssim n_s^N \lesssim N^{-1}$, where the Coulomb repulsion in the crystal is replaced by the logarithmic potential $U(r) \simeq (\hbar\omega_c/2N) \ln(R_c^2/a_B r)$. (Conventional

parameter r_s characterizing the interaction strength is related to the total electron density n_e by $\pi r_s^2 = n_e a_B^2$.

Tunnelling into a Wigner crystal leads to a sudden formation of an interstitial in it. The energy of such a defect determines the width of the gap Δ_g in the tunnelling density of states (Fig. 2a), and it is of the order of interaction energy $U(r \simeq \lambda/\sqrt{\Delta\nu})$ between the nearest neighbors:

$$\Delta_g \simeq \frac{\hbar\omega_c}{4N} \ln(N^3 r_s^2 \Delta\nu). \quad (4)$$

It is worth noticing that unlike the case of small filling factors $\nu \lesssim 1$ (see Refs. [5]), here Δ_g depends on the interaction strength and on the electron density of the PFLL only logarithmically.

At larger concentrations, $\Delta\nu \gtrsim N^{-1}$, the single electron wave functions are still orthogonal to each other, but the densities corresponding to these wave functions have a significant spatial overlap. Because for the fully spin polarized electron system of the PFLL the orbital part of the many-electron wave function is antisymmetric, the Hartree and Fock terms in the interaction energy largely compensate each other. The resulting difference is almost independent of $\Delta\nu$, and it is of the order of $U(R_c)$. Therefore, the dependence of the gap in the tunnelling density of states on $\Delta\nu$, see Fig. 2b, saturates at a constant value:

$$\Delta_g \simeq \frac{\hbar\omega_c}{2N} \ln(r_s N). \quad (5)$$

This estimate was obtained previously in the framework of the hydrodynamic approach [3].

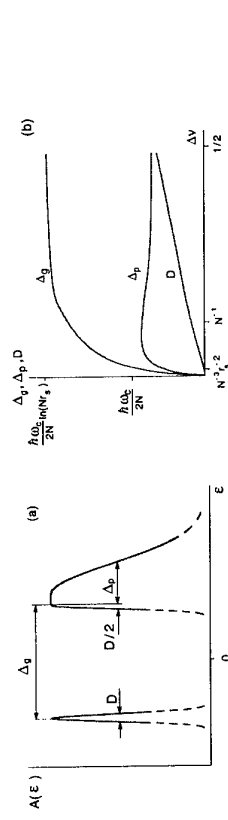


FIG. 2. (a): The spectral density as a function of energy. (b): The dependence of the characteristic energy scales on filling factor of the partially filled Landau level $\Delta\nu$. The asymptotic behavior of the width of the pseudogap, Δ_g is given by Eqs. (4) and (5). The width of the peak in the one-electron spectral density Δ_p is determined by the variation of the interstitial energy and it is smaller than $\hbar\omega_c/2N$ at all filling factors. The width D of the peak corresponding to vacancies ($\epsilon < 0$) is even smaller than Δ_p .

The thermodynamic density of states in a large region of filling factors, $N^{-1} < \Delta\nu < 1 - N^{-1}$ is contributed mainly by the Fock energy and it has a negative, independent of the magnetic field value:

$$\left(\frac{\partial n_e}{\partial \mu}\right) \simeq -\frac{m}{\hbar^2} \left[\sqrt{2} r_s \ln\left(\frac{2^{3/2}}{r_s}\right) \right]^{-1}. \quad (6)$$

We turn now to the discussion of the spin excitations. Flipping the spin of a single electron affects the exchange interaction of this electron with all the other electrons of the same Landau level. All the lower Landau levels carry equal number of electrons of both spin polarizations, and do not contribute to the energy associated with the spin flip, Δ_s . Therefore, only $1/2N$ -th fraction of the total electron density participates in the exchange enhancement, and the corresponding contribution to Δ_s is approximately N times smaller than the exchange energy per electron at zero magnetic field. For a 2D electron gas with Fermi wave vector k_F , the latter energy is of the order $e^2 k_F / \kappa$, and the contribution to Δ_s is of the order $e^2 k_F^2 / \kappa N$. The rigorous result [2] obtained for a large odd ν differs from this estimate only by a logarithmic factor. For the effective g -factor defined by the relation $g_{\text{eff}} \equiv \Delta_s / \hbar\omega_c$, we find

$$g_{\text{eff}} = g_0 + \frac{r_s}{\sqrt{2\pi}} \ln\left(\frac{2^{3/2}}{r_s}\right). \quad (7)$$

Here g_0 is determined by the Zeeman splitting in the absence of the interaction, and it is usually small (in $GaAs$ the value of g_0 is only 0.029). For the even filling factors, the value of Δ_s is determined solely by g_0 [6].

In conclusion, we constructed a theory of the low-energy properties of 2D electron liquid in a weak magnetic field. This theory enabled us to describe the tunnelling and thermodynamic densities of states, and the spin excitations. We found that in a weak magnetic field, $\nu \gg 1$, the energy scale of charge excitations $(\hbar\omega_c/\nu) \ln(\nu/\nu_s)$ is parametrically smaller than the energy scale for spin excitations $r_s \hbar\omega_c$. This is qualitatively different from the situation at small filling factors, $\nu \lesssim 1$, where these excitations are characterized by the same energy scale $e^2/k\ell$.

Helpful discussions with B. L. Altshuler, B. I. Halperin, A. I. Larkin, L. S. Levitov, Yu. B. Lyanda-Geller, A. H. MacDonald, B. I. Shklovskii, and X. Zhu are acknowledged with gratitude. This work was supported by NSF Grant DMR-9423244.

References

- [1] *The Quantum Hall Effect*, edited by R. E. Prange and S. M. Girvin (Springer-Verlag, New York, 1990), 2nd ed.
- [2] I. L. Aleiner and L. I. Glazman, preprint cond-mat/9505026.
- [3] I. L. Aleiner and L. I. Glazman, Phys. Rev. Lett. **74**, 3435 (1995).
- [4] K. Maki and X. Zotos, Phys. Rev. B **28**, 4349 (1983); S. Kivelson, C. Kallin, D. P. Arovas, and J. R. Schrieffer, Phys. Rev. B **36**, 1620 (1987).
- [5] S.-R. E. Yang and A. H. MacDonald, Phys. Rev. Lett. **70**, 4110 (1993); Y. Hatsugai, P.-A. Bares, and X. G. Wen, Phys. Rev. Lett. **71**, 424 (1993); Song He, P. M. Platzman, and B. I. Halperin, Phys. Rev. Lett. **71**, 777 (1993); Y. B. Kim and X. G. Wen, Phys. Rev. B **50**, 8078 (1994); A. L. Efros and F. G. Pikus, Phys. Rev. B **48**, 14694 (1993); P. Johansson and J. M. Kinaret, Phys. Rev. Lett. **71**, 1435 (1993); Phys. Rev. B **50**, 4671 (1994).
- [6] T. Ando and Y. Uemura, J. Phys. Soc. Japan **37**, 1044 (1974).

Berry Phase, Conductance Oscillations and Phase Breaking in Mesoscopic Transport

Yuli Lyanda-Geller

Beckmann Institute for Advanced Science and Technology,
University of Illinois at Urbana-Champaign, Urbana, IL 61801

Abstract

A novel class of interference phenomena originating from the geometric phase is discussed. Spin-orbit interaction results in the geometric phase and leads to the destructive interference and a phase shift of the Aharonov-Bohm conductance oscillations in ballistic and diffusive rings. In-plane magnetoresistance of rings exhibits abrupt "topological" transitions from destructive to constructive interference. The origin of the phase breaking due to the spin-orbit interaction in the weak localization conductance and in the universal conductance fluctuations is clarified.

1. Introduction. A concept of the topological (geometric) phase introduced by M.Berry¹ generalizes the Aharonov-Bohm (AB) effect. AB effect manifests itself in a variety of exciting mesoscopic phenomena. Berry's phase (BP) may result in similarly important contributions. The simplest example of BP is the phase acquired by the spin wave function in magnetic field. When the value of the field is constant and its direction follows adiabatically the closed path, the wave function picks up BP equal to a half of a solid angle ($\pi/2$), subtended by the magnetic field while this closed path is circumnavigated. The total phase acquired by the wavefunction is the sum of BP and dynamical phase $\omega_L t$, t being the time in which the field returns to the original direction. ω_L is the Larmor frequency.

Aharonov and Casher² considered the phase (ACP) picked by the wavefunction of a particle with fixed projection of a spin or the orbital angular momentum. This phase is the direct analogue of the AB phase. In the present paper I describe how the spin-orbit (SO) interaction in low dimensional structures leads to the interference phenomena in mesoscopic transport due to these spin phases. I show the difference between BP and ACP and discuss other spin vector-potential (topological) effects.

2. Spin-orbit geometric phase in conducting rings. SO interaction in low dimensional structures includes not only the coupling with random impurity fields but also zero magnetic field spin splitting; the electron spin is influenced by the momentum-dependent magnetic field (MDF). For instance, in 2D GaAs the electron Hamiltonian has the form

$$\mathcal{H} = \frac{\mathbf{p}^2}{2m} + \alpha(\sigma_x p_x - \sigma_y p_y), \quad (1)$$

where \mathbf{p} is the electron momentum, σ_i are the Pauli matrices, m is the effective mass, α is the coefficient describing the leading term in the SO splitting of the electron states at $p \neq 0$.

Consider a ring of radius r coupled to leads and confined to the interface plane of a heterostructure. The electron coming from a lead is characterized by the Fermi momentum p_F . The value of the momentum is constant, but its direction changes while electron traverses a ring³. The MDF (in the particular case of Eq.1) also encloses a circle, i.e. the solid angle subtended is 2π . If the two branches of a ring are symmetric, the dynamical phases acquired by electrons in branches are equal and the phase difference of the electron waves interfering at the outgoing lead is determined solely by the geometric phase, being the half of the solid angle. Correspondingly, if there is no external magnetic field, then the geometric phase is π and the interference is destructive. As a result, electrons are completely reflected by the ring due to SO interaction, while in the absence of the MDF the ring is transparent. It is only necessary that the electron spin motion should be adiabatic, i.e. the frequency of the variation of the MDF, p_F/mr , is less than the effective Larmour frequency αp_F , or $\alpha mr \gg 1$.

When an electron circumnavigates the ring, the external magnetic field applied perpendicular to its plane results in the cone-shape path of the total effective spin magnetic field. SO BP is then given by $\Phi_B = \pm\pi \left(1 - \omega_s / \left((\alpha p_{\pm})^2 + \omega_s^2 \right)^{1/2} \right)$, where p_{\pm} are the momenta of the incident electrons with spin up and down. The phase difference between waves passing the opposite branches of a ring contains the SO BP Φ_B and the conventional AB phase $2\pi \frac{\Phi_0}{\Phi_B}$, where Φ_0 are the magnetic and the unit flux, correspondingly. As a result the phase shift of AB oscillations should be observed. This geometry, in which the direction of the momentum and the effective magnetic field varies, with the electron spin adiabatically following the direction of the field, is the natural example for BP manifestation. ACP concept is not applicable in this case.

3. Topological Transitions. A special case of BP occurs when the trajectory around which the spin magnetic field is transported is confined to a plane. As it was discussed in the previous section, in the absence of external magnetic field the interference is destructive. Consider the effect of the external in-plane magnetic field⁴. At small fields the total spin magnetic field, which is the sum of the external field and the in-plane MDF, subtends a circle around the the point of zero total field (the origin) in the magnetic field space, when an electron encircles a ring. Correspondingly, BP is π and the conductance is still zero. This situation holds until the values of the external field and the MDF become equal (the transition point). Then the trajectory subtended by the total field is the circle, but it does not subtend the origin. It only crosses it, when directions of the two fields coincide. It is easily seen that BP then is $\pm\pi/2$, since only the half of a plane is seen from the origin. Rigorous consideration of this case with the proof of the applicability of the adiabatic phase concept is given in⁴. At larger external fields, the circle which is subtended by the total magnetic field, while the electron traverses the ring, does not subtend the origin any more, and the solid angle and BP are zero. This is an abrupt topological transition from the solid angle 2π to zero solid angle as a result of the external magnetic field variation. The value of the conductance undergoes the transition from zero to e^2/h , due to the transition from destructive to constructive interference. In a ring with a number of spin-resolved transverse modes (channels), each channel is characterized by its specific kinetic energy, momentum and MDF. Correspondingly, a sequence of transitions should be observed: with increasing the external field the character of interference changes from destructive to constructive in more

and more channels and the step-like current-magnetic field characteristics should appear.

4. Spin-orbit flux effect in disordered conductors. Transport properties of mesoscopic systems in diffusive regime are sensitive to interactions affecting the phase coherence. In the weak localization (WL) regime, the external magnetic field leads to the anomalous magnetoresistance which, due to SO interaction, is positive at low fields but negative at higher fields⁵. Magnetic flux⁶ results in AB oscillations of resistivity in disordered rings.

It turns out that oscillations of the resistivity and the phase shift of AB oscillations in rings result from the variation of the SO constant α with the gate voltage.⁷ SO oscillations in rings from the viewpoint of ACP were considered in⁸. The aim of the present discussion is to clarify the origin of these effects and to find when oscillations are not destroyed by the phase-breaking, which may also be caused by SO interaction.

The recognition that important difference exists between SO coupling arising from random fields and SO splitting of the electron states, is crucial. The unique symmetry of the Hamiltonian given by Eq.(1) with terms containing the first Legendre polynomial of the electron momentum (MDFI) leads, as we will illustrate below, to the spin vector potential effect. SO oscillations in rings due to AC effect considered in⁸ may result exclusively from this vector potential in the conditions of the "frozen" electron spin. If the electron spin is not frozen, i.e. it is impossible to choose the coordinate system in which the electron Hamiltonian contains only one projection of the spin operator, then SO oscillations may be smeared by the SO phase-breaking. Note that all types of SO interaction, distinct from MDFI, i.e. due to the third Legendre polynomial term in the spin Hamiltonian or due to random impurity fields result only in the phase breaking, irrespective of the topology of samples. We discuss here only MDFI term, the equation for the cooperon accounting for cubic terms, SO and magnetic impurity scattering and general form of linear terms was considered in⁷.

Electrons in a weakly disordered conductor ($\epsilon_F \tau \sim Dm \gg 1$) are described by the diffusivity D (ϵ_F is the Fermi energy,⁷ τ is the collision time). Let two electrons propagate in two different MDFI characterized by SO constants α and α' , correspondingly, (both MDFI are of the same symmetry described by Eq.1). Then the cooperon correlator, which determines the WL corrections and the universal conductance fluctuations, has the form

$$D(q_i + A_i + A'_i)^2 C = \frac{1}{\pi \nu \tau^2}, \quad (2)$$

where ν is the single spin electron density of states, the effective spin vector-potentials $A = m\langle \boldsymbol{\sigma}_x^{(1)}, -\boldsymbol{\sigma}_y^{(1)} \rangle$, $A' = m\langle \boldsymbol{\sigma}_x^{(2)}, -\boldsymbol{\sigma}_y^{(2)} \rangle$, $\boldsymbol{\sigma}^{(i)}$ is the spin operator for the i^{th} particle. The universal conductance fluctuations can be characterized by the Fourier power spectrum $F_{ijkl}(\alpha, (\alpha - \alpha')) = \langle \sigma_{ij}(\alpha) \sigma_{kl}(\alpha') \rangle - \langle \sigma_{ij}(\alpha) \rangle \langle \sigma_{kl}(\alpha') \rangle$, where $\sigma_{ij}(\alpha)$ is the conductivity of the sample and angular brackets denote averaging over various random potentials. The quantity $\sqrt{F(\alpha, 0)}$ characterizes the amplitude of random variation of $\sigma(\alpha)$, and the scale $\alpha - \alpha'$ on which $F(\alpha, (\alpha - \alpha'))$ varies, determines the typical variation scale of $\sigma(\alpha)$. $F(\alpha, (\alpha - \alpha'))$ is described by the cooperon and the diffusion contributions similarly to the Fourier spectrum of magnetoresistance^{9,10}. Equation (2) for the cooperon is easily solved in a narrow ring (the width of a ring is less than the SO phase breaking length discussed below) and one finds that *the Fourier spectrum is periodic in both α and $\alpha - \alpha'$* . The diffusion contribution to fluctuations is characterized by the same spectrum. This is a difference between SO oscillations effect and AB effects in mesoscopic conductors.

The SO effect connected with the MDFI term in the WL regime (for this case $\alpha = \alpha'$) is related to the effective spin vector-potential determined by the total spin of particles. Equation (2) then reduces to the cooperon equation derived in coordinate representation in⁸ and in momentum representation in⁷. For the narrow ring we obtain the phase shift of the AB conductance oscillations, $2m\alpha\Phi_0$. Note, that the contribution of the Zeeman interaction (ZI) to the left hand side of Eq.2 is proportional to the difference of spins $\boldsymbol{\sigma}^{(1)} - \boldsymbol{\sigma}^{(2)}$ and contains the parameter $\frac{1}{Dm}$. ZI "has no information" about the massive diffusive trajectory characteristic for disordered conductor. Its influence onto the cooperon propagator is negligible, while the role of the MDFI, which knows about diffusion, is enhanced. Since ZI is ineffective, the solid angle subtended by MDFI, while electron circumnavigates a loop, is 2π . The relevant for WL (which is the result of the interference of waves traversing the loop counter and clockwise) phase difference is twice BP or 2π . Consequently, BP is irrelevant in WL regime, only the dynamical phase is important.

With ineffective ZI and the electron spin frozen this dynamical phase is just ACP. However, in many cases, and in 2D in particular, the electron spin is not frozen. As a result an anisotropic phase breaking of the triplet cooperon (diffusion) components, described by the SO length $L_{so} = (\alpha m)^{-1}$, appears. It results in diminishing of oscillations of the mesoscopic fluctuations and of the WL conductance as well as changes the anomalous magnetoresistance. The origin of this phase breaking is that an electron moving along different trajectories from one point to another accumulate different phases due to the spin vector potential. This phase difference breaks the coherence analogously to AB flux. We note that conventionally¹¹ the dephasing due to SO splitting of electron states was attributed to Dyakonov-Perel spin relaxation mechanism, which is the spin precession in momentum-dependent SO field varying its direction due to elastic scattering. However, as we demonstrated⁷, the phase breaking is absent in 1D wire, where such a spin relaxation exists. We conclude that in the case of MDFI term SO phase breaking has the topological (vector potential) origin.

Finally we note that the spin vector potential leads to unusual values of conductance variance¹². Compensating the AB flux for one of the spin eigenvalues of the cooperon (or diffusion), SO vector potential essentially changes level statistics in mesoscopic ring.

I am grateful to I. Aleiner, P. Dresselhaus, H. Matlub, A. Mirin, J. Pieper, G. Pilks, A. D. Stone and R. Wheeler for stimulating discussions. I am greatly indebted to Arkyd Aronov, with whom we started the work on the spin-orbit geometric phase. Untimely death unlabeled him to become a coauthor of the present article.

5. References

1. M.V.Berry, Proc.Roy.Soc.(London) A392, 45 (1984).
2. V.Aharanov, Yu.V.Sharvin, Phys.Rev.Lett., 53, 319 (1984).
3. A.G.Aronov, Yu.B.Lyanda-Geller, Phys.Rev.Lett., 70, 343 (1993).
4. Yu.B.Lyanda-Geller, Phys.Rev.Lett., 71, 657 (1993).
5. G.Bergmann, Phys.Rep., 107, 1 (1984).
6. A.G.Aronov, Yu.V.Sharvin, Rev.Mod.Phys., 59, 755 (1987).
7. A.G.Aronov, Yu.B.Lyanda-Geller, preprint, University of Karlsruhe (1993).
8. H.Matlub and A.D.Stone, Phys.Rev.Lett., 68, 2964 (1992).
9. P.A.Lee and A.D.Stone, Phys.Rev.Lett., 55, 1622 (1985).
10. B.I.Altshuler and D.E.Khmelnitskii, JETP Lett., 42, 44 (1985).
11. B.I.Altshuler, A.G.Aronov, D.E.Khmelnitskii, A.I.Larkin, JETP, 54, 411 (1981).
12. Yu.B.Lyanda-Geller and A.D.Mirlin, Phys.Rev.Lett., 72, 1894 (1994).

Detection of the Oscillation of the Fermi Energy of a 2DEG

CHW Barnes[†], DR Mace[†], G Faini[†], D Mailly[‡], MY Simmone[‡], CJB Fordt, and M Peppert.

[†]Cavendish Laboratory, Madingley Road, Cambridge, CB3 0HE, UK.
[‡]L2M - CNRS, 196, avenue Henri Ravera, 92220 Bagneux, FRANCE.

We have used a Quantum Antidot (QAD) to detect the oscillation of the Fermi energy in a two dimensional electron gas (2DEG) as a function of magnetic field. At a magnetic field $B_0 = n_s h^2 / (e^2 \pi R^2)$ (where n_s is the carrier density and R is the radius of the QAD at the Fermi energy) the Shubnikov de-Haas (SdH) oscillation period becomes greater than the period of the Aharonov-Bohm (AB) oscillations from the QAD. Hence above this field the corresponding oscillation of the Fermi energy is superimposed onto the period of the AB oscillations. We have taken measurements of the AB period as a function of magnetic field at a number of different QAD radii. These measurements reveal an average oscillatory period which is consistent with the motion of the Fermi energy through the predicted QAD eigen spectrum.

In a metal the carrier density is a fixed quantity determined by a background of positive charge from ion sites independent of any external magnetic field. However when a magnetic field is imposed the density of states picks up an oscillatory component due to the quantisation of cyclotron motion. The condition that the carrier density is constant is then only met if the Fermi energy oscillates. An experiment to measure this effect was first proposed by Kaganov in 1957 [1] nearly thirty years after Landau's [2] celebrated paper detailing the eigen spectrum of a metal in a magnetic field. In most metals the effect is very small, microvolts or less, however oscillations were seen as reviewed in Schoenberg (1985) [3]. With the advent of Si MOSFETs and GaAs/AlGaAs heterostructures, in which a 2DEG may be formed, came the possibility to repeat these measurements on a system where the oscillations are accentuated due to the simpler spectrum and lower effective masses. The contact potential method was used successfully first by Pudalov *et al* [4] and then Dabiran *et al* [5] and a direct measurement of the density of states was made by Smith *et al* [6].

In our experiment we have attempted to detect the oscillation of the Fermi energy in a 2DEG formed in a GaAs/AlGaAs heterostructure using a local probe - a QAD. The idea is that as the Fermi energy oscillates the QAD effective potential changes: firstly the potential difference between the conduction band edge and the potential peak of the QAD oscillates, and secondly, the shape changes as the screening oscillates with the density of states [7]. The QAD is measured in a regime where it exhibits sharp transmission resonances (due to inter-edge state scattering between states in the first Landau level (LL) bound to the QAD and extended states in the second [8]) at specific magnetic fields determined by the QAD potential. The oscillation of the Fermi energy is then superimposed on the positions of the observed peaks.

The experimental QAD is defined using an independently contacted gate placed in the center of a split gate (SG) to form two parallel ballistic constrictions [9,10]. The QAD lithographic diameter is 0.2μm, the SG lengths are 0.3μm and the separation between the side gates and the QAD is 0.3μm. The device was fabricated on a GaAs/AlGaAs heterostructure with the 2DEG 100nm below the surface, carrier density $n_s = 3.05 \times 10^{15} \text{ m}^{-2}$, and mobility $60 \text{ m}^2 \text{ V}^{-1} \text{ s}^{-1}$ after brief illumination. The device was measured at temperatures below 50mK.

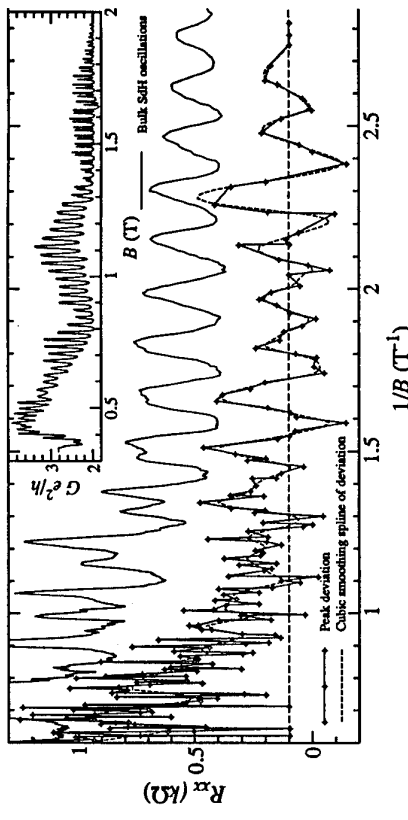


Figure 1 Inset: A typical conductance trace in which an aperiodicity in the AB oscillations is clearly seen near 0.6T. Upper solid line: Bulk ρ_{xx} . At high field, the QAD is defined at zero gate voltage accounting for the absence of zeros. Lower solid line with points: Derived from plotting peak position against peak index, and removing a smoothed background to yield the peak deviation for four different QAD radii. Dashed line: Cubic smoothing spline performed on the solid line with points.

Figure 1 (inset) shows a typical conductance trace obtained in our experiment. At low fields ($B < 0.7$ T) a clear aperiodicity of order 0.01T can be seen by eye in the positions of some peaks. By looking at a gray scale plot of many traces taken for different gate voltages we can see which peaks belong to which LL - peaks in different LLs move at different angles [8]. We can then find the aperiodicity in the peaks by removing a smoothed background. Figure 1 shows the result of analyzing the spectra of four different dot radii (gate voltages) similar to the inset. Although an oscillatory signal can be seen in all traces, experimental conditions and noise do not permit the comparison of too many traces at one time. We see, at low fields, a strong oscillatory signal which aligns well with the experimental bulk SdH measurement. At higher fields noise swamps the oscillatory signal.

In order to quantify our observation, we now consider in detail the effect of the oscillation of the Fermi energy within a simple model of our system. Our model comes in two parts: the QAD and the bulk properties. The QAD: There is no simple way to determine the selfconsistent potential profile of a QAD in a magnetic field [7,11] particularly in light of the recent development that a strong magnetic field is likely to produce steps in the effective potential [12-15]. For our purposes a reasonable guess is sufficient: $V(B) = V_0(B) \exp(-r^2/\sigma^2(B)) - E_f(B)$, $V_0(B) = V_0 + (E_f(B) - E_f(0))$ and $\sigma(B) = \sigma(0) + \alpha(1 - \pi r^2 \rho_{total}(E_f(B))) / m^2$. This choice reflects the experimental fact that the 2DEG is earthed and the gate voltage which determines V_0 in the depleted region is measured with respect to this zero. It assumes that the 'height' of the dot $V_0(B)$ is determined by $E_f(B)$ and the 'shape' of the dot, $\sigma^2(B)$, is determined by $\rho_{total}(E_f(B))$ the total density of states at the Fermi energy [7]. α is a small coupling constant. We use this potential in the single particle Schrödinger equation to determine the magnetic field positions at which bound states in the first

LL pass the Fermi energy and therefore for inter-edge state scattering to lead to transmission resonances [8]. The oscillation in period is a small effect and therefore we can fit approximate values for the parameters V_0 and $\sigma^2(0)$ by comparing the experimental peak positions with the above model. We find very good fits for values $V_0 = 65\text{-}100\text{ meV}$ (for gate voltages in the region $-0.27V - -0.3V$) and $\sigma = 1.22\text{ nm}$. It is interesting to note that the usual semiclassical $\Delta B A = \hbar/e$ is a poor approximation when compared to the quantum mechanical solution for this QAD.

The Bulk: We calculate the oscillation of the Fermi energy and density of states by solving: $\rho_{\text{total}}(E) = eBh\sum_{n_s}(\Gamma/\pi(\Gamma^2 + (E - E_{n_s})^2))$ with $n_s = \int_0^{E_F} \rho_{\text{total}}(E)dE$ constant (for a review of the theory of the quantum Hall effect see [16]). The sums are over $s=\pm 1, n=0, 1, \dots, \infty$, $E_{n_s} = (n+1/2)\hbar\omega_c + 1/2sg\mu_B B$ and $g = 0.44$, the bare spin splitting. In order to find the parameters n_s and Γ we can fit the experimental SdH oscillations using the approximate relation $\rho_{xx} \propto \rho_{\text{trans}}(E_f(B))n_s = \text{const.}$ The transport density of states has the form $\rho_{\text{trans}}(E) = \sum_{n_s} -\partial/(E - E_{n_s})/\partial E$, where f is the Fermi-Dirac distribution evaluated at the nominal temperature of the device $\approx 50\text{ mK}$. Within this model Γ determines the apparent spin splitting and n_s determines the period in $1/B$. We find a good fit to the experimental ρ_{xx} with $\Gamma = 0.007\text{ meV}$, $n_s = 3.05 \times 10^{15}\text{ m}^{-2}$. Figure 2a shows the calculated oscillation in peak positions assuming $\sigma^2(B) = \sigma^2(0)$ (i.e. pure E_f oscillation) together with $E_f(B)$. Figure 2b shows the calculated oscillation assuming $V_0(B) = V_0$ (i.e. pure oscillation in screening) together with $\rho_{\text{total}}(E_f)$. Figure 2c shows a combination of the two effects with the

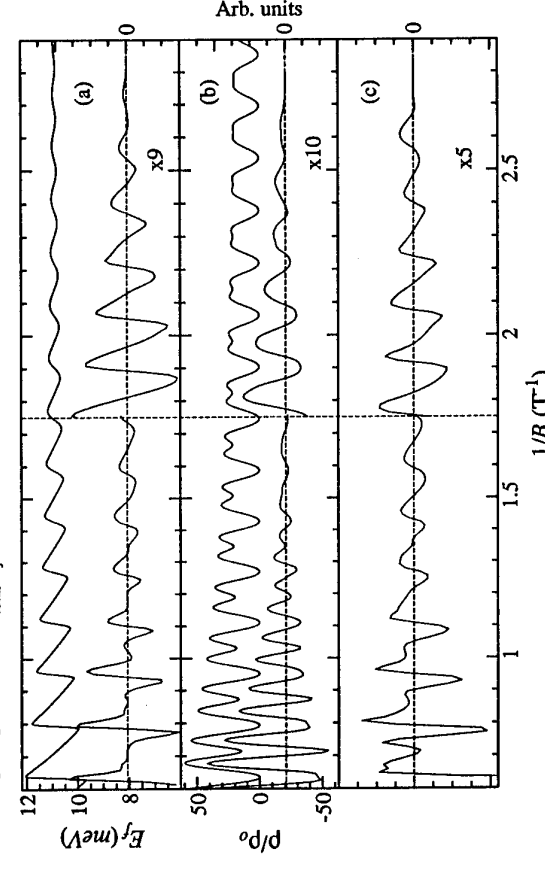


Figure 2 (a) Upper line: Oscillation of E_f . Lower line: Aperiodicity in model peak positions for QAD subject to pure E_f oscillation. (b) Upper line: Oscillation of E_f . Lower line: Aperiodicity in model peak positions for QAD subject to pure screening oscillation. (c) The aperiodicity for a combination of (a) and (b) using $\alpha=0.2$. In all three cases, the calculated aperiodicity was determined using the same method for as that used for experiment (figure 1). For case (c) we use four different QAD radii.

arbitrary choice $\alpha = 0.2$.

Low field: The shape of the oscillations can readily be compared (figures 1 and 2). However, our simple model imposes an aperiodicity an order of magnitude greater than that measured experimentally. A more thorough understanding of the effective QAD potential will be necessary to resolve this.

High field: At high fields the numerical results predict extreme oscillations which are not born out experimentally. The pure E_f oscillation shows flat regions separated by very sharp peaks at even integer filling factors. The closest experiment comes to matching this behaviour in our analysis of a number of different QADs is to perhaps generate enhanced noise near these positions separated by flat regions. The explanation for the absence of the density of states oscillation can be seen in the inset in figure 1. It shows a linear increase in spin splitting with magnetic field [8]. Measurements of this type of oscillation in high field show that the spin-splitting is caused by the coulomb interaction between neighbouring states with different spins bound to the QAD [17,18]. Such coulomb interaction is only strong when it is not screened by a neighbouring body of electrons. Our explanation is therefore that the screening of the QAD potential decreases as the increasing cyclotron energy pulls electrons away from the QAD.

Summary: We have detected an oscillation in the period of the AB oscillations of a QAD which aligns with the bulk SdH oscillations. We have performed numerical calculations which show that the result is consistent with the oscillation of the Fermi energy and the concomitant oscillation of the density of states. We acknowledge C. Mayeux and D. Arquey for technical support and the UK EPSRC and ESPRIT basic research action 6556 for financial support.

References

- [1] M. I. Kaganov, I. M. Lifshitz and K. D. Sinehnikov, Sov. Phys. JETP **5** 500 (1957).
- [2] L. Landau Z. Phys. **64** 629 (1930).
- [3] D. Schoenberg, 'Magnetic oscillations in metals', Camb. Univ. Press (1984).
- [4] V. M. Pudalov, S. G. Semenchinskii and V. S. Edel'man, Sov. Phys. JETP **62** 1079 (1985); V. M. Pudalov, S. G. Semenchinskii and V. S. Edel'man, JETP Lett. **39** 576 (1984); V. M. Pudalov, S. G. Semenchinskii and V. S. Edel'man, JETP Lett. **41** 713 (1984); V. M. Pudalov, S. G. Semenchinskii and V. S. Edel'man, JETP Lett. **41** 325 (1985).
- [5] A. M. Dabiran, R. T. Zeller, F. F. Fang, S. L. Wright and P. J. Stiles A. M. Dabiran, Surf. Sci. **196** 712 (1988).
- [6] T. P. Smith, B. B. Goldberg and P. J. Stiles, Phys. Rev. B **34** 2995 (1986).
- [7] T. Ando, A. B. Fowler, F. Stern, Rev. Mod. Phys. **54** 437 (1982).
- [8] D. R. Mace, C. H. W. Barnes, G. Faini, D. Mailly, M. Y. Simmons, M. Pepper, To be published.
- [9] P. J. Simpson, D. R. Mace, C. J. B. Ford, I. Zeller, M. Pepper, D. A. Ritchie, J. E. F. Frost, M. P. Grinshaw and G. C. Jones, Appl. Phys. Lett. **63** 3191 (1993).
- [10] R. P. Taylor, J. A. Adams, M. Davies, P. A. Marshall and R. Barber, J. Vac. Sci. Technol. B **11** 628 (1993).
- [11] J. H. Davies, I. A. Larkin, E. V. Sakhnenko, J. Appl. Phys. **77** 4504 (1995).
- [12] A. M. Chang, Solid State Commun. **74** 871 (1990).
- [13] D. B. Chklovskii, B. I. Shklovskii and L. I. Glazman, Phys. Rev. B **46**, 4026 (1992).
- [14] K. Leir and R. R. Gerhardt, Phys. Rev. B **50** 7757 (1994).
- [15] M. Stopa, Private communication.
- [16] M. Jansen, O. Viehweger, U. Fastenrath and J. Hajdu, 'Introduction to the theory of the integer quantum Hall effect', VCH Verlagsgesellschaft mbH (1994).
- [17] R. P. Taylor, Y. Feng, A. S. Sachrajda, J. A. Adams, M. Davies, P. T. Coleridge and P. Zawadski, Surf. Sci. **263** 247 (1992); R. P. Taylor, A. S. Sachrajda, P. Zawadski, P. T. Coleridge and J. A. Adams, Phys. Rev. Lett. **69** 1989 (1992); A. S. Sachrajda, R. P. Taylor, C. Dharma-Wardana, P. Zawadski, J. A. Adams and P. T. Coleridge, Phys. Rev. B **47** (1993).
- [18] C. J. B. Ford, P. J. Simpson, I. Zeller, J. D. F. Franklin, C. H. W. Barnes J. E. F. Frost, D. A. Ritchie and M. Pepper, Phys. Rev. B **49** 17456 (1994).

Many-electron Magnetococonductivity in 2D Electrons on Liquid Helium

P J Richardson ^a, A Blackburn ^b, K Djerfi ^a, M I Dykman ^c, C Fang-Yen ^d,
P Fozzani ^a, A Kristensen ^a, M J Lea ^a and A Santrich-Batista ^a

^a Physics Department, Royal Holloway, University of London, TW20 0EX, UK.

^b Department of Electronics and Computer Science, Southampton University, SO17 1BJ, UK.

^c Department of Physics and Astronomy, Michigan State University, Michigan 48824, USA.

^d Department of Physics, Stanford University, Stanford, California 94305 , USA.

Abstract

The magnetoconductivity $\sigma(B)$ of nondegenerate two-dimensional electrons on superfluid helium was measured and calculated below 1 K in fields B up to 8 Tesla. The results show that the internal electric fields from electron-electron interactions strongly influence $\sigma(B)$ in the 2D electron fluid. This internal field strength is in good agreement with Monte Carlo simulations. The magnetococonductivity increases at the transition to the 2D solid phase.

Introduction

Experimentally the simplest possible conductor is a sheet of nondegenerate two-dimensional (2D) electrons, density n , on the surface of superfluid helium. They can have higher mobilities μ than any solid state conductor and are a prime example of a strongly interacting system. The ratio of the Coulomb energy to the kinetic energy, the plasma parameter $\Gamma = e^2(\pi n)^{1/2}/4\pi e\hbar kT \gg 1$, there is short-range order in the electron system and, for $\Gamma > 127$, a 2D electron crystal forms. A fundamental question is the extent to which these interactions influence the conductivity. It is now known that fluctuating internal electric fields, magnitude E_f , control the diffusion of cyclotron orbits and hence the magnetoresistivity $\rho(B)$ [1] and magnetoconductivity $\sigma(B)$ [2]. We present new measurements of $\sigma(B)$ below 1 K in the electron fluid (see [3] for some previous work), and obtain values of E_f , in good agreement with Monte Carlo simulations. The transition to the 2D solid is also observed.

Experimental

The magnetococonductivity was measured using a 4 mm diameter Corbino disk (see figure 1) made by optical lithography at the Southampton University Microelectronics Centre [2]. A central electrode **A** was surrounded by a ring **E** which separated the annular receiving electrode **B** into three segments **B1**, **B2** and **B3**, all enclosed by a guard electrode **G**. Electrons were produced by glow discharge and held on the helium surface (typically 50 μm above the electrodes) by DC potentials. The gaps in the electrode pattern were only 10 μm so the electron sheet was very homogeneous. An AC voltage V_0 (typically 1 - 10 mV) at a frequency f ($= \omega/2\pi$) between 2 and 70 kHz was applied to electrode **A** and $\sigma(B)$ was obtained from the phase of the AC current to electrode **B**. The electron density was found from the -ve DC bias voltage on electrode **E** needed to "cut-off" this current.

The Drude Region

In low fields, $B < 0.5$ T, the data for $\sigma(B)$ follow the simple Drude-like result, even for classically strong fields with $\mu B \leq 500$,

$$\sigma(B) = \frac{\sigma(0)}{1 + (\mu B)^2} \quad (1)$$

where $\sigma(0) = ne\mu$. The mobility μ was obtained from the B^2 dependence of $\sigma^{-1}(B)$ [4] in good agreement with measurements at $B = 0$ by Mehrotra *et al* [5]. The mobility is density dependent because the vertical electric pressing field, and the electron-ripplon coupling, increases with density. Figure 1 shows measurements of $ne/\mu\sigma(B)$ versus B for several densities, using the experimental μ values. In the Drude region, the data all lie on the line, $ne/\mu\sigma(B) = B^2$ (line **a**).

Initially, these results seem to confirm a single-particle approach to magnetoconductivity. In fact they come about through electron-electron interactions. First, the many-electron correlation time is less than the relaxation time τ from scattering by He vapour atoms and ripplons [6]. This changes the averaging over the Boltzmann distribution and, for the energy-dependent ripplon interaction, decreases the mobility, compared to independent electrons, in satisfactory agreement with experiment. The agreement of the experimental μ values in zero and classically strong ($\mu B \gg 1$) fields implies that the relaxation rate is independent of magnetic field, $\tau^{-1}(0) = \tau^{-1}(B)$ even where Landau level quantisation (energy spacing $\hbar\omega_c$, $\omega_c = eB/m$ is the cyclotron frequency) might be expected to change the density of states and the scattering rate for quasi-elastic scattering. But the fluctuating internal electric field E_f produces an energy uncertainty $eE_f kT$ over an electronic thermal wavelength λ_T and, for $kT \gg eE_f kT > \hbar\omega_c$, smears out the Landau levels. This also holds for $eE_f R_c > \hbar\omega_c$ ($R_c = \sqrt{2mkT/eB}$ is the classical cyclotron orbit radius), which corresponds to $B < B_o$, an onset field for deviations from the Drude model (typically 0.2 to 1 Tesla). The Drude model is followed because of the internal electric fields, and the many-electron theory gives $ne/\mu\sigma = B^2$ for $\mu B \gg 1$, independent of n , in this region.

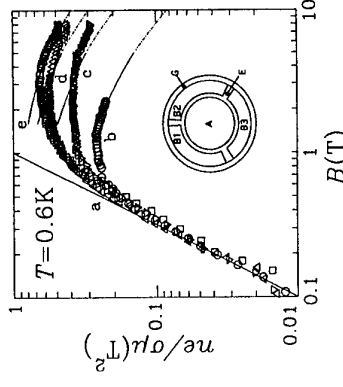


Figure 1. $ne/\mu\sigma$ versus B for $n = 0.51$ (**b**), 1.21 (**c**), 1.60 (**d**) and 2.07 (**d**) $\times 10^{12} \text{ m}^{-2}$. The lines show the many-electron theory. Inset: Corbino disk electrodes.

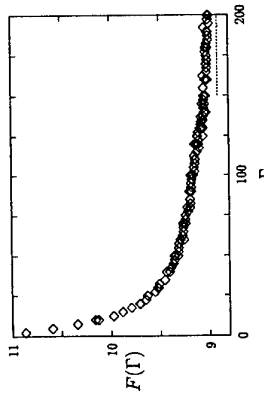


Figure 2. The many-electron internal field scaling function $F(\Gamma)$ from Monte Carlo calculations.

Many-electron magnetocconductivity

A distinctive feature in Figure 1 is that the conductivity saturates above the Drude region. Moreover, the plots of $n\sigma_1(B)$ are then density and temperature dependent. The energy uncertainty $eE_f E_C < \hbar\omega_c$ and the scattering rate $\tau^{-1}(B)$ is enhanced by a density of states factor $\approx \hbar\omega_c/eE_f E_C = B^2/B_0^2$. Hence we find [7]

$$\frac{n\sigma}{\mu_0 B} = K\pi B_0^2, \quad (2)$$

where K is a dimensionless factor, depending on the scattering mechanism. For short range scattering, such as ${}^4\text{He}$ atoms, $K \equiv K_g(\hbar\omega_c/kT)$ reflects the change in the cyclotron orbit radius, and hence the diffusion length, from R_c for $\hbar\omega_c/kT \ll 1$, $K_g = 1$, to the magnetic length, $l = (\hbar/eB)^{1/2}$ for $\hbar\omega_c/kT \gg 1$, $K_g = 4(\hbar\omega_c/kT)^{-1/2}\pi$. For ripplons $K \equiv K_r$ depends on $\hbar\omega_c/kT$ in the same way but the interaction strength also changes with field as the dominant scattering ripplon wavelength is proportional to the cyclotron orbit radius. This extra factor is numerically close to unity in these experiments. Thus, for $\hbar\omega_c/kT = 1.34$, $B/T \gg 1$, $n\sigma_1(B)$ decreases with field as seen in Figure 1 above 2 Tesla. An important conclusion is that, above the Drude region, $\sigma_1(B)$ is proportional to the internal electric field E_f .

The internal electric field

For a classical electron fluid with thermal fluctuations, the mean-square internal electric field has a nearly Gaussian distribution and can be written as

$$E_f^2 - \langle E_f^2 \rangle = \frac{n^2 k T}{4\pi e_0} F(\Gamma) = E_0^2 F(\Gamma) \quad (3)$$

where E_0 sets the scale for the internal field strength. The dimensionless function $F(\Gamma)$ is plotted in Figure 2, from Monte Carlo computer simulations [8], for $10 < \Gamma < 200$. The variation of F is surprisingly small, given that the structure changes dramatically from a crystal to a liquid with short-range correlations. In the harmonic crystal, Γ can be calculated analytically as 8.91 (dashed line).

The magnetocconductivity was calculated using the many-electron theory for $\hbar\omega_c > kT$, using the internal fields from Figure 2, as shown in Figure 1 for several densities at 0.6 K. As B increases the data cross over from the many-electron low field theory (equivalent to the Drude model, line a) to the density dependent behaviour, eq. (2) (lines b, c, d and e).

Conversely, the measured $\sigma_1^{-1}(B)$, at $B = 2$ Tesla, was used to obtain experimental values of the internal electric field E_f as plotted in Figure 3 versus E_0 from eq.(3). The points come from over 40 combinations of density and temperature at 0.6 and 0.9 K. Within the errors the measured field $E_f = vE_0$ with $v = 3.11 \pm 0.10$ in close agreement with $v = \sqrt{F} = 3.07 \pm 0.03$ from the Monte Carlo calculations for $20 < \Gamma < 70$.

The 2D electron solid

At lower temperatures, the 2D electron system forms a classical solid below $T_m = 0.216 \times 10^{-6} n^{1/2}$ K. The zero-field mobility decreases at the transition [5] but little is known about the magnetotransport. Hysteresis in the highly non-linear magnetoconductivity has been interpreted as shear-induced melting [9] or the decoupling of the crystal from commensurate “dimples” in the helium surface [10]. Figure 4(a) shows $\sigma_1^{-1}(B)$ in the fluid at 0.25 K, (good agreement with eqs(1) and (2)) and in the solid at 0.1 K for $n = 0.80 \times 10^{12} \text{ m}^{-2}$ ($T_m = 0.19$ K), assuming that the phase shifts are due to magnetoconductivity (i.e. neglecting Lorentz force coupling to shear modes in the crystal). The many-electron $\sigma(B)$ is not expected to change substantially at the transition from a highly correlated fluid to a crystal for comparatively high

fields where $2\pi^{1/2}\hbar\omega_l/m\omega_c \ll 1$ [7, 11]. This is seen in Figure 4(b) where the change in $\sigma_1^{-1}(B, T)$ in low fields corresponds to a change in mobility [5], though the B^2 Drude region is no longer clear experimentally at 0.1 K. However at higher fields the transition (at the same T_m) is much less pronounced. The many-electron theory must now be extended to include the region where the electron motion in the field created by the other electrons is quantum, and the field E_f is non-uniform over the electron wavelength.

This work was supported by the EPSRC, UK, and EU Contract CHRXCT 930374.

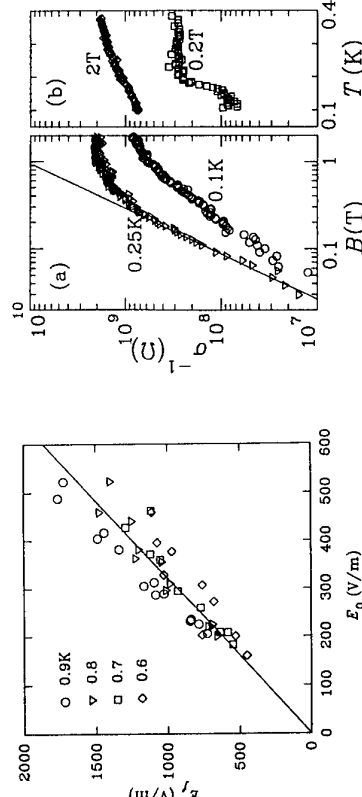


Figure 3. The internal field E_f , measured for a range of electron densities at 0.6, 0.7, 0.8 and 0.9 K, versus the reference field E_0 .

References

- [1] M.I.Dykman, M.J.Lea, P.Fozooni and J.Frost, *Phys.Rev.Lett.* **70**, 3975 (1993).
- [2] M.J.Lea, P.Fozooni, P.J.Richardson and A.Blackburn, *Phys.Rev.Lett.* **73**, 1142 (1994).
- [3] Yu.Z.Kovdyra et al., J.Low Temp.Phys. **91**, 371 (1993); J.Neunenschwander, W.Joss and P.Wyder, *Helv.Phys.Acta* **65**, 325 (1992); *Physica B* **194 - 196**, 1231 (1994).
- [4] Y.Iye, *J.Low Temp.Phys.* **40**, 441 (1980).
- [5] R.Méntriva, C.J.Guo, Y.Z.Ruan, D.B.Mast and A.J.Dahm, *Phys.Rev. B* **29**, 5239 (1984).
- [6] M.Saitoh, *J.Phys.Soc.Japan* **42**, 201 (1977); *Solid State Commun.* **52**, 63 (1984); V.A. Buntar' et al., *J.Low Temp.Phys.* **79**, 323 (1990).
- [7] M.I.Dykman and L.S.Rhazan, *Zh.Eksp.Teor.Fiz.* **77**, 1488 (1979) [*Sov.Phys.JETP*, **50**, 747 (1979)]; M.I.Dykman, *J.Phys.C* **15**, 7397 (1982). M.I.Dykman et al. to be published.
- [8] M.I.Dykman and C.Fang-Yen, to be published.
- [9] L.Wilen and R.Giametta, *J.Phys.Soc.Japan* (1988)
- [10] K.Shirahama and K.Kono, *Phys.Rev.Lett.* **74** (1995) 781.
- [11] M.Saitoh, *J.Phys.Soc.Japan* **56** (1987) 706.

Interplay of Landau Band Width and Band Separation in a Square Lateral Superlattice

T. Schlösser, K. Ensslin, and J. P. Kotthaus
Sektion Physik, LMU München, D-80539 München, Germany

M. Holland

Dept. of Electronics, University of Glasgow, United Kingdom

A laterally modulated gate electrode is evaporated on high-mobility two dimensional electron systems embedded in GaAs-AlGaAs heterostructures. At small lateral potential modulation of square geometry as induced by a suitable gate voltage commensurability oscillations dominate the low-field magnetoresistance indicating the oscillating width of the Landau bands. For increasing potential modulation the width of the Landau bands increases, the band contributions to the conductivity are suppressed and scattering conductivity dominates reflecting our beginning to resolve the internal structure of a Landau band.

Introduction

In a magnetic field the energy spectrum of a homogeneous two-dimensional electron gas (2DEG) splits up into Landau levels whose width is determined by the single particle life time of the carriers. If a laterally periodic potential modulation is superimposed onto the 2DEG the Landau levels transform into Landau bands [1] that are theoretically expected to have a rich internal energy spectrum in the two-dimensional case [2]. At low magnetic fields commensurability oscillations have been observed in the magnetoresistance [3]. Landau bands generally oscillate as a function of center coordinate leading to a finite group velocity and therefore to a band contribution to the conductivity. At flat band condition the Landau band width vanishes explaining the observed minima in the conductivity. To the best of our knowledge there is no convincing experiment so far that unambiguously demonstrates additional subbands and gaps within one Landau band. [2] In this paper we present experimental data that clearly exhibits suppression of band conductivity for increasing potential modulation. We argue that this is caused by our beginning to resolve the internal structure of the Landau bands eventually leading to additional substructure superimposed on the maxima of the Shubnikov-de Haas oscillations.

Small Potential Modulation

The AlGaAs/GaAs heterojunctions containing a 2DEG only 36 nm below the surface were grown by molecular beam epitaxy. At liquid He temperatures the 2DEG has a mobility $\mu = 400$ cm²/Vs and a carrier density $N_s = 5 \times 10^{11}$ cm⁻², corresponding to a mean free path of $\ell = 4.7$ μ m and a Fermi wavelength of $\lambda_F = 35$ nm. A Hall bar geometry is defined by wet chemical etching with an area of $20 \mu\text{m} \times 8 \mu\text{m}$ between the voltage probes, i.e. dimensions that are larger than the elastic and inelastic mean free path. With electron beam lithography a resist layer on the sample surface is suitably exposed and developed to create a lattice of voids and then covered by an evaporated gate metal. Since the 2DEG is so close to the sample surface this gives us the unique possibility to induce lateral superlattices with periods as small as 80 nm and relatively large potential modulation.

We study square superlattice devices with periods of 205 nm, 139 nm, 105 nm and 80 nm. In the following we will concentrate on the sample with $a = 139$ nm because there the compromise

between small lattice periods and moderate potential modulation is best achieved and the observed effects are most pronounced. However, the main features are also observed on the other short period samples.

With low current levels (≤ 10 nA) we measure the magnetoresistance of the samples immersed in the mixing chamber of a dilution refrigerator at a bath temperature of 30 mK as exemplified in Fig. 1 (a). For low magnetic fields commensurability oscillations occur that are superimposed by SdH oscillations. The vertical dashed lines indicate the condition where the Landau bands are flat [1]. In this case the Landau bands have no dispersion leading to a vanishing band conductivity and therefore to a minimum in the resistance. The amplitude of the Shubnikov-de Haas (SdH) oscillations generally increases with magnetic field B (see envelopes). It is obvious from Fig. 1 (a), however, that the SdH amplitudes are especially large in the minima of the lower envelope, i.e. at flat band. Scattering contributions to the conductivity essentially resemble the density of states. For flat Landau bands the gaps between the Landau bands widen and one expects large contributions of the scattering conductivity. The amplitude of the SdH oscillations is thus a qualitative measure for the Landau gap and therefore for the width of the Landau bands. We like to mention here that we can detect well defined commensurability oscillations down to magnetic fields of 0.1 T corresponding to a classical cyclotron diameter as large as 12 lattice periods. This indicates the homogeneity of our sample as well as of the fabrication process.

Medium Potential Modulation

Figure 1 (b) displays experimental results for the magnetoresistance for $V_g=0$ which leads to a larger potential modulation. The envelopes of the SdH oscillations are indicated by dashed lines. The positions of the minima of the lower envelope experimentally defines flat band condition for all three cases of potential modulation (Fig. 1 (a)-(c)). The envelope connecting the maxima shows minima at flat prediction (vertical dashed lines) [1]. The envelope connecting the maxima shows minima at flat band for low magnetic fields going over to maxima at high magnetic fields. This is an indication that the importance of scattering conductivity increases with increasing magnetic field [1,4]. In comparing the results presented in Fig. 1 (a) and (b) it is obvious that the contributions of scattering conductivity to the total conductivity increases for increasing potential modulation as the amplitude of the SdH oscillations becomes especially large at flat band.

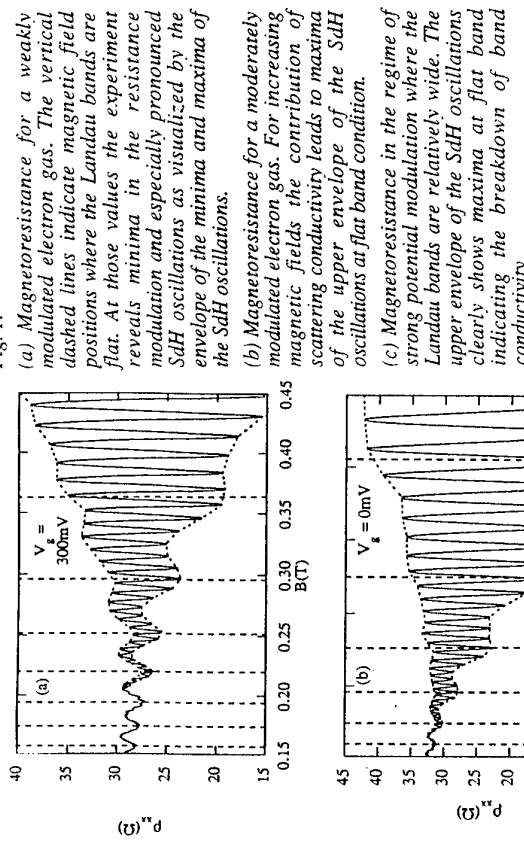
Strong Potential Modulation

At $V_g = -200$ mV (see Fig. 1 (c)) band conductivity is completely suppressed and the maxima of the upper envelope of the SdH oscillations clearly lie at flat band condition as marked by the vertical dashed lines. The features of the upper envelope, however, show a continuous transition from minima to maxima at flat band. We argue that the suppression of band conductivity is caused by the beginning resolution of the internal structure of the Landau bands. [1] In order to illustrate this effect more clearly Fig. 2 shows only the envelopes of the SdH maxima plotted as a function of classical cyclotron diameter covering typically two lattice constants in this regime. For strong potential modulation (lowest curve) a maximum is observed at flat band (vertical dashed line) indicating the dominance of scattering conductivity. For decreasing potential modulation the maximum shifts to larger values of $2R_C$ as indicated by the solid line finally leaving a minimum close to the flat band condition which resembles the band conductivity contributions.

In general band conductivity as well as scattering conductivity contribute to the commensurability oscillations. The extreme cases however, clearly show that for weak potential modulation band conductivity dominates (Fig. 1(a)) and for strong potential modulation scattering conductivity (Fig. 1(c)) takes over.

It is important to note that the suppression of band conductivity is observed for increasing potential modulation in contrast to Ref. [4] where band conductivity was detected to vanish for increasing mobility and decreasing potential modulation. In our case the mobility as deduced

Fig. 1:

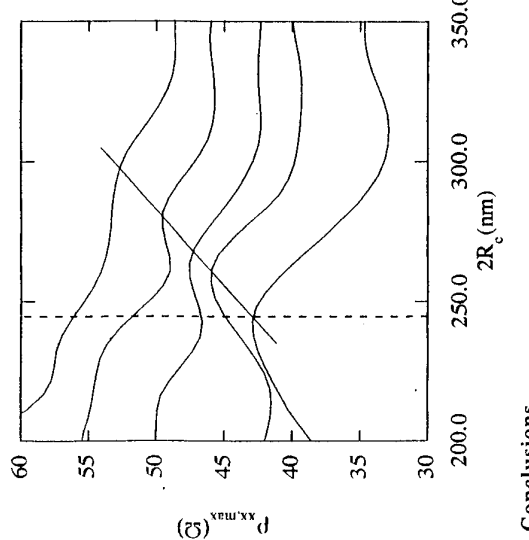


from the zero field resistance hardly changes in our set of data as presented in Fig. 1(a)-(c). The collision broadening of minibands within a Landau band should therefore hardly change in the regime of interest. We argue that the likelihood for the resolution of the internal structure of a Landau band improves for increasing band width which generally increases with increasing potential modulation.

We like to mention that we observe additional structure superimposed on the maxima of the SdH oscillations for very strong potential modulation close to the antidot regime. Silberbauer and Rössler [6] showed that the energy spectrum of a realistic antidot potential is very complicated and that the Landau bands may strongly overlap and mix. It is not

clear in our sample how the exact potential looks like and it is difficult to predict how the coupling of the Landau bands [7] might influence the various subbands and gaps. Electron-electron interactions may further complicate the experimentally detectable bandstructure. The fact, however, that I/B periodic SdH oscillations can be resolved in the experiment indicates that the terminology of Landau bands is basically still valid.

Fig. 2: Envelope of the SdH maxima as a function of classical cyclotron diameter for various values of the potential modulation as tuned by a gate voltage from lowest trace $V_g = -200 \text{ mV}$ to uppermost trace $V_g = +200 \text{ mV}$ with $\Delta V_g = 100 \text{ mV}$.



Conclusions

The magnetic field dependent width of Landau bands in a lateral superlattice leads to pronounced oscillations in the magnetoresistance of such systems. Our experiments demonstrate the breakdown of bandconductivity for increasing potential modulation indicating our beginning to resolve the internal structure of a Landau band.

We are grateful to the Deutsche Forschungsgemeinschaft and the ESPRIT Basic Research Action for financial support.

References

- [1] D. Piankache and R. R. Gerhardts, Phys. Rev. B46, 12606 (1992)
- [2] D. Langbein, Phys. Rev. B14, 2239 (1976)
- [3] D. Weiss, K. v. Klitzing, K. Ploog, and G. Weimann, Europhys. Lett. 8, 179 (1989).
- [4] W. Winkler, J. P. Kotthaus, and K. Ploog, Phys. Rev. Lett. 62, 1177 (1989), E. S. Alyes, P. H. Beton, M. Henini, L. Eaves, P. C. Main, O. H. Hughes, G. A. Toombs, S. P. Beaumont, C. D. W. Wilkinson, J. Phys. C1, 8257 (1989)
- [5] D. Weiss, A. Mensching, K. v. Klitzing, and G. Weimann, Surf. Sci. 263, 314 (1992), for a review see R. Schuster and K. Ensslin, Advances in Solid State Physics 34, 195 (1994), Springer, Berlin
- [6] H. Silberbauer and U. Rössler, Phys. Rev. B50, 11911 (1994)
- [7] G. Petschelt and T. Geisel, Phys. Rev. Lett. 71, 239 (1993)

The Unifying Role of Effective Field in the Composite Fermion Model of the Fractional Quantum Hall Effect

D.R. Leadley*, M. van der Burgt*, R.J. Nicholas*, P.J. Gee*, J. Singleton*,
J.J. Harris* and C.T. Foxon†

*Department of Physics, Clarendon Laboratory, Parks Road, Oxford, OX1 3PU

†Department of Electronics and Electrical Engineering, University College, London

#Department of Physics, Nottingham University, University Park, Nottingham NG7 2RD

Fractional Quantum Hall Effect measurements in 50T pulsed magnetic fields, are analysed in the Composite Fermion (CF) model. Energy gaps of all fractions in the principal series around $v=1/2$ show a simple, sample independent, increase with the CF effective field following $\sqrt{B^*}$. The spin polarised state at $v=5/3$ follows exactly the same behaviour, but for mixed spin states like 4/3 the energy gap collapses when $B^*>1\text{T}$.

The Fractional Quantum Hall Effect (FQHE) may be neatly described by a model of composite Fermions (CFs) formed by a gauge transformation [1]. This is equivalent to attaching pairs of flux quanta ($\Phi_0=\hbar/e$) to each electron in a partially filled Landau level (LL). At even denominator filling factors like $v=1/2$ these CFs see zero magnetic field and away from such points they move in an effective magnetic field $B^*=B-2\Phi_0/\ell_e$, which is the resultant of the gauge and external fields. All the observed FQHE features may be interpreted as the Integer QHE of the CFs in the effective field, without reference to the strong underlying many body interactions. The experiments reported in this paper show that the single parameter B^* unifies the observations from all the fractions across all the samples we have studied. This represents a major advance over the hierarchical model where each filling factor had to be considered separately.

By treating the FQHE features in ρ_{xx} as CF Shubnikov-de Haas oscillations, we previously used the Ando formula to obtain values for the CF effective mass M^* and the energy gap E^* between CF LLs in very high mobility, low density, GaAs-GaAlAs heterojunctions [2]. We have now extended this work to higher magnetic fields using higher electron density samples, with a ^3He cryostat in 50T pulsed fields giving the large range of B/T required to obtain accurate mass values. Details of these heterojunctions grown by MBE at Philips Research Laboratories are given in Table 1.

Fig. 1 Resistivity of samples G627 and G902 showing FQHE at the highest fields yet observed.

Figure 1 shows the temperature evolution of the FQHE features for: (a) sample G627 where $v=1/3$ is seen at 38T and the well developed 2/7 at 45T is the highest field FQHE has been observed; (b) sample G902 which is the highest electron density sample yet studied with $v=2/3$ at 30T. This figure shows that FQHE states survive to very high magnetic fields in much the same form as at lower fields, but can then be observed at much higher temperatures.

The temperature variation of the resistance oscillations are fitted to the Ando formula [3] to extract values of M^* , taking care only to consider those oscillations that are approximately sinusoidal. In practice we chose a temperature range for each feature such that $\Delta\rho/p<0.5$. Figure 2 shows the results as a function of n_e for several different fractions. There is no unique n_e dependence covering all fractions. Instead the mass values fall in pairs, corresponding to states with a common numerator p , e.g. 2/3 and 2/5. These have equal numbers of occupied CF Landau levels, but occur on either side of $v=1/2$ with effective fields in opposite senses. This provides a simple demonstration of the symmetry of their states about $v=1/2$, consistent with the CF model rather than that of particle-hole conjugation where states of common denominator q (e.g. 1/3 and 2/3) look similar. In the low density limit all states tend to the same effective mass, but the lower index CF Landau levels show an increasing "non-parabolicity". By $n_e=3\times 10^{15}\text{m}^{-2}$ the effective masses for $v=1/3$ and $v=2/5$ differ by approximately 40%, while the masses for $v=2/3$ and $v=2/5$ differ by less than 5%. Furthermore the gradients of each line on Fig. 2 follow accurately a $1/p$ dependence. The CF mass may then be given by $M^*=0.510+0.35n_e/p$, in units of the free electron mass m_e , with n_e in 10^{15}m^{-2} . Since $B^*=\Phi_0\rho_e/B$ this shows there is no additional dependence on n_e other than that produced by the effective field.

Accordingly, M^* is shown as a function of the effective field in Fig. 3a, where data from a large number of different fractions and from samples with densities varying by an order of magnitude all lie on the single dashed line

$$M^* = (0.510 \pm 0.015) + (0.083 \pm 0.005)B^*, \quad (1)$$

which is the same approximately linear increase seen earlier at low fields [2].

Again there is no noticeable difference (m_e) between data taken from either side of $v=1/2$ showing that the sign of B^* is not important. The data show that there is a simple functional dependence of the CF mass on the single parameter B^* , covering more than a factor of 25 variation of B^* . At the highest effective field $M^*=1.6m_e$, which represents an increase of $\sim 200\%$ over our range of B^* , and a factor of 24 enhancement over the GaAs band edge mass.

CF4 WEDNESDAY

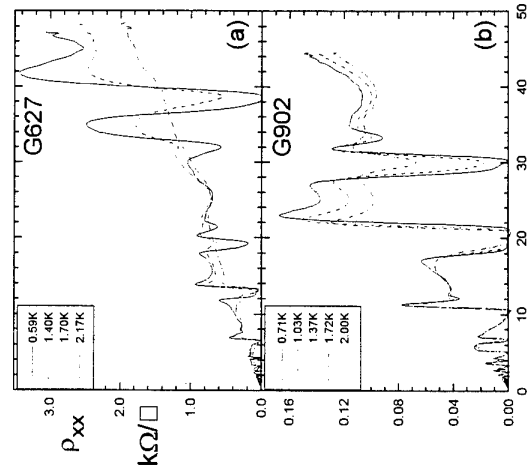


Fig. 1 Resistivity of samples G627 and G902 showing FQHE at the highest fields yet observed.

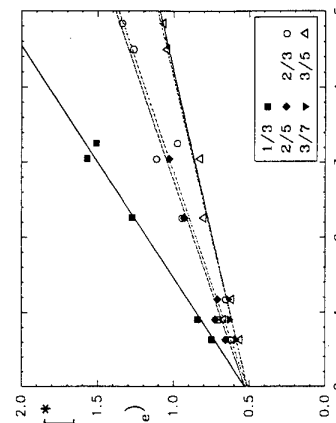


Fig. 2 CF effective mass as a function of density for different fractions p/q . The fitted lines have gradients $\propto 1/p$.

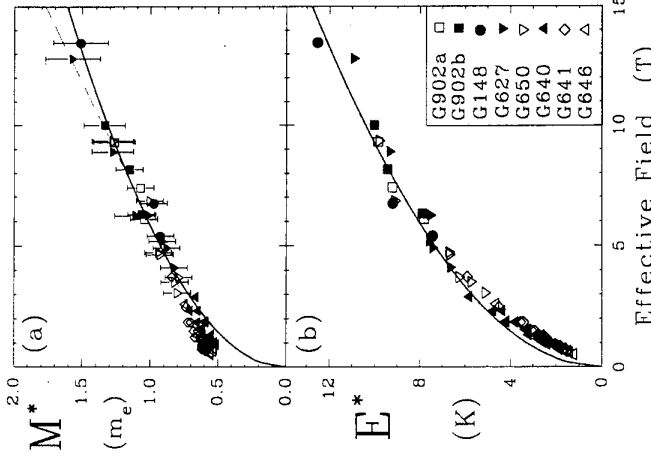


Fig. 3 (a) CF effective mass and (b) energy gap as a function of B^* . The dashed line is a linear fit of the mass data and the solid lines are a fit to \sqrt{B} .

The FQHE is the result of a many body Coulomb interaction and so theoretically the energy gap may be written $\Delta = C_v e^2 / (4\pi \epsilon_0 l_0)$, which gives rise to a \sqrt{B} dependence for both the energy gap and mass *for any given fraction* through l_0 the cyclotron radius, proportional to the interparticle spacing. Since $B^* = B/(1-2v)$ there will also be a $\sqrt{B^*}$ dependence for a given fraction. C_v is however different for each v so previously energy gaps had to be shown following separate \sqrt{B} curves for each fraction [4]. However our data clearly shows that although there is not a single functional dependence on n_e (and hence B^*) covering *all* fractions, when we use B^* a single dependence does cover *all fractions and all densities*. In this spirit the data of Fig. 3b has been fitted to $E^* = \alpha/\sqrt{B^*}$ and we find a good fit to the high field data (solid line) with $\alpha = 3.3(±0.2)KT^{-1/2}$. This $\sqrt{B^*}$ dependence may be related to the Coulomb interaction between CFs via the effective cyclotron radius $l^* = (l_0/\epsilon_0 B^*)^{1/2}$, in which we have effectively ignored the presence of all filled CF levels in determining the inter (composite) particle spacing. This is reasonable because the orthogonality of CF wavefunctions means there will only be strong interactions between CFs of the same LL. Below about 2T the energy gap is smaller than predicted by the strict square root behaviour, as can be seen clearly in the mass plot Fig. 3a. So although the high field data can be described quite well with a $\sqrt{B^*}$ dependence, this breaks

The measurement of M^* is equally a measurement of the CF cyclotron energy since $E^* = \hbar e B^*/M^*$. In fact it is the ratio kT/E^* (independent of B^*) that determines the oscillation amplitudes so we could regard the energy gap as the more fundamental quantity, with M^* being a consequence of the model considering CFs in an effective field. Unlike activation energy measurements which only give the gap between extended state regions, the method used here directly probes the energy difference between the centres of the CF LLs. In Fig. 3b we show E^* as a function of the effective field for all the samples. With $B^* = 1/4$ T there is an energy gap of 12K for the 1/3 fraction, allowing FQHE features to be seen at quite high temperatures. It is again remarkable how plotting E^* against the effective field yields a single curve for all samples and all fractions considering both maxima, minima and either sense of B^* . By contrast plotting the gap against external field shows no such orderly behaviour. Thus we make our claim that the Composite Fermion effective magnetic field is the single parameter that unifies all the experimental Fractional Quantum Hall Effect data.

The FQHE is the result of a many body Coulomb interaction and so theoretically the energy gap may be written $\Delta = C_v e^2 / (4\pi \epsilon_0 l_0)$, which gives rise to a \sqrt{B} dependence for both the energy gap and mass *for any given fraction* through l_0 the cyclotron radius, proportional to the interparticle spacing. Since $B^* = B/(1-2v)$ there will also be a $\sqrt{B^*}$ dependence for a given fraction. C_v is however different for each v so previously energy gaps had to be shown following separate

down as $v=1/2$ is approached. In the low field region our original description of the data with a linearly increasing mass remains far more accurate and still adequately describes the high field behaviour, so from a purely empirical point of view this provides the most general description.

In addition we have studied the FQHE features between $v=1$ and 2, where both spin states of the lowest LL may be occupied [5]. In this region the number of CFs changes with the LL degeneracy as the external field is changed, but the effective field is still given by B/g . Energy gaps for these fractions deduced from the Ando formula are shown in Fig. 4, using data from several samples measured in a dilution refrigerator and 1.5T superconducting magnet. At low B^* all the fractions exhibit the *same* 2 $>v>1$ showing the collapse of 4/3. The line represents the $v<1$ data of Fig. 3b.

universal behaviour as seen earlier for $v<1$ and shown by the line in Fig. 4. Thus we conclude initially that all first generation CFs behave the same whether they emanate from 1/2 or 3/2. However, while the gap for $v=5/3$ continues to increase to the highest fields measured at exactly the same rate as for the fractions around $v=1/2$, the gap at 4/3 collapses for $B^* > 1.5$ T. This is consistent with earlier observations of 4/3 disappearing on sample rotation [6], which also increases the Zeeman energy, and strengthening at high pressure where the g-factor is reduced [7]. Interpreting this in the CF model, we deduce that the excitation at 5/3 is always a spin preserving cyclotron transition between CF LLs and so not affected by the Zeeman energy, whereas for 4/3 this is only true at low effective field. As the Zeeman energy is increased LLs from the two spin states cross and reduce the energy gap for 4/3. The rotation experiments also show 4/3 reappearing at high angles, which suggests that at higher B^* the states may again uncross and restore a cyclotron like gap.

In conclusion measurements of M^* in pulsed magnetic fields of up to 50T show the same linear increase with effective magnetic field that we found earlier at low fields. The CF cyclotron energy increases sub-linearly with B^* and a single $\sqrt{B^*}$ behaviour describes the high field data. The results strongly support the Composite Fermion interpretation of the FQHE and show the effective field B^* to be a parameter that unifies the data for all fractions and all samples. For CFs formed around $v=3/2$ the behaviour of the energy gap depends on the state's spin polarisation.

- [1] J.K. Jain, *Adv. Phys.* **41** 105 (1992).
- [2] B.I. Halperin, P.A. Lee and N. Read, *Phys. Rev. B* **47** 7312 (1993)
- [3] D.R. Leadley, R.J. Nicholas, C.T. Foxon and J.J. Harris, *Phys. Rev. Lett.* **72** 1906 (1994)
- [4] T. Ando, *J. Phys. Soc. Jpn.* **37** 1233 (1974)
- [5] V. Kukushkin, N.J. Pulsford, K. von Klitzing, K. Ploog, R.J. Haug, S. Koch and V.B. Timofeev, *Europhys. Lett.* **18** 63 (1992)
- [6] D.R. Leadley, R.J. Nicholas, P.J. Gee, J. Singleton, C.T. Foxon and J.J. Harris, in *The Physics of Semiconductors*, p983 Ed D.J. Lockwood (World Scientific, Singapore, 1995).
- [7] R.G. Clark, S.R. Haynes, A.M. Stuckling, J.R. Mallett, P.A. Wright, J.J. Harris and C.T. Foxon, *Phys. Rev. Lett.* **62** 1536 (1989)
- [8] N.G. Morawietz, K. Barnham, A. Briggs, C.T. Foxon, J.J. Harris, S.P. Najda, J.C. Portal and M.L. Williams, *Semicond. Sci. Technol.* **8** 333 (1993)

Composite fermions around Landau level filling factor $\nu = 3/2$

R.R. Du^{**}, A.S. Yeh^{*}, H.L. Stormer^{*}, D.C. Tsui^{*},
L.N. Pfeiffer^{*}, and K.W. West^{*}

^{*}Princeton University, Princeton, N.J. 08540
^{**}AT&T Bell Laboratories, Murray Hill, N.J. 07974
^{*}University of Utah, Salt Lake City, UT 84112

Abstract

Our magneto-transport experiments on a low-density two-dimensional electron sample detect an alternating strength of the fractional quantum Hall effect (FQHE) states around Landau level filling factor $\nu=3/2$ as the magnetic field is moving away from $\nu=3/2$. It is viewed as a manifestation of spin-split levels of composite fermions around $\nu=3/2$. A cyclotron effective mass $m^*_d \sim 0.4 m_o$ (where m_o is the free electron mass) of composite fermions around $\nu=3/2$ is deduced from Shubnikov-de Haas oscillations in a tilted ($\theta=73^\circ$) magnetic field. This value is found to be in keeping with a mass of $m^*_d \sim 0.7 m_o$ determined around $\nu=1/2$ in the same sample once the $B^{1/2}$ -dependence is taken into account.

1. Introduction

The composite fermion model [1,2] has been very successful in interpreting the experimental data on higher-order states $\nu=p/(2p\pm 1)$ in the fractional quantum Hall effect (FQHE) [3] around Landau level filling factor $\nu=1/2$. These states are being viewed as the integer quantum Hall effect (IQHE) [3] of composite particles consisting of electrons to which two magnetic-flux quanta $\Phi_0=\hbar/e$ have been attached by virtue of the electron-electron interaction. Quite remarkably, activation energy measurements [4] and Shubnikov-de Haas (SdH) data [5,6] in this filling factor regime can be interpreted largely as resulting from Landau quantization of a fermion with a mass m^*_d about ten times the band electron mass, m_b , in GaAs.

These experiments around $\nu=1/2$ have so far conformed to a scheme of spin-polarized composite fermions. At the next higher half-filling $\nu=3/2$ the lower spin state of the lowest electron Landau level is totally occupied, whereas its upper spin state is half filled. Naively, one may regard $\nu=3/2$ as the upper-spin version of the well studied, down-spin $\nu=1/2$ state expecting to interpret the surrounding FQHE states in terms of Landau levels of spin-polarized composite fermions formed at $\nu=3/2$. Our recent activation energy and SdH experiments however, do not agree with a picture of spin-polarized composite fermions around $\nu=3/2$.

Specifically, our experiments in low-density samples detect an alternating strength of the FQHE states around $\nu=3/2$ as one moves away from $\nu=3/2$. The alternation is reminiscent of the alternation seen between spin-gaps and cyclotron-gaps in the IQHE around zero magnetic fields. Our angular dependent magneto-transport measurements on the FQHE states around $\nu=3/2$ are explained very effectively in terms of a composite fermion model complemented by a spin degree of freedom [7]. These experiments establish that the composite fermions around $\nu=3/2$ form spin-split "Landau levels". While the "Landau splitting" scales with *effective* magnetic field, having its origin at $\nu=3/2$, the spin-splitting scales with *total* external magnetic field having its origin at $B=0$.

2. Experiment

Our sample is a high-mobility GaAs-AlGaAs heterostructure. The specimen has electron density $n=1.1 \times 10^{11}/\text{cm}^2$, and mobility $\mu=6.8 \times 10^6 \text{ cm}^2/\text{Vs}$. Such density and mobility are achieved after a brief illumination from a light-emitting diode at low temperature. The specimen is a 5mm by 5mm square with eight Indium contacts placed around the edges. Magneto-transport experiments were performed in a top-loading Oxford ^3He - ^4He mixture dilution refrigerator in a 20 Tesla superconducting magnet. Both the sample and a calibrated RuO_2 resistor thermometer are immersed in the liquid of the mixture. A standard low-frequency (3-7 Hz) lock-in technique is employed for resistance measurement.

3. Results and discussion

The Magneto-resistance around $\nu=3/2$ at temperature $T=40 \text{ mK}$ is shown in Fig. 1. The resolution of many FQHE states at fields as low as 3 T attests to the high quality of the specimen. The fractional filling factor (marked near the resistance structures) $\nu=n\hbar/eB$ is calculated from the electron density n and magnetic field B .

Remarkably, the magneto-resistance reveal an *alternating strength* of the FQHE states around $\nu=3/2$. *Even-numerator* states are consistently weaker than their *odd-numerator* successors. For example, the $\nu=10/7$ minimum is evidently weaker than its neighboring $\nu=7/5$ and $\nu=13/9$ minima. The FQHE state at $\nu=14/9$ is very weak rendering the resistance as a maximum. This pattern also applies to the stronger states at $\nu=5/3$, $8/5$, and $11/7$ at higher temperatures (not shown here). This is in sharp contrast to the SdH oscillation around $\nu=1/2$ in the same sample, where the amplitudes decrease monotonically towards zero magnetic field [5].

The alternation is reminiscent of the alternation seen between spin-split Landau levels of electrons, the spin-split gap (given by the Zeeman energy $g^* \mu_h B$, where g^* is the effective g-factor and μ_h a



Fig. 1. Magneto-resistance of low-density, two-dimensional electron system around Landau level filling factor $\nu=3/2$ at 40 mK.

Bohr magneton) is considerably smaller than the cyclotron gap $\hbar eB/m_b$, giving rise to the alternating strength of magneto-resistance minima at finite temperatures.

Earlier experiments [8,9] in this filling factor regime, published prior to the composite fermion model, clearly indicated the impact of the electron spin on the FQHE states around $v = 3/2$. Generalizing from the $v = 8/5$ state and $v = 4/3$ state (both are considered to be spin-unpolarized), we may expect that the alternation is caused by an alternation of spin-polarized (or partially-polarized) and un-polarized states around $v = 3/2$. In terms of the composite fermion model, the alternation is a manifestation of spin-split “Landau levels” around $v = 3/2$ [7].

Applying a strong in-plane magnetic field will polarize the composite fermion system. Experimentally this is achieved by tilting the magnetic field away (tilt angle θ) from normal. We expect that at very high tilt angles the ground states of the FQHE around $v = 3/2$ should be largely spin-polarized, and the SdH oscillations should conform to those around $v = 1/2$. It is thus possible (and necessary) to determine the cyclotron effective mass of composite fermions around $v = 3/2$ at a high tilt angle.

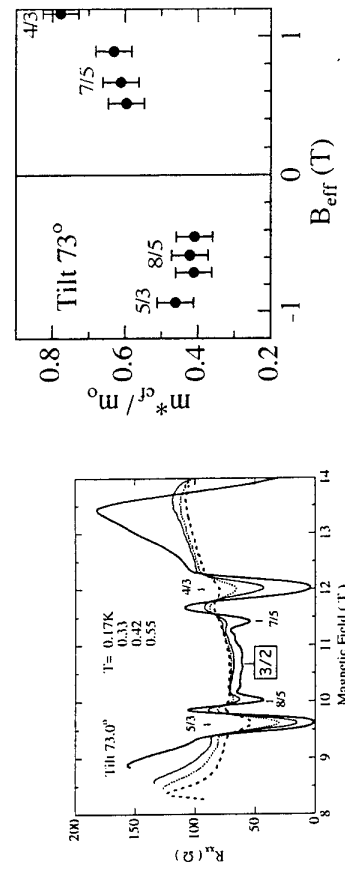


Fig. 2. Magneto-resistance around $v = 3/2$ at several T at a tilt angle $\theta = 73^\circ$.

The composite fermion mass is deduced from the T -dependence (From 0.07 to 0.6 K) of SdH oscillations (representatives are shown in Fig.2) around $v = 3/2$, at $\theta = 73^\circ$. The angle θ is determined from the $\cos\theta$ shift of prominent features in the data which defines the perpendicular field, $B_{\perp} = B \cos\theta$. At this tilt angle, the SdH amplitudes decrease monotonically towards half-filling, where the effective field seen by the fermions is zero.

Exploiting the correct electron-hole symmetry in the lowest Landau level (taking into account the spin degree of freedom), we regard the FQHE states at filling factor around $v = 3/2$ as the $v' = (2-v)$

states around $v = 3/2$ are equivalent to IQHE states of fermions of mass m^*_d originating from $v = 3/2$. These fermions see an effective magnetic field $[2] B_{\text{eff}} = 3(B_{\perp} - B_{\perp,3/2})$.

The amplitude of the SdH oscillation around $v = 3/2$ at this high tilt angle follow very well the traditional sinh-dependence of the SdH formalism $\Delta R/R_o = A_r/\sinh A_r \times 4 \exp(-\pi i/\omega_c \tau)$ with $A_r = 2\pi^2 kT/\hbar \omega_c$, once the magnetic field is replaced by B_{eff} in the cyclotron energy $\hbar \omega_c$ [5]. The effective mass m^*_d so determined are plotted against the effective field B_{eff} in Fig.3.

We observe a mass of $m^*_d \sim 0.4 m_o$ for negative B_{eff} whereas the masses for positive B_{eff} are considerably higher, $m^*_d \sim 0.6 m_o$. Inspection of the level diagram of composite fermions around $v = 3/2$ indicates that only for the states at $v = 5/3$ and $8/5$ does the energy gap represent a pure “Landau level splitting” $\hbar B_{\text{eff}} / m^*_d$, all other FQHE states in Fig. 3 represent combinations of “Landau splitting” and spin-splitting. For this reason, these gaps are reduced and the associate masses appear to be enhanced. The most reliable determination of the mass is made at $v = 8/5$, yielding $m^*_d = 0.42 m_o$. As compared to $v = 5/3$, this fraction is not affected by amplitude distortion around $v = 7/4$. The mass value of $m^*_d = 0.42 m_o$ is in keeping with a mass of $m^* \sim 0.7 m_o$ determined around $v = 1/2$ in the same sample once the $B^{1/2}$ -dependence is taken into account.

In conclusion, magneto-resistances around $v = 3/2$ reveal an alternating strength of the FQHE states. The alternation is a manifestation of spin-split levels of composite fermions around $v = 3/2$. A cyclotron effective mass of $m^*_d = 0.42 m_o$ is deduced from the spin-polarized composite fermion state.

4. References

- [1] J. K. Jain, Phys. Rev. Lett. 63, 199 (1989); Phys. Rev. B40, 8079 (1989); 41, 7653 (1990).
- [2] B. I. Halperin, P. A. Lee, and N. Read, Phys. Rev. B47, 7312 (1993).
- [3] R. E. Prange and S. M. Girvin, Eds.; The Quantum Hall Effect (Springer, New York, 1990).
- [4] R. R. Du, H. L. Stormer, D. C. Tsui, L. N. Pfeiffer, and K. W. West, Phys. Rev. Lett. 70, 2944 (1993).
- [5] R. R. Du, H. L. Stormer, D. C. Tsui, L. N. Pfeiffer, and K. W. West, Phys. Rev. Lett. 70, Communication 90, 71 (1994).
- [6] D. R. Leadley, R. J. Nicholas, C. T. Foxon, and J. J. Harris, Phys. Rev. Lett. 72, 1906 (1994).
- [7] R. R. Du, A. S. Yeh, H. L. Stormer, D. C. Tsui, L. N. Pfeiffer, and K. W. West, “The Fractional Quantum Hall Effect around $v = 3/2$: Composite Fermions with a Spin”, submitted to Phys. Rev. Lett.
- [8] J. P. Eisenstein, H. L. Stormer, L. N. Pfeiffer, and K. W. West, Phys. Rev. Lett. 62, 1540 (1989).
- [9] R. G. Clark, S. R. Haynes, A. M. Suckling, J. R. Mallett, P. A. Wright, J. J. Harris, and C. T. Foxon, Phys. Rev. Lett. 62, 1536 (1989).

Magnetoexciton Luminescence at 1/3 Landau Filling as a Function of Electron-Hole Separation

Francis Bitter National Magnet Lab, Massachusetts Institute of Technology
Cambridge, MA 02139

F. Plenz, D. Heiman

A. Pinczuk, L.N. Pfeiffer, K.W. West
AT&T Bell Laboratories Murray Hill, NJ 07974

The luminescence spectrum of magnetoexcitons in a 2D electron system in GaAs/AlGaAs is studied as a function of electron-hole separation, h , which is varied by applying front- and back-gate voltages. For Landau filling, $v < 1$ the energy splitting between the doublet components *decreases* for increasing h . For $v = 1/3$ two regimes are observed — at small h the upper component has a positive-going cusp, while for larger h a positive-going step is observed. This may be related to charge fractionalization associated with anyon excitons consisting of three quasielectrons and a valence band hole.

Optical experiments in high magnetic fields are useful for studying several aspects of electron-electron correlations in 2D electron systems that are not accessible with conductivity experiments. Both photoluminescence (PL) [1-6] and inelastic light scattering [7,8] measurements have been used to investigate correlations leading to formation of the incompressible liquid associated with the fractional quantum Hall effect. In the case of PL arising from the recombination of dressed excitons — composed of a photoexcited valence hole that carries with it an electronic polarization charge — several distinguishing characteristics have been observed. For $v < 1$ Landau filling, a doublet structure is observed in the PL spectrum, having a peculiar temperature dependence in which the upper peak only appears at lower temperatures.[1,3] For $v = 1/3$, experimental results show a transfer of intensity from the lower energy component (L-peak) to the upper energy component (U-peak).[4,5,9] and a *positive-going cusp* in the energy. Subsequent time-resolved PL measurements related the intensity transfer to a reduction in electron-hole (e-h) overlap.[9]

Recent theoretical work indicates that a key parameter in determining the behavior of the magnetoexciton PL is the separation, h , between the electrons and the photoexcited holes, scaled by the magnetic length.[10-13] In the case of charge symmetric systems, corresponding to $h=0$ and equal charge distributions for the electrons and holes, no anomaly in the energy is expected to occur at $v=1/3$.[10,11] This is a manifestation of the hidden symmetry inherent to the system. Even though no energy shift is predicted, there is a spread of charge distribution around the hole and the magnetoexciton dispersion relation becomes flatter.[11] In the case of charge asymmetric systems, the perturbation of the hole on the electron-electron correlations is reduced and the energy is expected to show a shift at $v=1/3$. A strong dependence of the emission spectra on the charge asymmetry parameter h is predicted. In the regime of the incompressible quantum fluid, we expect the formation of anyon excitons (AE), a multiparticle complex composed of a valence band hole and a number of quasiparticles.[14] The major problem in experimentally accessing AE formation is controlling the e-h separation. This problem has not yet been addressed.

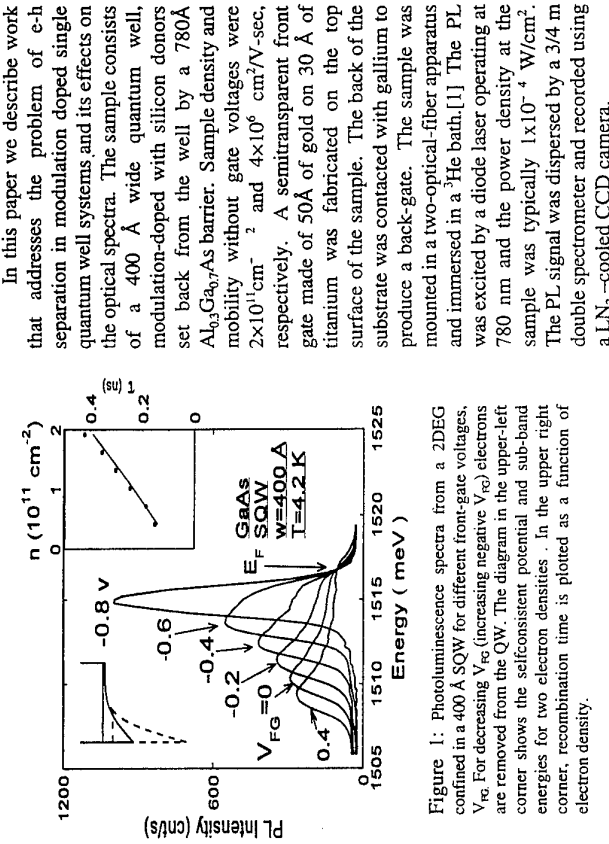


Figure 1: Photoluminescence spectra from a 2DEG confined in a 400 Å SQW for different front-gate voltages, V_{FG} . For decreasing V_{FG} (increasing negative V_{BG}) electrons are removed from the QW. The diagram in the upper-left corner shows the selfconsistent potential and sub-band energies for two electron densities. In the upper right corner, recombination time is plotted as a function of electron density.

Electron-hole separation was controlled either by applying an electric field through the use of a back-gate voltage, or by changing the built-in selfconsistently Hartree potential by changing the electron density using a front-gate. In Fig. 1 we show how the PL spectra at $B=0$ changes as a function of a voltage applied to the front gate, V_{FG} . For decreasing V_{FG} (increasing negative V_{BG}), the overall width of the PL decreases. The peak on the low-energy side, corresponding to the band edge minima, moves to higher energies, while the high-energy cutoff at the Fermi edge remains fixed. The spectral changes can be understood from the diagram in the upper-left inset, showing the potentials and subband energies calculated selfconsistently. For higher electron density, shown by the dashed curves, the larger Hartree potential lowers the subband energy. An increased Hartree potential produces an increased electric field that separates the electrons and holes — the electrons are pushed to the left and the hole wavefunction is pushed to the right. This increased e-h separation is revealed in the measured radiative recombination time (τ) through the reduced e-h overlap. The upper-right inset shows τ as a function of electron density, n , determined from the Fermi energy. The solid curve is the result of a selfconsistent calculation and good fit is achieved using a single scaling parameter. Note that a large increase in the recombination time is observed as n increases. Since τ^{-1} is proportional to the e-h overlap squared, it is clear that electrons and holes move apart as a consequence of the enhancement in the built-in electric field generated by the excess of charge that moves into the well. A study of electric-field-induced e-h separation can be found in Ref. 15. Results at $v=1/3$ Landau filling are shown in Fig. 2. Here, two PL peaks are evident. In these spectra a positive back-gate voltage of $V_{BG}=0.128$ V is applied to push the electrons and holes

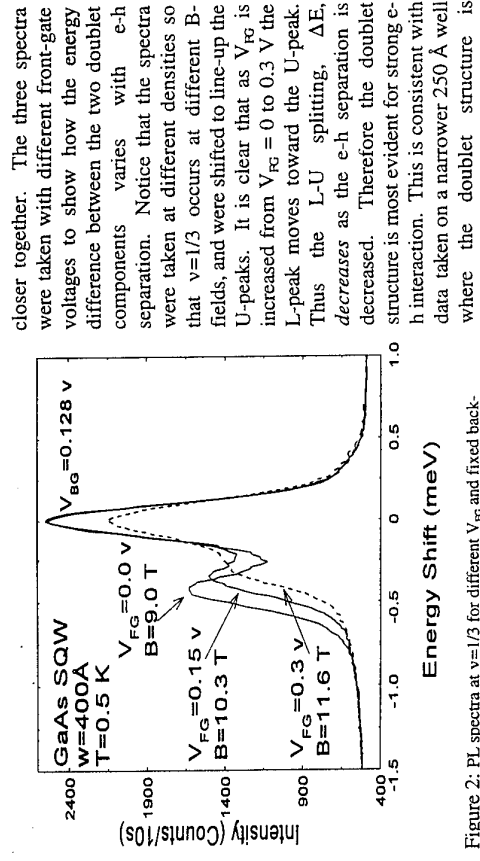


Figure 2. PL spectra at $v=1/3$ for different V_{FG} and fixed back-gate voltage. For larger V_{FG} , i.e., higher electron density and e-h separation, the L-peak moves towards U-peak.

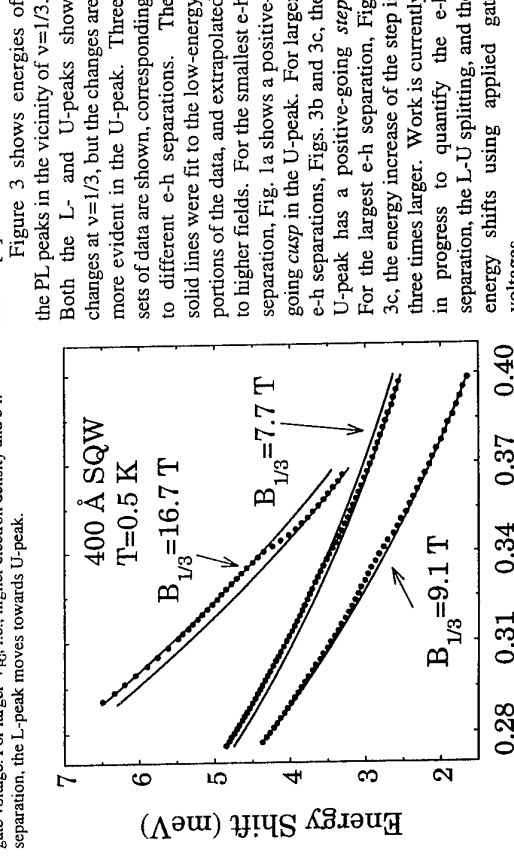


Figure 3. U-peak energy versus filling factor in the $v=1/3$ region. The electron hole separation increases from (a) to (b) to (c). Curves were shifted in energy for clarity. Solid lines are linear fits to the high filling factor portion of each curve.

closer together. The three spectra were taken with different front-gate voltages to show how the energy difference between the two doublet components varies with e-h separation. Notice that the spectra were taken at different densities so that $v=1/3$ occurs at different B-fields and were shifted to line-up the U-peaks. It is clear that as V_{FG} is increased from $V_{FG} = 0$ to 0.3 V the L-peak moves toward the U-peak. Thus the L-U splitting, ΔE , decreases as the e-h separation is decreased. Therefore the doublet structure is most evident for strong e-h interaction. This is consistent with data taken on a narrower 250 Å well where the doublet structure is robust.[9]

Figure 3 shows energies of the PL peaks in the vicinity of $v=1/3$. Both the L- and U-peaks show changes at $v=1/3$, but the changes are more evident in the U-peak. Three sets of data are shown, corresponding to different e-h separations. The solid lines were fit to the low-energy portions of the data, and extrapolated to higher fields. For the smallest e-h separation, Fig. 1a shows a positive-going cusp in the U-peak. For larger e-h separations, Figs. 3b and 3c, the U-peak has a positive-going step. For the largest e-h separation, Fig. 3c, the energy increase of the step is three times larger. Work is currently in progress to quantify the e-h separation, the L-U splitting, and the energy shifts using applied gate voltages.

The character of the optical transitions is shown to be related to the electron-hole separation. Due to the extra degrees of freedom

introduced by attaching more than one charged particles to the valence hole, the anyon exciton has a multibranch structure. What branch forms the ground state depends fundamentally on the separation between the electron and hole 2D layers. In the case of $v=1/3$ for small e-h separation, $h \lesssim 1$, the ground state is the branch L_0 . Two characteristics of that branch are a larger spread of charge density around the hole and a much "flatter" dispersion relation. This is the so-called "dressed exciton". As the h increases, an upper branch L_0 falls below the L_0 branch and becomes the ground state of the quasiparticle-hole complex. That branch describes an anyon exciton, a complex of a valence hole with three quasiparticles attached to it, two on an inner shell and one in an outer shell. This behavior can be understood as follows. When $h < 1$ the perturbation of the positive charge on the 2D electron system is strong enough to locally overcome the electron-electron correlations. Although the FQHE gap goes to zero in the vicinity of the hole, the build up of charge around it gives rise to a broader distribution due to the weaker polarizability of the underlying fluid. In the case where $h > 1$, real quasiparticles can be attached to the hole and an anyon exciton forms. This leads to a larger effective Bohr radius, a smaller binding energy and an upward shift of the peak energy.

The authors would like to thank E.I. Rashba for helpful conversations. The work was supported by the National Science Foundation grant DMR-9201614. F.P. acknowledges support from the Brazilian agency CNPq. The Francis Bitter Magnet Lab. is supported by the NSF.

References

- [1] D. Heiman, *Laser Spectroscopy of Semiconductors*, Vol. 36, Semiconductors and Semimetals, eds. C. Little and D.G. Seiter (Academic Press, 1992), p. 1; and references cited therein.
- [2] C.H. Perry, J.M. Worlock, M.C. Smith, and A. Petrou, *High Magnetic Fields In Semiconductor Physics*, ed. G. Landwehr (Springer-Verlag, 1987) p. 202.
- [3] D. Heiman, B.B. Goldberg, A. Pinczuk, C.W. Tu, A.C. Gossard, and J.H. English, Phys. Rev. Lett. **61**, 605 (1988).
- [4] A.J. Turberfield, S.R. Haynes, P.A. Wright, R.A. Ford, R.G. Clark, J.F. Ryan, J.J. Harris, and C.T. Foxon, Phys. Rev. Lett. **65**, 637 (1990).
- [5] B.B. Goldberg, D. Heiman, A. Pinczuk, L.N. Pfeiffer, K.W. West, Phys. Rev. Lett. **65**, 64 (1990).
- [6] H. Buhmann, W. Joss, K. von Klitzing, I.V. Kukushkin, G. Martinez, A.S. Plaut, K. Ploog, and V.B. Timofeev, Phys. Rev. Lett. **65**, 1056 (1990).
- [7] A. Pinczuk, B.S. Dennis, D. Heiman, C. Kallin, L. Brey, C. Tejedor, S. Schmitt-Rink, L.N. Pfeiffer, and K.W. West, Phys. Rev. Lett. **68**, 3623 (1992).
- [8] A. Pinczuk, B.S. Dennis, L.N. Pfeiffer, and K.W. West, Phys. Rev. Lett. **70**, 3983 (1993).
- [9] D. Heiman, A. Pinczuk, M. Dahl, B.S. Dennis, L.N. Pfeiffer, and K.W. West, Surf. Sci. **305**, 50, (1994); and Physica B **201**, 315 (1994).
- [10] A.H. MacDonald, E.H. Rezayi, and David Keller, Phys. Rev. Lett. **68**, 1939 (1992).
- [11] V.M. Apalkov and E.I. Rashba, Phys. Rev. B**46**, 1628 (1992); and *ibid.* **48**, 18312 (1993).
- [12] B.S. Wang, J.L. Birman, Z.B. Su, Phys. Rev. Lett. **68** (1992) 1605.
- [13] X.M. Chen and J.J. Quinn, Phys. Rev. B**50**, 2354 (1994).
- [14] E.I. Rashba and M.E. Portnoi, Phys. Rev. Lett **70**, 3315 (1993).
- [15] F. Plentz, D. Heiman, A. Pinczuk, L.N. Pfeiffer, and K.W. West, Phys. Rev. B (1995).

Josephson Phenomena in Bi-Layer Quantum Hall Systems

ZYUN FRANCIS EZAWA

Department of Physics, Tohoku University, Sendai 980, Japan

Abstract

In certain bi-layer quantum Hall systems it is shown that an interlayer phase coherence develops spontaneously due to a strong interlayer electron correlation. It leads to various Josephson phenomena but for the Meissner effect. The Josephson frequency in the DC-voltage circuit is eV/h , as reflects the condensation of bosonic composite electrons in the quantum Hall state.

1. Introduction

We analyze bi-layer quantum Hall (BLQH) systems at the Landau level filling factor $\nu = 1/m$ with m an odd integer. When the interlayer distance d is nearly equal to the magnetic length $\ell_B (= 1/\sqrt{eB_\perp})$, where $d \approx \ell_B \approx 10\text{nm}$, it is shown [1, 2, 3] that an interlayer quantum coherence is spontaneously developed and induces various Josephson phenomena. We use the *composite electron* picture to derive an effective Hamiltonian describing these dynamics. See also related works in different approaches [4, 5]. Our results read:

- (A) The Josephson effect occurs but the Meissner effect does not.
- (B) The Josephson frequency in the DC-voltage circuit is eV/h , as reflects the condensation of bosonic composite electrons in the quantum Hall state.
- (C) The system has two phases, the commensurate (C) and incommensurate (IC) phases, as a function of the parallel magnetic field $B_{||}$ applied externally.
- (D) The low lying excitation modes are the plasmon excitations in each of these phases.
- (E) The parallel magnetic field actually penetrates the junction rather freely in the C phase as sine-Gordon vortices because the screening effect is extremely small. The energy of plasmons emitted from the vortices decreases rapidly as a function of $B_{||}$. The size of the vortex is 250nm in a typical sample.
- (F) The activation energy anomaly found at Bell Lab [6] in a BLQH system can be accounted for by the plasmon excitations based on this picture.

2. Interlayer Quantum Coherence

Since no intrinsic spin-statistics relation exists in planar systems, the statistics of the electron may be altered externally. This can be done explicitly by making *composite electrons*, which are electrons bound to statistics flux. When the statistics flux cancels the external magnetic flux in the mean-field sense, composite electrons acquire a physical reality. Indeed, when the filling factor is $\nu = 1/m$ with m an odd integer, they become bosons and undergo a bose condensation. This is the fractional quantum Hall state [7, 1].

Let us analyze a BLQH system based on this picture. We label two electron fields ψ_f^x by the layer index x ($= 1, 2$). The composite electron fields ψ^x and the statistics gauge field a_k are defined by $\psi^x \equiv \exp[i\chi]\psi_f^x$ and $a_k = \partial_k\chi$, respectively, where $\chi(x)$ is the phase field defined by

$$\chi(x)[\{x_r^1\}; \{x_p^2\}] = m(\sum_r \theta(x - x_r)[\{x_r^1\}; \{x_p^2\}]) + \sum_p \theta(x - x_p)[\{x_r^1\}; \{x_p^2\}], \quad (1)$$

in the basis $[\{x_r^1\}; \{x_p^2\}]$ with the electron positions diagonalized. Eq.(1) gives rise to

$$\varepsilon_{ij}\partial_i a_j(x) = 2\pi m(\rho^1(x) + \rho^2(x)), \quad (2)$$

where ρ^α is the electron density in each layer. The fields $a_k(x)$ and $\chi(x)$ are not dynamical since they are determined by this constraint equation. Examining the commutation relation the composite electrons are found to be bosons for an odd integer m .

The momentum operator of the composite electron is $P_k^\alpha = i\partial_k + a_k - eA_k$. Hence, it follows that $\langle P_k^\alpha \rangle = i\partial_k$ when $\langle a_k(x) \rangle = eA_k(x)$. Due to eq.(2) this mean-field solution is possible when the sum of the electron distributions is uniform ($\rho_0 \equiv \langle \rho^1 \rangle + \langle \rho^2 \rangle$ =constant) at the filling factor $\nu \equiv 2\pi\rho_0/eB_\perp = 1/m$. (Note that $\varepsilon_{ij}\partial_i A_j = B_\perp$.) In this case the statistics flux cancels the external magnetic flux, and composite electrons do not feel the external magnetic field. Being bosons, they undergo a condensation:

$$\langle \psi^\alpha(x) \rangle = \sqrt{\langle \rho^\alpha \rangle} e^{i\theta}, \quad (3)$$

where $\langle \rho^1 \rangle \neq \langle \rho^2 \rangle$ in general. These are the BLQH states [1] realized at $\nu = 1/m$. There are many BLQH states corresponding to the interlayer density difference $\Delta\rho \equiv (\rho^1 - \rho^2)/2$. These states are mixed among themselves by a weak interlayer tunneling interaction.

The phase difference θ is the canonical conjugate to the density difference $\Delta\rho$, with $\langle \theta \rangle = \theta_1 - \theta_2$. The effective Hamiltonian is given by [3]

$$\mathcal{H} = \frac{1}{2}\rho_s(\partial_k\theta)^2 + \frac{2\pi e^2 d}{\varepsilon}(\Delta\rho)^2 - \Delta_{\text{SAS}}\sqrt{\rho_0^2 - (\Delta\rho)^2} \cos\theta. \quad (4)$$

The first term of the r.h.s. is the kinetic energy of the interlayer phase field. Here, $\rho_s \approx 0.32\text{ K}$ is obtained by a microscopic analysis [5]. The second term is the electric capacitance energy, and the last term is the tunneling interaction term with Δ_{SAS} the gap energy between the one-particle symmetric and antisymmetric states ($\Delta_{\text{SAS}} \approx |K|$).

3. Josephson Effect

The field equations are $d\theta/dt = -\partial\mathcal{H}/\partial\Delta\rho$ and $d\Delta\rho/dt = \partial\mathcal{H}/\partial\theta$. It follows that $\langle \theta \rangle = 0$ and $\langle \Delta\rho \rangle = 0$ in the ground state. However, by applying voltage or current externally, we can modulate the interlayer phase $\langle \theta \rangle$. The first equation leads to

$$d\langle \theta \rangle / dt = eV_{\text{ext}}, \quad (5)$$

The physical meaning is that the time evolution of $\langle \theta \rangle$ is determined by the energy change due to the movement of electrons $\langle \Delta\rho \rangle$ from one layer to the other, and this energy is equal to the work done by the external voltage V_{ext} . The other equation leads to

$$J_{\text{ext}} = J_0 \sin\langle \theta \rangle, \quad (6)$$

with $J_0 = e\rho_0\Delta_{\text{SAS}}$, which physically means the current conservation. In the system with DC-current feed, for $|J/J_0| < 1$, the Josephson current $J = J_0 \sin\theta_0$ flows between the two layers. The tunneling current is a superconducting current since $V_{\text{ext}} = 0$ for $\langle \theta \rangle = \theta_0$. In the system with DC-voltage feed, where $\langle \theta \rangle = \theta_0 + eV_{\text{ext}}t$, the Josephson frequency becomes $eV_{\text{ext}}/\Delta_{\text{SAS}}$, which reflects the condensation of bosonic composite electrons carrying a unit charge.

4. Meissner Effect and C-IC Phase Transition

The present BLQH system closely resembles the superconductor Josephson junction. However, the Meissner effect does not occur, as we now show. We apply a constant parallel magnetic field B_{\parallel} along the y axis and choose the gauge such that $B_y = -\partial_x A_z$. The penetrated parallel magnetic field induces a screening current $J_x = \mp c\rho_s \partial_x \theta$ in each layer, and as a result we obtain $B_y = -4\pi e\rho_s \partial_x \theta + B_{\parallel}$. The Hamiltonian is given by [3]

$$\mathcal{H} = \frac{d}{8\pi} B_y^2 + \frac{1}{2} \rho_s (\partial_x \theta)^2 + \frac{2\pi e^2 d}{\epsilon} (\Delta_p)^2 - \Delta_{SAS} \sqrt{\tilde{J}_0^2 - (\Delta_p)^2} \cos(\theta + \epsilon d A_z). \quad (7)$$

By analyzing the Gibbs free energy, $\mathcal{G} = \mathcal{H} - (d/4\pi) B_y B_{\parallel}$, we obtain the following physical picture of the ground state [3], as in the superconductor Josephson junction.

When B_{\parallel} is sufficiently small, B_y is equal to B_{\parallel} at the edge and gradually decreases to the screened value B_0 deep inside the junction with the penetration depth $\lambda_J = \sqrt{\kappa/4\pi e^2 d \Delta_{SAS} \rho_b}$, where $\kappa = 4\pi e^2 \rho_s d / (1 + 4\pi e^2 \rho_s d) \approx 2.7 \times 10^{-7}$ and $B_0 = B_{\parallel} / (1 + 4\pi e^2 \rho_s d)$. This is the C phase. Therefore, there exists a Meissner effect ($B_0 \neq 0$). The Meissner effect would occur if $\rho_s \rightarrow \infty$, as was assumed in Ref.[8].

As B_{\parallel} is increased, the magnetic flux begins to penetrate the junction as sine-Gordon vortices on top of B_0 . The increase of the Gibbs free energy due to one vortex penetration at B_{\parallel} is given by [9]

$$\Delta \mathcal{G} = (\kappa/2e)(B_{\parallel}^* - B_{\parallel}), \quad (8)$$

where $B_{\parallel}^* = 4/\pi e d \lambda_J$, which is the phase transition point. When B_{\parallel} becomes sufficiently large, it penetrates the junction freely. This is the IC phase. In a typical sample we estimate [3, 5] that $B_{\parallel}^* \sim 1.6$ T and that $J_x^{se} \sim 0.37$ A/m for the screening current at B_{\parallel}^* .

5. Plasmon Excitations and Activation Energy Anomaly

The BLQH system has the C and IC phases. Small fluctuations around the mean-field ground state are the plasmon excitations in each phase. It is easy to evaluate the plasmon energy at zero momentum [2]. In the C phase it is given by

$$\omega_C^2 = \omega_J^2 + \Delta_{SAS}^2, \quad (9)$$

with $\omega_J^2 = 4\pi e^2 d \rho_0 \Delta_{SAS} / \epsilon$. On the other hand, in the IC phase it is given by

$$\omega_{IC}^2 = \omega_J^2 \left| \frac{\sin(edB_{\parallel}/2)}{edB_{\parallel}/2} \right|^2 + \Delta_{SAS}^2. \quad (10)$$

If the size ℓ of the IC phase is very small, the plasmon energy ω_{IC} depends on the parallel field B_{\parallel} in an interesting way. However, if the size ℓ is very large, it is just a constant ($\omega_{IC} \rightarrow \Delta_{SAS}$). See Fig.1.

Plasmons are neutral but affect the transport property since they induce the oscillation of the charging $e\Delta\rho$ in each layer as well as that of the electric field associated with it. The activation energy must be given by the plasmon energy at zero momentum. Then, the activation energy would be given by a different constant in each phase as in Fig.1. This behavior agrees with the experimental data for $B_{\parallel} > B_{\parallel}^*$.

In order to account for the data for $B_{\parallel} < B_{\parallel}^*$, we question the rigidity of the C phase against the vortex penetration. The increase of the Gibbs free energy due to one vortex penetration is given by

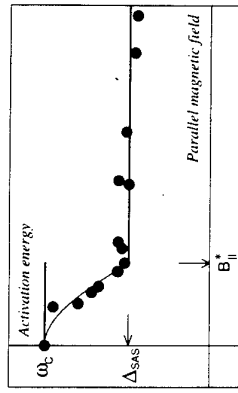


Fig.1: The activation energy is given theoretically by a different constant (thick line) in the C phase and IC phase, which is actually modified (thin curve) in the C phase by vortices penetrating the junction. Solid circles represent data points for a typical sample.

(8), but it is actually negligible since $\kappa \approx 2.7 \times 10^{-7}$. (We cannot give a physical significance to such a small quantity in our approximation where various small quantities have been neglected.) Consequently the parallel magnetic field may penetrate the junction rather freely as sine-Gordon vortices in the C phase. Here, each vortex separates two C domains, and vortices themselves act as IC domains. Thus, when $B_{\parallel} < B_{\parallel}^*$, the sample contains C domains as well as IC domains (vortices). Now, the main contribution to the activation energy is from the IC domains, that is ω_{IC} given by eq.(10), with $\ell = \ell_M$, the size of the vortex. The energy ω_{IC} decreases very rapidly from ω_C to Δ_{SAS} as B_{\parallel} increases from $B_{\parallel} = 0$ to B_{\parallel}^* , as in Fig.1. This rapid decrease is precisely the feature observed in the data [6].

In a typical sample the size of the vortex penetrating the C phase is estimated as $\ell_M \sim 250$ nm from the observed value $B_{\parallel}^* \sim 0.8$ T. The activation energy formula contains three parameters; the maximum energy ω_C , the minimum energy Δ_{SAS} and the critical point B_{\parallel}^* ; see Fig.1. If we adjust these parameters phenomenologically, we can explain all the reported data [6] quite well by plasmon excitations [3, 2]. This gives strong support to our physical picture of the BLQH state.

The domain structure made of vortices in the C phase affects detailed properties of the Josephson effects. We would like to report the results of our analysis elsewhere [10].

I am very grateful to Aichi Iwazaki and Hideo Ohno for fruitful discussions.

References

- [1] Z.F. Ezawa and A. Iwazaki, Int. J. Mod. Phys. B **6**, 3205 (1992); Phys. Rev. B **47**, 7295 (1993); Phys. Rev. B **48**, 15189 (1993).
- [2] Z.F. Ezawa and A. Iwazaki, Int. J. Mod. Phys. B **8**, 2111 (1994).
- [3] Z.F. Ezawa, Phys. Rev. B **51**, 11152 (1995).
- [4] X.G. Wen and A. Zee, Phys. Rev. Lett. **69**, 1811 (1992); Phys. Rev. B **47**(1993)2265.
- [5] K. Yang, K. Moon, L. Zheng, A.H. MacDonald, S.M. Girvin, D. Yoshioka and S.C. Zhang, Phys. Rev. Lett. **72**, 732 (1994); K. Moon, H. Mori, K. Yang, S.M. Girvin, A.H. MacDonald, L. Zheng, D. Yoshioka and S.C. Zhang, Phys. Rev. B **51**, 5138 (1995).
- [6] S.Q. Murphy, J.P. Eisenstein, G.S. Boebinger, L.N. Pfeiffer and K.W. West, Phys. Rev. Lett. **72**, 728 (1994).
- [7] Z.F. Ezawa, M. Hotta and A. Iwazaki, Phys. Rev. B **46**, 7765 (1992).
- [8] Z.F. Ezawa and A. Iwazaki, Phys. Rev. Lett. **70**, 3119 (1993).
- [9] P. Bak, Rep. Prog. Phys. **45**, 587 (1982).
- [10] Z.F. Ezawa, in preparation.

Time-Resolved Phonon Absorption in the Fractional Quantum Hall Regime

J.E. Digby, C.J. Mellor, A.J. Kent, K.A. Benedict, L.J. Challis, J.R. Middleton, and T. Cheng
 Physics Department, University of Nottingham, Nottingham, NG7 2RD, UK

We report time-resolved measurements of phonon absorption in the fractional quantum Hall regime. Experiments have been conducted on an n-type heterojunction grown on a 1.8mm GaAs wafer. The start of the absorption signal is consistent with the ballistic phonon time-of-flight. An unusually slow rise time in the longitudinal voltage is observed. The most likely explanation is that multiple reflections of the phonon pulse are being integrated by the long time constant of the device/cabling combination.

Introduction

The fractional quantum Hall effect which occurs in high mobility two-dimensional carrier systems, such two dimensional electron (2DES) and hole (2DHS) systems, subject to a strong perpendicular magnetic field is ascribed to the existence of an incompressible quantum liquid at certain rational filling factors. It is believed that the low-lying excited states of the liquid are collective modes that are never gapless (except at the sample boundaries). Girvin, MacDonald and Platzman (GMP) [1] have developed a theory for these collective modes at the primary filling factors $v=2\pi e^2 h_c / l_c = 1/m$ (l_c is the cyclotron length, and m is an odd integer); they find that the dispersion of the collective mode has a deep minimum for wavelengths comparable to the mean interparticle spacing. This "magneto-roton" minimum occurs, as in liquid helium, because of the peak in the static structure factor. What has been lacking experimentally is a means of measuring the gap close to the magneto-roton minimum. We report a study of these excitations using phonon absorption.

Activated magneto-transport studies have provided a measure of the energy gap that is found to depend on the mobility of the sample [2]. Theoretically it is also expected that this measurement probes the dispersion at high wavevectors rather than close to the magneto-roton minimum. Pinczuk et al [3] observe a feature in the inelastic light scattering spectrum that is attributed to the low wave-vector excitations of the FQHE in a quantum well. More recent measurements have been reported at finite wavevector in the integer quantum Hall effect regime [4].

Ballistic acoustic phonons have proved to be a unique probe of low dimensional systems [5]. The typical energies and wave-vectors are well matched to those of the 2DES and 2DHS and since, in the FQHE state, the magnetorotons are the only low energy modes which can couple to the ground state through the electron density, they should provide the principal channel for the absorption of acoustic phonons. This makes phonon absorption a promising method to investigate the energy gap of the FQHE in this region.

Phonon Absorption Experiments

To measure the phonon absorption signal, a constantan heater was evaporated onto the polished rear face of the GaAs wafer. A heterojunction had previously been grown on the front face by molecular beam epitaxy, and a Hall bar fabricated opposite the heater position. The carrier system was supplied with a constant bias current. The phonon absorption is measured from the change in longitudinal resistance produced by a burst of non-equilibrium ballistic phonons

generated by a 100ns voltage pulse applied to the heater. The transient voltage was measured using a gated amplifier with an 8μs gate length. The apparatus and methodology of these time-averaged studies is described in more detail elsewhere [6].

Theoretical Model

The spectral distribution of the non-equilibrium phonon pulse is assumed to approximate to that of a black body at a temperature, T_h , which is calculated from the total power dissipated in the heater by acoustic mismatch theory and confirmed by measuring the energy gaps at $v=12$ and $v=14$ on a high mobility 2DES under the same conditions as the fractional energy gaps were obtained.

The rate of energy transfer from the non-equilibrium phonon pulse to the carrier system depends on the dynamic structure factor of the latter. At long wavelengths this is believed to be well described by the single-mode approximation of [1]. This predicts that the dominant energy transfer process is the absorption of a phonon with energy and wavevector which match those of a magneto-roton at the minimum of the dispersion curve allowing the creation of such an excitation. The absorption of lower energy phonons is forbidden by energy conservation while the absorption matrix elements for higher energy phonons are exponentially smaller (as are their occupation probabilities in the black-body distribution).

Previous results

Two 2DES samples with approximately the same carrier density but with zero field mobilities of $1\times 10^6 \text{ cm}^2 \text{V}^{-1} \text{s}^{-1}$ and $8\times 10^6 \text{ cm}^2 \text{V}^{-1} \text{s}^{-1}$ have been studied previously [6]. We find that the energy gaps at $v=2/3$ for the lower and higher mobility samples measured by the temperature dependence of the longitudinal magno-resistance are $2.7\pm 0.2 \text{ K}$ and $5.5\pm 0.5 \text{ K}$ respectively whereas the gaps determined by phonon absorption at $6.2\pm 0.2 \text{ K}$ and $6.9\pm 0.4 \text{ K}$ are very similar. This leads us to believe that the phonon absorption technique is largely independent of the effects of disorder. The experimental values obtained are in good agreement with the theory of GMP, corrected for the effects of the finite thickness of the carriers and Landau level mixing. The experimental values of the energy gap expressed in units of $(e^2/4\pi\hbar c)^{1/2}$ are 0.041 ± 0.002 and 0.045 ± 0.003 respectively compared to a predicted gap of around 0.04. The measured energy gaps are independent of the substrate temperature. These results are discussed in more detail in ref. [6]. The nature of the absorption and the time development of the longitudinal voltage, although of great importance to the understanding of phonon absorption in the FQHE, could not be determined from these studies.

Time-resolved Measurements

All results reported previously have been made using a gated amplifier with a minimum gate length of 8μs. This was chosen because performing time-resolved measurements at these low (micro-volt) signal levels was not possible with the equipment available. We now describe preliminary time-resolved measurements in the FQH regime.

The sample used in these experiments is a 1.8 mm (100) GaAs wafer with a 2DES at the front surface. The sheet density of electrons at the heterojunction is $1.1\times 10^{11} \text{ cm}^{-2}$; the zero-field mobility at 100mK is $1.5\times 10^6 \text{ cm}^2 \text{V}^{-1} \text{s}^{-1}$. On the front surface two Hall bars, 1.4mm long and 0.35mm wide have been defined by wet-etching. The rear face is polished to an optical finish and two $60 \mu\text{m} \times 600 \mu\text{m}$ constantan heaters are fabricated as before. The heaters are aligned with the Hall bars so that angle-resolved measurements may be performed; for example the non-equilibrium phonons can be selected to travel normal to the 2DES or at 45° to it. All results reported here are

for the heater directly under the Hall bar, ie most of the phonons that interact with the 2DES will have travelled along the 100 crystal direction. The sample was mounted *in vacuo* on the tail of a dilution refrigerator.

A dc current was passed along the sample Hall bar by a floating constant current source. Two longitudinal voltage probes along the bar are connected to a high impedance ac-coupled differential amplifier which has a bandwidth greater than 30MHz. The output of this amplifier is itself amplified before recording the signal with an EG&G 9825-200 signal averaging board in a computer. This board has a 5ns time resolution and can average over a thousand complete signal traces per second. Voltage pulses are applied to the heater on the rear face of the sample. The resulting non-equilibrium phonons traverse the 1.8mm wafer in about 0.4μs. The response of the sample to the heater pulse is measured using the differential amplifier. To reduce the noise inherent in this wide-bandwidth signal to an acceptable level long averaging times were required. Great care has been taken to prevent noise from the computer and averaging board from reaching the sample and affecting the measurement. The cryostat and analogue amplifiers are all housed in a screened room, whilst the computer is outside this room.

As expected there is a small electrostatic breakthrough signal when the voltage pulse is applied to the heater. This signal reverses sign when the polarity of the heater pulse is reversed. The signal we ascribe to the interaction of the phonons with the 2DES is unchanged with the polarity of the voltage pulse. Measurements are taken in both forward and reversed direction of current flow along the Hall bar. These are then subtracted from each other to eliminate any thermo-electric effects which might arise from the non-equilibrium phonons. Thermo-electric effects were small as the zero-current trace hardly showed anything above the noise level (see figure 1). This observation along with the use of a differential amplifier helps to ensure that we measure the true response of the carriers rather than a thermo-electric effect in the contacts. A typical set of traces at different heater temperatures is shown in figure 2.

The most unusual feature of this trace is the very slow-time response of the system. In work reported in higher carrier density, higher temperature experiments it is possible to measure a ballistic response [7]. The slow rise in the sample begins after a time delay consistent with the time of flight of the phonons across the wafer. In our lower carrier density samples the contact resistance can be considerable, 1kΩ at zero field rising to 50kΩ at high magnetic fields. This is consistent with the observation that the size of the electrostatic breakthrough signal reduces as the magnetic field is increased, integrated over the long RC time constant of the contacts and cable capacitance. If we estimate the cable capacitance to be 200pF and the contact resistance to be 50kΩ, this leads to an RC time constant of 10μs. A puzzling feature is why the signal continues to rise after the

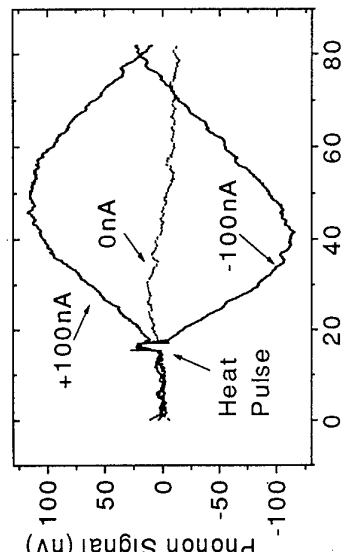


Figure 1: Phonon signal vs time at $v=2/3$.

computer. This board has a 5ns time resolution and can average over a thousand complete signal traces per second. Voltage pulses are applied to the heater on the rear face of the sample. The resulting non-equilibrium phonons traverse the 1.8mm wafer in about 0.4μs. The response of the sample to the heater pulse is measured using the differential amplifier. To reduce the noise inherent in this wide-bandwidth signal to an acceptable level long averaging times were required. Great care has been taken to prevent noise from the computer and averaging board from reaching the sample and affecting the measurement. The cryostat and analogue amplifiers are all housed in a screened room, whilst the computer is outside this room.

As expected there is a small electrostatic breakthrough signal when the voltage pulse is applied to the heater. This signal reverses sign when the polarity of the heater pulse is reversed. The signal we ascribe to the interaction of the phonons with the 2DES is unchanged with the polarity of the voltage pulse. Measurements are taken in both forward and reversed direction of current flow along the Hall bar. These are then subtracted from each other to eliminate any thermo-electric effects which might arise from the non-equilibrium phonons. Thermo-electric effects were small as the zero-current trace hardly showed anything above the noise level (see figure 1). This observation along with the use of a differential amplifier helps to ensure that we measure the true response of the carriers rather than a thermo-electric effect in the contacts. A typical set of traces at different heater temperatures is shown in figure 2.

The most unusual feature of this trace is the very slow-time response of the system. In work reported in higher carrier density, higher temperature experiments it is possible to measure a ballistic response [7]. The slow rise in the sample begins after a time delay consistent with the time of flight of the phonons across the wafer. In our lower carrier density samples the contact resistance can be considerable, 1kΩ at zero field rising to 50kΩ at high magnetic fields. This is consistent with the observation that the size of the electrostatic breakthrough signal reduces as the magnetic field is increased, integrated over the long RC time constant of the contacts and cable capacitance. If we estimate the cable capacitance to be 200pF and the contact resistance to be 50kΩ, this leads to an RC time constant of 10μs. A puzzling feature is why the signal continues to rise after the

driving pulse has ended. A possible explanation is that the non-equilibrium distribution of phonons injected into the GaAs will take some time to equilibrate. At the temperatures used in these experiments ($\approx 100\text{mK}$) the mean free path of low frequency phonons such as those used in this experiment ($T_h < 4\text{K}$) is much longer than the 1.8mm thickness of the sample. Whether multiple reflections and down-conversion of higher energy phonons can explain this rise is a matter of further investigation.

Conclusion

Time-averaged measurements suggest that phonon absorption experiments provide a means of measuring energy gaps in the FQHE which is independent of the sample mobility and lattice temperature. The measured energy gap at a given filling factor depends only on the heater temperature. The results on 2DES samples are in good agreement with the predictions of GMP. Time-resolved experiments demonstrate that the system has a very slow time-response. The exact reason for this is the subject of continuing investigation.

Acknowledgements

We would like to thank Dr W Dietsche for useful discussions and the EPSRC and EU for funding this work.

References

1. S.M Girvin, A.H Macdonald, and P.M. Platzman, Phys. Rev. B **33** (1986) 2481.
2. R.L. Willett, H.L. Stormer, D.C. Tsui, A.C. Gossard, and J.H. English, Phys. Rev. B **37** (1988) 8476.
3. A. Pinczuk, B.S. Dennis, L.N. Pfeiffer, and K. West, Phys. Rev. Lett. **70** (1993) 3983.
4. L. L. Sohn, A. Pinczuk, B.S. Dennis, L.N. Pfeiffer and K.W. West, Solid State Comm. **93** (1995) 897.
5. J.C. Hensel, R.C. Dynes and D.C. Tsui, Phys. Rev. B **28** (1983) 1124; M. Rothenfusser, L. Koster, and W. Dietsche, Phys. Rev. B **34** (1986) 5518.
6. C. J. Mellor, R.H. Eyles, J.E. Digby, A.J. Kent, K.A. Benedict, L.J. Challis, M. Henini and C.T. Foxon, Phys. Rev. Lett. **74** (1995) 2339.
7. D.J. McKitterick, A. Shik, A.J. Kent and M. Henini Phys. Rev. B **49** (1994) 2585.

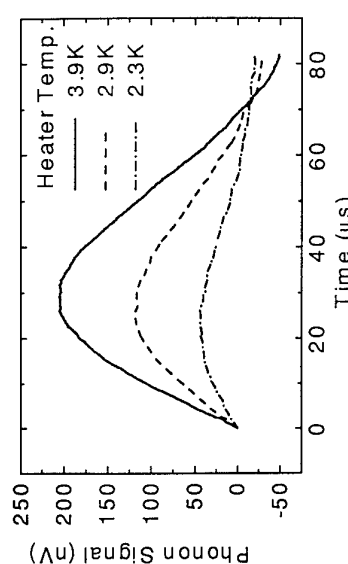


Figure 2: Phonon Signal ($I_r - I_0$) for different heater temperatures at $v=2/3$.

Optical Spectroscopy of Single Quantum Dots

A. Zrenner*

Walter Schottky Institut, Technische Universität München,
D-85748 Garching, Germany

Abstract

Fully confined excitons are observed in natural quantum dots, which are formed by well width fluctuations in narrow GaAs quantum wells. Contributions from a single quantum dot can be isolated by using spatially resolved spectroscopy and resonant charge injection in an electric-field-tunable coupled quantum well structure. In optical and magneto-optical experiments the excitonic and biexcitonic ground states are identified and analyzed.

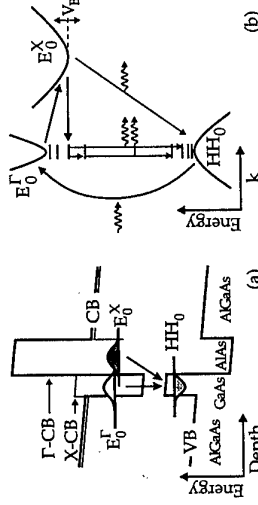
From fully quantized excitons in semiconductor quantum dot structures enhanced optical properties are expected as compared to systems of higher dimensionality. This enhancement originates mainly from the strongly peaked oscillator strength of such atom-like objects. Because of the absence of inhomogeneous broadening effects in a single quantum dot, the width of the optical absorption and recombination lines should be lifetime limited. From technological point of view, however, the controlled preparation of quantum dots has remained a problem. So far the incorporation of impurities and structural imperfections via lateral patterning processes can not be avoided. As a consequence, nonradiative recombination will be enhanced, and, within an array of quantum dots, fluctuations in composition and size will appear. In optical experiments zero-dimensional confinement in patterned structures was demonstrated in single quantum dots [1] as well as in arrays of dots [2, 3]. Recently two strongly disordered, but yet defect-free quantum dot systems have been introduced. Those are quantum dots formed by well width fluctuations in narrow GaAs quantum wells (QWs) [4-6], so-called natural quantum dots, and self organized, pyramid shaped InAs (InP) clusters in GaAs [7-9] ($In_{0.48}Ga_{0.51}P$ [10]). Both systems exhibit extremely narrow photoluminescence (PL) linewidth, as expected for fully quantized objects. Typically, however, the areal density of quantum dots in those systems is so high, that several dots with different ground state excitation energies contribute with their narrow emission lines to the observed PL spectra.

In the present contribution we report on the optical properties of single natural quantum dots. In particular we will describe a GaAs/AlAs coupled QW (CQW) structure, which allows the selection of a single natural quantum dot out of a statistically distributed array of dots with different shape and depth. Natural quantum dots originate from well width fluctuations in narrow QWs. Interface roughness with enhanced well width.

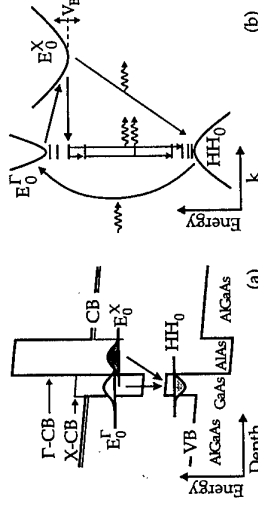
an amplitude of at least one monolayer (ML) in growth direction is known to appear in III/V semiconductor heterostructures [11]. The lateral length scale of those fluctuations covers a broad range reaching from atomic scale to water scale. In a narrow QW well width fluctuations of several monolayers result in sizable lateral potential variations. As shown schematically in figure 1, excitons can be localized in regions with locally enhanced well width. On this basis it is justified to describe a narrow QW as a disordered array of quantum dots with arbitrary dimensions. The amplitudes of the expected potential variations are respectable. For a GaAs QW a local variation of the well width from 10 ML to 12 ML will result in a local reduction of the exciton energy by 43 meV [12]. The most difficult part in the spectroscopy of fully quantized excitons in natural quantum dots is the selection of an individual dot. Only if it can be arranged experimentally, that the observed recombination originates from the radiative decay of ground state excitons in exclusively one selected quantum dot, we can expect to observe a single narrow emission line with homogeneous linewidth. For non-resonant optical excitation this condition requires, that every photoexcited exciton can reach within its lifetime a predefined quantum dot, where it finally recombines radiatively.

The experimental realization of such a selectivity is however difficult. Several selection mechanisms have to be combined to meet this requirement. Spatially resolved photoluminescence (PL) spectroscopy at the diffraction limit is one of the techniques which is thereby used. It allows a restriction of the optically excited and probed area down to about $1 \mu\text{m}^2$. With such a resolution it is already possible to resolve an inhomogeneously broadened line in its constituents, in form of many discrete narrow emission lines [5]. Under the assumption, that typical quantum dots should have dimensions in the range of a few exciton diameter ($300 \text{ \AA} - 1000 \text{ \AA}$) in the x-y-plane, about 100 to 1000 dots are expected to exist within a region of $1 \mu\text{m}^2$. A further enhancement of the spatial resolution in the excitation channel, for example by means of near field spectroscopy [6] is possible, doesn't result however in a dramatic improvement, since the exciton diffusion length in GaAs/AlGaAs QW structures is typically $1 \mu\text{m}$ [13]. A conceptionally different and more promising technique is the resonant optical excitation of single constituents in the low energy tail of a dilute, inhomogeneously broadened system. This approach for instance has been successfully used for single molecule spectroscopy [14].

For the present study we use a closely related approach to isolate the contribution of a single quantum dot, which is resonant charge injection in an electric-field-tunable coupled quantum well (CQW) structure as shown in figure 2a. With a typical GaAs layer width around 30 \AA the strongly confined electron ground state subband at the energy E_0^r in this system is almost degenerate with the corresponding subband state in the neighboring AlAs layer at energy E_0^x [15]. Application of an additional electric field results in an electric-field-induced Γ -X transition. The



(a)



(b)

Fig. 2: (a) Schematic band diagram of a GaAs/AlAs CQW structure. Direct and indirect transitions are indicated. (b) Relevant relaxation and recombination channels after optical excitation in the GaAs QW. The energy levels of a natural quantum dot in the GaAs QW are indicated by horizontal lines.

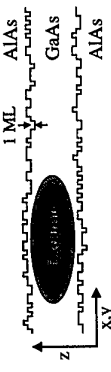


Fig. 1: Interface roughness in a QW structure on an atomic length scale. Excitons can be localized in regions with locally enhanced well width.

excitonic ground state is thereby tuned from direct to indirect (in real- and k-space).

Compared to the case of a single QW, the CQW structure has important new features which makes it extremely attractive for optical studies on natural quantum dots in narrow GaAs QWs [4]. Those new features originate from the relaxation of photo excited electrons in real- and k-space as indicated in figure 2b. After optical excitation in the GaAs QW the electrons undergo an ultrafast scattering process to the X-point subband in the AlAs layer forming thereby both real- and k-space indirect excitons with the associated holes in the GaAs QW. The lifetime of those indirect excitons is enhanced by up to a factor of 1000 as compared to a direct exciton in a GaAs QW [16]. Furthermore the energy of the AlAs X-point subband E_0^X is tunable by more than 70 meV with respect to E_0^r , allowing therefore for a resonant back-injection of electrons into the energy levels of natural quantum dots in the GaAs layer. This means, that the tunable X-point level E_0^X can be used as a charge reservoir and internal energy spectrometer to populate natural quantum dots in the neighboring GaAs QW.

In our optical studies on GaAs/AlAs CQWs we make use of both spatially resolved techniques at the diffraction limit and the above described resonant charge injection. For spatially resolved spectroscopy we use the cryogenic microscope setup shown in figure 3a and, for experiments at high magnetic fields, the optical fiber coupled scanning laser microscope shown in figure 3b. The spatial resolution of those instruments is 1.5 μm and 4 μm respectively. With this setup we can systematically look for the energetically lowest quantum dot in the investigated sample. By performing x-y-scans at fixed injection energies, we are able to pump selectively only a subset of natural quantum dots within the area of investigation, namely those with energies below the injection energy. By subsequently reducing the external bias voltage V_B the injection energy is lowered and we can realize a situation in which only one single quantum dot or eventually only its groundstate is pumped.

This is demonstrated in figure 4, where PL results from a GaAs/AlAs 30Å/40Å structure are shown for a set of different V_B . In steps of 0.05V V_B is tuned from the direct regime at 0.5V to the indirect regime all the way down to -0.5V. The electric-field-induced Γ -X transition appears at $V_B \sim -0.35\text{V}$. Below this threshold the linear Stark shift of the indirect line is evident as a global redshift of the background from which the narrow emission lines from the natural quantum dots emerge. In general we expect to find of course more than one local potential minimum in an optically probed area of 1.5 μm . For small Γ -X separations ($V_B=0\text{V}$) carrier injection into a big variety of shallow and deep local potential minima is possible and a complex superposition of sets of narrow emission lines results. For large separations only sufficiently deep potential minima can be populated and the spectra simplify up to a point, where only a single narrow emission line ($0\text{D}-\text{X}$) contributes ($V_B=-0.35\text{V}$).

This line originates from the groundstate of the deepest quantum dot in the area under investigation and it is attributed to a single exciton decay. Slightly Stark-shifted and less intense this transition can be also observed in the purely direct regime at $V_B=0.5\text{V}$. The width of the $0\text{D}-\text{X}$ line is smaller than the experimental resolution (50 μeV) for out-of-resonance conditions and therefore believed to be lifetime limited.

Under the condition of resonant charge injection into the lowest energy levels of the dot ($V_B \sim -0.2\text{V}$) the population of excitons can be dramatically enhanced. This leads to the formation of excitonic molecules (in the simplest form biexcitons) and the appearance of the corresponding emission line ($0\text{D}-\text{XX}$), which is about 3 meV below the ground-state single exciton line ($0\text{D}-\text{X}$) for the present dot [17]. In the regime of strong injection the exciton and biexciton lines appear to be broadened, which could be caused by random correlations with remote excitons. The biexciton line may be resolved as doublet or triplet [17].

The origin of an additional line between $0\text{D}-\text{X}$ and $0\text{D}-\text{XX}$ around $V_B=0\text{V}$ is still unknown. Biexcitons are characterized by their correlation energy $E_{\text{Cor}}=2E_{\text{Ex}}-E_{\text{Biexc}}$, where E_{Ex} (E_{Biexc}) is the ground state energy of the exciton (biexciton). Compared to two-dimensional QW structures E_{Cor} was found to be substantially enhanced in quantum dot structures [17, 18]. For out-of-resonance conditions the biexciton line vanishes. An almost quantitatively similar behaviour was found in various different dots. In this regime an increase of the excitation power P_L results in a quadratic increase of the intensity of the biexciton line. Under the condition of resonant charge injection ($V_B \sim -0.1\text{V} \dots -0.2\text{V}$) the biexciton line can be even the most prominent feature in the single quantum dot emission spectrum. In this regime the $0\text{D}-\text{XX}$ intensity has a linear dependence on P_L . According to simple rate equations, which include biexciton formation from two single excitons, such a behaviour is expected [19]. In this limit the recombination originates almost exclusively from biexciton decay. The decay of one of the correlated excitons, leaving behind a single uncorrelated exciton, is thereby followed by the capture of a new incoming exciton and hence the formation of a new biexciton. The fact that the $0\text{D}-\text{XX}$ is by far more intense as $0\text{D}-\text{X}$ denotes, that the formation and decay time

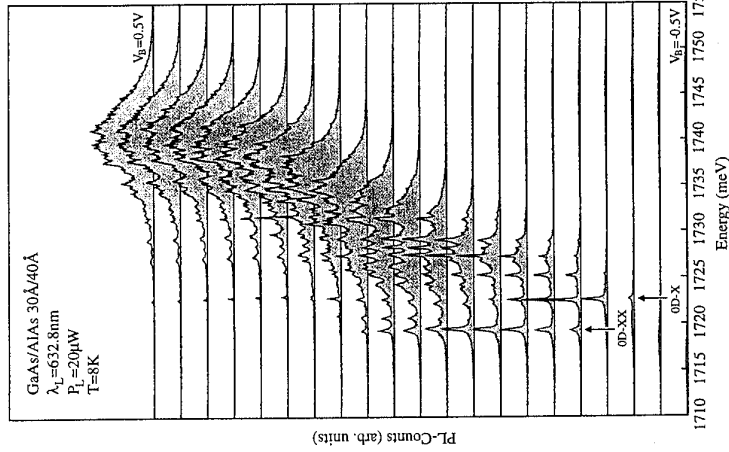


Fig. 4: Narrow emission lines from natural quantum dots for different V_B . The ground state exciton in the deepest quantum dot ($0\text{D}-\text{X}$) and the corresponding biexciton line ($0\text{D}-\text{XX}$) are indicated.

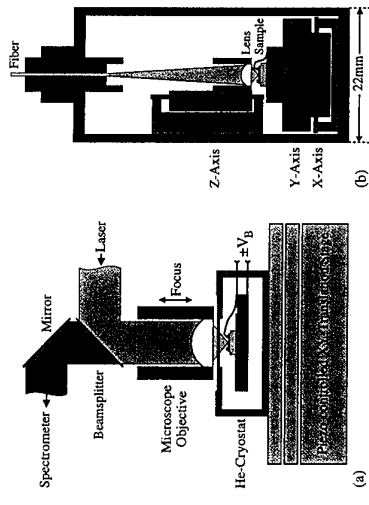


Fig. 3: (a) Cryogenic microscope setup for spatially resolved spectroscopy at the diffraction limit. (b) Scanning laser microscope for PL spectroscopy at high magnetic fields.

of a biexciton is much shorter than the single exciton lifetime.

Magneto-optical data of the excitonic and biexcitonic ground states in a single natural quantum dot are shown in figure 5. The data was obtained from a GaAs/AlAs 30Å/50Å CQW structure and is displayed for different perpendicular magnetic fields between $B_z=0$ and 12 T in steps of 0.5 T. The experimental conditions in terms of V_b have been chosen such, that only the excitonic ground state and the corresponding biexciton state contribute to the spectra. With increasing B_z the ground state exciton 0D-X splits linearly into a pair of optically active Zeeman sublevels $|c, \hbar\omega> = |s=1/2, j=3/2>$ and $|s=1/2, j=1/2>$. The observed level splitting amounts to 81.7 μeV/T. Almost the same coefficient is found for excitons in different dots with different energies. We conclude therefore, that the corresponding g-factor is predominantly given by confinement effects in the z-direction. The x-y-components, which lead to the formation of the natural quantum dots, seem to play a minor role. Not understood so far are the relative intensities of the individual Zeeman components. Whereas the low-energy branch exhibits a monotonic, slightly decreasing behaviour with increasing B_z , the high energy branch exhibits strong variations. For different dots different relative intensities are observed. The diamagnetic shift of the ground state exciton, given by the average shift of the two Zeeman sublevels, is purely quadratic with a magnitude of 8.25 μeV/T².

More complicated is the behaviour of the biexciton line 0D-XX, which appears as a doublet under the given conditions. With increasing B_z both lines exhibit a Zeeman splitting. Whereas for small magnetic fields the individual lines are difficult to attribute, clearly four lines (the original doublet for each Zeeman sublevel) appear at $B_z=12$ T. Compared to the exciton, the biexciton exhibits a larger Zeeman splitting (96.2 μeV/T) and a smaller diamagnetic shift (6.92 μeV/T²) (evaluated at $B_z=12$ T). From the differences in diamagnetic shift between the exciton and the biexciton a magnetic-field-induced enhancement of the biexciton correlation energy is apparent. The obtained shift is quadratic and has a magnitude of about 1.4 μeV/T². Since from theoretical point of view the biexciton correlation energy scales with the effective Rydberg, we believe, that the observed shift is a direct consequence of the enhancement of the exciton binding energy caused by the presence of a magnetic field. Various experimental findings, however, remain further unexplained. Those are in particular the unexpected enhancement of the biexciton intensity between $B_z=1$ T and 2 T and the origin of the 0D-XX doublet structure.

In summary we have investigated natural quantum dots in narrow GaAs QWs. Using spatially resolved PL spectroscopy and resonant charge injection in an electric-field-tunable GaAs/AlAs CQW structure we have been able to analyze excitonic and biexcitonic ground states in single quantum dots.

The authors like to acknowledge financial support by the DFG (SFB 348).

*This work has been performed in cooperation with M. Hagn, L. V. Butov, G. Abstreiter, G. Böhm, and G. Weimann.

References

- [1] K. Brunner, U. Bockelmann, G. Abstreiter, M. Walther, G. Böhm, G. Tränkle, and G. Weimann, Phys. Rev. Lett. **69**, 3216 (1992).
- [2] Y. Arakawa, Solid-State Electronics **37**, 523 (1994).
- [3] M. Bayer, A. Schmid, A. Forchel, F. Faller, T. L. Reinecke, P. A. Knipp, A. A. Demrin, and V. D. Kulakovskii, Phys. Rev. Lett. **74**, 3439 (1995).
- [4] A. Zrenner, L. V. Butov, M. Hagn, G. Abstreiter, G. Böhm and G. Weimann, Phys. Rev. Lett. **72**, 3382 (1994).
- [5] K. Brunner, G. Abstreiter, G. Böhm, G. Tränkle and G. Weimann, Appl. Phys. Lett. **64**, 3320 (1994).
- [6] H. F. Hess, E. Betzig, T. D. Harris, L. N. Pfeiffer and K. W. West, Science **264**, 1740 (1994).
- [7] J.-Y. Marzin, J.-M. Gérard, A. Izraël, D. Barrier, and G. Bastard, Phys. Rev. Lett. **73**, 716 (1994).
- [8] H. Drexler, D. Leonard, W. Hansen, J. P. Kotthaus, and P. M. Petroff, Phys. Rev. Lett. **73**, 2252 (1994).
- [9] M. Grundmann, J. Christen, N. N. Ledentsov, J. Böhmer, D. Bimberg, S. S. Ruvimov, P. Werner, U. Richter, U. Gösele, J. Heydenreich, V. M. Usmanov, A. Yu. Egorov, A. E. Zhukov, P. S. Kop'ev, and Zh. I. Alferov, Phys. Rev. Lett. **74**, 4043 (1995).
- [10] A. Kunzenbach, K. Eberl, and T. Shitara, Appl. Phys. Lett. **66**, 361 (1995).
- [11] C. A. Warwick, W. Y. Jan, A. Ourmazd, and T. D. Harris, Appl. Phys. Lett. **56**, 2666 (1990).
- [12] This result was obtained by numerical computation. The total shift of 43 meV is caused by a shift of the subband levels, which is 36 meV in the CB and 7 meV in the VB. Variations of the exciton binding energy can be neglected.
- [13] H. Hilmer, A. Forchel, R. Sauermann, and C. W. Tu, Phys. Rev. B **42**, 3220 (1990).
- [14] W. E. Moerner, Science **265**, 46 (1994).
- [15] A. Zrenner, Festkörperprobleme/Advances in Solid State Physics, Vol. 32 (ed. by U. Rössler, Vieweg, Braunschweig/Wiesbaden 1992), pp. 61-80.
- [16] A. Zrenner, P. Leeb, J. Schäfer, G. Böhm, G. Weimann, J. M. Worlock, L. T. Florez and I. P. Harbison, Surf. Sci. **253**, 496 (1992).
- [17] K. Brunner, G. Abstreiter, G. Böhm, G. Tränkle, and G. Weimann, Phys. Rev. Lett. **73**, 1138 (1994).
- [18] Y.Z. Hu, S. W. Koch, M. Lindberg, N. Peyghambarian, E. L. Pollock, and Farid F. Abraham, Phys. Rev. Lett. **64**, 1805 (1990).
- [19] J. C. Kim, D. R. Wake, and J. P. Wolfe, Phys. Rev. B **50**, 15099 (1994).

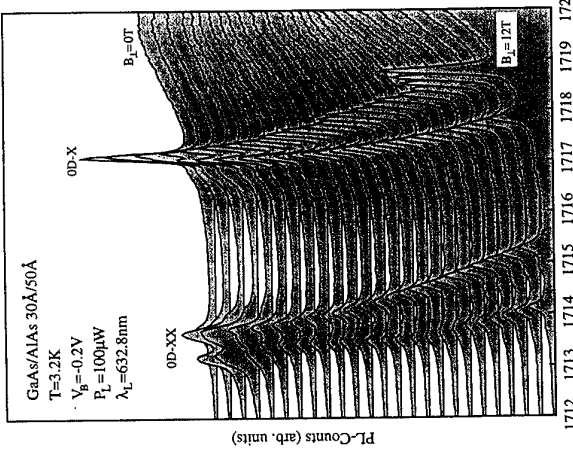


Fig. 5: Magnetic field dependence of a ground state exciton (0D-X) and the corresponding biexciton line (0D-XX) in a natural quantum dot.

Coupled Modes and Filling Factor Dependent Edge Potentials in Double-Layered Antidot Arrays

K. Bollweg, T. Kurth, and D. Heitmann

Institut für Angewandte Physik und Zentrum für Mikrostrukturforschung,
Universität Hamburg, Jungiusstraße 11, D-2035 Hamburg, Germany

E. Vasiliadou, P. Grambow, and K. Eberl
Max-Planck-Institut für Festkörperforschung, Heisenbergstraße 1, D-70569 Stuttgart,
Germany

Abstract

Double-layered antidot arrays have been prepared by deep mesa etching of modulation-doped $\text{Al}_x\text{Ga}_{1-x}\text{As} - \text{GaAs}$ double-quantum-wells. In far infrared transmission spectroscopy we observe a rich mode spectrum arising from collective optical (in phase) and acoustic (out of phase) oscillation in the two layers. In a magnetic field we find huge filling factor dependent oscillations of the frequency of the edge magnetoplasmon modes which are caused by self-consistent screening of the edge potential.

Quantum confined electronic systems in laterally microstructured semiconductor heterostructures, in particular quantum dots and antidots, have attracted increasing interest. With confinement energies in the meV regime far infrared (FIR) spectroscopy is a direct tool to study the excitations in these systems (for a recent review see Ref. [1]). It is found that the excitations are strongly dominated by collective effects. In this paper we have investigated two-layered antidot systems to study the long range Coulomb interaction between separated antidot layers. We find a rich mode spectrum with features resembling the optical and acoustic plasmon modes in multi-layered two-dimensional electron systems (2DES) [2-4] and 1DES [5].

Antidot arrays have been prepared starting from modulation-doped $\text{Al}_{0.36}\text{Ga}_{0.64}\text{As} - \text{GaAs}$ double-quantum-well structures, which have been grown by molecular beam epitaxy. The width of both quantum wells was 7.0nm, separated by a 55nm barrier. Three doping layers, as sketched in Fig. 1(b), were separated by 15nm spacers on each side of the wells. The electron density of the 2DES was $N_s = 9 \cdot 10^{11} \text{ cm}^{-2}$ in each well. The antidot arrays were fabricated by deep mesa etching starting from holographically prepared grid masks, similar as described in Ref.[5]. We concentrate here on an antidot sample with period $a = 400\text{nm}$ and a geometrical hole radius of $R_g = 100\text{nm}$. The FIR experiments were performed in perpendicular magnetic fields at $T=2.2\text{K}$ by Fourier transform spectroscopy.

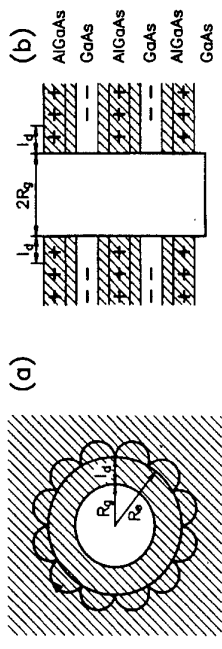


Fig. 1: (a) Sketch of an antidot. The area inside the radius R_g has been etched away. Electrons are depleted in the region with a lateral depletion length l_d . The ω_- mode is a collective mode where the individual electrons perform skipping orbits around the effective radius $R_e = R_g + l_d$. (b) Cut through an antidot in a double-quantum-well structure with three doping layers.

Experimental spectra of an antidot array are shown in Fig. 2. Several modes are observed. The B -dispersion of these modes is shown in Fig. 3. The strongest modes are the two labeled $\omega_{\pm 1}^e$. Two modes with similar dispersions have been observed before in one-layered antidot arrays [6-8].

To give an explanation for this complex mode spectrum we start from the microscopic model given in Ref.[6] and expand it to the two-layered system here. The antidot dispersions at large B resemble the excitations in quantum dots. The eigenmodes of a dot have dispersions [1]:

$$\omega_{\pm i} = \sqrt{\omega_0^2 + \frac{\omega_c^2}{4}} \pm \frac{\omega_c}{2}, \quad i = 1, 2, 3, \dots \quad (1)$$

For dots with hard wall confinement several sets of modes with index i arising from confined plasmon modes [9] exist with:

$$\omega_0^2 = f_1 \cdot \frac{N_s e^2}{2 \epsilon_0 \pi m} \cdot \frac{i}{R}, \quad i = 1, 2, 3, \dots \quad (2)$$

where R is the radius of the dot, ϵ the effective dielectric constant, and $\omega_c = \frac{eB}{m}$ is the cyclotron frequency. The prefactor f_1 depends on the shape of the confining potential and is $f_1 = 0.81$ in the model of Ref.[9]. For large B , $\omega_c > \omega_0$, we can expand (1) and find for the low frequency branch: $\omega_{-1} \approx \omega_0^2/\omega_c \propto 1/(\omega_c \cdot R)$. Microscopically the ω_- modes correspond to collective magnetoplasmon excitations where the individual electrons perform cyclotron motions between the antidots. The ω_- modes at large B are collective edge magnetoplasmons where the individual electrons perform skipping orbits around the outer boundary of the antidots as sketched in Fig. 1(a). The interesting point is that, which decreasing B and thus increasing cyclotron orbit, the electrons can eventually perform a classical cyclotron motion with radius $r_c = v_F/\omega_c$ (v_F = Fermi velocity) around the antidot. Therefore, in contrast to the dispersion of dots (1), the ω_- mode decreases for small B . The modes labeled ω_{+1}^e and ω_{-1}^e dominate the spectrum. (We will see below that for these modes both layers oscillate in phase.) Higher modes with index $i = 2$ are expected in our model

at $\omega_{+2} = \sqrt{2} \cdot \omega_{+1}$ for $B = 0$. In Fig. 3 we find one mode with $\omega_{+2}^o/\omega_{+1}^o = 1.4$ which we therefore identify with this type of mode. The intensity of this mode is weaker, about 20% of the ω_{+1}^o mode. Similar higher lying modes have been observed in one-layered dot arrays [5] with frequency ratios ω_{+2}/ω_{+1} varying from 1.4 to 1.8. $\omega_{+2}/\omega_{+1}^o = 2$ is expected for a parabolic confinement in small dots if the confinement energy is much stronger than Coulomb interaction. It is well known in multi-layered 2DES that two types of plasma oscillations, optical and acoustic, exist ('acoustic', because of the linear q -dependence at small q) [2-4]. For the optical branch both layers oscillate in phase. This increases the frequency of the coupled oscillation ω_p^o with respect to the plasmon frequency ω_p of a separated layer, up to $\omega_p^o = \sqrt{2} \cdot \omega_p$ in the limit $qd \ll 1$ if d is the separation between the layers. In a two-layer system we have one acoustic branch where the electrons oscillate out of phase which decreases the frequency ω_a^a with respect to ω_p . We attribute the experimentally observed modes in Fig. 3 to coupled in-phase and antiphase magnetoplasmon and edge magnetoplasmon modes. We identify the modes labeled ω_{+2}^o with collective excitations where both layers oscillate in phase. In addition we find acoustic ω_{+1}^a modes. These modes can be identified since they have smaller frequencies and intensities as compared to the ω_{+1}^o modes. The mode ω_{+2}^a in Fig. 3 with $\omega_{+2}^a/\omega_{+1}^a \approx 1.6$ is attributed to a higher index mode where the acoustic plasmons are quantized with index $i = 2$. We note that on other samples we also observe acoustic modes of the ω_- branch.

acoustic modes cannot be excited with FIR dipole excitation. It is our observation that the excitation strength of the acoustic mode increases if one has different carrier concentrations in the two layers. We can produce this behavior for example by a short illumination with a LED.

Another interesting finding is that the ω_- branch in Fig. 3 shows well pronounced oscillations of the frequency with increasing magnetic field. If we plot this frequency versus $1/B$ we find a periodic behavior. We can relate the oscillations to the filling factor $\nu = \frac{N_e}{eB}$. We find, as shown in Fig. 3, that maxima occur at half filled Landau levels (ν odd) and minima for fully occupied Landau levels (ν even). We attribute these frequency oscillations to oscillations of the edge potential and the related effective antidot radius. To demonstrate this we consider Fig. 1. The electrons are separated by a lateral depletion length l_d [5] from the geometrical hole Radius R_g on an effective radius $R_e = R_g + l_d$. We can deduce from our experiments that this depletion length depends strongly on the Landau level occupation. For fully occupied Landau levels screening is weak leading to a large value of l_d and corresponding effective radius R_e in the antidot system. Since we have shown above that for large B , $\omega_- \propto 1/R$, we expect a small resonance frequency as observed in the experiments. For half filled Landau levels we have good screening which gives rise to small R_e and to the observed large resonance frequency. If we apply the model potential of Fetter [9], formula (2), we can fit the maxima and minima of the ω_- dispersion and find for the antidot array $R_{remax} = 160\text{nm}$ and $R_{remin} = 140\text{nm}$. Thus we have relative radius oscillation of about 15% for the antidots.

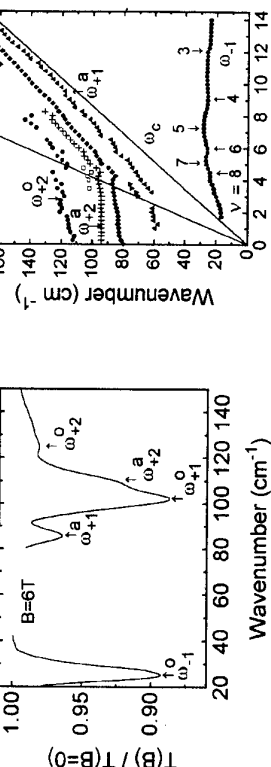


Fig. 2: Normalized transmission spectra of an antidot array with a period $a = 400\text{nm}$ and a geometrical hole radius $R_g = 100\text{nm}$ at $B = 6\text{T}$.

We find that the intensity of the acoustic modes depends strongly on the sample, in particular on the symmetry between the layers. For symmetric layers we expect that the filling factor ν .

In summary, two-layered antidot arrays exhibit a rich mode spectrum of in-phase-optical and antiphase-acoustic magnetoplasmon and edge magnetoplasmon modes. The low frequency edge magnetoplasmon mode shows pronounced oscillations of the frequency indicating directly the self-consistent oscillations of the edge potential in a magnetic field.

References

- [1] D. Heitmann and J.P. Kotthaus, Physics Today **46**, 56 (June 1993).
- [2] J.K. Jain and P.B. Allen, Phys. Rev. Lett. **54**, 2437 (1985).
- [3] A. Pinczak, M. G. Lanson, and A.C. Gossard, Phys. Rev. Lett. **56**, 2092 (1986).
- [4] G. Fasol, N. Mestres, H.P. Hughes, A. Fischer, and K. Ploog, Phys. Rev. Lett. **56**, 2517 (1986).
- [5] T. Denel, D. Heitmann, P. Grambow, and K. Ploog, Phys. Rev. Lett. **53**, 2176 (1988).
- [6] K. Kern, D. Heitmann, P. Grambow, Y.H. Zhang, and K. Ploog, Phys. Rev. Lett. **66**, 1618 (1991).
- [7] G.Y. Wu and Y. Zhao, Phys. Rev. Lett. **71**, 2114 (1993).
- [8] D. Huang and G. Gumbs, Phys. Rev. B **47**, 9597 (1993).
- [9] A.J. Fetter, Phys. Rev. B **32**, 7676 (1985).

Efficient Exciton-relaxation in Self-organized InAs/GaAs Quantum Dots

R. Heitz, M. Grundmann, N.N. Ledentsov*, L. Eckey, M. Veit, and D. Bimberg
Institut für Festkörperfysik, Technische Universität Berlin, 10623 Berlin, Germany

V.M. Ustinov, A.Yu. Egorov, A.E. Zhukov, P.S. Kop'ev, and Zh. I. Alferov
A.F. Ioffe Physical-Technical Institute, 194021, St. Petersburg, Russia

We report on optical studies of relaxation processes in self-organized InAs/GaAs quantum dots (QDs). Photoluminescence excitation spectra reveal a series of almost equidistant lines. Their energy with respect to the detection energy does not depend on QD size. The energy separations are close to the LO phonon energy of 32.1 meV estimated numerically for strained pyramid-like InAs QDs. Carrier relaxation is found to proceed by multphonon processes involving QD and wetting layer LO phonons, and an interface mode.

Introduction

The δ -function density of states of quantum dots (QD's) is expected to lead to an exceedingly low threshold current density independent of temperature for semiconductor lasers [e.g. 1,2]. Recently, indeed an injection laser based on InGaAs QDs with promising low threshold current density and large T_0 of 350 K at low temperatures has been demonstrated [3]. Defect-free nm-size QDs can be realized for the (InGa)As/GaAs system in the Stranskí-Krastanow growth mode [4-7]. However, carrier relaxation, being crucial e.g. for high speed device performance, is expected to be drastically slowed down due to energy conservation, resulting in the so called 'phonon bottleneck'. Only transitions involving one low frequency LA, one LO phonon [8] or a combination of both [9] were predicted to be efficient. Photoluminescence excitation (PLE) spectroscopy presents a well known approach to obtain information on such relaxation processes. Recently, Fafard et al. reported PLE and selectively excited luminescence (SEL) spectra of InGaAs/GaAs QDs [10] and interpreted the results with absorption into an excited electron state assuming a large Stokes shift and a symmetry-forbidden transition.

Here we present PLE measurements of nm-size InAs QDs embedded in GaAs. Instead of a simple correlation of PLE maxima with excited QD states, relaxation processes are found to dominate the shape of the PLE spectra. Multphonon processes mainly involving the InAs QD LO phonon are identified.

Samples and Experimental

The investigated InAs QD structures are grown by solid source molecular beam epitaxy as described in [6]. A single layer of self-organized QDs on a wetting layer is formed upon deposition of 4ML InAs at 480 °C on GaAs (001). TEM images show highly symmetric InAs pyramids with a base-plane size of approximately 12 nm and a density of 10^{11} cm^{-2} [6,7].

Luminescence is excited with a HeNe or a Nd:YAG laser and spectrally resolved with a 0.5 m monochromator. PLE spectra are recorded with a tungsten halogen lamp dispersed by a 0.35 m double grating monochromator as tunable light source and detected with a 0.75 m double grating monochromator and a cooled Ge photodiode.

Experimental Results

For excitation far above the GaAs bandgap QD luminescence at 1.11 eV with a full width at half maximum (FWHM) of 45 meV (dotted line in Fig. 1) dominates the spectrum. Calorimetric

absorption spectra (CAS) of the same sample [6] prove absorption coinciding in energy with the QD luminescence. For excitation at the high energy onset of the QD luminescence (solid line in Fig. 1), the broad QD peak decomposes into three bands in the energy range of 1, 2 and 3 LO phonon replica, respectively. Four phonon modes with energies of 29.6 (InAs₁), 31.9 (InAs₂), 35.0 (IF) and 36.6 meV (GaAs) account for the fine structure. We note that the FWHM of the fine structure is much narrower in the 1 than in the 2 and 3 LO band indicating different processes causing them. Tentatively, we assign the 1 LO band to resonant Raman scattering and the 2 and 3 LO bands to hot excitation relaxation.

Fig. 2 depicts excitation spectra detected at different parts of the QD luminescence. All spectra reveal excitation via absorption of the InAs wetting layer at 1.388 eV. At their low energy onset occurs a characteristic series and 3 LO bands to hot excitation (A,B,C,D) of excitation peaks increasing in intensity with increasing separation from the detection energy (except for lowest detection energies). The QD ground state absorption is obscured by stray light.

Fig. 3 compiles the energy differences ΔE between the PLE peaks A - D and the detection energy as function of the detection energy. The energies are obtained from lineshape fits assuming a sum of Gaussians as illustrated in Fig. 4(a). The FWHMs of the excitation lines are between 8 and 12 meV and allow the determination of their peak positions within 1 meV. Most important, the energy differences ΔE are independent of the detection energy. Dotted lines in Fig. 3 correspond to energy differences of 34.1, 65.6, 95.0 and 124.8 meV. It is most surprising after the results shown in Fig. 1 that this ladder is not equidistant. The experimental resolution of the PLE measurements, however, is only 6 meV, which is not sufficient to distinguish the various phonon modes resolved in Fig. 1.

Discussion and Conclusions

We calculated the electronic states of the QDs taking into account the strain distribution resulting from the pyramid-like structure on top of the wetting layer

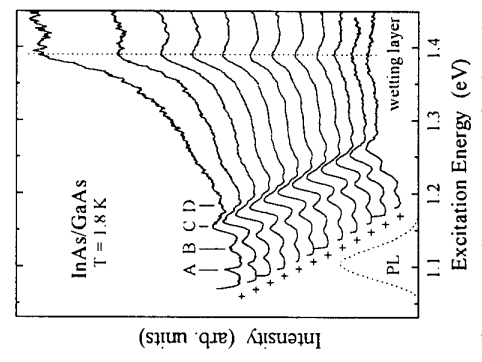
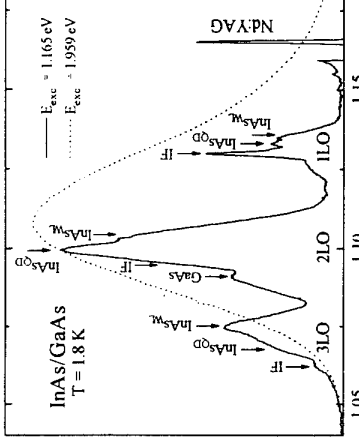


Fig. 2: PLE spectra of the luminescence. The detection energies are indicated by crosses.

[11]. Simulation of the strain by a finite differences method yields a transfer of anisotropic strain into the GaAs barrier. From the strain distribution the 3D confinement potential is generated for which the single particle effective mass Schrödinger equation is solved. Only one electron but several hole states are confined in our QDs as schematically indicated in the inset of Fig. 4(b). The states are classified by the number of nodes in different directions. Transitions between the electron and the $|000\rangle$ and the $|001\rangle$ hole states are expected to have a much larger oscillator strength than any other one. The reliability of the calculations has been proven recently by comparison with CARS and photoluminescence spectra for high excitation densities revealing excited hole states [12].

The solid lines in Fig. 3 show the calculated energy differences between the hole ground state and excited hole states as a function of the fundamental transition energy. The calculations predict for all cases at least a 15 meV variation of ΔE in Fig. 3 across the PLE peaks and the detection energy as function of the detection energy. Solid lines represent the calculated energies of the investigated energy range which is clearly absent in experiment. Our experimental findings thus exclude the attribution of the excitation lines A - D to excited electronic states. We conclude phonon-related processes as origin of the excitation resonances.

In our strained nanostructures the LO phonon energy is altered by both the strain and phonon confinement. Both effects almost perfectly compensate each other for the thin InAs quantum well (wetting layer) [13], leading to a phonon energy of 29.6 meV (InAsw). For the InAs QD the phonon confinement can be neglected. In [11] a QD LO phonon energy of 32.1 meV is predicted from the simulated strain distribution which is in excellent agreement with the InAs mode energy of 31.9 meV determined from Fig. 1. The IF mode with an energy of 35.0 meV is tentatively assigned to an interface phonon.

Fig. 4(b) illustrates the the relaxation processes

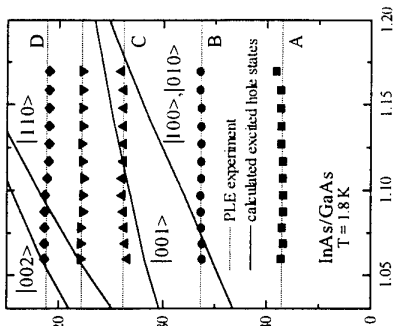


Fig. 3: Energy difference between PLE peaks and the detection energy as function of the detection energy. Solid lines represent calculated energies of excited hole states.

processes as origin of the excitation resonances.

In our strained nanostructures the LO phonon energy is altered by both the strain and phonon confinement. Both effects almost perfectly compensate each other for the thin InAs quantum well (wetting layer) [13], leading to a phonon energy of 29.6 meV (InAsw). For the InAs QD the phonon confinement can be neglected. In [11] a QD LO phonon energy of 32.1 meV is predicted from the simulated strain distribution which is in excellent agreement with the InAs mode energy of 31.9 meV determined from Fig. 1. The IF mode with an energy of 35.0 meV is tentatively assigned to an interface phonon.

Fig. 4(b) illustrates the the relaxation processes

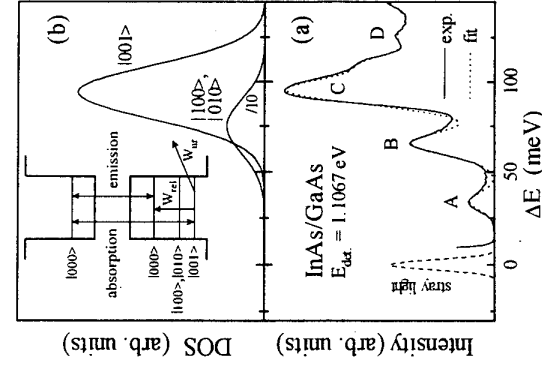


Fig. 4: (a) High-resolution PLE spectrum and lineshape fit for one detection energy. (b) The estimated variation of excited hole state energies leading to inhomogeneous broadening ($\Delta E_{inh} = 30$ meV) for a fixed ground state transition energy. The inset depicts a schematic model of relaxation processes for the QDs.

leading to the observed PLE spectra of QD ground state luminescence. Any QD ensemble shows inhomogeneous broadening of the ground state transition energy due to size, shape and strain fluctuations. For a fixed ground state transition energy the excited state absorption energy can vary additionally leading to inhomogeneous broadening ΔE_{inh} . From luminescence spectra [12] ΔE_{inh} can be estimated to 30 meV. The dominating PLE line C is nearly resonant to the allowed $e_{|100>} h_{|001>}$ transition. For excited hole states energy transfer to deep nonradiative relaxation centers in the low temperature GaAs barrier (W_m) competes with intradot relaxation (W_{rel}) processes. Only QDs with hole state splittings allowing rapid population of the ground state via LO phonon scattering processes contribute to the PLE signal. The relaxation process must be a multiphonon process since no matching intermediate states are available (Fig. 3). The relative large FWHM of the 2 and 3 LO lines in Fig. 1 might be due to additional scattering of LA phonons as proposed in [9].

In conclusion, we have studied excitation processes of self-organized pyramidal InAs QDs in a GaAs matrix. Carrier relaxation is found to proceed by multiphonon processes and the decisive role of phonon scattering for the shape of the PLE spectra is pointed out. Scattering of LO phonons from different regions of the QD structure due to the extended QD wavefunctions probably together with acoustical phonon bradening circumvents the ‘phonon bottleneck’ effect allowing exciton relaxation.

Parts of this work were supported by the Volkswagen Stiftung, by the Deutsche Forschungsgemeinschaft in the framework of the SFB 296 and by INTAS.

References

- * On leave from A.F. Ioffe Physical-Technical Institute, St. Petersburg, Russia.
- [1] Y. Arakawa, H. Sakaki, *Appl. Phys. Lett.* **40**, 939 (1982).
- [2] M. Asada, Y. Miyamoto, and Y. Siematsu, *IEEE J. Quant. Electr.* **QE-22**, 1915 (1986).
- [3] N. Kirstaedter, N.N. Ledentsov, M. Grundmann, D. Bimberg, V.M. Ustinov, S.S. Ruvimov, M.V. Maximov, P.S. Kop'ev, Zh.I. Alferov, U. Richter, P. Werner, U. Gösele, and J. Heydenreich, *Electr. Lett.* **30**, 1416 (1994).
- [4] D. Leonard, M. Krishnamurthy, S. Fafard, J.L. Merz, and P.M. Petroff, *J. Vac. Sci. Technol. B* **12**, 1063 (1994).
- [5] J.M. Moison, F. Houzay, F. Barthe, L. Leprinse, E. André, and O. Vatel, *Appl. Phys. Lett.* **64**, 196 (1994).
- [6] M. Grundmann, N.N. Ledentsov, R. Heitz, L. Ecke, J. Christen, J. Böhmer, D. Bimberg, S.S. Ruvimov, P. Werner, U. Richter, J. Heydenreich, V.M. Ustinov, A.Yu. Egorov, A.E. Zhukov, P.S. Kop'ev, and Zh.I. Alferov, *phys. stat. sol. (b)* **188**, 249 (1995).
- [7] M. Grundmann, J. Christen, N.N. Ledentsov, J. Böhmer, D. Bimberg, S.S. Ruvimov, P. Werner, U. Richter, U. Gösele, J. Heydenreich, V.M. Ustinov, A.Yu. Egorov, A.E. Zhukov, P.S. Kop'ev, and Zh.I. Alferov, *Phys. Rev. Lett.* **74**, 4043 (1995).
- [8] H. Benisty, C.M. Sotonayor Torres, and C. Weisbuch, *Phys. Rev. B* **44**, 10945 (1991).
- [9] T. Inoshita and H. Sakaki, *Phys. Rev. B* **46**, 7260 (1992).
- [10] S. Fafard, D. Leonard, J.L. Merz, and P.M. Petroff, *Appl. Phys. Lett.* **65**, 1388 (1994).
- [11] M. Grundmann, O. Stier, and D. Bimberg, *Phys. Rev. B* (1995), in print.
- [12] M. Grundmann, N.N. Ledentsov, O. Stier, R. Heitz, J. Böhmer, D. Bimberg, V.M. Ustinov, P.S. Kop'ev, and Zh.I. Alferov, to be published in *Appl. Phys. Lett.*
- [13] P.D. Wang, N.N. Ledentsov, C.M. Sotonayor Torres, I.N. Yassievich, A. Pakhomov, A.Yu. Egorov, A.E. Zhukov, V.M. Ustinov, *Phys. Rev. B* **50**, 1604 (1994).

Optical Spectroscopies of Electronic Excitations in Quantum Dots

P.Hawrylak^a, A.Wojs^{a,d,*} D.J.Lockwood^{a*} P.D.Wang^b C.M.Sotomayor Torres^b

A.Pinczak^c and B.S.Dennis^c
(a) Institute for Microstructural Sciences, National Research Council of Canada,

(b) Nanoelectronics Research Center, Glasgow University, Glasgow, UK
(c) AT&T Bell Laboratories, Murray Hill, NJ, USA

(d) Institute of Physics, Technical University of Wroclaw, Wroclaw, Poland
(June 12, 1995)

Calculations of the electronic and optical properties of quantum dots (QD) reveal that optical absorption and emission and inelastic light scattering may probe a rich spectrum of ground and excited states of QD in a magnetic field. Comparisons are made with Raman measurements for deep-etched GaAs/AlGaAs modulation doped QD in a magnetic field.

I. INTRODUCTION

We discuss here electronic and optical properties of dots with soft (parabolic [1-4]) and hard-wall (disks [5]) confinement and present preliminary results of inelastic light scattering from deep-etched GaAs/AlGaAs modulation doped disks in a magnetic field. The disks with radii R , ($50\text{nm} < R < 100\text{nm}$), were etched from a modulation doped multi-quantum well structure [5] with carrier density $n = 8.5 \cdot 10^{11}\text{cm}^{-2}$.

II. THEORY

The electronic states of a quantum dot in a magnetic field are determined by the competition between kinetic, Zeeman, and potential energy due to confinement V_c and positive charges V_+ , and by electron-electron interactions and correlations.

For quantum dots with soft (parabolic) confinement we can replace the net confining potential $V_c(\vec{r}_i) + V_+(\vec{r}_i)$ by an effective parabolic potential [4]. For deep-etched dots the confining potential is modelled by a disk of radius R with infinite walls and the positive potential is a potential of a disk of positive charge with density $N/\pi R^2$ at a distance D from the plane of the dot.

Electronic states of QD's in a magnetic field with N electrons ($N=1,\dots,130$) were calculated using exact diagonalization techniques for $N < 15$, and Hartree and Hartree-Fock methods for large number of electrons. All states are labelled by a total angular momentum J and excitations are labeled by an excess angular momentum M .

Results of calculations are illustrated in Figure 1. Figure 1a shows excited state energies $E(M)$ as a function of the excess angular momentum M of a $N = 10$ spin polarized compact parabolic dot with $\omega_N = 2.1\text{meV}$ in the magnetic field $B = 2\text{Tesla}$. The well separated low lying excitations of the droplet, the edge magneto-rotons, are clearly visible, while the higher excited states form pairs of edge magneto-rotons. Increasing the magnetic field and the strength of e-e interactions leads to a softening of edge magneto-roton dispersion and

to a reconstruction of the dot's charge density. The reconstruction of the dot in terms of freezing of edge magneto-rotons is equivalent to "magic" angular momentum transitions in few electron dots [4].

Figure 1b shows the low angular momentum Hartree excitation spectrum of a disk with $R = 70\text{nm}$ and $N = 124$ electrons ($n_s \approx 8 \cdot 10^{11}\text{cm}^{-2}$) in a magnetic field $B = 2\text{T}$. There is a low lying branch of excitations followed by a band of excitations at $\approx 4\text{meV}$. The inset shows charge density profiles $n(r/R)$ of a noninteracting disk (almost uniform charge density) and an interacting disk. Because of the spatial separation $D \approx 300\text{\AA}$ of the positive background from the disk, electrons repel each other very effectively and the electron charge density is depressed inside the disk and enhanced at the edges of the disk.

III. ABSORPTION/EMISSION

In absorption/emission, an exciton probes the magnetic field induced reconstruction of charge density of the parabolic dot and repopulation of quantum levels in a disk. The detailed calculations of a magneto-exciton in an N electron parabolic droplet were carried out using exact diagonalization techniques. In Figure 2 we illustrate our results by showing the absorption peaks for the $N = 3$ electron dot as a function of the magnetic field. Insets show the charge density of the ground state of the dot. For low values of the magnetic field the dot is compact and excitons can be added outside the dot. When the dot undergoes reconstruction, vacancies (holes) appear in the dot , and a photo-excited electron can annihilate these holes. A new , low energy, absorption line (b) appears then as a direct signature of a phase transition in the dot. The phase transition is also visible in the main absorption line (a) which undergoes discontinues jumps whenever the ground state changes it's angular momentum.

IV. RAMAN SCATTERING

Resonant inelastic light scattering is a useful probe of the spectrum of electronic excitations [5,6] since it does not involve adding or subtracting particles [7]. Slightly off-resonance, the Raman cross section $I(q,\omega)$ corresponding to the transfer of energy ω and momentum q is proportional to the imaginary part of the dynamical structure factor $S(q,\omega)$ of a quantum dot [7].

The Raman spectrum and the dynamical structure factor for few-electron quantum dots has been calculated in Ref. [7]. In a strong magnetic field induced transitions correspond to the closing and opening of gaps in the excitation spectrum. It was shown that the Raman spectrum should exhibit the appearance of soft modes corresponding to the collapse of gaps and freezing of edge-magneto-rotons as a signature of magnetic field induced phase transitions.

We now turn to inelastic light scattering from deep-etched quantum dots. Photoluminescence and resonant electronic Raman spectra of deep-etched GaAs/GaAlAs quantum dots were measured in magnetic fields up to 17 Tesla . The rich spectrum of excitations with Raman shifts in the range 1-35meV was observed. The spectra show level-splitting , level-

crossing, and mode-softening with increasing magnetic field. The spectra for $B=0, 1$ and 2T are shown in Figure 3 for a dot with radius $R=75\text{nm}$.

Since the spectra do not show a clear polarization dependence, they are a mixture of spin density (SDE), charge density (CDE), and single particle (SPE) excitations. Broad features visible in the spectra are on the scale of several meV, yet single-particle 0D excitations in Figure 1 show quantization on the scale of a fraction of a meV. Thus the interpretation of experimental spectra is difficult, and we initially restrict ourselves to SPE based on Hartree calculations.

The effect of the magnetic field is to remove the degeneracy of states with angular momenta $+/- M$ and to change the Hartree fields and the equilibrium charge distribution. This results in a splitting and rearrangement of transition energies and hence in changes of the Hartree SPE spectra.

We show in Fig.3 the evolution of the calculated Hartree SPE spectra $E(\omega) = \sum_{i,j} (1 - f_i) f_j \delta(E_i - E_j - \omega)$ with the magnetic field \mathbf{B} (f_i is the Fermi occupation function for a Hartree state E_i) superimposed with the measured spectra. We assumed in our model a slight loss of the carrier density (from $8.5 \cdot 10^{11} \text{cm}^{-2}$ to $8.0 \cdot 10^{11} \text{cm}^{-2}$) and a reduction in the dot size from $R = 75\text{nm}$ to $R = 70\text{nm}$ due to the etching. We do not resolve transitions that are less than 0.5meV apart, and do not include matrix elements nor finite state interactions. We see that the spectrum consists of many transitions with a typical spacing of $\approx 0.5\text{meV}$. The magnetic field induces the splitting of transition energies and some transitions move to lower energies with increasing magnetic field. The envelope of the spectrum shows magnetic field tunable modulations, with a number of bands spaced by several meV. This situation is qualitatively consistent with experiment but more work, and in particular a realistic calculation of edge magneto-plasmons and spin density excitations, is needed for a quantitative interpretation of experiment.

*supported by NATO HTECH LG 930746.

References

- [1] For recent reviews and references see M.Kastner, Physics Today **24**, January 1993; T.Chakraborty,Comments in Cond.Matter Physics **16**,35(1992).
- [2] H.Drexel,D.Leonard,W.Hansen,J.P.Kotthaus ,and P.M.Petroff, Phys.Rev.Lett.**73**,2252(1994).
- [3] R. C. Ashoori, H. L. Stormer, J. S. Weiner, L. N. Pfeiffer, K. W. Baldwin, and K. W. West, Phys. Rev. Lett. **71**, 613 (1993);
- [4] P. Hawrylak, Phys. Rev. Lett. **71**, 3347 (1993).
- [5] P.D.Wang, Y.P.Song, C.M.Sotomayor Torres, M.C.Holland, D.J.Lockwood, P.Hawrylak, J.J.Palacios, P.C.M.Christianen, J.C.Maan, and J.A.Perenboom, Superlattices and Microstructures **15**,23,(1994)
- [6] R.Strempel,U.Bockelmann,F.Hirler,G.Abstreiter,G.Bohm, and G.Weimann, Phys. Rev. Lett. **73**, 3022 (1994).
- [7] P.Hawrylak,Solid State Commun.**93**,915(1995)

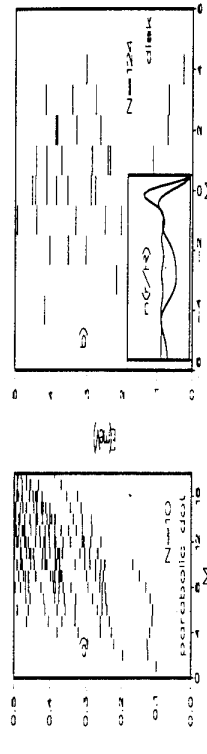


FIG. 1. Electronic excitation energies as a function of excess angular momentum M at magnetic field $B = 2\text{T}$. (a) $N = 10$ compact droplet in a parabolic dot (b) Hartree energies of a disk with $N = 124$ electrons.

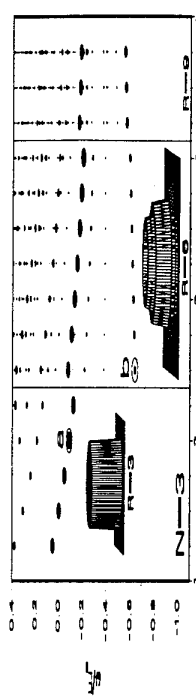


FIG. 2. Absorption spectrum $A(\omega)$ of a $N = 3$ electron dot as a function of the magnetic field. Insets show approximate charge density of the dot.

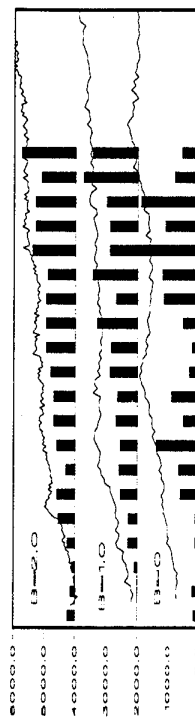


FIG. 3. (a) Raman spectrum $I(q \approx 0, \omega)$ of an array of deep-etched disks with nominal carrier density $n_s = 8.5 \cdot 10^{11} \text{cm}^{-2}$ and radius $r = 75\text{nm}$ for magnetic fields $B = 0 - 2\text{Tesla}$. (b) Hartree Single Particle excitations of a disk with carrier density $n_s = 8.0 \cdot 10^{11} \text{cm}^{-2}$ and radius $R = 70\text{nm}$ for magnetic fields $B = 0 - 2\text{Tesla}$.

Temperature effects on the Radiative Recombination in Self-Assembled Quantum Dots

S. Fafard¹, S. Raymond^{1*}, G. Wang², R. Leon^{2†}, D. Leonard², S. Charbonneau¹, J. L. Merz^{2‡}, P.M. Petroff², and J.E. Bowers².

¹Institute for Quantized Electronic Structures (QUEST), Materials department, and Electrical and computer Engineering Department, University of California, Santa Barbara, California 93106
(June 1995)

Abstract

Several ensembles of self-assembled quantum dots (QDs) based on the AlInAs/AlGaAs and InGaAs/GaAs material systems have been investigated using photoluminescence (PL), PL excitation (PLE), and time-resolved PL (TRPL). The influence of the temperature (T) is measured by monitoring sharp spectral features (as narrow as $\sim 90 \mu\text{eV}$) obtained when probing the PL of small QD ensembles (few hundreds QDs). Thermionic emission of the photocarriers out of the QD potential is found to be the dominant mechanism leading to the thermal quenching of the PL, and temperature-independent linewidths are observed up to the onset of the PL quenching.

The spontaneous island formation in the Stranski-Krastanow growth mode of highly strained semiconductors have been exploited to produce self-assembled $\text{Al}_y\text{In}_{1-y}\text{As}/\text{Al}_x\text{Ga}_{1-x}\text{As}$ and $\text{In}_x\text{Ga}_{1-x}\text{As}/\text{GaAs}$ QDs with emission in the visible [1-4] and the infrared [5-7] respectively. Non-resonant PL experiments, performed on ensembles with a different number of QDs, exposed the sharpness of the single-dot emission forming the smooth gaussian lineshape which is often observed when probing a larger number of slightly different QDs. Resonant PL or PLE experiments also revealed the discrete nature of the density of state (DOS) [6]. Enhanced radiative recombinations for excitation energies permitting resonant phonon (multi-phonon) relaxation were also observed [4], thus suggesting different 0-Dimensional (0-D) induced carriers/excitons relaxation/capture mechanisms. Time-resolved PL studies obtained with InGaAs/GaAs self-assembled QDs also demonstrated a different carrier dynamics and/or temperature behavior [5]. To further elucidate these temperature effects and the mechanism(s) leading to the thermal quenching of the PL in such 0-D structures, we present here a detailed

investigation performed on several infrared and visible QD ensembles. The samples for this work were grown by molecular beam epitaxy using the spontaneous island formation in the Stranski-Krastanow growth mode [8]. They are either based on the InGaAs/GaAs or the AlInAs/AlGaAs material systems. This method is capable of producing high material quality QDs with typical diameters of $\sim 20 \pm 2 \text{ nm}$, thicknesses of few nm, and densities between few per μm^2 to few hundreds per μm^2 . More specific sample and growth descriptions can be found in the above references.

Fig. 1 displays the temperature dependence of the PL intensities for various QD samples. From such Arrhenius plots, the activation energy (E_a) for the PL quenching can be extracted [9-12]. For the first 3 samples, the E_a values thus found are close to the energy difference between the barrier band gap (E_b) and the peak of the QD emission. This suggests that thermionic emission of the photocarriers over the barrier is responsible for the thermal quenching of the PL. The agreement for the last 2 samples is not as good, and this might be attributed to a much broader PL spectrum in the case of this InAs/AlGaAs QD

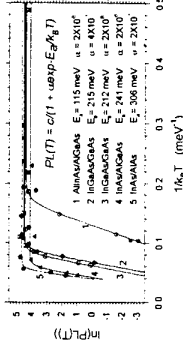


Fig. 1: Temperature dependence of the PL intensity, probing a large number of QDs, for various material systems. The activation energy E_a is derived from the Arrhenius plots by fitting the data with $I/I_0 \propto e^{(E_a/T)}$. These E_a values can be compared with the energy difference between the barrier band gap (E_b) and the peak of the QD emission: 115 meV for (1), 232 meV for (2), 242 meV for (3), 600 meV for (4), and 450 meV for (5).

sample [3], and perhaps the indirect gap of the barrier in the case of the InAs/AlAs QDs. Alternatively thermionic emission in the wetting layer (underlying the QDs [8]) might lead to a reduced activation energy since its ground state energy is lower than that of the barrier. Carrier hopping in the wetting layer would contribute to the thermal quenching if it contains large enough densities of non-radiative interface defects. In any cases, a deeper confinement clearly leads to thermal quenching at higher T, with here an onset as high as $T = 210 \text{ K}$.

To better clarify the effects of the temperature on the single QD emission, temperature-dependent PL experiments were performed on ensembles with only a few hundred QDs [2]. Fig. 2 and 3 give the results for AlInAs/AlGaAs and InGaAs/GaAs QDs respectively. The PL displays several sharp spectral features with a FWHM ranging from 190 to 400 μeV for fig. 2 and fig. 3. Other ensembles of AlInAs/AlGaAs QDs excited above E_b ($E_{exc} = 2.0 \text{ eV}$) with very low power densities ($25 \text{ nW}/\mu\text{m}^2$) exhibited spectral features as narrow as $90 \mu\text{eV}$. Spectral features for which the intensity remains well above the collective emission background show very little broadening as the temperature is increased up to the onset of the thermal quenching. Some lines, such as G, do show some broadening, although much less than the increase in the thermal energy ($k_B T$). This small effect can be attributed to the reduced signal to noise ratio caused by the thermal quenching. These temperature-independent

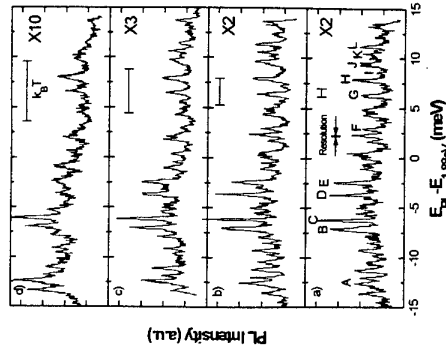


Fig. 2: PL spectra for 600 AlInAs/AlGaAs /AlGaAs/GaAs QDs, $18 \pm 2 \text{ nm}$ in diameter and 5.2 nm thick, obtained with an excitation intensity of $250 \text{ nW}/\mu\text{m}^2$ at 1.96 eV , for temperatures of $T = 1.5 \text{ K}$ (d), 30 K (b), 50 K (c), and 70 K (d). Temperature-independent sharp spectral features, $\sim 200 \mu\text{eV}$ wide, are observed up to the onset of the PL quenching.

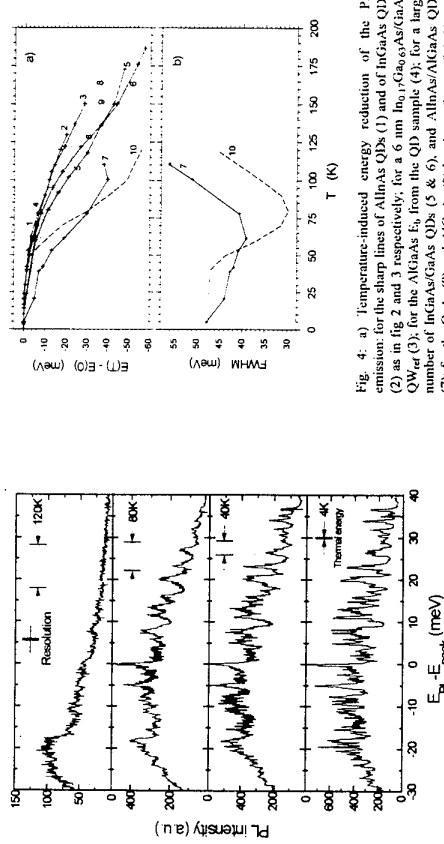


Fig. 3: Temperature-dependence of the sharp spectral features obtained with 100 In_xGa_{1-x}As/GaAs QDs, 25 ± 5 nm in diameter.

4b. This behavior is readily understood considering the effects of the thermionic emission. Fig. 5 clearly demonstrate the influence of the thermionic emission by comparing the measured PL with the calculated $PL(E, T)$ obtained considering the thermionic emission [9-12] out of the QDs and the gaussian lineshape associated with QDs having slightly different ground state energies [2]. We obtain:

$$PL(E, T) = C \exp(-(E-E_g)/\Gamma)^2 / (1+\exp-(E_g-E)/KT) \quad (1)$$

Comparing fig. 5a and b, it is clear that this simple model taking into account the thermionic emission is in good qualitative agreement with the observed temperature effects for the changes in the emission energy and the FWHM. However, the temperature at which the effects are predicted and the magnitude of the shifts are different. This might be linked to carrier retrapping by the lower energy QDs which is likely to occur, as in the case of QWs [10,12]. In the absence of thermionic emission, 0-D quantum structures are expected to be characterized with temperature-independent decay-times [5]. The

PL results obtained with the AlInAs/AlGaAs QDs are shown in fig. 5c for $T=2$ K where thermionic emission should be negligible for all QDs, and for $T=55$ K where the decay times for the lower energy QDs remain unaffected, but the higher energy QDs suffer from the enhanced thermionic emission rates. The thermionic emission rate can be deduced from the $(1/\tau_{55K} - 1/\tau_{2K})^{-1}$ plot in fig. 5d which demonstrates a clear dependence on the emission energy, and thus the confinement potential.

To illustrate that the retrapping of thermionically emitted photocarriers might be important amongst the distribution of QDs in a given ensemble, fig. 6 displays the PL spectra obtained at different T for a sample containing a reference QW 100 nm away from the QD layer. The peak observed at ~ 100 meV above E_{det} corresponds to photocarriers created in the QW_{ref} and transferred to the QDs via thermionic emission. Clearly this process becomes more important as T is increased.

In conclusions, the temperature-independent extremely narrow linewidths observed with the

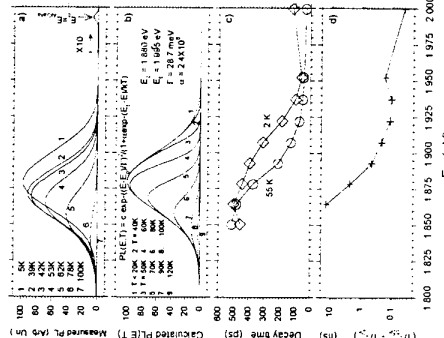


Fig. 4: a) Temperature-induced energy reduction of the PL emission for the sharp lines of AlInAs QDs (1) and of InGaAs QDs (2), as in fig. 3 and 3 respectively; for a 6 nm In_xGa_{1-x}As/GaAs QW (3); for the AlInAs QDs (5 & 6); for a large number of InGaAs/GaAs QDs (5 & 6), and AlInAs/AlGaAs QDs (7); for the GaAs (8) and AlGaAs (9) band gap from ref. [13]; and for the thermionic emission model of fig. 5b. In b), the temperature dependence of the FWHM is shown for the PL spectra thermionic emission model (10). Fig. 5b, also shown in fig. 5a, and for the thermionic emission model (10), fig. 5b.

TRPL results obtained with the AlInAs/AlGaAs QDs are shown in fig. 5c for $T=2$ K where thermionic emission should be negligible for all QDs, and for $T=55$ K where the decay times for the lower energy QDs remain unaffected, but the higher energy QDs suffer from the enhanced thermionic emission rates. The thermionic emission rate can be deduced from the $(1/\tau_{55K} - 1/\tau_{2K})^{-1}$ plot in fig. 5d which demonstrates a clear dependence on the emission energy, and thus the confinement potential.

This research was supported by NSF Science and Technology Center QUEST (DMR #91-20077), by an AFOSR grant (#F49620-92-J-0124). Some of us (S.F. and S.R.) would also like to acknowledge NSERC for their additional support.

*Also at Department of Physics, University of Ottawa, Ottawa, Ontario, Canada K1N 6N5.

†Present address: Department of Electronic Materials Engineering, The Australian National University, Canberra, ACT, 0200, Australia.

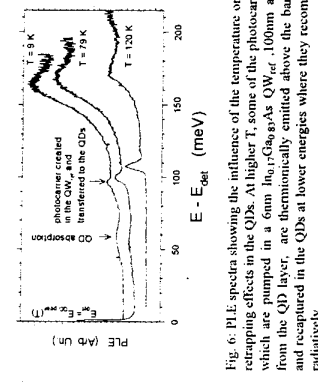


Fig. 6: PL spectra showing the influence of the temperature on the retrapping effects in the QDs. At higher T, some of the photocarriers which are pumped in a 6 nm In_xGa_{1-x}As QW_{ref} 100nm away from the QD layer, are thermionically emitted above the barrier, and reabsorbed in the QDs at lower energies where they recombine radiatively.
Present address: Department of Electrical Engineering, University of Notre Dame, Notre Dame, Indiana U.S.A. 40536-5602.

References

- [1] R. Leon, P.M. Petroff, D. Leonard, and S. Falard, Science 267, 1966 (1995).
- [2] S. Falard, R. Leon, D. Leonard, J.L. Merz, and P.M. Petroff, Phys. Rev. B 50, 8086 (1994).
- [3] I. Leon, S. Falard, D. Leonard, J.L. Merz, and P.M. Petroff, Appl. Phys. Lett. 64, 2815 (1994).
- [4] S. Falard, R. Leon, D. Leonard, J.L. Merz, and P.M. Petroff, Phys. Rev. B (1995).
- [5] G. Wang, S. Falard, D. Leonard, J.J. Bowers, J.L. Merz, and P.M. Petroff, Appl. Phys. Lett. 64, 2815 (1994).
- [6] S. Falard, D. Leonard, J.L. Merz, and P.M. Petroff, Appl. Phys. Lett. 65, 1388 (1994).
- [7] D. Leonard, S. Falard, K. Pond, Y.H. Zhang, J.M. Merz, and P.M. Petroff, J. Vac. Sci. Technol. B12, 2516 (1994).
- [8] D. Leonard, K. Pond, and P.M. Petroff, Phys. Rev. B 50, 11 687 (1994).
- [9] G. Buehler, H. Schweizer, J. Kovace, A. Forchel, H. Nickel, W. Schiltlapp, and R. Lischl, Phys. Rev. B 43, 9312 (1991).
- [10] G. Buehler, C. Hartmann, H. Schweizer, F. Held, G. Maher, and H. Nickel, Phys. Rev. B47, 9535 (1993).
- [11] J.D. Lambkin, D.J. Dunstan, K.P. Homewood, I.K. Howard, and M.T. Emeny, Appl. Phys. Lett. 57, 1886 (1990).
- [12] M. Vening, D.J. Dunstan, K.P. Homewood, Phys. Rev. B48, 2412 (1993).
- [13] M. El allali, C.B. Storaasen, E. Veijo, and P. Friedland-Peterson, Phys. Rev. B48, 4398 (1993).

RESONANT INELASTIC LIGHT SCATTERING BY ELECTRONIC EXCITATIONS IN TUNABLE QUANTUM WIRE STRUCTURES

G. Schiedelbeck, E. Silveira, R. Strenz, U. Bockelmann, G. Abstreiter,
G. Böhm and G. Weimann
Walter Schottky Institut, Technische Universität München, Germany

Abstract

Resonant inelastic light scattering is used to investigate both charge density excitations and spin density excitations in shallow etched GaAs/AlGaAs quantum wires. A semitransparent Schottky gate is evaporated on top of the samples which allows a strong tunability of the electron density and the lateral confinement even under high illumination conditions used for inelastic light scattering. The range of charge density excitations extends from confined plasmons to a plasmon band structure. Both intra- and intersubband single particle excitations are observed. The occurrence of a tunable doublet structure in depolarized plane wave spectra is attributed to spin flip intersubband single particle excitations.

1. Introduction

The investigation of elementary excitations in low dimensional electron systems with inelastic light scattering has been subject of extensive research for many years. Plasmons in quantum wires have been investigated with various methods. In cases where the Fermi energy is smaller than the lateral potential modulation and the Fermi wavelength is several times larger than the inverse confinement length, the observed modes are explained in terms of confined plasmons [1]. A plasmon band structure is expected for systems with a Fermi energy larger than the lateral potential modulation [2]. Intersubband single particle excitations (SPE) in quantum wires have been observed as well [3]. It was found that the energies and spacings of the modes depend on the effective electrical wire width. In 2D quantum wells a doublet structure in the intrasubband SPE has been attributed to transitions between the two spin split conduction bands of GaAs [4]. In this communication we discuss plasmons as well as inter- and intrasubband SPE in tunable wire structures.

Two n-type modulation doped single quantum well (SQW) AlGaAs/GaAs structures are used as starting material. The location of the SQW beneath the surface and the 2D-carrier density determined by magnetotransport measurements, are 650 Å and $5.7 \times 10^{11} \text{ cm}^{-2}$ for structure A, and 360 Å and $10.8 \times 10^{11} \text{ cm}^{-2}$ for structure B. The samples are laterally structured with holographic lithography and wet chemical etching as described in reference [1]. For sample B the wires are oriented along the (110) direction. The nominal period lengths for both samples are in the range of 600 nm. The etching process of A (B) is stopped in a depth of 200 Å (85 Å). On top of the surface a 50 Å titanium Schottky gate is evaporated and an Ohmic contact is alloyed to the SQW (inset fig. 1). By applying a bias voltage between the electron system and the Schottky contact, the electron density and the confining potential can be tuned even under high illumination conditions used for electronic Raman scattering. The experiments are performed in conventional backscattering geometry in a continuous flow He cryostat at a temperature of about 5 K. The samples are excited by a dye laser in the range of the second allowed electron heavy hole

transition. The transferred in plane wavevector \mathbf{q} is varied by tilting the sample normal by an angle α with respect to the incident linearly polarized laser beam : $\mathbf{q} = (4\pi \sin \alpha)/\lambda$. Wavevector transfer parallel to the wire grating is called plane wave geometry (PW), while wavevector transfer perpendicular is called standing wave geometry (SW).

2. Plasmons

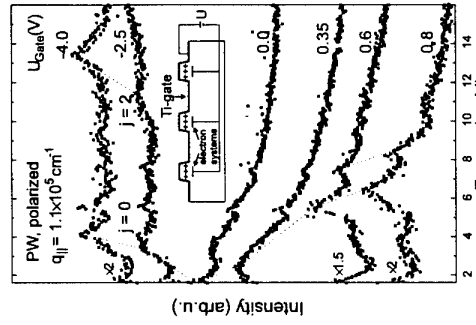


Figure 1. Polarized spectra from sample A for different gate voltages.

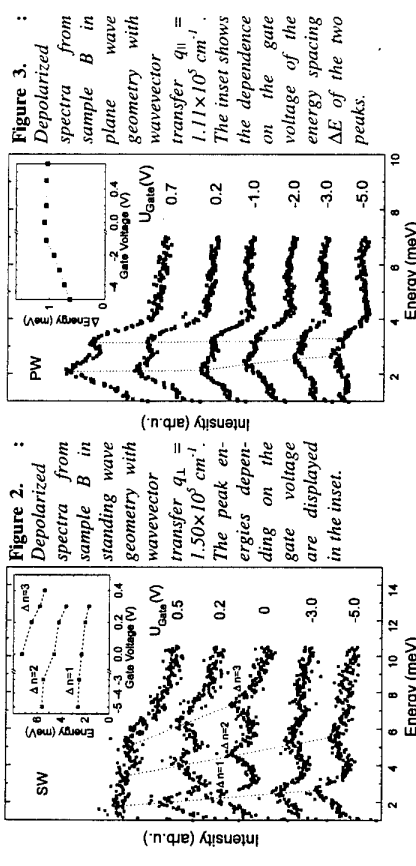
The dotted lines are guides to the eye. The inset shows a schematic cross section view valid for both structures. Thus we conclude that in this regime the potential modulation is larger than the Fermi energy and a pattern of standing wave geometry, reveal the typical features of confined plasmons [1]. Thus we conclude that in this regime the potential modulation is larger than the Fermi energy and a pattern of isolated wires is formed. A fit, using the simple picture of standing waves [7] in connection with an effective dielectric constant due to the metallic surface [8], yields for $U_{\text{Gate}} = -4.0 \text{ V}$ an electron density in the wire of approximately $2.5 \times 10^{11} \text{ cm}^{-2}$ and an effective electrical wire width of about 54 nm. At $U_{\text{Gate}} > 0.3 \text{ V}$ we observe a strong anisotropic dispersion for wavevector transfer parallel as well as perpendicular to the potential modulation. For these gate voltages the potential modulation is expected to be smaller than the Fermi energy, which leads to a charge density modulated 2D system. Due to the periodic potential for wavevectors parallel to the modulation the dispersion is folded back into the first Brillouin zone. The observed regular ladder scheme, which is in good qualitative agreement with theoretically expected dispersions, is a typical signature of plasmon bandstructure. In the regime for $-2.0 \text{ V} < U_{\text{Gate}} < 0.3 \text{ V}$ no plasmons are observable. Here the Fermi energy is approximately equal to the potential modulation. The excitation of plasmons is then located at points with minimal charge density ('asymptotic localization' [9]) and therefore, the peaks collapse towards energies below the experimentally accessible range.

3. Single Particle Excitations

Figure 2 shows depolarized spectra from sample B in standing wave geometry for fixed wavevector transfer but varying gate voltages. For vanishing gate voltage three modes are observed, which are spaced nearly equidistantly. They are attributed to intersubband SPE [3].

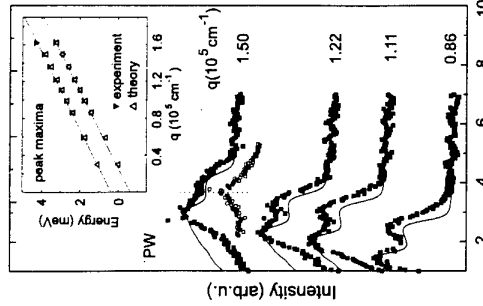
For increasing negative gate voltages these modes shift to higher energies and the spacing increases. With increasing positive gate voltages on the other hand the energies and the spacings decrease (see also inset of figure 2). This blueshift of the intersubband SPE with decreasing voltage is explained by a decreasing effective electrical wire width, which leads to a stronger lateral confinement of the electrons with higher quantization energies.

In figure 3 depolarized spectra of the same sample, but in plane wave geometry are displayed. As in figure 2, the wavevector is fixed and the gate voltage is varied. In this geometry, intrasubband SPE are expected to be the dominant feature. The observed mode shows a clear doublet structure. Both peaks shift with decreasing voltage to higher energies. For increasing negative gate voltages below 0V the shift of the low energy peak is stronger, which leads to a decrease of the spacing. In addition, the intensity of the mode decreases monotonically for decreasing gate voltage.



The doublet structure in the intrasubband SPE may be attributed to spin splitting of the conduction band [10]. Due to the lack of inversion symmetry in the zinc-blende structure of GaAs the conduction band is non-degenerate even at zero magnetic field. In 2D quantum wells the effects of the spin split conduction band on SPE have been studied extensively [4, 11, 12]. In addition to non spin flip processes, which are allowed in both polarizations, in crossed polarization transitions between the two spin split conduction bands can contribute to the observed spectra. Neglecting anisotropy effects, the lineshapes of the SPE continua with spin flip from down to up and vice versa are essentially not modified, but their cutoff energies are different: $E_c^*(\mathbf{q}) = \hbar q v_F \pm \Delta E(k_F)$ [4].

To support the interpretation, that also in our microstructured sample spin flip processes lead to the doublet structure of the intrasubband SPE, we have studied the wave vector dependence of depolarized spectra (Fig. 4). A gate voltage of 0.2V is applied to obtain well resolved two peaks. Both peak maxima show a linear dependence on the wavevector transfer, while the spacing nearly stays constant. For a wavevector transfer of $1.50 \times 10^5 \text{ cm}^{-1}$ the polarized spectrum is also displayed with hollow symbols. In this geometry no doublet structure of the SPE is observable. The energy of the peak in polarized geometry is between the energies of the peaks in depolarized geometry.



The straight lines are fitted to the experimental data. The lineshape of SPE is given by the imaginary part of the polarizability of the non-interacting electron gas [5]. Only spin flip intrasubband transitions are considered. The conduction band dispersion along the $(1\bar{1}0)$ direction is derived from the effective mass Hamiltonian including spin splitting [10], replacing the wavevectors in the confined directions by differential operators. In growth direction we assume a rectangular and in lateral direction a parabolic confinement potential. The field induced asymmetry of the SQW is neglected due to its small thickness of 80Å. For $U_{\text{Gate}} = 0.2V$ we obtain from the inset of figure 2 a subband spacing energy of 2.0meV. We use a single-particle scattering time of 6ps, a carrier temperature of 10K and a Fermi energy of 30meV. The spin splitting parameter $\gamma = 8.9 \text{ eV}^3$ is taken from [13]. The calculated lineshapes are in reasonable agreement with the experiment. The positions of the peak maxima (inset of figure 4) are very well reproduced.

4. Acknowledgments

We thank C. Obermüller and M. Holzmann for numerous SEM and AFM investigations and gratefully acknowledge financial support by the Deutsche Forschungsgemeinschaft via SFB 348.

5. References

- [1] R. Strenz, V. Roßkopf, F. Hirler, G. Abstreiter, G. Böhm, G. Tränkle, and G. Weimann, *Semicond. Sci. Technol.* **9**, 399 (1994)
- [2] G. Eliasson, P. Hawrylak, J.-W. Wu, and J.J. Quinn, *Solid State Comm.* **60**, 3 (1986)
- [3] R. Strenz, U. Bockelmann, F. Hirler, G. Abstreiter, G. Böhm, and G. Weimann, *Phys. Rev. Lett.* **73**, 22 (1994)
- [4] B. Jusserand, D. Richards, H. Peric, and B. Etienne, *Phys. Rev. Lett.* **69**, 5 (1992)
- [5] Pinczak and G. Abstreiter, in *Light Scattering in Solids V*, Eds. M. Cardona and G. Güntherodt (Springer Verlag, Berlin, 1989) p. 153.
- [6] G. Schedelbeck, R. Strenz, G. Abstreiter, G. Böhm, and G. Weimann, *Solid State Comm.* **93**, 569 (1995)
- [7] T. Egele, G. Abstreiter, and G. Weimann, *T. Denel, D. Heitmann, and P. Grambow, W. Schiapp, Phys. Rev. Lett.* **65**, 14 (1990)
- [8] A. V. Chaplik, *Surf. Sci. Rep.* **5**, 293 (1985)
- [9] V. Cataudella and V. Marijano Ramalho, *Phys. Rev. B* **38**, 3 (1988)
- [10] U. Rössler, *Solid State Comm.* **49**, 943 (1984)
- [11] D. Richards, B. Jusserand, H. Peric, and B. Etienne, *Phys. Rev. B* **47**, 23 (1993)
- [12] B. Jusserand, D. Richards, G. Allan and C. Priester, B. Etienne, *Phys. Rev. B* **51**, 7 (1995)
- [13] P. Santos and M. Cardona, *Phys. Rev. Lett.* **72**, 432 (1994)

Chaos in Quantum Dots

B.L. Altshuler

NEC Research Institute, 4 Independence Way, Princeton, NJ 08540, USA
 Department of Physics, Massachusetts Institute of Technology,
 77 Massachusetts Ave., Cambridge, MA 02139, USA

Abstract

The majority of studies of quantum effects in transport phenomena focus on the properties of *open* systems where the size of the leads are comparable to the system size, L . In such structures quantum interference arising from the scattering from impurities eventually induces the phenomenon of localization as the system size or degree of disorder is increased. Even before localization, sample to sample fluctuations of the conductance δg are universal of order unity (weak localization), so that close to the insulating state they become of the same order as the average conductance, $\langle g \rangle$.

However, there are other ways in which quantum interference effects are manifest. One can decrease the size of the leads while keeping L and the mean free path, l , constant. This clearly decreases $\langle g \rangle$ without changing the magnitude of the fluctuations $\delta g \sim 1$. As a result, the relative fluctuations of the conductance g as a function of Fermi energy E_F , or magnetic field becomes increasingly pronounced. For a single channel lead, $\delta g \sim \langle g \rangle$.

Indeed it is possible to go further and apply to the system tunnel contacts with very low transmittance. If Coulomb Blockade effects can be neglected, $g(E_F)$ is described by a series of resonance peaks. Their location is determined by the spectrum of the system while the widths are set by the escape rate \hbar/τ_{esc} . If the latter is smaller than the typical inverse transport time or Thouless energy $E_c = \hbar D/L^2$, then E_c is irrelevant. Such devices are known as ‘quantum dots’.

When the system was open there were two relevant energy scales,

E_c and the mean level spacing Δ , which can be combined into the

dimensionless ratio $g = E_c/\Delta$. Here we consider only systems with g/g_1 and will be concerned with time scales $t \geq \hbar/\Delta \equiv t_H$ ($t \leq \tau_{\text{esc}}$) when the individual levels are well resolved. In this case we have only one relevant energy scale Δ (or, equivalently, one time scale, the Heisenberg time, t_H). Therefore, the statistical properties of the system should become universal after proper rescaling.

The question of level statistics in metallic grains or quantum dots has a long history. Universality of the statistical properties was first conjectured by Gorkov and Eliashberg in a study of the dielectric properties of an ensemble of metallic grains. However, it was not until a pioneering work by Efetov almost twenty years later that a formal theoretical framework was developed that confirmed this hypothesis. From a field theoretic description of weakly disordered conductors, Efetov demonstrated that the single-particle spectral properties of disordered metallic grains obey the same statistics as random matrix ensembles.

Here we will discuss some general results which have been found from the study of weakly disordered metallic conductors but which have an application that encompasses all quantum chaotic systems. In particular, we will explore universal statistical correlations associated with the response of matrix elements as well as spectra to the change in arbitrary external perturbations. We will illustrate the universality of parametric correlation functions by investigating several types of correlation function and discuss a variety of general relations which connect different types of response functions. We will also describe several applications of these results.

EVIDENCE FOR PERIODIC 'SCAR' PATTERNS IN THE WAVEFUNCTIONS OF A CHAOTIC QUANTUM WELL

P.B. Wilkinson, T.M. Fromhold, L. Eaves, F.W. Sheard,
N. Miura*, and T. Takamatsu.

*Department of Physics, University of Nottingham, Nottingham NG7 2RD, UK
* Institute for Solid State Physics, University of Tokyo, Tokyo 106, Japan*

The tunnelling characteristics of GaAs/(AlGa)As double barrier structures are investigated when a large tilted magnetic field is applied to generate strongly chaotic (nonintegrable) classical motion in the wide (~ 100 nm) quantum well. In this regime, a transfer-Hamiltonian approach is used to calculate current-voltage characteristics $I(V)$ for the structures. The theoretical $I(V)$ curves reveal distinct series of resonant peaks which have been observed in recent experiments. These resonances are shown to originate primarily from dominant transitions into subsets of regularly spaced energy levels in the well whose wavefunctions contain regions of high probability density (scars) along the paths of particular unstable periodic classical orbits. The effects of very high magnetic fields (up to 37 T) on the tunnelling characteristics are investigated experimentally.

A clear link between the classical and quantum pictures of chaotic electron dynamics has been identified by considering the statistical properties of the quantised energy levels [1]. Despite the characteristic irregularity of the level spectra, periodic fluctuations in the density of levels can be identified and related to unstable but periodic classical orbits, as shown by the theoretical work of Gutzwiller [1] and Berry [2]. A particular orbit with period T_p produces fluctuations on an energy interval $\Delta_{\text{ep}} = \hbar/T_p$ [2]. These Gutzwiller oscillations have been observed experimentally in magnetoabsorption spectra of highly excited hydrogenic atoms [3]. More recently, resonant tunnelling spectroscopy has been used to investigate the energy level spectra of wide (~ 100 nm) quantum wells (QWs), which exhibit strongly chaotic classical motion in a large tilted magnetic field B [4,5]. Distinct sets of periodic resonances in the current-voltage characteristics $I(V)$ of the resonant tunnelling diodes (RTDs) were originally attributed to Gutzwiller oscillations in the QW associated with a small number of unstable closed classical orbits [4,5]. However, recent theoretical work [6] has shown that for certain tilt angles and voltage ranges, the tunnelling rates into individual "scarred" states in the QW whose wavefunctions are localised along the paths of particular closed classical orbits are much higher than for transitions into adjacent unscarred states. This scarring of individual eigenfunctions occurs periodically on exactly the same energy scale as the Gutzwiller fluctuations associated with the scarring orbit [6]. It is therefore unclear whether the observed peaks in $I(V)$ originate from Gutzwiller fluctuations in the density of levels or from dominant transitions into *individual* scarred states.

Here we address this question by calculating the tunnelling characteristics of a RTD containing a QW of width $w = 120$ nm when a high magnetic field of 11.4 T is applied at angles $\theta = 20^\circ$ and 40° to the normal to the well walls. For these angles, the electrons in the QW exhibit predominantly strong classical chaos. At $\theta = 20^\circ$ (40°), the calculated $I(V)$ resonances are shown to originate mainly from dominant transitions into individual scarred states in the QW. For a RTD containing a 60 nm wide QW, we have investigated how the resonant

peaks in $I(V)$ change as B is increased to 37 T. The oscillatory structure associated with a particular type of periodic classical orbit is found to persist over a wide range of magnetic field values.

4. Details of the sample composition are given in Ref. 7. Under bias voltage V , a two-dimensional electron gas (2DEG) is formed in the undoped spacer layer adjacent to the left-hand (LH) barrier. Current flows as electrons tunnel from the 2DEG into the quantised energy levels of the QW [4-6]. Close to the electron injection energy, individual energy levels in the QW cannot be resolved because the mean level spacing ~ 1 meV is much smaller than the level broadening ~ 6 meV produced by the emission of longitudinal optic phonons and interface scattering [4,5]. This can be seen from Fig. 1(a) where we show energy levels calculated for $V = 176$ mV, together with the density of levels D , obtained by broadening each level to a width of ~ 6 meV. The energy levels are calculated by diagonalising the Hamiltonian matrix for the QW, assuming finite barriers of height 330 meV [6]. Conduction band nonparabolicity is included phenomenologically by using a mean effective mass $m^* = 0.067m_e(1 + \alpha K(V))$, where $K(V)$ is the kinetic energy of the electrons at the centre of the QW under bias V , and $\alpha = 2$ eV⁻¹ [8]. For the energy range shown in Fig. 1, the classical phase space exhibits predominantly strong chaos [8]. Although the level spacing is too small for individual energy levels to be resolved, periodic Gutzwiller fluctuations in the density of levels can be identified. These oscillations can be related to unstable periodic orbits in which the electron makes two successive collisions on the right-hand (RH) barrier for each collision on the LH barrier (Fig. 1(b) RH inset) [4]. Henceforth we refer to an unstable periodic orbit in which the electron makes λ successive collisions on the RH barrier for each collision on the LH barrier as a type λ orbit. As V is varied, resonant tunnelling into the quantised energy levels in the QW is expected to generate resonant peaks in $I(V)$. The current due to transitions from the emitter 2DEG into the n^{th} bound state of the QW is proportional to the transition rate $W_n \propto M_n^2$, where the matrix element M_n depends on the overlap between the emitter and QW states [6]. We have calculated these matrix elements within the Bardeen transfer-Hamiltonian formalism [9], using an approximate separable wavefunction for the emitter state [8].

Fig. 1(b) shows M_n^2 for tunnelling transitions into the discrete energy levels in Fig. 1(a). These matrix elements are much larger for transitions into a subset of almost equally-spaced energy levels than for the remaining states. The reason for this can be seen by examining the probability distributions of the corresponding wavefunctions which are shown in inset [6]. These wavefunctions all reveal remarkably strong scars of type 2 orbits (RH inset). The energies of these scarred states can be accurately located using a simple quantisation rule $S(\epsilon) = (\nu + \phi)\hbar$, where $S(\epsilon)$ is the classical action of the scarring orbit, the quantum number ν gives the number of antinodes in the scar pattern along the classical path, and ϕ is fixed for a given type of orbit [6]. The rates of tunnelling transitions into these scarred states are high because the LH antinode in the scar pattern is aligned in the z -direction with the maximum in the probability density of the occupied ($n = 0$) Landau level in the emitter accumulation layer [8]. Unscarred QW states generally have several antinodes close to the LH barrier and therefore couple weakly to the emitter states. Note that the energy spacing of the scarred states is identical to the period of the Gutzwiller oscillations in Fig. 1(a).

We have investigated how transitions into individual scarred states in the QW influence the tunnelling characteristics of the RTDs. Fig. 2(a) shows the $I(V)$ curve calculated for $B =$

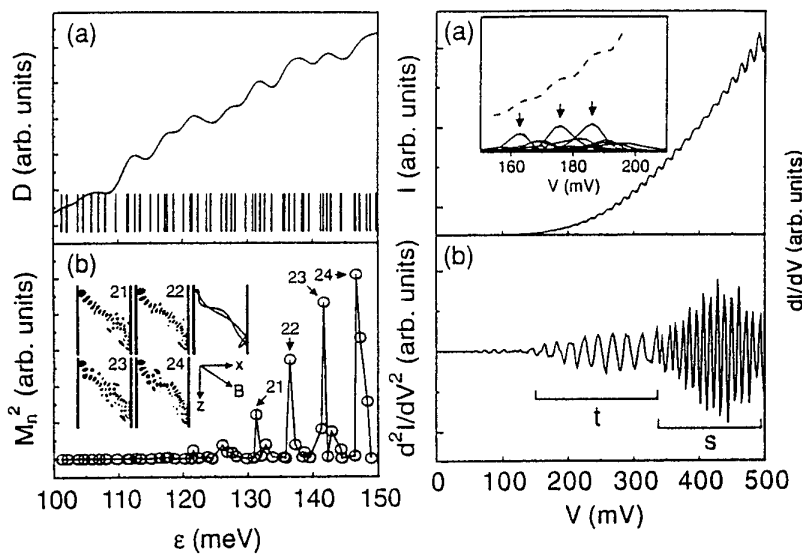


Fig. 1 (a) Energy levels (vertical lines) and density of levels D versus electron energy ϵ measured from conduction band edge at RH side of the QW. (b) M_n^2 for transitions into QW states close to the electron injection energy. Insets: probability density in x - z plane for eigenfunctions (with quantum numbers ν shown) scarred by the type 2 orbit shown in RH inset. $B = 11.4$ T, $\theta = 40^\circ$, $V = 176$ mV, $\alpha = 2$ eV $^{-1}$, $w = 120$ nm.

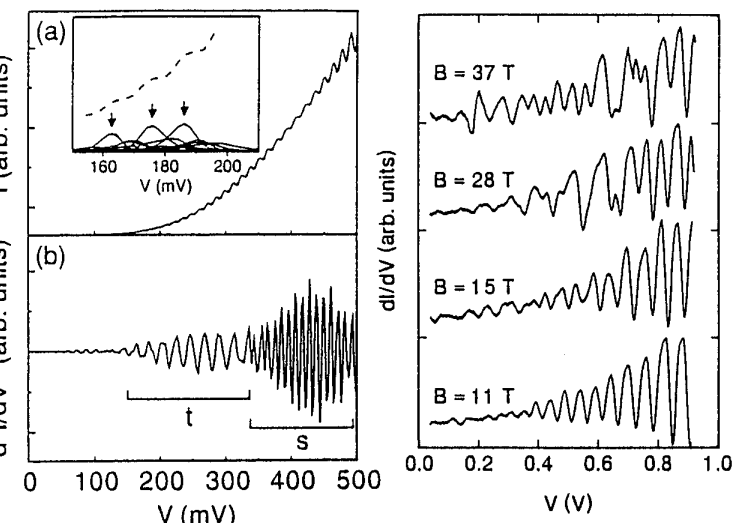


Fig. 2 (a) $I(V)$ characteristic calculated for $\theta = 40^\circ$. Inset: $I(V)$ (broken curve) and current contributions (solid curves). Dominant contributions (arrowed) originate from transitions into individual QW states scarred by type 2 orbits. (b) d^2I/dV^2 versus V plot calculated for $\theta = 20^\circ$ showing s - and t -series of resonances. $B = 11.4$ T, $\alpha = 2$ eV $^{-1}$, $w = 120$ nm.

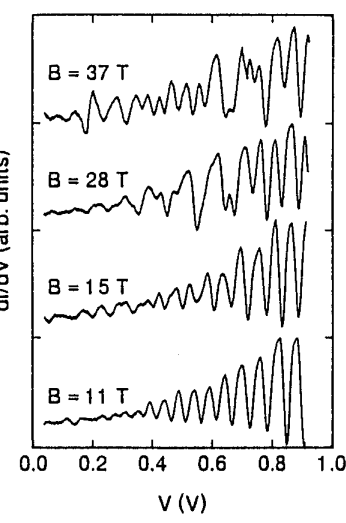


Fig. 3 dI/dV versus V plots for a RTD containing a 60 nm wide QW with $\theta = 40^\circ$ and magnetic field values indicated.

11.4 T and $\theta = 40^\circ$, together with current contributions (arrowed) originate from resonant tunnelling into scarred states in the QW similar to those shown in Fig. 1(b) and generate strong resonant peaks in $I(V)$. Similar resonant features have been observed in the corresponding experimental data [4]. When $\theta = 20^\circ$ (Fig. 2(b)), the calculated d^2I/dV^2 versus V plot reveals two different sets of oscillations, as in the experiments [4]. The s - and t -series originate primarily from dominant transitions into individual states in the QW whose wavefunctions are scarred by type 2 and type 1 orbits respectively. However, Gutzwiller oscillations may also contribute to the resonant structure observed for this tilt angle, particularly at high V [8].

We have investigated how the resonant peaks observed in the $I(V)$ characteristics of a RTD containing a 60 nm wide QW evolves with increasing B . Pulsed magnetic fields up to 37 T were used to generate strongly chaotic classical motion in the QW over wider ranges of V and θ than in our previous experiments [5]. Fig. 3 shows dI/dV versus V plots for several field values at $\theta = 40^\circ$. When $B = 11$ T, a single series of resonant peaks is observed for $0.2 \leq V \leq 0.9$ V. These resonances can be related to type 3 orbits in the QW [5]. Orbit of this type exist for a wide range of B , and so associated resonant peaks can be seen in all of the tunnelling characteristics shown in Fig. 3. Additional lower frequency oscillations observed for $B = 15$ T, 28 T, and 37 T, probably originate from type 1 orbits in the QW [8].

In summary we have studied wavefunction scarring and its influence on tunnelling into a QW with chaotic electron dynamics. Transitions into periodic subsets of scarred states in the QW have been shown to generate dominant peaks in $I(V)$ which provide direct experimental evidence for the periodic scarring of individual wavefunctions. For a RTD containing a 60 nm wide well, resonant peaks associated with type 3 orbits persist over a remarkably wide range of magnetic field values. Our studies highlight the potential of RTDs for the study of wavefunction scarring.

This work is funded by the UK Engineering and Physical Sciences Research Council (EPSRC). LE (TMF) are supported by EPSRC Senior (Advanced) Fellowships.

- [1] M.C. Gutzwiller, *Chaos in Classical and Quantum Mechanics* (Springer-Verlag, New York, 1990).
- [2] M.V. Berry, Proc. R. Soc. London A 413 (1987) 183.
- [3] A. Holle, J. Main, G. Wiebusch, H. Rottke, and K.H. Welge, Phys. Rev. Lett. 61 (1988) 161.
- [4] T.M. Fromhold, L. Eaves, F.W. Sheard, M.L. Leadbeater, T.J. Foster and P.C. Main, Phys. Rev. Lett. 72 (1994) 2608.
- [5] T.M. Fromhold, A. Fogarty, L. Eaves, F.W. Sheard, M. Henini, T.J. Foster, P.C. Main, and G. Hill, Phys. Rev. B, accepted for publication.
- [6] T.M. Fromhold, P.B. Wilkinson, F.W. Sheard, L. Eaves, J. Miao, and G. Edwards, Phys. Rev. Lett., accepted for publication.
- [7] M. Henini, M.L. Leadbeater, E.S. Alves, L. Eaves, and O.H. Hughes, J. Phys.: Condens. Matter 1 (1989) 3025.
- [8] T.M. Fromhold, P.B. Wilkinson, L. Eaves, and F.W. Sheard, to be published.
- [9] I. Bardeen, Phys. Rev. Lett. 6 (1961) 57.

Persistent currents in the ballistic regime

Rodolfo A. Jalabert¹, Klaus Richter², and Denis Ullmo³

¹ Université Louis Pasteur, IPN-CNRS-GMME, 29 rue du Loess, 67037 Strasbourg Cedex, France

² Institut für Physik, Münsterstr. 6, 86135 Augsburg, Germany

³ AT&T Bell Laboratories, 1D-265, 600 Mountain Avenue, Murray Hill, New Jersey 07974-0636

We analyze the persistent currents of noninteracting electrons in mesoscopic ballistic rings. We provide a semiclassical approach stressing the relevance of the underlying classical mechanics, and in particular of short periodic trajectories. In the limit of thin rings we recover previous theoretical results that we compare with recent measurements in the ballistic regime.

I. INTRODUCTION

The existence of a magnetic moment in normal metal rings threaded by a magnetic flux, referred as the persistent current (PC) phenomenon, has received considerable theoretical attention since the experimental evidence provided by Levy et al. [1,2]. These first measurements were done in an ensemble of metallic rings, where the electron motion is *disordered*. Recent experiments in rings lithographically defined on high-mobility semiconductor heterostructures [3] measured the PC of a single ring in the *ballistic* regime, where the classical electron motion is essentially given by the bounces off the walls of the confining potential. The ballistic regime is particularly interesting since the nature of the underlying classical mechanics (in particular whether or not the hamiltonian is chaotic) becomes relevant for the quantum properties, like the conductance or the magnetic susceptibility [4-6].

Persistent currents have been analyzed up to now in models of diffusive [2] or ideal quasi-one dimensional [7] rings. Therefore, it is important to develop an approach that can interpolate between the two regimes. Semiclassical techniques are particularly suited for this purpose. In this communication we use these tools to calculate the PC of a ring billiard of finite width. This *clean* (disorder-free) model can be easily generalized to include the effect of weak disorder [8].

II. THERMODYNAMICS OF CLASSICALLY INTEGRABLE SYSTEMS

The magnetization M of a small ring (of outer and inner radius a and b) is usually expressed in terms of the persistent current I , given by the thermodynamical relation

$$I = \frac{e}{A} \mathcal{M} = -e \left(\frac{\partial F}{\partial \Phi} \right)_{T,N} \quad (1)$$

$F(T, H, N)$ is the free energy, $\Phi = HA$ is the total flux, with H the applied field and $A = \pi a^2$ the total area. The number of electrons N is finite and fixed, dictating the use of the canonical ensemble [2]. In the leading order in N , and for temperatures such that $k_B T$ is much larger than the level spacing Δ , the choice of the ensemble, (canonical vs. grand-canonical) is not important, and we can work with the thermodynamical potential

$$\Omega(T, \mu, H) = -\frac{1}{\beta} \int dE d(E) \ln(1 + \exp[\beta(\mu - E)]),$$

which is simply expressed in terms of the single-particle density of states (DOS) $d(E) = g_S \sum_\lambda \delta(E - E_\lambda)$. The factor $g_S = 2$ takes into account spin degeneracy, E_λ are the eigenenergies, and $\beta = 1/k_B T$. Using Ω instead of F in Eq. (1) (with the chemical potential μ dictated by the condition of having a mean number of particles equal to N) is appropriate when considering the magnetic response of a single mesoscopic sample. However, for an ensemble of microstructures the average magnetization vanishes in the leading order, and we need to calculate further corrections in $1/N$ [2,6].

The calculation of the PC in a noninteracting system reduces to that of the field-dependent DOS. Moreover, since the temperatures of experimental interest are much larger than the level spacing, only the features of the DOS on a scale larger than Δ are relevant. The semiclassical trace formulas [9,10] are particularly suited for obtaining this information. For chaotic dynamics the Gutzwiller formula expresses the DOS as a sum over (isolated) periodic orbits (POs). For integrable systems the POs appear in families and the Berry-Tabor formula expresses the DOS as a sum over these families. Generically,

systems which are integrable at zero field lose their integrability by the effect of an applied magnetic field. In that case an interpolation scheme between the two trace formulas is needed [5,6]. An exception within the integrable systems are those with rotation symmetry, where a finite field does not break the integrability. Circle and ring billiards belong to this category. The magnetic susceptibility of a disk [5,6] and the PC in a ring can be calculated as a direct application of the Berry-Tabor formula.

The classical hamiltonian $H(p, q)$ is integrable if there exist as many constants of motion as degrees of freedom (2 in our case). For bounded systems all trajectories are trapped on torus-like manifolds, each of which can be labeled by the actions integrals

$$I_j = \frac{1}{2\pi} \int_C p dq, \quad j = 1, 2, \quad (2)$$

taken along two independent paths C_1 and C_2 . The Berry-Tabor formula writes the DOS as [10]

$$d(E) = d(E) + d^{ss}(E).$$

The mean component $d(E)$ is in leading order in h , the Weyl term, while $d^{ss}(E)$ is given as the sum

$$d^{ss}(E) = \sum_{\mathbf{M} \neq 0, 0} d_{\mathbf{M}}(E), \quad (3)$$

$d_{\mathbf{M}}(E) = \frac{8\pi \mathbf{M} \cos(\mathbf{M}/h - i\mathbf{M}\pi/2 + \gamma\pi/4)}{\pi h^{3/2} M_z^{3/2} |g_E^*(E)|^{1/2}}, \quad (4)$

over families of POs at energy E , labeled by their topology $\mathbf{M} = (M_1, M_2)$, $S_{\mathbf{M}}$ and $\tau_{\mathbf{M}}$ are, respectively, the action integral and the period. (In billiards we use $k = p/h = \sqrt{2mE/h}$, $\tau = L/v_F$, and $S/h = kL$, with L the trajectory length.) \mathbf{M} takes into account the Maslov indices and the phase acquired at each bounce on the walls. Given the energy surface E in action-space whose implicit form is $\mathcal{H}(I_1, I_2) = E$, the function g_E^* defines it explicitly by $I_2 = g_E^*(I_1)$, and $\gamma = \text{sign}(g_E^*(E))$. Using the DOS from (4) we can write $\Omega = \Omega + \Omega^{ss}$. The smooth part yields the standard Landau diamagnetism [8], while $\Omega^{ss}(E) = \sum_{\mathbf{M}} \Omega_{\mathbf{M}}(E)$ with

$$\Omega_{\mathbf{M}}(E) = \left(\frac{h v_F}{L_{\mathbf{M}}} \right)^2 d_{\mathbf{M}}(E) R_T(L_{\mathbf{M}}).$$

$R_T(L) = L/L_c(\sinh(L/L_c))^{-1}$, with $L_c = h v_F \beta/\pi$, yields an exponential suppression for the contribution of trajectories with $L > L_c$.

The PC is obtained from Eq. (1) once the shortest POs are identified. While this procedure works

at arbitrary fields [8], we concentrate here in the weak-field regime where classical perturbation theory yields the modifications of the zero-field PO. The most sensitive change is through the classical action and given by $\delta S = (e/c) H A$, where A is the algebraic area enclosed by the unperturbed orbit. Since the system is time-reversal invariant at zero field, each PO is associated with a time-reversed partner having exactly the same characteristics except for an opposite enclosed area. Grouping time-reversal trajectories in Eq. (3), we obtain for weak fields

$$d_{\mathbf{M}}(E, H) = d_{\mathbf{M}}^0(E) \cos\left(\frac{eH}{\hbar c} \mathbf{A}_{\mathbf{M}}\right),$$

where $d_{\mathbf{M}}^0(E)$ is the zero-field contribution.

III. PERIODIC ORBITS IN THE RING BILLIARD

The characteristics of the zero-field periodic orbits is the remaining information to be incorporated. There are two types of POs: those which do not touch the inner disk (type-I), and those which do hit it (type-II) (insets Fig. 1). Type-I trajectories can be labeled by the topology $\mathbf{M} = (M_1, M_2)$, where M_1 represents the number of turns in coming to the initial point after M_2 bounces on the outer circle, and $M_2 \geq M_2 = \text{Int}[M_1\pi/2 \arccos(r)]$, $r = b/a$. Type-II trajectories can be labeled by $\mathbf{M} = (M_1, M_2)$, where M_1 is the number of turns in coming to the initial point after M_2 bounces on the outer circle (with the same restriction $M_2 \geq M_2$ as for type-I). The length and area of type-I trajectories with topology \mathbf{M} are respectively $L_{\mathbf{M}} = 2M_2 \sin(\pi M_1/M_2)$ and $\mathcal{A}_{\mathbf{M}} = (M_2 a^2/2) \sin(2\pi M_1/M_2)$. For type-II trajectories we have $L_{\mathbf{M}} = 2M_2 a^2 [1 + r^2 - 2r \cos(\theta/2)]^{1/2}$ and $\mathcal{A}_{\mathbf{M}} = M_2 abh(\pi M_1/M_2)$. The function $g_E^*(E)$ has two branches corresponding to the interval to which the angular momentum I_1 belongs ($I_1 b \leq I_1 \leq pa$ for type-I and $0 \leq I_1 < pb$ for type-II). It can be obtained by performing the integral of Eq. (2) along two independent paths on the invariant torus [8]. The contributions to the zero-field DOS from topology \mathbf{M} trajectories of type-I and type-II are respectively given by

$$d_{\mathbf{M}}^0(E) = \sqrt{\frac{2}{\pi}} \frac{\mathbf{g}_{\mathbf{M}} L_{\mathbf{M}}^{3/2}}{h^2 k^{1/2} M_2^2} \cos\left(k L_{\mathbf{M}} + \frac{\pi}{4} - \frac{3\pi}{2} M_2\right),$$

$$\tilde{d}_{\mathbf{M}}^0(E) = 4 \sqrt{\frac{2}{\pi}} \frac{\mathbf{g}_{\mathbf{M}}^2 m}{h^2 (k L_{\mathbf{M}})^{1/2}} \sin\left(k L_{\mathbf{M}} + \frac{\pi}{4}\right) \times \times [(1 - r \cos \delta)(r \cos \delta - r^2)]^{1/2}.$$

IV. TYPICAL CURRENT

Noting $I_0 = e\tau_e/2\pi a$, the typical current of one-dimensional electrons at the Fermi energy, we can express the PC as the sum of two contributions corresponding to both types of trajectories:

$$\frac{I}{I_0} = \frac{1}{8\pi(k_F a)^{1/2}} \sum_{M_1, M_2 \geq M_2} \left\{ L_{\text{M},I} \sin \left(\frac{eH\bar{A}_{\text{M}}}{\hbar c} \right) \times R_T(L_{\text{M}}) + I_{\text{M},II} \sin \left(\frac{eH\bar{A}_{\text{M}}}{\hbar c} \right) R_T(\bar{L}_{\text{M}}) \right\}, \quad (5)$$

$$I_{\text{M},I} = \frac{2\sqrt{2}}{\sqrt{\pi} M_2^2} (L_{\text{M}}/a)^{1/2} \cos \left(k_F L_{\text{M}} + \frac{\pi}{4} - \frac{3\pi}{2} M_2 \right), \quad (6)$$

$$I_{\text{M},II} = 8\sqrt{\frac{2}{\pi}} \frac{(\bar{A}_{\text{M}}/a^2)}{(L_{\text{M}}/a)^{5/2}} \sin \left(k_F \bar{L}_{\text{M}} + \frac{\pi}{4} \right) \times [(1 - r \cos \delta) [r \cos \delta - r^2]]^{1/2},$$

$$\frac{I}{I_0} \approx \frac{8\pi}{\sqrt{3}} \left(\frac{\bar{A}_{\text{M}}/a^2}{(L_{\text{M}}/a)^{5/2}} \right)^{1/2} \sum_{M_1, M_2 \geq M_2} \left[\langle (\mathcal{T}_{\text{M},I}^{(t)})^2 \rangle \sin^2 \left(\frac{eH\bar{A}_{\text{M}}}{\hbar c} \right) R_T^2(L_{\text{M}}) \right]^{1/2}$$

$$R_T^2(L_{\text{M}}) + \langle (\mathcal{T}_{\text{M},II}^{(t)})^2 \rangle \sin^2 \left(\frac{eH\bar{A}_{\text{M}}}{\hbar c} \right) R_T^2(\bar{L}_{\text{M}}) \right],$$

where $\langle (\mathcal{T}_{\text{M},I}^{(t)})^2 \rangle$ and $\langle (\mathcal{T}_{\text{M},II}^{(t)})^2 \rangle$ are obtained by replacing the corresponding sinusoidal terms by 1/2. In Fig. 2 we present the typical PC and its two contributions for various r and L_c . The contribution of type-I trajectories dominates for small r , while type-II trajectories take over for narrow rings.

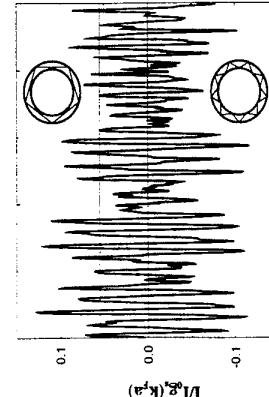


FIG. 1. Persistent current in a ring with $r = b/a = 0.9$ for a magnetic field giving a total flux of $\Phi_0/4$. The typical current is represented by the dashed horizontal line. Upper and lower insets: type-I and type-II trajectories.

In Fig. 1 we show the persistent current according to Eq. (5) for a cut-off length $L_c = 10a$ and a thickness ($r = b/a$) for cut-off lengths $L_c = 30a$ (circles), $6a$ (diamonds) and $3a$ (triangles). Filled symbols: total current, unfilled symbols: contribution from type-I trajectories (dotted) and type-II (dashed). Arrows: asymptotic behavior according to Eq. (7).

Thin rings ($r \leq 1$) are particularly interesting since they are the configuration used in the experiments. Even for other fields, the higher width numbers ($M_1 > 1$) are strongly suppressed at the temperatures of experimental relevance because L_{M} is roughly proportional to M_1 . We will therefore restrict ourselves in what follows to $M_1 = 1$. The PC of a given sample can be parabolic or diamagnetic with a characteristic period in k given by the

circle perimeter $L = 2\pi a$. Since these oscillations are quite irregular, in order to characterize the typical value of the magnetic response we average I^2 over a $k_F a$ -interval containing many oscillations, but negligible on the classical scale. In practice, we scale out the secular ($k_F a)^{3/2}$ dependence and define

$$\frac{I}{I_0} = (k_F a)^{1/2} \left[\frac{1}{\Delta k} \int \frac{dk}{k_F a} \left(\frac{I}{h} \right)^2 \right]^{1/2}, \quad (6)$$

which gives the dashed horizontal line of Fig. 1. At finite temperatures and for sufficiently large integration interval Δk , the nondiagonal terms of I^2 (involving two different families of trajectories) are unimportant and we have

$$\frac{I}{I_0} = 2g\pi(k_F a)^{1/2} \left[\frac{1}{2} \sum_{M_1 > M_2} \left\{ \frac{1}{M_2^4} + \frac{\pi^2((1-r)^2 + \delta^2)^{5/2}}{M_2^5((1-r)^2 + \delta^2)^{5/2}} \right\} \right]^{1/2} R_T(L), \quad (7)$$

Since $M_2 \gg 1$ we can convert the sum into an integral obtaining $I^2/I_0 = 1/(2\pi\Phi_0/\Phi_b) R_T(L)$ where

$$J = \frac{2g\pi\sqrt{\Lambda}}{\pi\sqrt{3}} \left(1 + [2(1-r)]^{1/4} \right), \quad (7)$$

and $\Lambda' = k_F(a-b)/\pi$ is the number of transverse occupied channels. The leading order term [$(1-r)^2$] is consistent with result of Ref. [7]. It comes from type-II trajectories, and is indicated by arrows in Fig. 2. The second contribution arises from type-I trajectories and decreases with r .

VI. DISCUSSION

- In the experiment of Ref. [3], the persistent current of a thin ring ($a = 1.43\mu\text{m}$, $r = 0.9$) with $\Lambda \approx 4$, was measured in the phase-coherent ($L_c = 25\mu\text{m}$), ballistic ($L = 11\mu\text{m}$) regime. The quoted temperature of $T = 15mK$ makes the temperature-reduction factor irrelevant ($L_c \approx 30a$, $R_T(L) \approx 1$). The magnetic response exhibits a Φ_0 flux periodicity and oscillates from diamagnetic to paramagnetic by changing the microscopic configuration, consistently with Eq. (5). The typical PC was found to be $4\pi A$, while Eq. (7) and Ref. [7] would yield $7\pi A$. The difference between the theoretical and measured values is not significant given the experimental uncertainties, as discussed in Refs. [3] and [5]. Moreover, the residual disorder is not completely negligible and causes a reduction of the magnetic response (without altering the physical picture presented or giving any additional contribution [8]). Also, from the highly structured curve of Fig. 1, we see that obtaining the

typical current $I^{(t)}$ necessitates a very large $k_F a$ average, which in experimental terms means considering many different configurations.

A salient feature of our semiclassical analysis is the relevance of the classical dynamics in determining thermodynamical properties of ballistic mesoscopic samples. The magnetic response in noninteracting model is a measure of the field dependence of the oscillating part of the density of states. Integrable systems (where the periodic orbits appear in families) show much larger oscillations than chaotic systems (where the POs are generally isolated), and therefore a much larger magnetic response [5,6]. The finite temperature of the mesoscopic regime limits the relevance of POs to only the shortest ones. This simplifies considerably the calculations and limits the effect of long diffusive trajectories.

We have not considered the persistent currents in an ensemble of ballistic rings, as no experiment is available in this domain yet. As indicated in the introduction, higher order terms (in $1/N$) from the expansion of the free energy are necessary in that case. These corrections can also be expressed in terms of the DOS, which can be obtained semiclassically in the same way as presented here [8]. The average current also depends on the nature of the underlying classical mechanics, presenting an experimentally accessible means for the distinction between integrable and chaotic structures at μm scale.

**WEAK LOCALIZATION IN CHAOTIC VERSUS NON-CHAOTIC CAVITIES:
A STRIKING DIFFERENCE IN THE LINE SHAPE**

A.M. Chang, H.U. Baranger, L.N. Pfeiffer, and K.W. West AT&T Bell Laboratories,
Murray Hill, NJ 07974

We report evidence that chaotic (non-integrable) and non-chaotic (integrable) scattering through ballistic cavities display distinct signatures in quantum transport. In the non-chaotic case, we observe a linear decrease in the magneto-resistance with field. This contrasts markedly with a Lorenzian behavior for a chaotic cavity. The weak localization, negative magneto-resistance peak is associated with coherent back-scattering of electrons from the walls of the cavities; its shape sheds information on the distribution of areas enclosed by classical and non-classical trajectories. According to the theory of Baranger, Jalabert and Stone, [Phys. Rev. Lett. 70, 3876 (1993)], in the non-chaotic case the linear dependence arises from a power law area distribution rather than the exponential distribution in the chaotic case. Our results are directly compared to exact numerical calculations on cavity geometries nominally identical to experiment. The agreement between experiment and theory is substantial in both the line shape and magnitude of the weak localization peak.

Our measurements are performed on structures fabricated on a high mobility $\text{GaAs}/\text{Al}_x\text{Ga}_{1-x}\text{As}$ heterostructure crystal. The typical dimension is $\sim 1.2\mu\text{m}$, compared to a transport elastic mean free path of $17\mu\text{m}$, and more importantly, a small angle scattering length of $\sim 4.5\mu\text{m}$. Sample averaging is employed to reduce the contributions of universal conductance fluctuations. In addition to the negative magneto-resistance peak, periodic Aharonov Bohm oscillations are observed which are likely associated with periodic orbits within the cavities.

References

- 1) "Weak Localization in Chaotic versus Nonchaotic Cavities: A Striking Difference in the Line Shape," A.M. Chang, H.U. Baranger, L.N. Pfeiffer, and K.W. West, Phys. Rev. Lett. 73, 2111 (1995).
- 2) "The Signature of Chaos," in the News and Views section, R.V. Jensen, Nature 373, 16 (1995).

Experimental Investigation of Pauli Exclusion Principle Using Noise in Coherent Electron Transport

C. Kurdak*, C.-J. Chen, D. C. Tsui, J. P. Lu, M. Shayegan, S. Parikh, and S. A. Lyon
Department of Electrical Engineering, Princeton University, Princeton, NJ 08544, USA

Abstract

We study low frequency noise and noise correlation in two kinds of mesoscopic conductors to investigate the contribution of Fermi statistics in coherent electron transport. In Y-shaped triple quantum point contact structures, we observe multi-level switching noise which is much bigger than the expected contribution due to Fermi statistics. In a second device structure, a partially transmitting surface gate is used to split ballistic electrons injected from a quantum point contact. In our noise measurements on these second kind of structures, within the resolution of our noise measurement setup (10-20 V²/Hz), no excess noise correlation between the reflection and transmission voltages is observed.

Excess noise in a conductor contains valuable information that cannot be obtained from other transport measurements and can be used to complement ordinary transport measurements where time averaged currents and voltages are measured. Recent attention has been focused on noise in the coherent electron transport regime where low frequency current fluctuations are theoretically calculated in terms of scattering matrix elements of the conductor. These calculations suggest that the excess noise of a mesoscopic conductor has corrections resulting from the Pauli exclusion principle of the carriers [1]. We note that there is a direct analogy between these corrections in mesoscopic conductors and the noise correlations observed in the Hanbury Brown-Twiss experiment with photons [2]. In the photon experiment, the quantum corrections in noise have different sign due to the bosonic nature of photons. In principle, these corrections can be used to determine the statistics of carriers. Naturally, it would be most exciting to carry out these experiments in the fractional quantum Hall effect regime where the statistics of the excitations are unknown.

Experimentally such corrections would be most pronounced in split-structures by measuring the correlation between the two current fluctuations when the injected beam is truly random (full shot noise). In that case, the classical contribution to the noise correlation becomes zero and only the quantum corrections survive. If this condition is not satisfied, as in the case when the injected beam is noise free, the noise correlation between the split beams would be overwhelmed by the partition noise which is purely a classical effect [3].

To investigate the contribution of these quantum effects, we fabricated two kinds of mesoscopic structures on GaAs/AlGaAs heterojunctions using electron-beam lithography. All samples are grown by molecular beam epitaxy such that the two-dimensional (2D) electrons are close to the top surface (700-1000 Å). The 2D electron density ($1.5 \times 10^{11} \text{ cm}^{-2}$) and mobility ($0.5-1.5 \times 10^6 \text{ cm}^2/\text{V}\cdot\text{s}$) are determined by Hall measurements at $T = 4.2 \text{ K}$. In the first structure, we use three metal gates to define a Y-shaped triple quantum point contact (QPC) geometry (shown in Fig. 1 a). At applied gate voltages of less than -0.3 V, the electrons under the gates are depleted to form the Y-shaped constriction. The electrical widths of this constriction are controlled by changing the gate voltages. The QPCs exhibit quantized channel conductances, G , in units of

$e^2/2h$ as a function of gate voltage at $T = 1.5 \text{ K}$. The second structure (shown in Fig. 1 b) consists of three QPCs and a surface gate which acts like a partially transmitting mirror for the ballistic electrons injected from the injector QPC. The transmissivity of this mirror can be tuned by changing the gate voltage. In typical operation of the device, electrons are injected from the injector QPC and some of these ballistic electrons are detected by either of the two QPCs after being reflected or transmitted by the partially transmitting mirror. Transport measurements on a similar mesoscopic split-structure are discussed in detail elsewhere [4]. We made two such split-structures with different overall dimensions where the injected electrons before reaching the detector QPCs travel a distance of $3 \mu\text{m}$ in one of the structures and $6 \mu\text{m}$ in the other.

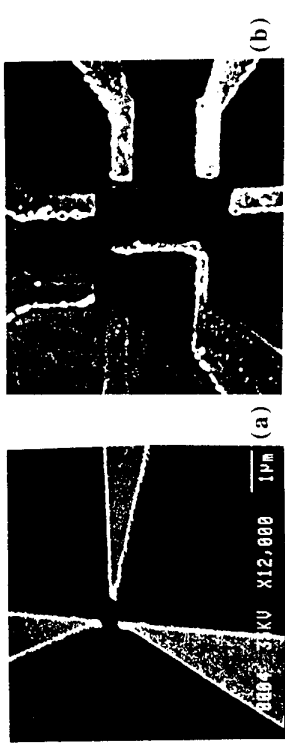


Figure 1. (a) SEM micrograph of the Y-shaped QPC structure. (b) AFM picture of the mirror structure. The central surface gate is $0.1 \mu\text{m}$ wide and all three QPCs are spaced $1.5 \mu\text{m}$ from the center. The injector QPC is located on the lower right.

All noise measurements are made at $T = 4.2 \text{ K}$. In the Y-shaped sample, the current signals and, in the mirror structure, the voltage signals are amplified by low noise current and voltage amplifiers which are then fed to a HP 3562A two-channel spectrum analyzer for Fourier analysis. To calibrate the noise measurement setup metal resistor networks are measured and the results are in agreement with the expected thermal noise of these resistors.

It is known from early noise measurements that the white noise component of excess noise of a multi-channel QPC is less than the full-shot noise [5]. This is due to fact that the channels with a transmission coefficient of close to unity do not contribute to excess noise [6]. In the Y-shaped sample, in order to suppress the noise correlation contribution that would result from the partition noise of such noise free channels, the devices have to be operated in the weakly coupled limit (all transmission coefficients are much less than unity or $G \ll e^2/2h$). However, in the frequency range of our measurement, when the QPCs are operated in the weakly coupled regime, the measured excess noise was dominated by a different noise source. A typical noise spectrum of a QPC has a Lorentzian shape as shown in Fig. 2. Note that the measured excess noise is much larger than the expected contribution of the quantum corrections (on the order of full shot noise) and scaled with current quadratically instead of linearly. Furthermore, the spectrum is sample dependent and is different for different cool-downs of the same sample. Similar Lorentzian noise in a QPC has been observed previously and explained by electron trapping and detrapping events occurring around the QPC [7]. However, in some cases, as shown in the inset of Fig. 2, we observed multi-level switching events which cannot be explained by trapping events are rare and that it is unlikely to find active trapping events in the close vicinity of a QPC [8]. We

* Present address: Physics Department, University of California, Berkeley, CA 94720

suggest that these switching events are actually caused by the fluctuations in the remote donor configuration.

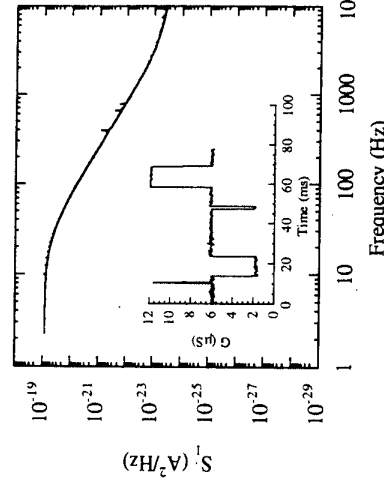


Figure 2 Excess noise spectrum of a QPC for a bias current of 5 nA. Inset shows a typical time trace of the QPC conductance. Sample exhibits a three-level switching noise.

To extract quantum corrections in the presence of such switching noise, one has to measure the noise of the Y-shaped samples at microwave frequencies. Major modifications are required to achieve such measurements [9].

In the noise measurements of the second structure, electrons are injected from the injector QPC and the surface gate is biased such that half of the incident electrons are reflected and the other half are transmitted. In this structure, only a very small percentage of the injected electrons is actually detected by the detector QPCs. Thus, the condition to suppress the classical partition noise is satisfied. The transmission and reflection voltages on detector QPCs are measured with respect to different voltage leads so that the thermal noise of the leads would be uncorrelated. The phase and the magnitude of the cross spectrum between the transmission and reflection voltages obtained from the 6 μ m sample is shown in Fig. 3. The data are obtained after averaging 10000 traces of cross-spectrum. By doing such a long measurement one can measure signals that are much smaller than the intrinsic noise of the amplifiers (10^{-18} V $\sqrt{\text{Hz}}$); the resolution of the noise measurement is proportional to the intrinsic noise of the amplifiers and inversely proportional to the square root of the total measurement time. The cross-spectrum does not change with injector current and the measured spectrum is the background spectrum coming from our measurement setup. This is further illustrated in Fig. 4 where we plot the magnitude of the cross spectrum averaged in the frequency range of 80 to 100 kHz as function of injector current.

This measurement only sets an upper bound to the magnitude of the quantum corrections for this sample. We know from ordinary transport measurements that, when the detector QPC resistances are 1.3 k Ω , only about 2-3 percent of the electrons reach the detector QPCs. For the maximum injector current used in the noise measurements (1 μ A), we estimate the size of the quantum contribution coming from the Fermi statistics of carriers as 0.55-0.8 10^{-20} V $\sqrt{\text{Hz}}$ (assuming that it is on the order of shot noise [1]) which is close to the resolution of our noise measurement setup. Note that the theory does not take into account finite temperature effects, disorder, carrier-carrier interactions, and various imperfections in the sample such as misalignment of the detector QPCs which can further suppress these quantum corrections.

In conclusion, we studied two kinds of sample structures to investigate the contribution of the Pauli exclusion principle on excess noise. In the Y-shaped structure, in the frequency range of our measurement, excess noise is dominated by switching events that are due to changes in donor configuration. The quantum corrections in this Y-shaped sample, in the presence of such switching events, can only be measured at microwave frequencies. In the partially transmitting mirror structure the quantum effects are so far not observed. The resolution of our measurement setup puts an upper limit of 10^{-20} V $\sqrt{\text{Hz}}$ for the quantum corrections from Fermi statistics.

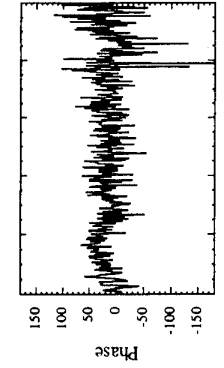


Figure 2 Excess noise spectrum of a QPC for a bias current of 5 nA. Inset shows a typical time trace of the QPC conductance. Sample exhibits a three-level switching noise.

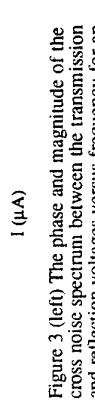


Figure 3 (left) The phase and magnitude of the cross noise spectrum between the transmission and reflection voltages versus frequency for an injector current of 0.6 μ A.

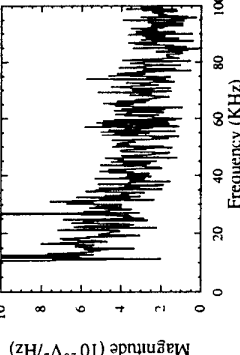


Figure 3 (up) The magnitude of the cross noise spectrum averaged in the frequency range of 80 to 100 kHz versus injector current.

We would like to thank D. Shahar, L. Engel, and Y. P. Li for their help and useful discussions. This work is supported by the NSF and the ONR.

References

- [1] Th. Martin and R. Landauer, Phys. Rev. B 45, 1742 (1992); M. Buttiker, Phys. Rev. B 46, 12485 (1992)
- [2] R. Hanbury Brown and R. Q. Twiss, Nature 177, 27 (1956); 178, 1447 (1957); E. M. Purcell, Nature 178, 1149 (1957)
- [3] R. E. Burgess, Brit. J. of Appl. Phys. 6, 185 (1955)
- [4] X. Ying, J. P. Lu, J. J. Heremans, M. B. Santos, M. Shayegan, S. A. Lyon, M. Litman, P. Gross, and H. Rabitz, Appl. Phys. Lett. 65, 1154 (1994)
- [5] Y. P. Li, D. C. Tsui, J. J. Heremans, J. A. Simmons, and G. W. Weimann, Appl. Phys. Lett. 57, 774 (1990)
- [6] G. B. Lesovik, Pis'ma Zh. Eksp. Teor. Fiz. 49, 514 (1989) [JETP Lett. 49, 593 (1989)]
- [7] C. Dekker, A. J. Scholtens, and F. Lierink, R. Eppenga, H. van Houten, and C. T. Foxon, Phys. Rev. Lett. 66, 2148 (1991)
- [8] C. Kurdak, C.-J. Chen, D. C. Tsui, S. Parikh, S. A. Lyon, and G. W. Weimann, in preparation
- [9] M. Reznikov, M. Heiblum, H. Shtrikman, and D. Mahalu, preprint

Magnetic field-dependent Fermi surfaces in quasi-2D organic conductors

J. Singleton¹, A. House¹, N.A. Harrison², S.J. Blundell¹, J.A.A.J. Perenboom³, A. Polisski¹, W. Hayes¹, M. Kurmoo⁴ and P. Day⁴

¹University of Oxford Department of Physics, The Clarendon Laboratory, Parks Road, UK-Oxford OX1-3PU, United Kingdom.

²Laboratorium voor Vaste-Stoffysica en Magnetisme, Katholieke Universiteit Leuven, Celestijnenlaan 200 D, B-3030 Leuven, Belgium.

³High Field Magnet Laboratory and Research Institute for Materials, NL 6525 ED Nijmegen, The Netherlands.

⁴The Royal Institution, 21 Albemarle Street, London W1X 4BS, U.K.

Abstract

We review recent studies of charge-transfer salts of the ion bis-(ethylenedithio)-tetraphiafulvalene which exhibit spin-density wave groundstates, concentrating on techniques involving high magnetic fields and experiments carried out by the Oxford group and coworkers.

Introduction

Traditionally, fundamental solid-state physics has almost exclusively involved the study of *inorganic* elements, alloys, and simple compounds, the underlying assumption being that fundamental physics research is most usefully concentrated on *chemically simple* materials. Our recent work is built upon the realisation that such an assumption is quite misplaced, that in fact some of the most exciting studies in solid-state physics can and should be attempted on organic materials which are chemically very complicated. The attraction of organic molecular systems is that though chemically complex, in other ways they are beautifully simple and can often provide much information about basic phenomena like superconductivity and magnetism (see [1, 2, 3] and references therein). As an example of this, charge-transfer salts of the ion bis-(ethylenedithio)-tetraphiafulvalene (ET or BEDT-TTF) form a versatile and interesting system for the studies of many problems in solid-state physics; by varying the anion X incorporated into the charge-transfer salt (ET)_nX, the stoichiometry and band-filling may be adjusted, producing compounds which are metallic, semimetallic, semiconducting, or superconducting [1, 2, 3]. The charge-transfer salts have a very simple quasi-two dimensional (q2D) bandstructure and a well defined Fermi surface, and single crystals of high quality are available, making them amenable to bandstructure characterisation techniques such as the Shubnikov-de Haas (SdH) effect.

In previous reviews [2, 3], we have concentrated on some of the similarities between the ET salts and semiconductor systems such as superlattices. In this paper, we shall instead describe some of the contrasts between the two systems and focus on two experimental techniques which are now regularly applied in the study of organic molecular metals but not in semiconductors.

Field-dependent Fermi surfaces 1: the de Haas-van Alphen effect up to 54 T.

The areal carrier densities in ET salts are 100-1000 times higher than those in semiconductor heterostructures, so that many interactions which are of negligible size in the latter systems exert a major influence. In particular, carrier-phonon and carrier-carrier interactions are strong, often resulting in heavy effective masses ($1.5 - 10m_e$), large densities of states at the Fermi energy and superconducting or spin-density wave (SDW) groundstates [1, 3]. Furthermore, typical laboratory magnetic fields cause significant perturbations of the bandstructure and can result in field-induced changes in the Fermi surface [4, 5, 6].

These points are illustrated by the salts $\alpha\text{-}(ET)_2\text{Mhg}(\text{NCS})_4$, where $M=\text{NH}_4$, K, Rb or Tl. Although all possess very similar calculated Fermi surfaces (Figure 1a inset [7]), consisting of an open 1D electron section and a closed 2D hole pocket, the salt with $M=\text{NH}_4$ is a superconductor below 1 K, whilst those with $M=\text{K}$, Tl or Rb exhibit SDW groundstates at low temperature (see [4, 5, 6] and references therein). When a SDW forms, a so called nesting vector in k -space translates one side of the 1D Fermi surface into the other, thereby opening up a band gap and lowering the energy of the system [8]. The nesting vector introduces a new periodicity in the crystal which results in a smaller Brillouin zone. In turn, the new zone boundaries "cut and paste" any remaining pieces

of Fermi surface into a new arrangement. Additional small pockets of Fermi surface may occur due to imperfect nesting of the 1D parts. Such a proposed reconstruction of the Fermi surface for $\alpha\text{-}(ET)_2\text{Mhg}(\text{NCS})_4$ ($M=\text{Tl}, \text{K}$) due to a SDW [9] is shown as an inset to Figure 1b.

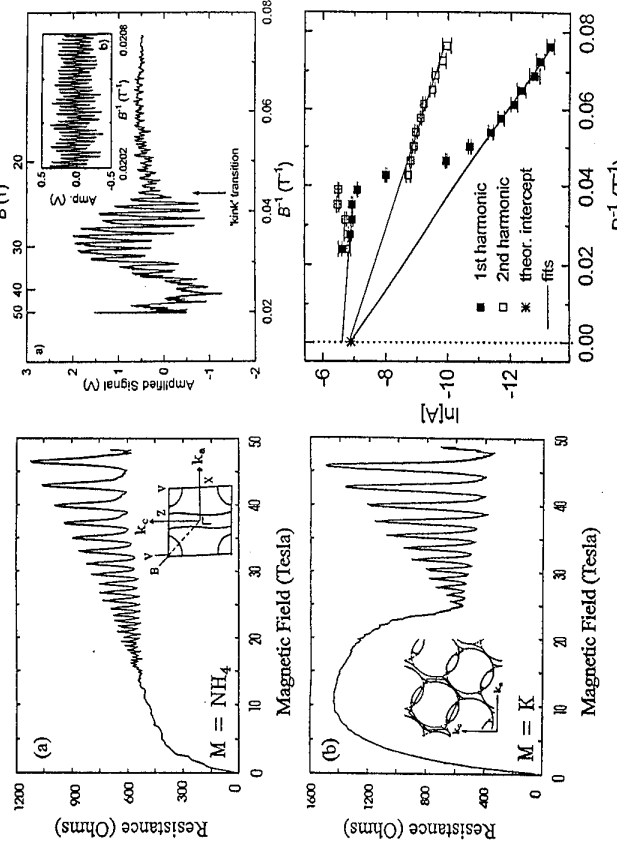


Figure 1. Magnetoresistance of $\alpha\text{-}(ET)_2\text{Mhg}(\text{NCS})_4$ at $T \approx 1$ K for $M=\text{NH}_4$ (Figure 1a) and $M=\text{K}$ (Figure 1b). The insets show the calculated Fermi surface (Figure 1a) and a proposed Fermi surface in the SDW state (Figure 1b).

One of the most notable features of the M=K, Rb and Tl salts is observed as a sharp kink in the magnetoresistance (MR) (Figure 1b); it has become known as the "kink transition". The kink occurs at around 23 T in the $M=\text{K}$ salt, and is thought to represent destruction of the SDW groundstate (i.e. a transition from a Fermi surface possibly like the one in Figure 1b to that in Figure 1a; see [4, 5, 6] and references therein); the kink is absent in the $M=\text{NH}_4$ salt (c.f. Figures 1a and 1b).

Recently we have studied the de Haas-van Alphen (dHvA) effect (i.e. oscillatory magnetisation) of $\alpha\text{-}(ET)_2\text{Khg}(\text{NCS})_4$ in pulsed magnetic fields of up to 54 T, in order to clarify the field-induced changes in bandstructure occurring at the kink [10]. Figure 2a shows a typical dHvA signal from a single $1 \times 0.5 \times 0.1 \text{ mm}^3$ crystal of $\alpha\text{-}(ET)_2\text{Khg}(\text{NCS})_4$, recorded using a compensated pick-up coil technique (a direct measurement of dM/dB). The data were measured on the rising side of the field pulse; the higher dB/dt produces a higher signal to noise ratio, allowing dHvA oscillations at

fields below the kink to be clearly resolved. The dHvA oscillations above 23 T are attributed to the 2D hole pocket of the Fermi surface shown in Figure 1e; note that the oscillations for fields below the kink exhibit the same frequency, $F = 670 \pm 3$ T, but with a stronger second harmonic component. The apparent increase in noise towards peak field is partly due to copper belly dHvA originating from the copper wire of the detection coils (Figure 2b), illustrating the sensitivity of the technique [10].

The importance of using the highest possible fields is illustrated by Figure 2c, which shows “Dingle plots” (i.e. logarithmic corrected dHvA oscillation amplitudes versus $1/B$ [11]) for the first and second harmonics of the 670 T series. The new feature revealed using high fields is the region of the Dingle plot with a very small gradient, corresponding to $B > \sim 27$ T. Earlier studies up to ~ 30 T had only accessed the steeply sloping middle and flatter low field regions of the Dingle plots [4, 6], and the authors had incorrectly taken this to imply that the scattering rate at high fields increased. However, it is apparent from Figure 2c that the gently sloping region corresponding to $B > \sim 27$ T represents the true behaviour of the high field state; the other shallow sloped region ($B < \sim 20$ T) corresponds to the low field state. The region between can therefore be considered as a gradual transition between the two regimes, and is roughly centred on the kink at ~ 23 T. The close correlation between the infinite field intercepts above and below the kink together suggest that the quantum dHvA frequency F is the same above and below the kink, although the quantum oscillations detected in both regimes originate from similar, if not identical, pieces of Fermi surface. However, the quasiparticle scattering rate increases greatly from $\tau^{-1} \sim 2 \times 10^{11}$ s $^{-1}$ above ~ 27 T to $\tau^{-1} \sim 2 \times 10^{12}$ s $^{-1}$ below ~ 20 T, indicating that additional scattering processes occur at fields below the kink, probably due to the formation of the SDW [10].

The temperature dependence of data such as those in Figure 2a may be analysed to yield effective masses m^* for the 2D carriers; the availability of data up to ~ 54 T allows reliable values to be obtained at fields well above the kink. Values of $m^* \sim 1.5m_e$ were obtained for $B < 20$ T, whilst for $B > 27$ T, $m^* \sim 2.7m_e$. This large increase probably signals an enhancement of the carrier-carrier and/or carrier-phonon interactions above the kink. It is notable that the effective mass of the 2D holes in $\alpha\text{-}(ET)_2\text{KHg(NCS)}_4$, measured at fields below the kink is anomalously low compared to those of isostructural salts (e.g. $\alpha\text{-}(ET)_2\text{NH}_4\text{Hg(NCS)}_4$ [12]) which do not exhibit a SDW groundstate; the larger mass in the high-field state may therefore be a more representative value.

Finally, note that the dHvA oscillations at fields above 30 T contain unusually large contributions from higher harmonics [10]. These higher harmonics do not obey the Lifschitz-Kosevich formula, which predicts the behaviour of ‘conventional’ metals successfully. Such anomalous behaviour and its cause is currently a focus for study in the organic metals [13, 14, 15]. The utility of the dHvA pick-up coil technique in this context cannot be overemphasised; in contrast to either SdH [13, 14] or torque dHvA measurements [15], the signal derived from the sample may be simply related in a quantitative manner to theoretical expressions for the density of states at the Fermi energy [10]. In addition, its sensitivity is now sufficient to study some semiconductor systems.

Field-dependent Fermi surfaces 2: angle-dependent magnetoresistance oscillations

We have glibly been referring to the sections of Fermi surface in the ET salts as “1D” and “2D” thus far. In fact, there is a small contribution to the bandstructure from molecular overlaps in the interplane direction, leading to slightly warped or corrugated q1D and q2D Fermi surfaces. The SdH and dHvA effects tend not to pick up any information about the warping, because each frequency observed is proportional to the area of an *extremal orbit* of the Fermi surface [11]. Furthermore, the warping of the q2D sections is in fact small, so that separate neck and belly orbits are rarely seen [2]. The orbits which are not extremal do not contribute to this oscillatory signal but give rise to e.g. the non-oscillatory background MR. However, this background MR can depend quite dramatically on the direction of the applied magnetic field, and can give information about Fermi surface warping; the effect has been exploited in the technique known as “angle-dependent magnetoresistance oscillations” (AMRO), now commonly used to characterise the Fermi surfaces of charge-transfer salts. AMRO can be observed at much higher temperatures and in much lower applied fields than either the SdH or dHvA effects [1]. The latter arise due to well resolved Landau levels moving through a sharply defined Fermi surface, and this restriction does not apply so stringently to AMRO. The information obtained from AMRO can therefore be complementary to SdH and dHvA effects since it is due to all carriers on the Fermi surface and not just those performing

extremal orbits.

Semiclassical calculations of AMRO can be performed using the Boltzmann transport equation, an integral (over all states at the Fermi surface) of the velocity-velocity correlation function for each Fermi surface orbit [16]. This can change dramatically as the direction of the magnetic field is changed, altering the paths of all the Fermi surface orbits. For q2D Fermi surfaces, this manifests itself as the Yamaji effect [17, 18]; as the field is tilted away from the axis of the warped cylindrical Fermi surface, MR oscillations can be observed which can be directly related to the degree of warping. In order to apply such models to AMRO in substances like $\alpha\text{-}(ET)_2\text{KHg(NCS)}_4$, one must also include the effect of the q1D part of the Fermi surface. This can be considered to be two slightly warped sheets with a dispersion relation given by

$$E(\mathbf{k}) = \hbar v_F(|\mathbf{k}_x| - k_F) - \sum_{m,n} t_{mn} \cos(m\mathbf{k}_y + n\mathbf{k}_z) \quad (1)$$

where the parameters t_{mn} are the Fourier components of the corrugation of the Fermi sheets [16].

Figure 3. Angle-dependent magnetoresistance oscillations for $\alpha\text{-}(ET)_2\text{KHg(NCS)}_4$ at 1.5 K for several values of the angle ϕ at an applied field of (a) 15 T and (b) 24 T.

Turning to experimental data, Figure 3 shows the MR of $\alpha\text{-}(ET)_2\text{KHg(NCS)}_4$ as a function of the angle θ between the normal to the 2D plane and the field [4]. The azimuthal angle ϕ in Figure 3 describes the plane of rotation of the magnetic field. At 15 T, the AMRO appear as sharp dips in the MR, periodic in $\tan(\theta)$, and the period is proportional to $1/\cos(\phi - \phi_0)$, with $\phi_0 \approx 21^\circ$. Such AMRO are characteristic of a q1D section of Fermi surface inclined at $\sim 21^\circ$ to the crystallographic ‘c’ plane. At 24 T, the AMRO appear instead as broader peaks which do not exhibit a strong ϕ dependence; this is the characteristic behaviour of the Yamaji oscillations caused by 2D sections of Fermi surface [4, 6].

The AMRO clearly sense a Fermi surface reconstruction in this material as the kink field is exceeded. We have already seen that above the kink field, the Fermi surface is thought to contain both q1D and q2D sections (Figure 1a), whilst below the kink field, q2D sections must occur for the dHvA and SdH effects to be observed (see Figure 2a)[4], in addition to the q1D sections which dominate the AMRO. If both types of Fermi surface occur above and below the kink, why is a transition in the AMRO observed? A second problem concerns the parameters t_{mn} ; these are often related to the transfer integrals associated with the lattice vector $\mathbf{R}_{mn} = (0, m_b, n_c)$ [19]. Simulations of AMRO

seen at low fields in $(ET)_2KHg(SCN)_4$ require these to decay relatively slowly with increasing m and n in order to model the data [4, 16, 20], whereas one might expect anything other than the nearest neighbour and next-nearest neighbour overlaps to be negligibly small [8]. This is in fact why no AMRO due to q1D sections of the Fermi surface are generally observed in other ET salts, and in particular, why none is observed above the kink, the nesting of the Fermi surface. Thus, only q2D AMRO is observed above the kink. However, below the kink, the nesting of the Fermi surface removes the weakly corrugated q1D sections of Fermi surface and “cuts up and glues together” pieces of q2D Fermi surface. The reconstructed Fermi surface consists of a very highly and irregularly corrugated Fermi sheet (see Figure 1b for a possible candidate) since it consists of a periodic assembly of cylindrical sections; the corrugation thus has a high harmonic content; thus the t_{mn} are not transfer integrals so much as Fourier components of the corrugation. Although the AMRO (perhaps because they themselves are irregularly corrugated, and the q2D “Yamaji” AMRO effect relies on cylindrical sections of Fermi surface with weak and regular corrugation), the AMRO in this q1D case arises from the fact that for any Fourier component of corrugation, the velocity is more effectively averaged when electrons are not travelling along the axis of the corrugation than when they are; thus sharp resistance minima are obtained when the orbits run along a Fourier component of the corrugation.

Field-dependent Fermi surfaces 3: another example.

Figure 4 shows the MR of $\beta''-(ET)_2AuBr_2$, recorded using a pulsed magnet and a $10 \mu A$, 250 kHz ac current [21]. The Fermi surface calculated for $\beta''-(ET)_2AuBr_2$ only contains one closed 2D hole pocket, and so a single series of SdH oscillations is expected. However, even a cursory inspection of Figure 4 indicates that there are many sets of oscillations present, and a Fourier transform of the entire field range shows no less than fourteen different frequencies, ranging from 38 T to 414 T. E

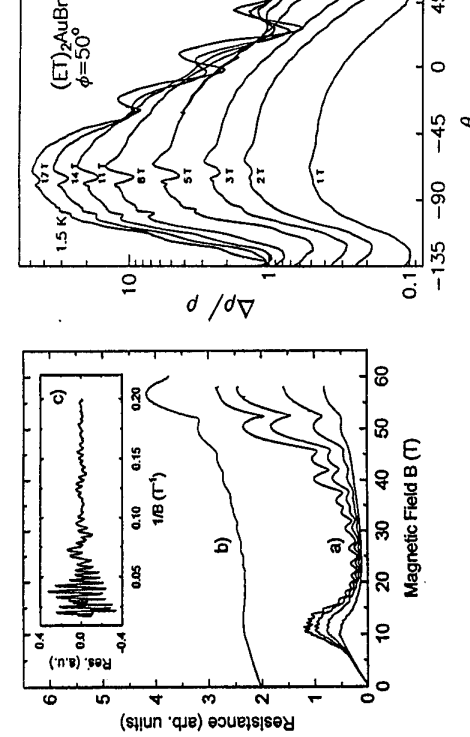


Figure 4. MR of $\beta''-(ET)_2AuBr_2$, Figure 4a, top to bottom, 490 mK, 690 mK, 960 mK and 1.44 K data; Figure 4b, Data for a lower quality sample (380 mK); Figure 4c, Oscillatory component of MR in Figure 4a at 490 mK.

The plethora of frequencies results from the presence of a SDW, evidence for which is also seen in the spin susceptibility [22]. Four of the SdH frequencies can be explained using a SDW model [22], but the problem of accounting for the remaining four sets of oscillations remains. The answer is provided by the AMRO data in Figure 5; note that most of the features in the MR do not shift as B is increased, but merely grow in amplitude. However, for $B > \sim 11$ T, a new series of AMRO appears, indicating that the Fermi surface has changed in form. This transition at $B \sim 11$ T results in shifts of the SdH frequencies, and herein lies the explanation for the eight frequencies seen in the Fourier transforms of Figure 4; four correspond to the Fermi surface below 11 T, and the other four result from the altered Fermi surface above 11 T. This has been confirmed by analysis of the SdH frequencies over restricted field ranges [21].

The smallest of the Fermi surface pockets, corresponding to a frequency of 38 T, approaches the quantum limit ($\nu = 2$) at peak field. The background MR increases dramatically above 40 T, rising by over an order of magnitude in some samples (Figure 4a); the increase is suppressed by raising the temperature (Figure 4b). Effects such as simple depopulation of a small Fermi surface pocket or destruction of the SDW groundstate by the field are almost invariably expected to lead to a sharp decrease in resistance [2], rather than the increase observed experimentally. The data instead suggest that a further field-induced rearrangement of the SDW occurs at high magnetic fields. Theoretical papers have proposed that strong carrier self-energy effects will occur as a high carrier density 2D metal enters the ultraquantum limit, leading to an enhancement of the density of states (DOS) at the Fermi energy (e.g. [23]). It has been suggested that this could in turn promote phenomena such as re-entrant high field superconductivity [23], SDW groundstates often occur in competition with superconductivity in organic molecular metals [2, 3]; it is therefore possible that one of the suggested ultraquantum limit DOS enhancement mechanisms may be initiating a further modification of the SDW state at ~ 40 T rather than re-entrant superconductivity [21].

Acknowledgements

This work is supported by EPSRC, the EU and the Royal Society (UK). The Nijmegen High Field Magnet Laboratory is supported by FOM and the EU Large Installations Plan. We thank our many collaborators in Boston, Bristol, Cambridge, Chernogolovka, Leuven, London, Moscow, Nijmegen, Oxford, Sheffield and Tsukuba for invaluable help, discussions and access to unpublished data.

References

- [1] For a recent review, see Proc. ICSM'94, *Synth. Met.* vols. **69–71**, 1995.
- [2] J. Singleton, F. L. Pratt, *et al.*, *Physica B* **184**, 470–480 (1993).
- [3] J. Singleton, J. M. Caulfield, *et al.*, *Physica B*, **211**, 400 (1995).
- [4] J. Caulfield, S. J. Blundell, *et al.*, *Phys. Rev. B* **51**, 8325 (1995).
- [5] X. Chen, J.S. Brooks, *et al.*, *Phys. Rev. B*, in press.
- [6] T. Sasaki and N. Toyota, *Jpn. J. Appl. Phys.* **33**, 2183 (1990).
- [7] H. Mori, S. Tanaka, *et al.*, *Bull. Chem. Soc. Jpn.* **69**, 10120 (1994).
- [8] T. Ishiguro and K. Yamaji, *Organic Superconductors*, (Springer-Verlag, Berlin 1990).
- [9] M.V. Kartsovnik, H. Ito, *et al.*, *J. Phys.: Condens. Matter*, **6**, L479 (1994).
- [10] N. Harrison, A. House, *et al.*, *Phys. Rev. B*, **52**, 15 August (1995).
- [11] D. Shoenberg, *Magnetic oscillations in metals* (Cambridge University Press, 1984).
- [12] T. Osada, A. Kawasumi, *et al.*, *Solid State Commun.*, **75**, 901 (1990).
- [13] P.S. Sandhu, G.J. Athas, *et al.*, *Phys. Rev. B*, submitted.
- [14] V.N. Laukhin, N.D. Kusch, *et al.*, (unpublished).
- [15] P. Christ, W. Biberacher, *et al.*, this conference.
- [16] S.J. Blundell and J. Singleton, *Phys. Rev. B*, submitted.
- [17] K. Yamaji, *J. Phys. Soc. Jpn.* **58**, 1320 (1989).
- [18] M. V. Kartsovnik, V. N. Laukhin, *et al.*, *J. Physique I* **2**, 89 (1993).
- [19] T. Osada, S. Kagoshima, and N. Miura, *Phys. Rev. B* **46**, 1812 (1992).
- [20] Y. Iye, R. Yagi, *et al.*, *J. Phys. Soc. Jpn.* **63**, 674 (1994).
- [21] A. House, N. Harrison, *et al.*, *Phys. Rev. B*, submitted.
- [22] M. Donporto, J. Singleton, *et al.*, *Phys. Rev. B*, **49**, 3534 (1994).
- [23] H. Goto and Y. Natsume, *J. Phys. Soc. Jpn.* **63**, 1465 (1994).

Magneto-oscillations and field-induced phase transitions in organic conductors

R. H. McKenzie^a, J. S. Brooks^b, R. G. Clark^b, R. Newbury^c, R. P. Starrett^c, A. Skougarevsky^a, R. A. Lewis^d, S. Takasaki^d, J. Yamada^d, H. Anzai^e, Y. Tanaka^e, T. Kinoshita^e, N. Kinoshita^f, M. Tokumoto^f, and M. Kartovsnik^f

^a National Pulsed Magnet Laboratory, School of Physics, University of New South Wales, Sydney, 2052 Australia
^b National High Magnetic Field Laboratory, Florida State University, Tallahassee, FL 32306, U.S.A.
^c Department of Physics, University of Wollongong, Wollongong, 2522 Australia
^d Himeji Institute of Technology, 2167 Shosha, Himeji, Hyogo 671-22, Japan
^e Electrotechnical Laboratory, Tsukuba, Ibaraki 305, Japan
^f Institute of Solid State Physics, Chernogolovka, MD, 142432 Russia

Abstract

We have made a systematic study of the temperature and field dependence of the quantum oscillations in the magnetoresistance of the quasi-2D systems (BEDT-TTF)₂Mg(SCN)₄ ($M=K, Rb, Tl, NH_4$) and the quasi-1D system (TMTSF)₂ClO₄ at fields up to 51 T and temperatures down to 300 mK. Recent theoretical work can explain the high magnetic field-induced phase transitions observed in these systems.

Introduction

Organic conductors based on the TMTSF [tetramethyltetraselenafulvalene] and BEDT-TTF [bis(ethylenedithio)tetrafulvalene] molecules are model systems in which to investigate the fundamental physics of low-dimensional electronic systems. They have a very rich phase diagram as a function of temperature, pressure, magnetic field, and chemical substitution [1]. There is a subtle competition between metallic, superconducting, and spin-density-wave (SDW) phases. Furthermore, organic conductors are available in ultra-high purity single crystals that very clearly exhibit magnetic quantum oscillations. Previous studies have suggested that some of these organic conductors undergo magnetic field-induced phase transitions at fields around 25–35 tesla at low temperatures [1]. Consequently the National Pulsed Magnet Laboratory is an ideal facility to investigate these exciting materials.

Quasi-2D systems

The family (BEDT-TTF)₂Mg(SCN)₄ ($M=NH_4, K, Rb, Tl$) is particularly interesting because of the unique properties resulting from the co-existence of quasi-2D (cylindrical) and quasi-1D (planar) sections of the Fermi surface [1]. The $M=NH_4$ crystal is a superconductor at zero field. In contrast, the $M=K, Rb, Tl$ crystals have a SDW ground state below about 10 K [4]. This is believed to be due to the nesting of the quasi-1D part of the Fermi surface.

The Shubnikov - de Haas oscillations in the $M=NH_4$ salt exhibit up to seven harmonics of the α orbit (frequency 557 T) on the 2D Fermi surface. In addition we observe the β orbit (frequency 4212 T) due to magnetic breakdown between the co-existing 1D and 2D Fermi surfaces (Fig. 1). In $M=Rb$ and Tl salts the nature of the quantum oscillations, due to closed orbits on the 2D Fermi surface, changes above 27 T at which the density-wave state is destroyed (Fig. 2). Harrison et al. [5] recently obtained de Haas - van Alphen data showing similar behavior for the $M=K$ salt.

* Corresponding author. e-mail: ross@newt.phys.unsw.edu.au, fax: 61-2-663-3420

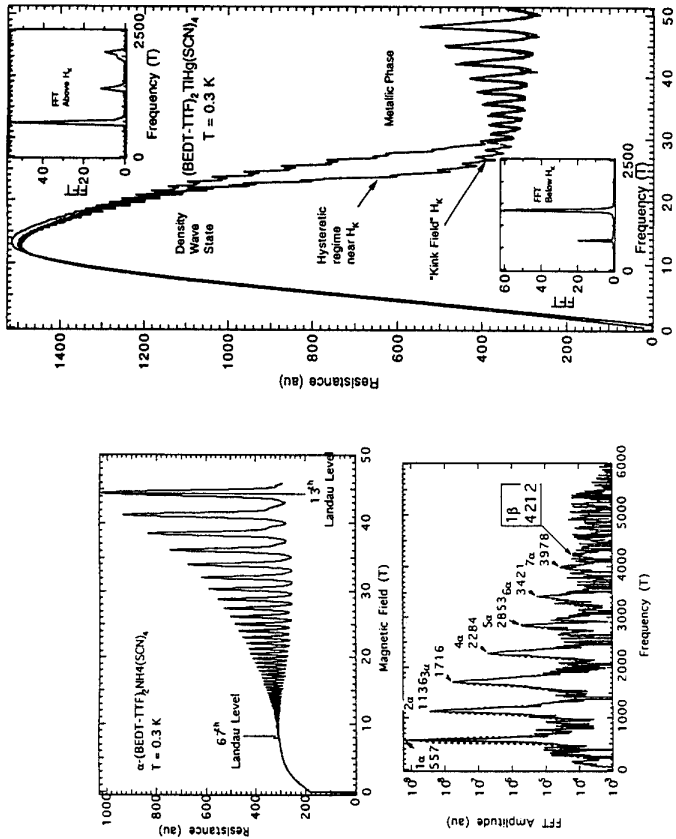


Fig. 1. Pulsed field measurement of the magnetoresistance in the quasi-2D compound (BEDT-TTF)₂Tl[SCN]₄. The magnetic field is parallel to the least conducting direction. The crystal is of such high purity that a FFT (Fast Fourier Transform in inverse field) of the Shubnikov - de Haas shows seven harmonics (inset) and the presence of the beta-orbit due to magnetic breakdown between the closed quasi-2D Fermi surface and the open quasi-1D Fermi surface.

Quasi-1D system

The Bechgaard salt (TMTSF)₂ClO₄ is a superconductor below 1.3 K and up to 30 mT. A cascade of phase transitions into field-induced-spin-density-wave (FISDW) phases occurs at fields above 4 T. Near 15 T the FISDW transition temperature reaches a maximum of 6 K. Another phase boundary is present at $H_{RE} \sim 27$ T, and the high field state (HFS) above H_{RE} is also known as the re-entrant phase. Its existence contradicts the "standard model" [1] of FISDW formation.

We have measured the magnetoresistance up to 51 T in (TMTSF)₂ClO₄, in both the most conducting (a-axis) and least conducting (c^* -axis) directions, and systematically from

0.3 to 4.2 K [2]. Fig. 3 shows two striking anomalies. First, the huge magnetoresistance is particularly puzzling because the current and field directions are parallel and so there is no Lorentz force on the electrons. Second, Shubnikov-de Haas like oscillations are not expected in a metal with a quasi-1D open Fermi surface. We find [2] that the field and temperature dependence of these oscillations is consistent with that expected for closed two-dimensional orbits [6].

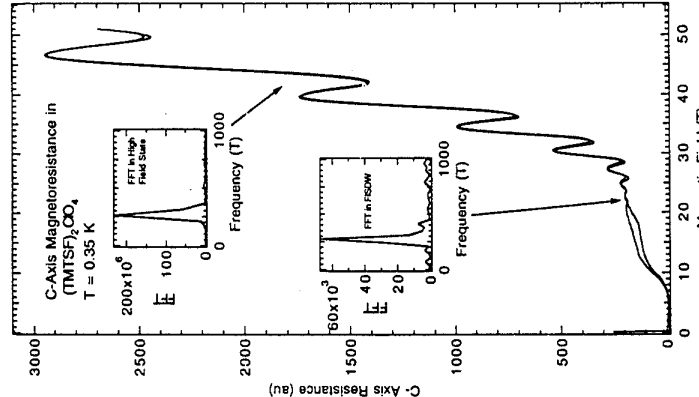


Fig. 3. Plotted field measurement of the magnetoresistance in the quasi-1D compound $(\text{TMTSF})_2\text{ClO}_4$ along the c^* -axis (least conducting) direction. The magnetic field is also parallel to the c^* -axis. At 27 tesla there is a transition from a spin-density-wave state to the re-entrant phase [1]. The insets show a FFT (Fast Fourier Transform in inverse field) below and above the transition.

Theory

Finally, a brief description is given of the essential physics of a new theory [3] describing the destruction by high magnetic field of spin-density-wave (SDW) phases in materials with a quasi-1D Fermi surface. The model is consistent with the high magnetic field-induced phase transitions observed in $(\text{TMTSF})_2\text{ClO}_4$ and $(\text{BEDT-TTF})_2\text{Mg}(\text{SCN})_4$ ($M=\text{K}, \text{Rb}, \text{Tl}$).

A SDW forms when the opening of an energy gap at the Fermi surface, due to the SDW, lowers the total electronic energy by more than the increase in Coulomb energy due to the SDW. The size of the energy gap is proportional to the amplitude of the SDW. However, quantum and thermal fluctuations in the SDW order parameter affect the electronic states [6]. Such effects are ignored in the standard mean-field model normally used to describe the SDW state [1]. Near the transition temperature the fluctuations increase and there are long-range SDW correlations. The SDW fluctuations produce a pseudo-gap in the density of states (Fig. 4 inset). This pseudo-gap gradually closes away from the phase boundary. The pseudo-gap reduces the transition temperature and for a sufficiently large pseudo-gap, formation of a SDW is not possible (Fig. 4). The reason for this is simple. In the presence of a large pseudo-gap, opening an energy gap due to a SDW will not lower the total energy sufficiently to make formation of a SDW energetically favourable. The size of the pseudo-gap is determined by the magnitude of the SDW fluctuations which are in turn affected by the size of the SDW correlations transverse to the chains. Recent work by Biehs and Maki [8] has shown that the transverse correlation length is a decreasing function of magnetic field. This provides a mechanism for the destruction of SDW's by high magnetic fields: as the field increases the transverse correlation length decreases and the fluctuation amplitude increases above a critical value (Fig. 4). The existence of a pseudo-gap is reasonable since in CDW systems, at zero field, optical and susceptibility measurements near the transition temperature are consistent with a pseudo-gap due to fluctuations.

Acknowledgements

This work was supported by the Australian Research Council and US National Science Foundation.

References

- [1] For a review, T. Ishiguro and K. Yamaji, *Organic Superconductors* (Springer-Verlag, Berlin, 1990); J. S. Brooks, *MRS Bull.*, August, 31 (1993).
- [2] J. S. Brooks, R. G. Clark, R. H. McKenzie, R. Newbury, R. P. Starratt, A. V. Skougarovsky, M. Tokunoto, S. Takasaki, J. Yamada, and H. Anzai, submitted to *Phys. Rev. Lett.*
- [3] R. H. McKenzie, *Phys. Rev. Lett.*, to appear.
- [4] F. L. Pratt, T. Sasaki, N. Toyota, and K. Nagamine, *Phys. Rev. Lett.* **74**, 3892 (1995), and references therein.
- [5] N. Harrison, A. House, I. Deckers, J. Caulfield, F. Herlach, W. Hayes, M. Kurmo, and P. Day, preprint.
- [6] Similar effects occur in CDW systems. See K. Kim, R. H. McKenzie, and J. W. Wilkins, *Phys. Rev. Lett.* **71**, 4015 (1993), and references therein.
- [7] D. Shoenberg, *Magnetic Oscillations in Metals*, (Cambridge University Press, Cambridge, 1984).
- [8] A. Biehs and K. Maki, *Phys. Rev. B* **44**, 6799 (1991).

Novel tunneling experiments on organic heterostructures

C. M. Fischer, M. Burghard, S. Roth, K.v. Klitzing
Max-Planck-Institut für Festkörperforschung,
Heisenbergstr. 1, 70569 Stuttgart, Germany

Abstract

In analogy to inorganic semiconductor devices tunnel junctions consisting of organic heterostructures incorporated between two gold electrodes are built. Molecular layers are formed by using Langmuir-Blodgett films of two different molecules, a phthalocyanine- and a perylene-derivative. Tunnel characteristics at 4.2K of junctions incorporating two different molecular layers exhibit rectifying behaviour and show equidistant steps in the current, reminiscent of single electron charging phenomena. At higher temperatures the tunneling current is superceded by thermal hopping processes through defect states which over-ride the steplike structure in the curves. The absolute tunneling current through the junction roughly scales with the active junction area.

In the field of molecular electronics several theoretical studies propose the use of complex organic molecules as functional units in electronic devices [1]. Molecules with extended conjugated electron systems are of major interest, since such molecules themselves can represent low-dimensional electron systems. Different energy levels of the highest occupied (HOMO) and lowest unoccupied molecular orbitals (LUMO) can be used to build up molecular structures. To perform tunneling experiments on molecular structures it is essential to assemble the molecules in a well ordered structure and to contact them with electrodes. Further, well defined tunnel barriers are needed.

In previous studies molecular films were incorporated into metal/inorganic oxide/metal tunnel junctions [2]. In this case the inorganic barriers dominate the transport properties, so that the interesting molecular features are only visible in the second derivative of the tunneling characteristic [3]. Recently, we reported the successful preparation of organic tunneling junctions with symmetric gold electrodes in which the molecules themselves act as both, the quantum dots and tunneling barrier systems [4]. In this case no additional inorganic barriers dominate the transport characteristic, so that tunneling processes through molecular orbitals are already observable in the current(I)/voltage(V)-curves. On tunnel junctions consisting of two different molecular layers we observed a rectifying behaviour which we attributed to asymmetric hole tunneling processes through the highest occupied molecular orbitals of the two different molecular complexes.

In the present paper we focus on this two-layer rectifying device and the dependence of the tunnel characteristics on the junction area and temperature is examined. The organic heterostructure is built up from Langmuir-Blodgett films of an octapentyloxy-substituted palladiumphthalocyanine (PcPd) and a perylene-3,4,9,10-tetracarboxydiimide derivative (PTCDI-SPent). Microstructured gold bottom electrodes were deposited onto polished BK7 glass substrates by a photolithographic lift-off process. On top of the gold electrodes 6 monolayers of PcPd are transferred, followed by 6 monolayers of PTCDI-SPent. Noteworthy, in both molecular

films the molecules are upright standing, leading to a total thickness of the organic heterostructure of about 20nm. After the film preparation, the gold top electrode with a thickness of 15nm is deposited perpendicular to the bottom electrode by employing a pulsed evaporation technique through a metal mask [5]. The intersection of the top and bottom contact defines the active junction area. Two different junctions were realized, with the area of $20 \times 100 \mu\text{m}^2$ and $3 \times 13 \mu\text{m}^2$, respectively (width of bottom electrode times width of top electrode). The chemical structure of the molecules and the arrangement of the molecular films between the electrodes are shown in figure 1.

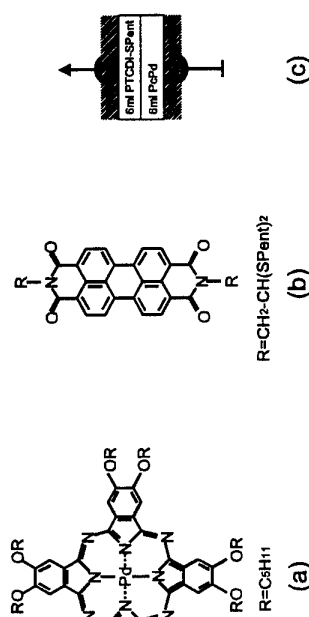


Figure 1: Chemical structure of the octapentyloxy-substituted palladiumphthalocyanine (a) and the perylene-3,4,9,10-tetracarboxydiimide derivative (b). Inset (c) shows the schematic arrangement of the molecular layers in the organic heterojunction.

In Figure 2(a) the I/V-curve of a heterojunction with an active junction area of $20 \times 100 \mu\text{m}^2$ is displayed. The device clearly exhibits rectifying behaviour. For negative voltages (applied to the top electrode), a strong current increase is observed at about -0.53V, whereas for positive voltage values a large current onset occurs at +0.65V. In the positive bias region the tunnel characteristic exhibits four equidistant steps which is underlined by the derivative in the inset of figure 2(a).

To interpret the observed structure we consider the energetic levels of the highest occupied (HOMO) and lowest unoccupied molecular orbitals (LUMO) compared to the gold Fermi level, as shown in figure 2(b). The HOMO levels of both molecules are within a few tenths of an eV below the gold Fermi energy with the HOMO of the PcPd slightly above the HOMO of the PTCDI-SPent [6,7]. When applying a voltage to the electrodes, the molecular orbitals will be shifted relative to the Fermi edges. At a certain voltage value, the HOMO of the PcPd becomes resonant with the positively charged electrode, by which a hole tunneling process through the molecular orbitals starts. The HOMOs of the PTCDI-SPent layer are still energetically below the Fermi edge and therefore act as barrier. For this reason the tunneling current only slightly increases. At higher voltages the HOMOs of the PTCDI-SPent layer become resonant with the positively charged electrode as well, leading to an additional tunneling channel. Since now the remaining tunnel barrier is only given by the aliphatic side chains of the molecules (see fig. 1), the current strongly increases. Due to the asymmetric location of the PcPd and PTCDI-SPent layers inside the junction, the strong current onsets occur at different absolute voltage values for positive and negative bias.

In addition, the I/V-characteristic in figure 2 (a) exhibits four equidistant steps in the positive bias region. These steps we attribute to single charge tunneling effects in the P_cPd layer. It has been suggested elsewhere that this effect might arise from charging of single molecules or molecular stacks, whereby the latter ones might be represented by highly ordered domains in the film plane [4]. Based on this, it has to be clarified whether this effect is dominated by a single, statistically defined pathway through the organic film (e.g. defined by a gold filament of the top electrode penetrating the organic film) or is arising from a collective tunneling process through a large number of channels connected in parallel.

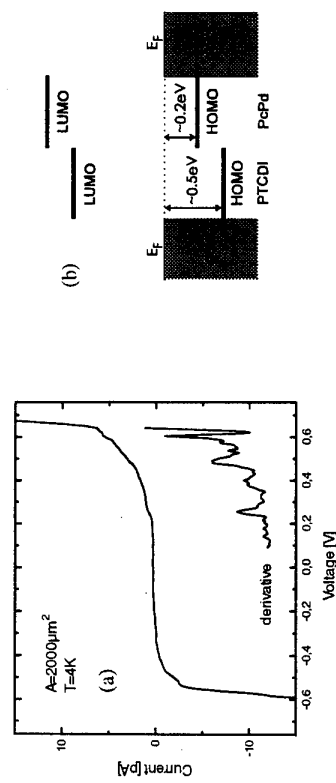


Figure 2: I/V-characteristic of a heterostructure consisting of 6 monolayers P_cPd and 6 monolayers PTCDI-SPT with a junction area of $2000 \mu\text{m}^2$ measured at 4.2K (a). In (b) the estimated energy levels of the molecular orbitals compared to the gold Fermi energy are schematically displayed.

For this purpose, an organic heterojunction with an identical sequence of organic layers and an active junction area of $3 \times 13 \mu\text{m}^2$ was prepared. The I/V-characteristic is shown in figure 3(a). The curve exhibits rectifying behaviour with large current onsets at -0.57V and +0.79V. For positive voltages a similar step-like increase in current is observed as for the larger junction. The absolute height of the current steps is about 30 times lower compared to figure 2(a), whereas the ratio of the two junction areas is about 50. The absolute current through the junction also strongly depends on the actual film thickness, influenced by different penetration depths of gold atoms into the organic film during the evaporation of the top electrode. For this reason, one can speak of the current step heights to scale with the active junction area. This underlines the above mentioned picture of a tunneling process through parallel connected tunneling channels. Indeed, we cannot define the exact nature of such a channel. But speaking of the molecules or molecular stacks as isolated dots surrounded by tunneling barriers represented by the insulating aliphatic chains, these organic heterostructures might be considered as arrays of more or less correlated quantum dots.

The voltage spacing of the current steps corresponds to an energy of a few tenths of an eV, which is much larger compared to the thermal energy kT at room temperature. Thus, the current steps should also be observable at room temperature. A room temperature measurement of the small area junction is displayed in figure 3(b). In comparison, the absolute current is much higher and the characteristic steps are not observed. Nevertheless, the rectifying behaviour is still manifested in a global asymmetry of the curve. Plotting the current versus temperature (not shown), the current steadily increases for temperatures up to about 150K and saturates for higher

temperatures [8]. This behaviour is not dependent on the applied voltage, i.e., there is no qualitative difference in the temperature dependence before and after the opening of tunneling channels through the molecular orbitals. Therefore the additional current might be explained by a thermal hopping conductivity between statistically distributed defects in the organic film which dominates the resonant tunneling through molecular states. To verify this assumption, a future task would be to further purify the organic substances.

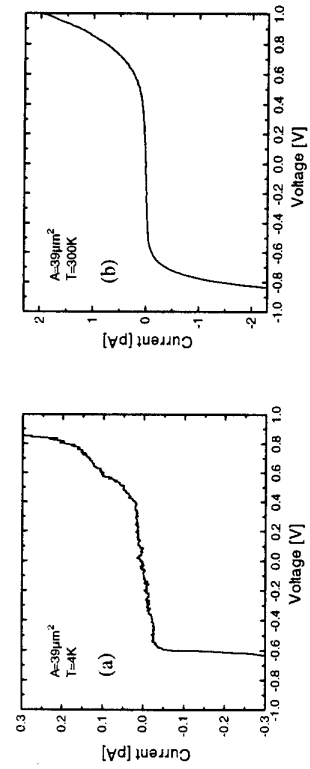


Figure 3: I/V-characteristic of an identical heterostructure as in fig. 2 but with a junction area of $39 \mu\text{m}^2$, measured at 4.2K (a) and room temperature (b).

In conclusion, we have presented transport measurements on organic tunnel junctions consisting of two different molecular layers. At liquid helium and room temperature the devices show rectifying I/V-characteristics. Only at low temperatures superimposing thermal hopping processes are frozen out and additional steps in the current occur, which are tentatively attributed to single charge tunneling effects. The current step height roughly scales with the active junction area, i.e. the tunneling process takes place in various parallel connected tunneling channels. From the present experiments we are not able to draw conclusions about the exact nature of these tunneling channels. One possible way to interpret the organic heterostructure would be the model of an array of single molecules or molecular stacks.

This work was supported by the Sonderforschungsbereich 329 of the Deutsche

Forschungsgemeinschaft and the ESPRIT network NEOME.

References

- [1] A. Aviram, M.A. Ratner, Chem. Phys. Lett. **29**, 25 (1974)
- [2] T.M. Ginnai, D.P. Oxtley, R.G. Pritchard, Thin Solid Films **68**, 241 (1980)
- [3] U. Mazur and K.W. Hippes, J. Phys. Chem. **99**, 6684 (1995).
- [4] C.M. Fischer, M. Burghard, S. Roth, K.v. Klitzing, Europhys. Lett. **28** (2), 129 (1994).
- [5] C.M. Fischer, M. Burghard, S. Roth, K.v. Klitzing, Appl. Phys. Lett. **66** (24), in print
- [6] J. Simon, J.J. André, *Molecular Semiconductors* (Springer Verlag, Berlin, 1985).
- [7] D. Wöhrl, D. Meissner, Adv. Mater. **3**, 129 (1991).
- [8] M. Burghard, C.M. Fischer, M. Schmelzer, S. Roth, M. Hanack, W. Göpel, Chem. Mater., to be published

Recent Progress in the Theory of Composite Fermions near Even-Denominator Filling Factors

N. Read

*Departments of Physics and Applied Physics, P.O. Box 208284,
Yale University, New Haven, CT 06520*

Theories of compressible and incompressible states at filling factors $\nu = 1/2, 1/4, 1/3, 2/5, \dots$ in the fractional quantum Hall regime, will be reviewed, using mainly physical pictures. Our current understanding, and its relation to experiments, will be discussed together with its limitations.

PACS Nos.

June, 1995

A lot of excitement has been generated in the past few years about composite fermions and compressible, Fermi-liquid-like states of the two-dimensional electron gas in high magnetic fields. In this talk I will attempt to review the basic concepts in simple terms, and to explain some recent advances.

In the approach I will describe, we will consider electrons in the lowest Landau level. The kinetic energy is then a constant $\frac{1}{2}hu_e$ per electron, and the potential energy of Coulomb interactions between electrons, and any background potentials, are all that is left in the Hamiltonian. To find the quantum-mechanical ground state, we must "minimize" this potential energy, which, however, is not a trivial problem because of the quantum mechanics of electron motion in the lowest Landau level. Even though we do not attempt a frontal assault on the eigenvalue spectrum, the necessity to obtain a low (expectation or eigen-) value of the potential energy must not be ignored.

Let us begin by recalling that the wavefunctions of a single electron in the lowest Landau level (LLL) are spanned by the basis states (working in the symmetric gauge [1] with the magnetic length $\ell_B \equiv \sqrt{\hbar/eB} = 1$) $u_m = z^m \exp(-\frac{1}{4}|z|^2)$, where $z = x + iy$ is the complex coordinate of the electron. Such a wavefunction has m zeroes at the origin; in general one finds that states for an electron within a certain area in the complex plane possess a total number of zeroes equal to the number of flux quanta N_ϕ that pass through the region, and that the total number of linearly independent states in the LLL is equal to $N_\phi + 1$ (note that, in general, some of the zeroes may lie at the boundary of the region, or at infinity). Because the wavefunctions are, apart from the ubiquitous Gaussian factor, analytic functions in z , two things happen at a zero: the wavefunction vanishes, implying that its probability density goes to zero there, and its phase winds by 2π as the location of the zero is encircled.

Next, we can consider a many-particle system, with electron coordinates z_j for the j th electron. An N particle wavefunction has the form

$$\Psi(z_1, \dots, z_N, \bar{z}_1, \dots, \bar{z}_N) = f(z_1, \dots, z_N) e^{-i \sum_i |z_i|^2} \quad (1)$$

where f is complex analytic and totally antisymmetric. If f contains a single zero for each electron at (or at least near) a position z , we say that it has a *vortex* there. It is represented in the wavefunction by the presence of a factor

$$U(z) = \prod_i (z_i - z). \quad (2)$$

$U(z)$ can be viewed as an operator, Laughlin's quasi-hole operator [1], acting on the remainder of the wavefunction by multiplication to produce f . We call it a *vortex*, by analogy with superfluids and superconductors, because of the winding of phase as any particle encircles z . At the same time, there is a depletion of charge there, because the amplitude for finding any particle goes to zero at z .

The next step is to consider vortices as objects having dynamics in their own right. This

is the crucial step; almost everything else can be easily obtained once this is understood. We will view vortices in any fluid state (a state with no positional order) as particle-like objects. One might ask whether these are stable excitations, but this is not relevant. The vortices will later be constituents in bound states, and it is the stability of the latter which is relevant. It is quite possible for the vortices to be stable in bound states and yet unstable outside them. An analogy can be made with neutrons, which are stable inside nuclei, yet decay when outside them.

The key property of a vortex is this: a vortex sees the density of electrons as a magnetic field, and the current as an electric field. Thus, for example, if we can exert a force on the center of a vortex, it will respond by drifting in the direction perpendicular to the force, just like the drift motion of the center of the cyclotron orbit of a charged particle in a magnetic field. The field strength, if the vortex is viewed as having unit charge, is one flux quantum per electron. This property of vortex dynamics is well-known in the context of superfluids, and also describes the (unquantized) vortices in classical fluid dynamics (in both cases, we must adapt the usual results to the two-dimensional case). Another situation is a vortex in the presence of a current, that is, a velocity field in the fluid. If no other forces act on it, the vortex will be carried along with the flow. It can be held fixed if a force is exerted on it; thus the vortex exerts a force, the Magnus force, which is perpendicular to the velocity and proportional to it in magnitude. Quantum-mechanically, magnetic fields can be observed, as in the Aharonov-Bohm effect, as the phase induced in the wavefunction when a particle is dragged adiabatically around a closed loop; the phase is equal to the number of flux quanta enclosed. For a vortex, the phase obtained is $[2/\hbar c_D d^2 z] \rho(z)$ where $\rho(z)$ is the density of electrons, and the integral is over the area enclosed by the loop, as is almost obvious from equation (2). Electric fields can similarly be obtained from a time-dependent phase, a change of phase in $U(z)$ being obtained by changing the positions of the electrons with time, i.e. when there is a current.

We are now ready to construct a theory for the electron fluid in high magnetic field. First we observe that an electron and a vortex are attracted to each other by the Coulomb interaction, because they have opposite charge. As the kinetic energy is constant, they can easily form a bound state, the electrons sitting at the center of the charge deficiency caused by the vortex. (The vortex is here a vortex in the wavefunction for the other electrons, not including the one bound; the whole function must be antisymmetrized, but this causes no difficulties.) More generally, we can repeat the process and bind a number, q , of vortices to the electron. The bound object now enjoys properties of both the electron and vortices that constitute it. The electron sees the external magnetic field and any external electric fields. The vortices see the electron density and current as magnetic and electric fields. In

particular, the total effective magnetic field is the sum of $\nabla \times \mathbf{A} = -B$, the real field as seen by the electron, and

$$\nabla \times \mathbf{a} = q\Phi_0\theta, \quad (3)$$

the field seen by q vortices (Φ_0 is the flux quantum). The total $\nabla \times (\mathbf{A} + \mathbf{a})$ vanishes if the average density $\bar{\rho}$ is $B/q\Phi_0$, which corresponds to the filling factor $\nu = \bar{\rho}\Phi_0/B = 1/q$. If we now suppose that every electron in the system is part of a bound state, then we have a many-particle system of the bound states, and at the special filling factors $1/q$, q integral, the bound states see zero net effective magnetic field.

In order to understand the many-bound-state problem, we must understand the effective Hamiltonian for the bound states, and their statistics, better. We already see that using each electron in a bound state will give a low potential energy, because the zeroes coincide with the electrons and there is a low amplitude for finding electrons close together. The wavefunction which has this property can be easily written down: it is

$$f_L = \prod_{i < j} (z_i - z_j)^q \quad (4)$$

the Laughlin-Jastrow product. It has long been realized that Laughlin's Jastrow-like ansatz [1] can be called a "binding of zeroes to electrons". We know that each bound state sees an effective magnetic field $B_{\text{eff}} = \nabla \times (\mathbf{A} + \mathbf{a})$, which vanishes at $\nu = 1/q$. Taking these cases first for simplicity, it is natural to expect that the bound state can occupy plane wave states, with a wavevector \mathbf{k} . In the many-particle wavefunctions, this is represented by a factor $e^{i\mathbf{k}\cdot\mathbf{r}_j}$ in the term where the j th electron is the bound in the state with wavevector \mathbf{k} . Now it turns out that this factor, acting by multiplication on some given state, displaces the j th particle by $ik = k_x + ik_y$ (recall that the magnetic length ℓ_B is 1). This arises because in the Hilbert space of many particle states of the form (1), \tilde{z}_j acts on f as $2\partial/\partial z_j$, which generates displacements [3]. A bound state with wavevector zero would have the electron exactly at the center of the multiple vortex. So a bound state with wavevector \mathbf{k} has the electron displaced by $|\mathbf{k}|$ from the centre of the vortex. The electron and the multiple other electrons, which are excluded from the vortex cores. A good understanding is now achieved semiclassically. The electron will drift along an equipotential of $V(|\mathbf{k}|)$. From the preceding discussion, at $\nu = 1/q$ the q -fold vortex experiences a magnetic field of the same strength as the electron, and so it will also drift with the same speed but in the opposite sense relative to the gradient of the potential, due to the opposite sign of its effective charge. This means that both components of the pair drift in the same direction, perpendicular to the vector connecting their centres, so that their separation ($= |\mathbf{k}|$) remains constant. The picture is like that of oppositely charged particles in a magnetic field, which can drift in a straight line as a pair. The energy of our pair is $V(|\mathbf{k}|)$ and the velocity is $\propto \partial V / \partial |\mathbf{k}|$ as it should be. Near the bottom of the potential, it will be quadratic, and we can obtain an effective mass $m^* \sim (\partial^2 V / \partial |\mathbf{k}|^2)^{-1}$ due to the Coulomb interactions (a similar calculation was performed in [4]). This shows clearly that the interactions favour "condensation" of the bound states into the smallest available wavevectors to minimize this effective kinetic energy, which arises solely from the Coulomb interactions and has nothing to do with the real kinetic energy or mass of the electrons, within our lowest Landau level approximation [10].

For q odd, (4) is an acceptable electron wavefunction because it is totally antisymmetric. For q even, it is not, and we must now consider particle statistics. The statistics of the

bound states can be derived from the fact that the vortices obey fractional statistics, which is a byproduct of the effective magnetic fields already described above. If a vortex makes a circuit around a loop enclosing another vortex, with the density otherwise uniform, the missing charge around the vortex core will make a difference of $2\pi\nu$ to the phase (independent of the size and shape of the loop, as long as the vortices remain far enough apart). But a circuit is equivalent to two exchanges, up to translations. So a similar calculation gives that adiabatic exchange of two vortices produces a phase $\theta = \pi\nu$ [2]. For two q -fold vortices, the result is $\pi q\nu$ which at $\nu = 1/q$ is πq . This shows that at these fillings, q -fold vortices are fermions for q odd, and bosons for q even. Hence the electron- q -vortex bound state is a boson for q odd, and a fermion for q even, and they are often termed "composite bosons" and "composite fermions", respectively. For q odd, we can now argue that the bosons in zero magnetic field can Bose condense (at $T = 0$) into the zero-momentum state and that this is the interpretation [4] of the Laughlin state [1]. For q even, we can instead form a Fermi sea, in the manner

$$(5) \quad f = \mathcal{P}_{LL} \det M \prod_{i < j} (z_i - z_j)^q.$$

The matrix M has elements that are essentially plane waves $M_{ij} \sim e^{i\mathbf{k}_i \cdot \mathbf{r}_j}$ for the bound states, filling the Fermi sea, $|\mathbf{k}| \leq k_F$. The Fermi wavevector k_F is determined by the density of particles in the usual way, and for $\nu = 1/2$ is $1/\ell_B$. \mathcal{P}_{LL} projects all electrons to the LLL (we never really left the LLL: this is simply the most convenient way to describe it). As explained above, the plane wave factors then act as operators within the LLL, on the Jastrow factor $\prod (z_i - z_j)^q$ which if not modified would be the Laughlin state for bosons at $\nu = 1/q$. The Slater determinant makes the state totally antisymmetric. The resulting theory is essentially equivalent to that of Halperin, Lee and the author [5], though they employed a transformation involving attaching delta function fluxes to the electrons. I find the present version more physical, and less potentially misleading: no flux is bound to the electrons in reality, as the magnetic field remains almost perfectly uniform when the electrons form this novel state of matter at low temperatures. It is vorticity which is bound to the electrons. The wavefunctions (5) have been tested numerically [6] and it has been found that this theoretical picture gives a good account of small size systems at $\nu = 1/2$.

The simple product form of (5) is similar to Jain's states off half-filling [7], to which we may now turn. Jain's argumentation was a little different from that above, but our approach can be easily extended. We again consider q even, so the bound states are fermions when $\nu = 1/q$. Away from that filling, while the electron and the q -fold vortex still see the same potential $V(|\mathbf{k}|)$, the drift velocities are different because that for the vortices is fixed by the electron density, not the true magnetic field, and B_{eff} is not zero. The separation still remains constant, so the bound pair moves (semiclassically) on two concentric circles separated by $|\mathbf{k}|$, giving an effective cyclotron radius for the bound states. This radius is given by the usual formula $\Phi_0 k / 2\pi B_{\text{eff}}$ for a particle of charge 1 in a magnetic field B_{eff} . If we now consider a fully quantum mechanical picture, then the bound states can occupy Landau level states, and if they fill an integer number $|p|$ of Landau levels, there will be a gap in the excitation spectrum, given, at least naively by the above "mean field" ideas, by $\hbar\omega_c^2 \sim B_{\text{eff}}/m^*$. In these states, the filling factor is $\nu = p/(qp+1)$, for either sign of p [7]. We see that, when the idea of a well-defined Fermi-liquid-like ground state at $\nu = 1/q$ has been understood, including the effective mass setting the basic energy scale, then we are led to predict that the energy gaps near, for example, $\nu = 1/2$, should scale as $|p| \rightarrow \infty$ [5]. (This scaling was later seen experimentally [8].) Notice that we have formulated the theory entirely in the lowest Landau level for the electrons; the Landau levels for the bound states, of which

infinitely many are occupied as $|p| \rightarrow \infty$, have nothing to do with the real excited Landau levels of the electrons.

Many of the physical properties of the states obtained in the above approach can be obtained quite easily if we keep in mind that the vortices see the electron density and current as magnetic and electric fields. These fields are described by the ‘internal’ vector and scalar (gauge) potentials, defined by (3) above, and by

$$-\nabla a_0 - \dot{\mathbf{a}} = q\Phi_0\hat{\mathbf{z}} \times \mathbf{j}, \quad (6)$$

where \mathbf{j} is the electronic current density. Since both ρ and \mathbf{j} fluctuate quantum mechanically in both space and time, so do a and a_0 , which determine B_{eff} and E_{eff} ; E_{eff} is the left hand side of (6), plus the real electric field experienced by an electron. The gauge fields, often described as Chern-Simons gauge fields because the equations (3), (6) can be obtained from an action containing a Chern-Simons term (see e.g., [5]), play an essential role in the physical properties of the states. Fortunately, for many basic properties, a self-consistent field (or random phase) approximation is adequate (or in many cases exact). In such an approach, the long range effects of the gauge fields (together with the Coulomb interaction) are treated explicitly and exactly, much like Coulomb interactions in ordinary Fermi liquid theory [7]. Short range effects of the fields are approximated, in the simplest case (the RPA), by simply neglecting them. Thus the bound states are treated as noninteracting bosons or fermions, in the gauge field B_{eff} , E_{eff} ; the fields are calculated from the equations (3), (6) using the expectation values of ρ , \mathbf{j} , and the whole system is then required to be consistent. For example, the gauge fields must be included to obtain the correct Hall conductance, since a naive use of the mean field picture that at $\nu = 1/2$ we have fermions in zero net magnetic field would appear to give $\sigma_{xy} = 0$, not $1/2!$ The correct argument is that when a current flows, there is a gauge field contribution to E_{eff} , which must be cancelled by a real electric field since the fermionic bound states respond to the total field and have no Hall conductance, so the component of E_{eff} perpendicular to the current flow must vanish. This gives the correct Hall field for the electrons. Other applications include the incompressibility of the fractional quantum Hall states at $\nu = 1/q$, q odd, where the bound states Bose condense. The Bose condensate would usually be compressible, but here the usual mechanism for flux quantization in a superfluid, applied to the internal gauge field in a vortex added to the ground state implies by Eq. (3) that a fractional charge $1/q$ is accumulated there, in agreement with Laughlin’s theory, and this object has finite energy, so there is an energy gap. Essentially, the Meissner effect implies incompressibility in this system. This does not occur in the Fermi liquid state at q even, so these states are compressible.

A more striking demonstration of the gauge fields occurs in relation to the surface acoustic wave experiments [9]. The basic observation, which helped stimulated the development of the theory of the Fermi liquid like states, is an anomaly in the longitudinal conductivity $\sigma_{xx}(k)$ at wavevector k and low frequency. At fractions such as $1/2$, $1/4$, $3/4$, \dots , but not at the incompressible fractions $1/3$, \dots , $\sigma_{xx}(k)$ increases linearly with k , and further the width of this feature in magnetic field near these fractions scales the same way. The theoretical explanation, based on the theory in [5], rests on two facts: (i) the bound states at $\nu = 1/2$ form a Fermi liquid which responds to a longitudinal electric field as $\sim \tilde{\sigma}_{xx}(k) \sim k_F/k$ (ii) the time- and space-dependent self-consistent field leads to the rule that the resistivity tensor of the bound states should be added to the resistivity tensor due to the Chern-Simons term (which appears in the right hand side of equations (3), (6)) to obtain that for the electrons. The second point leads to a matrix inversion to obtain $\sigma_{xx}(k) \sim k/k_F$ [5]. Ref [5] also predicted geometric resonances in the anomaly, due to the wavelength of the sound

waves coming into resonance with the cyclotron radius of the fermion bound states, which is determined by k_F . The subsequent observation of these resonances [9] confirmed the existence of a Fermi surface in the excitation spectrum of the compressible state at $\nu = 1/2$, as did other experiments [11].

There are also quantum fluctuations in the gauge fields that can scatter the bound states. These have the effect of causing the effective mass to diverge weakly, as a logarithm, as k of a bound state approaches k_F , or as the filling factor approaches a value $1/q$, q even [5]. (Later analyses have essentially confirmed the correctness of that given in [5].) This enhancement is on top of that already obtained because our effective mass is determined by electron-electron interactions, not by the GaAs band mass, and it was not included in our earlier statements about the mass. The effect is so weak that it will be very hard to observe. Recently, some experimental groups have reported both decreases [12] and increases [13] in effective mass on approaching $\nu = 1/2$; some other groups report increases much stronger than logarithmic if the trend persists all the way to $\nu = 1/2$. However, it is hard to extract a mass in this region from the data, and many data are also consistent with a constant mass as we have described here. While a non-singular systematic variation of effective mass with filling factor is not ruled out, I suspect the apparent increases are due to problems with the analysis.

I have not discussed the older hierarchy theory [14, 15] that describes the full set of incompressible fractional quantum Hall states at filling factors $\nu = p/q$, with q odd. If one examines the properties of these states and those obtained using the ‘composite fermion mapping’, that is the bound states occupying Landau levels, one finds that the properties that can be calculated using these simple analytical ideas, which are the universal ones of filling factors (or σ_{xy}), and charge, statistics and number of types of excitations, turn out to be the same [16]. The different approaches to these states are simply descriptions of the same physics in different variables or using different bases. In fact, even within a composite fermion approach, a fraction such as $1/3$ can be described in two ways: either as one Landau level of bound states containing two vortices each, or as one Landau level of bound states containing four vortices each. There is no question that these describe the same state of matter. The simplest way, however, to describe $1/3$, or other similar fractions, is to use the mapping that minimizes the effective magnetic field seen by the bound states; that is, in terms of ‘composite bosons’ containing an electron and three vortices [4]. If one can accept that a low energy emerges at even denominators from binding an even number of vortices to each electron, why not accept the same for odd denominators?

The many different ways of viewing the physics raises the question, when can one expect to see phenomena characteristic of the fermion bound states, that would not be easily explained otherwise? Results such as the scaling of the energy gap as ν approaches $1/2$ are hard to explain quantitatively in the old hierarchy, which is more useful for energetics near the primary fraction such as $1/3$. The most distinctive results, however, are for response functions in the wavevector range $R_c^* < k < k_F$, or the frequency range $\omega_c^* < \omega < E_F^*/E_F$ is the effective Fermi energy $\sim k_F^2/m'$, some of which is explored by the surface acoustic waves [9]. At higher energies or wavevectors, one is probing the microstructure of the bound states themselves. At energies or wavevectors below the stated limit, which vanishes as $\sim B_{\text{eff}}$, the fermions are screened so as to become the usual fractional charge, fractional statistics quasiparticles. It is only in the intermediate region that the fermion behaviour most characteristic of $\nu = 1/2$ becomes apparent, and this requires that the scales be well separated. By the time one reaches $\nu = 1/3$, the scales become essentially equal, and there is no dynamic range where the fermion behavior can be seen, whereas the bosonic behaviour now rules out to low energies or wavevectors, though this is harder to detect because the bosons are Bose

condensed and the system has an energy gap.
This research was supported by NSF grant no. DMR-9157484.

References

- [1] R.B. Laughlin, Phys. Rev. Lett. **50**, 1395 (1983).
- [2] D. Arovas, J.R. Schrieffer and F. Wilczek, Phys. Rev. Lett. **53**, 722 (1984).
- [3] S.M. Girvin and T. Jach, Phys. Rev. B **29**, 5617 (1984).
- [4] N. Read, Phys. Rev. Lett. **62**, 86 (1989).
- [5] B.I. Halperin, P.A. Lee and N. Read, Phys. Rev. B **47**, 7312 (1993).
- [6] E. Rezayi and N. Read, Phys. Rev. Lett. **71**, 900 (1994).
- [7] J.K. Jain, Phys. Rev. Lett. **63**, 199 (1989); Phys. Rev. B **40**, 8079 (1989); **41**, 7653 (1990).
- [8] R.-R. Du *et al.*, Phys. Rev. Lett. **70**, 2944 (1993).
- [9] See, e.g., D. Pines and P. Nozières, *The theory of quantum liquids*, Benjamin, New York, 1966.
- [10] R.L. Willett *et al.*, Phys. Rev. B **47**, 7344 (1993); Phys. Rev. Lett. **71**, 3846 (1993); preprint.
- [11] N. Read, Semicond. Sci. Technol. **9**, 1859 (1994).
- [12] W. Kang *et al.*, Phys. Rev. Lett. **71**, 3850 (1993).
- [13] D.R. Leadley, *et al.*, Phys. Rev. Lett. **72**, 1906 (1994).
- [14] R.-R. Du *et al.*, Phys. Rev. Lett. **73**, 3274 (1994).
- [15] F.D.M. Haldane, Phys. Rev. Lett. **51**, 605 (1983).
- [16] B.I. Halperin, Phys. Rev. Lett. **52**, 1583 (1984).
- [17] N. Read, Phys. Rev. Lett. **65**, 1502 (1990).

Composite Fermions Examined with Surface Acoustic Waves

R. L. Willett, L.N. Pfeiffer
AT&T Bell Laboratories, 600 Mountain Avenue
Murray Hill, New Jersey 07974, U.S.A.

Abstract

By using large wavevector surface acoustic waves (SAW) to probe the conductivity of 2D electron systems our studies have revealed directly the Fermi surface effects of the composite fermion (CF). Geometric resonances of the quasiparticles' cyclotron orbit and the SAW have allowed measurement of the CF Fermi wavevector. Recent results at larger SAW wavevector have demonstrated these geometric resonances at multiple even denominator filling factors. In addition, these new results expose an apparent inconsistency between the effective mass as measured in simple d.c. transport experiments and the mass necessary to observe the geometric resonances.

Introduction

Our experiments employ surface acoustic waves (SAW) propagated on GaAs/AlGaAs heterostructures to extract the 2D electron wavevector dependent conductivity $\sigma_{xx}(q)$. The SAW traverses the 2DES where it is attenuated and slowed by the interaction of its piezoelectric field and the 2D electrons. The sound velocity shift as measured here decreases monotonically with increasing 2DES conductivity: $\Delta v/v = \alpha/(1 + (\sigma_{xx}(q)/\sigma_m)^2)$, where the piezoelectric coupling constant $\alpha = 0.00032$, and σ_m is used as a scaling parameter. The essential point of the experiments is that the measured amplitude and velocity reflect the 2DES conductivity at the dimension of the SAW wavelength. We have developed new SAW that operate at up to 10.7 GHz, which allow examination of the 2DES conductivity at a length scale of ~270 Å. Measuring the 2DES response at small length scales has been crucial in exposing the properties of the gauge transformed or composite fermion [1]. In particular, surface acoustic waves have revealed the composite fermion's Fermi surface effects at even-denominator filling factors as delineated by Halperin, Lee, and Read [2] (HLR).

Results

At low SAW frequencies, the measured sound velocity shift describes a sheet conductivity throughout the magnetic field range essentially similar to that seen in d.c. transport. However, in our early results [3], SAW demonstrated an anomalous drop in transmitted amplitude and velocity at $v = 1/2$ and $1/4$, reflecting an enhanced conductivity of the 2DES at these specific v . Following HLR this anomaly is understood to occur when the SAW wavelength is smaller than or about the dimension of the composite fermion mean free path, so that the conductivity is enhanced since the quasiparticle can move in the direction of the piezoelectric field of the SAW without scattering. The width of the anomaly in magnetic field is determined by the cyclotron motion of the quasiparticle since the enhanced conductivity is cut off as the quasiparticle moves more laterally with respect to the SAW propagation direction as the effective B-field

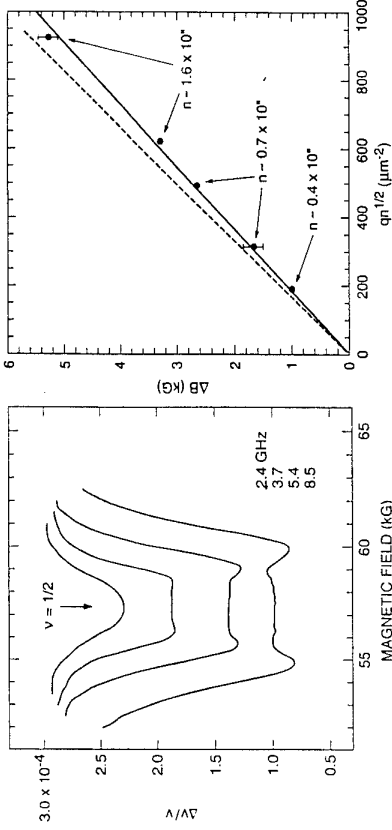


Figure 1. Sound velocity shift versus B-field at four SAW frequencies demonstrating geometric resonances developing symmetrically about $v = 1/2$. Right panel: principle resonance position in ΔB for samples of different densities using several q SAW, with the dashed theoretical line $\Delta B = qn^{1/2}$.

$\Delta B = B - B(1/2)$ increases. Further, the theory proposed that the conductivity at $v = 1/2$ should increase linearly with SAW wavevector as should the width of the anomaly: these predictions were found to be true experimentally [4].

Beyond these findings, theory predicted definitive evidence for the presence of a Fermi surface at 1/2 to be observation of geometric resonance of the quasiparticle cyclotron motion and the SAW wavelengths. That is, within the above described enhanced conductivity, resonance structure should appear in the conductivity ($\Delta v/v$) if cyclotron orbits can be completed within the SAW wavelength without scattering. By using smaller wavelength SAW, such resonances were indeed observed [5] in SAW measurements up to 8.5 GHz. In Figure 1 these resonances are shown to develop symmetrically about 1/2 as larger SAW wavevector is used, with the resonance positions in ΔB increasing linearly with SAW q : $\Delta B/B = q/(3/83 k_F)$ for the principle resonance positions, corresponding to resonance of the CF cyclotron orbit with a single SAW wavelength. This commensurability of the cyclotron orbits and the wavelength allows measurement of the quasiparticle k_F , which closely matches [5] the value prescribed by the system of density n , $k_F = (4\pi n)^{1/2}$. The density dependence of the resonance position in B_{eff} is confirmed by using samples of different densities and plotting the positions versus $qn^{1/2}$, as shown in Figure 1, right panel.

We have further developed the SAW technology and have studied the 2DES conductivity up to 10.7 GHz, corresponding to a wavelength of ~2700 Å. These new results demonstrate geometric resonance structure at multiple even denominator filling factors, show both secondary and principle resonances at $v = 1/2$, and most importantly reveal a fundamental inconsistency with the effective mass measurements [6] using simple d.c. transport.

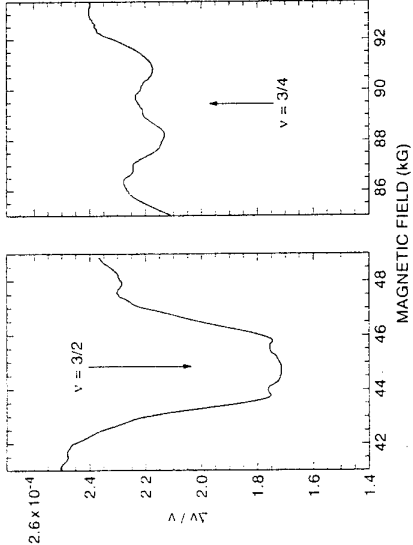


Figure 2. Geometric resonance structures around filling factors 3/2 and 3/4. SAW frequency is 10.7 GHz, temperature ~ 150 mK.

Using samples of density larger than that employed previously, the 10.7 GHz SAW show geometric resonance structure at filling factors 3/2 and 3/4; see Figure 2. The effective B-field positions of the resonances agree with theoretical predictions[2], and their observation confirms the presence of Fermi surface effects throughout the magnetic field spectrum.

The higher sample density and smaller SAW wavelengths also allow observation of both principle and secondary resonances around 1/2, corresponding to commensurability of the cyclotron orbits with both one and two SAW wavelengths; see Figure 3. The resonance structure agrees with the theoretical curve using experimentally derived values of quasiparticle mean free path and electron density inhomogeneity. The conditions necessary for resonance observation place constraints on the quasiparticle cyclotron frequency, and therefore the mass. In order to observe a resonance, the SAW must present a static spatial wave like a grating to the quasiparticle orbits; quantitatively this is equivalent to $\omega_c \gg \omega_{SAW}$ and $v_F > v_{SAW}$. Given observation of the resonances with high resolution, we then compare these satisfied constraints to the effective mass as derived from d.c. transport studies on these same samples. By measuring activation energies and Shubnikov-deHaas amplitudes of the FQHE states as done previously[7], we extract cyclotron frequency and effective mass values over a magnetic field range near the SAW resonance positions; see Figure 3, right panel. We find that these mass values are too large to be consistent with observation of the SAW resonances. As shown in the figure, when a quasiparticle mass of $1.2m_e$ is used, both the cyclotron frequencies at the principle and secondary resonance positions are less than or nearly equal to the SAW frequency, thus violating the static wave constraint.

The origin of the inconsistency is unclear. Three possibilities exist: the d.c. transport derived effective mass is wrong, the conditions considered above to be necessary for resonance observation are incorrect, or a different cyclotron frequency is applicable for the d.c. transport

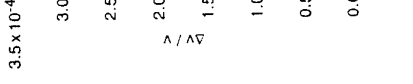


Figure 3. Sound velocity shift versus effective B-field for 10.7 GHz SAW near $v = 1/2$. The dotted line is a theoretical fit. Right panel shows energy gap, cyclotron energy, and effective mass as derived from d.c. transport. The cyclotron frequency using $m^* = 1.2m_e$, i.e. the electron mass, is compared to the SAW frequency in the upper right.

References

- [1] J.K. Jain, PRL 63, 199(1990).
- [2] B.I. Halperin, P.A. Lee, and N. Read, Phys. Rev. B 47, 7312(1993)
- [3] R.L. Willett et al., PRL 65, 112(1990).
- [4] R.L. Willett et al., Phys. Rev. B 47, 7344(1993).
- [5] R.L. Willett et al., PRL 71, 3846(1993).
- [6] R.L. Willett et al., submitted to PRL(1995).
- [7] R.R. Du et al., PRL 70, 2944(1993). D.R. Leadley et al., PRL 72, 1906(1994). R.R. Du et al., PRL 73, 3274(1994).

THE PHYSICAL SIGNIFICANCE OF SINGULARITIES IN THE CHERN SIMONS FERMI

LIQUID DESCRIPTION OF A PARTIALLY FILLED LANDAU LEVEL

Ady Stern* and Bertrand I. Halperin

Physics Department, Harvard University, Cambridge, MA 02138

Abstract

We analyze the linear response of a half filled Landau level to long wavelength and low frequency driving forces, using Fermi liquid theory for composite fermions. This response is determined by the composite fermions quasi particle effective mass, m^* and quasi-particle Landau interaction function $f(\theta - \theta')$. Analyzing infra-red divergences of perturbation theory, we get an exact expression for m^* , and conjecture the form of the $f(\theta - \theta')$. We then conclude that in the limit of infinite cyclotron frequency, and small \mathbf{q}, ω , the composite fermion excitation spectrum is continuous for $0 < \omega < \gamma_{\text{eff}}^2 q$, with γ an unknown number. For fractional quantum Hall states near a half filled Landau level, we derive an exact expression for the energy gap.

The fermionic Chern-Simons theory of the half filled Landau level maps the problem of interacting electrons in a strong magnetic field onto that of composite fermions at zero magnetic field, interacting with a Chern-Simons gauge field. This mapping opens the way to a study of low energy excitations of the system by an application of Fermi liquid theory. In this paper we discuss such an application. Due to space constraints, very few details are given. We refer the reader to Ref. [1] for further details.

Fermi liquid theory outlines a formal method for a calculation of the exact small wave-vector \mathbf{q} , low frequency ω and zero temperature limit of linear response functions. In practice, the exact calculation is usually intractable, and approximations are needed. In section (1) below, we remind the reader of the formal method. Then, in section (2), we attempt to use it to extract information about the linear response of electrons at, and near, a half filled Landau level.

1. Derivation of linear response function by Fermi liquid theory – a review

The Fermi liquid theory prescription for the calculation of linear response functions can be put into the following steps:

- Formulate the Hamiltonian of the system.
- Calculate the effective mass of quasi-particles at the Fermi level m^* and the quasi-particle Landau interaction function $f(\mathbf{k} - \mathbf{k}')$. This calculation is done in two stages. First, calculate the single particle self energy $\Sigma(\mathbf{k}, \omega)$ for states near the Fermi level,

and the two-particle interaction operator $\Gamma(\mathbf{k}_1, \omega_1; \mathbf{k}_2, \omega_2; \mathbf{k}_1 + \mathbf{q}, \omega_1 + \Omega; \mathbf{k}_2 - \mathbf{q}, \omega_2 - \Omega)$ for an exchange scattering near the Fermi level. Then, use the following formulae,

$$m^* = m \frac{1 + \frac{\partial \Sigma}{\partial \mathbf{q}}}{1 - \frac{m}{k_F} \frac{\partial \Sigma}{\partial \mathbf{q}}} \quad (1)$$

$$f(\mathbf{k} - \mathbf{k}') = z^2 \lim_{n \rightarrow 0} \Gamma(\mathbf{k}, 0; \mathbf{k}', 0; \mathbf{k}, \Omega; \mathbf{k}, -\Omega) \quad (2)$$

to extract m^* and f out of Σ and Γ . In Eq. (1), z is the single particle Green function residue at the Fermi level.

In most practical cases, the self energy and the interaction operator cannot be calculated exactly, and have to be approximated by a perturbative calculation.

- Consider now the response of a 2D fermion system to a driving force in the limit $\mathbf{q}, \omega \rightarrow 0$. In linear response to such a driving force, the shape of the Fermi surface acquires a space and time dependence characterized by the same Fourier components \mathbf{q}, ω , and is described by a function $\nu_{\mathbf{q}, \omega}(\theta)$. The angle θ parametrizes the Fermi surface, whose ground state shape is a circle. The function $\nu_{\mathbf{q}, \omega}(\theta)$ describes the distortion of the Fermi surface relative to its ground state shape. It is related to the driving force acting on the fermions by means of the Boltzmann equation, in which the effective mass and the Landau function are parameters:

$$(\omega - q \frac{k_F}{m^*} \cos \theta) \nu_{\mathbf{q}, \omega}(\theta) - \frac{1}{(2\pi)^2 q k_F} \cos \theta \int d\theta' f(\theta - \theta') \nu_{\mathbf{q}, \omega}(\theta') = \hat{\mathbf{k}} \cdot \mathbf{F}_{\mathbf{q}, \omega} \quad (2)$$

where the angle θ is measured relative to \mathbf{q} ; the function $f(\theta - \theta')$ is the quasi-particle interaction function $f(\mathbf{k}, \mathbf{k}')$ for two wave-vectors at the Fermi surface, at angles θ, θ' relative to \mathbf{q} ; and \mathbf{F} is the driving force. In the case of long range interaction the driving force \mathbf{F} deserves a further discussion, which is given below.

- In the absence of driving force ($\mathbf{F} = 0$), the solutions to the Boltzmann equation (2) are low energy excitation modes of the Fermi liquid. As long as $f(\theta - \theta')$ is regular, these modes are composed of a continuum, at $0 < \omega < v_F^2 q$, and possibly a number of discrete modes.
- The Boltzmann equation relates the driving force to the shape of the Fermi surface.
- The shape of the Fermi surface determines the three vector current $J_\mu(\mathbf{q}, \omega)$, according to:

$$J_0(\mathbf{q}, \omega) = k_F \int d\theta \nu_{\mathbf{q}, \omega}(\theta) \quad (3)$$

$$\mathbf{J}(\mathbf{q}, \omega) = \int d^2 k \delta(k - k_F) \mathbf{u}_k \nu_{\mathbf{q}, \omega}(\frac{k \mathbf{q}}{k_F}) \quad (3)$$

with $\mathbf{u}_k \equiv \frac{\mathbf{k}}{m^*} + \int d^2 k' f(\mathbf{k}, \mathbf{k}') (\epsilon_{\mathbf{k}'} - \mu) \frac{\mathbf{k}'}{m^*}$. Combined together, Eqs. (2) and (3) relate the current to the driving force, i.e., lead to the linear response functions.

- In the case of long range interactions between the fermions, the driving force appearing in the right hand side of the Boltzmann equation is the total driving force, composed of an externally imposed part and an internally induced part. The induced part is exerted by charge density and current induced by the driving force in the system.

2. Application to the $\nu = 1/2$ problem

- The fermions' Hamiltonian is:

$$H = \frac{1}{2m} \int d^2r \Psi^\dagger(\mathbf{r}) [-i\nabla - \mathbf{a}(\mathbf{r})]^2 \Psi(\mathbf{r}) + \frac{1}{2} \int d^2r' \int d^2r'' [\Psi^\dagger(\mathbf{r}) \Psi(\mathbf{r}) - n] V(\mathbf{r} - \mathbf{r}') [\Psi^\dagger(\mathbf{r}') \Psi(\mathbf{r}') - n]$$

supplemented by the gauge condition $\nabla \cdot \mathbf{a} = 0$ and the constraint $\nabla \times \mathbf{a}(\mathbf{r}) = 2\pi\tilde{\phi}\hat{\psi}^\dagger(\mathbf{r})\Psi(\mathbf{r}) - n$, where n is the average electron density. The parameter $\tilde{\phi}$ is the number of flux quanta attached to every fermion. While $\tilde{\phi} = 2$ for $\nu = 1/2$, it is useful to keep $\tilde{\phi}$ as a variable parameter (see below). In Eq. (4) we use a system of units where $\hbar = \frac{e}{c} = 1$.

Perturbative calculation: There are two dimensionless parameter in the present problem. The first, $\tilde{\phi}$, the number of flux quanta attached to each fermion, is the dimensionless fermion gauge field coupling constant. The second is the ratio of Coulomb and cyclotron energies, $\frac{e^2 k_F}{\omega_c}$. In the physical system $\tilde{\phi} = 2$ and $\frac{e^2 k_F}{\omega_c}$ is small.

We define the unperturbed problem as that in which both parameters are zero, and the problem is that of non-interacting fermions at zero magnetic field. In our perturbative scheme, $\tilde{\phi}$ is turned adiabatically on, and so is the external magnetic field B , such that $B = 2\pi\tilde{\phi}\hat{\psi}$. In parallel, $\frac{e^2 k_F}{\omega_c}$ is turned on from zero, too.

The effective mass: A calculation of the effective mass using a low order perturbation theory approximation for the self energy leads to the conclusion that the effective mass of a quasi-particle of energy ω above the Fermi energy diverges logarithmically for small ω [2]. We have studied the effect of higher order processes on this result, and concluded that *to all orders in $\tilde{\phi}$* ,

$$\lim_{\omega \rightarrow 0} m^*(\omega) = \frac{\tilde{\phi}^2 e k_F}{2\pi c^2} |\ln \omega| \quad (5)$$

This conclusion is based on two observations: first, following from general principles, the infra-red limit of the gauge field propagator can be calculated exactly. Second, by use of Ward identities, we are able to show that the renormalization of the vertices by high-momentum exchange processes does not affect the effective mass.

The Landau function: A calculation of the Landau function within low order perturbation theory leads to the conclusion that $f(\theta - \theta') = \frac{(2\pi)^2}{m} \delta(\theta')$. When substituted into the Boltzmann equation (2), this singular form of the Landau function leads to a renormalization of the effective mass from infinity back to its bare value, and to a cancellation of the logarithmically divergent effective mass from the linear response functions.

This cancellation is consistent with calculations of the response functions using perturbation theory, renormalization group and bosonization [3]. However, the re-renormalization of the mass back to its *bare* value is inconsistent with the requirement that the low energy spectrum of a partially filled Landau level should be independent of the bare mass at the limit of infinite cyclotron energy, and should depend on the Coulomb energy scale only. To

reconcile both arguments, we conjecture that the correct form of the Landau function is

$$f(\theta - \theta') = A\delta(\theta - \theta') + \text{regular part} \quad (6)$$

where A is of the order of $\frac{e^2}{ck_F}$. In the limit of infinite cyclotron energy, we expect the regular part to give a contribution of the order of $\frac{1}{m}$ to the first two Fourier components, f_0 and f_1 , only.

Low energy linear response: The Boltzmann equation can be used to calculate the density density component of the fermions' linear response function, $\Pi_{\mu\nu}(\mathbf{q}, \omega)$, which gives the response to the total scalar and vector potentials. The total potentials include both the Coulomb and Chern-Simons potentials resulting from the induced density and current fluctuations of wave vector \mathbf{q} and frequency ω . Poles in this polarizability function can be loosely interpreted as excitation modes of the fermion system, when the long range forces are suppressed. If our conjecture for the Landau function (Eq. (6)) is indeed correct, then the spectrum of density excitations is composed mostly of a continuum of modes at $\omega < v_F q$, where $v_F \propto \frac{e^2}{\hbar}$, with the proportionality constant being an unknown number. This continuum leads to a finite longitudinal electronic resistance in that range of \mathbf{q}, ω . On top of that continuum, our conjecture predicts, at the limit of infinite cyclotron energy, 1 or 2 discrete poles, whose energy depends on the bare mass of the electron. While these poles are not excitation modes of the electronic system, they do have an effect on its linear response.

3. Implications to FQHE states near $\nu = 1/2$

We have studied the energy gap corresponding to a fractional quantum Hall state of the form $\nu = \frac{p}{2p+1}$, by mapping the state onto that of p filled composite-fermion Landau levels, and directly calculating the discontinuity in the chemical potential when the density is varied. Similar to the case of the effective mass, we were able to obtain an exact result, namely,

$$\lim_{p \rightarrow \infty} E_g = \frac{\pi}{2} \frac{e^2}{ek_F} \frac{1}{(2p+1) \ln(2p+1)} \quad (7)$$

This work was supported in part by NSF grant DMR 94-16910. AS acknowledges financial support of the Harvard Society of Fellows.

References

- [*] Future address (starting from October 1995): Department of Condensed Matter Physics, Weizmann Institute of Sciences, Rehovot 76100, Israel.
- [1] A. Stern and Bertrand I. Halperin, preprint, cond-mat/9502032, and references therein.
- [2] B.I. Halperin, P.A. Lee and N. Read, Phys. Rev. B **47**, 7312 (1993).
- [3] Y.B. Kim, X.G. Wen, P.A. Lee and A. Furusaki, Phys. Rev. B **50**, 17917 (1994); B.L. Altshuler, L. Ioffe and A.J. Millis, preprint, C. Nayak and F. Wilczek, Nucl. Phys. B **417**, 359 (1994); H.J. Kwon, A. Houghton and J.B. Marston, Phys. Rev. Lett. **73**, 284 (1994).

UNIVERSAL BEHAVIOUR IN THE THERMOELECTRIC POWER OF COMPOSITE FERMIONS

B. Tieke^a, U. Zeitler^a, R. Fletcher^b,
S.A.J. Wiegers^a, A.K. Geim^a, J.C. Maan^a, and M. Henini^c

^a High Field Magnet Laboratory, University of Nijmegen, the Netherlands

^b Department of Physics, Queen's University, Kingston, Ontario, Canada
^c Department of Physics, University of Nottingham, UK

Abstract

The experimental phonon-drag thermoelectric power (TEP) of high mobility two-dimensional electron gases (2DEGs) at filling factors with even denominators reveals a remarkable similarity with the zero magnetic field TEP. It is identical for $\nu = \frac{1}{2}$ and $\nu = \frac{3}{2}$, and for $\nu = \frac{1}{4}$ and $\nu = \frac{3}{4}$, respectively, with an about two times higher absolute value. These results are interpreted as the "zero field" TEP of Composite Fermions belonging to the $m = 1$ and $m = 2$ family at filling factors $\nu = q/2m$.

Composite Fermions (CFs), quasi-particles which have recently been proposed theoretically [1, 2] to explain the fractional Quantum-Hall effect, have attracted a lot of interest from experimentalists in the last two years. In the CF-picture the FQHE is regarded as the integer Quantum-Hall effect (IQHE) of new quasi-particles around filling factors $\nu = \frac{1}{2m}$ ($\frac{1}{2}$, $\frac{1}{4}$, etc.). The external magnetic field transforms to an effective field for CFs which is zero at these particular filling factors.

Despite the great number of experiments having been reported on CFs, they were nearly exclusively of the type of electrical transport measurements [3, 4] with only few exceptions [5, 6]. To understand the nature of these quasi-particles investigations of their interaction with other (quasi-)particles are of great value. Thermoelectric power (TEP) as a tool to study the interaction of CFs with phonons can provide a whole new class of information. TEP in 2-dimensional systems is known to be caused by two different mechanisms: The diffusion TEP involving only intrinsic properties of the charge carrier system and the phonon drag TEP which is a consequence of the interaction between the phonons and the charge carriers. Measurements of diffusion TEP in a 2D hole gas have been reported for temperatures below 100 mK [6]. However, TEP in 2DEGs is dominated by phonon drag down to temperatures below 200 mK [7, 8] (see also Fig. 3).

In this paper, we will present extensive data on the phonon drag TEP of CFs, not only at $\nu = \frac{1}{4}$ but also at other even denominator filling factors.

The TEP of 2DEGs was measured in a $^3\text{He}/^4\text{He}$ -dilution refrigerator (100 mK to 1.2 K) and high magnetic fields (20 T) using the standard techniques – application of a temperature gradient ΔT to a sample in vacuum and detection of the created voltage – described in [7, 8]. The thermometry was checked at $B = 0$ as well as in high fields by inferring the thermal conductivity λ from the measured I , ΔT , and heater power P . λ was always found to be in excellent agreement with a T^3 -dependence expected for boundary scattering. The electron density and mobility of the sample could be adjusted in the range of $1.0...1.9 \times 10^{11} \text{ cm}^{-2}$ and $0.6...1.0 \times 10^6 \text{ cm}^2 \text{V}^{-1} \text{s}^{-1}$, respectively, by consecutive illumination with an IR-diode.

The magneto-TEP of a 2DEG with an electron density $n = 1.9 \times 10^{11} \text{ cm}^{-2}$ is shown in Fig. 1. At first glance, this picture looks similar to typical magneto-transport measurements on 2DEGs. However, there are a lot of subtle but very illustrating differences. To account for the strong temperature dependence of the absolute magnitude, the TEP-curves have been normalized by their value at filling factor $\nu = \frac{1}{2}$. This scaling is non-trivial since taking any other filling factor away from $\frac{1}{2}$ (and also $\frac{3}{3}$, $\frac{1}{4}$, and $\frac{3}{4}$) for the scaling would lead to an obviously chaotic picture. Thus, the natural scaling of the TEP by its value at a $\nu = \frac{1}{2}$ is already a demonstration of the particularity of this filling factor (as it is also the case for $\frac{3}{2}$, $\frac{3}{4}$, and $\frac{1}{4}$).

Furthermore, there is a striking symmetry around $\nu = \frac{1}{2}$ with quantum oscillations growing with decreasing temperature and increasing effective field $B^* = B - B_{\frac{1}{2}}$. This symmetry in S_{xx} is much more pronounced than in the resistivity where it is partly hidden by a quadratic background of classical magnetoresistance (see Fig. 2). The symmetry in the TEP resembles more the resistivity of 2DEGs with a 10 times higher mobility. Moreover, a similar behaviour – a plateau-like structure surrounded by symmetric peaks – is also observed around the other even denominator filling factors $\nu = \frac{3}{4}$ and $\nu = \frac{3}{2}$ at temperatures below 600 mK.

The most striking observation concerns the relative amplitudes of these plateaus. Below 600 mK, S_{xx} has the same value at $\nu = \frac{1}{2}$ and $\nu = \frac{3}{2}$ despite the enormously strong temperature dependence of its absolute values (about 2 orders of magnitude in this temperature range). This observation is all the more remarkable since such a similarity is not present in the resistivity ($R_{xx}(\nu = \frac{1}{2}) \simeq 5 \times R_{xx}(\nu = \frac{3}{2})$). Also at $\nu = \frac{3}{4}$ a plateau develops at low temperatures but with a 2.2 times higher value compared to the halves. To appreciate this result one should know that a constant ratio in the range of 2 to 3 has been observed between $\nu = \frac{1}{4}$ and $\nu = \frac{1}{2}$ in the TEP of many different 2DEGs before ([7]).

Although it was not yet possible to observe the plateaus at $\nu = \frac{3}{4}$ and $\nu = \frac{1}{4}$ at the same time (because of the limit in the magnetic field for high density samples and a too short quantum lifetime to observe the $\frac{3}{4}$ -CF in lower density samples) we were able to measure both CFs in the same device (see Fig. 3). This could be done using different electron densities which were adjusted by persistent photoconductivity. At low densities ($n = 1.1 \times 10^{11} \text{ cm}^{-2}$), we find $S_{xx}(\nu = \frac{1}{4}) \simeq 2.4 \times S_{xx}(\nu = \frac{1}{2})$, the ratio slightly decreasing with increasing concentration. S_{xx} at $\nu = \frac{3}{4}$ for these densities does not show a clear plateau and is clearly smaller than the $\frac{1}{4}$ -plateau, indicating that no $\frac{3}{4}$ -CF state has yet formed. The relative magnitude of the $\nu = \frac{3}{4}$ peak increases with n . At higher densities ($n = 1.7 \times 10^{11} \text{ cm}^{-2}$), a plateau develops at $\nu = \frac{3}{4}$, its relative magnitude being $S_{xx}(\nu = \frac{3}{4}) \simeq 2.2 \times S_{xx}(\nu = \frac{1}{2})$ and remaining constant when the electron concentration is increased further. This is the same value as the one we obtain for $\nu = \frac{1}{4}$ when extrapolating the lower density data to this electron density.

The temperature dependence of the TEP at $\nu = \frac{1}{2}$ is strictly proportional to the TEP at zero magnetic field over the whole temperature range where the absolute values are changing by 3 orders of magnitude (see Fig. 4), the proportionality factor being about 50 (at $n = 1.8 \times 10^{11} \text{ cm}^{-2}$). The temperature dependence follows roughly a T^3 -behaviour proving that the dominant process in TEP is phonon drag. No sign of diffusion TEP ($S_d \sim T$) is observed. The similarity in the temperature dependence of the TEP at $B = 0$ and at $\nu = \frac{1}{2}$ strongly suggests the interpretation of the $\frac{1}{2}$ -state as a CF in zero effective field.

Below 600 mK, the absolute magnitudes of the TEP at $\nu = \frac{3}{2}$ and $\nu = \frac{1}{2}$ are identical. Above this temperature, $S_{xx}(\nu = \frac{3}{2})$ starts to be smaller. This temperature coincides with the change of the shape of the magneto-TEP around $\nu = \frac{3}{2}$ from a plateau with surrounding peaks at low T to a 'conventional' peak at high T (marked by the arrow in Fig. 4). This transition might indicate the thermal destruction of the $\frac{3}{2}$ -CF. A similar behaviour is found for the $\frac{3}{4}$ -CF.

The phonon drag TEP S^g for electrons in zero magnetic field as well as for CFs in zero effective field is given by [7]:

$$S^g = -\frac{vLm^*}{eT\tau_{\text{fp}}} = -\rho^{\text{ph}} \frac{nevL}{T}, \quad (1)$$

where v is the sound velocity in the GaAs substrate, L the phonon mean free path, m^* the effective mass of the electrons, τ_{fp} the scattering time between the 3-dimensional phonons and the 2D electrons (CFs), and $\rho^{\text{ph}} = m^*/ne^2\tau_{\text{fp}}$ is the resistivity due to electron-phonon scattering. Thus, TEP is a direct measure for the product of the mass of a CF and the CF-phonon scattering rate $m^*\tau_{\text{fp}}^{-1}$.

Applying this result to the experimental findings we obtain that it is the product of the mass of a CF and the CF-phonon scattering rate $m^*\tau_{\text{fp}}^{-1}$ which is the same at $\nu = \frac{1}{2}$ and $\frac{3}{2}$ and has a 2.4 times higher value at $\frac{1}{4}$ and $\frac{3}{4}$. The strong enhancement of the TEP of CFs as compared to the zero field value S_0^g , can partly be explained as being the consequence of the enhanced effective mass between CFs and electrons ($m_{\text{ef}}^* \sim 10 \times m^*$ for $\nu = \frac{1}{2}$ [3, 4]). The remaining factor therefore has to come from an enhanced CF-phonon coupling.

However, a direct application of the CF effective mass obtained by Shubnikov-de Haas measurements to the TEP bears a fundamental difficulty. A SdH-analysis makes use of the quantum oscillations which inevitably fade away as $\nu = \frac{1}{2}$ is approached, while TEP-measurements are sensitive to m_{ef}^* directly at $\nu = \frac{1}{2}$ (essentially everywhere). The possibility of a diverging effective mass at $\nu = \frac{1}{2}$ gained a lot of interest and the observation of an enhancement of m_{ef}^* towards $\nu = \frac{1}{2}$ has been reported in SdH-studies of the resistivity [3]. In contrast, the TEP at $\nu = \frac{1}{2}$ does not show a diverging m_{ef}^* at $\nu = \frac{1}{2}$ but only a smooth but clear maximum is observed in S_{xx} . This peak becomes more pronounced with decreasing temperature and increasing electron density (see Figs. 1 and 3). The position of $\nu = \frac{1}{2}$ could always be obtained directly from this peak. This again differs from resistivity where there is only a minimum-like, smooth background. These results propose a slightly enhanced but finite effective mass of the CFs at $\nu = \frac{1}{2}$ compared to filling factors away from $\frac{1}{2}$.

In summary we have shown the universality of the thermopower at filling factors $\nu = q/2m$ with an identical behaviour for the same denominator. We attributed this as being due to an identical CF-phonon interaction for each CF family $2m$. Comparison with zero field data show that CFs behave as particles in zero effective field with enhanced mass and electron-phonon scattering rate.

References

- [1] J.K. Jain, Adv. Phys. **41** (1992) 105.
- [2] B.I. Halperin, P.A. Lee, and N. Read, Phys. Rev. **B47** (1993) 7312.
- [3] R.R. Du, H.L. Stormer, D.C. Tsui, A.S. Yeh, L.N. Pfeiffer, and K.W. West, Phys. Rev. Lett. **73** (1994) 3274, and references therein.

[4] D.R. Leadley, R.J. Nicholas, C.T. Foxon, and J.J. Harris, Phys. Rev. Lett. **72** (1994) 1906.

[5] R.L. Willett, R.R. Ruel, K.W. West, and L.N. Pfeiffer, Phys. Rev. Lett. **71** (1993) 3846.

[6] X. Ying, V. Bayot, M.B. Santos, and M. Shayegan, Phys. Rev. **B50** (1994) 4969.

[7] B. Tieke, R. Fletcher, S.A.J. Wiegers, U. Zeitler, J.C. Maan, C.T. Foxon, and J.J. Harris, Physica B in print (1995); U. Zeitler, B. Tieke, B. Tieke, S.A.J. Wiegers, J.C. Maan, R. Fletcher, V.I. Fal'ko, C.T. Foxon, and J.J. Harris, to be published in World Scientific (Proceedings of the 11th International Conference on High Magnetic Fields in Semiconductor Physics (SEMIAG-94), Cambridge, MA, USA, 1994).

[8] U. Zeitler, J.C. Maan, P. Wyder, R. Fletcher, C.T. Foxon, and J.J. Harris, Phys. Rev. B **47** (1993) 16008.

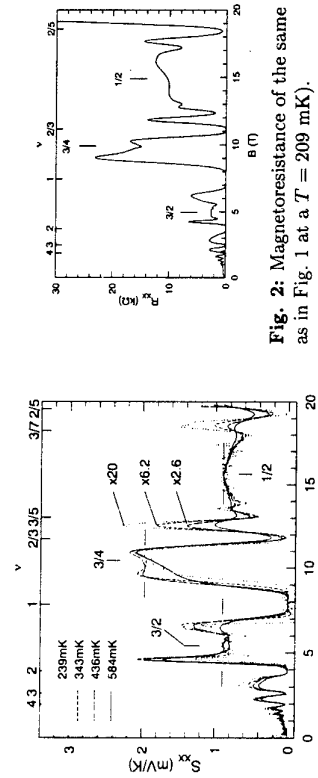


Figure 1: The magneto-TEP, renormalized by its value at $\nu = \frac{1}{2}$, for different temperatures.

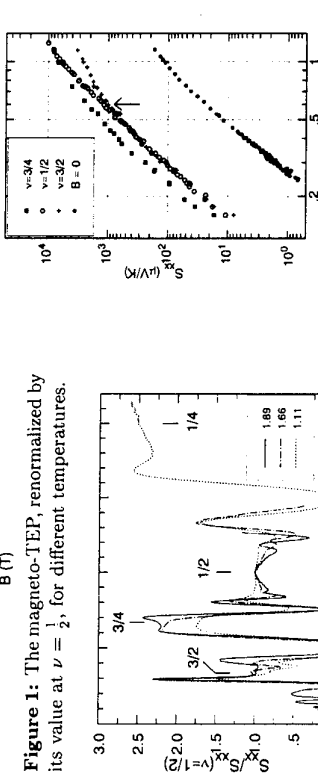


Figure 2: Magnetoresistance of the same 2DEG as in Fig. 1 at a $T = 209$ mK.

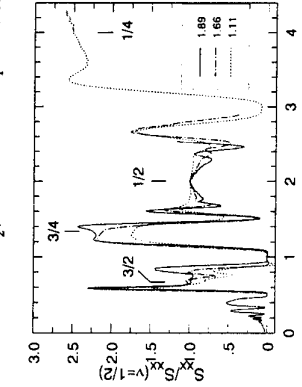


Figure 3: The renormalized TEP at 440 mK for different electron densities.

Figure 4: The temperature dependence of the TEP for $\nu = \frac{1}{2}$, $\nu = \frac{3}{2}$, and $\nu = \frac{1}{4}$ compared to the zero field TEP.

Quantum Interference in 2-d Atomic-Scale Structures

M. F. Crommie ^a, C. P. Lutz ^b, D. M. Eigler ^b, and E. J. Heller ^c

^a Department of Physics, Boston University, Boston, MA 02215
^b IBM Research Division, Almaden Research Center, 650 Harry Road, San Jose, California 95120-6099

^c Department of Physics and Harvard-Smithsonian Observatory, 17 Oxford St., Harvard University, Cambridge, MA 02138

Abstract

Electrons occupying surface states on the close-packed faces of the noble metals form a two-dimensional (2-d) electron gas that is accessible to the scanning tunneling microscope (STM). Using a cryogenic STM, we have observed quantum mechanical interference patterns arising from 2-d electrons on the surface of Cu. These interference patterns can be artificially controlled by arranging individual Fe atoms into "quantum corrals" on the Cu surface. Quantum corrals behave qualitatively like 2-d hard-wall boxes, but a quantitative understanding is obtained within a multiple scattering formalism. The scattering here is characterized by a complex phase shift which can be extracted from the electronic density pattern near a quantum corral.

1. Introduction

The behavior of low dimensional electrons has been studied in a variety of systems [1]. Semiconductor heterostructures are perhaps the most extensively explored [2]. Local, real-space studies, however, are elusive in this system because the electrons move in a subsurface plane. Here we discuss measurements performed on a different 2-d electronic system that is ideally suited to real-space imaging: noble metal surface states.

Surface states exist on the close-packed faces of the noble metals because of a gap along the Γ -L direction of their bulk band structure [3-4]. The 2-d nearly-free electron gas formed by this surface state can be directly imaged with a scanning tunneling microscope (STM) [5-7]. Here we show how the STM can be used to image the quantum mechanical interference patterns that arise due to the scattering of surface electrons off artificial structures fabricated from individual atoms ("quantum corrals"). The electronic behavior of quantum corrals can be qualitatively explained by modeling them as simple hard-wall "electron boxes" [8]. To gain a quantitative understanding, however, one must turn to multiple-scattering theory [9]. Here the principal physical quantity is the phase shift in electronic amplitude acquired when an electron scatters off a single adsorbate. Quantum corrals provide a new method for spectroscopically probing this quantity, and open new possibilities for studying the interaction of a 2-d electron gas with microscopic scattering objects.

2. Results and Discussion

The experiments were performed using an STM contained in ultra-high vacuum and cooled to 4K [10]. The single-crystal Cu sample was cleaned through repeated cycles of Ar-ion sputtering and annealing. The cooled Cu sample was dosed with Fe atoms using a calibrated electron-beam evaporator.

Figure 1 shows an STM image of a small region of the Cu(111) surface before deposition of Fe. A raised plateau can be seen surrounded by sharp step-edges (much larger terraces having widths up to 1000 Å were also seen on the Cu surface). Interference patterns can be seen covering the surface. These ripples are not due to lattice corrugation (which cannot be seen in this image),

but are rather manifestations of quantum mechanical interference in the 2-d electron gas formed by the Cu surface state. The interference rises from scattering of the surface state electrons by step-edges [6, 7]. This image shows the local density of states (LDOS) of the Cu surface at EF, where the wavelength of a free surface state electron is $\sim 30\text{ \AA}$ [6].

Figure 2 shows an STM image of the Cu(111) surface after depositing ~ 0.005 monolayer coverage of Fe. This image is a closeup of a single Fe atom resting on the Cu surface. The waves surrounding the Fe atom reflect the disturbance in surface state LDOS induced by this impurity. The Fe atom can thus be "seen" scattering the surface state electrons at EF [8].

Using the tip of the STM, it is possible to move Fe atoms into predetermined arrangements [10]. By moving Fe atoms into proximity with one another, one can observe the quantum interference pattern that forms as 2-d electrons scatter from one impurity atom to another. Figure 3 shows a ring of 20 Fe atoms, placed loosely in a circle having a diameter of 177 \AA . The complex interference pattern seen in the vicinity of this open structure reflects the multiple scattering behavior of 2-d surface state electrons at EF.

Reducing the interatomic distance of the Fe atoms down below the wavelength of a free surface state electron causes the atoms to behave more like a continuous scattering boundary in two dimensions. Figure 4 shows the process of extending a boundary of tightly spaced Fe atoms into a ring having a radius identical to the looser ring shown in Figure 3. Although the radii of the rings in Figs. 3 and 4 are identical, there is a strong qualitative difference between the observed interference patterns. The patterns in Fig. 4 behave much more as one might expect for a continuous, hard wall. A distinct change occurs between the patterns shown in Figs. 4 (b) and 4 (c), as the "wall" is closed off and forms a continuous, closed scattering boundary.

The STM can also be used to measure the energy dependence of the LDOS of the surface [11]. This is done by recording the position and bias dependence of the differential conductivity of the STM tunnel junction, $dI/dV(r, V)$. Changes in $dI/dV(r, V)$ correspond to changes in the surface LDOS($r, E_F + eV$) (dI/dV is also influenced by the LDOS of the STM tip). The solid line in Figure 5 shows the results of measuring dI/dV while holding the STM tip stationary over the center of the 60 atom ring shown in Figure 4(c). Peaks in dI/dV mark the location of seven resonances in the LDOS at the center of the 60 atom ring.

These resonances can be qualitatively explained by modeling the tight Fe atom boundary as a hard-wall barrier that the surface state electrons cannot pass [8]. The problem is then reduced to finding the eigenstates of a particle confined to a circular box. Here "the particle" is a surface state electron (of nominal effective mass) and the walls of the box are defined by the Fe adatoms. The eigenstates of a particle confined to a 2-d round box are [12]

$$\psi_{n,l}(\rho, \phi) \propto J_l(k_n \rho) e^{il\phi}, \quad (1)$$

where $k_n l = \frac{\pi n}{r}$ and the eigenenergies are

$$E_{n,l} = \frac{\hbar^2 k_n^2}{2m *}. \quad (2)$$

l is the angular momentum quantum number of an electron in the box, J_l is the l th order Bessel function, and $z_{n,l}$ is the n th zero crossing of $J_l(z)$. The eigenenergies of a round box having the same dimensions as the 60 atom ring are shown as vertical lines in Figure 5. The particle-in-a-box eigenenergies lie quite close to the observed resonances at the center of the ring. Only $l=0$ eigenstates are shown here, since all non-zero angular momentum states have a node at the origin and shouldn't contribute to the tunnel current.

Broadening of the spectroscopic peaks shows that the quantum corrals are leaky structures. In order to understand the broadening mechanism, and also to quantitatively explain LDOS patterns around more complex quantum corrals, we turn to multiple-scattering theory [9]. Multiple scattering theory takes into account the multiple reflections of an electron in the presence of many

scatters and treats motion of an electron outside a quantum corral on an equal footing with motion inside a corral. It is also possible to take into account "absorptive" behavior at the scattering sites. In the long wavelength limit the only physically adjustable parameter is the s-wave phase shift, η_0 , for a 2-d electron scattering off an atom on the surface. If the scattering is elastic, then η_0 is real, but if there are inelastic or absorptive components to the scattering, then η_0 is complex.

The LDOS in the vicinity of a quantum corral is calculated by treating the STM tip as a Green's function point source of electronic amplitude. The electronic amplitude arriving at the site of an adatom from the tip can be written as

$$a_T(r_j) = \sqrt{\frac{2}{\pi k_0 r}} e^{ikr_j - \frac{\pi}{4}} \quad (3)$$

where r_j is the distance from the tip to the j th adatom. This causes a scattered wave from the adatom

$$a_T(r_j) a(r) = a_T(r_j) \sqrt{\frac{2}{\pi k_0}} \frac{e^{2i\eta_0} - 1}{2i} \frac{e^{ik_0 r}}{\sqrt{r}} \quad (4)$$

The surface LDOS is obtained by taking into account the various possible scattering paths an electron can make before returning to the tip. This results in an interference term to the LDOS [9]:

$$\Delta \text{LDOS} \propto \text{Re}[\tilde{a}_T \cdot (1 - \mathbf{A})^{-1} \cdot \tilde{a}] \quad (5)$$

where $a_T(r_i)$, $a_i = a(r_i)$, and $\mathbf{A}_{ij} = a(\vec{r}_i - \vec{r}_j)$. For N scatterers \mathbf{A} is an $N \times N$ matrix. \tilde{a}_T and \tilde{a} change as the LDOS is calculated at each new point in space, but \mathbf{A} remains constant. We find that the quantum corral images are best described by Eq. (5) in the limit that $\text{Im}[\eta_0] \rightarrow \infty$ [9]. We call this the "black dot" limit, since all in-coming s-wave amplitude is absorbed by the scatterer, which consequently emits no outgoing s-wave amplitude (a *plane* wave incident upon a black dot scatterer still induces a scattered wave). The broken line in Figure 5 shows a multiple scattering calculation of the energy dependence of the LDOS at the center of the 60 atom quantum corral. Agreement with spectroscopic data is obtained over a wide energy range under the black dot assumption. The linewidth of the spectral peaks is thus explained within the multiple scattering framework.

The success of the black dot assumption shows that the Fe quantum corrals are rather "quiet" chambers. Only 25% of the amplitude incident on their walls is reflected, while 50% is absorbed [9]. We believe that the absorptive channel is due to scattering into bulk states. One result of this analysis is that we learn that greater electron confinement will not be achieved by simply packing Fe atoms more densely along the borders of the quantum corrals. The borders, themselves, act as "absorbers", and so greater confinement will likely come only from new surface state/adsorbate systems that do not couple surface state electrons so strongly to the bulk.

3. Conclusions

We show that it is possible to observe the quantum interference patterns that arise from 2-d electrons scattering off of artificially fabricated atomic-scale structures. These interference patterns are reminiscent of particle-in-a-box eigenfunctions, but more importantly they allow one to extract fundamental information, such as the s-wave scattering phase shift from STM images. A few possible future research directions are the study of 2-d electronic effects in a magnetic field, the

study of different varieties of adsorbed molecules, and investigation of more complex artificial structures.

4. References

- * Corresponding author.
- [1] T. Ando, A. B. Fowler and F. Stern, Rev. Mod. Phys. **54**, 437 (1982).
- [2] *Electronic Properties of Two-Dimensional Systems, Proceedings of the 10th International Conference on EP2DS, Newport, RI, 1993*, edited by B. McCombe and A. Nurmiikko (Elsevier, Amsterdam, 1994).
- [3] W. Shockley, Phys. Rev. **56**, 317 (1939).
- [4] F. Forstmann, Z. Physik **235**, 69 (1970).
- [5] M. P. Everson, R. C. Jaklevic and W. Shen, J. Vac. Sci. Technol. A **8**, 3662 (1990).
- [6] M. F. Crommie, C. P. Lutz and D. M. Eigler, Nature **363**, 524 (1993).
- [7] Y. Hasegawa and P. Avouris, Phys. Rev. Lett. **71**, 1071 (1993).
- [8] M. F. Crommie, C. P. Lutz and D. M. Eigler, Science **262**, 218 (1993).
- [9] E. J. Heller, M. F. Crommie, C. P. Lutz and D. M. Eigler, Nature **369**, 464 (1994).
- [10] D. M. Eigler and E. K. Schweizer, Nature **344**, 524 (1990).
- [11] *Scanning Tunneling Microscopy*, edited by J. A. Stroscio and W. J. Kaiser (Academic Press, Inc., San Diego, 1993).
- [12] R. Haberman, *Elementary Applied Partial Differential Equations* (Prentice-Hall, Inc., Englewood Cliffs, 1983).

Captions --

Fig. 1. $250\text{\AA} \times 250\text{\AA}$ constant-current STM image of the Cu(111) surface in the region of a raised plateau ($V=0.1$ volt, $I=1\text{nA}$). Visible step-edges have a height of either one or two atomic layers. Interference patterns are due to surface state electrons scattering off of step edges.

Fig. 2. $130\text{\AA} \times 130\text{\AA}$ constant current STM image of an isolated Fe atom on the Cu(111) surface ($V=0.02$ volt, $I=1.0\text{nA}$). Apparent height of adatom is 0.9\AA . Concentric circles reveal the effect of scattered surface state electrons.

Fig. 3. Constant-current STM image of 20Fe atoms arranged loosely at the boundary of a 177.4\AA diameter circle on Cu(111) ($V=0.01$ volt, $I=1\text{nA}$).

Fig. 4. Process of constructing 177.4\AA diameter ring of Fe atoms on Cu(111) (constant-current images, $V=0.01$ volt, $I=1\text{nA}$). Evolution of quantum interference pattern can be seen as structure is closed.

Fig. 5. Solid curve: dI/dV spectrum taken with the STM tip held stationary over the center of the 177.4\AA Fe ring seen in Fig. 4(c). The experimental curve has had a smooth background removed. Broken curve: results of multiple-scattering calculation performed in the "black dot" limit (the offset and normalization of the theoretical curve are treated here as free parameters). Vertical lines: theoretical eigenenergies for $l=0$ states of a round, 2-d hard-wall box having the same dimensions as the 177.4\AA Fe ring.

Universal Conductance Fluctuations in Carbon Nanotubes

L. Langer¹, V. Bayot¹, L. Stockman², E. Griveil¹, J.-P. Heremans³, C.H. Olk³, C. Van Haesendonck², Y. Bruynseraede², J.-P. Issi¹
¹Unité PCPM, Université Catholique de Louvain, I Place Croix du Sud, B-1348 Louvain-la-Neuve, Belgium
²Laboratorium voor Vaste Stof-Fysica en Magnete, Katholieke Universiteit Leuven, Celestijnenlaan 200 D, B-3000 Leuven, Belgium
³Physics Department, General Motors Research, Warren, MI 48090

Abstract

Using scanning-tunneling-microscopy lithography, electrical contacts were attached to an individual carbon nanotube of 20 nm diameter. Electrical conductance measurements have been performed on this nanotube down to very low temperature, T_c , and with a magnetic field, B , applied perpendicular to the tube axis. The conductance exhibits a $\ln T$ dependence followed by a saturation below a critical temperature $T_c \approx 0.3\text{K}$ at $B=0$. At low temperature, the magnetoconductance shows aperiodic fluctuations superimposed to a positive background. The amplitude of the fluctuations increases with decreasing T as a weak power law down to a critical temperature $T_c^* \approx 0.3\text{K}$ below which it saturates. While T_c increases with increasing B , T_c^* is found magnetic field independent. We show that the data find a global and coherent interpretation in terms of two dimensional weak localization and universal conductance fluctuations for mesoscopic systems. The observed dimensionality of the electronic system is discussed in terms of the peculiar structure of carbon nanotubes.

1. Introduction

It is now well established that in weakly disordered systems, the "quantum nature" of electrons is reflected in the observation of "quantum transport" phenomena which are not predicted by classical approaches [1,2]. While quantitative descriptions of these phenomena are based on scaling arguments [1] and the Landauer formalism [3], more intuitive approaches show that most of these effects can be understood through quantum interferences of electron wavefunctions within domains where their phase coherence is maintained [4]. One of these effects is the weak localization (WL), which occurs in weakly disordered systems ($k_F l > 1$, where k_F is the Fermi wave vector and l is the electron mean-free-path) when elastic scattering of carriers by lattice defects is more frequent than inelastic scattering processes due to carrier-phonon, carrier-carrier and carrier-magnetic impurities interactions. As long as scattering is elastic, time-reversal symmetry is maintained and electron partial wave-functions interfere constructively in the backward direction of propagation, leading to an enhanced backscattering probability, and hence to a reduced conductance. Both inelastic scattering processes and magnetic field, B , suppress time-reversal symmetry and, as a result, WL is observed at low temperature (T) and is progressively suppressed by an increasing B . The WL occurs whatever the dimensionality of the system, but is much more pronounced for two-dimensional (2D) than for three-dimensional (3D) systems [1]. For 2D systems, the two main features are a logarithmic T -dependence of the conductance, G , and a positive magnetoconductance MC defined by $[G(B)-G(B=0)]/G(B=0)$. The important characteristic length in the framework of WL is the electron phase coherence length L_ϕ which is limited by $L_\phi = (D_\phi T)^{1/2}$ or $L_\phi = (D_\phi \tau_s)^{1/2}$, when $L_\phi \ll L_m$ or $L_m \ll L_\phi$, respectively. D_ϕ , τ_s , and T are the diffusion constant, the magnetic scattering time, and the inelastic scattering time due to electron-phonon or electron-electron interaction, respectively. $\tau_{in} \propto T^p$, where p depends on scattering mechanism, dimensionality, etc.

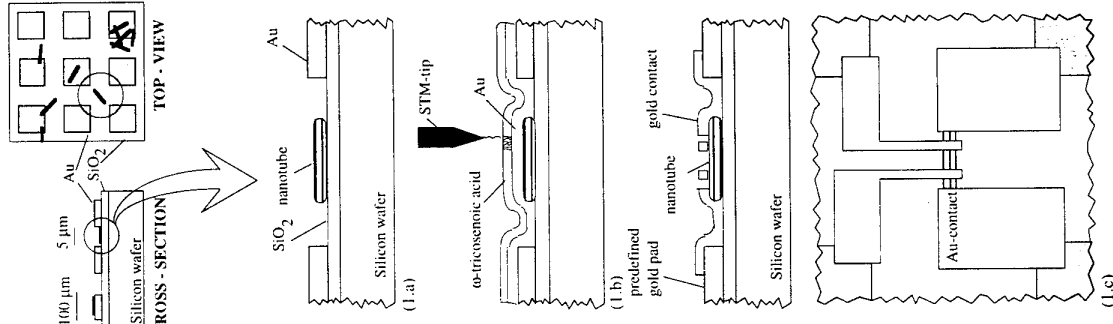


Figure 1 : Schematic representation of the STM-lithography technique used to make electrical contacts on a carbon nanotube.

Another type of quantum transport effect of a surprisingly universal character was observed in mesoscopic weakly disordered metals [5,6] and semiconductors [7,8] of various dimensionalities. In such systems, where the size of the sample, L , is smaller or comparable to both L_ϕ and the thermal scattering length $L_T = (D/k_B T)^{1/2}$, elastic scattering of electron wave functions generates an interference pattern which gives rise to a sample-specific, time-independent conductance [9]. The interference pattern, and hence the conductance, can be modified by either applying a magnetic field or by changing the electron energy in order to tune the phase or the wavelength of the electrons respectively [5-8]. The resulting phenomenon is called "universal conductance fluctuations" (UCFs), since the fluctuations have an average "universal" rms-amplitude $\Delta G \approx e^2/h$. When the relevant length scale, L_ϕ or L_T , is smaller than L , the amplitude of the observed fluctuations decreases due to self-averaging of UCFs in phase-coherent subunits. When the relevant length scale decreases with temperature, the amplitude of the fluctuations decreases as a weak power law, $T^{-\alpha}$ where α depends on dimensionality and limiting diffusion length, L_ϕ or L_T [9].

With the discovery by Iijima [10] of carbon nanotubes (CN), a new class of materials with respect to dimensionality has been introduced. These tubes are made of coaxial graphitic cylinders. Each cylinder can be visualized as the conformal mapping of a 2D honeycomb lattice onto its surface. This new quasi-1D structure built from rolled up 2D graphene sheets can either be a metal, or a semiconductor, depending on diameter and degree of helicity [11]. Also, the extremely small size of CNs combined with their hybrid dimensionality may induce specific quantum interference effects. Experimental observation of such effects is naturally very delicate because of the very small size of individual nanotubes.

In the first part of this work we will describe the experimental method that we developed to realize electrical contacts on very small nanotubes[12], while in the second part we will report on the electrical conductance and magnetoconductance measurements performed on an individual CN with a magnetic field applied perpendicular to tube axis. The data obtained give evidence for the effects of 2D weak localization and UCFs in this particular structure of hybrid dimensionality[13].

2. Experimental

Using ethanol in an ultrasonic bath, we disperse CN on an oxidized Si-wafer on which we had previously deposited an array of predefined gold pads using electron-beam lithography (Fig. 1.a). After thermal evaporation of a 25 nm thick gold film in helium atmosphere at reduced pressure in order to obtain a smooth film surface, we deposit Langmuir-Blodgett layers of a negative electron-beam resist (o-tricresylic acid) on top of the wafer. A scanning-tunneling microscope (STM) is then used to locate the position of a nanotube between the predefined gold pads at tunnelling voltages below 5 V. Then, the bias voltage is increased in order to locally expose and to polymerize the LB resist layers (Fig. 1.b) from both ends of the nanotube towards the contact pads. The LB-film act as a negative resist and the unexposed parts of the resist layer is removed by ethanol. Finally, the gold areas that are no longer protected by the LB-film were multiwalled carbon nanotube (Fig. 1.c) of 20 nm diameter as determined by atomic force microscopy (AFM)[14]. AC electrical conductance measurements were performed with a lock-in amplifier down to 20 mK in a magnetic field perpendicular to the tube axis up to 14 T.

3. Results and discussion

In figure 2 we present the conductance as a function of temperature for our sample at various magnetic fields. The conductance shows a $\ln T$ dependence followed by a saturation at low temperature. As discussed in more details later in the paper, the turnover in the temperature dependence of the conductance occurs at a critical temperature, T_c , which shifts to higher temperature in the presence of a magnetic field. A $\ln T$ dependence can either originate from weak localization [15] or electron-electron interactions [16] for 2D systems, or from a Kondo anomaly due to magnetic impurities[17]. A Kondo anomaly is most unlikely to be responsible for the effect since it has never been observed in graphitic materials that contain detectable amounts (≈ 100 ppm) of magnetic impurities [18]. Moreover, spectrographic analysis using DC-arc with a 10 ppm detection limit revealed no magnetic impurities in our CN material [19].

Figure 2 : Electrical conductance as a function of temperature at the indicated magnetic fields. The dashed line separates the contributions to the magnetoconductance due to both Landau levels (LL) and weak localization (WL).

In the presence of electron-electron interactions the relevant length scale is L/\hbar [2]. In a 2D mesoscopic sample the conductance is expected to follow a $\ln T$ dependence and to saturate when $L \ll L_T$. Electron-electron interactions give rise to a negative MC, while L_T , and hence the onset of the saturation is expected to be independent of B . Thus, our data in Figure 2 rule out the possibility of electron-electron interactions as they clearly show an opposite behavior: a positive MC and a saturation of the conductance occurring at higher temperature for higher B .

In the framework of the weak-localization theory the saturation of the conductance at low temperature may have two different origins. First, the scaling theory predicts that the conductance

saturates at low temperature when $L \ll L_\phi$. This corresponds to the "mesoscopic" regime. Second, in the "macroscopic" regime, i.e. when $L_\phi \ll L$, the conductance saturates at low temperature when L_ϕ is temperature independent ($L \ll L_{in}$). In order to discriminate between the two regimes, we consider the effect of B on the temperature dependence of the conductance. In the presence of a sufficiently large magnetic field, $L_H=(\hbar/eB)/2$ becomes the new limiting length scale for the weak-localization and the conductance saturates when $L_\phi > L_H$. T_c marks the critical temperature that separates the $\ln T$ dependence from the saturation and corresponds to either $L_\phi \approx L_{in}$ at low B or $L_\phi = L_{in} \approx L_H$ at high enough B .

Our data show that T_c increases with increasing magnetic field. This implies that at $B=14T$ and $T=T_c=1.5K$, $L_{in}=L_H=7$ nm. In the absence of magnetic field, and assuming $p=1$ in agreement with previous experiments[18], we finally obtain an estimation for $L_3=L_{in} \approx 20$ nm at $T=T_c=0.3K$. Since L_ϕ is always much smaller than L , we conclude that our sample is in the macroscopic regime for weak localization.

For fitting purposes, the conductance in the macroscopic regime for the 2D weak localization can be expressed as:[4]

$$G = \eta + \zeta \ln(L_H^{-2} + L_s^{-2} + L_m^{-2}) \quad (1)$$

where η and ζ are adjustable parameters. Since L_s and L_H are temperature independent and $L_m \propto T^{1/2}$, equation (1) can be reduced to :

$$G \approx \alpha + \beta \ln(T_c + T) \quad (2)$$

which α , β and T_c are the new fitting parameters. Fig. 1 shows that relation (2) (solid line) provides a good fit to the data in the whole temperature range investigated. Globally, the above discussion clearly shows the consistency of the interpretation of our results in terms of 2D WL. The particular cylindrical geometry of CN implies that, like in 2D graphite, the electron may have a diffusive motion on the grafithic cylinder without reaching the nanotube is comparable to L_ϕ .

The WL theory predicts that when $T > T_c$, the conductance is independent of B . The data in Fig. 2 show that there is an additional contribution to the MC of CN which is T -independent up to the highest temperature investigated. Ajiki and Ando [20] have predicted the formation of Landau states when a magnetic field is applied perpendicular to the nanotube axis. In particular, a Landau level should form at the crossing of the valence and conduction bands, thereby increasing the density of states at the Fermi level, and hence increasing the conductance. The resulting positive MC is expected to be temperature independent at low temperature as long as $k_B T$ remains smaller than the width of the Landau level. Previous results obtained on a CN-bundle [21] revealed a behavior consistent with these predictions. In the present work, we attribute the additional T -independent positive MC to the same mechanism. Both 2D WL and "Landau level" (LL) contributions to the MC can be separated as illustrated in Fig. 2 at $B=7$ T.

Representative MC data are shown in Figure 3. At low temperature a reproducible, aperiodic structure appears in the MC, which we will refer to as conductance fluctuations, CFs. The positions of peaks and valleys with respect to magnetic field are weakly temperature dependent. Figure 4 shows the temperature dependence of the peak-to-peak amplitude of the CFs (ΔG) for three selected peaks (see Fig. 3). ΔG is constant and of the order of 0.03 e^2/h up to 0.3 K, and then decreases slowly with increasing temperature as a weak power law. It is also worth noting that the turnover in the temperature dependence of the CFs occurs at a critical temperature $T_c^* \approx 0.3K$ [22] which, contrary to T_c discussed above, is independent of the magnetic field. At first sight this behavior seems consistent with the theory of UCFs [23-24].

Observation of UCFs requires that the sample length L must be smaller or comparable to L_ϕ . In general, the complexity of data analysis comes from the existence of two relevant T -dependent length scales: L_ϕ and L_T . The shortest of these two lengths governs the size of the fluctuations and the turnover in the temperature. In the present case, and unlike what is observed in most metals, we showed above that $L_\phi \ll L_T$. The limiting length scale is therefore L_ϕ for both 2D WL and CFs, consistent with $T_c(B=0)=T_c^*$. Contrary to the weak localization effect

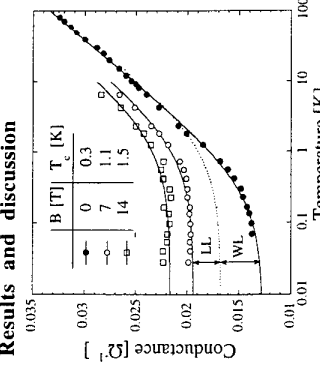


Figure 2 : Electrical conductance as a function of temperature at the indicated magnetic fields. The dashed line separates the contributions to the magnetoconductance due to both Landau levels (LL) and weak localization (WL).

In a 2D mesoscopic sample the conductance is expected to follow a $\ln T$ dependence and to saturate when $L \ll L_T$. Electron-electron interactions give rise to a negative MC, while L_T , and hence the onset of the saturation is expected to be independent of B . Thus, our data in Figure 2 rule out the possibility of electron-electron interactions as they clearly show an opposite behavior: a positive MC and a saturation of the conductance occurring at higher temperature for higher B .

In the framework of the weak-localization theory the saturation of the conductance at low temperature may have two different origins. First, the scaling theory predicts that the conductance

where L_H becomes the relevant cutoff length at high magnetic field, UCFs remain governed by L_ϕ which is magnetic field independent. This is consistent with the observed B -independent in our experiments.

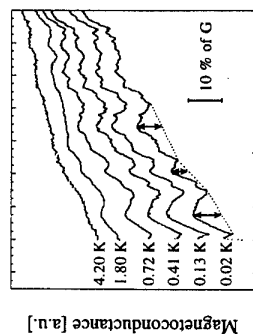


Figure 3 : Magnetic field dependence of the magnetoconductance at the indicated temperatures.

We now turn to the temperature dependence of the CFs' amplitude. In our case, $L_\phi < C < L$, where C is the circumference of the CN. The sample length and circumference can be divided into $N = L/L_\phi$ and $M = C/L_\phi$ phase coherent subunits. The CN can then be treated as M parallel and N series classical resistors with fluctuations of order e^2/h occurring in each one[9]. The rms-amplitude of the CFs is then given by :

$$\text{rms}[\Delta G] \approx \frac{e^2}{h} M^{1/2} N^{-3/2} = \frac{e^2}{h} \left(\frac{C}{L_\phi} \right)^{\frac{3}{2}} \left(\frac{L_\phi}{L} \right)^{\frac{3}{2}}$$

Using $C=20\pi$ nm, $L=800$ nm and $L_\phi=20$ nm for $T < T_c^*$, we find $\text{rms}[\Delta G] \approx 7 \cdot 10^{-3}$ e^2/h which is in good agreement with the observed value of $\text{rms}[\Delta G] \approx \Delta G/3 \approx 10^{-2}$ e^2/h .

$$\text{rms}[\Delta G] \propto L_\phi \propto T^{-1/2}$$

Above T_c^* ,

which is effectively observed over a decade in temperature.
Globally, we find that the observed conductance fluctuations can be interpreted in terms of UCFs for mesoscopic 2D systems. It is worth emphasizing that for smaller CN, C would eventually be smaller than L_ϕ resulting in a 2D-1D crossover for UCFs.

4. Conclusion

As foreseen on base of the peculiar structure of carbon nanotubes, conductance data obtained on a single multiwalled nanotube reveal specific quantum transport phenomena. Despite of the extremely small diameter of the nanotube, the cylindrical structure of the honeycomb lattice give rise to a 2D electron system for the weak localization effect. This fact has been evidenced by the $\ln T$ dependence of the conductance and the positive magnetoresistance. At low temperature and at $B=0$, the cutoff length is $L_\phi=L_s$ due to magnetic scattering, while L_H becomes the new cutoff length at high magnetic field. Consequently, T_c which marks the onset of the saturation of the conductance, increases with increasing magnetic field.

L_ϕ is also the relevant cutoff length for the observed conductance fluctuations in magnetic field. The amplitude of these CFs is constant ($\Delta G=0.03 \cdot e^2/h$) up to a magnetic field independent critical temperature $T_c^* \approx 0.3$ K and then decreases slowly with T as a weak power law $T^{-1/2}$. Both the amplitude and the T dependence of the CFs are consistent with the theory of universal conductance fluctuations applied to the particular cylindrical structure of our nanotube.

5. Acknowledgements

We are much indebted to J.-C. Charlier, X. Gonze, L. Filippozzi and L. Piraux for fruitful discussions and suggestions. This work has been financially supported by the Belgian Concerted Actions and Inter-University Attraction Poles programs. V.B. is a Senior Research Assistant at the National Fund for Scientific Research (Belgium).

6. References

- [1] P.A. Lee, T.V. Ramakrishnan, Rev. Mod. Phys. **57**, 287 (1985)
- [2] S. Washburn, R.A. Webb, Advances in Physics **35**, 375 (1986)
- [3] Landauer, Philos. Mag. **21**, 863 (1970)
- [4] G. Bergmann, Phys. Rep. **107**, 1 (1984)
- [5] C.P. Umbach, S. Washburn, R.B. Laibowitz, R.A. Webb, Phys. Rev. B **30**, 4048 (1984)
- [6] S. Washburn, C.P. Umbach, R.B. Laibowitz, R.A. Webb, Phys. Rev. B **32**, 4789 (1985)
- [7] I.C. Licini, D.J. Bishop, M.A. Kastner, J. Meingailis, Phys. Rev. Lett. **55**, 2987 (1985)
- [8] W.J. Skocpol, P.M. Mankiewich, R.E. Howard, L.D. Jackel, D.M. Tennant, A.D. Stone, Phys. Rev. Lett. **56**, 2865 (1986)
- [9] P.A. Lee, A.D. Stone, H. Fukuyama, Phys. Rev. B **35**, 1039 (1987)
- [10] S. Iijima, Nature **354**, 56 (1991)
- [11] J.C. Charlier, J.P. Michenaud, Phys. Rev. Lett. **70**, 1858 (1993), C.T. White, D.H. Robertson, J.W. Mintemire, Phys. Rev. B **47**, 5485 (1993), R. Saito, G. Dresselhaus, M.S. Dresselhaus, J. Appl. Phys. **73**, 494 (1993)
- [12] L. Langer, L. Stockman, J.P. Heremans, V. Bayot, C.H. Olk, C. Van Haesendonck, Y. Bruynseraede, J.P. Issi, Synthetic metals, **70**, 1393 (1995)
- [13] L. Langer, V. Bayot, L. Stockman, E. Grivete, J.P. Heremans, C.H. Olk, C. Van Haesendonck, Y. Bruynseraede, J.P. Issi, submitted
- [14] The size of the features which can be resolved by the AFM is smaller than the diameter of thinnest nanotubes present in the CN material as determined by TEM [12].
- [15] E. Abrahams, P.W. Anderson, D.C. Licciardello, T.V. Ramakrishnan, Phys. Rev. Lett. **42**, 673 (1979)
- [16] B.I. Altshuler, A.G. Aronov, P.A. Lee, Phys. Rev. Lett. **44**, 1288 (1980)
- [17] F.J. Okihawa, H. Fukuyama, K. Yosida, J. Phys. Soc. Jpn. **52**, 1701 (1983)
- [18] V. Bayot, L. Piraux, J.-P. Michenaud, J.-P. Issi, Phys. Rev. B **40**, 3514 (1989)
- [19] J. Heremans, C.H. Olk, D.T. Morell, Phys. Rev. B **49**, 15122 (1994)
- [20] H. Ajiki, T. Ando, J. Phys. Soc. Jpn. **62**, 1255 (1993)
- [21] L. Langer, L. Stockman, J.P. Heremans, V. Bayot, C.H. Olk, C. Van Haesendonck, Y. Bruynseraede, J.P. Issi, Mater. Res. **9**, 927 (1994)
- [22] T_c^* is taken from the intersect of the $T^{-1/2}$ dependence and the saturation.
- [23] B.I. Altshuler, JETP Lett. **41**, 648 (1985)
- [24] P.A. Lee, A.D. Stone, Phys. Rev. Lett. **55**, 1622 (1985)

Nanofabrication with Proximal Probes

P. M. Campbell⁺, E. S. Snow[†], and P. J. McMarr^{*}
 + Naval Research Laboratory, Washington, DC
 *SFA Incorporated, Landover, MD

ABSTRACT

We report the fabrication of nanometer-scale Si structures using an atomic force microscope. A conducting AFM tip was used to write nanometer-scale oxide patterns by the local anodic oxidation of a passivated Si (100) surface. These oxide patterns were used as masks for selective etching of the silicon to form the completed structures. Side-gated Si field effect transistors with critical features as small as 30 nm have been fabricated by this method.

Proximal probes such as the scanning tunneling microscope (STM) and the atomic force microscope (AFM), originally developed to image surfaces with atomic precision, have recently been used to modify surfaces at the nanometer scale [1] and even to manipulate and position single atoms on a surface [2]. This suggests that proximal probes may be useful in the fabrication of nanometer-scale structures, with a precision that may exceed the limits of electron beam lithography and perhaps approach the ultimate limit of atom-by-atom control of the surface. However, the application of proximal probe-induced surface patterning to the fabrication of nanometer-scale devices has been slowed by irreproducibilities in the surface modifications, low write speeds, and the difficulty of transferring such fine surface patterns (in some cases only a single monolayer thick) into usable structures. This last problem arises because proximal probes by their nature create thin surface patterns which are often not sufficiently robust to withstand transfer into the substrate by etching or other standard processing techniques.

We have developed a simple and reliable proximal probe-based technique for the fabrication of nanometer-scale structures [3]. We start with a Si (100) surface with a native oxide layer. Immersion in a 10% aqueous solution of HF strips this native oxide layer and terminates all the Si surface bonds with a passivating hydride layer. Exposing this H-passivated surface to a negatively biased electrically conducting AFM tip in air generates a high local electric field which strips the hydride layer and anodically oxidizes the surface in the immediate vicinity of the tip. We use a conventional insulating AFM tip made conducting by depositing a 30 nm Ti layer. Write speeds are usually $1 - 10 \mu\text{m/sec}$, but can exceed 1 mm/sec . The local oxide patterns so generated, typically only a few monolayers thick and as narrow as 10 nm, can act as etch masks for selective etches which attack Si but not its oxides. Other materials such as GaAs can be patterned by depositing a thin film of Si which, when so patterned and etched, can act as a resist to pattern the underlying substrate [4].

This local oxidation can also be performed with an STM [5,6]; however, use of a conducting tip AFM offers the unique advantage that the exposure mechanism (applied bias) is decoupled from the feedback control (contact force). As a result, writing and imaging are independent. One can therefore write a pattern and immediately thereafter image it with the same tip without fear of further exposure. With an STM tip, imaging of the pattern could cause additional exposure due to the tip bias required for feedback control.

We have used this technique of AFM-induced oxidation and selective etching to fabricate side-gated Si field effect transistors with critical dimensions (channel width and/or gate separation) as small as 30 nm [7]. The starting material was n-type (100) Si (doping between 10^{15} and 10^{17} cm^{-3}) with a buried SiO₂ layer formed by oxygen implantation and

anneal. Such material, called SIMOX, is described elsewhere [8]. Ohmic contact pads for source, gate, and drain contacts were formed on the above materials by liftoff of 2 nm of Cr and 150 nm of Au evaporated into windows in photoresist formed by standard optical lithography. A second level of 2 nm Cr and 15 nm of Au was patterned over the first level to form an etch mask for fingers from the source, gate, and drain contacts to the active regions of the device to be patterned by AFM.

The active area to be patterned was first scanned by AFM and the resulting image used to align the tip to the center of the active area between the source, drain, and gate fingers. The tip was then moved to the thin metal source finger, the exposing bias was applied between the tip and the sample (4 to 6 V, tip negative) and the tip was scanned slowly ($1 - 10 \mu\text{m/sec}$) across the surface from the source to the drain finger. This formed a thin line of surface oxide between the source and drain fingers. Next, an oxide line was drawn from the gate finger to a point near the source-drain line to form the gate pattern. Figure 1 shows the AFM image of a typical oxide device pattern taken immediately after it was written, and imaged with the same tip used to write the pattern [7]. The height of the oxide pattern above the Si surface is $\sim 1.5 \text{ nm}$.

The sample was next etched in warm (70° C) hydrazine, which etches Si but not its oxides. The hydrazine removes all the surface Si unprotected by the oxide pattern or the metal masks down to the buried oxide layer, which acts as an etch stop. Figure 2 is an SEM image after hydrazine etching of a single-gate structure fabricated on a top Si layer 40 nm thick [7]. The wire between source and drain is a conducting channel isolated from the substrate by the buried layer of implanted oxide. The source-drain wire shown in Figure 2 is $\sim 30 \text{ nm wide by } 40 \text{ nm high by } 6 \mu\text{m long}$. The side gate is a wire 220 nm wide connected at one end to a contact pad and at the other end separated by 160 nm from the source-drain wire. The gate wire in Figure 2 was purposely made wide and well-separated from the channel wire. Gate wires as narrow as 35 nm with separations of 40 nm from the channel wire have been fabricated. Because liquid etches such as hydrazine generally produce no better than a one-to-one ratio of wire height-to-width, the minimum wire width achievable depends not only on the minimum width of the oxide pattern that can be written but also on the thickness of the layer to be etched. Higher aspect ratios have recently been achieved through directionally selective dry etching of these anodic oxides [9].

Because of the buried oxide layer, backgating can drive the source-drain channel into accumulation, depletion, or inversion, thus allowing independent control of the conductance and carrier type of the channel [10]. The side gate can then be used to modulate the channel conductance. With the source-drain channel wire backgated into accumulation, the side gate can be biased negatively to pinch the source-drain channel near the side gate into depletion. Figure 3 shows the transistor characteristic of a device (channel dimensions 300 nm wide by 200 nm high, backgated +40 V into accumulation and depleted by a single side gate [7]). The side gate bias ranges from 0 V to 7 V in 1 volt steps. Similar transistor characteristics have been observed for devices with source-drain wires as thin as 40 nm and narrow as 30 nm but with correspondingly reduced currents because of the smaller size. Such small devices (like that shown in Figure 2) can by increased backgating be driven further into accumulation, achieving currents as high as $5 \times 10^{-7} \text{ amp}$ [7]. The device designs shown here were optimized for ease of fabrication, not for device performance, and several obvious improvements can be made. The channel resistance can be significantly reduced by replacing the long thin channel wire with a wide geometry which tapers to a thin wire only in the region near the gate. Gating action can be increased by using a split-gate geometry to modulate from both sides of the channel instead of one. Varying the gate-channel separation and the channel doping will affect the transconductance and maximum current density.

Recently, an otherwise conventional large-scale Si MOSFET was fabricated, in which a $0.1\ \mu\text{m}$ gate made of amorphous hydrogenated Si was defined by AFM-induced oxidation and dry etching [11]. The side-gated FET structures discussed here are uncommon for Si but are used in compound semiconductor devices such as quantum point contacts. Side-gated FETs offer some advantages over conventional device designs, including an inherently low gate-channel capacitance [12]. Low capacitances are essential to the operation of devices such as Coulomb blockade and single electron tunneling structures. Coulomb blockade effects have recently been reported in SiMOX structures made by conventional electron-beam methods [13]. Also, the exposed surface of the active area of side-gated devices affords the possibility of further modification of device properties. Proximal probe manipulation may allow tailoring of the surface of the active area to near-atomic precision. In structures with the charge carriers near or at the surface, such precise surface control may give corresponding control over the device properties.

The approach described here offers several advantages over conventional nanofabrication techniques. The modified surface layer can be as thin as one monolayer, suggesting patterning at the $1\ \text{nm}$ scale, and below may be achievable. Because only the top few monolayers are modified, the bulk properties underneath are not damaged. There are no proximity effects from backscattered beams, hence very densely packed patterns can be written. The conducting-tip AFM offers the additional advantage over STM of the exposure and imaging mechanisms being decoupled. Therefore, pre-exposure registration and post-exposure imaging and selective decoupling of patterns can be made without risk of accidental exposure. These and similar proximal probe techniques make possible the fabrication of nanometer-scale devices through simple, reliable, and easily adaptable processes using relatively inexpensive and widely available equipment. Optimization of proximal probe writing and subsequent pattern transfer techniques may allow the fabrication of structures with critical dimensions below the limits of conventional electron beam lithography. The atomic-level resolution already achieved by proximal probe imaging and single-atom manipulation suggests that such techniques may approach the ultimate processing limit of single-atom control of device structure.

REFERENCES

- [1] R. Wiesendanger, *Applied Surface Science* **54** (1992) 271.
- [2] D. M. Eigler and E. K. Schweizer, *Nature* **344** (1990) 524.
- [3] E. S. Snow and P. M. Campbell, *Appl. Phys. Lett.* **64** (1994) 1932.
- [4] E. S. Snow, P. M. Campbell, and B. V. Shanabrook, *Appl. Phys. Lett.* **63** (1994) 3488.
- [5] J. A. Dagata, J. Schneir, H. H. Harary, C. J. Evans, M. T. Postek, and J. Bennett, *Appl. Phys. Lett.* **56** (1990) 2001.
- [6] E. S. Snow, P. M. Campbell, and P. J. McMarr, *Appl. Phys. Lett.* **63** (1993) 749.
- [7] P. M. Campbell, E. S. Snow, and P. J. McMarr, *Appl. Phys. Lett.* **66** (1995) 1388.
- [8] P. J. McMarr, B. J. Mristik, M. S. Barger, G. Bowden, and J. R. Blanco, *J. Appl. Phys.* **67** (1990) 7211.
- [9] E. S. Snow, W. H. Juan, S. W. Pang, and P. M. Campbell, *Appl. Phys. Lett.* **66** (1995) 1729.
- [10] P. M. Campbell, E. S. Snow, and P. J. McMarr, *Solid-State Electronics* **37** (1994) 583.
- [11] S. C. Minne, H. T. Soh, Ph. Flueckiger, and C. F. Quate, *Appl. Phys. Lett.* **66** (1995) 703.
- [12] U. Meiners, H. Brugger, B. E. Maile, C. Wolk, and F. Koch, *Solid-State Electronics* **37** (1994) 1001.
- [13] D. Ali and H. Ahmed, *Appl. Phys. Lett.* **64** (1994) 2119.

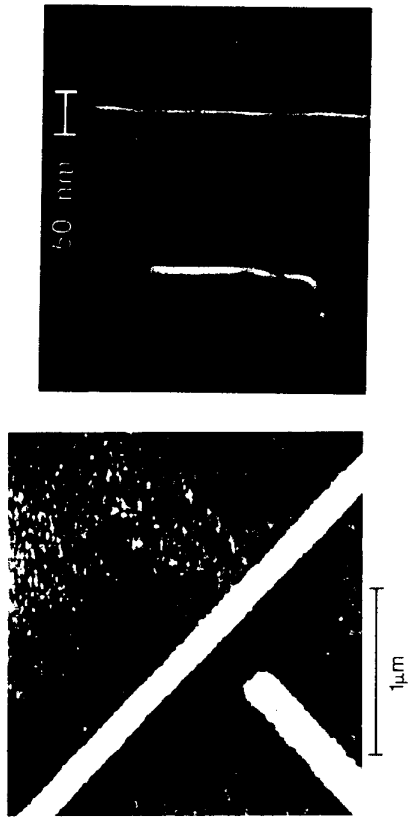


Figure 1. AFM image of a device oxide pattern (prior to etching) imaged with the same tip immediately after writing. Vertical scale (black to white) is $2\ \text{nm}$. The oxide pattern height is $\sim 1.5\ \text{nm}$.

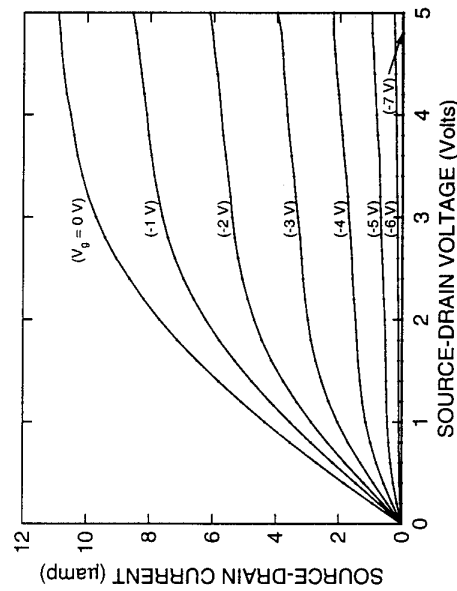


Figure 2. Scanning electron micrograph of the active region of a side-gated transistor after etching in hydrazine. The width of the source-drain channel (vertical line in picture) is $\sim 30\ \text{nm}$. The gate is to the left.

Figure 3. Drain current vs. drain voltage for various side-gate biases (ranging from 0 to -7 V in -1 V steps) for a side-gated Si transistor fabricated by AFM.

Fabrication of Metallic Nanostructures with an Atomic Force Microscope

L. L. Sohn and R. L. Willett
AT&T Bell Laboratories, 600 Mountain Ave., Murray Hill, NJ 07974

Abstract

We describe a novel technique for fabricating metallic nanostructures on an arbitrary substrate using an AFM. An AFM tip is used to plow a pattern through a bilayer resist spun onto a substrate. A development step is then performed to create a mask through which metal can be evaporated. By changing the applied force, the top resist-layer thickness, or the development time, the line width can be varied. Continuous metallic wires $600\text{ \AA} \times 400\text{ \AA} \times 15\mu\text{m}$ have been routinely fabricated on bare substrates and between contact pads.

Introduction

Recent advances in nanofabrication technology have provided access to continually smaller length scales. Consequently, a number of novel quantum phenomena, including single-electron charging effects [1], Aharonov-Bohm oscillations [2], and universal conductance fluctuations [2], have been observed in fabricated structures of size $\sim 1000\text{\AA}$. Because of the high probability that additional novel effects will manifest at even smaller dimensions, there is strong motivation to develop fabrication techniques that can *routinely* access sub- 500\AA length scales in various materials.

We have developed a novel technique [3] for fabricating *with ease* metallic nanostructures of width $\sim 400\text{\AA}$ and height $\sim 600\text{\AA}$ on an arbitrary, topographically-varying, substrate using an atomic force microscope (AFM). An AFM tip is used to plow a pattern through the first of two resist layers spun onto a substrate. A development step is then performed to create a mask through which up to $\sim 600\text{\AA}$ of metal can be evaporated. By changing the applied force, the thickness of the first resist layer, or the development time, the line width can be varied. This technique has advantages over other currently-investigated proximal-probe lithography methods, including direct deposition/chemical modification [4], low-voltage resist exposures [5], and more recently "tapping" [6]. The most important advantage is the *general use* of resist which allows for the deposition of a range of materials. Because the top-resist layer is plowed, a conductive tip and/or substrate is not needed and neither the tip nor the substrate is damaged. A bilayer-resist scheme is employed for three reasons: 1) the bottom resist layer *planarizes* a topographically-varying substrate; 2) the overall scheme offers an undercut profile for clean lift-offs; and 3) the resulting profile provides potentially excellent height-width aspect ratios (roughly 2:1 or 3:1).

Materials and Methods

To prepare for AFM-writing, we spin a 3000\AA film of PMMA/MAA [7] onto an arbitrary substrate and bake for 1 hr at $165-170^\circ\text{C}$. The resist-coated substrate is then blanket-exposed using e-beam lithography ($\sim 1\mu\text{C}/\text{cm}^2$) [8]. This particular step increases the solubility of the baked-resist when exposed to the standard developer, 1:3 Methyl Isobutylketone (MIBK):isopropyl

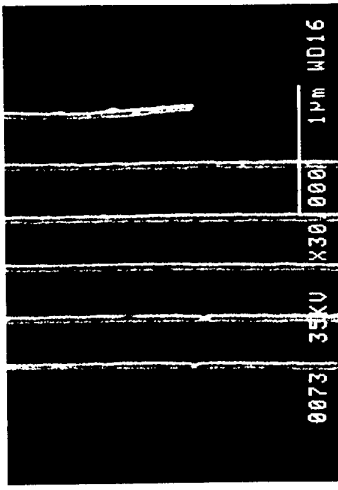


Fig. 1. Scanning-electron micrograph of 400\AA -wide, 500\AA -thick Cr wires fabricated on a GaAs substrate. Fabrication parameters include: $I=1100\text{nA}$, $t_{\text{dev}}=5\text{s}$, top resist-layer thickness= 240\AA .

alcohol (IPA). After blanket-exposure, a $\sim 240\text{\AA}$ film of 496K PMMA [9] is spun onto the sample which is then immediately placed in an AFM equipped with a standard Si_3N_4 cantilever tip. The top-resist layer is plowed with an applied force ranging from $1100-1180\text{nN}$ and a velocity of $\sim 0.2\text{\mu m/sec}$. After plowing, the sample is baked in an oven at $165-170^\circ\text{C}$ for 1 minute and cooled to ambient temperature. It is then developed in 1:3 MIBK: IPA for 5s . Material is deposited through the newly-created resist "mask" which is subsequently lifted off with acetone.

Results

Figure 1 shows $\sim 400\text{\AA}$ -wide, 500\AA -thick chromium (Cr) wires fabricated via the above technique. For the entire length ($\sim 1.5\text{\mu m}$), the wires are straight and parallel, thus indicating that the Si_3N_4 tip is not subject to any significant noise during plowing. As shown, the wires have smooth edges and are uniform in width, suggesting that the Si_3N_4 tip maintained a constant force over the substrate and neither degraded nor accumulated any appreciable PMMA residue while plowing. Although the wires shown in Fig. 1 have a $\sim 4300\text{\AA}$ period, a $\sim 1000\text{\AA}$ period can be realized without a change in parameters. A smaller period, however, is difficult to achieve due to displaced resist (a by-product of plowing), but may be attempted with a thinner top-resist layer or a sharper tip.

We have fabricated $\sim 400\text{\AA}$ -wide, 500\AA -thick Cr wires between gold (Au) contact pads set 3\mu m apart and measured their resistance. Figure 2a shows one set of wires. Although there are areas where lift-off was incomplete, they are displaced from the wires of interest and thus do not affect the measurement. For this particular sample, we measured a resistance $R=2k\Omega$. Close examination reveals that R corresponds to only one wire, free from any obvious breaks or defects, in the set. Nonetheless, this demonstrates that metallic wires fabricated with the our AFM method are *continuous over an appreciable distance*. A unique aspect of the bilayer technique employed is the ability to create continuous structures over *varying topography*. This is demonstrated in Fig. 2b which shows that all wires are continuous and uniform in width over the *edges* of the 500\AA -

Discussion and Conclusion

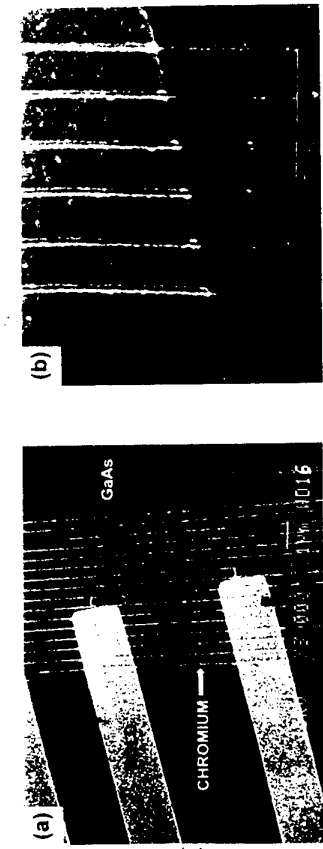


Fig. 2. 15 μ m-long, 400 \AA -wide, 500 \AA -thick Cr wires. (a) Fabricated with the parameters cited in Fig. 1, wires traverse 500 \AA -thick Au contact pads set 3 μ m apart on a GaAs substrate. Resistance of wires=2k Ω . (b) Magnified view of wires at the boundary of the Au contact pads and GaAs substrate.

thick contact pads. This result indicates that the AFM tip successfully maintained a constant force between itself and the varying sample topography. Moreover, it suggests that we have successfully planarized the substrate; i.e. smoothed the abrupt boundary edges of the contact pads, by spinning on a thick bottom-resist layer.

Three parameters—the applied force, the development time, and the top resist-layer thickness—determine line widths. Shown in Figure 3a is the linear dependence between the line width and the applied force F (a minimum force $F=1100\text{ mN}$ is needed to penetrate the resist with the tip). Keeping the force constant, we find that line width depends on the development time τ_{dev} . As shown in Fig. 3b, a minimum of 10s is needed before the developer begins to widen the resist profile, and therefore the line width, appreciably. The nonlinear dependence on $\tau_{\text{dev}} > 10\text{s}$ is due to a nonlinear PMMA dissolution. Finally, as shown in Fig. 3c, line width can depend on the top resist-layer thickness if F and τ_{dev} remain constant. Here, the nonlinear dependence reflects the higher residual-solvent concentration in thicker resist which ultimately increases the resist solubility in developer.

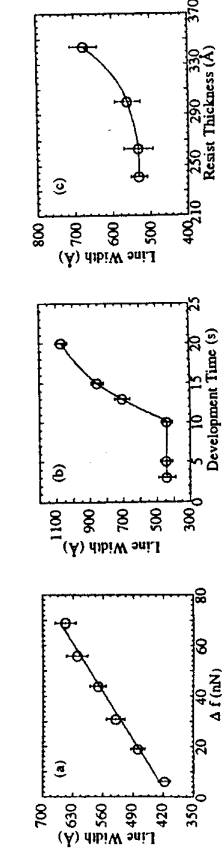


Fig. 3. Line width vs. (a) applied force ($F=1100 + \Delta f\text{ mN}$), (b) development time, and (c) resist thickness.

Our AFM-based lithography technique, using a bilayer-resist scheme, is distinctly advantageous. The generality of the presented technique is its most important feature—the good resist profiles obtained allow for many materials to now be deposited with small lateral length scales. Because the substrate surface is planarized with a thick bottom-resist layer, an arbitrary, topographically-varying, substrate can be used. Via the bilayer-resist scheme, nanostructures can be fabricated with potentially excellent height-width aspect ratios (roughly 2:1 or 3:1), thus allowing for practical device architecture consideration. Finally, because plowing is performed only on the top resist layer, the substrate and tip are not damaged. Presently, all fabricated lines have a minimum width of $\sim 400\text{\AA}$. Further optimization of the parameters that determine line width may decrease this, as may employing an entirely different resist.

To conclude, we have described a novel AFM-lithography technique. By plowing through the first of two resist layers on an arbitrary substrate and following with a development step, we can create a resist mask through which relatively thick material can be deposited. Line widths can be varied by changing the top resist-layer thickness, the force, and the development time.

References

- [1] T. A. Fulton and G. J. Dolan, Phys. Rev. Lett. **59**, 109 (1987).
- [2] See for instance, S. Washburn in *Mesoscopic Phenomena in Solids*, ed. by B. Altshuler, P. Lee, and R. Webb (Elsevier, 1991) and references therein; S. Washburn and R. A. Webb, Rep. Prog. Phys. **55**, 1311 (1992), and references therein.
- [3] L. Sohn and R. L. Willett, submitted for publication (1995).
- [4] J. A. Dagata, W. Tseng, J. Bennett, E. A. Dobisz, J. Schneir, and H. H. Harary, J. Vac. Sci. Technol. A **10**, 2105 (1992); E. S. Snow, P. M. Campbell, and P. J. McMarr, Appl. Phys. Lett. **63**, 749 (1993); and E. S. Snow, P. M. Campbell, and B. V. Shanabrook, Appl. Phys. Lett. **63**, 3488 (1993).
- [5] M. A. McCord and R. F. W. Pease, Appl. Phys. Lett. **50**, 569 (1987) and A. Majumdar, P. I. Oden, J. P. Carrejo, L. A. Nagahara, J. J. Graham, and J. Alexander, Appl. Phys. Lett. **61**, 2293 (1992).
- [6] M. Wendel, S. Kühn, H. Lorenz, J. P. Koithaus, and M. Holland, Appl. Phys. Lett. **65**, 1775 (1994).
- [7] 9% PMMA/MAA dissolved in cellosolve is used to obtain the proper thickness.
- [8] We can also expose the PMMA/MAA, which can be substituted with photoresist, using deep UV radiation.
- [9] A solution of 1% 496K PMMA dissolved in chlorobenzene obtains such a thin film.

SPIN-ORBIT SPLITTING OF THE SPECTRUM OF 2D ELECTRONS IN SURFACE QUANTUM WELL OF GAPLESS SEMICONDUCTORS

G.M.Minkov, A.V.Germanenko, V.A.Larionova, O.E.Rut
 Institute of Physics & Appl Mathematics, Ural University, Ekaterinburg 620083,
 Russia

Abstract

Spin-orbit splitting of the two-dimensional subbands in surface quantum well of gapless semiconductor HgCdTe has been measured by tunneling spectroscopy. The results have been analysed in the framework of the three band Kane model of the energy spectrum.

The spin-orbit interaction of 2D carriers localised in asymmetric quantum well leads to splitting of "spin-up" and "spin-down" subbands even at $B=0$. This effect in wide and narrow gap semiconductors was investigated experimentally and theoretically in many papers [1-3]. For 2D states in gapless semiconductors the role of spin-orbit interaction was discussed only in [4].

It is the aim of this work to study experimentally and theoretically the energy spectrum of size-quantized electron states in a surface quantum well in a gapless p-HgCdTe. The tunneling spectroscopy in quantizing magnetic field is used for experimental investigations. Theoretical investigation is based on numerical solution of the Schrödinger equation with three band Kane Hamiltonian.

We have measured the oscillations of the conductivity of the tunneling contacts Yb-oxide-p-HgCdTe in a magnetic field. All results reported here were obtained for two structures prepared on p-HgCdTe with $E_g = .70$ meV and concentration of uncompensated acceptors $N_{A-ND} = 6 \cdot 10^{18}$ cm $^{-3}$. The typical dependences of the oscillatory part of the tunneling conductivity versus reciprocal magnetic field $B \parallel n$ (n is the normal to the plane of the tunneling contact) at several biases are

presented in Fig.1. It is seen that the oscillation picture is a convolution of several components, which can best be distinguished by Fourier analysis (inset of the Fig.2). The fundamental fields are determined by the extreme cross-sections of the isoenergy surfaces $B_f = \frac{c\hbar S(E)}{2\pi \cdot e}$ at the energy $E = E_F + eV$. In semiconductors with isotropic spectrum $S(E) = \pi k^2 / E$. Thus the measurements of the oscillations of the tunneling conductivity at various biases allow to determine experimentally the energy spectrum of the bulk and 2D states. These results for two tunneling contacts which have different surface potential are presented in Fig.2.

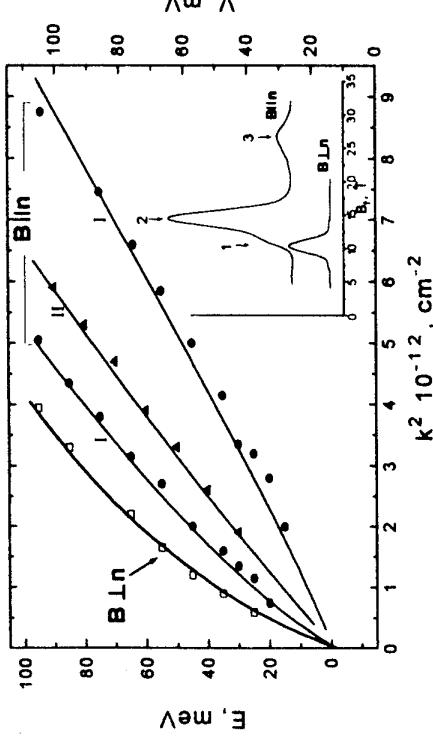


Fig.2. The energy spectrum of the bulk (□) and 2D (▲) states for the structure I with $\epsilon\varphi = 230$ meV and for the structure II with $\epsilon\varphi = 190$ meV. The curves are the results of the calculation (see text). Inset shows the results of the Fourier transformation of the oscillations for the structure I at $V = 100$ mV.

At $B \parallel n$ the oscillations of the tunneling conductivity are due to tunneling into Landau levels of the bulk states, therefore the energy spectrum of the bulk electrons is obtained from the analysis of the oscillations in this orientation of magnetic field. It is presented by the upper curve in Fig.2.

At $B \parallel n$ the oscillations are connected mainly with tunneling into 2D states localised in surface quantum well. It is clear from Fig.3, where angle dependence of the fundamental fields of these oscillations is shown. The positions of the maxima 2,3 of Fourier spectra (see Fig.2) depend on Θ roughly as $(\cos \Theta)^{-1}$, where Θ is the angle between B and n . The position of the shoulder 1 does not shift with changing of Θ and remains at about the position of maximum of Fourier spectra at $B \parallel n$, indicating that it is due to tunneling into Landau levels of the bulk states.

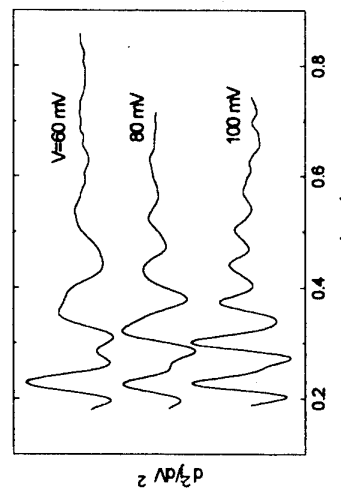


Fig.1. The oscillations of the derivative of the tunneling conductivity versus reciprocal magnetic field for structure I, $B \parallel n$. The results reported here were obtained for two structures prepared on p-HgCdTe with $E_g = .70$ meV and concentration of uncompensated acceptors $N_{A-ND} = 6 \cdot 10^{18}$ cm $^{-3}$. The typical dependences of the oscillatory part of the tunneling conductivity versus reciprocal magnetic field $B \parallel n$ (n is the normal to the plane of the tunneling contact) at several biases are

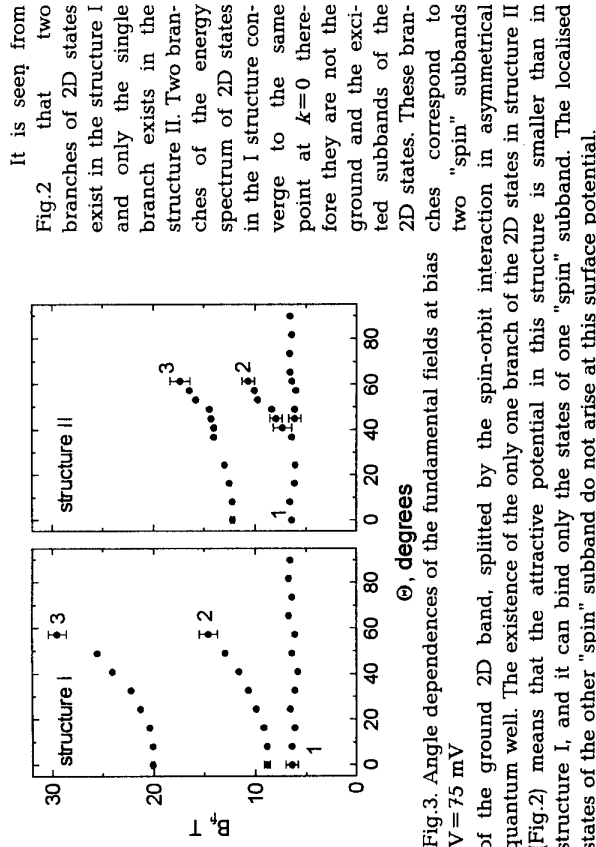


Fig. 3. Angle dependences of the fundamental fields at bias $V = 75$ mV of the ground 2D band, splitted by the spin-orbit interaction in asymmetrical quantum well. The existence of the only one branch of the 2D states in structure II (Fig. 2) means that the attractive potential in this structure is smaller than in structure I, and it can bind only the states of one "spin" subband. The localised states of the other "spin" subband do not arise at this surface potential.

For theoretical treatment of 2D states in wide gap semiconductors one can use one band model and take spin-orbit interaction into account as a perturbation. This approach is often used to describe the energy spectrum of 2D states in narrow gap semiconductors too. For gapless semiconductors the real band structure (nearest four-fold degenerated Γ_8 and two-fold degenerated Γ_6 bands) must be taken into account from the outset. The energy spectrum of the insulator must be specified in this case. The most acceptable model for such a problem was proposed in [5], where it was assumed that the insulator had the same band structure as the semiconductor had, but with large positive energy gap.

In our case the interaction with remote bands may be omitted and the Schrödinger equation in this approximation is the set of four differential and two algebraic equations. At $z < 0$ and $z > L$ the potential is constant (Fig. 4) and in these regions the wave functions are known, they are the same as for unbounded medium. The wave function of the 2D states must decay at $z < 0$ and $z > L$. Thus, requiring correct behaviour of the wave function outside the potential well we solved the set of equations numerically. The direct integration techniques were used. The behaviour of the potential in the space-charge layer was obtained from the Poisson equation which was easily solved when the charge of the 2D electrons was much less than the charge of uncompensated acceptors in the space-charge layer. This condition is fulfilled for our structures. Thus in our case the potential

has near parabolic shape $\phi(z) = \epsilon \phi_s (1-z/L)^2$, where $L = (2 \epsilon \epsilon_0 |\phi_s| / e(N_a - N_d))^{1/2}$, $\phi_s = \phi(z=0)$, and ϵ is dielectric constant. The value of the surface potential ϕ_s was used as an adjusting parameter.

The results of such a calculation with parameters E_g , $N_a - N_d$, corresponding to the investigated structures, and $P = 8.4 \cdot 10^{-8}$ eV·cm, $D_c = D_v = 1$ eV, $\epsilon = 20$, are presented in Fig. 2. One can see a good agreement between the results of the calculation, carried out with $e\phi_s = 230$ meV and 190 meV for structures I and II, respectively, and the experimental data. The agreement does not depend on parameters D_c , D_v , if D_c , $D_v \gg E_g$. Indeed, only one "spin" state, localised near the surface, exists in structure II. The states for another "spin" are pushed into continuous states. Unlike structure II, the both "spin" states exist in structure I with larger value of the surface potential.

Fig. 4. The model of the structure used in calculation. At intermediate value of the surface potential the binding energy is equal to zero at $k=0$ and grows with increasing of $|k|$.

Uncommon behaviour of the oscillations in tilted magnetic field was observed in structure II. As it is seen from Fig. 3 the fundamental field of only one of the 2D "spin" subbands is observed at $\Theta < 40^\circ$. But at larger angles another B_f which shifts with increasing of the angle as expected for a 2D system, arises, i.e. the Landau levels of both 2D "spin" subbands exist at intermediate angles. The theoretical analysis of the energy spectrum of the 2D carriers in a magnetic field performed in the framework of the foregoing model shows some peculiarities of the behaviour of the Landau levels at moderate potential values and gives a possibility for qualitative understanding of the specific feature of the angle dependence.

- References
1. B.Das and S.Datta, Phys.Rev. B 41 (1990) 8278.
 2. J.Luo, H.Munekata, F.F.Fang and P.J.Stiles, Phys.Rev.B 41 (1990) 7685.
 3. R.Wolrab, R.Sizmann, F.Koch, et al., Semicond. Sci. Technol. 4 (1989) 491.
 4. V.F.Radantsev, Sov.Phys. JETP 69 (1989) 1012.
 5. P.Sobkowicz, J.Semicond. Sci. Technol. 24 (1990) 1983.

LANDAU ASSISTED VERTICAL TRANSPORT IN MQW P-i-N GaAs/AlGaAs DIODES

R.J. Stone[†], J.G. Michels[†], S.L. Wong[†], C.T. Foxon^{*}, R.J. Nicholas[†] and A.M. Fox[†].

[†]Clarendon Laboratory, Physics Department, University of Oxford, Parks Road, Oxford, OX1 3PU, UK.

^{*}Department of Physics, University of Nottingham, University Park, Nottingham, NG7 2RD, UK.

Abstract

We report studies of inter-Landau level tunnelling in GaAs/AlGaAs multi-quantum well p-i-n structures. With the magnetic field parallel to the transport, we observe new resonances in the photocurrent characteristic of the devices. The new features are attributed to non-momentum conserving tunnelling between levels of different Landau index. In one of our samples, we also observe that the resonances move to lower bias and lose strength with increasing magnetic field.

1. Introduction

The physics of vertical transport in semiconductor multiple quantum well (MQW) p-i-n tunnelling devices is significantly different from other commonly-studied tunnelling structures. MQW devices allow the study of single particle tunnelling between 2D states. This contrasts with resonant tunnelling diodes (RTDs), where the carriers tunnel between 3D source and drain states via a confined 2D state. It also differs from the case of coupled 2DEGs, where the high carrier densities lead to many body effects.

In this paper we report the effect of a strong magnetic field normal to the growth direction on the vertical transport in an MQW tunnelling device. Previous studies have concentrated on the effect of magnetic fields applied perpendicular to the transport direction [1,2]. This is because it was expected that fields parallel to the transport would not have much effect due to the conservation of in-plane momentum for resonant 2D-2D tunnelling. Contrary to this expectation, we have observed clear inter-Landau level tunnelling resonances. This indicates a coupling of states of different in-plane momenta, and implies a non-momentum conserving process must be involved. We have also observed a suppression of the resonant tunnelling at high B-fields, similar to that reported in coupled 2DEG systems [3,4]. This is a surprising result, since the suppression has been attributed to many body effects which are clearly inappropriate to our case.

2. Samples and Technique

Vertical transport has been studied by injecting carriers into the wells optically, and measuring the photocurrent in GaAs/Al_{0.33}Ga_{0.67}As p-i-n diodes, with double quantum well (DQW) pairs grown into the 1 μm intrinsic region. Two samples were studied, with differing narrow well widths (see table (i)).

The samples were placed in a He cryostat, at a temperature of 2.2K, mounted with the growth axis parallel to the magnetic field. Carriers were injected selectively to the wells and not the barrier material using a 670nm diode laser delivered by optical fibre, giving diffuse illumination. Charge-build up in the wells was avoided by carefully reducing the optical power until the photocurrent response scaled linearly with power. Photocurrent was measured using a lock-in technique.

A linear electric field was applied across the wells, allowing tunnelling between adjacent DQW pairs to be studied. The resonances observed in the absence of magnetic field are well understood, agreeing closely with theory, allowing an accurate determination of the energy of the new magnetic-induced states. The thin barriers allow the DQW states to be hybridised, whilst still remaining localised by the thick barrier. Resonances observed in the photocurrent curves are due to slow tunnelling through the thick barrier (~10ns), at fields which align confined states of adjacent DQWs.

Sample	Thick Barrier	DQW Unit	
		Wide Well (WW)	Narrow Well (NW)
G953	152.6	158.3	56.5
G952	152.6	158.3	79.1

Table (i) : Sample growth details. The DQW / thick barrier unit is repeated 25 times in the intrinsic region of the diode (all thicknesses in Å)

It has been shown that the tunnelling processes observed in these samples at low temperature are dominated by the electrons [5]. This is because of the substantially lower effective mass of the electrons compared to the holes, which are consequently much slower to tunnel. We shall therefore consider only electron states. The carrier lifetime is longer in sample G952 due to the spatially indirect recombination which occurs at biases less than 0V. (G953 becomes indirect below -3V which is outside the range studied here.)

3. Results and Discussion

With no applied magnetic field, we observe peaks in the photocurrent response (figs. 1 and 4), corresponding to momentum-conserving resonant tunnelling through the thick barrier. This is in contrast to non-resonant tunnelling which must proceed by scattering. We first concentrate on the magnetic field dependence of the -1.3V resonance in G953 where the tunnelling is from the wide well (WW1) state to the WW3 state (see fig. 2). Figure 1 shows the effect of applying magnetic field. We observe new features which emerge out of the high bias side, indicating new states being brought into resonance. The position of these new resonances scales approximately linearly with magnetic field (fig. 3). This suggests a non-momentum conserving tunnelling process between states of different Landau index.

The magnetic field causes a ladder of states with spacing $\hbar\omega_c$ to be created, emanating from each subband. We would expect to observe tunnelling between states of the same Landau index. ($\Delta n = 0$) as this is a momentum conserving process. However, if we include processes involving some momentum transfer, transitions can be made with $\Delta n \neq 0$. We attribute the magnetic field induced peaks as a modification of the zero field resonance condition to include tunnelling between Landau states in adjacent well pairs. Specifically, in the case of G953, we see tunnelling from WW1 to WW3 with an associated $\Delta n = 1$ and 2 (fig. 3). The condition for this resonance is given by

$$E_{WW1}^{WW1} = E_{WW3}^{WW3} + \Delta n \hbar\omega_c - eFd \quad (1)$$

where E is the energy of the subband above the bandedge, F is the electric field, Δn is the change in Landau level number, d is the spatial separation of the well states and ω_c is the cyclotron frequency. Note that the carrier masses have been assumed to be identical in both wells at all subband energies.

This simple expression provides a theoretical prediction for the resonance positions in reasonable agreement with experiment. Fig. 3 shows the expected positions for tunnelling to the WW3 Landau levels from the WW1 state with $\Delta n = 0, 1$, and 2. The subband energies were calculated using a transfer matrix technique[6] which includes the electric field. There is a small discrepancy to lower bias of both the main and satellite peaks, but this is probably the result of band non-parabolicity.

The change of quantum number involved in tunnelling between Landau levels indicates that the in-plane momentum has not been conserved in the magneto-tunnelling process. A similar inter-Landau tunnelling effect has been observed in double barrier resonant tunnelling diodes[7] where the scattering mechanism is LO phonon emission. However the magnitude of the energy difference involved in our system is too small for this, and we also see no magnetic field threshold for the resonances. This may be due to scattering by either charged impurities, interface roughness or emission of acoustic phonons. We also observe that the magnetically induced features are stronger with increasing magnetic field, suggesting that the magneto-coupling of states with differing in-plane momentum also increases with field, possibly suggesting some mixing due to non-parabolicity.

Sample G952 shows comparable Landau resonances to G953 as would be expected for such a similar structure (see 9T trace in fig. 4). However the shift of the main resonance to lower electric field is more marked corresponding to $0.07 \hbar\omega_c$ as compared to $0.07 \hbar\omega_c$ in the case of G953. This shift is too large to be a band non-parabolicity effect in addition the magnitude of the resonant peaks in G952 fall off sharply with magnetic field (fig. 4 inset). This cannot be explained as a reduction in carrier lifetime, as the resonances are more strongly affected[5].

Differences in the response of the two samples could be due to the indirect exciton in G952, as in this sample the initial state is localised in the narrow well. Other recent studies[3,4] of vertical tunnelling between adjacent 2-D electron gases in the presence of parallel electric and magnetic fields have also reported a suppression of the tunnelling by the magnetic field and a shift of the resonances from the zero magnetic field value. These have been interpreted as many body "exciton-like" interactions. This many-body picture is not relevant in our case, as we have an essentially single particle tunnelling process, at substantially lower carrier densities.

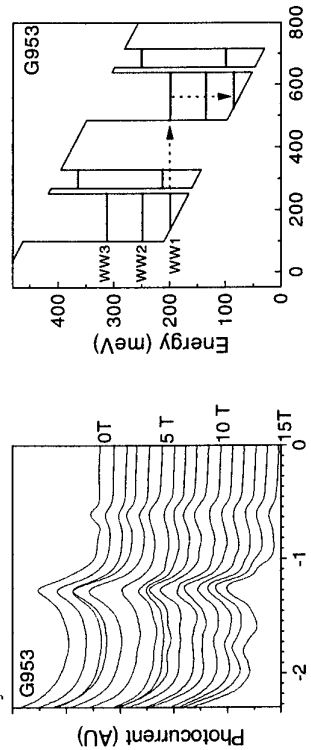


Fig. 2 : Conduction band profile of sample G953 at the $B = 0, -1.3V$ resonance.

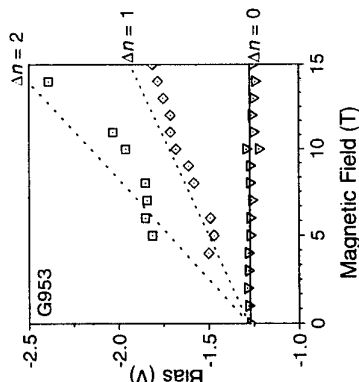


Fig. 3 : Peak positions of photocurrent response of sample G953 vs. magnetic field. (dotted lines indicate predicted Landau resonances according to Eq. 1)

4. Conclusion

We have observed a new non-momentum conserving inter-Landau level resonant tunnelling process in the photocurrent response of quantum well diodes. Unlike RTDs[7] we have shown that LO phonon emission is not the scattering effect at the magnetic fields investigated. Our experiment has been performed in the limit of the single carrier case, negating the many-body effects involved in experiments where the tunnelling is between 2-D electron gases. We see a similar suppression and shift of the resonances with magnetic field, but as yet have no explanation.

Acknowledgements - This work was partly supported by the EP SRC and Royal Society. The samples were grown at Philips Research Laboratories and processed by F.Stride at University College London, and M. Pate at the SERC III/V Facility at The University of Sheffield.

References

- [1] H. Schneider, K. von Klitzing, and K.Ploog, Superlatt. and Micros. **5** 383 (1989)
- [2] W. Müller H. Grahn, K. von Klitzing, K. Ploog, Phys. Rev. B **48** 1178 (1993)
- [3] J.P. Eisenstein, L.N. Pfeiffer and K.W. West, Phys. Rev. Lett. **74** 1419 (1994)
- [4] K.M. Brown, N. Turner, J.T. Nicholls, E.H. Linfield, M. Pepper, D.A. Ritchie and G.A.C. Jones, Phys. Rev. B **50** 15465 (1994)
- [5] R.G. Ispasoiu, A.M. Fox, C.T. Foxon, J.E. Cunningham, W.Y. Yan, Semicond. Sci. Technol. **9** 545 (1994)
- [6] R. Tsu and L. Esaki, Appl. Phys. Lett. **22** 11 (1973)
- [7] M.L. Leadbeater, E.S. Alves, L. Eaves, M. Henini and O.H. Hughes, Phys. Rev. B, **39** 3438 (1989)

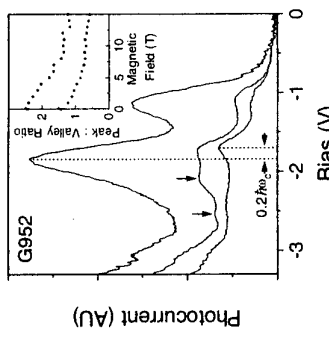


Fig. 4 : Photocurrent characteristic of sample G952 at 0, 9 and 15T (decreasing). The arrows on the 9T curve indicate Landau resonances. Inset : Peak to valley ratio vs. magnetic field

AN OPTICAL AND ELECTRICAL STUDY OF TUNNELLING MECHANISMS THROUGH INDIRECT GAP SINGLE BARRIER GaAs/AlAs/GaAs HETEROSTRUCTURES.

J.J. Finley[†], R.J. Tessler[§], M.S. Skolnick[†], J.W. Cockburn[†], R. Grey[‡], G. Hilt[‡] and M.A. Pate[‡].

[†]*Department of Physics, University of Sheffield, Sheffield, S3 7RH, UK.*

[‡]*Department of Electronic and Electrical Engineering, University of Sheffield, Sheffield, S1 3JD, UK*

[§]*Laboratoire de Microstructures et Microélectronique, 196 av. Henri Ravera, 92225 Bagneux, France.*

We present an electroluminescence (EL) and transport study of the tunnelling mechanisms in GaAs/AlAs/GaAs single barrier p-i-n tunnelling structures. We show that both Γ -X and X- Γ tunnelling processes arise from either elastic transfer involving the longitudinal X_z barrier states, or momentum conserving phonon assisted transfer involving transverse X_{xy} states. The tunnelling process is shown to be very strongly sequential.

Electroluminescence and transport studies are employed to identify the tunnelling mechanisms in GaAs/AlAs/GaAs single barrier structures. The tunnelling processes through such structures are particularly interesting since the lowest electron states in the GaAs and AlAs arise from different points of the Brillouin Zone (BZ) (Γ for GaAs, X for AlAs)[1-3]. Tunnelling through indirect gap AlAs barrier samples can then involve either Γ - Γ - Γ processes or Γ -X- Γ intervalley transfer, with the possible participation of momentum conserving (MC) zone boundary phonons. A further point of interest is that the tunnelling arises between regions of different effective mass, in contrast to the much more common case of tunnelling between regions of equal effective mass.

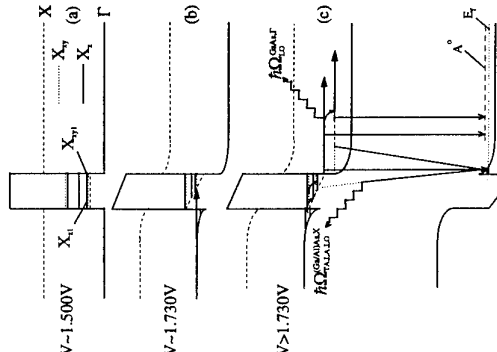


Figure 1-Band edge diagram:(a) Flat band condition (b) Onset of Γ -X- Γ tunnelling and (c) Observed EL transitions.

In the present work we investigate a series of single barrier p-i-n GaAs/AlAs/GaAs heterostructures of increasing AlAs layer width. When the structures are forward biased beyond the flat band condition (-1.5V fig 1a), electrons (holes) accumulate in a 2D layer close to the n-type(p-type) GaAs/AlAs interface. As the bias increases, the energy separation between the emitter 2D level and the confined X states in the barrier decreases until the 2D Fermi energy in the emitter crosses the lowest confined X state in the barrier and Γ -X tunnelling may begin (fig 1b). As the bias is increased further, tunnelling into excited X states takes place simultaneously with lower lying states, the result being that the emitter distribution may be quasi-resonant with a number of confined X states at a single forward bias (see fig 1c).

Electrons confined in the X potential of the AlAs layer may generate EL, via type-II recombination with the holes confined in their 2D accumulation layer (fig 1c). Populations of hot electrons are also produced by tunnelling out of the barrier into the p-type collector, with the characteristic production of EL arising from their recombination with holes bound to neutral acceptors, denoted by eA[7-8].

The single barrier structures studied comprised the following layers: 0.5 μm n+ ($n=2 \times 10^{18} \text{ cm}^{-3}$) GaAs buffer layer, 50 nm $n=1 \times 10^{17} \text{ cm}^{-3}$ GaAs emitter, 50 Å undoped GaAs spacer, 60.80 or 100 Å undoped AlAs barrier, 50 Å undoped GaAs spacer, 0.5 μm p= $1 \times 10^{17} \text{ cm}^{-3}$ collector and 0.5 μm GaAs p+ top contact. Details of the EL experiments can be found in ref 8.

Current ($I(V)$) and differential conductance ($\sigma_d(V)$) curves, as a function of bias are presented in figs 2(a)/(b) for the three samples. For V between 1.50V-1.70V the current arises from non-resonant Γ - Γ - Γ tunnelling. At forward bias in excess of ~1.70V, marked features are observed in the $I(V)$ characteristics of all three samples, as seen most clearly in the $\sigma_d(V)$ results of fig 2. These features, which correspond to resonant tunnelling into X_z and X_{xy} barrier states, are assigned in the following way. Magneto-transport measurements [9] (not presented here) confirm the 2D nature

of the emitter, and allow the electron density and hence electric field across the emitter-barrier region to be determined.

Based on these results, a self consistent calculation of the relative energy separation of emitter (Γ) and barrier (X) states was carried out. This calculation allows all the resonances observed in $\sigma_d(V)$ for all three samples to be assigned with confidence as indicated in Fig 2. Details of the calculation will be presented elsewhere. Resonances due to direct electron transfer into X_z states and with MC AlAs/GaAs TA and LO X point phonon assistance into X_{xy} states are observed. The X_z features occur without phonon assistance, due to the relatively strong Γ -X mixing by the potential discontinuity across the GaAs/AlAs interface. The X_{xy} - Γ mixing by contrast is much weaker, arising from in-plane inhomogeneity, with the result that MC phonon participation is required for the tunnelling process into X_{xy} states[10]. The

Figure 2-2a I(V) and 2b $\sigma_d(V)$ characteristics of 60.80

and 100 Å barrier samples.

above interpretation of the $I(V)$ characteristics contrasts with that in earlier studies where tunnelling only into X_x states was considered [1-3].

EL spectra for the 80Å barrier sample, between 1.760V and 1.820V, are shown in fig 3a. At 1.770V the EL spectrum consists of a sharp peak at 1731meV, X_{xy} , with three satellites to lower energy labelled γ_{xy}^i ($i=1,2$ and 3). The energy separations $X_{xy} - \gamma_{xy}^i$ are 12.2meV, 30 ± 2 meV and 48 ± 2 meV for $i=1,2$ and 3 respectively. From comparison with PL studies of type-II superlattices [10-11] we identify the relatively weak line X_{xy} as arising from the zero phonon (ZP) excitonic recombination, involving electrons in the lowest lying X_{xy} state in the barrier with holes bound in the hole accumulation layer (fig 1(c)). The energy spacings of the lines labelled γ_{xy}^i allow us to attribute these transitions to MC phonon replicas of X_{xy} involving X point AlAs LA (LA_x^{Al}), GaAs LO (LO_x^{Ga}) and AlAs LO (LO_x^{Al}) phonons respectively [11].

At 1.670meV a strong line labelled $e_b^{LO}A_x^0$ is observed. This feature exhibits a number of zone centre GaAs LO ($LO_x^{Ga} = 35$ meV) phonon satellites to lower energy, only the first of which $e_b^{LO}A_x^0$ is shown in fig 3. The observation of a LO_x^{Ga} phonon cascade is a clear signature of the relaxation of hot electrons [7]. We therefore identify the series $e_b^{LO}A_x^i$ ($i=0,1,\dots$) as e_xA recombination of ballistic and quasi ballistic electrons in the collector [8]. A much weaker LO_x^{Ga} phonon cascade, labelled $e_b^{LO}H_z$ in fig 3, originates from the γ_{xy}^3 phonon satellite, and is attributed to the recombination of quasi ballistic electrons close to the barrier with the hole accumulation layer (fig 1c). We conclude that the ballistic population, leading to both the $e_b^{LO}A_x^0$ and $e_b^{LO}H_z$ series is injected into the collector with MC LO_x^{Al} phonon assistance from the lowest 80Å barrier. The $e_b^{LO}A_x^0$ series is at 12.2 meV lower energy than $e_b^{LO}H_z$, corresponding to the energy separation between A_x^0 and the hole Fermi energy. Very similar results were obtained for the 100Å barrier sample.

Despite the fact that at higher bias, tunnelling occurs into excited X states, EL is only observed from the lowest X state of the barrier, which has X_{xy} character for the 80 and 100Å barrier samples. This indicates that the inter subband relaxation time between the X valleys is much more rapid than the tunnelling out time from the barrier and demonstrates that the Γ -X- Γ tunnelling process is strongly sequential in character.

In the narrower 60Å sample the effects of quantum confinement are more significant, with the result that the lowest confined X state has X_z symmetry. As discussed above, the Γ - X_z mixing at the AlAs/GaAs interface is considerably stronger than Γ - X_{xy} mixing. Fig 3a shows a representative EL spectrum from the 60Å sample at 1.740V. The spectrum differs very considerably from that obtained from the wider barrier samples at the equivalent forward bias. The feature labelled $e_b^{LO}A_x^0$ is identified as arising from e_xA recombination of ballistic electrons in the collector, since it is accompanied by characteristic LO_x^{Ga} phonon satellites, labelled $e_b^{LO}A_x^i$ ($i=1,2,\dots$) at multiples of 36meV to lower energy. At ~ 12 meV to higher energy than $e_b^{LO}A_x^0$ is an intense line labelled $e_b^{LO}H_z$ which, following the previous discussion, is attributed to ZP excitonic recombination of X_z electrons in the barrier with the hole accumulation layer. Due to the stronger X_z - Γ mixing the ZP line is expected to be several orders of magnitude stronger than any MC phonon satellites, which are consequently not observed [11]. The ballistic electron population in the collector is produced by direct injection from the lowest X_z quasi bound state, without MC phonon assistance.

The EL spectra from this sample are qualitatively similar to those obtained from single barrier Al_xGa_{1-x}As ($x=0.38$) structures [8], except that the ballistic population is injected from the lowest X_z state of the barrier, and not from the emitter distribution directly. A much weaker LO_x^{Ga} phonon cascade of the $X_z/e_b^{LO}H_z$ line, labelled $e_b^{LO}H_z$, is also observed. As discussed previously this series arises from the recombination of quasi ballistic electrons close to the barrier, with the hole accumulation layer.

At forward bias of 1.783V and 1.786V, the EL spectrum of the 80Å sample in figure 3a exhibits a sudden change of character. The ZP line becomes more intense relative to the γ_{xy}^i satellites. In addition a very weak feature labelled LO_x^{Ga} is observed, at 36 ± 2 meV to lower energy. We attribute the increase in intensity of the ZP line [11], and the appearance of a zone centre phonon satellite as being due to a change in nature of the lowest confined X state in the barrier, from X_{xy} to X_z . This is a consequence of the greater Stark shift of the heavier X_z state relative to the X_{xy} state with increasing bias. For $V > 1.786$ V the interpretation of the EL spectrum is complicated by the observation of features arising from X_{xy} and X_z states simultaneously, as seen in fig 3 at 1.820V. The lowest X_{xy} and X_z ZP transitions are less than 4meV apart at this bias and are not resolved. However, EL satellites arising from sets of both symmetry are observed on the figure.

In summary, transport and EL studies have permitted very clear identifications of the tunnelling mechanisms through AlAs single barrier structures. We have shown that tunnelling in the indirect gap barrier structures results both from elastic transfer via X_z states and phonon assisted transfer via X_{xy} states. The tunnelling process has been shown to be strongly sequential in nature.

References

- [1] E.E.Mendez, L.L.Chang, Surface Science 229 (1990) 173-176
- [2] D.Landheer, H.C.Liu, M.Buchanan, R.Stoner, Appl. Phys. Lett. 54 (18) (1989).
- [3] R.Beresford, L.F.Luo, W.I.Wang, Appl. Phys. Lett. 55 (15) (1989).
- [4] S.Adachi, J.Appl. Phys. 58 (3) (1985).
- [5] H.W. Van Kesteren, E.C. Cosman, Phys. Rev. B 39 (1989).
- [6] G.A.Toombs, F.W.Shead, Electronic properties of Multilayers and Low-Dimensional Semiconductor Structures, Plenum (1990).
- [7] S.A.Lyon,C.L.Petersen, Semicond. Sci. Technol. 7 (1992).
- [8] R.J.Tessier, J.W.Cockburn, J.J.Finley, M.S.Solntick, P.D.Buckle and D.J.Mowbray, Phys Rev B 51 8 (1995).
- [9] L.Eaves, G.A.Toombs, F.W.Shead, C.A.Paying, M.Leadbeater, Appl. Phys. Lett. 52 212 (1988).
- [10] E.Finkman, M.D.Sturge, M.-H.Meynadier, R.E.Nahory, M.C.Tamargo et al, J Lumim. 39 (1987) 57-54.
- [11] P.Dawson, I.Foxon, H.W.Van Kesteren, Semicond. Sci. Technol. 5 (1990).

Interband Tunneling of Holes through Single-Barrier Nanostructures

Masato MORIFUJI, Kenji TANIGUCHI and Chihiro HAMAGUCHI

Department of Electronic Engineering, Faculty of Engineering, Osaka University
Yamada-oka, Suita, Osaka 565, Japan

Abstract

Tunneling of holes through single-barrier structures is theoretically studied. Due to multi-band nature of valence band edge, it is necessary to take into account several paths of tunneling between bands with different effective masses. Calculated tunneling coefficients for GaAs/AlAs/GaAs and Si/GaAs/Si structures demonstrate that the interband tunneling is also affected by phase difference between amplitudes through different paths when in-channel states are coherent. Effect of such interference is discussed.

1. Introduction

Hole states in many semiconductors are considered to be unfavorable for device application, because they usually have heavier effective masses than electrons. Thus, tunneling phenomena of holes have been rarely studied neither theoretically nor experimentally, in contrast to electronic states which attract much interest.

In zinc-blende semiconductors, the valence band edge consists of two bands with different effective masses: the heavy-hole (hh) band and the light-hole (lh) band. There should be a mixing between these bands due to a hetero-junction or a potential drop, since an effective mass specifies a state only when translational symmetry exists. Such effect of interband mixing will be larger for holes than for electrons because of the multi-band nature, and may make the tunneling phenomena complicated. We have to take the mixing between different bands into account accurately and to consider tunneling paths between different bands.

2. Model

The system we consider is a single-barrier structure with *p*-type doped three-dimensional electrodes. Figure 1 shows a schematic band structure of the valence band of the system under an applied voltage. In the electrodes denoted by I and III, two bands with different effective masses lie at the valence band edge, *i.e.* the heavy-hole band and the light-hole band, which are denoted by parabolic curves. In addition to them, the spin-orbit split-off (so) band lies below the valence band edge. In an equilibrium, holes distribute in both of the hh band and the lh band as schematically denoted by thick part of the curves.

Holes which are injected from the region I tunnel through the potential barrier II to the region III with a certain probability. Usually tunneling current is calculated in the

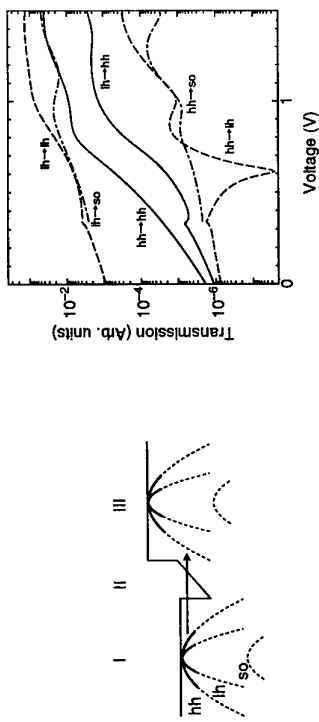


Figure 1: Schematic picture of band structure of the system. Parabolic curves denote the hh, lh and so bands, whose thick part indicates the region where holes exist.

framework of an effective mass approximation. For holes, however, conventional effective mass approximation will be insufficient to describe the mixing between bands with different effective masses. On the other hand, a tight-binding theory has advantage to describe the interband mixing, because no effective mass is used for specifying states. In this study, we calculated tunneling coefficient using the theory developed by Schulman *et al.*[1] This method based on the tight-binding picture has a capability to take into account the interband mixing associated with a hetero-junction or a potential drop. Using the tunneling coefficients, we evaluated current density within an elastic multi-channel scattering theory.[2]

In this study, we calculated the tunneling current using

$$J(V) = \frac{2e}{(2\pi)^3 \hbar} \sum_{n'} \int d^2 k_{\parallel} / \int dE \left| \sum_n t_{n,n'}(\mathbf{k}_{\parallel}, E) \right|^2 \frac{v_{n,k}}{v_{n',k}} [f_{in}(E_{n,k_{\parallel}} - V) - f_{in}(E_{n',k_{\parallel}})]. \quad (1)$$

In eq. (1), $t_{n,n'}(\mathbf{k}_{\parallel}, E)$ is a tunneling coefficient from the n th band in the region I to the n' th band in the region III (n stands for hh and lh, and n' for hh, lh and so). V is a total potential drop through the region II and $f_{in}(un)(E_{n,k_{\parallel}})$ is the Fermi distribution function. For single-band tunneling, phase of tunneling coefficient is trivial because only an absolute value of tunneling coefficient contributes to current density. On the other hand, when we consider multi-channel tunneling, the phase change during tunneling may have an important role. We consider two tunneling paths from different two states to one state such as $hh \rightarrow hh$ and $lh \rightarrow hh$. Since tunneling coefficients t 's are complex numbers, t 's can be written as $t_{n,n'} = |t_{n,n'}| e^{i\phi_{n,n'}}$. The phase of $t_{n,n'}$ is regarded as a phase shift of a state during tunneling. If an in-channel state from hh and that from lh are coherent, that is, they have a certain phase difference, an out-channel hh state will be a superposition of two kinds of components

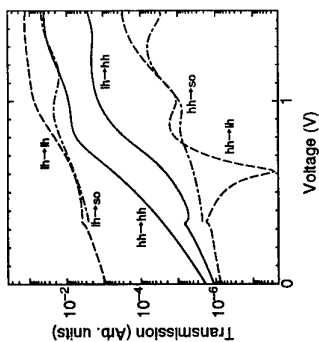


Figure 2: Calculated transmission coefficients $|t_{n,n'}|^2$ for GaAs/AlAs/GaAs as functions of applied voltage.

as $|t\psi_{hh} + t'\psi_{hh}|^2$ instead of $|t\psi_{hh}|^2 + |t'\psi_{hh}|^2$. Thus the interference effect will be seen; tunneling current density is affected by the phase difference between $t\psi_{hh}$ and $t'\psi_{hh}$. In this study, we consider that the hole density is high enough ($1.0 \times 10^{19} \text{ cm}^{-3}$) to degenerate. Furthermore, we assume that the temperature is low enough so as to regard the Fermi distribution function as a step function.

3. Results and Discussion

3.1 GaAs/AlAs/GaAs structure

In this section, we show calculated results for a GaAs/(AlAs)₁₀/GaAs single-barrier structure. Figure 2 shows calculated tunneling coefficients $|t_{n,n'}|^2$ for a state $\mathbf{k}_{\parallel} = 0$ as functions of applied voltage for in-channel state energy -0.2 eV . This energy corresponds to the Fermi energy when hole density is about $1.0 \times 10^{19} \text{ cm}^{-3}$. Gross feature of the curves is similar to that of a curve calculated by Mendez for electron tunneling within the effective mass approximation.[3] We can see that $|t_{ll,ll}|^2$ is largest at any applied voltage reflecting the light effective mass. $|t_{hh,hh}|^2$ is small at low voltages, while it becomes important when the voltage is about 1 V . Other interband components are small at any voltage. All of the tunneling coefficients show oscillatory behavior with increasing voltage. The oscillation occurs associated with barrier narrowing due to applied voltage and is known as Fowler-Nordheim tunneling. These results may suggest that interband tunneling is unimportant. However, from the calculation, we found that the interband tunneling coefficients increase rapidly with increasing \mathbf{k}_{\parallel} . This indicates that we have to take \mathbf{k}_{\parallel} -integration carefully when we consider the interband tunneling.

Current density vs. applied voltage is shown in Fig. 3. In this figure the solid curve shows the current density evaluated by using eq.(1). The dot, dashed and dot-dashed curves show the partial current density for hh-, ll- and so-out-channel state, respectively. From these curves, we see that tunneling current related to the ll states has largest component. The other components are small comparing with ll related current. Although $|t_{hh,so}|^2$ has a large value, tunneling current related to the so band is not so large. This is because the so states have smaller \mathbf{k} -vector comparing with hh and ll states at the same energy. However, the interband tunneling current becomes important for the voltage larger than 0.4 V .

3.2 Si/GaAs/Si structure

In Si, the hh effective mass and ll effective mass is close comparing with GaAs. This makes us expecting large interband tunneling coefficients for Si/GaAs/Si structure. Although some structural parameter at Si/GaAs interface are still ambiguous, we adopted in this calculation the valence band offset between Si and GaAs 0.23 eV [4] and introduced strain in the GaAs layer about 5%. Calculated current density vs. applied voltage for Si/(GaAs)₁₀/Si is shown in Fig. 4. In this figure the solid curve shows the current density evaluated by using eq.(1), where interference effect is considered. The dot curve is the current density when the interference is neglected, that is, coherency of in-channel states is not considered. The dot-dashed curve shows the current density where the interband tunneling is neglected, which is much smaller than other curves.

Except the magnitude, these curves are almost the same. The peak at 0.04 V is due to the band edge of the so band. Weak oscillation for voltage larger than 0.5 V is due to the Fowler-Nordheim tunneling. From these curves, we see that the interband mixing strongly enhances tunneling current and the interference effect results in an modulation of the current density.

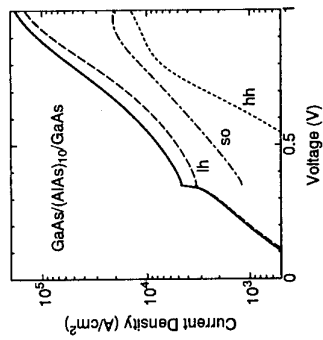


Figure 3: Calculated current density for GaAs/(AlAs)₁₀/GaAs as functions of applied voltage. Dot-, broken- and dot-dashed-curves denote component of current as out-channel state of heavy-hole, light-hole and spin-orbit split-off band, respectively.

Acknowledgements

This work is supported by a Grant-in-Aid for Scientific Research on Priority Area, ‘Quantum Coherent Electronics: Physics and Technology’ from the Ministry of Education, Science and Culture, Japan. M. M. acknowledges the support by a Grant-in-Aid for Encouragement of Young Scientists from the Ministry of Education, Science and Culture, Japan.

References

- [1] J. N. Schulman and Y.-C. Chang, Phys. Rev. **B 27**, 2346 (1983).
- [2] A. Di Carlo, P. Vogl and W. Pötz, Phys. Rev. **B 50**, 8358 (1994).
- [3] E. E. Mendez, Proc. of NATO Int'l School, Physics and Applications of Quantum Well and Superlattices, (1987).
- [4] R. S. List and W. E. Spicer, J. Vac. Sci. Technol. **B 6**, 1228 (1988).

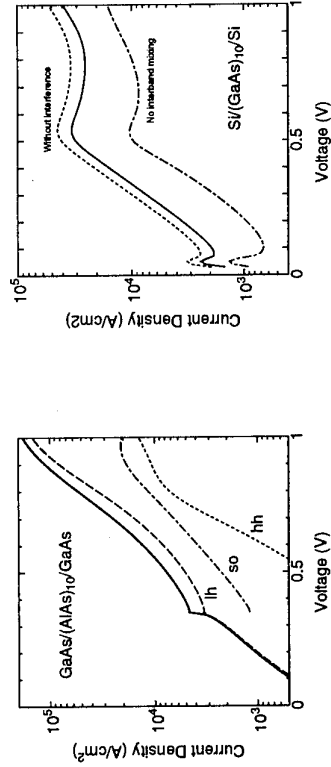


Figure 4: Calculated current density for Si/(GaAs)₁₀/Si as functions of applied voltage. Dot-, broken- and dot-dashed-curves denote component of current as out-channel state of heavy-hole, light-hole and spin-orbit split-off band, respectively.

Interface composition dependence of the band offset in InAs/GaSb

M.S. Daly, D.M. Symons, M. Lakrimi, R.J. Nicholas
 N.J. Mason, P.J. Walker
*Clarendon Laboratory, Physics Department, University of Oxford,
 Parks Road, Oxford, OX1 3PU, U.K.*

Abstract

We have performed 4K magnetotransport measurements on intrinsic InAs/GaSb superlattices (SL) under hydrostatic pressure. Through careful configuration of the growth we are able to produce samples that have differing interface monolayers (either InSb or GaAs). Analysing the data to calculate the band overlap (Δ), we find that InSb-like samples have an overlap about 30 meV larger than GaAs-like in good agreement with recent theoretical predictions.

The technologically essential problem of predicting the band line-ups in semiconductor heterostructures has received much interest recently. A key issue in the determination of the offset is the role played by the interface layer. In type I systems such as GaAs/AlGaAs the offset is notoriously hard to measure, in the InAs/GaSb type II system we have chosen to study however we are more fortunate. Due to its unusual crossed gap band alignment the InAs conduction band (CB) lies lower in energy than the GaSb valence band (VB), the system is semimetallic for long period structures with intrinsic carriers being transferred from the GaSb VB to the InAs CB. The concentration of intrinsic carriers and thus the electrical properties are very sensitive to the amount the bands overlap and this makes the offset much easier to measure and the system excellent for testing theories of band line-ups in heterostructures. Applying pressure to the InAs/GaSb system[1] leads to a decrease in the band overlap, and thus the transferred electron and hole densities. In this paper we have studied the magnetotransport of a series of intrinsic semimetallic SLs as a function of pressure. This allows us to deduce the band overlap (Δ) and its variations with pressure ($d\Delta/dP$). Evidence is presented that the interface layer composition has a significant effect on the overlap.

InAs and GaSb share no common atom, so both anion and cation change across the interface. Thus it is possible to produce two distinct types of interface with, in the ideal case, either an InSb or GaAs monolayer at the interface depending on the order in which the group III and group V elements are switched during the growth. The samples studied were grown by atmospheric pressure MOVPE, which is found to produce material with much lower levels of extrinsic charge than those grown by MBE[2]. Different types of switching sequences were also found to indirectly affect the overlap through the quality of the interface. Atomic layer epitaxial (ALE) growth at the interface, where only one species is switched into the reactor at any one time was found to give a more clearly defined difference between the interface quality and the electrical properties than those grown by 'binary' interface switching, where pairs of species are switched together[3]. Detection of the different interface modes via Raman spectroscopy of thinner layer samples has demonstrated the ability to produce material with well controlled interface compositions essential for this present study[4]. Both 20 and 80 period SLs were studied with layer thicknesses of 220 Å (InAs)/180 Å (GaSb). A summary of the sample characteristics and results is shown in Table 1.

The magnetoresistance and Hall resistivity were studied up to 15T at 4K for a series of pressures, the results of the 80 period InSb sample are shown in Fig.. 1. The Hall resistance shows strong curvature at low fields characteristic of a system with both electron and holes present. The carrier concentrations are obtained from classical fitting of the low field dependence of the Hall resistivity. Fourier transforms (FFT) of the magnetoresistance oscillations at lower fields confirm that all 20/80 layers of the superlattices are active and thus from ρ_{xy} and ρ_{xx} we can obtain the density per layer of electrons and holes in the structure. The layer thicknesses have been measured by TEM and the band overlap is then calculated self-consistently using the method of Symons *et al*[5]. The full band overlap is the sum of the electron and hole Fermi energies and confinement energies and must be calculated self-consistently using the carrier densities and the superlattice periodicity, because of the large band bending that occurs within the layers.

The electron carrier densities calculated from the low field FFTs are shown in Fig.. 2. These show consistently higher densities for the InSb-like interfaces, with the densities approaching zero at 14 kbar for InSb and 10 kbar for GaAs samples. The InSb-like samples are also better electrically with mobilities almost 10 times larger and a much lower net extrinsic charge density. The band overlaps calculated from the fitted data for a number of samples are shown in Fig. 3. Firstly it can be seen that the zero pressure band overlap for the GaAs interface is considerably smaller than that for InSb. The difference in zero pressure overlap being about 30meV, $d\Delta/dP$ is approximately the same for both samples -9.5±1meV/kbar which is consistent with the shift of the bulk InAs band gap with pressure. A second method of analysing the influence of the pressure is to plot the positions of the maxima in the large oscillations which are observed in the Hall resistivity as a function of magnetic field and pressure. The appearance of the strong oscillations is a characteristic feature of highly compensated semimetallic systems[6]. Maxima have been found to occur in ρ_{xy} whenever the Fermi energy lies in the extended states where the Nth. Landau levels of the electrons and the holes cross each other. Thus as we decrease the overlap with pressure these features scale down in field, so that extrapolating the positions of the maxima to zero field should yield the transition pressure where the confinement energy of the electrons moves above that of the holes and the structure becomes semiconducting. This transition from semimetallic to semiconducting behaviour can be clearly seen in Fig..1, where both ρ_{xx} and ρ_{xy} become very large above 10T at 11.5 kbar as the last electron and hole levels uncross with field and we are just left with a single residual 2DEG of low mobility electrons giving some conventional single carrier quantum Hall features. Plots of the field dependence of the maxima are shown in Fig.. 4 for the two 80 period samples. These show zero gap states of 10 and 14 kbar for the GaAs and InSb interfaces respectively, in excellent agreement with the extrapolations of the electron FFT density with pressure shown in Fig.. 2. The values for Δ and $d(\Delta)/dP$ are summarised in table I. Clearly the zero pressure overlap depends on the interface composition. This would not be the case if the band offset depended on the parameters of the bulk constituents alone so that there must be a contribution from the interface layer to Δ . The difference in the bond lengths between In-Sb and Ga-As is ~14%, and both are significantly (~7%) different from In-As and Ga-Sb. This will induce strains in the interface monolayer that may also influence the strength of the dipole and thus Δ for each interface.

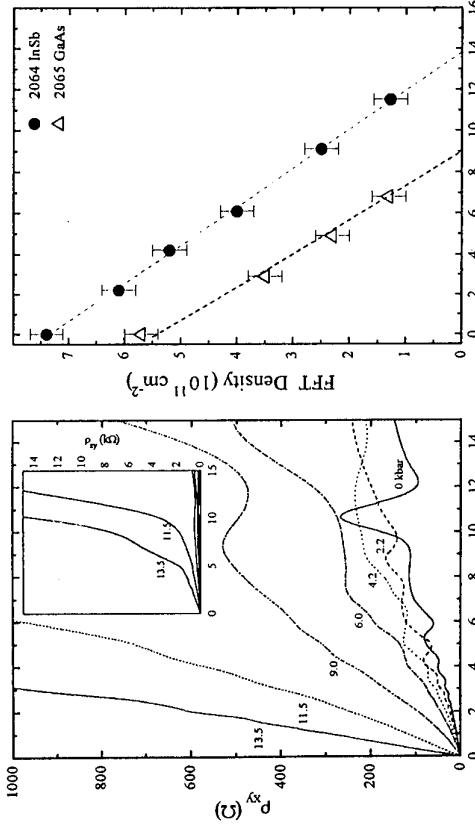


Figure 1. The Hall resistance to 15T as a function of pressure for sample 2064. The inset shows the divergence of R_H after the bands have uncrossed.

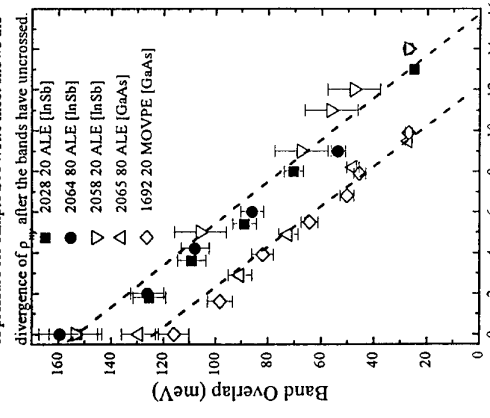


Figure 3. The band overlap as a function of pressure for the two differing interface types. InSb being 30(5) meV larger than GaAs. The slope is the same within error.

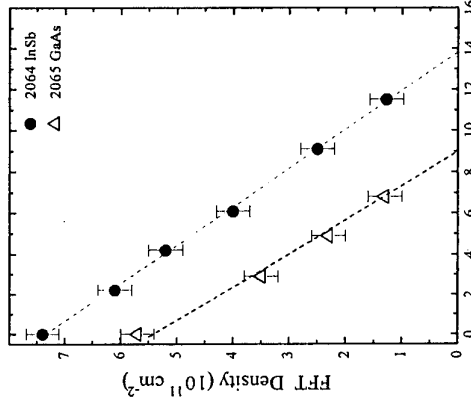


Figure 2. The electron densities determined from FFTs of ρ_{xx} 2064 (InSb) has a clearly higher density than 2065 (GaAs).

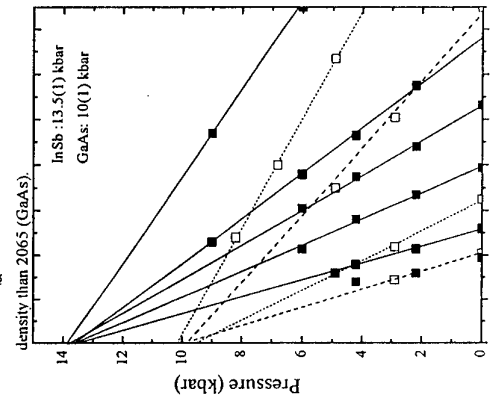


Figure 4. Extrapolations of maxima in ρ_{xy} as a function of pressure. Zero gap state occurs at higher pressure for InSb interfaces implying a larger overlap.

Recent calculations of the band offset for [001] interfaces[7],[8] have led to the conclusion that in systems where neither binary compound shares common elements the offset is not necessarily the same for each interface type. Meyer *et al.*[9] measuring MBE samples conclude that InSb interfaces produce larger overlaps by 14(5) meV, somewhat lower than our result, Khan-Cheema *et al.*[10] on the other hand using perpendicular transport measurements under pressure on heterojunctions grown in the same reactor find evidence of a larger Δ for InSb interfaces consistent with our results. Theoretically it is predicted that in this system InSb-like interfaces will have overlaps 30-45meV higher than GaAs-like interfaces which is in good agreement with our findings[7],[8]. Our results show $d(\Delta)/dP$ to be the same within experimental error for both interface types and are close to the predictions of the model solid theory of Van de Walle[11] of 10.1 ± 3 meV/kbar. They also agree with recent measurements by Symons *et al.*[5] on similar samples.

In conclusion, we have grown samples with good quality interfaces biased to either InSb or GaAs monolayers. Analysis of the magnetotransport measurements of a series of SLs with both types of interface shows the InSb to have superior electrical properties, more intrinsic charge and a band overlap that is ~30meV larger than that for GaAs. This difference in Δ may provide the possibility of growing in-built electric fields into structures for improved device characteristics. The results for the difference in overlap for the best samples are in excellent agreement with recent theoretical predictions of the interface composition dependence of the band offset in this system.

This work was funded by the Engineering and Physical Sciences Research Council of the U.K.

Table 1

Sample	Structure Type	Switch Sequence	Interface Type	$N_{\text{eff}}(0)$	$\frac{dN(0)}{dP}$	$\frac{\mu_x(0)}{dP}$	$\frac{\mu_y(0)}{dP}$	$\frac{d\mu_y}{dP}$
2064	80 Periods	ALE	InSb	7.3	7.2	115.490	8.140	-9.4
2058	20 Sand	ALE	InSb	6.9	6.9	54.719	9.491	-9.5
2078	20	ALE	InSb	7.0	6.9	94.240	11.560	-154.5
2065	80	ALE	GaAs	6.2	3.7	15.301	2.340	-129.4
1692	20	BINARY	GaAs	5.1	2.75	-	116.0	-9.0

References

- [1] J. Beerens, G. Grégoris, S. Ben Amor, J.C. Portal, E.E. Mendez, L.L. Chang, L. Eskil *Phys. Rev. B* **36** 4742 (1987); *ibid. B* **35** 3039 (1987)
- [2] M. Lakrimi *et al.* *J. Cryst. Growth* **124** 395 (1992)
- [3] G.R. Booker *et al.* *J. Cryst. Growth* **145** 778 (1994)
- [4] S. Lyapin, P.C. Klipstein, N.J. Mason, P.J. Walker, *Phys. Rev. Lett.*, **174** 3285 (1995)
- [5] D.M. Symons *et al.* *Phys. Rev. B* **49** 16614 (1994)
- [6] R.J. Nicholas *et al.* *Physica B* **184** 268 (1993)
- [7] Y. Foulon, C. Priester, *Phys. Rev. B* **45** 6259 (1992)
- [8] R.G. Dandrea, C.B. Duke *J. Vac. Sci. Technol. B* **10** 1744 (1992)
- [9] J.R. Meyer *et al.* *Proc. of 22nd ICPS, World Scientific* **1** 783 (1994) ed. D.J. Lockwood
- [10] U. Khan-Cheema, P.C. Klipstein, N.J. Mason, P.J. Walker, G. Hill *to be published.*,
- [11] C.G. Van de Walle, *Phys. Rev. B* **39** 1871 (1989)

Simulation of Bloch oscillations in a finite semiconductor superlattice

José Eduardo Manzoli* and Oscar Hipólito
Instituto de Física de São Carlos - USP
CP 369, 13560-970, São Carlos, SP, Brasil

Abstract

Using a self-consistent field approximation including exchange and correlation effects we calculated the mini-band, eigen-states, eigen-values, charge densities and the evolution of the electron wave packet in a finite superlattice of GaAs - Al_{0.35}Ga_{0.65}As with doped layers.

The recent observation of Bloch Oscillations and Tamm States in superlattices [1-5] has pointed out to a revolution in photodetectors, optical switches and infra-red emitters [6]. The infra-red radiation is usually explained as a charge oscillation whose frequency is proportional to the electric field through the heterostructure.

In this work we report a self-consistent numerical simulation to study charge oscillations in a finite superlattice (FSL) with the presence of a Tamm state in order to initially localize the electrons. By applying an electric field, the electronic wave packet will oscillate through the superlattice with the emission of resonant tunneling terahertz radiation. As far as we know this is the first calculation for the profile of an infra-red emitter without any optical pumping. A schematic view of the FSL is shown in Fig. 1.

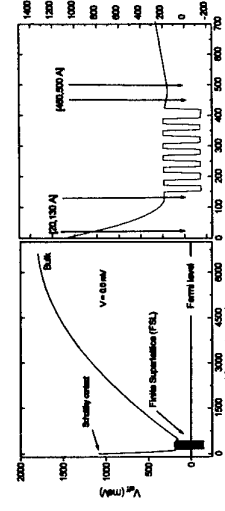


Figure 1: Schematic potential profile for a finite superlattice heterostructure. The system consists of six periods of GaAs (20 Å) quantum wells embedded Al_{0.35}Ga_{0.65}As (20 Å) barriers plus a wider well of GaAs (30 Å) - a Tamm well. In the right side of this figure the donor doping layers limits are shown by the brackets with donor densities of 8.25x10¹² cm⁻² [20, 130 Å] and 7.5x10¹¹ cm⁻² [450, 500 Å]. In the whole structure the residual acceptor doping density is 5x10¹⁵ cm⁻³.

The calculation is performed for many combinations of the FSL parameters, temperatures and doping densities in order to get: (a) only the Tamm state populated without the applied voltage V, (b) the sub-bands of the mini-band closed enough in such a way that a small voltage variation allows resonances, (c) a small size of the FSL with linear z-dependence in $V_{eff}(z)$ in order to generate the steps of the Stark ladder, (d) a minimal doping to avoid a bump in the V_{eff} which would drain the states.
We solve the time-dependent Schrödinger's equation by using the Split Operator technique[7,8],

$$\left[-\frac{\hbar^2}{2} \frac{\partial}{\partial z} \frac{1}{m^*(z)} \frac{\partial}{\partial z} + V_{eff}(z,t) \right] \Psi_n(z,t) = i\hbar \frac{\partial}{\partial t} \Psi_n(z,t) \quad (1)$$

where $V_{eff} = V_h + V_{ex} + V_s$ is the effective potential, V_h is the Hartree potential obtained self-consistently through Poisson's equation, V_{ex} is the exchange and correlation potential[9], and V_s is the FSL potential profile.

The real time evolution of the wave packet Ψ is then obtained numerically by solving Eq.1. For the numerical procedure, the time is discretized in intervals Δt .

In the Split Operator method, if we change (Δt) by (- Δt) we end up with the so called imaginary time evolution. In doing so we change the Schrödinger's equation to a diffusion-equation like with a wave function converging to the ground-state. By starting with a certain number of initial wave functions orthonormalized at every time step, they will converge to the first, second, etc. eigen-states.

The numerical calculation was performed for several heterostructures profiles. One of these profiles is shown in Fig.2.

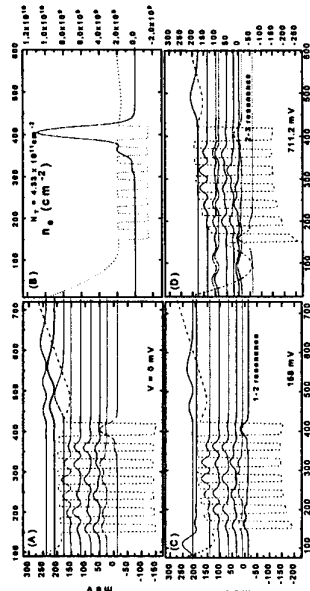


Figure 2: The selected finite superlattice heterostructure. (A) the potential profile and the electronic probability densities aligned with the respective sub-band. Note the localization of the Tamm State (ground-state). (B) the electronic charge density in the Tamm sub-band, the only one populated. (C) resonance of the first and second sub-band, note the delocalization of the Tamm state. (D) the second resonance. The bump in the doping layer at the left begins to drain the eigen-functions.

It can be used as an infra-red emitter under the resonance voltage as indicated in Fig.3 by the arrow A.

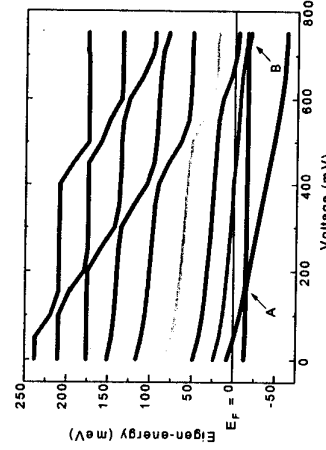


Figure 3: Modification of the sub-bands as function of the applied voltage. Note the intersections with the Fermi level and the resonances, where the formation of bound and anti-bound states occurs.

In our proposal, the wave packet is an initial Tamm state, Ψ_0 , which oscillates, by applying a suddenly voltage V. The oscillatory motion of this wave packet in real time can be seen in Fig.4. This oscillation can be interpreted as a movement of the electrons initially in the wider well. Due to the suddenly change in the Hamiltonian by the applied voltage, the wave function is not an eigen-function any more. This charge oscillation radiates in the far infra-red spectra with the emission of 0.6 THz radiation.

The numerical technique is of interesting for the studies of quantum well structures with doping layers and the simulation presented here could be important to avoid expensive production of samples.

Acknowledgment

We are grateful to Centro Nacional de Supercomputação of UFRGS.

* PhD FAPESP fellow.

References

- 1 I.Tanaka, M.Nakayama, H.Nishimura, K.Kawashima, K.Fujiwara - *Solid-State Electronics* - V37, N4-6, pp 863-866, 1994.
- 2 E.E.Mendez, G.Bastard - *Physics Today* - 06/1993 - pp 34.
- 3 C.Waschke, H.G.Roskos, K.Leo, H.Kurz, K.Köhler - *Semicond. Sci. Technol.* - 9 (1994) 416-418.
- 4 C.Waschke, H.G.Roskos, R.Schwendler, K.Leo, H.Kurz, K.Köhler - *Physical Review Letters* - 24/05/1993 - V70, N21, pp 3319.
- 5 H.Ohno, E.E.Mendez, J.A.Brum, J.M.Hong, F.Agulló-Rueda, L.L.Chang, L.Esaki - *Physical Review Letters* - 21/05/1990, V64, N21, pp 2555.
- 6 V.Ryzhii, M.Ershov - *Solid-State Electronics* - V38, N1, pp 149-150, 1995.
- 7 M.D.Feit, J.A.Fleck Jr. - *J. Chem. Phys.* - 80 (6), 1984, pp 2578.
- 8 A.Goldberg, H.M.Schey, J.L.Schwartz - *Am. J. Phys.* - V35, N3, 1967, pp 177.
- 9 F.Stern, S.Das Sarma - *Phys. Rev. B* - 30 (2), 840, 1984.

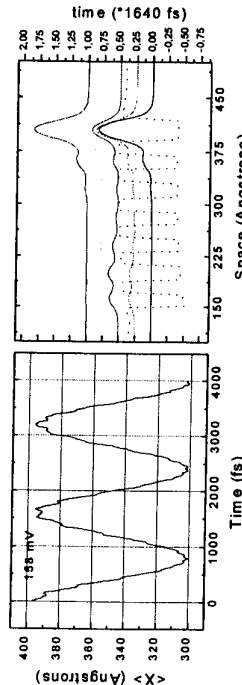


Figure 4: FSU under the first resonance. Expected position of the Tamm state as function of time. Probability density of this wave package in some selected instants.

In conclusion we have numerically simulated a charge oscillation in a proposal finite superlattice semiconductor where for the emission of terahertz radiation one does not need of any optical pumping arrangement.

Transfer Efficiency of Hot Electrons in a Metal(CoSi₂)/Insulator(CaF₂) Quantum Interference Transistor

T. Suematsu, W. Saitoh, Y. Kohno, K. Mori, M. Watanabe and M. Asada

Department of Electrical and Electronic Engineering, Tokyo Institute of Technology,
2-12-1, O-Okayama, Meguro-ku, Tokyo 152, Japan

Abstract

We report on the transfer efficiency of hot electrons with monochromatic energy across a nanometer-thick metal epilayer in a metal(CoSi₂)/insulator(CaF₂) quantum interference transistor. The transfer efficiency from emitter to collector is estimated to be more than 0.96.

Introduction

Metal-insulator (M-I) superlattices are very interesting due to the very large conduction-band discontinuity (> 10 eV) in comparison with semiconductor heterostructures, and therefore remarkable quantum effects are expected. In addition, it is also attractive for ultrahigh-speed devices [1-3], due to the higher carrier density in the metal and the lower dielectric constant of the insulator resulting in a high transconductance and a short charging time suitable for high-speed operation of electronic devices [3]. We have developed an epitaxial growth technique for M-I superlattices [4], and have demonstrated resonant tunneling and its device applications [5][6]. Recently, multiple NDRs due to quantum interference of hot electrons through the conduction band of M-I-M structure were observed [7]. Since novel devices can be expected with this quantum interference [3], the transfer efficiency of hot electrons with monochromatic energy across such a superlattice structure is very important for future device applications. In this report, we discuss the transfer efficiency of monochromatic hot electrons from the measured current-voltage ($I-V$) characteristics of a quantum interference transistor.

Experimental

Figure 1 shows the cross sectional view and the conduction-band diagram under bias conditions of the fabricated quantum interference transistor in order to measure the transfer efficiency. In this transistor, electrons with monochromatic energy are injected from the emitter through the quantized level in the 1.9-nm-thick metallic quantum well ($E_N = 13.6$ eV from the bottom of the conduction-band edge) into the conduction band of the collector barrier region. Strong quantum interference is exhibited between the two M-I interfaces in the same manner as a Fabry-Perot optical interferometer. This is due to the very large conduction-band discontinuity at the CoSi₂/CaF₂ interface (~ 15 eV), causing a sharp change in the transmission probability for the hot electron wave. When this sharp change in the transmission probability is applied to controlling the electrons going through the collector-barrier region by changing collector-base voltage V_{CB} , the collector current I_C is expected to exhibit multiple NDRs with respect to V_{CB} as a reflection of

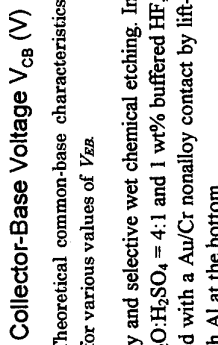
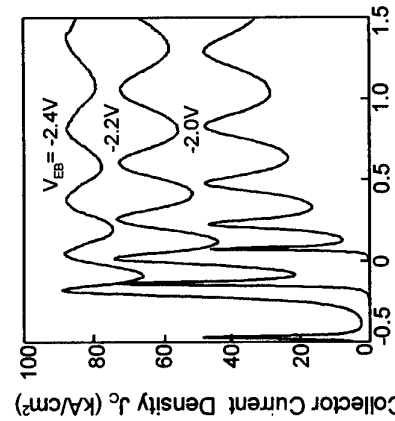
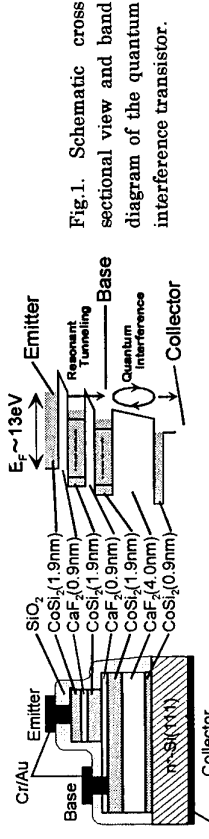
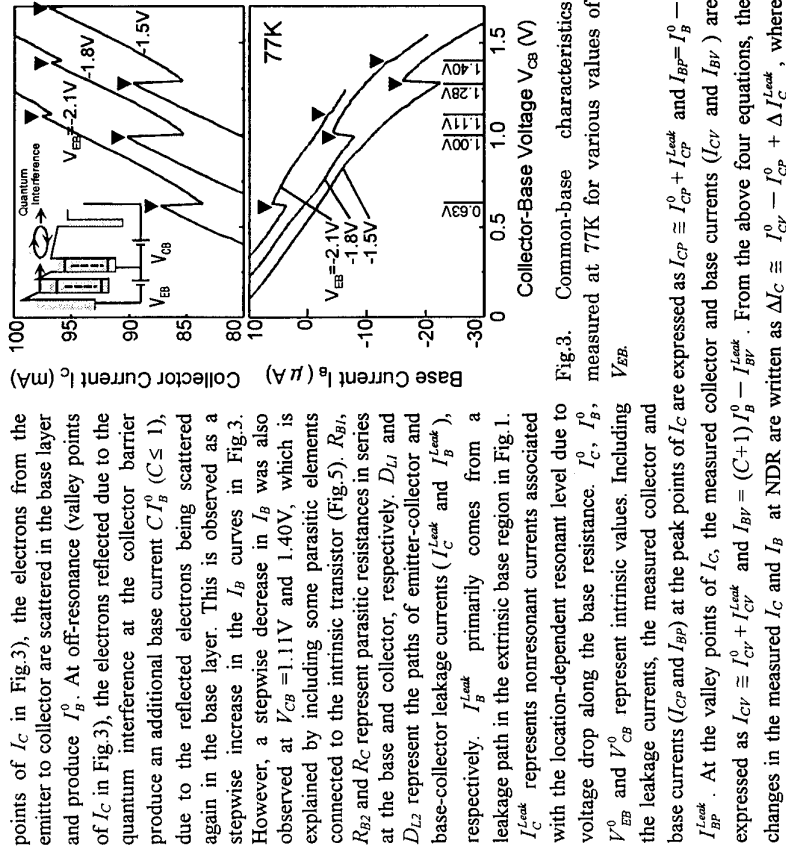


Fig.1. Schematic cross sectional view and band diagram of the quantum interference transistor.

Results and discussion

Figure 3 shows I_C and I_B at 77 K as a function of V_{CB} for various values of V_{EB} . Multiple NDRs are seen in I_C due to the quantum interference mentioned above. There are some degradations observed: low peak-to-valley current ratio at NDR, reverse base current and unsaturated I_C with respect to V_{CB} . Analysis, taking several parasitic elements into account (e.g., base resistance, substrate resistance and leakage currents connected to the intrinsic transistor), can explain the observed characteristics well [8]. Negative I_B is due to leakage current through a base-collector leakage path.

The stepwise change in I_B is interpreted as follows. As shown in Fig. 4, at resonance (peak



$\Delta I_C^{Leak} = I_{Cv}^{Leak} - I_{Cp}^{Leak}$, and $\Delta I_B = C I_B^0 - \Delta I_B^{Leak}$, where $\Delta I_B^{Leak} = I_{Bv}^{Leak} - I_{Bp}^{Leak}$. At the points of NDR, the voltage drop in R_C decreases rapidly due to the decrease in I_C . This results in the stepwise increase in V_{CB}^0 ($\equiv -R_C \Delta I_C$) and therefore, I_C^{Leak} and I_B^{Leak} are increased at NDRs, leading to ΔI_C^{Leak} and $\Delta I_B^{Leak} > 0$. Thus, the direction of the shift in I_B at NDRs depends on the magnitude of I_B^0 and ΔI_B^{Leak} . Since I_B^{Leak} increases with V_{CB} , the small stepwise decrease in I_B is obtained in high V_{CB} as in Fig.3.

From the above discussion, the transfer efficiency α from emitter to collector is estimated to be $I_{CP}^0 / (I_{CP}^0 + I_B^0) \approx 1 - I_B^0 / I_{CP}^0 \geq 1 + (\Delta_B + \Delta I_B^{Leak}) / C \Delta I_C$. Δ_B and ΔI_B^{Leak} are obtained from Fig.3. ΔI_C^{Leak} and C are calculated as follows using the NDR characteristics at $V_{CB}=0.63V$. It seems reasonable to assume that I_B^0 is saturated as I_C^0 of Fig.2 when $V_{CB}^0 > 0$ except at NDR positions. The saturated value of I_B^0 is estimated to be about $20\mu A$ from the I_B curves extrapolated to $V_{CB}=0$, where I_B^{Leak} is negligible. Thus, $\Delta I_B^{Leak} \leq 20\mu A$, as $\Delta I_B^{Leak} \leq I_B^0$ when $I_B > 0$. As for the value of C , $\Delta I_B^0 = C I_B^0 > \Delta_B$. Considering this and $I_B^0 \leq 20\mu A - \Delta_B = 17\mu A$ at the NDR, $C \geq 0.17$ is obtained. Therefore, as an example, $\alpha \geq 0.96$ is obtained at $V_{CB}=0.63V$. Assuming the expression $\alpha \sim \exp(-W/L_B)$, where W is the base width and L_B is the mean-free path, L_B is estimated to be more than $50nm$. Although this value limits the length of wave injected into the collector barrier, it is long enough for strong quantum interference at the M-I-M structure if scattering in the CaF_2 layer is negligible. Such a high value of α may be due to the very thin single-crystalline metallic layer.

Conclusions

Transfer efficiency of hot electrons with monochromatic energy across a nanometer-thick metal(CoSi₂) epilayer is estimated to be more than 0.96 from the NDR characteristics of a metal(CoSi₂)/insulator(CaF₂) quantum interference transistor. This fact implies that metal-insulator heterostructures have a potential for future high-speed quantum-effect devices.

References

- [1] C.A.Mead, *J.Appl.Phys.*, **32** (1961) 646.
- [2] M.Helium, *Solid-State Electron.*, **24** (1981) 343.
- [3] T.Sakaguchi et al., *IEICE Trans. E74* (1991) 3326.
- [4] M.Watanabe et al., *J.Electron.Mater.* **21** (1992) 128.
- [5] M.Watanabe et al., *Appl.Phys.Lett.* **62** (1993) 300.
- [6] T.Suematsu et al., *IEEE IEDM Tech.Dig.* (1993) 553.
- [7] T.Suematsu et al., *Jpn.J.Appl.Phys.* **33** (1994) L1762.
- [8] W.Saitoh et al., to be published in *Jpn.J.Appl.Phys.* (1995).

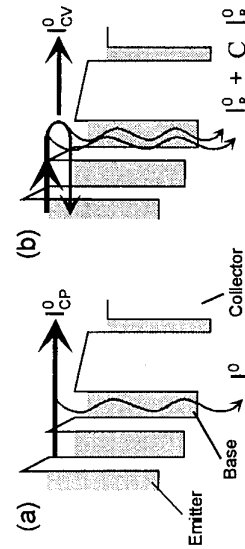


Fig.4. Schematic illustration of electron flow at (a) the peak points and (b) the valley points of I_C in Fig.3.

Resonant Tunneling through Pseudo-Quantum Well in Single-Barrier Heterostructure.

Yu. V. Dubrovskii, T. G. Andersson*, Yu. N. Khanin, I. A. Larkin**, E. E. Vdovin

Institute of Microelectronics Technology and High Purity Materials
Russian Academy of Sciences
Chemogolovka, Moscow District, 142432 Russia.

*Department of Physics, Chalmers University of Technology
S-412 96 Göteborg, Sweden

**Department of Electronics and Electrical Engineering
Glasgow University, Glasgow G12 8QQ, UK.

Resonant tunneling through virtual states in a wide pseudo-quantum well is observed at liquid He temperature. This well is formed in the spacer layer region ($n^+ - GaAs/n^- - GaAs/n^- - AlAs/n^- - GaAs/n^- - GaAs/n^-$). GaAs due to the electron reflection from the main barrier at one side and from the smooth potential drop through the n/n^+ junction in the GaAs at the other side.

The study of ballistic electron transport in GaAs [1] has demonstrated that about 15% of electrons injected through the barrier with energy up to 0.3 eV can travel a distance of more than 70 nm without any scattering and phase breaking process. As a result, a set of different interference phenomena have been observed in tunnelling experiments in heterostructures with wide quantum wells (30 - 100 nm) confined between two barriers [2-8]. In most cases the interference phenomena is due to the electron reflection from the discontinuities of the conductance band edge at the heterointerfaces when the current is normal to the layers.

Current oscillations due to tunnelling through states in wide quantum wells have first been observed by Levi et al [2] and Potter and Lakhani [3]. Some of the oscillations are related to the tunnelling through virtual states, i.e. the states with energy above barrier height. Application of a magnetic field transverse to the tunnelling current induces some additional phenomena. Helm et al. [4] have first observed the appearance of a new oscillations with voltage bias in the magnetic field $B \geq 11$ T ($\vec{B} \perp \vec{J}$). These oscillations are related to tunnelling through hybrid magnetoelectric quantum states in crossed electric and magnetic fields. Further studies of electron transport through wide quantum wells [5,7] have shown different types of oscillations in crossed fields related to the tunnelling into distinct types of magnetoelectric states: "transversing" orbits, "skipping" states, bulk states. Later Fromhold et al. [8] have investigated the energy-level spectrum of electrons in a trapezoidal potential well in the presence of a tilted magnetic field. A distinct series of quasiperiodic resonance's have been observed in the current-voltage tunnelling characteristics which change with tilt angle. The authors relate these resonance's to unstable closed orbits within the chaotic dynamical system.

In this work we study tunnelling resonances in wide pseudo-quantum well restricted by real heterobarrier on one side, and smooth potential drop in conductance band edge through a n^-/n^+ junction in GaAs at the other side (Fig. 1.). Aperiodic oscillations of the tunneling current have been observed as a function of applied voltage bias without magnetic field. We relate these oscillations to the resonant tunnelling through virtual quantum states in the pseudo-well. The application of a magnetic field perpendicular to the tunnelling current suppress the oscillations.

At the same time a new set of oscillations appears due to the tunnelling through hybrid magnetoelectric states. The main difference between our samples and those studied before [2-8] is the absence of one of the barriers which confines the quantum well. In our samples one barrier is replaced by the smooth potential drop in the region of low to high donor concentration due to the step like doping profile in the bulk GaAs. The electron reflection coefficient from the smooth potential drop is enough to observe electron interference in this pseudo-quantum well.

The samples were grown by molecular beam epitaxy (MBE) on a (100)-oriented Si doped n^+ -type GaAs wafer ($N_d = 2 \times 10^{18} \text{ cm}^{-3}$). The structure consists (in the order of growth) of a lightly Si-doped, 50 nm thick GaAs layer ($N_d = 2 \times 10^{16} \text{ cm}^{-3}$); undoped GaAs layer 10 nm thick; 3.5 nm thick AlAs barrier layer, 10 nm undoped GaAs; 50 nm lightly doped GaAs ($N_d = 2 \times 10^{16} \text{ cm}^{-3}$); and a GaAs cap-layer ($N_d = 2 \times 10^{18} \text{ cm}^{-3}$) which was 0.4 μm thick. To fabricate ohmic contacts an AuGe/Ni/Au metallic film was evaporated on the n^+ -type GaAs cap-layer. Mesa structures (80 μm in diameter) were defined by wet etching (2 μm depth) using the metal as mask. A second ohmic contact was prepared on the backside of the wafer by soldering. A standard annealing process (400°C, 2 min in N_2 atmosphere) gave good ohmic contacts ($10^{-6} - 10^{-5} \Omega\text{-cm}^2$).

Figure 2 shows the differential conductance as a function of external voltage bias at 4.2 K without magnetic field. Eight resonance's manifested as local minimum's can be seen clearly. We relate them to the resonant tunnelling through first eight quantum states in the pseudo-well.

In Fig. 3 the second derivatives of the current-voltage characteristic are shown for different values of magnetic field applied perpendicular to the current. The average distance between resonances without magnetic field is equal to $\Delta V_0 \cong 45 \text{ mV}$ in agreement with similar values obtained in previous experiments [2-4, 9] taking into the account different well width and effective electron mass. The amplitude of the oscillations in our experiment is two to three order of magnitude less. The amplitude of the resonance's decreases and the resonance positions are displaced to slightly higher voltages as the magnetic field increased up to $B \geq 3.5$ T. Similar behaviour has been observed in wide quantum wells [4] and has been explained by the action of the Lorentz force as the electron transverse the region of the barrier. The shift in the electron transverse momentum is given by $(eBd)/\hbar$ where d is the width of the barrier. The suppression of the oscillation amplitude in our samples can not be explained by the total magnetoresistance of the structure. This has been checked by direct measurements. The new set of oscillations appears at low bias voltage for magnetic fields $B > 4$ T. These oscillations are related to tunnelling through hybrid magnetoelectric states [5]. The application of a longitudinal magnetic field only slightly increases the amplitude of the oscillations observed at zero magnetic field. The same has been observed in wide quantum wells [2] and has been explained by a decrease of the scattering in the well due to the decrease of the density of final states for scattering events.

The main difference in our structures is the absence of one barrier which confines the well. It is replaced in our structure by the smooth potential drop with reflection coefficient equal to 0.3%-3% in the energy interval relevant here. Figure 4 shows the calculated values of the reflection coefficient from the step like potential as the function of applied voltage bias (solid line). In the calculations we have assumed that the electron energy is equal to the voltage bias and the height of the step potential is equal to 87 meV - the potential drop through n^-/n^+ junction in our samples. The experimental data (circles) are calculated in the following manner. It is known from resonant tunnelling theory [10] that for the tunnelling through double barrier structure with different barrier transparencies the relative resonant contribution to the total

current $\Delta I/I$ is equal to the reflection coefficient from the most transparent barrier (smooth potential drop in our case). Thus we can determine the reflection coefficients at different voltage biases directly from our experimental data. It is easy to explain difference between calculations and experimental values by considering smooth rather than step like potential drop which leads to the additional term for the reflection coefficient proportional to $\exp(-\frac{\Delta W}{\lambda})$ where ΔW is the potential change length and λ is the electron wave length [11].

Thus we believe that our results are consisted with the experimental data obtained for wide quantum wells [2-9] and the good agreement of the measured reflection coefficients with calculations confirm our preposition that observed oscillation structure is due to the resonant tunnelling through virtual states in the pseudo-quantum well.

In conclusion we have observed aperiodic oscillations in single barrier heterostructure related to the electron interference due to the quantum reflection from the smooth potential drop through n^-/n^+ junction in GaAs.

This work is supported by the Russian Fundamental Science Foundation and the International Science Foundation. We acknowledge helpful discussions with Professor V. A. Tulin.

References.

- [1] M. Heiblum, I. M. Anderson, C. M. Knoedler, *Appl. Phys. Lett.* **49** (1986) 207.
- [2] A. F. J. Levi, R. J. Spahn, J. H. English, *Phys. Rev. B* **36** (1987) 9402.
- [3] R. C. Porter, A. A. Lakhani, *Appl. Phys. Lett.* **52** (1988) 1349.
- [4] M. Helm, F. M. Peeters, P. England, J. R. Hayes, E. Coles, *Phys. Rev. B* **39** (1989) 3427.
- [5] M. L. Leadbeater, E. S. Alves, L. Eaves, M. Henini, O. H. Hughes, A. Celeste, J.-C. Portal, G. Hill, M. A. Pate, *J. Phys.: Condens. Matter* **1** (1989) 4865.
- [6] N. Miura, K. Yamada, N. Kamata, T. Osada, L. Eaves, *Superlat. Microstr.* **9** (1991) 527.
- [7] K. P. Martin, S. Ben Amor, J. J. L. Rascol, R. J. Higgins, R. C. Potter, H. Hier, *Appl. Phys. Lett.* **56** (1990) 1772.
- [8] T. M. Fromhold, L. Eaves, F. W. Sheard, M. L. Leadbeater, T. J. Foster, P. C. Main, *Phys. Rev. Lett.* **72** (1994) 2608.
- [9] E. S. Alves, M. L. Leadbeater, L. Eaves, M. Henini, O. H. Hughes, *Sol. State Electr.* **32** (1989) 1627.
- [10] B. Ricco and M. Ya. Azbel, *Phys. Rev. B* **29** (1984) 1970.
- [11] L. D. Landau and E. M. Lifshitz, *Quantum Mechanics (non relativistic theory)*, Course of theoretical physics v. 3, Third edition (Pergamon Press, 1977) p. 214.

Figure captions.

Fig. 1. The schematic conduction energy-band diagram for the structure at an applied external bias V_b .

Fig. 2. The differential conductance, $\partial I / \partial V_b$, as a function of an applied external voltage bias V_b at zero magnetic field.

Fig. 3. The second derivative of the current voltage characteristics, $\partial^2 I / \partial V_b^2$, as a function of an applied external voltage bias V_b . The magnitude of magnetic field is a parameter. Curves are shifted arbitrary in vertical direction.

Fig. 4. The electron reflection coefficient from potential drop as a function of voltage bias.

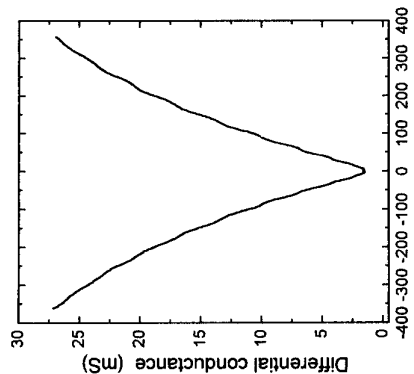


Fig. 2

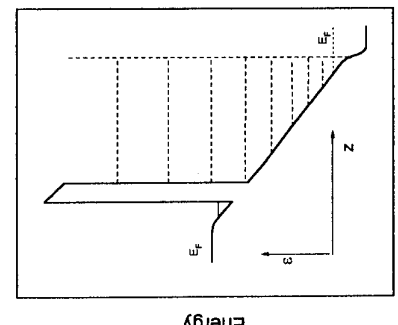


Fig. 1

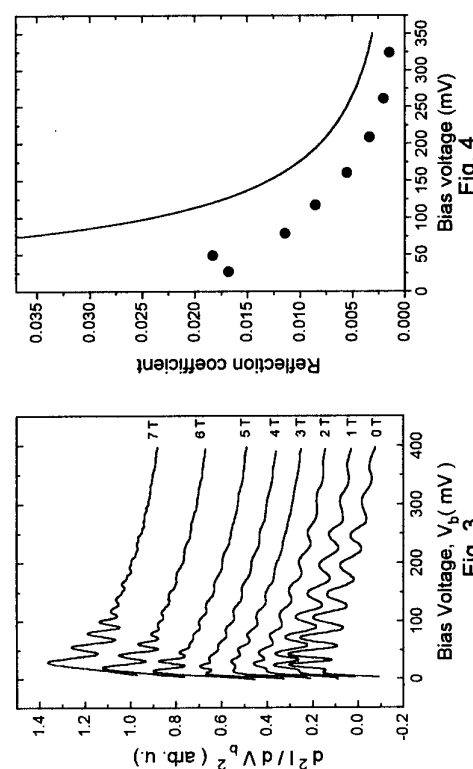


Fig. 3



Fig. 4

Resonant tunneling in time dependent fields through laterally confined double barriers.

Ramón Aguado, Jesús Iñarrea and Gloria Platero

Instituto de Ciencia de Materiales (CSIC) and Departamento de Física de la Materia
Condensada C-III, Universidad Autónoma, Cantoblanco, 28049 Madrid, Spain.

Abstract

We analyze the tunneling current through resonant heterostructures in the presence of a time dependent field. We compare two different cases : an AC potential where the external field is position-dependent through the heterostructure versus the case where an electromagnetic field irradiates homogeneously the whole sample. While in the presence of an AC potential the tunneling takes place mainly through photoiside bands, in the case of homogeneous illumination the main effective tunneling channels correspond to the coupling between different electronic states due to photon absorption and emission. The difference of tunneling mechanisms between these configurations is strongly reflected in the transmission and current which present different features in both cases. In order to analyze these effects we have obtained the transition probability for coherent resonant tunneling in terms of the Green's function of the system. We have applied this model to analyze the effect of light in the current steps which presents a laterally confined double barrier where the Coulomb interaction is considered in a mean field approximation.

In the last years several works have been devoted to analyze of the effect of a time-dependent field on the transport properties of resonant heterostructures. However there is not yet a systematic discussion of the different experimental situations corresponding to an AC potential applied between the left and right leads and which implies a position-dependent dephasing of the external field on the sample , and the case where the whole sample is homogeneously illuminated, i.e., where the electron-photon coupling depends on position just through the momentum matrix elements [1]. In spite of the increasing interest in this field, most of the theoretical work has been done considering an AC potential but the experimental information includes both configurations. Both situations however are physically different because the effective tunneling channels for the flowing of current are different in both cases. In this work we have extended the GTH [2] (Generalized Transfer Hamiltonian) which allows to analyze the coherent tunneling, to obtain the transition probability for the coherent tunneling in the presence of a time dependent potential in the two configurations discussed above. We analyze first the effect of an AC field applied just to the left and right leads with a dephasing of π between them. In this case the Hamiltonian is such that [3,4] the AC potential $H_2(t) = V_{AC} \cos(\omega t)$ does not couple electronic states within the same spatial region but just diagonal terms: $\langle k_L | H_2(t) | k_L \rangle c_{kL}^\dagger c_{kL}$, appear in the Hamiltonian. Following

the GTH scheme we obtain the stationary transition probability [4]:

$$P_{RL} = \frac{2\pi}{\hbar} \sum_{n,m} J_n^2 \left(\frac{V_{AC}}{\hbar\omega_0} \right) J_m^2 \left(\frac{V_{AC}}{\hbar\omega_0} \right) \delta(\epsilon_{p_R} - \epsilon_{k_L} - n\hbar\omega_0 - m\hbar\omega_0) \\ + \langle p_R | V_L + V_R G^+(\epsilon_{k_L} + n\hbar\omega_0) V_L | k_L \rangle^2 \quad (1)$$

Where G is the total Green's function of the system [2,4]. We consider now homogeneous illumination of the sample. In this case, there is no a position-dependent phase shift of the external field and the spatial dependence appears through the matrix elements of P_{RL} . The light considered is linearly polarized in the tunnel direction . In this case the e-ph interaction imply coupling of different electronic states: $\langle k'_L | P_z | k_L \rangle c_{k'_L}^\dagger c_{k_L} (\alpha e^{-i\omega_0 t} + \alpha^* e^{i\omega_0 t})$ and these terms are the reason for the differences observed in the transmission with respect to the previous case. In the AC case, however, the effect of the field on the transition probability comes from the photoiside bands [1] which appear in the regions affected by the field and which behave as additional tunneling channels. Applying the same procedure as in the case of the AC field including the non-diagonal coupling terms we obtain:

$$P_{RL} = \frac{2\pi}{\hbar} \{ |A_{RL}|^2 \delta(\epsilon_{p_R} - \epsilon_{k_L}) + |B_{RL}|^2 \delta(\epsilon_{p_R} - \epsilon_{k_L} + \hbar\omega_0) + (\omega_0 \rightarrow -\omega_0) \} \\ A_{RL} = J_0(\beta_{p_R}) J_0(\beta_{k_L}) \langle p_R | V_L + V_R G^+(\epsilon_{k_L}) V_L | k_L \rangle \\ B_{RL} = \frac{eF}{2m^*\omega_0} \{ \langle p_R | V_R G_T^-(\epsilon_{p_R}) P_z | k_L \rangle + \langle p_R | P_z G_R^+(\epsilon_{k_L}) V_L | k_L \rangle + \\ \langle p_R | V_R G^-(\epsilon_{p_R}) V_L G_T^-(\epsilon_{p_R}) P_z | k_L \rangle + \langle p_R | P_z G_R^+(\epsilon_{k_L}) V_R G^+(\epsilon_{k_L}) V_L | k_L \rangle \\ \langle p_R | V_R G^-(\epsilon_{p_R}) P_z G^+(\epsilon_{k_L}) V_L | k_L \rangle \} \quad (3)$$

Where G_L and G_R are the Green's functions of the left and right regions respectively. The interesting thing here is that $\beta_k = \frac{eF/m^*E_F}{\hbar^2 k^2}$ is very small and just J_0 terms have been considered. In fig.(1.a) the transmission coefficient T through a DB for an AC potential has been drawn. The ratio between the amplitude and the energy of the field determines the number of photoiside bands participating in the current and in this case is 0.77. We include in the calculation the Bessel functions up to forth order (it is reflected in the four satellites appearing at both sides of the main peak). We have plotted (fig. 1.c) the current density J for this case: the threshold current moves to lower bias and for higher bias J is smaller in the presence of the AC field. Also a step-like behaviour is observed in J/V . We can explain it in terms of the photoiside bands: The threshold bias moves to lower values due to the fact that there are photoiside bands associated to electronic states close to E_F which contribute to the resonant tunneling even when the resonant state (E_r) is higher in energy than E_F . If E_r is higher than E_F in several photon energies the photoiside bands which allow the flow of current have a low spectral weight and their contribution to J is small. As E_r closes into E_F increasing V , the lower indexes photo-side bands, i.e., those which are more intense in the spectral function can be aligned with E_r and their contribution to J increases. Once E_r crosses E_F J increases but remains smaller than in the case with no AC applied. That is due again to the fact that the spectral function has finite weight in all the photoiside bands and not only in the main one whose weight is smaller than one. In fig. 1.b) we plot T for a DB in

FIGURES

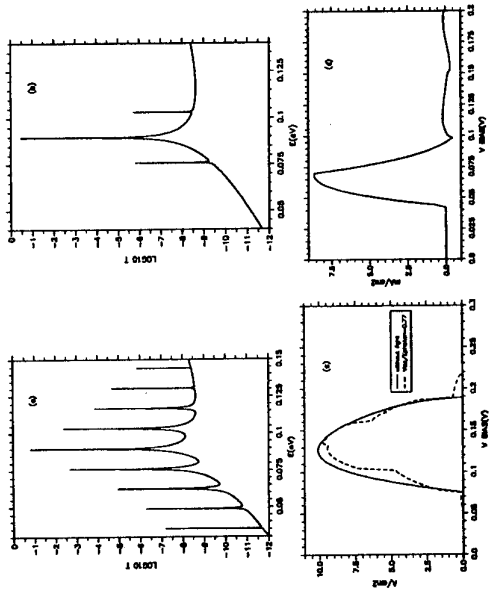


FIG. 1. \log_{10} of T as a function of energy with a) an AC field : $\frac{V_{AC}}{\hbar\omega_0} = 0.77$; b) homogeneous light $F = 1.10^5 \frac{V}{m}$ $\hbar\omega_0 = 13.6 \text{ meV}$; c) $1/V$ with (dotted line) and without (continuous line) the AC field d) Current density diff. (with minus without light) for different ratios between the intensity and the energy of the AC field ($\hbar\omega_0 = 13.6 \text{ meV}$). (GaAs/AlGaAs DB 100-50-100 Å).

the presence of light. The main difference between 1.a and 1.b is that the momentum matrix elements are very small, for typical values of the intensities and frequencies of the light, then the contribution of the photoiside bands of higher order than zero are negligible. That is the reason why to consider just the main peak ($m=0$) makes sense. However we observe in fig. 1.b the presence of two satellites in T : they come from the coupling of electronic states due to the light (in this case just processes involving one photon are considered). Therefore, the tunneling channels for the two configurations are different: in the case of AC the off-diagonal terms cancel if the field is considered constant within each region (left, center and right). In this case, the main channels (the only ones within this approximation) are the photoiside bands: those in the emitter aligne in energy with the photoiside bands in the well producing additional contributions to the current. In the case of light the off-diagonal terms are those which modify the current. Those channels, involving different electronic states (fig. 1.b) contribute in principle also with all their photoiside bands, however, just the zero index one is non-negligible and gives a contribution to the current. Therefore the three peaks in T come from the main bands (index zero) corresponding to three electronic states differing in one photon energy. In fig. 2 we analyze a DBS laterally confined by a 2-D parabolic potential and a magnetic field parallel to the current [6] in the presence of light. We consider (fig. 2.a) the confinement very small. Then the number of electrons crossing the well is large and a mean field model for the electron-electron interaction is a good approximation. We define an equivalent capacitance [1] and we evaluate the coherent tunneling current within a single electron model considering the additional electrostatic potential induced by the charge into the well in a self-consistent way. One can observe that in this case, many lateral states are very close and contribute to the current giving a current step which, for the zero confinement limit corresponds to a Landau level [5] involving many electrons in the confined region. The additional steps in the current reflect the 1 photon absorption and emission processes [1] which assists the tunneling. Also the light modifies the charge in the well for a fixed bias and this affects also the current. In fig. 2.b), the confinement is important and a mean field model for the e-e interaction is not good. However we expect that the effect of light on J should be qualitatively the same as for the low confinement case. Here the current steps correspond to the contribution of each lateral state and each step involves one electron at most, passing through the well and only the current at high bias, which involves more electrons [6], could be qualitatively consider in order to discuss the effect of the light on the characteristic curve.

This work has been supported in part by the Comision Interministerial de Ciencia y Tecnologia of Spain under contract MAT 94-0982 -02-02.

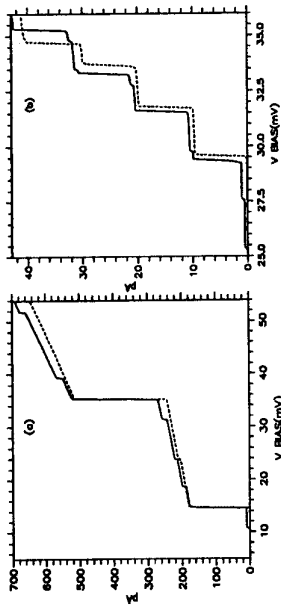


FIG. 2. J/V for a laterally confined DB (50-90-100 Å) with (continuous line) and without (dotted line) homogeneous light: $F = 1.10^5$ and $\hbar\omega_0 = 2meV$. $B = 6T$ and the parabolic confinement is a) 0.01 meV; b) 3.6 meV

- [1] J.Iñarrea, G.Platero and C.Tejedor, Phys. Rev. B **50** 4581 (1994)
- [2] L.Brey G.Platero and C.Tejedor, Phys. Rev. B **38** 10507 (1988)
- [3] P.Johansson, Phys. Rev. B **41** 14 (1990)
- [4] R.Aguado,J.Iñarrea and G.Platero, to be published.
- [5] J.Iñarrea and G.Platero,Phys.Rev.B **51** 5244 (1995)
- [6] B.Su,V.J.Goldman and J.E.Cunningham, Phys.Rev.B **46** 7644 (1992)

Broadening of Resonance Level Induced by Interface Roughness Scattering in Double Barrier Tunneling Structures

T. Hoshida, M. Tsuchiya and T. Kamiya
Department of Electronic Engineering, University of Tokyo,
Hongo 7-3-1, Tokyo 113, Japan.

Abstract

Energy spectral line shapes of resonance states in double barrier (DB) structures have been studied using (a) tunneling spectroscopy measurements and (b) a semi-quantitative theoretical analysis on elastic scattering by hetero-interface roughness (IR). Obvious broadening in resonance levels were observed when interface morphology was modified by interface smoothing time periods during molecular beam epitaxy. IR scattering probability calculation suggested that such broadening could be attributed to enhanced dephasing of vertical momentum induced by the IR scattering inside the quantum well of DB.

1. Introduction

Energy spectral line shape of resonance level is one of the basic characteristics of resonant tunneling (RT) phenomena in a semiconductor double barrier (DB) structure. Its investigation is not only interesting in the physical sense, but since line shapes are expected to affect the ultimate performance in RT schemes with ultrafast electronic device [1] and quantum cascade lasers [2], it also plays an important role in applications. The line shape, however, had not been exhaustively studied partially because attention of RT researches had been paid mostly on the characteristics of *I-V* and/or negative differential resistance. One of the authors (M.T.) used a novel method using tunneling spectroscopy (TS) and applied it around the onset voltage of RT current [3] and was, thus, able to provide means for experimental treatment of this phenomena. It was reported in Ref. 3 that a drastic peak broadening in second derivatives of *I-V* curves, which correspond to the RT energy spectra, was observed and the interface roughness (IR) was speculated to be one possible origin of the broadening among other possibilities concerning doped donors [4] and phonons.

In this paper, we report a more systematic experimental study on the RT spectral line shapes of DB tunneling structures having different interface morphologies. The difference was provided by the growth interruption technique during molecular beam epitaxy (MBE). We also performed a theoretical analysis of elastic scattering by IR under the Born approximation incorporating more realistic model for interface morphology than those in other works [5,6,7]. The experimental and theoretical results show that the RT spectra does not narrow down but broadens with the insertion of the interface smoothing time periods (ISTP) in the MBE. Thus, spectral broadening can be attributed to the IR scattering (IRS) enhanced by the modification of interface morphology.

2. Tunneling Spectroscopy Experiments

Two kinds of DB structures were compared by low temperature TS measurement. They were grown by MBE on 2-inch-diameter n -GaAs (001) substrates separately. The layer thicknesses at the centers of two wafers were chosen to construct DB structures with 3.25-nm AlAs barriers and a 6-nm-wide GaAs quantum well (QW). The only difference between the

two was whether a 60-second ISTP was inserted at each AlAs-on-GaAs interface or not. The insertion of such growth interruption is known to enhance diffusion of Ga adatoms on the substrate surface, and hence, modify morphologies of these hetero-interfaces. Therefore, IR effects were expected to appear in different degrees between the two wafers if the tunneling electrons were sensitive to this change.

Several tens of diodes with 80- μm -diameter mesas and Ni/AuGe/Au ohmic contacts were fabricated on each wafer. All the diodes exhibited negative differential resistance in their *I-V* characteristics. It should be noted here that their peak current I_p changed continuously depending on their position on the wafer: the diodes near the wafer edges showed about ten times larger I_p than the diodes at the center. This variation in I_p is due to the layer thickness deviation in the wafer originating from in-plane variation of Al and Ga beam flux in MBE growth. Since a tenfold increase in RT current corresponds to a reduction of a few monolayers in AlAs barrier thickness, the well width and the barrier thickness were estimated to decrease down to 80% along the radius of each wafer. Thus, by investigating this variation among all of the diodes, we were able to make a systematic and reliable study, and came to the conclusion that I_p can be used to indicate the real layer thicknesses in each diode.

The d^2I/dV^2 -*V* spectra at the onset voltage of RT current, which correspond to the tunneling transmission coefficient through DB structures, were measured at 10.4 K for the diodes. In each spectrum a peaked structure was observed corresponding to the first resonance level. The width of the peak was about several hundred times broader than the values predicted for ideal DB structures of square potential shapes as reported in a previous paper [3]. Figure 1 shows typical tunneling spectra for the diodes with $I_p=27$ mA, whose well and barrier are estimated to be 5.5-nm wide and 3-nm thick, respectively. The peaks at approximately 0.18 V correspond to the first resonance levels. Note that the spectral shapes were broadened further with the insertion of ISTP, which seems to contradict the well-known results where introduction of ISTP sharpens the photoluminescence peak width in QW structures [8,9]. Layer thickness dependence of tunneling spectra was analyzed by plotting the position, the height, and the width of the spectral peaks as functions of I_p (Fig. 2); for example, increase in

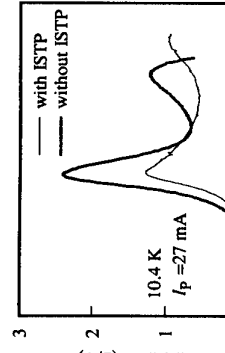


FIG. 1 Typical tunneling spectra measured for diodes with the same peak current but different wafers.

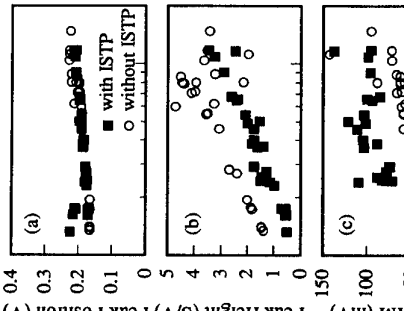


FIG. 1 Typical tunneling spectra measured for diodes with the same peak current but different wafers.

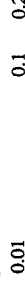


FIG. 2 Variation of spectral (a) peak position, (b) peak height, (c) peak width as functions of diode peak current, which is closely related to the thicknesses of the layers.

peak voltage with I_P shown in Fig. 2(a) corresponds to the elevation in resonance levels with decreasing well width. It is clearly shown that the insertion of ISTP introduce (a) negligible change in spectral peak position, (b) significant decrease in spectral peak height, and (c) broadening of the peaks.

3. Theoretical Analysis on Resonance Linewidth

In our calculations for the investigation on the effects of IRS in quasi two-dimensional states, we interpreted the broadening as a result of vertical momentum dephasing caused by elastic scattering that changes the direction of momentum vector. The energy width ΔE of a resonance level is assumed to be

$$\Delta E \cdot \tau = \Delta E / (\tau_{\text{tunel}}^{-1} + \tau_{\text{scatter}}^{-1}) = \hbar,$$

where τ_{tunel} is the tunneling escape time from QW, and τ_{scatter} is the relaxation time of vertical momentum defined by scattering. Since τ_{scatter} itself is dependent on ΔE , we determined ΔE with a self-consistent calculation, in which τ_{scatter} is obtained under the Born approximation for each loop [10]. Note here that ΔE for electron of small parallel momentum should be examined. This is because the TS measurement was performed where the Fermi level in the emitter electrode coincides with the resonance level. The detailed framework of the calculation will be reported elsewhere.

In the calculation of τ_{scatter} spatial Fourier spectra (SFS) of the scatterer, the IR potential in this case, were obtained as follows. Assuming one atomic monolayer roughness, the interface morphology was created by using a Monte-Carlo simulation of Ga-atom diffusion on a substrate surface during MBE growth [11]. The duration of simulation time T_S was found to cause a drastic change in the morphology. For example, as T_S increased, initially, "island-like" structures started to form and eventually expanded to larger structures (Fig. 3(a)). This change was analyzed by evaluating SFS of simulated interface morphology as functions of an absolute value of the spatial frequency. We found that each spectrum showed a peak at the spatial frequency corresponding to the average island size and that the peak moved to lower frequencies as ISTP was increased.

In the following discussion the SFS peak

wavelength Λ , which is twice the average island size, is used to refer each morphology instead of ISTP.

The simulations were very time-consuming, and thus calculation was made only for cases where $\Lambda < 6$ nm. For larger Λ as we extrapolated SFS from simulated results

assuming a simple spectral shape as shown in Fig. 3(b), but was careful not to violate the assumption of a single atomic monolayer roughness.

ΔE , calculated for the case of 6-nm well and 3-nm barriers, is plotted as a function of Λ in Fig. 4. Although no significant state broadening was seen when $\Lambda < 5$ nm, a drastic degradation of resonance level starts to occur as Λ exceeds 10 nm, causing ΔE to shoot up to several tens of meV for $\Lambda \sim 100$ nm. This agrees fairly well with the experimental results in which a 60-second ISTP broadened the resonance peaks by a few tens of meV (provided that the generally accepted idea that the island size grows to more than tens of nm after the 60-second ISTP is correct [9].)

Since our model does not eliminate the forward scattering probability from momentum relaxation rate, ΔE is overestimated for larger Λ s. Yet this is the first analysis that discusses the cases where $\Lambda > 50$ nm and gives an interpretation for the experimental results. One should note also that it can be concluded that the RT process is incoherent with respect to the vertical direction in a DB structure with such narrow QWs, provided that our scenario is fully acceptable.

4. Conclusion

With the first systematic TS measurement on resonance line shapes in DB tunneling structures, impact of IR effects on resonant tunneling was confirmed. It was found that the insertion of ISTP further broadened the resonance peak shape rather than sharpening it. Analysis of interface roughness scattering incorporating a realistic model for interface morphology provided a possible explanation to the dramatic broadening of resonance levels, suggesting that the RT process does accompany the IRS in a narrow QW.

Acknowledgment

The authors would like to appreciate discussion with Prof. T. Ando on the theoretical work. They also thank Mr. Y. Nakamura and Prof. H. Sakaki for their help in sample preparation.

References

- [1] T.C.L.G. Solner, W.D. Goodhue, P.E. Tannenwald, C.D. Parker and D.D. Peck, *Appl. Phys. Lett.* **43** (1983) 288.
- [2] J. Faist, F. Capasso, D.L. Sivco, C. Sirtori, A.L. Hutchinson and A.Y. Cho, *SCIENCE* **264** (1994) 553.
- [3] M. Tsuchiya and H. Sakaki, *Jpn. J. Appl. Phys.* **30** (1991) 1164.
- [4] H. Fukuyama, T. Waho and T. Mizunari, *Jpn. J. Appl. Phys.* **31** (1992) L823.
- [5] D.Z.-Y. Ting, S.K. Kirby and T.C. McGill, *Appl. Phys. Lett.* **64** (1994) 2004.
- [6] P. Johansson, *Phys. Rev. B* **46** (1992) 12865.
- [7] J. Leo and A.H. MacDonald, *Phys. Rev. B* **43** (1992) 12865.
- [8] C. Weisbuch, R. Dingle, A.C. Gossard and W. Wiegman, *Solid State Commun.* **38** (1981) 709.
- [9] H. Sakaki, M. Tanaka and J. Yoshino, *Jpn. J. Appl. Phys.* **24** (1985) L417.
- [10] T. Hoshida, M. Tsuchiya and T. Kamiya, *Proceedings of Eighth International Conference on Molecular Beam Epitaxy* (1994) (to be published).
- [11] P. Smilauer and D.D. Vvedensky, *Phys. Rev. Lett.* **72** (1994) 3194.

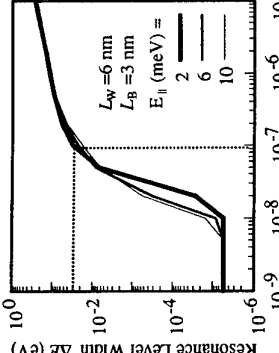


FIG. 4 Energy width of resonance level calculated at the presence of IR with various Λ . The resonance level is indicated by a horizontal dotted line at $\Delta E \approx 10^{-2}$ meV.

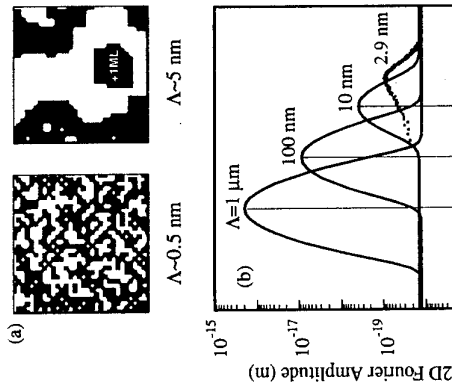


FIG. 3 (a) One atomic monolayer interface roughness (IR) generated by a Monte-Carlo simulation. (b) Examples of IR spatial Fourier spectra obtained from simulation ($\Lambda=2.9$ nm) and their extrapolation ($\Lambda=10,100,1000$ nm).

Charge Accumulation over a region of Electrical Multistability in a Double Barrier Structure

M. L. F. Lerch¹, D. J. Fisher¹, A. D. Martin¹, C. Zhang¹, and L. Eaves²

¹ Department of Physics, University of Wollongong, New South Wales 2522, Australia
² Department of Physics, University of Nottingham, Nottingham, NG7 2RD, England

When a double barrier semiconductor structure is biased near a tunneling resonance, charge can accumulate in the central quantum well. We report photoluminescence measurements of the 2D charge density over the full range of a tunneling resonance with emphasis on the region of multistability. An active load line technique was used to bias the device into this region, which is otherwise inaccessible. The charge density vs. current graph shows hysteresis and the plasmon excitation, which is a strong feature in the current-voltage characteristic, appears only weakly. Both these results are consistent with a model calculation based on charge conservation and the electron-electron interaction.

The electron tunneling current through a semiconductor double barrier structure (DBS) can show large resonances when an applied bias gives incoming electrons the same energy and transverse momentum as quantum states quasilocalised in the central quantum well[1]. In specially designed devices, the tunneling resonance is accompanied by significant charge accumulation in the well [2,3]. The predicted effect of this charge accumulation is to tip the normally bell-shaped resonance in the current-voltage, $I(V)$, characteristic over to the right, to give a Z shaped curve [4,5]. The central arm of the Z however is inaccessible to conventional measuring techniques, which give the appearance of a bistable and discontinuous characteristic[6]. Fig. 1 shows the $I(V)$ curve for an asymmetric $GaAs/Al_{0.4}Ga_{0.6}As$ DBS measured conventionally in both bias directions.

Fig. 1. $I(V)$ characteristic at 4 K of the first tunneling resonance. Arrows indicate where current switching occurs, delineating the region of apparent bistability. The broad peak near 0.9 V is due to LO-phonon assisted tunneling. Inset: Schematic conduction band diagram for the device under forward bias. Resonant tunneling occurs when one of the quasi-bound states in the well is brought into energy coincidence with E_0 in the emitter.

Full details of the layer structure, $I(V)$ curve and resonant charge accumulation, over that part of the resonance accessible to the conventional load line technique, have been reported previously for this DBS[2,3]. A recently developed technique using an active load line, equivalent to a voltage source and negative series resistance, enables the region of apparent bistability and hence the detailed structure of the entire resonance, to be probed [7]. This technique reveals the predicted Z shaped curve, with additional structure associated with a 2D plasmon developing at lower temperatures[8]. The interior of the bistability and the plasmon structure are shown in Fig. 2. As can be seen from Fig. 2(b), there can be as many as five stable current states for this particular device and the bistability is more correctly referred to as a multistable region.

Photoluminescence(PL) measurements made on the device, biased using the active load line technique, enabled the accumulation of charge in the well to be followed over the complete resonance. PL was excited using the 1.96 eV

line from a He-Ne laser incident onto the collector side of the device through ring electrodes. Weak illumination conditions minimised perturbations to the $I(V)$ characteristic. PL signals, measured at each of the five stable current points at the same bias of 0.723 V, are shown in Fig. 3. PL is caused predominantly by carrier recombination between the lowest energy electron and heavy hole states in the quantum well (see Fig. 3 inset). As charge accumulates, band filling causes the PL linewidth itself to increase[3]. Although the linewidth itself provides only a qualitative measure of the charge density, linefitting, to a model which includes the effects of a Fermi function and varying oscillator strength, has been shown to provide a good measure of the sheet charge density, n , in the quantum well at this first resonance [9].

Fig. 4(a) shows the PL linewidth variation with applied bias and the charge density vs. current relation is plotted in Fig. 4(b). It is noted that n is known quite accurately over the conveniently measured $I(V)$ curve from independent measurements[2,3] and that our deduced n over the same bias range agrees quantitatively. This provides confidence in the deduced n , and certainly in the trend, within the multistable region. It should also be noted that the plasmon structure in the $I(V)$ curve is clearly visible in the $n(V)$ and PL peak energy vs V data. Two features of interest in the $n(V)$ data are the hysteresis (or bistability) and the apparent lack of any structure associated with the plasma excitation. These features are, perhaps, to be expected and can be explained qualitatively as follows. In the absence of any change to the collector barrier, the tunneling current could be assumed to be proportional to n . Over the region of the plasmon excitation there is little change in the applied bias and the well level is close to that of the emitter, so this assumption is quite valid and is supported by the almost linear behaviour of the lower branch of the $n(I)$ curve. The upper branch corresponds to much lower applied bias conditions, where the collector barrier is higher. The increased charge density represented by this branch corresponds to a reduced probability for tunneling out of the well.

A quantitative description of the experimental data can be obtained from the density dependence of the electron tunneling life time and the effect of the electron-electron interaction ($e-e$) on resonant tunneling. The tunneling process is assumed to be sequential[2]. The current is determined by $\frac{\partial n_b}{\partial t} + \nabla \cdot \mathbf{J} = 0$, where n_b is the 3D charge density in the resonant well. The effective two-dimensional density is given by $n = n_b L$. For small devices, $\nabla \cdot \mathbf{J} \approx J/L$ where L is the width of the well. For electrons with a constant escape rate, $\frac{\partial n}{\partial t} = -[n]/\hbar$ and $n \propto \exp(-\Gamma t/\hbar)$. In this case, the current is linearly dependent on the density. Such a linear

Fig. 2. (a) $I(V)$ characteristic at 4 K showing the interior of the apparently bistable region. Measurements were taken with a positively sloping active load line. (b) Region of apparent bistability on an expanded voltage scale. The broad satellite, which appears as a shoulder on the high energy side of the main resonance, is associated with plasmon assisted tunneling.

A quantitative description of the experimental data can be obtained from the density dependence of the electron tunneling life time and the effect of the electron-electron interaction ($e-e$) on resonant tunneling. The tunneling process is assumed to be sequential[2]. The current is determined by $\frac{\partial n_b}{\partial t} + \nabla \cdot \mathbf{J} = 0$, where n_b is the 3D charge density in the resonant well. The effective two-dimensional density is given by $n = n_b L$. For small devices, $\nabla \cdot \mathbf{J} \approx J/L$ where L is the width of the well. For electrons with a constant escape rate, $\frac{\partial n}{\partial t} = -[n]/\hbar$ and $n \propto \exp(-\Gamma t/\hbar)$. In this case, the current is linearly dependent on the density. Such a linear

relation has been widely used in studying the static level shift and the resulting current bistability. However, it is clear from our measurements that the deviation from linearity is significant, indicating that the n -dependence of Γ can not be neglected. Γ is the nett escape rate due to elastic coupling with both left and right barriers. However, throughout the resonance, Γ_L is negligible and $\Gamma \approx \Gamma_r$. When the density in the well decays with a density (or current) dependent rate, $\partial n_i / \partial t = -n\Gamma(n)/\hbar$, the rate equation has to solved selfconsistently. Here $\Gamma(n)$ depends on n through the resonant level shift due to $e - e$. In the Hartree-Fock(HF) approximation, this shift is given as $\Delta\epsilon_r(n) = \alpha n$ where α is a parameter which depends on the sample and model static dielectric function[6]. Within the WKB approximation, the tunneling decay rate can be written as

$$\Gamma(n, V) = \frac{\hbar}{2m} \exp\left(-\frac{2}{\hbar} \int_{r.b.} [2m(V(x) - \epsilon_r(n))]^{1/2} dx\right) \left[\int_{well} \frac{dx}{\sqrt{2m(\epsilon_r(n) - V(x))}} \right]^{-1} \quad (1)$$

where $r.b.$ stands for the right barrier and $V(x)$ is the one-dimensional potential including the band discontinuity and applied bias. If the HF shift is much smaller than $\epsilon_r(n)$ and $V(x) - \epsilon_r(n)$, we only retain the linear density correction in the escape rate, $\Gamma(n, V) \approx \Gamma(0)[1 + C\alpha n/(2\epsilon_r(0))]$, and $C = 1 + (2\epsilon_r(0)d/\hbar)\sqrt{2m/(V_0 - \epsilon_r(0))}$, where V_0 and d are the average height and width of the collector barrier. The charge density in the well is now $n(1 + C\alpha n/(2\epsilon_r(0)))^{-1} = \text{constant} \times e^{-V_0/J}$. From the continuity equation, the tunneling current density can be written as

$$J = n\Gamma(n, V)/\hbar. \quad (2)$$

The bias-current relation in resonant tunneling including $e - e$ is given as

$$V = V_0 + \alpha n \pm \Gamma [J_0/J - 1]^{1/2} \quad (3)$$

where J_0 is the maximum current density, V_0 is the energy difference between the emitter and the well at zero bias, and αn again represents the level shift due to $e - e$. Equations (1)-(3) can be evaluated iteratively. The result is presented in Fig. 4. All the parameters used in our calculation are taken directly from the experiment with the strength of $e - e$ adjusted by the parameter α . It linewidth for five current values, all at the same applied bias of 0.723 V. The shift of the peak to lower energy with increasing current is due to bandgap renormalisation as charge accumulates. Inset: Schematic conduction and valence band profiles under bias. Laser excitation from the right creates holes which form a 2D hole gas (HH_0) at the collector barrier. These holes tunnel into the well and thermalise to HH_1 before recombining with electrons to give the PL signal.

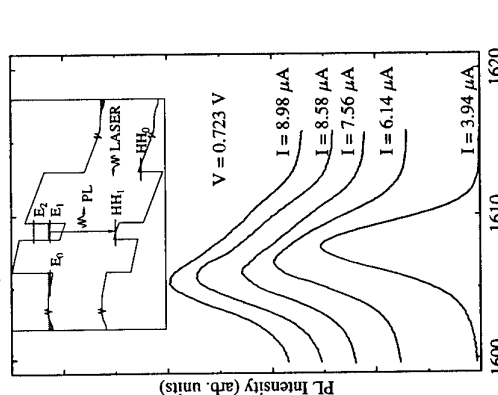


Fig. 3. PL spectra, taken from the multistable region and showing the variation of linewidth for five current values, all at the same applied bias of 0.723 V. The shift of the peak to lower energy with increasing current is due to bandgap renormalisation as charge accumulates. Inset: Schematic conduction and valence band profiles under bias. Laser excitation from the right creates holes which form a 2D hole gas (HH_0) at the collector barrier. These holes tunnel into the well and thermalise to HH_1 before recombining with electrons to give the PL signal.

In conclusion, simultaneous PL and transport measurements have been made on the charge accumulation in the central quantum well of a $\text{GaAs}/\text{Al}_{0.4}\text{Ga}_{0.6}\text{As}$ double barrier structure as the device is biased over the full range of a tunneling resonance. The charge density varies nonlinearly with the tunneling current. We attribute this nonlinearity to the density dependent tunneling escape rate. The authors would like to thank M. Henini for growing the sample and P. E. Simmonds for many helpful discussions. This work is supported in part by the Australian Research Council.

References

1. See, e.g., E. E. Mendez, "Physics of resonant tunneling in semiconductors", in Physics and Applications of Quantum Wells and Superlattices, edited by E. E. Mendez and K. von Klitzing, NATO ASI, Series B Physics (Plenum, New York, 1988), Vol 170, p. 159.
2. M. L. Leadbeater, E. S. Alves, F. W. Sheard, L. Eaves, M. Henini, O. H. Hughes and G. A. Toombs, J. Phys.: Condens. Matter **1**, 10605 (1989).
3. M. S. Skolnick, D. G. Hayes, P. E. Simmonds, A. W. Higgs, G. W. Smith, H. J. Hutchinson, C. R. Whethouse, L. Eaves, O. H. Hughes, M. L. Leadbeater and D. P. Halliday, Phys. Rev. B, **41**, 10754 (1990).
4. A. Zaslavsky, V. J. Goldinan, D. C. Tsui and J. E. Cunningham, Appl. Phys. Lett. **53**, 1408 (1988).
5. F. W. Sheard and G. A. Toombs, Appl. Phys. Lett. **52**, 1228 (1988).
6. D. D. Coon, K. M. S. V. Bandara and H. Zhao, Appl. Phys. Lett. **54**, 2115 (1989).
7. A. D. Martin, M. L. F. Lerch, P. E. Simmonds and L. Eaves, Appl. Phys. Lett. **64**, 1248 (1994).
8. C. Zhang, M. L. F. Lerch, A. D. Martin, P. E. Simmonds and L. Eaves, Phys. Rev. Lett. **72**, 3397 (1994).
9. T. A. Fisher, P. E. Simmonds, M. S. Skolnick, A. D. Martin and R. S. Smith, Phys. Rev. B, **48**, 14253 (1993).

Origin of Current Broadening in Resonant Tunnelling via Localised States

C. Zhang, D. J. Fisher, S. M. Stewart.

Department of Physics, University of Wollongong, New South Wales 2522, Australia

Abstract

It is found that in electron resonant tunnelling via localised states, the current exhibits a very strong temperature dependence and power nonconservation. This subtle behaviour is due to the impurity states induced tunneling which is subsequently renormalised by an overlap integral of many-electron states in the emitter. By using a temperature dependent dynamical approach, an analysis of this interesting tunneling process is performed. It is found that the temperature dependence of the current has very different origin than the thermal activation. It is also found that plasmon excitation in the emitter further renormalises the tunneling current by a factor of two to three orders of magnitude.

When electrons tunnel from a two dimensional state to a localised state, the tunneling current exhibits several interesting behaviours[1]. (i) The current is singular at the Fermi energy at zero temperature; (ii) The current near the resonance has a very strong temperature dependence which can not be explained by ordinary thermal activation; (iii) The area under the I-V curve (power) decreases as temperature increases. The singularity has been attributed to a many-body contribution which arises due to the strong interaction of a tunneling electron with the Fermi sea in the emitter [2-7]. The purpose of this work is to study the strong temperature dependence of the tunneling current. We shall show that the temperature dependence of the Fermi edge singularity (FES) is predominantly due to increased overlap of the manybody wavefunction rather than broadening of the single-particle distribution. Here we propose that the singularity is associated with the tunneling process from the two-dimensional emitter to an impurity state, which is accompanied by a sudden destruction of the impurity potential in the centre well. When an electron tunnels into the impurity site, it can also excite electron-hole pairs with small excitation energy. These low energy electrons may not be able to rearrange their wavefunctions according to the sudden change of the impurity potential. As a consequence, the true tunneling rate is renormalized by a factor which is proportional to the overlap integral between the initial and final wavefunctions of the emitter electrons[8,9].

We consider a process in a double barrier structure (DBS) where an electron tunnels from the emitter (L) to an impurity site in the central well (C) then tunnels out of the well to the collector (R). Suppose the whole process is sequential, that is the two tunneling processes are independent and the tunneling rate is just the product of the two independent tunneling rates. The first process ($L-C$) can be described by a resonant-like rate and the second process ($C-R$) is described by an escaping rate Γ_R , which in the wide band approximation can be regarded as energy independent. The level width of the impurity states in the well due to tunneling escape Γ , however, is determined by both Γ_L and Γ_R , i.e., $\Gamma = \Gamma_L + \Gamma_R$. Below

we shall describe the $L-C$ tunneling process in detail with the inclusion of electron-electron and electron-impurity interactions. The Hamiltonian for the electron-impurity system can be written as $H = H_0 + H_T + H_{\text{int}}$ where H_0 is the electronic part including electron-electron interactions in the emitter,

$$H_0 = \sum_{\mathbf{k}} (\epsilon_{\mathbf{k}} + \epsilon_{\mathbf{k}}^*) a_{i,\mathbf{k}}^\dagger a_{i,\mathbf{k}} + \sum_{\mathbf{k}} \epsilon_{\mathbf{c}} c^\dagger c + \sum_{\mathbf{k},\mathbf{q}} v_{\mathbf{q}} a_{i,\mathbf{k}+\mathbf{q}}^\dagger a_{i,\mathbf{k}-\mathbf{q}} a_{i,\mathbf{k}} a_{i,\mathbf{k}} \quad (1)$$

where $a_{i,\mathbf{k}}^\dagger (a_{i,\mathbf{k}})$ is the creation (annihilation) operator for an electron with quantum number \mathbf{k} in the emitter, $c^\dagger (c)$ is the creation (annihilation) operator in the well. $v_{\mathbf{q}}$ is the Fourier transform of the electron-electron interaction. H_T is the transfer Hamiltonian given as, $H_T = \sum_{\mathbf{k}} (V_{\mathbf{k}} c^\dagger a_{i,\mathbf{k}} + \text{c.c.})$ where $V_{\mathbf{k}}$ is the transfer Hamiltonian given as, $H_T = \sum_{\mathbf{k}} (V_{\mathbf{k}} c^\dagger a_{i,\mathbf{k}} + \text{c.c.})$ where $V_{\mathbf{k}}$ is the static coupling between the electrons and the left barrier. The electron-impurity interaction H_{int} can be written as, $H_{\text{int}}(\nu) = \sum_{\mathbf{k},\mathbf{q}} g_{\nu}(\mathbf{q}) a_{i,\mathbf{k}+\mathbf{q}}^\dagger a_{i,\mathbf{k}}$ where $\nu = \text{initial } (i)$ or final (f) , i.e. $g_{i(f)}(q)$ is the electron-impurity interaction when the impurity orbital is empty (occupied).

The probability per unit time for the tunneling from $L-C$ to occur, to the lowest order in the transfer Hamiltonian is[9,10],

$$w = 2\pi \sum_f | \langle f | H_T | i \rangle |^2 \delta(E_i - E_f - \zeta) = \sum_{\mathbf{k},\mathbf{k}'} V_{\mathbf{k}} V_{\mathbf{k}'}^* \int_0^\infty dt L_{\mathbf{k}\mathbf{k}'}(t) e^{-it} \langle e^{iH_t} e^{-iH_f t} \rangle \quad (2)$$

where ζ is the energy shift between the quasi 2D level in the emitter and in the well. We use the units in which $\hbar = k_B = 1$ for notational convenience. The above expression can be understood as follows. Due to the electron-impurity interaction, a new tunneling channel becomes available, this impurity level mediated tunneling is described by $L_{\mathbf{k}\mathbf{k}'}(t)$. However, this tunneling rate should be greatly reduced due to the vanishing overlap integral of the many-electron wavefunctions of the emitter. The average in eq.(2) is carried out over all possible initial states, $\langle O \rangle = \text{Tr}[e^{-\beta H_i} O] / \text{Tr}(e^{-\beta H_i})$. The bare tunneling probability, $L(t) = \sum_{\mathbf{k},\mathbf{k}'} V_{\mathbf{k}} V_{\mathbf{k}'}^* L_{\mathbf{k}\mathbf{k}'}(t) e^{iE_i + iE_f t}$, only depends on the temperature very weakly at low temperature and therefore can be treated in the zero temperature limit. The result is well documented[7,11]. If we adopt a \mathbf{q} -independent electrostatic barrier coupling ($V_{\mathbf{k}} = V_0$) and only consider the eigenstates of the scattering matrix with maximum phase shift, δ_0 , its long time behaviour is given as[7], $L(t) = \tau_0^2 (1 + \eta t)^{2\alpha/\pi} / t$ where $\tau_0 = \sqrt{\rho/V_0} f_0$, ρ is the two dimensional density of states and f_0 is the eigenstate with eigenvalue δ_0 . The cutoff η is of the order of the bandwidth. The renormalization due to the overlap integral $\phi(t) = \langle e^{iH_t} e^{-iH_f t} \rangle$ is strongly dependent on temperature, (much stronger than the bare distribution function effect in a non-interacting system). The procedure to evaluate the temperature dependent $\phi(t)$ is a standard one[9]. By using a technique of linked cluster expansion and only retaining terms up to the second order of electron-impurity interaction, we obtain $\phi(t) = \exp[F_{ph}(t) + F_p(t)]$, where $F_{ph}(t)$ is due to the particle-hole contribution,

$$F_{ph}(t) = 2\alpha \left[\ln \left(\frac{\sinh(\pi T t)}{\pi T t} \right) \sqrt{1 + \eta^2 t^2} \right] + i \arctan(\eta t) \quad (3)$$

$$\alpha = \frac{m k_F^2}{2\pi E_F} \int_0^{2k_F} \frac{dq}{2\pi} \frac{1}{q\sqrt{4k_F^2 - q^2}} \frac{1}{D_q(0)^2} |G(q)|^2 \quad (4)$$

where η is a cutoff frequency of order E_F , $D(0)$ is the static dielectric function of the emitter, T is the absolute temperature in energy units, and $G(\vec{q})$ is the Fourier transform of the electron-impurity interaction. The contribution due to plasmon excitation, $F_p(t)$, is given as,

$$F_p(t) = - \int_0^{\infty} \frac{qdq}{4} \frac{|G(\vec{q})|^2}{v_q \omega_p(\vec{q})} \left[\frac{1 - e^{-\omega_p(\vec{q})t}}{1 - e^{-\theta \omega_p(\vec{q})}} + \frac{1 - e^{\omega_p(\vec{q})t}}{1 - e^{\theta \omega_p(\vec{q})}} \right] \quad (5)$$

where v_q is the cutoff frequency beyond which the plasmon becomes heavily damped. $F_p(t)$ can be written as a time-independent term plus a time-dependent term. Now the transition rate can be written as,

$$w = \Re \left[\int_0^{\infty} dt e^{-i\epsilon t} L(t) \phi(t) \right] \quad (6)$$

Equations (3) and (6) are the central result of this work, they contain both electron-electron and electron-impurity interactions, as well as effects due to the finite temperature of the system and finite width of the impurity levels ($\epsilon_i = \epsilon_i - i\Gamma$). The result in eq.(6) indicates that the additional tunneling channel via the impurity state is, to the lowest order, proportional to the electron-impurity interaction. This is expected physically because electrons can only occupy the impurity states when there is a finite electron-impurity coupling. In the zero temperature limit, the inverse power law dependence of ref.[7] can be readily recovered.

We now examine the renormalization of the tunneling probability via an impurity state due to plasmon excitation. We take $|G(\vec{q})|^2 = v_q^2 e^{-2qd}$ and consider the low temperature limit. In the long wavelength approximation, $\omega_p = \sqrt{2\pi^2 n q/m}$. We obtain,

$$F_p(t) = -\sqrt{\frac{m 2\pi e^2}{\pi}} \int_0^{\infty} dq \frac{e^{-2qd}}{4\sqrt{q}} (1 - e^{-\omega_p(\vec{q})t}) \simeq -\pi \sqrt{r_s b} (1 - \exp(-r_s \epsilon_F^2 t^2 / 2k_F d)) \quad (7)$$

where $b = q_c/k_F$ if $1/2d > q_c$ or $b = 1/2k_F d$ if $1/2d < q_c$. We see that the tunneling rate is renormalised due to plasma excitation by a factor $\exp(-\pi\sqrt{r_s}b)$. For $r_s = 2.0$, $4k_F d = 1.0$, the tunneling rate is reduced by a factor of about 600.

We have numerically calculated the tunneling current by using eqs.(3,6) and $I = ew$. The result is plotted in Fig.1 with $\epsilon_i = V - V_{th}$, where V_{th} is the difference between the Fermi level in the emitter and the impurity level in the well at zero bias. The left panel shows the temperature dependence of the current. For small Γ and at low temperature, the current is essentially zero below V_{th} and has a sharp increase at around V_{th} . The inverse-power-law like singularity is clearly shown even at nonzero temperature and nonvanishing level width. There are three noticeable effects as temperature increases further: (i) The singularity is smeared out by the thermal excitation making the effective inverse-power decay somewhat weaker; (ii) The current also appears below the threshold; (iii) The area under the I-V curve increases with decreasing temperature. This is due to the interplay of temperature dependent wavefunction overlap and the level width and is a very particular feature of the present system where the resonant tunneling occurs via a strongly localized state. It should not be confused with the temperature smearing in a single-electron model which is due to the broadening of the Fermi distribution function. One can hardly notice any effect of the Fermi step smearing on the many-body current even if the temperature is varied by a few Kelvins. To clearly distinguish the present result from normal thermal activation, we

have deliberately set the temperature in those distribution functions responsible for thermal activation to be zero. Therefore all temperature dependence obtained in this work is due to manybody interactions. The calculations show excellent qualitative agreement with the experimental behaviour [1]. The fact that the area under the I-V curve around the resonance decreases as temperature increases strongly indicates that the temperature dependence in this case is of manybody nature because the single particle activation picture would predict that the power should increase with temperature. The right panel of Fig.1 shows that current decreases exponentially with decreasing wavefunction overlap.

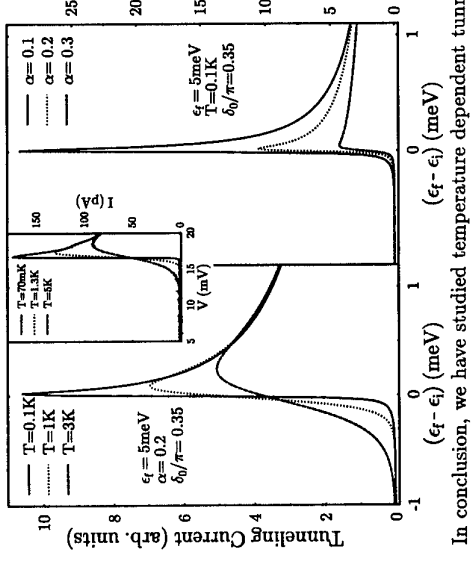


Figure 1: Left: Calculated tunneling current via the localised state in the well. Insets: Measured I-V characteristic of the tunneling current via the localised state in the well, taken from ref.[1]. Right: Calculated tunneling current at low temperature for several different wavefunction overlaps.

In conclusion, we have studied temperature dependent tunneling in a DBS via localised states. We argue that the temperature dependence of the Fermi-edge singularity observed experimentally is mainly due to the manybody wavefunction overlap effect which leads to a strong increase in the power of the FES as the temperature decreases.

The authors would like to thank P. E. Simmonds and A. K. Geim for valuable discussions.

References

- [1] A. K. Geim et al, Phys. Rev. Lett. **72**, 2061 (1994); Phys. Rev. B **50**, 8074 (1994)
- [2] G. D. Mahan, "Many-Particle Physics" (Plenum, New York 1981) p.748
- [3] G. D. Mahan, Phys. Rev. **153**, 882 (1967); D. L. Langreth, Phys. Rev. B **1**, 471 (1970)
- [4] J. Kondo, Physica B+C **84B**, 40 (1976); B+C **123B**, 175 (1984)
- [5] C. Zhang, Phys. Lett. **A148**, 193 (1990)
- [6] P. Hawrylak, Phys. Rev. **B45**, 8464 (1992); W. Chen et al, Phys. Rev. **B45**, 4237 (1992); K. J. Nash et al, Phys. Rev. Lett. **70**, 3115 (1993)
- [7] K. A. Matveev and A. I. Larkin, Phys. Rev. B **46**, 15337 (1992). See also G.E.W.Bauer, Sur. Sci. **305**, 358 (1994)
- [8] C. Zhang, G. Gumbs and N. Tzoar, Phys. Rev. B **43**, 1463 (1991)
- [9] G. Gumbs, C. Zhang and H. L. Cui, J. Phys. Condens Matter **3**, 1429 (1991)
- [10] K. Yamada, A. Sakurai, and S. Miyazima, Prog. Theor. Phys. **73**, 1342 (1985)
- [11] P. Nozieres and C. T. de Dominicis, Phys. Rev. **178**, 1097 (1969)

EFFECT OF SPACER LAYER ON QUANTUM INTERFERENCE IN DOUBLE BARRIER RESONANT TUNNELING STRUCTURES

A.E.Belyaev^{a)}, S.A.Vitusovich^{a)}, T.Figieliski^{b)}, B.A.Glavin^{a)}, R.V.Konakova^{a)}, L.N.Kravchenko^{c)}, A.Makosa^{b)}, T.Wosinski^{b)}

a) Institute of Semiconductor Physics, National Academy of Sciences of Ukraine, Kiev, 252028, UKRAINE

b) Institute of Physics, Polish Academy of Sciences, Warsaw, 02-668, POLAND

c) Science and Research Institute of Molecular Electronics, Moscow, 103460, RUSSIA

Abstract

The oscillations of tunnel current in Double Barrier Resonant Tunneling Structures incorporating a variety types of spacer layers in both emitter and collector sides have been studied. In some structures the period of oscillations was found to be considerably lesser than LO-phonon energy. Simple model based on quantum interference effect arising in the structures having wide spacer layer is proposed to explain the experimental results.

Introduction

In 1984, Hickmott et al. [1] discovered oscillatory structure in the low-temperature reverse-bias current-voltage characteristics of single barrier heterostructures. Its origin is stipulated by LO-phonon assisted processes occurring in the depletion region on the collector side. Recently we have observed oscillations of tunnel current in double barrier resonant tunneling structure (DBRTS) based on AlAs/GaAs/AlAs incorporating one-sided wide spacer layer [2]. The oscillations had a period that closes to $\hbar\omega_{LO}/e$, where $\hbar\omega_{LO}$ is the longitudinal optic phonon energy in GaAs, if to suppose the scaling factor is nearly one. It was surprisingly to observe the similar oscillation picture in both polarities of the applied voltage. Our further investigations of the DBRTS incorporating variety types of spacer layers in both emitter and collector sides showed the strong dependence of fine structure of the resonant current on DBRTS's parameters. Moreover, in some structures the period of oscillations was found to be considerably lesser than LO-phonon energy. The decrease of the period of oscillations occurs independently on whether the buildup of space charge in the well takes place or not. In this work we present the results of these experiments and give their interpretation in framework of quantum interference model.

Experimental details

Our device structures were grown by molecular beam epitaxy (MBE) on a n^+ -GaAs substrate. They comprise two highly doped ($\sim 10^{18} \text{ cm}^{-3}$ Si) n^+ -GaAs electrode regions (emitter and collector) having widths of 100 nm on the average between which the active part of structures is sandwiched. The sequence of layers in the active part starting from substrate side was following:

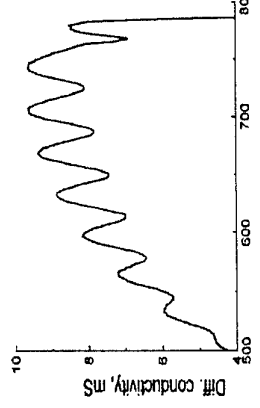


Fig.1. Experimental dependence of differential conductivity on voltage for the structure A (the first peak, forward bias).

structure A (spacer, GaAs undoped, 100 nm; barrier, AlAs undoped, 2 nm; well, GaAs undoped, 4 nm; barrier, AlAs undoped, 2 nm);
 structure B (buffer, GaAs doped by Si ($2 \times 10^{16} \text{ cm}^{-3}$), 1000 nm; spacer, GaAs undoped, 10 nm; barrier, AlAs undoped, 1.7 nm; well, GaAs undoped, 5.6 nm; barrier, AlAs undoped, 1.7 nm; spacer, GaAs undoped, 1.7 nm);
 structure C (buffer, n-GaAs(Si) graded from $3 \times 10^{18} \text{ cm}^{-3}$ to $1 \times 10^{17} \text{ cm}^{-3}$, 70 nm; spacer, p-GaAs ($5 \times 10^{14} \text{ cm}^{-3}$), 14 nm; barrier, $Al_{0.3}Ga_{0.7}$ As undoped, 1.7 nm; well, GaAs undoped, 5.6 nm; barrier, $Al_{0.3}Ga_{0.7}$ As undoped, 1.7 nm; spacer, p-GaAs ($5 \times 10^{14} \text{ cm}^{-3}$), 1.5 nm; buffer, n-GaAs(Si) graded from $3 \times 10^{18} \text{ cm}^{-3}$ to $1 \times 10^{17} \text{ cm}^{-3}$, 50 nm).

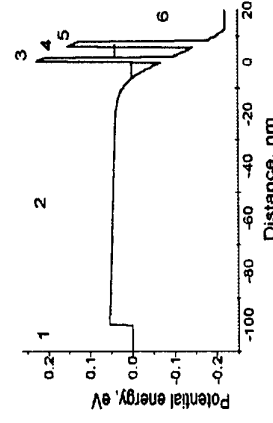


Fig.2. Calculated potential profile of the structure A under applied bias (The barrier's height is decreased 3 times)
 We measured the current-voltage characteristics (CVC) I(V) and differential conductance dI/dU of square mesa diodes of the area $1.6 \times 1.6 \text{ nm}^2$. Two quasi-bound states of the well are expected to appear in the structures A and B. Surprisingly, three resonant peaks were observed at low temperature under forward bias, instead of two peaks which actually appeared when the bias polarity was reversed. In all cases the forward bias corresponds to negatively biased substrate. The oscillatory structure is too weak to be seen directly on the I(V) characteristics, but it is clearly revealed by voltage modulation (Fig.1). Up to ten peaks are seen on the low-voltage slope of the first and second resonant peaks in both bias directions. The period of oscillations (ΔV) exhibits a weak dependence on number of resonant peak, while it shows the strong dependence on DBRTS's parameters. Really, ΔV equals to 36 mV and 38 mV for the first and second peaks in the case of structure A, whereas in the case of structure B the period of oscillations is considerably lesser: 22 mV and 24 mV, respectively. The oscillations are clearly observed up to temperature of 120K, and their amplitude monotonously increases with applied voltage. There are no oscillations for the third peak in the forward bias.

The only quasi-bound state of the well is expected to appear in the structure C. According to this the only resonant peak is observed in both bias polarities. There are no oscillations observed in such structure.

Theory

A number of mechanisms were proposed for explanation of fine structure of the tunnel current. In spite of their peculiarities most of them associate periodicity with electron scattering on LO phonons whose energy is 36 meV. This assumption is not appropriate in our case because of the fact that in some our structures the period of oscillations is definitely lesser than 36 mV, whereas observed behaviour must be due to dropping of this voltage on some part of the structure. To explain the above mentioned peculiarities we suggested the model based on quantum interference effect arising in the structures having a wide spacer layer. The model predicts appearance of fine structure in the tunnel current, but the period of oscillations is determined exclusively by the structure design. Speaking about interference we mean that quantum properties of transport take place not only in barriers and quantum well, but also in spacer, either emitter or collector. Potential distribution over spacer is nonuniform and the length of the latter is of order 100 nm, so transport in it is ballistic. In terms of wave mechanics, we have additional resonator (spacer region) before the Fabry-Perot interferometer (double-barrier structure). As a result, transparency of resonant tunneling through the quantum well is modulated by that one through the spacer.

wave function was taken in the form of plane waves. In quantum well (region 4) it was expressed through the Airy functions. In barriers (regions 3 and 5) it was taken in semiclassical form. In spacer (region 2) wave function was described by Airy functions in weak-field region and by corresponding semiclassical ones in the region of 2D electrons confinement. Result is shown on the Fig.3. We really see clear oscillations on CVC. It should be noted that they originate as a result of interference of electrons passing through the spacer. Resulting quasilevels are semiclassical on their nature and distance between them and thus the period of oscillations on CVC are determined mainly by electron movement in the weak-field region of spacer, in other words by the value F_s .

Discussion

We observed some disagreement with experimental curves: the frequency and amplitude of oscillations in experiment are smaller. Besides, position of resonant peak is shifted to the lower bias and peak is narrower. But we believe that these disagreements may be simply explained. The amplitude decreasing most probably is because of spoiling of quantum interference in spacer in result of scattering, which broads reflecting resonances. Different voltage scale arises due to some voltage drop on contacts. The latter does not explain the different number of oscillations on CVC, which may originates as a result of the nonequilibrium population of quantum level in spacer well. In connection with this point we must consider two characteristic times: time of tunneling (nonresonant) escape from the spacer level to collector through the barriers (τ_{tra}) and average time of electron scattering to the level (τ_{scat}). The population of the level is equilibrium if $\tau_{\text{tra}} > \tau_{\text{scat}}$. In our case barriers are relatively thin and this condition may violate. In this case spacer level would be deeper and electric field F_s stronger. As we mentioned above, the period of oscillations depends on the F_s (approximate dependence is $\propto F_s^{2/3}$), so described reason may lead to the observed difference between experimental and numerical results. To check suggested model we designed the potential profile of structure to eliminate the accumulation layer. It was done by using a graded layer or multilayered structure in front of the emitter barrier. The profile of structure C was chosen by such a manner to obtain the flat band regime in the emitter spacer at the work point of resonant tunneling. As result there are no oscillations observed in this structure.

Conclusion

In conclusion we have shown that quantum ballistic transport of electrons through a wide spacer causes the appearance of fine structure of the tunnel current. Most of experimentally observed peculiarities in CVC (in particular, the period of oscillations lesser than LO-phonon energy) may be explained in frame of this model.

References

1. T.W.Hickmott, P.M.Solomon, F.F.Fang, F.Stern, Phys.Rev.Lett., 52 (1984) 2053.
2. A.E.Belyaev, S.A.Vitusevich, R.V.Konakova, T.Figielki, A.Makosa, T.Wosinski, L.N.Kravchenko, JETP Lett., 60 (1994) 403.

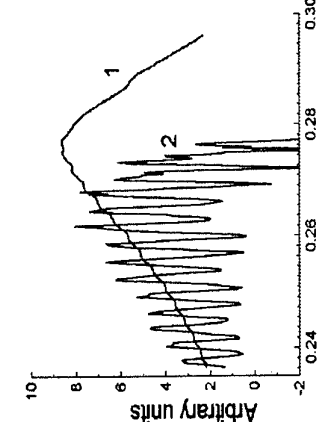


Fig.3 Numerical results obtained for the structure A: CVC (curve 1) and Differential Conductivity (curve 2)

For illustration we undertook selfconsistent calculation of CVC in the region of the first resonant peak for the structure A in the case when spacer layer is in emitter. It was assumed that charge accumulation in spacer is due to 2D electrons confined in the spacer well. Position of spacer level and potential profile were calculated through the selfconsistent solution of Poisson and Schrodinger equations (variational method was used for the quantum mechanical part of the problem) and demand of equilibrium population of 2D electrons (the latter assumption is questionable and will be discussed in the next section).

Voltage drop on the depletion layer of collector was calculated as well. Resulting potential profile is depicted on the Fig.2. We can see that there are two regions in spacer: short area of electron confinement and long area with weak electric field F_s . On the next step transparency of the system and, after averaging over Fermi-Dirac distribution, current were obtained. In these calculations Schrodinger equation was solved analytically with the use of boundary conditions on the interfaces between all regions, marked on the Fig.2. In regions 1 and 6

Quantum box energy spectroscopy by 3D–0D resonant tunnelling

G. Fain,[†] C. Vieu, F. Larnelle
L2M-CNRS, 196 Avenue H. Ravéra , B.P. 107, 92225 Bagneux Cedex – France
P. Krauz
CNET – Lab. de Bagneux, 196 Avenue H. Ravéra , B.P. 107, 92225 Bagneux Cedex – France
E. Bedel, C. Fontaine
LAAS-CNRS, 7 Avenue du Colonel Roche, 31077 Toulouse Cedex – France

[†]tel: (33 1) 42 31 74 30; fax: (33 1) 42 31 73 78; e-mail: giancarlo.fain@bagnieux.cnet.fr

Abstract

Nanometer resonant tunnelling diodes with independent control of the electrodes and quantum well dimensionalities have been fabricated by a novel technique. Liquid helium temperature current-voltage (I–V) characteristics exhibit a set of resonance lines due to the tunnelling of the 3D electrode electrons through the 0D states of the quantum box. Preliminary results on the line shape and on the relative intensity dependence of the lines with the radius of the box and the principal quantum number are discussed.

1. Introduction

Advances in Molecular Beam Epitaxy (MBE), and in processing techniques such as Electron Beam Lithography (EBL) and transfer associated methods, have allowed the fabrication and study of nanoscopic systems in which the electron wavefunction behavior, and in particular quantum interferences, is the relevant mechanism of the carrier transport. Among all these studies, evidence of the transport through the discrete states of quantum boxes has been addressed by several groups in the last past years[1]. In particular, double barrier resonant tunnelling structures (DBRTS) have revealed their good capability as a tool to probe the quantum boxes spectra by means of transport measurements [2,3,4]. In such structures, the current flows through the hetero-interfaces and senses the effects of the additional fabrication imposed lateral confinement. Previous technological approaches to fabricate such quantum boxes [2,3,4], induce the reduction of the dimensionality not only in the quantum well but also in the electrodes. For the smallest structures, the system consists in a quantum box coupled to two quantum wire electrodes so that the measured current is due to 1D–0D tunnelling. As the radius varies, the quantum box level and the quantum wire subband splitting change leading to the analysis of complex spectra [4,5,6]. In this work we report on the experimental study of the tunnelling of 3D emitter electrons through the 0D states of the quantum box based on a new fabrication technique allowing us to separate the dimensionality of the quantum well from that of the electrodes. With this approach, we can really investigate the radius dependence of quantum boxes without varying the nature of the electrodes, in order to perform a real spectroscopy of the discrete states of the three dimensionally confined quantum well.

2. Sample fabrication

This new fabrication process involves two MBE growth steps, separated by a set of technological runs. The MBE sample was conventionally grown on a n⁺ Si doped GaAs substrate. The DBRTS was chosen similar to our standard structure [3]. It consists on a 480nm 1x10¹⁸ cm⁻³ Si doped GaAs buffer layer followed by a 480nm 2x10¹⁷ cm⁻³ Si doped GaAs electrode. The active layer region is the following: an undoped 20nm GaAs spacer grown in order to prevent Si segregation in the DBRTS with consequent degradation on the I–V characteristics [7]; then an undoped 5.1nm GaAs quantum well cladded in between two undoped Al_{0.33}Ga_{0.67}As 8.7nm thick barriers and, finally, a last layer composed by a 30nm undoped GaAs spacer.

EBL is used in order to define a Ni layer pattern by conventional lift-off. This layer acts as a mask for the implantation at 200°C of 5x10¹⁴ cm⁻² Ga ions, with an energy of 50keV. Areas ranging from 50nm to 50μm in width are thus protected from the effects induced by the implantation process. After the removal of the mask in an aqueous solution of HNO₃, the sample is prepared for the epitaxial regrowth of the top electrode. The regrown layer consists in a 500nm 2x10¹⁷ cm⁻³ Si doped GaAs top electrode followed by a 500nm 1x10¹⁸ cm⁻³ Si doped GaAs cap layer. Details on the cleaning of the surface for the regrowth and on the structural and electrical characteristics of the epitaxial

hetero-interface are given on reference [8]. EBL is then used to define a new Ni mask for a deep SiCl₄ reactive ion etching for devices isolation or localized TEM investigations [9]. Finally a last EBL level is used for conventional ohmic contacts deposition. Figure 1 summarizes the whole process, the top contact electrode is 100μm×100μm wide, whereas the quantum boxes dimensions are defined by the first EBL on the buried hetero-interface. With this unique process, we are able to measure I–V spectra of diodes having identical 3D electrodes but effective physical quantum well radius varying from 50nm to 50μm.

3. 3D–0D resonant tunnelling: experimental results and discussion

In figure 2-a we plot the liquid helium temperature I–V characteristic of a nominal 400nm physical radius quantum box. Superimposed on the main broad resonant peak, we observe multiple peaks clearly resolved. The magnitude of these features is surprisingly high as compared to our previous measurements carried out on the deep etched structures [3,4]. Their amplitude is more than 100 times greater than the magnitude of the current for voltage biases less than the threshold voltage. This is depicted in the figure 2-b where we plot the spectrum of a nominal 50nm physical radius quantum box for voltage bias values close to the threshold voltage: the noisy current measured before the resonance sets in is of the order of 500fA. This, jointly to the variation of the splitting between lines with the radius of the quantum box, confirms that the observed resonance lines are associated to the quantum lateral confinement in the quantum well. In the following, we mainly focus on the shape and relative intensity of the resonance lines.

A very different line shape is expected in the 3D–0D tunnelling case as compared to the 1D–0D one. In 1D–0D tunnelling, as previously observed [3,4], the spectra show a steplike structure in the I–V characteristics because the contribution of each conducting channel to the total current is constant. A downward staircase due to the closing of the conducting channels is observed [3, 4], if Coulomb repulsion inside the quantum box is relevant [6].

Let us consider now a 3D electrode. The qualitative behavior of the I–V spectra can be quite easily described considering energy and momentum conservations in the different cases of the quantum box dimensionality [10]. In the quantum box case all the directions are quantized so that only the total energy is conserved: the current is thus maximal when E_{QB} is aligned with E_F and decreases with the increase of the voltage bias [10].

The behavior of the 1D–0D and the 3D–0D tunnelling cases are thus strongly different. The shape of the resonance lines we observe in our experiments is appreciably different than that we measured in the deep etched structures [3,4] as clearly shown in figure 2-a. The three successive more pronounced lines above 0.55V exhibit unambiguously a sharp current increase as the resonance sets in, followed by a quite slow rounded decrease as the voltage bias increases. The rounded shape for the resonance line as the voltage bias increases is also predicted by more realistic calculations of the I–V spectra taking into account the temperature effects and quantum box levels width [11]. This behavior is observed in almost all the lines measured in our spectra, as shown e.g. in figure 2-a: the rounded shape of the features in the differential negative resistance region (0.6<|V|<0.65) are thus attributed to the closing of the higher energy quantum box levels conducting channels.

In figure 3 we plot the relative intensity of the lines as a function of the quantum box radius for the first four quantum box energy levels. The relative intensity has been deduced from the experimental spectra as following. From each spectra we have extrapolate an average curve fitting the data without taking into account the resonance lines due to the tunnelling through the 0D states of the quantum box. This give a baseline which fits the main resonant broad peak described above for the figure 2-a. We subtract this baseline to the experimental data in order to get only the contribution of each resonance line to the current. Due to the quite low voltage step resolution for the smallest measured device (R=50nm), some lines seems split in several sublines due in fact to some digital error. Thus, an average value of the current is taken to account for each level contribution. These values are reported in figure 3 for the first four lines.

We consider as usually that the electron motion of the electrons in the longitudinal and transverse directions can be separated and we assume a parabolic approximation for the lateral confining potential [4, 6]. This assumption turns out to be realistic for an implantation induced lateral confinement. Thus the eigenfunctions of the quantum box are those of the harmonic oscillator. The current driven by each resonance channel can be evaluated by the estimation of the coupling between the emitter

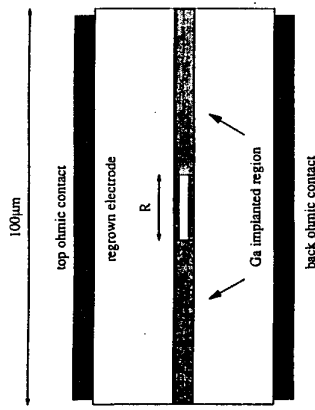


Figure 1: Scheme of the 3D-0D devices. The values of R range from 50nm to 50μm

electron plane waves and the eigenfunctions of the quantum box [11,12]; the current is in fact proportional to the overlap between the considered eigenfunction of the quantum box level and a particular plane wave of the emitter electrons conserving the energy during the tunnelling [11]. Calculations of the relative intensity ΔI of the tunnelling current through the quantum box levels have been carried out as a function of the box radius R and the level index n [11]. For the first few levels the $\Delta I=f(R)$ curve displays an almost linear increasing behavior until a critical radius value R_0 is reached. Above R_0 the relative intensity ΔI slightly decreases with R. The calculation shows that the value of R_0 is level dependent. This result implies that if one considers the first 4 levels (as those plotted in figure 3), for large enough radius (say $R>300$ nm) the magnitude of the intensities increases with n, whereas in the other limit ($R<100$ nm) the magnitude of the ground state of the quantum box ($n=0$) is the larger one, the contribution of the higher excited states of the quantum box being negligible as n increases. The calculation exhibits a crossover region for 100 nm< $R<250$ nm where the first excited states have a larger magnitude than the ground state whereas as n continues to increase the relative intensity become negligible.

In figure 3 we observe qualitatively the behavior expected from this calculation. If we focus on the 400nm data we clearly observe that the magnitude of the line intensities increases with n. For the 50nm nominal radius, the predicted behavior is also observed except for the $n=1$ level. Since it remains some uncertainty to evaluate correctly the relative line intensities for this device as mentioned above, the experimental data are in quite good agreement with theoretical expectations. The remarkable feature we want to stress concerns the 150nm radius data. This radius value is included in the theoretical crossover region [11]: $n=1$ and $n=2$ are predicted to have a slightly high magnitude than the ground state (but a magnitude less than the $n=1$ and $n=2$ contributions for $R=400$ nm) and $n=3$ has a negligible value. Here again, taking into account the relative line intensity uncertainty ($n=1,2$ have very close values), our experimental observations agree qualitatively well with the theoretical predictions.

4. Conclusion

A novel processing technique allowing the fabrication of nanometer resonant tunnelling diodes with a full control of the electrodes and quantum well dimensionalities have been realized. The I-V spectra exhibit resonance lines attributed to the 3D-0D electron tunnelling. The preliminary results described here are in good agreement with theoretical expectations for the line shape and for the relative intensity dependence of the lines with the radius and with the level index of the quantum box.

Acknowledgments

We wish to thank C. Mayeux and D. Arquey for technical help. We gratefully acknowledge fruitful discussions with M. Boero, J. Inkson and A. Munoz-Yagüe. This work was in part supported by ESPRIT Basic Research Action 6336, LATMIC II.

References

- 1 see e.g. "Coulomb and interference effects in small electronic structures" ed. by D.C. Glattly, M. Sanguer and J. Trân Thành Ván, (Editions Frontières, 1994), and references therein
- 2 M.A. Reed, J.N. Randall, R.J. Aggarwal, R.J. Matyi, T.M. Moore and A.E. Weissel, Phys. Rev. Lett. **60** (1988) 535; M. Tewordt, L. Martin-Moreno, V.I. Law, M.J. Kelly, R. Newbury, M. Pepper, D.A. Ritchie, J.E.F. Frost and G.A.C. Jones, Phys. Rev. B **46** (1992) 3548; B. Su, V.J. Goldman and J.E. Cunningham, Phys. Rev. B **46** (1992) 7644; J. Wang, P.H. Beton, N. Mori, L. Eaves, H. Bühmann, L. Mansouri, P.C. Main, T.J. Foster and M. Henini, Phys. Rev. Lett. **73** (1994) 1146
- 3 G. Faini, A. Ramdane, F. Mollet and H. Launois, Inst. Phys. Conf. Ser. **112** (1990) 357
- 4 A. Ramdane, G. Faini and H. Launois, Z. Phys. B **85** (1991) 389
- 5 Y. Gaivao-Gobato, J.M. Berroir, Y. Guldner, G. Faini, H. Launois, Super. Micr. **12** (1992) 473
- 6 M. Boero and J. Inkson, Phys. Rev. B **50** (1994) 2479
- 7 F. Laroche, A. Ramdane and G. Faini, Surf. Sci. **267** (1992) 396
- 8 E. Bedel, G. Faini, C. Fontaine, F. Laroche, and C. Vieu, to be published
- 9 C. Vieu, A. Pepin, G. Ben Assayag, J. Gierak, F.R. Ladan, Inst. Phys. Conf. Ser. **134** (1993) 385
- 10 H.C. Liu and G.C. Aers, J. Appl. Phys. **65** (1989) 4908
- 11 M. Boero (private communication)
- 12 Y. Meir and N.S. Wingreen, Phys. Rev. Lett. **68** (1992) 2512

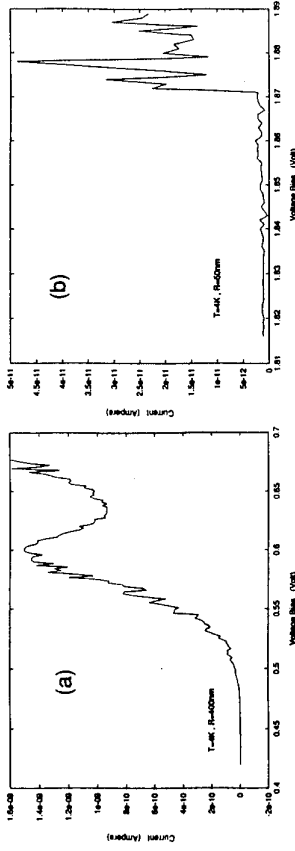


Figure 2:I-V characteristics measured at $T=4K$ on single quantum boxes with nominal physical radius of (a) 400nm and (b) 50nm; in (b) only the spectrum close to the threshold voltage is shown.

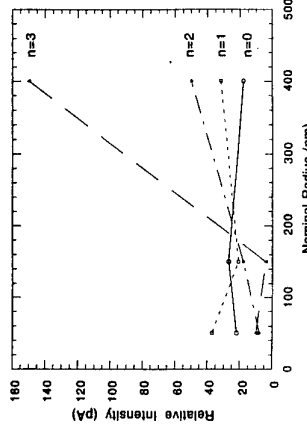


Figure 3:Relative intensity of the quantum box level number as a function of the physical radius and for different values of the quantum box level number. The drawn lines are only for eye-guide.

1 Introduction

ULTRA-HIGH-FREQUENCY COHERENT SOUND GENERATION IN RESONANT TUNNELING

Sergio S. Makler, Diana E. Tuyarot, Enrique V. Anda *

Instituto de Física, Universidade Federal Fluminense,
Campus da Praia Vermelha, Av. Gal. Milton Tavares de Souza s/n

24210-340 - Niterói - RJ, Brazil
and

Mikhail I. Vasilevskiy

Faculty of Applied Physics, N. Novgorod University,
Nizhni Novgorod, 603600 Russia

Abstract

In this paper we propose a device capable to generate ultra-high-frequency coherent sound. It is called SASER by analogy to laser. The device consists of a double barrier heterostructure (DBHS) tailored to permit phonons to resonate with the electronic system. The condition for resonance is fulfilled when the energy difference between the first and second resonant peaks of the electronic DOS in the well matches the LO phonon frequency.

Due to the low energy and short wavelength of the phonon beam this device could be useful for imaging and for non-destructive characterization of nanostructures. It could be also used to build phono-electronic systems (analogous to optoelectronics).

We establish kinetic equations for the number of electrons in each level, the number of LO phonons in the well and for the number of coherently generated secondary TA phonons that results from the LO phonon decay due to anharmonicity. Coefficients of the equations that describe the tunneling process have to be obtained in a self-consistent way considering the effects of space charge inside the well and the accumulation and depletion layers in the emitter and collector, respectively. The steady solution of the system is analyzed and the conditions for "SASER action" are discussed. The characteristic curve $I - V$ shows the well known bistability at the negative differential resistance region. Besides, at the beginning of the SASER emission this curve shows a chaotic behaviour.

In our device the $GaAs - AlGaAs$ DBHS is constructed such that $\Delta_e = \epsilon_1 - \epsilon_0$, that depends slightly upon the applied bias V , satisfies the resonant condition $\Delta_e = \hbar\omega_0$, when the electrons are injected directly into the first excited level through the application of the external potential[1, 2]. Here ϵ_0 is the energy of the ground-state in the well, ϵ_1 is the energy of the first excited level and ω_0 is the LO-phonon frequency. Therefore the electrons could decay to the ground state by emitting an LO-phonon. These phonons have a very small group velocity and, if the Al concentration in the barriers is greater than 0.3, they are confined inside the well [3]. Therefore they accumulate there. This accumulation represents an increase of the oscillation amplitude that makes important the anharmonic effects. Then the LO-phonons decay coherently by anharmonicity with more the short wavelength and low energy a short lifetime into a pair of phonons [4]. We are interested in this secondary intense beam of coherent TA phonons. The details of the proposed device and the processes involved in it will be described below.

A coherent beam of short wavelength ultrasound would be a useful tool to study nanostructures. To obtain images of a small structure we need waves much shorter than the size of the details of the system. The SASER beam proposed here will have wavelength smaller than 25 \AA , capable to see in detail structures of about 50 nm. On the other hand if we try to see structures at the submicron scale by using light we realize that these soft X-rays with the same wavelength will have energies greater than 0.5 KeV. That could affect strongly the system to be studied. As a possible application of the device it is possible to built near it thin barriers of $AlGaAs$ designed as semimirrors placed at 45° to split the beam and to force to pass one half through the part of the sample we are interested in and the other across a very pure reference $GaAs$. After

that we can use again semimirrors to superpose them and record the interference pattern with a detector. This pattern could be processed in a computer to get a hologram of the sample showing the three-dimensional shape of the nanostructure.

We have shown that the amplitude of the SASER beam can be easily modulated by varying the applied bias. This permit to use the phonon beam to transmit information from a component of a circuit to another at very short distance. These "phono-electronic" devices could work at lower distances and energies that the optoelectronic ones thus improving the computing performance.

A third potential application is to use the SASER beam to make sensitive under control a "phonoresist" (a compound with a soft mode close to the SASER frequency) for lithography at mesoscopic scale. Once more the short wavelength and low energy of this beam could turn out it better than the traditional methods.

It is important to notice that the amplification of sound by stimulated emission has been already observed experimentally. It was reported by Prieur et al. [5] in a letter whose title has precisely in its initials the word SASER (that we have had already used in a work in which the rough initial sketch of our device was presented [1]). In the paper of Prieur the phonon emission occurs between the two level system well known in glasses. Therefore the energy of that beam is distributed in a very wide range. Furthermore that energy is distributed about 0.01 meV far away from the phonon energy expected for our SASER. In another paper referring to coherent sound of lower energy [6], acoustical phonons are optically generated in a superlattice so that its wavelength is the same as the period of the superlattice (i.e., 500 Å what is about 20 times more than we expect from the device described below).

*This work has been financially supported by brazilian agencies CNPq and FINEP and by project Autorchas/Vtae/Andes grant 2021-10.

2 The device

Our system consists of a standard double barrier heterostructure. The distance between levels is determined basically by the well width but it depends also on the barriers' height because the penetration of the wave function into the barriers diminishes the confinement and then reduces the energy of the levels. For the same reason this energy difference $\Delta\epsilon$ depends also upon the applied bias. Besides, an electron-phonon interaction of strength g reduces the energy of each level by a quantity $gh\omega_0$ [7]. Other factors that modify the level position are the slope of the well due to the applied bias and its curvature due to the effect of accumulated charge. All these factors were taken into account in this work.

The system is prepared such that $\Delta\epsilon < \hbar\omega_0$ before the voltage is applied. When the voltage is increased this difference augments and after the first excited level merges below the Fermi level but remaining above the bottom of the conduction band the condition $\Delta\epsilon = \hbar\omega_0$ is fulfilled. We have calculated the transition rate of this process following the evaluation of the electron-phonon interaction given by Trallero Giner and Comas [8] and we have shown that the situation $\Delta\epsilon > \hbar\omega_0$ that occurs for higher applied bias is still compatible with energy and momentum conservation in the process of LO-phonon emission. The tunneling current and the phonon emission continue till the excited level merges below the bottom of the conduction band.

We have studied a DBHS under the effect of an external potential V using an one-dimensional tight-binding model. The widths of the levels involved in the process are about $\Gamma_0 = 0.005\text{meV}$ and $\Gamma_1 = 0.030\text{meV}$, depending slightly on V , when the barriers have the sizes used in our calculation, i.e., $b_L = b_R = 56.5\text{\AA}$, corresponding to 20 layers of $\text{Ga}_{1-x}\text{Al}_x\text{As}$, with a height of 300meV . It can be seen that the level positions ϵ_0 and

ϵ_1 depend upon the well width d and the applied bias V . For $d = 197.8\text{\AA}$, that corresponds to 70 layers of GaAs grown in the [100] direction, we found that when the applied bias varies between 59.4mV to 96.0mV , the position of the first excited level goes down from about 15meV to zero. Simultaneously the energy difference $\Delta\epsilon$ increases from 35.5meV to 36.8meV . That means that for a device prepared with a Fermi level $\epsilon_F = 15\text{meV}$, the system would have electrons injected into the excited level when V sweeps the region referred above. This includes the resonant value $\Delta\epsilon = 36.8\text{meV}$.

The accumulated charge inside the well, the phonon population and the potential profile have to be calculated selfconsistently. The electron and phonon populations must fulfill the following system of kinetic equations (in the steady state)

$$\begin{aligned} I &= R_0 n_0 + R_1 n_1 \\ R_0 n_0 &= w[n_1(n_{LO} + 1) - n_0 n_{LO}] \\ R_0 n_0 &= \gamma_0(1 + n_{TA})n_{LO} \\ n_{TA}/\tau &= \gamma_0(1 + n_{TA})n_{LO} \end{aligned}$$

where n_1, n_0 are the number of electrons at levels 1 and 0, and n_{LO}, n_{TA} are the number of primary and secondary phonons respectively. Here I is the current of electrons entering the well through the left barrier, R_1 and R_0 are the escape rates of electrons through the right barrier before and after the phonon emission respectively, τ is the escape rate of TA-phonons through the barriers and γ_0 is the decay rate of LO-phonons.

The LO-phonon emission rate w that varies strongly from zero to an almost constant value when $\Delta\epsilon$ becomes greater than $\hbar\omega_0$. This produces a strong oscillating behaviour on the characteristic curve for values of V close to the beginning of the SASER effect where n_0, n_{LO} and n_{TA} begin to be different from zero. These oscillations have the

characteristics of a chaotic behaviour. We have calculated the intensity of the SASER beam that is typically of the order of 4000 phonons per ps (see figure 2). This is of the same order of the intensity, in photons per ps, of a standard He-Ne laser with a power of about 1.25mw and a wavelength of about 6300\AA . Admittedly, as the energy of each photon is here 200 times greater than the phonon energy, the SASER power is very much lower.

References

- [1] E. V. Anda, S. S. Makler, H. M. Pastawski and R. G. Barrera, *Braz. J. of Phys.* **24** (1), 330 (1994).
- [2] E. V. Anda, S. S. Makler, H. M. Pastawski and R. G. Barrera, XII SLAFES, Pichidangui - Chile, Nov. 1992.
- [3] J.M. Jacob, D.M. Kim, A. Bouchalkha, J.J. Sony, J.F. Klem, H. Hou, C.W. Tu, H. Morkoc, *Sol. State Comm.* **91** (9), 721 (1994).
- [4] Fabrice Vallée, *Phys. Rev. B* **49** (4), 2460 (1994).
- [5] J.-Y. Prieur, R. Höhler, J. Joffrin and M. Devaud, *Europhys. Lett.* **24** (5), 409 (1993).
- [6] P. Basseras, S. M. Gracewski, G. W. Wicks and R. J. D. Miller, *J. Appl. Phys.* **75** (6), 2761 (1990).
- [7] N.S. Wingreen, K.W. Jacobsen and J.W. Wilkins, *Phys. Rev. B* **40** (17) 11 834 (1989).
- [8] C. Trallero Giner and F. Comas, *Phys. Rev. B* **37** (9) 4583 (1988).
- [9] L. Pavese and M. Guzzi, *J. Appl. Phys.* **75** (10) 4779 (1994).

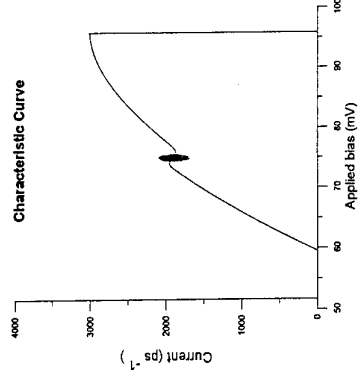


Figure 1: The characteristic curve shows a chaotic behaviour at the beginning of the SASER emission. The current is expressed in electrons per ps.

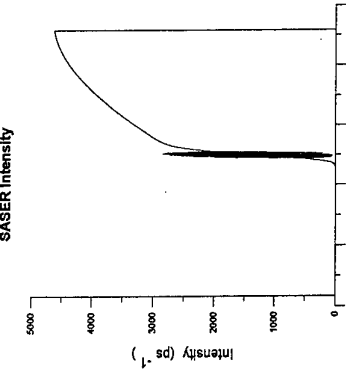


Figure 2: The SASER intensity measured in phonons per ps. After the initial chaotic regime the emission stabilizes. The linear region could be useful to modulate the SASER amplitude.

The Effect of Confining Electric Fields on New Magnetoplasma Excitations in a 2-D Electron System

P.K.H. Sonnenfeld, A.M.C. Valkering, R.W. van der Heijden, and A.T.A.M. de Waele
 Department of Physics, Eindhoven University of Technology,
 P.O. Box 513, NL-5600 MB Eindhoven, The Netherlands

Abstract

The effects of spatially varying electrostatic holding fields on several new types of edge excitations in a magnetic field are investigated for the 2DES on liquid helium. They clearly show that (a) the modes are localized near inhomogeneity boundaries of the sample and (b) different, independent edge modes exist.

1. Introduction.

The electrical and optical properties of two-dimensional electron systems (2DES's) are strongly determined by their lateral confinement [1]. Under Quantum Hall conditions, the boundaries are crucially important even for the DC electrical transport in large samples [2]. At very high frequencies (far-infrared) the magneto-optical properties of arrays of classical-[3] and quantum-[4] dots, anti-dots [5], rings [6] or wires [7] exhibit a frequency-magnetic field ($\omega(B)$) dispersion quite different from that of bulk samples. One of the most salient properties, the existence of regions where $\omega(B)$ has a negative slope, can basically be traced back to the classical phenomenon of edge magnetoplasma (EMP) waves [3,8]. These correspond to a collective excitation of the 2DES which is localized near a boundary of the sample as a result of the classical Hall effect [9]. These EMP's can be easily investigated in large samples of low density at high magnetic fields, where the frequencies of their resonant modes can be made arbitrarily low ($\omega \sim ne/BL$) [9], n , electron density, e , elementary charge, L (sample dimension). The 2DES on liquid helium is very suited to investigate EMP's. Because of the low densities attainable, the frequencies can easily be brought down to the 100 kHz regime or even much lower. Due to the absence of quantum degeneracy, it is the only 2DES in which the purely classical EMP can be studied. Recently, a new type of edge mode was found in this system [10]. The confining potentials can be easily varied with the use of a structured electrode system beneath the 2DES that serve as gates. This leads to new modes localized at inhomogeneity boundaries [11].

In this paper, the effect of spatially varying the holding field is investigated on the entire spectrum of low-frequency excitations in a magnetic field, which is an important help in identifying the spectra and locating the region of the sample that contributes to the different resonances.

2. Experimental method.

The charged helium surface was located about 1 mm above an array of electrodes with 14 mm diameter, shown in the inset of Fig. 2. The electrodes couple capacitively to the electron sheet. Overall confinement of the electrons is accomplished by negative potentials on

a plate about 2 mm above the surface and on a circular guard electrode of 15 mm diameter. In the reference situation, all segments of the lower plate are at DC ground. To spatially modulate the density distribution, some segments of the lower plate, usually the central disk M and surrounding ring, are biased at a positive or negative DC potential to increase or decrease the density above that segment. The densities, including their detailed profiles can be calculated from the electrostatics of the cell including the electron layer. For the measurements one of the outer electrodes (say 1) is excited with an ac-voltage of $10 \text{ mV}^{\text{max}}$ within the linear regime. The induced voltage at one of the other electrodes (usually the opposite one, 5), which is capacitively shunted to ground by the coaxial lead capacitance, is measured phase sensitively.

3. Results and Discussion.

A typical spectrum at a fixed magnetic field is shown in Fig. 1(a). The main peaks correspond to the harmonic series of resonances of conventional EMP's $\omega_i = i\omega_1$ ($i=1,2,\dots$) [12]. The variation of mode amplitude with harmonic number is caused by the excitation and detection efficiency, depending on the ratio ω/λ , with λ the wavelength and ω the width along the perimeter of the small electrodes. Obviously the amplitude must be zero when $\omega=\lambda$, and when $\omega=\lambda$.

A series of resonances is visible in the low-frequency region. As was recently shown [10], the dispersion relation for these resonances is very similar to those of EMP's, namely $\omega^* = \omega_1^* \propto neB$, just as for the EMP's. For this reason it was suggested that the new modes might correspond to the higher order EMP's, that were predicted theoretically by several groups [13]. These higher order modes are just like EMP's localized at the boundary region with the varying density, but have a multi-node structure also in radial direction unlike EMP's. Another possibility is that they are a coupled mode of a boundary oscillation and an edge.

The inset to Fig. 1(a) shows the variation of the frequencies ω of the EMP and these new modes with V_g (for another data set). Changing V_g changes the radius of the electron pool and the full lines give the expected $\omega(L)$ relations, assuming that the resonant frequencies in both cases vary as $1/L$. It follows that the

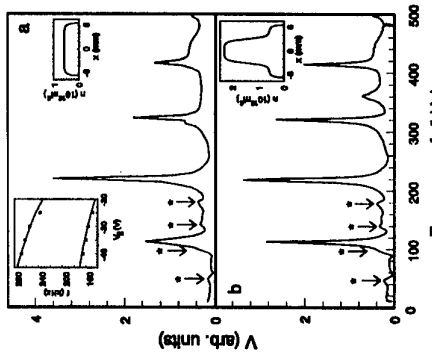


Fig. 1. (a) Spectrum for a magnetic field of 1 T, temperature 0.56 K, $V_{\text{top plane}} = 15 \text{ V}$, $V_b = 0$. Right inset: corresponding calculated cross-sectional density profile. Left inset: V_b -dependence of the position of one large and one small (*) peak (for other data) with the full line showing the calculated dependence. (b) Same as (a) but with a positive voltage of 30 V on the bottom central (M) and ring electrodes. Inset: corresponding calculated cross-sectional density profile.

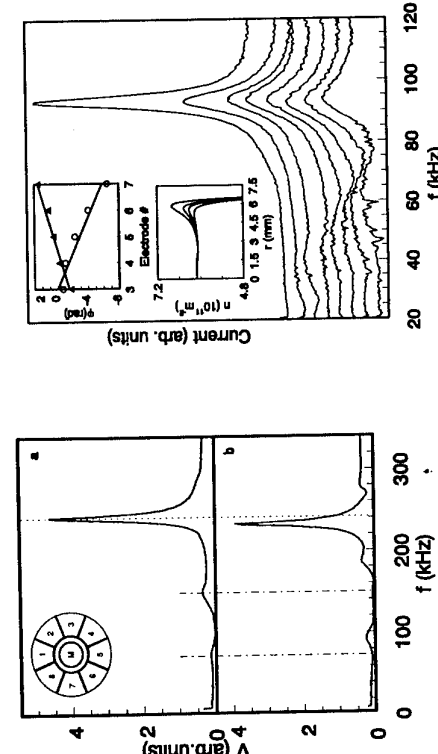


Fig. 2. Two spectra, under nearly identical circumstances ($V_{top} = -10$ V, $V_s = -15$ V, $B = 0.5$ T, $T = 0.5$ K) but with slight (uncontrolled) differences in confining potentials. Inset: electrode geometry of lower plate.

changing the potential of the top plate without changing the total charge at the surface. This will change the confining potential profile at the edge and also the density profile. The effects of this on the small ω -modes have so far not been addressed, because another unexpected major effect occurred as illustrated in Fig. 3, where a part of a spectrum is given for increasing pressing fields. In this experiment, the position of the large EMP resonance was kept fixed by adjusting the guard potential (and therefore L) at each pressing field. When the electrons are pressed stronger onto the surface, the linewidth increases as a result of increased electron-ripple scattering. Theories for linewidths, even for the conventional EMP's, are not well developed so far.

The unexpected feature in Fig. 3 is a broad resonance that appears with increasing E_1 at low frequencies and shifts towards higher frequencies. Analyzing the phase of this resonance at different electrodes like in Ref. 11, it could be established that it belongs to an excitation that propagates in a direction opposite to that of the EMP (see inset in Fig. 3). This is indicative of an IEMP [11]. Indeed a profile calculation for a pool at fixed total charge for increasing holding fields develops a maximum in the density profile near the edge (see inset). The IEMP is expected to be associated with the inner leading edge of the maxima, the EMP with the outer trailing edge.

4. Acknowledgement.

The European Commission is acknowledged for grants from the HCM programme (ERBCHBCT930490 and ERBCHRXC7930374).

5. References.

- [1] C.W.J. Beenakker and H. van Houten, in *Solid State Physics*, edited by H. Ehrenreich and D. Turnbull (Academic, New York, 1991), Vol. 44.
- [2] M. Büttiker, Phys. Rev. B **38** (1988) 9375; D.B. Chklovskii, B.I. Shklovskii and L.I. Glazman, Phys. Rev. B **46** (1992) 4026; R.J.F. van Haren, F.A.P. Blom, and J.H. Wolter, Phys. Rev. Lett. **74** (1995) 1198.
- [3] S.J. Allen, Jr., H.L. Störmer, and J.C.M. Hwang, Phys. Rev. B **28** (1983) 4875.
- [4] T. Denel, D. Heitmann, P. Grambow, and K. Ploog, Phys. Rev. Lett. **64** (1990) 788.
- [5] K. Kern, D. Heitmann, P. Grambow, Y.H. Zhang, and K. Ploog, Phys. Rev. Lett. **66** (1991) 1618; G.Y. Wu and Y. Zhao, Surf. Sci. **305** (1994) 601.
- [6] C. Dahl, J.P. Koithaus, H. Nickel, and W. Schlapp, Phys. Rev. B **48** (1993) 15480.
- [7] T. Denel, D. Heitmann, P. Grambow, and K. Ploog, Phys. Rev. Lett. **66** (1991) 2657.
- [8] D.C. Glattli, E.Y. Andrei, G. Deville, J. Pinenrein, and F.B. Williams, Phys. Rev. Lett. **54** (1985) 1710; D.B. Mast, A.J. Dahm, and A.L. Fetter, Phys. Rev. Lett. **54** (1985) 1706.
- [9] V.A. Volkov and S.A. Mikhalov, in *Modern Problems in Condensed Matter Sciences*, edited by V.M. Agranovich and A.A. Maradudin (North-Holland, Amsterdam, 1991), Vol. 27/2, p. 855.
- [10] O.I. Kirichek, P.K.H. Sommerfeld, Yu.P. Monarkha, P.J.M. Peters, Yu-Z. Kovdyra, P.P. Siejka, R.W. van der Heijden, and A.T.A.M. de Waele, Phys. Rev. Lett. **74** (1995) 1190.
- [11] P.K.H. Sommerfeld, P.P. Siejka, P.J.M. Peters, and R.W. van der Heijden, Phys. Rev. Lett. **74** (1995) 2359.
- [12] P.K.H. Sommerfeld, P.J.M. Peters, H.F.W.J. Vorstenbosch, R.W. van der Heijden, A.T.A.M. de Waele, and M.J. Lea, Physica B **194-196** (1994) 1311.
- [13] S.S. Nazin and V.B. Shikin, Sov. Phys. JETP **67**, 238 (1988); I.I. Aleiner and L.I. Glazman, Phys. Rev. Lett. **72**, 2935 (1994); X. Xia and J.J. Quinn, Phys. Rev. B **50**, 11187 (1994); S.A. Mikhailov, JETP Lett. **61**, No 6 (1995).

ω^* resonances are indeed a type of geometrical resonance, just as the EMP's. Fig. 1(b) shows a similar spectrum as Fig. 1(a), but now for a sample where the central region has a higher density, using a positive potential on the central electrode. The conventional EMP's as well as the new modes are completely unaffected and therefore are independent of the interior region of the sample. These observations show that the new mode also corresponds to an edge excitation.

A new resonance has appeared in Fig. 1(b) at a frequency near 360 kHz. This peak belongs to a plasmon localized at the boundary between the two regions with different density (inter-edge magnetoplasmon, IEMP) [11]. It is important to rule out that the new modes are some artificial derivative of the EMP's. In [10], only indirect arguments could be given. Fig. 2 proves that the modes are independent. Both traces are made under nearly the same circumstances, but with some small unintentional variation in the confining fields, caused by slightly different densities in the two cases. This leads to slight shifts in the resonance positions, but the shifts for the conventional and the new resonances are in opposite directions. Note that in Fig. 2(b) the EMP-frequency lies in between the second and third harmonic of the ω^* resonances, which firmly rules out a harmonic relation between the frequencies of both sets [10].

To further investigate the edge resonances, the holding electric field E_1 was varied by

Shear Modes in 2D Ion Crystals Trapped below the Surface of Superfluid Helium

P. L. Elliott, A.A. Levchenko*, C.I. Pakes, L. Skrbek† & W.F. Vinen
 School of Physics & Space Research, University of Birmingham,
 Birmingham B15 2TT, UK

Abstract

An experimental study is reported of shear modes in the crystal phase of a circular 2D pool of charged ions trapped just below the free surface of superfluid ^4He . The frequencies of the modes are in good agreement with theory. Preliminary studies are included of the damping of the modes, of the temperature dependence of the mode frequencies, and of the effect on the modes of damage to the crystal.

Introduction

Positive ions can be produced in superfluid ^4He by field ionization, and they consist of ${}^4\text{He}$ ions surrounded by a shell of solid helium formed by electrostriction; the ions have an effective mass of about 30 helium atomic masses. A two-dimensional pool of such ions can be trapped just below the free surface of the liquid by the combination of an image potential pushing the ions away from the surface and a uniform external electric field (E_0) pushing them towards the surface [1]. The trapping depth depends on the magnitude of E_0 , and is typically 40 nm. At a typical pool density (n_0) of 10^{12} m^{-2} the ions form a 2D classical Coulomb crystal below a melting temperature (T_m) of about 230 mK [2,3]. We report an observation and study of shear modes in this type of Coulomb crystal.

Shear modes in a 2D classical electron crystal trapped above the surface of liquid helium were observed by Deville *et al* [4]. The modes concerned had high frequencies which were shifted significantly by interaction of the electrons with dimples in the helium surface that form beneath each electron in the crystal phase, but good measurements of the shear modulus of the crystal and its temperature dependence were obtained. In the case of the ion crystals with which we are concerned, the corresponding surface dimples are very small and have a negligible effect. It is therefore possible to study shear modes of low frequency without interference from the dimples.

Experimental techniques

The circular pools of ions of typical radius 1.3 mm are surrounded by a system of electrodes that serve to provide the holding electric field and to allow the generation and detection of the various modes of oscillation of the pool. Direct generation and direct detection of these modes is possible only through electrostatic interaction with one or more of the electrodes. However, pure shear modes involve no charge fluctuation, and therefore they do not couple to the electrodes. A coupling can be induced by applying a vertical magnetic field (as was done by Deville *et al*), the shear modes then acquiring a small longitudinal component, but for

the ions the coupling turns out to be too small to allow the modes to be both excited and detected electrostatically. We have therefore relied only on electrostatic excitation, and we have detected the modes through a non-linear coupling that exists between different modes of oscillation [3,5], and in particular between the shear modes and the (longitudinal) plasma modes. The lowest axisymmetric plasma mode is driven at or close to its natural frequency of about 100 kHz, and a second drive is applied over the frequency range up to about 3 kHz, where the lowest shear modes of the pool are expected to appear. Strong excitation of a shear mode is observed as a change in the response of the plasma mode. Typically we observe the change in the amplitude of response of the plasma mode when it is driven slightly off resonance. The damping of the plasma mode, which is determined by the ripplon-limited mobility of the ions, is small at the low temperatures concerned, so that this technique is quite sensitive and does not require that the shear mode be driven very hard. It is important to remember, however, that the detection is inherently non-linear, which must be taken into account when measuring shear-mode linewidths.

Experimental results

The simplest experimental results, which we shall interpret with some confidence in the next section, relate to ion pools that are trapped at depths exceeding 50 nm ("deep pools") and to low temperatures (less than $0.5T_m$). Otherwise the results are complicated in ways that we have not yet fully explored and do not understand. As we shall explain in the next section, the behaviour of deep pools seems to be affected by ripplon interactions only to the extent that these interactions limit the mobility of the ions. The observation that shallow pools seem to behave differently suggests they are influenced in a more complicated way by ripplon interactions. The situation near the melting temperature seems to be affected by the appearance of other low-frequency modes, to which we shall return later. Furthermore, the quality of the experimental data deteriorates as the temperature is raised. The results that we now describe relate only to deep pools and low temperatures.

A typical observed spectrum that we ascribe to shear modes is shown in figure 1. The predicted frequencies, obtained in a way that we describe in the next section, are indicated by the vertical arrows, and we see that there is good agreement with experiment. The dependence of these frequencies on pool radius, pool density, and magnetic field has been studied, and there is again good agreement between experiment and theory. Shear mode linewidths increase (reversibly) with increasing amplitude of the driving voltage, but they tend to limiting values at low drives. For the case of axisymmetric modes, which are the most easily observed and studied, the limiting linewidths increase with increasing frequency in the way shown in figure 2. The frequencies of the shear modes are observed to decrease with increasing temperature, although the quality of our data at the higher temperatures does not yet allow us to make firm statements about the precise form of the dependence.

The response of a shear mode to a low drive is found to be reduced if the mode has previously been driven hard; a very strong drive will cause the response to disappear altogether.

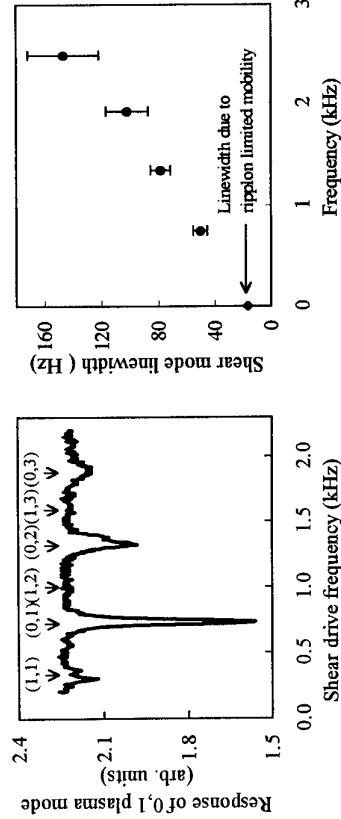


Fig. 1 Observed spectrum of shear modes
 $(m_0 = 7.51 \cdot 10^{11} \text{ m}^{-2}, T=30 \text{ mK})$

We attribute this behaviour to damage in the crystal, the shear required to produce substantial damage being found to be very roughly 9%. It is found that the crystal will recover if it is either remelted and slowly cooled or annealed at a temperature just below T_m .

Theoretical instrumentation

The predicted response of the pool is based on the equations of motion of a continuum solid of charged particles with a shear modulus μ ; we take $\mu = 0.245 \rho_0^3 e^2 / 4\pi \varepsilon_0$ at $T=7$ [6], with the temperature dependence predicted in [7] (and references therein) and verified in [4]. Such a solid supports both longitudinal (plasma) modes and shear modes, the latter modes having in practice much lower frequencies. The modes cease to be purely longitudinal or purely transverse in the presence of a vertical magnetic field, although those of low (high) frequency are still largely transverse (longitudinal). An ion pool has a density profile that is flat except within a small distance, h , of its edge. Provided that the wavenumber of the mode that we are considering is small compared with $1/h$, the effect of the edge can be represented by imposing two boundary conditions. The first is that the radial displacement of the ions vanishes at the edge (the validity of this condition is confirmed by the observed frequencies of the plasma modes); the second is that the shear stress at the pool edge shall also vanish. Since the shear (transverse) modes must be observed in the presence of a magnetic field, they must have associated with them a small longitudinal component. No mode with a single wavenumber can then satisfy both the boundary conditions. The resonant modes of the pool are therefore formed from mixtures of two wavenumbers; for shear modes in the presence of a large magnetic field, one of these wavenumbers is real and the other is pure imaginary (i.e. an edge mode). The predicted

The observed temperature dependence of the mode frequencies is *consistent* with that predicted from the temperature dependence of μ , but our data do not yet allow us to make a stronger statement.

The ions have a finite mobility, which is determined by collisions with ripples. Within experimental error the observed damping of plasma waves in the ion pools is independent of frequency and due entirely to this finite mobility. The observed damping of the shear modes at low temperatures increases with increasing frequency and is significantly larger (by a factor of typically three) than can be accounted for by the finite mobility; the situation at higher temperatures is less clear, although there is some evidence that the finite mobility then accounts for a larger fraction of the damping. The extra damping is presumably due to internal friction in the crystal, although there might be a contribution also from the low-density edge of the pool, which must be molten or in a hexatic phase. If this internal friction leads to a relaxation process characterized by a single relaxation time τ , the resulting frequency dependence of the damping will be of the form $A\omega^2\tau/(1+\omega^2\tau^2)$, where A is a constant. The observed extra damping

The internal friction must be due to defects, and, as we have seen, deliberate damage to the crystal, which introduces defects in excess of any present in equilibrium, does certainly increase the shear mode damping. It is not yet clear whether the damping observed in an annealed crystal is due entirely to intrinsic defects, such as dislocation pairs present in equilibrium [8,9].

As we have noted, extra modes seem to appear at temperatures close to T_m . Among them are modes with frequencies that decrease with decreasing magnetic field, and it is possible that they can be identified with those predicted by Nazin & Shikin [10]. Modes are also present above T_m ; they may be characteristic of a hexatic phase, and we aim in future to study them in

Present address: Institute of Physics, AVCR, 25068 Řež, Czech Republic.
† Permanent address: Institute of Physics, AVCR, 142432 Černogorovka, Russia.

- [1] C F Barenghi *et al*, *Phil. Trans. Roy. Soc. London A334*, 139 (1991)
 [2] C J Mellor & W F Vinen, *Surf. Sci.* 229, 368 (1990)
 [3] W F Vinen *et al*, *Physica B197*, 360 (1994)
 [4] G Deville *et al*, *Phys. Rev. Letters*, 53, 388 (1984)
 [5] N. J. Applebyard *et al*, *Phys. Rev. B51*, 5892 (1995)
 [6] L. Bonsall & A. A. Maradudin, *Phys. Rev. B15*, 1959 (1977)
 [7] M.C. Chang & K. Maki, *Phys. Rev. B27*, 1646 (1983)
 [8] J. M. Kosterlitz & J. Thouless, *J. Phys. C6*, 1181 (1979)
 [9] A. Zippelius, B. I. Halperin & D. R. Nelson, *Phys. Rev. B22*, 2514 (1980)
 [10] S. S. Nazin & V. B. Shuklin, *Sov. Phys. JETP* 67, 288 (1988)

Single particle and electron-electron scattering rates in coupled quantum wells

Y. Berk¹, A. Kamenev², A. Palevski¹, H. Shtrikman², M. Shatzky¹

¹School of Physics and Astronomy, Raymond and Beverly Sackler Faculty of Exact Sciences, Tel Aviv University, Tel Aviv 69978, Israel

²Department of Condensed Matter, The Weizmann Institute of Science, Rehovot 76100, Israel.

We have studied experimentally the single-particle (small angle) and electron-electron scattering in coupled double-quantum well systems. These scattering rates were determined by analysis of resistance resonance (RR) effect in the in-plane magnetic field. We have demonstrated that the values for single-particle scattering rate are in fair agreement with Shubnikov-de Haas data and electron-electron scattering rates are consistent with the theoretical calculations.

The resonant coupling of electrons in double quantum wells (QWs) leads to delocalization of electronic states in such systems. It was demonstrated experimentally [1,2] that this quantum mechanical phenomenon strongly influences the electrical resistance of QWs measured in parallel, giving rise to "resistance resonance" (RR) peak when QWs have different mobilities. Recently it was demonstrated [3,4] that the *in-plane* magnetic field suppresses the coupling between electronic states. The microscopic description of the lateral magnetoresistance of the coupled QWs was developed and verified [4] by the experimental data. Some microscopic parameters, namely coupling energy Δ , and single-particle (or small angle) scattering time τ incorporated in the theory were estimated, but not independently experimentally verified in the above mentioned investigation. In this paper we present an extensive experimental studies of magnetoresistance in double QWs in different limits of quantum mechanical coupling between QWs, mobilities and temperature. These measurements are supplemented by the the analysis of Shubnikov-de Haas (SdH) oscillations in perpendicular magnetic field which allows to deduce independently the parameters used in the theory. The main points, following from our studies, are:

- (i) the *in-plane* magnetic field destroys the coupling between QWs; the lineshape of the magnetoresistance fits the microscopic formula with a single-particle scattering time being the only fitting parameter.
- (ii) the *width* (i.e. the characteristic magnetic field, H_c) of the RR is sensitive to the single electron scattering time, providing a new method of measuring the small angle scattering time on the remote impurities;
- (iii) the dependence of H_c on temperature at elevated temperatures and on Fermi energy suggests that the electron-electron scattering rate (intralayer and interlayer) may be tested as well.

The detailed diagrammatic calculation, based on the Kubo formula [4] leads to the following dependence of the resistance resistance, R , on the in-plane magnetic field, H (H is perpendicular to the direction of the excitation current, j):

$$R^{-1}(H) - R_{off}^{-1} = (R^{-1}(0) - R_{off}^{-1})f(H/H_c), \quad (1)$$

where

$$f(x) = \frac{2(\sqrt{1+x^2}-1)}{x^2\sqrt{1+x^2}}, \quad (2)$$

and the characteristic field is given by

$$H_c = \frac{\hbar c}{e v_F \tau b} \sqrt{1 + \left(\frac{\Delta}{\hbar}\right)^2 \frac{\tau_F + \tau_2^r}{2}}, \quad (3)$$

with $2\tau^{-1} \equiv \tau_1^{-1} + \tau_2^{-1}$. The above relations are valid until $H \approx H_F$, where $H_F \equiv 2\pi\hbar c/(e \lambda_F b)$; λ_F is a Fermi wavelength. Note also that $H_c \ll H_F$, when $v_F \tau / \hbar \gg 1$. Here $\tau_{1,2}, \tau_{1,2}^r$ are single-particle (small angle) and two-particle (transport) scattering times in the first and the second QWs respectively, v_F is the Fermi velocity, and b is the distance between the centers of the QWs. Note that, all the parameters can be measured directly from SdH oscillations of the resistance in perpendicular magnetic field at low temperatures.

Two sets of double QW structures were grown on a N^+ -GaAs substrate by molecular-beam epitaxy and consist of two GaAs wells of 139 Å width separated by 14 Å, and 28 Å Al_{0.3}Ga_{0.7}As barriers. The electrons were provided by remote delta-doped donor layers set back by spacer layers from the top and the bottom well correspondingly. In all our samples the bottom well had lower mobility due to the rougher AlGaAs/AlGaAs interface for that well. The schematic cross-section of the device may be found in Ref. [1]. Measurements were done on 10 μm-wide and 200 μm-long channels with Au/Ge/Ni Ohmic contacts. Top and bottom gates were patterned using the standard photolithography fabrication method. The top Schottky gate covered 150 μm of the channel. The data were taken using a lock-in four terminal technique at $f = 37$ Hz. The voltage probes connected to the gated segment of the channel were separated by 100 μm.

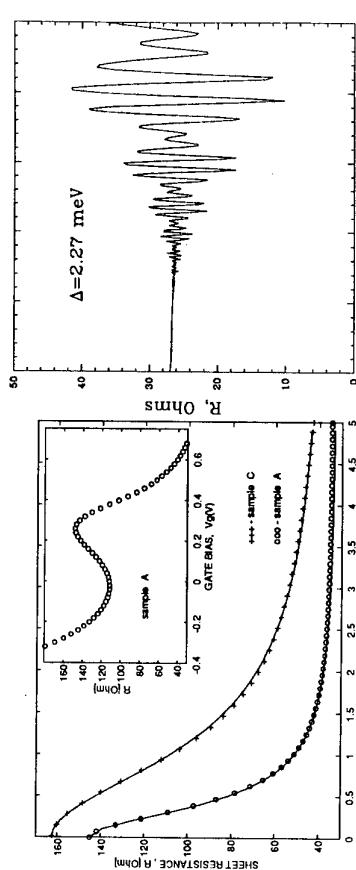


Fig. 1. The resistance resistance (RR) vs. magnetic field at 4.2 K (solid lines – theory). The inset – lineshape of the RR vs. gate voltage.

The variation of the top gate voltage, V_g allows to sweep the potential profile of the QWs through the resonant configuration. The resistance vs. top gate voltage for the sample with 28 Å barrier at $T = 4.2K$ is plotted in the inset of Fig. 1. The resistance resonance is clearly observed at $V_g \approx 0.28V$. A similar procedure allows to determine resonance values for V_g for structures with 14 Å barrier.

Next we fix the gate voltages, corresponding to the exact resonance position, and measure the resistance as a function of the in-plane magnetic field perpendicular to the direction of the current, $\mathbf{H} \perp \mathbf{j}$. Fig. 1 shows the behavior of the RR for two structures with 14 Å and 28 Å barriers.

The experimental data clearly demonstrate the suppression of the RR by the magnetic field, as well as the expected broadening for stronger coupled structures, i.e. the resistance

decreases slower for samples with larger barrier width. In order to establish the microscopic parameters employed in the theoretical description we perform the analysis of SdH oscillations of the resistance, for the samples with applied gate voltage corresponding to RR. Fig. 2. shows beats of the resistance, which are an indication of two subbands with different E_F present at resonance [5].

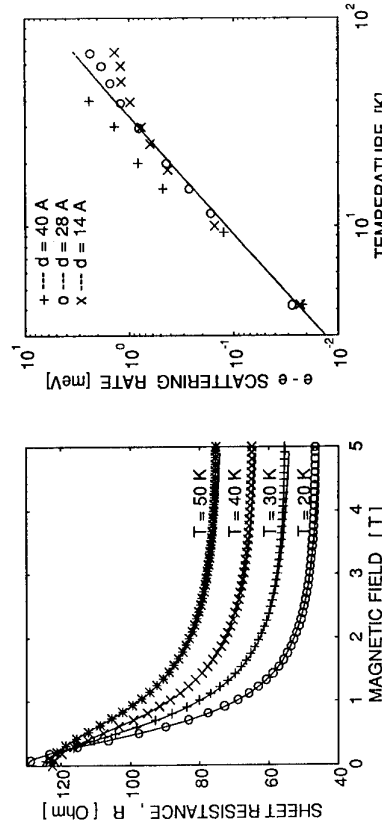


Fig. 3. The resonance resistance (RR) vs. magnetic field for different temperatures (the solid lines are the theoretical curves)

The distance between the nodes of the curve allows us to find the separation between the subbands $\Delta = E_{F1} - E_{F2}$. For the samples with 14\AA and 28\AA barriers we obtain Δ s of 2.3meV and 1.1meV corresponding. These values are in a good agreement with the theoretical estimates. In addition to the parameter Δ we extract for each sample a small-angle scattering time τ . Their values are tabulated in Table 1. The complementary measurements of the Hall effect and the sample resistance versus gate voltage provide us the rest of the parameters entering into the definition of H_c , namely $\tau_{1,2}^{tr}$.

The theoretical expression (1) fits perfectly the experimental data shown in Fig. 1 (solid line is the theoretical curve) and the values of τ used as the *only* fitting parameter are tabulated in Table 1. The agreement between values of τ obtained from RR and SdH measurements is quite fair for samples with low mobilities of one of the wells and rather poor for the high-mobility samples.

We follow the identical fitting procedure for the RR vs H curves obtained at elevated temperatures (see Fig. 3). As the temperature is increased, the experimental curves become broader and therefore $\tau(T)$ obtained in the fitting procedure attains smaller values. The correction of τ^{tr} due to increase in temperature is measured by the method mentioned above.

The values of the scattering rate $\tau(T)^{-1}$ are temperature-independent (within experimental resolution) below 4.2K for low-mobility samples and below 2.2K for high-mobility samples. These saturated values which we denote as $\tau(0)^{-1}$ are subtracted from $\tau(T)^{-1}$, and the variation of $\tau(T)^{-1} - \tau(0)^{-1}$ versus temperature is plotted in Fig. 4 for samples with different barrier width d. The data for sample with $d = 40\text{\AA}$ is taken from Ref. [4]. The solid line represents the theoretical expression [6] for $\tau^{-1}(T)$ in a clean 2D gas:

$$\frac{\hbar}{\tau_{ee}} = \frac{1}{\pi} \frac{(k_B T)^2}{\epsilon_F} \left(1 + \ln 2 + \ln \frac{\lambda_{TF}}{\lambda_{TF}} - \ln \frac{k_B T}{\epsilon_F} \right), \quad (4)$$

where $\lambda_{TF} = 276\text{\AA}$ is Thomas-Fermi screening length in GaAs.

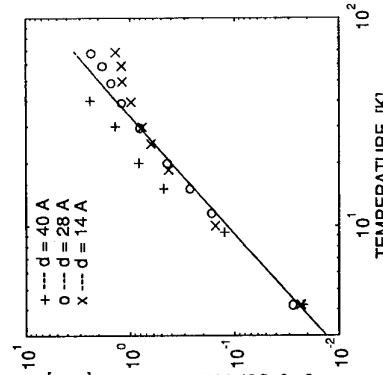
The agreement between the experimental points and the theoretical curve Eq. (4) is quite remarkable. This equation is valid only in the limit $k_B T \ll \epsilon_F$. Therefore the deviations of the experimental points from the theory at high temperatures are not surprising.

Table 1

Sample	d (barrier width), [\AA]	Δ from SdH, [meV]	$(\tau_1^{tr})^{-1}$ [meV]	$(\tau_2^{tr})^{-1}$ [meV]	τ^{-1} from SdH, [meV]	$\tau(0)^{-1}$ from RR, [meV]
A	28	1.1	0.02	0.38	0.8	0.6
B	28	1.1	0.04	0.07	0.5	0.18
C	14	2.27	0.02	0.39	0.9	0.84
D	14	2.27	0.02	0.05	0.34	0.16

Thus we believe that the RR in two coupled QWs with different mobilities provides a powerful and relatively simple method of measuring of small angle and e - e scattering rates. We have benefited from the useful discussions with O. Entin and M. Karpovski. The experimental research was supported by the Israel Academy of Sciences and Humanities. A.K. was supported by the German-Israel Foundation (GIF) and the U.S.-Israel Binational Science Foundation (BSF).

Fig. 4. Electron-electron scattering rate vs. temperature.



- [1] A. Palevski, F. Beltram, F. Capasso, L. N. Pfeiffer and K. W. West, Phys. Rev. Lett. **65**, 1929 (1990).
[2] Y. Ohno, M. Tsukada and H. Sakaki, Appl. Phys. Lett. **62**, 1952 (1993).
[3] J. P. Eisenstein, T. J. Gramila, L. N. Pfeiffer, K. W. West, Phys. Rev. **B44**, 6511 (1991).
[4] Y. Berk, A. Kamenev, A. Palevski, L. N. Pfeiffer, and K. W. West, Phys. Rev. **B51**, 2604 (1995).
[5] G. S. Boebinger, A. Passner, L. N. Pfeiffer, K. W. West, Phys. Rev. B **43**, 12673 (1991).
[6] G. F. Giuliani, and J. J. Quinn, Phys. Rev. **B** **26**, 4421 (1982).

Strong enhancement of Coulomb drag in double layer systems due to correlations among carriers

L. Świertkowski^(a), J. Szymański^(b), and Z.W. Gorzel^(c)

^(a)School of Physics, The University of New South Wales, Sydney 2052, Australia

^(b)Telstra Research Laboratories, 770 Blackburn Road, Clayton, Vic. 3168, Australia

^(c)Department of Physics, University of Alberta, Edmonton, Alberta, T6G 2J1, Canada

Abstract

We investigate the influence of many-body correlations on Coulomb drag between spatially separated conducting layers of electrons or holes. We show that the correlations can enhance the drag at low carrier densities and small layer separations by up to an order of magnitude. Good agreement between observed and calculated temperature and concentration dependence of transresistance is obtained.

Introduction

Transport properties of a system composed of two parallel, spatially separated 2D electron and electron or hole gases are affected by Coulomb scattering between carriers in different layers. Coulomb interaction competes directly with the coupling between the carriers due to the exchange of phonons across the barrier. The relative importance of these scattering mechanisms depends strongly on the thickness of the barrier separating the gases: for larger separations the phonon mechanism dominates becoming relatively less important for smaller separations [1,2]. In order to isolate the effects due to the Coulomb interactions, experiments are performed for thin barriers (~ 20 nm) but persistent disagreement exists between recent transresistance measurements [3] and theories of this effect [3-6]. We demonstrate in this work that the Coulomb correlations account for most of the discrepancies.

The system under consideration consists of two adjacent layers of carriers (electrons or holes) in GaAs-Al_xGa_{1-x}As heterojunctions. The electronic systems on both sides of the barrier are very well described as 2D electron/hole gases, particularly at low temperatures. When an electric current is set in one of the layers it drags the carriers in the other one. If, however, the current is not allowed to flow in the second layer, the carriers in it are swept to one of its ends until the induced electric field balances exactly the drag force. Transresistance is defined as the ratio of the potential difference induced in the stopped layer to the current in the drag layer.

Theory

Expression for transresistance in a double layer system was derived repeatedly in the past [3-6] using variety of approaches. In our derivation quantum kinetic equations for the relaxation functions of the double layer system are derived using the Mori's projection operator method in analogy to the procedure followed for the single layer system [7]. Solution of these equations in the hydrodynamic limit leads to the expression for the conductivity tensor from which the

DC transresistance can be obtained. It incorporates, in a fully consistent way, the effects of dynamical screening and of short range intra- and interlayer correlations. The resulting expression for transresistance of a square double layer sandwich is [8]

$$R_T = \frac{-\beta\hbar^2}{4\pi^2 e_1 e_2 n_1 n_2} \int_0^\infty dq q^3 \int_0^\infty d\omega \left| \frac{V_{eff}^{12}(q)}{\epsilon(q, \omega)} \right|^2 \frac{\text{Im} \chi_0^1(q, \omega) \text{Im} \chi_0^2(q, \omega)}{\cosh(\beta\hbar\omega) - 1}, \quad (1)$$

where $\beta = 1/k_B T$ and subscripts or superscripts $\alpha = 1, 2$ refer to two layers of the system and $e_\alpha = +e$ for the hole-filled layer and $-e$ for the electron-filled one. Derivation and physical interpretation of this result for a simpler case of no correlations can be found in Ref. [6]. The most important feature of our approach, distinguishing it from previous attempts, is that short range Coulombic correlations are inherent in it. The correlations are accounted for by static local field correction factors $1 - G^{\alpha\alpha}(q)$ multiplying the bare Coulomb potentials [9]. Thus, the effective intra- and interlayer interaction between the carriers are

$$V_{eff}^{\alpha\alpha'}(q) = \frac{2\pi e_\alpha e_{\alpha'}}{\epsilon_0 q} F^{\alpha\alpha'}(q) [1 - G^{\alpha\alpha'}(q)] \exp[-qd/(1 - \delta_{\alpha\alpha'})], \quad (2)$$

where ϵ_0 is the background static dielectric constant of the host material, and d is the thickness of the potential barrier. We use standard form factors $F^{\alpha\alpha'}(q)$ for the square well potential model of the layers. The intra- and interlayer ones static local field corrections are calculated using the self-consistent Singwi-Tosi-Land-Sjölander (STLS) procedure [9] generalized to double layer systems [10,11].

The dielectric function

$$\epsilon(q, \omega) = [1 + V_{eff}^{11}(q) \chi_0^1(q, \omega)][1 + V_{eff}^{22}(q) \chi_0^2(q, \omega)] - [V_{eff}^{12}(q)]^2 \chi_0^1(q, \omega) \chi_0^2(q, \omega) \quad (3)$$

in Eq. (1) screens the effective Coulomb interaction $V_{eff}^{12}(q)$ between the carriers from different layers accounting for the modification of the excitation spectrum of the system due to the interaction between gases. Essentially, two collective plasmon modes emerge: the acoustic plasmon with linear dispersion in the long wavelength limit in which both subsystems oscillate out of phase, and the optical plasmon with the square root dispersion law in which they oscillate in phase [12,13]. At finite temperatures, the momentum and the energy transfers corresponding to the plasmon poles, in particular the acoustic ones which are easier to excite thermally, significantly contribute to the transresistance.

The role of correlations can be summarised as follows. The *intralayer correlations* (included through $G^{\alpha\alpha}(q)$) account for the depletion of the probability of finding an electron (or a hole) around a particular charge carrier within the same layer since the carriers tend to avoid each other. This, in turn, suppresses the screening of the *interlayer* interaction and, consequently, enhances the Coulomb drag in the electron-electron and the electron-hole systems alike. The *interlayer correlations* influence the drag more directly. In the electron-hole system it enhances the probability of finding an electron and a hole close to each other on the opposite sides of the barrier. The correlated motion of electrons and holes (excitonic effect) enhances the drag. In the electron-electron system the effect of the interlayer correlations is opposite due to the repulsion between carriers.

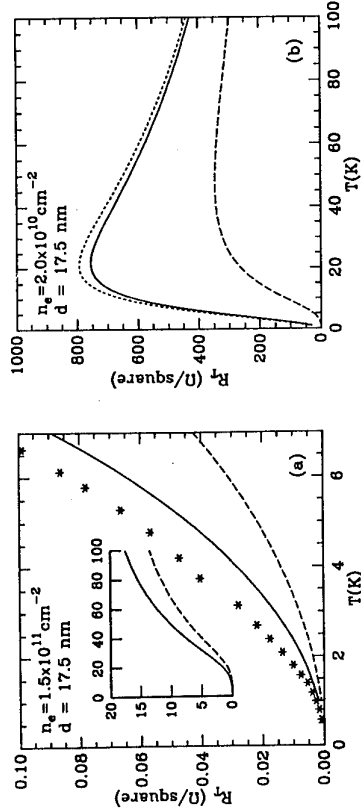


Figure 1: Temperature dependence of the transresistance for the electron - electron double layer system experimentally investigated by Gramila et. al [1]. As seen in Fig. 1(a) the mean field approach underestimates the transresistance by at least a factor of three and the inclusion of correlations significantly improves the agreement with the experiment. The remaining discrepancy can be attributed [1,2] to the phonon exchange mechanism. It is clear that without accurate accounting for the correlations it is impossible to assess the strength of the phonon contribution from the experimental data. The temperature dependence of the transresistance for higher temperatures is shown in the insert. Fig. 1(b) gives the results for the system with lower carrier concentration. It is clear that, as expected, the many - body correlations play a more prominent role in systems with lower carrier densities.

Numerical results and discussion

We have calculated temperature dependence of the transresistance for the electron - electron double layer system experimentally investigated by Gramila et. al [1]. As seen in Fig. 1(a) the mean field approach underestimates the transresistance by at least a factor of three and the inclusion of correlations significantly improves the agreement with the experiment. The remaining discrepancy can be attributed [1,2] to the phonon exchange mechanism. It is clear that without accurate accounting for the correlations it is impossible to assess the strength of the phonon contribution from the experimental data. The temperature dependence of the transresistance for higher temperatures is shown in the insert. Fig. 1(b) gives the results for the system with lower carrier concentration. It is clear that, as expected, the many - body correlations play a more prominent role in systems with lower carrier densities.

The qualitative difference between the temperature dependence of the transresistance for different carrier concentrations, seen in Figs. 1(a) and (b) is somewhat illusory. For higher densities a maximum of transresistance also occurs but at temperatures well above 100 K since its position scales approximately with the Fermi temperature of the system.

In order to show the relative importance of the intra- and interlayer correlations we also present in Fig. 1(b) the transresistance with the interlayer correlations suppressed ($G_{12} \equiv 0$). As expected, the intralayer correlations tend to decrease the strength of the Coulomb drag in the electron-electron system. At lower concentrations as in Fig. 1(a) the role of interlayer correlations is negligible.

From the theoretical point of view the electron-hole double layer systems are more interesting since for experimentally attainable carrier concentrations the correlations effects are stronger than in the electron-electron systems due to much higher effective mass of holes. In Fig. 2 the electron/hole concentration dependence of the transresistance in such a system is shown for several temperatures. As seen there, the correlations not only enhance the drag but also change the

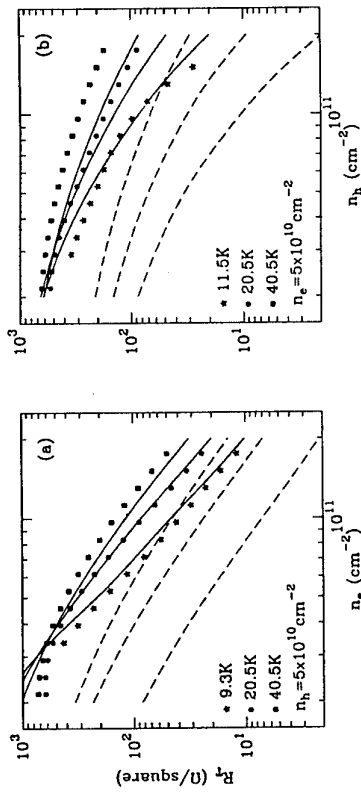


Figure 2: Electron (a) and hole (b) concentration dependence of the transresistance for the electron-hole double layer system for experimental temperatures of Ref. [3]. Full theory with correlations (disorder scattering included). Ref. [8], solid lines), mean field approximation (dashes), experiment (squares, full circles, asterisks).

character of its temperature dependence, suppressing it at lower carrier concentrations. The carrier concentration dependence is stronger with the correlations included in the theory, particularly electrons. We conclude that a good agreement between the theoretical and the experimental results is unattainable within theories which ignore many-body correlations.

This work was supported by grants from the Australian Research Council and from the Natural Sciences and Engineering Research Council of Canada. J.S. acknowledges the permission of Director of Telstra Research Laboratories to publish the paper.

References

- [1] T.J. Gramila, J.P. Eisenstein, A.H. MacDonald, L.N. Pfeiffer, and K.W. West, Phys. Rev. Lett. 66 (1991) 1216.
- [2] T.J. Gramila, J.P. Eisenstein, A.H. MacDonald, L.N. Pfeiffer, and K.W. West, Phys. Rev. B 47 (1993) 12957.
- [3] U. Sivan, P.M. Solomon, and H. Shtrikman, Phys. Rev. Lett. 68 (1992) 1196.
- [4] H.C. Tso and P. Vasilopoulos, and F.M. Peeters, Phys. Rev. Lett. 70 (1993) 2146.
- [5] A.-P. Jauho and H. Smith, Phys. Rev. B 47 (1993) 4420.
- [6] L. Zheng and A.H. MacDonald, Phys. Rev. B 48 (1993) 8203.
- [7] D. Neilson, L. Świerkowski, A. Sjölander, and J. Szymański, Phys. Rev. B 44 (1991) 6291.
- [8] L. Świerkowski, J. Szymański, and Z.W. Gorzel, Phys. Rev. Lett. 74 (1995) 3245.
- [9] K.S. Singwi, M.P. Tosi, R.H. Land, and A. Sjölander, Phys. Rev. 176 (1968) 589.
- [10] L. Zheng and A.H. MacDonald, Phys. Rev. B 49 (1994) 5522.
- [11] J. Szymański, L. Świerkowski, and D. Neilson, Phys. Rev. B 50 (1994) 11002.
- [12] S. Das Sarma and A. Madhukar, Phys. Rev. B 23 (1981) 805.
- [13] D. Neilson, L. Świerkowski, J. Szymański, and L. Liu, Phys. Rev. Lett. 71 (1993) 4035.

Frictional Drag between Closely Spaced Two-Dimensional Electron Gases

H. Rubel[#], E.H. Linfield, N.P.R. Hill, J.T. Nicholls, D.A. Ritchie, K.M. Brown, M. Pepper, and G.A.C. Jones.

Cavendish Laboratory, Madingley Road, Cambridge CB3 0HE, United Kingdom
now at: Max-Planck-Institut für Festkörperforschung, Heisenbergstrasse 1, 70569 Stuttgart, Germany

Abstract

We have studied electron transport in two closely spaced, electrically isolated, two-dimensional electron gases (2DEGs) using GaAs/AlGaAs double quantum wells. A frictional drag voltage due to interlayer electron-electron ($e\text{-}e$) scattering is induced in one layer when a current is passed through the other. We present new experimental data based on a detailed carrier-density dependence of these $e\text{-}e$ interactions. We have shown, in particular, that the interlayer scattering rate is a function of the relative electron densities in the layers, with a maximum scattering rate when the two carrier densities are matched.

In addition, we present preliminary magnetic field measurements of the frictional drag. We have observed strong quantum oscillations in the measured drag voltage, with an amplitude two orders of magnitude greater than the zero magnetic field signal. The drag oscillations in I/B are determined solely by the density of states of the dragged electron gas.

Double-layer two-dimensional electron gas systems, where electrons are confined to nearby parallel planes, exhibit many interesting phenomena due to interlayer $e\text{-}e$ interactions. These $e\text{-}e$ interactions can be studied directly by measuring the drag voltage V_{drag} induced in one layer when a current is passed through the other. The drag voltage is generated by momentum transfer from the electrons in the drive layer, which undergo $e\text{-}e$ scattering events with electrons in the dragged layer. The induced voltage has the opposite polarity to the resistive voltage drop in the drive well and an interlayer scattering rate $1/\tau_0$ is defined as [1]:

$$\frac{1}{\tau_0} = \frac{e^2}{m} \left(\frac{W}{L} \right) \frac{n_{drive}}{I_{drive}} |V_{drag}| \quad (1)$$

where e is the electron charge, m the effective mass of the electron, (WL) is the width to length ratio of the Hall bar, and n_{drive} is the carrier density of the drive well. Note that $\tau_0 \gg \tau_e$, where τ_e is the elastic scattering time.

The frictional drag between barrier-separated 2DEGs was first proposed and discussed theoretically by Pogrebinskii [2] and later by Price [3]. Difficulties in making independent contacts to the layers delayed experimental investigation until the measurements of Gramila *et al.* [4] and Solomon *et al.* [5]. Gramila *et al.* [4] mainly investigated the temperature and barrier separation dependence of the drag from which they concluded that these interactions are dominated, for small barrier widths, by direct Coulomb scattering between the electrons of the two 2DEGs. For thicker barriers, however, the strength of the interaction could not be explained with the Coulomb interaction alone. Recently the exchange of virtual phonons was shown to account for this unexpected long range coupling between layers [6, 7]. Tsu *et al.* [7] predicted that the low temperature interlayer scattering rate mediated by the phonon coupling is a strong function of the relative electron densities in the two wells, with the interaction strongest when there are equal carrier densities in the two layers.

Results are presented from a wafer which consists of two 200 Å modulation-doped GaAs quantum wells separated by a 300 Å Al_{0.33}Ga_{0.67}As barrier (Fig. 1). The barrier width was chosen to be sufficiently large that tunneling between the two layers [8] is negligible. The upper 2DEG has an as-grown carrier density of 3.3x10¹¹cm⁻² and a mobility of 9x10⁵cm²/Vs, the corresponding values for the lower 2DEG being 2.2x10¹¹cm⁻² and 1.3x10⁵cm²/Vs, respectively. The wafer also includes a buried n⁺ GaAs back-gate layer which was patterned during growth using *in situ* Ga focused ion beam lithography, the details of which have been discussed elsewhere [8-10]. The back-gate is 3500 Å below the lower 2DEG. The carrier densities of the upper and lower 2DEGs could be controlled independently by voltages applied to standard NiCr/Au full front-gates and the buried back-gates. This control over carrier densities allows us to present a detailed study of the carrier dependence of the interlayer scattering rate.

The device was put into an independent contact configuration using a selective depletion scheme [10, 11], where negative voltages were applied to the side front- and back-gates independently, by applying negative voltages to 40mV could be applied between the layers with leakage currents less than 0.1nA, showing that the layers were indeed electrically separated. Drag measurements were carried out using standard lock-in techniques with drive currents in the range 200 nA to 1 μA, at a typical frequency of 17 Hz. The induced drag voltage was proportional to the drive current and independent of the excitation frequency, indicating an absence of heating effects and capacitive coupling. While passing a drive current through one 2DEG, the drag voltage developed in the other was measured in an open circuit configuration. Earth loops, a problem in this type of measurement, were avoided using a floating current in the drive well, which was generated via an isolation transformer.

The carrier density dependence of the drag voltage can be investigated by varying the density in the upper 2DEG with the front-gate, whilst the density in the lower 2DEG is kept at a constant value determined by the back-gate. The result of such a measurement, where the upper 2DEG serves as the drive and the lower as the dragged layer, is shown for $T = 4.2$ K in the inset of Fig. 2a). Also shown is the expected behaviour for pure Coulomb interaction, as calculated from theory [1]. Two basic features can be extracted from this graph: First, we can confirm that the measured scattering rate is higher than expected for Coulomb interaction alone, showing that a second mechanism is involved. Second, we can observe a clear peak in the scattering rate, when the carrier densities in the two wells are matched. Both features are characteristic of an interaction mediated by virtual phonons [6, 7].

The dependence on $n_{matched}$ of the phonon contribution, which is obtained by subtracting the calculated Coulomb contribution [1] from the measured total scattering rate, is shown in Fig. 2a).

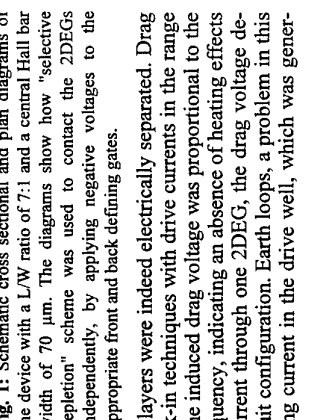
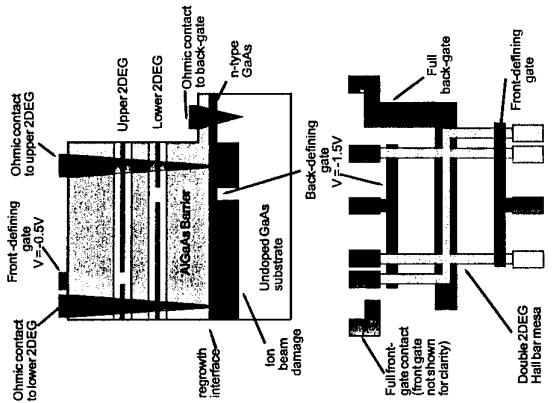


Fig. 1: Schematic cross sectional and plan diagrams of the device with a L/W ratio of 7:1 and a central Hall bar contact configuration using a selective depletion scheme [10, 11], where negative voltages were applied to the side front- and back-gates independently, by applying negative voltages to 40mV could be applied between the layers with leakage currents less than 0.1nA, showing that the layers were indeed electrically separated. Drag measurements were carried out using standard lock-in techniques with drive currents in the range 200 nA to 1 μA, at a typical frequency of 17 Hz. The induced drag voltage was proportional to the drive current and independent of the excitation frequency, indicating an absence of heating effects and capacitive coupling. While passing a drive current through one 2DEG, the drag voltage developed in the other was measured in an open circuit configuration. Earth loops, a problem in this type of measurement, were avoided using a floating current in the drive well, which was generated via an isolation transformer.

The carrier density dependence of the drag voltage can be investigated by varying the density in the upper 2DEG with the front-gate, whilst the density in the lower 2DEG is kept at a constant value determined by the back-gate. The result of such a measurement, where the upper 2DEG serves as the drive and the lower as the dragged layer, is shown for $T = 4.2$ K in the inset of Fig. 2a). Also shown is the expected behaviour for pure Coulomb interaction, as calculated from theory [1]. Two basic features can be extracted from this graph: First, we can confirm that the measured scattering rate is higher than expected for Coulomb interaction alone, showing that a second mechanism is involved. Second, we can observe a clear peak in the scattering rate, when the carrier densities in the two wells are matched. Both features are characteristic of an interaction mediated by virtual phonons [6, 7].

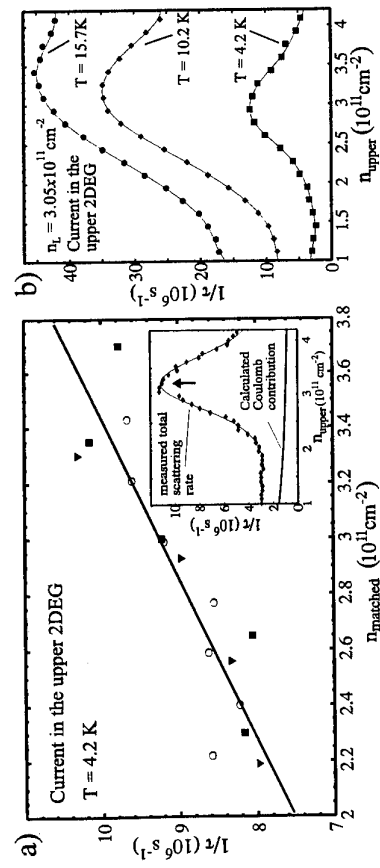


Fig. 2. a) The peak height of the phonon contribution of the scattering rate as a function of the matched carrier density in the wells, as obtained from different measurements. The squares correspond to data where n_{upper} was continuously varied for fixed n_{lower} , whilst the triangles represent data in which n_{lower} was continuously varied at fixed n_{upper} . Results obtained by applying an interlayer bias between the two 2DEGs are represented by circles. The solid line in the figure is a linear fit to all of the data shown. The inset shows the measured total scattering rate, together with the calculated Coulomb contribution, as a function n_{upper} for $n_{\text{lower}} = 3.5 \times 10^{11} \text{ cm}^{-2}$. The solid line through the data points is intended only as a guide to the eye. The arrow indicates the point at which the carrier density in the two wells is equal. b) The phonon contribution of the scattering as a function of n_{upper} for different temperatures. The scattering rate is an increasing function of the carrier density, similar to the behaviour observed in earlier experiments [12, 13] on electron-phonon interactions.

The effect of different temperatures on the phonon contribution to the interlayer scattering rate is shown in Fig. 2(b). In contrast to the previous measurements of Gramila *et al.* [6] we observe clear maxima in the phonon contribution above 10K. The persistence of the maxima in the phonon contribution is probably due to the measurements being carried out at higher n_{matched} , resulting in a larger peak (see Fig. 2(a)) occurring at a carrier density where the Coulomb contribution is smaller.

Preliminary measurements of the drag voltage at 1.5 K as a function of the perpendicular magnetic field are shown in Fig. 3. The data were obtained at a matched carrier density of $n_{\text{drag}} = n_{\text{drive}}$ = $3 \times 10^{11} \text{ cm}^{-2}$. The experimental conditions used to measure the drag in a magnetic field were similar to those used at zero field. At low fields, $B < 0.3 \text{ T}$, the drag voltage is the same sign and magnitude as at zero magnetic field (within our convention the zero field sign is negative). At higher fields the drag voltage oscillates between positive and negative values periodic in $\ln B$, following the density of states of the two 2DEGs, as evidenced by comparison with the SdH trace of the dragged layer. The amplitude of the oscillations is two orders of magnitude greater than the zero-field signal. The drag signal is negative when the Landau levels (LLs) are partially filled and transport is mainly through the bulk. This negative signal shows spin splitting following that observed in the SdH trace. In contrast, the positive drag observed near integer LL filling shows a double peak structure that cannot be attributed to spin splitting.

The inset to Fig. 3 shows drag traces obtained for different drive layer carrier concentrations n_{drive} whilst keeping n_{drag} fixed at $3.5 \times 10^{11} \text{ cm}^{-2}$. There appears to be no dependence of the period of the drag oscillations on n_{drive} . However, the amplitude of the induced voltage does show some dependence on n_{drive} , increasing as n_{drive} is reduced towards $1 \times 10^{11} \text{ cm}^{-2}$.

The oscillations of the drag voltage about zero might be accounted for in a recent paper by

Kusmartsev [14] where it is suggested that the creation of fluctuating bound virtual electron-hole pairs can lead to a positive contribution in the frictional drag and thus to a drag voltage that oscillates between positive and negative values.

In conclusion, new experimental data has been presented on the carrier density dependence of interlayer electron-electron scattering rates in double 2DEG systems. We have shown, in particular that the phonon contribution of the interlayer scattering rate is a strong function of the relative electron densities in the layers, with a maximum value at matched carrier densities. We have also investigated the magnetic field behaviour of the frictional drag. Strong quantum oscillations between positive and negative values were found, two orders of magnitude higher than the signals in zero magnetic field. Their periodicity was determined only by the density of states of the dragged electron gas.

References

- 1 A.P. Jauho, and H. Smith; *Phys. Rev. B* **47**, 4420 (1993)
- 2 M.B. Progribinskii; *Sov. Phys. Semicond.* **11**, 372 (1977)
- 3 P.J. Price; *Physica B* **111**, 750 (1983)
- 4 T.J. Gramila, J.P. Eisenstein, A.H. MacDonald, L.N. Pfeiffer, and K.W. West; *Phys. Rev. Lett.* **66**, 1216 (1991); T.J. Gramila, J.P. Eisenstein, A.H. MacDonald, L.N. Pfeiffer, and K.W. West; *Surf. Sci.* **263**, 446 (1992)
- 5 B. Laikhanov, and P.M. Solomon; *Semiconduct. Microstruct.* **10**, 39 (1991)
- 6 T.J. Gramila, J.P. Eisenstein, A.H. MacDonald, L.N. Pfeiffer, and K.W. West; *Phys. Rev. B* **47**, 12957 (1993)
- 7 H.C. Tso, P. Vasilopoulos, and F.M. Peeters; *Phys. Rev. Lett.* **68**, 2516 (1992)
- 8 K.M. Brown, E.H. Linfield, D.A. Ritchie, G.A.C. Jones, M.P. Grimeshaw, and M. Pepper; *Appl. Phys. Lett.* **64**, 1827 (1994)
- 9 E.H. Linfield, G.A.C. Jones, D.A. Ritchie, J.H. Thompson; *Semiconduct. Sci. Technol.* **9**, 415 (1993)
- 10 K.M. Brown, E.H. Linfield, D.A. Ritchie, G.A.C. Jones, M.P. Grimeshaw, and A.C. Churchill; *J. Vac. Sci. Technol. B12*, 1293 (1994)
- 11 J.P. Eisenstein, L.N. Pfeiffer, and K.W. West; *Appl. Phys. Lett.* **57**, 2324 (1990)
- 12 J.C. Hensel, R.C. Dynes, and D.C. Tsui; *Phys. Rev. B* **28**, 1124 (1983); J.C. Hensel, B.I. Halperin, and R.C. Dynes; *Phys. Rev. Lett.* **51**, 2302 (1983)
- 13 M. Rothenfusser, L. Köster, and W. Dieische; *Phys. Rev. B* **34**, 5518 (1986)
- 14 F.V. Kusmartsev, *Preprint* (1995)

Tuning a Double Quantum Well Fermi Surface with In-Plane Magnetic Fields

J. A. Simmons, N. E. Harff, T. M. Eiles, S. K. Lyo, and J. F. Klem
Sandia National Laboratories
Albuquerque, New Mexico 87185-1415 USA

Abstract

A double quantum well (QW) subject to in-plane magnetic fields B_{\parallel} has the dispersion curves of its two QWs shifted in \mathbf{k} -space. When the QWs are strongly coupled, an anticrossing and partial energy gap occur, yielding a tunable multi-component Fermi surface. We report measurements of the resultant features in the conductance, the capacitive density of states, and giant deviations in the cyclotron effective masses.

Double quantum wells (DQWs) constitute a system in which an additional degree of freedom can be controllably introduced to a two dimensional electron gas by changing the thickness and height of the grown interwell barrier. In the case of purely in-plane fields B_{\parallel} , single particle tunneling dynamics dominate the interactions, with the primary effect of B_{\parallel} being a linear transverse shift in the momenta $\hbar \mathbf{k}$ of electrons in one QW relative to those in the other [1,2].

Here we describe our studies of a strongly coupled DQW subject to a high B_{\parallel} . The strong tunneling causes the shifted QW dispersion curves to distort into an anticrossing, opening a partial energy gap or minigap. The presence of the gap mixes the two (displaced) QW Fermi circles to produce a Fermi surface (FS) with orbits of greatly differing area. At the edges of the gap, van Hove singularities in the density of states $D(\epsilon)$ appear, and the electron group velocities approach zero. By sweeping B_{\parallel} , the FS can be tuned and the gap can be made to pass through the chemical potential μ , with the gap edges producing dramatic effects in the transport properties [3,4]. These include sharp features in both the conductance and the capacitance as a function of B_{\parallel} , and giant deviations in the cyclotron mass m_c .

The two samples studied were grown by MBE. Sample A (*B*) consisted of a modulation-doped pair of GaAs QWs of equal width $w = 150 \text{ \AA}$ (100 \AA) separated by an $\text{Al}_0.3\text{Ga}_0.7\text{As}$ barrier of thickness $t = 25 \text{ \AA}$ (35 \AA). Each QW had density $n = 1.5 \times 10^{11} (1.2 \times 10^{11}) \text{ cm}^{-2}$, as measured by Shubnikov-de Haas oscillations (SdHO) for $B_{\parallel}=0$. Top and bottom QW mobilities were ~ 2.7 and $\sim 2.2 \times 10^5$ (~ 1.2 and $\sim 0.6 \times 10^5$) $\text{cm}^2/\text{V}\cdot\text{s}$. Four-terminal 17 Hz lock-in measurements were performed on Hall bars with Cr/Au top gates. Measurements of m_c required a simultaneous small B_{\perp} and large B_{\parallel} , achieved by applying a uniform total field B_T at angles $\theta = 0^\circ, 2.5^\circ, 3.0^\circ$, and 3.5° from parallel, with rotations performed *in situ*.

In Fig. 1(a) we show the normalized in-plane resistance $R_{\parallel}(B_{\parallel})$ for sample A, at $T=0.5 \text{ K}$ and $\theta=0$. A minimum occurs at 5.9 T , followed by a maximum at 6.5 T . We now briefly discuss the origin of these two features [3,4]. Shown in Fig. 2(a) is a tight-binding calculation for sample A of the DQW dispersion $\epsilon(\mathbf{k})$, for $B_{\parallel}=7.5 \text{ T}$ in the x -direction [5]. B_{\parallel} shifts the two QW dispersion curves relative to one another by an amount $\Delta k_y = eB_{\parallel}/\hbar$. The strong QW coupling produces an anticrossing and minigap whose width ϵ_G (of order 1 meV) is independent of B_{\parallel} and $\approx \Delta S\text{AS}$, the zero-field symmetric-antisymmetric gap [6]. The minigap dramatically distorts $D(\epsilon)$

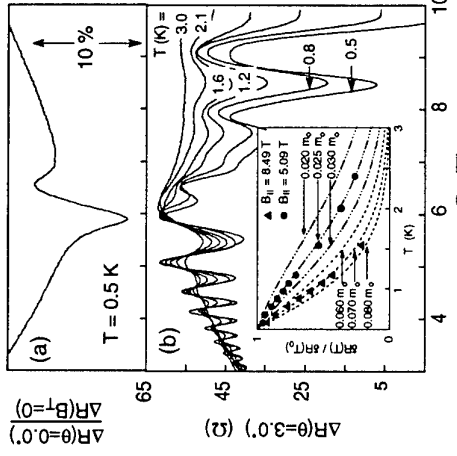


FIG. 1. (a) Normalized $R_{\parallel}(B_{\parallel})$ of sample A at $\theta=0$. (b) $\Delta R(B_{\parallel})/3.0$ for several T . Inset: SdHO amplitudes vs. T and fits to Eq. (1) for two B_{\parallel} .

present. As B_{\parallel} is increased further, μ touches the lower gap edge, causing the hourglass "waist" to pinch off. For $B_{\parallel} > 6.5 \text{ T}$, the FS separates into two Fermi circles of roughly equal size.

Changes $\Delta D(\epsilon)$ in $D(\epsilon)$ can be measured directly via changes $\Delta C(B_{\parallel})$ in the capacitance between the surface gate and the DQW. For $\Delta D(\epsilon)$ small relative to the full 2D density of states, $\Delta C(B_{\parallel}) \propto \Delta D(\epsilon)$ [7]. This condition appears to hold for our sample, based on a calculation of the geometrical capacitance. In Fig. 3 we show $\Delta C(B_{\parallel})$ of sample B (gate area $\sim 5.4 \text{ mm}^2$) for several different gate voltages. In contrast to the conductance data, $C(B_{\parallel})$ remains relatively constant at low B_{\parallel} , until a sudden step-like decrease appears. This corresponds to the disappearance of the lens orbit, occurring when the upper gap edge crosses μ . $C(B_{\parallel})$ then increases monotonically, and ends in a slight peak before settling at a value nearly the same as just before the step-decrease. The peak is due to the lower gap edge, with a logarithmic singularity in $D(E)$, crossing μ , and is washed out due to damping. The relative constancy of $C(B_{\parallel})$ outside the anticrossing region is in stark contrast to R_{\parallel} [see Fig. 1(a)], which convolves the changing Fermi velocities. The overall shape of $C(B_{\parallel})$ bears a striking resemblance to the calculated $D(\epsilon)$ of Fig. 2(b). The slight oscillations just below the step-decrease are SdHO due to a slight misalignment of the sample from $\theta=0$, which brings us to our next topic.

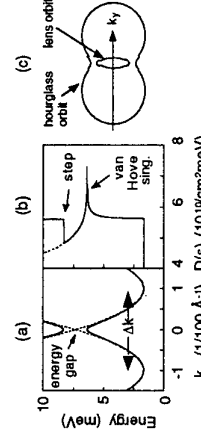


FIG. 2. Sample A calculations at $B_{\parallel}=7.5 \text{ T}$. (a): $\epsilon(\mathbf{k})$ with (solid lines) and without (dotted lines) coupling. (b): $D(\epsilon)$ for lower energy branch (dotted line) and both branches (solid line). (c): Fermi surface sketch for $\mu=9 \text{ meV}$.

FIG. 3. Change in capacitance $\Delta C(B_{\parallel})$, proportional to $\Delta dE/dx$, for several gate biases. The curves are strikingly similar to Fig. 2(b).

FIG. 3. Change in capacitance $\Delta C(B_1)$, proportional to $\Delta D(\epsilon)$, for several gate biases. The curves are strikingly similar to Fig. 2(b).

and hence $B_{||}$ are sufficiently small, electrons in the hourglass are unable to complete the orbit without scattering, contributing negligibly to the SdHO. However, because v_k is nearly the same for the two orbits (except very close to the gap edge), enough electrons complete the lens orbit to produce SdHO. This assumption agrees with the data for $B_{||} < 5.9$ T, where only a single period occurs for all three Θ . For 5.9 T $< B_{||} < 6.5$ T, the FS consists of only the hourglass, while for $B_{||} > 6.5$ T, the FS consists of two separated Fermi circles of equal size, producing SdHO of the same period and T -dependence. Thus for all three ranges, the SdHO arises from a single orbit of the FS period. For a single FS orbit, the SdHO are in general described by a series of terms [9]. However when $B_{||}$ is small enough that $\omega_{\perp}T$ is of order unity (where $\omega_{\perp} = eB_{||}/mc$, and τ is the scattering

With Δt so small enough that we do not exceed the limit of the numerical scheme (which is $\Delta t = \frac{L}{c}$), the higher order terms become negligible.

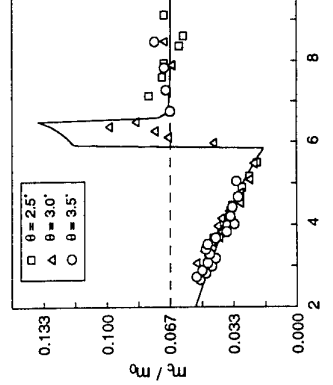


FIG. 4. Summary of measured m_c values vs. B_{\parallel} . Solid line is theoretical calculation of Ref. [10].

between $\Delta R(B_{||}, \theta)$ evaluated at adjacent Si/HgO extrema, and subtracting the magnetoresistance background.) While for 8.49 T $m_c = 0.070 m_0$, for 5.09 T $m_c = 0.025 m_0$, a factor of three lower than m^*_{GaAs} . In general, the fits yield m_c to $\pm 10\%$ error. For the range $5.9 \leq B_{||} \leq 6.5$ T, however, m_c is changing rapidly, yielding larger errors of roughly $\pm 20\%$.

Fig. 4 shows $m_c^*(B_{||})$ for all three θ . At 2.7 T, $m_c = 0.050 m_0$, considerably lower than m^*_{GaAs} . Raising $B_{||}$ causes m_c to decrease, reaching 0.021 m_0 near the upper gap edge at 5.6 T. As $B_{||}$ is increased further, m_c suddenly increases, reaching a value of 0.099 m_0 just below 6.5 T, where μ crosses the lower gap edge, or saddle point. m_c then rapidly converges to m^*_{GaAs} near 7 T and remains roughly constant thereafter.

Following Lyo [10], an understanding of the behavior of m_c can be gained by examining Fig. 2 and employing the expression $m_c = (\hbar/2\pi) \int V_k^{-1} d\mathbf{k}$, where the integration is along the dominant orbit. As $B_{||}$ is increased, the upper gap edge moves upward towards μ . As a result, the size of the lens orbit decreases, while V_k decreases more slowly, resulting in a monotonic decrease of m_c . The lens orbit vanishes at 5.9 T, but because V_k also vanishes, m_c does not go to zero. Above 5.9 T, the orbit size increases abruptly as electrons move to the hourglass, causing an abrupt increase in m_c . As $B_{||}$ increases from 5.9 to 6.5 T, m_c lies in the minibar and moves towards the saddle point. At the same time, V_k becomes smaller near the saddle-point, yielding now a monotonic *increase* of $m_c(B_{||})$. The divergence of m_c at the saddlepoint, due to V_k vanishing, is suppressed in the data by damping. Above 6.5 T, μ falls below the saddle point, causing the hourglass to split into two roughly circular orbits with nearly parabolic dispersion. The two QWs are thus effectively uncoupled, and m_c approaches $m^*(B_{||})$. In Fig. 4 we plot Lyo's calculation of $m_c(B_{||})$ for sample A, where $B_{||}$ has been scaled by 0.96. Excellent agreement is seen.

Preferences

- [1] J.P. Eisenstein, T.J. Gramila, L.N. Pfeiffer, and K.W. West, Phys. Rev. B **44**, (1991) 6511.

[2] J.A. Simmons, S.K. Lyo, J.F. Klem, M.E. Sherwin, and J.R. Wendt, Phys. Rev. B **47**, (1993) 15 741; S.K. Lyo and J.A. Simmons, J. Phys.: Condens. Matter **5**, (1993) L299.

[3] J.A. Simmons, S.K. Lyo, N.E. Harff, and J.F. Klem, Phys. Rev. Lett. **73**, (1994) 2256.

[4] S.K. Lyo, Phys. Rev. B **50**, (1994) 4965.

[5] Including the Hartree term increases the center-to-center distance between the wavefunctions of the two QWs, thus lowering the B_{\parallel} at which the minigap crosses H_0 and reducing EG.

[6] G.S. Boebinger, H.W. Jiang, L.N. Pfeiffer, and K.W. West, Phys. Rev. Lett. **64**, (1990) 1793.

[7] M. Buttiker, J. Phys.: Condens. Matter **5**, (1993) 9361, and references therein.

[8] N.E. Harff, J.A. Simmons, S.K. Lyo, J.E. Schirber, J.F. Klem, and S.M. Goodnick, in The Physics of Semiconductors, Vol. 1, Ed. D.J. Lockwood, (World Scientific, Singapore, 1995) p. 831.

[9] T. Ando, A.B. Fowler, and F. Stern, Rev. Mod. Phys. **54**, (1982) 437.

[10] S.K. Lyo, Phys. Rev. B **51**, (1995) 11 160.

Effects of a floating channel on magnetotransport properties of two dimensional electron gases in a resonantly coupled double quantum well structure

Yuzo Ohno and Hiroyuki Sakaki

Research Center for Advanced Science and Technology, University of Tokyo
4-6-1 Komaba, Meguro-ku, Tokyo 153, Japan
and
Institute of Industrial Science, University of Tokyo
7-22-1 Roppongi, Minato-ku, Tokyo 107 Japan

Effects of an electrically "floating" two dimensional electron gas (2DEG) on the magnetoresistivities ρ_{xx} and ρ_{xy} of the other 2DEG channel where the coupling of two channels is controlled by the gate voltage are studied in double quantum well (DQW) structures. At resonance, both ρ_{xx} and ρ_{xy} in low magnetic fields are found to be identical to those measured when the top 2DEG is connected in parallel with the bottom 2DEG (parallelly connected case). This indicates that the tunnel resistance between the two channels is sufficiently reduced. When ρ_{xx} and ρ_{xy} are studied under strong magnetic fields, however, the quantized plateaus of Hall resistance are found to no longer coincide with those of parallel-connected case but abruptly increase to the level twice as the latter. This phenomenon indicates that at the resonant inter-well tunneling of electrons is significantly suppressed under the quantizing magnetic fields when they are localized in the in-plane direction.

Recently, two dimensional electron gases (2DEGs) in coupled double quantum well (DQW) structures have attracted much attention. For example, a number of experimental studies have been done on such topics as gate-controlled resonant tunneling and Coulomb interaction. In order to evaluate the contribution of the individual 2DEG channels and to perform spectroscopic measurements, some unique and elaborate techniques have been devised. One of these schemes is making ohmic contacts to individual 2DEG independently [1-3]. This method makes it possible to study the lateral transport properties of each of two 2DEGs separately [2], and observe the 2D-2D tunneling current [1].

In this paper, we investigate the gate-induced resonant tunneling phenomena in a novel GaAs / AlGaAs DQW structure by measuring the in-plane resistivities ρ_{xx} and ρ_{xy} with magnetic fields B applied normal to the 2DEGs. Using the selective depletion technique [1], the two limiting situations are realized where the 2DEG in the top QW is electrically isolated from or connected to that in the bottom QW. We study both the channel resistivity (ρ_{xx}) and Hall resistivity (ρ_{xy}) of primarily the bottom QW for these two cases, and demonstrate that a drastic change of magnetotransport appears in the quantum Hall regime as the inter-well coupling is suppressed when electronic states at the Fermi energy alter from extended to localized states with B .

A selectively doped GaAs/AlGaAs DQW structure studied in this work was

not deplete the top 2DEG of each side arm so that the ohmic contacts can probe only the bottom 2DEG or both the top and bottom 2DEGs. By two-terminal resistance measurements, we find the threshold voltage V_{th} of the top 2DEG channel to be -0.5V, which is confirmed also by the Shubnikov-de Haas measurement with both 2DEGs connected in parallel at all the ohmic contact (parallelly connected case). Hence by setting the voltage of these five small gates to -0.5V, the top 2DEG under the main gate can be electrically separated from all the ohmic contacts, and thereby from the bottom 2DEG. We demonstrate this situation as the "floating" case.

First, we study the resonant tunneling effect under lower magnetic fields with the top 2DEG in the "floating" states. For this purpose, we measured at 1.5K the resistivity ρ_{xx} and the Hall resistivity ρ_{xy} at $B=0.3$ T as functions of V_{gs} . The results are shown in Fig. 2 by solid lines for the case of "floating", and by dotted lines for the parallelly connected case. Note that ρ_{xy} of the dotted line decreases as V_{gs} increases, indicating that the total number of electrons ($N=N_{top}+N_{bot}$) increases up to $V_{gs}=-0.2$ V, and then saturates. For $V_{gs}>-0.5$ V, newly induced electrons mainly populate in the top QW, while the number of electrons N_{bot} in the bottom QW does not change. Therefore, for the "floating" case both ρ_{xx} and ρ_{xy} should be kept unchanged in this range of V_{gs} as the top 2DEG does not contribute to the current flow. One notices in Fig. 2, however, solid curves show dip structures centered at $V_{gs}=-0.1$ V and coincide with dotted curves. This is due to the resonant tunneling [3], which results in the reduction of tunnel resistance between two 2DEGs. The intrinsic energy splitting ΔE_{SAS} of two levels caused by the resonant coupling is calculated to be 0.02meV. This value is much smaller than the broadening of each level (-0.1meV) which is estimated from their mobility $\mu = 2 \times 10^5$ cm²/Vs at low temperatures. It indicates that a simple picture of delocalized single-particle wavefunctions over the two QWs may not be accurate [4]. The data in Fig. 2 clearly show, however, that the solid and the dotted curves coincide at resonance, which suggests that the tunnel coupling is quite strong.

Next we discuss the situation under strong magnetic fields, where inter-well tunneling of electrons takes place between Landau levels [5]. Note that the resonant bias is still the same ($N_{bot}=0.1$ V), since the energy spectra in both QWs are still identical at resonance. If both the top and the bottom 2DEGs with the same densities are connected in parallel at all the ohmic contacts, ρ_{xx} and ρ_{xy} of the DQW channel should be similar to those of one QW channel except that their magnitude is halved. To test this expectation, we measured at 1.5K ρ_{xx} and ρ_{xy} at $V_{gs}=-0.1$ V, and the results are plotted as functions of magnetic fields up to 8.5T. Solid lines correspond to the case that the top 2DEG is "floating". Contrary to the expectation, they exhibit peculiar behaviors. Especially, ρ_{xy} shows an abrupt increase each time ρ_{xy} reaches quantized Hall plateaus. The height of ρ_{xy} at these peaks are almost the same as those of the bottom 2DEG, i.e. twice as high as that of the case of parallel transport.

This unique behavior suggests that the inter-QW resonant tunneling of electrons is suppressed at certain magnetic fields, since the contribution of the top 2DEG to the resistivities will be modified when the tunnel coupling is reduced, as shown in Fig. 2. Based on the bulk-picture of Landau states [6], one of the simplest explanations is given as follows: When the Fermi energy E_F lies in middle region of the Landau level, electrons will be in the extended states. In such a case, the resonant tunneling of electrons can take place between the two QWs, just as the case of low magnetic fields. On the other hand, when E_F is in the localized states, the extended states below E_F are fully occupied and the tunnel transition of electrons perpendicular to the QW plane is also inhibited. The latter corresponds to the range of the magnetic fields where quantized Hall plateau appears in $\rho_{xy}(B)$. This localization effect for electronic motion across the layers is also theoretically predicted [7]. More detailed discussion together with results of more systematic studies will be presented elsewhere.

Finally, we briefly mention the result of a similar experiment using another DQW sample of weak-coupling in which a 10nm-wide AlGaAs barrier is replaced by 7nm AlAs

barrier. In the latter sample, it is expected that tunnel-transfer is more strongly suppressed, but the Coulomb interaction between 2DEGs might be enhanced. In Fig. 4, V_{gs} - ρ_{xy} characteristics of this sample at 0.3T are shown. It is clearly seen that ρ_{xy} of the sample in the "floating" case shows only a small signature of dip and remains almost constant once the number of electrons in the bottom 2DEG saturates for $V_{gs} > 0.4V$. We studied ρ_{xx} and ρ_{xy} of the bottom 2DEG also in high magnetic fields and confirmed that they hardly change for $V_{gs} > 0.4V$.

These results support our explanation and suggest that the inter-2DEG Coulomb effect is negligibly small. It is interesting to note in Fig. 4, that the dependence of ρ_{xx} on V_{gs} shows a small but distinct dip structure, which calls for the future study.

In summary, we have found that quantized Hall resistance in a double quantum well structure shows an abrupt increase when the top 2DEG is on resonance with the bottom 2DEG but is electrically isolated. This feature is qualitatively explained by the suppression of inter-well resonant tunneling, which is caused by the localization of electronic states at the Fermi energy in the quantum Hall regime.

The authors wish to acknowledge Prof. M. Tsuchiya, Drs. T. Noda, M. Foley, and Y. Nagamune for useful discussions. This work was partly supported by a Grant-in-Aid for Scientific Research from the Ministry of Education, Science and Culture and partly by the Japan Research and Development Corporation.

References

- [1] J. P. Eisenstein et. al., Appl. Phys. Lett. **57**, 2324 (1990)
- [2] N. K. Patel et. al. Appl. Phys. Lett. **65**, 831 (1994)
- [3] N. K. Patel et. al. Appl. Phys. Lett. **64**, 3018 (1994)
- [4] F. T. Vasko, Phys. Rev. B **47**, 2410 (1993)
- [5] E. E. Mendez et. al. Phys. Rev. B **33**, 2893 (1986)
- [6] K. von Klitzing, Rev. Mod. Phys. **58**, 519 (1986)
- [7] T. Ohtsuki, et. al. J. Phys. Soc. Jpn. **62**, 224 (1993)

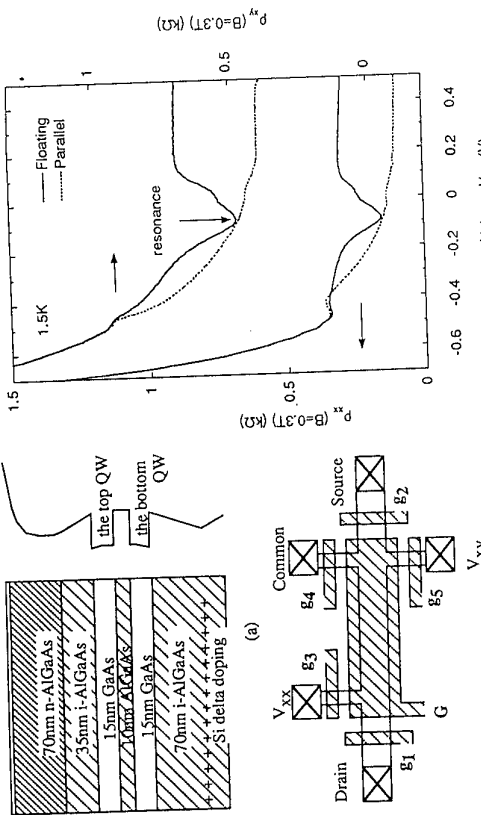


Fig. 1 (a) The cross sectional view of the double quantum well structure. (b) The top view of the Hall bar device.

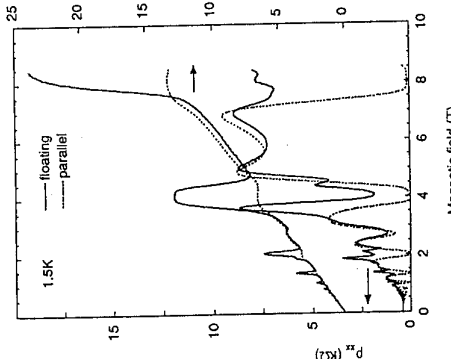


Fig. 2 ρ_{xx} and ρ_{xy} at 0.3T are shown as functions of the gate voltage V_{gs} . Solid lines indicate the case when the top 2DEG is in the "floating" state, and dotted lines are of the case where the top 2DEG is connected in parallel with the bottom 2DEG.

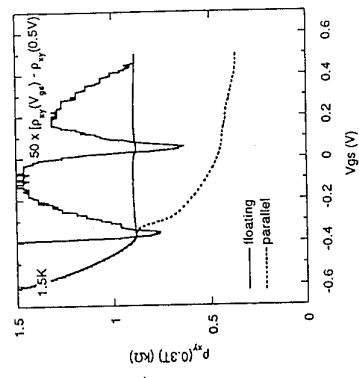


Fig. 3 ρ_{xx} and ρ_{xy} at $V_{gs}=0.1V$ are plotted as functions of B for both "floating" (solid lines) and "parallel" (dotted lines) cases.

Fig. 4 The Hall resistivity ρ_{xy} at 0.3T of the sample with a 7nm AlAs barrier plotted as functions of V_{gs} for both "floating" (solid line) and "parallel" (dotted line) cases.

Superfluid ground state in electron-hole double layer systems

Z.W. Gortel^(a) and L. Świerkowski^(b)

^(a)Department of Physics, University of Alberta, Edmonton, Alberta, T6G 2J1, Canada
^(b)School of Physics, The University of New South Wales, Sydney 2052, Australia

Abstract

Superfluid ground state in the electron-hole double layer systems is investigated within the mean field approach at zero temperature. The single particle excitation spectrum is obtained for various densities and barrier widths separating the layers. The electron-hole pairing gap is shown to be significantly reduced by the dielectric screening shifting the most favourable conditions for the condensation towards lower carrier concentrations.

Introduction

Systems of mobile charges trapped in a semiconductor quantum well structure became over the past several years the searching ground for novel physical phenomena and ground states of the systems related to the cooperative many-body effects which are for them at play. The existence of the Wigner crystal ground state was theoretically demonstrated for a single layer of charges [1] but the carrier concentrations at which this might occur are well below the limits available today. Systems like GaAs-Al_xGa_{1-x}A_y heterojunctions in which two layers of charges may interact with each other without particle tunneling across the potential barrier separating them offer more favourable conditions for the observation of the charge-density-wave and the Wigner crystal phases [2] because the changes in one layer form a polarizable background to which the carriers in the other one adjust.

The most intriguing feature of electron - hole double layer systems [3], in which two dimensional electron and hole gases fill the respective layers, is the possibility of formation of a superfluid state due to the attractive interactions across the barrier [4,5]. At low concentrations the electrons and holes may pair into excitons undergoing Bose condensation. At higher concentrations, at which the picture of noninteracting excitons does not apply, the attractive interaction between the carriers may still induce transition to the superfluid ground state similar to the BCS ground state in the theory of superconductivity. The idea is not entirely new and has a long history of theoretical research in the realm of three dimensional semiconductors [6]. The main experimental difficulty in the bulk materials, however, is the high rate of recombination of photoexcited carriers preventing at low temperatures a build up of a sufficiently high concentration of excitons. Recent experiments of Butov *et al* [7] indicate that these difficulties may be somewhat reduced by spatially separating the wave functions of photoexcited electrons and holes in 2D systems. Perfect separation, however, of electrons and holes in thermal equilibrium may be achieved in electron - hole double layer systems making them good candidates for the observation of the superfluid transition.

Dielectric screening must be included in a realistic description of properties of the double layer systems. In this work we report on our preliminary investigation into the condensation

problem in electron - hole double layers. We account for screening in the simplest approximation in which the effects of condensation on the dielectric function are ignored.

Theory

To model the system we consider infinitely thin layers of electrons ($l = 1$) and holes ($l = 2$), separated by a potential barrier d and interacting through the Coulomb potential whose intra- and inter-layer Fourier transforms are $v_{11}(\mathbf{k}) = 2\pi^2/\epsilon_0$, and $v_{12}(\mathbf{k}) = 2\pi^2 \exp(-k_d)/\epsilon_0$, respectively. Here, ϵ_0 is the background dielectric constant. The total Hamiltonian of the system contains the potential interaction energy between electrons and holes and a sum of single particle energies, $\epsilon_{\mathbf{k}}^{1,2} = \hbar^2 k^2 / 2m_{1,2} \mp \epsilon_g/2 - \mu$, where μ is the chemical potential with respect to which the single particle energies are measured. The spin degree of freedom is ignored. Intralayer interactions are ignored in the mean field treatment of the Hamiltonian but their role in screening is accounted for in the RPA dielectric function appropriate for the double layer system:

$$\epsilon(\mathbf{k}) = (1 + v_{11}(\mathbf{k})\chi_1(\mathbf{k})) (1 + v_{22}(\mathbf{k})\chi_2(\mathbf{k})) - v_{12}^2(\mathbf{k})\chi_1(\mathbf{k})\chi_2(\mathbf{k}). \quad (1)$$

Here, $\chi_l(\mathbf{k})$ is the 2D Lindhardt susceptibility for *spinless* charged particles in the l -th layer. The effective interlayer interaction is then $v_{\text{eff}}(\mathbf{k}) = v_{12}(\mathbf{k})/\epsilon(\mathbf{k})$. In the mean field approach, the product of two creation/annihilation operators from different layers is replaced with their ground state expectation value, and the gap function, $\Delta_{\mathbf{k}} = \Omega^{-1} \sum_{\mathbf{k}} v_{\text{eff}}(\mathbf{k} + \mathbf{k}') \ll \epsilon_{\mathbf{k}+2c-k'} \gg$, is introduced (Ω is the surface area of the system). Diagonalization of the mean field Hamiltonian is achieved through the Bogoliubov transformation. For the system with equal concentrations of electron and holes, $n_1 = n_2 = n$, the resulting excitation energies, the integral equation for the gap function, and the concentration in either layer are, respectively,

$$E_{\mathbf{k}}^{\pm} = \pm(\epsilon_{\mathbf{k}}^l - \epsilon_{\mathbf{k}}^2)/2 + \bar{E}_{\mathbf{k}}, \quad (2)$$

$$\Delta_{\mathbf{k}} = -(1/2\Omega) \sum_{\mathbf{k}'} v_{\text{eff}}(\mathbf{k} + \mathbf{k}') \Delta_{\mathbf{k}'} / \bar{E}_{\mathbf{k}'}, \quad (3)$$

$$n = (1/2\Omega) \sum_{\mathbf{k}'} (1 - \epsilon_{\mathbf{k}'} / \bar{E}_{\mathbf{k}'}). \quad (4)$$

Here $\bar{E}_{\mathbf{k}} = \sqrt{\epsilon_{\mathbf{k}}^2 + \Delta_{\mathbf{k}}^2}/2$, $\epsilon_{\mathbf{k}} = (\epsilon_{\mathbf{k}}^l + \epsilon_{\mathbf{k}}^2)/2$, and the last equation is the condition for the chemical potential. For a given concentration, Eqs. (2) – (4) must be solved simultaneously for $\Delta_{\mathbf{k}}$ and μ . The concentration enters not only through Eq. (4) but it is also present in the static dielectric function so, in practice, one fixes μ and looks for the self-consistent solutions for both, $\Delta_{\mathbf{k}}$ and n . In principle, more accurate treatment of the intralayer interactions is possible [6] in which the Fock self-energies are added to the unperturbed single particle energies $\epsilon_{\mathbf{k}}^l$. Such a modification is not expected to alter significantly the conclusions reached in this work.

Numerical results and discussion

The numerical calculations were performed using the effective Bohr radius and the effective Rydberg, $a_B^* = \hbar^2 \epsilon_0 / e^2 m_{\text{eff}}$ and $Ry^* = \hbar^2 a_B^* / 2m_{\text{eff}}$, as units of length and energy, respectively ($1/m_{\text{eff}} = 1/m_1 + 1/m_2$). For GaAs, $m_1 = 0.067m_e$, $m_2 = 0.4m_e$, and $\epsilon_0 = 13$, resulting in $a_B^* = 12$ nm and $Ry^* = 4.62$ meV. The concentration n is expressed in terms of $r_s = 1/\sqrt{\pi n a_B^*}$.

and the Fermi momentum used in the Lindhardt functions is $k_F = 2\sqrt{\pi n}$, differing from the standard expression on the account of the ignored spin degree of freedom.

An example of typical plots of E_k^\pm , Δ_k and of the excitonic excitation energy, $(E_k^+ + E_k^-)/2$, as functions of k are presented in Fig. 1a for high concentrations corresponding to $r_s \approx 1$. Note that Δ_k is not a monotonic function of k and its maximum value is larger than the gap in the single particle excitation spectrum. In Fig. 1b the r_s dependence of the chemical potential with and without screening is compared for two values of the barrier thickness and contrasted with the $2/r_s^2$ dependence for noninteracting layers of ideal 2D gases. The latter limit is reached for high concentrations. For low concentrations the chemical potential becomes negative indicating at an excitonic bonding between electrons and holes. Without screening, the curves level out quickly at the barrier-thickness dependent binding energy of an isolated exciton. With screening, the same limits are reached at much lower concentrations (beyond the scale of the figure) at which the effects of screening are negligible.

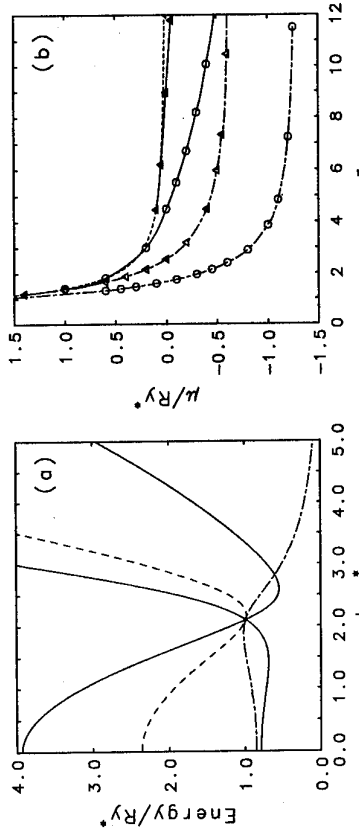


Fig. 1. (a): E_k^\pm (solid lines), their arithmetical average (excitonic excitation energy, dashes), and Δ_k vs k (chain curve) for $d = a_B^*/2$, $\epsilon_g = 3.14 Ry^*$ and $n = 2.38 \cdot 10^{11} \text{ cm}^{-2}$ ($r_s = 0.96$) with screening ignored; (b): μ vs r_s for $d = a_B^*/10$ (circles), $d = a_B^*/2$ (triangles), with (solid lines) and without (chain curves) screening, and $\mu = 2/r_s^2$ (for the ideal 2D gas, dashes).

Screening affects strongly the gap function. The maximum value reached by Δ_k is shown in Fig. 2 as a function of r_s . Without screening (Fig. 2a), the largest Δ_k 's, corresponding to temperatures 148 and 64 K, respectively, are reached for r_s changing from 1 to about 2 (i.e. the concentrations dropping from $2.2 \cdot 10^{11} \text{ cm}^{-2}$ as the barrier thickness increases from 0.1 to 0.5 of a_B^*). These concentrations correspond to $\mu > 0$ so Δ_{\max} is a fair estimate of the gap in the single particle excitation spectrum. With screening (Fig. 2b), the maximum values reached are by about an order of magnitude lower and occur at much lower concentrations (12 K at $7.3 \cdot 10^9 \text{ cm}^{-2}$, and 3.6 K at concentrations lower than $1.6 \cdot 10^8 \text{ cm}^{-2}$) at which $\mu \leq 0$ and the gap in the excitation spectrum is $\approx \sqrt{\mu^2 + \Delta_{\max}^2}$.

We conclude that the effects of screening are significant and shift the most favourable

conditions for the occurrence of the condensation towards lower carrier concentrations. We note, however, that the screening itself is probably overestimated in our approach because Coulombic correlations and the existence of the excitation gap in the condensed phase tend to diminish the screening, particularly at low concentrations.

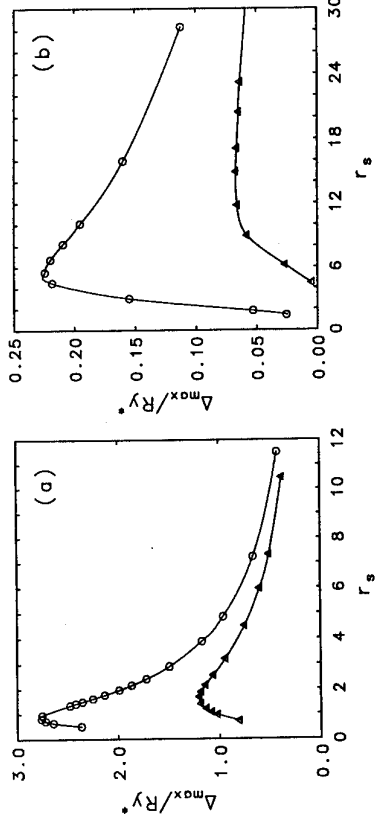


Fig. 2. Maximum value of Δ_k vs r_s without (a) and with (b) screening for $d = a_B^*/10$ (circles) and $d = a_B^*/2$ (triangles).

We thank Dr. A.H. MacDonald and Dr. J. Szymanski for informative discussions. This work was supported by grants from the Australian Research Council and from the Natural Sciences and Engineering Research Council of Canada.

References

- [1] B. Tanatar and D.M. Ceperley, Phys. Rev. B 39 (1989) 5005.
- [2] L. Świernowski, D. Neilson, and J. Szymanski, Phys. Rev. Lett. 67 (1991) 240.
- [3] U. Sivan, P.M. Solomon, and H. Shtrikman, Phys. Rev. Lett. 68, (1992) 1196.
- [4] Yu.E. Lozovik and V.I. Yudson, Pis'ma Zh. Eksp. Teor. Fiz. 22 (1975) 556 [JETP Lett. 22 (1975) 274]; Solid State Commun. 19 (1976) 391.
- [5] S.I. Shevchenko, Fiz. Nizk. Temp. 2 (1976) 505 [Sov. J. Low. Temp. Phys. 2 (1976) 251].
- [6] L.V. Keldysh and Yu.V. Kopaev, Fiz. Tverd. Tela. 6 (1964) 2791 [Sov. Phys. Solid State 6 (1965) 2219; A.N. Kozlov and L.A. Maksimov, Zh. Eksp. Teor. Fiz. 48 (1965) 1184 [JETP 21 (1965) 790]; D. Jerome, T.M. Rice, and W. Kohn, Phys. Rev. 158 (1967) 462; C. Comte and P. Nozières, J. Physique 43 (1982) 1069.
- [7] L.V. Butov, A. Zrenner, G. Abstreiter, G. Böhm, and G. Weimann, Phys. Rev. Lett. 73 (1994) 304.

An Unusual Superconductivity Mechanism in the Systems with Pairing of Spatially Separated Electrons and Holes.

S.I. Shevchenko
 B.I. Verkin Institute for Low Temperature Physics and Engineering,
 Academy of Sciences of Ukraine, Kharkov, 310164, Ukraine

Abstract

The conditions of transition of the systems with pairing of spatially separated electrons and holes into a superconducting phase have been formulated. Principal properties of this very unusual phase are described.

First, a possibility of superfluidity at the pairing of electrons and holes was analysed in [1, 2] in application to the system of real excitons. Then this problem was discussed in connection with exciton dielectric [3, 4]. By analogy with He-II and superconductors it was assumed that the appearance of Bose-condensate of excitons would result in superfluidity of excitons. The summary of these studies is given in the review [5] where it is asserted that since the Meissner effect is absent in an exciton phase, and the impossibility of electric and heat superflows has been proved, then the assumptions of exciton superfluidity are not correct.

The situation changed after the appearance of the works [6, 7] where attention was paid to a possibility of pairing of spatially separated electrons and holes (PSSEH) and transition of the system to a superfluid state. In the system with PSSEH, a local compensation of electron current by hole one does not occur that allows one to observe equal and oppositely directed supercurrents in electron and hole layers. In this connection, in [8] it is proposed to call a coherent phase of the system with PSSEH condenser superconductivity. Progress in microelectronic technology made it possible to create the required structures, and lately a considerable number of experimental [9-12] and theoretical works [13-15] appeared dedicated to the study of the systems with PSSEH. All the above makes actual the careful analysis of realization conditions of condenser superconductivity in the systems with PSSEH.

The first problem to be solved is to provide PSSEH. The length determining the pairing regime is the effective Bohr radius $a_0 = \hbar^2/e^2/m_e^2$. If a_0 is much less than the average distance a between electrons and holes (which densities will be taken coinciding: $n_e = n_h = n$), then the electron and hole pairing will take place according to the one particle scheme. In the opposite limiting case, electrons and holes are collectively paired (as it is in low-temperature superconductors). But there is an important difference between the case of high-density of the pairs ($n a_0^2 \gg 1$) and the case of usual superconductors. The collective electron and hole pairing occurs only when their Fermi-surfaces are almost congruent. Keldysh and Kopaev [3] were the first to pay attention to this fact. Since it is practically impossible to

reach congruent Fermi-surfaces then from here a restriction follows at which the pairing of electrons and holes takes place: $n a_0^2 \leq 1$.

At temperatures much less than the binding energy of a pair, all electrons will be paired with holes, and we obtain the system of two-dimensional bosons formed by spatially separated electrons and holes. As in other two-dimensional systems, the temperature of the transition into a superfluid state must satisfy the Kosterlitz-Thouless relationship:

$$T_c = \frac{\pi \hbar^2 n_s(T_c)}{2 M}, \quad (1)$$

where $M = m_e + m_h$ is the mass of an electron-hole pair. In the case of rare gas of pairs to estimate the transition temperature T_c with a good degree of accuracy, one can substitute $n_s(T_c)$ in (1) by total density of pairs n .

The crystallization of pairs, i.e. the formation of a two-dimensional dipole crystal, in the system may compete with the transition of pairs into a superfluid state. When neglecting quantum effects, a melting temperature T_m may be easily estimated assuming that the melting of a two-dimensional dipole crystal occurs by dissociation of dislocation pairs with antiparallel Burgers vectors. To obtain the temperature T_m one needs to calculate the Lame coefficients for a dipole crystal. These coefficients may be easily found making use of the similarity in the behaviour of spatially separated electrons and holes and the system of surface electrons on the film covering a metallic substrate. Such similarity allows one to avoid the necessity of calculating lattice sums connected with Coulomb interaction of charges. Generalizing the results found earlier for surface electrons [16], it is not difficult to show that at $d \geq a_0$ the melting temperature is [17]

$$T_m \approx 6 \cdot 10^{-2} \eta^2 d^2 n^{3/2} \quad (2)$$

Here η is the numerical coefficient of the order of unity depending on dielectric permeabilities of a dielectric film and conducting media. The dependence of the Lame coefficients on the temperature was neglected when obtaining (2).

Condenser superconductivity realizes evidently provided that $T_m < T_c$. The consequence of this inequality is the restriction to the magnitude d

$$6d^2 < 10^2 a \cdot \alpha_B \eta^{-1} \quad (3)$$

Restriction (3) results in important consequences. If d is large, then the distance between electron-hole pairs a must be large too, i.e. the density of pairs must be small. In this case, the temperature of superfluid transition T_c decreases essentially. Besides, at small densities n , the localization of pairs by impurities or roughness of boundaries may take place. If because of boundary roughness, two-dimensional potential wells with the depth of the order of U_0 and characteristic dimension in the structure plane ℓ , appear, then in the limit of low-density of pairs it will lead to pair localization near the roughness with a localisation length $\lambda \approx \ell \exp(\hbar^2/M^2|U_0|)$.

As a result of it, at the large density of roughnesses or impurities, all pairs will be localized if their density $n < \lambda^{-2}$. On the other hand, small thicknesses d make it possible to increase density of electron-hole pairs avoiding localisation and increasing the temperature of a superfluid transition T_c . At very small thicknesses of a dielectric layer d , however, tunneling transitions between layers with electron and hole conductivities become important. The

presence of such transitions cardinally changes the situation. Interlayer tunneling transitions coinciding with interband transitions for the systems treated lead to the appearance in the Hamiltonian of the system of additional terms fixing the phase φ of the order parameter: since the magnitude of the superfluid flow is proportional to $\nabla\varphi$, then the phase fixation transforms the system from a superfluid state to dielectric one. Guseinov and Keldysh [17] were the first to pay attention to this fact (in application to exciton dielectric). More careful analysis shows, however, that the problem of current states in the presence of interband transitions is not reduced to the question of fixation of the order parameter phase [8].

Interband transitions lead to a possibility of the appearance of solitons in the systems, i.e. vortices which axes ℓ lie in the structure plane. The energy of solitons is positive and their number is exponentially small, if a current I , flowing into the structure on the boundary, is small. At $I > I_{C1}$, where the critical current I_{C1} is a function of matrix elements of interband tunneling, the energy of solitons is negative, and the number of solitons is determined by the magnitude of the current I . Solitons fix the phase. Their appearance make it possible for supercurrent to flow but the state, in which the system transforms, is determined by the presence or absence of phase coherence in the system. If solitons form a lattice, then at large $|f - f'|$ the correlator $\langle \exp(i(\varphi(f) - \varphi(f')) \rangle$ falls off by a power law that is the evidence of the presence of phase coherence. In this case the gas of electron-hole pairs is superfluid, i.e. condenser superconductivity is realized. Melting of a soliton lattice destroys the phase coherence and thus transforms electron-hole pairs into a normal state. The melting temperature of a lattice may be found assuming that melting occurs by the Kosterlitz-Thouless mechanism. At $I_{C2} \gg I \gg I_{C1}$, where I_{C2} is the current destroying the condenser superconductivity, the melting temperature of a soliton lattice coincides with T_C from [1].

The discovery of zero electric resistivity of the current into the structure plane would be the most direct proof of the transition of the system with PSSEH to a superconductivity state. In this case, by virtue of the specificity of the treated systems, it is necessary that the regions with electron and hole conductivities should form a successive circuit for the current, that is, at $x = 0$ the current must flow, for example, into the region with electron conductivity. At $x = L$ the current must flow out of this region and flow into the region with hole conductivity. And at last, it must flow out of the region with hole conductivity at $x = 0$. It is also necessary that at very thin dielectric interlayer separating the regions with electron and hole conductivities for which interlayer tunneling transitions are essential, the supercurrent I would exceed the critical value I_{C1} .

Magnetic properties of condenser superconductors are also rather interesting. A superconducting phase represent a condensate of electron-hole pairs with a mass M , zero charge, and nonzero dipole moment $e\vec{d}$. That's why, assigning the order parameter ψ to a superconducting phase we have an addition to the density of the energy specified by a magnetic field

$$\Delta F = \frac{1}{2M} |(-i\vec{\nabla} - \frac{e}{c}\vec{J} \times \vec{H})\psi|^2 + \frac{H^2}{8\pi} - \frac{\vec{H} \cdot \vec{H}_0}{4\pi}, \quad (4)$$

where \vec{H}_0 is the external magnetic field, and \vec{H} is a local field related to supercurrents by the Maxwell equation, $\nabla \times \vec{H} = (4\pi/c)\vec{j}_s$, and with spatially separated electron and hole currents being equal and oppositely directed. So, in spite of the electric neutrality of pairs, they interact with a magnetic field. It results in a number of interesting effects. In

particular, if the field \vec{H}_0 is created by ring currents flowing over a plane and the currents exceed some critical value, then in a condenser superconductor quantized vortices appear, in which electron-hole pairs rotate around an axis normal to conducting layers. Vortices form an regular structure which, however, does not possess translational invariance. This structure may be found due to regular distribution of a magnetic field related to vortices. The research described in this publication was made possible in part by Grant No. U2D200 from the Joint Fund of the Government of Ukraine and International Science Foundation.

References

- [1] J.M.Blaat, K.W.Boer, and W.Brandt, Phys. Rev., **126**, (1962) 1691.
- [2] S.A.Moshalenko Fiz. Tverd. Tela **4**, (1962) 276.
- [3] L.V.Keldysh and Yu.V.Kopaev Fiz. Tverd. Tela **6** (1964) 2791.
- [4] B.I.Halperin and T.M.Rice Solid State Phys. **21**, (1968) 116.
- [5] W.Kohn, D.Sherrington Rev. Mod. Phys. **42**, (1970) 1.
- [6] S.I.Shevchenko, Fiz. Nizk. Temp. **2**, (1976) 505.
- [7] Yu.E.Lozovik and V.I.Yudson Zh. Eksp. Teor. Fiz. **71**, (1976) 738.
- [8] S.I.Shevchenko Phys. Rev. Lett. **72**, (1994) 3242.
- [9] J.E.Golub, K.Kash, J.P.Harbison, L.T.Flores Phys. Rev. B **41**, (1990) 8564.
- [10] U.Sivan, P.M.Solomon, H.Shtrikman Phys. Rev. Lett. **68**, (1992) 1196.
- [11] J.P.Eisenstein, L.N.Pfeiffer, K.W.West Phys. Rev. Lett. **74**, (1995) 1419.
- [12] L.V.Butov, A.Zrenner, G.Abdetreiter, G.Böhm, G.Weimann Phys. Rev. Lett. **73**, (1994) 304.
- [13] X.M.Chen and J.J.Quinn Phys. Rev. Lett. **67**, (1991) 895.
- [14] X.Zhu, P.B.Littlewood, M.S.Hyberseen, T.M.Rice Phys. Rev. Lett. **74**, (1995) 1633.
- [15] I.Swierkowski, J.Szymanski, and Z.W.Goretz Phys. Rev. Lett. **74**, (1995) 3245.
- [16] F.M.Peeters Phys. Rev. B **30**, 159 (1984).
- [17] S.I.Shevchenko, S.V.Terent'yev, Yu.Z.Kovdrya Fiz. Nizk. Temp. **21**, (1995) N 9.
- [18] R.R.Guseinov, L.V.Keldysh Zh. Eksp. Teor. Fiz. **63**, (1972) 2255.

Coulomb Blockade as a Non-Invasive Probe in Double Layer 2DEG Systems

M. Field, C.G. Smith, M. Pepper, K.M. Brown, E.H. Linfield,
M.P. Grimsditch, D.A. Ritchie and G.A.C. Jones
Cavendish Laboratory, Madingley Road, Cambridge CB3 0HE, United Kingdom

We have used a double two dimensional electron gas (double 2DEG) sample to measure the density of states in one of the 2DEGs over a submicron area. The lower 2DEG screens the electric field between the plates of a mesoscopic capacitor made up of a quantum dot in the upper 2DEG and a backgate behind both 2DEGs. The capacitance is measured by observing the Coulomb blockade period of the dot as function of backgate voltage. The density of states is inferred from the screening, the technique is sensitive to both localised and extended electronic states.

Direct transport measurements disrupt the system being measured and only reveal information about the diffusivity of electrons in states contributing to conduction. The use of a "non-invasive" technique in which the local conditions in one circuit affect a nearby measuring circuit allows the system to remain undisturbed and measures properties over the small length scale in which the two circuits are brought close enough together to interact [1]. One such class of non-invasive measurement is the determination of the screening properties of a sample by capacitance techniques. In this paper we use a two dimensional electron gas (2DEG) to screen a perpendicular electric field between the plates of a mesoscopic capacitor, allowing the compressibility of the screening layer to be measured over a microscopic area.

Measuring the density of states experimentally requires a technique which measures a thermodynamic property of the 2DEG, such as specific heat [2,3], magnetisation [4] or magnetocapacitance [5,6,7]. Using samples with two separate, independently contacted, 2DEG's [8] together with a back gate behind both 2DEGs allows the capacitance between the upper 2DEG and the backgate to be measured [7]. The back 2DEG screening can then be inferred over a large area from which the compressibility and the density of states are deduced.

A double 2DEG sample was grown with two 200 Å quantum wells a distance of 200 Å apart, and a backgate 3300 Å beneath the lower 2DEG. The mobility of the upper layer was 7×10^5 cm²/V·s at a carrier concentration $N_i = 4.5 \times 10^{11}$ cm⁻², while the lower layer had a low mobility of 3×10^4 cm²/V·s at the same carrier concentration, $N_b = N_i$. The carrier concentration in the lower layer was controllable via the backgate, complete depletion occurring at approximately -1.4 V. The sample was patterned into a thin Hall bar shape (0.6 μm wide by 2 μm long) by low energy gallium ion beam damage [8]. Two independent surface Schottky gates of width approximately 500 Å cross the Hall bar a distance of 0.4 μm apart. Using these surface gates a quantum box can be induced in the upper 2DEG. The completed device is shown schematically in figure 1. Measurements were made in a dilution refrigerator with a base temperature of less than 50 mK. The conductance of both the top and bottom 2DEG were measured simultaneously by ac phase sensitive detection using an excitation

voltage of 10 μV.

We measure the screening non-invasively over a small area using the quantum box in the upper 2DEG layer. This small island of charge exhibits Coulomb blockade (CB) effects [9]. The conductance of the upper layer oscillates on changing the potential of a nearby gate; the period of oscillation being inversely proportional to the capacitance between the gate and the dot. Using the back gate to induce CB oscillations in the quantum box allows the capacitance to be measured directly, including any screening effects of the back 2DEG. By making the backgate voltage extremely negative, the carriers in the back 2DEG can be depleted out and the direct capacitance between the back gate and the quantum box measured in the absence of screening. Similarly applying a voltage directly to the back 2DEG allows it to be used as a gate, the capacitance between the back 2DEG and the dot can be measured as well as the active area, $A = 0.51 \times 0.51 \mu\text{m}^2$, of the dot. In the quantum Hall regime, the dot exhibits Aharonov - Bohm oscillations as the magnetic field is swept [10]. The area extracted from this measurement agrees with that obtained from the Coulomb blockade measurement above.

The total capacitance seen by the back gate can be modelled by the equivalent circuit proposed by Luryi [11] which has an extra capacitance C_Q in parallel with the geometric capacitance due to the extra energy required to place electrons in the quantum well due to the finite density of states. This quantum capacitance was first measured by Smith [5] and calculated explicitly by Büttiker [12], who also derived the full 3x3 capacitance matrix for this system. Effects due to electron-electron interactions or the non-zero extent of the wavefunction perpendicular to the 2DEG were considered explicitly by Eisenstein [7].

The equivalent circuit gives the total capacitance as seen by the backgate. The CB period allows the capacitance from the backgate to the dot to be measured, from which the quantum capacitance and hence the density of states can be extracted.

$$\frac{1}{C_Q} = \frac{1}{e^2} \left(\frac{1}{dN_s/dE} \right) \quad (1)$$

Applying the above theory, the density of states can be extracted from the observed period of CB oscillations as the backgate voltage is swept with the back 2DEG grounded.

The model introduced above will be used for small voltage swings (± 0.075 V) around $V_{bg} = 0$. In this region there is little variation of CB period with backgate voltage and the constant density of states model can be applied. The corrections due to the exchange and correlation energies, together with effects due to charge movement perpendicular to the 2DEG within the confines of the well, will tend to reduce the capacitance [5,7]. We have introduced a numerical factor γ ($\gamma = 0.725$, compared with the numerical constant of 0.7 found by Smith [5]) to the quantum capacitance C_Q which brings the predicted CB period in to line with the observed period at $V_{bg} = 0$. Using this value the deduced density of states is computed to be the same as the theoretical value of $\text{m}^* / \pi \hbar^2$.

On changing the magnetic field the period of CB oscillations without the back 2DEG is not substantially affected, whereas the screening component oscillates with inverse magnetic field. At zero back gate voltage the oscillation period is 16.2 mV in zero magnetic field and the lower 2DEG carrier concentration measured by Shubnikov - de Haas $\sim 2.7 \times 10^{11}$ cm⁻². The upper trace (a) in figure 2 shows both the CB period as a function of the inverse magnetic field (right hand axis), and the derived density of states of the back 2DEG (left hand axis). The screening oscillates with a period in $1/B$ of 0.135 Tesla⁻¹, giving a carrier concentration of 3.5×10^{11} cm⁻² compared with a measured lower layer concentration of 2.7×10^{11} cm⁻².

The carrier concentration in the lower layer immediately under the dot may well be higher than the carrier concentration at the most constricted part of the Hall bar. There is some evidence that the dot is not aligned with the narrowest portion of the ion beam defined channel.

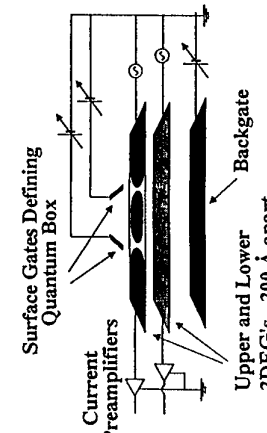


Figure 1: A schematic diagram of the double 2DEG device.

The lower trace, figure 2(b), is the measured R_{xx} of the back 2DEG showing Shubnikov - de Haas oscillations. This was taken at a more positive backgate voltage such that the measured carrier density (determined by the density at the most constricted point along the channel) is the same as that found under the dot from the change in density of states. The low field Shubnikov - de Haas oscillations follow the modulation of the density of states. At higher fields R_{xx} drops to zero in the minima as the Fermi energy sits in localised states, the peak width is noticeably narrower. The density of states however continues to oscillate with the same peak width. Unlike the transport measurements the screening technique is sensitive to localised as well as extended states. The dot is detecting densities of states of order $1 - 5 \times 10^{13} \text{ cm}^{-2} \text{ eV}^{-1}$, with a resolution of $\pm 5 \times 10^{12} \text{ cm}^{-2} \text{ eV}^{-1}$. Since the area and the energy scales are both known, the actual number of electron states can be deduced (a carrier density of $N_b = 3.5 \times 10^{11} \text{ cm}^2$ implies a Fermi energy $E_F = 12.5 \text{ meV}$, the majority of screening occurs in the area of equal size directly below the dot). The system is thus measuring the screening varying by $330 - 1700$ electron states, with a sensitivity of ± 170 electron states.

At zero magnetic field the period of CB oscillations is seen to change dramatically at a backgate voltage of -1.42 V (figure 3) from 7 mV to 2 mV as the screening layer is depleted. The conductance of the back 2DEG dropped below the sensitivity of the measurement at a more positive gate voltage (-1.3 V), the point of complete depletion can only be observed in the screening. As the back 2DEG depletes out it may undergo an Anderson transition, screening then occurs by thermal activation to the mobility edge or by variable range hopping. The carrier density in the lower 2DEG at the transition point is estimated by extrapolating the known dependence at higher backgate voltages at $N_b = 1.2 \times 10^{11} \text{ cm}^{-2}$, $E_F = 4.4 \text{ meV}$.

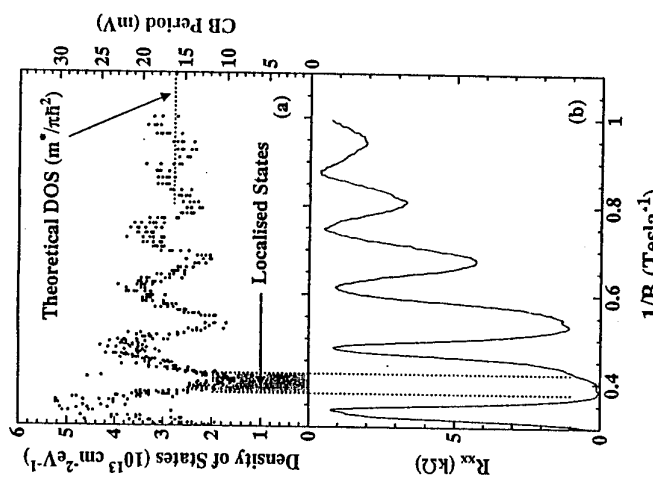


Figure 2: (a) The Coulomb blockade period as a function of inverse magnetic field (right hand axis) and the deduced density of states at the Fermi energy (left hand axis). (b) R_{xx} of the back 2DEG showing Shubnikov - de Haas oscillations, taken at a more positive backgate voltage such that the measured carrier density is the same as that found under the dot. The density of states measurement is sensitive to both the extended and localised electronic states.

The product $N_b^{1/2}a_H = 0.35$ (a_H being the Bohr radius corrected for dielectric constant and effective mass) is close to the predicted value for an Anderson transition of 0.27 [13]. Increasing the temperature moves the point of depletion to more negative gate voltages and flattens out the transition. The backgate voltage can be recalibrated in terms of back 2DEG Fermi energy giving an estimate of the mobility edge at $E_c = 4.4 \text{ meV}$. The actual pinch off underneath the quantum dot may well occur at different back gate voltages to the observed turn on of the back 2DEG conductivity. The screening will depend on whether the states underneath the dot are localised, and if not whether they can reach the ohmic contacts which define the ground potential.

In conclusion we have measured the density of states in a submicron area of a 2DEG using a non-invasive capacitance technique. The technique is sensitive to both the extended and localised electronic states.

This work was supported by the Engineering and Physical Sciences Research Council and ESPRIT project No. BRA6536.

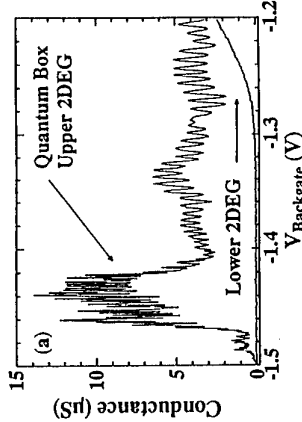


Figure 3: Coulomb blockade oscillations which change period suddenly when the lower 2DEG is fully depleted and can no longer screen. The conductance of the lower 2DEG falls below the minimum sensitivity of the equipment before the 2DEG is completely depleted.

- [1] M. Field, C.G. Smith, M. Pepper, D.A. Ritchie, J.E.F. Frost, G.A.C. Jones and D.G. Hasko; Phys. Rev. Lett. **70**, 1311 (1993)
- [2] E. Gorink, R. Lassing, G. Strasser, H.L. Störmer, A.C. Gossard and W. Wiegmann; Phys. Rev. Lett. **54**, 1820 (1985)
- [3] J.K. Wang, J.H. Campbell, D.C. Tsui and A.Y. Cho; Phys. Rev. B **38**, 6174 (1988)
- [4] T. Haavajoen, H.L. Störmer, D.J. Bishop, V. Narayanamurti, A.C. Gossard and W. Wiegmenn, Surface Science **142**, 294 (1984)
- [5] T.P. Smith, B.B. Goldberg, P.J. Stiles and M. Heiblum; Phys. Rev. B **32**, 2696 (1985)
- [6] R.C. Ashoori and R.H. Silsbee; Solid State Communications **81**, 821 (1992)
- [7] J.P. Eisenstein, L.N. Pfeiffer and K.W. West; Phys. Rev. B **50**, 1760 (1994)
- [8] K.M. Brown, E.H. Linfield, D.A. Ritchie, G.A.C. Jones, M.P. Grimshaw and A.C. Churchill; J. Vac. Sci. Tech. B **12**, 1293 (1994)
- [9] For a review of Coulomb blockade effects see H. Grabert and M.H. Devoret, eds "Single Charge Tunneling", Vol. B294 NATO ASI Series B; New York, Plenum Press (1992)
- [10] R.J. Brown, C.G. Smith, M. Pepper, M.J. Kelly, R. Newbury, H. Ahmed, D.G. Hasko, J.E.F. Frost, D.C. Peacock and G.A.C. Jones; J. Phys.: Cond. Matter **1**, 6291 (1989)
- [11] S. Luryi; Appl. Phys. Lett. **52**, (6) 501 (1988)
- [12] M. Büttiker, H. Thomas and A. Prêtre; Phys. Lett. A **180**, 364 (1993)

Observation of many-body interactions of electrons in coupled double quantum wells

A.S. Plaut*, A. Pinczuk, B.S. Dennis, J.P. Eisenstein, L.N. Pfeiffer, and

K.W. West
AT&T Bell Laboratories, Murray Hill, New Jersey 07974, USA
Exeter University, Exeter EX4 4QL, UK

Abstract

We have investigated, by resonant inelastic light scattering, the finite in-plane wavevector dispersion of the collective excitations of electron bilayers in AlGaAs/GaAs double quantum wells. As the wavevector is increased the plasmon mode first becomes Landau damped and then at larger wavevectors it reappears as it emerges from one of the two maxima of the continuum of single-particle excitations in a two-dimensional system with two occupied subbands. These measurements enable quantitative determination of many-body interactions in dilute electron bi-layers.

Single-layer two-dimensional electron systems (2DES) have been intensively studied in recent years [1]. Optical experiments have been particularly important in revealing the nature of electron-electron interactions in these systems [2,3]. Raman spectroscopy, for instance, probes the collective excitations of the electron gas [4]. In the last five years, further advances in molecular beam epitaxial (MBE) growth have produced double-layer 2DES with mobilities comparable to single-layer 2DES [5-7]. The separation of the two 2D electron gases in such structures is 100 Å or less, resulting in quantum states with strong correlations between the layers [5-7]. Recently, it has been suggested [8] that an exchange-correlation induced many-body excitonic vertex correction may lead to an instability in the normal ground state of these double quantum well (DQW) structures. A novel zero-field electronic phase transition to a many-body triplet excitonic liquid ground state is predicted to occur, which would manifest itself by the disappearance of the intersubband spin-density excitation gap at low electron densities.

We have investigated, by resonant inelastic light-scattering, the collective charge-density and spin-density excitations associated with electron transitions between the lowest symmetric and antisymmetric states of DQW structures. For $q \ll K_F$, where q is the in-plane wavevector transfer and K_F the Fermi wavevector, the intersubband single-particle excitations (SPE) occur within the continuum of energies bounded by $\Delta_{SAS} \pm h\nu_F$ [9], where Δ_{SAS} is the symmetric-antisymmetric splitting (or tunneling gap of the DQW) and ν_F is the Fermi velocity. Thus for $q=0$, the energy of the SPE equals that of Δ_{SAS} . Δ_{SAS} can be easily tuned by changing the thickness and Al content of the central barrier [5]. In the samples used in these studies, the value of Δ_{SAS} was adjusted to be small (about 1 meV), as required for investigations of instabilities induced by electron interactions [8].

The modulation-doped DQWs investigated were grown by MBE. They consist of two nominally identical GaAs quantum wells of width $d_w = 180 \text{ \AA}$ separated by composite barriers consisting of two 8.5 Å wide Al_{0.3}Ga_{0.7}As layers with an 11 Å AlAs layer in the middle (Figure 1). Si-doped layers grown both above and below the DQW create two equivalent 2DES with combined total carrier concentrations in the range $0.8 \cdot 10^{11} \text{ cm}^{-2} < n < 1.5 \cdot 10^{11} \text{ cm}^{-2}$ and low-temperature mobilities $0.70 - 1.24 \cdot 10^6 \text{ cm}^2/\text{Vs}$. Raman spectra were obtained at 1.7 K using a dye laser tuned to the excitonic optical transitions. A conventional backscattering geometry allowed in-plane wavevector transfer by rotating the sample relative to the incident light beam [10]. In this configuration $q = 4r\sin\theta/\lambda$, where λ is the wavelength of the incident light and θ the angle between the incident beam and the normal to the sample.

Figure 2 shows Raman spectra obtained from Sample 1 at $q \geq 0$. The peaks have well defined polarization selection rules. They arise from collective charge-density excitations (CDE) and spin-density excitations (SDE) of the 2DES. Collective SDE are shifted to lower

energies than the SPE due to exchange vertex corrections (excitonic shift). The CDE are shifted upwards from the SPE due to the direct (Hartree) term of the Coulomb interaction (depolarisation shift). As the depolarisation shift is usually greater than the excitonic shift, the CDE appear higher in energy than the SPE. SDE are active in depolarised spectra, where incident and scattered light polarisations are perpendicular and CDE occur in polarised spectra measured with parallel polarisations. The sharpness of the collective excitation peaks is indicative of the high quality of the 2DES.

Quantitative determination of many-body interactions also require measurement of the SPE energy. A broad peak positioned in energy between the SDE and CDE peaks has in previous work [7,10,11] been assigned to SPE. Deco *et al.* [7] have seen this SPE peak broaden with increasing q to the expected width of $2\hbar\nu_F$, and in addition to exhibit two well defined maxima as predicted theoretically [9]. Unfortunately, it was difficult to observe the band of SPE in the $q=0$ light-scattering spectra from these low density samples. In order to determine the energy position of the SPE at $q=0$ we have measured the finite in-plane wavevector dispersion of the collective excitations of these electron bilayers. Figure 3a shows polarised spectra at various q . Not only does the CDE peak move to higher energy with increasing q , but first it broadens and then sharpens again at yet higher q . In Figure 3b the full width half maximum (FWHM) of the CDE is plotted. As the wavevector is increased, by changing the scattering angle, the plasmon mode enters the electron-hole continuum of SPE and becomes Landau damped due to its decay into electron-hole pairs [10]. At larger wavevectors still, we observe the collective charge-density excitation (CDE) peak re-appearing as it leaves one of the two maxima of the density of states for the SPE in a two-dimensional (2D) system with two occupied subbands [9]. This scenario is depicted schematically in the inset of Figure 3.

From such novel re-entrant behaviour we can extrapolate Δ_{SAS} even when the SPE peak is not apparent in the zero-wavevector spectra. We know the wavevector and energy of the CDE when it first intersects the SPE continuum and when it emerges from the higher energy wing. Since this SPE region is bounded by $\Delta_{SAS} + h\nu_F$ on the high energy side and $\Delta_{SAS} + h\nu_F$ on the low energy side (where ν_F is the Fermi velocity of the (anti)symmetric state), we can derive a value for Δ_{SAS} at $q=0$. We estimate that the uncertainty involved in this procedure to be about $\pm 0.03 \text{ meV}$. The values obtained from the samples exhibiting this behaviour are given in Table 1. Also included in Table 1 are the values calculated self-consistently within a Hartree approximation. These calculated values are in good agreement with the measured ones.

In Sample 3, with $n = 0.8 \cdot 10^{11} \text{ cm}^{-2}$, we observed not only the FWHM of the CDE increasing and then suddenly dropping as described above, but it then proceeded yet greater q to broaden for a second time (Figure 4). We interpret this striking anomaly as the CDE passing through both wings of the continuum of SPE as shown in the inset of Figure 4. Analysing this behaviour in a similar manner to that described above, we extract a value of $\Delta_{SAS} = 0.90 \text{ meV}$, which implies that the energy of CDE falls below that of the SPE in this sample. This phenomenon, observed for the first time in bilayer 2D electron systems, is a many-body effect arising from the excitonic vertex correction becoming larger than the depolarisation shift at low electron densities [12].

The energy position of the SDE in these samples is often too low to be accurately determined experimentally. The reason is simply a consequence of the small value of Δ_{SAS} . At finite wavevector in the sample with a resolvable SDE ($\omega_{SDE} = 0.35 \text{ meV}$ at $q=0$) the energy position of the SDE decreases sharply until it becomes Landau damped as it moves coincident in energy with either the intersubband SPE or intrasubband excitations. We have not, as yet, observed the spin-density excitonic instability predicted to occur around similar electron densities [8].

From the measured energies of the excitations (Table 1) we can determine the direct and exchange terms of the Coulomb interaction as a function of electron density [7]: The depolarisation shift is given by

Table 1: Electron densities; Δ_{SAS} measured by experiment; Δ_{SAS} calculated self-consistently within a Hartree approximation; transition energies of the collective excitations; the depolarisation shift (α), the excitonic shift (β) and their ratio.

Sample	1	2	3
$n \times 10^{11} \text{ cm}^{-2}$	1.5	1.1	0.8
$\Delta_{SAS} \text{ (meV) measured}$	0.75 ± 0.05	0.55 ± 0.05	0.90 ± 0.05
$\Delta_{SAS} \text{ (meV) calculated}$	0.62	0.65	0.79
$\alpha \text{SDE} \text{ (meV)}$	0.35	<0.2	<0.3
$\alpha \text{CDE} \text{ (meV)}$	0.80	0.55	0.70
$\alpha \times 10^{-11} \text{ meV cm}^2$	1.61	-1.5	-0.9
$\beta \times 10^{-11} \text{ meV cm}^2$	1.37	-1.5	-1.6
β / α	0.85	-1.0	-1.8

and the excitonic shift by

$$\beta = \frac{\Delta_{SAS}^2 - \omega_{SDE}^2}{2\Delta_{SAS}(n_S - n_{AS})}$$

where ω_{CDE} (ω_{SDE}) is the energy of the CDE (SDE) and $n_{(A)S}$ is the electron density of the (anti)symmetric state. The factor $(n_S - n_{AS})$ takes into account the reduction in available phase space when two subbands are occupied. The values of α and β so determined are also given in Table 1. β remains relatively constant across the range of electron densities investigated, whereas α decreases dramatically at the lowest density.

In summary, we have measured in-plane wavevector dispersions of the spin- and charge-density excitations of the bilayer 2DES of double quantum wells. We have observed the re-emergence of the CDE as it moves in-between the two maxima of the SPE continuum. We have, hence, determined Δ_{SAS} and the Hartree and exchange terms of the Coulomb interaction. At low electron densities we have observed the CDE crossing the SPE of these strongly coupled 2DES as a result of a significant decrease in the depolarisation shift of the intersubband CDE.

One of us (A.S.P.) is grateful for financial support from The Leverhulme Trust.

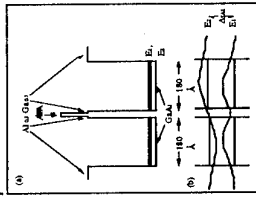


Figure 1: The double quantum well (DQW) structure (a) with composite barriers totalling 28 Å in width. (b) is a schematic of the symmetric and anti-symmetric states of the DQW.

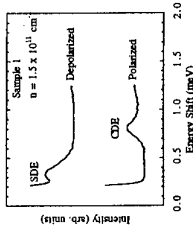


Figure 2: Inelastic light scattering spectra of the intersubband excitations of the double quantum well. The peaks of the spin-density excitations (SDE) and charge-density excitations (CDE) are shown. The spectral resolution is 0.15 meV.

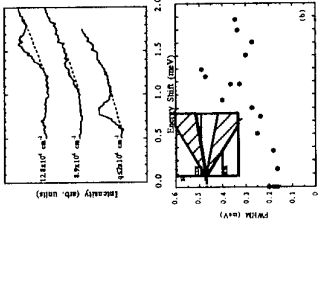


Figure 3: Wavevector dependence of the intersubband CDE of Sample 1 with $n = 1.5 \times 10^{11} \text{ cm}^{-2}$; (a) inelastic light scattering spectra and (b) the full width half maximum (FWHM) of the CDE peak. The error in the FWHM is of the order of the scatter in the data. Inset: A sketch of the q dependence of intersubband excitations in the long-wavelength limit $q \ll K_F$.

- [1] Proceedings of the 10th International Conference on Electronic Properties of 2-Dimensional Systems (EP2DS), Newport, USA, 1993 [Surf. Sci. **305** (1994)].
- [2] For example: I.V. Lukushkin et al., JETP Lett. **44**, 228 (1986); H. Buhmann et al., Phys. Rev. Lett. **65**, 1056 (1990); H. Buhmann et al., Phys. Rev. Lett. **66**, 926 (1990); D. Heiman et al., Phys. Rev. Lett. **61**, 605 (1988); B.B. Goldberg et al., Phys. Rev. Lett. **65**, 641 (1990); A.J. Turberfield et al., Phys. Rev. Lett. **65**, 637 (1990); E.M. Goldys et al., Phys. Rev. B **46**, 7957 (1992).
- [3] A. Pinczuk, B.S. Dennis, L.N. Pfeiffer and K. West, Phys. Rev. Lett. **70**, 3983 (1993).
- [4] For a review: A. Pinczuk, Festkörperprobleme/Advances in Solid State Physics, **32**, 45 (1992).
- [5] G.S. Boebinger et al., Phys. Rev. Lett. **64**, 1793 (1990); J.P. Eisenstein et al., Phys. Rev. Lett. **68**, 1383 (1992); S.Q. Murphy et al., Phys. Rev. Lett. **72**, 728 (1994).
- [6] J.P. Eisenstein, L.N. Pfeiffer and K.W. West, Phys. Rev. Lett. **69**, 3804 (1992).
- [7] R. Decca, A. Pinczuk, S. Das Sarma, B.S. Dennis, L.N. Pfeiffer and K.W. West, Phys. Rev. Lett. **72**, 1506 (1994).
- [8] S. Das Sarma and P.I. Tamborenea, Phys. Rev. Lett. **73**, 1971 (1994).
- [9] J.K. Jain and S. Das Sarma, Phys. Rev. B **36**, 5949 (1987).
- [10] A. Pinczuk, S. Schmitz-Rink, G. Danan, J.P. Valdáres, L.N. Pfeiffer and K.W. West, Phys. Rev. Lett. **63**, 1633 (1989).
- [11] D. Gammon et al., Phys. Rev. B **41**, 12311 (1990); D. Gammon et al., Phys. Rev. Lett. **68**, 1884 (1992).
- [12] S. Das Sarma and I.K. Marmorkos, Phys. Rev. B **47**, 16343 (1993); I.K. Marmorkos and S. Das Sarma, Phys. Rev. B **48**, 1544 (1993); S. Ernst, A.R. Goni, K. Syassen and K. Eberl, Phys. Rev. Lett. **72**, 4029 (1994).

Stability and dynamical properties of a double-layer Wigner crystal in two dimensions

G. Goldoni, V. Schweigert, and F. M. Peeters
Department of physics, University of Antwerp, B-2610 Antwerp, Belgium

(June 13, 1995)

We investigate the zero-temperature phase diagram and melting transition of a two-dimensional Wigner crystal (WC) of classical Coulomb particles in a double-layer structure. In contrast with the single-layer WC, we find that five different crystalline phases are stable in different ranges of inter-layer distance/particle density. Phase boundaries consist of both continuous and discontinuous transitions. From the phonon frequencies of the system we evaluate the melting temperature of the WC. We suggest the possibility of structural phase transitions as a function of temperature.

Classical charged particles confined in a single two-dimensional (2D) layer are known to localize into a triangular lattice (Wigner crystal) for sufficiently large densities and low temperatures. A single-layer Wigner crystal (SLWC) can be realized, e.g., on the surface of liquid helium.¹

In this paper we study the static and dynamical properties of a classical Wigner crystal realized in a double-layer structure (DLWC). This is a very promising system for the investigation of phase transitions in 2D since, contrary to the SLWC, which crystallizes in the triangular lattice at any charge density, several different lattice geometries are stable in the DLWC, and the energetically favoured configuration can be tuned by changing either the inter-layer distance D or the particle density n . Therefore, melting of different crystalline structures can be investigated. Moreover, structural phase transitions as a function of temperature T in 2D can be studied. Recent theoretical studies of the DLWC include the investigation of the $T = 0$ phase diagram in the quantum regime,² the effect of a magnetic field,³ and systems of coupled electron-hole layers.³ To our knowledge, no investigation of the phase diagram at finite T exists.

In this paper we study both the $T = 0$ phase diagram and the melting transition of the classical DLWC in zero magnetic field. The DLWC is characterized by the dimensionless parameter $\eta = D\sqrt{n}$ which gives a measure of the relative strength of the interaction between particles in the same layer and particles in different layers. We find that the $T=0$ phase diagram of the classical DLWC consists of five different crystalline structures which are stable in different ranges of η . These phases evolve one into the other through both first and second order phase transitions.

From the calculated phonon frequencies we have computed the mean square displacements, which allowed us to evaluate the melting temperature of the different phases using a modified Lindemann criterion, appropriate to 2D systems.

We consider a DLWC consisting of classical, spinless particles with Coulomb interaction e^2/r both between particles in the same layer and in different layers. Electrons localized in the two layers constitute two sub-lattices which are equivalent by symmetry. The particle density is $n/2$ in each sub-lattice, so that if $\eta \rightarrow 0$ we recover a SLWC of density n .

First we discuss the $T=0$ phase diagram. In Fig. 1 we show the calculated total energy of five different lattice geometries as a function of η ; three of the lattice geometries are sketched in the insets. The five phases are as follows. Phase I (inset I in Fig. 1), which is energetically

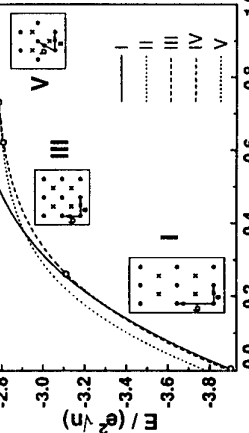


FIG. 1. Static energy of the five different phases at $T=0$. In the insets we show the lattice geometries of lowest energy in the various ranges. Dots and crosses identify the two sub-lattices. Phases II and IV, whose energy is nearly indistinguishable on the scale of the figure, have a geometry which evolve in a continuous way from I to III, and from III to V, respectively (see text). White dots identify phase boundaries.

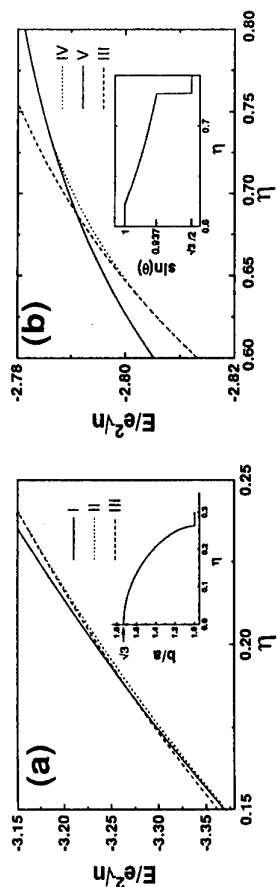


FIG. 2. Detail of Fig. 1 showing the transitions between (a) phases I and III and (b) phases III and V. The insets show how (a) the ratio b/a and (b) the sine of the angle b/a between a and b evolves during the transitions.

favoured at small η , is composed of two rectangular sub-lattices. In the limit $\eta \rightarrow 0$, the two sub-lattices merge and one recovers the energy of the one-component triangular lattice of the SLWC.⁴ At the opposite limit of very large η , the two sub-lattices become less and less coupled and the favoured geometry is two triangular SLWC (see inset V); due to the long-range Coulomb interaction, the two sub-lattices are staggered to maximize the inter-layer particle distance (phase V). Eventually, the energy converges to the energy of a SLWC with density $n/2$. At intermediate values of η the favoured geometry is two staggered square sub-lattices (phase III). This is in contrast with the SLWC, where the square lattice is not even electrostatically stable.⁴

We next discuss how phases I, III and V evolve one into the other as a function of η . Phase I is composed of two rectangular sub-lattices, where the ratio of the lengths of the two axes a and b is $\sqrt{3}$; phase I evolves into phase II through an anisotropic shrinking of the rectangular unit cell. In fact, as η exceeds a critical value (0.006), a rectangular unit cell with $b/a < \sqrt{3}$ becomes energetically favoured (phase II) and eventually $b/a = 1$, corresponding to the square lattice (phase III), is reached in a continuous way. Fig. 2(a) shows a detail of the I \rightarrow III transition. At each value of η we report the minimum energy as a function of b/a ; the value of b/a for which the minimum is obtained is shown in the inset. For $\eta > 0.621$ a rhombic lattice becomes favoured (phase IV). Its energy is reported

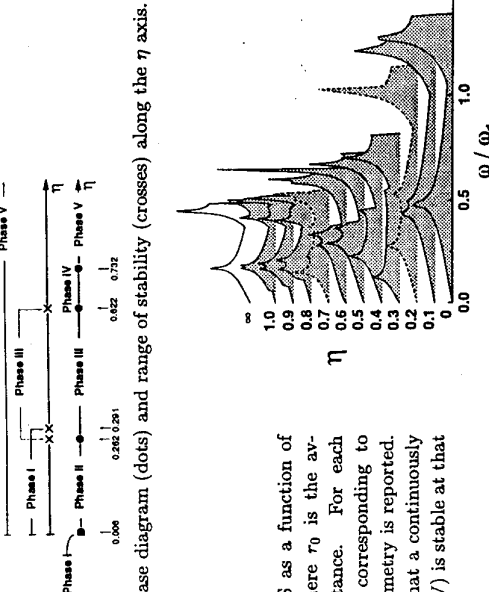


FIG. 3. $T=0$ phase diagram (dots) and range of stability (crosses) along the η axis.
 $\eta = e^2/mr_0^3$, where r_0 is the average interparticle distance. For each value of η , the DOS corresponding to the favoured lattice geometry is reported. Dashed lines indicate that a continuously changing phase (II or IV) is stable at that value of η .

in Fig. 2(b). As shown in the inset, the angle θ between its axes evolves continuously from 90° , corresponding to the square lattice (phase III) to 69.48° and suddenly drops to 60° , corresponding to the staggered triangular phase (phase V). The $T=0$ phase diagram of the classical DLWC found here agrees well with a recent calculation of the WC phases in a bi-layer quantum Hall system.²

We now consider the dynamical properties of the DLWC. The phonon dispersion curves of the five phases was calculated in the whole range of η within the harmonic approximation. The phonon modes (not shown here) reveal that each phase, except phase V, is electrostatically stable only in a finite range of η . The softening of low-frequency modes in particular directions sets an upper limit to the range of stability of each phase. The $T=0$ phase diagram, deduced from Figs. 1,2 and the range of stability, deduced by the softening of phonon modes, are summarized in Fig. 3. Anharmonic effects, not included here, will renormalize the low-frequency modes to lower frequencies and will narrow the range of stability of the different phases.

Fig. 4 shows the phonon density of states (DOS) as a function of η . Since each lattice geometry has a different Brillouin zone, phonon frequencies are measured in units of $\omega_1 = e^2/mr_0^3$, where r_0 is defined by $n = 1/\pi r_0^2$. Both at $\eta = 0$ and $\eta = \infty$ the favoured lattice is the triangular lattice; therefore, the corresponding DOS curves are equal and scaled due to the different particle density. Note in Fig. 4 the high frequency peak which narrows at $\eta \approx 0.5$, corresponding to the η -range where the in-plane component of the average interaction of one particle with its nearest neighbours in the same layer and in the opposite layer are similar. Also note the low-frequency peak which moves to very low frequencies around $\eta \sim 0.3$ and $\eta \sim 0.7$. This behaviour is reminiscent of the softening of some of the modes of the square lattice (phase III). The high density of low-frequency modes suggests that very large fluctuations of particles around equilibrium lattice sites are possible; correspondingly, a low melting temperature is expected in proximity of these points.

Finally, we consider the finite temperature properties of the DLWC. To evaluate the melting temperature of each crystalline phase we used the calculated phonon frequencies to

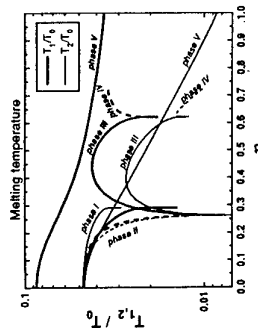


FIG. 5. Melting temperatures T_1 (thick lines) and T_2 (thin lines) for the five lattices. $T_0 = e^2/K_B a$, where a is the lattice parameter and K_B the Boltzmann constant. For phases II and IV (dashed lines) we used the value of the continuously changing parameter, either the ratio b/a or the angle between a and b , respectively, for which the energy is at its minimum at $T=0$.

evaluate the mean square relative displacement of each lattice site with respect to the cage of its nearest neighbours. As confirmed by simulations of 2D systems, melting occurs when this quantity exceeds roughly 10 % of the lattice parameter.⁵ We define two melting temperatures, T_1 and T_2 , calculating the mean square relative displacement with respect to the cage of its nearest neighbours either in the same layer or in the opposite layer, respectively. In this way we can evaluate the critical temperature of two different phase transitions, one in which the inter-layer correlation is lost even if each layer separately remains ordered (T_2), and one in which melting occurs within each layer (T_1).

Fig. 5 show the calculated T_1, T_2 for the five lattice geometries in their range of stability, according to Fig. 3. As expected, $T_1 > T_2$ except at $\eta = 0$ where $T_1 = T_2$, as the two sub-lattices are equivalent; furthermore, T_2 vanishes exponentially for very large η , as the interaction between the sub-lattices decreases. As $\eta \rightarrow \infty$, T_1 approaches $T_1(\eta = 0)/\sqrt{2}$, because at large η each layer consists of a triangular lattice with density $n/2$. At the phase interfaces I/III and III/V the melting temperature shows pronounced dips. This is a consequence of mode softening.

In conclusion we have studied the $T = 0$ phase diagram and melting of a classical DLWC. The presence of several stable crystalline phases of similar energy suggests the possibility of structural phase transitions as a function of T and η . We are currently investigating the phase boundaries in the $T - \eta$ plane; these results will be presented elsewhere. The present calculations have been performed within the harmonic approximation, which are expected to give qualitatively reliable results. More quantitative calculations, including anharmonic corrections and comparison with Monte Carlo simulations are in progress.

We acknowledge financial support from the HCM network No. ERBCHRXCT930374, INTAS and the Belgian National Science Foundation.

¹ C. C. Grims and G. Adams, Phys. Rev. Lett. **42**, 795 (1979)

² S. Narasimhan and T.-L. Ho (unpublished).

³ A. Chan and A. H. Mac Donald (unpublished).

⁴ L. Bonsall and A. A. Maradudin, Phys. Rev. B **15**, 1959 (1977).

⁵ In 2D this value is rather insensitive to the details of the interactions (see Ref. 6) and therefore we use the same value for all lattice geometries.

⁶ V. M. Bedanov, G. V. Gadiyak, Y. E. Lozovik, Phys. Lett. **109A**, 289 (1985).

Tunneling between Parallel Two-dimensional Electron liquids

T. Jungwirth
Institute of Physics ASCR, Cukrovarnická 10, CZ-162 00 Praha.

A.H. MacDonald
Department of Physics, Indiana University, Bloomington, IN 47405

Abstract

We derive and evaluate expression for the dc tunneling conductance between interacting two-dimensional electron systems at non-zero temperatures. The possibility of using the dependence of the tunneling conductance on voltage and temperature to determine the temperature-dependent electron-electron scattering rate at the Fermi energy is discussed. The finite electronic lifetime produced by electron-electron interactions is calculated as a function of temperature for quasiparticles near the Fermi circle. Our results are in a reasonable agreement with existing experiments.

Introduction

Recently developed experimental techniques for measuring the tunneling conductance between parallel two-dimensional electron systems have provided a new probe of the underlying electronic structure. Crucial to the success of this method is the conservation of in-plane momentum which is achieved to a remarkable degree in GaAs/AlGaAs double-quantum-well structures [1,2]. Zheng *et al* [3] studied theoretically the influence of disorder on the zero-temperature tunneling conductance and found that 2D-2D tunneling experiments can provide a direct measure of the elastic scattering rate of electrons.

Murphy *et al* [4] extended this idea to inelastic processes by measuring the temperature dependent tunneling conductance. By comparing with the measured mobility of their system, they concluded that electron-phonon scattering could not account for their observations and suggested that the experiment provides information about electron-electron scattering rates which cannot be obtained from standard in-plane transport measurements. However, the energy dependence of the electronic lifetime due to electron-electron interactions makes the relation to the tunneling conductance more complicated than in the case of the elastic scattering. To examine this relation we derive an expression for the 2D-2D tunneling conductance as a function of applied voltage and temperature using the linear-response formalism. The problem of calculating the quasiparticle lifetime due to Coulomb interactions is a standard problem in the many-body theory of the electron gas. Nevertheless, for the two-dimensional electron gas confusing disagreements exist among the various analytical calculations [5-7] published to date. To clarify the situation we perform both analytical and numerical calculations of the energy and temperature-dependent electron-electron scattering rate based on the Fermi golden rule. We show that the widely accepted approximation where the general four-point scattering function is replaced by the *forward* scattering limit

of the RPA screened Coulomb potential is not adequate. Moreover, even the full momentum-dependent dynamical RPA fails for electron systems typical of tunneling experiments and vertex corrections have to be taken into account.

2D-2D tunneling conductance at $T > 0$

We consider a GaAs/AlGaAs heterostructure with two identical quantum wells and equal layer densities. The Hamiltonian can be written as the sum of three terms:

$$\begin{aligned} H &= H_R + H_L + H_T \\ H_T &= \sum_{\vec{k}, \vec{k}'} (t_{\vec{k}, \vec{k}'} c_{\vec{k}, R}^\dagger c_{\vec{k}', L} + \text{h.c.}) \end{aligned} \quad (1)$$

The first term H_R is the Hamiltonian for particles in the right well. Generally, it contains all many-body interactions. Similarly, H_L has all the physics for particles in the left well and the tunneling is caused by the term H_T . (We ignore inter-layer interactions in this paper.) Because of the conservation of in-plane momentum $t_{\vec{k}, \vec{k}'}$ is zero for $\vec{k} \neq \vec{k}'$, i.e., $t_{\vec{k}, \vec{k}'} = t \delta_{\vec{k}, \vec{k}'}$. For the samples used in experiments the tunneling rate t , which in the absence of scattering determines the difference in energy between symmetric and antisymmetric states for each \vec{k} , is much smaller than the elastic scattering rate of electrons in the 2D layer. In this regime the tunneling Hamiltonian can be treated as a perturbation and the linear response formalism can be employed to find the formula for the tunneling current I as a function of applied voltage V between the 2D layers. Following a familiar line [8] we obtain

$$I(V, T) = \gamma t \int_{-E_F}^{\infty} d\xi \int_{-\infty}^{\infty} dE A(\xi - E, \Gamma(\xi, T)) A(\xi - E - eV, \Gamma(\xi, T)) \times \times [n_F(E, T) - n_F(E + eV, T)], \quad (2)$$

where γ is a constant, $A(x, \Gamma) = \Gamma / [\pi(x^2 + \Gamma^2/4)]$ is the spectral function in the quasi-particle peak approximation, $\Gamma(\xi, T)$ is the quasiparticle energy and temperature dependent electronic scattering rate and n_F is the Fermi distribution function. At $T = 0$ the lifetime of electrons close to Fermi energy is dominated by elastic scattering and the scattering rate $\Gamma(\xi) = \Gamma_{\text{elast.}}$ is a constant much less than the Fermi energy E_F of the 2D electron system. The tunneling conductance $G(V) \equiv I/V$ is a Lorentzian, in this case, with the full width at half maximum equal to $2\Gamma_{\text{elast.}}$.

At higher temperatures, neglecting electron-phonon interactions, $\Gamma(\xi, T)$ can be written as a sum of $\Gamma_{\text{elast.}}$ and the electron-electron scattering rate $\Gamma_{\text{el.-el.}}(\xi, T)$. Since the energy dependence of $\Gamma_{\text{el.-el.}}(\xi, T)$ is not negligible compared to its temperature dependence, the zero-temperature relationship between the scattering rate of an electron on the Fermi energy and the width of the $G(V)$ curve is altered. Subtracting the constant elastic scattering rate, it follows from Eq.(2) that the width at half maximum of the $G(V)$ function overestimates the electron-electron scattering rate at the Fermi energy. Introducing $\Gamma_{\text{el.-el.}}(\xi, T)$, calculated below, into Eq.(2) and performing the numerical integration we obtain that the overestimate is about 30% for the whole range of temperatures, for the electron concentrations used in the tunneling experiments [4] ($T \leq 10K$, $N_e = 0.8$ and $1.6 \times 10^{11} \text{ cm}^{-2}$).

Electron-electron scattering rate

As explained above both the temperature dependence and the energy dependence of the electron-electron scattering rate at the Fermi energy have to be calculated to compare theory to measured $I - V$ characteristics. From the Fermi golden rule we obtain

$$\Gamma_{el-el}(\epsilon_1) = 2 \int \frac{d^2 p_1}{(2\pi)^2} \int \frac{d^2 p_2}{(2\pi)^2} W (1 - n_F(\vec{p}_1)) \times \\ \times n_F(\vec{p}_2) (1 - n_F(\vec{p}_1 + \vec{p}_2 - \vec{p}_1')) \delta(\epsilon_1 + \epsilon_2 - \epsilon_1' - \epsilon_2'), \quad (3)$$

where W is the four-point scattering function and the energies $\epsilon_i = \hbar^2 \vec{p}_i^2 / 2m$. In the Born approximation W is equal to $2\pi |V_c(\vec{p}_1, \vec{p}_1')|^2$ where $V_c(\vec{p}_1, \vec{p}_1')$ is the matrix element of a suitable electron-electron interaction potential. Using the random-phase approximation the dynamically screened interaction in units of N_0^{-2} (the 2D density of states $N_0 = m/\pi\hbar^2$) can be written as a function of transferred momentum $\vec{q} \equiv \vec{p}_1' - \vec{p}_1$ and energy $\hbar\omega \equiv \epsilon_1 - \epsilon_1'$

$$(q\chi_E)^2 = \frac{(q\chi_E)^2}{\left(1 + \frac{\pi q E}{4} \text{Re}\chi_0(q, \hbar\omega)\right)^2 + \left(\frac{\pi q E}{4} \text{Im}\chi_0(q, \hbar\omega)\right)^2}. \quad (4)$$

($q\chi_E$ is the Thomas-Fermi screening wave vector and χ_0 is the susceptibility of a noninteracting 2D electron gas in units of N_0 .)

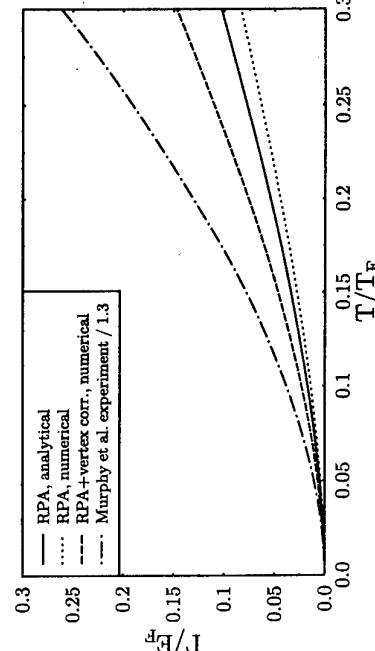


Figure 1: Temperature dependent el-el. scattering rate at the Fermi energy given by Eq. (5) (full line), numerically calculated using the RPA screened Coulomb interaction (dotted line) and numerically calculated with vertex corrections to RPA (dashed line). The dotted-dashed line corresponds to half-width of measured $G(V)$ curves at half-maxima divided by 1.3.

Integrating over the angle θ_2 between the incoming momenta \vec{p}_1 and \vec{p}_2 in Eq. (3), we find that the forward and backward limits of the scattering processes contribute to the leading term in the energy and temperature dependence of Γ_{el-el} . To obtain analytical expressions for the electron-electron scattering rate we replace $|V_c(q, \hbar\omega)|^2$ by a constant $|V_c^0|^2 = (|V_c(0, 0)|^2 + |V_c(2p_F, 0)|^2)/2$. In this approximation Eq.(3) and Eq.(4) give

$$\frac{\Gamma_{el-el}(\xi)}{E_F} = |V_c^0|^2 \frac{1}{2\pi} \left[\ln\left(\frac{\xi}{E_F}\right)^2 + \frac{\ln(8)}{2} + \frac{1}{2} + \dots \right], \quad T=0, \xi \ll E_F \quad (3)$$

$$\frac{\Gamma_{el-el}(T)}{E_F} = |V_c^0|^2 \frac{\pi}{4} \left(\frac{k_B T}{E_F} \right)^2 \left[\ln\left(\frac{E_F}{k_B T}\right) + \frac{\ln(8)}{2} - .08 + \dots \right], \quad \xi=0, k_B T \ll E_F \quad (5)$$

In figure 1 the approximate formula (5) for $\Gamma_{el-el}(T)$ at the Fermi energy is compared to the exact numerical calculation with the four-point scattering function in the form given by Eq.(4). Results obtained when vertex corrections to the RPA are approximated in the way proposed by A.H. MacDonald *et al.* [9] are also shown in figure 1. These corrections significantly modify the calculated electronic lifetime and shift the theoretical curve closer to the experimentally measured $\Gamma_{el-el}(T)$.

Conclusions

Tunneling conductance between parallel 2D electron systems at $T > 0$ provides a measure of the electron-electron scattering rate. The theoretical calculations of the electronic lifetime presented here demonstrate that low-temperature scattering is dominated by both forward and backward scattering processes. Corrections to the RPA are expected to be substantial (for electron concentrations typical of existing tunneling experiments) and bring theoretical results into reasonable agreement with experimental data. Existing quantitative differences motivate more accurate evaluation of the four-point electron-electron scattering function. Also the derivation of the tunneling conductance should be carefully examined to account for inter-layer electron-electron interactions and the role of plasmon excitations.

It is a pleasure to acknowledge many stimulating conversations with J.P. Eisenstein. This work was supported by National Science Foundation under Grant No. INT-9106888.

References

- [1] J.P. Eisenstein, L.N. Pfeiffer and K.W. West, Appl. Phys. Lett., 57, 1497 (1991)
- [2] Y. Katayama, D.C. Tsui, H.C. Manoharan and M. Shayegan, to be published
- [3] L. Zheng and A.H. MacDonald, Phys. Rev. B47, 10619 (1993)
- [4] S.Q. Murphy, J.P. Eisenstein, L.N. Pfeiffer, K.W. West, to be published
- [5] C. Hodges, H. Smith and J.W. Wilkins, Phys. Rev. B42, 302 (1971)
- [6] G.F. Giuliani and J.J. Quinn, Phys. Rev. B26, 4421 (1982)
- [7] H. Fukuyama and E. Abrahams, Phys. Rev. B27, 5976 (1983)
- [8] G.D. Mahan, *Many-Particle Physics* (Plenum, New York, 1981)
- [9] A.H. MacDonald and D.J.W. Geldart, Can. J. Phys., 60, 1016 (1982)

Magnetotransport of a low-disorder triple-layer electron system in perpendicular or parallel magnetic fields

T.S. Lay, S.P. Shukla, J. Jo, X. Ying, and M. Shayegan
Department of Electrical Engineering, Princeton University, Princeton, NJ 08544, USA

We report magnetotransport measurements on a coupled, triple-layer electron system subjected to either perpendicular (B_{\perp}) or parallel (B_{\parallel}) magnetic fields. The B_{\perp} data reveal an abrupt collapse of the $v = 1$ quantum Hall state as we increase the density in the side-wells. The results suggest the system makes a triple- to a double-layer transition at high B_{\perp} , which is driven by interlayer electron-electron interactions. In B_{\parallel} data, we observe two types of resistance oscillations as we decrease front-gate bias; one corresponds to the passage of the Fermi level through the partial energy gaps arising from the B_{\parallel} -induced level anticrossings, the other is due to the enhanced Coulomb scattering as the system makes layer transitions.

Coupled bilayer electron systems subjected to a perpendicular or parallel magnetic field (B_{\perp} or B_{\parallel}) exhibit intriguing physical phenomena arising from the Coulomb interaction and tunneling. Examples include, for B_{\perp} , an interaction-driven collapse of the quantum Hall effect (QHE) at odd -integer filling factor (v) [1-4] and the creation of new even-denominator fractional QHE states at $v = 1/2$ and $3/2$ [3,5,6]. For B_{\parallel} , new resistance oscillations arising from a partial energy gap induced by an anticrossing of the energy levels have been reported [7]. *Triple*-layer electron systems (TLEs) possessing interlayer and intralayer interactions are also expected to display rich transport properties [8]. The fabrication of high-quality TLEs is particularly challenging, however, and very little experimental work has been reported so far [9].

Here we report magnetotransport measurements on a low-disorder ($\mu \approx 7 \times 10^5 \text{ cm}^2/\text{Vs}$) TLE confined to three GaAs quantum wells which are separated by thin AlAs barriers (≈ 4 monolayers thick). We applied front- and back-gate biases (V_{FG} and V_{BG}) to change the layer densities and measured the resistance of the sample in the presence of either a B_{\perp} or B_{\parallel} .
 B_{\perp} data -- We measured the longitudinal and Hall resistances (R_{XX} and R_{XY}) as a function of B_{\perp} . At low B_{\perp} , R_{XX} exhibits Shubnikov-de Haas oscillations from which we obtain the electric subband densities (Fig. 1). The data are in excellent agreement with the results of our self-consistent calculations and enable us to determine the layer densities as a function of V_{FG} (Fig. 1). It is worth emphasizing that we find good agreement between the measured and calculated electrical subband densities only if we include the exchange-correlation energies; this we do via a local-density approximation. The exchange-correlation term is responsible for the significant charge transfer from top layer to the central layer when the top layer is depleted near $V_{\text{FG}} = -0.3 \text{ V}$. We use such data to determine the voltage pair (V_{BG} and V_{FG}) which result in a symmetric charge distribution in the TLE. As shown in Fig. 1, e.g., at $V_{\text{BG}} = 0$ and $V_{\text{FG}} = 0.030 \text{ V}$, the top and bottom layers have equal densities of $5.75 \times 10^{10} \text{ cm}^{-2}$ and the central layer has a density of $3.30 \times 10^{10} \text{ cm}^{-2}$ (total density $N_s = 14.8 \times 10^{10} \text{ cm}^{-2}$).

Figure 2 shows R_{XX} vs B_{\perp} data for two states of the TLE with symmetric charge distribution. The gate bias voltages ($V_{\text{BG}}, V_{\text{FG}}$) for the state with $N_s = 14.8 \times 10^{10} \text{ cm}^{-2}$ are $(0, 0.030 \text{ V})$ and for $N_s = 13.8 \times 10^{10} \text{ cm}^{-2}$ are $(-40 \text{ V}, -0.005 \text{ V})$. The data of Fig. 2 exhibit well-developed integer and fractional QHE attesting to the high quality of the sample. Of particular interest is the $v = 1$ state which is strong for $N_s = 13.8 \times 10^{10} \text{ cm}^{-2}$ but collapses when $N_s = 14.8 \times 10^{10} \text{ cm}^{-2}$. Note that this increase in N_s corresponds to adding only $\approx 5 \times 10^9 \text{ cm}^{-2}$ electrons to the side layers (the central layer density remains constant). At present we do not fully understand

either the origin of the $v = 1$ QHE in this system at $N_s = 13.8 \times 10^{10} \text{ cm}^{-2}$ or the reason for its collapse at slightly higher N_s . The striking resemblance of the data in Fig. 2 to the observations made on interacting *bilayer* electron systems [1-4] suggests that this TLE makes a transition to a bilayer system at high B_{\perp} . The fact that all other QHE states observed near $v = 1$ at both N_s have even numerators supports this conjecture. Future work to understand the origin of the $v = 1$ QHE in this system is planned.

B_{\parallel} data -- In a separate set of experiments on the same sample at fixed B_{\parallel} , we measured the capacitance (C) between the front-gate and the TLE, and also the magnetoresistance of the TLE as a function of V_{FG} . The details are reported elsewhere [10]; here we give a brief summary of some of the results. Figure 3(a) shows the step-like C-VFG data at $B_{\parallel} = 0 \text{ T}$ and $V_{\text{BG}} = 0 \text{ V}$. The capacitance drops observed with decreasing V_{FG} result from the depopulation of the layers which increases the distance from the front-gate to the nearest electron layer. The TLE makes a

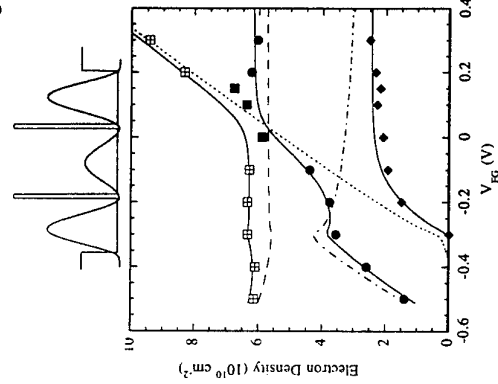


Fig. 1 The electric subband densities vs V_{FG} for the TLEs at $V_{\text{BG}} = 0$. The symbols represent the measured data from Fourier transforms of Shubnikov-de Haas oscillations and the solid curves show the self-consistent calculation results which are in excellent agreement with the measured data. Also, the calculated top, central, and bottom layer densities are shown by dotted, dot-dashed, and dashed curves, respectively. The exchange-induced charge transfer from the top to the central layer takes place near $V_{\text{FG}} = -0.3 \text{ V}$ as the top layer is depleted. Top figure shows the calculated conduction-band edge and charge distribution for $N_s = 14.8 \times 10^{10} \text{ cm}^{-2}$ ($V_{\text{FG}} = 0.03 \text{ V}$) when the top and bottom layers have equal densities.

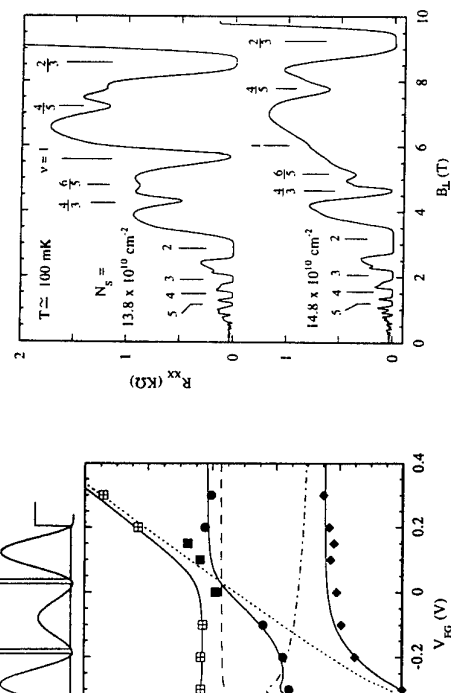


Fig. 2 R_{XX} vs perpendicular magnetic field data for the TLEs at two different total areal densities, N_s . For each N_s , the TLEs has a symmetric charge distribution but the ratio of side- to central-layer density is larger for higher N_s . At $N_s = 13.8 \times 10^{10} \text{ cm}^{-2}$, the $v = 1$ QHE is well developed. With increasing N_s to $14.8 \times 10^{10} \text{ cm}^{-2}$, the $v = 1$ QHE collapses while the fractional states at $v = 2/3, 4/5, 6/5$, and $4/3$ become stronger. Note that at both N_s , $v = 3$ QHE is present.

triple-to-double layer transition near $V_{FG} = -0.35$ V, and a double-to-single layer transition near $V_{FG} = -0.60$ V. These layer-depopulation V_{FG} values are consistent with the results of our subband density measurements, presented in Fig. 1.

Figure 3(b) shows the resistance (R) of the sample at $V_{BG} = 0$ as a function of V_{FG} for several values of B_{\parallel}/B_{\perp} applied in the plane of the sample and perpendicular to the current direction. For all values of B_{\parallel}/B_{\perp} , R increases with decreasing V_{FG} (density) but exhibits pronounced maxima and minima as the TLES undergoes transitions from a triple to a double and finally to a single layer system. The positions of the oscillations are consistent with the positions of steps in capacitance data (Fig. 3(a)) and with the results of Fig. 1. A similar oscillation has been observed at $B_{\parallel} = 0$ in double-layer systems with appropriate coupling, and has been attributed to the enhanced interlayer Coulomb scattering before the top layer is depleted [11]. In addition to these oscillations, at $B_{\parallel} = 2.8$ and 3.0 T we observe two additional oscillations in R as a function of V_{FG} , marked by arrows in Fig. 3(b), one in the triple-layer regime ($V_{FG} > -0.35$ V) and the other in the double-layer regime ($-0.60 < V_{FG} < -0.35$ V). These oscillations correspond to the B_{\parallel}/B_{\perp} induced level anticrossings and are observed in the intermediate field range $2.0 < B_{\parallel} < 3.5$ T.

To provide an analysis of the data, we first briefly review the explanation given in Ref. 7 for the resistance oscillation observed as a function of B_{\parallel} in bilayer electron systems. In a bilayer system at $B_{\parallel} = 0$, the energy vs in-plane wavevector (E_k) dispersions for the electron layers can be represented by two parabolae centered at the origin. Application of a B_{\parallel} in \mathbf{x} -direction displaces the crystal momenta \mathbf{k}_y of the two layers, and therefore their dispersion parabolae, by an amount $\Delta \mathbf{k}_y = d/l^2$, where d is the interlayer distance and $l = (\hbar/eB_{\parallel})^{1/2}$ is the magnetic length. If the two layers are coupled, a level anticrossing takes place at the intersection of the dispersion parabolae leading to a partial energy gap (for electron motion in the \mathbf{y} -direction). While the upper subband above this energy gap maintains a parabolic shape, the lower subband has a saddle point which results in a van Hove singularity in the density of states. With increasing B_{\parallel} , as the bottom of the upper subband moves above E_F , the density of states that contribute to scattering at the Fermi surface suddenly decreases, resulting in a minimum in R . As B_{\parallel} is further increased, the top (saddle point) of the lower subband rises above E_F . Since the density of states at the saddle point diverges and electrons have zero group velocity, a resistance maximum is expected as the saddle point passes through E_F .

The two B_{\parallel} -induced R oscillations marked by arrows in Fig. 3(b) can be explained from the evolution of the dispersion parabolae for our TLES with V_{FG} at fixed B_{\parallel} . As shown in Fig. 3(c), at $B_{\parallel} = 3$ T, for example, besides the layer-depopulation R oscillations at $V_{FG} = -0.36$ V and -0.62 V, we expect two other R oscillations near $V_{FG} = -0.21$ V and -0.53 V as the anticrossing energy gaps of the top-central and central-bottom layers are swept above E_F , respectively. We attribute the R minima marked by arrows in Fig. 3(b) to the E_F passing through the upper level of these two anticrossing gaps. In agreement with this explanation, we observe these minima at progressively larger V_{FG} as B_{\parallel} is increased from 2.0 to 3.5 T, in contrast to layer-depopulation R oscillations whose V_{FG} positions are independent of B_{\parallel} . We note, however, that the shape and position of these two oscillations are severely distorted because of the strongly increasing R background with decreasing V_{FG} and the R oscillations observed near the layer-depopulation V_{FG} . We have also measured R as a function of B_{\parallel} at fixed values of V_{FG} [10]; we observe R oscillations whose positions in B_{\parallel} we can quantitatively explain using dispersion parabolae similar to those in Fig. 3(c).

We thank S. Patilhar for help in self-consistent subband calculations and M.B. Santos in sample fabrication. This work was supported by the National Science Foundation.

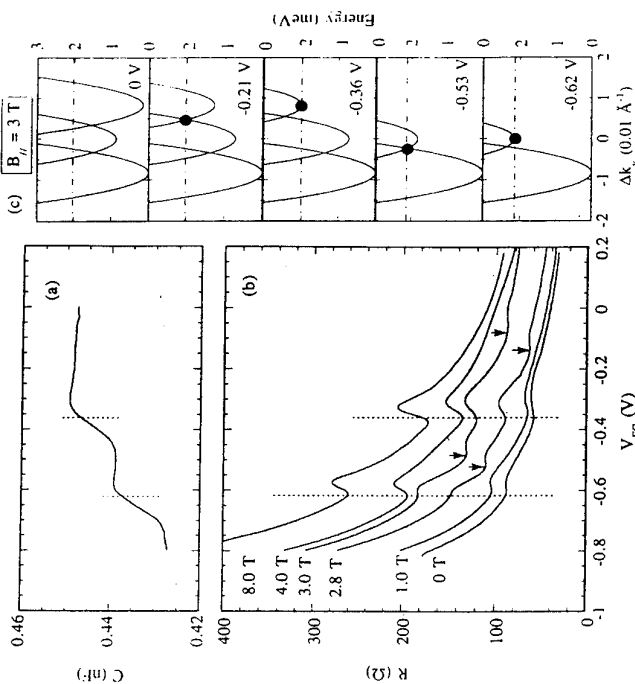


Fig. 3 (a) Capacitance-voltage (C - V_{FG}) taken at $V_{BG} = 0$ showing the depopulation of the TLES layers. (b) The resistance R vs V_{FG} data at different parallel magnetic fields showing minima in R at the same V_{FG} where the layer depopulation occurs. In an intermediate field range near 3 T, two additional oscillations (marked by arrows) are observed; these correspond to the level anticrossings. The R scale is for the 0 T and 1.0 T data. The 2.8 T data is shifted up by 10 Ω and the higher field traces by 40 Ω for clarity. (c) Evolution of the dispersion parabolae for the TLES in the case where a negative V_{FG} is applied at fixed $B_{\parallel} = 3$ T. The Fermi level is indicated by the dash-dotted line. The solid circles denote layer depopulations or level anticrossings near which we expect resistance oscillations.

1. G.S. Boebinger et al., Phys. Rev. **B45**, 11391 (1992).
2. Y.W. Suen et al., Phys. Rev. **B44**, 5947 (1991).
3. Y.W. Suen et al., Phys. Rev. Lett. **68**, 1379 (1992).
4. T.S. Lay et al., Phys. Rev. **B50**, 17725 (1994).
5. J.P. Eisenstein et al., Phys. Rev. Lett. **68**, 1383 (1992).
6. Y.W. Suen et al., Phys. Rev. Lett. **72**, 3405 (1994).
7. J.A. Simmons et al., Phys. Rev. Lett. **73**, 2256 (1994).
8. A.H. MacDonald, Surf. Sci. **229**, 1 (1990).
9. J. Jo et al., Phys. Rev. **B46**, 9776 (1992).
10. T.S. Lay et al., unpublished.
11. Y. Katayama et al., Surf. Sci. **305**, 405 (1994).

Collective Excitonic Phase with Spatial Order in Quantum Wires

A.L. Ivanov and H. Haug

Institut für Theoretische Physik, J.W. Goethe Universität Frankfurt
 Robert-Mayer-Str. 8, D-60054 Frankfurt/Main, Germany

A quantum exciton crystal (EC) as a ground-state of squeezed quasi-1D Wannier-Mott excitons (x 's) has been recently proposed and examined [1-2]. This quantum EC is due to the repulsive interaction between singlet x 's with fixed spin structure. Spatial squeezing of the x -system can be realized by the surface or interface potentials at the ends of a quasi-1D quantum wire (QWR). Thus, in comparison with a Wigner electron crystal, the quantum EC has a negative binding energy. A classical analog of this model has been realized for the laser-cooled Mg^+ ions stored in a closed 1D ring trap [3].

According to our estimates within a Heitler-London approximation, the quantum EC can exist for intermediate x densities ($1 < r_s < 5.5$). For these densities, the complete removal of the Fermi surfaces due to $e-h$ coupling to the x ground-state takes place. In Fig. 1 the x - x interaction potential is compared with the corresponding zero-point and thermal energies (the Mott criterion of stability). A phase diagram of the dense quasi-1D x -system with x - x repulsion is shown in Fig. 2. Here, the regions P and G refer to degenerate $e-h$ plasma and dense x -gas, respectively.

The expected short crystallization time (ps) makes an EC formation very likely even for the optically active x 's in $GaAs/Ga_xAl_{1-x}As$ quantum-well wires.

In this report we propose and analyze superradiance of the quantum EC. Due to the large zero-point x 's motion the onset of EC condensation should result in a drop of incoherent x 's luminescence along the wire axis. On the other hand, the quantum EC can be considered as a 1D lattice with the completely inverted two-level "atoms" in its sites. Such a system is able to emit a coherent, short, superradiant light pulse. In comparison with the conventional Dicke's theory, the specific features of the possible EC superradiance are connected both with a spatial translational symmetry of the EC and with a large degree of the hybridization of the x states due to longitudinal Coulombic interaction. In a sense, the quantum EC is a giant molecule which is able to annihilate radiatively at whole.

This work has been supported by the Volkswagen Stiftung.

- [1] A.L. Ivanov and H. Haug, Phys. Rev. Lett. 71, 3182 (1993).
- [2] A.L. Ivanov and H. Haug, Phys. Status Solidi (b) 188, in print (1995).
- [3] I. Waki, S. Kassner, G. Birk, and H. Walter, Phys. Rev. Lett. 68, 2007 (1992).

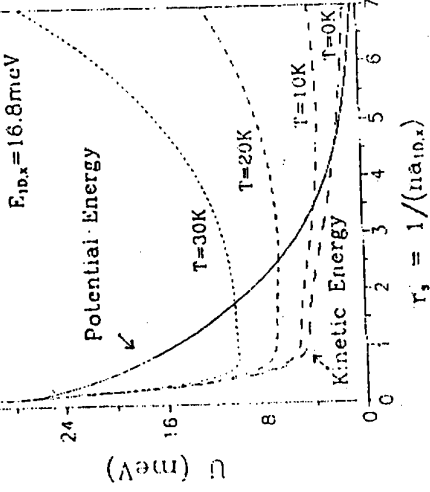


FIG. 1. Potential W_{x-x} (solid line), kinetic energy $\varepsilon_{kin} = \varepsilon_0 + \varepsilon_{th}$ at various temperatures (dashed lines) and zero-point energy ε_0 ($T = 0K$) per one x versus lattice parameter r_s . The x -interaction potential is compared with the corresponding zero-point and thermal energies (the dimensionless energy $|\epsilon| = \epsilon_0 / (E_{1D,x} = 16.8 \text{ meV})$

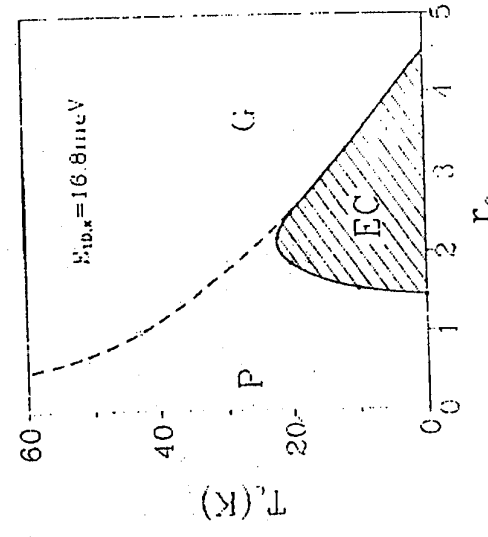


FIG. 2. Phase diagram for the quantum EC ($E_{1D,x} = 16.8 \text{ meV}$). Regions P and G refer to the degenerate $e-h$ plasma and dense x -gas, respectively. The bold square dots are determined by the condition $W_{x-x}(r_s) + \varepsilon_0(r_s) + \varepsilon_{th}(r_s) = E_{1D,x}$ for the family of the curves given in Fig. 1

PA31

MONDAY

Phase of magnetic oscillation of luminescence energy in asymmetric quantum wells

Takuma Tsuchiya, Shin'ichi Katayama, and Tsuneya Ando¹
*Japan Advanced Institute of Science and Technology (JAIST), 15 Asahidai, Tatsunokuchi,
 Ibaraki 980-42, Japan*

¹*Institute for Solid State Physics, University of Tokyo, Roppongi, Minato-ku, Tokyo 106, Japan*

The energy of photoluminescence due to recombination of a photo-generated free hole and a two-dimensional electron is calculated in an n-type GaAs/AlGaAs asymmetric single quantum well in high magnetic fields. The magnetic oscillation undergoes a phase change at a certain strength of the applied electric field because of the change in the strength of the electron-hole interaction.

I. INTRODUCTION

A two-dimensional (2D) electron gas in strong magnetic fields exhibits various interesting phenomena coming from its discrete density of states of Landau levels [1]. They can directly be observed, for example, by magneto-photoluminescence measurements [2,3]. In this paper, a magnetic field dependence of luminescence energy of an n-type GaAs/AlGaAs asymmetric quantum well is calculated and it is demonstrated that the phase of the magnetic oscillation can be controlled by changing electron-hole distance due to applied electric field.

Magnetic oscillation of the luminescence energy was observed experimentally [4] and has also been investigated theoretically [5–8]. In these theoretical calculations the oscillation in the self-energies of electrons and holes has been shown to be the origin of that of the luminescence energy. However, there remains a possibility that the observed energy oscillation comes from other mechanisms such as Landau level pinning at donor levels in the barrier layers [9], oscillation of the Hartree-potential by possible occupation of higher subbands, [10] or electron-phonon interactions [11].

Asymmetric n-type quantum wells [12] have the advantage that electron-hole distance and consequently the strength of the electron-hole interaction can be controlled by electric field applied perpendicular to the layer. In this paper, a magnetic field dependence of luminescence energy is calculated in such an asymmetric quantum well as a function of applied electric field. It is demonstrated that the phase of the oscillation due to self-energy effects changes at a certain crossover electric field. This phase change can be a critical test for identifying the clear mechanism of the magnetic oscillation of luminescence energy observed experimentally.

II. METHOD OF CALCULATION

Figure 1 shows the schematic band diagram of an n-type single quantum well with a front-back-gate electrodes made of transparent materials. Donors are modulation-doped in the AlGaAs barriers. The potential energy is asymmetric, because of external electric field applied by the gate electrodes. A photo-generated hole and 2D electrons move to opposite sides to each other in the well.

The luminescence energy is given by the energy difference between the initial and final states. In the initial state, we have a photo-generated free hole in the ground Landau subband. The energy is given by

$$E_i = E_g - E_{\text{band}} + E_{\text{subband}}^h + \frac{1}{2} E_{\text{cy}}^h + \Sigma^h, \quad (1)$$

where E_g is the band-gap energy of GaAs, E_{band} is the energy of the bottom of the conduction band of GaAs at the right-side GaAs/AlGaAs interface measured from that at the left-side, E_{subband}^h is the energy of the hole in the ground subband, E_{cy}^h is the cyclotron energy of the hole, and Σ^h is its self-energy. In the final state, the hole and a 2D electron in the ground Landau subband are annihilated by recombination and the energy becomes

$$E_f = -(E_{\text{subband}}^e + \frac{1}{2} E_{\text{cy}}^e + \Sigma^e), \quad (2)$$

where E_{subband}^e is the energy of the electron in the ground subband, E_{cy}^e is the cyclotron energy of the recombining electron, and Σ^e is its self-energy.

The electronic state and the potential are calculated self-consistently and the hole state is calculated from the self-consistent potential. We assume that the wave functions are completely confined in the GaAs layer. This assumption is expected to be appropriate for wells wider than 100 Å. The electron density is assumed to be independent of the applied electric field.

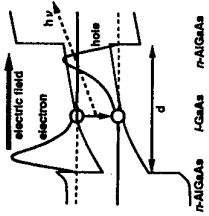
In the present calculation, we employ the same method developed for symmetric quantum wells [5]. For broadening of Landau levels, we employ the self-consistent Born approximation [13] and the width of the Landau levels is assumed to be 1 meV. For the dynamical dielectric function of 2D electron gas, we employ the plasmon-pole approximation, which works quite well in the present system in the absence of magnetic field. Spin splitting is ignored, because the g factor is small in GaAs. In the following example, we assume that the electron sheet-density is $2.2 \times 10^{11} \text{ cm}^{-2}$, the effective masses of electrons and holes are $0.067 m_0$ and $0.4 m_0$ with m_0 the electron rest mass, and the static dielectric constant is 12.53.

III. NUMERICAL RESULTS

Figure 2 shows magnetic-field dependence of luminescence energy of the quantum well with width $d = 300$ Å for applied electric field $E = 0, 1.5 \times 10^4$, and $3 \times 10^4 \text{ V/cm}$. These field strength is usual in this type of structure [14]. The luminescence energy decreases with increasing E , because the difference between ground-subband energies of the electron and hole decreases. Since the cyclotron energies of electrons and holes increase linearly, the luminescence energy increases with the magnetic field. When the filling factor of Landau levels, ν , is an even integer, however, the energy shows an anomalous shift from the linear magnetic field dependence. Furthermore, it is found that the direction of the shift depends on E , i.e., the energy shows blueshift for $E = 0$, but shows redshift for $E = 1.5 \times 10^4$ and $3 \times 10^4 \text{ V/cm}$.

The energy shift is the result of oscillation of self-energies of the recombining 2D electron and free hole. In Fig. 3, Σ^e and Σ^h for $E = 0$ and $3 \times 10^4 \text{ V/cm}$ are shown. At even ν , Σ^e shows redshift and Σ^h shows blueshift. This self-energy shift is due to the oscillation of the screening strength which comes from the discrete density of states of Landau levels of 2D electron gas. Here, Σ^h consists only of the Coulomb-hole term, which comes from the interaction between the free hole and the 2D screening charge induced by the hole itself. On the contrary, Σ^e consists of not only the Coulomb-hole but the screened exchange term and

FIG. 1. Schematic band diagram of an n-type asymmetric GaAs/AlGaAs single quantum well [2] with electric field applied by gate electrodes.



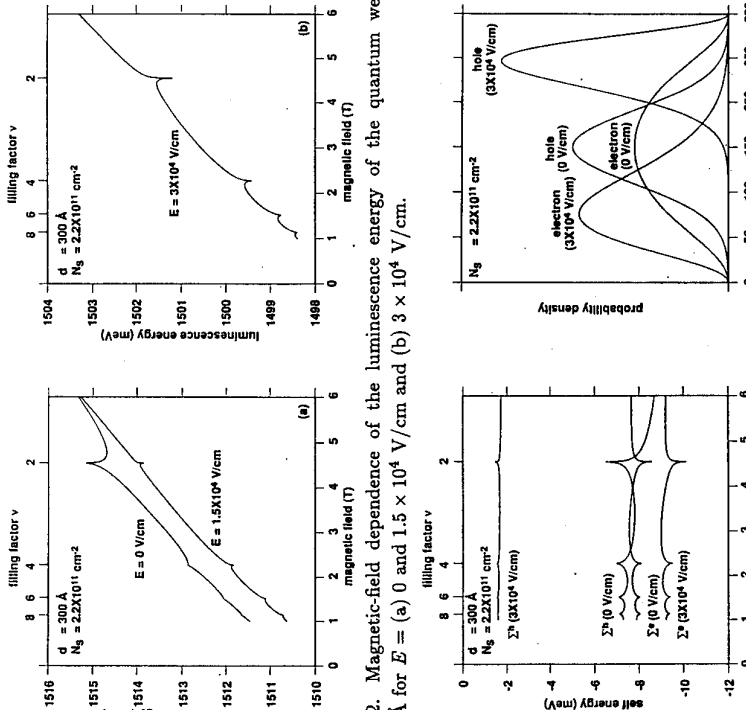


FIG. 2. Magnetic-field dependence of the luminescence energy of the quantum well with $d = 300 \text{ \AA}$ for $E =$ (a) 0 and $1.5 \times 10^4 \text{ V/cm}$ and (b) $3 \times 10^4 \text{ V/cm}$.

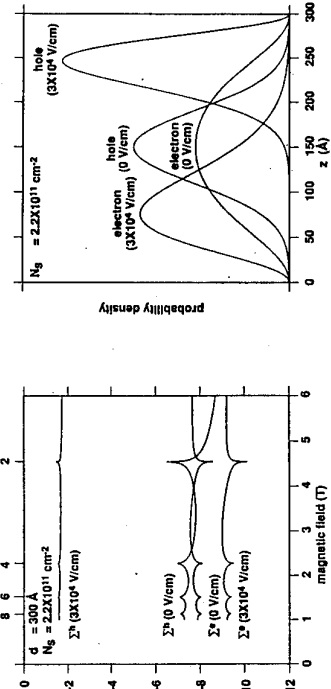


FIG. 3. Magnetic-field dependence of self-energy of an electron, Σ_e , and a hole, Σ_h , for $E = 0$ and $3 \times 10^4 \text{ V/cm}$.

FIG. 4. Probability density of electrons and holes in the ground subband for $E = 0$ and $3 \times 10^4 \text{ V/cm}$.

The oscillation amplitude of the latter is dominant. This explains the difference of the direction of the shift between Σ_e and Σ_h [5]. For $E = 0$, the amplitude of the oscillation of Σ_h is larger than that of Σ_e . On the other hand, for $E = 3 \times 10^4 \text{ V/cm}$, $|\Sigma_h|$ and its oscillation amplitude are much smaller than those at $E = 0$ and Σ_e is dominant. This is because the screening strength of the 2D electron gas for the photo-generated free holes decreases as E increases. In Fig. 4, we show probability density of the electrons and the holes in the ground subbands for $E = 0$ and $3 \times 10^4 \text{ V/cm}$. For $E = 0$, the peak positions of the density for electrons and holes are both at the center of the well and the screening strength of the 2D electron gas for the electrons themselves and that for the holes are almost the same. On the other hand, for $E = 3 \times 10^4 \text{ V/cm}$, the distance between the peak positions is about 200 \AA and the screening strength for the holes are much smaller than that for the electrons.

The phase change is the characteristic of the oscillation of the luminescence energy comes from that of the self-energies. The phase change of the same origin is also predicted in an n -type one-side-doped quantum well [15]. In this structure, the phase can be controlled by the well width. Goldberg *et al.* observed a well-width dependence of the phase in a one-side-doped well at $\nu = 1$, using polarized light measurement [12]. Though the result of our calculation seems to be consistent with that of their experiment, it is difficult to compare these results directly. This is because the spin splitting seems to shift the luminescence energy at $\nu = 1$ in their experiment.

IV. CONCLUSIONS

We have calculated magnetic-field dependence of the luminescence energy due to recombination of a two-dimensional electron and a photo-generated free hole for n -type GaAs/AlGaAs asymmetric single quantum wells, taking into account the self-energy of the electron and hole. We found that the direction of the luminescence-energy shift at even integer filling-factor of Landau levels depends on the distance between the 2D electron gas and hole. This dependence gives a method to identify the origin of the observed luminescence energy oscillation.

ACKNOWLEDGMENTS

This work is supported in part by Grant-in-Aid for Scientific Research from the Ministry of Education, Science and Culture, Japan.

- [1] See for example, T. Ando: *High Magnetic Fields in Semiconductor Physics II*, ed. G. Landwehr (Springer, Berlin, 1989) p. 164.
- [2] D. Heiman: *Semiconductors and Semimetals*, eds. D.G. Seiler and C.L. Little (Academic Press, 1982) Vol. 36, Chap. 1, p. 1.
- [3] A. Nurmiiko and A. Pinczuk: Phys. Today **46** (6) (1993) 24-32.
- [4] M. C. Smith, A. Petrou, C. H. Perry, J. M. Worlock, and R. L. Aggarwal: *Proc. 17th Int. Conf. Physics of Semiconductors, San Francisco*, 1984 (Springer, New York, 1985) p. 547.
- [5] S. Katayama and T. Ando: Solid State Commun. **70** (1989) 97.
- [6] T. Uenoyama and L. J. Sham: Phys. Rev. B **39** (1989) 11044.
- [7] S. Katayama and T. Ando: Physica B **184** (1993) 115.
- [8] T. Tsuchiya, K. Katayama, and T. Ando: *Proc. Int. Conf. Optical Properties of Nanostructures, Sendai*, 1994, Jpn. J. Appl. Phys. **34** (1995) Suppl. 34-1, p. 240.
- [9] See for example, G.A. Baraff and D.C. Tsui: Phys. Rev. B **24** (1981) 2274.
- [10] D.G. Hayes, M.S. Shorick, D.M. Whittaker, P.E. Simmonds, L.I. Taylor, and S.J. Bass: Phys. Rev. B **44** (1991) 3436.
- [11] W. Chen, M. Fritzze, W. Wailecki, A. V. Nurmikko, D. Ackley, J. M. Hong and L. L. Chang: Phys. Rev. B **45** (1992) 8464.
- [12] B. B. Goldberg, D. Heiman, A. Pinczuk, L. Pfeiffer, and K. West: Phys. Rev. Lett. **65** (1990) 641.
- [13] T. Ando and Y. Uemura: J. Phys. Soc. Jpn. **36** (1974) 959.
- [14] K. Hirakawa, H. Sakaki, and J. Yoshino: Phys. Rev. Lett. **54** (1985) 1279.
- [15] T. Tsuchiya, K. Katayama, and T. Ando: *Proc. Int. Workshop Mesoscopic Physics and Electronics, Tokyo*, 1995, Jpn. J. Appl. Phys. Suppl. (in press).

Strain-induced suppression of spin splitting in asymmetric p-type quantum wells

O. Mauritz and U. Ekenberg

Department of Physics
Royal Institute of Technology, S-100 44 Stockholm, Sweden

Abstract

The strain dependence of the spin splitting of hole subbands in an asymmetric quantum well is investigated. It is found that the spin splitting can be suppressed both by compressive and tensile strain. The maximum spin splitting occurs when the tensile strain is about one third of that required to make the two uppermost subbands coincide at $k_{\parallel} = 0$.

1. Introduction

It is well-known that strain in quantum wells may decrease the parallel mass of the uppermost heavy-hole subband and this has been found to decrease the threshold current in lasers [1]. Here one important mechanism is that the increased energy separation between heavy- and light-hole subbands decreases the interaction between them. This effect can be enhanced further by spatial separation of heavy and light holes [2].

In this paper we examine to which extent one can influence also the subband spin splitting by strain. In a symmetric potential each hole subband has a two-fold spin degeneracy. If the potential becomes asymmetric, as is the case for a modulation-doped interface, this degeneracy is lifted for finite values of k_{\parallel} , the wave vector parallel to the interfaces. This theoretical prediction has been verified experimentally [3]. A similar potential appears in a quantum well intentionally doped on one side only. In this case we have the possibility of introducing strain across a layer of finite width without causing dislocations.

2. Method

The valence band structure is calculated self-consistently in the multiband envelope-function approximation using the Luttinger-Kohn 6×6 Hamiltonian [4]. It incorporates the heavy-hole (HH), light-hole (LH) and spin-orbit split-off (SO) band. Even if we are interested in subband energies which are small compared to the spin-orbit splitting Δ it is important to take the SO band into account because of its strain-induced coupling with the LH band. The 6×6 matrix can be decoupled into two 3×3 matrices, which can be written [5]

$$H = \frac{\hbar^2}{m_0} \begin{pmatrix} A_+ + S & C \mp iB & \sqrt{2}C \pm iB/\sqrt{2} \\ C \pm iB & A_- - S & F + \sqrt{2}S \mp i\sqrt{\frac{3}{2}}B \\ \sqrt{2}C \mp iB/\sqrt{2} & F + \sqrt{2}S \pm i\sqrt{\frac{3}{2}}B & D \end{pmatrix}$$

where

$$\begin{aligned} A_{\pm} &= -\frac{i}{2}(\gamma_1 \mp 2\gamma_2)k_z^2 - \frac{i}{2}(\gamma_1 \pm \gamma_2)k_{\parallel}^2 \\ B &= \sqrt{3}\gamma_3 k_{\parallel} k_z \end{aligned}$$

$$\begin{aligned} C &= (\sqrt{3}/2)k_{\parallel}^2(\gamma_2^2 \cos^2 2\theta + \gamma_3^2 \sin^2 2\theta)^{1/2} \\ D &= -\Delta - \frac{i}{2}\gamma_1(k_{\parallel}^2 + k_z^2) \\ F &= \gamma_2(\sqrt{2}k_z^2 - k_{\parallel}^2)/\sqrt{2} \end{aligned}$$

γ_1, γ_2 and γ_3 are the Luttinger parameters, θ is the angle between $\mathbf{k}_{\parallel} = (k_x, k_y)$ and the (100)-direction and Δ is the spin-orbit splitting. The parameter $S = b(|\epsilon| - \epsilon_{\perp})$ gives the upward shift of the heavy-hole band edge due to strain. Here ϵ_{\parallel} is the strain parallel to the layers, which is determined by the lattice constant of the substrate, ϵ_{\perp} is the strain along the growth direction and b is the deformation potential. We use the axial approximation which neglects the θ -dependence of the term C :

$$C \approx (\sqrt{3}/4)k_{\parallel}^2(\gamma_2 + \gamma_3)$$

The subband dispersions $E(k_{\parallel})$ are calculated by means of a self-consistent variational method described elsewhere [6]. The upper and lower signs in the matrix give different solutions (denoted \uparrow and \downarrow) for $k_{\parallel} \neq 0$ in the case of an asymmetric potential. The spin splitting discussed below is the energy separation between these solutions. It often has a maximum near $k_{\parallel} = 1.6 \cdot 10^6 \text{ cm}^{-1}$ and therefore we have calculated the spin splitting at this wave vector in this paper.

3. Results

We have studied a quantum well structure with a 200 Å wide $\text{Ga}_{0.75}\text{In}_{0.25}\text{As}$ well and lattice-matched $\text{Ga}_{0.618}\text{In}_{0.382}\text{P}_{0.271}\text{As}_{0.729}$ barriers. Asymmetry is achieved by letting one barrier have intentional p-type doping ($N_a = 3 \cdot 10^{18} \text{ cm}^{-3}$) while the other barrier has an n-type background ($N_d = 10^{15} \text{ cm}^{-3}$). By varying the composition of the barriers we could vary the strain in the quantum well but at the same time the barrier heights would change. In order to study the "pure" effect of strain in the quantum well we instead consider thin barriers lattice-matched to the quantum well with the p-type barrier grown on a lattice-mismatched $\text{Ga}_x\text{In}_{1-x}\text{P}_y\text{As}_{1-y}$ substrate with a combination of x and y such that the valence band edge is the same in barrier and substrate. By varying the composition of the substrate under the condition of essentially constant valence band edge (to avoid complications with the band bending) the lattice mismatch and hence the strain of both the quantum well and the thin barriers is tuned. The input parameters including interpolation procedures for the band edges are taken from ref. [7]. The Luttinger parameters for the alloys are obtained from linear approximation of appropriate effective masses.

In figure 1 we display the subband structure in the case where the spin splitting has a maximum. The spin splittings at $k_{\parallel} = 1.6 \cdot 10^6 \text{ cm}^{-1}$ for the two highest subbands are given in figure 2. For $S < -5 \text{ meV}$ the highest subband is light-hole type, otherwise heavy-hole type. ($S < 0$ corresponds to biaxial tension). Let's denote the highest hole subband $H1$, the next one $H2$ and so on without considering whether they are heavy-hole type or light-hole type. It is worth noting that the spin splittings of $H1, H2$, etc. are continuous even at the points where they change type, i.e. at the points where two subbands coincide at $k_{\parallel} = 0$. This continuous transition is demonstrated in figure 3, where the behaviour of the

subband structure in this region is shown. The spin splitting at $k_{\parallel} = 1.6 \cdot 10^6 \text{ cm}^{-1}$ is not much affected by the subband interchange at $k_{\parallel} = 0$. For large values of both compressive and biaxial strain ($\approx 20 \text{ meV}$) the spin splitting has been almost completely suppressed. When the strain is increased the heavy- and light-hole subbands become separated and their interaction is reduced.

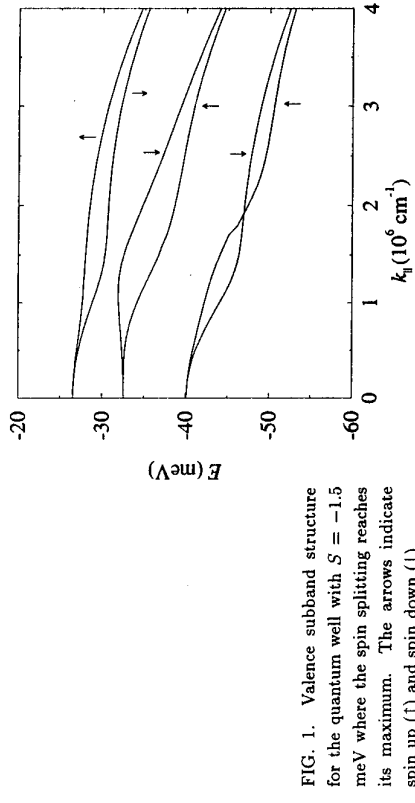


FIG. 1. Valence subband structure for the quantum well with $S = -1.5 \text{ meV}$ where the spin splitting reaches its maximum. The arrows indicate spin up (↑) and spin down (↓).

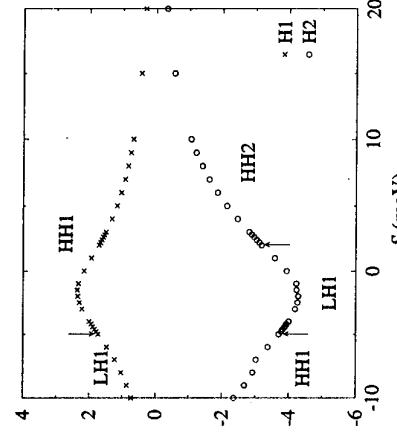


FIG. 2. Spin splitting for the two highest valence subbands $H1$ and $H2$ at $k_{\parallel} = 1.6 \cdot 10^6 \text{ cm}^{-1}$. $\Delta(E)$ means $E(↑) - E(↓)$. The arrows indicate the transition from heavy-hole type to light-hole type of the subbands at $k_{\parallel} = 0$.

However, it is interesting to note that the subband separation is not the only factor determining the spin splittings. For example, it is seen that the maximum splitting for the two highest subbands occurs at $S \approx -1.5 \text{ meV}$ and not at $S = -5 \text{ meV}$, when the energy separation of $HH1$ and $LH1$ vanishes. One must invoke matrix element effects to explain

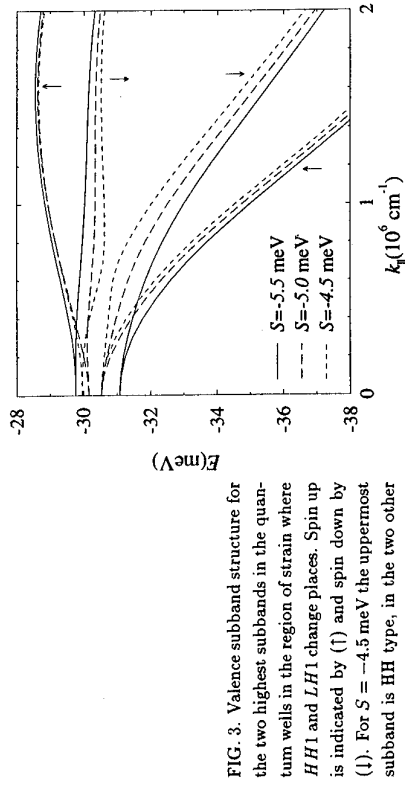


FIG. 3. Valence subband structure for the two highest subbands in the quantum wells in the region of strain where $HH1$ and $LH1$ change places. Spin up is indicated by (↑) and spin down by (↓). For $S = -4.5 \text{ meV}$ the uppermost subband is HH type, in the two other cases it is LH type.

4. Conclusion

It has been shown that the spin splitting of hole subbands which occurs in asymmetric quantum wells can be strongly modified by strain. For strong compressive or tensile strain when the uppermost subband is well separated from the other subbands the spin splitting is suppressed. The spin splitting is found to be continuous for the uppermost hole subband even when its character at $k_{\parallel} = 0$ changes from HH to LH type for tensile strain corresponding to $S = -5 \text{ meV}$. The maximal spin splitting is found for $S = -1.5 \text{ meV}$.

References

- [1] S. W. Corzine, R.-H. Yan, and L. A. Coldren in *Quantum Well Lasers*, Ed. P. S. Zory, Jr (Academic Press, San Diego, 1991) p 72.
- [2] A. Ghiti and U. Ekenberg, *Semicond. Sci. Technol.* **9** (1994) 1575.
- [3] See, e.g., J. P. Eisenstein, H. L. Störmer, V. Narayanamurti, A. C. Gossard and W. Wiegmann, *Phys. Rev. Lett.* **53** (1984) 2579.
- [4] J. M. Luttinger and W. Kohn, *Phys. Rev.* **97** (1955) 869.
- [5] U. Ekenberg, W. Batty and E. P. O'Reilly, *J. de Physique* **48** (1987) C5-553.
- [6] M. Altarelli, *Phys. Rev. B* **28** (1983) 842.
- [7] M. P. C. M. Krijn, *Semicond. Sci. Technol.* **6** (1991) 27.

Dependence of the optical absorption on the in-plane light polarization of QW's grown on low symmetry (011), (012), (112) and (113) surfaces

J. Los and A. Fasolino

Istituto Nazionale Fisica della Materia, Dipartimento di Fisica, Università di Modena, Via Campi 213/A, I-41100 Modena, Italy

We show, on the basis of $8 \times 8 \mathbf{k} \cdot \mathbf{p}$ electronic structure calculations, that, in contrast to the well known properties of high symmetry (001) Quantum Wells, the optical absorption for samples grown along low symmetry directions, such as the (011), (012), (112) and (113), strongly depend on the direction of the polarization of the light in the interface plane. No polarization dependence is instead found for circularly polarized light. Calculations performed for GaAs/AlGaAs and InGaAs/AlGaAs Quantum Wells show that this effect is largest for the (011) direction and is strongly enhanced in presence of strain.

We present a theoretical study of the electronic band structure and optical properties of semiconductor structures grown on novel index planes. The interest of non-(001) oriented semiconductor structures is manifold, concerning growth and impurities incorporation [1], self-organized growth [2], electronic properties [3,4] and lasing performances [4]. It is therefore desirable to identify fingerprints of successful growth. In the following, we show that growth on low symmetry planes results in a peculiar anisotropic dependence of the matrix elements for optical transitions on the in-plane light polarization.

We have developed a numerical real space method [5] for solving the $8 \times 8 \mathbf{k} \cdot \mathbf{p}$ hamiltonian [6] for any growth direction including strain and piezoelectric effects. We refer to Ref. 5 for details on the method of calculation. Here, it is important to notice that for a growth direction (hkl) we use the following spatial basis functions:

$$\begin{aligned} |X'> &= c_1 |h|X> + h|kY> - (h^2 + k^2)|Z> \\ |Y'> &= c_2 [-k|X> + h|Y> \\ |Z'> &= c_3 |h|X> + k|Y> + l|Z> \end{aligned} \quad (1)$$

where $|X>$, $|Y>$ and $|Z>$ are the three $L=1$ basisfunctions oriented along the edges of the simple cube. With the appropriate constants c_1 , c_2 and c_3 the rotated basisfunction (1) are orthonormal, with $|Z'>$ oriented along the (hkl) growth direction. With the basisfunctions (1) plus spin we can construct, for all growth directions, generalized heavy (hh), light (lh) and split-off (so) hole states in analogy to the (001) case by taking the quantization axis of J_z along the growth direction. Obviously, these generalized states have exactly the same selection rules for light incoming parallel or perpendicular to the interfaces as in the (001) case. The only difference is that, except for the (001) and (111) directions, the generalized hh and lh states are not exactly decoupled at $k_{\parallel} = 0$. In the following, we show that this residual coupling at $k_{\parallel} = 0$ leads to a strong dependence of the matrix elements for optical transitions on the linear polarization of the light in the interface plane. This effect is further enhanced in presence of strain due to the strain-induced coupling with the so band and its

observation would unambiguously establish the crystalline quality of the samples and the achievement of the desired crystallographic orientation.

In Figs. 1a and 1c, we show the calculated valence band structure of a 60 Å GaAs/Ga_{0.4}Al_{0.6}As unstrained Quantum Well (QW) grown along the (011) and (113) directions respectively. The marked differences in confinement energies, effective masses and warping make clear the enormous possibilities offered by growth on novel index planes for valence band engineering. Also, the number and ordering of confined hh and lh states varies with growth direction. It should be kept in mind, however, that even at $k_{\parallel} = 0$ all states have a mixed hh-lh character. In Figs. 1b and 1d, we show the calculated subbands for a strained 60 Å In_{0.25}Ga_{0.75}As/Ga_{0.4}Al_{0.6}As QW grown along (011) and (113) respectively. In both cases, the main effect of compressive strain is to shift the lh states at lower energy. As a consequence, the hh states become more parabolic, but this effect is much larger for (011) growth. It is also remarkable that, in the (011) case, successive hh states are almost equidistant, as if resulting from a parabolic potential. Besides, the built-in piezoelectric field removes the spin degeneracy at $k_{\parallel} \neq 0$ in the (113) case.

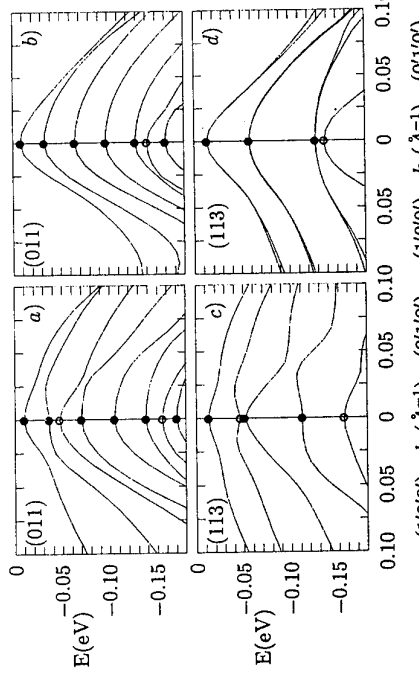


Fig. 1 : Hole-dispersion along the directions (1'0'0') and (0'1'0') with respect to the rotated basis for an unstrained 60 Å GaAs-Al_{0.4}Ga_{0.6}As-QW (a and c) and for a compressively strained 60 Å In_{0.25}Ga_{0.75}As-Al_{0.4}Ga_{0.6}As-QW (b and d) grown along the (011) (a and b) and (113) (c and d) directions. Closed and open dots indicate the hh and the lh subbands respectively.

The effect of the growth axis is however most remarkable in what concerns the optical properties. In Fig. 2 we show the calculated matrix element M for optical transitions from the first confined hh₁ and lh₁ states to the first conduction subband e₁ as a function of k_{\parallel} for strained and unstrained samples grown along the (001), (113) and (011) directions. The calculations are done, considering light impinging on the samples along the growth axis

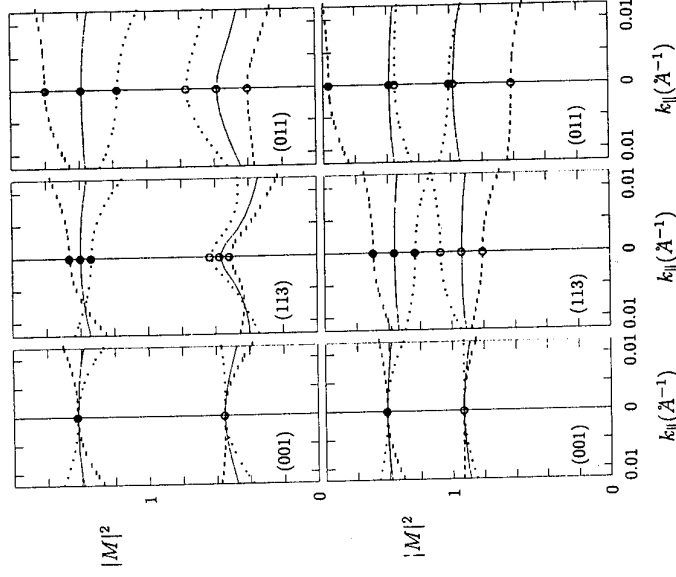


Fig. 2 : Squared absolute value of the dipolar matrix element M for circularly (solid line) and linearly polarised light (dashed line and dotted lines for polarization in the x' - and y' -directions respectively), incoming perpendicular to the layers, for the hh_1-e_1 (closed dots) and hh_1-e_1 transitions (open dots) as function of k_{\parallel} along the same in-plane directions and for the same structures as in Fig. 1. The upper figures are for the unstrained case and the lower figures for the strained case. The results for the usual (011) case are shown for comparison.

with the two helicities of circular polarization or with light linearly polarized along the two X' and Y' orthogonal in-plane directions. The dependence on the direction of the linear light polarization is particularly strong for the (011) case but is certainly not negligible also for the (113) case. We have calculated M for a range of k_{\parallel} vectors in the interface planes comparable to $1/a_b$, where a_b is the excitonic Bohr radius in GaAs. Since, at least for the (011) case, the difference persists over the whole range of k_{\parallel} , the above dependence of M on the linear light polarization should not be removed by excitonic effects, not considered here. It is important to notice that M is instead the same for the two helicities of circular polarization. The anisotropy of M is strongly enhanced in presence of strain, as shown in the bottom panels of Fig. 3 but remain largest for (011) growth. Results for the usual (011)

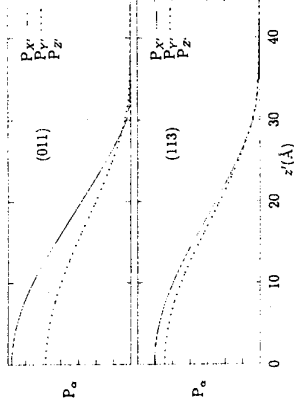


Fig. 3 : Squared absolute values of the envelope function components for the hh_1 eigenstate at $k_{\parallel} = 0$. Writing the eigenstate as $|\psi_{hh_1}\rangle = \sum_{\alpha} F_{\alpha}(z')| \alpha \sigma \rangle$ where $\alpha = S', X', Y', Z'$ and $\sigma = \uparrow, \downarrow$, $P_{\alpha}(z')$ is defined as $\sum_{\sigma} |F_{\alpha\sigma}(z')|^2$.

case are shown for comparison. It is, however, also interesting to notice that, in the case of (001) growth, the strain-induced mixing of lh states to so states makes that the approximate 1:3 ratio for the strength of the transition from hh and lh states is strongly modified. In order to find a rationale for the above peculiar dependence on the direction of the linear light polarization in the interface plane, we show in Fig. 3 the composition of the envelope function of the first confined hh state $|\psi_{hh_1}\rangle$ in terms of the rotated $|S\rangle$, $|X'\rangle$, $|Y'\rangle$ and $|Z'\rangle$ basisfunctions as a function of the coordinate z' along the growth direction. It can be seen that the $|X'\rangle$ and $|Y'\rangle$ components are different, in contrast to the (001) case and that the difference is largest for the (011) case, which justifies the strongest anisotropy of $|M|^2$ in the latter case.

In summary, we have shown that strong anisotropies of absorption of light linearly polarized in the interface plane should result from the lower spatial symmetry in QW's grown along directions other than (001) and (111). This prediction awaits experimental confirmation.

Acknowledgments: This work has been carried out within the European Community HC&M network for High Pressure Studies of Semiconductors and Semiconductor Structures ER-BCHRXCT 930321

- [1] M. Henini, P.J. Rodgers, P.A. Crump, B.I. Gallagher, G. Hill, Appl. Phys. Lett. **65** 2054 (1994)
- [2] R. Notzel, N.N. Ledentsov, L. Daweritz and K. Ploog, Phys. Rev. **B45**, 3507 (1992)
- [3] J.-B. Xia, Phys. Rev. **B43**, 9856 (1991).
- [4] A. T. Meny, Super. Microstr. **11**, 387 (1992)
- [5] J. Los, A. Catellani, A. Fasolino in preparation
- [6] R. Eppenga, M.F.H. Schuurmans, and S. Colak, Phys. Rev. **B36**, 1554 (1987)

Magnetooscillations in the electroluminescence intensity of excited subbands in resonantly coupled superlattices

D. Bertram^a, H.T. Grahn^b, O. Kuhn^c, D.K. Maude^c, J.C. Porta^c, K. Ploog^a, and K. von Klitzing^a

^aMax-Planck-Institut für Festkörperforschung, Heisenbergstraße 1, D-70569 Stuttgart, Germany

^bPaul-Drude-Institut für Festkörperelektronik, Hausvogteiplatz 5-7, D-10117 Berlin, Germany

^cCNRS-LCMI, Rue de martyrs 9, F-38042 Grenoble, France

Abstract

We have measured the electroluminescence (EL) from excited conduction subband populations in resonantly coupled GaAs/AlAs superlattices in magnetic fields up to 23 T perpendicular to the layers. Strong oscillations are observed in the EL intensity of the second electronic subband with increasing magnetic field exhibiting two different periods in 1/B for a subband spacing below the optical phonon energy. The EL intensity of the third electronic subband with a separation above the optical phonon energy only shows a distinct minimum with increasing magnetic field, which coincides with a maximum in the measured current.

There has been a large number of proposals concerning superlattices (SL) as a source of far-infrared radiation created by radiative transitions from excited states which are populated by resonant tunneling.[1-3] Recently Faist et al.[4] demonstrated the first infrared laser based on such a type of device. This discovery increased the interest in the properties of SL based devices.[5] One particular feature is the relaxation mechanism of excited state populations created by resonant tunneling under an externally applied electric field.

In order to investigate the interplay between carrier transport by resonant tunneling and different relaxation processes, we recorded the intensity variation of the interband transitions of excited conduction subband populations of a SL in magnetic fields up to 23 T. A very different behavior of the magnetic field dependence of the electroluminescence (EL) intensity is observed, when the subband spacing is varied from below the optical phonon energy ($\hbar\omega_{LO}$) to a value above $\hbar\omega_{LO}$. The sample used in our experiment is a GaAs/AlAs SL consisting of 40 periods of 21 nm GaAs and 2.2 nm AlAs. The SL represents the intrinsic region of a p-n diode with contact-layers consisting of $Al_0.9Ga_0.1As$, which are transparent for the investigated optical transitions of the SL. The front side of the wafer is etched into mesas of 120 or 200 μm diameter. Ohmic contacts are evaporated on the substrate side as well as on the top of the mesa providing electrical access to the structure. The sample is mounted in a continuous helium flow cryostat which is inserted into the bore of a resistive magnet delivering field strengths up to 23 T. Optical access to the structures is provided by an optical fiber which is attached to the monochromator. Carriers, i.e., electrons and holes, are injected electrically into the SL region of the p-n diode by applying a fixed dc forward bias to the structure. The EL originating from the recombination of electrons and holes in the SL is then recorded with an optical multichannel analyzer as a function of the applied magnetic field.

The parameters of the SL are chosen in such a way that the calculated spacing of the quantum well ground state C1 and the first excited conduction subband C2 at zero electric field

is 31 meV, which is below $\hbar\omega_{LO}$ in GaAs (36.4 meV). Through this design a fast relaxation of carriers from C2 into C1 via optical phonon emission is prevented. The spacing of C3 and C2 as well as C3 and C1 is, however, with 52 and 83 meV, respectively, larger than $\hbar\omega_{LO}$. Therefore, it is expected that the relaxation of carriers from the C3 conduction subband is dominated by energy loss via polar LO phonon emission.

The electric field dependence of the EL intensity of the different SL transitions CnHm, which denotes the recombination of electrons in the n-th subband with heavy holes in the m-th subband, have been published in Ref. [6,7]. In this paper we will focus on the magnetic field dependence of the C2H1 and C3H1 transitions at the respective electric field strength for resonant injection. The direction of the applied magnetic field is chosen to be parallel to the current, i.e., perpendicular to the layers. Fig. 1 schematically depicts part of the band-edge profile of the SL under C1 \rightarrow C2 resonance condition. Landau levels emerging from the confined states in the conduction and valence band are also shown. The investigated recombination transitions are indicated.

First, we will consider the C2H1 transition. An isointensity plot of the EL intensity versus magnetic field is shown in Fig. 2. The applied voltage was set to 3.7 V corresponding to the C1 \rightarrow C2 resonance condition at 0 T. The observed transition energy of the C2H1 recombination at 0 T is marked by an arrow. Oscillations in the EL intensity of C2H1 with increasing field are clearly observed. Furthermore, recombination from Landau levels of the C1H1 transition is also detected (lighter grey regions). These transitions shift upwards in energy until they cross the C2H1 line. At higher magnetic fields, i.e., above about 16 T, the C2H1 transitions can no longer be distinguished from the other transitions, which are shifting upwards from lower energies. An overall quadratic shift of the transition energies is observed, which points to an excitonic behaviour of the observed transitions. However, this is not really expected, since the carrier density is quite large. Furthermore, an electric field is applied to the structure, which pulls the wavefunctions of the electrons and holes apart. Analyzing the spectra we extracted the peak intensity of the C2H1 signal of the EL transition, which is shown together with the measured current (solid line) in Fig. 3. The filled squares are the measured values, while the dashed is added to the eye. The EL-peak intensity exhibits large oscillations with increasing magnetic field, which are periodic in 1/B, but with two different periodicities. However, neither the current, nor the C1H1 EL intensity show any pronounced oscillatory structure. A small maximum in the current can be seen at 7.5 T, which coincides with a distinct minimum in the EL intensity. The overall shape of the EL-peak intensity dependence shows at low magnetic fields an increase, but strongly falls off above 10 T. As mentioned above, the C2H1 transition disappears in the region of 15 T. Analyzing the maxima of the EL-peak intensity oscillations of the C2H1 transition, two different 1/B periodicities are identified. Fig. 4 shows the respective 1/B values versus the peak number N for both series. The linear regression of the data points is also shown. Converting the slope to an energy, the first series (filled squares) corresponds to an energy difference of $\Delta E_1 = 22.0$ meV using the effective mass of the electrons of GaAs ($m^* = 0.067 \text{ mo}$). The second series (filled circles) results in an energy difference of $\Delta E_2 = 22.3$ meV using the effective mass of the heavy holes in GeAs ($m^* = 0.45 \text{ mo}$). Due to the applied electric field F_{app} , carriers are injected with an energy of $F_{app} \cdot d$ (d denotes the SL period), which at resonance corresponds to the respective subband spacing. Therefore, the energy loss of the injected carriers is $F_{app} \cdot d - \Delta E_{1,2}$. For both types of carriers we find an energy loss of about 10 meV.

We propose that the origin of these oscillations is a modulation of the C2 population due

to a modulated intersubband scattering between C2 and C1 by resonant elastic scattering

between Landau levels of different subbands.[8,9]

The difference between the subband spacing and the energy deduced from the period of the oscillations is 10 meV.

This suggests that an inelastic process with an energy of 10 meV is involved.

The energy of transverse acoustic phonons is close to 10 meV, but the electron-phonon coupling is extremely weak. A more plausible explanation would therefore be the ionisation of an exciton, since the excitation

binding energy in a quantum well is of the order of 10 meV. This process is analogous to the magneto-impurity resonance.[10] The almost identical energy separation of C² and C¹ as well as H₄ and H₁ then explains the observation of oscillatory structure periodic in 1/B corresponding to the heavy-hole mass.

We will now discuss the C3H1 transition. The EL has been recorded at 5.8 V which corresponds to the C¹→C³ resonance at 0 T. The C3H1 transition energy again exhibits a quadratic shift with increasing magnetic field indicating the excitonic origin of this transition (not shown). Fig. 5 shows the magnetic field dependence of the integrated EL intensity of the C3H1 line together with the current. The magnetic field dependence of the EL intensity exhibits a camel-back shape with a distinct minimum at 15 T and a less pronounced one around 8 T. Both minima in the EL intensity coincide with maxima in the current, leading to the interpretation of a magnetic field induced enhancement of the current at the corresponding magnetic field values. However, since the energy spacing of C³ and C² is larger than the optical phonon energy, we expect that the main relaxation mechanism of carriers from the C³ subband is polar LO phonon emission. In contrast to the C2H1 transition, no oscillations with a well-defined periodicity are observed. The origin of the minimum is not clear. It may be possible that a crossing of the lowest light hole level L₁ with the H₁ state in the same well occurs at this magnetic field strength[5] leading to a reduced occupation of the H₁ level. Since the oscillator strength of the C1L1 transition is smaller than the C1H1 transition, the EL intensity would be reduced. At the same time, the hole density in the L₁ state is increased and the current through the structure becomes larger due to the smaller effective mass of the light holes.

In conclusion, we have investigated the EL properties of excited subband populations in magnetic fields in a SL p-i diode. If the energy spacing is smaller than the optical phonon energy, strong oscillations of the EL intensity as a function of the magnetic field are observed. When the subband spacing becomes larger than the optical phonon energy, no oscillations are found. Several mechanisms for the presence of these oscillations have been discussed. We would like to thank A. Fischer for sample growth and L. Eaves as well as V. Fa'ilko for stimulating discussions. This work was supported in part by the European Community ESPRIT Project no. 7193 PARTNERS.

References

- [1] M. Helm, in: Intersubband transitions in quantum wells, Eds. E. Rosencier et. al., (Plenum Press, New York, 1992) p. 151 and references therein.
- [2] Q. Hu and S. Feng, Appl. Phys. Lett. 59 (1991) 2923.
- [3] J.P. Loehr, J. Singh, R.K. Mains, and G.I. Haddad, Appl. Phys. Lett. 59 (1991) 2070.
- [4] J. Faist, F. Capasso, D.L. Sivco, C. Sirtori, A.L. Hutchinson, and A.Y. Cho, Science 264 (1994) 553.
- [5] T. Yasui, Y. Segawa, Y. Aoyagi, Y. Iimura, G.E.W. Bauer, I. Mogi, and G. Kido, Phys. Rev. B51 (1995) 9813.
- [6] D. Bertram, H. Lage, H.T. Grahn, and K. Ploog, Appl. Phys. Lett. 64 (1994) 1012.
- [7] R. Klann, H.T. Grahn, and K. Ploog, Phys. Rev. B50 (1994) 11037.
- [8] D.R. Leadley, R. Fletcher, R.J. Nicholas, F. Tao, C.T. Foxon, and J.J. Harris, Phys. Rev. B46 (1992) 12439.
- [9] M.E. Raikh and T.V. Shahbazyan, Phys. Rev. B49 (1994) 5531.
- [10] L. Eaves and J.C. Portal, J. Phys. C12 (1979) 2809.

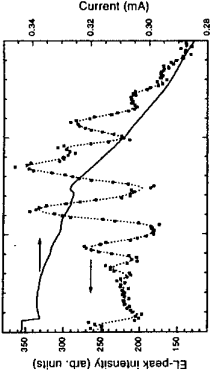


Fig. 3. EL-peak intensity of the C2H1 transition (squares) and current (solid line) versus magnetic field at 4.2 K. The dashed line is added as a guide to the eye.

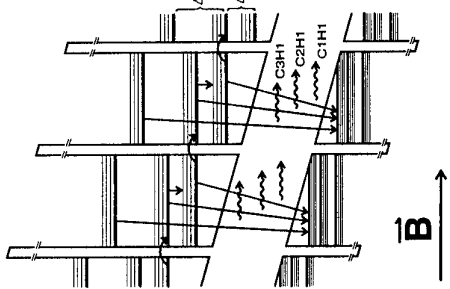


Fig. 1. Schematic view of the bandedges of the SL under forward bias in a perpendicular magnetic field. The electric field corresponds to the resonance condition between the first and second conduction band of adjacent wells. The observed interband transitions are indicated.

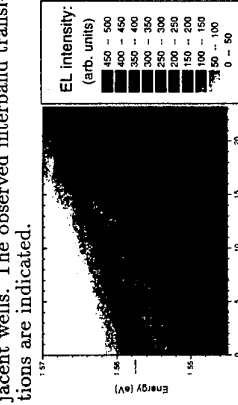


Fig. 2. Isointensity plot of the EL signal versus magnetic field in the energetic regime of the C2H1 transition for an applied voltage of 3.7 V (C1→C2 resonance) at 4.2 K. The arrow indicates the energetic position of the C2H1 transition at 0 T.

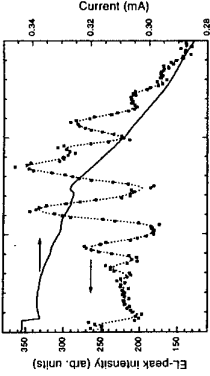


Fig. 3. EL-peak intensity of the C2H1 transition (squares) and current (solid line) versus magnetic field at 3.7 V (C1→C2 resonance) versus magnetic field at 4.2 K. The dashed line is added as a guide to the eye.

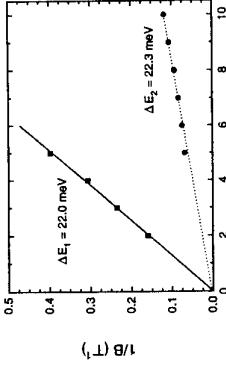


Fig. 4 Maxima of the EL intensity oscillations of the C2H1 transition in Fig. 3 vs peak number N. The solid and dashed lines are linear fits to the cyclotron energy with the effective electron (ΔE_1) and heavy hole mass (ΔE_2).

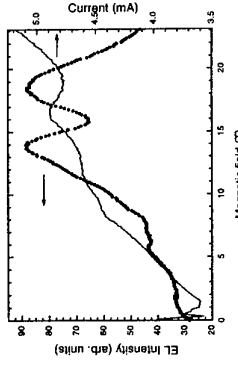


Fig. 5. Integrated EL intensity of the C3H1 transition (dots) and current (solid line) versus magnetic field for 5.8 V (C1→C3 resonance) at 4.2 K.

**PHOTOLUMINESCENCE STUDIES OF CURRENT-INDUCED
NON-EQUILIBRIUM POPULATION IN MAGNETICALLY QUANTIZED
TWO-DIMENSIONAL ELECTRON GASES.**

N. N. Zinov'ev, A. V. Andrianov
Ioffe Physical Technical Institute, St Petersburg 194021, Russia

L. J. Challis, C. T. Foxon
Physics Department, Nottingham University, Nottingham, NG7 2RD, UK

J. J. Harris
Department of Electrical Engineering, University College, London, WC1E 7JE, UK

We report PL studies of the kinetics of current-induced non-equilibrium Landau level (LL) populations in 2DEGs. The B^{-2} field dependence of the relaxation rate is inconsistent with theoretical rates for one and two-phonon inter LL processes suggesting relaxation takes place by extrinsic processes.

Photoluminescence (PL) has been widely used in the study of the equilibrium properties of magnetically quantized two-dimensional electron gases (2DEGs) [1,2]. In this paper we report PL studies of the kinetics of current-induced non-equilibrium Landau level populations. The 2DEG devices are Hall bars of modulation doped GaAs/Al_{0.32}Ga_{0.68}As heterostructures, G-635 and G-644, with saturation electron densities $\approx 1.2 \cdot 10^{15} \text{ m}^{-2}$ (filling factor $\nu \sim 2.5/B$) and mobilities of a few times $10^2 \text{ m}^2 \text{ V}^{-1} \text{ s}^{-1}$. They have dimensions $2 \times 3 \text{ mm}^2$ with source-drain contacts and four voltage probes and their band structure is shown schematically in Fig. 1. The GaAs buffer layer is weakly doped to flatten the bands and so enhance the quality of the PL. The samples are held at $T = 1.8 \text{ K}$ and magnetic fields B applied perpendicular to the plane of the 2DEG. An area $30 \mu\text{m}$ across at the centre of the device is weakly illuminated (power density $\lesssim 10^{-3} \text{ W cm}^{-2}$) by a low power cw He-Ne laser beam which leads to the well-known PL features caused by electrons in the 2DEG combining with photo-created holes in the buffer layer. The Landau level (LL) populations are now driven from equilibrium by $320 \mu\text{A}$ pulses of current I_{sd} in the range $1 - 150 \mu\text{A}$ (well below the value $\sim 1 \text{ Am}^{-1}$ at which quantum Hall breakdown occurs at $\nu \sim 1$, (Ref. [3] and references cited therein) which produce marked current and magnetic field dependent changes in both the energy and intensity of the PL features. These are investigated by taking two time-resolved PL spectra of resolution better than 0.2 meV. A reference spectrum is taken using a gate interval centred $100 \mu\text{s}$ before the start of the current pulse and a second spectrum is then taken after a preset and variable time delay. Simultaneous measurements of the source-drain resistance are also made.

Fig. 1 shows the PL spectra obtained for three values of B . The shaded curves are data for zero current and the curves shown by bold lines are for $I_{sd} = 30 \mu\text{A}$ taken with the gate set in the middle of the current pulse. For $B=0$, two familiar features are observed for zero current: a broad band E_0 and a narrower band or line E_1 . These have previously been assigned respectively to the recombination of electrons from the $n = 0$ and $n = 1$ 2DEG

subbands with photo-created holes in the buffer layer [1], 10-100nm from the plane of the 2DEG [2]. There is also a weak feature on the low energy side of E_1 due to the Fermi edge singularity (FES) [4]. The excitonic nature of E_1 is supported by the diamagnetic shift in its energy and also by the fact that no evidence of significant population in the $n = 1$ subband is found in the Shubnikov de Haas oscillations of the magnetoresistance.

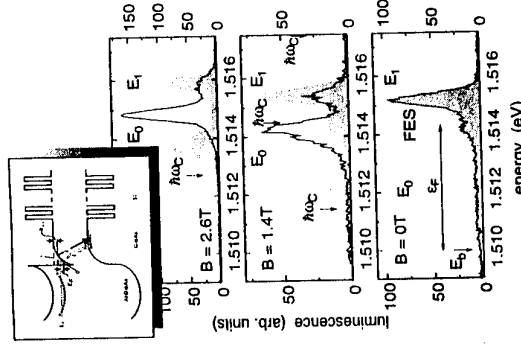


FIG. 1. PL spectra obtained at three magnetic fields. The curves shown shaded and in bold are for $I_{sd} = 0$ and $30 \mu\text{A}$ respectively. *Inset:* Schematic diagram of the potential in and optical transitions observed from n-type modulation doped heterostructures. 0 and 1 are the ground and the first excited 2D subbands. E_0 and E_1 are the radiative transitions between 2DEG and photoholes in the buffer layer.

E_0 narrows with increasing B and its peak energy E_0^p moves by an amount proportional to $\hbar\omega_c/2$ where $\omega_c = eB/\mu$ with $\mu^{-1} = m_e^{-1} + m_h^{-1}$, showing that the PL arises from transitions between the lowest LLs of the 2DEG $l_e = 0$ and photoexcited holes $l_h = 0$. The shift in E_0^p corresponds to a value of μ somewhat smaller than that calculated possibly as a result of interface strain effects. When a current flows through the 2DEG marked changes occur in the PL. Any change in zero or small magnetic fields is too small to detect but, for $B \gtrsim 0.5 \text{ T}$, current-dependent effects are observed in both E_0 and E_1 . The effects increase with current but are qualitatively the same up to the highest current measured. The dominant effect on E_0 is a shift to higher energy. For fixed B , the energy of E_0^p increases approximately linearly with current by an amount proportional to B . So the recombination energy in the illuminated region is increased by an amount proportional to the Hall voltage V_H presumably reflecting differences in the response of the electrons and holes to the Hall field. The dominant effect on E_1 is a change in intensity whose sign depends on the magnetic field. We attribute this to changes in the recombination rate caused by population changes of the LLs in the $n = 0$ subband. The exciton recombination is screened by electrons in

the LLs and in equilibrium this is known to depend on their distribution. It is weakest (PL intensity greatest) when the Fermi energy E_F lies midway between LLs where the 2DEG is least compressible [1] and increases when E_F is raised or lowered. The current-dependent changes observed in E_1 appear to arise from related effects associated with the broadening of the Fermi distribution caused by a rise in electron temperature. This increases the screening when E_F is midgap, or close to midgap, but reduces it when it lies within a LL leading to the changes in PL intensity seen in Fig. 2: the intensity falls for $\nu = 1.0$ (and 1.8) but rises for $\nu = 0.75$. Since the intensity changes in E_1 are due to changes in LL population they can be used to study the relaxation when the current is switched off. Fig. 2 shows the form of the current pulse through the 2DEG and the time-dependence of the PL intensity from E_1 at three different fields. The recovery after the current is switched off is seen to take longer as B increases and from the tail of the decay, we obtain a relaxation time $\tau(B)$ which agrees quite well with times obtained from the relaxation of the position and intensity of E_0^p and the intensity of E_1 . Values of $\tau(B)$ obtained from E_1 are given in the inset to Fig. 2 and at the higher fields are seen to lie approximately on a line $\tau_B = \gamma B^2$ where $\gamma = 38 \pm 7 \text{ T}^{-2} \mu\text{s}$ corresponding to a relaxation rate $\tau_B^{-1} \sim 1.1 \cdot 10^4 \cdot B^{-2} [\text{s}^{-1}]$.

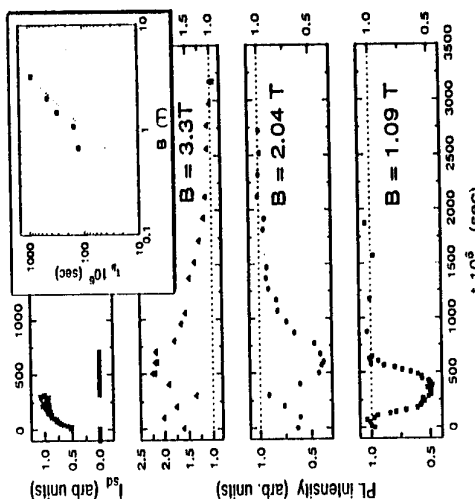


FIG. 2. The time dependence of the E_1 PL intensity for various magnetic fields: (a) $B = 3.3 \text{ T}$; (b) $B = 2.04 \text{ T}$ and (c) $B = 1.09 \text{ T}$. The inset shows the relaxation time determined from the approach of the PL to equilibrium as a function of B (squares); the dotted line shows the fit to $\tau_B = \gamma B^2$, where $\gamma = 38 \pm 7 \mu\text{s}$

This field dependence is too slow for relaxation via one-phonon inter-Landau level emission. For the $l_e = 1 \rightarrow l_e = 0$ transition, this has been shown theoretically [5] to vary as B^{-4} with

$$\tau_{1-m}^{-1} \approx \frac{2.3 \Xi^2 \beta^2 m^4 (1 - f_n^0)}{\hbar \rho a^6 \omega_c^4} \sim 7 \cdot 10^8 (1 - f_n^0) \cdot B^{-4} [\text{sec}^{-1}] \quad (1)$$

where we take $\Xi = 10 \text{ eV}$, $s = 5.5 \cdot 10^3 \text{ nm}^{-1}$, $a = 6 \text{ nm}$ and $\rho = 5.3 \cdot 10^3 \text{ kgm}^{-3}$ for the values of the deformation potential constant, the LA sound velocity, the width parameter of the well and the GaAs density respectively. f_n^0 is the Fermi distribution function of the final state. The strong field dependence is a consequence of the increasing severity of the constraints of momentum conservation on the emission process. In-plane momentum conservation confines the emission to directions approximately normal to the 2DEG plane and its probability falls rapidly with q_e/a where $q_e = \omega_c/s$.

Since the observed field dependence observed is much weaker than that for the one-phonon process we conclude that relaxation must be taking place through some faster parallel channel. (The one-phonon rate calculated using the parameters given is actually ~ 40 times faster than that measured but is very sensitive to a which appears to be increased by illumination [6]; the rate falls below the measured rate if $a \sim 10 \text{ nm}$). This cannot be the two-phonon process since the rate for that has been shown to vary as B [5] and we tentatively ascribe it an extrinsic process involving fast relaxing centres to which the electrons diffuse. Possible candidates for these are the potential fluctuations caused by inhomogeneities. A steep rise in potential would lead to "internal edges" where phonon relaxation could occur at frequencies less than ω_c . In this situation however the rate-limiting process may not be the phonon emission itself but the relatively slow diffusion of the excited electrons within the Landau levels.

We conclude that time-resolved photoluminescence provides a new and valuable method of studying non-equilibrium phenomena in magnetically quantized 2DEGs. The present studies, which focus on the non-equilibrium Landau level populations produced by a transport current, show that they relax at a rate proportional to B^{-2} . This is inconsistent with theoretical expressions for intrinsic processes of inter-Landau level phonon emission and suggests that the relaxation must take place through a faster extrinsic channel. If so it seems likely that a similar process may also be responsible for the electron excitation. The dependence of the shift in E_0 on Hall voltage suggests the technique could be used to map the potential across the sample. It may also be possible to extend it to study integer quantum Hall breakdown and perhaps also to the fractional quantum Hall regime. We gratefully acknowledge help with the device processing from Mr J Middleton and financial support from the Engineering and Physical Sciences Research Council and the European Commission.

[1] A.J. Turberfield, S.R. Haynes, P.A. Wright, R.A. Ford, R.G. Clark, J.F. Ryan, J.J. Harris and C.T. Foxon, Phys. Rev. Lett. **65** (1990) 637.

[2] The dependence of the PL decay on the spatial separation of electrons and photoholes bound to δ -doped impurities is reported by A.F. Dietz, I.V. Kukushkin, K. von Klitzing, V.B. Timofeev and A.I. Filin, JETP Lett. **54** (1991) 388; I.V. Kukushkin, R.J. Haug, K. von Klitzing K. Elbert and K. Tolemeier, Phys. Rev. B **50** (1994) 11259.

[3] S. Kawaji, K. Hirakawa, M. Nagata, T. Okamoto, T. Fukase and T. Gotoh, J. Phys. Soc. Jpn. **63** (1994) 2303.

[4] A.J. Turberfield, R.A. Ford, I.N. Harris, J.F. Ryan, C.T. Foxon and T. Gotoh, Phys. Rev. B **47** (1993) 4794.

[5] G.A. Toombs, F.W. Sheard, D. Neilson and L.J. Challis, Sol. State Communications **64** (1987) 577; V.I. Fal'ko and L.J. Challis, J. Phys. C Condensed Matter **5** (1993) 3945; H.L. Zhao and S. Feng, Phys. Rev. Lett. **70** (1993) 4134.

[6] I.V. Kukushkin, K. von Klitzing, K. v Klitzing, K. v Klitzing, K. v Klitzing and B.N. Shepel, Phys. Rev. B **40** (1989) 4179.

Anomalous Transport of Indirect Excitons in Coupled AlAs/GaAs Quantum Wells

L. V. Butov^{1,2*}, A. Zrenner¹, M. Hagn¹, G. Abstreiter¹, G. Böhm¹, G. Weimann¹

¹ Walter Schottky Institut, Technische Universität München, D-85748 Garching, Germany

² Institute of Solid State Physics, Russian Academy of Sciences, 142432 Chernogolovka, Moscow district, Russia

Abstract

Time-of-flight method is used to study the transport of indirect excitons in AlAs/GaAs CQW structures at $T \geq 350$ mK and $B \leq 14$ T. A large increase of the exciton diffusivity is observed at high magnetic fields and low temperatures, when exciton superfluidity is expected to occur.

Due to the long recombination lifetime of indirect (interwell) excitons the exciton condensation (analogous to the Bose-Einstein condensation of bosons) is expected to occur in coupled quantum wells (CQWs) [1-4]. High perpendicular magnetic fields improve the critical conditions for the exciton condensation [2,5]. Recently evidence for the condensation of indirect excitons in AlAs/GaAs CQWs, which manifests itself as the appearance of a huge broad band noise in the exciton photoluminescence (PL) intensity, has been observed at high magnetic fields [6]. The condensation should be accompanied by the appearance of exciton superfluidity. Rapid exciton transport has been observed in Cu₂O and attributed to the exciton superfluidity [7]. An evidence for anomalies in the exciton transport in AlAs/GaAs CQWs was already observed in Ref. [6]. In the present paper we study the transport of indirect excitons in AlAs/GaAs CQWs under conditions of expected exciton superfluidity. A time-of-flight technique is applied.

We have studied the same type of structures as used in Ref. [6], which are electric field tunable AlAs/GaAs CQWs. The active part of the structure is the i-region which consists of a 40 Å AlAs and 30 Å GaAs layer, surrounded by Al_{0.48}Ga_{0.52}As barrier layers (see insert of Fig. 1). In this structure the electrons and holes are confined in the AlAs and GaAs layers, respectively, for external gate voltage $V_g \lesssim 0.5$ V (indirect regime), which results in a long lifetime of indirect excitons. Data, obtained for $V_g=0$ are used throughout the paper. To derive the exciton diffusion constant D we have compared the PL decay from an unmasked part of the sample with that from a part of the sample which was covered by a nontransparent mask leaving 4 μm wide stripe windows separated from each other by 32 μm. Carriers were photoexcited in the GaAs QW by a pulsed semiconductor laser ($\hbar\omega=1.8$ eV, pulse duration 50 ns). Excitation and detection of the PL signal were performed using an optical fiber with a diameter of 100 μm positioned either in front of the part of the sample covered by the mask or in front of the unmasked part.

The PL decay curves from the unmasked part of the sample at $T=350$ mK and $B=6$ and 14 T are shown in Fig. 1. There is a clear difference of the initial PL intensity decay. This

initial decay time τ is plotted versus magnetic field in Fig. 3a. At $B \lesssim 7$ T the decay is only slightly nonexponential with a relatively long time constant of about 50 ns. At higher magnetic fields the fast initial decay is followed by slow decay at larger times. In the indirect regime the integrated PL intensity is more than an order of magnitude smaller than that in the direct region. Therefore in the indirect regime the radiative lifetime is much larger than the nonradiative lifetime, τ_{nr} , and $\tau \approx \tau_{nr}$. In the considered narrow CQW structures τ_{nr} is determined by the exciton transport to nonradiative recombination centers. Therefore, the variations of τ show that the increase of B first leads to a small reduction of the exciton diffusivity and then to a strong increase (Fig. 3a). The analogous dependence was observed already in Ref. [6].

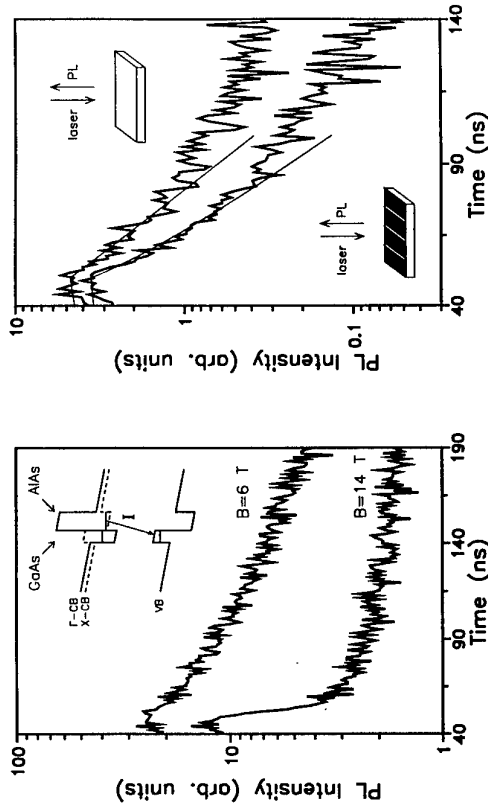


FIG. 1. PL decay curves for the unmasked part of the sample at $T = 350$ mK and $B = 6$ and 14 T. Insert: band diagram of an AlAs/GaAs CQW for $V_g=0$.

Information about the exciton transport obtained from the variations of τ , however, is

only qualitative and indirect. A direct measurement of the exciton transport is obtained by

time-of-flight technique. Fig. 2 shows an example of the PL decay curves for the unmasked and the masked part of the sample. In the presence of diffusion of photoexcited carriers into the metal covered regions the variation of the exciton density, n , is described by

$$\frac{\partial n}{\partial t} = D \frac{\partial^2 n}{\partial x^2} - \frac{n}{\tau} \quad (1)$$

where D is the exciton diffusion constant and x is the coordinate perpendicular to the direction of the stripes. For the PL decay in the unmasked part of the sample the first term

in Eq. (1) is absent, thus the comparison of the decays allows an independent determination of τ and D . The corresponding fitting curves for the PL decay are shown in Fig. 2 by thin lines.

Magnetic field dependence of D at $T=350$ mK is shown in Fig. 3b. D first slightly reduces with B and then strongly increases. The temperature dependence of τ and D for $B=6$ T and 14 T is shown in Fig. 4a and 4b, respectively. The data for $B=6$ T represent typical variations of τ and D at low magnetic fields while the data for $B=14$ T are characteristic for high fields where rapid exciton transport is observed at low temperatures. Fig. 4 shows that at $B=6$ T an increase of temperature results in a monotonic increase of D and a reduction of τ . Contrary to this, at $B=14$ T an increase of T results in a reduction of D and an increase of τ at $T \lesssim 5$ K. Only at higher temperatures τ starts to drop and D to increase approaching the behaviour observed for low magnetic fields. In all experiments the variations of τ describing the exciton transport to nonradiative recombination centers are consistent with the variations of D measured by the time-of-flight technique: an increase (reduction) of τ corresponds to a reduction (increase) of D .

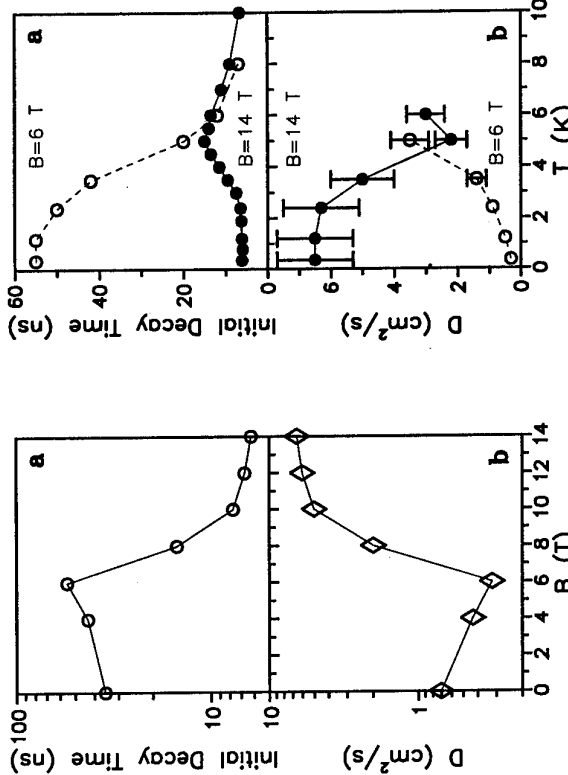


FIG. 3. Magnetic field dependence of the initial decay time (a) and the exciton diffusion coefficient (b) at $T = 350$ mK.

At low magnetic fields, $B \lesssim 7$ T, the temperature and magnetic field dependence of D are usual for the thermally activated exciton transport in a random potential. At zero magnetic field the analogous increase of the exciton diffusivity and reduction of the PL decay time with

increasing temperature were observed in many studies of AlAs/GaAs type-II superlattices (see, e.g., Ref. [8] and references therein). The monotonic reduction of the exciton diffusivity with the magnetic field can be qualitatively explained by the increase of the magnetoexciton mass, and is in a qualitative agreement with the theoretical consideration of the exciton transport in AlAs/GaAs CQWs [9]. The slow PL decay at large delay times corresponds to the recombination of strongly localized excitons.

The rapid exciton transport is observed at high magnetic fields and low temperatures when exciton superfluidity is expected to occur [6]. With increasing temperature the rapid exciton transport disappears, and at $T \gtrsim 5$ K the usual increase of D with temperature is recovered. The rapid exciton transport is observed in approximately the same temperature range where the optical signature of the exciton condensate — appearance of a huge broad-band noise in the integrated PL intensity — was observed [6]. The noise is observed at lower magnetic fields than the rapid exciton transport [6], therefore the noise may be considered as critical fluctuations near the phase transition, while the rapid exciton transport — as the appearance of the exciton superfluidity. A possible alternative explanation of the rapid exciton transport, the magnetic field induced suppression of the destructive interference between excitation paths [6], seems to be less realistic due to the total charge neutrality of the excitons. However this effect can not be totally ruled out and its relation to the observed rapid exciton transport has to be clarified by future theories of exciton transport in magnetic fields.

In our study the average characteristics of the exciton transport integrated over the stripe lengths are measured in time-of-flight experiments. For the exciton condensation in the presence of a random potential superfluid lakes with the boundary determined by the potential profile are expected to be formed. Therefore on a large scale the average exciton transport is a transport in a disordered array of normal and superfluid regions which are determined by potential fluctuations. The relatively low value of D characteristic for the observed exciton transport can be explained by such a simple picture.

We thank A. B. Dzyubenko for interesting discussions. The work was supported financially by the Volkswagen foundation (grant No. VW I/69361).

* E-mail: butov@issp.ac.ru

- [1] Yu. E. Lozovik and V. I. Yudson, Zh. Eksp. Teor. Fiz. **71**, 738 (1976) [Sov. Phys. JETP **44**, 389 (1976)].
- [2] Y. Kuramoto and C. Horie, Solid State Commun. **25**, 713 (1978).
- [3] T. Fukuzawa, S. S. Kano, T. K. Gustafson, T. Ogawa, Surf. Sci. **228**, 482 (1990).
- [4] X. Zhu, P. B. Littlewood, M. S. Hybersten, T. M. Rice, Phys. Rev. Lett. **74**, 1633 (1995).
- [5] I. V. Lerner and Yu. E. Lozovik, Zh. Eksp. Teor. Fiz. **78**, 1167 (1980) [Sov. Phys. JETP **51**, 588 (1980)].
- [6] L. V. Butov, A. Zrenner, G. Abstreiter, G. Böhm, and G. Weimann, Phys. Rev. Lett. **73**, 304 (1994).
- [7] D. W. Shoke, J. P. Wolfe, and A. Mysrowicz, Phys. Rev. Lett. **64**, 2543 (1990); E. Fortin, S. Faïfard, and A. Mysrowicz, Phys. Rev. Lett. **70**, 3591 (1993).
- [8] G. D. Gilliland, D. J. Wolford, J. A. Bradley, J. Klem, Proc. 21 Int. Conf. Phys. Sem., Beijing, China, 1992, Ed. by P. Jiang and H.-Z. Zheng (World Scientific), p. 1250.
- [9] A. B. Dzyubenko and G. E. W. Bauer, Phys. Rev. B (to be published).

Resonant Bound Bipolarons in a Superlattice in a High Magnetic Field

J.-M. Shi,^{†,*} F.M. Peeters,^{*} and J.T. Devreese^{*†}

^{*}Departement Natuurkunde, Universiteit Antwerpen (UIA), Universiteitsplein 1, B-2610 Antwerpen, Belgium

[†]Departement Technische Natuurkunde, Technische Universiteit Eindhoven, P.O. Box 513, NL-5600 MB Eindhoven, The Netherlands

Abstract

We present a theoretical study of a bound bipolaron in a GaAs/AlGaAs superlattice (SL) in a high magnetic field. Using a variational approach and second order perturbation theory, the influence of tunneling of the electrons into the adjacent wells, electron-electron (e-e) correlation, band nonparabolicity, and electron-phonon interaction on this system is described. Our numerical results are in good agreement with available experimental data.

1. Introduction

There has been an increasing interest in the study of electron-phonon interaction in quasi-two-dimensional (Q2D) systems [1]. Two electrons bound to a Coulomb impurity (D^-) in a polar material form a bound bipolaron, which can be made using selective doping of a GaAs/AlGaAs SL [2,7]. At a high magnetic field, resonant bipolaron effects occur, which influences strongly the electronic properties of the D^- states [8-11].

This paper presents a theoretical investigation of a D^- center in a SL in a magnetic field. The following effects on the D^- states are discussed: (1) tunneling of the electrons into the adjacent wells, (2) e-e correlation, (3) band nonparabolicity, and (4) the electron-phonon interaction. We have found that the electron tunneling effect and the e-e correlation are important for describing the D^- binding energy, band nonparabolicity becomes important with increasing magnetic field, and resonant bipolaron effect is responsible for the measured two-level resonance of the D^- transition [8,9].

2. D^- centers in a superlattice

In the absence of electron-phonon interaction, a D^- center at the well center of a GaAs/ $\text{Al}_x\text{Ga}_{1-x}\text{As}$ SL in a magnetic field $B = (0, 0, B)$ along the growth (z) axis is described by

$$H_{e,e}(\mathbf{r}_1, \mathbf{r}_2) = \frac{e^2}{\epsilon_0 r_{12}} + \sum_{j=1}^2 \left[\frac{1}{2m_e^*(z_j)} \left(\mathbf{p}_j + \frac{e}{c} \mathbf{A}_j \right)^2 - \frac{e^2}{\epsilon_0 r_j} + V(z_j) \right], \quad (1)$$

where $m_e^*(z_j)/m_e = 0.067 + 0.083z$ is the electron effective mass which depends on the electron in GaAs or in $\text{Al}_x\text{Ga}_{1-x}\text{As}$; $\epsilon_0 = 12.5$ is the static dielectric constant assumed to be uniform in the system; the position of the j th electron is indicated by $\mathbf{r}_j = (r_j, \phi_j, z_j)$; r_{12} is the distance between the two electrons; the vector potential \mathbf{A}_j is defined as $\mathbf{A}_j = \frac{1}{2} \mathbf{B} \times \mathbf{r}_j$; and the SL potential is modeled by a periodic square-well potential: $V(z_j) = 0$, for $|z_j| < w/2$; $V(z_j) = V_0$, for $w/2 < z_j < w+b$, and $V(z_j) = V[z_j + n(w+b)]$ with w (b) the well (barrier) width, n an integer, and $V_0 = 0.6(1.155x + 0.37x^2)$ in eV.

The Schrödinger equation with the Hamiltonian $H_{e,e}$ cannot be solved exactly, and therefore we rely on a variational approach to study the D^- states. Since no triplet states have been observed in the experiments [8], our attention will be focused on the singlet (s) states. The following trial functions are used for the D^- center

$$|I, O; s\rangle = [\Psi_I(\mathbf{r}_1)\Psi_O(\mathbf{r}_2) + \Psi_O(\mathbf{r}_1)\Psi_I(\mathbf{r}_2)]|1 + \Theta_{I,O}(z_1 - z_2)|^2 + \Xi_{I,O}(\rho_1 - \rho_2)^2], \quad (2)$$

where $|1s, 1s; s\rangle$ is the ground state, and $|1s, 2p^\pm; s\rangle$ the two lowest excited states. $\Psi_I(\Psi_O)$ is taken to be the form $\rho^{lm} f(z) \exp(i m\phi - \xi \rho - \eta z^2)$ with $f(z)$ the function of the lowest-energy solution of the SL. The terms $(z_1 - z_2)^2$ and $(\rho_1 - \rho_2)^2$ in Eq. (2) describe e-e correlation. Thus all the six variational parameters for each state are determined by minimizing the energy: $E_{I,O;s}^0 = \langle I, O; s | H_{e,e} | I, O; s \rangle / \langle I, O; s | I, O; s \rangle$.

In Fig. 1 we present the widths of the ground state in an $x = 0.25$, $100\text{\AA}/100\text{\AA}$ SL (solid curves) for $\langle \rho^2/2 \rangle^{1/2}$, $\langle z^2 \rangle^{1/2}$, and $\langle r_{12}^2 \rangle^{1/2}$ as function of B . The results for the $x = 0.25$, 100\AA QW (dotted curves) are also plotted. It is shown: that (1) the state widths decrease with increasing B ; (2) the difference between the SL and QW cases comes from the z direction which displays the influence of the adjacent wells; (3) due to stronger confinement the width in the z direction for the QW case is almost independent of the magnetic field, while it has still weak B -dependence for the SL case (i.e., it is 30.5\AA at $B = 0$, and 28.6\AA at $B = 25\text{T}$); and (4) the two electrons are relatively close to each other because of the Q2D confinement.

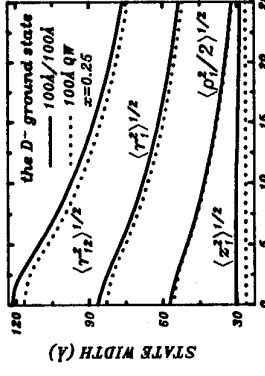


FIG. 1. Widths of the wave function of the D^- ground state in an $x = 0.25$, $100\text{\AA}/100\text{\AA}$ SL (solid curves) vs magnetic field. The corresponding results in the QW (dotted curves) are also plotted.

Figure 2 shows B -dependence of the binding energy of the ground state, which is defined by $E_b = E_1^0 + E_{1z}^{N=0} - E_{1z,1}^0$ with $E_{1z}^0 (E_{1z,1}^{N=0})$ the energy of the shallow donor (free electron) ground state, for the same systems as shown in Fig. 1. The binding energy in the SL (solid) is appreciably decreased as compared to that in the QW (dotted curve), which shows that is for the study of the D^- binding energy in such a SL, the single-QW theory is not a good approximation. The results without e-e correlation effect for the SL case (dashed curve) are also plotted, which show that e-e correlation becomes more important with increasing B due

to the fact that the magnetic field forces the electrons closer to the donor and consequently closer to each other (see, Fig. 1).

3. Bipolaron effects on the D^- states

Since GaAs is a weak polar material and the SLs have rather broad wells, we can use second-order perturbation theory and include only GaAs bulk-phonon modes to calculate the bipolaron correction to the energy of the μ [$\mu = (I, O; s)$] state

$$\Delta E_\mu = - \sum_{\mu'} \sum_{\mathbf{q}} \frac{|\langle \mu'; \mathbf{q} | H_I(\mathbf{r}_1) + H_I(\mathbf{r}_2) | \mu; 0 \rangle|^2}{\hbar\omega_{\mathbf{q}} + E_\mu^0 - E_\mu^0 - \Delta E_\mu + \Delta E_{1s,1s;s}} , \quad (3)$$

where H_I is the Fröhlich Hamiltonian given by $H_I(\mathbf{r}_j) = \sum_{\mathbf{q}} [V_{\mathbf{q}} b_{\mathbf{q}} \exp(i\mathbf{q} \cdot \mathbf{r}_j) + h.c.]$ with $b_{\mathbf{q}}$ ($b_{\mathbf{q}}^\dagger$) the annihilation (creation) operator of a LO phonon having momentum $\hbar\mathbf{q}$ and energy $\hbar\omega_{\mathbf{q}}$, and $|V_{\mathbf{q}}|^2 = 4\pi c(\hbar\omega_{\text{LO}})^{3/2}/q^2\Omega$ with Ω the volume. For GaAs we take $\hbar\omega_{\text{LO}} = 36.75\text{meV}$, and the electron-phonon coupling constant $\alpha = 0.068$.

In principle we should include all the D^- states in Eq. (3), but this is a formidable task. Using Platzman's iterations [12] Eq. (3) can be rewritten into a sum of a finite number of terms, and only the last term needs an approximation, which allows one to know only a few relevant states [11] to evaluate Eq. (3).

4. Comparison with experiments and conclusions

Now we compare our results with the experimental data. The $|1s, 1s; s\rangle \rightarrow |1s, 2p^-; s\rangle$ transition energy of a D^- center in an $x = 0.25, 100\text{\AA}/100\text{\AA}$ SL and in the QW is depicted in Fig. 3 with (solid) and without (dotted curves) polaron correction. The solid dots are the

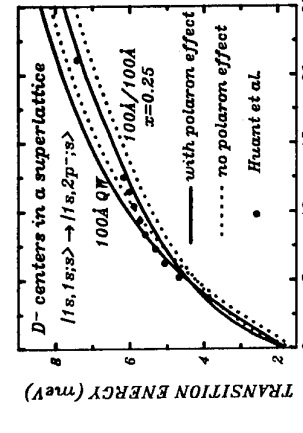


FIG. 3. Transition energy of $|1s, 1s; s\rangle \rightarrow |1s, 2p^-; s\rangle$ as a function of the magnetic field B (T) for a D^- center in an $x = 0.25, w = b = 100\text{\AA}$ SL with (solid) and without (dotted curves) polaron correction. The corresponding results are also plotted for the QW case for comparison. The solid dots are the experimental data in Ref. [2].

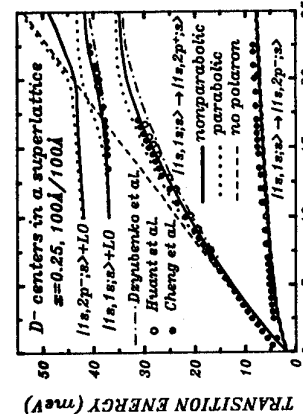


FIG. 4. $|1s, 1s; s\rangle \rightarrow |1s, 2p^+; s\rangle$ transition energies vs B for a D^- center in an $x = 0.25, 100\text{\AA}/100\text{\AA}$ SL without any (dashed), with polaron (dotted), and with polaron and band nonparabolicity (solid curves) corrections. The open (solid) dots are the measured data from Ref. [8] ([9]), and the dash-dotted curves are the calculated results from [10].

experimental data [2]. A reasonable agreement is found between experiment and theory for the SL case when we include the polaron effect. The transition energies for the QW case do not agree with experiment and in particular the slope of the curve differs appreciably. This slope is consistent with the results from a Monte Carlo calculation [6]. The polaron effect slightly increases the transition energy because of the larger polaron correction to the ground state than to the excited state.

The resonant bipolaron effects are shown in Fig. 4 together with the experimental results for the D^- transitions in an $x = 0.25, 100\text{\AA}/100\text{\AA}$ SL [8] (open) and in a SL with $x = 0.3, w = 100\text{\AA}$ [9] (solid circles). The variational-calculation results (dashed curves) are not able to explain the two-level resonance. Including the polaron effect (dotted curves) improves our results appreciably, and describes the higher branch of the measured $|1s, 1s; s\rangle \rightarrow |1s, 2p^+; s\rangle$ transition from resonance between the $|1s, 1s; s; \mathbf{q}\rangle$ and $|1s, 2p^+; s; 0\rangle$ states, which is consistent with a recent calculation [10] for an $x = 0.3, w = 100\text{\AA}$ QW shown by the dash-dotted curves. However, at high magnetic fields the agreement for the $|1s, 1s; s\rangle \rightarrow |1s, 2p^+; s\rangle$ transition is less satisfactory.

To improve this we include the effect of band nonparabolicity using the standard Kane model given by $E_{np} = E_g[-1 + (1 + 2E_p/E_g)^{1/2}]$ with E_{np} (E_p) the D^- center energy with (without) the effect of band nonparabolicity and $E_g = 1520\text{meV}$ the energy gap of GaAs. Here we have taken half of the D^- energy as the single-electron energy. The results are plotted in Fig. 4 by the solid curves which show that this effect becomes important for the $|1s, 1s; s\rangle \rightarrow |1s, 2p^+; s\rangle$ transition near resonance.

Acknowledgments: One of us (F.M.P.) is supported by the Belgian National Science Foundation, and JMS wishes to thank TUE for financial support. This work is sponsored by Fonds voor Kollktief Fundamenteel Onderzoek, Belgium, project No. 2.0093.91, "Diensten voor de Programmatie van het Wetenschapsbeleid," Belgium, under contract No. IT/SC/24.

References

- [1] See, e.g., J.P. Cheng, B.D. McCombe, G. Brozak, and W. Schaff, Phys. Rev. B **48** (1993) 17243; and references therein.
- [2] S. Huard, S.P. Najda, and B. Etienne, Phys. Rev. Lett. **65** (1990) 1486.
- [3] S. Holmes, J.P. Cheng, B.D. McCombe, and W. Schaff, Phys. Rev. Lett. **69** (1992) 2571.
- [4] T. Pang and S.G. Louie, Phys. Rev. Lett. **65** (1990) 1635.
- [5] D.M. Larsen and S.Y. McCann, Phys. Rev. B **45** (1992) 3485.
- [6] S. Huard, A. Mandray, J. Zhu, S.G. Louie, T. Pang, and B. Etienne, Phys. Rev. B **48** (1993) 2370.
- [7] J.M. Shi, F.M. Peeters and J.T. Devreese, Surf. Sci. **305** (1994) 220.
- [8] S. Huard, Physica B **204** (1995) 339.
- [9] J.P. Cheng, B.D. McCombe, and W. Schaff, in *Proceedings of the 11th International Conference on the Application of High Magnetic Fields in Semiconductor Physics* (Springer-Verlag, Berlin, 1994).
- [10] A.B. Dzyubenko and A.Y. Sivchenko, Phys. Rev. B **48**, (1993) 14690.
- [11] J.M. Shi, F.M. Peeters and J.T. Devreese, Phys. Rev. B **51** (1995) 7714.
- [12] P.M. Platzman, Phys. Rev. **125** (1962) 1961.

Luminescence Spectroscopy of the Two-Dimensional Hole Gas in p-Type Modulation-Doped SiGe Quantum Wells and Si Epilayers

I. A. Buyanova, W. M. Chen, A. Henry, W.-X. Ni, G. V. Hansson and B. Monemar
Department of Physics and Measurement Technology
Linköping University S-581 83 Linköping, Sweden

Abstract

Photoluminescence (PL) transitions related to the two-dimensional hole gas (2DHG), formed by boron δ -doping, are studied in detail in Si epilayers and modulation-doped SiGe quantum wells (QWs). New broad PL bands are observed and are shown to be characteristic for these modulation-doped structures. For SiGe QWs a strong enhancement of the PL intensity near the Fermi edge is shown to be related to carrier correlation effects, i. e. the Fermi edge singularity.

II. Introduction

Photoluminescence (PL) spectroscopy is known as a powerful technique in obtaining electronic properties of bulk semiconductors. Similar studies of Si-based electronic systems grown by epitaxial techniques have generally been lacking so far, however, mainly due to a lack of high quality crystals suitable for optical studies. Recent developments of advanced crystal growth techniques such as molecular beam epitaxy (MBE) enable the growth of high quality Si and SiGe with controlled changes of composition and doping and with a reasonably high radiative efficiency. These developments thus open the door for detailed studies of Si-based materials by a variety of PL spectroscopies. Of particular interest is modulation doping of Si thin films and SiGe/Si heterostructures, where the advantages of the Si technology could be combined with the possibilities of band-gap engineering provided by modulation doping. So far studies on modulation-doped Si-based systems have been limited to magnetotransport measurements [1, 2] and far-infrared absorption spectroscopy [3, 4]. Luminescence studies of such structures remain few [1]. In this work we shall demonstrate that useful information on p-type modulation-doped Si and SiGe/Si structures can be obtained from PL studies.

III. Results and Discussion

Boron modulation-doped Si epilayers

In Fig. 1(a) a schematic band diagram for the B modulation-doped Si epilayers is shown, where the space charges in the B-doped regions create V-shaped QWs filled with the 2DHG. Fig. 1(b) displays PL spectra from such modulation-doped Si layers of various B doping concentration. All samples show substrate-related P bound exciton (BE) luminescence, denoted as PNP and PTO. In addition two relatively broad asymmetric PL bands (denoted as the BD-

band in Fig. 1), corresponding to the weak TA and strong TO replicas, are observed below the shallow BE emission.

The BD PL observed can consistently be interpreted as being due to the radiative recombination of the 2DHG formed within the doped regions and nearby photo-created electrons, based on the following experimental facts. First of all, these BD-bands appear only in δ -doped structures with the doping concentration exceeding the degenerate limit. This is further confirmed by post-growth hydrogen treatments, where a reduction of the B doping concentration due to the hydrogen passivation has resulted in a disappearance of the BD PL, as shown by the dashed curve in Fig. 1(b). The width of the BD-band increases with an increasing the doping level (Fig. 1(b)), consistent with an increasing filling of the QWs. The width of the BD band in fact gives a measure of the Fermi level (E_F) position of the 2DHG.

A detailed study varying photo-excitation intensity and temperature reveals that the BD-band is composed of two overlapping components, arising from the recombination of the 2DHG with photo-excited free electrons (at a higher energy) and electrons bound to residual donors (at a lower energy), respectively (Fig. 1(a)). The former dominates at a low temperature and a high photo-excitation level, consistent with a shallow photo-induced potential well in the conduction band for the electrons near the doping spikes. The component related to the donors is easily saturated with photo-excitation due to a low ($\sim 10^{15} \text{ cm}^{-3}$) residual donor concentration.

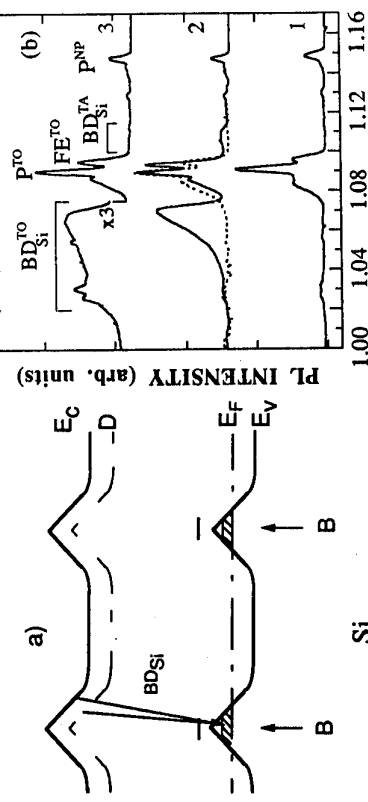


Fig. 1a) Schematic band diagram of p-type δ -doped Si epilayers; b) Normalized PL spectra at 2K from modulation-doped Si layers with B doping concentrations of $2 \times 10^{12} \text{ cm}^{-2}$ (curve 1), $1 \times 10^{13} \text{ cm}^{-2}$ (curve 2) and $5 \times 10^{13} \text{ cm}^{-2}$ (curve 3). The spectrum of a hydrogen-passivated sample is shown by the dashed curve.

Boron modulation-doped Si/SiGe/Si quantum structures

In Fig. 2(a) a schematic band diagram for the B modulation-doped SiGe/Si QW is given, where a 2DHG is formed as a result of the hole transfer from the remote B dopants. Fig. 2(b) shows PL spectra from such modulation-doped SiGe/Si QWs of various well and spacer widths. The previously discussed BD PL from Si is no longer observed. Instead, SiGe related emissions are dominating in the PL spectra with an enhanced intensity of the NP line as compared to the TO replica, due to the alloy effects. The PL properties are strongly dependent on the modulation doping conditions. The spectrum of a 500 Å SiGe QW resembles the sharp excitonic emission (X) from undoped SiGe. In the case of 30 Å wide SiGe QWs, the PL spectra

are, however, dominated by broad asymmetric PL bands (Fig. 2(b)). These PL bands are completely different not only from the sharp excitonic emission X, but also from the localized exciton emission often observed in undoped QW structures [5]. First of all, they are only observed in the structures with a significant filling of holes in the SiGe QW. In addition, localized exciton emission is usually observed only under very low excitation conditions [5] which is not so in our cases. We attribute the broad asymmetric PL to the band-to-band recombination between free electrons and the 2DHG, as shown in Fig. 2(a). The high energy cut-off in the PL spectra thus corresponds to the Fermi edge of the 2DHG, which is about 30 and 50 meV above the bottom of the first heavy hole (HH) subband for the 30 Å QWs with 300 Å and 250 Å spacer, respectively.

The energy position and the overall shape of the PL bands strongly depend not only on the filling of the SiGe QW (Fig. 2) but also on the experimental conditions. An increase of excitation intensity causes a shift of the PL bands towards higher energy followed, for the QW with 500 Å spacer, by an abrupt increase of the PL intensity at the Fermi edge - Fig. 3(a). Such a PL enhancement can be suppressed by an increase in temperature and is no longer observed for T > 42 K - Fig. 3(b).

The mechanisms responsible for such a PL enhancement near the Fermi edge could be manifold, including 1) excitonic recombination equivalent to that of an undoped QW when a near flat-band condition is reached upon an intense photoexcitation, 2) excitonic transition related to the higher lying light hole (LH) subband and 3) the Fermi-edge singularity (FES). The first mechanism can, however, be ruled out here as it is inconsistent with the observed temperature quenching of the PL enhancement, since the excitonic recombination detected from the reference undoped sample sustains within the same temperature range. The second alternative can also be discarded. This is because within this model an enhanced LH emission is expected with an increasing temperature, contradictory to the experimentally observed thermal quenching behaviour. By the third mechanism the observed strong enhancement near the Fermi level is interpreted as a direct consequence of carrier correlation, namely FES, which has been intensively studied for highly doped III-V quantum systems [6]. The peculiar features of the FES experimentally observed in our structures are represented by a the strong thermal quenching of the PL enhancement and its critical dependence on the separation between the EF quenching of the PL enhancement and its critical dependence on the separation between the EF

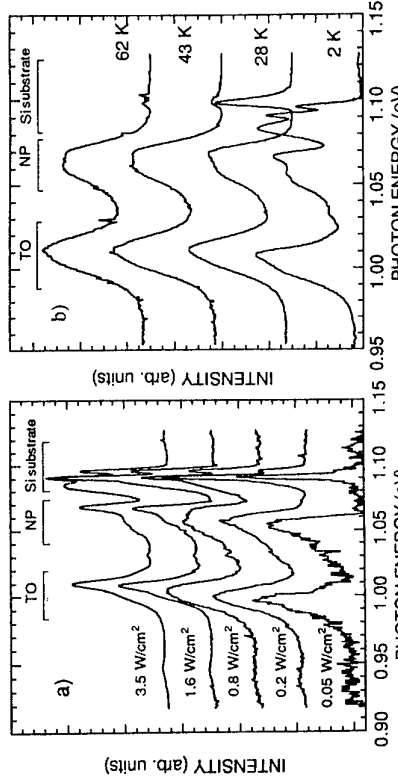


Fig. 3 a) Normalized excitation-dependent PL spectra of the 30 Å-wide SiGe QW separated by 500 Å spacer. b) Normalized temperature-dependent PL spectra of the same SiGe QW. The position and the next unoccupied subband [7]. The latter provides evidence that the enhancement occurs due to the coupling of excitons with excitations of the Fermi sea.

IV. Summary

The P-type modulation doping has been shown to strongly affect the radiative recombination processes in Si thin films and Si/SiGe/Si quantum structures grown by the MBE technique. In both cases, characteristic broad and asymmetric PL bands are observed as the result of the formation of the 2DHG due to the B-doping. Useful information about the charge transfer, filling of the QWs, subband structure of the 2DHG, recombination mechanisms etc. can be obtained by the PL studies. Interesting carrier correlation phenomena such as the Fermi-edge singularity are observed.

References

- [1] R. Loo, L. Vescan, A. Hartmann, R. Apetz, U. Zastrow, T. Schäpers, A. Leuther, C. Dicker, and H. Lüth, Phys. Rev. B50 (1994) 18113.
- [2] H. H. Radamson, M. R. Sardella, O. Nur, M. Willander, B. E. Sernelius, W. X. Ni, and G. V. Hansson, Appl. Phys. Lett. 64 (1994) 1842.
- [3] J. S. Park, R. P. G. Karunasiri, Y. J. Mii, and K. L. Wang, Appl. Phys. Lett. 58 (1991) 1083.
- [4] F. Fromherz, E. Koppensteiner, M. Helm, G. Bauer, J. F. Nutzel, and G. Abstreiter, Phys. Rev. B 50 (1994) 15073.
- [5] L. C. Lenchshyn, M. I. W. Thewalt, J. C. Sturm, P. V. Schwartz, E. J. Prinz, N. L. Rowell, J.-P. Noël and D. C. Houghton, Appl. Phys. Lett. 60 (1992) 3174.
- [6] M. S. Skolnick, J. M. Ronison, K. J. Nash, D. J. Mowbray, P. R. Tapster, S. J. Bass, and A. D. Pitt, Phys. Rev. Lett. 58 (1987) 2130; Y. F. Chen, L. Y. Lin, J. L. Shen, and D. W. Liu, Phys. Rev. B46 (1992) 12433.
- [7] P. Hawrylak, Phys. Rev. B44 (1991) 6262.

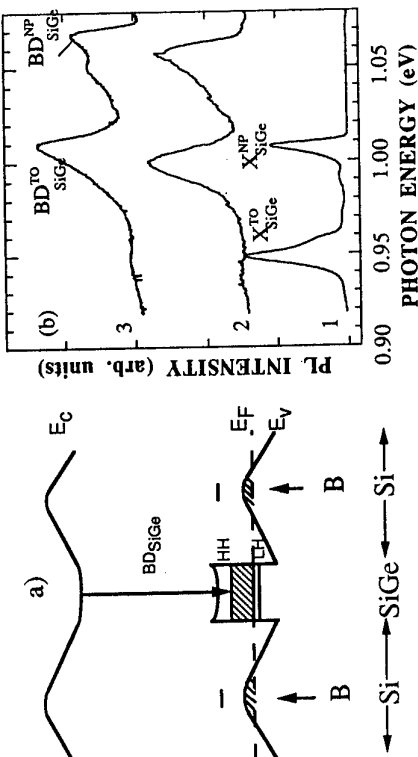


Fig. 2 a) Schematic band diagram of p-type δ -doped Si epilayers; b) Normalized PL spectra at 2 K from the 500 Å-wide SiGe QWs with a 500 Å spacer (curve 1) and from the 30 Å-wide SiGe QWs with 500 Å spacer (curve 2) and 250 Å spacer (curve 3).

Spatially Direct-to-Indirect Transition of Excitons in Step Quantum Wells

Kejian Luo, Houzhi Zheng, Shijie Xu, and Haiping Zhou*

National Laboratory for Superlattices and Microstructures, Institute of Semiconductors, Chinese Academy of Sciences, Beijing 100083, P.R. China

Abstract

Spatially direct-to-indirect transition of excitons induced by perpendicular electric field in a novel step quantum well is studied. From photoluminescence spectra at the temperature of 77K, we observe distinct blueshift of exciton peak stemming from this transition. We also calculate the exciton binding energies at various electric fields considering the effect of inhomogeneous broadening and reproduce the main feature of the observation.

It is well known that the effect of perpendicular electric field on the spectroscopic shift of exciton transition energy in quantum wells(QW) is two-fold: one effect is so-called quantum confined Stark effect (QCSE) which causes redshift; another is the reduction of exciton binding energy that leads to blueshift. In principle, the enlarged separation between electron and hole in electric field should give rise to the reduction of the exciton binding energy. As a result, a transition from spatially direct to spatially indirect excitons should be observed if the effect were sufficiently large. However, in general, the QCSE is dominate effect in QWs. Therefore, only the redshift of exciton peak has been observed experimentally [1-3] while the blueshift caused by the latter effect has not been observed from PL spectra so far.

In this paper, we employ photoluminescence (PL) spectroscopy to study the spatially direct-to-indirect transition of excitons in a novel step QW. We find, that the reduction of exciton binding energy due to this transition could dominate the spectroscopic shift of exciton peak and lead to a blueshift of PL spectrum in certain bias range in contrast to usually observed redshift arising from QCSE. This provides a possible way for measuring the exciton binding energy directly from conventional PL spectra.

The samples used in our experiments are multilayered n-i-n heterostructures grown by molecular beam epitaxy. After a 0.6μm thick, Si-doped($1 \times 10^{17} \text{ cm}^{-3}$), n-type GaAs buffer layer is deposited on a n-type (100) GaAs substrate(Si-doped to $2 \times 10^{18} \text{ cm}^{-3}$), a nominally undoped multilayer consisting of GaAs/AlAs/GaAs/AlAs/GaAs/Al_{0.2}Ga_{0.8}As /Al_{0.4}Ga_{0.6}As (the corresponding thicknesses are 100Å / 30Å / 40Å / 20Å / 25Å / 160Å /500Å) is grown in sequence. The top contact layer is composed of a 500Å-thick n-type ($n=1 \times 10^{17} \text{ cm}^{-3}$) GaAs layer and a 200Å-thick, n-type ($n=4 \times 10^{18} \text{ cm}^{-3}$) GaAs cap layer.

The samples are processed into circle mesas of the diameter 2mm by conventional photolithography, and annular ohmic contacts are fabricated by evaporating and subsequently alloying Au/Ge/Ni metals on the tops of the mesas. PL experiments are carried out both at 300K and 77K. For the latter, the samples are held in a liquid

nitrogen cryostat. The photoexcitation is usually provided by 4880Å line of Ar⁺-ion laser, and by 7300Å line of Ti:sapphire laser pumped by a Ar⁺-ion laser in case where a selective excitation is required. The excitation power density is controlled on the level of $\sim 0.5 \text{ W/cm}^2$.

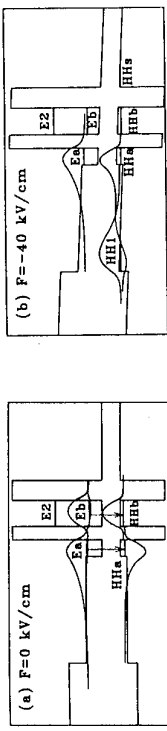


Fig. 1. Schematic band diagram of the structure and relevant states. (a) the wave functions of E_a, E_b, HH_a and HH_b states at F=0 kV/cm. (b) the functions of E_a, HH_a, and HH_b states at F=40 kV/cm. Here the ground heavy hole's state of the step QW is HH₁, HH₁ becomes the first excite state.

Fig. 1(a) schematically shows the energy band profile of the sample under flat-band condition. The main constituents of our structure are one step QW on the left and one conventional QW on the right. In-between is a 20Å thick AlAs barrier. The total width of the step QW is 185Å with a deep portion of 25Å. Fig. 2 gives the PL spectra, excited by 4880Å laser line, measured at 25K (solid line) and 300K (dashed line) under zero bias. As seen, at 77K, two PL peaks show up at the energies, 1.716eV and 1.693eV, which will hereafter be labeled by the letters A and B. Their PL peak energies will be denoted as E_a and E_b respectively. It is rather intuitive to assign the peak A to the transition from the electron's ground state E_a to the heavy hole's ground state HH₁ in the deep portion of the step QW, and the peak B to the transition from electron's ground state E_b to ground heavy hole's state HH_b in the conventional QW, as indicated by the arrows in Fig. 1(a). The corresponding PL spectra measured at 300K gives that E_a=1.636eV and E_b=1.612eV at zero bias. To verify the above assignment we have used simple envelope wave function method [4] to calculate the transition energies excluding the exciton effect. The result reveals that the transition energy for E_a→HH₁ is 1.639eV and the one for E_b→HH_b is 1.614eV in good agreement with the values measured at 300K. This is what one expected because the thermal ionization of excitons at 300K is to greatly suppress the exciton effect.

In order to provide further evidence for our assignment, we re-measure PL spectra at 77K by changing excitation wavelength from 4880Å to 7300Å, which amount to a photon energy of 1.702eV smaller than E_a(1.716eV). At zero bias, only peak B (E_b=1.693eV) is observable on the low energy side, peak A does not appear as shown in the inset to Fig. 2. However, the situation changes after applying a negative bias to our n-i-n structure. Here, by "negative" we refer to the top contact being negatively biased with respect to the substrate. In this case the electrons will be injected into QWs from n'-electrode. On the other hand, HH_b shifts downward more rapidly than HH₁ with the bias (linear Stark effect), and they cross each other as the electric field reaches a value of F=40 kV/cm (about V \approx 0.8V). From Fig. 1(b) it follows that as long as HH_b is below HH₁, the photoexcited holes in HH_b will partially be transferred to HH₁ in the step QW through nonresonant tunneling process, and recombine the injected electrons in situ by emitting photons. This gives rise to the re-

appearance of the peak A in the PL spectra at the biases higher than -0.8V, as seen in the inset to Fig.2, and justified our assignment further.

With right assignment in hand, we have systematically studied the bias dependences of Eaa and Ebb. Fig.3 plots an abrupt blueshift of about 6meV in the bias range from -0.5V to -1.0V in contrast to a somewhat expected redshift. We first claim tentatively that this anomalous blueshift is attributed to the reduction of exciton binding energy in the step QW, where a transition from spatially direct to spatially indirect excitons may easily occur after applying electric bias for the following reason. Under negative biases, as seen in Fig.1(b), the electron's wave function of Ea becomes more localized in the deep portion of the step QW, while the hole's wave function of Hb is going to extend from the deep portion to the whole step QW. As a result, the Coulomb interaction inside the exciton will significantly be weakened because of the enlarged spatial separation between the electron and hole. This will certainly result in a noticeable reduction of excitation binding energy. At the same time the Stark shift of Eaa is rather small (not more than 1meV according to our calculations) due to the very narrow width (25Å) of the deep portion in the step QW. Accordingly, the observed blueshift of Eaa is obviously caused by the reduction of the exciton binding energy in the bias range from -0.5V to -1.0V. To make our points more convincing, we calculate the exciton binding energies at various electric fields using a simple method presented by Leavitt and Little [5]. The results are given in Fig.4. The dashed line corresponds to results without considering any energy-level broadening and temperature effect. It shows that exciton binding energy decreases sharply from -40 kV/cm to -70 kV/cm (corresponding bias range is from -0.7V to -1.2V) in good agreement with experiment. Two dips appear at -26 kV/cm and -42 kV/cm corresponding to the hole level resonance of HH1 with HH1 (as seen in Fig.1(b)) and HH2 (not shown in Fig.1(b)). In reality the level broadening, either inhomogeneous or homogeneous, will smear out such sharp resonant feature. As an example, by considering the inhomogeneous broadening, we re-calculate the binding energies, and show corresponding results by the solid line in Fig.4, which is obtained after a weighted average when a Gauss-like fluctuation in the well width is assumed. We can see that the two dips are nearly washed away. Apparently, our calculation reproduces the main feature of our observation. The detail about the calculation is beyond the scope of this paper and will be reported elsewhere.

We have taken one step further and measured the same bias dependence of PL's peak position for both Eaa and Ebb at 300K. As mentioned previously, the thermal ionization of excitons will increasingly become important. A PL signal featuring the recombination of free electrons and holes is generally going to take over that of exciton-type. Especially, in our step QW the thermal occupation of high-lying states in a broadened subband makes the carriers spill out of the deep portion of the step QW more easily. That facilitates the dissociation of the excitons at 300K. Therefore, the blueshift of Eaa shown in Fig.3 is somewhat expected to disappear at 300K since the shift of PL peak will primarily be controlled by QCSE. The inset to Fig.3 indeed reveals the expected behavior with no any blueshift observed.

In conclusion, we have observed the spatially direct-to-indirect transition of excitons by studying the spectroscopic shift of PL peaks in a novel step QW position with increasing perpendicular electric field. The distinct blueshift of exciton's PL peak at 77K in the bias range from -0.5V to -1.0V and its absence at 300K provided the convincing evidence for the reduction of the exciton binding energy due to such a

transition. The calculated dependence on the biases of the exciton binding energy also reproduces the main feature of the experiment. Our work may give a convenient way to measure the exciton binding energy directly.

We would like to thank the technical assistance of C.F.Li and W.Liu. This work is supported by the State Science and Technology Commission and Chinese National Natural Science Foundation.

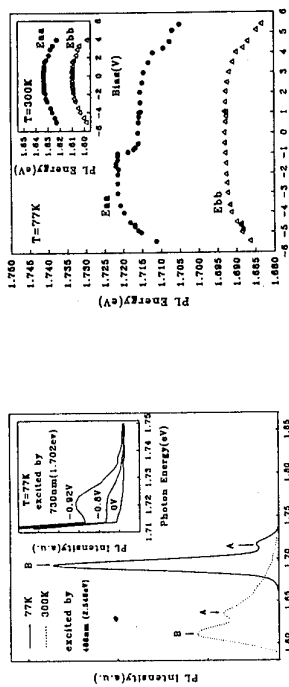


Fig.2. PL spectra at 77K (solid line) and 300K (dashed line) under zero bias. The inset shows selectively excited PL spectra under the biases of 0V, -0.8V, and -0.92V.

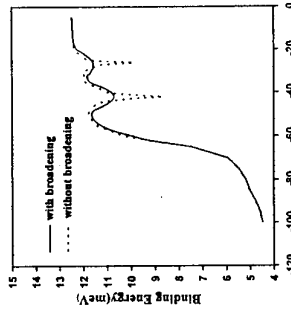


Fig.3. Variation of Eaa (●) and Ebb (△) with the bias at 77K. The inset shows the bias dependence of PL spectra at 77K and 300K.

References

- * present address: Department of Electronics & Electrical Engineering, University of Glasgow, UK
- [1] D.A.B.Miller, D.S.Chemla, T.C.Damen, A.C.Gossard, W.Wiegmann, T.H.Wood, and C.A.Burrus, Phys.Rev.B32, 1043 (1985)
- [2] R.T.Collins,K.v.Klitzing and K.Ploog, Phys.Rev.B33, 4378 (1986)
- [3] S.Tarucha and K.Ploog, Phys.Rev.B38, 4198 (1988)
- [4] C.Weisbuch and B.Vinter, *Quantum Semiconductor Structures* (Academic Press, INC., San Diego, 1991), chapter II. The parameters used in the calculation are listed as follows: the band offset is $\Delta E_c = 390$ meV, $\Delta E_v = 195$ meV for $Al_0.4Ga_{0.6}As/GaAs$, $\Delta E_c = 187$ meV, $\Delta E_v = 80$ meV for $Al_{0.2}Ga_{0.8}As/GaAs$ and $\Delta E_c = 1.038$ eV, $\Delta E_v = 530$ meV for AlAs/GaAs. The effective masses have Al content(x) dependences as given by $m_r^* = 0.067 + 0.063x$, $m_h^* = 0.38 - 0.32x$.
- [5] R.P.Leavitt and J.W.Little, Phys.Rev.B42, 11774 (1990)

Nonlinear Resonant Optical Rectification in a Coupled Quantum Well

K. Unterrainer¹, J.N. Heyman², K. Craig¹, B. Galdrikian¹, M.S. Shervin¹, H. Drexler¹, K. Campman³, P.F. Hopkins³, A.C. Gossard³

¹Quantum Institute, University of California at Santa Barbara
Santa Barbara, CA 93106

²Department of Physics, Macalester College, Saint Paul, MN 5505

³Materials Department, University of California at Santa Barbara.
Santa Barbara, CA 93106

Abstract

We have measured the rectification of far-infrared radiation resonant with the lowest intersubband transition of an AlGaAs/GaAs asymmetric coupled double-quantum well in which the subband spacing is 11 meV. From these measurements we can extract an intersubband lifetime of 1.2±0.4 ns at low excitation intensity and T=10 K, which appears promising for devices which can operate at low excitation and temperature, such as FIR detectors or mixers. From simultaneous measurements of the optical rectification and of the intersubband absorption coefficient we can determine the intensity-dependent intersubband lifetime which shows a strong decrease for increasing intensities.

Introduction

The recent development of a midinfrared intersubband laser has encouraged the study of the possibility for an intersubband laser in the far infrared spectral region which has a great demand for semiconductor radiation sources [1]. The most important parameter for such devices as well as for detectors is the intersubband relaxation time (T_1). We have measured this time using a new experimental technique based on the strong nonlinear susceptibility of an asymmetric double quantum well. Simultaneous measurements of the rectification of far-infrared radiation resonant with the intersubband transition and of the intersubband absorption enable the determination of the intensity dependent relaxation time. Optical rectification is the static polarization produced by difference-frequency mixing of a harmonic electric field $E(\omega)$ with itself through the second order susceptibility. In asymmetric quantum wells this static polarization is observed for intersubband transitions, because the expected value of the position of an electron in an excited state and in the ground state are different

$$P^{(2)}(0) = \chi_{(0,\omega,\omega)}^{(2)} E(\omega) E(\omega) = -e(n_2 - n_2^0)(z_{2,2} - z_{1,1}) \quad (1)$$

where n_2 is the population in the second subband, n_2^0 is the equilibrium population in the second subband, $z_{i,j}$ is the dipole-matrix element between states i and j .

Experimental

The coupled GaAs quantum wells in our heterostructure are 85 Å and 73 Å wide, separated by a $\text{Al}_{0.3}\text{Ga}_{0.7}\text{As}$ barrier 25 Å wide (see Fig. 1). The wavefunction of the ground state is centered in the wide well, the wavefunction of the first excited state in the narrow well (see Fig. 1, 0 V gate bias). The lowest electron-subband spacing was measured to be $E_2 - E_1 = 11$ meV using photoluminescence. Energies of the higher subbands $E_3 - E_1 = 110$ meV, and $E_4 - E_1 = 156$ meV were obtained from a self-consistent model described below. The measurements described below were performed near resonance, with $\hbar\nu = E_2 - E_1$. Under these conditions the heterostructure may be approximated as a two-subband system. At low temperatures ($T < 50\text{K}$), the zero-bias charge density obtained by Hall measurements is $N_s = 2 \cdot 10^{11} \text{ cm}^{-2}$ and the electron in-plane mobility is $\mu = 1.05 \text{ cm}^2/\text{Vs}$.

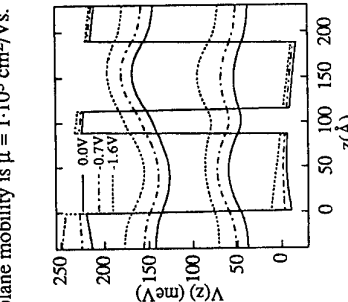


Fig. 1: Conduction band diagram for the coupled double well for different gate bias voltages. The envelope wavefunctions for the first and second subband are shown.

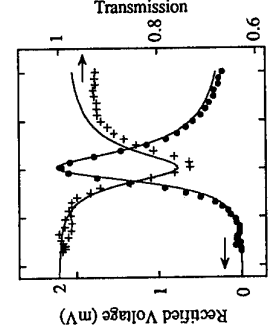


Fig. 2: Optical rectification and transmission in the linear regime ($T = 10\text{K}$, $I = 0.5 \text{ W/cm}^2$). Solid lines are calculated from theory (see text).

Results and Discussion

Figure 2 shows the amplitude of the optical rectification and the FIR transmission as a function of gate bias, measured at $T = 10\text{K}$ and at a laser intensity of 0.5 W/cm^2 . A resonance in

the rectification occurs when the intersubband-absorption frequency is tuned through the laser frequency at $V_G = -0.8$ V, indicating that the rectification is associated with the intersubband transition.

We have calculated the energies and envelope functions of electrons at the subband minima in our double well by self-consistently solving the Schrödinger and Poisson equations within the effective-mass approximation. Temperature effects were included by allowing thermal population of higher subbands. This model, together with the dephasing time determined from the linewidth of the absorption resonance, allows us to calculate the FIR transmission and optical rectification of our sample (Fig. 2, solid lines), and we find a good agreement with the experiment.

Figure 3(a) shows the sensitivity (rectified voltage/intensity) and the intersubband absorption at resonance as a function of pump intensity at $T=10$ K. At low intensities the sensitivity and the absorption are constant. The rectified signal starts to saturate (the sensitivity decreases) at about 1W/cm^2 , the absorption coefficient starts to decrease at about 200W/cm^2 . The saturation behavior of both the rectified signal and the absorption is described by the rate equations of a two level system. The intensity dependent rectified signal is then given by

$$\Delta V^{opr} = \frac{-4\pi e}{\epsilon} (z_{2,2} - z_{1,1}) \Delta n_{1,2}^0 \frac{I \sigma T_1}{\hbar \omega} \left(1 + 2 \frac{I \sigma T_1}{\hbar \omega} \right)^{-1}, \quad (2)$$

and the intensity-dependent absorption-coefficient is

$$\alpha(I) = (\Delta n_{1,2}^0) \frac{\sigma}{a} \left(1 + 2 \frac{I \sigma T_1}{\hbar \omega} \right)^{-1} \quad (3)$$

where σ is the linear absorption cross section, $\Delta n_{1,2}^0$ is the difference between the equilibrium populations of the first and second subbands, I is the intensity of the pump beam, and a is the thickness of the sample. Fitting the magnitude of the rectification voltage (Eq.2) to the experiment yields an intersubband lifetime $T_1 = 1.2 \pm 0.4$ ns. This lifetime is longer than the calculated lifetime of $T_1 = 215$ ps we obtain from Ferreira and Bastard's simple model for the acoustic-phonon scattering rate in our structure [3]. Since an intersubband excitation is in fact a collective excitation, the relaxation of a collective mode has to be treated in a different way from the single particle relaxation. This many body effect can reduce the relaxation rate.

The different saturation behavior of the rectified signal and of the absorption coefficient indicates that the relaxation time is intensity-dependent. This intensity dependence has not been considered in any other experiment. Moreover, most experimental results are derived from nearly saturated systems. However, the intensity dependent relaxation time can be obtained directly from the ratio between rectified signal and the absorption coefficient (see Eq. 2 and 3)

$$T_1 = - \frac{V^{opr}(I)}{I \alpha(I)} \frac{e \hbar \omega}{4 \pi (z_{2,2} - z_{1,1}) a} \quad (4)$$

Therefore, simultaneous measurements of optical rectification and intersubband absorption can determine T_1 over a wide range of conditions, including low intensities within the linear regime. The intersubband lifetime depends strongly on intensity (Fig. 3b). In the linear regime we measure $T_1 = 1.2$ ns (consistent with the result of the fit only to the rectified signal), while in the strongly saturated regime ($I = 2\text{kW/cm}^2$) we find $T_1 = 15$ ps. We suggest two mechanisms for the reduction in lifetime at high intensities. First, the electron-electron intersubband-scattering rate is predicted to depend strongly on the population in the second subband. If this mechanism controls the relaxation, the lifetime will decrease as the excited state is populated through absorption. Second, the excitation by the pump should heat the electron gas. In view of the strong temperature-dependence of the scattering rate, a reduction in the intersubband lifetime at high pump-intensities is expected due to heating [4].

In order to investigate the effect of carrier concentration on the relaxation time we have performed the same experiments in a logarithmically graded quantum well [5]. The intersubband energy can be tuned from 35cm^{-1} to 125cm^{-1} in this structure. Since we observe a considerable rectified voltage at the resonance, this structure acts as a widely tunable FIR detector. In addition, the carrier concentration can be adjusted by a backgate. As a function of carrier concentration the absorption coefficient increases as expected. However, the rectified signal decreases with increasing carrier concentration which indicates that the relaxation time gets shorter. Since the change of the carrier concentration is controlled by the back-gate voltage the electric field in the well changes. Therefore the matrix elements have to be evaluated for each carrier concentration. Fig. 4 shows preliminary results for the relaxation rate as obtained from the linear power dependence of the rectified signal.

In summary, we have observed resonant optical rectification in our coupled quantum-well. From simultaneous measurements of the rectified voltage and of the absorption we can extract the intersubband lifetime as a function of intensity. At low intensities the lifetime is 1.2 ± 0.4 ns at $T=10\text{K}$ which appears promising for devices which can operate at low excitation and temperature, such as FIR detectors or mixers. At high intensities the lifetime reduces to 15ps at 2kW/cm^2 which is still an order of magnitude larger than the lifetime for intersubband energies above the optical phonon energy.

Acknowledgment: The authors would like to thank the staff at the Center for Free-Electron Laser Studies J.R. Allen, D. Eynart, G. Ramian, and D. White. Funding for the Center for Free-Electron Laser studies is provided by the Office of Naval Research.

References:

1. J. Faist, F. Capasso, D.L. Sivco, C. Sitor, A.L. Hutchinson, and A.Y. Cho, Science **264**, 553-556 (1994).
2. J. N. Heyman, K. Craig, B. Galdrickian, K. Campman, P. F. Hopkins, S. Fafard, A. C. Gossard, and M.S. Sherwin, Phys. Rev. Lett. **72**, 2183-2186 (1994).
3. R. Ferreira, G. Bastard, Phys. Rev. **B40**, 1074 (1989).
4. J. N. Heyman, K. Unterreiner, K. Craig, B. Galdrickian, M. S. Sherwin, K. Campman, P. F. Hopkins, and A. C. Gossard, Phys. Rev. Lett. **74**, 2682 (1995).
5. P.F. Hopkins, K.L. Campman, G. Bellomi, A.C. Gossard, M. Sundaram, E.L. Yuh, E.G. Gwinn, Appl. Phys. Lett. **64**, 348 (1994).

Cyclotron Resonance in Short Period $(\text{GaAs})_n/(\text{AlAs})_n$ Superlattices

T. Fukuda[†], K. Yamamoto[‡], H. Momose[‡], N. Mori[†] and C. Hamaguchi[†]
[†]Department of Electronic Engineering, Osaka University
[‡]Low Temperature Center, Osaka University
 Suta City, Osaka 565, Japan

Y. Inanaka, Y. Shimamoto and N. Miura
 Institute for Solid State Physics, University of Tokyo, Roppongi, Minato-ku, Tokyo 106, Japan

Cyclotron resonance measurements have been carried out to evaluate the effective mass of electrons in short period $(\text{GaAs})_n/(\text{AlAs})_n$ superlattices (SLs). In order to clarify the $I^{\prime}-X$ crossover occur at $n \approx 12$ due to the zone folding effect, we have measured the effective masses in SLs with n ranged from 8 to 16 using the cyclotron resonance in high magnetic fields up to 150 T. We found a clear cyclotron resonance in the transmission of 10.61 μm radiation at 100 T in type-I SLs corresponding to the effective mass of 0.099 m_e and broad cyclotron resonances at around 90 T in type-II SLs in the transmission of 28 μm radiation which gives the effective mass $0.26 \pm 0.02 m_e$. These resonances were found to be nearly independent of the monolayer number n .

I. INTRODUCTION

Intensive studies have been reported on the type-I to type-II transition due to the crossover of the I^{\prime} - and X -like conduction bands in short period GaAs/AlAs superlattices(SLs) [1-9]. It has been accepted that the lowest conduction band states of $(\text{GaAs})_n/(\text{AlAs})_n$ SLs with n less than about 13 [3-6] have AlAs X -like character rather than GaAs I^{\prime} -like character because of the Brillouin zone folding effect of the I^{\prime} -like states and the X -like states. In addition, degeneracy of the six X valleys of the bulk AlAs crystals is removed in SLs, resulting in splitting of the states into X_z (the (001) minima) and X_{xy} (the (100) and (010) minima) in GaAs/AlAs SLs grown along the (100) axis. Although a simple effective mass model predicts that X_z is lower than X_{xy} , the ordering of the conduction states is not settled. The first principle energy band calculations such as tight-binding [6,7] or pseudopotential method [9] have revealed that their results are in disagreement with each other such as the monolayer number of the cross-over, direct or indirect levels except for $n = 1$ and so on. Our previous work shows that for type-II SLs X_z level lies below the X_{xy} levels for $n = 1$ [6]. It has been shown that the lowest conduction band states of type-II SLs are unambiguously determined by experimental methods such as emission time decay [10], optical measurement under high pressure [11] and magneto-photoluminescence [8]. Cyclotron resonance (CR) measurements under high magnetic fields enables us to investigate low mobility materials such as bulk AlAs, because the condition $\omega\tau > 1$ can easily be satisfied. For example, resonance peaks corresponding to $m_e = 0.44 \sim 0.5 m_0$ have been observed in bulk AlAs [12-14]. In addition a high magnetic field has been shown to cause the type-I-type-II transition in short period SLs [8]. In the present study, we have carried out CR measurements in short period $(\text{GaAs})_n/(\text{AlAs})_n$ SLs under pulsed high magnetic fields up to 150 T to determine the effective mass and to study the magnetic field induced type-I-type-II transition. We report the effective mass of the X_z state for the first time. The present results will be compared with the tight-binding calculations.

II. EXPERIMENTAL PROCEDURES

The SL samples used in the present study are $(\text{GaAs})_n/(\text{AlAs})_n$ SLs with $n = 8, 10, 12, 14, 16$ (Table I). All the samples were grown by molecular beam epitaxy (MBE) on semi-insulating GaAs (001)-oriented substrates. Two different doping profiles are adopted in order to get electrons in the superlattice region. The sample referred to as “ δ -doped” has a structure such that the n GaAs/AlAs region is delta-doped with Si donors in the center of each GaAs well, where 80 periods of n -GaAs/ AlAs region are sandwiched with 10 periods undoped GaAs/ AlAs SLs (total 100 periods). In the sample “GaAs-doped”, $(\text{GaAs})_{16}/(\text{AlAs})_{16}$ layers are grown with spatially doped GaAs layers, where 12 monolayers of each GaAs well was uniformly Si-doped and sandwiched by undoped GaAs 2 monolayer spacers (100 periods in the total). Hall effect measurements were carried out to obtain

the mobility and carrier density of the SLs at 77 K which are shown in Table I. The number of GaAs and AlAs layers were accurately controlled by counting the periods of the intensity oscillations of a specularly reflected beam in a reflection high-energy electron diffraction (RHEED).

A block-diagram of the experimental apparatus is shown in Fig. 1. Pulsed high magnetic fields up to 150 T were produced by a single-turn coil technique [16]. The fields were produced by supplying short large current pulses of about 2.5 MA to thin single turn coil from a fast condenser bank with a storing energy of 100 kJ at +0 kV. The pulse duration was about 7 μs and the magnetic field was measured by a pick-up coil wound on the sample. The error of the field measurement was less than 3% [17].

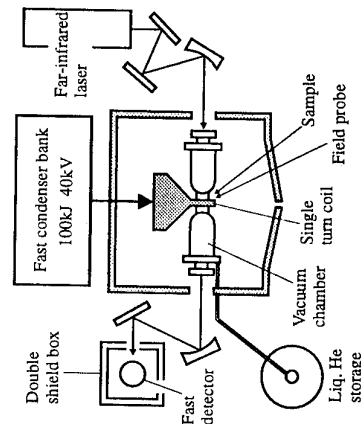


FIG. 1. The block-diagram for CR measurement. Pulsed high magnetic field up to 150 T is produced by a single-turn coil. The magnetic field is applied parallel to the growth direction of $(\text{GaAs})_n/(\text{AlAs})_n$ superlattices. $n = 8-16$

III. EXPERIMENTAL RESULTS

A. Effective mass of type II superlattices

Figure 2 shows experimental results of CR for $(\text{GaAs})_n/(\text{AlAs})_n$ SLs with $n = 8-16$ in the transmission of 28 μm radiation at low temperature (19 \sim 45 K). We find prominent CR signals by using persistent photoconductivity brought about by illumination from Ar^+ laser, which increases the mobility and the carrier density in SLs at low temperature. We obtained the cyclotron mass from the resonance position of SLs by fitting a CR curve with a sum of Lorentzian curves. For $n = 16$ SLs (type-I SLs) we found CR at 25 T, which gives $0.065 m_0$ (close to $0.067 m_0$ of GaAs I^{\prime} -like effective mass). In the samples with $n \leq 14$, on the other hand, the resonant absorption corresponding to the effective mass of I^{\prime} -like was not found, instead broad CR signals were observed at around 90 T which gives $0.232 \pm 0.008 m_0$. This abrupt change in the cyclotron mass at $n = 14$ is in contrast to the smooth change of the effective mass in $\text{GaAs}/\text{AlGaAs}$ multi quantum wells [18].

In the CR experiments for bulk AlAs, absorption peaks of CR were observed, giving the effective mass of $m_e^* = 0.44 m_0$ [12,13]. Miura *et al.* [12] regarded the peak as due to the effective mass of $(m_t^* m_e^*)^{1/2}$, where m_t and m_e are the transverse and the longitudinal effective masses respectively, because the peak position shifts to a lower field for tilting samples. On the other hand, Goiran *et al.* [13] assigned the two peaks as the transverse effective mass m_t^* and the effective mass of $(m_t^* m_e^*)^{1/2} = 1.05 m_0$. Sasaki *et al.* [8] obtained the transverse effective mass of the AlAs X -point as $m_t = 0.16 \pm 0.07 m_0$ using magneto-photoluminescence measurement under high magnetic fields.

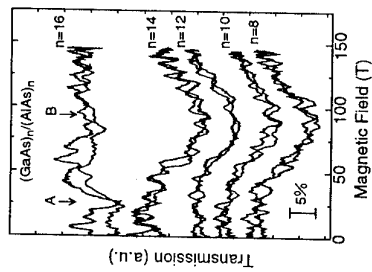


FIG. 2. Experimental results of CR for $(\text{GaAs})_n/(\text{AlAs})_n$ SLs with $n = 8-16$ in the transmission of 28 μm radiation. The resonance A gives the effective mass of 0.065 m_0 and B gives $\sim 0.232 m_0$.

and this value is in good agreement with the commonly used values ($m_e^* = 0.19m_0$) [15]. In the present study, we obtained the cyclotron mass of type-II SLs as $0.23m_0$ at low temperatures corresponding to the effective mass of X_z -point, which is expected to be close to the transverse effective mass of the AlAs X -point, and this value is in reasonable agreement with the effective mass obtained by Miura *et al.* ($m_t = 0.25m_0$) and Sasaki *et al.* ($m_t = 0.16m_0$).

B. Temperature dependence of cyclotron resonance

Figure 3 represents recordings of CRs at various temperatures. Fig. 3(a) shows a resonance position of 70 T at 34 K in $10.61\text{ }\mu\text{m}$ radiation for $n = 16$ SL, which gives $0.067m_0$. The resonance position shifts to 100 T at 300 K , corresponding to the effective mass $0.099m_0$. The temperature dependence of the effective mass is too big compared to the bulk effective mass and may be interpreted in terms of the impurity transition at lower temperature and free electron transition at higher temperature. The calculated effective mass of the SLs based on the tight-binding theory is about $0.080m_0$, which is in good agreement with the above result. Figure 3(b) shows temperature dependence of CR for $n = 12$ SL, where CR peak of 85 T at 30 K gives the effective mass $0.227m_0$, and the resonance position shifts to 95 T at 100 K , giving rise to the effective mass $0.248m_0$ at 100 K . At 170 K CR was not well resolved. Such a weak temperature-dependent CR was observed in other type-II SLs with $n = 10, 14$ (see Table I) and can be explained in terms of temperature dependence of the band gaps of GaAs and AlAs. In Table I we find no significant change in the effective mass in the SLs with $n = 8, 10, 12$ and 14 .

TABLE I. Hall mobility μ , carrier sheet density N_s and cyclotron mass m_e^* of $(\text{GaAs})_n/(\text{AlAs})_n$ SLs for $n = 8 \sim 16$. The Hall mobility and carrier density of SLs were measured at 77 K , and the cyclotron mass of SLs were measured at $19 \sim 45\text{ K}$ (low temperature), 100 K and 300 K .

Sample	doping	μ (cm^2/Vs)	N_s ($\text{cm}^{-2}/\text{period}$)	low temperature	m_e^*	100K	300K
8	δ	60,000	3.0×10^9	0.227			
10	δ	17,000	7.0×10^9	0.240	0.256		
12	δ	10,000	1.0×10^{10}	0.227	0.248		
14	δ	600	2.0×10^{11}	0.235	0.272		
16	δ	9,000	1.5×10^{10}	0.067	0.099		
16	GaAs	10,000	3.0×10^{10}	0.071			

In Fig. 3(b) we find the resonance peak for $n = 12$ SLs becomes weaker as the temperature increases, which is explained by the decrease in the mobility and the carrier density at higher temperatures. On the other hand, the resonance peak for $n = 16$ SLs becomes stronger at 300 K compared to the CR peak at 34 K , as shown in Fig. 3(a). This behavior seems to be associated with the temperature-dependence of T - X crossover in $(\text{GaAs})_{16}/(\text{AlAs})_{16}$ SLs [6] and magnetic field induced T - X crossover (see the next subsection).

C. T - X crossover in short period GaAs/AlAs superlattices

It is well known that high magnetic field causes the type-I-type-II transition (magnetic field induced T - X transition). Figure 4 shows CRs of $(\text{GaAs})_{16}/(\text{AlAs})_{16}$ SLs at 30 K in the various transmissions: $10.61\text{ }\mu\text{m}$, $28\text{ }\mu\text{m}$ and $119\text{ }\mu\text{m}$ radiation. We observed only one resonance for the transmission of $119\text{ }\mu\text{m}$ radiation which corresponds to T -like states, while two resonances were observed for the transmission of $28\text{ }\mu\text{m}$ radiation: one corresponds to T -like states ($0.055m_0$) and the other to X -like states ($0.222m_0$). CR peak due to the X -like states was not observed for the transmission of $10.61\text{ }\mu\text{m}$ because of the limited range of the applied magnetic field. This behavior may be explained in terms that the T - X crossover occurs at about 60 T for $n = 16$ SLs and that the CR peak of X_z states becomes visible at a higher magnetic field.

IV. CONCLUSION

We have studied T - X crossover in short period $(\text{GaAs})_n/(\text{AlAs})_n$ SLs using CR measurement at high magnetic fields, and found that the abrupt change in the effective mass of SLs at $n = 14$.

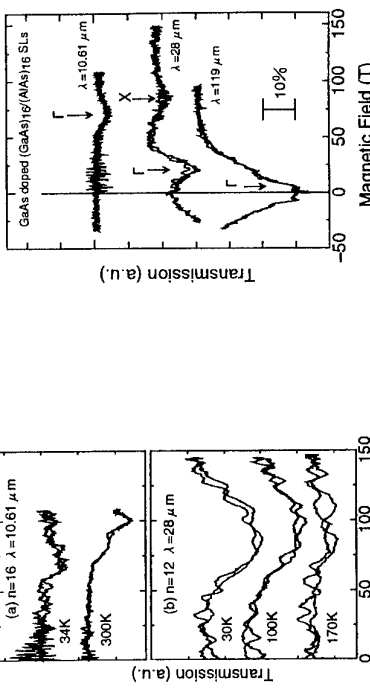


FIG. 3. Experimental results of CR for $(\text{GaAs})_n/(\text{AlAs})_n$ SLs. (a) CR for $n = 16$ SL in $10.61\text{ }\mu\text{m}$ radiation. Low temperature CR at 70 T gives $0.0865m_0$. (b) CR for $n = 12$ SL in $28\text{ }\mu\text{m}$ radiation. CR at 85 T corresponding to $0.227m_0$ was observed at 30 K , and the resonance position shifts to 95 T corresponding to $0.248m_0$ at 100 K .

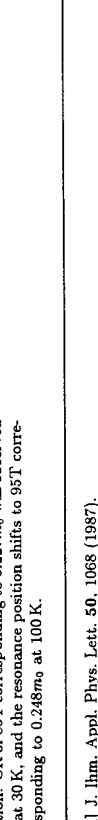


FIG. 4. Experimental results of CR for $(\text{GaAs})_n/(\text{AlAs})_n$ SLs in the various transmissions: $10.61\text{ }\mu\text{m}$, $28\text{ }\mu\text{m}$ and $119\text{ }\mu\text{m}$ radiation. The results clearly demonstrate the magnetic field induced T - X transition.

**Cyclotron resonance and subband-Landau level coupling
in 2D electron and hole gases**

R. Winkler*

Institut für Theoretische Physik, Universität Regensburg,
D-93040 Regensburg, Germany

May 26, 1995

We discuss the far-infrared absorption in quantum wells in the presence of a quantizing magnetic field. Our theory is applicable both to electrons and holes. Band structure effects are fully taken into account and our approach allows to consider different sample geometries and potential profiles. As an example we discuss the spin-split cyclotron resonance in the nonparabolic 2D electron gas in InAs-AlSb quantum wells. Our parameter-free calculations are in excellent agreement with recent experiments of Yang *et al.* [Phys. Rev. B 47, 6807 (1993)] and Scriba *et al.* [Solid State Commun. 88, 633, (1993)]. The complex valence band structure results in anticrossings between Landau levels of different hole subbands.

1. Introduction. Magneto-optical spectroscopy has proven to be a valuable tool for analyzing the subband structure of electrons and holes in semiconductor quantum wells (QW's) [1]. We present a theory for the absorption of far-infrared (FIR) radiation in the presence of a quantizing magnetic field \mathbf{B} that is capable of describing a variety of experimental situations. For long time attempts failed to observe the spin splitting of the cyclotron resonance (CR) in a nonparabolic 2D electron gas and various arguments were put forward to explain its suppression, see Refs. [2-4] and references therein. Here we show that the spin-splitting of the CR recently observed by Yang *et al.* [2] and Scriba *et al.* [3] can be reproduced quantitatively by using the $\mathbf{k} \cdot \mathbf{p}$ parameters known for the corresponding bulk materials.

2. Calculation of electron and hole states. Our theoretical analysis is based on an $8 \times 8 \text{ k}$ P Hamiltonian $H_{8 \times 8}$ (Γ_6^c , Γ_8^v and Γ_7^r), which fully takes into account heavy-hole light-hole (HH-LH) mixing and nonparabolicity [5]. We use the axial approximation.

First we discuss the case $B = 0$. Here the in-plane wave vector $\mathbf{k}_{||}$ is a good quantum number and the eigenfunctions of $H_{8 \times 8}$ can be written as

$$\Psi_{\nu, \mathbf{k}_{||}}(\mathbf{r}) = e^{i\mathbf{k}_{||}\mathbf{r}} \sum_{j=1}^8 \xi_{\nu, \mathbf{k}_{||}}^j(z) u_{j0}(\mathbf{r}), \quad (1)$$

where $\xi_{\nu, \mathbf{k}_{||}}^j(z)$ are the spinor components of the envelope function of subband ν and $u_{j0}(\mathbf{r})$ are bulk band edge Bloch functions. We self-consistently solve the Poisson equation and the eigenvalue problem defined by $H_{8 \times 8}$ to obtain the Hartree potential, which is superimposed to the z dependent band edge energies [6,7]. The density-of-states effective mass is defined by [6,7]

$$\frac{m^*_{\text{DOS}}(E)}{m_0} = \frac{1}{\pi} \frac{\hbar^2}{2m_0} \int \delta[E - \mathcal{E}_\nu(\mathbf{k}_{||})] d^2\mathbf{k}_{||}. \quad (2)$$

In Fig. 1 we show m^*_{DOS} for the samples investigated by Yang *et al.* [2] and Scriba *et al.* [3], a 149 Å wide and a 125 Å wide InAs-AlSb QW with 2D electron density $N_s = 6.5 \cdot 10^{11} \text{ cm}^{-2}$ and $N_s = 1.41 \cdot 10^{12} \text{ cm}^{-2}$, respectively. Band parameters were taken from Refs. [8,9]. The most striking feature besides the Van Hove singularities at the subband edges [6] is the strictly linear

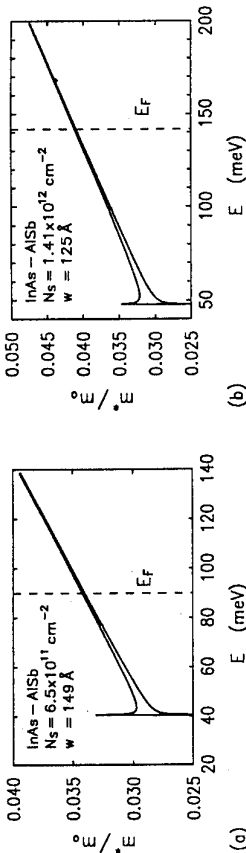


Figure 1: Density-of-states effective mass calculated (a) for the 149 Å wide and (b) for the 125 Å wide InAs-AlSb QW with 2D charge density $N_s = 6.5 \cdot 10^{11} \text{ cm}^{-2}$ and $N_s = 1.41 \cdot 10^{12} \text{ cm}^{-2}$, respectively, which were investigated experimentally by Yang *et al.* [2] and Scriba *et al.* [3]. dependence of m^*_{DOS} on energy E . This is due to the fact that basically our numerical calculations yield nonparabolic subband dispersion curves $\mathcal{E}_\nu(\mathbf{k}_{||})$, which can be parametrized by the well-known Kane formula $\mathcal{E}_\nu(\mathbf{k}_{||}) = \mathcal{E}_\nu(0) + \sqrt{\alpha_\nu^2 + \beta_\nu k_{||}^2} - \alpha_\nu$ with constants α_ν and β_ν [10]. For the calculation of Landau levels we use the Hartree potential obtained for $\mathbf{B} = 0$. The in-plane wave vector components k_x, k_y are replaced by Landau raising and lowering operators a^\dagger, a in the usual way [5,11]. Due to the axial symmetry the total Hamiltonian commutes with $\hat{F} = a^\dagger a + J_z$, which corresponds to the conservation of total angular momentum [5,11]. Therefore, the eigenfunctions of $H_{8 \times 8}$ can be written as

$$\Psi_{\nu, F}(\mathbf{r}) = \sum_{j=1}^8 |n_j = F - M_j\rangle \xi_{\nu, F}^j(z) u_{j0}(\mathbf{r}) \quad (3)$$

with Landau oscillators $|n\rangle$ and M_j is the z component of the angular momentum of $u_{j0}(\mathbf{r})$. In this basis the Hamiltonian falls into blocks for fixed eigenvalues $F = n_j + M_j$ of \hat{F} , which are treated in the same way as the subband problem for $\mathbf{B} = 0$, i.e., we use the numerical procedure described in Ref. [6].

In Fig. 2 (upper parts) we show the nonparabolic and spin-split Landau levels calculated for the samples of Yang *et al.* [2] and Scriba *et al.* [3].

3. Optical transitions and absorption. We consider the absorption of FIR radiation with an electric dipole field $\mathbf{E} = E_0 \hat{\mathbf{e}} e^{i\omega t}$, where $\hat{\mathbf{e}} = (e_x, e_y, e_z)$ denotes the polarization vector. Following Ref. [11] the transition probability between eigenstates $|s\rangle$ and $|t\rangle$ with eigenenergies E_s and E_t is given by

$$W_{st}(\omega) = \frac{\pi e^2 E_0^2}{2\hbar\omega^2} \left(\frac{\lambda_c E_s}{\hbar} \right)^2 |\langle s| \hat{e}_+ a + \hat{e}_- a^\dagger + e_z \lambda_c k_{||} |t\rangle|^2 [\delta(E_{st} - \hbar\omega) + \delta(E_{st} + \hbar\omega)], \quad (4)$$

where $E_{st} = E_s - E_t$, $e_\pm = (e_x \pm ie_y)/\sqrt{2}$ and $\lambda_c = \sqrt{\hbar/(eB)}$ is the cyclotron radius. Eq. (4) yields the selection rule $\Delta F = \pm 1$ for \pm polarization. The cyclotron mass is defined by

$$m_c^* = \frac{\hbar e B}{|\mathcal{E}_{\nu, F \pm 1} - \mathcal{E}_{\nu, F}|} \quad (5)$$

with $\mathcal{E}_{\nu, F}$ the energy of Landau level F of subband ν . In Eq. (5) in case of subband-Landau-level coupling (Sec. 4) we must consider also pairs of Landau levels with $\nu \neq \nu'$. In the limit $B \rightarrow 0$ the cyclotron mass equals $m^*_{\text{DOS}}(E)$ evaluated at the Fermi edge $E = E_F$. For 2D systems the absorption coefficient $\alpha(\nu)$ is defined as the energy absorbed per unit time

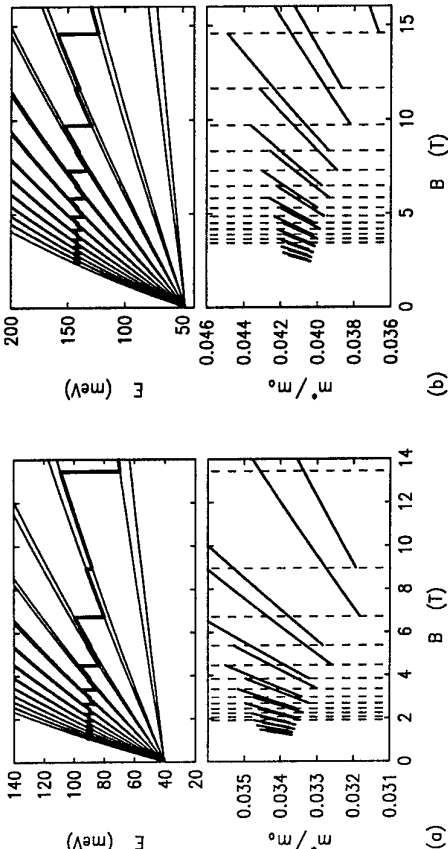


Figure 2: Landau levels (upper parts) and cyclotron masses (lower parts) calculated for the samples of Fig. 1. The dashed lines indicate integer filling factors.

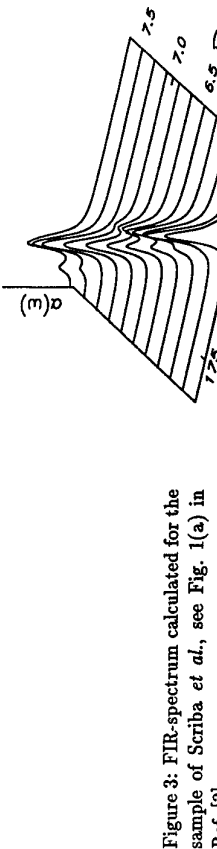


Figure 3: FIR-spectrum calculated for the sample of Scriba *et al.*, see Fig. 1(a) in Ref. [3],

$$\alpha(\omega) = \frac{2\pi}{n} \frac{e^2}{\hbar c} \sum_{s,t} (f_s - f_t) E_{st} |(s|e_s a + e_- a^\dagger + e_z \lambda_c k_z t)|^2 \delta(E_{st} - \hbar\omega), \quad (6)$$

with n the index of refraction and f_s, f_t are occupation factors, which depend on the 2D charge density and on the magnetic field. In our calculations we replace the δ -function by a Lorentzian broadening with the same phenomenological linewidth for all transitions. The absorption coefficient $\alpha(\omega)$ can be compared directly with experimental data.

In Fig. 2 (lower parts) we present the cyclotron masses calculated for the samples of Yang *et al.* and Scriba *et al.* Our parameter-free calculations are in excellent agreement with Fig. 2(b) of Ref. [2] and Fig. 3 of Ref. [3]. Fig. 3 shows $\alpha(\omega)$ for the sample of Scriba *et al.*, which also is in very good agreement with Fig. 1(a) of Ref. [3].

4 Subband-Landau level coupling. Due to their large separation in energy electron Landau levels (ν, F) and (ν', F) with $\nu \neq \nu'$ do not interfere with each other. It is known [12] that in case of electrons the subband-Landau level coupling requires a tilted magnetic field which breaks the axial symmetry. (Terms of cubic symmetry in H_{8x8} having the same effect are rather small [5].)

For hole states the complex valence band structure induces anticrossings between pairs of Landau levels (ν, F) and (ν', F) even in a magnetic field perfectly parallel to the growth direction. We found that these effects are the strongest either in slightly asymmetric double QW's or in QW's with [111] as growth direction, where the subbands are close together.

In Fig. 4 we show the hole Landau levels and cyclotron mass for a 100 Å wide GaAs-Al_{0.4}Ga_{0.6}As QW grown in [111] direction with $N_s = 5 \cdot 10^{11} \text{ cm}^{-2}$. Note that for [111] both the topmost and the first excited subband are HH-like at the subband edge. Two Landau levels of HH1 and HH2, which undergo an anticrossing at $B \approx 10 \text{ T}$ are marked by bold lines.

The author wishes to thank T. Darnhofer and U. Rössler for stimulating discussions. Work supported by the Graduiertenkolleg "Komplexität in Festkörpern: Phononen, Elektronen und Strukturen".

* Present address: Department of Physics and Astronomy, Vanderbilt University, Nashville, Tennessee 37235.

[1] See, e.g., J. C. Maan, in *Physics and Applications of quantum wells and superlattices*, Eds. E. E. Mendez and K. von Klitzing (Plenum, New York, 1987), p. 347, and references therein.

[2] M. J. Yang, R. J. Wagner, B. V. Shanabrock, J. R. Waterman, and W. J. Moore, Phys. Rev. B **47**, 6807 (1993).

[3] J. Scriba, A. Wixforth, J. P. Kotthaus, C. Bolognesi, C. Nguyen, and H. Kroemer, Solid State Commun. **86**, 633 (1993).

[4] N. R. Cooper and J. T. Chalker, Phys. Rev. Lett. **72**, 2057 (1994).

[5] H.-R. Trebin, U. Rössler, and R. Ranft, Phys. Rev. B **20**, 686 (1979).

[6] R. Winkler and U. Rössler, Phys. Rev. B **48** 8918 (1993).

[7] R. Winkler, J. Phys.: Condens. Matter **5**, 2321 (1993).

[8] Landolt/Börnstein, New Series Group III, Vol. 22a, Ed. O. Madelung, (Springer, Berlin, 1987).

[9] R. Winkler, U. Kunze und U. Rössler, Surf. Sci. **263**, 222 (1992).

[10] E. O. Kane, J. Phys. Chem. Solids **1**, 249 (1957).

[11] J. C. Hensel and K. Suzuki, Phys. Rev. B **9**, 4219 (1974).

[12] Z. Schlesinger, J. C. M. Hwang, and S. J. Allen, Phys. Rev. Lett. **50**, 2098 (1983)

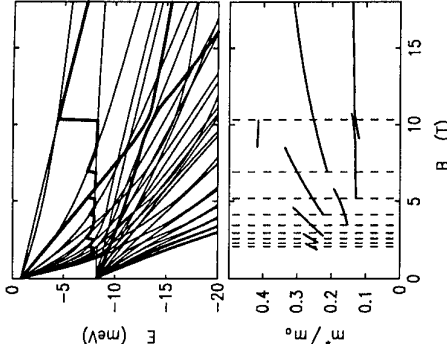


Figure 4: Self-consistently calculated hole Landau levels and cyclotron mass for a symmetrically *p*-doped 100 Å wide GaAs-Al_{0.4}Ga_{0.6}As QW grown in [111] direction with $N_s = 5 \cdot 10^{11} \text{ cm}^{-2}$.

Cyclotron Resonance in InAs Quantum Wells in Tilted Magnetic Fields

Yu.B.Vashyev, S.V.Ivanov, B.Ya.Melser, and S. D.Suchalkin
Ioffe Physical Technical Institute, 194021 St.Petersburg, Russia

P.Grambow
Max-Planck-Institut für Festkörperforschung, D-70569, Stuttgart,
Germany

Abstract

Cyclotron resonance (CR) experiments have been performed to study the two-dimensional gas in InAs-AlSb-GaSb structures in tilted magnetic fields. The CR spectra exhibit characteristic behavior associated with the trimerization of electron motion. New spectroscopic effects such as the appearance of additional lines in CR spectra and their strong dependence on electron density and tilt angle have been observed. The tilted-field CR technique allows us to probe the band bending of the InAs quantum wells.

Introduction

The technique of tilted magnetic fields have been used extensively to study transport and optical properties of two dimensional systems in the last 30 years [1]. This method is expected to be successful for investigation of the interaction of cyclotron resonance (CR) and spin resonance modes for systems with large values of effective g-factors such as in InAs [2]. Although the recent decade has produced a number of far-infrared (FIR) magneto-studies on InAs-Al_xGa_{1-x}Sb systems [3-6] but no CR experiments in tilted magnetic fields on InAs-AlSb-GaSb quantum wells (QW) have been reported.

In this paper we present results of FIR transmission measurements in tilted magnetic fields H for series of single InAs QWs with AlSb barriers.

Experimental

The samples used in the present work are asymmetric InAs-AlSb-GaSb single QW's grown by molecular-beam epitaxy. All the samples have the same well width of 200 Å and a cap GaSb layer width of 100 Å but different AlSb barrier widths of 100 Å, 300 Å, 20 Å for samples 2,3,4, respectively. Electron density in the InAs well depends on the AlSb barrier width. The constituent layer thicknesses were determined by high resolution transmission electron microscopy. CR measurements were performed using Fourier transform spectroscopy at different fixed angles α between the normal to the well plane and H direction. The sample transmission was always normalized by rationing it against a reference spectrum taken at H=0. The samples were wedged to avoid interference and supplied with contacts to measure magneto-resistance oscillations. The temperature was 2.2 K. The electron densities were determined from the oscillation periodicities and from transmission spectra using Drude model. Note that typical experimental recordings of

P_{xx} (not shown) are very similar to those observed in semimetallic InAs-GaSb structures [7]. The distinct features of the magneto-resistance traces confirm the presence of two separated layers of carriers: electrons in InAs and holes in GaSb in our structures.

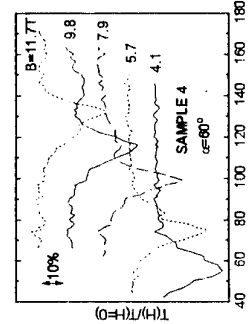


Fig.1a

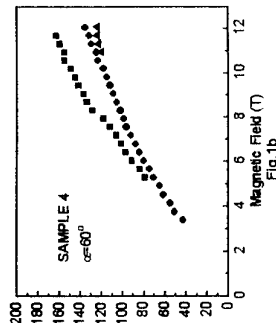


Fig.1b

Results and discussions

Figure 1a shows five traces of CR spectra obtained for sample 4 at various magnetic fields tilted at the angle $\alpha=60^\circ$. Similar series of CR spectra were obtained for all the samples. Detailed magnetic field dependence of the CR line position for the data from Fig.1a is shown in Fig.1b. It consists of the main CR line and two satellite lines at energies higher and lower than the CR energy. As tilt angle increases all peaks show non-linear dependence on magnetic field. Spectra with several peaks were found recently in perpendicular H for In-As-Al_xGa_{1-x}Sb [8] structures. The InAs-AlSb-GaSb system is very complicated and has many specific features which affect the CR spectra. It is known that CR line splitting may occur when CR line overlaps with another mode. The latter may be a crossing of Landau levels belonging to different subbands [9], cubic mode [10], and spin resonance mode [2]. Additionally the spectrum structure may be affected by the built-in electric field which may arise due to the difference in interface state concentrations and electron layers spaced on the distance equal to the AlSb barrier width. More detailed investigations concerning to the origin of CR splitting will be published elsewhere and here we would like to concentrate on the features of the main CR line.

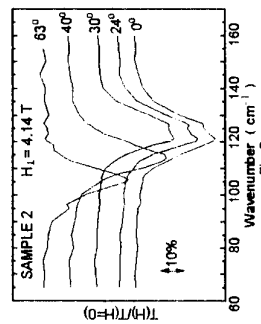


Fig.2

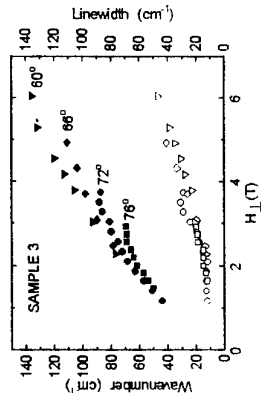


Fig.3

Figure 2 shows a set of spectra of the CR transmission in sample 2 in perpendicular and tilted H with the normal component $H_{\perp}=4.14$ T. One can see two groups of resonances with different magnetic field dependencies: at $\alpha < 30^{\circ}$ the CR positions are determined by H_{\perp} and therefore they are the same for all traces at small angles. In contrast the two resonances at $\alpha > 40^{\circ}$ do not obey the Hcos α dependence. There the CR peak positions are clearly shifted and correspond to the increase of the CR effective mass. This observation is in agreement with the results of Kukushkin *et al.* [12]. The effect is attributed to trimerization of electron motion by a strong parallel magnetic field [13]. The condition of the trimerization is the presence of a strong parallel component of magnetic field so that $\lambda_{||}=\lambda/\sin\alpha$ (λ is the magnetic length) is much less than the width of the well a . This condition is expected to be fulfilled at $\alpha > 40^{\circ}$ for the data in Fig.2. Evaluations show that the ratio $a/\lambda_{||}$ for the trace at $\alpha=40^{\circ}$ is approximately equal 4. Note an interesting feature of the spectra in Fig.2, namely, the satellite peak which occurs on the shoulder of the CR line at the wavenumber of $1.27/\text{cm}^{-1}$ in a perpendicular magnetic field does not change its position at small angles and disappears at the angles where the trimerization occurs. This fact also confirms that the parallel component of the magnetic field changes the effective mass of 2D electrons [1]. As far as the satellite peak is associated with the spin splitting at integer filling factors [5,6], we can attribute its disappearance to the increase of the effective mass in strong parallel magnetic field which results in shifting of Landau levels with respect to the Fermi energy. So this new configuration of the levels with another non-integer filling factor does not allow to observe the spin splitting of CR.

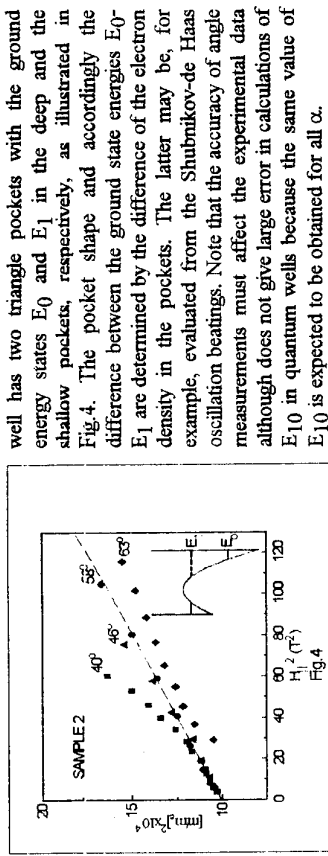
Detailed dependencies of the CR energy (solid symbols) versus the normal component of the magnetic field for sample 3 at different tilt angles are shown in Fig.3. One can see that the dependencies deviate from the straight line and furthermore at angles more than 72° one can clearly see a saturation which means that the CR energy is independent on H_{\perp} . The dependence of the linewidth (open symbols) depicted in the same figure is linear on H_{\perp} and independent on the angles. The data in Fig.3 also confirm the fact of innerization of the electron motion in a tilted H .

We use the method of tilted H to define the bottom of the subband in InAs quantum wells and follow the calculations performed recently by Kukushkin *et al.* [12]. Figure 4 shows the dependence of the square of the effective mass on the square of the parallel component of H derived from CR spectra for sample 2 at different tilt angles. Linear dependences are observed only at $\alpha > 40^{\circ}$. The dependences at α of 46° and 58° coincide except one point at 46° which is shifted due to influence of TO phonon absorption in InAs.

We can conclude that the linear dependence in Fig.4 is observed only for the parallel component of magnetic field larger than the perpendicular one. This is in accordance with the theory [14] which predicts the linear dependence for parallel magnetic fields:

$$m^2 = m_0^2 (1 + H_{\parallel}^2 / H_0^2), \text{ where } H_0 = E_1 / (m_e e \hbar).$$

The straight line in Fig.4 represents the fit by the equations with the $m_0 = 0.03118 m_e$ (m_e is the free electron mass) and $H_0 = 12.9$ T. From the fit one can find the intersubband energy E_{10} as 48 meV which is about two times less than expected for the 200 Å quantum well [15]. This evaluation gives important information on the conduction-band edge and the electron distribution in the well and may be attributed to the strong asymmetry of the quantum well. It is known that electrons in a wide quantum well may form two 2DES's at the well's sidewalls that results in formation of two coupled quantum wells. The asymmetry of the structures with the top GaSb cap layer is expected to result in considerable asymmetry of carrier localization at the direction normal to the layers: almost all the holes are located near only one barrier, the electrons in the well are forced to one of the interfaces and different band bending at the interfaces are realized. We suppose that the InAs



Summary

In conclusion this paper has presented several novel features of In-As-AlSb-GaSb systems studied in tilted magnetic fields. This method also has allowed us to evaluate intersubband energy in the InAs quantum well and make assumption on the presence of two triangle pockets of the bottom near interfaces with AlSb barriers.

Acknowledgments

We would like to thank V.I.Falko and K.v.Klitzing for very useful discussions. Yu.Vasilyev thanks the Max-Planck-Institut für Festkörperforschung for supporting and hospitality during his stay at Stuttgart.

References

- [1] T.Ando, A.B.Fowler and F.Stern, Rev.Mod.Phys. 54 (1982) 437.
- [2] V.I.Falko, Phys.Rev.Lett. 71 (1993) 141.
- [3] D.Heitmann, M.Ziesmann and L.J.Chang, Phys.Rev. B 34 (1986) 7463.
- [4] M.Lakrimi *et al.*, Solid St. Electron. 37 (1994) 1227.
- [5] J.Scriba *et al.*, Semicond. Sci. Technol. 8 (1993) S133.
- [6] M.J.Yang *et al.*, Phys. Rev. B 47 (1993) 6807.
- [7] D.M.Symons *et al.*, Phys.Rev. B 49 (1994) 16614.
- [8] I.Kono *et al.*, Phys.Rev. B 49 (1994) 12242.
- [9] A.D.Wieck *et al.*, Phys.Rev. B 39 (1989) 3785.
- [10] A.H.McDonald and C.Kallin, Phys.Rev. B 40 (1989) 5795.
- [11] D.L.Smith and C.Maitlhot, Rev.Mod.Phys. 62 (1990) 173.
- [12] I.V.Kukushkin, B.N.Shepel, O.V.Volkov and K.v.Klitzing, JETP Lett. 60 (1994) 556.
- [13] V.E.Kirichev, I.V.Kukushkin, V.B.Timofeev and V.I.Falko, JETP Lett. 51 (1990) 436.
- [14] H.Tang and P.N.Bucher, J.Phys. C: Solid State Phys. 21 (1988) 3313.
- [15] J.Lin-Chung and M.J.Yang, Phys. Rev. B 48 (1993) 5338.

Optical and Transport Studies of Highly Acceptor Doped GaAs/AlGaAs Quantum Wells

A.C. Ferreira, A. V. Buyanov, P.O. Holtz, B. E. Sernelius, B. Monemar,
Department of Physics and Measurements Technology
Linköping University, S-581 83 Linköping Sweden.

O. Mauritz, U. Ekenberg.
Department of Physics, Royal Institute of Technology,
S-100 44 Stockholm, Sweden

M. Sundaram, K. Campman, J.L. Merz and A.C. Gossard.
Center for Quantized Electronic Structures (QUEST),
University of California at Santa Barbara, CA 93016, USA.

We present a theoretical and experimental study of the properties on highly acceptor doped quantum wells (QWs), with doping levels varying from 9×10^9 up to $6 \times 10^{12} \text{ cm}^{-2}$. From variable temperature Hall measurements it is found that the temperature dependence of the mobility differs remarkably from p-type bulk GaAs as well as n-type QWs. For the moderately doped ($N_A < 3 \times 10^{11} \text{ cm}^{-2}$) sample, the mobility is almost constant with temperature up to $\approx 100 \text{ K}$, while the 2D hopping conduction dominates in the same temperature range for the degenerate samples. Steady state photoluminescence (PL) and PL excitation results are compared with theoretical predictions involving exchange and correlation effects for the electron-hole system and their interaction with acceptor ions. We finally report on the survival of the excitons well above the degenerate limit, due to the inefficient screening in the 2D case.

1. INTRODUCTION

The properties of quantum wells (QW's) doped with donors in the central part of the QW (CDQW's), up to the metallic limit, have recently been investigated [1,2]. For the case of p-doped bulk GaAs, B. Sernelius [3], has calculated the bandgap renormalisation in the high hole concentration regime including exchange and correlation effects of the electron-hole system together with the interaction with ionised impurities. However, no corresponding theoretical study of acceptor CDQW's structure has been presented in the literature up to now.

So far, most of the transport studies in 2D systems have been carried out on the modulation doped heterostructures, where the mobility was shown to be, in general, limited by the contributions to the scattering rate from acoustic and optical phonon modes, remote impurities, surface and interface roughness [4,5]. For n-type Si central doped QW's, it has been suggested

that mobility degradation is mainly induced by the increase of ionised-impurity scattering [6]. The enhancement of scattering was proposed to result from the larger overlap of the electronic wave function with impurities, a decrease in screening, and an increase in large angle scattering [6,7]. The transport properties of p-type 8-doped QW are even less studied.

2. THEORY

We have determined the hole subband dispersions by a self-consistent calculation of the Schrödinger and Poisson equations. The kinetic energy operator is given by the Luttinger-Kohn Hamiltonian [8] which includes the interaction between the heavy holes (HH) and the light holes (LH). We have applied the axial approximation [9] in which an average dispersion in the xy-plane is assumed. Current-conserving boundary conditions are fulfilled with the use of a

modified variational method described elsewhere [10].

The many-body (MB) effects are obtained in perturbation theory on the states determined before-hand, self-consistently neglecting the MB effects. We use the Rayleigh-Schrödinger perturbation theory or on-the-mass-shell perturbation theory [11]. The MB shifts are derived in a 2D approximation in the Random Phase Approximation with Hubbard's local field correction.

3. RESULTS AND DISCUSSION

The GaAs/AlGaAs quantum structure were grown by molecular beam epitaxy (MBE) on the semi-insulating (100) GaA substrate with a $0.35 \mu\text{m}$ buffer layer, including a smoothing superlattice, on top of the substrate. The growth temperature was nominally around 580°C . The central 3 \AA region of each GaAs QW was uniformly doped with Be at concentrations ranging from 9×10^9 to $6 \times 10^{12} \text{ cm}^{-2}$.

For the photoluminescence (PL) an photoluminescence excitation (PLE) measurement, an Ar⁺ ion laser was used to pump

a tunable titanium doped sapphire solid-state laser. The emitted light from the samples was focused on the slit of a 1-m double-grating monochromator and detected with a dry-ice cooled GaAs photomultiplier. All optical measurements presented were performed at 1.5 K . The transport studies were performed within the temperature range of 20 and 300 K in a superconductor solenoid "Oxford SM 2000". All the transport data presented in this paper were taken by a low-amplitude pulsed dc-current ($1-7 \text{ \mu A}$) technique. The magnetoresistance (MR) was measured under an applied magnetic field up to 5 T with direction normal to the plane of the CDQW's. Measurements were made in the dark on lithographically prepared Hall bars with six Au/Zn/Au ohmic contacts.

As illustrated in fig. 1, for a degenerate QW structure, not only the free exciton (FE) HH, but also the FELH can be monitored in PL. The relatively high FELH intensity in the PL spectrum, implies that there is a considerable LH population, i.e., the Fermi-level is close to the LH-band. Also the PLE

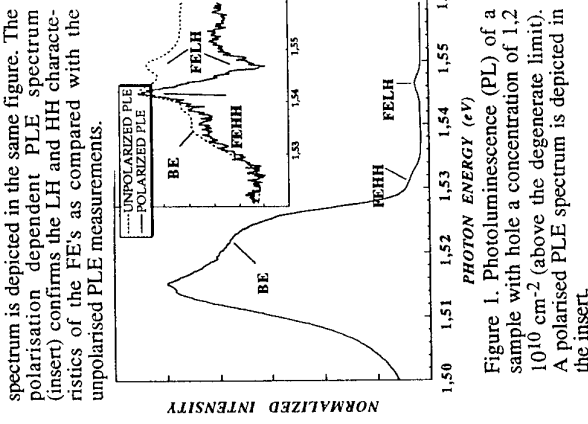


Figure 1. Photoluminescence (PL) of a sample with hole a concentration of $1.2 \times 10^{10} \text{ cm}^{-2}$ (above the degenerate limit). A polarised PLE spectrum is depicted in the insert.

In bulk GaAs, excitons are quenched at a hole concentration well below the metallic limit, around 10^{16} cm^{-3} , due to a strong screening of the electron-hole interaction [12]. It has earlier been found that excitons survive all the way up to the degenerate limit in n-type QW structures, due to the inefficiency of screening in a 2D system [2]. In our study of p-type QWs, we can confirm the same tendency and conclude that they can survive even above the degenerate limit. In fig. 2 we show the dependence of the FE's peak positions on the hole concentration. We compare our experimental data with two theoretical approaches. Our first theoretical model (A) includes only the band-filling effect (Burstein-Moss shift) while the theoretical model (B) includes in addition exchange-correlation effects, as mentioned in Sec. 2. The results of theory A deviates, as expected, from the experimental values when the MB effects become important. This effect is more clear when the

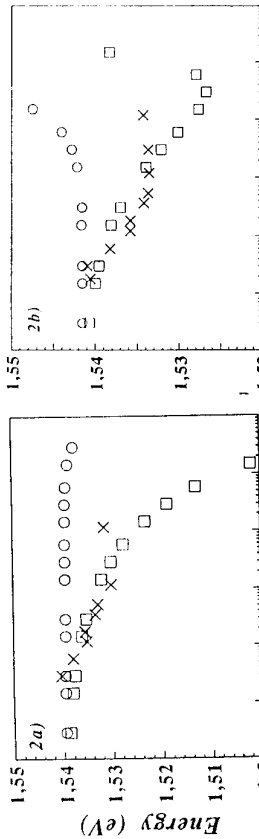


Figure 2. Peak position dependence of the free excitons (FE) heavy hole on the hole concentration in PL(a) and PLE(b). (X), (O) correspond to the experimental results of theory A and theory B respectively.

theoretical predictions are compared with the energy positions of the FEHH in PLE ($k=k_F$), where the theory A prescribes an increase of the exciton energy with hole concentration. The agreement with our second theoretical model is excellent. It should be pointed out that the exciton binding energy was assumed to be constant for all hole concentrations [13].

The variable temperature resistance data obtained for the degenerate CDQWs structures with Be concentrations of 1.5×10^{12} and $6 \times 10^{12} \text{ cm}^{-2}$, are presented in fig. 3. As can be seen, the resistance of these samples is practically constant between 100 and 300 K and indicate "degenerate conductivity". The resistance strongly increases with further decrease of the temperature and can be described by the law: $R=R_0 \exp(-eKT)$. As it is evident from fig. 3, the activation occurs within a rather narrow temperature range (70 to 120 K). The obtained values of e are $\sim 12 \pm 1$ and 8 ± 1 meV, respectively. For lower temperatures $R \propto \exp(T_0/T)^{1/3}$, and is known as Mott's law for noninteracting 2D carrier gas in the variable range hopping (VRH) regime [14].

The observation of a such temperature dependence of the conductivity in the degenerate system is quite remarkable. Firstly, the 2D-hopping conduction is usually observed below the metal-insulator transition after the formation of impurity bands. At low temperatures only the

4. REFERENCES

- [1] C.J. Harris, H. Kalt, B. Monemar and K. Köhler, *Surf. Sci.*, **263**, 462, 1991.
- [2] C.J. Harris, B. Monemar, H. Kalt and K. Köhler, *Phys. Rev. B* **48**, 4687, 1993.
- [3] B. Semmelius, *Phys. Rev. B* **34**, 5610, 1986.
- [4] P. Price, *Surf. Sci.* **143**, 145, 1984.
- [5] V. Walukiewicz, *J. Appl. Phys.* **59** 3577, 1986; *Phys. Rev. B* **31**, 5557, 1985.
- [6] (a) W. Ted Masselink, *Phys. Rev. Lett.* **66**, 1513, 1991 ; (b) *Appl. Phys. Lett.* **59**, 694, 1991.
- [7] B.K. Ridley, *Sol. Stat. Elec.* **34**, 111, 1991.
- [8] J.M. Luttinger and W. Kohn, *Phys. Rev.* **97**, 869, 1955 and J.M. Luttinger, *Phys. Rev.* **102**, 1030, 1956.
- [9] U. Ekenberg and M. Altarelli, *Phys. Rev. B* **32**, 3712, 1985.
- [10] M. Altarelli, *Phys. Rev. B* **28**, 842, 1983.
- [11] T.M. Rice, *Annals of Physics* **31**, 100, 1965.
- [12] J. Shah, R.F. Leheny, and W. Wiegmann, *Phys. Rev. B* **16**, 1577, 1977.
- [13] S. Nojima, to be published in *Phys. Rev. B*.
- [14] N.F. Mott, G.A. Davis, *Electronic Processes in Non-Crystalline Materials* (Clarendon, Oxford, 1979).
- [15] Q. Ye, B.I. Shklovskii, A. Zrenner, *Phys. Rev. B* **41**, 8477, 1990.
- [16] D.C. Look, D.C. Walters, M.O. Manastash, *Phys. Rev. B* **42**, 3578, 1990.

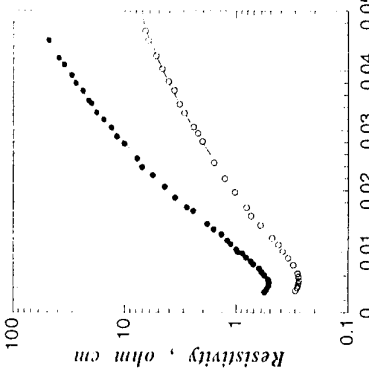


Figure 3. Resistivity vs. reciprocal temperature for samples with $p=6 \times 10^{12}$ (○) and $3 \times 10^{12} \text{ cm}^{-2}$ (●). The solid line models the VRH-transport with $T^{-1/3}$ slope.

Mobile excitons and Fermi edge singularities in an interacting 2D electron gas

J.A.Brum^(a,b), S.Brown^{c,d}, P.Hawrylak^a, J.F.Young^c and Z.Wasilewski^a

(a) Institute for Microstructural Sciences, National Research Council of Canada

(b) Instituto de Física, UNICAMP, Brasil

(c) Dept. of Physics, University of British Columbia, Canada

(d) School of Physics, University of New South Wales, Australia

Abstract

We present theoretical and experimental results on the evolution of the threshold absorption of a 2D electron gas as a function of electron density. We pay particular attention to the low density regime where the spectrum evolves from an exciton to a Fermi edge singularity. The many-body origin of the Moss-Burstein shift is emphasized.

I. INTRODUCTION

We present here theoretical and experimental results on Fermi edge singularities (FES) [1-4] in narrow (50 Å) modulation-doped quantum wells (QW). The non-perturbative treatment of FES addresses two remaining difficulties: the effect of electron-electron interactions and of a finite hole mass. The use of narrow QW separates the heavy- and light hole contributions to absorption and allows for a careful experimental study of the absorption position and lineshape as a function of carrier density. We concentrate here on extracting the position of the FES threshold as a function of electron density n_s , i.e., on the energy required to add an exciton to the two dimensional electron gas (2DEG). This gives a microscopic interpretation of the blue shift - the Moss-Burstein shift- observed in experiments.

II. EXPERIMENT

The samples investigated are 50 Å modulation doped multiple quantum wells with electron densities ranging from $n_s = 0$ to $n_s = 2 \times 10^{11} \text{ cm}^{-2}$. The samples were removed from their substrates using an epitaxial lift-off technique and subsequently Van der Waals bonded to glass substrates to allow absorption measurements. The only variation from sample to sample is the modulation doping density $N_D = 0, 0.5, 1.0, 2.0, 4.0 \times 10^1 \text{ cm}^{-3}$ giving nominal sheet densities of $n_s = 0, 0.25, 0.5, 1.0, 2.0 \times 10^{11} \text{ cm}^{-2}$. Numerical modelling of the samples shows that δ-doping near to the surfaces prevents electrons in the wells from being removed by surface states and so reduces well to well density variations. The samples show hh and

lh features in absorption well separated from each other. This allows a clear determination of the origin of the absorption lineshape.

The absorption measurements were performed at 5 K using a constant flow cryostat with optical windows and a Fourier transform spectrometer. To eliminate Fabry-Pérot interference effects in the measurements the sample was tilted at Brewster's angle relative to a polarised beam of white light.

Figure 1 shows the evolution of the absorption data, for different electron concentrations. The $n_s=0$ sample has strong hh and lh excitation peaks as well as a clear hh-continuum edge and a weaker lh-continuum edge. As in previous studies, when the electron density is increased the excitonic features weaken dramatically and broaden asymmetrically on the high energy side. The large hh-lh splitting (27 meV) allows the lineshape of the hh peak for the doped samples to be investigated independently of the lh peak. A remarkable feature of the data is that for finite n_s , the broadening of the hh peak is significantly greater than either the Fermi energy ($E_F = 3.5 \text{ meV}$ for $n_s = 1.0 \times 10^{11} \text{ cm}^{-2}$) or the exciton binding energy ($E_X = 12 \text{ meV}$). Also of interest is the complete lack of a continuum "edge" even for the lowest doping density. These facts constitute strong evidence for a many-body origin of the lineshape and lineposition, even at relative low n_s .

III. THEORY

We consider an initial Hamiltonian of N electrons in the conduction band and a final Hamiltonian of N+1 electrons and a valence hole. To treat the FES nonperturbatively and the effect of finite hole mass perturbatively the final Hamiltonian is transformed into a new set of relative coordinates via a canonical transformation: $\vec{\eta}_i = \vec{r}_i - \vec{r}_h$, $i = 1, \dots, N+1$, $R_{\text{tot}} = [m_h \vec{r}_h + m_e \sum_{i=1}^{N+1} \vec{r}_i]/M_{\text{tot}}$, where $M_{\text{tot}} = (N+1)m_e + m_h$ is the total mass and m_e and m_h are electron and hole effective masses. The effect of electron-electron interactions of relative particles is treated in local density approximation (LDA), with an LDA potential extracted from the screened exchange Σ_{SEX} and coulomb hole Σ_{CH} self-energy operators [4]. The final Hamiltonian can be finally written as a sum of the Kohn-Sham Hamiltonian H_0 of noninteracting Kohn-Sham particles and a momentum dependent interaction V, proportional to the inverse of the hole mass:

$$H = H_0 + V = \sum_{i=1}^{N+1} \left[\frac{1}{2\mu} \vec{p}_i^2 + V_{ch}(\eta_i) + V_{H}(\eta_i) + V_{xc}(\eta_i) \right] + \frac{1}{2m_h} \sum_{i < j, i,j=1}^{N+1} (\vec{p}_i \vec{p}_j) \quad (1)$$

$V_H(\eta_i)$ is the Hartree potential, $1/\mu = 1/m_e + 1/m_h$ and \vec{p} and $\vec{\eta}$ are momenta and positions of electrons relative to the valence hole. We first solve the Kohn-Sham equations self-consistently on a finite disk. The total final-state energy E_{tot}^f of $N+1$ relative particles on a disk of radius R and density $n_s = (N+1)/\pi R^2$ is given in terms of Kohn-Sham eigenvalues as :

$$E_{\text{tot}}^f(N+1, \mu) = \sum_{i=1, \text{occupied}}^{i=N+1} E_{\lambda_i} - \frac{1}{2} \int d\vec{p} n(\eta) V_H(\eta) + \int d\vec{p} n(\eta) (E_{exc}(n) - V_{exc}(n)), \quad (2)$$

$V_{exc}(n) = \delta[n E_{exc}(n)]/\delta n$, $E_{exc}(n)$ is the exchange-correlation energy per electron. The energy to add an exciton is the difference in total energies between final and initial states

plus a correction due to pairwise momentum dependent interaction V . We treat V as a perturbation and evaluate its contribution in the Hartree-Fock approximation. The final expression for the energy of adding an exciton E_X to the electron gas is:

$$E_X = E_{tot}^f(N+1,\mu) - E_{tot}^i(N,\mu) + \sum_{i=1}^{N+1} \frac{k_i^2}{2m_h} - \sum_{i,j=1, i \neq j}^{N+1} \frac{<\lambda_i | \vec{p} | \lambda_j > <\lambda_j | \vec{p} | \lambda_i >}{2m_h} \quad (3)$$

The first two terms describe the energy to add an exciton with a localised hole to a gas of electrons with mass μ . The last two terms give a correction due to finite hole mass m_h . In addition, for a mobile hole we should add a hole self-energy Σ_{CH} i.e. $E_X \rightarrow E_X + \Sigma_{CH}$ [5]. In the absence of electron-hole interactions the last term in Eq. 3 vanishes and the exciton energy is $E_X = \frac{k_\mu^2}{2\mu} + \Sigma_{SEX} + \Sigma_{CH}$. For the infinite hole mass case the last term vanishes altogether.

Figure 2 shows the calculated chemical potential μ , the renormalized single-particle band gap, E_g , the bound state energy, E_b , and the absorption threshold $\omega_0 = E_X$, as a function of the carrier concentration measured in terms of the Fermi energy of the free carriers ($E_F = 2\pi n_D a_0^2$), for the infinite hole mass. The chemical potential increases with the carrier concentration, as expected. The band gap shifts downwards as a consequence of the band gap renormalization. The binding energy remains fairly constant ($(E_b - E_g) \simeq -0.35 Ry$). Finally, the absorption threshold does not change significantly from the bare exciton energy for the carrier concentrations considered here.

Figure 3a shows the calculated absorption threshold as a function of the carrier concentration for the infinite and finite hole mass cases. We observe a clear blue shift when the finite hole mass is considered. Clearly the hole recoil is at the origin of the Moss-Burstein shift. It is important, however, to stress that the origin of this shift is a combination of several effects, namely the electron-hole interactions and the electron-electron interactions in the presence of a mobile hole. Figure 3b shows the measured absorption peak. We observe a qualitative agreement with the theory. To achieve a quantitative agreement we have to extend our calculations to include the finite QW width.

Parts of this work were supported by the Natural Science and Engineering Research Council of Canada, the Institute for Microstructural Sciences National Research Council of Canada, and the CNPq (Brazil).

REFERENCES

- [1] C. Delalande et al, Phys. Rev. Lett. **59**, (1987), 2690.
- [2] M. S. Skolnick et al, Phys. Rev. Lett. **58**, (1987), 2130.
- [3] T. Uenoyama and L.J. Sham, Phys. Rev. Lett. **65**, (1990), 1048.
- [4] P. Hawrylak, Phys. Rev. **B44**, 3821 (1991).
- [5] T. Uenoyama and L.J. Sham, Phys. Rev. **B39**, (1989), 11044.

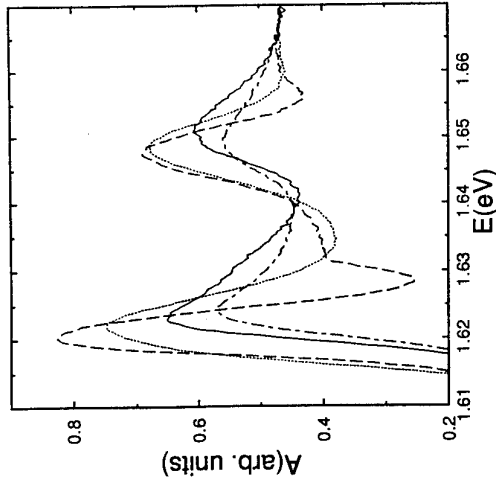


FIG. 1. Absorption spectra for a 50 Å multiple-quantum well with $n_s = 0$ (dashed line), $n_s = 0.5 \times 10^{11} \text{ cm}^{-2}$ (dot-dash line), $n_s = 1 \times 10^{11} \text{ cm}^{-2}$ (full line) and $n_s = 2 \times 10^{11} \text{ cm}^{-2}$ (dot-dash line).

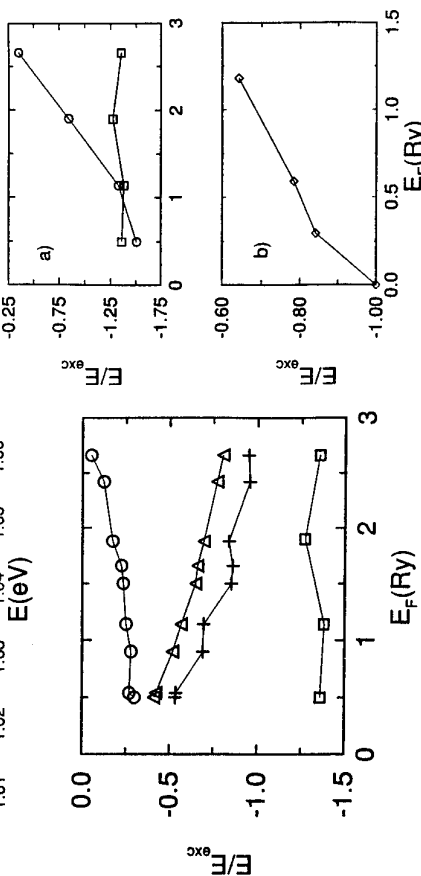


FIG. 2. The dependence of the absorption threshold ω_0 (squares), highest occupied level μ (circles), the bottom of the band, namely the second occupied level E_g (triangles), and bound-state energy E_b (crosses), as a function of Fermi energy E_F .

FIG. 3. (a) Theoretical absorption threshold ω_0 as a function of the Fermi energy E_F for a localised (infinite mass) hole (squares) and for a heavy hole with an effective mass of $0.45m_e$ (circles) and (b) experimental absorption peak position (diamonds) as a function of the Fermi energy E_F . The energies were scaled to the 2D exciton binding energy in (a) and the experimental exciton binding energy in (b).

Excitons in Dense Two-dimensional Electron Gas at a Semiconductor Surface

P.D. Altukhov
Laboratory of electronic semiconductors, A.F. Ioffe Physical-Technical Institute,
Politekhnicheskaya st. 26, St.-Petersburg 194021, Russia.

Abstract

The Fermi-edge singularity, increasing with increasing 2-D electron density, is observed in recombination radiation line of 2-D electrons and nonequilibrium holes in luminescence spectra of [100] silicon MOS-structures. A new effect of anisotropic paramagnetic reduction of the Fermi-edge singularity proves, that this singularity transforms itself into emission line of real excitons in dense 2-D electron gas before the second electron subband occupation.

Recombination radiation line (S-line) of 2-D electrons and 2-D nonequilibrium holes, bound to the [100] electron layer by the electron polarization attraction, is observed in luminescence spectra of silicon MOS structures [1]. The spectral position of the high energy edge of the S-line is very close to the spectral position of the bound exciton line and varies weakly with increasing electron density n_s . The S-line spectrum reproduces the 2-D electron energy spectrum at $n_s \approx (0.5 \div 1.5) \cdot 10^{12} \text{ cm}^{-2}$. In this region surface electron-hole pairs exist as a 2-D two-layer electron-hole plasma and the additional 2-D hole layer is formed [1]. At low surface pair density holes in the second layer are nongenerate and occupy the lowest quantum level with spin momentum $\pm 3/2$ in the hole quantum well. At $n_s < 0.5 \cdot 10^{12} \text{ cm}^{-2}$ surface pairs exist as excitons due to weak k-space occupation and weak screening [1]. At $n_s > 1.5 \cdot 10^{12} \text{ cm}^{-2}$ with increasing n_s a strong intensity enhancement arises at the high energy edge of the S-line (Fig. 1.2) due to an increase of the radiative transition probability for the electron levels close to the Fermi level. This Fermi-edge singularity at the beginning of its formation can be explained in terms of multiple electron-hole scattering [2] as a result of enhancement of the 2-D electron propagated wave functions at the Fermi level near a hole. Such enhancement of the electron-hole interaction may be also strongly stimulated by the appearance of the 2-D electron wave function tails in the region of the 2-D hole layer for the electrons close to the Fermi level [3], which becomes possible at large electron Fermi energy E_F before the second electron subband occupation.

The Fermi-edge singularity (excitonic resonance) in the S-line spectrum becomes very strong and narrow before the second electron subband occupation, which occurs at $n_s > 6.4 \cdot 10^{12} \text{ cm}^{-2}$ [4]. At the same time a new narrow line (S'-line) arises at the high energy edge of the S-line at low temperatures [1] (Fig. 1.2). The observed behaviour of the luminescence spectra has to be attributed to formation of real excitons in the system of surface pairs at $n_s = (3 \div 6) \cdot 10^{12} \text{ cm}^{-2}$. In this region excitonic resonance in the S-line spectrum corresponds to surface excitons, whose electrons originate from the lower electron subband.

Such S-exciton, strongly interacting with 2-D electron gas, can be considered as a bound state of a hole and its many-particle cloud of the electronic polarization. The S'-line corresponds to surface excitons, whose electrons originate from upper subbands. These excitons, arranged away from the 2-D electron layer, have the lowest energy [1]. A new effect of anisotropic paramagnetic reduction of the excitonic resonance in a tilt magnetic field proves the existence of real excitons in dense 2-D electron gas (Fig. 1.2,3). This effect is caused by a decrease of

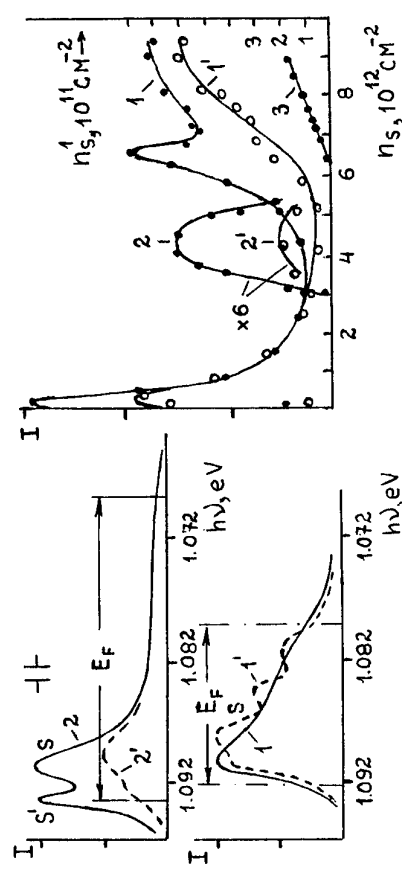


Fig.1. Recombination radiation spectra of 2-D electrons and nonequilibrium holes in [100] silicon MOS structures at $T=1.9 \text{ K}$ and excitation level $10^3 \text{ w} \cdot \text{cm}^{-2}$, TO-repllicas. 1,1' - $n_s = 2.2 \cdot 10^{12} \text{ cm}^{-2}$; 2,2' - $n_s = 4.3 \cdot 10^{12} \text{ cm}^{-2}$. The transverse magnetic field $B=B_{\parallel}$; 1,2 - $B=0$; 1',2' - $B=B_{\perp}=6.7 \text{ T}$.

Fig.2. The dependence of the intensity of the S-line maximum 1 (1,1') and the S'-line intensity (2,2') upon n_s at $T=1.9 \text{ K}$. The magnetic field $B: 1 - B=0$ and $B=B_{\parallel}=5.8 \text{ T}$; 1' - $B=B_{\perp}=5.8 \text{ T}$; 2 - $B=0$; 2' - $B=B_{\perp}=5.8 \text{ T}$ and $B=B_{\parallel}=5.8 \text{ T}$. 3 - the electron density n_s in the second subband.

hole g-factor anisotropy resulting from very small value of the 2-D hole g-factor in the longitudinal magnetic field.

The problem of electron paramagnetism of excitons in dense 2-D electron gas is very similar to the problem of impurity paramagnetism in metals [5]. Observation of the Curie paramagnetism of electrons in excitons is possible when the spin-correlation frequency $\hbar\omega_K$ for an electron in an exciton and 2-D electrons is lower than the electronic temperature. High spin-correlation frequency suppresses the electron paramagnetism of excitons. This spin-correlation frequency is analogous to the Kondo frequency for magnetic impurities in metals. The electron exchange between excitons and 2-D electrons results in a finite electron lifetime of excitons and defines an energy range of electron states at the Fermi level, which contribute considerably to the formation of an enhanced electron density near a hole. This enhanced electron density consists of an electron density of the exciton and an enhanced 2-D electron density. Hence, the amplitude of the excitonic resonance includes the "excitonic amplitude", resulting from recombination of a hole and its own electron, and the "enhanced amplitude", resulting from

where I_0 is the excitonic resonance intensity at $B=0$, $B^*=\mu_0 B/2kT$, μ_0 is the Bohr magneton, T is the temperature, $g=2$ is the electron g-factor, g_h is the hole g-factor, w_- and w_+ are the radiative transition probabilities. w_+ takes into account the recombination of a hole with spin momentum -3/2 and all electrons with spin momentum +1/2, including an electron in the exciton, w_- takes into account only the recombination of the hole with spin momentum -3/2 and 2-D electrons with spin momentum +1/2. The experiment (Fig.3) gives values of g_h and $w_-w_+^{-1}$. A deviation of the magnetic field dependence from the Curie behaviour is assumed to exist at $n_s \approx (3 \pm 3.5) \cdot 10^{12} \text{ cm}^{-2}$.

The "S"-line reveals the isotropic paramagnetic intensity reduction (Fig.2). The hole states in the S'-excitons are not splitted due to large distance of the S'-excitons from a surface, and the hole g-factor in the S'-excitons is isotropic. The second electron subband occupation is accompanied by disappearance of the S-line and S'-line and appearance of a new line [4], which does not reveal considerable paramagnetic reduction.

The formation of real excitons in dense 2-D electron gas can be explained as a result of a selforganization of surface electron-hole pairs, possessing an opportunity to choose their distance from a surface, which minimize the screening and the pair energy. This selforganization becomes essential for the case of [100] electron layer, when the surface pair energy is very close to the bulk exciton energy and combination of surface and bulk states causes the existence of two new excitonic states at a silicon surface.

References

- [1] P.D. Altukhov, A.A. Bakun, A.A. Rogachev and G.P. Rubtsov, *Fiz. Tverd. Tela* (Leningrad) 3560 (1988) 30.
- [2] G.D. Mahan, *Phys. Rev.* 882 (1967) 153.
- [3] S.V. Meshkov, *Zh. Eksp. Teor. Fiz.* 2252 (1986) 91.
- [4] P.D. Altukhov, A.A. Bakun and A.A. Kozlov, *Fiz. Tverd. Tela* (St.-Petersburg) 3747 (1992) 34.
- [5] A.J. Heeger in: *Solid State Physics*, Vol. 23, Eds. F. Seitz, D. Turnbull, H. Ehrenreich (Academic Press, New York and London, 1969) p.283.

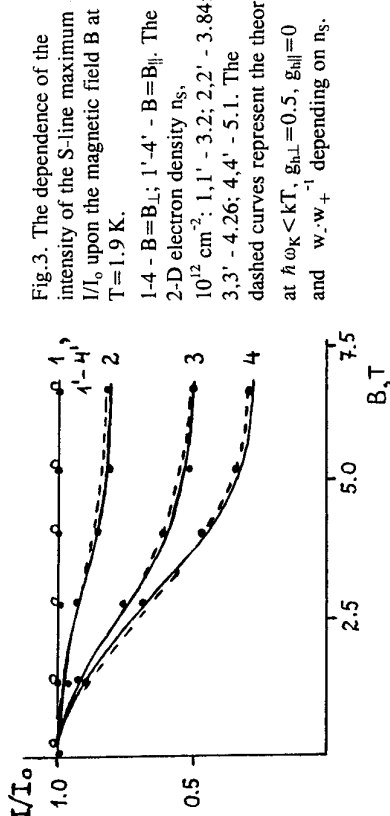


Fig.3. The dependence of the intensity of the S-line maximum I/I_0 upon the magnetic field B at $T = 1.9 \text{ K}$.
 1-4 - $B = B_{\perp}$; 1'-4' - $B = B_{\parallel}$. The 2-D electron density n_s , 10^{12} cm^{-2} ; 1, 1' - 3/2; 2, 2' - 3.84; 3, 3' - 4.26; 4, 4' - 5.1. The dashed curves represent the theory at $\hbar\omega_K < kT$, $g_{h\perp} = 0.5$, $g_{h\parallel} = 0$ and $w_-w_+^{-1}$ depending on n_s .

recombination of the hole and 2-D electrons. The "excitonic amplitude" is eliminated from the S-line spectrum by the paramagnetic reduction. So, the S-line spectrum represents the radiative recombination of holes and 2-D electrons in a strong transverse magnetic field (Fig.1). The magnetic field dependence of the paramagnetic reduction of the excitonic resonance shows the Curie behaviour at $n_s > 3.5 \cdot 10^{12} \text{ cm}^{-2}$ (Fig.3). In this case the dependence of the excitonic resonance intensity I on the magnetic field B is described by the formula

$$\frac{I}{I_0} = \frac{2}{1 + w_- \cdot w_+^{-1}} \frac{c\hbar[(3g_h - g)B^*] + w_- \cdot w_+^{-1}c\hbar[(3g_h + g)B^*]}{c\hbar[(3g_h - g)B^*] + c\hbar[(3g_h + g)B^*]} \quad (1)$$

HIGH DENSITY, SPATIALLY SEPARATED ELECTRON/HOLE PLASMAS IN MIXED TYPE I-TYPE II GaAs/AlAs HETEROSTRUCTURES

P. D. Buckle^a and P. Dawson.

Department of Pure and Applied Physics,

University of Manchester Institute of Science and Technology

Manchester, M60 1QD. UK.

Abstract

By the choice of appropriate layer thicknesses in the GaAs/AlAs materials system it is possible to create a mixed type I-type II band alignment. In such structures rapid electron scattering leads to a long lived spatially separated electron/hole plasma. In this paper we report measurements on such a structure and present evidence that it is possible to optically excite a two dimensional electron gas at the GaAs/AlAs interface.

Introduction

It is well established [1] that both type I and type II band alignments can be achieved in the GaAs/AlAs multilayer structures by controlling the alignment of the X conduction band minima in the AlAs and the Γ conduction band minima in the GaAs via the respective layer thicknesses. In structures where the GaAs layer thickness is less than 35 Å and the AlAs layer thickness is greater than 16 Å the Γ electron state in the GaAs layer lies above the X minima in the AlAs [2]. By utilising this phenomena a so called mixed type I - type II structure may be created [3] by the choice of appropriate AlAs and GaAs layer thicknesses. In mixed type I-type II structures optically excited electrons in the thin GaAs quantum well (<35 Å) are able to rapidly scatter via the X states in the AlAs barrier to the lower energy Γ states in the wider GaAs quantum well. The time for this scattering to occur is of the order of ps [4]. However at low temperatures the holes excited in the thin quantum well can only relax to the lower lying heavy hole states in the wide quantum well by tunnelling through the AlAs barrier. The combination of large heavy hole effective mass, large valence band barrier height and the choice of a suitable barrier thickness can lead to tunnelling times of many μ s. Thus a long lived spatially separated electron/hole plasma can be created. Because the density of the spatially separated electron/hole plasma is controlled by the heavy hole tunnelling time [5] large densities can be achieved by very low excitation power densities. In such mixed type I-type II quantum well structures it was shown [5] that exciton bleaching could be achieved with optical power densities as low as a few mW/cm² when the AlAs layer thickness was 102 Å.

In the sample studied here, the wide quantum well is replaced by a thick (1000 Å) layer of GaAs which approximates to a bulk layer of GaAs. This provides us with the possibility of optically creating a two dimensional electron gas (2DEG) at the GaAs/AlAs interface. On setting up the spatially separated electron/hole plasma by optical excitation where the narrow 25 Å well is occupied by free or loosely localised holes and the electrons have scattered to the thick GaAs layer we have an analogous situation to a modulation doped heterostructure. In such structures

the resulting electric field produces band bending at the GaAs/barrier interface and the subsequent production of a high mobility 2DEG. Such 2DEG structures have been extensively studied [6][7], not only the novel transport phenomena that can occur but also because they offer us the opportunity to study optically many body phenomena in semiconductors. If it is possible to set up a 2DEG optically it may offer new opportunities for the study of optical and transport phenomena in particular it should be possible to tune the carrier density and subband structure by varying the intensity of the optical excitation source.

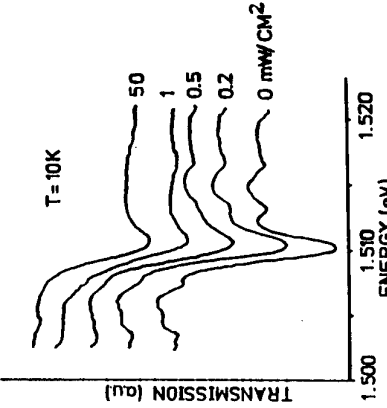
Experimental Details

The sample details have been reported elsewhere [5] except in the sample investigated here the 68 Å quantum well was replaced by 1000 Å of GaAs and the mixed type I-type II structure was repeated three times. For the pump/probe transmission experiments the sample was processed by polishing and etching and then mounted on a sapphire disk on the cold finger of a variable temperature (6-300 K) cryostat. The sample was simultaneously illuminated by pump light from a CW dye laser whose photon energy was greater than the energy of the $n=1$ electron/heavy (e-hh) exciton of the 25 Å quantum well and by chopped (130 Hz) white light. For the luminescence measurements, the unprocessed samples were mounted on the cold finger of the cryostat and illuminated by a chopped (230 Hz) light from a CW dye laser. The transmission spectra and luminescence spectra were analyzed by a double grating spectrometer and detected with a thermoelectrically cooled GaAs photomultiplier tube. A phase sensitive detection method was used to process the signal.

Results and Discussion

In figure 1 we show the zero pump power transmission spectrum at a temperature of 10 K which exhibits a dip at 1.511 eV. We ascribe the dip at 1.511 eV to be due to absorption by the 1S exciton of the thick GaAs layer. The energy of this feature at 10 K should be 1.515 eV [8], the discrepancy of 4 meV is ascribed to strain introduced by the sample processing and by mounting it on the sapphire disc. Figure 1 also shows the effect of increasing the pump power. At pump power densities of less than 1 mW/cm² we can see a significant reduction in the strength of the exciton absorption which denotes a sizeable population of free carriers in the bulk GaAs. As the pump power density is increased the exciton absorption is reduced in strength even further. As the pump power is increased beyond 10 mW/cm² we do not observe any further reduction of

Figure 1 Pump/probe transmission spectra at various pump power densities



the exciton absorption. It should be stressed that it was not possible to observe any exciton bleaching when the pump photon energy was tuned below the $n=1$ (e-hh) exciton energy of the 25Å quantum well. This indicates that a long lived spatially separated electron hole plasma was set up in the structure.

The luminescence spectra are shown in figure 2 for various excitation power densities. No luminescence was observed at all from the narrow quantum well region. This indicates a very fast non radiative path for optically excited carriers. This is ascribed to the rapid loss of electrons from the quantum well to the thick GaAs region via the X states in the AlAs barrier. At the lowest pump power density we observe a single line with a peak energy of 1.514 eV. As the pump power density is increased we observe two distinct phenomena. Firstly a lower energy feature (labelled M) emerges at a pump power density of 5 mW/cm² which as the pump power is increased continues to move to lower energy. At the highest pump power density used (400 mW/cm²) the peak position of M is 1.508 eV. Secondly as the pump power is increased we see the emergence of a series of sharp lines centred around 1.515 eV. We believe these spectral features are consistent with the occurrence of sufficient band bending at the GaAs/AlAs interface for the production of a confined electron state localised at the interface. In figure 3 we show a typical band diagram for the structure studied with an injected sheet hole density of $\sim 10^{11}/\text{cm}^2$. We assign the features seen in the PL spectra as follows. As can be seen from the figure the band bending at the interface allows the first ($n=1$) confined electron state to be localised at the interface. The higher lying ($n>1$) states extend over the bulk of the GaAs. Thus we assign the spectral feature M to recombination involving electrons at the confined state at the interface with holes that thermalise to the central part of the curved valence band as

illustrated in figure 3. As the pump power is increased the band bending at the interface will increase causing a corresponding decrease in the energy of M. At a sufficiently high carrier density we might expect sufficient band filling to occur in the interface subband so that the higher lying more delocalised states become occupied. We assign the sharp features seen at higher energy to recombination involving electrons in the higher lying states with holes that have thermalised to the central part of the GaAs. The lack of corresponding spectral detail in the transmission spectra is ascribed to broadening produced by the sample processing and mounting. The assignment of the high

energy luminescence lines is consistent with preliminary time resolved photoluminescence measurements where we observed a decay time $\sim 500\mu\text{s}$ when monitoring the intensity of line M as a function of time after switching off the excitation pulse. Thus a pump power density of 20mW/cm^2 would result in an estimated sheet carrier density at the interface of $10^{11}/\text{cm}^2$ which would result in a corresponding Fermi energy of 5 meV which is sufficient for the higher lying states to be occupied.

Conclusion

In conclusion we have demonstrated the formation of a long lived spatially separated electron/hole plasma in a mixed type I-type II structure where the thick layer of GaAs is 100Å thick. Detailed spectroscopic measurements have provided evidence for the formation of a 2DEG at the GaAs/AlAs interface. This type of structure opens up the opportunity of studying the carrier density dependent optical and transport properties of a 2DEG in a single structure.

Acknowledgement

We would like to acknowledge useful discussions with Dr I Galbraith. The samples used in this study were grown by Prof. C.T. Foxon.

*Department of Electrical and Electronic Engineering, UMIST.

References

- [1] P. Dawson, Optical and Quantum Electronics 22 (1990) S231.
- [2] K. J. Moore, P. Dawson and C. T. Foxon, Phys. Rev. B 38 (1988) 3368.
- [3] P. Dawson, I. Galbraith, A. I. Kucharska and C. T. Foxon, Appl. Phys. Lett. 58 (1991) 2889.
- [4] J. Feldmann, M. Preis, E. O. Gobel, P. Dawson, C. T. Foxon and I. Galbraith, Sol. State Comm. 83 (1992) 245.
- [5] I. Galbraith, P. Dawson and C. T. Foxon, Phys. Rev. B 45 (1992) 13499.
- [6] M.H. Meynadier, J.Orgonasi, C.Delalande, J.A.Brum, G.Bastard, M.Voos, G.Weimann, W.Schilapp, Phys. Rev. B 34 (1986) 2482
- [7] G. Abstreiter, Surface Science 98 (1980) 117-125.
- [8] E. H. Bogardus and H. B. Bebb, Phys. Rev. Lett. 176 (1968) 993.

Figure 2. Photoluminescence spectra as a function of excitation power density.

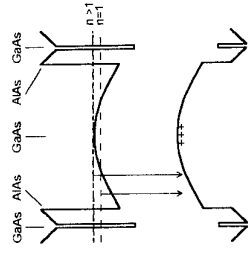
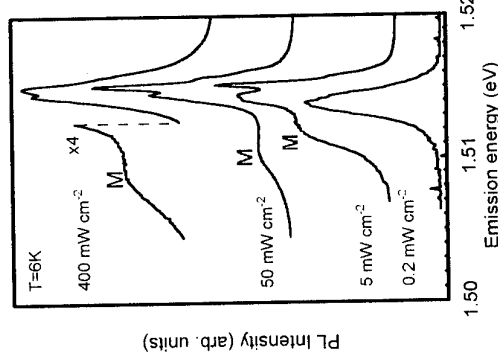


Figure 3. Schematic band profile with optical excitation of a mixed type I/II structure.

Investigation of g-factors, Zeeman splittings, exchange interactions and field-dependent spin relaxation in III-V quantum wells.

N.J.Traynor*, M.J.Snelling**, R.T.Harley*,
R.J.Warburton* and M.M.Hopkinson**.

* Physics Department, Southampton University, UK.
** Clarendon Laboratory, Parks Road, Oxford, UK.

Sektion Physik, Ludwig-Maximilians Univ., München, Germany.
EPSRC III-V Semiconductor Facility, Sheffield University, UK.

Abstract

Splittings of the $n=1$ heavy-hole exciton spin states in zero and small magnetic fields for several type I quantum well systems are investigated with μeV precision using cw photoluminescence techniques. Field dependent spin relaxation rates are also obtained.

Introduction

Symmetry dictates that in (001)-grown III-V quantum wells the $n=1$ heavy hole exciton consists of four spin states separated into two doublets, $J=1$ and $J=2$, by electron-hole exchange interaction [1,2]. $J=1$ is allowed with circular polarisation, σ^+ and σ^- , but $J=2$ is forbidden. Zeeman splittings for (001)-magnetic field occur without admixture of $J=1$ and $J=2$ [1-4]. These splittings are less than inhomogeneous broadening, necessitating special measurement techniques [5,6].

We describe 2K cw polarised PL measurements on several type I systems which give the sign and magnitude of Zeeman splittings with μeV precision. The measurements can also give the exchange interaction revealing strong enhancement relative to bulk [7]. Finally, based on time-resolved measurements at zero field [8], we extract the field-dependence of spin-relaxation rates.

Zeeman splitting of excitons in III-V systems

The PL was separated into σ^+ and σ^- components using a 50 kHz photoelastic modulator and linear polariser and the splittings were determined to $\pm 2\mu\text{eV}$ using a curve fitting method [3]. Figures 1-4 show results for the 3 material systems with theoretical calculations using an eight band k.p model.

Agreement for GaAs/AlGaAs is good up to 7.5 nm. The disagreement for wider wells may be because the light-hole (LH) - heavy-hole (HH) splitting becomes comparable to the exciton binding energy, leading to significant mixing of LH and HH states via the coulomb potential not included in our band calculation approach; in this system the LH - HH splitting is a maximum near 4nm. We note that Bauer and Ando [9] obtained good agreement for wide wells using an effective mass approximation including coulomb interaction. Non-linearity in the splitting is produced by repulsion of the LH and HH states with increasing field, the effect being strongest where the LH-HH splitting is least in zero field, eg for wide GaAs/AlGaAs wells. Only the spin-up HH state interacts while the spin-down state does not.

Inclusion of strain for InGaAs provides an additional test of k.p theory, and we find satisfactory agreement, within the constraints of well width and concentration uncertainty. Here the light holes are type II so that the LH - HH splitting is reduced by quantum confinement

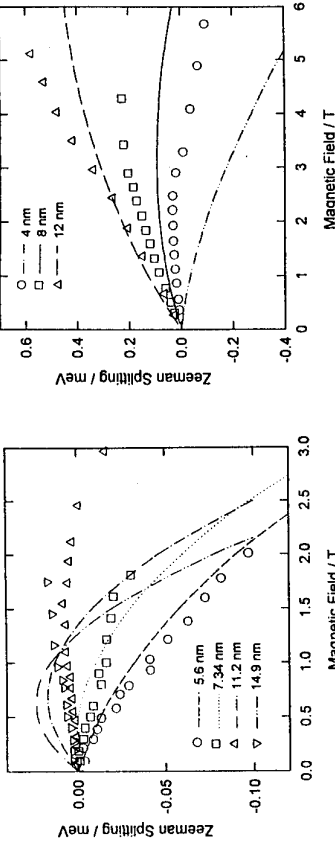


Figure 1 - Zeeman Splitting of $n=1$ HH excitons in $\text{GaAs}/\text{Al}_{0.34}\text{Ga}_{0.66}\text{As}$ multiple quantum wells

Figure 2 - Zeeman Splitting of $n=1$ HH excitons in $\text{In}_{0.075}\text{Ga}_{0.925}\text{As}/\text{GaAs}$ quantum wells

of the HH in contrast to GaAs/AlGaAs. Consequently there is no curvature due to the mixing of LH and HH states in wide wells whereas the effect is strong for narrow wells.

Figure 4 shows Zeeman data for GaNP/AlnP wells. Calculations have not yet been performed for this system but the data shows similar trends to the other systems, with the addition that there is an interesting change of both sign and curvature of Zeeman splitting at intermediate well widths, and also evidence of level crossing signals (see 4nm curve), [5,6].

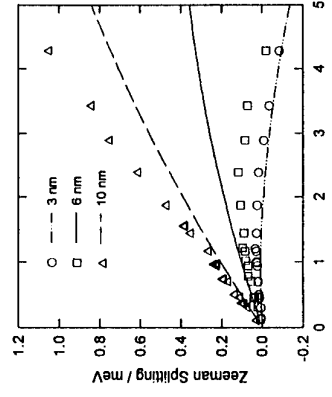


Figure 3 - Zeeman Splitting of $n=1$ HH excitons in $\text{In}_{0.11}\text{Ga}_{0.89}\text{As}/\text{GaAs}$ quantum wells

Figure 4 - Zeeman Splitting of $n=1$ HH excitons in $\text{Ga}_{0.52}\text{In}_{0.48}\text{P}/\text{Al}_{0.52}\text{In}_{0.48}\text{P}$ quantum wells.

Exchange interactions and spin-relaxation

Figure 5 shows the circular polarisation of integrated PL from GaAs/AlGaAs samples

reflecting the population difference of $J=1$ states. Excitation is into the continuum so excitons form at equal rates into each of the four spin states and populations are determined by the balance of spin relaxation and recombination from $J=1$ states. $J=1$ to $J=2$ transitions involve either electron or hole spin-flip whereas transitions between $J=1$ states require simultaneous (ie exciton) spin-flips [8]. We assign the uniform trend in polarisation to partial thermalisation of populations of the $J=1$ states and the peaks to extra population fed from one of the $J=2$ states where it crosses a $J=1$ state. Level crossings occur at $B = \Delta/g_h\beta$ and $\Delta/g_e\beta$ [1,2] where Δ is the exchange splitting in zero field (see inset in figure 5) and g_h and g_e are the hole and electron g-factors from the low field Zeeman splitting [3]. Since $|g_h| > |g_e|$ the observed peaks correspond to $B = \Delta/g_h\beta$, giving the points in figure 6. The curves in figure 6 are calculations [2] of exchange enhancements normalised to a bulk splitting of $6 \mu\text{eV}$, in agreement with the measured value ($10 \pm 5 \mu\text{eV}$) [7].

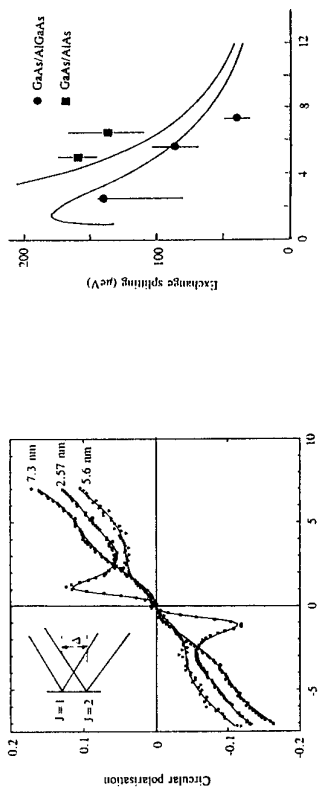


Figure 5 - Circular polarisation of PL from GaAs/AlGaAs MQWs of various widths. Inset:- exciton level structure.

The curves in figure 5 are fitted steady-state rate-equation solutions in which the recombination rate, τ_r^{-1} , is assumed field-independent. We write the transition probability from level i to level j as a sum of two terms, respectively 'direct' one-phonon processes [10] and zero-phonon transitions between quasidegenerate states

$$W_{ij} = \frac{\alpha_{ij} |E_j - E_i|^3}{\exp[(E_j - E_i)/kT] - 1} + \frac{\beta_{ij} \Gamma_y^2}{(E_j - E_i)^2 + \Gamma_y^2}$$

The E 's are the energies of the four exciton levels and the α 's, β 's and Γ 's adjustables of which there are three independent sets representing exciton, hole and electron spin transitions. The Γ 's are set close to inhomogeneous splittings of the levels found in independent experiments [2]. We then restrict the remaining parameters so that, in zero field, exciton spin-relaxation is faster than hole or electron relaxation [8]. Figure 7 shows the best-fit inter-level transition rates $\tau_{ij}^{-1} = W_{ij} + W_{ji}$; a single curve corresponds to exciton (ex) spin-flip whereas hole (h) and electron (e)

flips each produce transitions between two pairs of states.

With many adjustables the details of figure 7 may not be reliable but we can safely conclude that the exciton rate falls rapidly with field at low fields and that the peak in one hole spin-flip

rate at the level crossing produces the maximum in polarisation. The underlying reason for the rapid fall in exciton spin-flip rate is that at zero field it exceeds the recombination rate [8] and if this were also true at higher fields the $J=1$ level populations would be fully thermalised giving far higher values of polarisation than are observed and suppressing the level crossing signal. The fitting also shows that the $J=1$ states are higher in energy than the $J=2$ states.

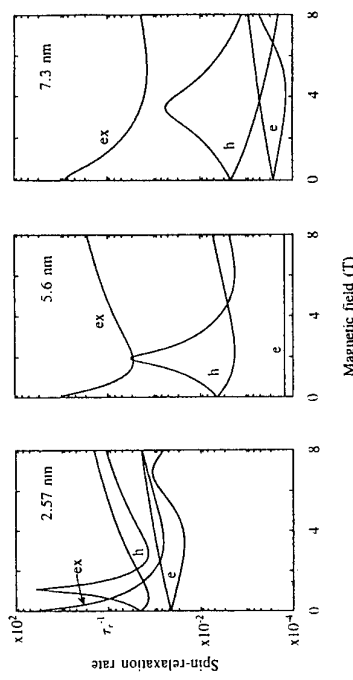


Figure 7 - Spin relaxation rates for the three MQW samples, derived from polarisation of PL

References

- [1] H.W.van Kesteren, E.C.Cosman, W.A.J.A.van der Poel and C.T.Foxon, Phys. Rev. B **41**, 5283 (1990).
- [2] E.Blackwood, M.J.Snelling, R.T.Harley, S.R.Andrews and C.T.Foxon, Phys. Rev. B **50**, 14246 (1994).
- [3] M.J.Snelling, E.Blackwood, C.J.McDonagh, R.T.Harley and C.T.Foxon, Phys. Rev. B **45**, 3922 (1992).
- [4] N.J.Traynor, R.T.Harley and R.J.Warburton, Phys. Rev. B **51**, 7361 (1995).
- [5] S.Bar-Ad and I.Bar-Joseph, Phys. Rev. Lett **66**, 2491 (1991); A.P.Heberle, W.W.Ruhle and K.Ploog, Phys. Rev. Lett. **72**, 3887 (1994).
- [6] H.Wang, M.Jiang, R.Merlin and D.G.Stein, Phys. Rev. Lett. **69**, 804 (1992).
- [7] W.Ekardt, K.Losch and D.Bimberg, Phys. Rev. B **20**, 3303 (1979).
- [8] A.Vinattieri, J.Shah, T.C.Damen, D.S.Kim, L.N.Pfeiffer, M.Z.Maialle and L.J.Sham, Phys. Rev. B **50**, 10868 (1994).
- [9] G.E.W.Bauer and T.Ando, Phys. Rev. B **37**, 3130, (1988).
- [10] R.Orbach, Proc. Roy. Soc. (London), **A264**, 458 (1961).

THE D⁻ BOUND EXCITON OBSERVED IN GaAs/AlGaAs QUANTUM WELLS

P.O. Holtz^a, Q.X. Zhao^a, B. Monemara^a, M. Willander^a, K. Campman^b, M. Sundaram^b, J.L. Merz^b, and A.C. Gossard^b

^a Departments of Physics and Measurement Technology, Linköping University,
S-581 83 Linköping, Sweden

^b Center for Quantized Electronic Structures (QUEST), University of California at Santa Barbara, CA 93106, USA

Abstract

We report on a well-defined peak, the F-line, in photoluminescence (PL) spectra interpreted as the exciton (D⁻X) bound at the negatively charged donor, the D⁻ state, in GaAs/AlGaAs quantum wells. The F-line exhibits an enhanced intensity with increasing magnetic field due to an increasing wave function overlap caused by the enhanced localization of the hole and electrons bound at the donor. An enhanced PL intensity together with a red shift is also observed for the F-line with increasing excitation intensity, i.e. a larger excitation binding energy with increasing thermal activation energy. The observed properties of the F-line with a striking dependence on the excitation intensity, magnetic field and temperature are all consistent with the observation of the exciton bound at the D⁻ triplet state. Another associated higher energy peak, the E-line, is observed in PL excitation spectra. The E-line has a similarly strong magnetic field and temperature dependence and is interpreted as the exciton bound at the D⁻ singlet state.

Introduction An impurity related system, which has been the source of considerable interest recently, is the D⁻ center, a neutral donor binding a second electron to form the negatively charged D⁻, i.e. an analogue of the H⁻ ion in atomic physics. Due to its fundamental character, there are numerous theoretical calculations on the D⁻ system [1-4], but the experimental results reported are scarce [5]. The two electrons bound at the donor form two states; a singlet and a triplet state. Only the lowest energy singlet state has been experimentally observed for GaAs/AlGaAs quantum wells (QWs) in far-IR magneto-optical measurements up to now [5, 6]. There is no experimental observation of either the triplet D⁻ state nor the D⁻ bound exciton reported so far to the best of our knowledge.

Experimental

The samples used in this study have been grown by molecular beam epitaxy (MBE). On top of the semi-insulating GaAs substrate, the following sequence of layers were grown: A 0.3 μm GaAs buffer layer, a 25 period superlattice (20 Å/20 Å GaAs/AlAs), 10 periods of 200 Å wide GaAs quantum wells (QWs) between 150 Å wide barriers and finally a 100 Å GaAs cap layer. The barrier layers are either 150 Å wide standard Al_{0.3}Ga_{0.7}As barriers or similar Al_{0.3}Ga_{0.7}As barriers, but with 2 monolayers (ML) AlAs at the QW/barrier interfaces. Both sets of samples exhibit similar PL spectra but with an increased line width for the standard interface structures. Both undoped and intentionally Si-doped structures were used in this study. The doped QWs were either center or edge doped with Si in a 40 Å wide dopant layer with a Si donor concentration of $1 \times 10^{16} \text{ cm}^{-3}$. Photoluminescence (PL) and PL excitation (PLE) measurements

were carried out, also in the presence of a magnetic field up to 16 T. A tunable Ti:Sapphire cw solid state laser was used as the excitation source.

Results and discussion

In the PL spectra of the donor doped samples, we observe in addition to the free excitons (FE), exciton peaks related to the shallow donor. In the center doped samples, the "normal" donor bound exciton (BE) is red shifted by about 1.7 meV relatively the FE, while the corresponding red shift in the edge-doped sample measures to about 1.1 meV. The edge donor BE can be observed also in the undoped samples due to segregation of the silicon impurities at the interfaces during the growth [7]. In fact, the undoped samples exhibit even better quality PL spectra than the doped samples, since the spatial distribution of interface donors is more well defined than in the intentionally doped samples.

We will now focus our attention on an additional novel feature appearing in the BE energy range, which can be monitored in these samples at about 1.3 meV below the FE (see Fig. 1), but dependent on the experimental conditions, as will be expounded below. One fingerprint of this novel feature, hereafter denoted the F-line, is its excitation intensity dependence. The F-line exhibits a red-shift with increasing excitation intensity (Fig. 1) i.e. a larger exciton binding energy with increasing excitation density. From the intensity dependence of the nominally undoped sample with AlAs ML interfaces, as illustrated in Fig. 1, it appears that there are two components involved in this exciton peak: The F-line is favoured at high excitation conditions, while the F-line is lower excitation intensity. The F-line is interpreted as an exciton (D⁻X) bound at the negatively charged donor, the D⁻ state, as will be further expounded below. The F-line intensity dependence is consistent with the D-X interpretation, since it has earlier been concluded by J P Cheng *et al* [5] from far infrared magneto-optical measurements that the D⁻ binding energy increases with increasing electron concentration.

Magnetic field dependent PL measurements show that the F-line exhibits

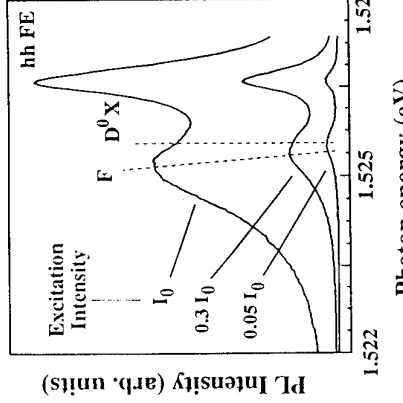


Fig. 1 Excitation intensity dependent PL spectra of QW structures with AlAs ML interfaces at zero magnetic field.

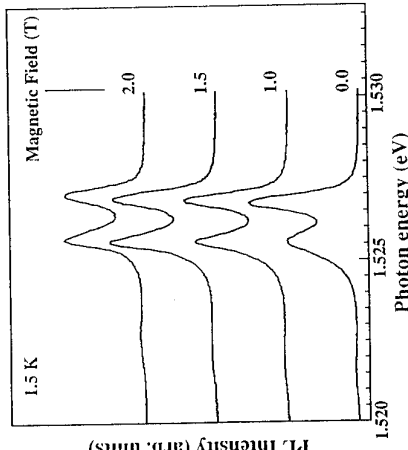


Fig. 2 Magnetic field dependence of the F-line in the PL spectra for the same sample as used in Fig. 1

a diamagnetic shift as expected for an excitonic transition. Another fingerprint of the F-line is its strong intensity dependence on the applied magnetic field already at small fields as illustrated in Fig. 2. The enhanced PL intensity with increasing field is due to an increasing wave function overlap caused by the enhanced localization of the hole and electrons bound at the donor. In accordance, the derived thermal activation energy for the F-line is magnetic field dependent. The stronger dependence on the magnetic field for the F-line relatively D^0X is also in agreement with earlier far infrared measurements [1, 5] from which it was concluded that the rate of binding energy increase with the applied magnetic field was faster for the D^- than for the D^0 .

When detecting the F-line in a PLE spectrum, a weak but novel feature (denoted E in Fig. 3) appears between the heavy hole (hh) and light hole (lh) FEes. There is no intrinsic transition in this region, and we instead conclude that the E-line is correlated with the F-line.

This correlation is proven in Fig. 4, which shows the selective PL spectrum, when the E peak is resonantly excited together with a reference spectrum with non-resonant excitation. This resonance behavior enables us to perform more sensitive temperature dependent PL and PLE measurements. From such investigations, we can conclude on a third fingerprint of the F-line (and E-line): The intensity exhibits a striking temperature dependence, and is quenched already at about 4 K. This small activation energy is consistent with a weakly bound D^- ground state for the BE transition.

The recombination of the D^- BE has three electrons and one hole in the initial BE state and the charged D^- donor with its two electrons in the final state. According to the fundamental $J-i$ coupling approximation, the lowest D^- BE states have $J = 2$ and $i = 1$, angular momentum, respectively. These states will split further in the reduced symmetry of our doped QW structures. The final D^- donor state with its two electrons form singlet and a triplet state with the singlet state at lowest energy. According to basic dipole transition rules, there are two allowed transitions: (1) The $J = 2$ state of the D^- BE as the initial state and the triplet D^- donor ground state as the final state and (2) the $J = 1$ state of the initial D^- BE state together with the singlet D^- as final state. Although the selection rules become relaxed due to the lowered symmetry, these transitions will presumably dominate. Based on these assumptions we propose that the F-line observed in PL originates from the recombination of the triplet D^- donor associated exciton (transition (1)), while the higher energy E-line observed in PLE is due to the singlet D^- donor associated exciton (transition (2)). Due to a very small energy splitting between the triplet and singlet states of the D^- donor, already a small temperature increase will reduce the thermal population of the D^- singlet ground state. The additional thermal activation needed to cause the dissociation of the D^- to the D^0 neutral donor is limited due to the small D^- binding energy. For

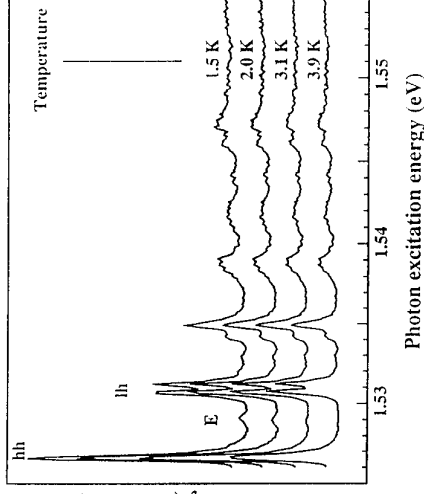


Fig. 3 PLE spectra of the same sample as used in Fig. 1 measured at 1.5 T and at four different temperatures. The detection energy is resonant with the F peak energy.

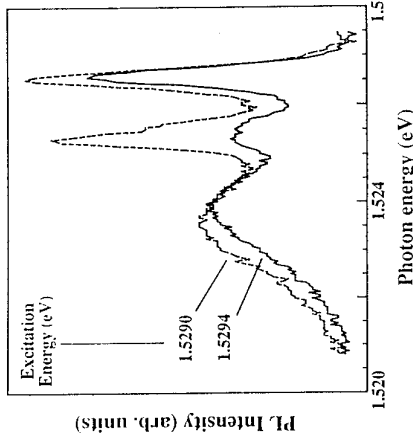


Fig. 4 Selective PL spectra measured at 1.5 T with excitation resonant with the E peak (1.5290 eV) compared with the non-resonant excitation (1.5294 eV). These spectra clearly demonstrate the correlation between the F-line and E-line.

instance, the binding energy of the D^- singlet state is less than 0.8 meV at 1.5 T according to theoretical calculations [5].

Summary

The observed properties of the F-line with a striking dependence on the excitation intensity, magnetic field and temperature are all consistent with the observation of the exciton bound at the negatively charged D^- donor triplet state confined in a GaAs/AlGaAs QW. The associated higher energy peak, the E-line, also exhibits a striking magnetic field and temperature dependence and is interpreted as the exciton bound at the D^- singlet state.

References

- [1] T. Pang and S.G. Louie, Phys. Rev. Lett. 65, 1635 (1990)
- [2] S. Huant, S.P. Naja and B. Etienne, Phys. Rev. Lett. 65, 1486 (1990)
- [3] S. Holmes, J.P. Cheng, B.D. McCombe and W. Schaff, Phys. Rev. Lett. 69, 2571 (1992)
- [4] P. Hawrylak, Phys. Rev. Lett. 72, 2943 (1994)
- [5] J.P. Cheng, Y.J. Wang, B.D. McCombe and W. Schaff, Phys. Rev. Lett. 70, 489 (1993)
- [6] S. Huant, A. Mandray, J. Zhu, S.G. Louie, T. Pang and B. Etienne, Phys. Rev. B48, 2370 (1993)
- [7] K. Inou et al, Appl. Phys. Lett. 46, 973 (1985)

RESONANT TUNNELLING THROUGH D^- STATES

J.G.S. Lok, A.K. Geim and J.C. Maan
High Field Magnet Laboratory, Research Institute for Materials,
University of Nijmegen, 6500 GL Nijmegen, Netherlands

I.Marmorkos and F.M.Peeters
Department of Physics, University of Antwerp, B-2610 Antwerpen, Belgium

N.Mori, L.Eaves, P.McDonnell, M.Henini and P.C.Main
Department of Physics, University of Nottingham, Nottingham NG7 2RD, England

We have studied tunnelling through Si donors incorporated in the quantum well of double barrier resonant tunnelling devices. In addition to a resonance associated with the ground state of a single donor (1s level), a novel donor-related resonance at a smaller binding energy is observed in high magnetic fields where it becomes dominant over the 1s resonance. We attribute this novel feature to a D -minus state of a shallow donor.

A shallow, hydrogenic atom which binds an extra electron is the simplest “many-body” electronic system. This system (D^- ion) has attracted significant interest, both theoretical and experimental, since the early days of quantum mechanics and is a basic test for our understanding of electron-electron interactions. The behaviour of D^- states becomes more prominent in a confined (quasi-2D) geometry and in strong magnetic fields where research has focused in recent years [1]. So far, all experimental information about D^- states has come from optical measurements.

In this paper we report a novel donor-related resonance in tunnelling spectroscopy which is attributed to the D^- state. The resonance is observed in double barrier resonant tunnelling devices (RTD) with intentional δ -doping by Si and appears in addition to a resonance due to tunnelling through the ground state (D^0 , 1s state) of the shallow donors [3]. The additional peak is clearly visible in high magnetic fields where its amplitude becomes significantly larger than the amplitude of the D^0 peak. The novel resonance cannot be explained by tunnelling via excited states of a shallow donor which are expected to yield a much smaller tunnel current and also a stronger field dependence of the peak position. The observed behaviour is in agreement with that expected from a D^- centre in high magnetic fields.

We have studied double-barrier RTD with δ -doping in the centre plane of the quantum well by Si donors with concentrations of 4×10^{19} and $8 \times 10^{19} \text{ cm}^{-2}$. The thickness of both $(\text{Al}_0\text{Ga}_{0.9})\text{As}$ barriers is 5.7 nm and the width of the quantum well is 9 nm. We also grew control devices without δ -doping. For the exact layer composition and experimental details we refer to papers [2,3].

Figure 1 shows a schematic energy band diagram of our devices under bias. A current flows when the energy of an electron in a two-dimensional electron gas (2DEG) formed at the emitter interface is resonant with a state in the quantum well. As the bias is increased, energy levels in the well pass through the resonant condition leading to a sequence of resonances in the I(V) characteristics. The lowest 2D subband in the well gives rise to the main resonance (Fig.1). The δ -doping gives rise to an additional resonance at smaller biases which originates from

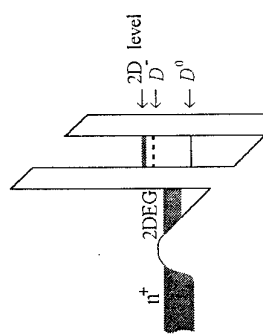
tunnelling through the localised ground state (D^0) of shallow donors (see Figure 2). This D^0 resonance has been studied earlier [2] and corresponds to electron flow via Si donors which switch between D^+ and D^0 states in the tunnelling process.

We focus below on a novel resonant feature which emerges at biases close to the onset of the main resonance when a strong magnetic field is applied. This resonance is shown in Figure 2 where it is clearly seen in the first derivative of a typical I(V) characteristic and also visible as a weak shoulder on the I(V) curve itself ($T=1.2\text{K}$). The peak amplitude increases linearly with increasing Si concentration in the well and the peak is absent in the undoped devices indicating unambiguously that the state is donor-related. The novel resonance has been observed in magnetic fields both parallel and perpendicular to the direction of the tunnel current. However, in the latter geometry resonant tunnelling is strongly field-dependent, making quantitative analysis more complicated. For brevity, we will discuss only the results for the parallel field orientation. Although the second donor-related resonance partially overlaps the onset of the main resonance, it can be traced in both I(V) curves and their derivatives for all magnetic fields above 6T. For a quantitative analysis, we have subtracted the background current due to the onset of the main resonance using I(V) characteristics obtained on the undoped devices in the same magnetic fields. The dashed curve in Fig.2 shows an example of the resulting resonance after such a subtraction. We emphasise that the essential behaviour of the donor resonance is not sensitive to details of the subtraction procedure.

Figure 3 plots peak positions and amplitudes of both donor resonances as a function of magnetic field for two samples with different doping concentrations. Also, two solid curves are shown that are measured at a constant current corresponding to the onset of the D^0 and the new resonances. These curves demonstrate that the onset of the donor resonance behaves somewhat differently from the peak. With increasing magnetic field the D^0 resonance exhibits a shift to lower biases which corresponds to a significant increase in its binding energy and indicates that this state is strongly localised [2]. In contrast, the second donor resonance is only weakly field dependent. In fields above 6T its peak position stays virtually constant while its onset shifts slowly to lower biases (i.e. the resonance broadens). Note that the position of the main resonance is essentially field independent for this field direction [2]. As the magnetic field increases, the amplitude of the second donor resonance increases first and saturates at higher fields while the 1s resonance decays monotonically. At 20T, the novel peak becomes nearly 10 times stronger than the D^0 resonance. The bias position, weak field dependence and relatively large amplitude of the novel resonance, all indicate a large spatial extent of the corresponding donor state.

The observed weakly bound level may be due to either excited states of a donor or a more complicated, many-body state such as D^- . To distinguish between these two possibilities

Figure 1. Schematic energy-band diagram for our RTD's under bias.



we have calculated the binding energies and tunnelling probabilities for states bound to the lowest Landau level in our structures following the procedure discussed in ref. [4]. The main results are shown in Figure 4 which plots the field dependence of the binding energies for 1s, 2p, 3d⁻² and D⁰ levels. The experimental data are presented by circles. A factor of 0.27 due to electrostatic leverage [3] has been used to convert the applied bias into energy. In the high field limit, the field dependence of the D⁰ peak is in excellent agreement with our calculations for the 1s state. As far as the second donor-related peak is concerned, only the D⁻ level gives a reasonable fit for both the absolute value of the binding energy and its field dependence (see Fig.4). In low fields, there is generally no agreement between the calculated and experimental dependences for the both donor-related resonances. However, we note that some of the non-monotonic behaviour observed in low magnetic fields is probably related to the transition of the emitter 2DEG into the quantum limit ($\nu=1$ at $B=5\text{ T}$).

Another major argument against the interpretation of the second resonance in terms of excited levels of a single donor comes from comparison of the tunnelling probabilities for the ground 1s and excited 2p, 3d⁻², 4f⁻³ states. In high magnetic fields ($\nu < 1$), we have found that the overlap integral for tunnelling between the first Landau level and the 1s state is respectively 6 and 30 times larger than for the 2p⁻ and 3d⁻² states. The overlap decays rapidly for higher excited states. This infers that tunnelling via the excited states is too weak to account for the strong new resonance. On the other hand, the calculated overlap for D⁻ is nearly twice as large as that for the 1s state in the fields between 1.5 and 20T and the high-field behaviour of the second donor-related resonance is in agreement with tunnelling through the D⁻ state.

The D⁻ resonance requires the presence of neutral donors in the quantum well since D⁰ is the initial state in this tunnelling process. Such neutral donors may appear only due to inelastic tunnelling of 2D electrons since, at biases corresponding to the D⁻ peak, the 1s state is below the bottom of the 2DEG and, hence, out of resonance. The inelastic tunnelling can occur with emission of plasmons in the 2DEG. Furthermore, we expect that a D⁻ centre in the quantum well does not emit its electrons directly into the collector contact but first lets one of them hop to the nearest positively charged Si atom in the well. The latter process has a much smaller tunnel barrier. This dissociation of D⁻ into two neutral donors is likely to give rise to a large concentration of neutral donors available for the D⁻ process and could explain a rather large amplitude of the D⁻ peak.

In conclusion, we have found a new strong tunnel resonance through a shallow donor in the quantum well whose behaviour in high magnetic fields is consistent with tunnelling via a D⁻ centre. Its large amplitude as well as a complicated behaviour in low magnetic fields ($\nu < 1$) remain to be explained.

This work is supported by the Stichting voor Fundamenteel Onderzoek der materie (FOM) (Netherlands), the Belgian National Science Foundation and EPSRC (UK).

[1] S.Huant, S.P.Najda, and B.Etienne, Phys.Rev.Lett. 65 (1990) 1486. See also refs. in [4].

[2] J.W.Sakai, T.M.Fromhold, P.H.Beton, M.Henini, L.Eaves, P.C.Main, F.W.Sheard, G.Hill, Physica B 184 (1993) 241; Phys. Rev. B 48 (1993) 5664.

[3] A.K.Geim, P.C.Main, N.J.a.Scal, L.Eaves, T.J.Foster, P.H.Beton, J.W.Sakai, F.W.Sheard, M.Henini, G.Hill, M.A.Pate, Phys.Rev.Lett. 72 (1994) 2061.

[4] J.M.Shi, F.M.Peeters, J.T.Devreese, Phys.Rev. B 51 (1995) 7714.

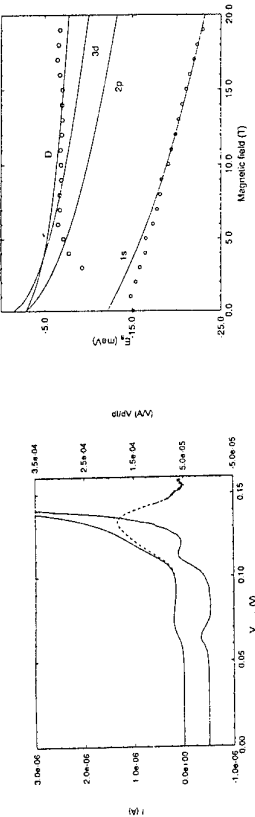


Figure 2: $I(V)$ and derivative for the sample with $N_i = 4 \cdot 10^{10} \text{ cm}^{-2}$; $T = 1.2 \text{ K}$; $B = 19 \text{ T}$; device area $= 12 \times 12 \mu\text{m}^2$. Also shown (dotted line) is the D⁻ resonance after subtracting the main resonance.

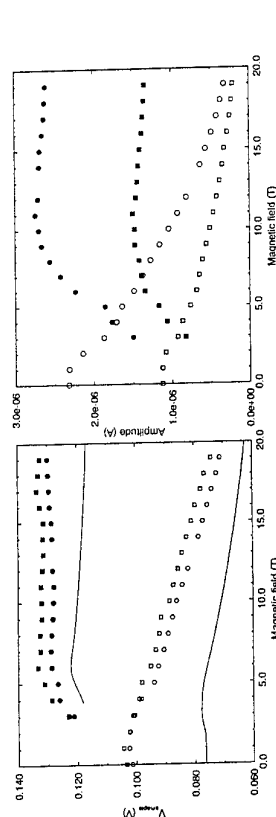


Figure 3: (a) Peak position and (b) amplitude as a function of magnetic field for D⁰ (open symbols) and D⁻ (filled symbols) resonances. (□) $N_i = 4 \cdot 10^{10} \text{ cm}^{-2}$; (○) $N_i = 8 \cdot 10^{10} \text{ cm}^{-2}$. Solid lines: curves measured at constant current, $I = 0.1 \mu\text{A}$ and $I = 0.9 \mu\text{A}$; $N_i = 4 \cdot 10^{10} \text{ cm}^{-2}$.

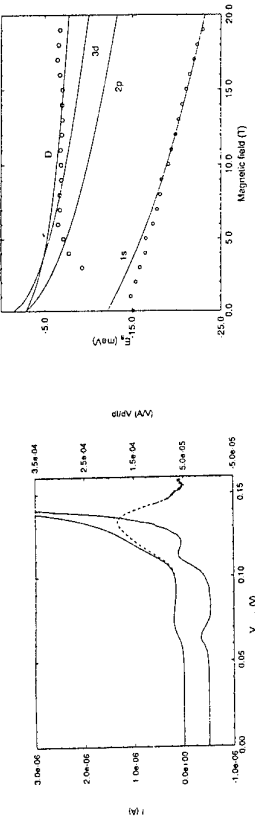


Figure 4: Binding energy of donor states that are bound to the lowest Landau level as a function of magnetic field for a 9nm quantum well.

COOPERATIVE EXCITON-ELECTRON TRANSITIONS IN QUANTUM WELLS

A. Manassen, R. Harel, E. Cohen, Arza Ron and E. Linder
Solid State Institute, Technion - Israel Institute of Technology, Haifa 32000, Israel
and L.N. Pfeiffer

AT&T Bell Laboratories, Murray Hill, NJ 07974, USA

Abstract

We report on the photoluminescence, transmission and reflection spectra of mixed type I - type II GaAs/AlAs quantum wells for various excitation intensities that create a 2DEG in the wide wells of these structures. The effect of the 2DEG on the spectra is analyzed in terms of cooperative exciton-electron transitions. We calculated the PL lineshape by explicitly considering the inelastic exciton-electron scattering rate for various 2DEG densities and show that this mechanism explains well the observed PL spectra.

Introduction

The optical properties of the two dimensional electron gas (2DEG) are usually investigated in modulation doped quantum wells (MDQW's) [1,2]. Phenomena such as band gap renormalization (BGR) due to exchange-correlation effects, and the Moss-Burstein shift due to phase space filling are observed [3]. These effects were studied extensively both experimentally and theoretically for $n_e > 10^{10} \text{ cm}^{-2}$ and only recent works deal with lower densities [4,5]. Low n_e was achieved by biasing the MDQW [2,4] or by applying external pressure [5]. Another useful method is controlling n_e by photogenerating separately confined 2DEG and 2DHG in a mixed type I - type II quantum well structure (MTQW) [6]. Then, a smooth transformation from excitonic to free carrier transition is observed with increasing n_e [7]. In this work we studied the effect of a 2DEG with $n_e < 10^{10} \text{ cm}^{-2}$ on the (e1:h1)1S exciton lineshape in a MTQW. We show that it is determined by both elastic and inelastic exciton-electron (x-e) scattering. The latter results in cooperative (x-e) transitions in which the exciton recombines radiatively and simultaneously excites an electron out of the Fermi sea.

Experiment

The GaAs/AlAs MTQW structure is schematically shown in Fig. 1a, by plotting the variation of the conduction bands (T and X) and the valence band with z (the growth direction). It consists of 30 periods of mixed wide GaAs wells ($L_W = 102 \text{ \AA}$ or $L_W = 198 \text{ \AA}$ in the cases reported here) and narrow wells ($L_N = 26 \text{ \AA}$) that are separated by AlAs

barriers ($L_B = 102 \text{ \AA}$). The MTQW's studied were grown by molecular beam epitaxy on undoped, [001] oriented GaAs substrates. A 2DEG with a controlled density is formed in the wide wells by photoexcitation with an Ar⁺ laser, $E_L = 2.41 \text{ eV}$. The intensities at the sample surface are $0 \leq I_L \leq 15 \frac{\text{mW}}{\text{m}^2}$. In addition, resonant excitation in the (e1 : hh1)W and (e1 : lh1)W excitons spectral range is done by using either a tungsten lamp or a Ti:Sapphire laser. The sample was immersed in liquid He at T=2K.

Fig. 2a presents the photoluminescence (PL) spectra for four values of I_L that yield the indicated n_e values. The density was estimated knowing the excitation intensity and the 2DEG lifetime to be $n_e = 3 \times 10^{10} \times I_L \frac{\text{cm}^2}{\text{mW}}$. Fig. 3 shows the absolute transmission T(E), reflection R(E) and absorption (obtained by $A(E) = 1 - (T(E) + R(E))$) of the etched MTQW with $L_W = 102 \text{ \AA}$. For $I_L > 0$, the PL spectrum was subtracted from the measured T(E) and R(E).

Analysis

The effects of the 2DEG on the exciton bands are clearly seen in Figs. 2 and 3. The T(E), R(E) and A(E) spectra show a weakening and broadening of the resonances at the excitation energies (with only a slight peak shift). The PL spectra at the (e1 : hh1)W 1S exciton band show an asymmetric broadening with increasing n_e ($< 10^{10} \text{ cm}^{-2}$). In this work we present a detailed analysis of the PL spectra. The underlying processes are elastic and inelastic (x-e) scattering. A schematic description of the inelastic case is shown in Fig. 1b. Excitons are photogenerated by the high energy laser in states with various \vec{K} . Then, an exciton in a state \vec{K} relaxes to $\vec{K} = 0$ state by a scattering event that excites an electron from \vec{k}_i to $\vec{k}_f = \vec{k}_i + \vec{K}$. The photon emitted by the $\vec{K} = 0$ excitonic recombination has an energy of $h\nu = E_g - E_b + \Delta E_x - \Delta E_r$. These are cooperative exciton-electron transitions analogous to the shake-up transitions [8]. We note that while the inelastic (x-e) scattering opens up new recombination channels, at energies different than the excitonic resonance, $E_0 = E_g - E_b$, the elastic scattering increases the excitonic dephasing rate and this leads to increasing linewidth. In the PL spectra, the cooperative transitions are observed at energies below E_0 by the appearance of a low energy tail. However, the increased broadening above E_0 is mainly due to elastic scattering. Therefore, the homogeneous broadening due to elastic (x-e) scattering is treated by fitting a Lorentzian lineshape to the high energy wing of the PL spectrum for each n_e . In order to calculate the inelastic (x-e) scattering rate, the simplest approach assumes a system of two electrons and a hole. The Hamiltonian is:

$$H = \frac{e^2}{\epsilon} \left(\frac{1}{r_{12}} - \frac{1}{r_{1A}} - \frac{1}{r_{2A}} \right).$$

The antisymmetrized wave function for the initial state is:

$$|1S, \vec{K} > | \vec{k}_i > = \frac{1}{\sqrt{2}} [e^{i(\vec{K} \cdot \vec{R}_1 + \vec{k}_i \cdot \vec{r}_1)} \phi_{1S}(\vec{r}_1) - e^{i(\vec{K} \cdot \vec{R}_2 + \vec{k}_i \cdot \vec{r}_1)} \phi_{1S}(\vec{r}_2)].$$

Here \vec{r}_j is the electron position vector, \vec{r}_h is that of the hole, $\vec{r}_{jh} = \vec{r}_j - \vec{r}_h$ and $\vec{R}_j = \frac{m_j \vec{r}_j + m_h \vec{r}_h}{M}$ is the exciton center of mass vector ($j = 1, 2$). $\phi_{1s}(\vec{r}_{jh})$ is the 1S excitonic wave function, and A is the QW area. A similar final state can be written. We then obtain four types of matrix elements that are calculated analytically. The leading element is:

$$U(K) = -\frac{128\pi e^2}{\omega K(16+(\frac{m_1}{M}K_0)^2)^{1/2}}.$$

We now sum over the phase space of both x and e with the constraint imposed by energy and momentum conservation. The $(x\text{-}e)$ inelastic scattering rate is proportional to

$$W(E_0 - h\nu) \propto \int \frac{d\vec{k} d\vec{k}_h}{(\frac{2\pi}{A})^2} U(K)^2 f_{BE}(K) f_{FD}(k_i)(1 - f_{FD}(|\vec{k}_i + \vec{K}|)) \\ \delta(E_0 - h\nu + \frac{\hbar^2 K^2}{2}(\frac{1}{M} - \frac{1}{m_e}) - \frac{\hbar^2}{m_e} \vec{k}_i \cdot \vec{K}).$$

The f 's are the appropriate exciton and electron distribution functions. We calculated this integral numerically for several n_e . The PL lineshape is then obtained by a convolution of $W(E_0 - h\nu)$ with the excitation Lorentzian lineshape obtained as described above for each n_e . The calculated PL spectra are shown in Fig. 2b. In order to reproduce all the features of the density dependent PL spectra, the center of the fitting Lorentzians were shifted by $\sim 0.2\text{meV}$ towards higher energies. We justify this adjustment by noting that we assumed an ideal QW while the spectra reflect a small inhomogeneous broadening (due to interface roughness).

The reflection and transmission spectra are analyzed by assuming an excitonic oscillator model in the $(e1\text{-}hh1)$ and $(e1\text{-lh1})$ interband transitions spectral range and by a broadened step function for the $e\text{-}h$ continuum. (Details will be given elsewhere).

Summary

We studied the PL spectra of the $(e1 : hh1)1S$ exciton in the presence of a 2DEG in the range of low densities ($n_e < 10^{10}\text{cm}^{-2}$), using mixed type I-type II QW's. With increasing n_e the exciton linewidth increases and a low energy tail appears. The model presented is based on cooperative exciton-electron transitions, which open up new channels of recombination for the excitons at energies lower than the excitonic resonance, and on an increased elastic scattering rate resulting in an increased linewidth.

Acknowledgement - The work at Technion was done in the Barbara and Norman Seiden Center for advanced Optoelectronics, and was supported by the US-Israel Binational Science Foundation (BSF), Jerusalem, Israel.

References

- [1] G. Livescu, D.A.B. Miller, D.S. Chemla, M. Ramaswamy, T.Y. Chang, N. Sauer, A.C. Gossard, and J.H. English, IEEE J. Quantum Electron. **QE24**, 1677 (1988).

[2] H. Yoshimura, and H. Sakaki, Phys. Rev. B **39**, 13024 (1989).

[3] A. Pinczuk, J. Shah, R.C. Miller, A.C. Gossard and W. Wiegmann, Solid State Comm. **50**, 735 (1984).

[4] G. Finkelstein, H. Shtrikman and I. Bar - Joseph, Phys. Rev. Lett. **74**, 976 (1995).

[5] S. Ernst, A.R. Goni, K. Syassen and K. Ebel, Phys. Rev. Lett. **72**, 4029 (1994).

[6] I. Galbraith, P. Dawson, and C.T. Foxon, Phys. Rev. B **45**, 13499 (1992).

[7] A. Manassen, E. Cohen, Arza Ron, and E. Linder, Superl. and Microst. **15**, 175 (1994).

[8] M.S. Skolnick, K.J. Nash, M.K. Saker and S.J. Bass, Phys. Rev. B **50**, 11771 (1994).

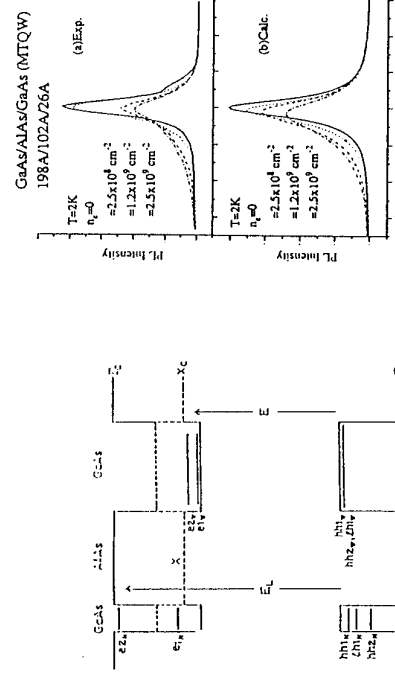


Fig. 1 (a) The PL spectra of the $(el:hh1)1S$ excitation measured for the following excitation intensities: $I_L = 0$ (solid), $I_L = 0.008\text{mW/cm}^2$ (dotted), $I_L = 0.04\text{mW/cm}^2$ (dashed), $I_L = 0.08\text{mW/cm}^2$ (dash-dot). (b) The corresponding calculated PL spectra.

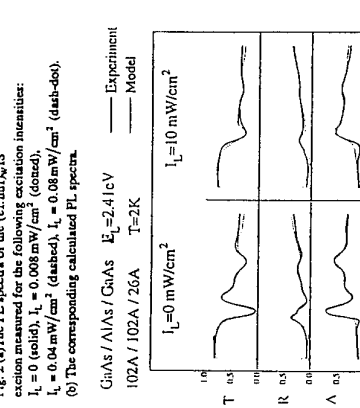


Fig. 1 (b) A schematic description of the mixed type I-type II QW structure. (b) A schematic description of the processes involved in the cooperative $(x \rightarrow)$ transition.

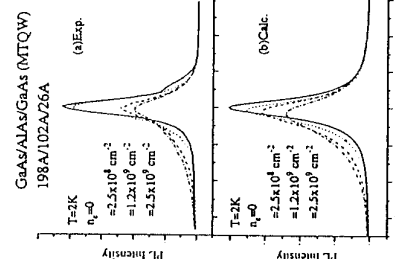


Fig. 2 (a) The PL spectra of the $(el:hh1)1S$ excitation measured for the following excitation intensities: $T=2K$, $I_L = 0$ (solid), $I_L = 2 \times 10^4 \text{ cm}^{-2}$ (dotted), $I_L = 1.2 \times 10^5 \text{ cm}^{-2}$ (dashed), $I_L = 2.5 \times 10^5 \text{ cm}^{-2}$ (dash-dot).

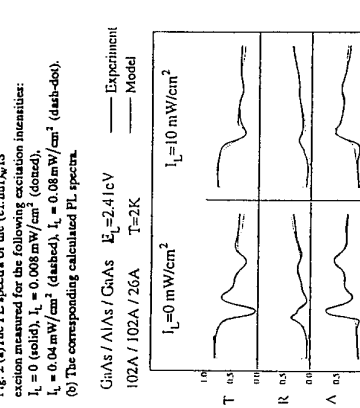


Fig. 2 (b) Measured (solid) and calculated (dotted) transmission, reflection and absorption spectra for an unexcited $I_L = 0$ and photoexcited ($I_L = 10\text{mW/cm}^2$) QW, in the spectral range of the $(el:hh1)_S$ and $(el:hh1)_W$ excitation bands.

CREATION AND ANNIHILATION OF POSITIVELY AND NEGATIVELY CHARGED EXCITONS IN GaAs QUANTUM WELLS

H. Buhmann, P.H. Beton L. Eaves and M. Henini

Dept. of Physics, University of Nottingham, Nottingham, NG7 2RD, U.K.

Abstract

The electro- and photoluminescence of p-i-n and n-i-n GaAs double barrier resonant tunnelling diodes have been investigated for various concentrations of free carriers (either holes or electrons) in the quantum well (QW). For these structures it is possible to change the relative electron or hole density quasi-continuously with applied bias-voltage. At electron densities well below that for exciton unbinding, the formation of negatively charged excitons (X^-) is demonstrated. In asymmetric QW structures the electron densities can be increased above the critical density and exciton unbinding is observed in the luminescence spectra. We also report the observation of the positively charged exciton (X_2^+) in the luminescence spectra of a GaAs quantum well. The conditions for forming X_2^+ are compared with those needed to see the negatively charged exciton (X^-), the heavy-hole free exciton (X) and free carrier recombination.

The low temperature recombination of free electrons and holes in semiconductors is excitonic in character with an enhanced binding energy in confined systems. Excitons ($X=e,h$) can become bound to various charged or electrically neutral impurities or defects located in the vicinity of the QW, which further decreases the exciton recombination energy. The effect of charged or neutral impurities on the excitonic recombination has been intensively investigated (see for example [1-3]). Results are also available on the luminescence spectra of exciton molecules (biexciton, BX or X_2) (see for example [2,4]). In addition, there have been recent reports on exciton complexes such as negatively charged excitons ($X^-=2e,h$) in confined system [5-7] but none so far on positively charged excitons ($X_2^+=e,2h$). X_2^+ and X^- are predicted to have larger binding energy than BX ($E_b(BX) \approx 1$ meV) and should therefore be resolved in the radiative recombination spectra. However, the conditions for their formation are constrained: excitons have to be created in an impurity-free environment of free carriers (electrons or holes) while the free carrier concentration has to be sufficiently low to prevent the unbinding of the exciton. Exciton unbinding should appear in the luminescence spectra as a sudden transition from an excitonic to an energetically lower free hole - free electron recombination (red-shift). However, this transition has only been treated theoretically [8-10] and the experimental evidence is still awaited.

In this paper we present results on the formation of X^- and the exciton unbinding transition observed in the luminescence spectra of a 9.0 nm QW. In the latter case, structures with asymmetric barrier were used to increase the electron density by charge accumulation in the QW above the critical transition value. Finally, evidence for the existence of X_2^+ is given for a 6.0 nm QW structure. We present results on three different structures. For electroluminescence (EL) studies we used p-i-n structures (n-doping near the surface) referred to as Sample 1 and 3 with two 6.1 nm (5.1 nm) barriers and 9.1 nm (6.0 nm) QW in the intrinsic region, respectively. Sample 2, a n-i-n structure consisting of a 8.5 nm (top) barrier 9.1 nm QW and a 6.5 nm (bottom)

barrier, was used for photoluminescence (PL) experiments. All structures incorporate large undoped spacer layer (20-30 nm) to separate the barriers from the doped contact regions. Optical lithography and wet-etching has been used to process mesas of 0.01-0.16 mm².

Figure 1 shows the current-voltage characteristic (I(V)) and EL spectra of Sample 1. The new recombination line ~ 2 meV lower in energy than the heavy-hole free exciton (X) recombination has previously been identified as a recombination related to X^- [6]. This line dominates the EL spectrum when the electron density in the QW reaches a maximum (alignment of emitter and first QW electron subband (E1)). However, the excitonic recombination is expected to disappear when the electron density exceeds $n_e \sim 10^{11} \text{ cm}^{-2}$ [8-10]. Since the electron density in the 9.1 nm QW structures with symmetric 6.1 nm tunnel barriers never exceeded a few 10^{10} cm^{-2} , we studied a new QW structure with asymmetric tunnel barriers (Sample 2) in order to increase further the electron density in the QW and to observe the quenching of the excitonic recombination. Figure 2 displays the I(V) and PL spectra of Sample 2. In this structure the X line vanishes abruptly when the device is biased onto the electron resonance. Figure 2 displays the I(V) and PL spectra of Sample 1. Simultaneously, a new line of lower oscillator strength and a strong electron-concentration-dependent recombination energy dominates the spectra in the region of the electron resonance at a recombination energy lower than X. The red shift with increasing electron concentration is indicated in Figure 2 by the dashed line. This behaviour differs from the observations on X⁻ in two ways: first, X⁻ appears at a constant energy while the electron density is increased; second, the oscillator strength of X⁻ is comparable to X. Furthermore, these features match the predicted properties for a free hole - free electron recombination [10]. An increased temperature should make the excitonic recombination reappear above the critical density as is observed for Sample 2. The inset in Fig. 3 shows PL spectra taken at 8 K.

Figure 1: (a) Current-voltage characteristic and (b) electroluminescence spectra of Sample 1, showing the formation of the negatively charged exciton X⁻. The inset in Fig. 1 (b) shows the formation of the exciton X. The red shift with increasing electron density is indicated in Figure 2 by the dashed line. This behaviour differs from the observations on X⁻ in two ways: first, X⁻ appears at a constant energy while the electron density is increased; second, the oscillator strength of X⁻ is comparable to X. Furthermore, these features match the predicted properties for a free hole - free electron recombination [10]. An increased temperature should make the excitonic recombination reappear above the critical density as is observed for Sample 2. The inset in Fig. 3 shows PL spectra taken at 8 K.

In order to form X_2^+ , excitons have to be present in an hole-rich environment. We searched for X_2^+ on the LHI resonance of Sample 1 but without success. The reason for this is that in the 9.1 nm QW structure the first light-hole (LHI) and the first electron (E1) resonance are close in bias position so that already a large number of electrons are present in the QW when LHI comes onto resonance (see I(V) Fig. 1 (b)) and X is the only feature observed in the EL spectra in this bias range. Resonantly tunnelling holes charge the QW and increase the potential drop across the tunnel barrier adjacent to the electron accumulation layer. This increase brings the electrons

closer to resonance and therefore increases the electron tunnel current, i.e. the electron density in the QW. By choosing a narrower QW, Sample 3, the separation of LH1 and E1 is increased and the number of electrons in the QW is expected to be lower on LH1 (Fig. 3 (a)). Figure 3 (b) gives an illustration of the EL of Sample 3. Indeed, the luminescence is dominated by a line ~ 3.0 meV lower in energy than X. This line has its maximum intensity on the LH1 resonance peak and rapidly decreases when the bias-voltage is increased. We attribute the new line to recombinations related to X_2^+ . The observed recombination energy is about 20% lower than the expected binding energy for X_2^+ in a strictly two-dimensional (2D) system ($E_b(X_2^+) \approx 3.7$ meV) [11]. However, this difference is apparently the same as for X- compared to its strictly 2D value. We rule out the possibility that the line is due to X- recombination with a lower recombination energy in a stronger confined system, because the expected increase for a decreased well-width from 9 to 6 nm is only $\sim 10\%$ [12] and it is unlikely to create negatively charged excitons on a hole resonance. We note that the X_2^+ -line exhibits a thermal activated behaviour resulting from the dissociation of X_2^+ into $X+h$, which is not shown in this report. A further increase of the bias-voltage (towards E1) does not show any signature of the X- formation. The spectra display the free hole-free electron characteristics observed for Sample 2 (Fig. 3 (b) inset). Here, the thin barriers (compared to Samples 1 and 2) cause a strong increase of the electron density in the QW so that electron-hole pairs relax into plane-wave- rather than excitonic-states and no X- is observed in the spectra for bias-voltage region.

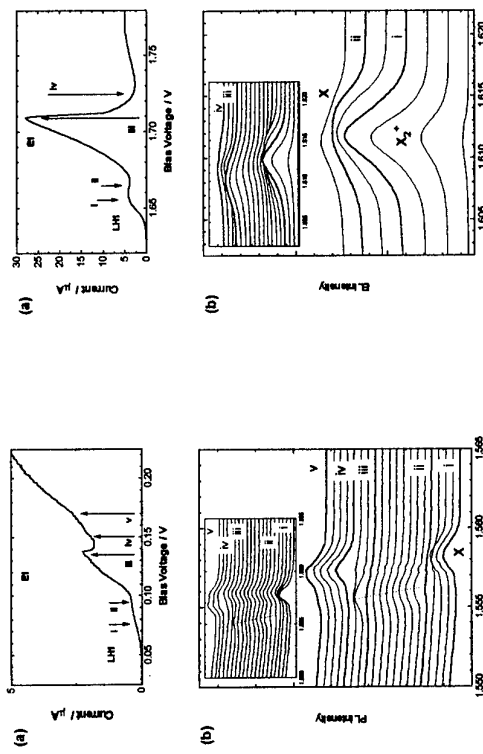


Figure 2: (a) Current-voltage characteristic and (b) electroluminescence spectra of Sample 2 at 4.2 K, showing the exciton unbinding transition. (Inset) EL spectra at 8 K.

To summarize, we have shown that a variety of excitonic recombination processes (X, X_2^+ and X-) can be observed in the QW of double barrier resonant tunnelling diodes (RTD). At high carrier densities in the well the exciton becomes unbound and recombination proceeds via free carrier recombination. The RTD provides us with a flexible means of studying these phenomena since both electron and hole densities in the well can be voltage-controlled over a wide range. Funding for this work was provided by ESPRIT Basic Research Grant No. 7193. LE acknowledges EPSRC for a Senior Fellowship.

References

- [1] D.C. Reynolds, C.E. Leak, K.K. Bajaj, C.E. Stutz, R.J. Jones, K.R. Evans, P.W. Yu and W.M. Theis, Phys. Rev. **B** **40** (1989) 6210.
- [2] R. Stepienowski, S. Huant, G. Martinez and B. Etienne, Phys. Rev. **B** **40** (1989) 9772.
- [3] H.B. Evans, L. Eaves, and M. Henini, Semicond. Sci. Technol. **9** (1994) 555.
- [4] D.C. Reynolds, K.K. Bajaj, C.E. Stutz, R.J. Jones, W.M. Theis, P.W. Yu and K.R. Evans, Phys. Rev. **B** **40** (1989) 3340.
- [5] K.Kheng, R.T. Cox, Y. Merle d'Aubigné, K. Bassani, K. Saminadayar and S. Tatarenko, Phys. Rev. Lett. **71** (1993) 1752.
- [6] H. Buhmann, L. Mansouri, J. Wang, P.H. Beton, L. Eaves, M. Henini and M. Potenski, Phys. Rev. **B51** (1995) 7969.
- [7] G. Finkelstein, H. Shtrikman and I. Bar-Joseph, Phys. Rev. Lett. **74** (1995) 976.
- [8] D.A. Kleinman, Phys. Rev. **B32** (1985) 3766.
- [9] G.E.W. Bauer, Solid State Commun. **78** (1991) 163.
- [10] G.E.W. Bauer, Phys. Rev. **B45** (1992) 9153.
- [11] B. Stébé and A. Aïanane, Superlattice and Microstructures **5** (1989) 545.
- [12] B. Stébé, D. Fristot, G. Munsch and L. Stauffer, in: 22nd International Conference on the Physics of Semiconductors, Vancouver, Canada, 1994, Vol 2, Ed. D.J. Lockwood, (World Scientific 1995) p.1403.

Figure 3: (a) Current-voltage characteristic and (b) electro-luminescence spectra of Sample 3 in the vicinity of LH1, showing the formation of the negatively charged exciton X_2^+ . (Inset) extended spectrum series.

Magneto-Optical Spectroscopy of Neutral and Negatively-Charged Excitons in GaAs Quantum Wells

A. J. Shields,^a M. Pepper,^{a,b} M. Y. Simmons,^b and D. A. Ritchie^b

^a Toshiba Cambridge Research Centre
260, Science Park, Milton Road, Cambridge CB4 4WE U.K.

^b Cavendish Laboratory, Madingley Road, Cambridge CB3 0HE

Abstract

We study interband optical spectra of GaAs quantum wells as a function of their excess electron density and an applied magnetic field. With increasing electron density we observe a sharp quenching of the neutral excitonic transitions (X), with the concurrent strengthening of a transition to lower energy due to the negatively-charged exciton (X^-). Application of a magnetic field enhances the second electron binding energy, increasing the separation of X and the ground state of X^- , as well as stabilising excited states of X^- where the two electrons have parallel spins.

1. Introduction

Optical spectroscopy of remotely-doped quantum wells (QWs) has concentrated upon high excess electron density effects, such as the lowering of the bandgap with density due to bandgap renormalisation, or the enhancement of the oscillator strength for transitions involving electrons near the Fermi energy.¹ Although there have been several theoretical studies^{1,2} concerning the effects of excess electrons upon the excitonic interaction, only recently have samples of sufficiently high quality been investigated to provide experimental^{3,4,5,6,7} insight into the low excess electron density regime.

We demonstrated recently that the bandedge neutral exciton (X) weakens sharply upon adding $\sim 10^{10}$ cm⁻² excess electrons to the QW and is replaced by a transition to a distinctly lower photon energy.⁵ This transfer of oscillator strength is caused by the neutral exciton binding an excess electron to form the so-called *negatively-charged exciton* (X^-). With further increasing density we observed X^- evolve smoothly into the Fermi-edge singularity seen for dense electron gases, while X was completely quenched from the spectra.

The Pauli exclusion principle requires the spin wavefunction of a two-electron system to be either anti-symmetric (*singlet*) or symmetric (*triplet*) upon interchange.⁸ For X^- , as for the analogous semiconductor negative Donor centre (D^-) and the negative Hydrogen ion (H^-), the only bound state is the ground spin singlet, although triplet levels are expected to stabilise in a magnetic field. Despite numerous calculations of this effect for D^- , clear observation of the triplet states by far infra-red optical spectroscopy has been prevented by the low population of the triplet ground state at low temperature.⁹ We demonstrate here that interband optical spectroscopy of X^- does not share these limitations and report clear observation of the binding of the triplet states at finite magnetic field. We show that the binding energy of the spin-singlet state also increases in a magnetic field.

2. Experimental Methods

We conducted our study on a number of remotely-doped GaAs/Al_{0.33}Ga_{0.67}As single QWs. Since the samples show qualitatively similar behaviour, we concentrate here on a structure with a 300 Å GaAs QW, 600 Å undoped AlGaAs spacer, and 2000 Å Si doped

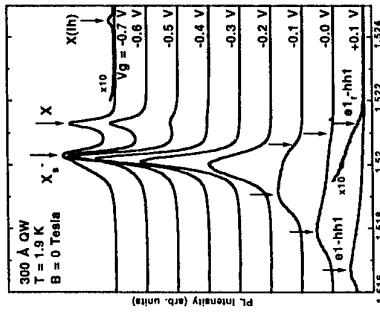


Figure 1. PL spectra recorded with the different applied gate biases indicated. The excess electron density is $\sim 8 \times 10^{10}$ cm⁻² at +0.1 V and negligible at -0.7 V.

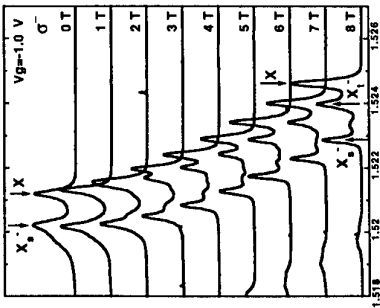


Figure 2. PL spectra measured with different applied magnetic fields, a fixed gate bias of -1.0 V and σ^- polarisation for the emitted light.

(10¹⁷ cm⁻²) AlGaAs, grown by MBE on a (100)-oriented GaAs substrate. An ungated Hall bar of this sample had a 2K mobility of 2.9×10^6 cm²V⁻¹s⁻¹. The excitonic linewidth of the QW when depleted is ~ 0.24 meV. The samples were processed into large area mesas with a semi-transparent Au Schottky gate layer and several ohmic contacts to the QW. The electron density could then be varied by application of a voltage (V_g) between the ohmic and Schottky contacts.

3. Electron Density Dependence

Fig.1 plots PL spectra taken on the 300 Å GaAs QW with different applied gate voltages. A broad band is observed for the largest biases, due to recombination of photo-excited holes and excess electrons with energies ranging from the bandedge to the Fermi energy. The shoulder on the high-energy side of the band, marked $e1_f - hh1$ in Fig.1, is associated with k -conserving recombination at the Fermi wavevector.⁴ Its observation allows the electron density to be determined directly from the PL spectra. As the gate bias is decreased the PL band narrows, as the Fermi energy reduces, until a single featureless peak is seen at -0.3 V. The blueshift of the PL peak with decreasing electron density is caused by a reduction in both bandgap renormalisation and the Stark shift due to the QW charge.¹⁰

Notice in Fig.1 that when the gate bias is decreased beyond -0.3 V, a second peak emerges to higher energy and grows in intensity. We ascribe this higher-energy peak to the neutral free exciton (X) formed between the lowest electron and heavy-hole subbands, $e1 - hh1(1s)$. The lower-energy component of the doublet (labelled X_s^-) we ascribe to recombination involving the negatively-charged exciton, according to $X^- \rightarrow \text{photon} + e^-$. This assignment explains

the weakening of X and concurrent strengthening of X^- with increasing electron density, as the excess electrons occupy an expanding proportion of the QW area. Analysis of the PL spectra demonstrates this sharp transfer of oscillator strength from X to X^- occurs around

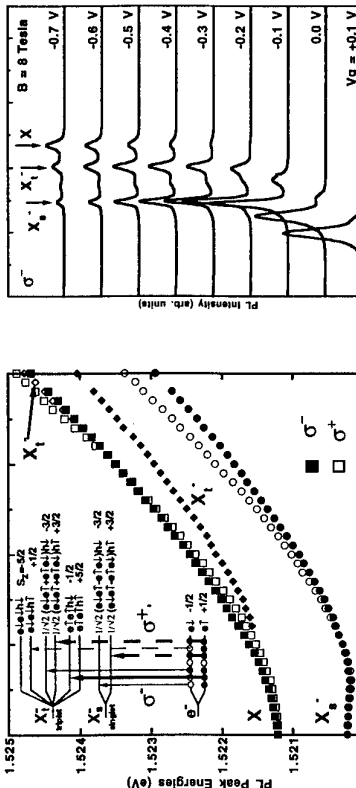


Figure 3. Magnetic field dependence of the PL peak energies. The inset schematises the spin-states of X^- and the possible optical transitions produced by circularly polarised light, according to $e^- + \text{photon} \rightarrow X^-$.

electron densities of a few 10^{10} cm^{-2} .⁵ This contrasts with measurements performed on samples with narrower undoped spacer layer thicknesses, which suggested neutral excitons can persist to much higher average excess electron densities $\geq 10^{11} \text{ cm}^{-2}$ due to electron localisation in spatial inhomogeneities.⁶ The separation of the X and X^- peaks ($\sim 1 \text{ meV}$) is roughly consistent with the expected binding energy for the second electron.⁵ Upon raising the sample temperature, the X^- peak weakens due to thermal dissociation into a neutral exciton and a free electron.

The X and X^- transitions are also observed in excitation spectra.⁵ Electroreflectance spectra, taken at the largest reverse biases are dominated by features due to the neutral excitonic transitions. However, as the electron density is increased these are seen to weaken, while the lower energy transition due to X^- strengthens, in qualitatively similar fashion to the PL spectra. Observation of the X^- transition in the excitation spectra, in addition to its electron density dependence, demonstrates that it cannot have an intrinsic origin, such as an impurity bound exciton. The electroreflectance spectra also demonstrate clearly that the X^- transition evolves smoothly into the Fermi-edge singularity with further increasing electron density.⁵

4. Magnetic Field Dependence and Spin-Triplet X^-

Figure 2 shows PL spectra taken with different magnetic fields applied perpendicular to the QW, and a fixed gate bias of -1.0 V, for which the excess electron density is small. The emitted light was circularly polarised in σ^- sense. The PL peak energies measured for both polarisations are plotted in Figure 3 as a function of magnetic field.

The diamagnetic shift and Zeeman splitting of X is very similar to that reported for undoped QWs.^{11,12} The change in sign of the Zeeman splitting with field is characteristic of

GaAs QWs and is caused by mixing of the heavy- and light-hole excitons. In contrast, the peak labelled X_s^- undergoes a rather different evolution, displaying an initial small red-shift with field, before increasing in energy less rapidly than X .

The increasing separation of the X and X_s^- peaks with field can be readily understood as due to an enhancement of the second electron binding energy. Insight is gained by regarding the X^- spatial wavefunction, in the usual manner, as a combination of two one-electron orbitals with different extents. The relatively weak binding of the second electron results in one of the orbitals being much larger than the other. The magnetic field forces this outer orbital towards the core of the exciton, thereby enhancing the Coulomb interaction and hence the binding energy. Notice also that the Zeeman splitting of X_s^- is rather larger than that of X and does not change sign. This suggests that mixing with the light-hole X^- is less significant than for the neutral exciton.

We ascribe the peak which emerges below the X line near 2.4 T in σ^- polarisation,

which is marked X_t^- in Figs. 2 and 3, to a spin-triplet X^- transition. As discussed in the Introduction, the triplet states are expected to bind only in the presence of a magnetic field. The inset of Fig. 3 schematises the spin states of X^- , along with the allowed optical transitions produced by circularly polarised light. The photon changes the z-component of the spin by ± 1 for σ^\pm polarisation. Notice that the circular polarisation of the observed transition is consistent with that expected for the lowest-energy triplet transition. The higher-energy triplet transition in σ^+ polarisation emerges below the X peak around the higher field of 6.8 T, see Fig. 3. The fact that we also observe the spin-triplet transitions in electroreflectance⁷ and PL excitation spectra taken with polarised light, at finite magnetic field, again excludes the possibility that the transition could have an intrinsic origin.

Further evidence for our assignment is provided by the gate bias dependence of PL spectra measured at 8 T, which are plotted in Figure 4 for σ^- polarisation. Notice that the triplet X^- transition strengthens with increasing electron density, in similar fashion to the ground-state singlet, and in contrast to the neutral exciton. This demonstrates that the transition requires the presence of an excess electron and therefore must be due to an excited state of X^- . A similar dependence of the X^- and X transitions with excess electron density is measured in electroreflectance spectra recorded at 8 T.⁷

5. References

1. for a review see S Schmitt-Rink, D S Chemla and D A B Miller, *Adv. Physics* **38**, 89 (1989).
2. for example, D A Kleimann, *Phys Rev B* **32**, 3766 (1985); P Hawrylak, *Phys Rev B* **44**, 3821 (1991); G E Bauer, *Phys Rev B* **45**, 9153 (1992).
3. K Kheng et al., *Phys Rev Lett* **71**, 1752 (1993).
4. A J Shields et al., *SIL and Microstruct.* **15**, 355 (1994).
5. A J Shields et al., *Phys Rev B* **51**, 19049 (1995).
6. G Finkelstein et al., *Phys Rev Lett* **74**, 976 (1995).
7. A J Shields et al., to be published in *Phys. Rev B*.
8. H A Bethe and E E Salpeter, *Quantum Mechanics of One- and Two-Electron Atoms*, (Plenum, New York, 1977).
9. A B Dzyubenko et al., *Phys Rev B* **50**, 4687 (1994) and references therein.
10. C Delalande et al., *Phys Rev Lett* **34**, 2482 (1987).
11. W Ossan et al., *NATO ASI Ser B* **183** (Plenum, New York, 1988), p285.
12. M J Snelling et al., *Phys Rev B* **45**, 3922 (1992).

INFLUENCE OF THE ELECTRON-ELECTRON AND ELECTRON-PHONON INTERACTION ON THE CYCLOTRON RESONANCE OF 2DEG IN GAAS

C. M. Hu and E. Baake
 Physikalisches Institut der Universität Würzburg
 Am Hubland, D-97074 Würzburg, Germany
 and

K. Köhler and P. Ganser
 Fraunhofer-Institut für Angewandte Festkörperforschung,
 Tullastr. 72, D-79108 Freiburg, Germany

2. Experiment

Cyclotron resonances were studied in Faraday geometry in transmission with an experimental set up as described elsewhere [3]. Our sample is a modulation doped Al_{0.3}G_{0.7}As-GaAs single-heterostructure of nearly standard design. For the electron density of order 10¹⁰ cm⁻² and magnetic fields as high as 14 T the population of the higher Landau-levels is achieved by increasing the temperature up to 100 K.

3. Results and discussion

The resonant polaron effect was investigated for cyclotron transitions N → N + 1 in magnetic field regimes where the Landau-levels N = 2 and 3 cross with the level N = 0 plus one bulk longitudinal optical phonon. The experiment is analyzed in the framework of the improved Wigner-Brillouin perturbation theory taking into account band coupling phenomena, a finite thickness of the inversion layer in growth direction and coupling of the cyclotron transitions due to electron-electron interactions. From the cyclotron mass enhancements a Fröhlich coupling constant $\alpha = 0.06$ to 0.07 was obtained.

1. Introduction

The electron mass renormalization due to the electron-phonon interaction for electron inversion layers in GaAs is still a subject of considerable experimental and theoretical interest. Usually information on the polaron mass is gained from cyclotron resonances (CR) where one studies the resonant coupling of the Landau-levels N (N ≥ 1) with the N = 0 level plus one bulk longitudinal optical (LO) phonon. In previous CR experiments performed on electron inversion layers in GaAs only the resonant coupling of the N = 1 level was investigated in samples with typical electron densities N of the order of 10¹¹ cm⁻². The resonant coupling of higher Landau-levels N ≥ 2 has not been investigated so far, although more moderate magnetic field strengths are sufficient to cover the resonant regimes. Very recently it was clarified that the coupling of high index Landau-levels cannot be studied in samples with electron densities of the order of 10¹¹ cm⁻², since electron-electron interactions couple the electrical dipole transitions from different Landau-levels [1]. This interaction coupling increases with electron density, and becomes important if the interaction energy

$$\hbar\omega_1 = C(\pi N_s)^{3/2} \frac{(e\ell)^2}{8\pi\varepsilon\varepsilon_0} \quad (1)$$

is comparable to the difference in the single-particle Landau-level transition energies. In Eq. (1) ε is the static dielectric constant of the semiconductor, $\ell = (\hbar/eB)^{1/2}$ the Landau orbit and C a dimensionless configuration constant reflecting the electron distribution in space. For ideally 2D electron systems $C = 1.6$ was obtained, whereas for quasi two-dimensional (Q2D) electron inversion layers generally a smaller value applies, which originates from the reduction of the effective electron-electron interaction due to the finite width of the inversion layer [2]. We report here the first investigation of the resonant polaron coupling for the Landau-levels N = 2 and 3 in GaAs heterostructures. The electron density is sufficiently low such that the strength of the interaction coupling is reduced.

Figure 1 shows the normalized transmission T(N_s)/T(0) measured at 100 K and N_s = 7 × 10¹⁰ cm⁻² in the magnetic field regime from 6.5 to 10 T. The dashed, dotted and dashed-dotted lines are fits to the experiment with Lorentzian lines. For B larger than 8.5 T the dotted and dashed lines represent the contributions of the 0 → 1 and 1 → 2 transitions to the CR line shape, respectively. Please note that with decreasing B in this regime the 1 → 2 transition starts to dominate. This cannot be expected in single-particle approximation, where the thermal populations rule the intensities, and is a result of the interaction coupling of both transitions. At 7 and 6.5 T the dashed-dotted lines reflect both transitions 0 → 1 and 1 → 2 which cannot be resolved experimentally, and the solid line indicates the contribution of the 2 → 3 transition. In Figs. 2 (a) and (b) resonance positions ω_{exp} and cyclotron masses m_c = eB/ω_{exp} are shown. The lines represent theoretical magnetic field dependences for the three cyclotron transitions in various approximations. At our low electron density screening and Landau-level population effects are negligible [4], thus we can calculate the polaron Landau-levels E_N^{pol} in the single-particle approximation. In the following it will be assumed that only the ground 2D subband is populated and that the electrons couple only to bulk LO phonons. In the framework of the improved Wigner-Brillouin perturbation theory we derive the analytical solution for the polaron Landau-level energies

$$E_{N,\pm}^{pol} = E_N + \frac{\hbar\omega_{LO}}{2} [1 - \delta_N + \Lambda_N \pm \sqrt{(1 - \delta_N - \Lambda_N)^2 + \frac{4P_{N0}^2}{(\hbar\omega_{LO})^2}}], \quad (2)$$

where we introduced the abbreviations $\delta_N = (E_N - E_0)/\hbar\omega_{LO}$ and $\Delta_N = P_{N0}^2(1 + \delta_N - \delta_N^2 + \delta_N^3)/(\hbar\omega_{LO})^2$. The E_N = (N + 1/2)h̄ω_c represent the Landau-level energies in the weak field limit (ω_c ≪ ω_{LO}) with the cyclotron frequency ω_c = eBm₀* determined by the polaron mass at band edge. If we describe the subband wave function in growth direction by the Fang-Howard variational envelope function [5] one obtains

$$P_{N0}^2 = \alpha(\hbar\omega_{LO})^2 \sqrt{\frac{\omega_c}{\omega_{LO}}} \frac{1}{N!} \int dx F\left(\frac{\sqrt{2}}{b}x\right) x^{2N} e^{-x^2}, \quad (3)$$

where $F(q/b) = (1 + 9q/8b + 3q^2/8b^2)(1 + q/b)^{-3}$ ruled by $b = [12m_0e^2(N_{dep} + 11N_g/32)/\varepsilon\varepsilon_0\hbar^2]^{1/3}$ is a form factor describing the reduction of the effective electron-phonon interaction due to the finite width of the inversion layer. In the 2D limit, F(q/b) = 1, the integral in Eq. (3) has to be replaced by (N - 1/2)!. Equation (2) provides a very accurate description of the transitions energies $\hbar\omega_N^{pol} = E_{N+1/2}^{pol} - E_N^{pol}$. This we tested by comparing our 0 → 1 cyclotron masses for ideally 2D electron systems in GaAs with the ones evaluated numerically in Ref. 6 and

found virtually no difference to our result. Band coupling phenomena cause a nonparabolicity of the GaAs conduction band and contribute in addition to the polaron effect to the energy dependence of the electron effective mass. The band nonparabolicity can simply be incorporated in Eqs. (2) by calculating the energies E_N in the framework of the two-band model. Although for GaAs the application of the two-band model is restricted, via the definition of an effective gap E_g^* one can account for the contributions of the far bands [7]. From the set of Eqs. (2 - 3) one can calculate the single-particle transitions energies $\hbar\omega_{N,N'}$ in a simple manner at arbitrary magnetic field strength. However, due to the breaking of the translational invariance by the energy dependence of the electron effective mass it is necessary to include also the interaction coupling of the electrical dipole transitions. We incorporated this coupling in a formalism developed recently [1, 2]. For the three transitions $N \rightarrow N+1$ ($N = 0, 1, 2$) the resulting frequencies are given by the solutions of

$$\begin{vmatrix} \omega_0^{\text{pol}} + (\phi_1 + \phi_2)\omega_1 - \omega & -\sqrt{\rho}\phi_1\omega_1 & -\sqrt{\rho}\phi_2\omega_1 \\ -\sqrt{\rho}\phi_0\omega_1 & \omega_0^{\text{pol}} + (\phi_0 + \phi_2)\omega_1 - \omega & -\sqrt{\rho}\phi_2\omega_1 \\ -\sqrt{\rho}\phi_0\omega_1 & -\sqrt{\rho}\phi_2\omega_1 & \omega_2^{\text{pol}} + (\phi_0 + \phi_1)\omega_1 - \omega \end{vmatrix} = 0, \quad (4)$$

where $\rho_N = (N+1)(m_N - m_{N+1})/N_S$, depending on the populations m_N of the Landau-levels, rule the intensities of the cyclotron transitions in the single-particle approximation. There are only two parameters C and α which have to be adjusted to explain the experiment, the other parameters are known or could be measured independently. We took $\omega_{1,0} = 295 \text{ cm}^{-1}$, $\epsilon = 12.8$ and $N_{\text{dep}} = 3 \times 10^{10} \text{ cm}^{-2}$, which was determined from resonant subband Landau-level couplings. The mass $m_0^* = 0.0663 \text{ me}$ and the gap $E_g^* = 0.85 \text{ eV}$ were essentially fixed from the $0 \rightarrow 1$ transition energies, and N_S was obtained from fits to the line shapes. In Fig. 2 the dashed-dotted and dotted lines represent the prediction for 2D and Q2D electron systems, respectively. The 2D model predicts a mass enhancement that is essentially too large, whereas the Q2D model is a good approximation in the magnetic field regimes where the interaction energy $\hbar\omega_{01}$ is small compared to the difference $\Delta\omega$ in the single-particle transition energies. A satisfactory description of the experiment at all magnetic fields is provided only if we include in addition the interaction coupling of the dipole transitions with $C = 1.2$, which is shown with a solid line. Please note, that the interaction coupling has essentially no influence in the strong resonant regime, since here $\omega_1 \ll \Delta\omega$. Our Fröhlich coupling constant α ranging between 0.06 and 0.07 agrees with the one obtained previously.

In conclusion we studied the resonant polaron coupling of the high index Landau-levels $N = 2$ and 3 for a low density electron inversion layer in GaAs heterostructures. The cyclotron mass enhancements are well described by coupling to bulk LO phonons only with $\alpha = 0.06$ to 0.07. A satisfactory description of the experiment required the inclusion of the finite thickness of the electron inversion layer in growth direction, the nonparabolicity of the GaAs conduction band and coupling of the cyclotron transitions by electron-electron interactions.

Acknowledgments

We would like to gratefully acknowledge financial support by the Deutsche Forschungsgemeinschaft and the VW-Stiftung.

References

- [1] C. M. Hu, E. Batke, K. Köhler and P. Ganser, to be published in PRL 1995.
- [2] C. M. Hu, E. Batke, K. Köhler and P. Ganser, to be published.
- [3] E. Batke and D. Heitmann, Infrared Phys. 24 (1984) 189.
- [4] F. M. Peeters, X. G. Wu, J. T. Devreese, G. J. G. M. Langerak, J. Singleton, D. J. Barnes, and R. J. Nicholas, Phys. Rev. B 45 (1992) 4296.
- [5] S. Das Sarma and A. Madhukar, Phys. Rev. B 22 (1980) 2823.
- [6] F. M. Peeters and J. T. Devreese, Phys. Rev. B 31 (1985) 3689.
- [7] M. Horst, U. Merkt, W. Zawadzki, J. C. Maan, and K. Ploog, Solid State Commun. 53 (1985) 403.

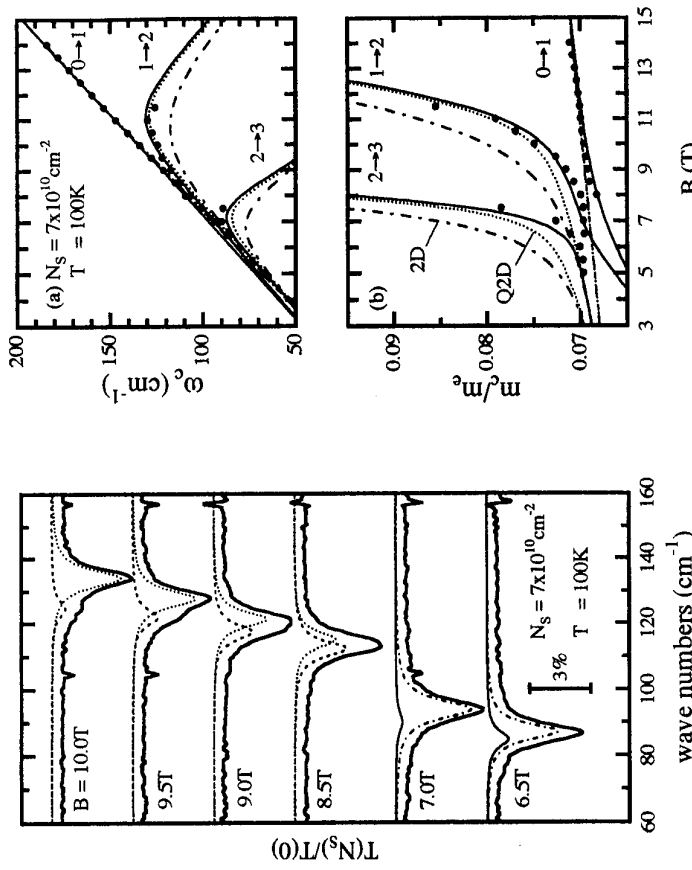


Fig. 1. Normalized transmission of a low density electron inversion layer in GaAs heterostructures at 100 K. Dashed, dotted, dashed-dotted and solid lines are Lorentzian line fits representing, respectively, the contributions from the $1 \rightarrow 2$, $0 \rightarrow 1$, combined $1 \rightarrow 2$ and $0 \rightarrow 1$ and $2 \rightarrow 3$ cyclotron transitions.

Electron and Hole g Factor Oscillations in CdTe-based Modulation Doped Quantum Wells

J. X. Shen, W. Ossau, F. Fischer, A. Waag and G. Landwehr
Physikalisch-Technische Universität Würzburg, Am Hubland, 97074 Würzburg, Germany

We have investigated g factor oscillations of electrons as well as of photo-excited holes in a quasi two dimensional electron gas (2 DEG) of CdTe/(CdMg)Te modulation doped single quantum wells by means of photoluminescence excitation (PLE) and photoluminescence excitation (PLE) spectroscopy. The oscillation amplitude is found to be related to Landau level numbers and filling factors as predicted by the theory. The exchange constants $A_{NN'}$ of the g factor enlargement have been obtained for the first time experimentally.

1. Introduction

The enhancement of the electronic g-factor has been a longstanding subject in the analysis of the spin splitting in Shubnikov-de Haas experiments [1,2]. Several attempts have been made to determine enhanced g factors, for example, magneto-transport measurements under tilted magnetic fields [3], photo-conductivity with microwave injection [4] and photoluminescence experiments [5]. The great advantage of the II-VI-compounds CdTe/(CdMgMn)Te, applied in this study, compared with the well known system GaAs/(GaAl)As, is the enlarged electron g-factor. On the one hand the electron g factor of CdTe is four times larger than that of GaAs. On the other hand the g factors are enlarged by the sp-d exchange interaction of the carriers with the Mn⁺⁺-ions in heterostructures with semimagnetic barriers like (CdMnMg)Te. Our high quality modulation doped CdTe/(CdMg)Te QW samples ($\mu > 4 \times 10^4$ cm²/Vs) enable us to measure the Zeeman splittings of the Landau levels with a better resolution as well below (PL) as above (PLE) the Fermi level, which allows us to study the variation of the g factor enhancement as a function of the Landau level quantum number in more detail.

Oscillations of the g factor in two dimensional electron gases (2 DEG) are assumed to be caused by the electron-electron coulomb interaction [2]. The Zeeman splitting enhancement of the Nth Landau level is determined by the difference of the electron concentration of spin up and spin down states:

$$g_N^* u_B H - \sum \sum \frac{\nu(q)}{q} J_{NN'}(q)(V_{N'\uparrow} - V_{N\downarrow}), \quad (1)$$

$$\text{where } J_{NN'} = \sqrt{\frac{N_2}{N_1}} \cdot \exp\left(-\frac{Pq^2}{4}\right) \cdot \left(\frac{Pq^2}{2}\right)^{N_1-N_2} L_{N_1}^{N_1-N_2} \left(\frac{Pq^2}{2}\right)$$

are the exchange constants with $N_1 = \max(N, N')$ and $N_2 = \min(N, N')$. N and N' are Landau level quantum numbers. $V_{N'}$ is the electron filling factor of Landau level N'. $L_{N_1}^x(x)$ are the associated Laguerre's polynomials. The important conclusion that can be drawn from equation (1) is that the exchange constants $J_{NN'}$ depend on N and N', which results in a different g factor enhancement for different Landau levels N and different Fermi level positions (maximum of N).

2. Experimental results and discussion

The samples we have investigated in this study are MBE grown modulation doped CdTe/(CdMg)Te quantum wells (QWs) with well widths between 60 Å and 100 Å as well as CdTe/(CdMgMn)Te QWs in order to increase the Zeeman splitting of electrons and holes via the sp-d exchange interaction of the carriers with the Mn-ions in the barrier. The electron carrier concentrations are obtained by optically detected Shubnikov-de Haas oscillations [6]. A low temperature cryostat (1.7 K) with a split coil magnetic is used for PL and PLE measurements up

to 10 T. Excitation was done by an argon ion laser for PL measurements and a dye laser with Pyridine 2 as dye for the PLE experiments.

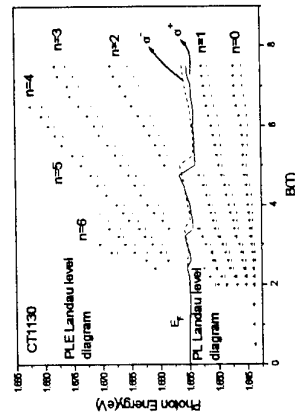


Fig. 1. Landau level diagram of sample CT1130. The Landau levels above the Fermi level are measured by PLE experiments. The Landau levels below the Fermi level are determined by PL measurements. The crosses(+) represent σ^+ and the bars (-) represent σ^- polarisation. The solid and dashed lines are the PLE absorption edges for σ^+ and σ^- polarisation, which represent the transition of electrons from the valence band to the Fermi level in the conduction band.

We have detected the luminescence of the 11 h-subband transition for σ^+ and σ^- polarisation and plotted the peak energies as a function of the magnetic field (Fig. 1). Besides an expected overall linear shift to higher energies we observe oscillatory deviations of the photon energies from the linear dependence as well as oscillations of the Zeeman splitting and the luminescence intensity [6]. As can be seen in Fig. 1 the slope of the photon energies with the magnetic field is different if we compare the same Landau level measured by PL or PLE experiments. The reduced effective mass values obtained from the energy shift are smaller if they are determined by PLE measurements. The mean reduction of the effective mass value comparing PLE with PL measurements is approximately 50%, which unambiguously demonstrates that the mass values of the carriers in the 2DEG are reduced by electron-electron interaction as theoretically predicted [7].

From the splitting of the magnetic subcomponents in the PL and PLE spectra, we can obtain an effective g factor $g^* = g_s^* - 3g_t^*$ only. However, in doped 2DEG systems, the absorption edge observed in the PLE spectra is determined by the Fermi level, which is identical for both spin up and spin down states of the electron. Therefore it is possible to determine the g factor of photo-excited holes from the energy difference in the PLE absorption edge measured for σ^+ and σ^- polarised excitation. If we assume that the hole g factor is identical for all valence band Landau levels, the electron g factor can also be determined separately. From our analysis we obtain strong oscillations of the g factors for both electrons and photo-excited holes (Fig. 2a). The electron g factor varies between 0.3 and -0.7. As the hole g factor changes its sign, we obtain a vanishing splitting for hole Landau levels at certain magnetic field strengths.

The oscillation of the electron g factor is caused by electron-electron coulomb interaction. As can be seen from equation (1), the g factor is proportional to the difference in the electron concentration of spin up and spin down states. This concentration difference will be large when the Fermi level lies between the spin up and spin down Landau levels. By increasing the external magnetic field, the Fermi level passes successively through spin up and spin down states, resulting in an oscillation of the concentration difference and as a consequence an oscillation of the electron g factor. The mechanism leading to an additional oscillation of the g factor of photo-excited holes is not clear yet. But from the data obtained in this work, it seems that the physical process is similar as that holding for electrons. However, the calculation of the self energy of photo-excited holes is complicated and beyond the scope of this paper.

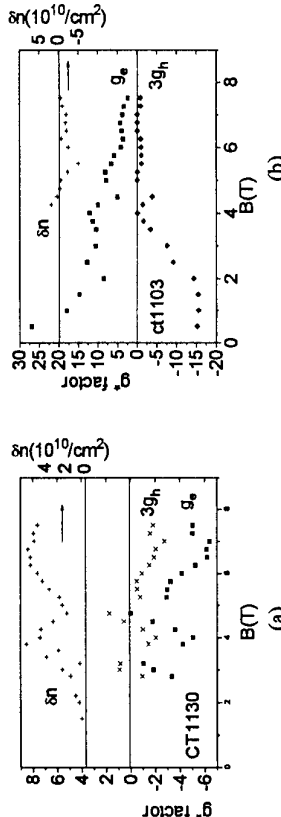


Fig. 2. g factor oscillations of electrons and holes observed for two different QWs a) with a non magnetic barrier layer b) with a semimagnetic barrier layer. When the Fermi level passes the centre of spin up and spin down states, the concentration difference and the g factor reaches a maximum value. A positive δn introduces a negative increase of the g factor (a), whereas a negative δn yields a positive increase of the g factor(b).

We have also added a small amount of Mn (0.5%) into the barriers of the CdTe-heterostructures investigated. Caused by the sp-d exchange interaction between the carriers and the Mn-ions in the barrier the sign of the electron g factor is changed from a negative to a positive value, resulting in a reversal of the ordering of spin up and spin down electron states and from that also in a reversal of the sign of $\delta n = n \uparrow - n \downarrow$. As can be seen in Fig. 2 the g factors are always positively (negatively) enlarged when the concentration difference is negative (positive).

We have also calculated the Fermi level position applying a Gaussian type function for the density of states together with the Landau level width directly from the PL spectra. From these calculations we obtained the concentration difference δn . Following the theory of Ando and Uemura [2] the g factor should be a linear function of $\delta V_{N'}/B^{1/2}$,

$$g_N^* \equiv g_{N''} - c \cdot \frac{\delta V_{N'}}{B^{1/2}} \cdot A_{NN'} \quad (2)$$

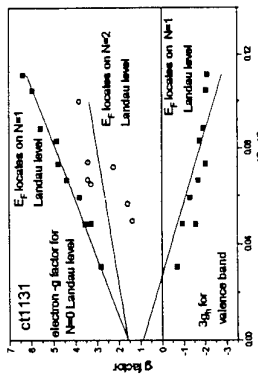
$$\delta V_{N'} = V_{N'\uparrow} - V_{N'\downarrow}, A_{NN'} = \frac{1}{\sqrt{\pi}} \int \frac{N_2!}{N_1!} \exp(-\frac{l^2 q^2}{2}) \cdot (\frac{l^2 q^2}{2})^{N_1-N_2} \cdot L_{N_2}^{N_1-N_2} \cdot d(l^2 q^2)$$

For simplicity, we have neglected the q dependence of dielectric function ϵ for Landau levels below the Fermi level. In Fig. 3a we have plotted the dependence of the g factor as a function of $\delta V_{N'}/B^{1/2}$ for both electrons and holes for Landau level $N = 0$ at different Fermi level positions. The experimentally obtained g factors show a good linear behaviour, with an increased slope when the Fermi level is located at a Landau level with a small quantum number. The constants c and $A_{NN'}$ are obtained from the slopes drawn in Fig. 3.

In Table 1 we have compared the ratios of different $A_{NN'}$ (data with *) with the values expected theoretically

A_{34}/A_{34}	48.8
A_{24}/A_{34}	4.7
A_{14}/A_{34}	1.07
A_{34}/A_{34}	5.6
A_{24}/A_{34}	-----
A_{14}/A_{34}	-----

Fig. 3. Experimentally obtained g factor enhancement as a function of $\delta V_{N'}/B^{1/2}$ for Landau level $N=0$ at different Fermi level position.



We have also chosen a constant magnetic field strength and determined the Zeeman splitting for different Landau level quantum numbers. Applying this condition the Fermi level position N' is fixed as well as the electron concentration difference δn . This means that for different Landau levels we should have different coefficient $A_{NN'}$. These coefficients increase rapidly with increasing N . The experimentally obtained coefficients prove this theoretically predicted increase, as can be seen in Table 1 (the data without *). Comparing the experimental data with the simplified theoretical values, where we have assumed a constant dielectric function ϵ in equation (2), we get a very good agreement. A better agreement can be expected when the theoretical values are calculated taking the q and ω dependence of dielectric function ϵ as well as the Landau level broadening into account.

4. Conclusion

We have investigated g factor oscillations of electrons and photo-excited holes in 2DEG of CdTe in different Landau level quantum numbers. Applying the Pauli principle and the electron-electron Coulomb interaction. The g factor is enlarged linearly with $\delta V_{N'}/B^{1/2}$ and the slope becomes stronger when the Fermi level is fixed on a small Landau level quantum number. The g factor is more strongly enhanced for the electrons occupying higher Landau levels.

Acknowledgements:
The authors want to thank Dr. Gunther Mack for helpful discussions. One of us (J.Shen.) also wants to thank the Volkswagen-Stiftung for the financial support.

Reference:

- I.F.F. Fang and P.J. Stiles, Phys. Rev. 174 (1968) 823.
- T. Ando and Y.Uemura, J. Phys. Soc. Japan, 37 (1974) 1044.
- R.J.Nicholas, R.J.Huang, K.v.Klitzing and G.Weiman, Phys. Rev. 37 (1988) 1294.
- D.Stein, K.v.Klitzing and G.Weiman, Phys. Rev. Lett. 51 (1983) 130.
- I.V.Kukushkin, Solid State Communication, 65 (1988) 1473.
- J.X.Shen, W.Ossau, F.Waag and G.Landwehr, XXIV International School on Physics of Semiconducting Compounds "Jaszowiec '95".
- J.L.Smith and P.J.Stiles, Phys. Rev. Lett., 29 (1972) 102.

Table 1

parameter	Theory	ct1130	ct1131
A_{30}/A_{30}	1.33	2.78*	2.35*
A_{12}/A_{30}	1.16	1.63*	1.95*
A_{30}/A_{30}	-----	2.55*	1.87*
A_{12}/A_{30}	1.16	1.73	2
A_{23}/A_{30}	5.1	3.77	4.4
A_{13}/A_{30}	1.1	1.98	2.97

Effective Mass Anisotropy and Many Body Effects in 2D GaAs/(Ga,Al)As Hole Gases Observed in Very High Magnetic Fields: Comparison of Theory and Experiment

B E Cole¹, S O Hill², Y Imanaka³, Y Shimamoto³, W Batty⁴, J Singleton²,
J M Chamberlain¹, N Miura³, M Henini¹, T Cheng¹

¹ Department of Physics, University of Nottingham, Nottingham NG7 2RD, UK.

² Clarendon Laboratory, University of Oxford, Oxford OX1 3PU, UK.

⁴ Electronics Department, The University of York, Heslington, York YO1 5DD, UK.

³ Institute for Solid State Physics, University of Tokyo, Minato-ku, Tokyo 106, Japan.

Abstract

The effective masses of 2D GaAs/(Ga,Al)As hole systems grown in (100), (311)B, (211)B, (111)B and (110) orientations have been measured in magnetic fields of up to 80T. The measured anisotropy is discussed in terms of bulk effects using newly developed theory. Low energy (millimetre wave) cyclotron resonance absorptions show a 15% shift to higher fields in the temperature range 1.4 to 4.2 K over two orders of magnitude of energy. Many-body effects are used to discuss this observation.

1. Introduction

The two dimensional hole system (2DHS) formed in GaAs/(Ga,Al)As heterostructures exhibits anisotropic effective mass behaviour in marked contrast to the companion electron system. We have previously investigated the cyclotron mass of (311)A grown 2DHSs of ultra-high mobility ($\mu > 100m^2V^{-1}s^{-1}$ at 300mK) and found this to be sensitively dependent on carrier density and magnetic field [1,2]. In this study we investigate the cyclotron mass (i.e. averaged in-plane mass in the ground subband) as a function of growth orientation. The cyclotron resonance (CR) measurements are made on a series of heterostructures with similar layer parameters and at magnetic fields of up to 80T. At these fields all of the 2DHS carriers are deep in the ultrarequantum limit so that the effects of varying carrier density (between the samples) are negligible. A new analytic calculation of the bulk mass characteristics in different crystallographic directions is used to discuss these results. We have also studied the temperature dependence of the CR at both high and very low energies and found a significant shift in resonant field with temperature. A shift on the scale observed has heretofore not been found in a semiconductor system and is interpreted as a consequence of the Coulomb-coupled different single-particle transitions, occurring at different energies as a result of the great nonparabolicity of the 2D hole dispersion. A similar effect, on a much smaller scale, has been observed in the companion 2D electron system, where in general the small spin splitting of the CR is not observed through Coulomb coupling [3]. Furthermore the combination of spin-orbit interaction and asymmetric confinement-potential results in very different dispersion relationships for the two spin projections. Measurements on the hole systems at low energies reveal CR transitions from both the spin subbands.

The samples used were grown by MBE; details are given in Table 1. The layer structure is: Si substrate, 1μm undoped GaAs, 50-period superlattice, 0.5μm undoped GaAs, 50nm undoped Al_{0.33}Ga_{0.67}As spacer, 40nm Be-doped 1x10¹⁸ cm⁻³ Al_{0.33}Ga_{0.67}As, 17nm GaAs capping layer.

Sample Identification	#1/ NU877	#2/ NU952	#3/ NU951	#4/ NU950	#5/ NU953
Growth Plane	(100)	(311)B	(211)B	(111)B	(110)
p _s (x10 ¹¹ cm ⁻²)	2.8	2.5	3.9	3.2	1.8
μ (m ² V ⁻¹ s ⁻¹)	12	5.6	1.45	3.8	7.2
CR mass @ 10.5meV ± 0.005	0.395	0.388	0.355	0.335	0.359
CR mass @ 7.6meV ± 0.002	0.428	0.399	-	-	-

Table 1: Sample Characteristics and Measured Effective Masses.

CR was measured down to 4K at high fields by direct absorption of far infrared (FIR) radiation using FIR lasers operating at 118μm and 163μm in pulsed fields up to 80T. Details of the magnet and measurement systems are given elsewhere [4]. Millimetre-wave Vector Network Analyzer (MVNA) measurements of transmission at fixed energy were also made between 1.4K and 4.2K for a further sample (#6NU942) grown on a (311)A substrate. For this sample, p_s=0.8x10¹¹ cm⁻² and μ>75 m²V⁻¹s⁻¹ at 2K.

2. Two Dimensional subband structure and the bulk Hamiltonian

The valence band structure of bulk GaAs/(Ga,Al)As is accurately described by the 4-band Luttinger Hamiltonian [5] and the QW valence subband structure can be derived from the bulk Hamiltonian in the envelope function approximation [6]. The standard form of the bulk Luttinger Hamiltonian has x, y, z along crystallographic <100> directions. By a rotation of axes, the bulk Hamiltonian can be expressed in terms of x', y', z' coordinates along non <100> directions. Consideration of the elements of the rotated Luttinger Hamiltonian shows that for non-<100> grown GaAs/(Ga,Al)As heterostructures the behaviour of the ground state hole subband is largely determined by the anisotropy of the bulk band structure. Thus the experimentally observed trends in CR masses can be qualitatively explained in terms of variation of bulk hole mass with crystallographic direction. Details of this calculation will be given elsewhere.

It is concluded from the form of the diagonal terms of the rotated Luttinger Hamiltonian that the general behaviour of the ground state, zone centre, QW hole, subband mass (as QW growth direction varies) will reflect the dependence of the bulk in-plane mass. Figure 1 illustrates how the bulk, in plane, heavy-hole mass for GaAs varies with crystallographic direction [11] (using γ₁=6.78, γ₂=1.92, γ₃=-2.70 [7]). Also shown are values of in-plane mass for the ground state heavy-hole subband in a square 10nm GaAs/(Ga,Al)As QW, obtained from full QW subband structure calculations [8], and the CR masses obtained experimentally at 10.5meV energy (118μm). {100} values are shown at the right of the figure, corresponding to the limit l→∞. The trend is seen to be the same in each case with

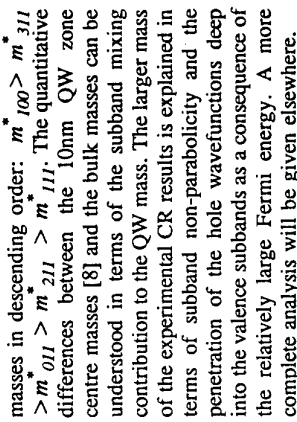


Figure 1 Calculated Hole Masses.

3. Temperature dependence of CR spectra

Figure 2 shows the CR at several temperatures for samples #1 and #2 at 7.6meV ($163\text{ }\mu\text{m}$) laser energy; Lorentzian fits are provided. The shift to lower field with increasing temperature for the (311) sample is apparent, but not for the (100) sample. In Figure 3 the temperature dependence of the resonant field is shown for sample #6 between 1.4K and 4.2K with incident radiation of 0.13meV energy (32GHz); a shift in resonant field to *higher* field of over 15% occurs. Similar temperature dependences were found for energies up to 0.62meV.

These results illustrate the importance of many-body interactions when considering the cyclotron excitations of a non-parabolic system such as the 2DHSS. Since the resonant field is a weighted average of single-particle transitions from both the ground Landau level and from the next level, the low energy temperature dependence follows from the cyclotron mass increase as the heavy-light hole anti-crossing is approached. At energies above this anti-crossing, the effective mass decreases (compare masses for the two FIR energies in Table 1). Thus a decreasing 'coupled' cyclotron mass with increasing temperature is expected. However, the reduction in mass between these two energies is slightly larger for the (100) direction compared to the (311); thus a similar temperature shift would be expected for the (100) sample. This difference may then imply the temperature dependence arises from contributions from transitions normally weak in the (100) system but allowed in the case of low-symmetry (311) samples. We note that the 7.6meV incident energy is larger than the first heavy-light hole subband splitting expected for this sample [1], so the next level above the ground state is the bottom Landau level of the first light hole; subband-subband interactions are known to be greater for (311) oriented samples [9]. Finally, the linewidths depicted in Fig 3 show little change with temperature,

masses in descending order: $m_{100}^* > m_{311}^*$ $> m_{111}^* > m_{211}^*$. The quantitative differences between the 10nm QW zone centre masses [8] and the bulk masses can be understood in terms of the subband mixing contribution to the QW mass. The larger mass of the experimental CR results is explained in terms of subband non-parabolicity and the penetration of the hole wavefunctions deep into the valence subbands as a consequence of the relatively large Fermi energy. A more complete analysis will be given elsewhere.

4. Conclusion

We have measured the anisotropy of the GaAs/(Ga,Al)As effective mass of carriers in 2DHSS for the first time. The results are discussed in terms of the anisotropy of a bulk Hamiltonian. A large temperature dependence of the CR mass is found, which is unparalleled in the companion electron system, and is explained in terms of a many-body cyclotron excitation.

Acknowledgements.

Support is gratefully acknowledged from: EPSRC, The European Community, The British Council and Monbusho (Japan).

References

- [1] S.J. Hawksworth, S.Hill, T.J.B.M.Janssen, J.M.Chamberlain, J.Singleton, U.Ekenberg, G.M.Summers, G.A.Davies, R.J.Nicholas, E.C.Valadares, M.Henini and J.A.A.J.Perenboom, *Semicond.Sci.Techol.* **8** (1993) 1465
- [2] S.Hill, B.E.Cole, J.M.Chamberlain, J.Singleton, P.J.Rodgers, T.J.B.M.Janssen, P.A.Pattenden, B.I.Gallagher, G.Hill and M.Henini, *Physica B* **211** (1995) 440
- [3] N.R.Cooper and J.T.Chalker, *Phys.Rev.Lett* **72** (1994) 2057
- [4] N.Miura, H.Nojiri and Y.Imanaka, Proc.22nd. Int. Conf.on Physics of Semiconductors, Ed. D.Lockwood (World Scientific, Singapore, 1995) p.1111
- [5] J.M.Luttinger, *Phys.Rev.* **102** (1956) 1030
- [6] G.Bastard, *Wave Mechanics applied to Semiconductor Heterostructures*, (Les Éditions de Physique, Les Ulis, 1988).
- [7] B.V.Shanabrook, O.J.Glembocki, D.A.Broido and W.I.Wang, *Superlattices and Microstructures* **5** (1989) 503.
- [8] A.T.Meney, *Superlattices and Microstructures* **11** (1992) 387.
- [9] E.C.Valadares, *Phys.Rev. B* **6** (1992) 3935.

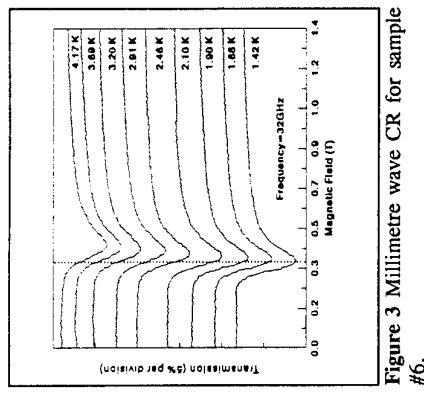


Figure 2 FIR CR for samples #1 and #2;

Figure 2 shows the low energy temperature sample temperatures are marked.

Figure 3 shows the FIR CR for samples #1 and #2; a weighted average of single-particle transitions from both the ground Landau level and from the next level, the low energy temperature dependence follows from the cyclotron mass increase as the heavy-light hole anti-crossing is approached. At energies above this anti-crossing, the effective mass decreases (compare masses for the two FIR energies in Table 1). Thus a decreasing 'coupled' cyclotron mass with increasing temperature is expected. However, the reduction in mass between these two energies is slightly larger for the (100) direction compared to the (311); thus a similar temperature shift would be expected for the (100) sample. This difference may then imply the temperature dependence arises from contributions from transitions normally weak in the (100) system but allowed in the case of low-symmetry (311) samples. We note that the 7.6meV incident energy is larger than the first heavy-light hole subband splitting expected for this sample [1], so the next level above the ground state is the bottom Landau level of the first light hole; subband-subband interactions are known to be greater for (311) oriented samples [9]. Finally, the linewidths depicted in Fig 3 show little change with temperature,

PHOTON DRAG SPECTROSCOPY OF A TWO-DIMENSIONAL ELECTRON SYSTEM

Hans Sigg, PSI-Z, Badenerstr. 569, CH-8048 Zürich, Switzerland
 Peter van Son, University of Delft, PO Box 5046, NL-2600 GA Delft, The Netherlands
 Klaus Köhler, FhG-IAF, Tullastr. 72, D-79108 Freiburg, Germany

The photon drag effect in a 2D electron gas of a GaAs/AlGaAs multi quantum well system is measured using the ps infrared pulses of the wavelength-tunable free electron laser source FELIX. The temporal response of the sample on a ps timescale has been verified, and the continuous spectral response through the intersubband resonance is investigated for low and high intensities at room temperature and at $T = 100\text{ K}$. An analysis of the lineshape yields information about the momentum relaxation times of the electrons in the ground and excited subbands.

The subband relaxation processes in quantum wells (QW's) are a subject of great current interest because of the development of high electron mobility transistors, QW infrared detectors, and QW infrared intersubband lasers. Traditional techniques for their investigation include time resolved spectroscopy [1], infrared saturation spectroscopy [2] and the differential absorption of excited states [3]. In general, these techniques probe energy relaxation times. The photon drag (PD) effect, on the other hand, (which produces a current directed along the path of the absorbed photons) is directly linked to the current or momentum relaxation times of the electrons in the ground and excited subbands [4, 5]. Here we study the PD effect in QWs with a high-density 2-dimensional electron gas (2DEG) and in which the intersubband transition energy $\epsilon_{12} \sim 120\text{ meV}$ is larger than the optical phonon energy. We use as the frequency-tunable source (with sufficient power) the Free Electron Laser for Infrared experiments (FELIX) [6].

The PD signal is on the one hand a consequence of direct momentum transfer from the photon to the electron system, and on the other hand a consequence of velocity-selective excitation (Doppler effect). The PD-induced current resulting from an intersubband absorption is conveniently represented as the sum of the momenta of the non-equilibrium states (NES) in the ground (1) and excited (2) subbands multiplied by the product of their respective charges, inverse effective masses and corresponding momentum relaxation times, τ_1 and τ_2 [4]. We call these NES of the first and second subband 'holes' and 'electrons' respectively because of their energy position below and above the Fermi energy E_F and due to their effective charges. As long as the momentum of the holes and electrons is unrelaxed ($t < \tau_1, \tau_2$), the current is proportional to the transferred photon momentum $h\nu/c$, where $h\nu$ is the photon energy and c/n is the light propagation velocity in the semiconductor. At later times $\tau_2 < t < \tau_1$ the net momentum of the hole distribution. Finally, for $t > \tau_1$ the current is solely due to the net momentum of the hole distribution. The net momentum of the hole distribution for $\tau_2 < t < \tau_1$ is zero exactly on resonance ($h\nu = \epsilon_{12}$), because excitation occurs with the electron wavevector k distributed symmetrically around $k = 0$. For slight detuning, excitation occurs at k -values given by $\hbar^2/m^* \mathbf{k} \cdot \mathbf{q} = h\nu - \epsilon_{12}$ (Doppler effect), where \mathbf{q} is the electron or hole wavevector [7]. This yields a large contribution to the PD signal proportional to $|\mathbf{k}| > |\mathbf{q}|$ which is, however, strongly smeared out, because the Doppler shift is usually much smaller than the linewidth of the transition. The two contributions lead to the following simple

frequency-dependence of the photon drag current [4, 7]:

$$i_{PD} \propto \alpha(\omega)\tau_2 + \frac{\partial\alpha}{\partial\omega}\frac{E_F}{2\hbar}(\tau_1 - \tau_2) \quad (1)$$

where $\alpha(\omega)$ is the absorption coefficient. The specific spectral dependence of the PD signal allows the separation of the two contributions and a relative determination of the momentum relaxation times. The momentum relaxation time τ_2 of the excited subband can be compared with the phase relaxation time T_2 which can be estimated from the linewidth Γ (FWHM) of the absorption: $T_2 \sim 2\hbar\Gamma^{-1}$. T_2 also includes phase relaxation processes, such as electron-electron scattering, that conserve the total momentum of the electron system, implying $\tau_2 > T_2$. The momentum relaxation time τ_1 of the ground subband can be compared with the current relaxation time τ_e as defined by the Hall mobility $\mu_{Hall} = e/m^* \tau_e$. The hole excitations in the PD effect, however, occupy a much larger energy range ($\sim E_F$) than the thermal energy range relevant for equilibrium transport ($\sim kT$). This implies that $\tau_1 < \tau_e$ and that the ratio τ_e/T_2 constitutes an upper limit for the ratio τ_1/τ_2 .

The experiments are performed on MBE grown AlGaAs/GaAs samples with 30 about 8 nm wide quantum wells each of which contains $\sim 0.810^{12}\text{ cm}^{-2}$ electrons. A Ge prism is pressed onto the sample surface, and the light is coupled into the 2DEG through a single-pass internal reflection at the Ge/GaAs interface [8], while the electrical signal is capacitively coupled out to a microstrip line [9]. This set-up allows the measurement of electrical transients up to 34 GHz, the bandwidth of the sampling oscilloscope. The true width of the PD signal is expected to be equal to the 2 ps length of the FELIX micropulse. FELIX produces micropulses at 1 ns intervals during a macropulse which is a few μs long. Best signal-to-noise performance is obtained by electrical low-pass filtering of the pulsed PD signal at $\sim 1\text{ MHz}$, the time scale of the macropulse. At room temperature, the continuous spectra thus obtained, were found to be in very good agreement with spectra obtained by digitally integrating the 20 ps long pulse transients (see inset of Fig. 1).

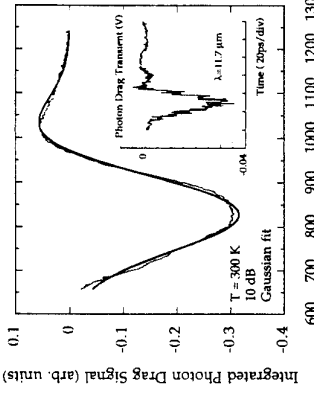


Fig. 1: Room-temperature spectrum of the photon drag signal taken at the high micropulse energy density of approximately $5\mu\text{J}/\text{cm}^2$. The fitted spectrum (full line) is obtained by inserting a Gaussian line profile into the predicted wavelength dependence (Eq. 1, text). The fast transient response of the detector is shown in the inset.

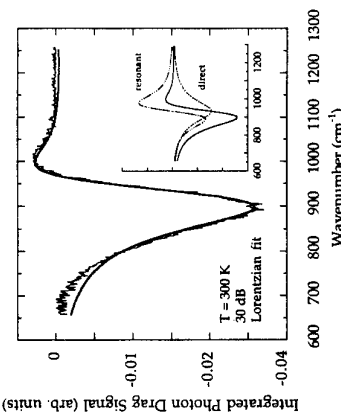


Fig. 2: Room-temperature spectrum of the photon drag signal taken at the low micropulse energy density of approximately $0.05 \mu\text{J}/\text{cm}^2$. The spectrum is fitted with a Lorentzian line profile. The Photon drag effect is the sum of direct and resonant contributions, which are respectively proportional to the absorption and its derivative with respect to energy (inset).

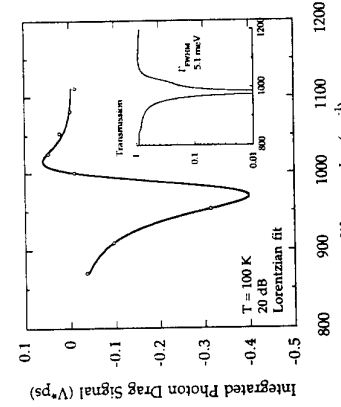


Fig. 3: Integrated transients of the photon drag signal taken at 100 K for various wavelengths (circles). The full line gives the Lorentzian fit to the data. Inset: Normalized transmission after a single reflection at the critical angle of $\sim 55^\circ$ at the Ge/iAs interface.

Unfortunately, the slightly different sample design used in the flow-cryostat did not allow continuous spectra to be taken at low temperatures. Typical micropulse energies impinging on the approximately 2mm^2 large samples were $1 \mu\text{J}$, attenuated by factors up to 1000 (30 dB).

The room temperature PD spectra taken at high (10dB) and low (30dB) excitation intensities (Figs. 1 and 2) are almost exactly reproduced by Eq. 1 using a Gaussian and a Lorentzian absorption profile, respectively. At 10 dB we obtain for the single coefficient of Eq. 1, $E_F \cdot (\tau_1 - \tau_2)/2\tau_2 \approx 13.6 \text{ meV}$. With $E_F = 27 \text{ meV}$, this implies $\tau_1/\tau_2 \approx 2.0$. This value for the ratio of the relaxation times is larger than the predicted upper limit obtained from $\mu_{Hart}(300K) \approx 7200 \text{ cm}^2/\text{Vs}$ and from the absorption linewidth measured at the very low intensities of a Fourier transform spectrometer, $\Gamma_{AB} \approx 8.7 \text{ meV}$: $\tau_e/T_2 \approx 1.9$. A possible explanation for the large relaxation time ratio is optical-phonon reabsorption, which would reduce T_2 and thus increase the upper bound. However, the linewidth obtained from the fit to the PD spectrum, $\Gamma_{PD} \approx 26.9 \text{ meV}$, is much larger than Γ_{AB} , indicating strong saturation. In this regime, the 2DEG is far from equilibrium, and the hole/electron excitation picture becomes questionable. The Lorentzian fit to the spectrum taken at 30 dB attenuation yields a linewidth of $\Gamma_{PD} = 19.3 \text{ meV}$, which still is much larger than Γ_{AB} . As before, the relaxation time ratio is high, from the fit shown in Fig. 2, we obtain $\tau_1/\tau_2 \approx 1.95$.

At low temperature, the situation changes dramatically. While similar relaxation time values are obtained at 200 K, the Lorentzian-line-fit to the integrated PD signal taken at 100 K (Fig. 3) yields the coefficient $E_F \cdot (\tau_1 - \tau_2)/2\tau_2 \approx 7.4 \text{ meV}$ and the linewidth $\Gamma_{PD} \approx 9.6 \text{ meV}$. Again with $E_F \approx 27 \text{ meV}$, the relaxation time ratio τ_1/τ_2 become 1.55, while the low temperature mobility value of $46000 \text{ cm}^2/\text{Vs}$ and $\Gamma_{AB} \approx 5.1 \text{ meV}$ yield $\tau_e/T_2 \approx 6.2$. The small relaxation time ratio seems to correlate with the reduced linewidth and corresponding reduced saturation. This trend is found to continue: At 40 K the line narrows further, while the ratio τ_1/τ_2 drops to ~ 1.3 .

References

- [1] D.Y. Oberli, D.R. Wake, M.V. Klein, J. Klem, T. Henderson, and H. Moroc, Phys. Rev. Lett. **59**, 696 (1987).
- [2] A. Seilmeyer, H.-J. Hubner, G. Absreiter, G. Weimann, and W. Schlapp, Phys. Rev. Lett. **59**, 1345 (1987).
- [3] J. Faist, C. Stoeni, F. Capasso, L. Pfeiffer, and K. West, Appl. Phys. Lett. **44**, 872 (1984).
- [4] S.Luryi, Phys. Rev. Lett. **58**, 2263 (1987); and A. Grinberg, and S.Luryi, Phys. Rev. **B38**, 87 (1988).
- [5] A.D. Wieck, H. Sigg, and K. Ploog, Phys. Rev. Lett. **64**, 463 (1990).
- [6] R.J. Bakker, C.A.J. van der Geer, D.A. Jarosynski, A.F.G. van der Meer, D. Oeps, and P.W. van Amersfoort, J. Appl. Phys. **74**, 1501 (1993).
- [7] H. Sigg in "Intersubband transitions in quantum wells", E. Rosenthal, B. Vinter, and B. Levine, eds; NATO ASI Series B, Vol. **288** (Plenum Press, NY (1992)); p: 83.
- [8] F. Keilmann, Solid State Commun. **92**, 223 (1994).
- [9] M. Kwakernaak, B. Margotte, Diplomthesis 1995 ETH-Z, unpublished

Zero-field spin-splitting in InAs/AlSb quantum wells

C. Gauer, M. Hartung, A. Wixforth, J.P. Kotthaus
 Sektion Physik der Ludwig-Maximilians-Universität München, D-80539 München, Germany
 B. Brar, H. Kroemer
 Department of Electrical and Computer Engineering, UC Santa Barbara, CA 93106, USA

Abstract

Zero-magnetic-field spin-splitting of two-dimensional conduction band electrons in InAs/AlSb multi-quantum wells is observed in intersubband absorption experiments. An in-plane magnetic field induces combined spin-flip intersubband transitions which for magnetic fields $B > 0$ T are separated in energy by as much as $\Delta E = 17$ meV. With increasing magnetic field this separation diminishes and a crossover between both resonances occurs at about $B = 1$ T. The excitation of spin-flip resonances as well as the zero-field spin-splitting are direct consequences of the bulk inversion asymmetry of InAs providing two independent methods to determine the relevant band structure parameter.

Introduction

The inversion asymmetry present in III-V semiconductors with zinc-blende structure is manifested in two prominent physical effects: First, the bulk crystalline electric field is Lorentz-transformed in the frame of a moving electron into an effective magnetic field B_{int} lifting the spin-degeneracy of the conduction band [1] for all directions in k -space except for $\vec{k} \parallel \{100\}$ and $\{111\}$ [2]. A k^3 -term in the electronic dispersion, whose strength is determined by a parameter γ makes the electronic energy spin-dependent and thus accounts for the so-called zero-field spin splitting [3]. Such a spin-splitting of the conduction band has been experimentally observed and theoretically described for bulk materials [4] as well as for two-dimensional electron systems (2DES) confined in semiconductor heterostructures [5,6]. Secondly, the additional spin-dependent terms in the Hamiltonian allow the excitation of electric dipole induced spin-flip resonances. These have been investigated in detail for bulk InSb [7]. To the best of our knowledge, however, there is no experimental evidence that both effects - the zero-field spin-splitting in combination with the excitation of spin-flip resonances - have been observed simultaneously thus allowing to independently determine the strength of the bulk inversion-asymmetry.

Experiment

Here, we report on the spectroscopic observation of combined spin-flip intersubband transitions in a symmetrically doped InAs/AlSb multi-quantum well structure. The oscillator strength of the resonances is found to increase strongly with an external magnetic field applied parallel to the plane of the layers. The excitation of the spin-flip transitions is made possible by a combination of both the in-plane magnetic field and the bulk inversion asymmetry of InAs [8]. In the framework of an 8-band matrix Hamiltonian the resonance strength is determined by inversion asymmetry terms $\propto G_{ij}P_j$ with the canonical momentum P_{ij} and $i, j \in x, y, z$ [8]. The combined spin-flip intersubband transitions remain spin-split even for $B \rightarrow 0$ [9] with a large energetic separation of $\Delta E = 17$ meV. This is caused by the high carrier density (large k -vector) in our samples and the narrow band gap of InAs. Hence, we are able to directly determine the

material constant γ as the spin-splitting at finite magnetic fields is about an order of magnitude larger than the magnetic energies in the experiment. Thus the oscillator strength of the excitations and the zero-field splitting constitute two different methods to experimentally deduce the strength of the bulk inversion-asymmetry.

The InAs/AlSb multi-quantum well structures were grown on a GaAs substrate followed by a 1 μm AlSb buffer and a 10 period superlattice [10] to accommodate the strain between the substrate and the active layers. The 20 period multi-quantum well consists of 15 nm InAs layers stacked between Te- δ -doped AlSb barriers of 10 nm width. Hall effect measurements at low temperatures revealed a carrier density per well of $N_s = 2.5 \cdot 10^{12} \text{ cm}^{-2}$.

Mid infrared (MIR) spectra were taken using a rapid scan Fourier transform spectrometer with the sample mounted in multiple reflection path geometry (MRPC, inset of Fig. 1). Experimentally, we determined the relative change in MIR transmission $T(B=0)/T(B=0)$ of the unpolarized radiation for different in-plane magnetic fields B . All experiments were performed at low temperatures $T = 4.2\text{K}$.

In Fig. 1 we depict typical relative transmission spectra taken at different in-plane magnetic fields $B \leq 13\text{T}$ ratioed against a reference spectrum at $B=0\text{T}$. We observe two well separated resonances I and II both of which gain oscillator strength as the field is increased. There is no resonant absorption of the 2DEG detectable at $B=0\text{T}$ which could be confirmed in a separate experiment by ratioing against a reference substrate. As the magnetic field is increased the low energy resonance I shifts to higher energies whereas the position of the high energy line II remains almost constant.

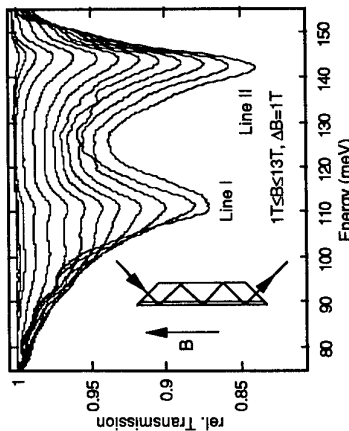


Fig.1: Relative transmission spectra for $B \leq 13\text{T}$ with $\Delta B = 1\text{T}$ in the multiple reflection path geometry (inset). At high magnetic fields two resonances I and II can be seen which both gain oscillator strength as the field is increased. At low fields resonance I splits into two lines giving experimental evidence for a zero-field spin-splitting.

This peculiar magnetic field dependence of the observed resonances has been observed and described in detail for a similar structure mounted in Voigt geometry [8]. We found that the radiation component perpendicular to the magnetic field induces both spin-conserving as well as spin-flip transitions. In these terms, line II is a superposition of the two allowed spin-conserving resonances $|0\uparrow\rangle \rightarrow |1\downarrow\rangle$ and $|0\downarrow\rangle \rightarrow |1\uparrow\rangle$, while line I corresponds to a superposition of the spin-flip excitations $|0\uparrow\rangle \rightarrow |1\uparrow\rangle$ and $|0\downarrow\rangle \rightarrow |1\downarrow\rangle$. Both lines I and II are separated in energy by the depolarization shift. While line I is induced by the parallel magnetic field the spin-flip transition II is made possible by a combination of the parallel magnetic field and the bulk inversion asymmetry of InAs. The combined resonances can only be excited at high $k_{||}$ -values as the transition matrix elements turn out to be strongly $k_{||}$ -dependent.

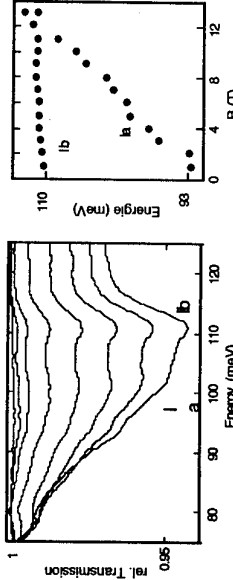


Fig. 2: The spin-flip resonances can be clearly resolved at low magnetic fields $B \leq 8\text{T}$ with $\Delta B=T$. Transition Ib is roughly constant in energy and has a greater oscillator strength (area under the curve) than transition Ia. Line Ia, on the other hand, shifts to higher energies as the magnetic field is increased.

In MRPC as described here, the magnetic field orientation is the same as in the Voigt geometry. In contrast to the latter where we observed only a pronounced asymmetry of line I, this resonance is now split into two well separated spin-flip transitions Ia and Ib at low magnetic fields $B \leq 8\text{T}$ as depicted in Fig. 2a. For $B \rightarrow 0$ the energetic difference is approximately $\Delta E=17\text{meV}$ and decreases with increasing magnetic field. With increasing B the low energy line Ia shifts to higher energies while the position of the high energy transition Ib remains roughly constant up to $B=13\text{T}$ (Fig. 2b). As can be seen from the figure, both lines cross each other at around $B=12\text{T}$.

Interpretation

Following Eppenga et al. [11] the zero-field spin splitting ΔE may be expressed as

$$\Delta E = 2\gamma \sqrt{k_x^2(k_y^2 - k_z^2)^2 + k_z^2(k_x^2 - k_y^2)^2}$$

with a calculated value of $\gamma(\text{InAs})=130\text{ eV}\text{\AA}^3$ [12]. The \mathbf{k} -value along the direction of electric confinement \mathbf{y} is taken to be $k_y = \pi/L$ for the ground state subband (well width L) and k_x and k_z denote the in the plane wavevectors. An analogous calculation for the first subband with $k_y = 2\pi/L$ yields the $\mathbf{k}\text{-dependence}$ of the splitting between the $|0\rangle \rightarrow |1+\rangle$ and $|0+\rangle \rightarrow |1-\rangle$ combined spin-flip resonances. For $\mathbf{k}=k_{\mathbf{F}}$ this calculation agrees reasonably well with the experimentally determined value of the splitting. Therefore our experiment confirms the calculated value of γ from reference [12].

We now turn to the comparison of γ inferred from the zero-field spin-splitting to its value deduced from the magnetic field dependence of the oscillator strength. In the 8-band matrix formalism the oscillator strength of the combined resonances is well described by the G -value of $\text{InSb } G = \frac{3\hbar^2}{2m_0}$ [8]. According to Cardona et al. [13] the parameter γ can be approximated by

$$\gamma = \frac{4}{3} G \hbar \kappa \frac{\Delta}{E_s(E_s + \Delta)}$$

Taking $E_g=0.42\text{eV}$, the spin-orbit-splitting $\Delta=0.38\text{eV}$, and the Kane energy $\kappa=22.9\text{eV}$ we find $\gamma=150\text{ eV}\text{\AA}^3$ in good agreement with the above result of the experiment as well as the theoretical value.

The magnetic field dependence of the spin-split lines Ia and Ib (Fig. 2b) may be qualitatively understood as follows: The cross-over at $B=12\text{T}$ is a clear signature that the sum of the effective g -factors in the respective subbands must be equal to zero. In other words, the Zeeman-term cancels the zero-field spin-splitting causing the effective g -factor to change its sign analogous to the Faraday configuration [3]. This cancellation occurs at different magnetic fields analogous to the two subbands because of the different values of \mathbf{k}_y and the energy-dependent g -factors.

Conclusion

In summary, we observe combined spin-flip intersubband transitions in a parallel magnetic field \mathbf{B} which are made possible by the bulk inversion asymmetry and the narrow band-gap of InAs in combination with the large Fermi-wavector. The large splitting of $\Delta E=17\text{meV}$ for $\mathbf{B} \rightarrow 0\text{T}$ is caused by the lack of inversion asymmetry in zinc-blende materials lifting the spin-degeneracy for finite \mathbf{k} . The observed oscillator strength of the combined resonance as well as the value of the zero-field splitting enables us to determine the inversion asymmetry parameter experimentally. Reasonably good agreement is found between these independent methods as well as the theoretical value. The cross-over of both lines at $B=12\text{T}$ can be explained by the influence of a parallel magnetic field on the electronic energies in a quantum well.

We gratefully acknowledge valuable discussions with U. Rössler, F. Pikus and W. Zawadzki. The work in Munich was sponsored by the Volkswagen Stiftung. The Santa Barbara group gratefully acknowledges support from the Office of Naval Research and from QUEST, the NSF Science and Technology Center for Quantized Electronic Structures (Grant DMR 91-20007).

References

- [1] G. Dresselhaus, Phys. Rev. **100**, 580 (1955)
- [2] N.E. Christensen, M. Cardona, Solid State Commun. **51**, 491 (1984)
- [3] G. Lommer, F. Malcher, and U. Rössler, Phys. Rev. Lett. **60**, 728 (1988)
- [4] H. Riechert, S.F. Alvarez, A.N. Tikkor, V.I. Safarov, Phys. Rev. Lett. **52**, 2297 (1984)
- [5] P.D. Dresselhaus, P.M.A. Papavassiliou, R.G. Wheeler, R.N. Sack, Phys. Rev. Lett. **68**, 106 (1992)
- [6] B. Jusserand, D. Richards, H. Peric, B. Etienne, Phys. Rev. Lett. **69**, 848 (1992)
- [7] Y.-F. Chen, M. Dobrowolska, J. K. Furdyna, S. Rodriguez, Phys. Rev. B **32**, 890 (1985)
- [8] C. Gauer, A. Wixforth, J.P. Kotthaus, M. Kubisa, W. Zawadzki, B. Brar, H. Kroemer, Phys. Rev. Lett. **74**, 2772 (1995)
- [9] C. Gauer, A. Wixforth, J.P. Kotthaus, B. Brar, H. Kroemer, submitted for publication
- [10] G. Tutte, H. Kroemer, J.H. English, J. Appl. Phys. **65**, 5239 (1989)
- [11] R. Eppenga, M.F.H. Schuurmans, Phys. Rev. B **37**, 10923 (1988)
- [12] E.A. de Andrade e Silva, G.C. La Rocca, F. Bassani, Phys. Rev. B **50**, 8523 (1994)
- [13] M. Cardona, N.E. Christensen, G. Fasol, Phys. Rev. B **38**, 1806 (1988)

Phase Transitions from Disorder in Two-Dimensional Solids

H.A. Fertig and M.C. Cha

Department of Physics and Astronomy,
University of Kentucky, Lexington,
Kentucky 40506-0055

$$(1)$$

We analyze a model of a two-dimensional crystal subject to a slowly varying random potential, and find evidence for the existence of a zero-temperature phase transition via the appearance of isolated dislocations above a critical disorder strength. The result is in contrast to earlier analyses of the model, which found that the crystal is always unstable with respect to dislocation formation. The argument is generalized to finite temperature and a phase boundary is derived. Molecular dynamics simulations of a model electron crystal show strong evidence of this phase transition at low temperatures.

It has long been appreciated that topological defects can drive interesting phase transitions in two-dimensional systems as a function of temperature. These defects, which carry a topological “charge,” are bound together into neutral pairs at low temperatures, and unbind above the Kosterlitz-Thouless transition temperature¹. For the case of XY ferromagnets, these excitations are vortices; for crystals, they may be dislocations or disclinations^{2,3}. The appearance of isolated defects in the system generally changes the behavior of certain correlation functions from power-law (quasi-long-range) to exponential (short-range) behavior.

An interesting question is whether this phenomenology has an analog for zero-temperature systems subject to various strengths of disorder. This question arises in a variety of situations: in this work, we will focus on crystal systems, with particular emphasis on their stability with respect to defect formation in the presence of a slowly varying random potential. The analysis may be applied, in particular, to the electron crystal in a two-dimensional system in the presence of a slowly varying disorder potential. We will give evidence, both analytical and numerical, that there is a zero-temperature phase transition in which isolated dislocations appear above a critical disorder strength. Analogous arguments for the appearance of isolated disclinations for stronger disorder⁴(b) may also be constructed⁵. We note that recent numerical simulations have shown strong evidence of a disorder induced disclination unbinding transition in the electron crystal⁴.

To further strengthen the case that such a transition is possible, we have performed large scale simulated annealing molecular dynamics simulations of electron

crystals in a slowly varying random potential. Our results show behavior indicative of such a transition: the positional correlation length rises sharply to above the system size at a critical disorder strength (see Fig. 1), and simultaneously one finds that the number of isolated dislocations in the low-temperature configuration drops sharply as the transition is approached from above. Results for the groundstate configurational energy also show structure at the transition (see Fig. 2).

We begin with a continuum elasticity theory model of the two-dimensional crystal, in which the energy to create a strain field $u_{ij}(\vec{r}) \equiv \frac{1}{2}(\partial_i u_j + \partial_j u_i)$, where \vec{u} is the displacement field of the lattice and $i, j = x, y$, is given by

$$E = \frac{1}{2} \int d^2r [2\mu u_{ij}^2 + \lambda(u_{kk} - \delta\rho(\vec{r}))^2]. \quad (1)$$

We have taken our unit of length in the above to be the lattice constant (i.e., $a_0 \equiv 1$), and μ and λ are Lamé coefficients. The quantity $\delta\rho$ represents a random field, which for simplicity we assign an uncorrelated Gaussian distribution, $P[\delta\rho(\vec{r})] = \frac{1}{\sqrt{2\pi\sigma}} e^{-\delta\rho(\vec{r})^2/2\sigma}$. One can see in this model that the coupling of the strain field to the disorder has the effect of forcing in fluctuations in the lattice density, which is proportional to u_{kk} . This model has been studied previously to describe a crystal with random substitutional disorder⁶; it has also been argued that the $\lambda \rightarrow \infty$ limit of this model may be used to describe the electron crystal in a random neutralizing background^{4,7}.

The strain field in Eq. 1 may be separated into a smoothly varying part ϕ_{ij} and a part due to dislocations with cores at sites \vec{r}_j and Burgers vectors \vec{b}_j . The energy of the resulting configuration turns out to be separable in these two contributions⁶. The contribution to the energy due to the presence of dislocations has the form

$$E_0^{dis} + \frac{K'}{4\pi} \int d^2r \delta\rho(\vec{r}) \sum_j \hat{z} \cdot [\vec{b}_j \times (\vec{r} - \vec{r}_j)], \quad (2)$$

where $K' = 4\mu\lambda/(2\mu + \lambda)$, and E_0^{dis} is the energy of the dislocations in the absence of the disorder field^{3,6}.

Suppose one attempts to find the ground state for a given disorder realization in a finite size system of area A . We can first minimize the energy with respect to the smooth displacements ϕ_{ij} without introducing any dislocations. We now ask: can one find a site in the sample for which the introduction of a dislocation lowers the energy? The energy to create a dislocation with Burgers vector \vec{b} in the absence of disorder has the form $E_0 = \frac{Kb^2}{16\pi} \ln A$ for large A where $K = 4\mu(\mu + \lambda)/(2\mu + \lambda)$; to be energetically favorable, the interaction energy between the dislocation and the disorder E_1 (i.e., the second term in Eq. (2)) must more than balance this energy cost. For a given site, the ensemble of disorder configurations will generate

a distribution of interaction energies $P(E_1)$ that in the limit of large sample sizes should be independent of the site location. The probability distribution $P(E_1)$ may be computed *exactly* by a functional integral, with the result $P(E_1) = \frac{1}{\sqrt{2\pi\eta}} e^{-E_1^2/2\eta}$, with

$$\eta = \left(\frac{K'}{4\pi}\right)^2 \frac{\sigma\pi b^2}{2} \ln A. \quad (3)$$

The probability that a site is energetically favorable for creation of a dislocation is then given by $p = \int_{-\infty}^{-E_0} P(E_1) dE_1$, which for large A is easily shown to have the form $p \sim e^{-E_0^2/2\eta} = A^{-\left(\frac{2K}{4K'}\right)^2/\pi\sigma}$. Since the number of sites in the sample scales as A , the number of sites for which it is energetically favorable to create the dislocation scales as $A^{1-\left(\frac{2K}{4K'}\right)^2/\pi\sigma}$, so that it will only be possible to find sites for the dislocation in the thermodynamic limit if

$$\sigma > \sigma_c = \frac{1}{\pi} \left(\frac{K}{4K'}\right)^2,$$

where we have set the Burgers vector to its lowest non-trivial value, $b = a_0 \equiv 1$.

In order to find the evidence of this zero-temperature transition, we performed a simulated annealing molecular simulation. We use a model electron system subject to a random potential, whose configurational energy is given by

$$E[\{\vec{r}_i\}] = \sum_{i \neq j}^{N_p} \frac{e^2}{|\vec{r}_i - \vec{r}_j|} - \sum_i^{N_p} \sum_j^{N_i} A_i \exp(-|\vec{r}_i - \vec{R}_j|^2/\xi_i^2)$$

where e is the electronic charge, \vec{r}_i are the position of particles, \vec{R}_j are the positions of randomly quenched impurities, and N_p and N_i are the number of particles and impurities respectively, ξ_i is the range of the random potential. A neutralizing uniform background is assumed to cancel out the diverging energy due to the long-range electron-electron interactions. We tune N_i to change the strength of the disorder, keeping A_i fixed.

The positional correlation is characterized as the correlation function of the field $\rho_{\tilde{G}}(\vec{r}_i) = e^{\tilde{G} \cdot \vec{r}_i}$ where \tilde{G} are reciprocal vectors. In practice the correlation function is averaged over six \tilde{G} 's with $|\tilde{G}| = 4\pi/\sqrt{3}a_0$, which give peaks of structure factors. It is important to determine such \tilde{G} 's carefully because the positional correlation length is sensitive to \tilde{G} . The positional correlation length ξ_G is determined by fitting the correlation function to an exponential form. Fig. 1 shows a rapid increase of the positional correlation lengths as N_i/N_p approaches to $n_c = 0.075 \pm 0.005$ from above. When $N_i/N_p \leq n_c$, either the correlation lengths are much longer than the system size or the long-range correlation cannot be fitted in an exponential form.

In conclusion, we argue that there is a dislocation-unbinding transition due to a quenched random potential at a finite strength of disorder down to zero temperature.

The difference of our approach from the previous theoretical works resides on the failure of the fugacity expansion on which previous RG studies are based. Numerical simulations of a model electron system in a slowly varying random potential shows evidence of this transition.

Acknowledgements. The authors would like to thank J.P. Straley and E. Kolomeisky for helpful discussions. This work was supported by the NSF through Grant No. DMR-92-02255, as well as by the Sloan Foundation and the Research Corporation.

REFERENCES

1. J.M. Kosterlitz and D.J. Thouless, *J. Phys. C* **6**, 1181 (1973).
2. For a review of two-dimensional melting, see K. Strandburg, *Rev. Mod. Phys.* **60**, 161 (1988).
3. B.I. Halperin and D.R. Nelson, *Phys. Rev. Lett.* **41**, 121 (1978); D.R. Nelson and B.I. Halperin, *Phys. Rev. B* **19**, 1855 (1979); A.P. Young, *Phys. Rev. B* **19**, 1855 (1979).
4. (a) M.C. Cha and H.A. Fertig, *Phys. Rev. Lett.* **73**, 870 (1994); (b) *Phys. Rev. B* **50**, 14368 (1994)
5. M.C. Cha and H.A. Fertig, to appear in *Physical Review Letters*; H.A. Fertig and M.C. Cha, unpublished.
6. D.R. Nelson, *Phys. Rev. B* **27**, 2902 (1983)
7. A.B. Dzyubenko and Y.E. Lozovik, *Surf. Sci.* **263**, 680 (1992)

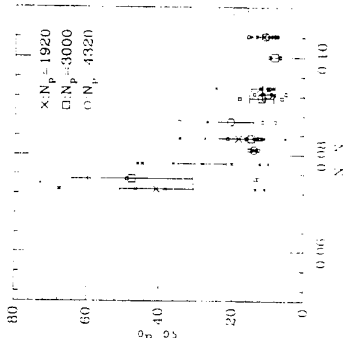


Fig. 1. The positional correlation lengths of two-dimensional electron systems at zero temperature where N_p is the number of electrons and N_i is the number of quenched impurities. Small symbols represent actual data, bigger symbols represent averages.

Phonon assisted energy relaxation for 2d electrons at high magnetic field

S.V.Iordanskii⁽¹⁾, Y.Levinson⁽²⁾ and S.Levit⁽²⁾

⁽¹⁾. Landau Institute for Theoretical Physics,
Kosygin str. 2, 117334 Moscow, Russia;

⁽²⁾. Physics Department, Weizmann Institute of Science,
Rehovot, Israel

Abstract

The energy relaxation rate due to one phonon processes for 2d electrons is calculated. An explicit dependence on the characteristics of random potential, magnetic field and electron energy is obtained.

Key words: electron-solid interaction, scattering.

For the calculation of the energy relaxation rate one need to know the proper two particle electron correlation function with given energy and momentum transfer. Such calculation was done numerically for white noise random potential in [1, 2]. In this paper we consider the energy relaxation rate for a test electron in a smooth random potential due to an emission of acoustical phonons. We exploit the semiclassical approximation used in a number of papers (see e.g. [3, 4]). The main difference as to compare to these papers is that we assume high enough magnetic field and high mobility when electron drift velocity v_d in a random potential U due to far off impurities is small compare to the velocity of sound s . Therefore the local approximation considered in these papers gives no possibility for phonon absorption or emission. We show that nevertheless at large enough phonon wave length one phonon processes are possible and give some universal relaxation rate defined by global structure of equipotential lines and the correlation length L of the random potential.

The relaxation rate due to phonon emission is defined by Golden Rule formula of the second order perturbation theory

$$\frac{1}{\tau(E)} = \frac{2\pi}{\hbar} \int |V(k)|^2 \frac{d^3 k}{(2\pi)^3} \ll S(\omega, k, E) \quad (1)$$

Here $S(\omega, k, E) = \sum_m \delta(E - E_m - \hbar\omega(k)) < E|e^{i\vec{q}\cdot\vec{r}}|E_m >^2$ is the pair correlation function for electrons, m labels the electron states, the double angular brackets denote the average over the random potential, \vec{q} is the in plane component of phonon momentum, $k, \omega(k) = sk$ is phonon frequency, $V(q)$ is the proper vertex, defining either piezoelectric or deformation potential electron-phonon coupling [5]. We neglect here k dependence of the formfactor for the transverse electron motion assuming small value of k .

2d electrons are in random Gaussian potential $U(\vec{r})$ with isotropical correlation function $\ll U(\vec{r})U(\vec{r}') \gg = R(|\vec{r} - \vec{r}'|/L)$ with correlation length $L > l_H$, where magnetic length $l_H^2 = c\hbar/eH$. The last assumption suggest a large enough magnetic field. As a measure we use the ratio of the average drift velocit v_d to the velicity of sound s $\gamma = s/v_d = \hbar s l_H^{-2} L / \sqrt{R(0)} \gg 1$.

We shall not try to perform the average of the relaxation rate over the random potential. Instead we shall evaluate "typical" cases which give the main contribution to this average.

1. Phonon emission at large electron energies. If electron energy is large $|E| \gg [R(0)]^{-1/2}$ (we assume $\hbar\omega_c \gg [R(0)]^{1/2}$) and the density of states is small then the random potential has a very simple form in the regions which give the main contribution to any average.

Using the properties of Gaussian distribution we can calculate the joint distribution to have at some point the values $U = E$, $\frac{\partial U}{\partial x_i} = a_i$, $\frac{\partial^2 U}{\partial x_i \partial x_j} = A_{ij}$. It turns out that this probability is independent Gaussian for quantities $a_i, A_{11} - A_{22}, A_{12}$ with "natural" dispersion around zero average defined by dimensional arguments from $R(0)$ and L . The quantity $A_{11} - A_{22}$ has Gaussian distribution around nonzero average $\sim E/L^2$ large compare to its "natural" dispersion $\sim [R(0)]^{1/2}/L^2$. That means that typically we are in the vicinity of almost isotropical maximum which is on the distance $r_0 \sim L[R(0)]^{1/2}/E \ll L$ from the point where $U = E$.

Therefore the relaxation rate (1) for typical electron with a large energy can be evaluated considering the states for circular oscillator in magnetic field with typical radius of state of the order of r_0 . We restrict ourselves by not very large energies so that still $r_0 \gg l_H$. The problem is quite simple because the exact wave functions are known and we get the matrix element analogous to (3):

$$M_{mm'} = \int J_{m-m'} \left(\frac{g}{k\gamma} (m - m') \right) r^{m+m'+1} e^{-r^2/2} dr N_m^{-1/2} N_{m'}^{-1/2} \quad (2)$$

Here m is the orbital momentum of the state, J_m is the Bessel function of the order m and normalization factor $N_m = 2\pi m!$

The Bessel function entering the matrix element has a large index compare to it's argument. Because of extremely rapid decrease of Bessel fuction with the increase of $m - m'$ the relaxation rate will be defined by $m - m' \sim 1$. We obtain from (1) and (4):

$$\frac{1}{\tau(E)} = \frac{1}{\tau_{pA}} \frac{1}{p_0 L} \frac{E}{[R(0)]^{1/2} \gamma^3} \text{ or } \frac{1}{\tau(E)} = \frac{1}{\tau_{DA}} \frac{1}{(p_0 L)^3} \left(\frac{E}{[R(0)]^{1/2}} \right)^3 \frac{1}{\gamma^5} \quad (3)$$

The first expression is for piezoacoustical and the second for deformation potential vertex [5]. For GaAs $\tau_{pA} = 8ns$, $\tau_{DA} = 4$ ns, $p_0 = 2.52 \cdot 10^8$ cm⁻¹.

The typical energy of emitted phonons is $\hbar\omega(k) \approx [R(0)]^{1/2} \cdot \frac{l_H^2}{L}$. The relaxation rate in this approximation is symmetrical and we can use these formulae for negative E if we change $E \rightarrow |E|$. The formulae (5), (6) are valid by the order of magnitude up to typical energy $|E| \sim [R(0)]^{1/2}$ and characteristic length of the order L .

2. Relaxation rate near the percolation threshold. The electrons with energies close to percolation threshold $E_c = < U > = 0$ (zero of energy coincide with some Landau level) have trajectories large compare to the correlation length L . Being almost delocalized these electrons define conductivity and their relaxation is of specil interest.

The accepted point of view confirmed by numerics and some exactly solved problems

treat the properties of the equipotential lines near the percolation threshold as universal

and not depending on the statistical model for random potential distribution [6, 7]. The

distribution of clusters upon their sizes is a power law till some critical diameter D_c . The clusters of larger sizes are exponentially rare and can be neglected. The power law indicate a complex fractal behaviour of critical clusters. By exact calculation it was shown that the perimeter \mathcal{L} of critical clusters is large compare to it's diameter and obeys the power law

$$D_c \sim L(\mathcal{L}/L)^\alpha \text{ with } \alpha = 4/7 \quad (4)$$

(see e.g. [8]) a bit more than for random walk where $\alpha = 1/2$.

We shall be interested in Fourier expansion of the perimeter curve in terms of it's length l :

$$\vec{r}(l) = \sum_n^{\max} \vec{r}_n \exp \frac{2\pi i nl}{\mathcal{L}} \quad (5)$$

For a wide class of random fractals [8] the Fourier coefficients are defined by power law with exponent defined by perimeter law (4):

$$\ll |r_n|^2 \gg = \frac{L^2}{n} \left(\frac{n_{\max}}{n} \right)^{2\alpha} \quad (6)$$

For the estimation of matrix element (3) we use the correspondence principle. It states that the matrix element of some operator in semiclassical region coincide with the time Fourier component along the classical trajectory with given energy E . For the matrix element of interest we have

$$M_{\omega,q}(E) = \frac{1}{T} \int_0^T e^{i\omega t} e^{i\vec{q}\vec{r}(t)} dt, \hbar\omega = E - E' \quad (7)$$

where T is the period for the motion along the equipotential line. The drift velocity can be represented as $v_d(l) = v_0 + \delta v(l)$ where v_0 is the average velocity along the equipotential and $\delta v(l)$ describes oscillating fluctuations. Fourier expansion of $\delta v(l)$ is concentrated near the largest component with $n \sim \mathcal{L}/L$ because this quantity changes essentially on the distance of the order L . We argue that for this reason we can neglect $\delta v(l)$ in the calculation of matrix element till the maximum $\omega \approx L/v_0$ where this neglection is still valid by the order of magnitude. Therefore we use (7) in a simplified form with $v_d = v_0 = \text{const}$.

Let us consider the case of small enough ω when $|\vec{q}\vec{r}(l)|^2 < 1$ for any l what is equivalent to $n(\omega) < \gamma(n_{\max})^{1-\alpha}$ if we use (4). In this case it is possible to use "dipole" approximation for the calculation the expression (7) and expanding the second exponent in $\vec{q}\vec{r}(l)$ we get:

$$|M_{\omega,q}(E)|^2 \approx \frac{1}{\gamma^2} \left(\frac{n_{\max}}{n(\omega)} \right)^{2\alpha-2} \frac{1}{n(\omega)} \quad (8)$$

For larger values of ω when $n(\omega) > \gamma(n_{\max})^{1-\alpha}$ the dipole approximation is not valid for smaller Fourier components of $\vec{r}(l)$ with $n < (n(\omega)/\gamma n_{\max}^{1-\alpha})^{2\alpha/1+2\alpha}$ and large amplitudes. In that case we must sum a number of Fourier harmonics with $n \sim n(\omega)$ instead of only one $n = n(\omega)$ in dipole approximation. But it turns out that the total contribution to $|M_{\omega,q}(E)|^2$ results in expression (11) aside some constant factor.

Because of large value of the perimeter length \mathcal{L} the electronic spectrum is rather dense. The value of the matrix element has a power dependence on the phonon frequency and does not change essentially when the frequency changes by the order of it's value. In order to

have the total relaxation rate we must sum all the transitions in the interval ω that gives additional factor $\omega T = n(\omega)$ as compare to the vertex and phonon density of states in (1). Therefore for the relaxation rate due to the emission of phonons with the energies of the order of ω we get

$$\frac{1}{\tau(E)} = \frac{1}{\hbar^2 S} k^2(\omega) |V(k\omega)|^2 \frac{1}{\gamma^2} \left(\frac{n(\omega)}{n_{\max}} \right)^{2-2\alpha} \quad (9)$$

We see that the relaxation rate increase with the phonon frequency. Therefore the relaxation rate for the test electrons will be defined by phonons with maximal frequency when $n(\omega) = n_{\max} = \mathcal{L}/L$ or $kL \sim \gamma^{-1}$ which coincide with (9) for $E = (R(0))^{1/2}$. Thus we have shown that the relaxation rate for a test electron in the vicinity of the percolation threshold will be approximately (up to a constant factor) the same as for electrons with the typical energy $E = [R(0)]^{1/2}$. That means that for a test electron we have a coherent emission only on the distance of the order of the correlation length for random potential. All formulae are valid up to constant factor. The energies of emitted phonons for electrons with Fermi distribution must be of the order of temperature and the relaxation rate is given by (8) with $\hbar\omega = \theta$.

The appearance of noninteger powers in ω for the structure factor was first established in [9] and confirmed numerically for electrons in magnetic field in [1, 2]. S.V.Iordanskii thanks JSF for financial support of this work by grant M9M000 and Russian Fund for Fundamental Research by grant 95-02-05-883.

References

- [1] I.T.Chalker, G.J.Daniel. Phys.Rev.Lett. **61**, 593 (1988).
- [2] T.Brandes, L.Schweizer, B.Kramer. Phys.Rev.Lett. **72**, 3582 (1994).
- [3] O.Heinonen, P.L.Taylor, S.M.Girvin. Phys.Rev. **B30**, 3016 (1984).
- [4] H.L.Zhao, S.Feng. Phys.Rev.Lett. **70**, 4134 (1993).
- [5] V.F.Gantmakher, Y.Levinson. The carrier scattering in metals and semiconductors. Moscow, Nauka (1984).
- [6] D.Stauffer, A.Aharony. Introduction to percolation theory, Taylor & Francis London-Washington, 1992.
- [7] A.Efros, B.Shklovskii. Electronic properties of Doped semiconductors, Springer, Berlin (1984).
- [8] B.Mandelbrot Fractals, Freeman W.H. Co. S.Francisco (1977).
- [9] F.Wegner. Z.Phys. **B25**, 327 (1976)

Electron-electron scattering in a two-dimensional electron gas in a strong magnetic field

Y. Levinson
Department of Condensed Matter Physics, The Weizmann Institute of Science,
Rehovot 76100, Israel.

Abstract

The electron-electron scattering rate $1/\tau$ is calculated for 2D electrons in a strong magnetic field B and a smooth random potential. The temperature $T = 0$ and all the electrons are in the lowest Landau level. Contrary to the case of $B = 0$ when $1/\tau \sim (\epsilon - \epsilon_F)^2$, for $B \neq 0$ the scattering rate of electrons far from the Fermi level is suppressed, $1/\tau \sim (\epsilon - \epsilon_F)^{-1}$.

Introduction

Since the pioneering work of Landau and Pomeranchuk [1] the effect of electron-electron (ee) interactions on the lifetime of electron states near the Fermi level has been one of the important problems in solid state physics. In the last decade the attention has been focused mostly on the properties of the 2DEG. The effect of ee-scattering in the 2DEG is more or less clear for $B = 0$ from the calculations of the ee-scattering rate done by Chaplik [2] (for $T = 0$) and by Giuliani and Quinn [3] (for $T \neq 0$). These calculations follow the lines of [1] and are relevant for "free" (Fermi-liquid) electrons. (When the electrons are "diffusive", i.e. when they are *strongly* scattered by a random *short range* static potential due to impurities, the Fermi-liquid picture is no longer valid in some energy intervals). There are no calculations of the ee-scattering rate for "free" electrons in strong quantizing magnetic fields. The point is that simple Fermi Golden Rule (FGR) calculations, used for $B = 0$ cannot be used for $B \neq 0$ due to the δ -function type singularities of the 2D Landau level (LL) density of states. If one neglects the width of the LL the argument of the energy conservation δ -function in the FGR is always zero, and therefore the FGR has no meaning.

Experimental evidence of the important role of ee-scattering in a 2DEG is provided by many experiments. Auger transitions (intra-LL and inter-LL) in a strong magnetic field were observed in luminescence [4] and cyclotron resonance [5]. ee-scattering is responsible for the signal decay in four-wave mixing experiments [6]. A dephasing time consistent with ee-scattering is observed in the interference of two electron beams [7].

Formulation of the problem

random potential, depending on one coordinate, $l(y)$. The correlation length Λ of the random potential, is assumed to be larger than the magnetic length l_B , and the amplitude of the random potential Δ , is assumed to be smaller than the separation between the LL's. All the electrons are in the lowest LL. With these assumptions the electron states in the gauge $A = (-By, 0, 0)$ are $\psi_k(xy) = L^{-1/2} \exp(i kx) \chi(y - k)$, where L^2 is the normalization area, k is the center of the oscillator, and $\chi(y) = \pi^{-1/4} \exp(-y^2/2)$. The energy of state k is $E_k = l(y)|_{y=k}$. All lengths and momenta are in magnetic units l_B and \hbar/l_B , respectively.

The scattering rate of an electron out state k_1 is

$$\frac{1}{\tau_{k_1}} = \sum_{k_2 k'_1 k'_2} \frac{2\pi}{h} | < k'_1 k'_2 | V | k_1 k_2 > |^2 f_{k_2}(1 - f_{k'_1})(1 - f_{k'_2}) \delta(E_{k_1} + E_{k_2} - E_{k'_1} - E_{k'_2}) |, \quad (1)$$

where $V(r_{12})$ is the ee -interaction potential, and $f_k = f(E_k)$ is the Fermi distribution. We average this scattering rate over the realizations of the random potential, *fixing* the energy of the test electron k_1 to be ϵ . Since the wave functions do not depend on the random potential, neither does the matrix element, so we have to average the scattering rate in the following manner

$$\begin{aligned} \left\langle \frac{1}{\tau} \right\rangle_\epsilon &= \sum_{k_2 k'_1 k'_2} \frac{2\pi}{h} | < k'_1 k'_2 | V | k_1 k_2 > |^2 \\ &\left\langle f_{k_2}(1 - f_{k'_1})(1 - f_{k'_2}) \delta(E_{k_1} + E_{k_2} - E_{k'_1} - E_{k'_2}) \right\rangle_\epsilon. \end{aligned} \quad (2)$$

The statistical average means

$$\begin{aligned} &\left\langle f_{k_2}(1 - f_{k'_1})(1 - f_{k'_2}) \delta(E_{k_1} + E_{k_2} - E_{k'_1} - E_{k'_2}) \right\rangle_\epsilon = \\ &\int d\epsilon_2 d\epsilon'_1 \int d\epsilon'_2 f(\epsilon_2)(1 - f(\epsilon'_1))(1 - f(\epsilon'_2)) \delta(\epsilon + \epsilon_2 - \epsilon'_1 - \epsilon'_2) \\ &\text{Prob}\{l'(k_1) = \epsilon \mid l'(k_2) = \epsilon_2, l'(k'_1) = \epsilon'_2, l'(k'_2) = \epsilon'_2\}, \end{aligned} \quad (3)$$

where *Prob*{...} is the *conditional* probability that the potential at point $y_2 = k_2$ will be equal ϵ_2 , the potential at point $y'_1 = k'_1$ will be equal ϵ'_1 and the potential at point $y'_2 = k'_2$ will be equal ϵ'_2 if the potential $l'(y)$ at point $y_1 = k_1$ is equal ϵ . This probability is calculated assuming the random potential is a Gaussian field and all its properties are defined by the average $< l' > = 0$ and the correlator $< l'(y)l'(0) > = \Delta^2 \exp(-|y|/\Lambda)$.

Coulomb matrix element

The key point of the calculations is the very unexpected behavior of the Coulomb matrix element $< k'_1 k'_2 | e^2/r | k_1 k_2 > = M(p, q)$. This matrix element can be reduced to the following integral

$$M(p, q) = M_0 \frac{1}{q} \exp\left(-\frac{q^2}{2}\right) \int_{-\infty}^{+\infty} dz K_0(|z|) \exp\left[-\frac{1}{2q^2}(pq - z)^2\right], \quad (4)$$

where K_0 is the MacDonald function, $M_0 = 2\varepsilon^2/\sqrt{2\pi}l_B$, $q = k'_1 - k_1 = k_2 - k'_2$ and $p = \frac{1}{2}(k_2 + k'_2) - \frac{1}{2}(k_1 + k'_1)$ is the "average" distance between them.

One can see from (1) that M is exponentially small if $q \gg 1$. This is trivial, since if the displacement q of each of the electrons in the scattering event is large compared to the magnetic length the wave functions of the initial and final states do not overlap in the y direction. The nontrivial property which follows from (1) is that M is exponentially small when $pq \gg 1$. It means that despite the smoothness and long range of the Coulomb potential, the matrix element is small for large p (if $q \gtrsim 1$). This result is related to the symmetry between the coordinates and the momenta for an electron in a magnetic field, where $\Delta y = \Delta k$ (in magnetic units) and the shift in y is equivalent to the transfer of the momentum k . The matrix element is effectively "short range" since in terms of Fourier components "smooth" is equivalent to "short range".

Due to the short range property of the matrix element, all the states in the scattering events contributing to the scattering rate are at small distances (compared to the correlation length). This greatly simplifies the calculation of the conditional probability.

Let us discuss the assumption that the random potential depends only on one coordinate. In a smooth random potential the electron wave functions are localized near the (closed) classical trajectories of the guiding center, $U(\mathbf{r}) = E$. The size and the radius of curvature of these equipotential lines are of the order of A if the state E is neither close to the center of the LL nor in its tails. As we mentioned earlier all the states in the scattering events are located at distances short compared to A and hence the potential can be considered as depending only on one coordinate (perpendicular to the local ∇U).

Due to quantization, the area between two adjacent trajectories is $2\pi l_B^2$ and the distance between them is of the order of $qQ \equiv l_B^2/A$. In a model with a random potential depending only on one coordinate there is no quantization, but one can check that the relevant q are larger than qQ and hence quantization can be neglected.

Scattering rate

The results of the calculations are as follows. The scattering rate is maximal when $\varepsilon \equiv \epsilon - \epsilon_F$ is of the order of $\Delta_B \equiv \Delta(l_B/\Lambda)^{1/2}$. This maximum scattering rate is of the order of $1/\tau_B = (\epsilon^2/l_B)^2/\Delta_B \sim B^{5/4}$. One can consider ϵ^2/l_B as the effective matrix element and $1/\Delta_B$ as the effective density of states. For energies larger and smaller than Δ_B the scattering rate is

$$\frac{1}{\tau_B} = 0.50 \frac{1}{\tau_B} \left(\frac{\varepsilon}{\Delta_B} \right)^{-1} \sim B, \quad \varepsilon \gg \Delta_B \quad (5)$$

and

$$\frac{1}{\tau_B} = 2.48 \frac{1}{\tau_B} \frac{\varepsilon}{\Delta_B} \sim B^{3/2} \quad \varepsilon \ll \Delta_B. \quad (6)$$

The unexpected result is that the scattering rate for an electron with energy ϵ depends only on the gap between its energy and the Fermi level ϵ_F and is independent of the density of states at ϵ . This is a consequence of the properties of conditional probabilities in Eq.(3) for a Gaussian-potential. The scattering rate is also independent of the filling factor (as long as ϵ_F is not in the tail of the LL density of states).

The scattering rate in a magnetic field $1/\tau_B$ can be compared with that of $B = 0$, which is $[2,3] 1/\tau_0 \simeq \varepsilon^2/\epsilon_F$ (neglecting the logarithmic factor $\ln \varepsilon$). The factor ε^2 in τ_0 comes from the statistical average in Eq.(3) and corresponds to the number of finite available states.

Contrary to the scattering rate $1/\tau_0$ for $B = 0$, which increases, with $\epsilon - \epsilon_F, 1/\tau_B$ decreases with increasing ϵ . The suppression of the scattering in a magnetic field can be explained as follows. Consider a scattering event $k_1, k_2 \rightarrow k'_1, k'_2$. The energy of test electron 1, $\epsilon = U(k_1)$ is above ϵ_F , while the energy of the scattering partner 2, $\epsilon_2 = U(k_2)$ is below ϵ_F and hence $\epsilon - \epsilon_2 > \varepsilon$. If $\varepsilon = \epsilon - \epsilon_F$ is large the positions $y_1 = k_1$ and $y_2 = k_2$ are far from each other since the potential is smooth. As a result, p is large. Since the matrix element is small unless $pq \ll 1$, large p means a small interval of available q values and thus the scattering is weakened. This reasoning is correct only when $\varepsilon \gg \Delta_B$. When $\varepsilon \ll \Delta_B$ the situation is closer to that of $B = 0$ when more finite states are available for larger ε .

References

- [1] L.Landau and I.Pomerantschuk, Phys. Z. Sowjetunion, **10** (1936) 649
- [2] A.V.Chaplik, Sov.Phys., JETP **33** (1971) 997
- [3] G.F.Gilman and J.J.Quinn, Phys.Rev. **B26** (1982) 4121
- [4] M.Potemski,R.Stepniowski,J.C.Maan,G.Martinez,P.Wyder, and B.Ettiene, Phys. Rev.Lett. **66** (1991) 2239
- [5] I.Mirav,W.Seidenblush,E.Gornik,G.Weinmann, and M.Shayegan, Semicond.Sci.Techol. **9** (1991) 700
- [6] S.Bar-Ad,I.Bar-Joseph, Y.Jevinson, and H.Shirikman, Phys.Rev.Lett. **72** (1991) 776
- [7] A.Yacoby, U.Sivan,C.P.Umbach, and J.M.Hong, Phys.Rev.Lett. **14** (1991) 1938

Inelastic Transport in a System of 2D Electrons Localized in a Smooth Potential: Giant Negative Magnetoresistance

M. E. Raikh,⁽¹⁾ L. I. Glazman⁽²⁾

⁽¹⁾ Physics Department, University of Utah, Salt Lake City, Utah 84112
⁽²⁾ Theoretical Physics Institute and Department of Physics, University of Minnesota, Minneapolis, Minnesota 55455

Abstract

We show that the tunnel coupling between semiclassical states localized in different minima of a smooth random potential increases when magnetic field is applied. We illustrate the increase of coupling by a model calculation of tunneling through a saddle point separating two adjacent lakes. The effect of the field on coupling constants leads to a negative magnetoresistance in low-temperature conduction.

In the present paper we consider inelastic transport in 2D electron gas subjected to a smooth random potential. For small enough concentrations electron gas breaks up into separate lakes, each lake accomodating many electrons. Within a certain temperature range the transport is dominated by tunneling of electrons through the saddle points of barriers separating adjacent lakes. Important is that the states active in transport (i.e., with energies close to the Fermi level) correspond to high-number levels of size quantization in the minima of the random potential. We show that the magnetoresistance of such a system is negative and is really giant in magnitude.

Consider two minima of the potential separated by a barrier. In the vicinity of a saddle point the barrier potential has the form:

$$U(x, y) = U_0 - \frac{m\omega_x^2 x^2}{2} + \frac{m\omega_y^2 y^2}{2}. \quad (1)$$

We define the coupling constant between the states p and k in the neighboring minima as a matrix element t_{pk} in the tunneling Hamiltonian:

$$H = \sum_p E_p^\ell a_p^\dagger b_p + \sum_k E_k^\ell b_k^\dagger a_k + \sum_{pk} (t_{pk} a_p^\dagger b_k + t_{pk}^* b_k^\dagger a_p), \quad (2)$$

where E_p^ℓ , E_k^ℓ are the energy levels in the two minima, and a_p^\dagger , b_k^\dagger are the corresponding creation operators. The expression for t_{pk} in terms of the wave functions $\psi_p^\ell(x, y)$ and $\psi_k^\ell(x, y)$ can be obtained using the procedure employed in the derivation of the tight-binding approximation

$$t_{pk} = \frac{\hbar^2}{2m} \int \int_{-\infty}^{\infty} dy_1 dy_2 G_E(y_1, y_2) \frac{\partial}{\partial x} \psi_p^\ell \left(-\frac{d}{2}, y_1 \right) \left[\frac{\partial}{\partial x} \psi_k^\ell \left(\frac{d}{2}, y_2 \right) \right]^*. \quad (3)$$

Here m is the electron mass, and $G_E(y_1, y_2)$ is the Green function describing the propagation of an electron under the barrier between the points $(-d/2, y_1)$ and $(d/2, y_2)$, see Fig. 1.

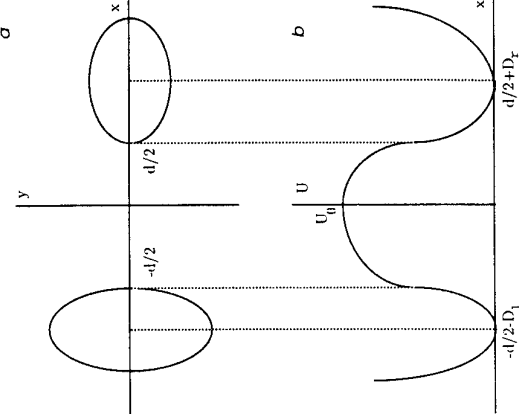


FIG. 1. Two electronic lakes separated by a saddle point (a), and the schematic potential profile in the crosssection $y=0$ (b)

At this point we will make a simplifying assumption which does not affect the final result for the magnetoresistance [1]. Namely, we will assume that $G_E(y_1, y_2)$ connects most effectively the points with $y_1 = y_2$. In other words we will take into account only direct tunneling paths in Eq. (3). For potential barrier (1) the amplitude of tunneling changes along y as $\exp[-\pi(U_0 - E + \frac{m\omega_x^2 y^2}{2})/\hbar\omega_x]$. Then the coupling matrix element reduces to following integral

$$t_{pk} \sim e^{-\pi(U_0-E)/\hbar\omega_x} \int_{-\infty}^{\infty} dy e^{-y^2/\lambda^2} \frac{\partial}{\partial x} \psi_p^\ell \left(-\frac{d}{2}, y \right) \left[\frac{\partial}{\partial x} \psi_k^\ell \left(\frac{d}{2}, y \right) \right]^*, \quad (4)$$

where parameter $\lambda = (2\hbar\omega_x/\pi m\omega_y^2)^{1/2}$ characterizes the electron motion near the saddle point (2). The prefactor in Eq. (4) is the tunneling amplitude in the central cross-section of the barrier while the integral describes the overlap of the "transverse" parts of the wave functions ψ_p^ℓ and ψ_k^ℓ . The main contribution to the integral comes from the region $y \sim \lambda$. Since this region is much smaller than the size of the lakes we will neglect the variation of the semiclassical momentum of electrons within this region. Thus, the behavior of the wave functions ψ_p^ℓ , ψ_k^ℓ at the barrier is simple sinusoidal

$$\psi_p^\ell \left(-\frac{d}{2}, y \right) \propto \sin(py - \chi_l), \quad \psi_k^\ell \left(\frac{d}{2}, y \right) \propto \sin(ky - \chi_r), \quad (5)$$

where χ_l and χ_r are some phases. Substituting (5) into (4) and performing the integration we obtain

$$t_{pk} \sim e^{-\pi(U_0 - E)/\hbar\omega_x} (\cos(\chi_l - \chi_r)e^{-(p-k)^2\lambda^2/4} - \cos(\chi_l + \chi_r)e^{-(p+k)^2\lambda^2/4}). \quad (6)$$

Let us study how a weak perpendicular magnetic field B affects the coupling matrix element t_{pk} . The prime effect of magnetic field is that the wave functions $\psi_p^l\left(-\frac{d}{2}, y\right)$ and $\psi_k^r\left(-\frac{d}{2}, y\right)$ acquire the gauge phase factors which can be presented as $\exp(2\pi i y D_l/\Phi_0)$ and $\exp(-2\pi i y D_r/\Phi_0)$ respectively (Φ_0 is the flux quantum). It is important to note that since the phase factor results from the motion of electron within the corresponding lake, the magnitudes of the parameters D_l, D_r are of the order of the size of the left and right lakes respectively (provided that D_l, D_r are much larger than the barrier thickness d). After introducing these factors into Eq. (4), the calculation of the coupling coefficient is quite similar to the case of zero magnetic field, and yields:

$$t_{kp}(B) = t_{kp}(0) \exp\left(-\frac{B^2}{2B_0^2}\right) \left[\cosh \frac{B}{B_1} + i \tan(\chi_l - \chi_r) \sinh \frac{B}{B_1} \right], \quad (7)$$

where parameters B_0 and B_1 are given by

$$B_0 = \frac{\Phi_0}{\sqrt{2}\pi(D_l + D_r)\lambda} \quad B_1 = \frac{\Phi_0}{\pi(D_l + D_r)|k - p|\lambda^2}. \quad (8)$$

Correspondingly the magnetoresistance between two lakes behaves as

$$\frac{R(B)}{R(0)} = \left(\frac{t_{kp}(B)}{t_{kp}(0)} \right)^{-2} = \exp\left(\frac{B^2}{B_0^2} \frac{1}{\cosh^2 B/B_1 + \tan^2(\chi_l - \chi_r) \sinh^2 B/B_1}\right). \quad (9)$$

The magnetoresistance at small B is quadratic,

$$\frac{\delta R(B)}{R(0)} = \left(\frac{1}{B_0^2} - \frac{1}{B_1^2 \cos^2(\chi_l - \chi_r)} \right) B^2, \quad (10)$$

and it is negative for any χ_l and χ_r if $B_0 > B_1$. The ratio $B_0/B_1 = |k - p|\lambda/\sqrt{2}$ can be estimated as $(E_F/\hbar\Omega)^{1/2}$, where E_F is the Fermi energy of an electron in a lake and $\Omega = \omega_y^2/\omega_x$. This ratio is large in the semiclassical regime. Hence, in the small field region the resistance decreases as $\delta R(B)/R(0) \simeq -B^2/B_1^2$, the characteristic value B_1 being of the order of Φ_0/S , where $S \sim D_l^2 \sim D_r^2$ is of the order of the area of the lake. The resistance falls off exponentially with B in the region $B_c \gg B \gg B_1$, where the crossover field is $B_c = B_0^2/B_1$. After reaching a minimum at $B \approx B_c$, the resistance rises sharply at higher fields. Note however that at $B = B_c$ the cyclotron frequency becomes of the order of $\hbar\Omega$ so that the effect of magnetic field on the eigenstates in the lakes cannot be reduced to the phase factors only.

The physical meaning of the negative magnetoresistance is that the phase factors acquired by the wavefunctions in magnetic field compensate effectively the difference in their wave numbers in the y -direction and, therefore, lead to the increase of the coupling.

The magnetoresistance (9) has no temperature dependence. This is because while deriving our main result (7),(8) we assumed the motion of electrons within each lake to be completely coherent. At a finite temperature, the phase-breaking length, L_ϕ , may become

smaller than D_l, D_r . This will eliminate effectively the phase factors acquired due to the electron motion within each of the lakes. However is $L_\phi > \lambda$ the wave functions on the opposite sides of the barrier retain their coherence within the tunneling region $y \sim \lambda$. Therefore at $L_\phi \lesssim D_l, D_r$ the parameters D_l, D_r in the phase factors should be replaced by the value of $d/2$. As a result, in the range of temperatures where $L_\phi \sim D_l, D_r$, the magnetoresistance must exhibit a strong temperature dependence, and become weaker at higher temperatures. The sign of the magnetoresistance remains negative, because for a semiclassical electron motion the condition $B_0 \gg B_1$ remains valid, even if $L_\phi \lesssim D_l, D_r$.

In conclusion, we have demonstrated that the conductivity of two-dimensional electron gas subjected to a smooth random potential should increase drastically with increasing magnetic field. The larger are the electron lakes (the closer is the Fermi level to the classical percolation threshold), the sharper is the raise of the conductivity with magnetic field. The principal assumption of the theory developed is the form (5) of the wave functions at the barrier. It might be argued that in the situation of "quantum chaos" ψ_p^l and ψ_k^r will contain *all* spatial harmonics, thus eliminating the sensitivity of coupling to the magnetic field. However the results of recent studies (see the book by Gutzwiller [1], and Heller's chapter in [2] and references therein) suggest that even in the case of chaotic motion a substantial portion of quantum eigenstates with high numbers are associated with periodic classical trajectories in the lakes. Then the tunneling between these states should still be strongly sensitive to the magnetic field.

Discussions with I. L. Aleiner, B. L. Altshuler and H. U. Baranger are gratefully acknowledged. The work at the University of Minnesota was supported by NSF Grant DMR-9423244.

References

- [1] The explicit calculation free from this simplification is presented in: M.E. Raikh and L.I. Glazman, Phys. Rev. Lett., **74**, (1995)
- [2] M. C. Gutzwiller, *Chaos in classical and quantum mechanics*, (Springer-Verlag, New York, 1991)
- [3] *Les Houches, Session LI, 1989, Chaos and Quantum Physics*, edited by M.-J. Giannoni, A. Voros, and J. Zinn-Justin (North Holland, Amsterdam, 1991)

Weak levitation of delocalized states as a result of Landau level mixing

T. V. Shalbazzyan and M. E. Raikh
Department of Physics, University of Utah, Salt Lake City, UT 84112, USA

Abstract

We study the effect of Landau level mixing on the energy positions of 2D delocalized states in a magnetic field. We show that a weak mixing can be incorporated into the Chalker-Coddington model by renormalization of parameters of the saddle-points. We demonstrate that after averaging over saddle-points, such a renormalization leads to floating of delocalized states upwards from the centers of Landau bands.

It is commonly accepted that in a strong magnetic field even a weak disorder leads to the localization of all electronic states with exception of a discrete set of delocalized states in the centers of Landau levels (LL). Such a structure of electronic spectrum was first conjectured in order to account for the behavior of the dissipative and Hall components of conductivity tensor in a strong magnetic field and later confirmed both by the renormalization group analysis and numerical simulations [1].

Since it is believed that there are no delocalized states at zero field ($B = 0$), the question arises: What is the fate of delocalized states as magnetic field decreases? It was suggested in [2] that with decreasing B , the energy positions of delocalized states depart gradually from the centers of Landau levels and float upwards. However, no microscopic theory for such a levitation has been developed so far. Here we present such a theory for the region of magnetic fields where the departure of the delocalized state from the center of the Landau band is relatively small. We demonstrate that the microscopic mechanism for the levitation is the resonant scattering of an electron with energy near the center of LL by localized states from neighboring LL.

A nice and physically transparent picture of delocalization was provided by Chalker and Coddington [3] for the case of a smooth disorder. In what follows we generalize their model in order to study the effects of LL mixing. In this model, delocalization results from the quantum tunneling of an electron through the saddle-points of a smooth potential which are connected by equipotential lines. The randomness of the potential is included by assuming the phase acquired by electron traversing a link (equipotential line) to be random. The probability amplitudes of incoming waves Z_1 and Z_2 and outgoing waves Z_3 and Z_4 (see Fig. 1) are related as

$$\begin{pmatrix} Z_1 \\ Z_3 \end{pmatrix} = \mathbf{M} \begin{pmatrix} Z_4 \\ Z_2 \end{pmatrix}, \quad \mathbf{M} = \begin{pmatrix} e^{i\phi_1} & 0 \\ 0 & e^{i\phi_2} \end{pmatrix} \begin{pmatrix} \cosh \theta & \sinh \theta \\ \sinh \theta & \cosh \theta \end{pmatrix} \begin{pmatrix} e^{i\phi_3} & 0 \\ 0 & e^{i\phi_4} \end{pmatrix}, \quad (1)$$

with parameter θ characterizing the tunneling and ϕ_i being gauge phases. For the potential expanded near the saddle point, $V(x, y) = V_0 - m\Omega_x^2x^2/2 + m\Omega_y^2y^2/2$, where m is the electron mass, this parameter can be presented as

$$\sinh \theta = \exp \left(\frac{E - V_0}{\gamma} \right), \quad \gamma = \hbar\Omega_x\Omega_y/\pi\omega_c, \quad (2)$$

where E is energy of the electron measured from the center of LL and ω_c is the cyclotron frequency. Since the saddle-point heights, V_0 , are distributed *symmetrically* around the value $V_0 = 0$ [corresponding to $\theta = \theta_c \equiv \ln(1 + \sqrt{2})$], the delocalized states occur at zero energy.

Now assume that the energy is close to the center of the $n = 0$ LL and study the change in the structure of electronic states caused by the $n = 1$ LL. The relevant $n = 1$ LL states are those with energies close to the center of $n = 0$ LL. The equipotentials corresponding to these states are depicted schematically in Fig. 1 by dashed loops. The prime role of these equipotentials is to shift the maximum of the density of states up from $E = 0$. However, such a shift does not affect the position of the delocalized state unless a coupling between the equipotentials of $n = 0$ and $n = 1$ LL is introduced. This coupling is illustrated in Fig. 1a. The line connecting the equipotentials stands for a scattering matrix \mathbf{S} defined as

$$\begin{pmatrix} Z \\ \tilde{Z} \end{pmatrix} = \mathbf{S} \begin{pmatrix} Z' \\ \tilde{Z}' \end{pmatrix}, \quad \mathbf{S} = \begin{pmatrix} e^{i\phi} & 0 \\ 0 & e^{i\tilde{\phi}} \end{pmatrix} \begin{pmatrix} \cos \alpha & -\sin \alpha \\ \sin \alpha & \cos \alpha \end{pmatrix} \begin{pmatrix} e^{i\phi'} & 0 \\ 0 & e^{i\tilde{\phi}'} \end{pmatrix}, \quad (3)$$

Such a form of \mathbf{S} insures the conservation of flux $|Z|^2 + |\tilde{Z}|^2 = |Z'|^2 + |\tilde{Z}'|^2$. The coupling strength is characterized by an angle α (gauge phases in matrix \mathbf{S} , as well as in \mathbf{M} , can be absorbed into the Z 's). It is clear that the only effect of such a coupling to a loop is a phase shift between the amplitudes Z and Z' which can be absorbed into the random phase on the link.

The situation is completely different when a loop occurs in the vicinity of the saddle-point so that it is coupled to both the incoming and outgoing links (see Fig. 1b). Below, we demonstrate that the effect of such loops is to shift the position of delocalized state upward. The crucial observation is that the saddle-point with the loops attached to the links can be viewed as some modified saddle-point and thus is characterized by a matrix $\mathbf{M}'(\theta')$ (relating Z'_i) with the same unitarity properties as $\mathbf{M}(\theta)$. The new parameter θ' can be expressed via θ and the elements of scattering matrices \mathbf{S}_i (see Fig. 1b) using the following equations

$$\begin{pmatrix} Z'_2 \\ Z'_5 \end{pmatrix} = \mathbf{S}_2 \begin{pmatrix} Z_2 \\ Z_6 \end{pmatrix}, \quad \begin{pmatrix} Z_3 \\ Z_6 \end{pmatrix} = \mathbf{S}_3 \begin{pmatrix} Z'_3 \\ Z_5 \end{pmatrix}, \quad \begin{pmatrix} Z'_1 \\ Z_7 \end{pmatrix} = \mathbf{S}_1 \begin{pmatrix} Z_1 \\ Z_7 \end{pmatrix}, \quad \begin{pmatrix} Z'_4 \\ Z_8 \end{pmatrix} = \mathbf{S}_4 \begin{pmatrix} Z'_4 \\ Z_8 \end{pmatrix}. \quad (4)$$

Consider for simplicity a case when all $\alpha_i = \alpha$ and there is only one loop (e.g., $\mathbf{S}_1 = \mathbf{S}_4 = \mathbf{1}$). Then the parameter θ' is given by

$$\begin{aligned} \sinh^2 \theta' &= \\ &= \frac{2 \sinh^2 \theta \cos^2 \alpha (1 - \cos \varphi)}{[\sin \varphi - \sin^2 \alpha \cosh \theta \sin(\psi - \varphi)]^2 + [\cos \varphi - \cos^2 \alpha + \sin^2 \alpha \cosh \theta \cos(\psi - \varphi)]^2}. \end{aligned} \quad (5)$$

Here φ is the phase acquired by electron traversing the loop while ψ is the phase acquired on the contour $Z_2 \rightarrow Z_3 \rightarrow Z_5$ (see Fig. 1b).

The conversion of the parameter θ into θ' can be viewed as an effective change in the height of the saddle-point, δV_0 , caused by $n = 1$ LL:

$$\delta V_0 = -\gamma \ln \left(\frac{\sinh \theta'}{\sinh \theta} \right). \quad (6)$$

The crucial observation is that the average (over φ and ψ) $\overline{\delta V_0}$ appears to be positive. For small α this average can be easily calculated analytically:

$$\overline{\delta V_0}(\theta) = \frac{\alpha^2 \gamma}{\pi} [\sinh \theta + \arcsin(1/\cosh \theta)], \quad (7)$$

where θ is related to V_0 by Eq. (2). We see that $\overline{\delta V_0}(\theta)$ is proportional to the width of the resonance, α^2 , since it is determined by resonant loops. Since $\overline{\delta V_0}(\theta)$ is finite, the average saddle-point height, $\overline{V_0}$, moves from $\overline{V_0} = 0$ to a finite value $\overline{V_0} = (\overline{\delta V_0}(\theta))v_0$, where $(\cdot)v_0$ stands for averaging over V_0 . The values of V_0 , relevant for delocalization, are of the order of γ , the relevant $E' - V_0$ being also of the order of γ , so that the relevant θ in (7) is $\theta \sim 1$. This leads to the following estimate for the energy shift of the delocalized state:

$$\delta E_0 \sim \langle \overline{V_0} \rangle_\alpha \sim \overline{\alpha^2} \gamma, \quad (8)$$

where $\overline{\alpha^2}$ is the coupling strength averaged over the loops. It can be seen that the shift is much smaller than a typical saddle-point height: $\delta E_0/\gamma \sim \overline{\alpha^2} \ll 1$.

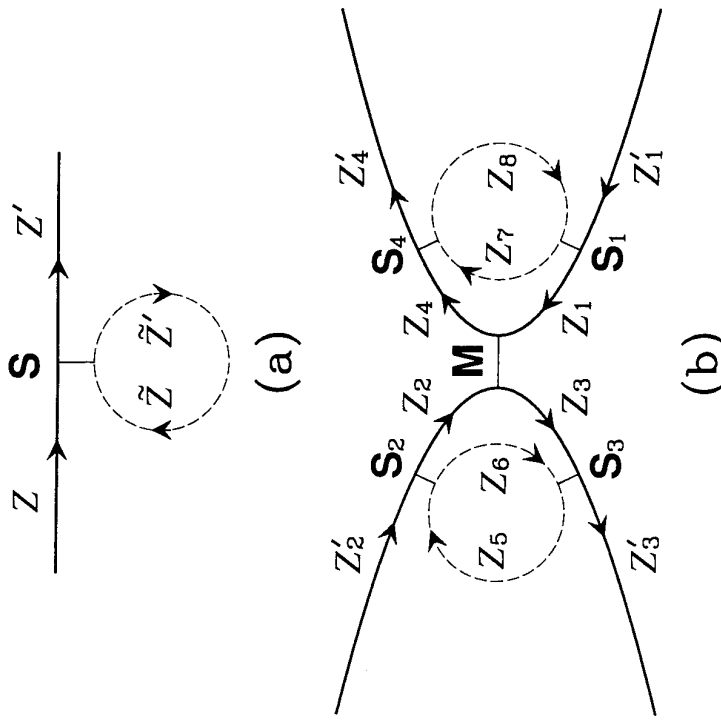
From a physical standpoint, the levitation (positive δE_0) originates from the loops providing a direct transmission between links, bypassing the saddle-point. Thus, in order to compensate the leakage of electrons to the opposite link via the loop, the energy of the delocalized state is raised *upwards*.

In the derivation of (7) we neglected the effect of the loop $Z_7 \rightarrow Z_8$ on the other side of the saddle-point (see Fig. 1b). It is easy to see, however, that the two loops cause essentially an additive effect. Indeed, an electron, traversing the link Z'_1 , can also bypass the saddle-point due to a resonant transmission to the opposite link Z'_4 . The key point in the consideration above was the fact that the loops can occur only in directions of the descend of a saddle-point potential (valleys), i.e., to the right and to the left from the saddle-point in Fig. 1b. This is the case when the effect of the $n = 1$ LL on the $n = 0$ delocalized state is studied. For the $n = 1$ delocalized state the situation is more complicated: the loops from the $n = 2$ LL occur in the directions of the valleys while the loops from the $n = 0$ LL occur in the directions of the hills. The latter loops cause an opposite trend, pulling the delocalized state downward. The resulting shift can be presented as $\delta E_1 \sim \gamma(\overline{\alpha_{12}^2} - \overline{\alpha_{10}^2})$. Note that the coupling, $\overline{\alpha_{12}^2}$, of $n = 1$ to $n = 2$ LL is stronger than the coupling, $\overline{\alpha_{10}^2}$, of $n = 1$ to $n = 0$ LL, due to a larger size of the $n = 2$ wave function. Thus, δE_1 is also positive. Another effect which we have neglected is coupling of the $n = 0$ links via loops corresponding to $n = 0$ equipotentials. Since these loops occur with equal probability in *all* directions from the saddle-point, it is obvious that positive and negative contributions to δE_0 from these loops cancel each other out.

In conclusion, the levitation of delocalized states due to LL mixing was demonstrated in the framework of a single-electron picture of the Quantum Hall effect.

References

- [1] For a review see B. Huckenstein, MPI preprint, 1995 (cond-mat/9501106).
- [2] D. E. Khmelnitskii, Phys. Lett. **106A**, 182 (1984); R. B. Laughlin, Phys. Rev. Lett. **52**, 2304 (1984); S. Kivelson, D.-H. Lee, and S.-C. Zhang, Phys. Rev. B **46**, 2223 (1992).
- [3] J. T. Chalker and P. D. Coddington, J. Phys. C **21**, 2665 (1988); D.-H. Lee, Z. Wang, and S. Kivelson, Phys. Rev. Lett. **70**, 4130 (1993).



Fermi-edge singularity of the Tomonaga-Luttinger liquids in a magnetic field

Tetsuo Ogawa and Hiroshi Otani

Department of Applied Physics, Osaka City University, Sumiyoshi-ku, Osaka 558, Japan

The Tomonaga-Luttinger liquid with spin-polarized Fermi points in an external magnetic field is studied theoretically to reveal that two gapless collective excitations result from hybridization between the charge- and spin-density fluctuations. The exponent of the Fermi-edge singularity is analytically obtained. Power-law divergence of optical edge spectra is possible even for repulsive electron-hole interactions.

1. Introduction

Fermi-surface effects in conductors have been one of the central topics in condensed-matter physics. One of the striking phenomena due to the existence of the Fermi surface is the Fermi-edge singularity (FES) [1,2] in optical spectra. The optical absorption (emission) spectrum $I(\omega)$ in the vicinity of the absorption (emission) edge E_{FES} behaves as $I(\omega) \sim |\hbar\omega - E_{\text{FES}}|^\beta$. Recently, the FES was experimentally observed in an n-type heavily-doped semiconductor wire in a magnetic field [3]. Then we need to extend the FES theory [2] to adapt it for the case of one-dimensional (1D) electron systems in a magnetic field [4] taking into account both the spin splitting of the Fermi surface and the spin-dependent interactions.

In this work, we first clarify the collective-excitation modes of 1D conductors with spin-split conduction bands in a magnetic field, and we then obtain an analytical expression of the FES exponent, β , in such systems. The FES in related spin-split systems is also discussed.

2. Bosonized Hamiltonian and the collective modes

We employ the Tomonaga-Luttinger (TL) bosonization method to describe the long-wavelength density fluctuations of the 1D degenerate conduction electrons. A valence hole can be safely assumed to be localized since the hole near recoil does not affect the FES exponent in 1D systems [2,5]. The conduction-band dispersion near Fermi points is linearized as $\epsilon(k) \approx \sum_{j=1,2} \sum_{\sigma=\pm 1} \epsilon_j^\sigma(k)$, where $\epsilon_1^\sigma(k) \equiv v_F^\sigma(k - k_F^\sigma)$ and $\epsilon_2^\sigma(k) \equiv -v_F^\sigma(k + k_F^\sigma)$. Here v_F^σ is the bare Fermi velocity of the conduction electrons with spin $\sigma = \uparrow, \downarrow = \pm 1$, and $j = 1, 2$ corresponds to the right (left) branch of the conduction bands. We note that the time-reversal symmetry is broken in this system. We shall consider the forward scatterings, the main processes of interactions in 1D, which are represented by $g_{2\parallel}^\sigma$, $g_{2\perp}^\sigma$, and $g_{4\perp}^\sigma$, according to the g-ology notation [6]. Effects of backward scatterings will be discussed later. The umklapp and spin-flip scatterings are neglected. Scatterings between an electron and a valence hole (when it exists) are represented by $g_{2\parallel}^{\text{sh}}$ and $g_{2\perp}^{\text{sh}}$.

The TL liquid with the spin polarization is described by the bosonized Hamiltonian: $\mathcal{H} = \frac{1}{2} \sum_{p>0} p b_p^\dagger b_p$, where $b_p^\dagger \equiv (2\pi/Lp)^{1/2} [\rho_{11}(p), \rho_{12}(p), \rho_{21}(p)]$ is a boson operator. Here $\rho_{j\sigma}(p) \equiv \sum_k a_{jk+\mathbf{p}\sigma}^\dagger a_{jk\sigma}$ and $a_{jk\sigma}^\dagger$ are operators for an electron with momentum k in j th branch of the spin- σ subband, and L is the system size. In order to diagonalize the Hamiltonian, we employ a unitary transformation:

$$\mathbf{Hb}_p = \mathbf{HUC}_p \equiv \begin{bmatrix} 2v_F^\perp + g_{2\parallel}^\sigma & g_{2\perp}^\sigma & g_{4\perp}^\sigma \\ g_{2\parallel}^\sigma & 2v_F^\perp + g_{4\parallel}^\sigma & g_{2\perp}^\sigma \\ g_{4\perp}^\sigma & g_{2\perp}^\sigma & 2v_F^\perp + g_{4\parallel}^\sigma \\ g_{2\perp}^\sigma & g_{4\parallel}^\sigma & 2v_F^\perp + g_{2\parallel}^\sigma \end{bmatrix} \begin{bmatrix} x_a^\dagger & y_a^\dagger & x_b^\dagger & y_b^\dagger \\ y_a^\dagger & x_a^\dagger & y_b^\dagger & x_b^\dagger \\ x_b^\dagger & y_b^\dagger & x_a^\dagger & y_a^\dagger \\ y_b^\dagger & x_b^\dagger & y_a^\dagger & x_a^\dagger \end{bmatrix} \begin{bmatrix} B_{\text{ap}} \\ A_{\text{ap}}^\dagger \\ B_{\text{ap}} \\ A_{\text{ap}}^\dagger \end{bmatrix}, \quad (1)$$

where $A_{\mu\text{p}}$ and $B_{\mu\text{p}}$ for $\mu = a, b$ are new boson operators. The matrix elements of $U, x_\mu^\dagger, y_\mu^\dagger, x_\mu^\perp$, and y_μ^\perp , are given as $x_\mu^\dagger = f_{2a}^\dagger f_{2a}^\perp \Delta_a$, $x_\mu^\perp = f_{2a}^\dagger f_{2a}^\perp \Delta_a$, $y_\mu^\dagger = f_{4a}^\dagger f_{4a}^\perp \Delta_a$, and $y_\mu^\perp = f_{4a}^\dagger f_{4a}^\perp \Delta_a$, where

$$\begin{aligned} \Delta_a &\equiv \left[\frac{N_6(f_{2b}^\perp)^2 - M_6(f_{2b}^\perp)^2}{M_a N_6(f_{2b}^\perp)^2 (f_{2a}^\perp)^2 - M_b N_a(f_{2b}^\perp)^2 (f_{2a}^\perp)^2} \right]^{1/2}, \\ f_{2\mu}^\perp &\equiv g_{2\perp}^\sigma [(g_{2\parallel}^\sigma)^2 + (g_{4\perp}^\sigma)^2 - (g_{2\perp}^\sigma)^2 + V_{\mu+}^\perp V_{\mu-}^\perp] - g_{2\parallel}^\sigma g_{4\perp}^\sigma (V_{\mu+}^\perp + V_{\mu-}^\perp), \\ f_{2\mu}^\perp &\equiv g_{2\parallel}^\sigma [(g_{2\parallel}^\sigma)^2 + (g_{4\perp}^\sigma)^2 - (g_{2\parallel}^\sigma)^2 + V_{\mu+}^\perp V_{\mu-}^\perp] - g_{2\perp}^\sigma g_{4\perp}^\sigma (V_{\mu+}^\perp + V_{\mu-}^\perp), \\ f_{2\mu}^\perp &\equiv g_{2\perp}^\sigma [(g_{2\parallel}^\sigma)^2 - (g_{2\perp}^\sigma)^2 + V_{\mu+}^\perp V_{\mu-}^\perp] - g_{2\parallel}^\sigma g_{4\perp}^\sigma (V_{\mu+}^\perp + V_{\mu-}^\perp), \\ f_{4\mu}^\perp &\equiv g_{4\perp}^\sigma [(g_{2\parallel}^\sigma)^2 + (g_{4\perp}^\sigma)^2 - (g_{2\parallel}^\sigma)^2 - V_{\mu+}^\perp V_{\mu-}^\perp] - g_{2\parallel}^\sigma g_{4\perp}^\sigma (V_{\mu+}^\perp + V_{\mu-}^\perp), \end{aligned} \quad (2)$$

with $M_\mu \equiv (f_{2\mu}^\perp)^2 - (f_{4\mu}^\perp)^2$, $N_\mu \equiv (f_{2\mu}^\perp)^2 - (f_{4\mu}^\perp)^2 + 2v_F^\perp + g_{4\parallel}^\sigma + 2v_\mu$, and $V_\mu^\perp \equiv 2v_F^\perp + g_{2\parallel}^\sigma - 2v_\mu$. Other elements, $x_b^\dagger, y_b^\dagger, x_b^\perp$, and y_b^\perp , are given by replacing the index a in above equations with b (a), and v_μ will be given soon.

After the diagonalization procedure, we find that A_{ap} and B_{ap} (A_{bp} and B_{bp}) describe the new normal mode of collective excitation, labeled a (b), which is a *hybrid* collective mode of the charge-density ($p_1 + p_1$) and spin-density ($p_1 - p_1$) excitations with momentum p . The velocity of the mode is given as $v_p \equiv [I \pm \Lambda]^{1/2}$, where $\mu = a$ (b) corresponds to the $+$ ($-$) sign, and

$$\begin{aligned} \Gamma &= \frac{1}{2} \left[(v_F^\perp)^2 + (v_F^\perp)^2 \right] + \frac{1}{4} \left[(g_{4\parallel}^\sigma)^2 + (g_{4\perp}^\sigma)^2 - (g_{2\perp}^\sigma)^2 - (g_{2\parallel}^\sigma)^2 \right] + g_4^\sigma v_F^\perp, \\ \Lambda &= \left[g_{4\perp}^\sigma v_F^\perp - \frac{1}{2} \left(g_{2\parallel}^\sigma g_{2\perp}^\sigma - g_{4\parallel}^\sigma g_{4\perp}^\sigma \right) \right]^2 + (v_F^\perp)^2 \left\{ (2v_F^\perp + g_{4\parallel}^\sigma)^2 - (g_{2\perp}^\sigma)^2 \right\}, \end{aligned} \quad (7) \quad (8)$$

with $v_F^\perp \equiv \frac{1}{2}(v_F^\perp + v_b^\perp)$ and $v_F^\perp \equiv \frac{1}{2}(v_F^\perp - v_b^\perp)$.

3. Exponent of the Fermi-edge singularity

Here we turn to the FES in a one-photon absorption process. The interaction between the $\mu = a, b$ mode of the conduction electrons and the valence hole with spin $-\sigma$ is $\mathcal{T}_\mu^{\text{eh}}(\sigma) = -\sqrt{\pi/2L} \sum_{\mathbf{p}>0} G_\mu^\sigma / \sqrt{A_{\mu\text{p}} + B_{\mu\text{p}}^\dagger + B_{\mu\text{p}}}$, where $G_\mu^\sigma = \frac{1}{2} \sum_{\sigma'=\pm 1} \left(g_{2\parallel}^{\sigma\text{h}} \delta_{\sigma, \sigma'} + g_{2\perp}^{\sigma\text{h}} \delta_{\sigma, \sigma'} \right) \times (x_\mu^{\sigma'} + y_\mu^{\sigma'})$. The optical spectrum $I(\omega)$ at zero temperature is given by the Fourier transform of the current correlation function $C_\sigma(t) = \sum_{k, \mu} (e^{i\hbar\omega t} a_{k\mu}^\dagger a_{k\mu}^{\sigma\text{h}})$. The FES exponent is determined by the asymptotic form of $C_\sigma(t) \sim (t^{-\beta_\sigma})$ (oscillating term) $\times t^{-\beta_{\sigma\text{h}}-1}$ for large t . The FES exponent consists of two parts: $\beta_\sigma = \beta_{\sigma\text{ex}} + \beta_{\sigma\text{oc}}$, where

$$\beta_{\sigma\text{ex}} = \sum_{\mu=a,b} \left[(x_\mu^\sigma)^2 + (y_\mu^\sigma)^2 - (x_\mu^\sigma - y_\mu^\sigma)^2 / v_\mu \right] - 1, \quad \beta_{\sigma\text{oc}} = \frac{1}{2} \sum_{\mu=a,b} \left(\frac{G_\mu^\sigma}{v_\mu} \right)^2. \quad (9)$$

These two terms correspond to the “excitonic (ex) correlation part” and the “orthogonality catastrophe (oc) part,” respectively [2]. Note that $\beta_\sigma \neq \beta_{\sigma\text{h}}$ in general. Hence the FES exponent depends on the rotation direction of a circularly-polarized incident light.

When $v_F^\perp = v_F^\parallel \equiv v_F$, the normal modes a and b coincide with the charge- and spin-density modes. Thus the conventional charge-spin separation is recovered in this case [7]. The FES exponent becomes independent of the hole spin, i.e., $\beta_1 \equiv \beta_1 = \beta = \beta^{\text{ex}} + \beta^{\text{oc}}$, where $\beta^{\text{ex}} = \mathcal{F}(g_{2\parallel}^{\text{eh}}, g_{2\perp}^{\text{eh}}) + \mathcal{F}(g_{2\perp}^{\text{eh}}, g_{2\parallel}^{\text{eh}}) - 1$ and $\beta^{\text{oc}} = \mathcal{G}(g_{2\parallel}^{\text{eh}}, g_{2\perp}^{\text{eh}}) + \mathcal{G}(g_{2\perp}^{\text{eh}}, g_{2\parallel}^{\text{eh}})$. Here $\mathcal{F}(x, y) \equiv \frac{1}{2}(1-x)(1-y^2)^{-1/2}$,

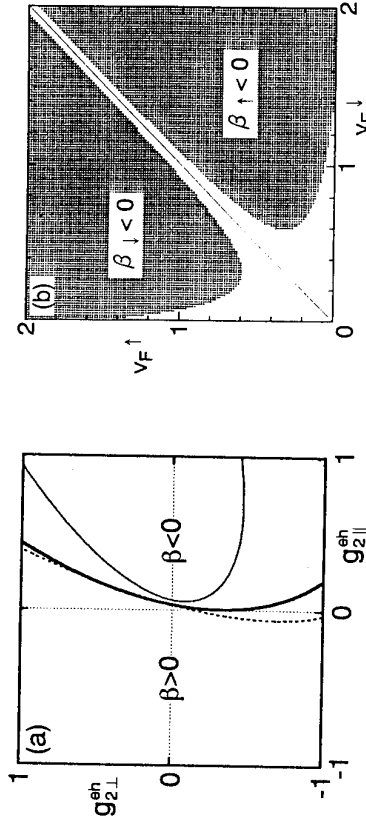


Figure 1: (a) The phase diagram for the sign of the FES exponent in the plane of $g_{2\parallel}^{eh}$ and v_F^γ , showing the boundary between the divergent edge ($\beta_\sigma < 0$) and the convergent one ($\beta_\sigma > 0$). Here $g_{2\parallel}^{eh} = g_{4\parallel}^e = 0.1$ and $g_{2\perp}^e = g_{4\perp}^e = 0.4$. Thin solid (broken) curve represents $\beta_1 = 0$ ($\beta_1 = 0$) for $v_F^\gamma = 0.5$ and $v_F^\gamma = 1.0$. Thick solid curve means $\beta_1 = \beta_1 = 0$ for $v_F^\gamma = v_F^\perp = 1.0$. (b) In the shaded region, the power-law divergence can take place ($\beta_\sigma < 0$) in edge spectra for a rotation direction of the circularly-polarized light even for a repulsive electron-hole interaction ($g_{2\parallel}^{eh} < 0$).

$\mathcal{G}(x, y) \equiv \frac{1}{4} x^2(1-y)^{-1/2}(1+y)^{-3/2}, g_{i+}^\gamma \equiv \frac{1}{2}(g_{i\parallel}^\gamma + g_{i\perp}^\gamma), g_{i-}^\gamma \equiv \frac{1}{2}(g_{i\parallel}^\gamma - g_{i\perp}^\gamma)$ for $i = 2, 4$ and $\gamma = e, eh$, and $\tilde{g}_{2\pm}^\gamma \equiv g_{2\pm}^\gamma / (v_F^\gamma + g_{2\pm}^e)$. Thus when $v_F^\gamma = v_F^\perp$, the FES exponent is independent of the rotation direction of a circularly-polarized light even for $g_{i\parallel}^\gamma \neq g_{i\perp}^\gamma$.

The phase diagram for the sign of β_σ is drawn in Fig. 1(a) on the $(g_{2\parallel}^{eh}, g_{2\perp}^{eh})$ plane. When $v_F^\gamma \neq v_F^\perp$, there are two striking features. (i) We find the region where $\beta_> < 0$ but $\beta_< > 0$. In such a region, the divergent or convergent edge spectrum can be negative even when the rotation direction of a circularly-polarized light. (ii) The exponent can be negative even when the electron-hole interaction is repulsive ($g_{2\parallel}^{eh} < 0$). In fact, there exists in Fig. 1(a) the region of $\beta_> < 0$ even for $g_{2\parallel}^{eh} < 0$ and $g_{2\perp}^{eh} < 0$. This is in striking contrast to the previous theories [1,2]. Figure 1(b) shows the condition on the (v_F^\perp, v_F^γ) plane for existence of such regions for fixed g^σ 's. One finds that $\beta_< > 0$ in the case of $g_{2\parallel}^{eh} < 0$ requires $v_F^\gamma < v_F^{-\sigma}$ [8].

4. Related spin-polarized systems

4.1. Spin-split systems with the time-reversal symmetry

There exists another spin-split band system with the time-reversal symmetry [9], where the band dispersion is $\tilde{\epsilon}(k) \approx \sum_{j=1,2} \sum_{\sigma=\uparrow,\downarrow} \tilde{\epsilon}_j^\sigma(k)$ with $\tilde{\epsilon}_1^\sigma(k) = v_F^\sigma(k - k_F^\sigma)$ and $\tilde{\epsilon}_2^\sigma(k) = -v_F^{-\sigma}(k + k_F^{-\sigma})$ for $\sigma = \uparrow, \downarrow$. The FES exponent in this system, denoted $\tilde{\beta}^\text{ex} + \tilde{\beta}^\text{oc}$, is independent of the hole spin $-\sigma$ in contrast to the case of broken time-reversal symmetry. The explicit form of the exponent is

$$\tilde{\beta}^\text{ex} = \min_{\sigma=\uparrow,\downarrow} \sum_{\mu=a,b} \left[(\tilde{x}_\mu^\sigma)^2 + (y_\mu^\sigma)^2 - \tilde{x}_\mu^{\sigma-\sigma} \frac{\tilde{G}_\mu^\sigma}{\tilde{v}_\mu} + \tilde{y}_\mu^{\sigma-\sigma} \right] - 1, \quad \tilde{\beta}^\text{oc} = \frac{1}{4} \sum_{\sigma=\uparrow,\downarrow} \sum_{\mu=a,b} \left(\frac{\tilde{G}_\mu^\sigma}{\tilde{v}_\mu} \right)^2, \quad (10)$$

where $\tilde{G}_\mu^\sigma = \frac{1}{2} \sum_{\sigma'=\uparrow,\downarrow} (g_{2\parallel}^{eh} \delta_{\sigma,\sigma'} + g_{2\perp}^{eh} \delta_{\sigma,-\sigma'}) \left(\tilde{x}_\mu^{\sigma-\sigma'} + \tilde{y}_\mu^{\sigma-\sigma'} \right)$. Here \tilde{x}_μ^σ , \tilde{y}_μ^σ , and \tilde{v}_μ are given respectively by x_μ^σ , y_μ^σ , and v_μ with interchanging $g_{2\parallel}^e \rightleftharpoons g_{2\perp}^e$. An interesting feature of the exponent is that $\tilde{\beta}^\text{ex}$ is given as the smaller one of two values. Consequently, “switching” phenomenon is observed in $\tilde{\beta}^\text{ex}$ as a function of g 's and v_F^σ [8].

4.2. Spin-split chiral Luttinger liquids

We here mention the FES exponent in the chiral Luttinger liquid, whose dispersion is defined as $\epsilon_{\text{chiral}}(k) \approx \sum_{\sigma=\uparrow,\downarrow} \epsilon_{\text{chiral}}^\sigma(k)$ with $\epsilon_{\text{chiral}}^\sigma(k) = v_F(k - k_F^\sigma)$. We write down here the result only of the FES exponent $\beta_{\text{chiral}} = \beta_{\text{chiral}}^{\text{ex}} + \beta_{\text{chiral}}^{\text{oc}}$ [8]: $\beta_{\text{chiral}}^{\text{ex}} = -\frac{1}{2} \left(\tilde{g}_{2+}^{\text{eh}} + \tilde{g}_{2-}^{\text{eh}} \right)$ and $\beta_{\text{chiral}}^{\text{oc}} = \frac{1}{8} \left[(\tilde{g}_{2+}^{\text{eh}})^2 + (\tilde{g}_{2-}^{\text{eh}})^2 \right]$. We note that the g_e^e process is absent in the chiral Luttinger liquid. Comparing these with β^{ex} and β^{oc} for $g_{2\parallel}^e = g_{2\perp}^e = 0$, one finds $\beta_{\text{chiral}}^{\text{ex}} = \beta^{\text{ex}}$ and $\beta_{\text{chiral}}^{\text{oc}} = \frac{1}{2} \beta^{\text{oc}}$. Since the orthogonality part, $\beta_{\text{chiral}}^{\text{oc}}$, is smaller, the edge spectra tend to diverge more strongly even in the case of $g_{2\parallel}^{\text{eh}} < 0$, $g_{2\perp}^{\text{eh}} < 0$ and $v_F^\perp = v_F^\parallel$, in comparison with the spin-polarized TL liquid.

5. Concluding remarks

We make a comment on the effects of the electron-hole backward scattering, denoted as $g_{1\parallel}^{\text{bh}}$ and $g_{1\perp}^{\text{bh}}$, on the FES exponent. In the case of $g_{1\parallel}^{\text{bh}} = g_{1\perp}^{\text{bh}} \equiv g_{1\parallel}^{\text{sh}} > 0$, the system is decoupled into two semi-infinite wires below a characteristic energy scale, ϵ_1 [10]. Then the exponent has additionally a universal constant, independent of $g_{1\parallel}^{\text{bh}}$ and $g_{1\perp}^{\text{bh}}$. Therefore, our results may be valid only when $\hbar\omega - E_{\text{FES}} > \epsilon_1$. However, the main features of the edge spectra are determined just by the forward-scattering correlations, i.e., by Eq. (9). Furthermore, interface roughness, impurity scatterings, and the Peierls transition in actual 1D systems may introduce effects on these effects is left for the future.

Acknowledgements. The authors thank K. Ohtaka and N. Nagaosa for discussion. This work is supported by Grant-in-Aid for the Scientific Research on Priority Areas, “Mutual Quantum Manipulation of Radiation Field and Matter,” from the Ministry of Education, Science and Culture of Japan.

References

- [1] K. Ohtaka and Y. Tanabe, Rev. Mod. Phys. **62** (1990) 929.
- [2] T. Ogawa, A. Furusaki and N. Nagaosa, Phys. Rev. Lett. **68** (1992) 3638.
- [3] J. M. Calleja *et al.*, Phys. Rev. B **51** (1995) 4285.
- [4] K. Penc and J. Sólyom, Phys. Rev. B **47** (1993) 6273; F. J. Rodriguez and C. Tejedor, Phys. Rev. B **49** (1994) 16781.
- [5] J. M. Calleja *et al.*, Solid State Commun. **79** (1991) 911; J. F. Mueller, A. E. Ruckenstein and S. Schmitt-Rink, Phys. Rev. B **45** (1992) 8902.
- [6] J. Sólyom, Adv. Phys. **28** (1979) 201.
- [7] T. Ogawa, Jpn. J. Appl. Phys., Suppl. **34** (1995) 146.
- [8] H. Oriani and T. Ogawa, (unpublished).
- [9] G. Pasol and H. Sakaki, Jpn. J. Appl. Phys. **33** (1994) 879.
- [10] C. L. Kane and M. P. A. Fisher, Phys. Rev. Lett. **68** (1992) 1220; C. L. Kane, K. A. Matveev and L. I. Glazman, Phys. Rev. B **49** (1994) 2253; N. V. Prokof'ev, *ibid.* **49** (1994) 2148.
- [11] N. Nagaosa and T. Ogawa, Solid State Commun. **88** (1993) 295; T. Ogawa, phys. stat. sol. (b) **188** (1995) 83.

Ordering in the ionized donor layer of modulation doped heterostructures

M. Stopa and Y. Aoyagi

RIKEN (The Institute of Physical and Chemical Research)

2-1, Hirosawa, Wako-Shi Saitama 351-01, Japan

e-mail stopa@sisyphus.riken.go.jp

Abstract We study the temperature dependent ordering of ionized impurities in the donor layer adjacent to a 2DEG layer via a Monte-Carlo simulation. We show that for a sufficiently small filling ratio the ionized donors become ordered among all donors, forming a Wigner-like lattice without long range order. We present evidence that the interacting donors on random sites form a glass, with a large number of nearly degenerate metastable states into which the system can decay, depending on initial conditions.

When the filling ratio \mathcal{F} of ionized donors among all donors in the dopant layer of a GaAs – AlGaAs modulation doped 2DEG heterostructure is less than unity, redistribution of the ionized sites through hopping can lead to ordering of the donor layer charge [1]. It has also been predicted [2] and observed experimentally [3] that the decrease in scattering rate of 2DEG electrons with remote donor layer impurities associated with ordering of the donor layer charge leads to enhanced mobility μ .

For mesoscopic structures, it is known that QPC resistance at cryostat temperatures can decay on a hyperexponential time scale. Furthermore, hysteresis in the IV curves of these and more complicated structures is commonly observed. These and other features of mesoscopic transport can be linked, we believe, to Coulomb regulation of ions in the donor layer.

A similar system which has received considerable scrutiny lately is that of coupled quantum dots, either in a “memory cell” configuration [4] or in a large square array [5]. Both of these devices show hysteresis resulting from Coulomb interaction of the dots, the former one by design. The physics of these devices is similar to that of the disordered donor layer in that both are characterized by Coulomb regulation of discrete charges on a disordered lattice. Both capacitively coupled quantum dot systems and ions distributed among randomly positioned donor sites are characterized by multiple metastable states, switching events and hyperexponential decay times. Both, in fact, are glasses.

Here we present the results of Monte-Carlo simulations on a system of ions hopping among randomly distributed donor sites in a modulation dopant layer (Si) of a GaAs – AlGaAs heterostructure [6,7]. We are particularly interested in the metastable quasi-ground states and the approach to equilibrium. We assume a system of N or donors, of which N_+ are ionized, located in a δ -doping layer separated by a distance a from a 2DEG which acts to screen the interionic Coulomb interaction. Here we simply assume that the 2DEG acts as a metal, producing an image charge of each ion at $2a$ away from the donor layer.

We note that our treatment of the Coulomb interaction is different from that of Sobkowicz *et al.* [7] in that we do not assume any Thomas-Fermi screening in the donor layer itself (those authors used a Yukawa type potential for the ion interaction). Rather we compute the direct Coulomb energy of a system of dipoles (the positive donor charges and their images in the 2DEG). Further in contrast to reference [7] we include the spatial dependence, $\exp(-2r_{ij}/a^*)$, of the hopping probability, where r_{ij} is the distance between sites i and j , and a^* is the effective Bohr radius. Thus we are not using the Monte-Carlo simulation simply to “anneal” the sample, but rather we are investigating the paths which the system takes to reach equilibrium.

We use the approximate hopping rates derived by Schmidt *et al.* [8] for hydrogenic states in GaAs. Since for $x > 0.22$ the ground state of an impurity in $Al_xGa_{1-x}As$ is a deep level or DX center, the current simulation actually depends upon the density of hydrogenic sites or “capture states” present in the sample.

Electrons bound to DX centers are assumed to be frozen out and immobile.

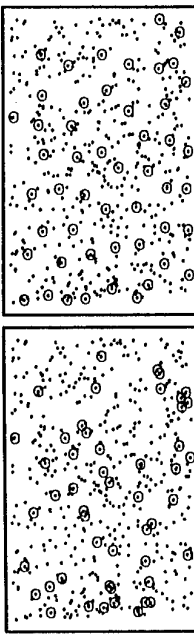


FIG. 1 Typical donor positions (dots) and ionized donor positions (open circles) within a 25 Bohr^* (250 nm) square. Left panel shows initial random distribution of ion positions, right panel shows distribution after time of 0.01 ns . Temperature is 5 K .

Figure 1 shows a typical example of a random set of donors of which ten percent are ionized. In the left panel the ionized sites are in their initial random configuration. On the right they have clearly evolved into a more ordered state with clear evidence of a triangular (Wigner crystal) symmetry. The degree of ordering in the system can be quantized in a number of ways. The most typical “order parameter” for such a system is the pair correlation function $g(r)$ which specifies the probability of finding an ion at distance r from another ion. This quantity, averaged over donor configurations and initial ion placement configurations, is shown in figure 2 as a function of \mathcal{F} . In this plot the total density of ions is held constant and the number of sites is varied.

In figure 3 we show the time development of the total electrostatic energy

of the system for a fixed $\mathcal{F} = 0.2$ (50 ions and 250 donors). In all of the displayed curves the donor distribution is unchanged, but the initial ion configuration among the donors is randomized. Thus we are simulating the raising of

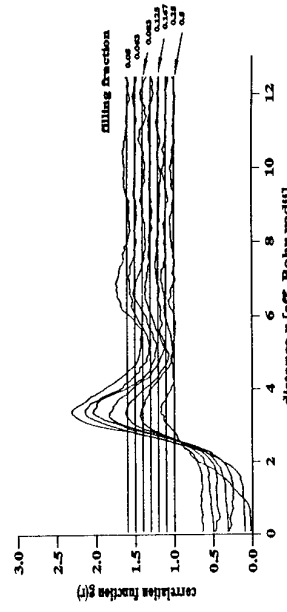


FIG. 2 Pair correlation function for a variety of filling ratios. The curves have been offset for clarity.

the sample to room temperature and the subsequent cool down, since in this case it is not expected that the silicon atoms will move, but rather only the ion positions. We note that even for fairly long simulation times, the fundamental rate governing hopping between sites allows our computation to extend at most to tenths of nanoseconds. Thus, based on our simulation, we cannot confidently predict the behaviour of the system, even at $T = 5$ K, for laboratory time scales.

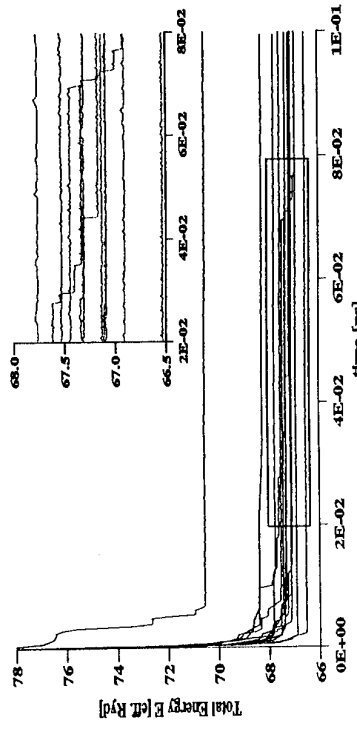


FIG. 3 Time development of the total energy of the ions for a variety of random initial ion distributions among a set of fixed donors. $\mathcal{F} = 0.2$. Inset is expanded view of boxed area.

Within the limitations of computation time, however, it is evident that the system proceeds very rapidly to a metastable state and remains there for a long time. Typically fluctuations between discrete states can be seen on individual curves. These are states that are separated from one another by a small number of hops. While these switching events are still on a nanosecond time scale it is still plausible that this kind of Coulomb governed multiple metastable quasi-ground state behaviour is responsible for some of the telegraph noise which is frequently observed in transport through mesoscopic structures.

Generally, an inspection of the actual ion configuration (not shown) of the various quasi-ground states shown in figure 3 reveals that the ion configurations differ by a large number of hops from one another. Thus a direct transition from one metastable state to another is overwhelmingly unlikely. Assuming that the ground state of a collection of dipoles in the limit of $\mathcal{F} \rightarrow 0$ is indeed a Wigner crystal, it is clear that for finite \mathcal{F} the system is similar to a pinned and deformed charge density wave.

We believe that further theoretical and numerical study is necessary to reveal precisely what observed phenomena in transport through mesoscopic 2DEG systems is attributable to the glassy behaviour of ions in the donor layer. Additionally, it is hoped that this numerical work can stimulate experimental effort toward probing the properties of the donor layer, which have heretofore been somewhat overlooked.

- [1] A. L. Efros, Solid State Comm. **65**, 1281 (1988); T. Stuski, P. Winiarski, I. Gorczyca, L. H. Dmowski, R. Piotrkowski, P. Sobkowicz, J. Smoliner, E. Gornik, G. Böhm and G. Weimann, Phys. Rev. B **50**, 2723 (1994).
- [2] A. L. Efros, F. G. Pikus and G. G. Samsonidze, Phys. Rev. B **41**, 2723 (1990).
- [3] E. Buks, M. Heiblum and Hadas Shtrikman, Phys. Rev. B **49**, 14790 (1994).
- [4] K. Nakazato *et al.*, Electron. Lett. **29**, 384 (1993); P. D. Dresselhaus *et al.*, Phys. Rev. Lett. **72**, 3226 (1994).
- [5] C. I. Duruoz, R. M. Clarke, C. M. Marcus and J. S. Harris, Phys. Rev. Lett. **74**, 3237 (1995).
- [6] F. A. Reboreda, Phys. Rev. B **51**, 5089 (1995).
- [7] P. Sobkowicz, Z. Wilamowski and J. Kosut, Semicond. Sci. Technol. **7**, 1155 (1992).
- [8] T. Schmidt, C. Metzner, St. G. Müller and G. H. Döhler, Phys. Rev. B **47**, 10633 (1993).

Electron Density Dependence of the Effective g-Factor in a

2-Dimensional Electron Gas at Strong Magnetic Fields

J. H. Oh*, K. J. Chang*, G. Ihm†, and S. J. Lee‡

*Department of Physics, Korea Advanced Institute of Science and Technology, Taejon 305-358, Korea.

†Department of Physics, Chungnam National University, Taejon 305-764, Korea

‡Department of Physics, Korea Military Academy, Seoul 139-799, Korea

Abstract

The dependences of the effective g-factor (g^*) on the electron density and the Landau level filling factor ν are studied for a two dimensional electron gas in strong magnetic fields. The trial many-body wavefunctions are constructed by multiplying the Jastrow correlation factor to the Laughlin-like wavefunctions, then, the ground state energy are calculated using a variational Monte Carlo method for $1 < \nu < 2$. For a dimensionless parameter $r_s = 1.33$, g^* is estimated to be about 11 at $\nu = 1.0$, while the measured value is 7.3. Considering the level broadening due to impurity and phonon scatterings, a better agreement of $g^* = 9$ is found.

Keywords: Many body and quasi-particle theories, Quantum effects.

Since Fang and Stiles [1] first observed an enhancement of the electronic g-factor (g^*) in two dimensional systems, the g^* -factor has been a subject of many theoretical and experimental studies. [2-8] The enhancement of g^* was first explained by Janak [2] in terms of the exchange interaction between electrons, and its value is largest at odd integer filling factors in the Landau levels. Ando and Uemura showed the oscillating behavior of g^* with magnetic field in two dimensional systems, which was attributed to the magnetic depolarization and spin Zeeman-splitting. [3] In most recent work, Xu and his co-workers [4] used a self-consistent scheme including the effects of impurity and phonon scatterings and obtained g^* , in good agreement with experimental data.

In this work, we examine the enhancement of g^* in a 2-dimensional electron gas. Using trial many-body wavefunctions, in which the Jastrow correlation factor is multiplied to the Laughlin-like wavefunction, [9] the dependence of g^* on the electron density is investigated and compared with experimental data. We also study the effect of the Landau level broadening due to impurity and phonon scatterings on g^* .

For the filling factors, $1 < \nu < 2$, where the first Landau level with up spin is fully occupied while the down-spin state is partially occupied with a fraction of $\nu - 1$, g^* is simply proportional to the energy difference between electrons with up and down spins. The ground state energy for each spin state is calculated by relaxing electrons on the surface of the Haldane's sphere. [10,11] In this model, electrons and uniform neutralizing positive background charges are assumed to be on the surface of the sphere with a radius R_s , and a magnetic monopole located at the center of the sphere gives rise to radially extended 2.5 flux quanta through the surface, with the magnetic field described by a vector potential $\vec{A} = -\hbar S \cot \theta \hat{\varphi} / eR$. The Hamiltonian of N electrons on the sphere is given by

$$H = \frac{4}{N r_s^2} \sum_i^N (|\vec{L}_i|^2 - S^2) + \frac{1}{r_s} \sum_{i \neq j} \frac{1}{|\vec{r}_i - \vec{r}_j|} + E_{ep} + E_{pp} \quad (1)$$

where the angular momentum operator \vec{L} is defined as $R\hat{r} \times (\vec{p} + e\vec{A}) + S\hat{r}$, E_{ep} ($= -4N^{3/2}/r_s$) is the interaction energy between the positive background and electrons, and E_{pp} ($= 2N^{3/2}/r_s$) is the self-energy of the positive background. Here the energy and length scales are chosen so that $e^2/2ca_B$ and $a = 2R/\sqrt{N}$ are set equal to one, and the dimensionless electron density is described by $r_s = a/a_B$, where the effective Bohr radius a_B is $e\hbar^2/m^*e^2$. If the numbers of up- and down-spin electrons are defined as N_u and N_d , respectively, their effective energies, E^1 and E^1 , can be evaluated for the ground state wavefunction Ψ :

$$E^1 = \frac{1}{N_u} \sum_{i=1}^{N_u} \int [T_i + V_i] \frac{\Psi^*(\vec{R})\Psi(\vec{R})}{<\Psi|\Psi>} d\vec{R} \quad E^1 = \frac{1}{N_d} \sum_{i=N_u+1}^N \int [T_i + V_i] \frac{\Psi^*(\vec{R})\Psi(\vec{R})}{<\Psi|\Psi>} d\vec{R} \quad (2)$$

where for each spin state the local energies T_i and V_i which depend on electron coordinates are defined as $T_i = \frac{4}{N r_s^2} \frac{1}{i} (|\vec{L}_i|^2 - S^2)\Psi$ and $V_i = \frac{1}{i} \sum_{j \neq i} \frac{1}{|\vec{r}_i - \vec{r}_j|}$. Since the Zeeman-splitting is represented by $m^*Sg^*/R^2r_s^2$ in the local energy unit, g^* can be written as, $g^* = (E^1 - E^1)R_s^2/m^*S + g_0$, where g_0 is the bare g-factor of 0.44 for GaAs.

A trial many-body wavefunction for a partially polarized interacting electron gas is usually assumed to be of the Jastrow-Slater form, [12,13]

$$\Psi(\vec{r}_{i1}, \vec{r}_{j1}) = D_u(\vec{r}_{i1})D_d(\vec{r}_{j1})J(\vec{r}_{i1}, \vec{r}_{j1}), \quad (3)$$

where D_u and D_d are the Slater determinants for the up- and down-spin states, respectively, and $J(\vec{r})$ is the Jastrow correlation factor. In our calculations, the Laughlin-type wavefunctions are used for the Slater determinants,

$$D_u(\vec{r}_{i1}) = \prod_{i < k} (u_i v_k - u_k v_i) \quad D_d(\vec{r}_{j1}) = \prod_{j < k} (u_j v_k - u_k v_j)^{m'}, \quad (4)$$

where $u (\equiv e^{-i\varphi/2} \cos \theta/2)$ and $v (\equiv e^{i\varphi/2} \sin \theta/2)$ are spinor coordinates, [11] and D_u and D_d represent the Laughlin states with the filling factors 1 and $1/m' (= \nu - 1)$, respectively. The Jastrow factor preserves the symmetric relation for particle permutations, and two different Jastrow factors with spin variables, s and s' , are tested;

$$J_1(\vec{r}) = \exp \left(\sum_{i < k} \frac{-\alpha}{|u_i v_k - u_k v_i|^{1/2}} \right) \quad J_2(\vec{r}) = \exp \left[\sum_{i < k} \frac{-\alpha}{|u_i v_k - u_k v_i|^{1/2}} \sqrt{1 - \exp(-b_{s,s'} |u_i v_k - u_k v_i|)} \right], \quad (5)$$

where α and $b_{s,s'}$ are the variational parameters. A variational Monte Carlo method is used to calculate the ground state energies, in which T_i and V_i are sampled by random walks generated by the standard Metropolis algorithm. [14] The maximum statistical errors for E^1 and E^1 are estimated to be about 0.0005 and 0.005 in the local energy unit, respectively, at $r_s = 1.0$. To examine the finite-size effect, we test several occupation numbers of electrons for the up- and down-spin states and find good convergence within the statistical error. In this work, we use a set of occupation numbers, $(N_u, N_d) = (100, 34)$, $(96, 20)$, $(99, 15)$, and $(100, 12)$ at $\nu = 4/3$, $6/5$, $8/7$, and $10/9$, respectively.

To see the effect of the exchange interaction on g^* , we first calculate the ground state energies only using the Slater determinants in Eq. (3). In this case, the energy difference between E^1 and E^1 results from the averaged potential energy $\langle V_i \rangle$ which reflects the exchange interaction. Since the exchange energy increases with increasing of $N_u - N_d$, the energy difference between the up- and down-spin states grows as the filling factor approaches one. Since the potential energy $\langle V_i \rangle$ is proportional to $1/r_s$, g^* increases linearly with r_s . At $r_s = 1.33$, the calculated values for g^* only from the exchange interaction are 7.5, 9.7, 10.9, and 11.5 at $\nu = 4/3$, 6/5, 8/7, and 10/9, respectively.

In the case of the many-body wavefunction with the Jastrow correlation factor, the total energy, $E_{\text{tot}}(\alpha) = N_u E(\alpha) + N_d E(\alpha) + E_{\text{cp}} + E_{\text{pp}}$, is minimized over the variational parameter α . The major role of the Jastrow factor is that electrons with the opposite as well as same spins no longer become closer together. Although this effect increases the kinetic energy of electrons, the decrease of the potential energy is more significant, thus, the resulting total energy is lowered. Moreover, we also find that g^* is reduced by introducing the Jastrow factor; with the form of J_1 , g^* are estimated to be 6.2, 7.8, 8.7, and 9.2 for $r_s = 1.33$ and $\nu = 4/3$, 6/5, 8/7, and 10/9, respectively, while they are generally further reduced by about 20 % in the case of J_2 , with the corresponding values of 4.9, 6.3, 7.0, and 7.6.

The dependence of g^* on the particle density r_s is drawn in Fig. 1. The difference between E^1 and E^1 decreases with r_s , however, g^* is found to increase because the Zeeman splitting decreases faster with a rate of $1/r_s^2$. In contrast to the case of $\alpha = 0$, which exhibits the linear dependence of g^* on r_s , g^* increases very rapidly at high densities, below $r_s = 5$, while at low densities it shows the linear behavior. The linear dependence of g^* mainly results from the dominant contribution of the potential energy $\langle V_i \rangle$ to the total energy at low electron densities because it is proportional to $1/r_s$, whereas the kinetic energy varies such as $1/r_s^2$.

In Fig. 2, g^* is plotted as a function of the filling factor and compared with other theoretical and experimental results. Our calculated values for g^* lie at higher values, and the differences are attributed to the neglect of the Landau level broadening due to impurity and phonon scatterings in our calculations. To include these scattering effects, we assume a Gaussian broadening such as $e^{-(E-E_b)^2/\Gamma^2}/\Gamma\sqrt{\pi}$ for the l -th Landau level E_l , where Γ is the broadening parameter. Since the up-spin state is fully occupied in our system, its associated energy is invariant by the Landau level broadening, however, the energy for the down-spin state is readily reduced by an amount of $\Delta E = -\frac{\Gamma}{2\sqrt{\pi}}e^{-\beta^2}$ where $\beta = \mu/\Gamma$ and μ is the chemical potential. Although Γ was shown to exhibit the oscillating behavior as ν varies, [4] we assume a constant broadening parameter of $\Gamma = 0.5$ meV for simplicity. Then, g^* is estimated to be about 9 for the Jastrow factor J_2 at $\nu = 1.0$, in good agreement with measured value of 7.3. Compared with other theoretical calculations [4], our results show that g^* decreases more rapidly as ν increases.

In conclusion we have studied the density dependence of g^* for a two-dimensional electron gas under strong magnetic fields. Using the Slater-Jastrow form of many-body wavefunctions, the electronic energies for the up- and down-spin states are calculated and used to determine g^* in the GaAs system. We estimate g^* to be about 11 for $r_s = 1.33$ and $\nu = 1.0$. Considering the Landau level broadening, the result for g^* is in better agreement with experimental data.

This work was supported by the CMS of Korea Advanced Institute of Science and Tech-

nology, the SPRC of Jeonbuk National University, Ministry of Education, and CTP at Seoul National University.

References

- [1] F. F. Fang and P. J. Stiles, Phys. Rev. 174 (1968) 823.
- [2] J. J. Janak, Phys. Rev. 178 (1969) 1416.
- [3] T. Ando and Y. Uemura, J. Phys. Soc. Japan 37 (1974) 1044.
- [4] W. Xu, P. Vasilopoulos, M. P. Das, and F. M. Peeters, 22nd International Conference on the Physics of Semiconductors, edited by D. J. Lockwood (World Scientific, London, 1995) p. 743.
- [5] Th. Englert, D. C. Tsui, A. C. Gossard, and Ch. Uhllein, Surf. Sci. 113 (1982) 295.
- [6] R. J. Nicholas, R. J. Haug, K. v. Klitzing, and G. Weimann, Phys. Rev. B 37 (1988) 1924.
- [7] A. Usher, R. J. Nicholas, J. J. Harris, and C. T. Foxton, Phys. Rev. B 41 (1990) 1129.
- [8] E. E. Mendez, J. Nocera, and W. I. Wang, Phys. Rev. B 47 (1993) 13937.
- [9] R. B. Laughlin, Phys. Rev. Lett. 50 (1983) 1395.
- [10] D. M. Haldane, Phys. Rev. Lett. 51 (1983) 605.
- [11] R. Price, P. M. Platzman, and S. He, Phys. Rev. Lett. 70 (1993) 339.
- [12] D. Ceperley, Phys. Rev. B 18 (1978) 3126.
- [13] S. Fahy, X. W. Wang, and S. G. Louie, Phys. Rev. Lett. 65 (1990) 1478.
- [14] N. Metropolis, A. W. Rosenbluth, M. N. Rosenbluth, A. H. Teller, and E. Teller, J. Chem. Phys. 32 (1953) 1087.

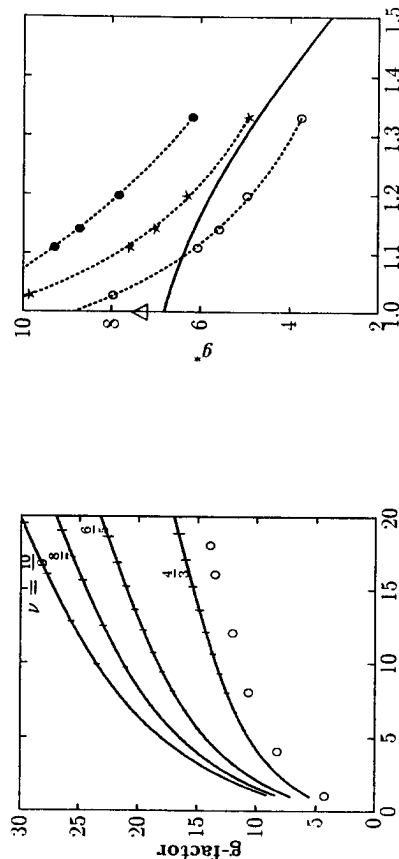


Fig. 1 g^* -factor vs r_s for the Landau level filling factors, $\nu = 10/9, 8/7, 6/5$, and $4/3$. Solid lines and vertical bars represent the results calculated with the Jastrow factor J_1 and their statistical errors, respectively. The results for J_2 at $\nu = 4/3$ are denoted by circles.

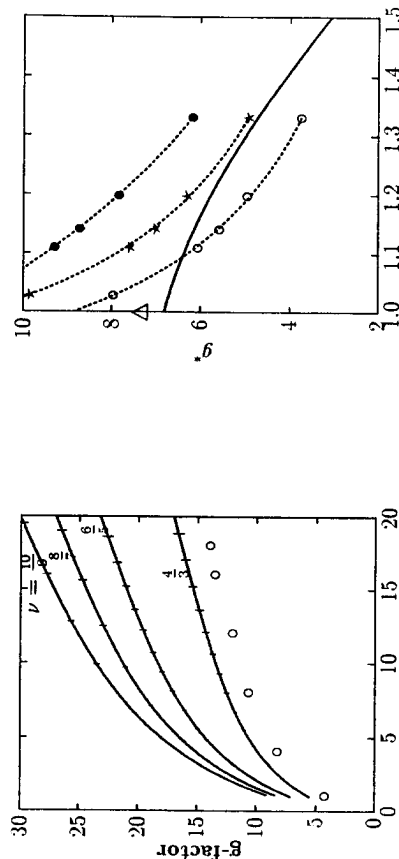


Fig. 2 For $r = 1.33$, the g^* factors are plotted as a function of the filling factor ν and compared with other theoretical[4] (solid line) and experimental[7] (Δ) results. Filled circles and stars represent the results calculated with the Jastrow factors, J_1 and J_2 , respectively, while empty circles denote the corrected values by including the level broadening for J_2 .

INEFFICIENCY OF ODD RELAXATION AND PROPAGATION OF ELECTRON BEAMS IN A TWO-DIMENSIONAL ELECTRON SYSTEM

R.N.Gurhi, A.N.Kalinenko, A.I.Kopeliovich,
B.Verkin Institute For Low Temperature Physics & Engineering,
National Ukr. Academy of Sciences,
47, Lenin Ave., Kharkov 310164, Ukraine.

Abstract

Evolution of sharp angular distributions in the degenerated two-dimensional electron gas of colliding electrons has been analyzed. It is shown that the part of the electron distribution function odd in momentum smears considerably slower than the even one, and this is the reason of the unusual behavior of propagation of two-dimensional electron beams.

Reduction of the degenerated electron gas dimensionality from three to two do not result in the rearrangement of its ground state but modifies essentially the momentum relaxation processes [1,2]. According to the laws of conservation, collisions of most electrons in the 2D system are of small-angular character, i.e. the scattering angle $\varphi \approx T/e_F \ll 1$ (T is the temperature, e_F is the Fermi energy). The exception is the collisions of electrons with almost opposite momenta ($|\vec{p}_1 + \vec{p}_2|/p_F \leq T/e_F$): as a result of the collision, an electron pair turns by the arbitrary angle $\varphi \approx 1$. (Note that, in contrast to the 3D case, in the 2D case both types of processes have equal, by the order of magnitude, probabilities.) The second type collisions are entirely effective in the relaxation of the part of the electron distribution function even in momentum. Thus, its relaxation time is the same as in the 3D case: $\tau_0 \sim (e_F/T)^2 \sim T^{-2}$. Both types of collisions are of small efficiency in the relaxation of the odd part of distribution. For the first type, it is connected with its small-angular character. For the second type, it is due to the fact that the turn of the electron pair with exactly opposite momenta by an arbitrary angle φ does not change, in general, the odd part of distribution. That is why, the odd distribution relaxation in the 2D case turns out to be far slower than in the 3D case: $\tau_a \approx \tau_0 (e_F/T)^2 \sim T^{-4}$.

The above refers to the case of the weakly anisotropic electron distribution with the characteristic angular scale $\delta\alpha \sim 1$. Decreasing the angle $\delta\alpha$, the relaxation rate of the

odd nonequilibrium correction to the distribution $(df_a/dt)f_a^{-1}$ increases and becomes of the order of τ_s^{-1} at $\delta\alpha \approx \sqrt{T/e_F}$ [3]. This rapid relaxation is connected, however, with scattering over small angles [3]. Roughly, for the time of the order of τ_s the even part of the distribution function becomes fully isotropic whereas the odd part only broadens by some times. In the present work it is shown that even in the case of the extremely anisotropic high-energy initial distribution, the odd nonequilibrium smears rather slowly in the space of the velocity directions. In particular, this fact provides stability of electron beams in 2DEG at the distances exceeding considerably a mean free-path length with respect to the electron-electron collisions $\approx \tau_0 v_F$. Thus, specific two-dimensional relaxation mechanisms may be found in experiments with electron beams. The problem on the electron beam propagation in 2DEG was previously treated by Laihltman [4], however, without taking account of the difference between relaxation of the odd and even distribution components, important for the given work.

The evolution of the nonequilibrium correction to the electron distribution in momenta is described by the following equation

$$\frac{\partial f_{\vec{p}}}{\partial t} = I\{f_{\vec{p}}\}, \quad (1)$$

$$I\{f_{\vec{p}}\} = - \int (\nu_{\vec{p}'\vec{p}} f_{\vec{p}} - \nu_{\vec{p}\vec{p}'} f_{\vec{p}'}) d^3 p', \quad (2)$$

where $I\{f_{\vec{p}}\}$ is the linearized integral of electron-electron collisions. At the "pretemperature" relaxation stage when the energy of electrons in a beam counted off from the Fermi-level, $|e| \gg T$, one can neglect the terms $\sim \exp(-|e|/T)$ in the collision integral. In this approximation $\nu_{\vec{p}\vec{p}'} = 0$ at $|\vec{e}_{\vec{p}'}| < |\vec{e}_{\vec{p}}|$. In other words, at the pretemperature stage, the departures from the stage \vec{p} occur downwards in the absolute energy value with the arrivals taking place from upwards. Assuming for the sake of simplicity the squared modulus of the matrix element of the electron-electron interaction W to be constant, we will obtain the following asymptotic expression for the core $\nu_{\vec{p}\vec{p}'}$ in the 2D system at not too small angles φ between the vectors \vec{p} and \vec{p}' :

$$\nu_{\vec{p}\vec{p}'} \simeq \frac{C}{\sin \varphi} \begin{cases} 2|\epsilon' - \epsilon|, & \epsilon' > 0; \varphi \rightarrow |\epsilon'|, \\ -|\epsilon + \epsilon'|, & \epsilon' < 0; \varphi, \pi - \varphi \rightarrow |\epsilon' - \epsilon|. \end{cases} \quad (3)$$

$\epsilon \equiv e_{\vec{p}}/e_F$, $\epsilon' \equiv e_{\vec{p}'}/e_F$, $|\epsilon|, |\epsilon'| \ll 1$; $C \equiv \frac{\pi^2 W m}{2 h^5}$, m is the electron mass. This expression turned out to be an even function of φ . The part of $\nu_{\vec{p}\vec{p}'}$ responsible for the odd relaxation appears in the following approximation

$$\frac{\nu_{\vec{p}\vec{p}'}}{\nu_{\vec{p}\vec{p}}} \simeq -C \frac{\cos \varphi}{\sin^3 \varphi} (\epsilon^2 - \epsilon'^2) \theta(\epsilon \epsilon') \operatorname{sign} \epsilon; \quad \varphi, \pi - \varphi \rightarrow \sqrt{|\epsilon|}, \quad (4)$$

$\theta(\epsilon \epsilon')$ is the Heaviside function.

One can prove mathematically in a strict form [5] that at $t \rightarrow \infty$, the solution of eqs.(1)-(3) under the initial condition $f_{\vec{p}} = A\delta(\vec{p} - \vec{p}_0)$ tends to:

$$f_{\infty\vec{p}} = A\delta(\epsilon)[\chi_s + \chi_a(\alpha)], \quad \chi_s = (2\pi m)^{-1}, \quad (5)$$

$$\chi_a(\alpha) = -\frac{\epsilon_0}{|\ln|\epsilon_0||} \frac{\cos\alpha}{\sin^2\alpha}, \quad |\alpha|, |\pi - \alpha| \gg \sqrt{|\epsilon_0|}, \quad (6)$$

α is the angle between the vectors \vec{p} and \vec{p}' . Present here not a strict but more obvious proof of this result. After each collision, the nonequilibrium electron energy decreases on the average, by about 3 times. For the sake of simplicity, let us take that it is exactly 3 times decrease, i.e. we substitute $\nu_{\vec{p}\vec{p}'}^*$ by the model core

$$\tilde{\nu}(\varphi, \epsilon_n) = m \frac{\int \nu_{\vec{p}\vec{p}'}^* d\vec{p} d\vec{p}'}{\int \nu_{\vec{p}\vec{p}'}^* d\vec{p} d\vec{p}'}. \quad (7)$$

Here $\tilde{\nu}(\varphi, \epsilon_n)$ is the probability for the electron with the energy $\epsilon_{\vec{p}'} = \epsilon_{\vec{n}-1} = \epsilon_0 3^{n-1}$ after the $n-1$ collision to be scattered in the n -th collision to the state \vec{p}' at the angle φ to \vec{p}' . Assume that by the moment of the n -th collision, the distribution has been mainly concentrated in the angular region near \vec{p}_0 whose width is substantially less of some angle α . Then after the n -th collision, the electron density at the angle α may be written as

$$f_n(\alpha, \epsilon_n) = \sum_{k=1}^n \tilde{\nu}(\alpha, \epsilon_k). \quad (7)$$

The core part odd in α is $\tilde{\nu}_{\alpha} \sim \epsilon |\ln \epsilon|^{-1} \alpha^{-3}$, the even one is $\tilde{\nu}_s \sim |\ln \epsilon|^{-1} \alpha^{-1}$ at $\alpha \gg \sqrt{\epsilon}$. From (7) it is clear that the assumption on the angular distribution character appears to be self-consistent for the odd part f_{an} , at any large number of n , a series in k converges rapidly to the quantity f_{∞} from (4). As to the even part, it diverges when $n \rightarrow \infty$. At α the electron density becomes large enough after about $|\ln|\epsilon_0||$ collisions.

Thus, the even part of the sharp distribution at the pretemperatute relaxation stage becomes fully isotropic (practically it occurs after a number of collisions $|\ln|\epsilon_0||$). The odd part being broadened as a result of some first collisions ($t \simeq \tau_s(T/\epsilon_0)^2$) up to the angular width $\simeq \sqrt{\epsilon_0/\epsilon_F}$, conserves further its form. The consideration of the temperature stage ($t \gg \tau_s$) when $|\epsilon| \simeq T$ shows that the broadening of the odd component occurs rather slowly according to the law

$$\delta\alpha \simeq \sqrt{T/\epsilon_F(t/\tau_s)^{1/4}}. \quad (8)$$

Therefore, complete smearing of a beam takes place for the time $\tau_A \gg \tau_s$.

The long-lived odd component of a beam may be interpreted as two relatively narrow electron and hole beams (by holes we mean the absence of electrons under the Fermi level) moving in the opposite directions which are formed from the primary beam after some

first collision. The propagation of these secondary beams for the time $t \gg \tau_s$ represents one-dimensional diffusion of electron-hole formations since for the time τ_s , as a result of collision an electron turns into a hole (and vice versa). We believe that a number of effects resulting from it can be found in the experiments with beams in heterostructures of the type made in [6,7]. Namely, conservation of a beam at the distances exceeding the usual electron-electron mean free-path length, appearance of a positive charge (holes) near an emitter, dependence of the secondary beams width on the excitation energy, temperature, and propagation time. The above effects are rather sensitive to a weak magnetic field, i.e. at $H \geq mc(\epsilon\tau_s)^{-1}$ and $t \geq \tau_s$ the field results in considerable smearing of secondary beams. Similar effects may be also studied in electric conductivity experiments of 2DEG wires [8] under the conditions when electric current is determined by a narrow group (a beam) of grazing electrons. Note that at $A \geq m\epsilon_0^2/\epsilon_F$ a nonlinear behavior of electron-electron relaxation takes place. Nonlinear relaxation of odd deformations of the Fermi-surface has been shown to occur considerably slower than even ones: $(\tau_s/\tau_A) \simeq (\mu_{max}/\epsilon_F)^{2+\beta}$, $\mu(\alpha)$ is the electron chemical potential as a function of the velocity direction, $\mu_{max} \gg T$.

The research described in this publication was made possible in part by Grant No. U2D200 from the Joint Fund of the Government of Ukraine and International Science Foundation.

References

- [1] R.N.Gurzhi, A.I.Kopeliovich, S.B.Rutkevich, Zh. Eksp. Teor. Fiz., **83**, (1982) 290 .
- [2] R.N.Gurzhi, A.N.Kalinenko, A.I.Kopeliovich, Phys. Rev. Lett., **74**, (1995) 3872.
- [3] R.N.Gurzhi, A.N.Kalinenko, A.I.Kopeliovich. Phys. Low-Dim. Struct., **2**, (1994) 75 .
- [4] B.Laihtman, Phys. Rev. B, **45**, (1992) 1259.
- [5] R.N.Gurzhi, A.N.Kalinenko, A.I.Kopeliovich, Fiz. Nizk. Temp., **21**, (1995) 462.
- [6] L.W.Molenkamp, M.J.P.Brugman, H.Van Houten, C.T.Foron. Semicond. Sci. Technol., **7**, (1992) B228.
- [7] J.Spector, J.S.Weiner, H.L.Stormer, K.W.Baldwin, L.N.Pfeiffer, K.W.West. Surf. Science, **263**, (1992) 240.
- [8] L.W.Molenkamp, M.J.M.de Jong, Phys.Rev. B, **49**, (1994) 5038.

Thermoelectric Transport in Superlattices

D. A. Broido

Department of Physics, Boston College,
Chestnut Hill, Massachusetts 02167, USA

T. L. Reinecke

Naval Research Laboratory,
Washington, DC 20375, USA

Abstract

The electrical conductivity, the Seebeck coefficient, and the electrical contribution to the thermal conductivity are calculated for quantum well and quantum wire superlattices. The figure of merit for these structures exhibits a maximum as a function of superlattice period that can lie above the corresponding value for the bulk material. The effects of tunneling and thermal currents through the barrier material are shown to be essential to describe the thermoelectric properties of superlattices.

Introduction

Materials with desirable thermoelectric properties are of current interest for the development of cleaner, more efficient cooling systems [1]. In this paper, we examine the thermoelectric transport properties of quantum well and quantum wire superlattices and evaluate their potential for use in thermoelectric applications.

The historical development of the thermoelectric properties of materials dates back to the 1800s with the discoveries of the Seebeck (1822) and Peltier (1834) effects. In the Seebeck effect, a temperature difference, ΔT , at the junction between two conductors, a and b , induces an electromotive potential difference, ΔV . The differential Seebeck coefficient is defined by $\alpha_{a,b} = \Delta V / \Delta T$, where $\alpha_{a,b} = \alpha_a - \alpha_b$ and $\alpha_a(\alpha_b)$ is the Seebeck coefficient associated with conductor $a(b)$. In the Peltier effect, when an electric current passes through the junction between two conductors, heating or cooling occurs depending on the direction of the current. The heat current, J_Q , released or absorbed at the junction is related to the electrical current density, J_e by $J_Q = \Pi_{a,b} J_e$, where $\Pi_{a,b} = \Pi_a - \Pi_b$ is the differential Peltier coefficient, defining the difference between the Peltier coefficients for conductors a and b . In 1855, Lord Kelvin demonstrated from the principles of thermodynamics that the Seebeck and Peltier coefficients are related as: $\Pi_{a,b} = \alpha_{a,b} T$.

A schematic of a cooling device is shown in figure 1. It consists of two thermoelements of n - and p -type material which connect through metal (shaded) links a heat source at lower temperature, T_L and a heat sink at higher temperature, T_H . The n (p)-material has negative (positive) Peltier coefficient. If an electrical current is passed through the circuit in the clockwise fashion, heat currents in both thermoelements flow from the source to the sink. This Peltier cooling is opposed by 1) thermal conduction from the sink to the source whose magnitude depends on the thermal conductivity, κ , and 2) joule heating in the thermoelements which is inversely proportional to the electrical conductivity, σ . The efficiency of a device for thermoelectric cooling applications is characterized by the "figure

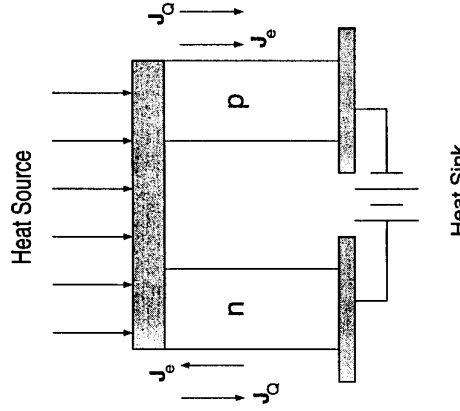


Figure 1: Schematic of thermoelectric cooling device.

of merit" for each material:

$$Z = \frac{\alpha^2 \sigma}{\kappa} \quad (1)$$

Here, the thermal conductivity consists of two parts, $\kappa = \kappa_e + \kappa_{ph}$, where κ_e and κ_{ph} correspond to the carrier and lattice contributions, respectively. The figure of merit, Z , reflects the effectiveness of a material for use in thermoelectric applications: 1) Large α (large Π), which enhances the thermal current carried from the source for given electrical current. 2) Large σ so as to minimize the Joule heating. 3) Small κ in order to minimize the thermal conduction from the sink to the source. While metals benefit from large electrical conductivities, they suffer from high thermal conductivities and low Seebeck coefficients. Insulators, on the other hand, have large Seebeck coefficients and comparably small thermal conductivities but suffer from extremely small electrical conductivities. Semiconductors achieve a balance of the above constraints and possess comparably the high figures of merit. Room temperature values of the dimensionless figure of merit, ZT , for bulk alloys of the semiconductor Bi_2Te_3 are the highest known to date, with $ZT \approx 1$.

Theory of Thermoelectric Transport

In a linear theory, the electrical and thermal current densities, J_e and J_Q , generated in response to electrochemical and thermal gradients are:

$$\mathbf{J}_e = L_{11} \frac{\nabla \eta}{e} + L_{12}(-\nabla T) \quad \mathbf{J}_q = L_{21} \frac{\nabla \eta}{e} + L_{22}(-\nabla T) \quad (2)$$

Here, $\eta = \mu - e\phi$ where μ is the chemical potential and ϕ is the scalar potential associated with the applied electric field, $\mathbf{E} = -\nabla\phi$. The L_{ij} 's can be related in a straightforward manner to the transport coefficients σ , α and κ_e : $L_{11} = \sigma$, $L_{12} = \sigma\alpha$, $L_{21} = \sigma\alpha T$ and $L_{22} = \gamma = \kappa_e - \sigma\alpha^2 T$. The transport coefficients can be obtained from a knowledge of the band structure, $\epsilon_n(\mathbf{k})$, and the carrier distribution function:

$$\left\{ \begin{array}{l} J_e \\ J_Q \end{array} \right\} = \sum_n \int \frac{d\mathbf{k}}{4\pi^3} \left\{ \begin{array}{l} -e \\ \epsilon_n(\mathbf{k}) - \mu \end{array} \right\} \mathbf{v}_n(\mathbf{k}) f_n(\mathbf{r}, \mathbf{k}) \quad (3)$$

where $\mathbf{v}_n(\mathbf{k}) = (1/\hbar)\nabla \epsilon_n(\mathbf{k})$. The distribution function, $f_n(\mathbf{r}, \mathbf{k})$, can be obtained in the relaxation-time approximation to the Boltzmann equation. For current and temperature gradients taken along the x -axis, the transport coefficients can then be expressed as:

$$\sigma = L_0 \quad \sigma\alpha = -\frac{1}{eT}L_1 \quad \gamma = \frac{1}{e^2 T}L_2 \quad (4)$$

where the L_j are given by:

$$L_j = e\mu_x \int_0^\infty d\epsilon f_0(\epsilon) \left[g_n(\epsilon)(\epsilon - \zeta)^j + j(\epsilon - \zeta)^{j-1} \int_0^\epsilon g_n(\epsilon') d\epsilon' \right] \quad (5)$$

In this expression, μ_x is the carrier mobility, f_0 is the equilibrium Fermi distribution, $g_n(\epsilon)$ is the density of states and ζ is the chemical potential of the carriers measured with respect to the bottom of the lowest band. σ , α and γ are varied by changing the chemical potential so as to maximize the ZT . Such variation could be achieved, for example, through doping.

Thermoelectric Transport in Superlattices

Although thermoelectric cooling systems have been available for some time, their poor efficiency has limited their use to specialized applications[2]. Recently, dramatic improvements in the figure of merit have been predicted for quantum well[3] and quantum wire[4] superlattice systems. These suggestions have attracted considerable attention because of the possibility that such confined systems may be desirable for thermoelectric applications. The authors of Refs. [3] and [4] approximate the superlattice systems as having zero barrier thicknesses and infinite barrier heights. The physical origin of the dramatic increase in ZT in the proposed systems then comes mainly from the enhancement in the density of electron states per unit volume that occurs for small well and wire thicknesses.

Here, we present the results of calculations of the thermoelectric figure of merit for Bi_2Te_3 quantum well and quantum wire superlattices with finite barrier heights and finite barrier widths. We employ the Bi_2Te_3 material parameters throughout the superlattice. The bulk conduction band is taken to be parabolic but anisotropic. The band structure of the superlattices is obtained from the solution of the one- and two-dimensional Kronig-Penney models, with the appropriate part of the bulk parabolic dispersion retained in the plane of the quantum well or along the quantum wire axis. Further details of these calculations will

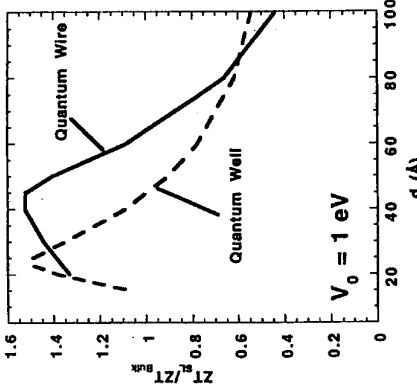


Figure 2: Figure of merit for quantum well and quantum wire superlattices.

be published elsewhere[5, 6]. The calculated figure of merit scaled by the value for bulk Bi_2Te_3 is shown in Figure 2 as a function of the superlattice period. The barrier width is taken to be equal to the well width, and the barrier height is chosen to be 1 eV.

For the larger periods, the ZTs for wells and wires lie below that of the bulk. This occurs because thermal currents flow throughout the superlattice material while electrical currents are confined mainly to the well and wire regions. For decreasing periods ZTs exhibits a maximum and then decreases. This behavior occurs because of tunnelling through the barrier which decreases the density of states and gives a decreased ZTs . At the maximum, ZTs lies above that of the bulk material. The amount of enhancement increases with the barrier height, V_0 . Above $V_0 = 1eV$, the enhancement for the wire superlattices is more substantial than for the wells. Additional enhancement might be obtained by employing a barrier material with lower thermal conductivity than that used for the wells or wires.

This work was supported in part by the U.S. Office of Naval Research (ONR).

References

- [1] H. J. Goldsmid, Thermoelectric Refrigeration, (Plenum, New York, 1964).
- [2] C. Wood, Rep. Prog. Phys. 51, 459 (1988).
- [3] L. D. Hicks and M. S. Dresselhaus, Phys. Rev. B47, 12727 (1993).
- [4] L. D. Hicks and M. S. Dresselhaus, Phys. Rev. B47, 16631 (1993).
- [5] D. A. Broido and T. L. Reinecke Phys. Rev. B (May 15 issue) (1995).
- [6] D. A. Broido and T. L. Reinecke, Appl. Phys. Lett., (July 3 issue) (1995).

Energy band diagrams of nano-size field effect transistors

Y. Fu and M. Willander

Department of Physics and Measurement Technology, Linköping University, S-581 83 Linköping, Sweden
Tel.: +46 13 282701, Fax: +46 13 197668, Email: fyg@fm.liu.se

soids: (1) the longitudinal effective mass is $m_l = 0.98$, the transverse effective mass $m_t = 0.19$, degeneracy $g = 4$; (2) $m_l = 0.19$, $m_t = 0.98$, $g = 2$. Here the effective mass is in the unit of free electron mass. Since the voltage between source and drain is very small compared with gate biases (50 mV with respect to 5 V), we only need to concentrate on stationary states. Equilibrium state can thus be assumed and the Fermi level is well defined. The electrons are described by the following Schrödinger and Poisson equations:

$$\begin{aligned} E_i F_i(\vec{r}) &= \left[-\frac{\hbar^2 \nabla^2}{2m} + E_c + V_{ex} - e\Phi(\vec{r}) \right] F_i(\vec{r}), \\ \nabla \cdot [e\nabla\Phi(\vec{r})] &= -e \left[N_D(\vec{r}) - \sum f_i |F_i(\vec{r})|^2 \right], \end{aligned} \quad (1)$$

where, F_i is the envelope function of subband E_i , m is the carrier effective mass, N_D is the spatial distribution of impurities, f_i is the occupation probability of state E_i , V_{ex} is the exchange-correlation energy approximated by the Hedin and Lundqvist formula [7].

I. INTRODUCTION

Many experiments have shown that in nano-size semiconductor device structures, the conductance along the conducting channel oscillates periodically with the gate biases at low temperature [1–4]. Common to all explanations was the single-electron transport between isolated or partially isolated segments in the structures. As summarized by Matsuo, Ichiguchi, Yoshimura, and Takeda recently [5], these segments are either the strong scatterers of randomly distributed impurities or defects [3], or artificially designed conducting quantum dots [4,5].

In this work we concentrate on the possibility of artificially designing quantum dots from theoretical point of view. In Sec. II and III we calculate self-consistently the energy-bandstructures from three-dimensional Schrödinger and Poisson equations for the dual-gate Si metal-oxide-semiconductor field effect transistor (MOSFET) recently studied by Matsuo *et al.* [5] and the GaAs/AlGaAs field effect transistor (FET) of Meirav *et al.* [6]. We will see in these two sections that, because of the relatively large structure size from quantum mechanical point of view, the realization of an artificial quantum dot is difficult. A brief summary will be made in Sec. IV together with a proposed FET structure for quantum dot system.

II. DUAL-GATE SI MOSFET

The device structure of Matsuo *et al.* is shown in Fig. 1. The conduction band of Si consists of six X ellip-

The upper gate is biased at -6 V while the lower gate at 3.5 V. The conducting channel induced by the lower gate is not transformed into quantum dots, as expected by Matsuo *et al.* The reason is very simple. Without free carriers, the upper gate can be simplified as an array of metal cylinders (Fig. 3). Analytical solution exists for the corresponding Poisson equation

$$\Phi = A \sum_{i=-3}^3 \ln \sqrt{(y - 300i)^2 + z^2} + B, \quad (2)$$

where A and B are constant determined by boundary conditions. 300 nm is the distance between two adjacent metal cylinders. Only when the surface under investigation is very close to the metal cylinders can we observe some ripples in the potential, otherwise there is only a big potential barrier (Fig. 4). The barrier in Fig. 2 is divided into two parts by the conducting channel because of the large free carrier density there (external voltage applies on the region of large resistance, i.e., small free carrier density).

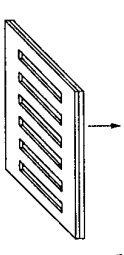


FIG. 3. Simplification of the upper gate.

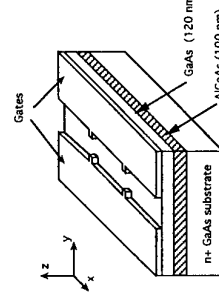


FIG. 5. The GaAs/AlGaAs FET [4].

We first look at the energy band diagram along the sample growth direction neglecting the existence of the gate on the top GaAs layer. In this case, the calculation is one-dimensional and the results are presented in Fig. 6. The FET is coordinated at $z \leq 0$ (this is the reason that there is a negative sign in the horizontal axis in Fig. 6). For $z \geq 0$, it is vacuum. At the GaAs-vacuum interface, the Fermi level is at the middle of the band gap due to the surface states. Biasing the substrate by V_g is equivalent to biasing the top layer. In Fig. 6 and later on, the reference value of V_g is the one when the conduction band edge at the GaAs-vacuum interface is zero (the conduction band edge of the substrate far away from the surface is zero). As compared with the works of Meirav *et al.*, we see that the two dimensional electron gas (2DEG) is formed at the GaAs side of the GaAs-vacuum interface, not the GaAs/AlGaAs heterointerface. This is because the top GaAs layer is undoped. When electrons flow in from the substrate by increasing V_g , the second-derivative of the conduction band edge of the top GaAs layer is negative, because of the negative charges on

ductances is most possibly due to carrier transport from source to drain through sublevels in the conducting channel.

III. GAAS/ALGAAS FET

Meirav *et al.* tried GaAs/AlGaAs FET for an artificial quantum dot (Fig. 5) [4,6,8]. They *et al.* [6] also made three-dimensional Poisson equation calculation where electrons are treated semiclassical. It was shown from their calculation that the oscillation period in conductances matches with the increment in substrate bias V_g when the number of carrier in the quantum dot is increased by one, single-electron charging effect is thus indicated.

Our calculation here is based on Eq. (1), with $m = 0.067 + 0.083x$ and $E_c = 0.7482x$ eV for the Γ electrons, where x is the Al concentration in $\text{Al}_x\text{Ga}_{1-x}\text{As}$. The three-dimensional calculation of Eq. (1) is much simpler for the GaAs/AlGaAs system because of the isotropic Γ band as compared with elliptical X bands in Si.

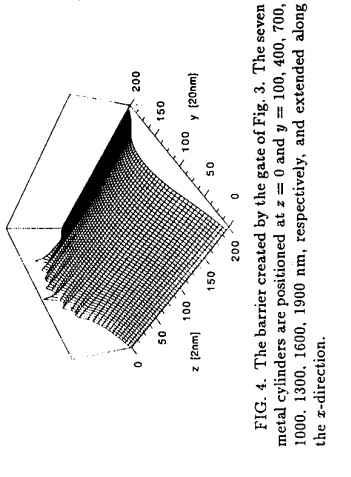


FIG. 4. The barrier created by the gate of Fig. 3. The seven metal cylinders are positioned at $z = 0$ and $y = 100, 400, 700, 1000, 1300, 1600, 1900$ nm, respectively, and extended along the x -direction.

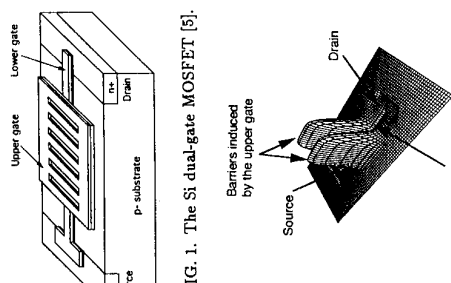


FIG. 1. The Si dual-gate MOSFET [5].

FIG. 2. Energy band structure at the Si side of the oxide-semiconductor interface. $V_g = 3.5$ V and $V_{tg} = -6$ V.

In Fig. 2 we present the numerical result of the energy band diagram at the Si side of the Si-oxide interface.

electrons. The spatial variation in the conduction band diagram of Fig. 1 in Ref. [6] is therefore unrealistic. n is the number of electrons in the quantum dot. We have difficulties to accept this explanation. First of all, the relation between $\partial n / \partial V_g$ and V_g is highly nonlinear. At the beginning of carrier accumulation in the quantum dot, $\partial n / \partial V_g = 0.07 \text{ meV}^{-1}$; when $V_g = 150 \text{ meV}$, $\partial n / \partial V_g = 1.5 \text{ meV}^{-1}$ [6] for the FET structure of Fig. 7(a), where the observed period of fine peaks in conductances is about 1 meV. Secondly, it must be remembered that the increment in n as a function of V_g is not an integer.

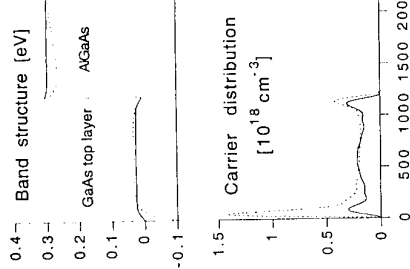


FIG. 6. Energy band structure and carrier distribution along the sample growth direction. Solid lines: $V_g = 0$; Dashed lines: $V_g = 100 \text{ meV}$.

The 2DEG formed at the GaAs side of the GaAs-vacuum interface is under direct control of the gate on the top GaAs layer, thus the problem facing the upper gate in the Si MOSFET (the upper gate is too far away from the conducting channel) is now removed. Free carriers directly under the gate are completely depleted, and the form of the conducting channel is exactly determined by the top gate. However, because of the large carrier concentration, external voltage drop on the conducting channel is small so that quantum barriers created by the four fingers in the top gate, as expected by Meirav *et al.*, are not that high and wide enough to separate carriers in the segment formed by the four fingers from the source and drain. The height and width of the barriers are further reduced by the quantum factor, i.e., the penetration of carrier waves into barrier regions.

Fig. 7 shows the energy band diagrams at the GaAs sides of the GaAs/AlGaAs heterointerface and GaAs-vacuum interface. We see here that the conducting channel is not cut off by the four fingers in the top gate and therefore wave functions of electrons are continuous from the source to the drain through the conducting channel. The reason is the same as in Si MOSFET where the barrier created by the upper gate is divided into two by the conducting channel because of the larger carrier concentration there in the conducting channel.

To explain the periods of fine peaks in conductances,

Meirav *et al.* used an averaged value of $\partial n / \partial V_g$, where

We have difficulties to accept this explanation. First of all, the relation between $\partial n / \partial V_g$ and V_g is highly nonlinear. At the beginning of carrier accumulation in the quantum dot, $\partial n / \partial V_g = 0.07 \text{ meV}^{-1}$; when $V_g = 150 \text{ meV}$, $\partial n / \partial V_g = 1.5 \text{ meV}^{-1}$ [6] for the FET structure of Fig. 7(a), where the observed period of fine peaks in conductances is about 1 meV. Secondly, it must be remembered that the increment in n as a function of V_g is not an integer.

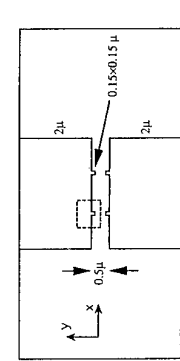


FIG. 7. Energy band structures of the area marked by dashed lines in (a) at the GaAs sides of (b) GaAs/AlGaAs heterointerface and (c) GaAs-vacuum interface. The top gate is biased at 0.4 V and $V_g = 0$.

From our calculation it is easy to estimate the energy separation between sublevels in the narrowest part of the conducting channel (due to the fingers in the top gate). It is about 1 meV. We therefore believe that the oscillation in conductances measured by Meirav *et al.* is not

the result of single-electron charging into the quantum dot formed by the four fingers in the top gate, it is the result of carrier transport through the sublevels in the conducting channel.

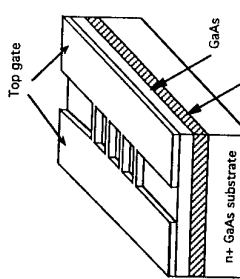
IV. SUMMARY

In a brief summary, we have shown by the three-dimensional energy band diagram calculations of Schrödinger and Poisson equations, that the upper gate in the Si MOSFET designed by Matsuoaka *et al.* does not transfer the conducting channel created by the lower gate into coupled quantum dots. It only makes the conducting channel narrower. The main reason is the characteristic of three-dimensional solution of Poisson's equation (in this case, the potential induced by the upper gate varies as $\ln r$, where r is the distance to the upper gate). The oscillations observed in the conductances are understood by the carrier transport through the quantized sublevels in the narrower conducting channel.

The advantage of the GaAs/AlGaAs FET design of Meirav *et al.* is the direct control of the conducting channel by the top gate. The segment defined by the four gate fingers in the GaAs/AlGaAs FET is not that isolated as expected by Meirav *et al.*. The reasons are as follows. First of all, the second-order derivative of the conduction band edge of the top GaAs layer is either zero when V_g is small, or negative when V_g is large enough so that carriers begin to accumulate in the top GaAs layer. Thus 2DEG forms at the GaAs side of the GaAs-vacuum interface. The carrier distribution not directly under the top gate is not much affected by the top gate due to its larger concentration. Thus, electrons are extended from the source to the drain through the conducting channel. The oscillations observed in the conductances are understood by the carrier transport through the quantized sublevels in the part of the conducting channel compressed by the fingers in the top gate.

Quantum effects, e.g., the wave penetrations into the classically forbidden region, also reduce the spatial variation of the carrier distribution and make the electron wave functions more extended.

FIG. 8. FET structure designed for quantum dot.



- [1] T. A. Fulton and G. J. Dolan, Phys. Rev. Lett. 59, 109 (1987).
- [2] C. G. Smith, J. Phys. C21, L893 (1988).
- [3] J. H. F. Scott-Thomas, S. B. Field, M. A. Kastner, D. A. Antoniadis, and H. I. Smith, Phys. Rev. Lett. 62, 583 (1989).
- [4] U. Meirav, M. A. Kastner, and S. J. Wind, Phys. Rev. Lett. 65, 771 (1990).
- [5] H. Matsuoka, T. Ichiguchi, T. Yoshimura, and E. Takeda, Appl. Phys. Lett. 64, 586 (1994).
- [6] U. Meirav, P. L. McEuen, M. A. Kastner, E. B. Foxman, A. Kumar, and S. J. Wind, Z. Phys. B-Conденсed Matter 85, 357 (1991).
- [7] L. Hedin and B. I. Lundqvist, J. Phys. C 4, 2064 (1971).
- [8] E. B. Foxman, U. Meirav, P. L. McEuen, M. A. Kastner, O. Klein, P. A. Belk, D. M. Abusch, and S. J. Wind, Phys. Rev. B50, 14139 (1994).

The Hofstadter Energy Spectrum for an Interacting 2DEG.

Vidar Gudmundsson¹ and Rolf R. Gerhardts²

¹Science Institute, University of Iceland, Dunhaga 3,

IS-107 Reykjavik, Iceland. vider@raunvis.hi.is

²Max-Planck-Institut für Festkörperforschung, Heisenbergstraße 1, D-70569 Stuttgart,

Federal Republic of Germany. gerha@klizix.mpg.de

We study the effects of the Coulomb interactions between electrons on the Hofstadter butterfly, which characterizes the subband structure of the Landau levels of a two-dimensional electron gas in a perpendicular homogeneous magnetic field and a periodic lateral superlattice potential. The interactions essentially preserve the intricate gap structure of the Hofstadter spectra, but with a lower symmetry that depends on the filling of the Landau bands. For short enough periods and strong enough modulation the miniband structure can be resolved in the thermodynamic density of states.

Measurements of the magnetotransport in superlattices weakly modulated in one or two directions have revealed novel oscillations in the conductivity, the Weiss oscillations, reflecting the commensurability of the cyclotron radius $R_c = l^2 k_F = v_F/\omega_c$ of the electrons at the Fermi energy $E_F = \hbar^2 k_F^2/(2m^*)$ and the modulation period l ; $l = (\hbar/eB)^{1/2}$ is the magnetic length, and $\omega_c = eB/(mc)$ the cyclotron frequency [1]. The Weiss oscillations are superimposed on the Shubnikov-de Haas oscillations which are well known in a homogeneous two-dimensional electron gas (2DEG) and caused by the commensurability of the Fermi wavelength λ_F and l . The single-particle energy spectrum for this problem has been investigated by several researchers culminating in Hofstadter's butterfly, a graph showing the complicated self-similar splitting of a Landau band (LB) into minibands as a function of the magnetic flux through a unit cell of the lattice (for a review see [2]). The effects of the splitting of LB's into minibands has, to the best of our knowledge, not been observed directly in the currently common superlattices ($L \sim 300$ nm $n_s = 3 \times 10^{11}$ cm $^{-2}$) since usually several LB's are occupied, which may overlap near E_F . The energy spectrum has been investigated in the intermediate region in the absence of collision broadening. The coupling of the LL's by the external periodic potential strongly reduces the original high symmetry of the Hofstadter spectrum but retains a very complicated subband structure [3, 4]. All the above-mentioned theoretical investigations of the energy spectrum of a 2DEG in a periodic potential and a homogeneous perpendicular magnetic field have neglected the effects of the electron-electron interaction. Here we study, within the Hartree approximation (HA), these effects on the electronic energy spectrum and the thermodynamic density of states.

To describe the electrons in the conduction band in the presence of a lateral superlattice

at the AlGaAs-GaAs interface in a constant perpendicular magnetic field $\vec{B} = B\hat{z}$ we employ a model of a 2DEG, with the three-dimensional charge density given by $-\epsilon n_s(\vec{r})\delta(z)$, and

$\vec{r} = (x, y)$. The square superlattice is spanned by orthogonal lattice vectors of length L ,

the primitive translations of the Bravais lattice \mathcal{B} . The corresponding reciprocal lattice \mathcal{R}

is spanned by $\vec{G} = G_1\vec{g}_1 + G_2\vec{g}_2$, with $G_1, G_2 \in \mathbb{Z}$, $\vec{g}_1 = 2\pi\hat{x}/L$, and $\vec{g}_2 = 2\pi\hat{y}/L$. The

external periodic potential the electrons are moving in is taken to be of the simple form

$V(\vec{r}) = V_0\{\cos(g_1x) + \cos(g_2y)\}$. The electron-electron interaction is included in the HA

leading to an effective single-electron Hamiltonian $H = H_0 + V_H(\vec{r}) + V(\vec{r})$, where $V_H(\vec{r})$ is the effective potential in a medium with a dielectric constant κ , felt by each electron and caused by the total charge density of the 2DEG, $-\epsilon n_s(\vec{r})$, and the neutralizing background charge density $+\epsilon n_s = +e\langle n_s(\vec{r}) \rangle$. The periodic external potential $V(\vec{r})$ and the constant external magnetic field imply that all physical quantities of the noninteracting system are periodic with respect to translations of $\vec{R} \in \mathcal{B}$. The periodicity of the Hartree potential follows from that of $n_s(\vec{r})$. In the following calculations we use the symmetric basis functions constructed by Ferrari [5] and used by Silberbauer [6]. The set of Hartree equations has to be solved iteratively together with the condition that the average electron density $n_s = N_s/A$ is constant, which determines the chemical potential μ . N_s is the number of electrons per unit cell with area A in \mathcal{B} .

The Coulomb interaction not only couples directly the subbands of a particular LL, but also the subbands of different LL's. If only the basis states in the same LL are taken into account, the modulation strength is irrelevant since it can be factored out of the Hamiltonian matrix. In this situation, corresponding to the usual discussion of Hofstadter's butterfly on the basis of Harper's equation, a highly symmetric energy spectrum is expected. Of course, this restricted model is only appropriate for describing a system with very weak modulation (as compared with the inter-Landau-level energy spacing $\hbar\omega_c$). The bandwidth of the subbands of the first LB is shown in Fig. 1, for the two cases, $pq = 3, 6$, identifiable from the number of subbands appearing in each figure. The period is short, $L = 50$ nm, the modulation strong, $V_0 = 4.0$ meV, and $T = 1.0$ K. However only one LL is used in the calculation, so that the results apply to the case of a weak superlattice potential. The electron-hole symmetry is exact, as is reflected in each case by the point symmetry of the subband structure around μ at half filling. The screening is strongly dependent on N_s and the average filling factor. It is, therefore, strongest for $pq = 6$ when maximum six electrons can occupy the lowest Landau level in the unit cell and when the LB is half filled, $N_s = 3$. The (dimensionlessly written) thermodynamic density of states $D_T = l^2\hbar\omega_c(\partial n_s/\partial\mu)_{TB}$, with $n_s = \langle n_s(\vec{r}) \rangle$, is shown in Fig. 2. Clearly the strong screening in the $pq = 6$ case obscures the fine structure in D_T leading to only one pronounced peak. The subbands in the other cases turn up as separate peaks in D_T . The Hofstadter butterfly should be recovered when the calculation is performed for $N_s = 0$ and only one LL, and if the width and location of the subbands are plotted as functions of the inverse of the number of magnetic flux quanta through a unit cell of the lattice, i.e. of $\Phi_0/\Phi = 1/(pq)$. In addition, all energies have to be scaled according to: $E \rightarrow (E - \hbar\omega_c/2)/V_0$. For interacting electrons N_s , or the average filling factor of the LB turns out to be a new parameter controlling the bandstructure. We therefore, present in Fig. 2 the subband structure for four values of the inverse flux $1/(pq)$ in the case of $N_s = 1.50$ together with the location of μ . For low density, the subband structure is almost symmetric around the energy zero, like in the noninteracting case, but the subbands become quite asymmetric for a higher density of electrons. For the short-period superlattice studied here, and for a low density of electrons, the essential gap structure does survive in the presence of interaction. The presentation in Fig. 2 corresponds to the experimental procedure of keeping the density of electrons fixed but changing the magnetic field. Another way to investigate the screening is to keep the average filling factor ν constant but vary the magnetic field and, thus, also the average density of the 2DEG. Fig. 3 compares the subband structures for $1/(pq) = 1/2, 1/3, 1/4, 1/6$ and $\nu = 1/2$ with the complete Hofstadter butterfly. Here the

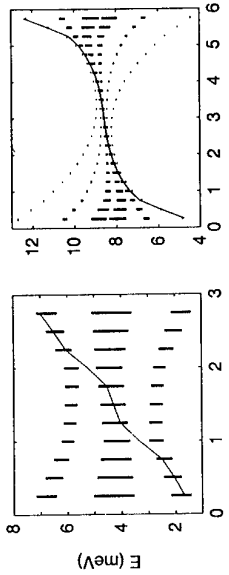


Figure 1: The bandwidth of the minibands of the lowest Landau band as a function of N_s for a Hartree interacting 2DEG and ($p = 1, q = 3$) (left), ($p = 2, q = 3$) (right). The chemical potential μ is indicated by a continuous curve. $L = 50 \text{ nm}$, $T = 1.0 \text{ K}$, $V_0 = 4.0 \text{ meV}$. One Landau level is included in the HA. $m^* = 0.067m_0$, $\kappa = 12.4$.

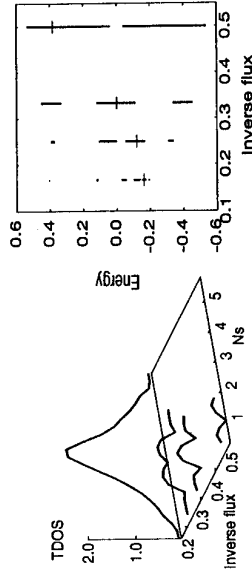


Figure 2: The thermodynamic density of states (left) $D_T = \frac{1}{2}\hbar\omega_c(\partial n_s / \partial \mu)_T$ as a function of $1/pq$ and N_s . The scaled bandwidth (right) of the subbands of the lowest Landau band, $(E - \hbar\omega_c/2)/V_0$, as function of $1/pq$ for $N_s = 1.5$. The chemical potential μ is indicated by crosses. $L = 50 \text{ nm}$, $T = 1.0 \text{ K}$, $V_0 = 4.0 \text{ meV}$. One Landau level is included in the HA.

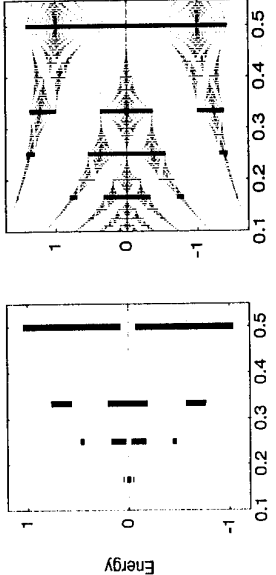


Figure 3: The scaled bandwidth $(E - \hbar\omega_c/2)\exp(\pi/L)^2/V_0$ of the subbands of the lowest Landau band as function of $1/pq$ for the Hartree interacting 2DEG with $\nu = 1/2$ (left), and for the noninteracting 2DEG (right), the Hofstadter butterfly. One Landau level is included in the calculations. In the left subfigure the 6 minibands for the case $pq = 6$ can not all be resolved due to vanishing band gaps. The parameters used for the left subfigure are: $L = 50 \text{ nm}$, $T = 1.0 \text{ K}$, $V_0 = 4.0 \text{ meV}$.

energies have been scaled with the factor $(E - \hbar\omega_c/2)\exp\{(\pi l/L)^2\}/V_0$ so that the results can be directly compared with earlier calculations of the Hofstadter spectrum [2]. The energy spectrum in the interacting case shows an overall reduction in dispersion or bandwidth due to the strong screening that is most effective for large flux and large number of available states. The bandwidths of the subbands for the interacting case has been evaluated here on a discrete lattice in the magnetic Brillouin zone without attempting an interpolation between the lattice points; thus, the actual bandwidths can be larger by a small percentage of the widths shown.

In an interacting 2DEG subject to a superlattice potential and a homogeneous perpendicular magnetic field not only the magnetic flux through a unit cell but also the density of electrons determines the complicated splitting of the LL's into subbands. We have shown that in the HA the essential gap structure of the energy spectrum remains, although the screening leads to a quenching of the Hofstadter butterfly at small values of the inverse flux. The symmetry of the butterfly is also lowered by the coupling to higher LL's due to increased strength of the periodic potential, as has already been discussed by other authors [3, 4]. For periods around $L = 200 \text{ nm}$ (currently attainable in experiments on superlattices) the 2DEG can effectively screen the periodic potential even for a very low density n_s when only one or two Landau bands are partly occupied. Only at shorter lattice constants ($L < 100 \text{ nm}$) and thus much higher magnetic fields we can, on the basis of our Hartree calculation, expect the subband structure to be resolvable in experiments, when n_s is maintained low enough. These predictions are made on the basis of the calculated energy spectrum and the structure observed in the thermodynamic density of states D_T . The transport coefficients do not depend on D_T in any simple way, and may be more sensitive to the subband structure of the energy spectrum [2]. In order to keep the computational efforts in reasonable limits, we have restricted our calculations to a few characteristic values of the magnetic field. Our results indicate in which manner screening effects will change the overall appearance of the Hofstadter energy spectrum. Unfortunately, there is no simple way to extrapolate from these special values to arbitrary rational numbers of flux quanta per unit cell. From the experimental point of view these details of the energy spectrum seem not to be accessible anyway. The challenge for the near future is to resolve the most prominent gaps of the energy spectrum experimentally.

This research was supported in part by the Icelandic Natural Science Foundation, the University of Iceland Research Fund, and a NATO collaborative research Grant No. CRG 921204.

References

- [1] D. Weiss, K. v. Klitzing, K. Ploog, and G. Weimann, *Europhys. Lett.* **8**, 179 (1989), and R. R. Gerhardts, D. Weiss, and K. v. Klitzing, *Phys. Rev. Lett.* **62**, 1173 (1989).
- [2] D. Pfannkuche and R. Gerhardts, *Phys. Rev. B* **46**, 12606 (1992).
- [3] O. Kühn, P. E. Selbmann, V. Fossatidis, and H. L. Cui, *J. Phys. C* **5**, 8225 (1993).
- [4] G. Petrichel and T. Geisel, *Phys. Rev. Lett.* **71**, 239 (1993).
- [5] R. Ferrari, *Phys. Rev. B* **42**, 4598 (1990).
- [6] H. Silberbauer, *J. Phys. C* **4**, 7355 (1992).

Fermi contour of 2D electron layer at $\text{GaAs}/\text{Al}_x\text{Ga}_{1-x}\text{As}$ heterojunction subject to in-plane magnetic fields

L. Smrká, P. Vášek, J. Koláček, T. Jungwirth, M. Cukr
Institute of Physics, Academy of Sciences of Czech Republic,
Cukrovarnická 10, 162 00 Prague 6, Czech Republic

Abstract

The magnetic-field-induced distortion of the Fermi contour of the 2D electron gas is investigated. The resulting increase of the cyclotron effective mass (the density of states) is measured by the cyclotron resonance, the temperature damping of Shubnikov-de Haas oscillations and the longitudinal magnetoresistance. The experimental data are compared with results of self-consistent calculations.

Introduction

In 1986, Zawadzki et al [1] have shown that the Fermi contour of a 2D electron gas confined inside a triangular well $V(z)$ is distorted by the in-plane magnetic field B_x and has, instead of the standard circular shape, an 'egg-like' form. Later, the more realistic Fermi lines shapes of a 2D gas at $\text{GaAs}/\text{Al}_x\text{Ga}_{1-x}\text{As}$ heterojunctions subjected to in-plane magnetic fields have been obtained, based on semi-empirical self-consistent calculations of the electron energy spectra [2,3]. The changes of the electron structure of a 2D gas due to the in-plane magnetic field can be investigated experimentally by adding a perpendicular component B_x to B_y . If the perpendicular field component is weak, the rather complicated dynamic of an electron in a tilted field [4] can be reduced to a simple quasiclassical picture [5], in which electrons move, in a real space, along trajectories with shapes similar to the shape of the Fermi contour, but multiplied by the scale factor $\hbar/e|B_z|$ and rotated by $\pi/2$. This quasiclassical electron motion can be subsequently quantized using the standard Bohr-Sommerfeld quantization rule which states that each real space trajectory encloses an integer number of flux quanta $\hbar/e|e|$. Such procedure yields a discrete spectrum of Landau levels separated by energy $\hbar\omega_c$.

The cyclotron effective mass, $m_e = |e|B_\perp/\omega_c$, is related to the shape of the Fermi contour by

$$m_e = \frac{\hbar}{2\pi} \oint \frac{dk}{|\mathbf{v}_k|}, \quad (1)$$

where dk denotes an element of a length of the Fermi line and $\mathbf{v}_k = 1/\hbar \nabla_k E$ is the velocity of an electron. Moreover, the density of states g and the cyclotron mass m_e of a single subband are related by a simple expression

$$g = \frac{m_e}{\pi\hbar^2}. \quad (2)$$

The validity of this relation is restricted to a 2D electron gas, the equation (2) has no analogy in three-dimensional electron systems.

Experimental results

The samples employed in experiments were $\text{GaAs}/\text{Al}_x\text{Ga}_{1-x}\text{As}$ modulation doped heterojunctions prepared by molecular beam epitaxy (MBE) on the top of (100) semi-insulating substrate. We have grown first AlAs/GaAs superlattice, followed by a $2\mu\text{m}$ undoped GaAs buffer layer, an undoped 10 nm $\text{GaAs}/\text{Al}_{0.32}\text{Ga}_{0.68}\text{As}$ spacer layer, a 100 nm n -doped $\text{GaAs}/\text{Al}_{0.32}\text{Ga}_{0.68}\text{As}$ layer ($1.7 \times 10^{18} \text{ cm}^{-3} \text{ Si}$), and finally a 20 nm GaAs cap layer. A part of the wafer was used to prepare a rectangular sample $8 \times 8 \text{ mm}$ for the cyclotron resonance experiments, the sample for the magnetoresistance measurements was shaped into Hall-bar geometry using a standard lithographic technique. Its length and width were $1100\mu\text{m}$ and $100\mu\text{m}$, respectively. The concentration of 2D electron gas at a heterojunction, $N_e = 5.2 \times 10^{11} \text{ cm}^{-2}$, and the mobility $\mu = 4.1 \times 10^5 \text{ cm}^2/\text{Vs}$, were determined from the Shubnikov-de Haas oscillations (SdH) of the magnetoresistance and the resistivity, respectively, measured at a temperature of 4.2 K.

Firstly, the dependence of m_e on the in-plane magnetic field was studied by means of the cyclotron resonance measurement, using a laser based far-infrared spectrometer. The sample was placed in the 9 T superconducting solenoid and cooled down to 2 K, with a laser beam oriented in parallel with the coil axis and the magnetic field direction. A coated silicon bolometer served to record the radiation transmitted through the sample.

To determine $m_e = m_e(B_{||})$, the sample was mounted at a tilt. Six wavelengths of the laser radiation and three different angles between a normal to the sample plane and the field direction, 0° , $43^\circ 47'$ and an angle close to 78° , were employed. The cyclotron mass was calculated from the position of a transmission minimum on the magnetic field scale according to an equation

$$m_e = \frac{|e|B_\perp\lambda}{2\pi c}, \quad (3)$$

where B_\perp denotes the perpendicular component of a magnetic field for which the resonance occurs, λ is the laser line wavelength and c the light velocity. The accuracy of results is given by an error in determination of B and the angle of the tilt. To minimize the systematic error in B , the ratio $m_e(B_{||})/m_e(0)$ is presented in Fig. 1. Due to the uncertainty in the angle determination, the data taken at 78° (denoted by empty squares) should be considered as less reliable.

The damping of SdH oscillations was investigated in the superconducting magnet reaching the maximum field 7 T, with the sample immersed in the pumped ^4He bath. Its temperature varied in the range 2.7 K - 4.2 K and was determined from the pressure of the gas. The perpendicular configuration and a configuration with the tilt angle $80^\circ 30'$ were employed.

The Hall voltage detected on the sample itself was used as a measure of the perpendicular field component.

The interpretation of experimental data is not so straightforward as in the case of cyclotron resonance. For the perpendicular magnetic field configuration, the oscillating part of the magnetoresistance is known to be proportional to the oscillating part of the 2D density of states, broadened by the zero field relaxation time τ . We assume that this type of behaviour is preserved also in the case of tilted magnetic fields, only the quantities corresponding to $B_{||} = 0$ should be replaced by that in $B_{||} \neq 0$. Then we obtain an expression

$$\frac{\Delta \varrho}{\varrho_0} \propto \frac{\Delta g}{g} = 2 \sum_{s=1}^{\infty} \frac{X}{\sinh X} \exp(-\frac{\pi s}{\omega_c \tau}) \cos(\frac{2\pi^2 N_e s}{|e|B_{\perp}} - \pi s), \quad (4)$$

where the temperature damping factor X is given by

$$X = \frac{2\pi^2 k_B T}{\hbar |e|} \frac{m_e}{B_{\perp}}. \quad (5)$$

We started our study with the sample subjected to a perpendicular field. In that case the full Dingle plot can be used to find the effective mass m_e and the Dingle temperature $T_D = \hbar/2\pi k_B T$ with a high accuracy. The value $m_e = 0.0658$ is in good agreement with $m_e = 0.0645$ obtained from the cyclotron resonance measurement and the widely accepted value $m_e = 0.067$. The Dingle temperature was equal to 1.31 K.

Discussion

The theoretical curves are also shown in Figs. 1,2, together with the experimental data. To calculate the in-plane field dependence of m_e , we have used a standard semi-empirical model. The coupled Poisson and Schrödinger equations were solved self-consistently for $B_{\parallel} \neq 0$, the Schrödinger equation was treated in the envelope function approximation and we used the local density-functional approximation of the exchange-correlation part of the self-consistent potential. The input parameters for calculations were taken from our knowledge of samples described above.

We have found in the course of calculations that the results are relatively insensitive to the exact values of most of these parameters, except of the concentration of residual acceptors in GaAs. Unfortunately, this quantity is difficult to measure and there is almost no information concerning the homogeneity of their distribution in the direction perpendicular to the interface. Therefore, we have chosen two different ‘realistic’ values corresponding to the standard level of impurities in our MBE samples, $N_a = 1.3 \times 10^{14} \text{ cm}^{-3}$ and $N_a = 2.3 \times 10^{14} \text{ cm}^{-3}$, and accepted the usual approximation of the constant ionized impurities concentration in the depletion layer, the width of which is determined from the condition of charge neutrality and the thermodynamic equilibrium.

Having in mind the above note about a semi-empirical nature of the self-consistent calculations, we can conclude that there is a good agreement between the theoretically predicted field dependence of the cyclotron effective mass (density of states) and the experimental data.

This work has been supported by the Academy of Science of the Czech Republic under Contract No. 110 423, the Grant Agency of the Czech Republic under Contract No. 202/94/1278, and by NSF, U. S., through the Grant NSF INT-9106888.

References

- [1] W. Zawadzki, S. Klahn and U. Merkt, Phys. Rev. B **33**, 6916 (1986).
- [2] J. M. Heisz and E. Zaremba, Semicond. Sci. Technol. **8**, 575 (1993).
- [3] T. Jungwirth and L. Smrčka, J. Phys. C.: Condens. Matter **5**, L217 (1993).
- [4] G. Bastard, *Wave mechanics applied to semiconductor heterostructures*, les éditions de physique Paris (1990) p. 317
- [5] L. Smrčka and T. Jungwirth, J. Phys.: Condens. Matter **6**, 55 (1994).
- [6] N. E. Harf, J. A. Simmons, S. K. Lyo, J. F. Klem, S. M. Goodnick, *22nd International Conference on Physics of Semiconductors*, Vancouver, ed. D. J. Lockwood, World Scientific Publishing Co., Singapore 1995, p. 831.

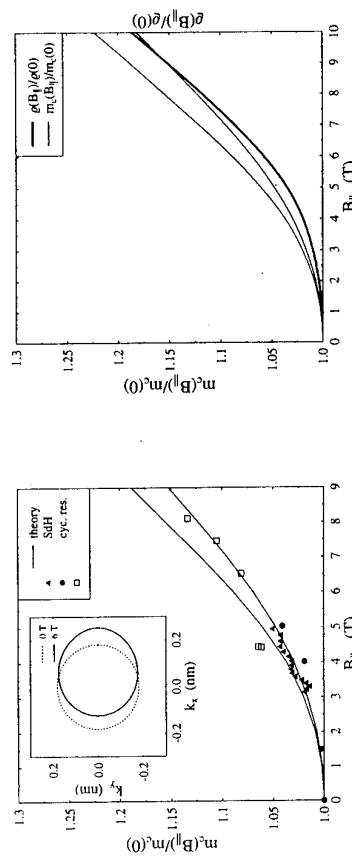


Fig. 1: Relative changes of the cyclotron effective mass m_e obtained from the cyclotron resonance measurement and the damping of SdH oscillation. The upper theoretical curve corresponds to the concentration of acceptors $N_a = 1.3 \times 10^{14} \text{ cm}^{-3}$, the second line for $N_a = 2.3 \times 10^{14} \text{ cm}^{-3}$. The inset demonstrates the variation of the Fermi line corresponding to the lower N_a .

In a tilted magnetic field with a fixed angle between the sample plane and the field direction, each peak corresponds to a different B_{\parallel} and, therefore, $m_e(B_{\parallel})$ was determined from the temperature damping of individual peaks with a limited accuracy. The analogous approach was used in [6], where the SdH oscillations in a double-well structure were investigated.

The last measurement of the magnetoresistance of a sample subjected to in-plane magnetic field with $j \parallel B_{\parallel}$, represents an attempt to relate the field dependence of $\varrho(B_{\parallel})$ to the

Coulomb interaction effects on the magnetoconductivity of laterally modulated two-dimensional electron systems

A. Manolescu*, R. R. Gerhardts, M. Tornow, D. Weiss, K. v. Klitzing and G. Weimann **
 Max-Planck-Institut für Festkörperforschung, Heisenbergstraße 1, D-70569 Stuttgart,
 Federal Republic of Germany, *Institutul de Fizica și Tehnologia Materialelor, C.P. MG-7
 București-Măgurele, Romania, **Walter-Schottky-Institut der Technischen Universität
 München, 85748 Garching, Federal Republic of Germany

Abstract

For a 2D electron system in a 1D periodic potential modulation, a complicated structure of Shubnikov-de Haas (SdH) oscillations of the diagonal resistivities ρ_{xx} and ρ_{yy} become periodically modulated in amplitude (so called Weiss oscillations) with a relative phase shift of π . In this paper we study the situation at higher magnetic fields, where the interplay between modulation broadening of the Landau levels, resulting in van Hove singularities (VHS), and exchange enhanced spin-splitting leads to an intricate internal structure of the SdH peaks.

Previous measurements [3], carried out on holographically modulated GaAs-AlGaAs heterojunctions already displayed an unusual splitting of the SdH maxima ascribed to the van Hove singularities of the 1D Landau band structure. In Fig.1 we show new experimental results obtained from a lateral superlattice with period $a=500$ nm which was fabricated on a GaAs-AlGaAs heterojunction by using electron beam lithography and selective wet chemical etching (for details see [4]). In Fig.1, the SdH peaks at high magnetic fields show a rich internal structure. Besides the spin-splitting (at filling factor $\nu = 3$) additional fine structure is resolved in the second Landau band. The low field spin-down SdH peak shows a splitting into two single peaks, while the high field spin-up maximum is threefold split. This internal structure can be understood as a consequence of the 1D Landau band structure involving enhanced spin splitting, pointed out below. From the amplitude of the commensurability (Weiss) oscillations at low magnetic field, displayed in the upper inset of Fig.1, we estimate the modulation amplitude $V_0 \approx 0.7$ meV.

While the results for low magnetic fields could be explained without including the electron-electron interaction, the latter is important at high B . The bare g-factor of GaAs is very small, $g \approx 0.4$, and only the exchange enhancement of the energy gaps, which occurs in homogeneous [5], as well as in modulated systems [6], allows to resolve the Zeeman splitting displayed in Fig.1. For a closer understanding of the observed structure we calculate the single-particle states in the Hartree-Fock approximation (HFA), the simplest

approximation which is able to include exchange effects, and the conductivity tensor from the Kubo formula.

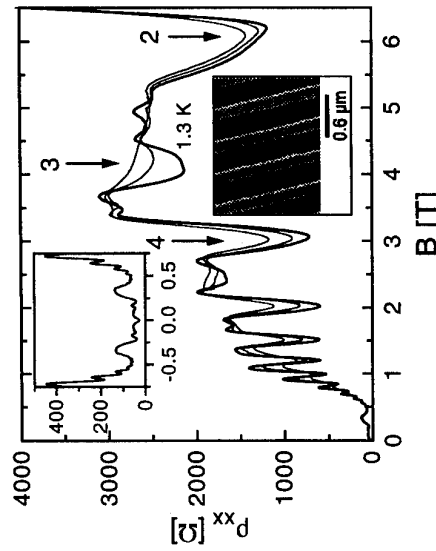


Fig.1: ρ_{xx} measured perpendicular to the 1D modulation for three temperatures $T=4.2$ K, 2.5 K, and 1.3 K. Due to slight parallel conduction in the doping layer after illuminating the sample the SdH minima at higher B do not reach zero. Note the rich internal structure of the SdH peak corresponding to the Landau band $n = 1$ (between filling factor 4 and 2). Upper inset: Weiss oscillations at low B , used to estimate the modulation strength. Lower inset: Electron micrograph of the 1D-superlattice fabricated by removing selectively the GaAs cap layer from the heterojunction.

The HFA has a tendency towards charge-density-wave instabilities, which may lead to artificial oscillations in the Landau energy bands and the particle density, for homogeneous and even for long-period modulated systems [6,7]. To avoid such artifacts, we consider a system with a shorter modulation period than in the experiment, $a \equiv 2\pi/K = 100$ nm. For the bare modulation potential we take $V \cos(Kx)$ with $V = 12$ meV, and we solve numerically the thermodynamic Hartree-Fock (HF) equations in the basis of the first 5-7 Landau levels. The material parameters are as for GaAs and the carrier density is fixed, such that the filling factor is $\nu = 13/B(T)$. In Fig.2 we show two energy spectra, $E_{n\sigma\omega}$, with n , x_0 , σ the orbital, center coordinate and spin quantum numbers. The band widths oscillate with the Landau level index n , as in the noninteracting case, but here they are reduced by a factor of two due to screening. On the other hand, the exchange contribution to each single-particle state, which is roughly proportional to its occupation number and negative, broadens the partially occupied Landau bands [6], Fig.2a. The exchange broadening reduces the density of states at the Fermi level, $D(E_F)$, even when

the latter is very close to the band edges, like in Fig.2b. This will make the expected VHS very sharp.

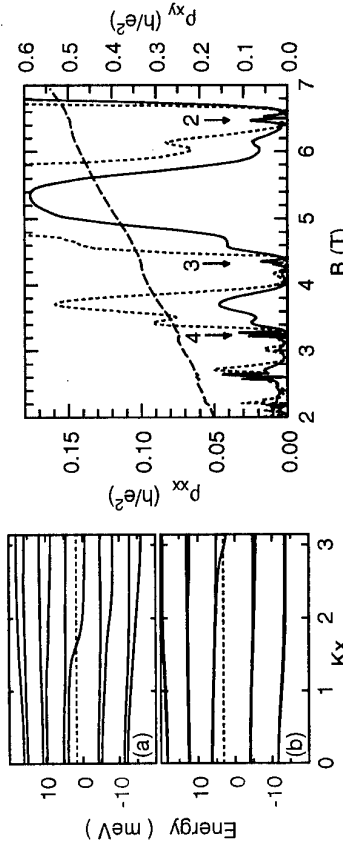


Fig.2: Energy bandstructures for (a) $B=2.9\text{ T}$ and (b) $B=3.2\text{ T}$. The dotted line is the chemical potential, $T=4\text{ K}$.

Fig.3: Calculated resistivities at $T=4\text{ K}$. ρ_{xx} : full line, with a disorder parameter $\gamma=0.4$, and dotted line, with $\gamma=0.2$. ρ_{xy} : dashed curve, both γ : filling factors are indicated by arrows.

We calculate the conductivities along the line of Ref. [2], where we replace the noninteracting single-particle states with the solutions of the HF equations. The impurity scattering is described in the same phenomenological self-consistent Born approximation, with a constant self-energy $\Sigma_b^{\text{imp}}(E)$ in the Green function $G_{n\alpha\sigma}(E) = (E - E_{n\alpha\sigma} - \Sigma_b^{\text{imp}}(E))^{-1}$. The characteristic energy parameter, $\Gamma = \sqrt{B/T}$ meV, will be assumed sufficiently small, such that the collision broadening does not considerably reduce the exchange enhancement of the energy gaps. Therefore, we can use in the Kubo formula the HF states calculated in the absence of impurities.

The Kubo formula for the diagonal conductivities can be written as:

$$\sigma_{\alpha\alpha} = \frac{\hbar e^2}{2l_B^2\pi^2} \int dE \left(-\frac{d\mathcal{F}}{dE} \right) \int_0^\infty \frac{dx_0}{a} \sum_{nn'\sigma} |\langle n x_0 \sigma | v_\alpha | n' x_0 \sigma \rangle|^2 \text{Im } G_{n x_0 \sigma} \text{Im } G_{n' x_0 \sigma}, \quad (1)$$

where $\alpha = x, y$, and l_B is the magnetic length, \mathcal{F} is the Fermi function, and $|nx_0\sigma\rangle$ are the HF states. The Coulomb interaction is also present in the velocity operators, $v_\alpha \equiv i[H, \alpha]/\hbar$. The nonlocal Fock term of the HF Hamiltonian does not commute with the position operators, yielding an exchange contribution to the velocity matrix elements, which is essential in reproducing (with the Kubo formula analogous to Eq.1, see Ref. [2]) the classical values of the Hall conductivity at integer filling factors.

Due to the anisotropy of the modulation, $D(E_F) = \sum_\sigma \text{Im } \Sigma_\sigma^{\text{imp}}(E_F)/(2\pi^2 l_B^2 \Gamma^2)$ is differently reflected in the longitudinal, σ_{xx} , and transversal, σ_{yy} , conductivities. σ_{xx} is given only by the off-diagonal terms in Eq.1, with $n' \neq n$, describing interband scattering processes, and is called a scattering conductivity [2]. For σ_{yy} also intraband processes, with $n = n'$, contribute (band conductivity). Hence $\sigma_{xx} \equiv \sigma_{x\text{scatt}} + \sigma_{yy}^{\text{band}}$ and $\sigma_{yy} \equiv \sigma_{y\text{scatt}} + \sigma_{yy}^{\text{band}}$. One can show the approximate proportionality relations [2] $\sigma_{xx}^{\text{scatt}} \sim (\Gamma D(E_F))^2$, while $\sigma_{yy}^{\text{band}} \sim (\Gamma D(E_F))^{-2}$, i.e. the scattering conductivities vanish for small disorder, but are sensitive to the VHS, while the band conductivity diverges for $\Gamma \rightarrow 0$, but vanishes for high $D(E_F)$. Fig.3 shows the calculated resistivity $\rho_{xx} = \sigma_{yy}/(\sigma_{xx}\sigma_{yy} + \sigma_{xy}^2) \approx \sigma_{yy}/\sigma_{xy}^2$ (since $\sigma_{xx}\sigma_{yy} \ll \sigma_{xy}^2$).

The sharp peaks in the vicinity of integer filling factors correspond to the VHS in $\sigma_{yy}^{\text{scatt}}$. The exchange broadening makes these peaks much sharper than in the absence of the Coulomb interaction, especially at lower temperatures. A similar structure is obtained for σ_{xx} . The broad peak structure is stable with the temperature and corresponds to $\sigma_{yy}^{\text{band}}$. The band conductivity is small for the "flat" bands with $n = 2$, and increases globally for the wider bands, with a lower density of states, in antiphase with the scattering conductivities, like in the Weiss oscillations. Close to the band edges the local reduction of D/E_F by exchange broadening determines the lateral shoulders in $\sigma_{yy}^{\text{band}}$. Experimentally, the contribution of scattering and band conductivities could be separated by a measurement of both ρ_{xx} and ρ_{yy} , which is now in progress.

In conclusion, comparing Figs.1 and 3, the observed spin splitting is reproduced in

the HFA. Apart from tiny structures near integer filling factors, which may vanish for a more realistic treatment of disorder, the calculated broad peak structure is similar to the experimental one, with a double structure between $\nu = 4$ and $\nu = 3$, and a triple structure between $\nu = 3$ and $\nu = 2$. For a more quantitative agreement with the experiment more realistic model parameters should be chosen. This especially includes screening effects, which are more important for a larger modulation period. But, due to the mentioned shortcomings of the HFA, this requires a more sophisticated many-body approach.

References

- [1] D. Weiss, K. v. Klitzing, K. Ploog, and G. Weimann, Europhys. Lett. **8** (1989) 179; R.R. Gerhardts, D. Weiss and K. v. Klitzing, Phys. Rev. Lett. **62** (1989) 1173.
- [2] C. Zhang and R. R. Gerhardts, Phys. Rev. B **41** (1990) 12850.
- [3] D. Weiss, K. v. Klitzing, K. Ploog, and G. Weimann, Surf. Sci. **229** (1990) 88.
- [4] M. Tornow et al. (unpublished); G. Müller, D. Weiss, K. v. Klitzing, P. Streda, and G. Weimann, Phys. Rev. B **51** (1995) 10236.
- [5] T. Ando and Y. Uemura, J. Phys. Soc. Jpn. **37** (1974) 1044.
- [6] A. Manolescu and R. R. Gerhardts, Phys. Rev. B **51** (1995) 1703.
- [7] A. Manolescu, Phys. Rev. B **52** (15 July, 1995).

Edge of the Two-Dimensional Electron Gas in a Gated Heterostructure

Ivan A. Larkin¹ and John H. Davies
*Department of Electronics and Electrical Engineering,
Glasgow University, Glasgow, G12 8QQ, U.K.*

Abstract

We describe a quantitative electrostatic theory of the two-dimensional electron gas (2DEG) confined by a semi-infinite gate. It includes the finite depth of the 2DEG below the surface of heterostructure, which enables us to treat the whole range of gate voltages. Two models are used for the boundary condition on the free surface, with either pinned potential or frozen charge. Our results predict the position and width of the strips of incompressible liquid in the quantum Hall regime, and are in good agreement with recent experiments.

Introduction

Many of the developments in electronic transport through ultra-small semiconductor devices have been seen by restricting a two-dimensional electron gas (2DEG) to a controlled channel. Even the quantum Hall effect, is believed to be dominated by edge states and therefore by the confinement of the 2DEG. Here we study the simplest geometry, a semi-infinite gate on the surface of a heterostructure. Variation of the bias on the gate controls the distance between the edge of the gate and that of the 2DEG. The density of the 2DEG then recovers from zero at the edge to its full value far away. This region divides into strips of compressible and incompressible liquid in a large magnetic field [1,2] and a quantitative theory was given by Chklovskii, Shklovskii, and Glazman [3] (CSG). The position and width of the strips of incompressible liquid can be calculated from the density of the 2DEG in zero magnetic field [3–6].

Previous analytical solutions [7–9] have set the depth of the 2DEG $d = 0$. This works well at large gate voltage but loses sense as the edge of 2DEG approaches the gate and moves underneath. Here we find a self-consistent solution of a gated 2DEG with a finite depth below the surface of the heterostructure, which holds over the whole range of gate voltages. We use an electrostatic approximation [3–9] in which the kinetic energy of the 2DEG is neglected. This relies on the relation $\epsilon_F/(-eV_g) \ll 1$ where $V_g \approx -en/d/\epsilon_{\infty}$ is the threshold voltage and n_0 is the unperturbed density of the 2DEG.

We consider two models [10] for boundary conditions on the surface. It is commonly assumed that the high density of surface states on GaAs pins the Fermi energy in the middle of the gap. We shall idealize this as an electrostatic potential fixed at zero to give a 'pinned' surface. The alternative 'frozen' model assumes that the charge on the surface is fixed and cannot move in response to a gate voltage. We expect this to be a more realistic model for devices operated at low temperature.

II. Solution of the electrostatic problem

Our idealized model of a heterostructure shown in Fig. 1. The system is translationally invariant along y so we need treat only the x - z plane, with $z > 0$ inside the semiconductor. The semi-infinite gate occupies $x < 0$ on the surface $z = 0$, and the 2DEG lies in the plane $z = d$ with electrons occupying the region $x > a$.

We first consider the free surface of the heterostructure to have its potential pinned at zero. The electrostatic potential Φ satisfies Poisson's equation with two charge densities, from the donors and 2DEG. The boundary conditions are $\Phi = 0$ on the exposed surface and $\Phi = V_g$ on the gate, with $\partial\Phi/\partial z = 0$ as $z \rightarrow \infty$. The potential of the donors can be subtracted out to leave φ which satisfies Poisson's equation with the charge density from the 2DEG alone. Within the electrostatic approximation we can replace this with Laplace's equation, and the additional boundary condition $\varphi(x > a, z = d) = V_g$ on the 2DEG.

We solve this electrostatic problem by conformal mapping. The function $w = \xi + \ln \zeta$ with $w = \pi(iz + a - x)d - 1$ gives the mapping from (x, z) to ζ illustrated in Fig. 1b where the geometry is simple. The edge of the gate maps to $\xi = \alpha + \ln \alpha + 1 = \frac{\pi a}{d}$. The potential is specified along the line $\text{Im } \xi = 0$ and the solution for all ξ is straightforward. The result satisfies the boundary conditions for any α but, in general, it gives an infinite charge density at the edge of 2DEG. A physically acceptable solution, however, must have $n(\mathbf{r}) = 0$ at the edge of the 2DEG. [7] The point $\xi = -1$ corresponds to the edge of the 2DEG, so we enforce $d\varphi/d\xi = 0$ here to suppress the electric field.

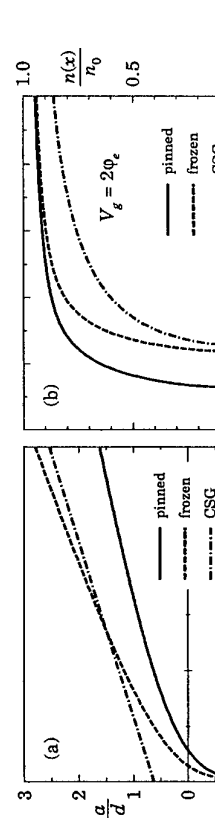


Figure 1. (a) Geometry of semi-infinite gate on the surface of a heterostructure above a 2DEG. (b) Conformal transformation to ξ .

¹ Email: larkin@elec.gla.ac.uk; jdavies@elec.gla.ac.uk

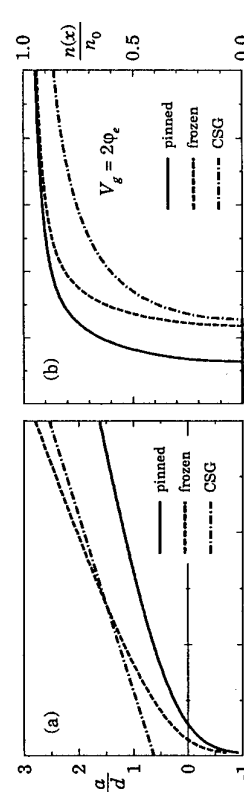


Figure 2. (a) Position of the edge a of a 2DEG as a function of the gate bias V_g . (b) Density of electrons as a function of position, with gate bias $V_g = 2V_\tau$.

This in turn fixes α , and we find $\alpha_p = V_g/V_T - 1$ for the pinned surface. Eliminating α gives the dependence of a , the edge of the 2DEG, on gate voltage V_g which is plotted in Fig. 2a. The density of the 2DEG is shown in Fig. 2b for $V_g = 2V_T$. There is a square-root singularity at the edge of the 2DEG and the density only approaches its unperturbed value as $1/x$.

Our second model has a frozen surface, where the charge on the exposed surface is fixed at its value in equilibrium and is not permitted to change in response to V_g . This was also used by CSG. The same conformal mapping works, and the boundary conditions on φ are as before except that $\partial\varphi/\partial z = V_T/d$ on the exposed surface. The condition of zero density at the edge of the 2DEG leads to the different relation $\alpha_f = 2(V_g/V_T - 1)$ for the frozen surface. The position of the edge is shown in Fig. 2a with the result of CSG for the same value of n_0 . The density is plotted in Fig. 2b, again for $V_g = 2V_T$, with the corresponding result for

III. Position and width of dipolar strips

An important application of our results is to predict the positions x_k of the dipolar strips of incompressible liquid in the quantum Hall effect. These can be calculated from our density using $n(x_k)/n_0 = k/v_0$ where k is an integer and v_0 is the filling factor of the bulk 2DEG. [3] The width a_k of the incompressible liquid was also given by CSG. If $a_k \ll d$ the general result

$$a_k = \sqrt{2} \left(\frac{4\hbar\omega_c \epsilon \epsilon_0}{\pi^2 dn/dx|_{x=x_k}} \right)^{1/2} \quad (1)$$

holds independent of the model. For $a_k \gg d$ and a frozen surface, the equation for a_k lacks the prefactor in Eq. (1). For a pinned surface the equation for a_{kp} is quite different and can be derived by the method of Ref. [19],

$$a_{kp} = \frac{\hbar\omega_c \epsilon \epsilon_0}{4\pi e^2 d^2 dn/dx|_{x=x_k}}. \quad (2)$$

The position of the edge states has been measured in two recent experiments, the first [11] using the lateral photoeffect. A gradient of concentration was created in the 2DEG by applying an electric field E_h to a parallel two-dimensional hole gas (2DHG), separated by d_{eh} . The position of incompressible strips does not depend on the behaviour of the surface, but their width does. Note that the 2DHG acts as an equipotential surface, so the width obeys an equation similar to Eq. (2),

$$a_{hf} = \frac{\hbar\omega_c}{eE_h}; \quad a_{kp} = \frac{\hbar\omega_c}{eE_h} \frac{d + d_{eh}}{d}, \quad (3)$$

for the frozen and pinned surface. For the experimental conditions $a_{hf} = 5 \mu\text{m}$ and $a_{kp} = 50 \mu\text{m}$. However, if their laser excites electrons in the doping layer, an

equipotential plane appears closer to the 2DEG and $a_* = 100 \mu\text{m}$ independent of the surface. This is roughly the scale of the features seen.

Marcus et al. [12] used Aharonov-Bohm oscillations of conductance in a large quantum dot to locate the edge states. The area enclosed by the edge states follows from the frequencies $f_k = |A - px_k - pB(\partial x_k/\partial B)|/\Phi_0$ of Aharonov-Bohm oscillation, where A is the area and p the perimeter of the dot, x_k being measured from the edge of the 2DEG. We find a depletion width $a_f = 80 \mu\text{m}$ and $a_p = 40 \mu\text{m}$ for frozen and pinned surfaces, with corresponding frequencies of $f_1^p = 101 \text{T}^{-1}$ and 128T^{-1} . Experiment gives 107T^{-1} , in favour of a frozen surface, and further support comes from the average value of the conductance.

IV. Conclusions

We have presented a quantitative theory of the gate-induced confinement of a 2DEG including the finite depth of the 2DEG below the surface of heterostructure, and applied it to the integral quantum Hall regime. Our model is applicable to the whole range of gate voltage. We are also able to treat the surface more accurately and have considered models with either pinned potential or frozen charge, which show large differences. Comparison with experiment [12] supports the picture of frozen charge on free surfaces of GaAs at helium temperatures. We have also considered the influence of a nearby 2D hole gas [11] and found that the interaction between electrons and holes alters considerably the CSG theory. Our results are also useful to estimate the depletion region around a large negatively biased gate; very little effort is needed to go beyond the common rule of thumb that the width of the depletion region equals the depth of the 2DEG.

This work was supported by the U.K. EPSRC. [13]

References

- [1] C. W. J. Beenakker, *Phys. Rev. Lett.* **64**, 216 (1990).
- [2] A. M. Chang, *Solid State Commun.* **74**, 871 (1990).
- [3] D. B. Chklovskii, B. I. Shklovskii, and L. I. Glazman, *Phys. Rev. B* **46**, 4026 (1992).
- [4] D. B. Chklovskii, K. A. Matveev, and B. I. Shklovskii, *Phys. Rev. B* **47**, 12650 (1992).
- [5] N. R. Cooper and J. T. Chalker, *Phys. Rev. B* **48**, 4530 (1993).
- [6] B. Y. Gelfand, J. Dempsey, and B. I. Halperin, *Surf. Sci.* **305**, 166 (1994).
- [7] L. I. Glazman and I. A. Larkin, *Semicond. Sci. Technol.* **6**, 32 (1991).
- [8] I. A. Larkin and V. B. Shikin, *Phys. Lett. A* **151**, 335 (1990).
- [9] I. A. Larkin and E. V. Sukhorukov, *Phys. Rev. B* **49**, 5498 (1994).
- [10] See, for example, J. H. Davies and I. A. Larkin, *Phys. Rev. B* **49**, 4800 (1994).
- [11] R. J. F. van Haren, F. A. P. Blom, and J. H. Wolter, *Phys. Rev. Lett.* **74**, 1198 (1995).
- [12] C. M. Marcus, R. M. Westervelt, P. F. Hopkins, and A. C. Gossard, *Surf. Sci.* **305**, 408 (1994).
- [13] A fuller account has been submitted to Physical Review B.

CALCULATED I-V CHARACTERISTICS OF LOW-DIMENSIONAL STRUCTURES

M. Boero and J.C. Inkson

Department of physics, University of Exeter, Stocker Road, Exeter EX4 4QL

Abstract. In this work we calculate the I-V characteristics of quantum dot devices. The I-V curves of such structures are not only dependent upon the dot spectrum, but also on whether they are connected to bulk contacts or to contacts confined in one or more direction. Here we concentrate on 1D-0D-1D and 3D-0D-3D devices, using two different techniques, a transfer-matrix approach and a non-equilibrium Green function formalism. The Coulomb interaction and the single particle aspects are included in the theory. For 1D-0D-1D structures the I-V curve consists of a series of upward and downward steps, the latter being present only if the Coulomb repulsion inside the dot is important. These downward steps prove to be thermally robust. For 3D-0D-3D devices the I-V curve is dominated by peaks rather than steps, reflecting the difference in density of states in the contacts. Comparison with experiments shows very good agreement.

Introduction

Recent progress in nanotechnology has allowed to fabricate semiconductor nanostructures in which electrons are confined in all directions, i.e. quantum dots^{1,2}. The interest in such systems is twofold, from the physics point of view they allow to study and control the behaviour of very few electrons, on the other hand the possibility of controlling the dynamics of individual electrons has raised hopes of a new devices based on single electron mechanisms.

We focus our attention on the transport properties of etched GaAs quantum dots or quantum pillars. The discrete nature of the quantum dot spectrum manifest itself by producing a series of fine features in the I-V curve of double-barrier structures^{1,2}. Depending on the lateral size of the pillar, the contacts can either be classical 3D contacts or they can themselves show size quantisation if the pillar diameter is less than ~500 nm³. We present results of I-V curves calculated by means of a transfer-matrix technique and by a non-equilibrium Green's function method, which is easier to deal with when conservation of lateral state does not occur during tunnelling, as in 3D-0D-3D structures. In both cases we include size quantisation and coulombic effects in modelling the quantum dot⁴. This is necessary since in typical quantum dots the two quantities are of the same order of magnitude.

Coulombic effects are modelled by a Hubbard-type hamiltonian. Our results are compared with experimental I-V curves and we find that we can explain the observed fine-structures as well their thermal behaviour. Particularly interesting is the finding that, due to the Coulomb repulsion inside the dot, fine features appear in the negative as well as the positive differential resistance region. The latter are found to be thermally robust, in accordance with experiment, so that they are a very good candidate to obtain quantum-dot devices working at room temperature⁴. We provide the explanation for such thermal robustness along with ways to further improve such thermal performances.

Method

The study of quantum dot spectra is simplified by the fact that in all practical cases, the dimension of the dot in the growth direction is much smaller than in the lateral ones. Therefore quantisation in the growth direction produces a very large energy splitting between the levels so that only the ground state is important in determining the electron spectrum. One can therefore treat a quantum dot as a two-dimensional system⁵. As for the shape of the laterally confining potential there is now sound evidence that the parabolic assumption is the correct one⁵. To determine its strength in etched devices, we assume a mid-gap pinning of the Fermi level at the outer surface. The electrostatic energy U of two electrons in the dot is given by:

$$U = \frac{e^2(2m\Delta V)^{\frac{1}{4}}}{4\pi e\sqrt{\hbar R}} \quad (1)$$

R is the dot radius, ΔV is the confining potential, m is the effective mass. Size confinement and repulsive energy U are approximately equal for R=90 nm in GaAs⁴, therefore for typical dots (R~50–200nm) both energies are important. We treat the electrostatic repulsion within a Hubbard-like approach⁴. In this way the electron-electron interaction is approximated by the average repulsive energy U of eq.(1). Together with the parabolic confining potential the hamiltonian for the N electron dot reads:

$$H = \frac{1}{2m} \sum_i \left(p_{xi}^2 + p_{yi}^2 \right) + \frac{1}{2} m\omega^2 \sum_i (x_i^2 + y_i^2) + \frac{1}{N(N-1)} U \quad (2)$$

N is the total number of electrons inside the dot and ω is the strength of the confinement. The main reason for adopting the Hubbard hamiltonian lies in the fact that it allows to include the electrostatic effects while maintaining at the same time a single particle picture, which greatly helps in calculating the I-V characteristics⁶. As for the energy U, it should be seen as an adjustable parameter to best account for all those effects such as surface charges, confinement, etc., that non-trivially modify the Coulomb interaction.

To calculate I-V curves we also need information about the contacts to which the dot is coupled. For etched devices the lateral dimensions of the contacts coincide with those of the dot. However this does not mean that the two regions possess the same spectrum. Inside the dot there is also the Coulomb repulsion present and, especially for relative large area devices, the latter dominates over size quantisation. Etched structures with radius less than ~200 nm behave as 1D-0D-1D devices whilst larger structures show 3D behaviour in the contacts since size confinement is too small⁴. To model 1D-0D-1D structures we used a transfer-matrix technique that enabled us to calculate the electron wave functions throughout the structure. Hence we deduced the occupancy of each state inside the dot as well as the transmission coefficient for each electron and the total current. Since the energy of the dot states is a function of the occupancy of the dot, one has to iterate the whole procedure to self-consistency⁴. The effects of finite temperature can easily be taken into account by the inclusion of the Fermi-Dirac distribution factor⁴.

Alternatively, one can use a formula derived by Meir and Wingreen⁶ for the current flowing through a quantum dot. Such formula, which generalises the Landauer formula to the case of interacting systems, reads:

$$I = -\frac{2e}{h} \int de [f_L(e) - f_R(e)] \text{Im}(\tau(\Gamma(e))G^R(e)) \quad (3)$$

the integral is extended to all possible energies, I is the current flowing through the system, $f_{L,R}$ are the Fermi-Dirac functions for the left (right) contact, G^R is the quantum dot retarded Green's function and Γ represents the coupling between the dot states and the contacts:

$$\Gamma = \frac{\Gamma^L \Gamma^R}{\Gamma^L + \Gamma^R}, \quad \Gamma_{a,n} = \sum_b \rho_n^L(e) V_{a,n}^L V_{n,b}^R \quad (4)$$

$\rho_n(e)$ is the density of states in the contact in the n-th subband, $V_{a,n}$ • $V_{n,b}$ are the matrix elements between the dot states and the contacts

To obtain the current one needs to calculate the widths Γ for every applied bias. Since these quantities involve the sum over all the contact subbands, they allow to treat dots with contacts of various dimensionality. The dependence of Γ on the energy and the dimensionality determines the behaviour of tunnelling through quantum dots from 1D, 2D, 3D contacts.

For 1D-0D-1D devices the calculation of the width Γ is simple since the lateral state is conserved during the tunnelling process. The case of 3D-0D-3D devices is more complicated since many states from the contacts can couple to each dot state. Basically the calculation of Γ amounts to first

Fourier transform the dot wave functions and then sum all the contributions from the states with different lateral momenta. Such sum is performed numerically.

Results

We applied the transfer-matrix method to the structure of radius 100 nm studied by Ramdane *et al.*². For such radius size confinement and Coulomb energy U are almost equal⁴. Fig. 1 shows the calculated I-V curves at various temperatures as well as the experimental characteristics at 77 K (d). At low temperature upward and downward steps are present in the I-V curve corresponding to states crossing the emitter Fermi level or a subband minimum. As the temperature is raised, the upward steps quickly disappear whilst the downward ones survive almost unaltered beyond 77 K. This is in very good agreement with experiments (fig. 1d). Our calculations correctly reproduce the number of fine features found experimentally as well their thermal behaviour. The fact that the downward staircase survives at high temperatures has important implications towards individualizing a route to obtain high temperature devices⁴. The physical reason for such thermal robustness lies in the fact that such features when a dot state crosses a subband minimum in the emitter. Since subband minima lie far in energy from the Fermi level, the occupancy of such states is little affected by raises in temperature⁴. In contrast the upward steps are produced by dot states crossing the emitter Fermi energy, which is quickly smeared by temperature increases⁴.

Electrostatic repulsion is a crucial ingredient for the observation of downward steps. The energy separation between the dot states is the sum of size confinement and Coulomb repulsion⁴. In the contacts only the former is present so that the energy separation between the dot states is different from that of the contacts. This fact ensures that the various tunnelling channels close one at a time therefore producing the downward staircase observed experimentally (fig. 1d). From this analysis it emerges that the downward staircase will be smeared at temperatures of the order of the energy separation between the Fermi energy and the subbands minima⁴. Therefore one way of further improving the thermal performances of 1D-0D-1D devices consists in raising the Fermi energy in the contacts by increasing the doping level in the structure. As previously reported, we have also successfully modelled the smaller device of Reed *et al.*¹

Finally in fig. 2a we show a calculation of the I-V characteristics performed by means of eq. (4) for a GaAs pillar of radius 200 nm. For such size the behaviour of the region between the barriers is 0D while for the contacts one is very close to the dimensions for which the effects of size quantisation become too weak to be detected. We therefore treated the contacts as bulk 3D regions. In fig. 2b one can see the experimental I-V curves for the same device. Fig. 2a well compares with fig. 2b and reproduces the peaks found in the upward region of the curve and the undulations in the downward one. The fact that such structure behaves as 3D-0D-3D is confirmed by the peak-like shape of the fine features observed, contrary to the step-like ones found for 1D-0D-1D structures. Eqs. (3) and (4) have the advantage of being more flexible and less computationally demanding than the transfer matrix formalism.

In conclusion we have presented two methods that successfully model the I-V curves of quantum dots for different types of contacts. Our calculations have individuated a route to obtain high temperature devices and can be applied to other types of low-dimensional structures.

References

1. M.A. Reed, J.N. Randall, R.J. Aggarwal, R.J. Matyi, T.M. Moore and A.E. Wetsel, Phys. Rev. Letters **60**, 535 (1988)
2. A. Ramdane, G. Faini, H. Launois, Zeit für Physik B-Conденсed Matter **85**, 389 (1991)
3. B. Su, V.J. Goldman and J.E. Cunningham, Phys. Rev. B **46**, 7644 (1992)
4. M. Boero and J.C. Inkson, Phys. Rev. B **50**, 2479 (1994)
5. D. Pfannkuche and S. Ulloa, Phys. Rev. Lett. **74**, 1194 (1995)
6. Y. Meir and N. Wingreen, Phys. Rev. Lett. **68**, 2512 (1992)

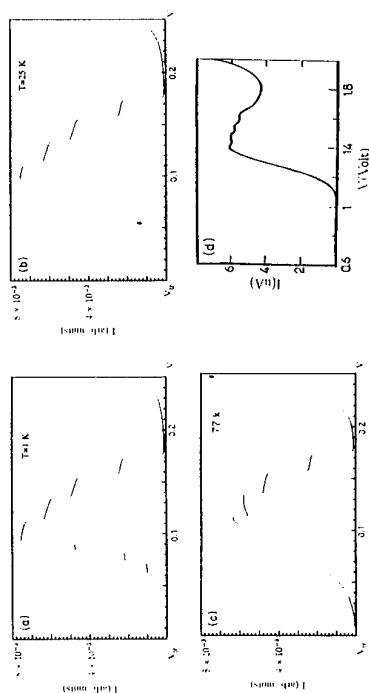


FIG. 1 Experimental I-V curves of a double-barrier structure of Faini *et al.*: (a) I-V curve at 90 K; (b) I-V curve at 77 K showing very good agreement with (d); (c) I-V curve at 52 K showing very good agreement with (d); (d) I-V curve at 77 K showing very good agreement with (d). All calculated curves are shown from threshold voltage.

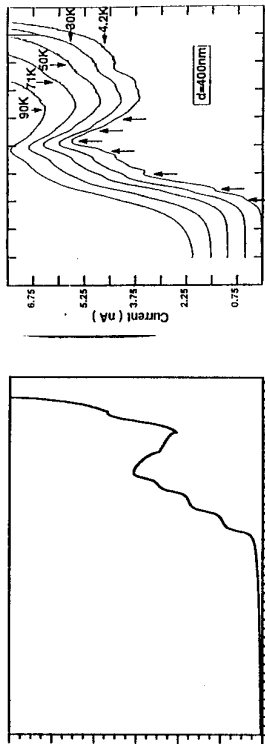


FIG. 2a Calculated I-V curve at 1 K for the double-barrier structure of Faini *et al.*

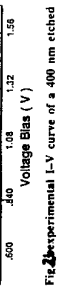


FIG. 2b Experimental I-V curve of a 400 nm etched quantum dot pillar.

Collapse of Quantum Hall State by Floating-up of Extended-State Bands with Increasing Disorder

Tohru Okamoto, Yoshinori Shinohara, Shinji Kawai and Atsuo Yagi*
Gakushuin University, Mejiro, Toshima-ku, Tokyo 171, Japan
 *NPC Ltd., Tochigi 329-28, Japan

Abstract

We measured the diagonal and Hall conductivities across the transition between the integer quantum Hall effect state and the insulating state in a two-dimensional electron system formed in Si-MOSFETs. Sample dependence of the transition indicates that the insulating state is caused by Anderson localization due to disorder, not by a formation of an electron solid.

Introduction

The metal-insulator transition from an integer quantum Hall effect (IQHE) state to an insulating state at very low temperatures has been investigated in many theoretical and experimental studies. In Si-MOSFETs, the insulating phase appears with decreasing electron concentration N_s . The electron concentration value at the transition depends on the strength of magnetic field B and takes local minima at Landau level filling factors $\nu \approx 1$ and $\nu \approx 2$. The insulating phase and the oscillation of the phase boundary in the N_s - B plane have been explained based on two theoretical pictures. One is a formation of a pinned electron solid and the other is Anderson localization. The former was proposed by Kravchenko, Perenboom and Pudalov [1], D'Iorio, Pudalov and Semenchinsky [2], and Pudalov and Chui [3]. They performed magnetotransport measurements on very-high-peaked-electron-mobility Si-MOSFETs, and observed large magnetoresistance in the insulating phase which oscillates as a function of ν . On the other hand, in the previous works, we measured the diagonal and Hall conductivity σ_{xx} , σ_{xy} as functions of a dimensionless parameter $a_c r = \mu B$ [4, 5]. We demonstrated the floating-up of the extended-state bands in energy from the center of the Landau levels with increasing disorder (with decreasing $a_c r$). The floating-up of the extended-state bands had been shown by Ando's numerical study on mixing of Landau levels [6] and proposed by Khmelevitskii [7] and Laughlin [8]. The electron mobility μ was determined in the absence of magnetic field as a function of N_s . We considered that strength of disorder depends on N_s strongly due to the screening effect by electrons against bare random potential fluctuations, and assumed that electrons are localized due to disorder at low- N_s even in their very-high-peaked-electron-mobility Si-MOSFET. However, the electron concentration we observed at the transition is almost the same as those in Refs. [1-3] and ranges from 0.7 to $1 \times 10^{15} \text{ m}^{-2}$ in the region of $\nu \geq 1$. Therefore, our experimental results do not exclude the possibility of the formation of an electron solid. In order to clarify a problem whether the insulating phase is induced by the formation of an electron solid or by the Anderson localization due to disorder, measurements for Si-MOSFETs with low peak electron mobility μ_{peak} is needed.

In the present work, we extend magnetotransport measurements to a Si-MOSFET with low peak electron mobility of $\mu_{\text{peak}} = 0.91 \text{ m}^2/\text{Vs}$ at $N_s = 6 \times 10^{15} \text{ m}^{-2}$ (denoted by Sample-09) and compare the results with those observed in a Si-MOSFET with high electron mobility of $\mu_{\text{peak}} = 2.7 \text{ m}^2/\text{Vs}$ at $N_s = 3.5 \times 10^{15} \text{ m}^{-2}$ (denoted by Sample-27) used in the previous works [4, 5].

Experimental Results and Discussions

An experimental procedure is the same as that used in the previous works. All magnetotransport data were obtained at a fixed temperature $T = 60 \text{ mK}$. Temperature dependences of the magnetotransport data were almost saturated below 100 mK except in the very-high-resistivity-regions of $\rho_{xx} \geq 1 \text{ MQ}$.

Figure 1 shows the N_s -dependence of σ_{xx} and σ_{xy} through the transition from the IQHE state of $i = 2$ to the insulating state with keeping the Landau level filling factor at $\nu = 2.0$. The transition is identified by the decrease in σ_{xy} and concomitant peak of σ_{xx} with decreasing N_s as discussed in our previous papers [4, 5]. Sample-09 which has the lower peak electron mobility has a higher electron concentration at the transition by a factor of about 2 than Sample-27. If a two-dimensional electron system (2DES) takes a crystalline configuration or an electron solid configuration, the critical concentration at the formation of an electron solid depends on the ratio of the electron-electron Coulomb energy ($\propto N_s^{1/2}$) to the Fermi energy of 2DES ($\propto N_s$). The ratio is proportional to $N_s^{-1/2}$. And if the magnetic field plays an important role in the formation of an electron solid, the Landau level filling factor ν gives a measure of the strength of the magnetic field in the solidification. If this is the case, the transition should occur at the same electron concentration in Fig. 1 because two samples have the same ν value. Therefore, the electron concentration dependence of the transition in Fig. 1 clearly shows that the insulating state is caused not by a formation of an electron solid but by the Anderson localization.

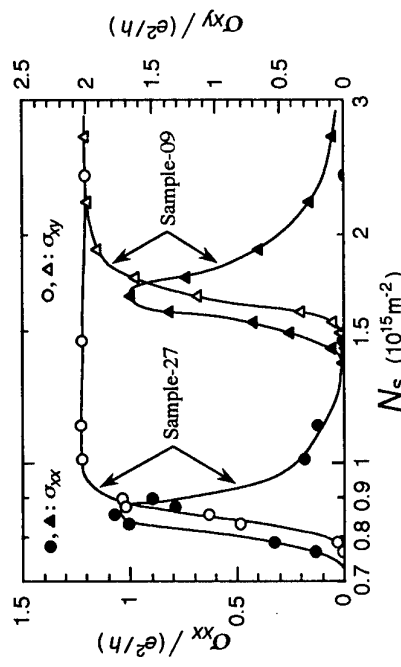


Fig. 1. Diagonal and Hall conductivities at a constant filling factor of $\nu = 2.0$.

In order to see how the electron concentration at the transition depends on the Landau level filling factor $\nu = hN_s/eB$, we show contour maps of the Hall conductivity σ_{xy} on the strength of disorder vs. $1/\nu$ plane in Figs. 2(a) and 2(b). These experimental phase diagrams are constructed by interpolating and smoothing $\sigma_{xy}(B)$ data obtained at different electron concentrations (about ten) in Sample-09 and Sample-27, respectively. The inverse of the Landau level filling factor $1/\nu$ equals to the normalized Hall resistivity of $\rho_{xy} / (h/e^2)$ at high temperature limit. The strength of disorder is determined as a function of N_s and represented by zero-magnetic-field resistivity ρ_0 . Figs. 2(a) and 2(b) are similar with each other while the electron concentration at the transition are different by a factor of about two in the region of $\nu \gtrsim 1$ [9]. Thus, we are convinced that ρ_0 is a good parameter which expresses a strength of disorder in a two dimensional electron system on the occasion of the metal-insulator transition. We have explained observed two peaks of the experimental phase boundary at $\nu \approx 1$ and at $\nu \approx 2$ based on the enhancement effect of the spin and valley splittings by the many-body exchange-interactions [5]. The peaks in Fig. 2(b) are sharper than those in Fig. 2(a). The enhancement effect of the splittings in Sample-27 is stronger than that in Sample-09. This fact might be due to the difference in the ratio of the strength of the e - e exchange interactions to that of the random potential fluctuations which causes the mixing of the Landau levels.

The theoretical phase diagram for the IQHE by Kivelson, Lee and Zhang [10] is also shown in Fig. 2(c). The disorder axis $\rho_{xx}^{(0)} / (h/e^2)$ indicates some microscopic measure of the longitudinal resistance, and the magnetic-field axis $\rho_{xy}^{(0)} / (h/e^2)$ indicates the dimensionless measure of the magnetic-field strength. The phase boundaries were determined as

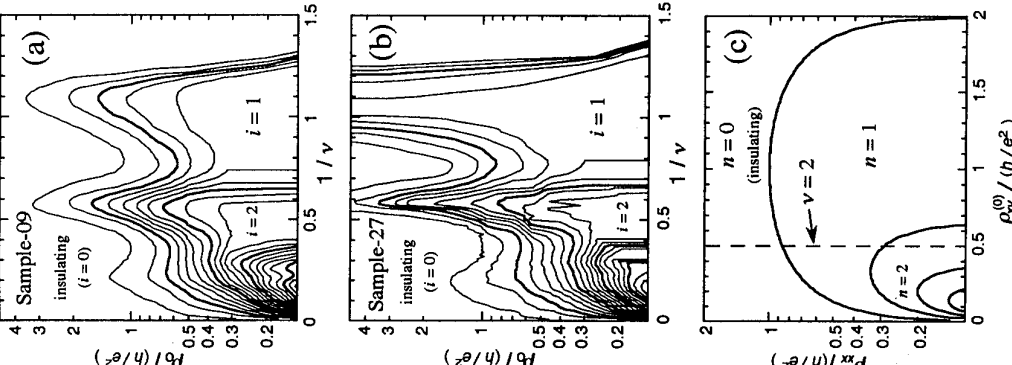


Fig. 2. Phase diagrams for the IQHE.
 (a) Sample-09. Thick lines represent $\sigma_{xy} = (p + 0.5)e^2/h$, $p = \text{integer}$. Thin lines represent $\sigma_{xy} = (p + 0.1, 0.3, 0.7 \text{ or } 0.9)e^2/h$.
 (b) Sample-27. (c) Theoretical one from Ref. 10.

$$\sigma_{xy}^{(0)} = \rho_{xy}^{(0)} / \left[(\rho_{xx}^{(0)})^2 + (\rho_{yy}^{(0)})^2 \right] = (e^2/h)(n + \frac{1}{2}). \quad (1)$$

These boundaries divide the integer quantum Hall states with different quantized Hall conductivities of $\sigma_{xy} = n(e^2/h)$ and $\sigma_{xy} = (n - 1)(e^2/h)$. Though the valley and spin splittings are ignored in Fig. 2(c), the experimental phase diagrams are not very different from the theoretical one in the low- ρ_0 region. The Hall plateaus of $\sigma_{xy} = i(e^2/h)$ with $i = 1$ and $i = 2$ are observed obviously in Figs. 2(a) and 2(b). If the valley and spin gaps are large enough in comparison with the level broadening, the topology of the phase diagram should be the same if the Landau quantum number n is simply replaced by i . However, the Hall plateaus, where σ_{xy} takes constant value of $\sigma_{xy} = i(e^2/h)$ with $\sigma_{xx} = 0$, disappear in the higher- ρ_0 region. The stepwise transitions between the IQHE states $i \leftrightarrow i \pm 1$ at a constant ν -value induced by disorder are not shown clearly in Figs. 2(a) and 2(b). Actually, no Hall plateau is observed in Fig. 1 with decreasing σ_{xy} from $\sigma_{xy} = 2(e^2/h)$ to $\sigma_{xy} = 0$ at $1/\nu = 0.5$; while Fig. 2(c) suggests a stepwise decrease in σ_{xy} along the dashed line with increasing disorder. In strong random potential fluctuations, the energy widths of the extended-state bands might be broadened even at very low temperature by mixing of the higher Landau levels as shown in the numerical calculation by Ando [6, 11].

The authors wish to thank K. Hayashi, T. Okuno, A. Fukano and T. Ohnri for their experimental assistance. This work is supported in part by Grants-in-Aid for Scientific Research from the Ministry of Education, Science and Culture.

References

- [1] S. V. Kravchenko, J. A. A. J. Perenboom, and V. M. Pudalov, Phys. Rev. B 44 (1991) 13513.
- [2] M. D'Inorio, V. M. Pudalov, and S. G. Semenchinsky, Phys. Rev. B 46 (1992) 15992.
- [3] V. M. Pudalov and S. T. Chu, Phys. Rev. B 49 (1994) 14062.
- [4] T. Okamoto, Y. Shinohara, S. Kawaji, and A. Yagi, Proc. 11th Int. Conf. on High Magnetic Fields in Semiconductor Physics.
- [5] T. Okamoto, Y. Shinohara, S. Kawaji, and A. Yagi, to be published in J. Phys. Soc. Jpn. 64 (1995) No. 7.
- [6] T. Ando, J. Phys. Soc. Jpn. 53 (1984) 3126.
- [7] D. E. Khmel'nitskii, Phys. Lett. 106A (1984) 182.
- [8] R. B. Laughlin, Phys. Rev. Lett. 52 (1984) 2304.
- [9] T. Okamoto, Y. Shinohara, and S. Kawaji, to be published elsewhere.
- [10] S. Kivelson, D. H. Lee, and S. C. Zhang, Phys. Rev. B 46 (1992) 2223.
- [11] T. Ando, Phys. Rev. B 40 (1989) 5325.

I-V CHARACTERISTIC OF A 2D ELECTRON CHANNEL WITH
THE FILLING FACTOR CLOSE TO INTEGER

V.B.Shikin

Institute of Solid State Physics Russian Academy of Sci.

142432, Chernogolovka, Moscow District, Russia

A method is proposed for calculating I-V characteristic of a 2D electron channel in a high magnetic field at approximately integer values of the filling factor. In this method, most of the Hall current is of edge origin. The bulk component, exponentially small in the linear regime, begins to grow rapidly above a threshold. At low temperatures this abrupt process corresponds to breakdown of the quantum Hall effect.

Our purpose in the present paper is to derive a current-voltage (I-V) characteristic for an extended 2D electron channel in a high magnetic field, directed normally to the plane of the channel, at filling factor ν which is approximately integer: $\nu=1, 2, 3$. We use the interpretation of Ref. [1] of magnetoelectric phenomena in 2D electron systems. The calculations verify that there is a critical current I_c in the problem, and the dependence of I_c on the channel width is fairly weak. The scale observed in [2]. The information presented below is also useful for refining the conditions and approximations under which the edge interpretation of the quantum Hall effect is valid (Refs [3] and [4], for example).

1. Let us consider an electron channel of width $2W$, $-W < x < +W$ elongated along the Y axis which is immersed in a magnetic field H normal to the channel plane. Assuming $\sigma_{xx} \ll \sigma_{xy}$, using Ohm's law in the form

$$j_1 = \sigma_{1k} \partial \phi / \partial x_k, \quad (1)$$

($\phi(x)$ is the electro-potential in bulk of 2DEG), the continuity equation $\partial j_1 / \partial x_1 = 0$, Poisson equation, the determination of electrochemical potential $\mu(x)$ for ideal, uniform 2DEG and quantum conductance for edge states, we have the following relations between total Hall current I , Hall voltage V , boundary values $\mu(\pm W)$, $\varphi(\pm W)$ and bulk current density $j_y = \text{const}$

$$I = I_e + I_b = \nu e^2 V / h \quad (2)$$

$$I_e = e^2 [\mu(+W) - \mu(-W) - e \varphi(+W) + e \varphi(-W)] / h \quad (3)$$

$$I_b = e^2 [\epsilon \varphi(+W) - \epsilon \varphi(-W)] / h \quad (4)$$

$$\mu(+W) - \mu(-W) = \epsilon V \quad (5)$$

$$\phi(+W) - \phi(-W) = \sigma j \quad (6)$$

$$\phi = e \varphi / \omega_c, \quad j = j_y / j_* \quad j_* = \nu n_s e^3 / \kappa, \quad \gamma = 2 W n_s e^2 / \kappa \omega_c, \\ V = \gamma j - t \ln S_+ / S_-, \quad V = e V / \omega_c, \quad t = T / \omega_c \quad (7)$$

$$2 S_+ = (\nu_{\pm}^{-1} - 1) + \sqrt{(\nu_{\pm}^{-1} - 1)^2 + 4 \epsilon^2 (2\nu_{\pm}^{-1} - 1)} \quad (8)$$

$$V_{\pm} = \nu \pm j / 4\delta, \quad \delta = 1_H / W, \quad 1_H^2 = C / eH, \\ V = \pi l_H^2 n_s, \quad \epsilon = \exp(-t^{-1}) \ll 1 \quad (9)$$

where n_s is the equilibrium electron density in the channel, l_H is the magnetic length, $\nu = 1$.
For $j < \epsilon$ the definition $v(j)$ (7) linearizes

$$V \approx \gamma j + t j / \sqrt{4 - 28\epsilon} \quad (9)$$

If the parameter ϵ is exponentially small, the second term in the right part of (9) is the leading term and the bulk current density j for a given ν is exponentially small. This result complements the model [3], according to which the quantum Hall effect in a linear region $eV \ll \omega_c$ is of the edge origin. In our case the total current I is mainly the edge current if $I_e \gg I_b$. According to (7), (6), (4) and (3) this inequality is really fulfilled.

In the general case the formula $v(j)$ (7) is strongly non-linear. The dependences $v(j)$ for $\nu = 1$, different t and the other parameters of the problem corresponding to the data [2] are presented in fig.1. In the region $t \ll 1$ non-linearity is quite spectacular for $\nu \approx 1$. For typical values $t \approx 10^{-3}$ used in experiments [2] non-linearity acquires the form of a cusp. Fig.2 illustrates the effect of the channel width $2W$ on I - V characteristic. Obviously, there is a dependence here (the critical voltage increases with the increase of the channel width) and it is weaker than linear.

In experiments [2] the voltage V_{yy} is measured

$$\sigma_{xy} V_{yy} = \sigma_{xx} \int_1^2 dy \partial \varphi (\pm w) / dx \quad (10)$$

Points 1 and 2 are the positions of the probes. Formula (10) shows that V_{yy} is a non-lineare function of V simultaneously with $j(v)$. Fig.1. This dependence corresponds to breakdown of QEH.

2. In a classical limit general Ohm's law has a form

$$j_i = \sigma_{ik} \partial \mu / \partial x_k \quad (11)$$

This law cannot be correct in a quantum case. The point is that in a this limit the equilibrium condition $\mu = \text{const}$ coexists with diamagnetic currents in 2DEG. Formula (11) has no this property.

A suitable compromise between (1) and (11) for a quantum Ohm's law could be written as

$$j_x = \sigma_{xx} \partial \mu / \partial x + \sigma_{xy} \partial \varphi / \partial x, \quad j_y = \sigma_{yy} \partial \mu / \partial y + \sigma_{yx} \partial \varphi / \partial x \quad (12)$$

In this case the general picture, presented above, is kepted. The difference is only in the behaviour of $\varphi(x)$ and $\mu(x)$. In the case (1) electro-potential φ is a harmonic function of coordinates. In the case (12) the function $\mu(x)$ is harmonic.

This work is supported by INTAS (Grant 93-933) and RFBI (Grant 95-02-06108-a)

References :

1. V.B.Shikin JETP Lett. 59 (1994) 826
2. N.Q.Balabani, U.Meirav, H.Shtarkman, Y.Levinson Phys.Rev.Let
3. M. Buttiker 71 (1993) 1443
4. K.von Klitzing Phys.Rev. B38 (1988) 9375
Physica B 184 (1993) 1

Figs captions.

Fig. 1 Hall voltage v versus of bulk current's density j from (7). The lines 1-3 correspond to different temperatures: 1. $t = 0.075$; 2. $= 0.050$; 3. $= 0.025$.

Parameters for the τ estimation are the following : $\kappa = 10$, $W = 10^{-3}$ cm., $n_d = 10^{11}$ cm $^{-2}$, $m_* = 0.07$ m $_e$, $H = 10$ T.

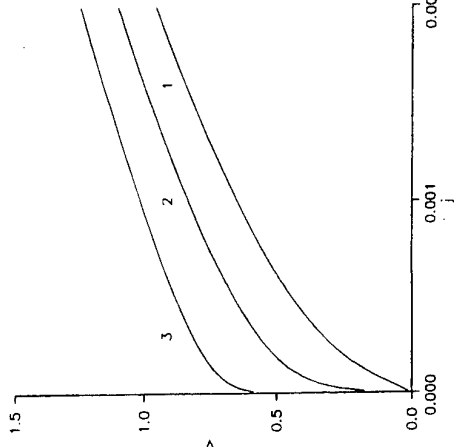


Fig.1

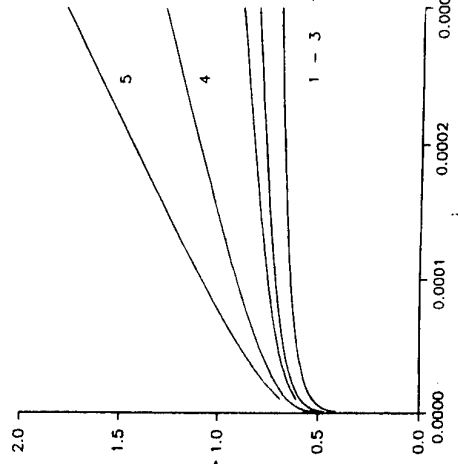
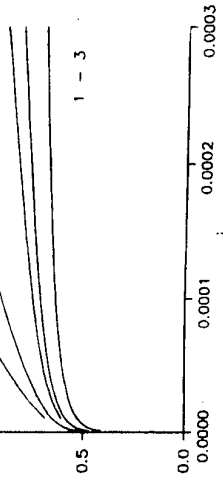
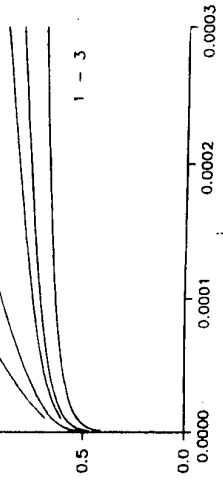
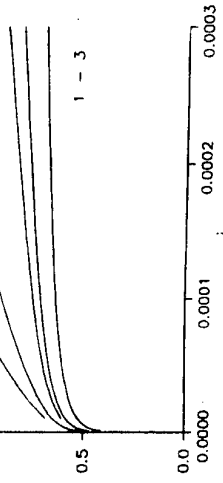


Fig.2



QUANTUM HALL EFFECT WITH STRONG SPIN-ORBIT MIXING OF ZEEMAN STATES

D. G. POLYAKOV^{1,*} AND M. E. RAIKH²

¹Institut für Theoretische Physik, Universität zu Köln, 50937 Köln, Germany
²Department of Physics, University of Utah, Salt Lake City, Utah 84112, USA

ABSTRACT

The conductivity in the quantum Hall regime is considered when two disorder-broadened Zeeman levels overlap strongly and are coupled by a spin-orbit interaction. Electron states of the overlapping Zeeman levels are studied in the limit of smooth disorder. The spin-orbit coupling is found to cause a drastic change in the percolation network, which leads to a strong enhancement of the dissipative conductivity at finite temperature, provided the Fermi level E_F lies between the energies of two delocalized states $E = \pm\Delta$, 2Δ being the Zeeman splitting. The conductivity is shown to exhibit a box-like behavior with changing magnetic field: σ_{xx} is $\sim e^2/h$ at $|E_F| < \Delta$ and exponentially small otherwise. Two peaks of σ_{xx} arising as $T \rightarrow 0$ are found to be strongly asymmetric: σ_{xx} between the peaks falls off with lowering T only in a power-law manner.

There has been considerable recent interest in understanding the quantum Hall effect (QHE) in spin-degenerate Landau levels. If the disorder-induced width of the Landau level Γ exceeds the Zeeman splitting 2Δ , two delocalized states exist within a single peak of the density of states, each corresponding to a different projection of spin. As a result, a single spin-unresolved σ_{xx} -peak, arising on sweeping the Fermi energy through the Landau level, splits into two with lowering temperature. Much attention to the spin-unresolved σ_{xx} -peaks has been attracted since an anomaly in the critical behavior of their width with temperature [1,2], as well as frequency and current [3], was reported: the peaks were claimed to shrink anomalously slow. In fact, the conclusion that overlapping of Zeeman levels strongly promotes delocalization of electron states could have been drawn from the very first experiments on the critical behavior of spin-split σ_{xx} -peaks [4]: if the width $\Delta\nu$ of the peaks, ν being the filling factor, is represented in the form $\Delta\nu = (T/T_1)^\kappa$, the characteristic temperature T_1 for $N = 1 \downarrow$ and $N = 1 \uparrow$ peaks is more than by order of magnitude smaller than that for $N = 0 \downarrow$ peak (while all the spin-split peaks were characterized by the same critical exponent κ). This difference in T_1 can be attributed to much stronger overlapping of Zeeman levels at $N = 1$.

The anomalous behavior of $\Delta\nu$ for two overlapping Zeeman levels can be accounted only for the spin-orbit (SO) interaction. The question is, How can the weak SO-interaction manifest itself strongly in the conductivity? In the paper, we generalize a quasiclassical model of electron motion in a long-range random potential in order to take spin into account. We will show that in this case the SO-interaction can lead to a drastic change in the percolation network, which indeed causes a strong enhancement of the conductivity in the QHE regime. Soon after discovery of the QHE a completely classical approach to the localization of Landau level states in a smooth random potential $V(\rho)$ with a correlation radius d much

larger than the magnetic length λ was developed [5]. In the classical picture, electrons move along the equipotential lines $V(\rho) = E$, so that their trajectories are closed except one of the equipotentials $V(\rho) = 0$ which penetrates through the entire system. Only electrons on this percolating trajectory contribute to σ_{xx} at $T = 0$. However, as it was first pointed out by Chalker and Coddington [6], the picture has the defect that tunneling through saddle-points of $V(\rho)$ is ignored. The tunneling causes coupling of electron states in adjacent cells of the percolation network and becomes crucial in an energy band of the width $\Delta_t \sim \Gamma(\lambda/d)^2$ around the level $E = 0$.

Since $\Delta_t \ll \Gamma$ in the smooth potential, a plausible situation is that the Zeeman splitting, being much smaller than Γ , is still much larger than Δ_t ($\Delta_t \ll \Delta \ll \Gamma$). In other words, the Zeeman levels may overlap while the tunneling through the saddle-points may be neglected. It is this case that is considered here (the opposite case, $\Delta \lesssim \Delta_t$, has been considered numerically in Refs. [7,8]). The absence of the tunneling makes it reasonable to start with the classical picture of electron states. The way we generalize the picture to include spin and SO-interactions is illustrated in Fig. 1 where a pattern of classical trajectories for electrons with spin-up and spin-down is depicted. All trajectories shown correspond to the same energy. They are solutions of the equations $V(\rho) \mp \Delta = E$. The trajectories for spin-down are separated by a saddle-point which is supposed to be non-transparent (its height is much larger than Δ_t) so that two spin-down states are decoupled in the absence of the SO-interaction. If the height of the barrier for spin-down is smaller than

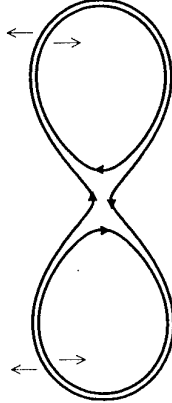
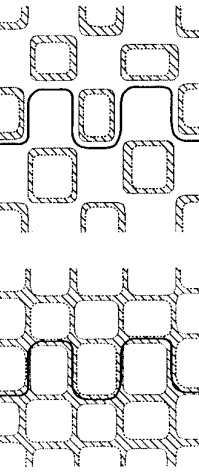


FIG. 1. Classical trajectories corresponding to the same energy, close to that of a saddle-point, in the presence of spin-splitting. The saddle-point separates two trajectories for spin-down but does not split up the trajectory for spin-up. Arrows on the trajectories indicate direction of motion. Due to the spin-orbit interaction, an effective coupling between the spin-down states is provided by the spin-up trajectory without any tunneling through the saddle-point.

To introduce characteristic lengths, consider the energy $E = 0$ in the middle between two percolation thresholds $E = \pm\Delta$ for two projections of spin. The equipotentials $V(\rho) \pm \Delta = 0$ are two sets of closed lines nonintersecting with each other. As we assume that $\Delta \ll \Gamma$, any of the spin-up equipotentials goes parallel with a neighboring spin-down one (typically the distance between them is $\sim d\Delta/\Gamma$). At the same time, percolating trajectories corresponding to either projection of spin form critical clusters with the same characteristic radius $R(\Delta) \sim d(T/\Delta)^{4/3} \gg d$ [9]. As the two percolating networks cannot cross each other, they must share critical saddle-points. Important to us is the characteristic length of the trajectories $L(\Delta) \sim d(\Gamma/\Delta)^{7/3}$ [9] between two critical saddle-points since $L(\Delta)$ determines the length of

close contact of two percolating trajectories with opposite spins: after traveling together this distance they hit a critical saddle-point which separates them. Hence, the crucial parameter is the ratio $L_{so}/L(\Delta)$, where L_{so} is the SO-scattering length.

Suppose $L_{so} \lesssim L(\Delta)$, how then will a classical electron travel over the system? Let us demonstrate that if $|E| < \Delta$, the electron, following the classical trajectories, can percolate. On the contrary, if E is outside the band $(-\Delta, \Delta)$, its motion is restricted to a finite area. It is convenient to color in the area between the spin-up and spin-down trajectories with the energy E . Then at $|E| < \Delta$ the dashed regions form an infinite network [Fig. 2(a)]. To prove this statement, notice that the trajectories with opposite spins at a given E may be obtained as the equipotentials $V(\rho) = E \pm \Delta$. Consequently, the infinite equipotential $V(\rho) = 0$ goes at $|E| < \Delta$ exclusively inside the dashed space. Therefore, an electron can travel throughout the entire system following the boundaries of the dashed regions. Treating $R(\Delta)$ as an elementary step we may view the electron motion as a random walk process. Consider now the case $|E| > \Delta$. Then there is no percolation as the dashed area contains now equipotentials either with only positive or only negative energies [Fig. 2(b)]. As a result, passage through the sample is unavoidably associated with tunneling between the finite clusters the characteristic distance between which is $\lambda[(|E| - \Delta)/\Delta]^{1/2}$. Hence, if $|E|$ exceeds Δ by the small energy Δ , the transport is exponentially suppressed. We thus conclude that the SO-enhancement of the classical transport occurs in the interval $|E| < \Delta$.



a) b)

The classical treatment above is valid if the phase-breaking length L_ϕ , associated with inelastic scattering at finite T , is much shorter than $\xi(0)$, where $\xi(0) \sim R(\Delta)$ [7]. This is the quantum localization length at $E = 0$. We thus predict that at $L_\phi \lesssim \xi(0)$, $T \ll \Delta$, and $L_{so} \lesssim L(\Delta)$ the dissipative conductivity σ_{xx} as a function of the Fermi energy E_F exhibits a box-like behavior [Fig. 3]: $\sigma_{xx} \sim e^2/h$ inside the band $|E_F| < \Delta$ and is exponentially small otherwise. The point is that for $|E_F| > \Delta$ the conductivity is only due to activation to the nearest percolation threshold, while a *metallic band with well-pronounced boundaries* exists between the percolation thresholds. The easiest way to see that $\sigma_{xx} \sim e^2/h$ at $|E_F| < \Delta$ is as follows. The diffusion coefficient provided by the SO-coupling of neighboring clusters is $D \sim R^2(\Delta)v_d/L(\Delta)$, where v_d is the typical drift velocity. The density of electron states on the loop of the length $L(\Delta)$ is $g \sim [1/R^2(\Delta)]L(\Delta)/hv_d$. Thus, if the SO-coupling is strong enough, i.e. $L_{so} \lesssim L(\Delta)$, we have $\sigma_{xx} = e^2gD \sim e^2/h$. In the absence of the SO-coupling, the wave functions would fall off on the scale of λ from the equipotentials and so the conductivity inside the band $|E_F| < \Delta$ would be dominated by activation.

When L_ϕ exceeds $\xi(0)$ with lowering T , then a drop of σ_{xx} occurs between the centers of the Zeeman levels and two well-pronounced σ_{xx} -peaks appear. To estimate σ_{xx} between the peaks, note that owing to the SO-coupling the wave functions of the localized states at

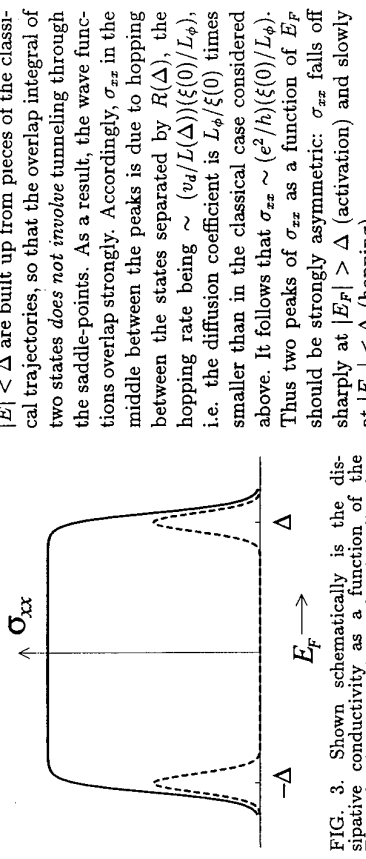


FIG. 3. Shown schematically is the dissipative conductivity as a function of the Fermi level position in overlapping disorder-broadened Zeeman levels separated by the energy 2Δ with (solid line) and without (dashed line) spin-orbit coupling. Both pictures correspond to the same temperature.

We thank J. Hajdu and B. I. Shklovskii for interesting discussions. M. R. is grateful to the Theoretical Physics Institute at the University of Cologne for hospitality. The work was supported by the Humboldt Foundation.

* Also at A. F. Ioffe Physico-Technical Institute, 194021 St. Petersburg, Russia.

1. S. W. Hwang, H. P. Wei, L. W. Engel, D. C. Tsui, and A. M. M. Pruisken, Phys. Rev. B **48**, 11416 (1993).
2. S. Koch, R. J. Haug, K. v. Klitzing, and K. Ploog, Phys. Rev. Lett. **67**, 883 (1991).
3. L. W. Engel, D. Shahar, C. Kurdak, and D. C. Tsui, Phys. Rev. Lett. **71**, 2638 (1993); H. P. Wei, L. W. Engel, and D. C. Tsui, Phys. Rev. B **50**, 14609 (1994).
4. H. P. Wei, D. C. Paasinen, and A. M. M. Pruisken, Phys. Rev. Lett. **61**, 1294 (1988).
5. See, for example, S. A. Trugman, Phys. Rev. B **27**, 7539 (1983) and references therein.
6. J. T. Chalker and P. D. Coddington, J. Phys. C **21**, 2665 (1988).
7. D. K. K. Lee and J. T. Chalker, Phys. Rev. Lett. **72**, 1510 (1994); D. K. K. Lee, J. T. Chalker, and D. Y. K. Ko, Phys. Rev. B **50**, 5272 (1994).
8. Z. Wang, D.-H. Lee, and X.-G. Wen, Phys. Rev. Lett. **72**, 2454 (1994).
9. M. B. Isichenko, Rev. Mod. Phys. **64**, 961 (1992).

POTENTIAL DROPS ACROSS QUANTUM HALL EFFECT SAMPLES - IN THE BULK OR NEAR THE EDGES ?

W. Dietsche, K. v. Klitzing and K. Ploog^(a)

Max-Planck-Institut für Festkörperforschung, Stuttgart, Germany

Abstract

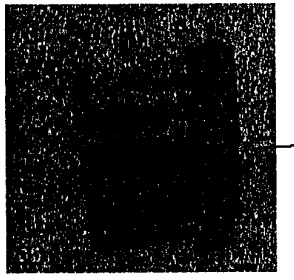
The electrostatic potential distribution in two-dimensional electron gases has been imaged using the electro-optic effect. A potential drop over a length of about $100 \mu\text{m}$ has been found. This edge potential runs along one sample edge only. It switches to the other edge upon current direction reversal.

Introduction

The electrostatic potential distribution inside Quantum-Hall-effect samples can be imaged using the linear electro-optic effect in GaAs [1,2]. A laser beam ($\lambda = 850 \text{ nm}$) with circular polarisation is focussed onto the sample. The potential differences between the illuminated spot of the sample and a metal ground plane on the far surface cause an elliptic distortion of the light after it is either passed through the sample or reflected back. Symmetric potential drops near both sample edges were observed by Fontaine e.a. [1]. On the other hand, Knott et al. [2] found a step-like potential drop near the center of the sample. The latter result could be explained in terms of phenomenological models which allow a variation of the carrier concentration over the sample width leading to a pronounced minimum of the conductivity along a stripe in the bulk of the sample [3,4]. In this work we present new data showing that this description is not necessarily valid for all sample configurations. The results may also clarify the seemingly differences between the data of [1] and [2].

Experimental results and discussion

The layout of our first sample is visible from Fig. 1. It has the shape of a hand, the widths of the fingers are 800, 400, 200, 100, and $50 \mu\text{m}$, respectively. The 2DEG has a carrier concentration of $3.7 \cdot 10^{11} \text{ cm}^{-2}$ and a mobility of $6 \cdot 10^5 \text{ cm}^2/\text{Vsec}$. The figure actually shows electro-optic images taken at 1.2 K where the polarisation changes are converted into grey tones.



+ 2 V ... - 2 V (4 kHz)



+ 2 V ... - 2 V

+ 2 V ... - 2 V

Fig. 1. Electrooptic image of a 2DEG sample in zero magnetic field and under 7.7 T. The width of the images corresponds to about 4 mm.

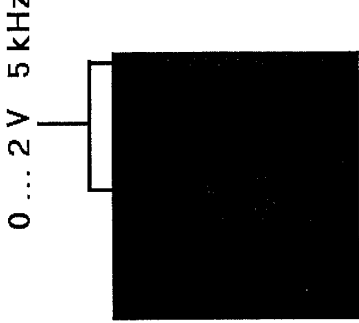
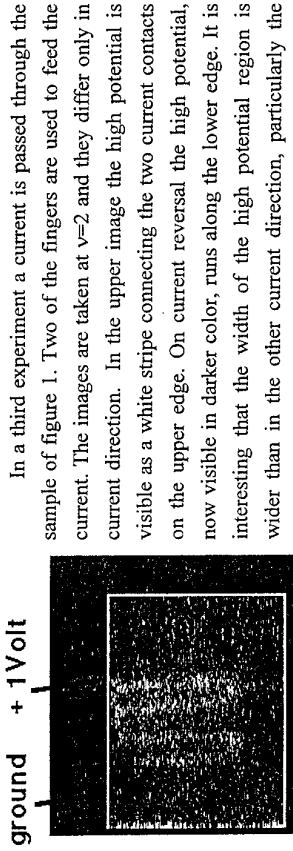


Fig. 2. Electro-optic image of a Corbino sample (filling factor 2). An oscillating voltage is applied simultaneously to both contacts with respect to the ground plane at the far surface.

Therefore the contacts are not visible because the potential there does not contribute to the signal. The two images in Fig. 1 correspond to the zero magnetic field and to the filling factor $v=2$ states. An oscillating voltage (-2V..2V) is applied to one contact only, thus no current flows through the sample and the 2DEG should show up in a constant grey tone. This is indeed the case for $B=0$. At $v=2$, however, we find that only the edge of the sample follows the external potential. The "penetration length" of this voltage drop is of the order of $100 \mu\text{m}$ which is much more than the spatial resolution of the experiment $\leq 20 \mu\text{m}$ and also much larger than the width of the frequently discussed edge states which would be the magnetic length. In the previous work of [2] the sample width was only $200 \mu\text{m}$. Therefore this large penetration length could not be resolved.

A similar penetration length is observed in Corbino samples (figure 2) where the 2DEG boundary is formed by metallic contacts. In this case, both contacts, the center disk and the outer ring, are set to the same voltage. Again, only the 2DEG regions near the contacts follow the applied voltage over a penetration length of about $100 \mu\text{m}$ while the interior of the $500 \mu\text{m}$ wide annulus remains near the ground potential.



Conclusion

In a third experiment a current is passed through the sample of figure 1. Two of the fingers are used to feed the current. The images are taken at $\nu=2$ and they differ only in current direction. In the upper image the high potential is visible as a white stripe connecting the two current contacts on the upper edge. On current reversal the high potential, now visible in darker color, runs along the lower edge. It is interesting that the width of the high potential region is wider than in the other current direction, particularly the "dead-end" in the lower right is completely filled. The interchange of the ground in this experiment is irrelevant to the result as shown by other tests. The change in color on current reversal is an artefact due to the reversal in the phase of the lock-in.

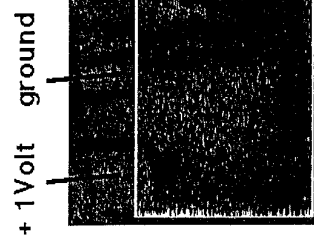
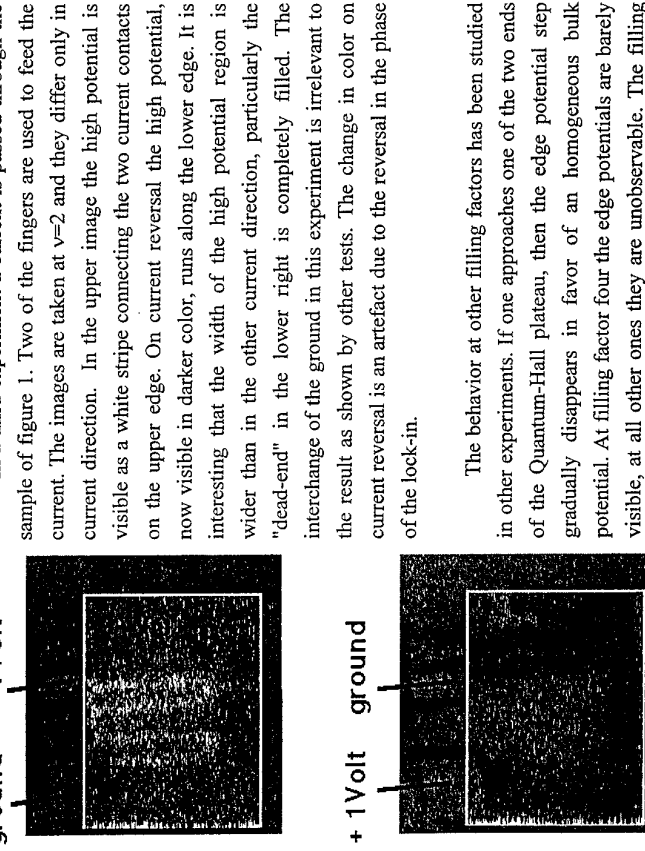


Fig. 3. Electrooptic image of the sample of Fig. 1 with current flow. The applied voltage oscillates between zero and 1 Volt with 4 kHz.

ground + 1 Volt



References

- (a) Now at Paul-Drude-Institut, Berlin, Germany
- [1] P.F. Fontein, P. Hendriks, F.A.P. Blom, J.H. Wolter, L.J. Giling and C.W.J. Beenakker, Surf. Sci. 263, 91 (1992)
- [2] R.Knott, W. Dietsche, K. v.Klitzing, K.Ploog, K.Eberl, Semic.Sci.Technol. 10, 117 (1995).
- [3] G. Diener and J. Collazzo, J. Phys. C'21, 3305 (1989).
- [4] H. Nielsen, preprint.

The behavior at other filling factors has been studied in other experiments. If one approaches one of the two ends of the Quantum-Hall plateau, then the edge potential step gradually disappears in favor of an homogeneous bulk potential. At filling factor four the edge potentials are barely visible, at all other ones they are unobservable. The filling factor $\nu=1$ was not accessible. The sensitivity of this experiment is not sufficient to decrease the voltage down to mV range where the edge effects in the Büttiker sense should become visible.

The fact that the potential drop switches from one edge to the other with reversal of current direction has interesting consequences for the observed potential distribution: if an ac-current without any dc-offset would have been used then potential drops near both edges would have been observed by the lock-in technique. It might be possible that the differences between our results and the ones of [1] are due to the differences in the modulation techniques. Both the qualitative shape of the potential drops and the magnitude of the penetration lengths (100 μm) observed in [1] would then agree with our data.

ground + 1 Volt

In conclusion, we have found that the electrostatic potential at low integer filling factors penetrates in our samples over a length of the order of 100 μm . Since this length does not vary with magnetic field one can not apply the phenomenological descriptions directly which worked very well in narrower samples. The discrepancies between the different electro-optic experiments can be easily explained if one takes both the effect of a dc offset and of the sample size into account.

- (a) Now at Paul-Drude-Institut, Berlin, Germany
- [1] P.F. Fontein, P. Hendriks, F.A.P. Blom, J.H. Wolter, L.J. Giling and C.W.J. Beenakker, Surf. Sci. 263, 91 (1992)
- [2] R.Knott, W. Dietsche, K. v.Klitzing, K.Ploog, K.Eberl, Semic.Sci.Technol. 10, 117 (1995).
- [3] G. Diener and J. Collazzo, J. Phys. C'21, 3305 (1989).
- [4] H. Nielsen, preprint.

Weak Localisation in Ballistic Cavities filled with Antidot-Arrays

G. Lütjering¹, K. Richter², D. Weiss¹, J. Mao¹, R. H. Blick¹, K. v. Klitzing¹, and C. T. Foxon³

¹ Max-Planck-Institut für Festkörperforschung, 70569 Stuttgart, Germany

² Universität Augsburg, 86135 Augsburg, Germany

³ University of Nottingham, Nottingham, UK

Abstract. We present experimental data on the ballistic weak localisation in square cavities filled with antidot arrays. The weak localisation peak is cusp-like at mK temperatures and clearly deviates from a Lorentzian line shape, which is the theoretical prediction for a classical chaotic system. Although the ideal system, a Sinai billiard, is in principle purely chaotic, directly reflected, non-chaotic trajectories lead to the behaviour of a mixed system in experiment. We demonstrate this by detailed semiclassical analysis. In comparison, empty cavities of equal geometry show a sharper peak in the form of a Lorentzian. Here, imperfections of the experimental structure (boundary roughness, small-angle scattering) seem to change the dynamics of the nominally regular system to chaotic, contrary to the antidot case.

The quantum interference phenomena observable in ballistic devices, in which the elastic mean free path exceeds all system dimensions, are a result of scattering from the walls and can thus be used to experimentally probe the scattering properties of regular and chaotic systems. This was originally proposed by Baranger, Jalabert and Stone [1]. Marcus et al. [2] observed aperiodic magnetoconductance fluctuations in single cavities and reported differences between power spectra of these fluctuations for nominally chaotic and non-chaotic cavities. Semiclassical theory also predicted regular and chaotic scattering to produce a qualitative difference on the line shape of the ballistic weak localisation (WL) peak at zero-field [3], which is directly accessible in experiment without the need for a statistical analysis. Recently, a Lorentzian line shape for chaotic stadia, and a triangular lineshape for regular circular billiards has been reported [4]. Here, we study the ballistic WL in square cavities either empty or filled with antidot arrays. The addition of antidots changes the ideally integrable squares to a chaotic system.

The devices have been fabricated on a modulation doped GaAs/AlGaAs heterostructure with a carrier density of $3 \times 10^{11} \text{ cm}^2$ and a mobility of $0.9 \times 10^6 \text{ cm}^2/\text{Vs}$ at 4.2 K which corresponds to a transport mean free path of $8 \mu\text{m}$. We used electron beam lithography and subsequent reactive ion etching to pattern the cavities. In order to do ensemble averaging in a single measurement we employed the technique of Chang et al. [4] by arranging many cavities on a single Hall bar in the geometry shown in fig. 1. For the sample discussed, 52 squares, in 4 rows of 13, were structured with a spacing of $10 \mu\text{m}$ between the rows. The lithographic length of the squares L is $2.3 \mu\text{m}$ and the width of the entrance and exit leads $W \approx 280 \text{ nm}$. The period of the antidot array which is placed symmetrically inside the square, a , is 300 nm with an antidot diameter of 80 nm . The boundaries of the cavities are defined by 100 nm wide trenches, etched 110 nm deep into the crystal, compared to 75 nm for the distance of the electron gas below the surface. Magnetotransport measurements were performed by using standard lock-in techniques at 13.5 Hz in four terminal geometry in a dilution refrigerator with a base temperature less than 30 mK . During initial cooling, the sample pinched off but became conducting after illumination by a short light pulse. In a single cavity ($L = 1.1 \mu\text{m}$, $W = 180 \text{ nm}$) we observe reproducible aperiodic conductance fluctuations on the order of $0.1 \text{ e}^2/\text{h}$ both in empty and antidot filled squares (Conductance fluc-

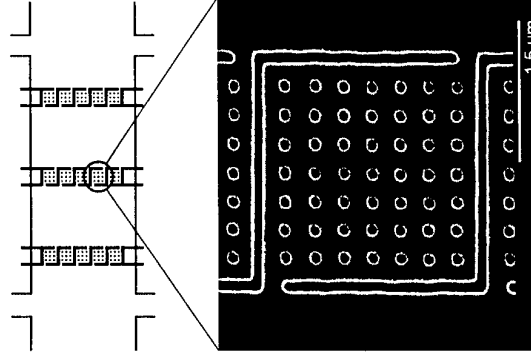


Figure 1: (a) Schematic arrangement of the ensembles of cavities on a Hall bar. The sample consists of 52 cavities arranged in 4 rows in series of 13 in parallel. (b) SEM-micrograph of a structure similar to the sample discussed, showing one cavity containing antidots.

tuations in mesoscopic antidot arrays have previously been discussed in Ref. [5]). The typical frequency of these fluctuations is strongly reduced by the addition of 3×3 antidots. This is clearly reflected in averaged power spectra which give a nearly exponential decay over three orders of magnitude in power for both cases but with different decay factors (not shown). Fits to the power spectra yield corresponding characteristic areas enclosed by trajectories of $1.7 \mu\text{m}^2$ for the empty squares and $0.9 \mu\text{m}^2$ for the antidot filled cavities.

Such conductance fluctuations are effectively suppressed by the ensemble average of 52 squares, enabling the unperturbed observation of the WL peak. Figure 2 shows the resistance peak at small fields, centred at $B = 0$, which was simultaneously measured for the antidot-filled (a) and empty cavities (c). The phase coherence length was decreased from top to bottom for the traces shown by a successive increase of the bias current from 4 nA to $5 \mu\text{A}$ which leads to current heating of the electrons, while the refrigerator was kept at base temperature of approximately 30 mK [6]. For the structure with antidots the line shape evolves from a Lorentzian profile to a cusplike breaking length from a Lorentzian profile to a cusplike peak at lowest current (temperature). This strong deviation from a Lorentzian line shape is rather unexpected for a chaotic ballistic cavity. For regular cavities, deviations from a Lorentzian are in accordance with predictions and have also been reported [4]. In our experiment, however, the empty cavities show a Lorentzian-like WL peak even for the lowest temperatures. The width of the WL peak is reduced by the insertion of the antidots from 6.3 to 0.7 mT . This demonstrates, that the area distribution of the backscattered trajectories is changed as a result of the diffusive dynamics in the antidot array on a length scale given by their period a .

To understand these surprising experimental results we applied semiclassical transport theory, following recent work [3]. The magnetic field dependence of the quantum corrections to the reflection coefficient R , which is linked to the resistance by the Landauer transport theory, is given by

$$\langle \delta R(B) \rangle \propto \int_{-\pi/2}^{\pi/2} d\Theta N(\Theta) \cos \left(\frac{2\Theta B}{\phi_0} \right) \quad (1)$$

This equation represents the cosine transform of the area distribution $N(\Theta)$ of backscattered paths which enclose an effective area Θ , with $\phi_0 = hc/e$ denoting the flux quantum. Equation (1) yields the correct peak profile of the WL on which we focus here, while an accurate semiclassical description of the peak magnitude remains an open problem (see Ref. [3]).

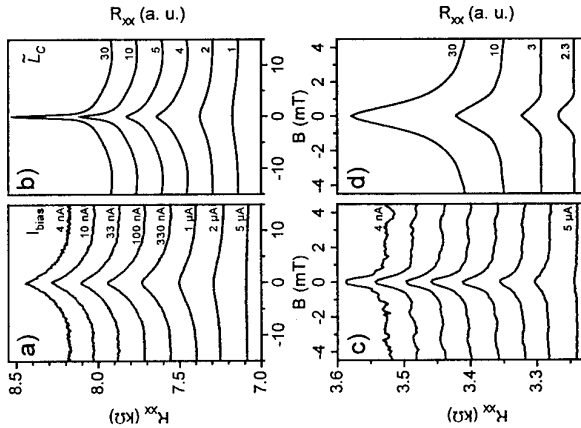


Figure 2: (a) Measured magnetoresistance of the ensemble of square cavities containing antidots as a function of bias current (corresponding to temperature). An offset was added for clarity. (b) Calculated quantum corrections to the resistance in dependence of the cut-off parameter \tilde{L}_c . (c) Experimental and (d) calculated WL peak for the empty cavities.

As illustrated in figure 3a, the backscattered trajectories in an antidot cavity can be categorised into two types: Short paths of electrons directly reflected by the antidots near to the entrance leads or by the opposing cavity wall (dashed and dotted paths), and longer trajectories where the electrons move diffusively through the array of scatterers before leaving the cavity (e.g., the orbit depicted as a solid line in fig. 3a). Directly backscattered paths enclose small areas and thus contribute to the normalised area distribution, $N(\Theta)/N_0$, as a peak at small Θ (see fig. 3b). On the other hand the long chaotic trajectories show an exponential decrease of the area distribution in accordance with chaotic scattering theory [1]. The cosine transform of $N(\Theta)$ yields a sharp Lorentzian $\partial R(B)$ profile from the long chaotic orbits, and a non-universal broad peak from the short orbits, as sketched in the inset of fig. 3b. Therefore the spike in the resistance peak for $\tilde{L}_c = 30$ (fig. 2b) is a signature of long chaotic orbits. With decreasing phase breaking length longer paths are successively eliminated and a cusp - remnant of a sharp Lorentzian imbedded into a smooth background resistance from short paths - can be observed.

In fig. 2d the numerical results for an empty square are shown for different cut-off lengths. The experimentally observed decrease of the peak width is also found in the simulations. This is mainly due to the fact that short paths directly reflected by antidots are no longer present. However, the experimentally observed peaks are slightly narrower than those calculated. Also, the simulated peaks show a crossover to triangular shape for long \tilde{L}_c , whereas the measured peaks remain Lorentzian even for the lowest current. We attribute this to small-angle scattering in our

For the calculation we use the model cavity sketched in fig. 3a containing an array of 7×7 antidots. First the trajectories of $N_0 = 10^6$ electrons injected with appropriate angular distribution are calculated for zero field. The correction to the classical resistance is then obtained from the area distribution $N(\Theta)$ of all backscattered particles by eq. (1). To take phase breaking into account, we introduce a cut-off length L_c and include only those orbits which are shorter than L_c into $N(\Theta)$. Fig. 2b shows the evolution of the computed peak profile by decreasing the normalised cut-off length $\tilde{L}_c = L_c/L$ from 30 to 1. Clearly this results in a crossover from a cusp-like peak to a smooth, flat profile very similar to that found in experiment. By relating the simulations to the experimental traces we can obtain an estimate for the phase coherence length L_ϕ . The WL peak for the lowest current ($I = 4 \text{ nA}$) in fig. 2a shows a close agreement with the calculation for $\tilde{L}_c = 5$, corresponding to an experimental phase breaking length of $L_\phi \approx 12 \mu\text{m}$.

As illustrated in figure 3a, the backscattered trajectories in an antidot cavity can be categorised into two types: Short paths of electrons directly reflected by the antidots near to the entrance leads or by the opposing cavity wall (dashed and dotted paths), and longer trajectories where the electrons move diffusively through the array of scatterers before leaving the cavity (e.g., the orbit depicted as a solid line in fig. 3a). Directly backscattered paths enclose small areas and thus contribute to the normalised area distribution, $N(\Theta)/N_0$, as a peak at small Θ (see fig. 3b). On the other hand the long chaotic trajectories show an exponential decrease of the area distribution in accordance with chaotic scattering theory [1]. The cosine transform of $N(\Theta)$ yields a sharp Lorentzian $\partial R(B)$ profile from the long chaotic orbits, and a non-universal broad peak from the short orbits, as sketched in the inset of fig. 3b. Therefore the spike in the resistance peak for $\tilde{L}_c = 30$ (fig. 2b) is a signature of long chaotic orbits. With decreasing phase breaking length longer paths are successively eliminated and a cusp - remnant of a sharp Lorentzian imbedded into a smooth background resistance from short paths - can be observed.

In fig. 2d the numerical results for an empty square are shown for different cut-off lengths.

The experimentally observed decrease of the peak width is also found in the simulations. This is

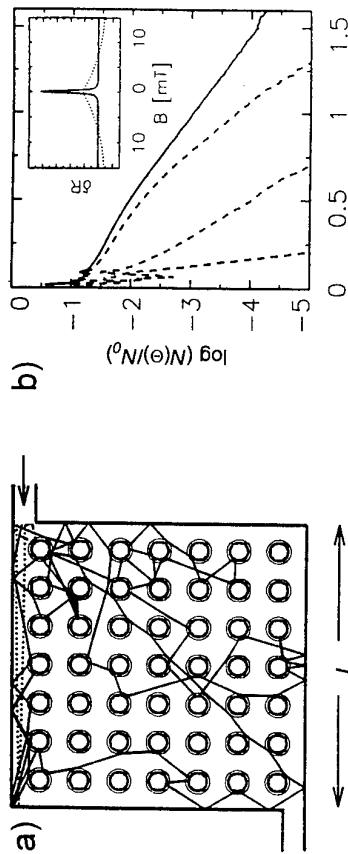


Figure 3: (a) Model of a 7×7 antidot cavity. Classical electrons injected from the right lead are either directly backscattered by nearby antidots (dashed line) or the opposite wall (dotted line) or follow chaotic diffusive paths through the array of scatterers (solid line). (b) Classical distribution $N(\Theta)/N_0$ of the effective areas Θ enclosed by backscattered paths for the antidot billiard (solid line). The nearly linear part at larger Θ , representing the diffusive particles, is suppressed by a decrease of the cut-off length \tilde{L}_c as shown for the dashed lines for $\tilde{L}_c \approx 30, 5, 2$. Inset: Decomposition of the WL peak into the contribution from long chaotic orbits (Lorentzian like spike, solid line) and orbits shorter than $3L$ (dotted line).

devices, which can change the classical distribution of areas from a power law to exponential in regular systems making them indistinguishable from chaotic systems [7].

We also addressed the influence of geometric imperfections of the cavities on the transport properties. Irregular, rippled boundaries were introduced by assuming a random Gaussian distribution for the reflection angles, centred at the angle of specular reflection. However, we found only slight changes in the width of the ∂R peaks for a RMS deviation of the reflection angles up to $\pi/10$ [7]. The influence of rounded corners was also found to be small.

In summary, we observe strong differences in the measured small field magnetoresistance between empty cavities and cavities containing antidots. For the antidot case our semiclassical calculations accurately reproduce the shape and width of the measured weak localisation peaks. We conclude that in a typical chaotic system which may even exhibit hard chaos (as the Sinai billiard), quantum transport phenomena usually reflect the coexistence of short time dynamics of non-universal paths and chaotic behaviour on longer time scales. Therefore, the generic chaotic feature of a pure Lorentzian weak localisation line shape appears to be rather exceptional while in general the resistance profile is more complex and not unique. We would like to thank T. Schmidt for helpful discussions and M. Rieck, B. Schönherr, and U. Witzmann for help in the sample preparation.

- [1] H. U. Baranger, R. A. Jalabert, and A. D. Stone, Phys. Rev. Lett. **65**, 2442 (1990)
- [2] C. M. Marcus, A. J. Rimberg, R. M. Westervelt, P. F. Gossard, Phys. Rev. Lett. **69**, 506 (1992)
- [3] H. U. Baranger, R. A. Jalabert, and A. D. Stone, Chaos **3**, 665 (1993); Phys. Rev. Lett. **70**, 3876 (1993)
- [4] A. M. Chang, H. U. Baranger, L. N. Pfeiffer, K. W. West, Phys. Rev. Lett. **73**, 2111 (1994)
- [5] R. Schuster, K. Ensslin, D. Wharam, S. Kuhn, and J. P. Kotthaus, Phys. Rev. B, **49**, 8510 (1994)
- [6] We also directly varied the temperature of the sample between 40 mK and 2.2 K and found a similar change in the WL lineshape (2.2 K $\approx 1 \mu\text{A}$). Here the current dependence is shown, since it covers a greater range.
- [7] W. A. Lin, J. B. Delos, and R. V. Jensen, Chaos **3**, 655 (1993)

Calculations of Magneto-transport Fluctuations in Ballistic Quantum Dots

G. Edwards, Anna Grincwraig and D. K. Ferry
 Center for Solid State Electronics Research, Arizona State University
 Tempe, Arizona 85287-6206, U. S. A.

Abstract

We examine the magneto-conductance in ballistic quantum dot structures, using the recursive Green's function technique. We find conductance fluctuations at weak B field strengths and Aharonov-Bohm oscillations at strong B field strengths.

Introduction

Recent magneto-transport experiments have examined the conductance properties of mesoscopic quantum dots, with quantum point contact (QPC) 'ports', in both 'weak' and 'strong' magnetic field regimes [1-3]. The quantum dots are defined in the 2DEG of a GaAs-AlGaAs heterostructure by the split-gate technique. Generally, very high mobility modulation-doped structures are used, so that the mean-free path is significantly larger than the quantum dot structure; hence, the transport through the dot is ballistic in nature. The 'weak' B field quantum dot measurements show magneto-conductance fluctuations, which have been attributed to the underlying chaotic classical scattering dynamics through semi-classical arguments [4]. The scattering dynamics of a 2D square billiard dot structure, subject to a B field perpendicular to the plane of the billiard, is chaotic. This can be understood from the mixing of 'degrees of freedom' between the cyclotron and the box-bouncing motion along the two Cartesian directions.

Aharonov - Bohm (AB) oscillations also have been observed in the in the experiments in the case of a 'strong' B field [3]. They are due to resonant tunnelling through the saddle point potential of the point contacts into a circulating edge state inside the dot. The circulating edge state encloses magnetic flux and the B field sweep every time the area of the dot encloses an additional flux quantum. We present simulation results for the quantum dot structures which illustrate both fluctuations in the 'weak' B field regime and AB oscillations in the 'strong' B field regime.

Recursive Green's Function Method

We use the recursive Green's function (RGF) method for calculating the conductance of the 2D mesoscopic waveguide system [5-8]. The philosophy of this method is to numerically calculate the single-particle Green's function exactly, for a discretized representation of the 2D Schrödinger equation (SE) for the mesoscopic waveguide system. The RGF technique is an efficient way of generating the elements of the Green's function for the system, which can be associated with the S matrix [9-11]. The conductance then can be obtained by using the Landauer-Büttiker formula which gives the total conductance in terms of the transmission coefficient. The discretized SE is equivalent to a 2D tight-binding lattice model, with a modified Peierls' phase factor describing the presence of the B field. In the lattice model, the lattice

constant a is the fundamental unit in which the Schrödinger equation is discretized. This provides a convenient scaling of the energy by the energy V which is related to a by

$$V = \frac{\hbar^2}{2m^* a^2}, \quad (1)$$

where m^* is the effective mass. For an accurate representation of the 2DEG, the momentum must be kept less than π/a , as the discretization induces a periodic structure in momentum space. In fact, the momentum should be well below this value to avoid "superlattice" effects in the energy structure from the discretization of the lattice [12], a point to which we return later.

The full Green's function of the discrete problem is calculated recursively using Dyson's equation. The entire lattice system is 'cut' into slices, where each slice is a decoupled column of the lattice. Starting with the known analytical expression for the Green's function in the semi-infinite left lead, the Green's function can be 'propagated' through the system by adding one slice at a time. Recursion equations are used to relate the left lead Green's function to the Green's function for the 'new' system consisting of the left lead plus one slice and the coupling between them. Repeating this procedure across the whole system and then finally attaching the right lead semi-infinite Green's function, we obtain the total Green's function. An important advantage of the recursion technique is its numerical stability [13]. Simple transfer matrix techniques are unstable for multimode wave propagation problems in heterogeneous media due to exponential numerical overflow resulting from the presence of evanescent waves [13].

The geometry of the waveguide is treated by considering an overall rectangular strip, where the waveguide boundary is contained inside this rectangular region. Then the site energies are set to be very large outside the boundary of the waveguide. This effectively defines the waveguide geometry with "hard-wall" boundary conditions. This method has considerable flexibility to vary the quantum wire geometry to enable direct modeling of the experimental situation. Here, we focus on idealized "rectangle-based" confining waveguide profiles, which must be calculated numerically by matrix diagonalisation and the more complicated B field Green's function-S matrix relation must be employed [11]. This will be discussed further elsewhere.

Boundary roughness can also be incorporated by allowing the boundary profile to deviate from an 'average' profile on the scale of the lattice [13,14]. To ensure numerical reliability of our computational scheme we check current conservation and find it to hold within machine accuracy.

Numerical Results

The length of the dot (inner dimension) is 20x23 sites. The 'entrance' and 'exit' QPC's of the dot have a length and width of 3 sites. The QPC's are then connected to a 63 site-wide rectangular region (the 'wide' lead region). The dot is located centrally with respect to the wide regions. The magnetic field strength is measured in terms of frustration

$$f = \frac{Ba^2}{\Phi_0}, \quad (2)$$

a dimensionless quantity, where Φ_0 is the flux quantum and B the magnetic field. f is the number of flux quanta enclosed in a unit cell of the lattice. For our calculations the conductance g is in units of $2e^2/h$. Figure 1 is a plot of g against f , for a Fermi energy of $2V$ over a range of f corresponding to a ‘weak’ B field. It is clear that aperiodic structure exists in the conductance, and we associate this with the experimentally observed “fluctuations” in such dot structures.

If the energy is raised to $4V$, then periodic oscillations are found to occur, but these do not correspond to any characteristic area of the dot. At this energy, the “superlattice” characteristics of the discretized lattice dominate the results. This energy corresponds to the half-filled band of points of the 2D energy surfaces and a divergent density of states, exists [15]. This reinforces our earlier statement that the momentum must be kept well below that corresponding to the “zone boundary” of the periodic momentum space created by the discretization.

In figure 2, we plot the conductance (for a Fermi energy of $2V$) over a range of f corresponding to a ‘strong’ B field. The strong field results show periodic oscillations with a period $\Delta f \sim 2.0 \times 10^{-3}$. A dot area of 20×23 sites has a corresponding AB period $\Delta f = 2.17 \times 10^{-3}$, which is consistent with an interpretation of the strong B field numerical oscillations as being AB-like in origin. Sivan *et al.* [16] have seen similar AB-like oscillations in their calculations of g as a function of f for a quantum dot structure, which they attribute to edge states circulating in the dot ‘probed’ by the ‘entrance’ and ‘exit’ leads.

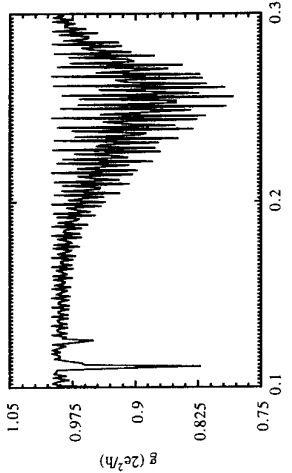


Figure 1 Conductance as a function of the flux through a unit cell, over the ‘weak’ B field range, for a 20×23 site quantum dot at a Fermi energy of $2V$.

This work is supported by NEDO under the international joint research program “Nanostructures and Electron Waves Project.” A. G. acknowledges support from the Swedish Research Council for Engineering Sciences (TFR), the Swedish Institute (SI), and the Ericsson ISS’90 Foundation.

References

- [1] C. M. Marcus, R. M. Westervelt, P. F. Hopkins, and A. C. Gossard, *Chaos* **3** (1993) 643.
- [2] J. P. Bird, K. Ishibashi, Y. Aoyagi, T. Sugano and Y. Ochiai, *Phys. Rev. B* **50** (1994) 18678.
- [3] J. P. Bird, K. Ishibashi, M. Stopa, Y. Aoyagi, and T. Sugano, *Phys. Rev. B* **50** (1994) 14983.
- [4] R. Blümel and U. Smilansky, *Phys. Rev. Lett.* **60** (1988) 477.
- [5] G. Czycholl and B. Kramer, *Sol. State Commun.* **32** (1979) 945.
- [6] D. J. Thouless and S. Kirkpatrick, *J. Phys. C* **14** (1981) 235.
- [7] P. Lee and D. S. Fisher, *Phys. Rev. Lett.* **47** (1981) 882.
- [8] H. U. Baranger, D. P. DiVincenzo, R. A. Jalabert, and A. D. Stone, *Phys. Rev. B* **44** (1991) 10637.
- [9] M. J. McLennan, Y. Lee, and S. Datta, *Phys. Rev. B* **43** (1991) 13846.
- [10] A. Szafer and A. D. Stone, *IBM J. Res. & Dev.* **32** (1988) 384.
- [11] H. U. Baranger and A. D. Stone, *Phys. Rev. B* **40** (1989) 8169.
- [12] See, e.g., the discussion in N. C. Klukstad, A. M. Kruman, D. K. Ferry, and C. Ringhofer, *Phys. Rev. B* **39** (1989) 7720.
- [13] Y. Takagaki and D. K. Ferry, *J. Phys. Condens. Matter* **4** (1992) 10421.
- [14] H. Akera and T. Ando, *Phys. Rev. B* **43** (1991) 11676.
- [15] See, e.g., R. K. Reich, R. O. Grondin, and D. K. Ferry, *Phys. Rev. B* **27** (1983) 3483.
- [16] U. Sivan, Y. Imry, and C. Hartzstein, *Phys. Rev. B* **39** (1989) 1242.

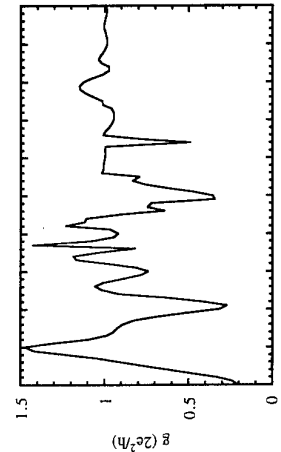


Figure 2 Conductance g in the ‘strong’ field range, for a 20×23 site quantum dot at energy of $2V$.

Conclusions

We have numerically investigated the conductance properties of a quantum-dot structure as a function of magnetic field using a recursive Green’s function technique. Our calculations demonstrate conductance fluctuations at weak B field strengths and Aharonov-Bohm like oscillations at strong B field strengths.

Conductance Fluctuations in Nanostructures of Doped CdTe and $\text{Cd}_{1-x}\text{Mn}_x\text{Te}$ Epilayers

J. Jaroszyński, J. Wróbel, M. Sawicki, T. Skośkiewicz, G. Karczewski, T. Wojtowicz,
J. J. Kosut and T. Dietl
Institute of Physics, Polish Academy of Sciences, al. Lotników 32/46, PL-02668 Warsaw, Poland

E. Kamińska, E. Papis and A. Piotrowska
Institute of Electron Technology, al. Lotników 32/46, PL-02668 Warsaw, Poland

Abstract

Weak-field magnetoresistance and universal conductance fluctuations have been studied at millikelvin temperatures in submicron wires of In-doped n^+ -CdTe and n^+ -Cd_{0.99}Mn_{0.01}Te. The fluctuations contain a periodic component of unknown origin. The giant spin-splitting of the electron states, caused by the s - d exchange interaction with the Mn spins results in the positive magnetoresistance and the temperature dependence of the fluctuation pattern.

We report here on a study of millikelvin magnetoresistance in submicron wires of CdTe and Cd_{0.99}Mn_{0.01}Te doped with In donors to the electron concentration $\sim 10^{18} \text{ cm}^{-3}$, more than five times greater than that corresponding to the metal-to-insulator transition in bulk n^+ -CdTe. Our results provide informations on the behaviour of the magnetoresistance [1] and universal conductance fluctuations (UCF) [2] at the localisation boundary as well as point to a dramatic effect of the s - d exchange interaction on quantum transport phenomena in the mesoscopic regime [2-5].

Cd_{1-x}Mn_xTe:In films with thickness of $\sim 0.3 \mu\text{m}$ were grown by MBE on semiconducting (001) GaAs substrates with 10 Å ZnTe and 3 μm undoped CdTe buffer layers. SIMS, high-resolution TEM, X-ray diffraction, photoluminescence, DLTS, conductivity, and Hall effect studies showed homogeneous impurity distribution and good structural properties of the epilayers. The studied wires had the form of six-terminal Hall bars with a square cross section, S , with a side $W = 0.3 \pm 0.05 \mu\text{m}$, and the distance between the voltage probes, $L = 5 \mu\text{m}$, as shown in the inset to Fig. 1. They were fabricated by means of 30 keV electron-beam lithography, followed by wet etching in 0.5% solution of Br₂ in ethylene glycol. No degradation in the carrier concentration or mobility was noted after nanostructurization. Ohmic contacts were formed by alloying Indium. Low-frequency a.c. currents down to 100 pA were employed for the resistance measurements in a dilution refrigerator.

Figure 1 presents resistance at 30 mK as a function of the magnetic field for a CdTe:In wire with the electron concentration $n = 1.0 \cdot 10^{18} \text{ cm}^{-3}$. Weak-field negative magnetoresistance and irregular resistance fluctuations are well resolved. The latter, in addition to a remarkable reproducibility, show several other features characteristic for UCF under conditions that the cyclotron energy is smaller than the inverse relaxation time, whereas the distance L is greater than both the phase breaking length $L_\varphi = \sqrt{D\tau_\varphi(T)}$ and the thermal diffusion length $L_T = \sqrt{\hbar D/k_B T}$ [2]. In particular, the root mean square of the fluctuation amplitude $\Delta G = \text{rms}(\Delta R)/R^2$ is independent of the magnetic field but decreases with the temperature according to $\Delta G \approx (C/T)^r e^2/h$, where $C \approx 0.1 \text{ mK}$ and $r \approx 0.5$. Besides, ΔG becomes by a factor of 3 smaller in a sample with S/L 10 times greater. However, the

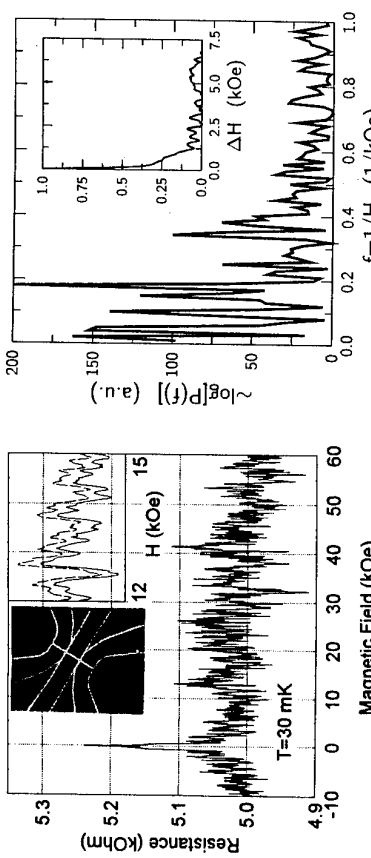


Fig. 1 Resistance as a function of the magnetic field perpendicular to n^+ -CdTe wire. Insets show micrograph of the sample and reproducibility of the fluctuations.

fluctuations are not entirely aperiodic. This is visible in Fig. 2, where both the Student t -distribution of the characteristic frequencies and the fluctuation correlation function single out a component with a period of 6 kOe. A similar effect has recently been observed in n^+ -GaAs [6] and n^+ -PbSe [7]. Guided by results of magnetoresistance studies in antidot lattices [8], we suggest that the periodic component observed by us may be related to correlation in the distribution of scattering centers.

Turning to the weak-field magnetoresistance we note that because $L_T < W$ above 100 mK, the studied wires are three dimensional (3D) with respect to phenomena determined by diffusions such as electron-electron interactions. Since, however, $L_\varphi > L_T$ [9], we may expect a dimensional cross-over in the negative magnetoresistance as it is governed by a pole in the cooperon channel. This is shown in Fig. 3 which displays the magnetoresistance in n^+ -CdTe at various temperatures. The theoretical curves were calculated for 3D from weak-localisation theory [1] according to the well known procedure [9] assuming $L_\varphi = A/T^{3/4}$, with A being a fitting parameter determined to be $0.9 \mu\text{m K}^{3/4}$. The effect of the electron-electron interactions on the magnetoresistance was neglected as, because of a small value of the Landé factor, $g^* \approx -1.7$, and relatively weak disorder, $k_F \ell \approx 4$, its contribution was found to be below 10%. We take the disagreement between the experimental and theoretical results below $\sim 2 \text{ K}$ as an evidence for the temperature-induced cross-over from 3D to 1D.

A striking influence of magnetic impurities on the magnetoresistance and UCF is shown in Fig. 4, where data for Cd_{1-x}Mn_xTe:In with $x = 1 \pm 0.1\%$ and $n = 8 \cdot 10^{17} \text{ cm}^{-3}$ are shown together with the results of a theoretical computation [1, 9]. The positive magnetoresistance is caused by modifications of electron-electron interaction related to giant spin-splitting. The spin-splitting depends on the temperature and the magnetic field according to [9, 10]

$$\hbar\omega_s \equiv \tilde{g}\mu_B H = g^* \mu_B H + \alpha M(T, H)/(g\mu_B),$$

where $\alpha N_0 = 0.22 \text{ eV}$ [11] is the s - d exchange integral, $M(T, H)$ is the magnetization of Mn spins given by a modified Brillouin function, $M(T, H) = \pi N g \mu_B S B_S(T + T_o, H)$, where

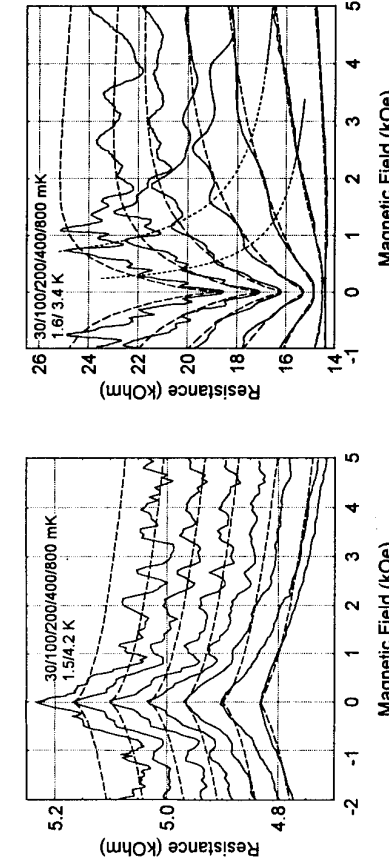


Fig. 3 Resistance changes as a function of the magnetic field perpendicular to the wire of n⁺-CdTe (traces for the lowest temperatures are vertically shifted). Dashed lines represent magnetoresistance calculated in the framework of 3D [1, 9] weak-localization theory with parameters given in the main text.

$N_e = 1.48 \cdot 10^{22} \text{ cm}^{-3}$, $g = 2.0$, $S = 5/2$ and, for $\bar{x} = 1\%$, $T_0 \approx 80 \text{ mK}$ [11, 12]. These parameter values imply $\tilde{g}\mu_B H = 5.5 \text{ meV}$ for $g\mu_B H \gg k_B(T + T_0)$ and $\tilde{q} = 150 \text{ K}/(T + T_0)$ in the opposite limit. In that way, the Coulomb amplitude was the only adjustable parameter and its fitting yielded $g_3 + g_4 = 1.3$. No dimensional cross-over to 1D is observed in the positive magnetoresistance, as it is controlled by a short length scale: L_T . Last point to discuss is the resistance fluctuations in Cd_{0.99}Mn_{0.01}Te. Their root mean square amplitude is independent of the magnetic field and varies with the temperature similarly to CdTe. This points to a minor efficiency of spin-disorder scattering, a conclusion consistent with a small density of states in semiconductors. In contrast to CdTe, the fluctuation pattern exhibits a distinct temperature dependence. This new effect may have its origin in the spin splitting-induced redistribution of carriers between the spin subbands. The redistribution, and a corresponding shift of the Fermi energy ε_F with respect to spin-up and spin-down subband edges, result in a gradual change of energy levels of the system that contribute to the conductance. If $\varepsilon_F \gg \hbar\omega_s > \mu_e$, where μ_e is the energy correlation range of the chemical potential, the correlation field for the spin effect assumes a simple form,

$$H_{\text{spin}} = \sqrt{2}\mu_c \left(\frac{\partial \hbar\omega_s}{\partial H} \right)^{-1}, \quad (2)$$

with [2] $\mu_c \approx \min(k_B T, \hbar/\tau_\varphi)$. By taking a known form of the correlation field for the orbital effects [2] we get, in the case when L_φ is the relevant length scale,

$$\frac{H_{\text{orb}}}{H_{\text{spin}}} \approx \left| g^* + \frac{\alpha N_o \chi(T, H)}{g\mu_B^2} \right| \frac{m^*}{m_0 k_F \ell}. \quad (3)$$

We see that for sufficiently large magnetic susceptibility $\chi(T, H) = \partial M(T, H)/\partial H$ and a small value of diffusion constant $D \approx \hbar k_F \ell/(3m^*)$ the spin effect will dominate. For the material parameters quoted above this is a case of n⁺-Cd_{0.99}Mn_{0.01}Te at $T \leq 1 \text{ K}$.

In summary, our results have provided a new evidence for the presence of the periodic component in the UCF spectrum as well as have led to a discovery of a new driving mechanism of the magnetoresistance fluctuations – the redistribution of electrons between the spin-subbands.

This work has been supported by Polish State Committee for Scientific Research under contracts No. P0Z-Z01/2011/P/4/P/03/01 and 8-T11B-02-108.

References

- [1] see, B.L. Al'tshuler and A.G. Aronov, in *Electron-Electron Interaction in Disordered Systems*, edited by A.L. Efros and M. Pollak (North-Holland, Amsterdam, 1985), p. 1; H. Fukuyama, *ibid*, p. 155; P.A. Lee and T.V. Ramakrishnan, *Rev. Mod. Phys.* **57**, 287 (1985); D. Belitz and T.R. Kirkpatrick, *ibid* **66**, 261 (1994).
- [2] see, *Mesoscopic Phenomena in Solids*, edited by B.L. Al'tshuler, P.A. Lee, and R.A. Webb (Amsterdam, Elsevier, 1991); C.V.J. Beenakker and H. Van Houten, *Solid State Phys.* **44**, 1 (1991); S. Washburn and R.A. Webb, *Rep. Prog. Phys.* **55**, 1311 (1992).
- [3] A. Benoit, S. Washburn, R.A. Webb, D. Mailly, and L. Dumoulin, in *Anderson Localization*, edited by T. Ando and H. Fukuyama (Berlin, Springer, 1988), p. 346; C. Van Haesendonck, H. Vloeberghs, Y. Bruynseraede, and R. Jonchere, in *Nanostructures Physics and Fabrication*, edited by M.A. Reed and W.P. Kirk (Academic Press, Boston, 1989), p. 467; A. Benoit, D. Mailly, P. Perrier, and P. Nedellec, *Superlattices and Microstructures* **11**, 313 (1992); T. Dietl, G. Grabecki, and J. Jaroszynski, *Semicond. Sci. Technol.* **8**, S141 (1993).
- [4] P.G.N. de Veger and T.A. Fulton, *Phys. Rev. Lett.* **71**, 357 (1993); G. Grabecki, T. Dietl, W. Pleskiewicz, A. Lenard, T. Skokiewicz, E. Kamińska, and A. Piotrowska, *Physica B* **194-196**, 1107 (1994).
- [5] A.A. Bobkov, V.I. Falko, and D.E. Khmelnitskii, *Zh. Eksp. Teor. Fiz.* **98**, 703 (1990) [Sov. Phys.: JETP **71**, 393 (1990)]; V. Chandrasekhar, P. Santhanam, and D.E. Prober, *Phys. Rev. B* **42**, 6823 (1990); V.I. Falko, *J. Phys.: Condens. Matter* **4**, 3943 (1992).
- [6] A. Ramon, M. Heiblum and H. Shtrikman, *Semicon. Sci. Technol.* **8**, 2175 (1994).
- [7] G. Grabecki, S. Takeyama, S. Adachi, Y. Takagi, T. Dietl, E. Kamińska, A. Piotrowska, E. Papis, N. Frank and G. Bauer, *Japan J. Appl. Phys.*, in press.
- [8] R.B.S. Oakeshott and A. MacKinnon, *J. Phys. Condens. Matter* **6**, 1519, (1994); D. Weiss, K. Richter, E. Vasiliadou and G. Lütjering, *Surf. Sc.* **305**, 408 (1994).
- [9] M. Sawicki, T. Dietl, J. Kossut, J. Igłosion, T. Wojtowicz, and W. Pleskiewicz, *Phys. Rev. Lett.* **56**, 508 (1986).
- [10] see, e.g., T. Dietl, in *Handbook on Semiconductors*, edited by T.S. Moss, (North-Holland, Amsterdam, 1994), p. 1251.
- [11] see, J.A. Gai, W. Grieshaber, C. Bondin-Deshayes, J. Gibert, G. Feuillet, Y. Merle d'Aubigné and A. Wasieła, *Phys. Rev. B* **50**, 5512 (1994).
- [12] M.A. Novak, O.G. Symko, D.J. Zheng, and S. Oseroff, *J. Appl. Phys.* **57**, 3418 (1985).

Shot Noise in the Mesoscopic 2D Diffusive Systems in the Limit of Strong Electron-Electron Scattering

V.I.Kozub and A.M.Rudin
A.F.Ioffe Physico-Technical Institute, 194021, St.-Petersburg, Russia

Abstract

The shot noise power of a diffusive conductor in a presence of both strong inelastic electron-electron and electron-phonon scattering is calculated. It is shown, that electron-electron inelastic scattering does not suppress shot noise strongly and the noise power is $(\sqrt{3}/2)e|\bar{I}|$. In contrast to this, inelastic coupling with phonons affects the nonequilibrium current noise substantially leading to a non-linear deviation from a standard shot noise formulae.

Introduction

Electric current noise in small devices has attracted recently a substantial attention. Contribution to this noise proportional to the current itself and persisting down to zero temperatures is known as a shot noise. In the absence of correlations between the carriers, as it is, for instance, for tunnel junction, the noise power has a form analogous to the Poisson process ("full shot noise") $P_{\text{full}} = 2eV|G = \bar{G}V|$, where $\bar{I} = GV$ is the average current and G the conductance. All correlations reduce the shot noise, so that P remains below the full shot noise level. In perfect ballistic metallic systems the shot noise is completely suppressed due to Fermi correlation [1]. This clearly does not hold for not-perfectly transmitting systems, for which general expression for the shot noise power (current-noise spectral density) P in the case of full quantum coherence [2] was recently derived. In particular, the shot noise power in a disordered diffusive conductor with purely elastic electron scattering was shown [3] to be reduced with respect to the "full shot noise" level with the reduction factor $\gamma = 1/3$. All these papers mainly dealt with the situation of elastic electron scattering and it is generally believed that inelastic scattering leads to strong suppression of the shot noise.

In the present work we show that while inelastic coupling with phonons indeed suppresses shot noise strongly, electron-electron inelastic scattering, even being very effective, leads only to some change in its magnitude. As we will show, the results obtained are in excellent agreement with experiment [4], where a shot noise of 2D diffusive mesoscopic conductor in the limit of strong electron-electron interaction was studied.

Shot noise in the "electron temperature" approximation

Let us consider a diffusive conductor with a length L . In order to find an expression for the shot noise in this system we will use the semiclassical kinetic theory due to Gantsevich, Gurevich and Katinus [5], which allows to express the correlation function of the fluctuating distribution function $\bar{F}(\mathbf{r}, \mathbf{p}, t)$ in terms of the average over the temporal fluctuations $\langle F \rangle \equiv \bar{F}(\mathbf{r}, \mathbf{p}, t)$. This average is the solution of the Boltzmann equation, which we, for simplicity,

$$\frac{d}{dt} \bar{F}(\mathbf{r}, \mathbf{p}, t) = -\bar{f}_p^{\text{coll}} \{ \bar{F}(\mathbf{r}, \mathbf{p}, t) \}, \quad (1)$$

where the derivative $(d/dt) \equiv (\partial/\partial t) + v_x(\partial/\partial x) + eE(\partial/\partial p)$ accounts for semiclassical motion of an electron with momentum $\mathbf{p} = mv$ in the electric field E . $\bar{f}_p^{\text{coll}} = \bar{f}_p^{\text{ee}} + \bar{f}_p^{\text{ep}}$ is the collisional operator, which includes terms responsible for impurity scattering (i_m), electron-phonon (e_p), and electron-electron (ee) interaction. We assume stationary Fermi distribution \bar{f}_p in the leads of the conductor as the boundary conditions for Eq. (1):

$$\bar{F}(\pm(L/2), \mathbf{p}, t) = f_F(\epsilon_p - \mu_{\pm}, T_{\text{bath}}), \quad \mu_{\pm} = \mu_0 \pm \frac{eV}{2}, \quad (2)$$

where μ_0 is the chemical potential of the electron gas in the absence of the bias, T_{bath} is the thermal bath temperature. Note that the boundary conditions of such form imply that the channel length L is much larger than the channel width.

It is a rather hard task to solve Eq. (1). In order to simplify the problem, we consider the situation, when electron-electron scattering is effective enough to make description in terms of electron temperature possible. On the other hand, that the momentum relaxation, and, therefore, relaxation of \bar{F}^- , is governed mainly by scattering on impurities, not on phonons or other electrons. In other words, we assume $\tau_{im} \ll \tau_{ee}$ and $\tau_{im} \ll \tau_{ep}$ to hold, where τ_{im} , τ_{ee} , τ_{ep} are characteristic times for corresponding scattering processes. In this approximation even with respect to $\mathbf{p} \rightarrow -\mathbf{p}$ transformation part of the electron distribution has the Fermi form along the whole sample:

$$\bar{F}(\mathbf{r}, \epsilon_p) = f_F(\epsilon_p - \mu(\mathbf{r}), T_e(\mathbf{r})) \quad (3)$$

with chemical potential $\mu(\mathbf{r}) \approx (eV/L)x$ and temperature $T_e(\mathbf{r})$, which depend on coordinate and on the voltage applied, while odd with respect to this transformation part is considered as small. The task reduces in this case to calculation of electron temperature profile $T_e(x)$ along the sample. The most direct way to do this is to derive the equation for the total energy of quasiparticle gas, which is uniquely related to T_e .

Let us first neglect electron-phonon interaction. Making use of the relaxation time approximation for the impurity scattering $\bar{f}_p^{\text{im}}\{F\} = F/\tau_p$, we can obtain the equation for $\bar{F}(\mathbf{r}, \epsilon_p)$. Then we multiply all terms in this equation by quasiparticle energy $\epsilon_p - \mu$ and sum over all ϵ_p . The final equation for the obtained this way total energy of quasiparticle gas takes the form:

$$D \frac{\partial^2}{\partial x^2} \sum_{\epsilon_p} (\epsilon_p - \mu) \bar{F}(\mathbf{r}, \epsilon_p) + (eE)^2 D \sum_{\epsilon_p} (\epsilon_p - \mu) \frac{\partial^2 \bar{F}(\mathbf{r}, \epsilon_p)}{\partial \epsilon_p^2} = 0, \quad (4)$$

where $D = v_F^2 \tau_p / 3$ is a diffusion coefficient. Both terms of Eq. (4) have a straightforward physical meaning. First one is a diffusion term, while the second is a Joule source of heat. Deriving Eq. (4) we have taken into account that electron-electron collisions conserve the total energy of quasiparticle gas and thus $\sum_{\epsilon_p} (\epsilon_p - \mu) \bar{f}_p^{\text{ee}} \bar{F}(\mathbf{r}, \epsilon_p) = 0$. Summation in Eq. (4) results in the equation for $T_e(\mathbf{r})$:

$$\frac{\pi^2}{6} \frac{\partial^2}{\partial x^2} [T_e(\mathbf{r})]^2 + (eE)^2 = 0. \quad (5)$$

Making use of the boundary conditions (compare with Eq. (2)) $T_d(x = \pm L/2) = T_{\text{bulk}}$ and $E = V/L$ we finally obtain the expression, which describes the electron temperature profile along the sample. In the most interesting case $eV \gg T_{\text{bulk}}$ this takes the form:

$$T_d(x) = \frac{\sqrt{3}}{2\pi} e|V| \sqrt{1 - \left(\frac{2x}{L}\right)^2}. \quad (6)$$

At this point we have found the explicit form of the nonequilibrium distribution function.

Now we will calculate the shot noise power in the conductor in a way similar to that used by Nagaev [3]. Current density in the point \mathbf{r} of the conductor is $\mathbf{j}(\mathbf{r}, t) = (e/\Omega_0) \sum_{\mathbf{p}} \mathbf{v}_p F(\mathbf{r}, \mathbf{p}, t)$, where $F(\mathbf{r}, \mathbf{p}, t)$ is a non-averaged over temporal fluctuations electron distribution function, the conductor is $I(t) = (S/\Omega_0) \int d^3\mathbf{r} j_z(\mathbf{r}, t)$. Therefore, zero-frequency shot noise power equals to

$$\begin{aligned} P &= 4 \int_0^\infty dt \langle \delta I(t) \delta I(0) \rangle \\ &= 4 \frac{e^2}{S^2 L^4} \int d^3\mathbf{r} d^3\mathbf{r}' \sum_{\mathbf{pp}'} v_z v'_z \int_0^\infty dt \langle \delta F(\mathbf{r}, \mathbf{p}, t) \delta F(\mathbf{r}', \mathbf{p}', 0) \rangle, \end{aligned} \quad (7)$$

where $\delta F = F - \bar{F}$. According to the kinetic theory [5] and within the electron temperature approximation we use throughout this paper

$$\int_0^\infty dt \langle \delta F(\mathbf{r}, \mathbf{p}, t) \delta F(\mathbf{r}', \mathbf{p}', 0) \rangle = \Omega_0 \delta(\mathbf{r} - \mathbf{r}') \tau_p \bar{F}(\mathbf{r}, \mathbf{p}) [1 - \bar{F}(\mathbf{r}', \mathbf{p}')] \delta_{\mathbf{pp}'}.$$
 (8)

After integration in Eq. (7) with account of Eq. (3) we arrive at the result:

$$P = \frac{4G}{L} \int_{-L/2}^{L/2} dx \int_0^\infty d\epsilon_p \bar{F}(x, \epsilon_p) [1 - \bar{F}(x, \epsilon_p)] = \frac{4G}{L} \int_{-L/2}^{L/2} dx T_d(x). \quad (9)$$

Here $G = e^2 D(\nu_F/\Omega_0)(S/L)$ is the total conductance, ν_F density of electron states at the Fermi level. Taking into account the obtained earlier profile of $T_d(x)$, Eq. (6), we arrive at the final expression for the shot noise power in the diffusive conductor in the presence of strong electron-electron scattering:

$$P_{ee} = \frac{\sqrt{3}}{2} e|V|G. \quad (10)$$

The obtained value is only $4/\sqrt{3}$ times smaller than the “full shot noise” level P_{full} , which corresponds to the reduction factor $\gamma = 0.43$. Therefore, electron-electron inelastic scattering, even being very effective, does not suppress shot noise strongly and lead only to not too large change in its magnitude.

Shot noise under phonon emission conditions

Until now we have neglected electron-phonon interaction. It is clear that this interaction results in decay of the electron gas energy and thus in reduction of $T_d(x)$. If the electron

diffusion length with respect to electron-phonon collisions $l_d(e \approx eV) = \sqrt{D \tau_{ep}(e \approx eV)}$ is smaller than L this channel of energy decay is substantial and strongly affects current noise spectrum making it nonlinear in voltage. Explicit form of this non-linearity depends on the type of the diffusive conductor. We will consider the case of 2D electron gas in semiconductor.

Account for electron-phonon interaction leads to an additional term in l.h.s. of Eq.(4), which corresponds to a decay of the total electron gas energy due to phonon emission per unit time Q_{2D}^{sp} . The momentum must be conserved only in the plane of 2DEG, while in the other direction (z -axis) this is not necessary. Under this condition and assuming $T_d \gg T_{\text{bulk}}$ straightforward calculation gives:

$$Q_{2D}^{\text{sp}} \approx \left(\frac{T_d}{\epsilon_F}\right)^2 \left(\frac{T_{\text{el}}d}{\hbar s}\right)^2 \frac{T_d^2}{m_e s^2 \tau_{\text{bulk}}^{\text{sp}}} \propto T_d^6, \quad (11)$$

where m_e is the electron effective mass, s - sound velocity, d is the thickness of 2DEG, $\tau_{\text{bulk}}^{\text{sp}}$ is the mean time of phonon emission by the electrons with the energy $\approx \epsilon_F$ in the bulk semiconductor. Finally, we have

$$\bar{T}_d^{\text{sp}} \approx [GV^2 m_e s^2 \tau_{\text{bulk}}^{\text{sp}} \epsilon_F^2 (\hbar s/d)^2]^{1/6} \propto V^{1/3}. \quad (12)$$

Zero-frequency shot noise power, Eq. (9), in this limit equals to $P = 4G \bar{T}_d^{\text{sp}} \propto V^{1/3}$.

Our results are in excellent agreement with recent experiment by Liefink et al., Ref. [4], where $\gamma \approx 0.45$ was found in the limit of weak electron-phonon scattering. This value is very close to that given by our Eq. (10). With relative increase of the electron-phonon interaction the authors of Ref. [4] observed the systematic deviation of γ towards smaller values, which is in accordance with our results.

References

- [1] I.O.Kulinik and A.N.Omel'yanichuk, *Fiz. Nizk. Temp.* **10**, 305 (1984) [Sov. J. Low. Temp. Phys. **10**, 158 (1984)].
- [2] V.A.Khlas, Zh. Eksp. Teor. Fiz. **93**, 2179 (1987) [Sov. Phys. - JETP **66**, 1243 (1987)]; G.B.Lesovik, Pis'ma Zh. Tekn. Fiz. **49**, 513 (1989) [JETP Lett. **49**, 592 (1989)]; M.Büttiker, *Phys. Rev. Lett.* **65**, 2901 (1990).
- [3] C.W.J.Benaakker and M.Büttiker, *Phys. Rev. B* **46**, 1889 (1992); K.E.Nagaev, *Phys. Lett. A* **169**, 103 (1992).
- [4] F.Liefink, J.I.Dijkhuis, M.J.M.de Jong, L.W.Molenkamp, and H.van Houten, *Phys. Rev. B* **49**, 14066 (1994).
- [5] S.V.Gantsevich, V.L.Gurevich, and R.Katilus, *Rivista Nuovo Cimento* **2** (5), (1979); E.M.Lifshitz and L.P.Pitaevskii, *Physical Kinetics* (Pergamon, Oxford, 1981).

TEMPORALLY CORRELATED TRANSPORT AND SHOT NOISE SUPPRESSION IN A BALLISTIC QUANTUM POINT CONTACT

M. Reznikov, M. Heiblum, Hadar Shtrikman and D. Mahalu

Braun Center for Submicron Research, Dept. of Condensed Matter Physics
Weizmann Institute of Science, Rehovot 76100, Israel

Wide band shot noise, associated with DC current flow through a quantum point contact (QPC), is measured in the microwave frequency range of 8 - 18 GHz. As the number of conducting channels in the QPC changes, the noise power oscillates, with almost zero value at the conductance plateaus. Consistent with existing theories the noise peaks depend linearly on the DC current. Surprisingly, however, in the pinch off region, where QPC is expected to behave as a classical injector, we find strong noise suppression, possibly mediated by the Coulomb interaction in the QPC region.

It is well known that the conductance of a QPC, e.g. a smooth one dimensional (1D) constriction made in a two dimensional electron gas, is quantized in units of $2e^2/h$. This quantization is a direct result of almost perfect transmission ($T \approx 1$) through the 1D channels confined in the QPC. Aside from that quantization, it was predicted by Khlus [1] and Lesovik [2] that when $T = I$ another remarkable effect is taking place: a total suppression of shot noise in the QPC. The shot noise, originating from the granularity of the electrons and their stochastic injection, is characterized by averaged squared current fluctuations. In classical systems such as the vacuum diode where electron emission can be considered as a truly stochastic (Poisson like) process, the average of the squared current fluctuations, Δi , measured in a frequency range Δv , is given by the *classical shot noise* expression $S(v) \cdot \Delta v = \langle (\Delta i)^2 \rangle_{\Delta v} = 2eI \cdot \Delta v$. $S(v)$ is the white (frequency independent) spectral density and I the average current. In a QPC the theoretically obtained low frequency spectral density of the current fluctuations, at zero temperature θ , for energy independent T_i 's is [1-3]:

$$S(v=0) = 2e^2 \cdot \frac{2e^2}{h} \cdot V_{ns} \cdot \sum_{i=1}^N T_i (1 - T_i), \quad k_B \theta < eV_{ns}, \quad (1)$$

with V_{ns} the voltage across the QPC, N the number of occupied channels in the QPC and T_i the transmission coefficient through the channel i . Since $\frac{2e^2}{h} \cdot V_{ns} \cdot T_i = I_i$ is the i 'th channel current, a noise suppression of $(1 - T_i)$, relative to the classical noise for the i 'th channel, is expected. In an experiment where the T_i 's are continuously varied, the shot noise is expected to have a maximum (half of the classical shot noise due to one channel) whenever the transmission of the uppermost conducting channel is 1/2. Note that the frequency dependence of $S(v)$ was shown (neglecting Coulomb interactions between electrons) to decrease linearly with v with $S(v_{cutoff}) = 0$ for $\hbar v_{cutoff} = eV_{ns}$ (i.e., for $V_{ns} = 1 \text{ mV}$, $v_{cutoff} \approx 250 \text{ GHz}$) [4].

Several attempts to measure shot noise in a QPC [5,6] were published. However, they had been restricted to low frequencies ($v < 100 \text{ kHz}$) where *1/f* noise or fluctuations and instabilities of the conductance are dominant. Moreover, the noise power was found to have a square

dependence on the DC current and not the expected linear dependence. A linear dependence, though, was observed for noise measured in diffusive mesoscopic conductors [7].

First some order of magnitude estimates. The injected DC current, I_{in} , and the applied voltage, V_{ns} , should be as small as possible in order to: (a) prevent electron heating, and (b) prevent injection into higher 1D channels. However, the applied voltage V_{ns} should be greater than $K_B \theta / e$ in order to make Eq. (3) applicable. For example, $V_{ns} = I_{in} mV$ leads, according to Eq. (3), to a peak noise $S(\theta) = 6.2 \cdot 10^{-2} \cdot A^2 / Hz$. At high enough frequencies this *shot noise signal* has to compete with the noise of the amplifiers. Even a cold amplifier has an equivalent noise temperature of 40 K at its 50 Ω input impedance, leading to a spectral density of unwanted noise $k_B \theta / 50 = 10^{-21} \cdot A^2 / Hz$, more than three orders of magnitude higher than the shot noise we are searching for. Consequently, in order to improve the *signal-to-noise ratio* (S/N) we modulate the DC current through the QPC at a low frequency f (less than 1 kHz) and measure the amplified noise, synchronously with f , using a lock in technique. It turns out that the wide band measurements improve the S/N relative to the ratio of the spectral densities given above by a factor of $(\Delta v / \Delta f)^{1/2}$, where Δf is the low frequency bandwidth (determined by the time constant of the lock-in amplifier). We thus expect that measuring the shot noise synchronously, in a band $v = 8 - 18 \text{ GHz}$ ($\Delta v = 10 \text{ GHz}$) with $\Delta f < 1 \text{ Hz}$ will improve the S/N ratio by a factor of $(I - 3) \cdot 10^5$, leading to an acceptable $S/N \approx 10^2$.

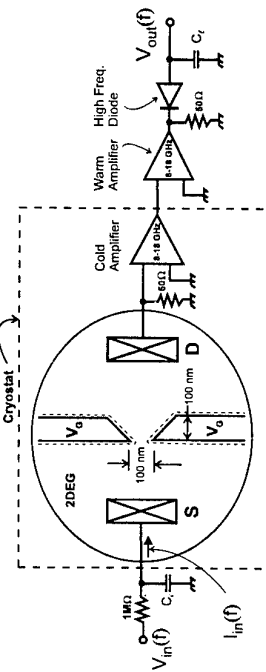


Fig. 1.

The experimental setup. The voltage V_G controls the number of 1D conducting channels in the QPC. The current, modulated at low frequency f , is provided to the QPC via a variable current source, with a voltage $V_{as(f)}$ appearing across the QPC. A high frequency path to ground is provided via a capacitor C_p .

Our QPC is induced electrostatically in the plane of a 2DEG, embedded in a GaAs - AlGaAs heterostructure only 33 nm below the surface. The 2DEG has an area electron density of $4.6 \cdot 10^{14} \text{ cm}^{-2}$ and a low temperature mobility of $5 \cdot 10^5 \text{ cm}^2 / Vs$. The QPC is formed by direct electron beam writing and metal gate (TiAu) deposition, with a 100 nm gap between two gates (shown schematically in Fig. 1). The voltage V_G , applied to the gates via a low pass filter with

an upper frequency of 1 MHz , controls the number of 1D conducting channels in the QPC. The DC voltage drop across the sample was monitored during the measurement with a lock-in amplifier and was kept constant via a feedback loop (taking into account series contact resistance). Similarly, the DC current was kept constant by monitoring the DC voltage drop on a series $1 \text{ M}\Omega\text{m}$ resistor. Note that high frequency path to ground is provided via the capacitor C_{hs} effectively maintaining a **constant voltage** on the sample. The high frequency current fluctuations are amplified in the $8 - 18 \text{ GHz}$ band, and are finally applied to a high frequency diode and a load capacitor C_r . The low frequency output $V_{\text{out}}(f) \propto <(\Delta t)^2>_{\text{noise}}$ is converted, after a calibration of the system gain and the diode sensitivity, to the spectral density at the input $S / \text{A}^2/\text{Hz} f$.

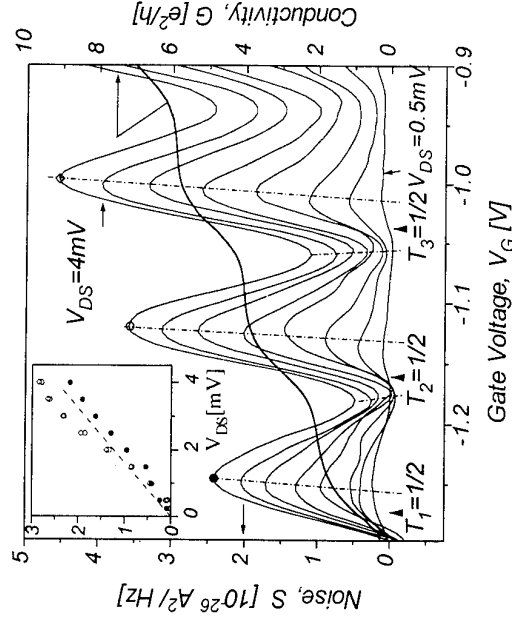


Fig. 2.

Noise spectral density $S(f)$ and normalized linear conductance G , measured with current 10nA vs. gate voltage V_G . The noise is measured for $V_{\text{DS}} = 0.5, 1, 2, \dots, 4 \text{ mV}$. The lines through the maxima and minima of the peaks are only guides to the eye. Positions of $T_1, 1/2$, where the noise maxima are theoretically expected to be, are marked with arrows. Inset: Dependence of the peaks height (same scale as in main figure) on injection voltage V_{DS} . \bullet , \circ , \diamond mark the first three conducting 1D channels. The dashed straight line is the predicted behavior.

Typical results for the DC conductance G and the noise signal $V_{\text{out}}(f)$, measured as a function of gates voltage V_G , at $T = 1.5 \text{ K}$, are shown in Fig. 2. The linear conductance is quantized in units of $2e^2/h$, after subtracting the series resistance of the ohmic contacts. The **noise - signal**, $S \propto V_{\text{out}}(f)$, is measured for different injection voltages, V_{DS} . As predicted by Eq. (3), keeping V_{DS} **constant** allows the injected current $I_m(f)$ to change

as the conductance of the QPC varies, leading to a noise dependence proportional to $T(l-T)$. Indeed the measured **noise - signal**, as a function of V_G and for different V_{DS} , exhibits strong oscillations. The magnitude of the peaks (each peak relative to the average of two adjacent minima) grows almost linearly with the current, as seen in the inset of Fig. 2. This linear dependence of the spectral density agrees with Eq. (3) also quantitatively and is a crucial fact in substantiating the origin of the noise.

Even though the peaks magnitude agree rather well with the predicted noise maxima, being $(l/4) \cdot 2e^2 \cdot (2e^2/h) \cdot V_{\text{DS}}$, the peak positions (and respective minima) shift from the predicted positions at V_G ($T_l=1/2$) and $T_l=1$ for the minima) to V_G (*higher* T_l 's) - a shift that increases with V_{DS} . This shift is not understood yet. As possible explanations one may consider injection into the upper channel of the QPC, mediated by the finite temperature and injection voltage, thus leading to added noise from this channel and to an apparent shift in the peaks position. However, the fact that the measured **noise - signal** for relatively small injection voltages drops almost to ‘zero’ at the minima, implies that $T_l=1$, $T_{i,l} \approx 0$ at the minima, making the above hypothesis questionable. Another possible explanation for the shift is the finite temperature and the fact that T is energy dependent ($T=T(E)$) [8,9]. Taking this into account we find that the calculated noise peaks shift toward **smaller** T 's, contrary to our data.

We performed detailed investigations of the noise in the *pinch off* region of the QPC, namely, when all carriers are depleted from the QPC and transport is via tunneling or via thermally assisted emission. As the gate voltage becomes more negative and the resistance of the QPC increases, the current and its fluctuations tend to zero. We thus performed noise measurements at a **constant current**, I , expecting to get the behavior $S=2eI \cdot (l-T_l)$, which is nearly classical when $T_l < l$. Contrary we find that the noise tends to saturate and become **independent** of the DC current above 100 nA ; contradictory to the expected *classical* behavior. Since at this regime the estimated *dwell time* in the QPC is similar to e/I (the *impinging time interval*) we suggest that **Coulomb repulsion** between the electrons leads to temporally correlated transport in the pinched QPC and thus to *noise suppression*.

References

- [1] V.A. Khlyus, Sov. Phys. JETP **66**, 1243 (1987).
- [2] G. B. Lesovik, JETP Lett. **49**, 592 (1989).
- [3] M. Buttiker, Phys. Rev. Lett. **65**, 2901 (1990).
- [4] G. B. Lesovik and L. S. Levitov, Phys. Rev. Lett. **72**, 538 (1990).
- [5] Y. P. Li et al., Appl. Phys. Lett. **57**, 774 (1990).
- [6] F. Lielink, J. I. Dijkhuis and H. van Houten, Semicond. Sci. Technol. **9**, 2178 (1994), and references therein.
- [7] F. Lielink et al. Phys. Rev. B **49**, 14066 (1994).
- [8] R. Landauer and Th. Martin, Physica B **175**, 167 (1991).
- [9] G. B. Lesovik and R. Loosken, Zeitschrift für Physik, B **91**, 531 (1993).

Phase Breaking in Ballistic Quantum Dots: A Correlation Field Analysis

J.P. Bird¹, K. Ishibashi², R. Newbury³, D.K. Ferry², R. Ochiai⁴, Y. Aoyagi¹, &

T. Sugano¹

1: Nanoelectronics Materials Laboratory, Frontier Research Program, RIKEN, 2-1 Hirosawa,

Wako, Saitama 351-01, JAPAN

2: Center for Solid State Electronics Research, Arizona State University, AZ 85287-6206, USA

3: School of Physics, University of New South Wales, Sydney 2052, AUSTRALIA

4: Department of Materials Science, Chiba University, Inage-ku, Chiba 263, JAPAN

We use a novel technique to determine the phase breaking time (τ_ϕ) of electrons in ballistic quantum dots, from the aperiodic fluctuations observed in their low temperature magneto-resistance. At temperatures below 100 mK, roughly similar values of τ_ϕ are obtained in both sizes of dot studied, suggesting a strong materials related influence on τ_ϕ . Analysing the temperature dependent characteristics of the fluctuations, τ_ϕ is found to scale roughly inversely with temperature close to a degree Kelvin, reminiscent of electron-electron scattering in two dimensional disordered systems. At much lower temperatures, however, a saturation in τ_ϕ is observed, and is thought to result from a transition from two to zero dimensional transport, which occurs as the discrete level structure of the dot becomes resolved.

1. Introduction

Electron interference is an important process in determining the electrical properties of mesoscopic devices, in which phase coherence of the electron wavefunction is maintained over considerable distances [1]. A useful quantity for characterising the interference is the phase breaking time (τ_ϕ), the time scale over which the phase of electrons is typically conserved, and a thorough understanding of the processes which limit τ_ϕ is therefore crucial to a full description of transport. In the case of ballistic quantum dots no well established theory for phase breaking exists, and in this report we therefore discuss a novel experimental approach for determining τ_ϕ in such devices. In particular, we obtain values for τ_ϕ from the reproducible fluctuations, observed in the low temperature magneto-conductance of the dots [2]. The fluctuations result from interference between electrons, ballistically confined within the dot, and their properties have recently attracted much interest as a potential probe of quantum chaos [3]. In a previous study, estimates for τ_ϕ were obtained from the Fourier spectra of the fluctuations in a stadium shaped dot [2]. The approach the authors employed is only valid if the motion of classical particles in the geometry is chaotic, however, and a more general analysis, independent of device geometry, is therefore required. In this report we formulate such a model, by considering the high field characteristics of the fluctuations. More specifically, as the magnetic field is increased, such that the cyclotron orbit size becomes smaller than the dot dimensions, a transition to edge-state transport occurs. Considering electron motion in this regime to occur via ballistic skipping orbits, we then obtain values for τ_ϕ from the corresponding, magnetically induced shrinkage in the effective area for coherent interference [4]. Values of τ_ϕ deduced in this fashion are then found to provide important information, on the origin of phase breaking in ballistic dots.

2. Sample Fabrication and Basic Experimental Results

Split gate quantum dots were realised in a GaAs/AlGaAs heterojunction, using standard electron-beam lithographic techniques [5]. The wafer was patterned in to a Hall bar geometry, with a typical carrier density 4.10^{15} m^{-2} , and mobility $40 \text{ m}^2/\text{V}\cdot\text{s}$. The gates consisted of a stub like design, in which a lithographically square dot was separated from the source and drain by quantum point contacts (Fig. 1 inset). Independently tunable dots, with lithographic dimensions 0.6- and $1.0\text{-}\mu\text{m}$ were defined within close separation on the same Hall bar. The dots were therefore considerably smaller than the calculated mean free path in the bulk wafer ($5 \text{ }\mu\text{m}$), and in a previous study we demonstrated the ballistic nature of transport in the devices [6]. Samples were clamped to the mixing chamber of a dilution refrigerator, and audio frequency magneto-

transport measurements were made at cryostat temperatures down to 10 mK. The four probe configuration employed [5] included a series contribution due to the source and drain regions, and at low magnetic fields the resistance of this was much smaller than that of the dot. At higher fields, however, the configuration was only sensitive to the edge state transmission of the dot. Great care was taken to ensure good thermal contact to the samples, and a source-drain excitation of less than $3 \text{ }\mu\text{V}$ was employed for the current bias measurements. As an example of the typical behaviour, observed in the different dots at low temperatures, consider the magneto-conductance traces shown in Fig. 1. Reproducible, aperiodic fluctuations persist across the entire range of magnetic field, and at suitably low fields the average amplitude and period of these are independent of magnetic field. As the magnetic field is increased, however, a marked increase in the average period of fluctuation can be clearly resolved in the raw data (also see Fig. 2 inset).

3. Correlation Field Analysis of τ_ϕ

In order to place the above observations on a quantitative footing, we first define the correlation function of the fluctuations [3]:

$$F(\Delta B) = \langle g(B) \cdot g(B + \Delta B) \rangle - \langle g(B) \rangle \langle g(B + \Delta B) \rangle, \quad [1]$$

where $g(B)$ is the conductance in units of e^2/h and at magnetic field B , and the angled brackets indicate an average over a suitably large field range. The correlation field B_c is then defined from the half-width of the correlation function $F(B_c) = F(0)/2$, while the root mean square amplitude of fluctuation $\delta g = \sqrt{F(0)}$. In Fig. 2 we show typical correlation functions, obtained by analysing the fluctuations over distinctly different magnetic field ranges. These reveal a strong field induced increase in B_c and, plotting the evolution of B_c with magnetic field, it can be seen that B_c increases roughly linearly at higher fields (Fig. 3).

A magnetically induced increase in B_c implies a corresponding reduction in the area over which coherent interference occurs, and is understood to be related to the formation of edge states at high fields [5, 7]. In particular, as the magnetic field is increased, such that the cyclotron orbit size becomes smaller than the dot dimensions, electronic motion should exhibit a transition to ballistically propagating, skipping orbits. The characteristic area for interference is then essentially determined by that enclosed between the dot walls and the skipping trajectories. Considering the path of an average electron, we obtain the coherent area $A_c = 0.5[N\pi r_c^2]$, where N is the average number of bounces made before losing phase coherence, and $r_c = \hbar k_F/2eB$ is the cyclotron radius (Fig. 3 inset). Since the phase breaking length can be written as $l = v_F \tau_\phi = N\pi r_c$, this then leads to the correlation field:

$$B_c(B) = [\pi R^2 m^* B / \hbar k_F v_F], \quad [2]$$

where m^* is the effective electron mass, and v_F is the Fermi velocity. Under conditions where τ_ϕ remains field independent, we therefore expect a linear field dependence to B_c , in good agreement with the behaviour we observe experimentally (Fig. 3). More importantly, however, from the slope of the straight line graph we can obtain an estimate for τ_ϕ in the dots.

4. Discussion

While space limitations prevent us from presenting a full analysis here, application of the above considerations to the results of Fig. 1 yields $\tau_\phi = 0.38 \text{ ns}$ and $\tau_\phi = 0.26 \text{ ns}$, for the $0.6-$ and $1.0\text{-}\mu\text{m}$ dots respectively. These values are in rough agreement with each other, suggesting that τ_ϕ in the dots is largely dominated by the properties of the host semiconductor, although further studies are required to establish whether the 50% difference in the deduced values actually reflects the influence of some additional process. In particular, in addition to phase breaking processes occurring within the dot, at suitably low temperatures it is also possible that the deduced value of τ_ϕ is influenced by the escape of electrons from the dot [2, 3]. With regards to this possibility, however, it seems reasonable that we would then obtain a lower value of τ_ϕ in the smaller dot, in which the point contact openings represent a larger fraction of the total dot perimeter, whereas we actually deduce a slightly larger value. We therefore once again

emphasise the need for more detailed experimental studies, characterising the dependence of τ_ϕ on both dot size and point contact opening.

We have also determined the temperature dependence of τ_ϕ , by measuring the corresponding dependence of the fluctuations in a 1- μm dot, and the results of such an analysis are summarised in Fig. 4. From this it is clear that the phase breaking time exhibits two distinct regimes of temperature dependent behaviour. Around a degree Kelvin τ_ϕ is inversely proportional to temperature $\tau_\phi(T) = 0.03/T(\text{K})$, reminiscent of electron-electron scattering in two dimensional disordered systems [8]. This is also in quantitative agreement with the results of a recent study [9], but is in contrast to a theoretical analysis for *diffusive* dots [10]. As the temperature is lowered below 150 mK, τ_ϕ ultimately becomes independent of temperature. We emphasise that this saturation does not result from a loss of thermal contact to the sample, since other features in the magneto-conductance showed consistent changes down to at least 30 mK [5]. An intrinsic origin is therefore the likely explanation, and we suggest an interpretation based upon a dimensional crossover of transport.

In particular, the dimensionality of a given system can be rigorously defined by appealing to the form of its density of states. In a quantum dot at sufficiently low temperatures this is zero dimensional in nature, due to the complete quantisation of motion in to discrete energy levels. For a dot of cross sectional area A the average level splitting $\Delta = \hbar^2/2\pi m^* A$ and, taking in to account the expected fringing field around each gate [5], we obtain $\Delta/k_B = 130 \text{ mK}$ for the 1- μm dot we study. As can be seen from Fig. 4, this calculated temperature is almost precisely equivalent to that, at which the transition is observed to occur in the measured values of τ_ϕ . In other words, the saturation in τ_ϕ appears to correspond to a transition, from two to zero dimensional phase breaking, which occurs as the discrete levels of the dot become resolved (a fuller discussion of this issue will be given elsewhere [11].)

5. Conclusions

We have used a novel technique to determine the phase breaking time of electrons in ballistic quantum dots. Roughly similar values of τ_ϕ were obtained in both sizes of dot studied, suggesting a strong materials related influence on τ_ϕ , although further experimental studies are required to investigate the influence of escape from the dot. Analysing the temperature dependent characteristics of the fluctuations, τ_ϕ was found to scale roughly inversely with temperature close to a degree Kelvin, reminiscent of electron-electron scattering in two dimensional disordered systems. At much lower temperatures, however, a saturation in τ_ϕ was observed, with the transition between the two regimes occurring once the thermal smearing becomes smaller than the expected level spacing in the dot. The saturation is therefore thought to result from a transition from two to zero dimensional transport, as the discrete level structure of the dot becomes resolved.

- [1] For a suitable review see C W J Beenakker and H van Houten, Solid State Physics **44** (1991) 1.
- [2] CM Marcus, RM Westervelt, PF Hopkins, and AC Gossard, Phys. Rev. B **48** (1993) 2460.
- [3] RA Jalabert, HU Baranger, and AD Stone, Phys. Rev. Lett. **65** (1990) 2442.
- [4] CV Brown, AK Geim, TJ Foster, CJGM Langerak, and PC Main, Phys. Rev. B **47** (1993) 10935.
- [5] JP Bird, K Ishibashi, M Stopa, Y Aoyagi, and T Sugano, Phys. Rev. B **50** (1994) 14983.
- [6] JP Bird, K Ishibashi, Y Aoyagi, T Sugano, and Y Ochiai, Phys. Rev. B **50** (1994) 18678.
- [7] DK Ferry, G Edwards, Y Ochiai, K Yamamoto, JP Bird, K Ishibashi, Y Aoyagi, and T Sugano, Jap. J. Appl. Phys., in press.
- [8] BL Alshuler, AG Aronov, and DE Khmel'nitsky, J. Phys. C **15** (1982) 7367.
- [9] RM Clarke, IH Chan, CM Marcus, CJ Duruoz, JS Harris Jr., K Campman, and AC Gossard, submitted for publication.
- [10] U Sivan, Y Imry, and AG Aronov, Europhys. Lett. **28**, 115 (1994).
- [11] JP Bird, K Ishibashi, DK Ferry, Y Aoyagi, and T Sugano, Phys. Rev. B, in press.

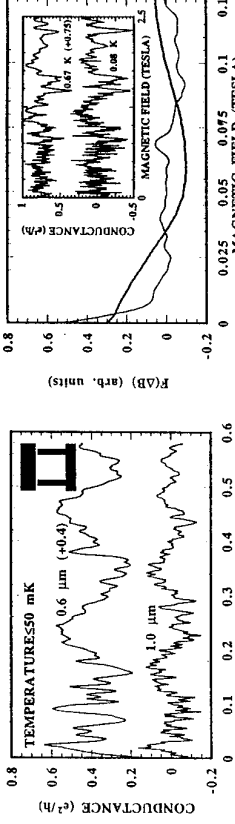


Fig. 1: Conductance fluctuations measured in 0.6- and 1.0- μm quantum dots. In both cases the traces were obtained by subtracting a smoothed polynomial fit from the raw data, leaving conductance fluctuations with an average value of zero. The gate voltage was adjusted in both measurements to give zero field dot-resistance of order 20 k Ω . Inset; Schematic of the split gate geometry employed in the devices.

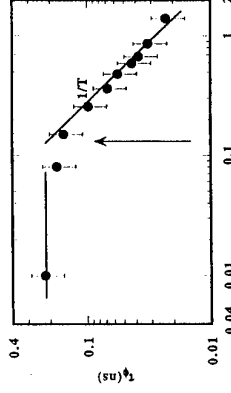


Fig. 2: Inset; Conductance fluctuations obtained in a separate 1- μm dot to that of Fig. 1. The traces were again obtained by subtracting a smoothed polynomial fit from the raw data, with an average resistance of roughly 16 k Ω . Note the high degree of reproducibility of the measurements, as evidenced by the common features in both traces. Main Figure; Plotting the correlation function of the fluctuations, shown in the inset, over two distinct field ranges reveals a marked increase in B_c with magnetic field (Temperature: 0.67 K, Thin Line: 0.00-0.25 T, Solid Line: 2.25-2.50 T.)

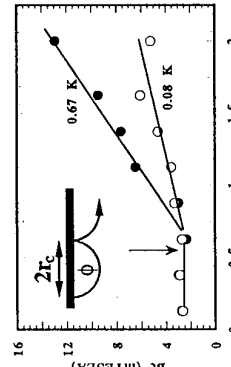


Fig. 3: Evolution of the correlation field B_c with magnetic field, for the 1- μm dot of Fig. 2. As the magnetic field is increased, however, B_c becomes field dependent once the cyclotron orbit size $2r_c$ becomes smaller than the effective "radius" of the dot (0.4 μm , marked by the arrow in the figure.) Inset; Schematic diagram showing the formation of skipping orbits at the dot walls. Each phase coherent bounce encloses magnetic flux Φ .

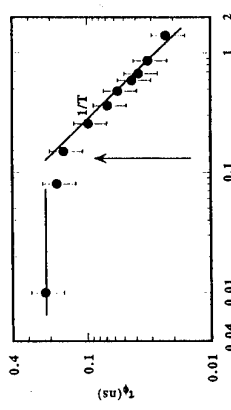


Fig. 4: Deducing temperature dependence of the phase breaking time τ_ϕ in the 1- μm quantum dot of Fig. 2. The arrow marks the temperature at which the thermal broadening $k_B T$ is calculated to be comparable to the mean level spacing Δ in the dot.

Multifractal Statistics of Eigenstates of 2D Disordered Conductors

Vladimir I. Fal'ko¹ and K.B. Efetov²

¹ Max-Planck-Institut für Fesökperforschung Heisenbergstr. 1, 70569 Stuttgart, Germany

² Max-Planck-Institut für Physik Komplexe Systeme, Heisenbergstr. 1, 70569 Stuttgart, Germany

We study the manifestation of pre-localized states in the distribution of local amplitudes of wave functions of a 2D disordered metal. Although the distribution of comparatively small amplitudes obeys the universal laws known from the random matrix theory, its large-amplitude tails are non-universal and have the logarithmically-normal dependence. The inverse participation numbers (IPN) calculated on the basis of the exact form of the distribution function in the weak localization regime indicate the multifractal behavior.

Our calculation is based on the derivation of the non-trivial saddle-point of the reduced supersymmetric σ -model.

The ideas of the fractal and multifractal analysis has penetrated to the theory of disordered systems for characterizing the complexity of wave functions in the vicinity of the localization transitions [1]. Due to the progress in numerical simulations, it has been recognized that, at criticality, the wave functions are really multifractal which gives rise to a spectrum of critical exponents [2]. Since the dimension $d = 2$ is commonly believed to be a critical one, the multifractal states have to be represented in 2D conductors at weak disorder manifesting the tendency of the system to show the localized behavior at long distances. This, probably, was the origin of the non-Gaussian distribution of fluctuations of the local density of states predicted in Ref. [3]. The analytical basis for the concept of multifractality is provided by the non-trivial dependence of the inverse participation numbers (IPN) on the size L of the system. The latter are the moments of the distribution function $f(t)$ of local amplitudes $t \equiv |\psi(\mathbf{r})|^2$ of wave functions at an arbitrary point \mathbf{r}_o inside a sample,

$$t_n = \int_0^\infty t^n f(t) dt, \quad f(t) = (V_\nu)^{-1} \left(\sum_\alpha \delta(t - |\psi_\alpha(\mathbf{r})|^2) \delta(\epsilon - \epsilon_\alpha) \right), \quad (1)$$

where $\psi_\alpha(\mathbf{r})$ and ϵ_α are the eigenfunctions and eigenvalues of a confined system, $\langle \rangle$ means averaging over disorder, ν is the average density of states, $V \propto L^2$ is the system area. In a ballistic chaotic cavity where the wave functions extend over the whole system, one has $V t_n \propto V^{-n}$. If disorder makes the localization length L_c much shorter than the sample size, the IPN's are insensitive to L . However, a very interesting information about the development of localization comes from the analysis of $t_n(L)$ for small samples with $L < L_c$. Below, we show that the *multipfractality of wave functions is a generic property of diffusive 2D disordered systems* as soon as the sample size L does not exceed the formal localization length L_c . In the language of the coefficients t_n , this is described as

$$t_n(\epsilon) \propto L^{-\tau(n)-2}, \quad \tau(n) = (n-1)d^*(n), \quad (2)$$

where the fractal dimension $d^*(n)$ differs from the physical dimension $d = 2$ and is a function of n [2]. To anticipate a little, we find that

$$d^*(n) \approx 2 - \beta n / (4\pi^2\nu D) \quad (3)$$

for $n \leq 2\pi\nu D\beta$, which can be associated with power-law tails of the envelopes of pre-localized states $|\psi(\mathbf{r}_o + \mathbf{r})|^2 \propto r^{-2\mu}$ (at distances longer than the mean free path). The exponent μ is individual for each wave function which has a locally too high amplitude $t \gg V^{-1}$, and $\mu(t) < 1$. The parameter β distinguishes between different fundamental symmetry classes: unitary, $\beta_u = 1$; orthogonal, $\beta_o = 1/2$, and symplectic, $\beta_s = 2$.

Our theory is based on the use of the supersymmetry technique [4]. Analytical study of wave functions using this method has been started recently [5] and made possible to calculate the distribution function of local amplitudes $f(t)$ as a whole [6], rather than to reconstruct it from the full set of IPN's, as has been done before [1,5]. The use of the supermatrix field theory reduces the calculation of the distribution function $f(t)$ to the evaluation of a functional integral with the free energy functional

$$F[\tilde{Q}] = \frac{\pi\nu}{8} \int \text{Str} [D(\nabla Q(\mathbf{r}))^2 - 2\gamma\Lambda Q(\mathbf{r})]. \quad (4)$$

In Eq. (4), D is the diffusion coefficient, γ is a level width which has to be taken in the limit of $\gamma \rightarrow 0$. The latter move is sufficient, since the degeneracy space of the field Q is non-compact, so that γ determines the limits of integration over Q 's. The notations for the supermatrices Q and Λ , and for the supertrace "Str" are the same as in Ref. [4]. A general form of the functional integral valid for an arbitrary magnetic field and technical details of our calculation can be found in Ref. [6]. Below, we schematically mention its key points.

Our most important step consists in the extension of the functional integration over Q to the non-uniform configurations of the superfield. Restricting the integration only to the uniform configurations, one would rederive [5,6] the universal Porter-Thomas distribution renown in the random matrix theory [7]. But this is not enough for probing the localization effects, since the latter are related to the non-uniform $Q(\mathbf{r})$ [4]. It has been recently understood [8] that the treatment of rate localization events in the metallic regime is related to the study of the saddle-point of the σ -model. The integration over the zero harmonics is only our first step which enables us to reformulate the problem in terms of only relative variations of the field Q . To realize this plan, we exploit the invariance of the Q -space and write $Q(\mathbf{r}) = V(\mathbf{r}) \Lambda \tilde{V}(\mathbf{r})$, where $V(\mathbf{r}) \tilde{V}(\mathbf{r}) = 1$. Then, we substitute $V(\mathbf{r}) = V(\mathbf{r}_o) \tilde{V}(\mathbf{r})$ and $Q(\mathbf{r}) = V(\mathbf{r}_o) \tilde{Q}(\mathbf{r}) \tilde{V}(\mathbf{r}_o)$ (where $\tilde{Q}(\mathbf{r}_o) = \Lambda$) and integrate over all orientations of the Q -field in the sample as a whole, i.e., over $Q_o = V(\mathbf{r}_o) \Lambda \tilde{V}(\mathbf{r}_o)$. This reduces the theory to the functional integration over the field \tilde{Q} alone [9],

$$f(t) = V^{-1} \hat{R}\{\Phi(t)\}; \quad \Phi = \int_{\tilde{Q}(\mathbf{r}_o)=\Lambda} \exp \left(-F[t, \tilde{Q}] \right) D\tilde{Q}(\mathbf{r}) \quad (5)$$

where the integro-differential operation \hat{R} depends on the fundamental symmetry class and acts on generating functional $\Phi(t)$ of the reduced σ -model determined by the free energy

$$F[t, \tilde{Q}] = \int d\mathbf{r} \text{Str} \left(\frac{\pi\nu D}{8} (\nabla \tilde{Q}(\mathbf{r}))^2 - \frac{t}{4} \Lambda \Pi \tilde{Q}(\mathbf{r}) \right). \quad (6)$$

The matrix Π selects from \tilde{Q} its non-compact sector $Q_b = V_b \Lambda \tilde{V}_b$:

$$\Pi = \begin{pmatrix} \pi_b & \pi_b \\ \pi_b & \pi_b \end{pmatrix}, \quad V_b = \exp \begin{pmatrix} 0 & u \tau_b \theta_1 / 2 \\ u + \pi_b \theta_1 / 2 & 0 \end{pmatrix}, \quad u = e^{i\chi\tau_b}, \quad \theta_1 \geq 0 \quad (7)$$

The universal statistics can be obtained by putting $\hat{Q}(\mathbf{r}) = \Lambda$ for all \mathbf{r} , and one ends with the distribution $f(t) = V\varphi(Vt)\exp(-\beta Vt)$ ($\varphi_u = 1$, $\varphi_o(x) = 1/\sqrt{2\pi x}$ and $\varphi_s(x) = 4x$), which gives IPN's with metallic-type behavior. However, the value $\hat{Q}(\mathbf{r}) \equiv \Lambda$ does not correspond to the minimum of the functional F when $t \neq 0$. The second term in F acts on \hat{Q} as if some external field tends to "align" the matrix Q_b along such a direction that $\theta_1 \rightarrow \infty$, whereas the condition $\hat{Q}(\mathbf{r}_o) = \Lambda$ prevents from that. The minimum corresponds to a non-uniform finite $Q_b(\mathbf{r})$. The solution θ_1 minimizing the functional F can be found after substituting Eqs. (7) into (6) and varying θ_1 under the condition $\mathbf{n}\nabla\theta_1 = 0$ at the boundary of the sample, and $\theta_1(\mathbf{r}_o) = 0$ at the origin. As the result, we obtain

$$\Delta\theta_t(\mathbf{r}) = -\frac{t}{\pi\nu D} \exp(-\theta_t(\mathbf{r})), \quad \chi(\mathbf{r}) = \pi, \quad (8)$$

where Δ is the Laplacian, and the optimal value of the free energy has the form

$$F_t = \beta f \left(\frac{\pi\nu D}{2} (\nabla\theta_t)^2 + t \exp(-\theta_t) \right) dr. \quad (9)$$

When solving Eq. (8) in the 2D case, we have to cut off the radii $r < l$ shorter than the value of the mean free path l and replace the conditions $\hat{Q} = \Lambda$ ($\theta_1 = 0$) at the origin by the same requirement at $\mathbf{r} = \mathbf{r}_o \sim l$. For the sake of simplicity, we consider the sample in the form of a disk of a radius L , $\ln(L/l) \ll (2\pi\nu D)^2$, and place the observation point \mathbf{r}_o in its center. This geometry allows us to seek for an axially symmetric solution of Eq. (8) which, with the parameter $\rho = \sqrt{2\pi\nu D}/l^2$, takes the exact form

$$e^{-\theta_t} = \frac{2(l/r)^{1-\lambda} [\sqrt{(\frac{1}{\Lambda\rho})^2 + 1 + 1}]^2}{[\sqrt{(\frac{1}{\Lambda\rho})^2 + 1 + 1}]^2 - (\frac{1}{\Lambda\rho})^2 (\frac{l}{r})^{2\lambda}]^2} \sim \left(\frac{l}{r} \right)^{2\mu}, \quad \sqrt{\Lambda^2 + \rho^{-2}} + \Lambda = \frac{(l/l)^A}{\rho} \sqrt{\frac{1+A}{1-A}}, \quad (10)$$

where the latter equation on $\Lambda = 1 - \mu$ is determined from the boundary conditions. This equation has positive roots if $\rho > \ln \frac{L}{l} \gg 1$, which limits the amplitude t by the value $(\lambda_F l)^{-1}$, the density of a plane wave forward-and-backward scattered within the mean free path length. In this limit, $\mu < 1$, which is the reason for the power-law asymptotics of the optimal $\exp(-\theta_t)$. The same condition also simplifies the consistency equation on $A \equiv 1 - \mu$ and the expression for the leading term of the optimal free energy:

$$\mu = \frac{z(T)}{2\ln(l/\rho)}, \quad z e^z = T \equiv \frac{V \ln(l/\rho)}{2\pi^2 \nu D} \quad \text{and} \quad F_t \approx \beta(2\pi)^2 \nu D (\mu + \mu^2 \ln \frac{l}{r}). \quad (10)$$

We can also evaluate the pre-factor J and find that $J = 1 + 0(T^2)$ at $T \ll 1$, and $J \propto \mu \exp(\mu \ln \frac{L}{l}) \sim T \ln T$ at $T \gg 1$. This approves the use of the saddle-point method and enables us to find the form of the distribution function $f(t)$ for small, $t <$, and large, $t > 2\pi^2 \nu D / (V \ln \frac{l}{r})$, amplitudes with the exponential accuracy:

$$f \approx V \begin{cases} \exp(-\beta V t [1 - T/2 + \dots]), & T \ll 1 \\ \exp\left(-\frac{\beta V \nu D}{\ln(l/\rho)} \ln^2 T\right), & T \gg 1. \end{cases} \quad (11)$$

From this expression, one can conclude that disorder makes the appearance of high-amplitude splashes of wave functions much more probable than one would expect from the Porter-Thomas formulae. Moreover, the striking similarity between the asymptotics of $f(t)$ in Eq.

(11) and the log-normal laws governing the distributions of rare fluctuations of the density of states discovered in Ref. [3] reveals their deep relationship. Both are due to the localization effects. But the tails of the states which are responsible for these rare events do not decay exponentially. Even in the asymptotical regime $T \gg 1$, the size L of the system influences the distribution. The structure of pre-localized states can be anticipated from the way how their distribution feels the boundary or - directly - by calculating more complicated cross-correlation functions [9]. It turns out that the envelope of the tail of a state associated with a large-amplitude splash $|\psi(\mathbf{r}_o)|^2 = t$ follows the form of the optimal solution. Therefore, it has the tail $|\psi(\mathbf{r})|^2 \propto e^{-\theta_t(\mathbf{r})} \approx (l/r)^{2\mu}$, with the individual exponent $\mu = \mu(t) < 1$ for each amplitude t , approaching the r^{-2} dependence for the limiting values of $t \sim (l\lambda_F)^{-1}$.

Moreover, the form of IPN's, t_n derived on the basis of Eq. (11) shows a scaling with the size of a system which forces us to assign them a multifractal nature. To find the moments t_n accurately enough, we have to take into account that the universal statistics fails unless the condition $tV \ll \sqrt{2\pi\nu D}$ is satisfied (see eq. (11)). Hence, only first few ratios t_n , $2 \leq n \ll \sqrt{2\pi\nu D}$, can be estimated using a finite polynomial expansion of $f(t)$ into the series on T , and their first terms reproduce the perturbatively found corrections [10] to the Porter-Thomas distributions. Alternatively, we derive the higher order IPN's directly from the generating functional. The IPN's calculated in both ways are in a good agreement with each other and, in the leading order, take the form

$$t_n \approx \frac{\min\{n!, [2\pi\nu D / \ln \frac{L}{r}]^n\}}{l^{2s}} \left(\frac{1}{V} \right)^{n-\delta}, \quad \delta \approx \frac{\beta n(n-1)}{8\pi^2 \nu D}.$$

To summarize the result for the statistics of wave functions in mesoscopic disordered conductors derived above, we end up with such a volume-dependence of the inverse participation numbers t_n which manifests the multifractal behavior of quantum states, Eq. (2.3). The multifractality seems to be the generic property of 2D disordered systems. The multifractal dimensions are $d^* = 2 - \beta n(4\pi^2 \nu D)^{-1}$ ($d^* > 0$) in the leading order on $1/D$.

- [1] F. Wegner, Z. Phys. B **36**, 209 (1980); C. Castellani, L. Peliti, J. Phys. A **19**, L429 (1986)
- [2] H. Aoki, J. Phys. C **16**, L205 (1983); Phys. Rev. B **33**, 7310 (1985); M. Schreiber, J. Phys. C **18**, 2493, (1985); B. Kramer *et al*, Surf. Sci. **198**, 127 (1988)
- [3] B.L. Altshuler, V.E. Kravtsov and I.V. Lerner, in *Mesoscopic Phenomena in Solids*, ed. B. Altshuler *et al*, Elsevier, Amsterdam 1991, p.449, and refs. therein
- [4] K.B. Efetov, Adv. Phys. **32**, 53 (1983)
- [5] K.B. Efetov and V.N. Prigodin, Phys. Rev. Lett. **70**, 1315 (1993)
- [6] V.I. Fal'ko and K.B. Efetov, Phys. Rev. B **50**, 11267 (1994)
- [7] T.A. Brody *et al*, Rev. Mod. Phys. **53**, 385 (1981)
- [8] B.A. Muzykantskii and D.E. Khmelnitskii, Phys. Rev. B **51**, 5480 (1995)
- [9] V.I. Fal'ko and K.B. Efetov, submitted to PRL
- [10] Y.V. Fyodorov and A.D. Mirlin, Phys. Rev. B **51**, 13403 (1995)

Transport in One-Dimensional Electron Sinai Billiards

M.V. Budantsev, Z.D Kvon, A.G.Pogosov,

N.T. Moschegov, A.I.Plotnikov, A.I.Toropov

Institute of Semiconductor Physics, Russian Academy of sciences,
Siberian Branch, Novosibirsk, RUSSIA

Abstract

Transport phenomena in a new type of electron Sinai billiards, one-dimensional "caterpillar"-like billiard, have been investigated for the first time. Magnetoresistance oscillations caused by commensurability of cyclotron diameter and the period of billiards, and originating from the trajectories running along its walls have been found. Quenching of the Hall effect has been also found near zero magnetic field and in magnetic fields corresponding to appearance of commensurability oscillations.

Recent advances in semiconductor technology made it possible to turn to experimental investigation of a list of exotic physical systems which have long been subjects of only theoretical study. The most prominent of such systems are electron Sinai billiards, which are the classical systems with dynamic chaos [1]. However the only type of these billiards experimentally studied up to now is a two-dimensional electron gas (2DEG) in a periodic lattice of antidots, which is an experimental realization of the Sinai billiard of scattering disks [2-5].

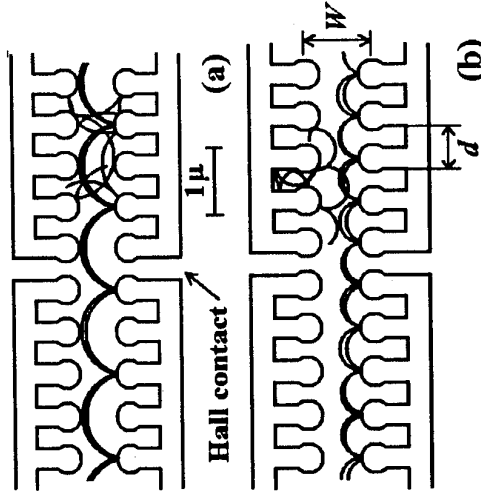
In the present work the new type of electron billiard (EB), the "caterpillar"-like Sinai billiard, serving as a glowing example of one-dimensional EB has been experimentally investigated for the first time. A large variety of anomalies in behaviour of the magnetoresistance (MR) and the Hall effect of this billiard has been found characterizing it as an extremely interesting and prominent system with dynamic chaos.

Experimental samples were fabricated on the basis of 2DEG with concentration $n = (3.5 \pm 6) \cdot 10^{11} \text{ cm}^{-2}$ and mobility $\mu = (6 \pm 8) \cdot 10^5 \text{ cm}^2/\text{Vs}$ by means of electron lithography and subsequent reactive plasma etching. The billiard was formed by two chains of antidots situated on the tops of antisegments and was separated from the other part of 2DEG by two antivires. The schematic diagram of the billiard is presented in Fig.1. The described type of the billiard makes it possible to estimate the width of the depletion layer by means of the Hall contacts as well as to avoid the influence of the antivires' depletion layer that might smoothen the potential around antidots.

Billiards of different sizes were investigated. In the present work we report the data for the billiard with the period $d = 0.6 \mu\text{m}$, the distance between antidots chains $W = 0.9 \mu\text{m}$ and the length $L = 7.8 \mu\text{m}$. The measurements of the billiard resistance and the Hall effect were carried out at temperatures $1.7 \pm 4.2 \text{ K}$ in magnetic fields up to 8 T . It was possible to change the effective width W_{eff} of the billiards by interband illumination due to the change of the depletion layer width.

The typical experimental curves of the magnetoresistance and the Hall resistance are presented in Fig.2a. The similar curves for the wire with smooth edges are shown in Fig.2b for the comparison. The geometrical width of the wire was $0.7 \mu\text{m}$ (equaled to the narrow part of the billiard) and the length was the same as that of the billiard. One can see that $R(B)$ dependence for the wire exhibits the monotonous decrease with increasing magnetic field which is typical for the quasiballistic wires with specular edges. The behaviour of MR of the billiard is quite different. In weak magnetic field the positive magnetoresistance (PMR) is observed. Its magnitude reaches 15% of the total sample resistance. This PMR has the same features (its magnitude increases with decreasing W_{eff} and the maximum shifts to weaker magnetic field approximately following the relation $W_{\text{eff}} = 0.55 R_c$, where R_c is a cyclotron radius) as the ones observed in [6] for the wires

with irregular edges and is caused by diffusive scattering of electrons by the edges. It should be noted however that in wires the diffusive scattering originates from irregularities of edges while in the billiards it is caused by the dynamic stochasticization by the regularly arranged scatterers.



In stronger magnetic fields the $R(B)$ dependence exhibits two well-pronounced features together with ordinary monotonous decrease of resistance. Positions of these features correspond to the conditions $R_c = d$ and $2R_c = d$. We believe that these features appear due to the running trajectories. Under these conditions they can run over the distances limited by the impurity scattering length l which is an order of magnitude larger than W_{eff} and d in the samples investigated ($l = 7 \pm 10 \mu\text{m}$). Such trajectories were first found theoretically in [4] for 2DEG in periodic lattice of antidots. What is more important is that these trajectories were shown in [4] as being the stable states occupying a large fraction of the phase space, thus making a noticeable contribution to the conductivity. It is these trajectories that give rise to the commensurability oscillations of MR. However in the case of 2D billiards in the Hall geometry samples (which are used in experiments) they lead to the maximum in the resistance. That is why there is still an alternative idea that the commensurability maxima originate from the stable localized trajectories [7] but not the running ones. Hence the data presented in Fig.2a are the first direct experimental evidence that running trajectories essentially influence the MR of electron Sinai billiards.

The Hall component of MR R_{xy} also has features. First, the suppression of the Hall signal is observed in magnetic fields below 300 Gs. Second, the quasiplateaus appear in magnetic fields corresponding to the running trajectories. It should also be noted that R_{xy} is nonzero at $B = 0$. Most likely it is caused by irregularities of the real billiard and represents no interest. Besides the described anomalies the dependencies $R(B)$ and $R_{xy}(B)$ have some less-pronounced irregular features.

Let us discuss the experimental results described above in more detail. Let's start with the quenching of the Hall effect signal near zero magnetic field. It is known that this phenomenon was first found in wires with specular reflecting edges [8] and is caused by the trajectories reflected from both edges of the wire in weak magnetic fields [9]. As it was ascertained in [8] the effect disappears rapidly with the increase of the effective wire width W_{eff} and is practically absent in the wires with $W_{\text{eff}} > 0.1 \mu\text{m}$. The width of the investigated EB measured even in their narrowest part was $W_{\text{eff}} > 0.5 \mu\text{m}$. (This estimation is based on the fact that there are running trajectories at $R_c = d$ and the overlapping of antidots forming EB is absent.) Nevertheless, Fig. 2a clearly shows that the quenching of the Hall effect in EB does exist in contrast to the smooth wire of the width equal to that of the narrowest part of the billiard (see Fig. 2b). We believe this behaviour of the Hall effect in EB to be caused by the diffusive nature of scattering of electrons by the walls of the billiard opposite to the case of a smooth wire. This is just the chaotic scattering of electrons by the walls of EB that leads to much slower decrease of the number of trajectories reflecting from both walls with increasing of the width of EB, than in a wire with specular edges as it was shown by numerical simulations. Thus, in the present work it has been first shown that quenching of the Hall effect in ballistic wires is determined not only by the size of the wire, but also by the character of scattering by its edges. As it was mentioned above two other features of the curve $R_{xy}(B)$ (the quasiplateaus) appear in the magnetic fields corresponding to the existence of the running trajectories under the conditions $R_c = d$ and $2R_c = d$ (see Fig. 2a) They appear because trajectories running along the walls of EB bypass the Hall contact and therefore do not contribute to the Hall voltage leading to the drastic slowing down of its increase with magnetic field. From this fact one can draw a conclusion that in certain magnetic fields the stable states in EB make crucial and noticeable changes in kinetic coefficients of the billiards.

References

- [1] Ya. G. Sinai, Usp. Mat. Nauk. 25 (1970) 141.
- [2] K. Ensslin and P. M. Petroff, Phys. Rev. B 41 (1990) 12307.
- [3] D. Weiss, M. L. Roukes, A. Mensching, P. Grambow, K. v. Klitzing, and G. Weimann, Phys. Rev. Lett. 66 (1991) 2790.
- [4] E. M. Baskin, G. M. Gusev, Z. D. Kvon, A. G. Pogosov, M. V. Entin, JETP Lett. 55 (1992) 678.
- [5] M. V. Budantsev, Z. D. Kvon, A. G. Pogosov, L. V. Litvin, V. G. Mansurov, V. P. Migai, S. P. Moshchenko, and Yu. V. Nastaushev JETP Lett. 59 (1994) 645.
- [6] T. J. Thornton, M. L. Roukes, A. Scherer, and B. P. Van de Gaag, Phys. Rev. Lett. 63 (1989) 2128.
- [7] R. Fleischmann, T. Geisel, R. Ketzmerick Phys. Rev. Lett. 68 (1992) 1367.
- [8] M. L. Roukes, A. Scheer, S. J. Allen, Jr., H. G. Craighead, R. M. Ruthen, E. D. Beebe, and J. P. Harbison Phys. Rev. Lett. 59 (1987) 3011.
- [9] C. W. J. Beenakker and H. van Houten Phys. Rev. Lett. 60 (1988) 2406.

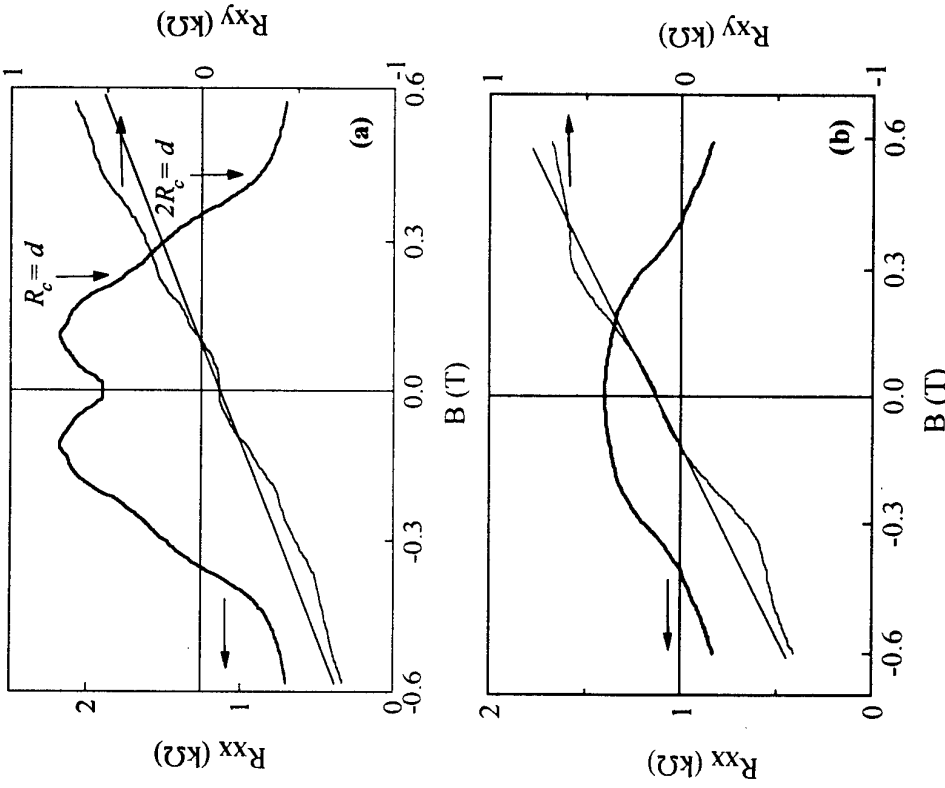


Fig. 2. The magnetoresistance (thick line) and the Hall resistance (thin line) of (a) the "caterpillar"-like electron billiard and (b) the wire with specular edges. The slope of the dash-dotted lines illustrates the Hall concentrations corresponding to that of the experimental samples measured from Shubnikov — de Haas oscillations.
 (a) $n_s = 6 \cdot 10^{11} \text{ cm}^{-2}$, (b) $n_s = 5 \cdot 10^{11} \text{ cm}^{-2}$.

Stable Orbit Bifurcations in a Quantum Well in a Tilted Magnetic Field

G. S. Boebinger, G. Müller*, H. Mathur, L. N. Pfeiffer, and K. W. West
AT&T Bell Laboratories, 600 Mountain Ave., Murray Hill, NJ 07974 USA

Abstract

Peak doubling regions are observed in resonant tunneling spectroscopy of a quantum well in a tilted magnetic field. They are identified with bifurcations of stable periodic orbits. The narrowness of the peak doubling region at small tilt angles arises from a “double bifurcation” which destabilizes the original periodic orbit.

Introduction

There is great theoretical interest in simple quantum systems whose classical counterparts exhibit chaotic dynamics [1], which has motivated experiments in semiconducting microstructures [2,3]. Recently, Fronhold, et al [4] have introduced a new quantum system for chaos studies: the wide quantum well in a tilted magnetic field. Using resonant tunneling spectroscopy, they studied chaotic dynamics at a fixed magnetic field of sufficient intensity that the quantum well was in a completely chaotic regime [4,5].

We have recently found a distinct transition from regular to chaotic dynamics in a quantum well [6]. By systematically varying the three *in-situ* experimental parameters of bias voltage, magnetic field and tilt angle, we mapped the parabolic magnetic field dependence of the transition. Poincaré section (PS) calculations identified the precursors of the chaos transition as the bifurcation and trifurcation of stable periodic orbits. In this paper, we concentrate on the earliest precursor of the chaos transition: a “double bifurcation” which occurs in small magnetic field tilt angles. We conclude that quantum wells provide a particularly clear manifestation of the break-up and restabilization of stable orbits.

Experimental Procedure

The sample is a resonant tunneling structure with a 1200Å wide GaAs quantum well confined between two layers of AlAs (Fig. 1). An applied bias voltage, U , creates a degenerate two-dimensional electron gas (2DEG) emitter which acts as a source of electrons which tunnel into the quantum well. Unwanted accumulation of charge in the quantum well is avoided by making the second AlAs barrier substantially thinner than the first (37Å compared to 57Å). Details of the sample growth and characterization are given in Ref. [6].

The experimental procedure is to rotate the sample to a measured tilt angle θ ($\theta = 0^\circ$ is magnetic field perpendicular to the quantum well). Resonant tunneling current-voltage (I-V) traces at a temperature of 1.5K are recorded in 0.1T magnetic field steps over a range from $B=0$ to 12T. Traces (a) and (b) in Fig. 1 are the same I-V data for $\theta = 27^\circ$ at $B=0$. In trace (b), a smooth background current is subtracted to emphasize the current peaks. The same procedure is applied at (c) $B=6\text{T}$ and (d) $B=12\text{T}$. A peak in an I-V trace evidences a corresponding peak in the quantum well density of states.

In Figure 2 the voltages at which peaks occur in the I-V traces are plotted (filled circles) versus total magnetic field for two of eleven angles studied from $\theta = 0^\circ$ to 45° . At $\theta = 0^\circ$, a tunneling peak occurs when the energy level in the 2DEG emitter aligns with the energy of a confinement subband in the quantum well. As expected, these subband peaks show no strong dependence on magnetic field. At $\theta = 11^\circ$ (Fig. 2a), most of the data resemble

the subbands at $\theta = 0^\circ$. Now, however, a doubling of the number of peaks occurs in two distinct regions of bias voltage versus magnetic field. These two regions gradually broaden and merge as the tilt angle is increased to $\theta = 27^\circ$ (Fig. 2b). Upon increasing the tilt angle further, the low field region remains subband-like, but there is a sharp transition to a region of disordered peaks, which has been identified as the chaos transition [5,6].

Poincaré Section Calculations

A classical model that corresponds to the resonant tunneling structure is a charged particle that bounces between hard walls (the emitter and collector barriers). Between specular collisions with the walls, the particle describes helical trajectories under the influence of electric and magnetic fields. The electric field arises from the applied bias (Fig. 1) and is perpendicular to the walls. As the magnetic field is tilted, the system becomes more chaotic because the angle of reflection becomes increasingly sensitive to the phase of the helical motion at the time of impact.

To visualize the complicated classical dynamics, we calculate Poincaré sections as follows: Trajectories of tunneling electrons are calculated in the quantum well. Upon each collision with the collector barrier, a point is plotted in the PS at (v_x, v_y) , the in-plane velocity components. Details of the PS calculations are given in Ref. [6].

At zero tilt angle, the electron moves along a helix and the orbit traces out a circle in the PS. Thus at $\theta = 0^\circ$, the PS is a pattern of concentric circles characteristic of an integrable system. At finite tilt angle, as magnetic field is increased, the motion grows progressively more chaotic. In the PS's, islands of regular motion are centered on stable periodic orbits, which are surrounded by a chaotic sea. As the system becomes more chaotic, the islands of integrability become smaller and disappear. Although classical dynamics usually change gradually, occasionally a stable periodic orbit will abruptly bifurcate, as shown in Fig. 3 for $\theta = 27^\circ$. Upon bifurcating, a stable periodic orbit (Fig. 3a) loses stability and simultaneously gives birth to two stable periodic orbits with exactly twice the period time of the original orbit (Figs. 3b,3c). Bifurcations are well-established precursors to chaos.

Following the analysis in Refs. [4] and [6], oscillations in the I-V traces are interpreted as oscillations in the density of states which arise from periodic orbits. According to semi-classical trace formulas [1], each periodic orbit contributes an oscillation to the density of states with energy period h/T_P (T_P is the period time of the orbit). Whereas Fronhold, et al. studied unstable periodic orbits, we concentrate on *stable* periodic orbits which undergo bifurcation when the system is en route to chaos. We find that the sharp onset of peak doubling in the data results from the bifurcation of a stable periodic orbit [6]. Upon bifurcation, the stable orbit period, T_P , doubles and, thus, the observed peak spacing halves. The calculated bifurcation onsets at $\theta = 11^\circ$ and 27° (lines in Fig. 2 marked “1 → 2”) agree reasonably well with the observed onset of peak doubling.

We now concentrate on the data at 11° , where the low-field peak doubling is followed at $\sim 2\Gamma$ higher magnetic field by a restabilization of the subband spacing. This restabilization is also seen in the PS's of Fig. 4, due to a “double bifurcation”. Although the sequence begins like the 27° bifurcation, the unstable orbit at the center of Fig. 4b quickly undergoes its own bifurcation, which restabilizes the original period orbit. I-V traces from this region are shown in Figure 5. The bracket under the $B = 7T$ data highlights the peak doubling region. Note that this data contrasts with the data at 27° , where all peaks in the peak

- doubling region have equal weight (Fig. 1c).
- In conclusion, we have studied the bifurcation precursors of the order to chaos transition in a quantum well. Poincaré section calculations find quantitative agreement with two qualitatively different bifurcations observed at magnetic field tilt angles $\theta = 11^\circ$ and 27° . We thank D. Shepelyansky and A. D. Stone for pointing out the importance of bifurcations in this system. G.M. thanks the Max-Planck-Gesellschaft for financial support via the Otto-Hahn-Medaille.
- *Present address: Philips Research Laboratories, Prof. Holstlaan 4, 5656 AA Eindhoven, The Netherlands
- [3] C. M. Marcus, A. J. Rimberg, R. M. Westervelt, P. F. Hopkins, and A. C. Gossard, Phys. Rev. Lett. **69**, 506 (1992); M. W. Keller, O. Millo, A. Mittal, D. E. Prober, and R. N. W. West, Phys. Rev. Lett. **73**, 501 (1994); and A. M. Chang, H. U. Baranger, L. N. Pfeiffer, and K. W. West, Phys. Rev. Lett. **73**, 2111 (1994).
- [4] T. M. Fromhold, L. Eaves, F. W. Sheard, M. L. Leadbeater, T. J. Foster, and P. C. Main, Phys. Rev. Lett. **72**, 2608 (1994).
- [5] D. Shepelyansky and A.D. Stone, Phys. Rev. Lett. **74**, 2094 (1995).
- [6] G. Müller, G. S. Boebinger, H. Mathur, L. N. Pfeiffer, and K. W. West (unpublished).

References

- [1] M. C. Gutzwiller, *Chaos in Classical and Quantum Mechanics*, (Springer, Berlin, 1990).
- [2] D. Weiss, K. Richter, A. Mensching, R. Bergmann, H. Schweitzer, K. von Klitzing, and G. Weimann, Phys. Rev. Lett. **70**, 4118 (1993); R. Schuster, K. Ensslin, D. Wharam, S. Kühn, J.P. Kotthaus, G. Böhm, W. Klein, G. Tränkle, and G. Weimann, Phys. Rev. B**49**, 8510 (1994).

• $a = 11^\circ$ $1 \rightarrow 2$

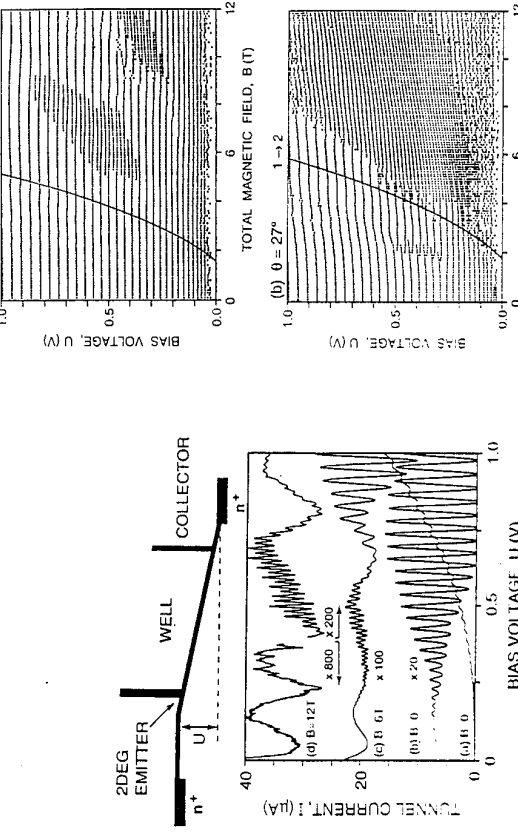


FIGURE 2: Peak positions from the resonant tunneling I-V traces at $T = 1.5\text{K}$ as a function of total magnetic field. At (a) $\theta = 11^\circ$, quantum well subbands dominate, but two regions of peak doubling are evident. At (b) $\theta = 27^\circ$, the peak doubling regions have broadened and merged. The solid lines are bifurcation boundaries from Poincaré section calculations.

3

FIGURE 3: Examples of Poincaré sections for $\theta = 27^\circ$ at $U = 0.5\text{V}$ showing (a) a stable periodic orbit at $B = 4.2\text{T}$ undergoing (b) bifurcation at $B = 4.4\text{T}$ and becoming (c) two separated stable orbits at $B = 4.6\text{T}$. This accounts for the sudden onset of peak doubling in Fig. 2a.

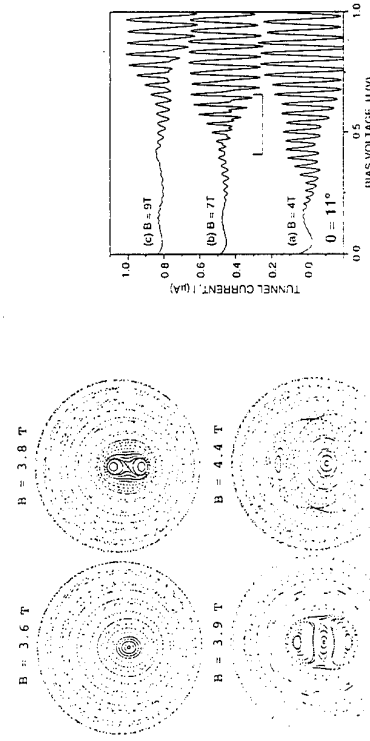
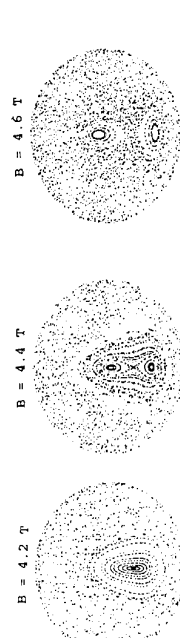


FIGURE 5: I-V traces taken at tilt angle $\theta = 11^\circ$ at $B = 4\text{T}, 7\text{T}$, and 9T . A smooth background has been subtracted as in Fig. 1. Note the unequal peaks in the peak doubling region [highlighted by the bracket in (b)], in contrast to the equal peak weights observed at $\theta = 27^\circ$ in Fig. 1c.

4

Theory of Coulomb Blockade of Tunneling through a Double Quantum Dot

K. A. Matveev,⁽¹⁾ L. I. Glazman,⁽²⁾ and H. U. Baranger⁽³⁾

⁽¹⁾Massachusetts Institute of Technology, 12-105, Cambridge MA 02139

⁽²⁾Theoretical Physics Institute, University of Minnesota, Minneapolis MN 55455

⁽³⁾AT&T Bell Laboratories, 600 Mountain Ave. 1D-230, Murray Hill NJ 07974

Abstract

We present a theory of Coulomb blockade oscillations in tunneling through a pair of quantum dots connected by a tunable tunneling junction. The positions and amplitudes of peaks in the linear conductance are directly related, respectively, to the ground state energy and to the dynamics of charge fluctuations. Our theory allows for a quantitative comparison with the experimentally observed peak positions. In the strong tunneling limit, we predict a striking power law temperature dependence of the peak amplitudes.

The simplest system which shows a Coulomb blockade consists of a small metallic grain separated from a bulk lead by a thin dielectric layer [1]. An electron tunneling through the layer inevitably charges the grain, thus increasing its energy by $E_C = e^2/2C$, where C is the capacitance of the grain. At temperatures $T \ll E_C$ a negligible fraction of the electrons in the lead have an energy of order E_C , and one might expect that no tunneling into the grain is possible. More careful consideration shows, however, that even at $T = 0$ the electrons can tunnel to the virtual states in the grain, thus lowering the ground state energy of the system [2]. Due to this virtual tunneling, the average charge of the grain is no longer quantized and acquires a correction proportional to the conductance of the barrier. Unfortunately a direct measurement of the equilibrium properties, such as the average grain charge, is a difficult experiment. In a recent experiment of Waugh *et al.* [4], the equilibrium properties were inferred from measurements of the tunneling conductance through a pair of coupled quantum dots. Focusing on this experiment, we develop a quantitative theory of the linear conductance in such a system; in particular, we predict the gate voltage and temperature dependence of the conductance.

We will study the properties of a two-dot system which is schematically shown in Fig. 1. The electrostatic energy of this system is a quadratic form of three variables: the charges of each dot, eN_1 and eN_2 , and the gate voltage V_g . In the most general case, this energy can be written in the following form:

$$U(N_1, N_2) = E_C(N_1 + N_2 - 2X)^2 + \tilde{E}_C[N_1 - N_2 + \lambda(N_1 + N_2) - \alpha X]^2. \quad (1)$$

Here X is a dimensionless parameter proportional to V_g , and the constants E_C , \tilde{E}_C , λ , and α are determined by the geometry of the system. In Eq. (1) we expressed the energy in terms of the total number of particles in the two dots $N_1 + N_2$ and the relative number $N_1 - N_2$; the former is constant in the absence of tunneling into the leads, and the latter describes charge fluctuations between the dots. We will concentrate here on the case of symmetric geometry of the system ($\lambda = \alpha = 0$), which apparently corresponds to the experiment [4].

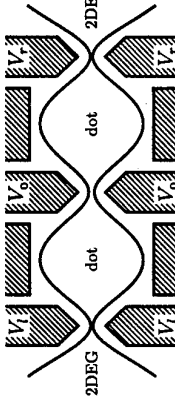


Fig. 1. Schematic view of the double quantum dot system. The dots are formed by applying negative voltage to the gates (shaded); the solid line shows the boundary of the 2D electron gas (2DEG). V_t and V_b create tunnel barriers between the dots and the leads while V_g controls the transmission coefficient through the constriction connecting the dots.

In order to study the effect of quantum fluctuations on the ground state energy of the system, one can vary the inter-dot conductance G_0 , keeping all other conductances small. Under these conditions, the sum $N \equiv N_1 + N_2$ can be treated as a c -number, but $N_1 - N_2$ fluctuates. These fluctuations affect the ground state energy E_N . In order to find E_N , one should consider the quantum mechanical problem with the Hamiltonian

$$H = H_0 + H_T + E_C(N - 2X)^2 + 4\tilde{E}_C\left(\hat{N}_1 - \frac{N}{2}\right)^2. \quad (2)$$

Here the terms H_0 and H_T describe, respectively, free electrons in the dots and tunneling between the dots; the last two terms in (2) correspond to the charging energy (1). Typically the size of the dots exceeds the effective Bohr radius, and therefore the level spacing for electrons in the dots is much smaller than the charging energy. We will neglect the level spacing and assume a continuous spectrum in H_0 .

The ground-state energy E_N of the Hamiltonian (2) is a function of the gate voltage X . The positions of the peaks can be found from the condition of the degeneracy of E_N with respect to the total number of particles in the two-dot system: $E_N(X) = E_{N+1}(X)$. The ground state energy of the Hamiltonian identical to (2) was found in the limits of weak and strong tunneling in Refs. [2, 3]. We will now use these results to find the peak positions. For weak tunneling, $G_0 \ll e^2/h$, the ground-state energy can be found [2] from the second-order perturbation theory in H_T . Corresponding peak positions are

$$X^* \approx n + \frac{1}{2} \pm \frac{1}{4} \left[1 - \frac{\tilde{E}_C}{E_C} \left(1 - \frac{4 \ln 2 \hbar G_0}{\pi e^2} \right) \right]. \quad (3)$$

Weak electrostatic coupling between the dots corresponds to $E_C - \tilde{E}_C \ll E_C$. In this case, the splitting between two peaks with the same n in sequence (3) is proportional to G_0 , and two such peaks merge at $G_0 \rightarrow 0$. This behavior is observed in [4].

In the limit of strong tunneling the discreteness of charge N_1 is no longer important, $\langle \hat{N}_1 \rangle \rightarrow \frac{1}{2}N$, see Eq. (2), and the peaks are equidistant, $X^* = (2N + 1)/4$. To find the peak positions as the system approaches the strong-tunneling limit, one has to specify a model of the junction between the dots. For electrostatically controlled dots in semiconductor heterostructures, the junction is a microconstriction with smooth boundaries [5]. The ground state energy of such a system near the strong-tunneling limit, when the reflection coefficient for the single transverse mode propagating through the constriction is small $\mathcal{R} = 1 - \pi \hbar G_0/e^2 \ll 1$, was found in Ref. [3] [see Eq. (48)]. Using that result, we get

$$X^* \approx \frac{2N + 1}{4} + (-1)^N \frac{4e^2 C \tilde{E}_C}{\pi^3} \mathcal{R} \ln \frac{1}{\mathcal{R}}, \quad C \approx 0.5772. \quad (4)$$

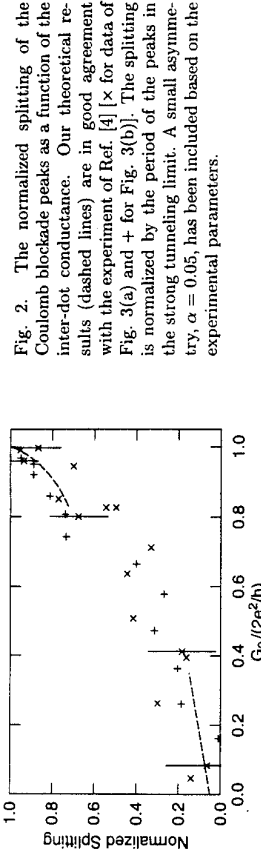


Fig. 2. The normalized splitting of the Coulomb blockade peaks as a function of the interdot conductance. Our theoretical results (dashed lines) are in good agreement with the experiment of Ref. [4] [\times] for data of Fig. 3(a) and + for Fig. 3(b)]. The splitting is normalized by the period of the peaks in the strong tunneling limit. A small asymmetry, $\alpha = 0.05$, has been included based on the experimental parameters.

Fig. 2 compares our results (3) and (4) with the observations of Waugh *et al.* [4]. Similar interpretation of the experiment [4] was independently suggested in [6]. As we have seen, the *positions* of peaks in the linear conductance carry information only about the ground-state energy of the two-dot system. To study the excitations, one can analyze the *heights and shapes* of the peaks. If the inter-dot tunneling is weak, $G_0 \ll e^2/h$, the excitation spectrum consists of two independent quasiparticle spectra of the two dots. This enables us to apply the standard master-equation technique [1] and find

$$G \propto \frac{4E_C(X - X^*)/T}{\sinh[4E_C(X - X^*)/T]} \quad (5)$$

Here X^* is the position of the center of a peak given by one of the values in the sequence (3). This simple formula is valid only at sufficiently low temperatures, $T \ll (hG_0/e^2)E_C$.

In contrast to weak tunneling, at $G_0 \sim e^2/h$ the excitation spectra of the two dots are not independent. In this regime an electron tunneling into the left dot shakes up the quantum state of the whole two-dot system, leading to a suppression of the conductance at low temperature. To illustrate this phenomenon, we calculate the temperature dependence of the peak heights in the case of perfect inter-dot transmission, $G_0 = e^2/\pi\hbar$. As we have seen, the conductance peaks in this limit are equally spaced, as if the double dot system were a single dot. However, the specific geometry of the system—whether it is one or two dots—will show up in the peak heights. Unlike in a single dot, the single-mode constriction impedes charge propagation between the two dots, thus producing effects similar to those for a single junction coupled to an environment [1]. When an electron tunnels from the lead into the left dot, the other electrons in both dots must redistribute in order to minimize the electrostatic energy: a charge $e/2$ must pass through the constriction. As a result, the overlap of the two ground states, before and after the tunneling, vanishes, as in Anderson's orthogonality catastrophe.

At non-zero temperature, the tunneling density of states is suppressed as T^γ , where the exponent is related [7] to the scattering phase shifts δ_m in each one-dimensional channel m by $\gamma = \sum_m (\delta_m/\pi)^2$. According to the Friedel sum rule, δ_m/π is the average charge transferred into each channel. A single-mode constriction provides two channels for each dot (two spins), yielding 4 channels in total. In our case, $\delta_m/\pi = \pm 1/4$, where the plus (minus) sign is for the channels in the right (left) dot. Thus, the rate of tunneling into the left dot is suppressed

by the factor $T^{1/4}$. An explicit formula for peak shapes may be obtained in the spirit of the bosonization approach [7], which yields

$$G \propto \left(\frac{T}{E_C} \right)^{1/4} F \left(\frac{4E_C(X - X^*)}{T} \right), \quad F(x) = \frac{1}{\cosh(x/2)} \frac{\left| \Gamma \left(\frac{9}{8} + \frac{ix}{2\pi} \right) \right|^2}{\Gamma(9/4)}. \quad (6)$$

Comparing our results in the weak and strong tunneling limits [Eqs. (5) and (6)], we see that when G_0 grows the conductance of the system decreases due to the orthogonality catastrophe. For inter-dot conductances between these limits, the system must cross over from temperature independent peak heights for weak tunneling to the power-law suppression of the conductance for strong tunneling.

In conclusion, the fluctuations of charge between two quantum dots strongly affect tunneling through such a structure. First, the conductance peaks are split because of the lowering of the *ground state energy* by charge fluctuations. This splitting and eventual halving of the period of the conductance peaks as the inter-dot conductance grows, is a dramatic feature of the experimental data [4] which is fully confirmed in our theory. Second, the temperature dependence of the peak height and shape is directly related to the *dynamics* of the quantum charge fluctuations. For a pair of dots connected by a reflectionless constriction, this produces a striking fractional power law temperature dependence. Our theory is valid for a wide range of temperatures, limited only by the charging energy from above, and by the discrete energy level spacing from below.

The research at MIT was sponsored by Joint Services Electronics Program Contract DAAH04-95-1-0038 and at the University of Minnesota by NSF Grant DMR-9423244.

References

- [1] *Single Charge Tunneling*, edited by H. Grabert and M. H. Devoret (Plenum Press, New York, 1992).
- [2] L. I. Glazman and K. A. Matveev, *Zh. Eksp. Teor. Fiz.* **98**, 1834 (1990) [Sov. Phys. JETP **71**, 1031 (1990)] and K. A. Matveev, *Zh. Eksp. Teor. Fiz.* **99**, 1598 (1991) [Sov. Phys. JETP **72**, 892 (1991)].
- [3] K. A. Matveev, *Phys. Rev. B* **51**, 1743 (1995).
- [4] F. R. Waugh, M. J. Berry, D. J. Mar, R. M. Westervelt, K. C. Campman, and A. C. Gossard, preprint (9/94).
- [5] L. I. Glazman, G. B. Lesovik, D. E. Khmel'nitskii, and R. I. Shekhter, *Pis'ma Zh. Eksp. Teor. Fiz.* **48**, 218 (1988) [JETP Lett. **48**, 238 (1988)].
- [6] J. M. Golden and B. I. Halperin, preprint (5/95).
- [7] K. Schotte and U. Schotte, *Phys. Rev.* **182**, 479 (1969).

Tunnelling Experiments Through Coupled Zero-Dimensional Systems

A.S.Sachraida, C.Gould¹, Y.Peng, M.W.C.Dharma-wardana and P.T.Coleridge,
Institute for Microstructural Sciences, NRC, Ottawa, Canada K1A 0R6

¹Département de Physique and CRPS, Université de Sherbrooke, Sherbrooke, Canada J1K 2R1

Transport measurements have been made through the bound states of two parallel antidots in a quantum wire in the edge state regime. The results are compared with a non-interacting independent-electron model. The experimental results are consistent with the model but only above a certain magnetic field ($\sim 1.5T$).

Introduction

A device was expressly fabricated to make a 'controlled' investigation of a variety of processes which occur in antidot lattice systems. These effects include cyclotron trajectory trapping (and related phase coherent effects) at low magnetic fields [1] and coupled antidot tunnelling processes. In particular we were able to study the tunnelling events between two antidots in series or parallel from low to high magnetic fields. The unique versatility of this device allowed us, in addition, to form and investigate a new system, the 'antidot molecule', in which some magnetic edge states encircled both antidots while others encircled the individual ones. In this short paper, however, we concentrate on only one of the many possible configurations; tunnelling through two antidots in parallel in the edge state regime. We investigate how closely the experimental results can be understood in terms of non-interacting independent-electron models which have been successfully employed in previous studies on single antidots[2].

Experimental Results and Theoretical model

Figure 1 contains a schematic of the device. It comprises of several electrostatic gates used to define a quantum wire (lithographically 5 microns long and 1 micron wide) in a high mobility GaAs/AlGaAs heterostructure. Two additional gates are used to define 200nm antidots within the wire (separated from each other and the wire gates by 200nm). The antidot gates were contacted 'individually' using our multilevel architecture technique[3]. The measurements were made using standard low excitation AC techniques on a dilution refrigerator. The results presented in this paper were taken after maximizing the electron density by illumination with a red LED. More details of the device and sample are given elsewhere [1]. The antidots formed three parallel constrictions within the wire, each of which could be independently tuned. Extensive calibrations were performed to set exact device configurations for different applied gate voltages and magnetic fields. Data was taken in two distinct ways. We stress that for both cases we began by calibrating all the potentials for the complete gate voltage and field regime used (something impossible to achieve in larger antidot lattices). In the first technique the magnetic field was swept while all gate voltages were kept fixed. In these measurements the resonances associated with the bound states of both antidots were swept at roughly the same rate. In the second technique one of antidot gate voltages was swept while the magnetic field and all the other gate voltages were kept fixed. Since the one-particle states of

both antidots are dependent on the potential between the antidots this technique also swept the levels of both antidots through the Fermi level but at different rates ($\sim 1:3$). The sweeps were repeated at small magnetic field intervals (compared to the resonant period of the antidots). The gate voltage sweeps were then combined to form greyscale composite pictures. An example is given in figure 2.

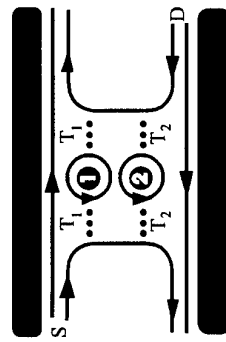


Figure 1:- A schematic diagram of the device and edge states (nb. only one reflected edge state is drawn for simplicity)

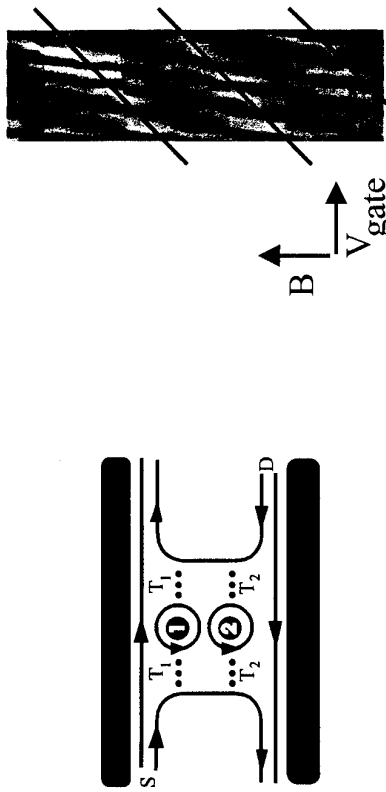


Figure 2:- A greyscale composite obtained from sweeping the gate of one antidot. (see text for details)

The edge state configuration used for tunnelling through antidots in parallel is shown in figure 1. In the simplest model no transmission of current is allowed directly between the two antidots. A new feature in this scenario is the conductance modulation resulting from an interference of the two individual antidot tunnelling paths. The situation of a single antidot has been studied theoretically by Kirzenow[5] and experimentally by several groups [2,4,6]. For simplicity and to reduce the number of model parameters only a single coupling point has been used at each antidot. In the case of a single antidot it was found by Kirzenow et al [2] that two coupling points (consistent with geometrical considerations) produced an additional slower beating effect observed in the data. The Landauer-Büttiker type of conductance formula for two antidots in parallel (assuming unitarity at all scattering events) for the conditions of figure 1 is given by

$$G(2e^2/h) = 1 + |f|^2$$

$$f = \frac{1}{I_0} / I_0$$

$$I_0 = t_{ab} e^{i(k_x x - k_y y)} (1 - r_p e^{i k_x r}) + t_{ba} (t_{ab} r_p e^{-i k_x r})$$

$$f_d = (1 - r_p e^{i k_x r}) (1 - r_b t_p e^{i k_x r}) - t_{ab} t_p t_q e^{i k_x r}$$

where G is the total conductance of the device. The coefficients t_{ab} , t_b , t_p , t_q are transmission amplitudes at the left and right sides of the upper (lower) antidots and were taken to be equal to T_1

(Γ_1). The corresponding reflection coefficients are r_1 , r_2 , r_p and r_q . The expression contains the phase factors χ_1 , χ_2 (dependent on the effective areas of the trapped states around the two antidots) as well as χ_3 (dependent on the area of the loop formed by part of the electron-wave going through each of the two antidots). A slightly more complicated expression involving more loops has also been derived for a model containing a finite transmission probability between the two antidots. To limit the number of free parameters in the model the transmission amplitudes and areas of individual antidots could be estimated from experiments on individual antidots (obtained experimentally by pinching off each side constriction in turn with the wire gates). The results for each antidot were consistent with our previous work on single antidots [2]. The oscillation period for the two antidots differed by up to 10%.

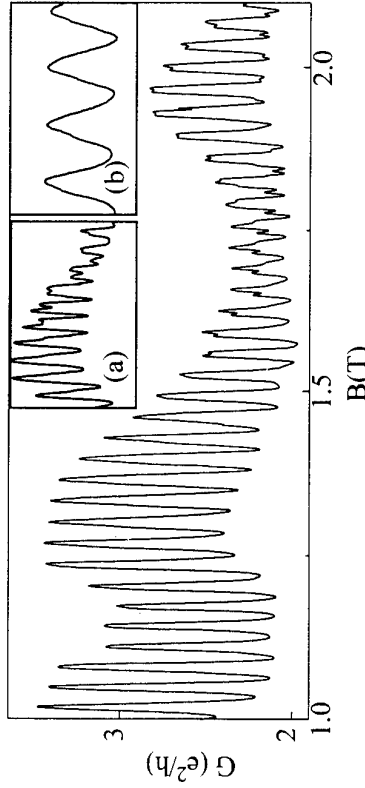


Figure 3:- Results from tunnelling experiments through parallel antidots. Inset(a) is for different gate voltage settings (see text for details). Inset (b) illustrates the 'triangular' lineshape of the lower field oscillations.

Figure 3 shows typical data obtained under the conditions of figure 1. The data falls roughly into two regimes. Starting with an apparent 'unlocking' feature at about 1.5T, we observe complex behaviour at higher fields in comparison to the single period oscillations obtained in measurements on single antidots in the same field regime. At these magnetic fields, however, it is found that the data can indeed be well accounted for by the above model. More details on the results obtained from the model in this regime will be given elsewhere. From about 0.8T to 1.5T we observe regular oscillations with a period and amplitude similar to that obtained for the single antidots (at these fields both of the individual antidots produced equally large amplitude resonant transmission oscillations). These magnetocapacitance oscillations, however, have a very triangular line shape (shown in the inset) which is quite distinct from the almost sinusoidal oscillations observed with single antidots. Whilst repeating measurements under slightly different conditions (e.g. using different gate voltages to increase the difference between antidot areas) altered the features above 1.5T in ways which could be easily modelled by adjusting the model parameters by reasonable amounts, the low field data remained very regular and could not be accounted for in the model. An inset in figure 2 illustrates an example of a field sweep under slightly different gate

voltage conditions. Above 2T additional structure due to spin resolution was observed while above 3T the resonances ceased to exist as a result of the decoupling between the antidot and reflected edge modes. Theoretical models are currently being investigated which take into account the coupling between antidots at lower magnetic fields. Since this is expected to switch off at higher fields it would explain the transition to a behaviour consistent with the simple model shown in figure 1.

Figure 2 is a greyscale diagram obtained by sweeping one of the antidot gate voltages at 3mV intervals between 1.6 and 1.7T. Such diagrams do not have enough resolution to identify the fine features of figure 3. However they provide useful additional information. As the gate voltage of an individual antidot is swept the individual levels of the two antidots pass through the Fermi energy at very different rates. This makes it easier to create and identify different regimes such as (i) both antidots on resonance (ii) both off resonance or (iii) one on and one off resonance. We find (as is intuitively obvious) that the difference corresponding to these regimes is especially dramatic for experiments involving tunnelling through antidots in series. The slanted vertical lines in figure 2 correspond to the resonances of the particular antidot being swept. The bright regions correspond to high resistance regions. In addition , however, there exist weaker stripes of bright and darker regions. The three lines are drawn to highlight these regions. These additional stripes are absent in experiments on single antidots. From measurements in which we studied tunnelling through antidots in series (as well as estimates from geometrical considerations) we identify the weak stripes as resulting from the single particle levels of the second antidot, brought into resonance indirectly due to the change in the potential between the two antidots induced by sweeping the first antidot. The magnetic field period (i.e. in the vertical direction of figure 2) is in good agreement with that expected for this second antidot. The observation of these stripes can be understood qualitatively as resulting from a higher(lower) total transmission when both antidots are both on (off) resonance. These observations confirm that the more complex structure observed above 1.5T results from the presence of two parallel and in this field regime 'independent' tunnelling paths.

Conclusions

We have used a novel device to study tunnelling through the single particle levels of two antidots in parallel. We have compared our results to a non-interacting independent electron model and found good agreement above a certain magnetic field. At lower magnetic fields we observe single period 'triangular' shaped oscillations with are not reproduced by the model. We acknowledge useful discussions with G.Kirczenow and the assistance of P.Zawadzki and K.Ieung with the experiments.

References

- [1] C.Gould et al., Phys. Rev. B51 (1995) 11213
- [2] G.Kirczenow et al., Phys. Rev. Lett. 72 (1994) 2069
- [3] Y.Feng et al., Appl. Phys. Lett. 63 (1993) 1666
- [4] S.W.Jhwang et al., Phys. Rev. B44 (1991) 13497
- [5] G.Kirczenow Phys. Rev. B50 (1994) 10856
- [6] C.J.B.Ford et al., Phys. Rev. B49 (1994) 17456

COULOMB GAP OF COUPLED QUANTUM DOTS WITH ADJUSTABLE INTERDOT TUNNELING

C.H. Crouch, C. Livermore, F.R. Waugh, [†] R.M. Westervelt,
Division of Applied Sciences and Department of Physics,
Harvard University, Cambridge, MA 02138

K.L. Campman, A.C. Gossard
Materials Department, University of California, Santa Barbara, California, 93106

ABSTRACT

We report low-temperature tunneling measurements at zero magnetic field through a double quantum dot with adjustable interdot tunneling rate, fabricated in a GaAs/AlGaAs heterostructure. We have measured the dependence of the current-voltage characteristic on interdot tunneling, and find that the Coulomb gap decreases continuously from that of two dots in series to that of a single large dot with twice the total capacitance as the interdot tunneling is increased from near zero to $2e^2/h$. These results are in agreement with many-body charge fluctuations due to tunneling between the dots.

INTRODUCTION

Conductance peak splitting, the stochastic Coulomb blockade, and single-particle states of individual dots have recently been observed in linear arrays of two and three dots [1-5] and in a parallel double dot [6]. Theories describing weakly coupled quantum dot systems include capacitive charging models [7] and Hubbard models [8]. Waugh et al. [1] discovered zero-bias conductance peak splitting of nominally identical double and triple quantum dots with tunable interdot tunneling, which correlates strongly with measured interdot tunnel conductance G_{int} and saturates for $G_{int} \approx 2e^2/h$. Golden and Halperin [9] and Matveev et al. [10] find that peak splitting arises theoretically from quantum mechanical charge fluctuations due to interdot tunneling, which reduce the energy of states with unequal numbers of electrons on the dots.

We report here low-temperature measurements of the Coulomb blockade in the current-voltage (I-V) characteristics of a double quantum dot with tunable interdot tunneling G_{int} . Figure 1a shows the device, a linear quantum dot array electrostatically defined by Cr/Au surface gates in a high mobility (5×10^5 cm²/V·s) near-surface (470 Å) two-dimensional electron gas with sheet density 3.7×10^{11} cm⁻² formed in a GaAs/AlGaAs heterostructure. The device was wired with six independently tunable gate voltages (Fig. 1b), one for each quantum point contact (V_1 through V_4), one for the top set of confining walls (V_5), and one for the bottom walls (V_6). Fourteen gates define up to three lithographically identical quantum dots in series; the double dot was formed by grounding V_1 to the electron gas. The total capacitance of a single dot of the array was measured to be $C_{2s} = 356 \text{ aF} \pm 8 \text{ aF}$ [1]. Increasing the voltage on the point contact which separates the dots (V_3) tunes G_{int} from near zero to $\geq 2e^2/h$; as G_{int} approaches $2e^2/h$, the two dots merge into a single large dot. G_{int} was measured separately by energizing gates 3 only. An equivalent circuit is shown in Fig. 1c; the gate voltage V_g was applied to side gates 5 to achieve matched gate-to-dot capacitances. Ac lockin

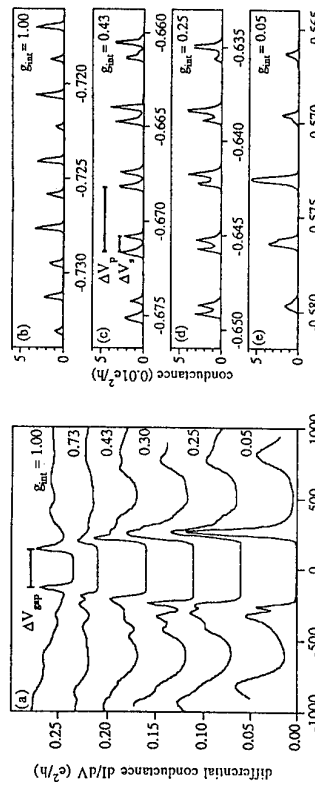


Fig. 2. (a) dI/dV vs. V_{ds} curves for the double dot for six values of dimensionless interdot tunnel conductance $G_{int}=Q_{int}/(2e^2/h)$ with V_5 constant. Traces have been offset vertically for clarity and have been centered for easy comparison of the Coulomb gap ΔV_{gap} . (b-e) Conductance measurements (zero dc bias) for values of G_{int} indicated.

measurements of the differential conductance dI/dV were made with ac drain-source bias $10 \mu\text{V}$ rms and dc drain-source bias V_{ds} . The device was cooled in a He dilution refrigerator to base temperature (18 mK).

RESULTS AND DISCUSSION

Figure 2a shows a series of dI/dV curves for the double dot taken for increasing values of the dimensionless interdot tunnel conductance $G_{int} \equiv G_{int}/(2e^2/h)$. A corresponding series of zero bias conductance measurements (Figs. 2b-e) show the peak splitting first reported by Waugh et al. [1]. As shown, both the Coulomb gap ΔV gap (see Fig. 2a) in the I-V measurements and the conductance peak splitting correlate strongly with G_{int} . The Coulomb gap and the peak separation decrease by a factor ≈ 2 as the interdot conductance increases from $G_{int}=0$ to $G_{int}=1.00$, as predicted by many-body theory [9,10].

The measured fractional peak splitting $F=2\Delta V/\Delta V_p$ (see Fig. 2c) is plotted in Fig. 3 (squares) versus G_{int} . Charge fluctuation theory [9,10] predicts that with negligible interdot capacitance, $F(G_{int} \rightarrow 0) = \frac{4\ln 2}{\pi^2} G_{int}$ and $F(G_{int} \rightarrow 1) = 1 + \frac{16e^2}{\pi^3} (1-G_{int})\ln(1-G_{int})$, where $\gamma \approx 0.577$. The measured peak splitting extrapolates to $F=0.115$ as $G_{int} \rightarrow 0$ due to capacitive splitting; we add this constant offset to the theory. Both expressions (solid lines in Fig. 3) agree well with the data and show the predicted saturation at $G_{int}=1$.

The Coulomb gap ΔV gap is also plotted in Fig. 3 (open circles) versus G_{int} . For $G_{int} < 1$, the tunneling contribution to the energy, $E_{int}(P)$, of the double-dot system in the presence of interdot polarization $P = CV_{ds}/e$ can be calculated from charge fluctuation theory [9]

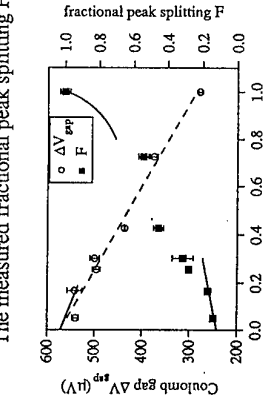


Fig. 3. Fractional peak splitting (filled squares) vs. dimensionless interdot tunnel conductance G_{int} . Solid lines are theory [9] described in the text. Coulomb gap ΔV_{gap} (open circles) vs. G_{int} . A linear fit to the data (dashed line) and theory described in [11] (solid line) are shown.

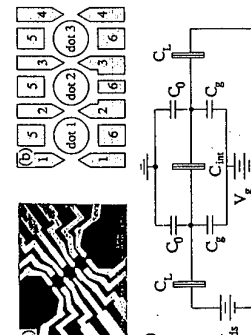


Fig. 1. (a) SEM micrograph of the device, an array of three coupled quantum dots with tunable interdot tunnel barriers in a GaAs/AlGaAs heterostructure. Scale bar is 1 μm ; lithographic size of dots is $0.5 \times 0.8 \mu\text{m}^2$. (b) Schematic device wiring. (c) Equivalent circuit for double dot differential conductance measurements. Ac lockin

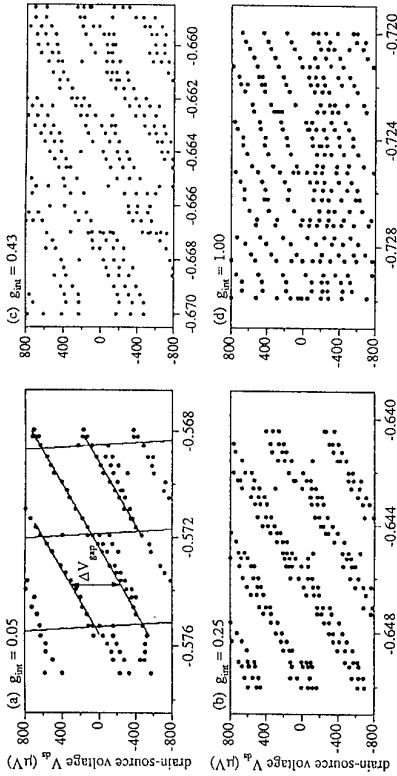


Fig. 4. (a-d) Position of peaks in the differential conductance dI/dV as a function of V_{ds} and V_g for the four C_{int} indicated.

to find the tunneling correction to ΔV_{gap} [11], $\Delta V_{gap} = -(271 \mu eV)C_{int}$, as shown by the solid straight dashed line is drawn through the ΔV_{gap} data in Fig. 3 to guide the eye.

Figures 4a to 4d show the positions of peaks in the differential conductance dI/dV in the (V_{ds}, V_g) plane for four increasing values of C_{int} . The diamond-shaped regions around $V_g=0$, bounded by peaks are the regions of Coulomb blockade. As shown, the Coulomb gap, ΔV_{gap} , decreases as C_{int} increases. We also observe bands of differential conductance peaks beginning just outside the Coulomb gap. These bands widen as C_{int} increases. The peak spacing within these bands is comparable to the single-particle state spacing of a single dot of the array [1] and remains roughly constant as C_{int} changes.

We can use capacitive charging models [7] in the $C_{int}=0$ limit to find the gap and peak splitting which arise from the interdot capacitance C_{int} alone (see Fig. 1c). Charging theory for Fig. 1c predicts diamond-shaped regions of Coulomb blockade with positive boundary slope

$$S_+ = \frac{C_g(C_{2d} + 2C_{int})}{(C_{int}(2C_{2d} - C_{int}) + C_{2d}^2 - C_L C_{2d})}, \text{ negative boundary slope } S_- = -\frac{C_{2d}}{C_{int} C_L},$$

$$\Delta V_{gap} = \frac{e(C_{2d} + C_{int})}{(C_{int}(2C_{2d} - C_{int}) + C_{2d}^2 - C_L C_{2d})}, \text{ and fractional peak splitting } F = \frac{2C_{int}}{C_{2d} + 2C_{int}},$$

where $C_{2d} \equiv C_C + C_B + C_g$. Assuming $C_{2d} + C_{int} \equiv C_{2s}$, appropriate for our geometry, we obtain $C_{int} = 22 \text{ aF} \pm 8 \text{ aF}$ and $C_{2s} = 334 \pm 8 \text{ aF}$ from the measured fractional splitting extrapolated to $C_{int}=0$. The dot-to-lead capacitance $C_L = 80 \text{ aF} \pm 10 \text{ aF}$ is obtained from single dot measurements [1]. Using these values of C_L , C_{2d} and C_{int} in Fig. 1c predicts $\Delta V_{gap}(C_{int}=0) = 583 \mu V$, in agreement with the value $\Delta V_{gap}(C_{int}=0) = 572 \mu V$ from Fig. 3; predicts $S_+ = 0.166$, in agreement with $S_+ = 0.169 \pm .002$ from Fig. 4a; and predicts $S_- = -4.6$, in agreement with $S_- < -1.8$ for Fig. 4a. (Negative slope boundaries drawn in Fig. 4a have $S_- = -4.6$.) The data of Fig. 4a are thus consistent with a small interdot capacitance C_{int} which determines the $C_{int}=0$ peak splitting and Coulomb gap and remains approximately constant as C_{int} changes, as discussed below.

For large interdot tunneling $C_{int} \geq e^2/h$ achieved in these experiments, classical charging theory is not applicable, and many-body charge fluctuation theory [9,10] should be used.

ACKNOWLEDGMENTS
We thank J. Golden, B. Halperin, K. Marveev, M. Stopa, and M. Eriksson for helpful discussions, and A. Adourian, J. Hergenrother, J. Katine, J. Liu, and D. Ralph for experimental assistance. This research was supported at Harvard by the ONR under grants N00014-95-1-0104 and N00014-95-1-0886, by the NSF under grant DMR-91-19386, and by ARPA under grant AFOSR-F49620-92-1-0466, and at UCSB by AFOSR-91-0214, C.H.C., and C.L. acknowledge support from the NSF Graduate Fellows program and C.H.C. from the AT&T Graduate Research Program for Women.

REFERENCES

- [1] F.R. Waugh, M.J. Berry, D.J. Mar, R.M. Westervelt, K.I. Campman, and A.C. Gossard, Phys. Rev. Lett., in press; F.R. Waugh, M.I. Berry, C.H. Crouch, C. Livermore, D.J. Mar, R.M. Westervelt, K.I. Campman, and A.C. Gossard, submitted to Phys. Rev. B.
- [2] M. Kemerink and L.W. Molenkamp, Appl. Phys. Lett. **65**, 1012 (1994).
- [3] T. Sakamoto, S. W. Hwang, F. Ninive, Y. Nakamura, and K. Nakamura, Jpn. J. Appl. Phys. **33**, 4876 (1994).
- [4] N.C. van der Vaart, S.F. Godijn, Y.V. Nazarov, C.J.P.M. Harmans, J.E. Mooij, L.W. Molenkamp, and C.T. Foxon, Phys. Rev. Lett. **74**, 4702 (1995).
- [5] D. Dixon, L.P. Kouwenhoven, P.L. McEuen, Y. Nagamune, J. Motohisa, and N. Sakaki, submitted to Phys. Rev. B.
- [6] F. Hofmann, T. Heinzel, D.A. Wharam, J. P. Kotthaus, G. Böhm, W. Klein, G. Frankle, and G. Weimann, Phys. Rev. B **51**, 13872 (1995).
- [7] M. H. Devoret and H. Grabert, in *Single Charge Tunneling*, ed. H. Grabert and M. H. Devoret (Plenum Press, New York, 1992), and references therein.
- [8] C. A. Stafford and S. Das Sarma, Phys. Rev. Lett. **72**, 3590 (1994), and references therein.
- [9] John M. Golden and Bertrand I. Halperin, submitted to Phys. Rev. B.
- [10] K.A. Marveev, L.I. Glazman, and H.U. Baranger, submitted to Phys. Rev. Lett.
- [11] The $C_{int} \rightarrow 0$ theory presented in [9] applies to a voltage-biased double dot with interdot polarization $p = CV_{ds}/e$ due to the bias. The gap correction is $\Delta V_{gap} = E_{int}(1-p) - E_{int}(p)$, evaluating p at $V_{ds} = \Delta V_{gap}/2$, the bias voltage at which the Coulomb gap is overcome. Including capacitive coupling between the dots gives, to first order in perturbation theory,
- $$E_{int}(p) = \frac{e^2}{2\pi C_{2s}} \left(\frac{C_{int} + C_{2s}}{C_{int} + 2C_{2s}} \right) \left[(1-p)\ln(1-p) + (1+p)\ln(1+p) \right].$$

Evaluating this result with $C_{int} = 22 \text{ aF}$, $C_{2s} = 334 \text{ aF}$, and $\Delta V_{gap} = 572 \mu V$ (treated as constant over the range of interest) gives the expression for ΔV_{gap} in the text.

Linear and Non-linear Transport Through Coupled Quantum Dots

D. Dixon, L. P. Kouwenhoven*, P. L. McEuen

*Department of Physics, University of California at Berkeley and Materials Science Division,
Lawrence Berkeley Laboratory, Mail Stop 2-200, Berkeley, California 94720*

Y. Nagamune, J. Motohisa**, H. Sakaki

*Research Center for Advanced Science and Technology, University of Tokyo, 4-6-1 Komaba,
Meguro-ku, Tokyo 153, Japan*

Abstract

We have measured linear and non-linear transport through a double quantum-dot system fabricated from the two-dimensional electron gas (2DEG) formed by a GaAs/AlGaAs heterostructure. At small source-drain bias, we observe Coulomb oscillations when the gate voltages of the two dots are tuned so that both dots conduct, in agreement with classical models of the two-dot system. At higher source-drain bias these Coulomb oscillations develop sharp overstructure, which arises from the alignment and de-alignment of quantized energy levels of the two dots.

Considerable interest recently has been directed to the study of electron transport through double quantum dots [1-15]. Much attention already has been paid to metallic and metallic-like systems [1-5], where the average quantum level spacing ΔE is very fine ($\Delta E < kT$), making these systems well-suited to classical models. Coupled quantum dots with well-separated 0D energy levels have also been studied theoretically [8-10] and experimentally [11-14]. Theories predict that the current through a double-dot system will be enhanced when the 0D-levels of the dots are in alignment, and that the current will be suppressed when the levels are dealigned. In this paper, we examine the effects of both charging and level quantization on electron transport through two dots connected in series.

Our device, fabricated from a GaAs/AlGaAs heterostructure, consists of an etched narrow channel of width $0.8 \mu\text{m}$ with five metal gates deposited over its width [15]. Two of the gates are held open at all times; the other three gates define the dots. Figure 1(a) shows a diagram of the device. When negative voltages are applied to the three gates (V_g^l , V_g^r , V_{gm}), the two-dimensional electron gas (2DEG) is depleted beneath the gates, forming two dots. The electron density was $3.64.0 \times 10^{11} \text{ electrons/cm}^2$ after illumination with an infrared diode at 4.2 K . The experiments were carried out in a dilution refrigerator, with the temperature of the electron gas determined to be $80-120 \text{ mK}$. All measurements were carried out near filling factor $v=4$ ($B=3.7-4.0 \text{ T}$), where the level spectra of the dots are very regular. The dots were measured individually and found to have a charging energy $e^2/C = 300-500 \mu\text{eV}$, and an average 0D-state energy separation $\Delta E=80-100 \mu\text{eV}$.

Before discussing our experimental results, we begin by considering the double-dot system using a classical model, where the effects of energy level quantization are ignored. It is useful to analyze this system by means of a "phase diagram" (Fig. (b)) [1], which details the charge state of the dots as a function of the two gate voltages. The phase diagram shown is for the case of the two gate voltages being nearly equal, with vanishing cross-capacitance between one gate and the other dot. Beginning at any point in the diagram, sweeping $V_g^l(V_g^r)$ positively will add electrons to dot 1(2) one by one. If the two dots are completely independent (meaning the interdot capacitance $C_{12}=0$), the phase diagram will simply be an array of squares, with vertical (horizontal) lines corresponding to the location of Coulomb oscillations for dot 1(2). Transport occurs at low bias for two dots in series only when these lines intersect, so that charge fluctuations can occur for both dots. If the interdot capacitance C_{12} between the dots is included, the charge-state domains become hexagonal, as the (M,N) and $(M+1,N+1)$ charge states are separated in energy due to electrostatic repulsion of electrons on different dots. At low bias, current can only flow through the two dots in series when the gate voltages are tuned to coincide with one of the triple-points (indicated by solid circles in Fig. 1(b)), where the three charge states involved in shuttling one electron across the double-dot system come together. For example, at the triple-point indicated by an arrow in the Figure, the double-dot system can fluctuate between charge states (M,N) , $(M+1,N)$, and $(M,N+1)$.

By applying a small bias,

electrons are driven across the device as the system cycles from (M,N) to $(M+1,N)$ to $(M,N+1)$ and back to (M,N) . At its neighbor triple-point, the sequence is $(M+1,N+1)$ to $(M+1,N)$ to $(M,N+1)$ and back to $(M+1,N)$, which shuffles a "hole" backwards across the device. Note that both triple points involve a transition from $(M+1,N)$ to $(M+1,N+1)$, when an electron is moved from one dot to the other. We will return to this interdot transition later in this paper.

Figure 1(c) shows a measurement of the current

through our double-dot system as a function of V_g^l and V_{g2} , with the current plotted in grayscale (black corresponds to zero current, white to $\sim 5 \text{ pA}$). This roughly square array of Coulomb peaks demonstrates that we have two well-formed dots. The array is slightly skewed, due to a small cross-capacitance between gate voltages and their opposite dots. In addition, a pair of triple points can be resolved in the upper right region of the plot. Nearly all the pairs of triple points are blurred together because of a finite source-drain bias ($50 \mu\text{V}$) and thermal smearing, both of which limit resolution.

We now discuss the nonlinear properties of the two dots in the classical model. At high bias (in this case, negative bias), the regions of phase space where current is allowed grow from triple-points into triangular regions (Figure 2(a)). The size and orientation of these triangles can be accounted for by the condition that electrons, while moving through the two-dot system, never jump uphill in energy, i.e. $\mu_L \geq \mu_1 \geq \mu_2 \geq \mu_R$ (or $\mu_L \leq \mu_1 \leq \mu_2 \leq \mu_R$ for positive bias) where $\mu_{L(R)}$ is the potential of the left (right) lead and $\mu_{1(2)}$ is the potential of dot 1 (2) when an extra electron is

capacitances being nearly equal, with vanishing cross-capacitance between one gate and the other dot. Beginning at any point in the diagram, sweeping $V_g^l(V_g^r)$ positively will add electrons to dot 1(2) one by one. If the two dots are completely independent (meaning the interdot capacitance $C_{12}=0$), the phase diagram will simply be an array of squares, with vertical (horizontal) lines corresponding to the location of Coulomb oscillations for dot 1(2). Transport occurs at low bias for two dots in series only when these lines intersect, so that charge fluctuations can occur for both dots. If the interdot capacitance C_{12} between the dots is included, the charge-state domains become hexagonal, as the (M,N) and $(M+1,N+1)$ charge states are separated in energy due to electrostatic repulsion of electrons on different dots. At low bias, current can only flow through the two dots in series when the gate voltages are tuned to coincide with one of the triple-points (indicated by solid circles in Fig. 1(b)), where the three charge states involved in shuttling one electron across the double-dot system come together. For example, at the triple-point indicated by an arrow in the Figure, the double-dot system can fluctuate between charge states (M,N) , $(M+1,N)$, and $(M,N+1)$.

By applying a small bias, electrons are driven across the device as the system cycles from (M,N) to $(M+1,N)$ to $(M,N+1)$ and back to (M,N) . At its neighbor triple-point, the sequence is $(M+1,N+1)$ to $(M+1,N)$ to $(M,N+1)$ and back to $(M+1,N)$, which shuffles a "hole" backwards across the device. Note that both triple points involve a transition from $(M+1,N)$ to $(M+1,N+1)$, when an electron is moved from one dot to the other. We will return to this interdot transition later in this paper.

Figure 1(c) shows a measurement of the current through our double-dot system as a function of V_g^l and V_{g2} , with the current plotted in grayscale (black corresponds to zero current, white to $\sim 5 \text{ pA}$). This roughly square array of Coulomb peaks demonstrates that we have two well-formed dots. The array is slightly skewed, due to a small cross-capacitance between gate voltages and their opposite dots. In addition, a pair of triple points can be resolved in the upper right region of the plot. Nearly all the pairs of triple points are blurred together because of a finite source-drain bias ($50 \mu\text{V}$) and thermal smearing, both of which limit resolution.

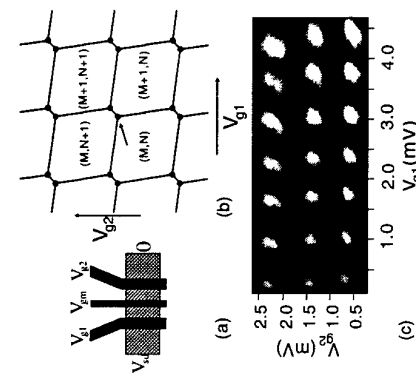


Figure 1: (a) Schematic view of the double-dot device. Three gates (V_g^l , V_g^r , V_gm) define the dots and modify their charge state. The source-drain bias V_{sd} is applied to the left lead, and the right lead is anchored to ground. (b) Theoretical phase diagram of a double-dot at low bias; current is only seen at the triple-points (denoted by solid circles). (c) Measurement of the current (plotted in grayscale) through the double-dot at low source-drain bias (50 μV) as a function of the two gate voltages. Distinct triple-points can be observed at approximately $V_g^l = 3.6 \text{ mV}$, $V_g^r = 2.2 \text{ mV}$.

added to that dot. The three equations that must be satisfied— $\mu_1 \geq \mu_1$, $\mu_1 \geq \mu_2$, and $\mu_2 \geq \mu_2$ —define the borders of the current-carrying triangular regions.

We repeat the type of measurement plotted in Fig. 1(c), but now with a high source-drain bias ($-350 \mu\text{V}$). In Figure 2(b), the current through the two-dot system is plotted in grayscale (black corresponds to zero current, white to $\sim 12 \text{ pA}$). At high source-drain bias, we indeed see a square array of nearly-right-tangled triangles. We also see extra features that cannot be accounted for by the classical model, namely a set of diagonal stripes moving up and to the right at a 45° angle; the point "X" is located on one of these stripes. Above and parallel to this primary stripe is a darker stripe, corresponding to a lower current, and further above is a second bright stripe which is less well-defined than the primary stripe. These stripes represent overstructure on each Coulomb oscillation. This overstructure is dramatically present in the line trace of Figure 4 (taken during a different measurement run). Here the applied bias ($+380 \mu\text{V}$) is of the opposite sign of the bias used to generate Figure 2(b), but the explanation is similar. The plot shows four Coulomb oscillations with two or three sharp features per oscillation.

To understand this overstructure, we must consider the influence of the quantum levels on the transport step that involves tunneling between the two dots. Note that the stripes in Fig. 2(b) are all parallel to the $\mu_1 = \mu_2$ line shown in Fig. 2(a), so that at every point along these stripes, $\mu_1 - \mu_2 = \text{const}$. This condition singles out the interdot tunneling step as being the origin of these features. Fig. 2(c) shows the potential landscape of the two-dot system at the point indicated by "X" in Fig. 2(b). The quantum ground state for any particular charge state of dot 1 (2) is labelled 0 (0') and the first few excited states are labeled 1, 1' (2, 2') [16]. The primary stripe of each triangle corresponds to the alignment of the ground-state energies of the two dots, $\mu_1(0) = \mu_2(0)$. If V_{g2}^2 is increased, the ground states of the dots are taken out of alignment, and the current drops (dark stripe). As we change V_{g2} further, $\mu_1(0)$ aligns with $\mu_2(1')$, and the current increases (second bright stripe). These stripes have no dependence on interdot charging effects, because, as mentioned previously, the "electron" and "hole" sequences of current flow both contain the step, $(M+1, N) \rightarrow (M, N+1)$. It is the influence of 0D-states on this transition rate that gives rise to the stripes in Fig. 2(b).

The alignment of 0D-states is responsible for the overstructure in the data of Figure 3. The sharp peaks are due to alignment of the 0D-states indicated next to each peak; for example, $|1-0'$ labels the peak in current which results from the first excited state of dot 1 (1) aligning with the ground state of dot 2 (0'). The spacing ΔE between energy levels on dot 1 can be deduced from

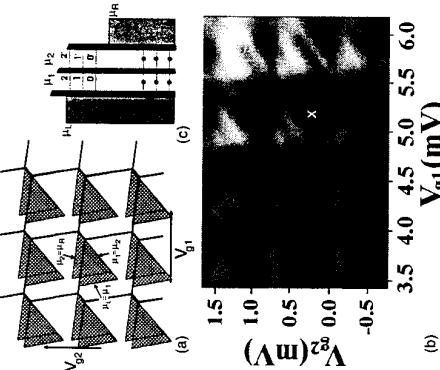


Figure 2: (a) Theoretical phase diagram at high-bias ($0 < V_{g2} < V_d/2e^2/C$). The hatched areas represent the gate voltages where current is observed, and the conditions for current flow define the borders of the hatched areas. (b) Grayscale plot of the measured current through the double-dot system at high bias ($V_d=0.35 \text{ mV}$). The diagonal stripes are due to the alignment of energy levels. (c) Potential landscape at the point "X" in Figure 2(b).

the spacing ΔV_{g2} between the $0-0'$ and $1-0'$ resonances on any Coulomb oscillation. We obtain $\Delta E \sim 90 \mu\text{eV}$, in agreement with single-dot measurements.

In conclusion, we have examined linear and nonlinear transport through two dots in series. We observed that the alignment of 0D-states can dramatically affect transport through a double-dot system. Similar results to ours have been recently published by van der Vaart, *et al.* [14].

We would like to thank Ned Wingreen and David Cobden for useful discussions. This work was supported by the Office of Naval Research, the Packard Foundation, and the Royal Netherlands Academy of Arts and Sciences (L. P. K.).

References

- * Present address: Department of Applied Physics, Delft University of Technology, P.O. Box 5046, 2600 GA Delft, The Netherlands.
- ** Present address: Research Center for Interface Quantum Electronics, Hokkaido University, North 13 West 8, Sapporo 060, Japan.
- [1] H. Pothier *et al.*, Europhys. Lett. **17**, 249 (1992).
- [2] Bart Geerligs *et al.*, Physica B **165&166**, 973 (1990).
- [3] I. M. Ruzin *et al.*, Phys. Rev. B **45**, 13469 (1992).
- [4] M. Kemerink and L. W. Molenkamp, Appl. Phys. Lett. **65**, 1012 (1994).
- [5] F. Hofmann *et al.*, Phys. Rev. B **51**, 13872 (1995).
- [6] R. Blick *et al.*, to be published (1994).
- [7] F. R. Waugh, Ph. D. thesis, Harvard University (1994).
- [8] Gerhard Klimeck, Guanlong Chen and Supriyo Datta, Phys. Rev. B **50**, 2316 (1994).
- [9] C. Y. Fong, *et al.*, Phys. Rev. B **46**, 9538 (1992).
- [10] J. Garnett W. Bryant, Phys. Rev. B **48**, 8024 (1993), Phys. Rev. B **44**, 3064 (1991).
- [11] L. P. Kouwenhoven *et al.*, Phys. Rev. Lett. **65**, 361 (1990).
- [12] M. A. Reed *et al.*, Adv. Solid State Phys. **29**, 267 (1989).
- [13] M. Tewordt *et al.*, Appl. Phys. Lett. **60**, 595 (1992).
- [14] Nijs van der Vaart *et al.*, Phys. Rev. Lett. **74**, 4702 (1995).
- [15] L. P. Kouwenhoven *et al.*, Phys. Rev. Lett. **73**, 3443 (1994).
- [16] Figure 3 shows the energy splittings for both dots being constant and equal. This assumption is not necessary to explain the main features of this paper, it just simplifies the analysis. Nevertheless, our experiments indicate that the energy splittings of each dot are not appreciably different.

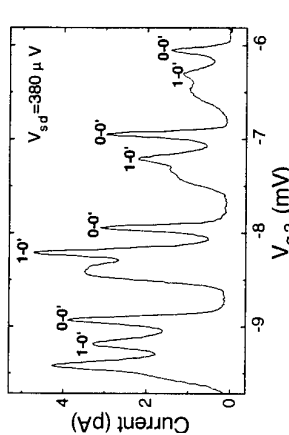


Figure 3: Four double-dot Coulomb oscillations at high bias. The rightmost peak on each dot corresponds to the alignment of the ground-states of both dots (0-0'). The next peak corresponds to alignment of the excited state of dot 1 to the ground state of dot 2 (1-0').

Coulomb blockade in coupled quantum dots

F. Hofmann, T. Heinzel, D.A. Wharam, J.P. Kotthaus
Sektion Physik der Ludwig-Maximilians Universität,
Geschwister-Scholl-Platz 1, D 80539 München, Germany.

&
G. Böhm, W. Klein, G. Träffke, G. Weimann
Walter Schottky Institut, Technische Universität München,
D 85748 Garching, Germany

Abstract

Low temperature conductance measurements have been performed upon a coupled quantum dot structure defined in the plane of a two-dimensional electron gas. The observed oscillatory conductance, reflecting the charge quantisation in the structure, is significantly modified due to the additional inter-dot coupling. This behaviour has been simulated using a simple capacitance model for the coupled dot structure. Interestingly, the addition of a single electron to the weakly coupled dot can switch the observed conductance from a conductance maximum to a conductance minimum.

The Coulomb blockade (CB) of transport in mesoscopic devices has created significant recent interest due both to the possible technological significance of such devices, as well as to the fascination of the fundamental physics. In metallic systems the CB is well described within an essentially classical picture of the charging effects [1]; in semiconducting devices however, the large separation between quantum states is expected to lead to a significant modification of this simple classical picture. These expectations have been confirmed by a large number of recent investigations upon single quantum dots [2], however, to date only a few experiments have been performed upon coupled quantum dot systems.

conducting dot to the surrounding reservoirs, as well as the tuning of the tunnel barrier between the two dots.

Here, we present results of low-temperature conductance measurements performed upon a coupled quantum dot structure defined in the plane of a high-mobility two-dimensional electron gas (2DEG). The lithographically defined electrodes used to deplete the underlying 2DEG are shown in Fig. 1; the application of appropriate negative bias voltages leads to the definition of a coupled quantum dot structure in a parallel configuration. In this geometry the current flow through the device is constrained to flow through the main, conducting dot which is weakly coupled via an internal tunnel barrier to the second, non-conducting dot. Previous investigations of coupled quantum dots [3] have concentrated on the series configuration of dots where the current flow is through both of the dots. The resulting CB structure has been coined the stochastic CB [4] due to the aperiodic nature of the resulting conductance oscillations whose observation requires the simultaneous lifting of the CB in both quantum dots. In the parallel geometry considered here these additional complications of the stochastic CB have been avoided and thus permit the inter-dot coupling to be investigated directly.

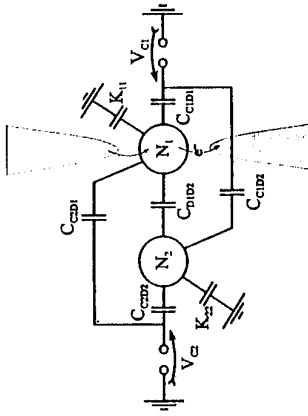


Figure 2. The system of capacitances used to model the parallel dot structure shown in Fig. 1. The coupling of the main dot to the reservoirs is schematically indicated.

The CB of transport in this device has been modelled using a simple capacitance model of the quantum dots and surrounding electrodes (see Fig. 2) as has been discussed elsewhere in detail [5,6]. Within the context of this model the energy of the coupled dot structure has been minimised as a function of both the centre-gate voltages (V_{C1} , V_{C2}) used to separately tune each dot and the quantised charges on the two dots. The resulting energy function yields the stable configuration (N_1, N_2) (i.e. the number of electrons stored on each dot) of the coupled dot device. The character of this configuration space depends essentially upon the magnitude of the inter-dot capacitance, C_{D1D2} , relative to the other partial capacitances of the device. The magnitude of the former, capacitance can be continuously tuned via the bias applied to the electrodes defining the internal tunnel barrier and the device behaviour accordingly. In the limit of vanishing inter-dot capacitance the two dots are essentially decoupled and standard CB of transport pertains. In the other extreme limit of large inter-dot capacitance the two dots merge into one contiguous region and the device operates as a large quantum

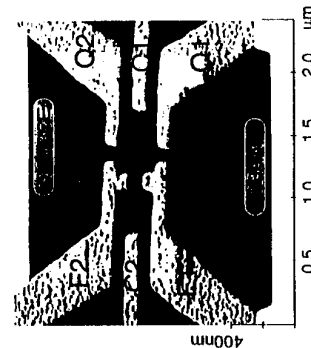


Figure 1. An atomic force micrograph of the parallel coupled dot structure used in these experiments. This geometry permits the independent control of both the coupling of the

dot [5,6]; the observed linewidth of the conductance oscillations is significantly broadened reflecting the larger total capacitance.

Between these two extremes the character of the stable configuration space is highly reminiscent of the charging diagram for the single electron pump [7] and is illustrated in Fig. 3. The interpretation, however, of this charging diagram is significantly different. For the single electron pump the CB is lifted at the nodes of the charging diagram where three configurations are simultaneously degenerate; for the parallel geometry considered here, the boundaries separating configurations with different numbers of electrons in the main dot correspond to those points where the CB is lifted as indicated by the thick lines in Fig. 3. Also indicated as thin continuous lines are the boundaries corresponding to a change in the occupancy of the second dot, and as dotted lines the boundaries corresponding to an internal transfer of an electron.

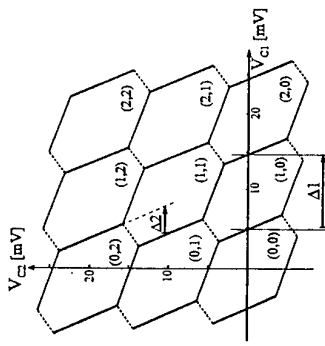


Figure 3. The periodic structure of the configuration space is illustrated as a function of the two centre-gate voltages used to tune each dot. The three fundamentally different types of boundary between stable configurations are indicated, as is the stable charge configuration of the two quantum dots.

Low-temperature ($T = 30$ mK) conductance measurements of the coupled dot have been performed for a wide range of center-gate voltages and the resulting data clearly showed both the CB and the quasi-periodic conductance oscillations expected [5,6]. In Fig. 4 the maxima of these conductance measurements have been plotted as a function of the two centre-gate voltages and the best fit to the simple capacitance model indicated. As discussed above, the CB is clearly lifted along those boundaries corresponding to a change in the occupancy of the main dot. Furthermore, a change in the occupancy of the second dot is also weakly visible. The observation of these boundaries cannot be explained by an activated transport mechanism via states in the main dot, and we attribute the observation of this boundary to cotunneling through virtual states [8].

Of particular interest is the tunability of the conductance via the charge state in the second dot. The charge quantisation condition in the second dot leads to a discrete change in the conductance when the occupancy of the second dot is altered [5]. This switching behaviour is more robust than the normal conductance oscillations themselves and is reminiscent of the switch in polarisation of a coupled quantum dot state which has been theoretically investigated as a possible quantum-mechanical realisation of a cellular automaton [9].

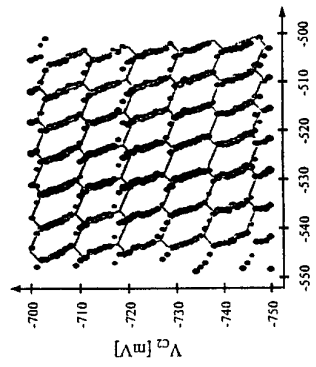


Figure 4. The gate-voltage dependence of the observed conductance maxima are plotted as a function of the applied centre-gate voltages. In addition the best fit according to the simple capacitance model is also illustrated.

In conclusion, we have investigated the CB of transport in a parallel, coupled dot geometry and demonstrated that the salient features of the observed conductance oscillations can be explained within a simple, classical capacitance model. The quantum mechanical nature of the device has, as yet, to be fully investigated but is clearly evident both in the statistical fluctuations of the periodic conductance oscillations as well as in the observation of cotunneling through states of the second dot.

References:

- [1] H. van Houten, C.W.J. Beenakker, and A.A.M. Staring, *Single Charge Tunneling*, Eds. H. Grabert and M.H. Devoret, (Plenum Press, 1992).
- [2] *Physica B* **189**, 1-278, Eds. L.J. Geerligs, C.J.P.M. Harmans, and L.P. Kouwenhoven (North-Holland, Amsterdam, 1993).
- [3] M. Kemerink and L.W. Molenkamp, *Appl. Phys. Lett.* **65**, 1012, (1994).
- [4] I.M. Ruzin, V. Chandrasekhar, E.I. Levin, and L.I. Glazman, *Phys. Rev. B* **45**, 13469, (1992).
- [5] F. Hofmann, T. Heinzel, D.A. Wharam, J.P. Kotthaus, G. Böhm, W. Klein, G. Tränkle, and G. Weimann, *Phys. Rev. B* **51**, 13872, (1995).
- [6] F. Hofmann and D.A. Wharam, *Festkörperprobleme* **35**, (1995).
- [7] H. Pothier, P. Lafarge, C. Urbina, D. Esteve, and M.H. Devoret, *Europhys. Lett.* **17**, 249, (1992).
- [8] D.C. Glattli, *Physica B* **189**, 88, (1993).
- [9] C.S. Lent, P.D. Tougaw, and W. Porod, *Appl. Phys. Lett.* **62**, 714, (1993).

Wave Function and Conductance Calculations for a Quantum Dot at Resonant Tunnelling Peaks

P.N. Butcher^a and J.A. McInnes^b

^a Physics Department, University of Warwick, Coventry CV4 7AL, U.K.
^b Computer Science Department, University of Strathclyde, Glasgow G1 1XH, U.K.

Abstract

We use a recently developed numerical matching procedure to calculate conductances g_{12} and scattering wave functions ψ for a quantum dot. The dot is formed in a 2D quantum wire by pushing in two hard wall fingers with height h , width d and separation s . Calculations are made for rectangular and capped fingers when $d/w = 0.1$, $s/w = 0.47$ and $h/w = 0.70, 0.60$ and 0.53 . We find two resonant tunnelling peaks in g_{12} below the transmission threshold at wave numbers which decrease with decreasing h/w . We use contour plots of $|\psi|/2$ to show that this behaviour when h decreases is due to increasing "spillage" of $|\psi|/2$ over the tops of the fingers and above the space between them. The higher resonance finally merges with the first continuous region of strong transmission.

1. Introduction

In a recent paper [1] the authors describe a widely applicable new procedure for calculating conductances and scattering wave functions for 2D hard wall nanostructures. In this paper we use the procedure to calculate conductances and scattering wave functions when two hard wall fingers are pushed in through one side of a quantum wire to form a quantum dot. Studies of wave functions in other structures using different matching procedures are reported in references [2-14]. We suppose that the 2DEG is at absolute zero and is spin degenerate with a Fermi wavelength denoted by λ . The conductance g_{12} is calculated in units of $2e^2/h$ as a function of $2w/\lambda$ where w is the width of the quantum wire. Our concern is the resonant tunnelling peaks which arise when $2w/\lambda$ is below the nominal propagation threshold of the structure.

2. The dependence of conductance on the Fermi wavelength

In Fig.1 we sketch the structure to be considered. We always take $d/w = 0.1$, $s/w = 0.47$ and vary $h/w = 0.70, 0.60$ and 0.53 . Resonant tunnelling peaks are found at $2w/\lambda = 2.214$ and 2.743 when $h/w = 0.70$ as shown by the full line in Fig.2. The location of the peaks is close to the two lowest resonant $2w/\lambda$ values for the open-ended space between the fingers. We write the resonant values of λ in this space in the form λ_{mn} where m is a positive integer and n is a positive odd integer. Then

$$(1) \quad \frac{2w}{\lambda_{mn}} = \left[\left(\frac{mw}{s} \right)^2 + \left(\frac{nw}{2h} \right)^2 \right]^{\frac{1}{2}}$$

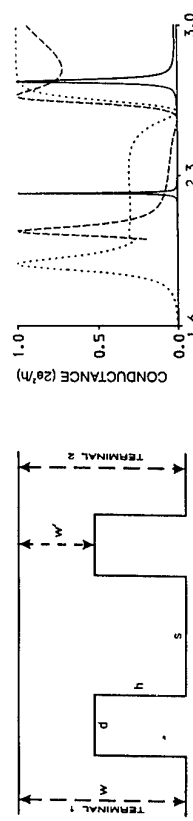


Fig. 1 A sketch of the nanostructure giving the notation used for its dimensions. The full lines are hard potential walls.

The corresponding solutions of the wave equation (in which the potential energy is zero) vanish on the hard walls at the bottom and the sides of the space considered and has zero normal derivative on a horizontal straight line joining the tops of the fingers. The two lowest values of $2w/\lambda_{mn}$ derived from equation (1) are $2w/\lambda_{11} = 2.26$ and $2w/\lambda = 3.03$ which are within 2% and 10% respectively of the values at the resonant peaks in Fig.2. The error arises because Eq.(1) is a crude approximation. It takes no account of the spillage of the wave functions above the tops of the fingers and the space between them which we discuss in Section 3.

To illustrate further the effect of spillage we also plot the resonant peaks in Fig.2 for $h/w = 0.60$ (dashes), and 0.53 (dotted). Eq.(1) predicts that $2w/\lambda_{11}$ and $2w/\lambda_{13}$ both increase as h is reduced. We see from Fig.2 that the opposite happens because decreasing h increases the aperture $w' = w-h$ above the fingers which increases the wave function spillage. In the next section we present wave function contours which confirm this explanation. We also see in Fig.2 that the width of the resonances increases as h/w is reduced which is consistent with increasing leakage into the region above the fingers. We would also expect spillage to increase when the flat fingers considered up till now are replaced by shorter fingers (with h reduced by r) capped with semicircles of radius r . Our calculations confirm this expectation.

The dashed curve in Fig.2 has $h/w = 0.6$. The nominal threshold is at $2w/\lambda = 2.5$ and the second resonance is now almost obscured by the beginning of the first region of strong propagation. Finally, the dotted curve has $h/w = 0.53$. The nominal threshold is at $2w/\lambda = 2.14$ and a short plateau with $g_{12} = 1$ completely obscures the second resonance. In this case the first resonance peak has moved to $2w/\lambda = 1.89$ and is followed by a pseudo-plateau with $g_{12} = 0.26$ extending from $2w/\lambda = 2.0$ to 2.4 . We notice that, in all three cases, $g_{12} = 0$ near to $2w/\lambda = 2.6$ which is just below the second resonance. When $h/w = 0.533$ this zero delays the onset of the region where $g \sim 1$ until $2w/\lambda$ is well above the nominal threshold.

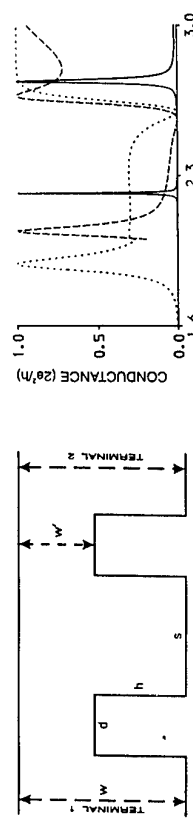


Fig. 2 The dependence of the resonance peaks on finger height for $d/w = 0.1$, $s/w = 0.467$ and $h/w = 0.7$ (solid line), 0.6 (dashed line), 0.533 (dotted line).

3. The behaviour of the wave function contours

4. Conclusion

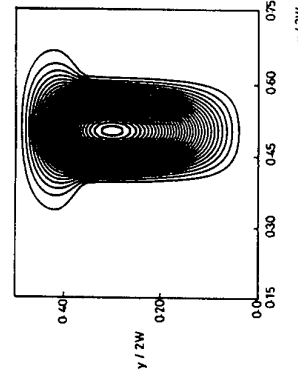


Fig.3 Contours of $|\psi|^2$ for the structure which produces the solid line in Fig.2. The contours are drawn for $2w/\lambda = 2.214$ which is at the centre of the first resonance peak.

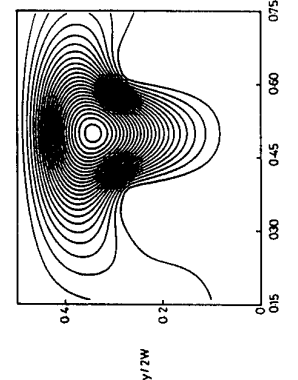


Fig.4 Contours of $|\psi|^2$ for the structure which produces the dotted line in Fig.2. The contours are drawn for $2w/\lambda = 1.89$ which is at the centre of the first resonance peak.

In this Section we present contour plots of $|\psi|^2$ when the dominant mode is incident in terminal 1. (The dominant mode begins to propagate in the terminals when $2w/\lambda = 1$). Fig. 3 shows the contours when $h/w = 0.7$ and $2w/\lambda = 2.214$, i.e. at the centre of the first resonance peak. The contours are confined in the regions between the fingers ($0.38 < x/2w < 0.60$ on the length scale used in Fig.3) but there is considerable "spillage" into the space above both the fingers and the space between them. In both terminals $|\psi|^2$ is too small to appear on the contour scale used in Fig.3. The contours are almost symmetrical about the centre line of the structure (at $x/2w = 0.5$) in spite of the asymmetric excitation. This is because the dominant mode incident in terminal 1 strongly excites the lowest organ pipe resonance between the fingers which is symmetrical.

In Fig.4 we plot contours of $|\psi|^2$ when h/w is reduced from 0.7 to 0.533. The variation of g_{12} in this case is given by the dotted line in Fig.2. The contours in Fig.4 are drawn for $2w/\lambda = 1.89$ which is at the centre of the first resonance peak. We see that there is a fairly strong build up of $|\psi|^2$ over the entire region in the space between and above the fingers and above the space between them. Moreover, the position of the maximum in $|\psi|^2$ has moved from just inside the space between the fingers in Fig.3 to just outside it in Fig.4 which is why $2w/\lambda$ decreases.

References

- [1] P.N. Butcher and J.A. McInnes, J. Phys.: Condens. Matter 7, 1995, 745.
- [2] F. Huariang and X. Xide, Phys. Rev. B 50, 1994.
- [3] A. Szafr and A.D. Stone, Phys. Rev. Lett. 62, 1990, 300.
- [4] H.U. Baranger and A.D. Stone, Phys. Rev. B 40, 1989, 8169.
- [5] H.U. Baranger, D.P. DiVicenzo, R.A. Jalabert and A.D. Stone, Phys. Rev. B 44, 1991, 10637.
- [6] G. Kirzenow, Solid State Commun. 68, 1988, 715.
- [7] G. Kirzenow, J. Phys.: Condens. Matter 1, 1989, 305.
- [8] G. Kirzenow, Phys. Rev. B 32, 1989, 10452.
- [9] D.L. Maslov, C. Barnes and G. Kirzenow, Phys. Rev. B 48, 1993, 2543.
- [10] L. Escapa and N. Garcia, J. Phys.: Condens. Matter 1, 1989, 2125.
- [11] N. Garcia and L. Escapa, Appl. Phys. Lett. 54, 1989, 1418.
- [12] E. Tekman and S. Ciraci, Phys. Rev. B 39, 1989, 8772.
- [13] Y. Avishai and Y.B. Band, Phys. Rev. B 40, 3429, 12535; Phys. Rev. Lett. 52, 1989, 2527; Phys. Rev. B 41, 3253; 1991, Phys. Rev. Lett. 66, 1990, 1761.
- [14] Z-L. Li and K-L. Berggren, Phys. Rev. B 45, 1992, 6652.
- [15] P.N. Butcher and J.A. McInnes, submitted to Journ. Phys.: Condens. Matter.

Magneto-tunnelling Spectroscopy of a Quantum Dot Charged with a Few Electrons

A.Nogaret, M.J.Gompertz, P.C.Main, L.Eaves, T.J.Foster, M.Hennini, S.P.Beaumont[◆]
 Department of Physics, University of Nottingham, NG7 2RD, UK
 ◆ Department of Electronics and Electrical Engineering, University of Glasgow,
 Glasgow G12 8QQ, UK

Abstract:

We have measured the tunnelling current through a two-dimensional quantum dot formed at the intersection between two wires. Near the onset, the current-voltage curves display a step-like current structure characteristic of incremental charging of the quantum well controlled by Coulomb blockade. Using a magnetic field, we probe the energy levels within the dot when charged with either one or two electrons. These results are compared to the Darwin-Fock calculation for a parabolic quantum dot.

The physics of electrons which are electrostatically confined in three dimensional dots is currently attracting considerable interest. Dots with capacitance, C , sufficiently small so that $kT < e^2/C$ exhibit properties controlled by Coulomb blockade [1]. In semiconductor dots, the low effective mass of electrons permits the investigation of a regime where both energy and charge quantization are comparable in size [2]. Unlike the situation with metal islands, semiconductor dots can be incrementally charged from zero [3] thus permitting an experimental study of interacting systems of few electrons [4].

The quantum dot investigated in this paper is formed in the 10.2 nm wide quantum well of an asymmetric double barrier structure. The mesa (Fig.1) is shaped as a submicron square loop with 900nm (500nm) external (internal) sidelengths. We assume zero dimensional states are formed in its four corners [5] and are bound to the one dimensional subbands that extend over the straight parts of the wire. The influence of both types of states in the tunnel current has been previously reported [6]. In forward (reverse) bias, fig. 1b, electrons traverse first the thinner, 5.6nm, (thicker, 6.6nm) barrier. 200nm spacer layers placed between the barriers and the doped contact regions are effective in preventing the segregation of ionized donors away from the active region since no sub-threshold current structure has been observed in any of the samples investigated [7].

Near the current onset in forward bias, the current increases incrementally in steps $\Delta I \approx 210\text{pA}$ in height and $\Delta V \approx 5\text{mV}$ in width (Fig.2). In contrast, only a single step is seen in reverse bias (inset Fig.3a). Moreover, ΔI is independent of mesa area whereas ΔV is not. This suggests that electrons at the Fermi level in the emitter start filling 0D states locally bound inside the square loop and within the quantum well. The current staircase is then a manifestation of single electron tunnelling controlled by Coulomb blockade. The single electron tunnelling time is independent of the mesa area and is $\tau_{\text{meas}} \approx 760\text{ps}$ ($\tau_{\text{meas}} = e/\Delta I$). This is in reasonable agreement with the theoretical expectation $\tau_{\text{theo}} \approx 580\text{ps}$ calculated from a sequential tunnelling picture [8].

The $\alpha=0.25\text{eV/V}$ bias to energy conversion factor [9] gives the charging energy of the dot to be: $e^2/C=1.2\pm0.2\text{meV}$ ($e^2/C=\alpha.\Delta V$). By treating each barrier as an independent capacitor, we estimate the conducting radius of the dot to be $r \approx 37\text{nm}$. Incremental charging of the dot only occurs in forward bias because the thicker collector barrier inhibits tunnelling out of the well and allows charge build-up. If the incremental charging were occurring in the emitter accumulation layer rather than the well, the Coulomb staircase would be seen in reverse bias instead.

A magnetic field (B) applied to the dot as indicated in fig.1b can increase the onset position in forward bias by up to $\approx 8\text{ mV}$ at $B \approx 5\text{T}$. Above this field, it remains unchanged. In reverse bias, the maximum shift of the onset is $\approx 7\text{ mV}$ at $B \approx 5\text{T}$. We interpret the $B < 5\text{T}$ regime as due to the diamagnetic shift of the ground energy state of the quantum dot with respect to the emitter Fermi energy. Since its energy increases as:

$$E_{0,0}(B)=\{(h\omega_c/2)^2+(h\omega_0)^2\}^{1/2} \quad (\text{Eq.1})$$

one can fit the B-dependence of the onset position (inset Fig.2) with the separation between the dot energy levels, $\hbar\omega_0$, as the only adjustable parameter. $\hbar\omega_c$ is the cyclotron energy. The inset of fig.2 shows that Eq.1 reasonably fits the data for $\hbar\omega_0$ being $1.25 - 2.00\text{ meV}$. Above $B=5\text{T}$ tunnelling starts through the first 1D subband.

Fig.3a plots the current through the quantum dot as a function of B when the bias is kept constant. The current steps are again due to the discreteness of the charge but, here, the number of electrons in the dot is controlled by the magnetic field. In turn, the fine current structure (arrows, Fig.3a) is due to oscillations in the tunnelling rate when the Darwin-Fock [10] energy levels in the dot (Fig.3b) successively cross the emitter Fermi level. The thick traces in fig.3b show the oscillations of the maximum in-plane energy of the electrons in the $V=105\text{mV}$ curve as a function of B. At $B > 4.2\text{T}$ the current is non resonant because all states in the well have too high an energy to align with the emitter Fermi level. As B is reduced to about 4.2T , a single electron current starts through the ground state of the dot. The four following features seen as B is decreased, are due to states of lower angular momentum ($m=-1,-2,\dots$) becoming resonant. Note that the spacing between the current features increases with decreasing magnetic field as is expected from the Darwin-Fock energy spectrum (Fig.3b). At $B=2.2\text{T}$, the dot ground state lies e^2/C lower than the maximum in-plane energy of the first electron. Hence, a second electron can now be admitted into the well and this two-electron current gives rise to the second step. Two of the current peaks observed next, in the $0 < B < 2.2\text{T}$ field range, correspond to values of the magnetic field where the $m=-1$ state cross the emitter Fermi level (Fig.3b). However the explanation of the peak at $B=0.95\text{T}$ seems to require the presence of one additional state which does not exist in the single particle spectrum. This extra peak could possibly arise from the spin singlet-spin triplet splitting of the $m=-1$ level which is expected when electron-electron interactions are taken into account [11]. At $V=100\text{mV}$, only one electron can be admitted in the dot with an in-plane energy of about $\alpha(100-97)=0.75\text{ meV} (< e^2/C)$. The structure in fig.3a is therefore ascribed to the two lowest single particle states successively becoming resonant.

The Darwin-Fock spectrum quantitatively describes the fine structure at $V=105\text{mV}$. Our fit shown in Fig.3b gives a unique value for $\hbar\omega_0 = 1.25 \pm 0.05\text{ meV}$. From this fit we can deduce *independently* the values of other device parameters and compare them with the values obtained earlier. (i) In Fig.3b, the emitter Fermi energy

lies 2.5meV above the dot ground state [c.f. $\alpha(105\text{-}97)=2\text{meV}$]; (ii) at $B \approx 2.2\text{T}$, one reads on fig.3b, $e^2/C=1.4\text{ meV}$ (c.f. 1.2meV) and (iii) from the result of the fit: $r=(2\hbar/(m^*\omega_0))^{1/2}=43\pm0.8\mu\text{m}$ (c.f. 37.37nm).

In summary, we have been able to control the charge of a quantum dot using either applied electric or magnetic fields. This allows us to investigate by resonant tunnelling the regime where charge and energy quantization are of the same order of magnitude. The measured energy excitations for a one and two electron system are in good agreement with the single particle energy spectrum of a parabolic quantum dot.

This work is supported by EPSRC (UK).

References:

- [1] D.V.Averin and K.K.Likharev, in Mesoscopic Phenomena in Solids, edited by B.L.Altshuler, P.A.Lee, R.A.Webb (Elsevier, Amsterdam, 1991)
- [2] P.L.McEuen et al., Phys.Rev.Lett. **66**, 1926 (1991)
- [3] B.Su, V.J.Goldman, J.E.Cunningham, Phys.Rev.B **46**, 7644 (1992)
- [4] for a review see: N.F.Johnson, J.Phys.Cond.Matter **7**, 965 (1995)
- [5] J.Goldstone and R.L.Jaffe, Phys.Rev.B **45**, 14100 (1992)
- [6] A.Nogaret et al., Proceedings of the MSS-7 conference (1995)
- [7] J.W.Sakai et al., Appl.Phys.Lett. **64**, 2563 (1994)
- [8] T.Weil, B.Vinter, Appl.Phys.Lett. **50**, 1281 (1987)
- [9] α is derived from the known values of the LO phonon and cyclotron energy in GaAs, see: M.L.Leadbeater et al., Phys.Rev.B **39**, 3438 (1989)
- [10] V.Fock, Z.Phys. **47**, 446 (1928); C.G.Darwin, Proc.Cambridge Phil. Soc. **27**, 85 (1930)
- [11] G.W.Bryant, Phys.Rev.Lett. **59**, 1140 (1987)

Figure Captions:

Figure 1:

(a) Top view micrograph and (b) diagram of a resonant tunnelling structure whose mesa is tailored as a square loop with 900 nm (500 nm) external (internal) sidelength. Lower confinement in the corners produces 0D states bound to the 1D subbands in the straight arms of the loop. The tunnel current is measured when the top electrode is biased with respect to the substrate.

Figure 2:
The current-voltage characteristic near the current onset for forward biases. Inset shows the bias shift of the first and second current steps as a function of magnetic field. The series of dashed lines are plots of Eq.1 with different $\hbar\omega_0$.

Figure 3:

(a) Magnetic field dependence of the current through the dot. The inset shows reverse bias I-V characteristics. The Darwin-Fock energy spectrum is plotted in (b). The fine structure indicated by arrows in (a) corresponds to states with different angular momentum traversing the Fermi level in the emitter (b). Both thick lines in (b) trace the energy oscillations undergone by the two electron system at $V=105\text{mV}$.

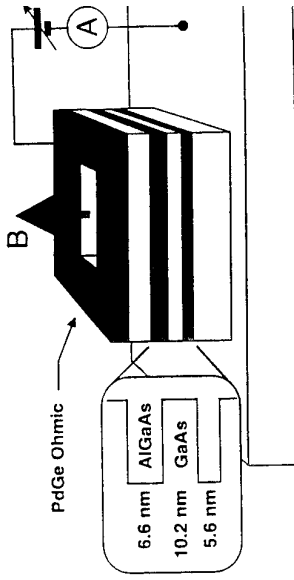
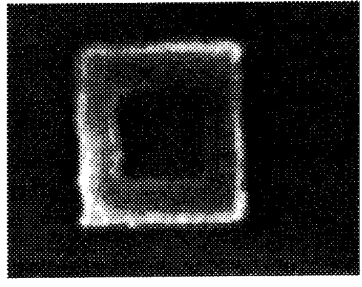


Figure 1:
(a) Top view micrograph and (b) diagram of a resonant tunnelling structure whose mesa is tailored as a square loop with 900 nm (500 nm) external (internal) sidelength. Lower confinement in the corners produces 0D states bound to the 1D subbands in the straight arms of the loop. The tunnel current is measured when the top electrode is biased with respect to the substrate.

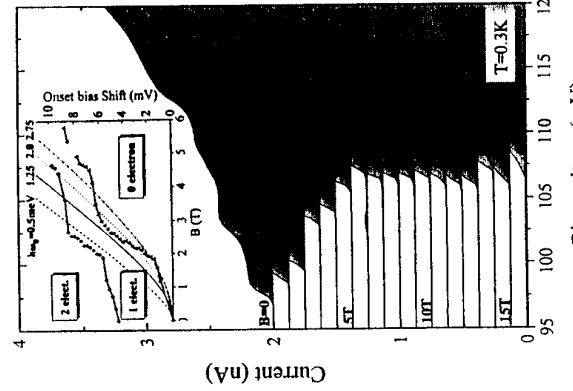
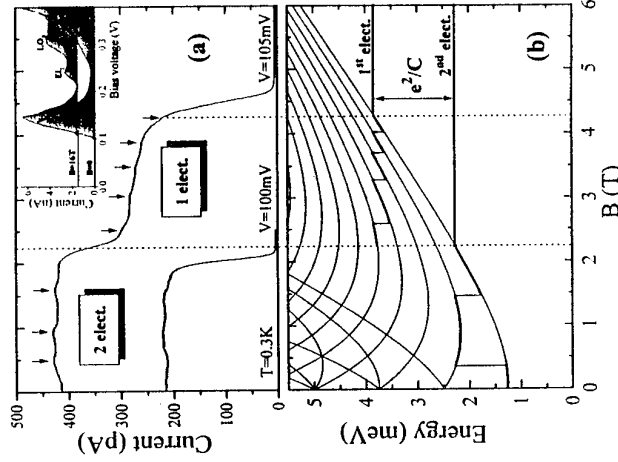


Figure 2:
(a) Magnetic field dependence of the current through the dot. The inset shows reverse bias I-V characteristics. The Darwin-Fock energy spectrum is plotted in (b). The fine structure indicated by arrows in (a) corresponds to states with different angular momentum traversing the Fermi level in the emitter (b). Both thick lines in (b) trace the energy oscillations undergone by the two electron system at $V=105\text{mV}$.

Figure 3:
(a) Current-voltage characteristic near the current onset for forward biases. Inset shows the bias shift of the first and second current steps as a function of magnetic field. The series of dashed lines are plots of Eq.1 with different $\hbar\omega_0$.
(b) The current-momentum characteristics. The fine structure indicated by arrows in (a) corresponds to states with different angular momentum traversing the Fermi level in the emitter (b). Both thick lines in (b) trace the energy oscillations undergone by the two electron system at $V=105\text{mV}$.

complicated structures occur for larger electron numbers [4]. For spin polarized electrons the magnetic angular momenta, J , are given by $J = N(N-1)/2 + kN$ [5] and $J = N(N-1)/2 + k(N-1)$ [3] where k is a positive integer, for N and $(N-1)$ -fold symmetry respectively. For example, figure 1 shows correlation functions, $C \langle \sum_i \hat{r}_i \delta(\mathbf{r}_i - \mathbf{r}_0) \delta(\mathbf{r}_j - \mathbf{r}_0) \rangle$ where C is a normalisation constant (the black spots denote \mathbf{r}_0). The correlation functions are for the lowest energy states of 6 electrons at $J = 40$ and $J = 45$ and they were obtained by numerically diagonalizing the ideal 2D hamiltonian for a GaAs/AlGaAs interface by a 6 fold symmetry difference between the 5 and 6-fold classical minima is rather small, only about 0.57meV at $J = 45$. In addition, symmetry allows both types of minima to occur only at certain J values, the lowest of which is 45. In this case quantum tunnelling mixes the two types of symmetry and, as can be seen in the figure, the peaks in the $J = 45$ correlation function are less sharp. This is possibly relevant to the fractional quantum Hall effect because the equivalent filling factor, calculated from $\nu = N(N-1)/2J$ is 1/3.

Next, consider the quantum states of electrons in a real device. The central problem of calculating these states is that the electrons are localised at a GaAs/AlGaAs interface by a potential that depends on the electron density as well as the densities of the dopants in the device and the gate electrode potential. This means that there is no obvious basis in which to diagonalize the interacting electron hamiltonian. To overcome this difficulty the interacting electron states are first calculated approximately by means of a variational Hartree-Fock (HF) approximation. This gives not only electron energies but also an orthonormal basis that is localised at the interface and may be used as the input to an exact diagonalization. However, the variational approximation alone is able to reproduce the ground state transitions that occur in the ideal 2D model so it is interesting to explore this approach in detail.

In the variational calculation the trial wave function is taken to have the form $\Phi(\mathbf{r}_1 \dots \mathbf{r}_N) = \Psi(\rho_1 \dots \rho_N) \prod_i \chi(z_i)$ where ρ_i and z_i are the parallel and perpendicular co-ordinates, χ is a function to be determined and Ψ is a Slater determinant of states, ψ , which are taken to have the Fock-Darwin form: $\psi_{nl}(\rho) = A_n(\lambda) \rho^{|l|} \exp(-i\phi) L_n^{(|l|)}(\rho^2/4\lambda^2) \exp(-\rho^2/4\lambda^2)$ where λ is treated as a variational parameter, n and l are radial and angular momentum quantum numbers, the $L_n^{(|l|)}$ are associated Laguerre polynomials and A_n is a normalisation constant. In the ideal 2D case these states are eigenstates of non-interacting electrons provided that λ satisfies the relation $\lambda^2 = \hbar/2m^* \Omega$, where $\Omega^2 = \omega_0^2 + \omega_c^2/4$ and ω_c is the cyclotron frequency, eB/m^* . A Hartree (H) approximation is also considered and in this case Ψ is taken to be a product of the ψ instead of a Slater determinant. The exact hamiltonian of the system may be written in the form $H = \sum_i T_{||i} + T_{\perp i} + U(\mathbf{r}_i) + V$, where $T_{||i} = (\mathbf{P}_{||i})^2/2m^*$, $T_{\perp i} = (\mathbf{P}_{\perp i})^2/2m^*$, $\mathbf{A}(\mathbf{r}_i)$ is the magnetic vector potential, $U(\mathbf{r}_i)$ is the electrostatic potential of the device in the absence of conduction band electrons and V is the electron-electron interaction. An equation for $\chi(z)$ is obtained by evaluating the matrix element of this hamiltonian with the state Φ and demanding that the result be stationary with respect to first order variations in χ . This leads to the 1D HF equation $(T_{\perp i} + \tilde{U} + V_{HF})\chi = \varepsilon\chi$ where ε is the HF eigenvalue and \tilde{U} and V_{HF} are laterally averaged potentials whose form is too complicated to reproduce here [6]. Self-consistent solution of the 1D HF equation together with minimisation of the total energy with respect to λ gives the solution of the variational problem for a particular set of single electron states ψ_n . The global minimum energy for a given J value is found by repeating the calculations for all sets of l values that sum to the required J .

Calculations were performed for a structure identical to that studied by Kumar *et al.* [7].

A relaxation method was used to calculate the electrostatic potential on a grid of $51 \times 51 \times 51$

Ground states of 2D and 3D quantum dots

L.D. Hallam*, N.A. Bruce and P.A. Maksym
Department of Physics and Astronomy
University of Leicester
Leicester LE1 7RH, UK.

June 13, 1995

Abstract

Ground states of spin polarized electrons in 2D and 3D quantum dots are studied theoretically. It is shown that new and interesting transitions occur in the 2D case when the number of electrons is 6 or more and it is shown that the transitions survive when the ideal 2D model is replaced by a realistic device model.

KEYWORDS: Many body and quasiparticle theories, Semiconductor-semiconductor interfaces.

One of the most interesting features of quantum dots is that the ground state undergoes a series of transitions with increasing magnetic field. Its angular momentum generally increases in a step like way and only certain 'magic' combinations of angular momentum and spin are allowed [1]. These transitions affect physical properties of dots such as the magnetization and the rate of tunnelling through dots and some of them have possibly been observed [2]. Most theoretical studies of these transitions have been done for very small numbers of electrons (up to 3 or 4) with the aid of an ideal 2D model of quantum dots in which the electron motion is perfectly two dimensional and the confining potential is parabolic. The present work extends these studies in two ways: first it is shown that new and interesting transitions occur in the ideal 2D model when the number of electrons is 6 or more and secondly it is shown that the 3 electron transitions survive when the ideal 2D model is replaced by a realistic device model.

Roughly speaking, the reason why the magic numbers occur is that the quantum ground state of few electron dots is normally localised about the classical minimum energy configuration. This minimum has a well defined symmetry which is only compatible with the permutational symmetry of the electron wave function at the magic combinations of angular momentum and spin. For a ground state, the two symmetries must be compatible so ground states only have the magic quantum numbers. More precisely, the classical symmetry is seen in a special moving reference frame in which vibrational motion is approximately decoupled from rotational motion. By considering the quantum states in the moving frame and antisymmetrizing them it is possible to derive expressions for the magic angular momentum and spin combinations of the quantum ground states in the laboratory frame [3].

For small electron numbers, N , the classical minimum always has well defined rotational symmetry. For $N \leq 5$ the minimum is ring shaped with N -fold symmetry but for $N = 6$ and $N = 7$ the symmetry is $(N-1)$ -fold with $N-1$ electrons on the ring and one in the centre. More

points and a standard differential equation package (NAC) was used to solve the 1D HF equation. The electron-electron interaction was taken to be a pure Coulomb potential. For more accurate studies, screening by the gate electrodes should be taken into account [8] but this does not affect conclusions about existence of transitions. The search for the minimum energy configuration was restricted to the zeroth Landau level and J values up to 21 were considered. At first sight the use of circularly symmetric basis states may seem at variance with the square cap of the structure of Kumar *et al.*, however the potential is circularly symmetric to within 1% at 500Å from the center of the dot. Thus the circularly symmetric basis states should give accurate results.

Figure 2 shows the ground state energy as a function of magnetic field. The minimum energies vary smoothly for both the H and HF approximations, with very slight changes in gradient at the transitions between total angular momentum. The H approximation gives consistently higher energies than the HF approximation. The magnetic fields at which transitions in the total angular momentum occur are shown in Table 1. The row labeled 2D gives transition fields calculated in the ideal 2D model. In this case the value of $\hbar\omega_0$ (4.962 meV) was determined from the curvature of the electrostatic potential at the GaAs/AlGaAs interface. The HF approximation reproduces the same sequence of transitions that occur in the ideal 2D model but the H approximation does not. The HF minimum energy states have consecutive l values, for example 2,3,4 at $J = 9$ and thus same Slater determinant occurs with highest probability in the ideal 2D ground state [5]. However the minimum energy states in the H approximation do not have this property, for example the l values at $J = 9$ are 1,3,5.

Figure 3 shows the optimal value of λ as a function of magnetic field. Results for H, HF and ideal 2D cases are shown. For high fields both H and HF converge to the 2D case. The H approximation shows large discontinuities at the transition points, whereas the HF approximation shows very small if any discontinuities. As expected, λ approaches the ideal 2D magnetic length in the strong field limit when the electrons are restricted to move in the very bottom of the confining potential.

This work was supported by the UK Engineering and Physical Sciences Research Council.

References

- [*] Present address: Computer Centre, University of Leicester, Leicester LE1 7RH.
- [1] P.A. Maksym, Physica B **184**, 385 (1993).
- [2] R.C. Ashoori, H.L. Störmer, J.S. Weiner, L.N. Pfeiffer, K.W. Baldwin and K.W. West, Phys. Rev. Lett. **71**, 613 (1993).
- [3] P.A. Maksym, submitted to Phys. Rev. B.
- [4] V. M. Bedanov and F. M. Peeters, Phys. Rev. B **49**, 2667 (1994).
- [5] P.A. Maksym and T. Chakraborty, Phys. Rev. B **45**, 1947 (1992).
- [6] N.A. Bruce, L. D. Hallam and P.A. Maksym, in preparation.
- [7] A. Kumar, S.E. Laux and F. Stern, Phys. Rev. B **42**, 5166 (1990).
- [8] L.D. Hallam, J. Weis and P.A. Maksym, submitted to Phys. Rev. B.

	3 → 6	6 → 9	9 → 12	6 → 12	12 → 18
H	8.9 ± 0.1	-	-	11.7 ± 0.1	11.9 ± 0.1
HF	11.8 ± 0.1	17.5 ± 0.1	> 20.0	-	-
2D	9.5 ± 0.1	14.5 ± 0.1	> 20.0	-	-

Table 1. Transitions of total angular momentum and the field at which they occur in Tesla.

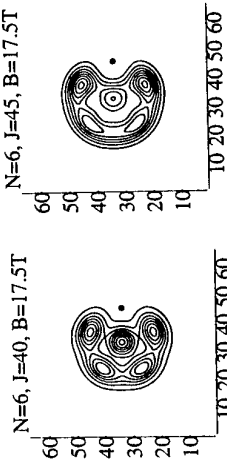


Figure 1. Correlation functions for 6 electrons in the ideal 2D model. Note the weakened peak structure at $J = 45$.

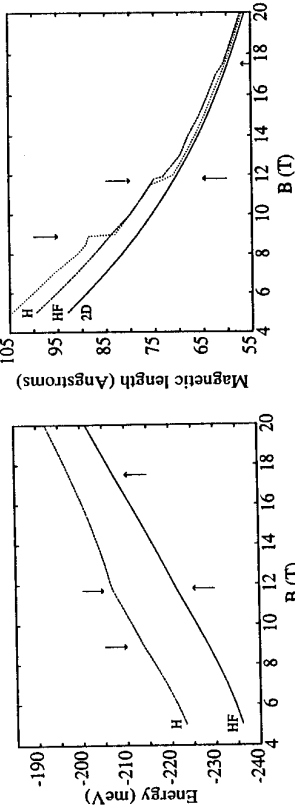


Figure 2. Ground state energy against magnetic field for 3 electrons in a realistic magnetic field. Arrows denote transition fields.

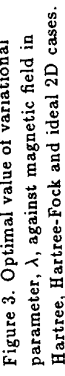


Figure 3. Optimal value of variational parameter, λ , against magnetic field in Hartree, Hartree-Fock and ideal 2D cases.

Intrinsic Bistability in Nonlinear Transport Through a Submicron Lateral Barrier

G. Pilling, D. H. Cobden, and P. L. McEuen

Department of Physics, University of California and Materials Science Division,
Lawrence Berkeley Laboratory, Berkeley, CA 94720, USA

C. I. Duruöz, J. S. Harris, Jr.

Solid State Laboratory, Stanford University, Stanford CA 94305-4055, USA

Abstract

We investigate nonlinear transport between regions of 2DEG separated by a submicron barrier produced by a shallow etch in a GaAs/AlGaAs heterostructure. After illumination a region of bistability appears in the *I*-*V* characteristic, where the current jumps randomly between zero and a finite value. The bistability is seen routinely in all similar devices, and it occurs even if the etch is deeper than the 2DEG, implying that the current-carrying electrons leave the plane of the heterojunction.

Introduction

Nonlinearities and instabilities in the electrical characteristics of semiconductor devices result from rapid spatial or temporal variations in the distribution of mobile carriers and impurity charges, fed with energy by a large electric field. Many varieties exist and they have been observed and studied intensively for their potential uses in high-frequency electronics [1], and because they can exhibit non-equilibrium phase transitions and classical chaos [2].

Here we present our investigations of a new and particularly simple kind of nonlinear instability which appears in submicron lateral barriers in 2DEGs. Whereas for macroscopic systems, the instabilities occur at large biases (of the order of volts), in this mesoscopic system the typical bias required is of the order of only 10 mV. Also, the phenomenon has a very regular form, a similar instability being seen in every one of a large number of devices of suitable dimensions. The mechanism, which we do not yet fully understand, should take into account that the electrons must leave

the plane of the heterojunction in the barrier region to carry current.

Experiment

The devices were standard GaAs/AlGaAs heterostructures made from a wafer with a 2DEG of density $3 \times 10^{15} \text{ m}^{-2}$ (Fermi energy 10 meV) and mobility $20 \text{ m}^2 \text{ V}^{-1} \text{ s}^{-1}$ located 800 Å below the surface. Patterns were defined by electron-beam lithography and wet etched in the conducting mesa using 40:1:1 $\text{H}_2\text{O}_2:\text{H}_2\text{PO}_4$. Fig. 1 (a) shows an atomic-force microscope image of a typical single barrier device, and Fig. 1 (b) shows a schematic cross-section through the center along the current direction. The depth of the etched trench was between 500 and 1000 Å. The devices were immersed in liquid helium at 4.2 K and voltage biased, and the current was measured using a dc-coupled virtual-earth preamplifier. A red or infrared LED mounted nearby was used for illumination.

The *I*-*V* characteristics of a device with a 100 nm wide, 800 Å deep trench before and after illumination are shown in Fig. 2 (a). Before illumination (trace A) no current flows below a threshold bias of more than 1 V. The threshold bias is dramatically reduced after illumination (traces B and C).

Fig. 2 (b) shows the characteristic of the same device at biases below 20 mV in one direction, after increasing amounts of illumination using an infrared LED. A much smaller amount of illumination using a red LED has an equivalent effect. All devices exhibit similar behaviour to that seen here. For each trace in this figure, *V* was swept up and down several times. During each sweep a sudden jump occurs between a zero current and a finite current state. The jump is at a slightly different position each time, and there is hysteresis between the up and down sweeps. With increasing illumination the differential conductance dI/dV in the current-carrying state increases until it saturates at a value between 10 and 100 μS for all devices. Also after high illumination the *I*-*V* of this state always extrapolates down to a threshold *V* of about 6 mV. At the same time the average positions of both up and

FIG. 1. (a) Atomic force microscope image of an etched barrier. All coordinates are in microns. The current flows along the mesa from left to right. The etched region has a bow-tie shape, so that the barrier is narrowest in a very small region at the center. (b) Schematic cross-section along the current direction. The arrow indicates how the current flows out of the heterojunction to pass the etched region.

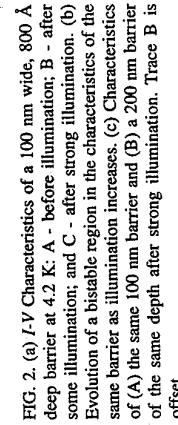


FIG. 2. (a) *I*-*V* Characteristics of a 100 nm wide, 800 Å deep barrier at 4.2 K: A - before illumination; B - after some illumination; and C - after strong illumination. (b) Evolution of a bistable region in the characteristics of the same barrier as illumination increases. (c) Characteristics of (A) the same 100 nm barrier and (B) a 200 nm barrier of the same depth after strong illumination. Trace B is offset.

down jumps move towards the threshold bias, and the hysteresis decreases and eventually vanishes. If V is then swept in one direction a series of jumps may be seen, as illustrated in Fig. 3 (a).

The inset here shows I as a function of time at a fixed V in the middle of the bistable region. It exhibits a random telegraph signal [3] with characteristic (mean) time constants τ_1 and τ_0 for the conducting and insulating states respectively. Both the telegraph signal and the hysteresis can be described by specifying the values of τ_1 , τ_0 and I (in the conducting state) at each value of V . The time constants vary exponentially with V , and therefore I , with gradients of similar magnitude but opposite sign on a log-linear plot, as illustrated in Fig. 3 (b). Hysteresis loops like those in Fig. 2 (b) are seen when the time constants at the crossing point, at which $\tau_1 = \tau_0$, are much longer than the measurement time.

Fig. 2 (c) shows the post-illumination characteristics of the same barrier (trace A) and another (width 200 nm - trace B) over a wider range of V . The difference between these traces represents the typical variation from device to device, which shows no obvious correlation with barrier width. In both traces, bistability is apparent in the region of 10 mV. At higher bias the detailed form of the I - V is more device specific. Further hysteresis loops are visible in trace B, but not in trace A. Nevertheless, the approximate symmetry of the I - V curve about $V = 0$ is always present.

Discussion

To begin to understand this phenomenon we must consider the effects of illumination in this system, which are thought to be twofold [4]. First, DX centers in the AlGaAs become ionized. Second, above-bandgap photons, far fewer of which are emitted by the infrared LED than by the red one, can create electron-hole pairs in the GaAs. The holes then recombine with ionized acceptors (mainly substitutional carbon) in the bulk GaAs and neutralize them. These processes together increase the carrier concentration in the 2DEG (by up to $\sim 20\%$ in our samples). The acceptor neutralization also has another consequence which we believe is crucial: it weakens the confinement potential seen by the electrons in the 2DEG, causing their wavefunctions to spread out more into the GaAs substrate. We believe that this allows electrons to leave the

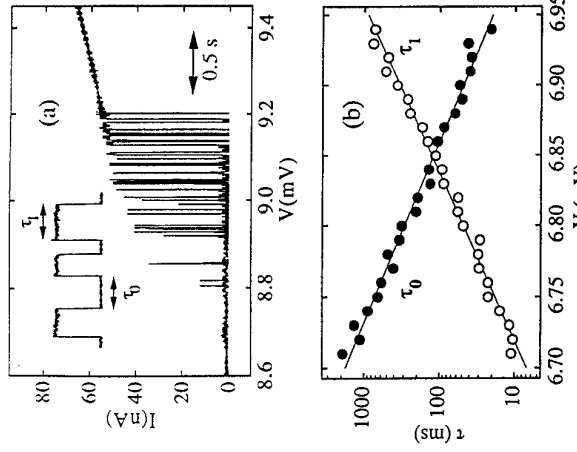


FIG. 3. (a) Main trace: slow sweep of V past the bistability for the 100 nm barrier after strong illumination. Inset: sample of I versus time at fixed V . (b) Dependence of the time constants on V , measured for a different device with a lower threshold. The solid lines are exponential fits. (c) Comparison of the I - V characteristics of two different devices. Trace A is for the 100 nm barrier and trace B is for a 200 nm barrier. The x-axis is V (mV) and the y-axis is I (A).

Conclusions

We have described a bistability which occurs at the onset of current flow across a mesoscopic barrier etched in a heterostructure. It is only seen after strong illumination and involves electrons leaving the plane of the heterojunction. The microscopic origin of this phenomenon remains a mystery. However, once understood, we believe this low-capacitance nonlinear device may be useful for creating high frequency circuits. It may also be a model system for studying non-equilibrium phase transitions in the mesoscopic regime. We are grateful to Per Hedegård, Kasper Eriksen, Boris Musykantskii, Dung-Hai Lee, Lisa Borland and Marc Bockrath for many stimulating discussions.

References

- [1] See, for example, *Physics of Semiconductor Devices*, by S. M. Sze (Wiley, 1981); and *Negative Differential Resistance and Instabilities in 2-D Semiconductors*, Eds. N. Balkan, B. K. Ridley and A. J. Vickers (Plenum, New York, 1993).
- [2] *Encounter with Chaos: Self-Organized Hierarchical Complexity in Semiconductor Experiments*, J. Pienke, J. Parisi, O. E. Roessler and R. Stoop (Springer, Berlin, 1992).
- [3] See, for example, M. J. Kirton and M. J. Uren, Adv. in Phys. **38**, 367 (1989).
- [4] R. Fletcher et al., Phys. Rev. B **41**, 10649 (1990).
- [5] C. Berven, M. N. Wybourne, A. Ecker, and S. M. Goodnick, Phys. Rev. B **50**, 14639 (1994).
- [6] J.C. Wu, M.N. Wybourne, C. Berven, S.M. Goodnick, and D.D. Smith, Appl. Phys. Lett. **61**, 2425 (1992).
- [7] C. I. Durñiz, R. M. Clarke, C. M. Marcus, and J. S. Harris Jr., Phys. Rev. Lett. **74**, 3237 (1995).
- [8] A. K. Savchenko, A. Woolfe, M. Pepper, J. E. F. Frost, D. A. Ritchie, M. P. Grimshaw, G. A. C. Jones, and V. V. Kuznetsov, preprint (1993).

CONDUCTION THRESHOLD, SWITCHING, AND HYSTERESIS IN QUANTUM DOT ARRAYS

C. I. Duru z,⁽¹⁾ C. M. Marcus,⁽²⁾ and J. S. Harris Jr.⁽¹⁾

*(1)Solid State Electronics Laboratory, Stanford University,
Stanford, CA94305-4055*

*(2)Department of Physics, Stanford University,
Stanford, CA94305-4060*

ABSTRACT

We investigate low temperature transport in 200x200 arrays of GaAs quantum dots in which coupling between dots and electron density are controlled by a single gate. Current-voltage curves obey a power law above a threshold voltage with exponent ~ 1.5 , and show discontinuous and hysteretic jumps in the current, or "switching events." Multiple switching events result in a hierarchy of hysteresis loops. Switching and hysteresis decrease with increasing temperature and disappear above 1 K. A possible mechanism for the hysteresis involving gate-to-dot tunneling, and the crossover from weak to strong localization in the array as a function of the gate voltage will be discussed.

Reference: C. I. Duru z, R. M. Clarke, C. M. Marcus, and J. S. Harris, Jr., "Conduction Threshold, Switching, and Hysteresis in Quantum Dot Arrays" *Phys. Rev. Lett.* (in press).

CONDUCTANCE INSTABILITIES IN QUANTUM POINT CONTACTS

J.C. Smith, C. Berven, and M.N. Wybourne
 Department of Physics, University of Oregon
 Eugene, OR 97403

S.M. Goodnick
Department of Electrical and Computer Engineering, Oregon State University
Covallis, OR 97331

Whitroot

We present low temperature electron transport measurements on quantum point contacts defined by electrostatic constrictions in the two-dimensional electron gas of a GaAs/AlGaAs heterostructure. Infrared illumination and annealing reversibly changes the nature of the electron transport through the point contact from ideal point contact behavior to transport that shows two-level conductance fluctuations. In the ideal case, the dependence of the differential conductance on the bias across the contact is used to determine the shape of the transverse confining potential. In the non-ideal case, current-controlled negative differential conductance in the device characteristic is observed, and is shown to be the average of a two-level random telegraph signal. The random telegraph signal consists of fluctuations between two well-defined differential conductance states. We suggest the fluctuations are due to changes in the transverse confining potential caused by the dynamics of DX centers in the AlGaAs near the point contact.

卷之三

Over the past few years, much work has been devoted to near equilibrium transport through quantum waveguides and point contacts [1]. In this case, the energy eV_{sd} associated with an applied bias V_{sd} is less than the one-dimensional subband separation. The current-voltage ($I-V$) characteristic is linear. There have also been reports of non-linear transport in these systems [2,3]. This occurs when eV_{sd} becomes comparable to the subband separation so that a different number of subbands are available for transport in the forward and reverse directions. We refer to these linear and non-linear transport regimes as ideal since they show no regions of instability. In certain circumstances, under high source-drain bias conditions and when the channel is pinched-off, the current-controlled s-shaped negative differential conductance (SNDC) has been observed. The SNDC has previously been explained by the heating and thermal runaway of a confined region of carriers [4]. We refer to this transport regime as non-ideal. In this paper we discuss the changeover from ideal to non-ideal behavior and present random telegraph switching data in the non-ideal regime, which indicates that the origin of the SNDC is associated with the dynamics of impurities close to the point contact.

Experiments

Quantum point contact devices of physical width 0.2 μm were fabricated on a molecular-beam epitaxy grown, uniform modulation doped GaAs/Al_{0.27}Ga_{0.73}As heterostructure, shown schematically in Fig. 1a. The GaAs cap and the doped AlGaAs layer both had a silicon donor concentration of $1 \times 10^{18} \text{ cm}^{-3}$. Electron-beam lithography was used to define the Schottky gate electrodes, which were made from 25 nm of Au thermally deposited on 7.5 nm of Ti. The point contact is formed by applying a negative gate bias, V_g , to both gate electrodes. At $V_g = 0.0 \text{ V}$ and 4.2 K the material has an electron density and mobility of $3 \times 10^{11} \text{ cm}^{-2}$ and $1 \times 10^6 \text{ cm}^2/\text{V}\cdot\text{s}$, respectively. The corresponding Fermi wavevector and energy are 46 nm and 10.7 meV, respectively.

The devices were mounted in a pumped 4He cryostat fitted with an infrared light emitting diode ($\lambda = 830$ nm) for device illumination. Typically, the devices were cooled in the dark from 200 to 12 K at a rate of 2 K min⁻¹ and the I - V characteristic was measured before and after illumination. During illumination the lattice temperature increased by less than 1 K, and after returning to thermal equilibrium the conductance had increased by up to 5%, showing that silicon donor ionization had taken place. Equilibrium conductance measurements were made using a 70 μ V amplitude, 23 Hz source-drain bias and lock-in amplifier detection of the current. Constant current measurements were used to study the non-equilibrium I - V characteristics. The two-level fluctuations were investigated by applying a constant voltage across a load resistor, R_L , in series with the device, and measuring the current through the device as a function of time.

Results and Discussion

Figure 2 shows the differential conductance as a function of V_{sd} for a point contact that has ideal transport behavior. The equilibrium conductance of this device shows eight high quality plateaus. Using the analysis of Martin-Moreno *et al.* [13], the shape of the confining potential in the constriction was determined by measuring the energy subband spacings which were obtained from the values of source-drain bias of the extrema of the second derivative of the $I-V$ characteristic. Comparing the ratios of the energy level spacings obtained this way to those obtained theoretically using a potential of the form $V(x) = a \sin^2 x$, where a is a function of V_{sd} and V

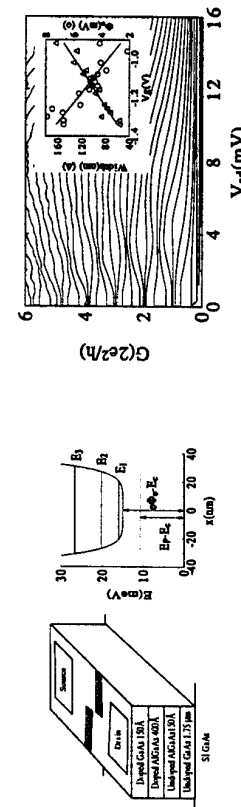


FIG. 1. (a) Schematic diagram of the point contact device. (b) The potential energy profile of the point contact. **FIG. 2.** Differential conductance as a function of voltage across a point contact. The measurements were made at 1.2 K. The inset shows the channel width and Φ_0 as a function of gate bias.



PB41 WEDNESDAY

is a positive even integer, we find the best fit with $V = 6$. As illustrated in Fig. 1b, this confining potential is offset above the conduction band edge by an energy Φ_0 that depends on V_g . From the data we have also determined the dependence of Φ_0 and the channel width on V_g , as shown in the inset to Fig. 2. As seen from the inset, at pinch-off ($V_g = -1.45$ V) the values of the channel width and Φ_0 approach the Fermi wavelength and energy, respectively. Furthermore, at the gate voltage corresponding to channel formation, the predicted width is close to the $0.2 \mu\text{m}$ lithographic width.

After cooling, ideal transport characteristics were obtained; however, infrared illumination or rapid quenching from room temperature produced non-ideal behavior, as shown in Fig. 3. Ideal behavior can be restored by annealing at or above 120 K for 12 hours. The annealing time and temperature are consistent with those required to deionize DX centers in Al_{0.27}Ga_{0.73}As [5] and provide strong evidence that ionized DX centers near the point contact are associated with the SNDIC [4]. Instabilities associated with the SNDIC were studied by measuring fluctuations in the device current and voltage at different DC operating points determined by the load resistor. When the bias conditions are such that the load line crosses the SNDIC, the current (voltage) fluctuates between a high (low) and low (high) value. The fluctuations correspond to switching between the low conductivity state found below the SNDIC region and the high conductivity state found above the SNDIC region. Figure 4 shows a typical device characteristic at a single gate voltage with the characteristic, but instead lie on projections of the characteristic above and below the SNDIC region. Hence, the SNDIC region appears to be a region of bistability between the two differential conductance states, and the steady-state I-V characteristic represents a time average of many individual switching events. The transitions between the high and low states have an exponential behavior that can be explained by the transient response of the load resistor in series with the device, which is in parallel with an 830 pF capacitor. The capacitor represents device and parasitic capacitance in the experimental arrangement. The transient is caused by the device switching between the two conductance states and as a consequence of the circuitry, the present experiment does not measure the time taken to switch between states.

The times spent in either state have an exponential distribution, characteristic of the Lorentzian spectrum of random telegraph noise. The time in each state is characterized by an individual switching event. The transitions between the high and low states have an exponential behavior that can be explained by the transient response of the load resistor in series with the device, which is in parallel with an 830 pF capacitor. The capacitor represents device and parasitic capacitance in the experimental arrangement. The transient is caused by the device switching between the two conductance states and as a consequence of the circuitry, the present experiment does not measure the time taken to switch between states.

The times spent in either state have an exponential distribution, characteristic of the

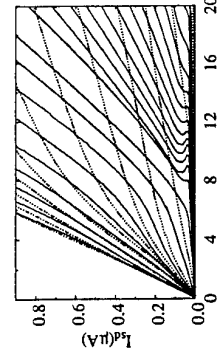


FIG. 3. The current-voltage relationship of a point contact showing ideal (dotted curves) and non-ideal (solid curves) behavior. The change was caused by infrared illumination at 1.2 K.

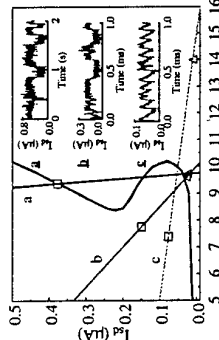


FIG. 4. The I-V characteristic for one gate voltage (-2.3 V) indicating three bias conditions given by the load resistors, a 1 kΩ, b 15 kΩ, and c 100 kΩ. Switching occurs between a high conductance state (square) and a low conductance state (triangle). The inset shows the time dependence for bias conditions a, b, and c.

average lifetime, τ . For different values of V_g and different bias voltages, the lifetime of the high conductance state takes the form $\tau_h \propto \exp(I/I_0)$. The lifetime in the low conductance state appears to be independent of current.

Random telegraph signals associated with discrete resistance switching have been reported in several small devices, including silicon MOSFETs [6] and tunnel diodes [7]. Such behavior has been attributed to potential fluctuations caused by the trapping and detrapping of electrons from a single localized state, or by the interaction of a collection of localized states [8]. That the switching observed in our devices is a random telegraph process suggests that a dynamic process involving DX centers may be the origin of the conductance instability.

According to the multi-channel Landauer-Büttiker formalism, the current through a quasi-adiabatic point contact is determined in part by the barrier height (Φ_0) and profile, which is characterized by a parameter α [4]. If a DX center, or collection of centers, near the point contact is fluctuating between two charge states, this may cause Φ_0 or α , or both, to fluctuate between two values. These changes will be seen as telegraph noise in the transport through the point contact. The region of SNDIC would then be the time average of the bistable current associated with each value of Φ_0 and/or α . Preliminary Monte Carlo simulations support these arguments, and further details will be presented elsewhere [9].

Acknowledgment

This work was supported in part by the Office of Naval Research N00014-93-1-0618.

References

- [1] See references in *Solid State Physics*, Vol. 44, edited by H. Ehrenreich and Turnbull (Academic Press, New York, 1991).
- [2] L. P. Kouwenhoven, B. J. van Wees, C. J. P. M. Harmans, J. G. Williamson, H. van Houten, C. W. J. Beenakker, C. T. Foxon, and J. J. Harris, Phys. Rev. B **39** (1989) 8040.
- [3] L. Martin-Moreno, J. T. Nicholls, N. K. Patel, and M. Pepper, J. Phys. Condens. Matter **4** (1992) 1323.
- [4] C. Berven, M. N. Wybourne, A. Ecker, and S. M. Goodnick, Phys. Rev. B **50** (1994) 14639.
- [5] P. M. Mooney, N. S. Caswell, and S. L. Wright, J. Appl. Phys. **62** (1987) 4786.
- [6] K. S. Ralls, W. J. Skocpol, L. D. Jackel, R. E. Howard, L. A. Fetter, R. W. Epworth, and D. M. Tennant, Phys. Rev. Lett. **52** (1984) 228.
- [7] K. R. Farmer, C. T. Rogers, and R. A. Buhrman, Phys. Rev. Lett. **58** (1987) 2255.
- [8] H. Korner and G. Mahler, Phys. Rev. E **47** (1993) 3206.
- [9] M. N. Wybourne, J. C. Smith, C. Berven, and S. M. Goodnick, *To be published*.

Phonoconductivity Measurements of the Electron-Phonon Interaction in Quantum Wire Structures

A J Naylor, K R Strickland, A J Kent[†] and M Henini

Department of Physics, University of Nottingham, University Park, Nottingham NG7 2RD, UK.

Abstract

We have used a phonoconductivity technique to investigate the electron-phonon interaction in quantum wires. This interaction has important consequences for certain aspects of device behaviour. The 10 μm long wires were formed in GaAs/AlGaAs heterojunctions using split-gate pulses. Ballistic phonon pulses, with an approximately Planckian frequency spectrum, were generated by a resistive film heater on the opposite side of the substrate. The interaction of the phonons with the quantum wire was detected via changes in conductance of the device. Oscillations in the phonoconductivity were observed with increasing (negative) gate bias. These oscillations were related to the Fermi level position relative to the one dimensional subband structure which was determined from electrical transport measurements. We give a qualitative explanation of the results in terms of phonon induced inter- and intra-1D subband electronic transitions leading to changes in the electron temperature which in turn affect the conductance. From our results we obtain a value for the effective width of the quantum wire.

1. Introduction

The carrier-phonon interaction plays an important role in the behaviour of semiconductor devices. For example, the energy relaxation of hot electrons is by the emission of phonons and this determines the effective electron temperature as well as some other properties in the system with hot electrons. The confinement of carriers in low-dimensional semiconductor structures can lead to a modification of the carrier-phonon interaction owing to restrictions in the available momentum space and changes in the energy spectrum of the carriers. Direct phonon experiments are able to give more detailed information regarding the carrier phonon interaction as has been demonstrated in the case of the two dimensional electron and hole gases, for a review see [1]. As well as giving information concerning the electron-phonon interaction, phonon methods can also be used to study the low-dimensional electronic states.

To date there have been no direct phonon experiments on quasi-one dimensional (1D) electron systems. However, a number of theoretical papers have appeared, see for example [2, 3]. It is expected that the electron-phonon interaction is strongly suppressed owing to the reduction of the momentum space to 1D. For example, if the electrons are confined in a wire of width w , then the maximum allowed perpendicular momentum component of an absorbed or emitted phonon is, by the uncertainty principle, about \hbar/w . For $w = 20 \text{ nm}$ in GaAs this restricts the interaction to very low frequency, < 35 GHz, modes which are not very effective at exchanging energy between the electron system and the lattice. However, it has also been suggested that electron-electron interactions [4] and possibly the effects of disorder may actually enhance the electron-phonon coupling by relaxing this momentum restriction.

The phonoconductivity technique has recently been used to probe edge states in the quantum Hall regime [5] and excitations in the fractional quantum Hall regime [6]. In this paper we describe the first such measurements on quantum wires in GaAs split gate structures.

2. Experimental details

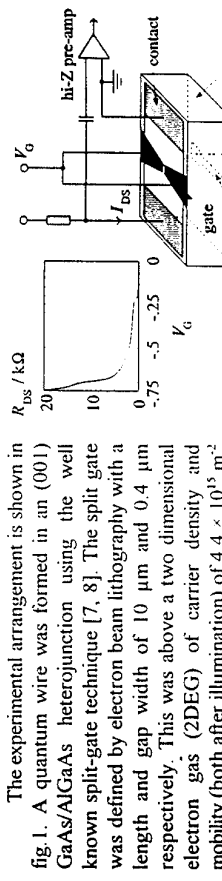


Fig. 1 The experimental geometry, the DC gate characteristics are shown in the inset.

The experimental arrangement is shown in fig. 1. A quantum wire was formed in an (001) GaAs/AlGaAs heterojunction using the well known split-gate technique [7, 8]. The split gate was defined by electron beam lithography with a length and gap width of 10 μm and 0.4 μm respectively. This was above a two dimensional electron gas (2DEG) of carrier density and mobility (both after illumination) of $4.4 \times 10^{15} \text{ m}^{-2}$ and $100 \text{ m}^2\text{V}^{-1}\text{s}^{-1}$ respectively. At the ends of the 2DEG MEESA structure, ohmic source and drain contacts were fabricated. The gate characteristics of the sample at a temperature of 1.3K and drain-source bias current, I_{DS} , of 100 nA are also shown in fig. 1. At a gate bias, V_g , of about -0.20 V the regions of 2DEG under the gate were depleted leaving a narrow channel beneath the gap, this channel was further narrowed by increasing the negative gate bias and hence the resistance increased. A distinct kink at $R_{DS} \approx 12.9 \text{ k}\Omega$ is seen at $V_g \approx -1.6 \text{ V}$, indicating that at this bias the channel width and carrier density were such that only one 1D subband was occupied.

On the other polished side of the 0.38 mm semi-insulating GaAs wafer, directly opposite the channel, was deposited a $100 \times 10 \mu\text{m}$ CuNi heater to be used as the phonon source. It was oriented using infrared front-to-back alignment with its long axis perpendicular to the length of the channel. The heater had an impedance of 50 Ω to match the transmission line from the pulse generator. Fig. 2 shows an example of the phonoconductivity signal detected by the device. The heater was excited by a pulse of 1 V amplitude and duration 50 ns, and the device parameters were: $V_g = -0.5 \text{ V}$ and $I_{DS} = 100 \text{nA}$. The onset of the signal is delayed from the start of the exciting pulse by 120 ns which corresponds to the time of flight for transverse (TA) phonons across the wafer, and is characterised by a rapid rise-time, approximately equal to the duration of the heat pulse, followed by a long decay given by the RC time constant of the device and the co-axial cable between the device and the pre-amplifier.

3. Results and discussion

Fig. 3 shows the intensity of the phonon signal as a function of the gate bias for two different heater pulse amplitudes. Also shown in fig. 3 is the device conductance. The effect of the phonon pulse is to cause a transient increase in the conductance of the channel. The intensity oscillates, with peaks occurring when the Fermi energy, E_F , is coincident with the bottom of any 1D band as deduced from the conductance data. At the higher heater power a further peak is clearly seen when E_F is in between

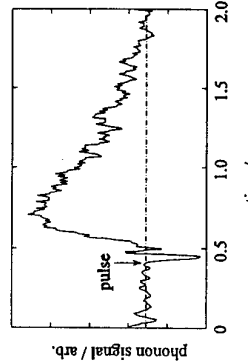


Fig. 2 Temporal response of the quantum wire to a pulse of nonequilibrium phonons, the start of the 50 ns heater pulse is indicated.

the bottom of the second and third subbands. This peak becomes dominant at much higher heater power.

In the discussion that follows, we make the a priori assumption that the electrons in the 1D system are in equilibrium and that we can assign an effective electron temperature, T_e . This assumption is commonly used in the case of 2D and 3D electron systems. However, we note that it has been suggested that suppression of the electron scattering in quantum wires may, under certain circumstances, lead to the breakdown of this assumption [9].

We postulate that the signals are due to changes in T_e brought about by phonon absorption. Steady state measurements of the device conductance as a function of temperature between 1.3 and 4.2 K show the conductance weakly increasing with increasing temperature over the complete range of gate bias. This is consistent with the polarity of the phonon signal. Two possible reasons for this temperature dependence are weak localisation phenomena and the energy dependence of remote ionised impurity scattering. In either case the conductance depends only on the electron temperature, and so it seems reasonable to use the conductance as a thermometer to measure T_e . Taking account of the RC time constant of the system, we can estimate from the size of the phonon signal that T_e increases by about 2.5 K for a heater power of 3.2 mW. This appears to be quite a large temperature increase, however, it is less than 6.3 K which would be expected if the quantum wire could be treated as a "black body" absorber of phonons.

It is also much greater than the increase in substrate temperature caused by thermalisation of the heat pulse which we estimate to be of the order a few mK (the sample is suspended in liquid helium).

We now consider the oscillations in the signal intensity. With the chosen heater geometry the phonons have little momentum component along the length of the quantum wire. This means that the in-line wavevectors, k_x and $k_{x'}$, of the initial and final electron states respectively must be close together, see fig. 4. The low energy phonon absorption will therefore follow the density of states (DOS) at the Fermi energy with strong peaks at the band edge. On the other hand, phonon emission processes have no such momentum restriction, although still dependent on the DOS, the emission will not be as strongly peaked as the absorption profile. The balance of these two processes determines the effective electron temperature and so we expect the latter to peak when E_F is close to the band edge. The number of available channels for phonon emission due to intersubband transitions decreases as the number of occupied subbands reduces, hence the peaks get stronger.

At higher heater temperatures a second phonon absorption process involving near vertical intersubband transitions becomes

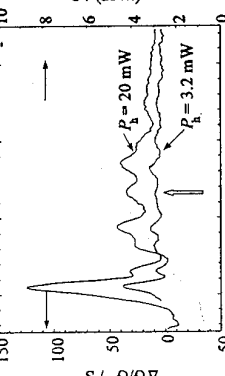


Fig.3 Boxcar sweep of the phononconductivity as a function of the gate bias at two heater powers. The interband peak is indicated by the arrow.

Fig.4 Electron energy bands in a quantum wire, intraband (a) and interband (b) transitions are shown. Transitions involving a large change in k_x (c) are disallowed in our geometry.

possible. The probability of such transitions will be a maximum when E_F is mid-way between the minima of the lower (filled) and higher (empty) bands. This we believe is the origin of the additional peak occurring when E_F is between the 2nd and 3rd 1D subbands. If the signal is due to interband transitions involving phonons in a narrow range of frequencies, then, following the method used in [6], we should be able to estimate the subband separation, Δ , by measuring the signal as a function of the heater temperature, T_h , which is determined by the power supplied to the heater. The signal size is dependent on the number of phonons in the heater spectrum of energy Δ , which is proportional to $\{\exp(\Delta/kT_h) - 1\}^2$. By fitting this function to a plot of the signal intensity as a function of T_h , we obtain $\Delta = 2.7$ meV. If we assume a parabolic confining potential this gives an effective channel width of about 20 nm at $V_G = -0.57$ V. This result is in good agreement with magnetotransport measurements which give a width of 25 nm at about the same value of gate bias. The interband signal is much weaker for E_F between the 1st and 2nd subbands. This is most probably due to the channel narrowing at increased negative gate bias, leading to a larger intersubband energy separation, coupled with the exponential dependence of the signal on the ratio Δ/T_h .

4. Conclusions and acknowledgements

We have presented the first direct phonon measurements of the electron-phonon interactions in a quantum wire using the photoconductivity technique. We see evidence for phonon induced intrasubband electronic transitions, for which the strength of the phonon absorption follows the density of states at E_F . We can also identify near vertical, $\Delta k_x \approx 0$, intersubband processes and have made a phonon-spectroscopic measurement of the intersubband energy gap. A qualitative description of the results has been given using as its basis a simple electron temperature model. Further study is required to determine whether this description is appropriate or if a nonequilibrium description of the electron system should be used instead.

The authors would like to thank Dr M Blencowe and Prof A Shik for valuable discussions relating to the theoretical interpretation of our results. The UK Central Microstructure Facility at DRAF for providing e-beam processing facilities. We would also like to thank EPSRC for support of the NUMBERS programme of which this project is a part.

References

- [1] J.J. Challis and A.J. Kent, in: *Physics of Phonons*, Eds. T. Paszkiewicz and K. Rapcewicz (Plenum, New York, 1994) p.159.
- [2] R. Mickevicius and C. Maitin, *Phys. Rev. B* **48** (1993) 17194.
- [3] B. Kramer, T. Brandes, W. Hänsler, K. Jauregui, W. Plaß and D. Weinmann, *Semicond. Sci. Technol.* **9** (1994) 1871.
- [4] J.R. Senna and S. Das Sarma, *Phys. Rev. Lett.* **70** (1993) 2593.
- [5] D.J. McKittrick, A. Shik, A.J. Kent and M. Henini, *Phys. Rev. B* **49** (1994) 2585.
- [6] C.J. Mellor, R.H. Eyles, J.E. Digby, A.J. Kent, K.A. Benedict, L.J. Challis, M. Henini and C.T. Foxon, *Phys. Rev. Lett.* **74** (1995) 2339.
- [7] T.J. Thornton, M. Pepper, H. Ahmed, D. Andrews and G.J. Davies, *Phys. Rev. Lett.* **56** (1986) 1198.
- [8] H.Z. Zhang, H.P. Wei, D.C. Tsui and G. Weimann, *Phys. Rev. B* **34** (1986) 5635.
- [9] J.P. Leburton, S. Briegs and J. Jovanovic, *Superlatt. and Microstr.* **8** (1990) 209.

**Microwave-induced Resonant Reflection and Localization of Ballistic Electrons
in Quantum Microchannels**

L. Y. Gorelik*, M. Jonson, and R. I. Shekhter
Chalmers University of Technology and Göteborg University, S-412 96 Göteborg, Sweden.
and •B. Verkin Institute for Low Temperature Physics and Engineering, Kharkov, Ukraine.

Abstract

We show that electron transport in a ballistic microchannel supporting both propagating and reflected modes can be completely blocked by applying a microwave electromagnetic field. The effect is due to resonant reflection caused by multiple coherent electron-photon scattering at least two spatially localized scattering centers in the channel. With many such scattering centers present the conductance is shown to have an irregular dependence on bias voltage, gate voltage and frequency with irregularly spaced dips corresponding to resonant reflection. When averaged over bias, gate voltage or frequency the conductance will decay exponentially with channel length in full analogy with the localization of 1D electrons caused by impurity scattering.

The dynamics of a mesoscopic system subject to a time dependent field depends crucially on the relation between the phase breaking time τ_ϕ and the time t_0 needed for electrons to pass through the system. In the absence of phase breaking processes, $\tau_\phi \gg t_0$, one could expect phase coherent dynamic phenomena to occur in mesoscopic systems in close analogy with the well known static phenomena. They should be highly tunable by for instance a magnetic field or by electric fields due to applied bias- or gate voltages. The photoconductance of a ballistic microchannel created in a gated AlGaAs heterostructure is an example. In a channel with a cross section that varies so slowly that the adiabatic approximation applies, coherent electron-photon scattering corresponding to transitions between different transverse modes has been shown to be localized in space and to lead to transitions between propagating and reflected modes [1]. This type of indirect backscattering has many features in common with impurity scattering and has been suggested [2] to give rise to quantum interference effects in the electron transport properties. In particular the photoconductance caused by single photon scattering (absorption) was shown to be an oscillating function of an applied gate voltage in a quasi-one dimensional channel containing a microwidening [2]. At large enough electromagnetic fields, multiple coherent electron-photon scattering results in a coherent resonant coupling of two different transverse modes in the channel. Because the electron-photon interaction is localized in space, this resonant coupling can be expressed in terms of a Landau-Zener breakdown [3]. In this paper we pursue this line of argument and show that resonant electron-photon scattering strongly modifies the electron transport and that it may lead to resonant (total) reflection of electrons and hence block the electron transport through a quasi-1D channel completely.

The channel geometry we have in mind is shown in Fig. 1a. We consider the simplest case where only a single transverse mode is ballistically propagating through the channel (schematically illustrated by the bold lines in Fig. 1a). The microwave-induced resonant coupling of this propagating mode with localized modes in the smooth widenings of the channel (thin lines in Fig. 1a) is the phenomena of interest here. Still referring to Fig. 1a, the longitudinal coordinates $x_1(n)$ and $x_2(n)$ give the positions where the resonant condition

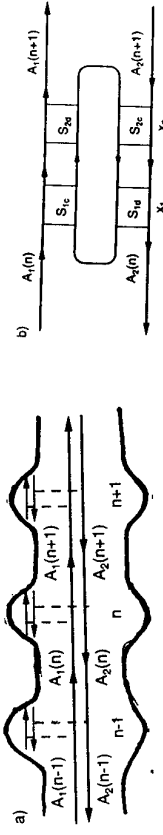


Figure 1: (a) Schematic view of a quasi-1D channel with one propagating mode (thick arrows) and several microwidenings with trapped modes (thin arrows). (b) Diagram describing scattering between propagating and trapped modes in a microwidening (see text)

$\Delta U \equiv U_2(x) - U_1(x) = \hbar\omega$ is satisfied and Landau-Zener scattering takes place. Here $U_n(x)$ is the effective potential barrier for the quasi-one dimensional motion of electrons in the n th transverse mode [1]. The total transmission through the channel is determined by the sum of the probability amplitudes for all electron paths. In the straight parts of the channel shown in Fig. 1a the electron states are superpositions of left- and right moving plane waves of amplitudes $A_1(n)$ and $A_2(n)$ respectively. Each widening is characterized by a scattering matrix S_n , which couples the amplitudes of incoming and outgoing waves,

$$\begin{pmatrix} A_1(n+1) \\ A_2(n) \end{pmatrix} = S_n \begin{pmatrix} A_1(n) \\ A_2(n+1) \end{pmatrix}, \quad S_n \equiv e^{i\varphi_n} \begin{pmatrix} iT_n & R_n^* \\ R_n & iT_n \end{pmatrix}. \quad (1)$$

We will first calculate the scattering matrix S_n and then later use the result to calculate the total transmission probability of the channel, which determines the conductance through the Landauer formula.

The internal structure of the scattering matrix S_n is schematically shown in Fig. 1b (where the index n is suppressed for convenience). Scattering is localized in space and may occur at x_1 or x_2 . At each site scattering of right moving electrons (upper part of Fig. 1b) and left moving electrons (lower part) must be considered separately. The closed curve in the middle of Fig. 1b represents the path of an electron state trapped in the widening. The scattering matrices S_{ic} and S_{id} that appear in Fig. 1b describe Landau-Zener transitions at point x ; for the case when the transverse energy levels are converging (c) and diverging (d) in the direction of longitudinal motion. They are related as $S_{id} = \sigma_y S_{ic} \sigma_y$, where σ_y is a Pauli spin matrix, and can be expressed in terms of two phases θ_i , ϑ_i — related to the amplitudes of the two resonantly coupled modes — and the probability r_i^2 for an intermode transition as

$$S_{ic} \equiv e^{i\theta_i} \begin{pmatrix} t_i & ir_i e^{i\vartheta_i} \\ ir_i e^{-i\vartheta_i} & t_i \end{pmatrix}, \quad t_i^2 + r_i^2 = 1, \quad r_i = (1 - e^{-\pi a_i})^{1/2}. \quad (2)$$

The quantity r_i is determined by the single parameter $a_i = e^2 \mathcal{E}^2 / p\omega |\Delta U'(x_i)|$ (as are θ_i , ϑ_i). \mathcal{E} and ω is the amplitude and frequency of the electromagnetic field polarized in the transverse direction, while p is the longitudinal momentum of the electron at the scattering sites.

There is a useful formal analogy between our scattering problem and the familiar case of electron scattering by (tunneling through) a double barrier structure. If we interpret $A_1(n)$ and $A_1(n+1)$ as the amplitudes of an incident and a reflected wave, then \mathbf{S}_{1c} and \mathbf{S}_{2d} correspond to the first and \mathbf{S}_{1d} and \mathbf{S}_{2c} to the second barrier in the analogous double barrier tunneling problem.

Note that the two barriers are identical, since each has one part corresponding to scattering at site x_1 and another part due to scattering at x_2 . This immediately tells us that there is a possibility for reflectionless transmission from $A_1(n)$ through the double barrier structure to $A_2(n)$ for certain values of the electron energy, which we can readily calculate. In the original problem, however, $A_2(n)$ is the amplitude of the reflected rather than the transmitted wave (cf. Fig. 2). Hence resonant coupling of two transverse modes by an electromagnetic field can lead to resonant reflection of electrons at a microwidening in an otherwise straight channel.

Straightforward calculations lead to the following result for the transmission probability through the microwidening:

$$T^2(E) = \frac{4T^2 \sin^2(\phi_L(E) - \eta(\Delta\varphi(E)))}{(1 - T^2)^2 + 4T^2 \sin^2(\phi_L(E) - \eta(\Delta\varphi(E)))} \quad (3)$$

Here the phase ϕ_L is the total phase gained by the electron as it propagates around the closed trajectory (middle part of Fig. 1b), while $\Delta\varphi$ is the difference in phase gained along the two different trajectories going from scatterer \mathbf{S}_{1c} to \mathbf{S}_{2d} . These two phases depend on two independent geometric parameters, say the length and width of the microwidening. In an experiment that implies they depend on applied gate voltages and on radiation frequency. While the phase $\eta(\varphi)$ in (3) is always less than $\pi/2$, the phase ϕ_L is a linear function of energy in the quasiclassical limit so that a discrete set of electron energies $\{E_m\}$ exists for which $\sin(\phi_L(E_m) - \eta(\Delta\varphi(E_m))) = 0$. At these energies the transmission probability T^2 goes to zero and resonant reflection takes place. The width of the resonance is determined by the parameter T^2 , which can be expressed in terms of the probability r^2 for inter-mode Landau-Zener transitions. In the simple case of a symmetric widening ($r_1 = r_2 = r$), we find

$$T^2 = 1 - 4t^2 r^2 \sin^2(\Delta\varphi/2) \quad (4)$$

It is interesting to note that T^2 is close to unity and the effect of the electromagnetic field is small for the two limiting cases of weak ($t \ll 1$) and strong ($r \ll 1$) field as long as we are outside the resonant regions (which are narrow in both cases). Corrections are due to the fact that $1 - T^2 \neq 0$ and coincide with those calculated in the single photon approximation [2]. This approximation breaks down at the resonant energies, however, where the transmission is suppressed to zero irrespective of the field strength. For a single microwidening in an otherwise straight channel the conductance $G = (2e^2/h)T^2(E = E_F)$ should therefore show a series of resonance “dips” as the gate voltage is varied. This resonant structure becomes richer and less regular if several microwidenings are present. The transmission amplitude can in this case be obtained from a product of transfer matrices describing the individual widenings. If the number of widenings is large — and if there are no correlations between the parameters describing their geometries — the theory of disordered one-dimensional systems

can be used to find the result [4]

$$G = \frac{2e^2}{h} \exp\left(\sum_{n=1}^N \ln |\mathcal{T}_n|\right). \quad (5)$$

Here \mathcal{T}_n is the transmission amplitude for the n :th widening as given by (2). The criterion $\mathcal{T}_n = 0$ for at least one n determines the gate voltages for which electron transport is completely blocked by the electromagnetic field. Taking an ensemble average in the standard theory of disordered systems corresponds here to averaging over gate voltage. Hence we get for our problem the same exponential decay of conductance found for the electron localization problem in disordered (equilibrium) conductors, i.e.

$$G = \frac{2e^2}{h} e^{-N/R_L}, \quad R_L^{-1} = \langle \ln \text{Max}(r_n, t_n) \rangle, \quad \langle f_n \rangle \equiv \lim_{N \rightarrow \infty} \frac{1}{N} \sum_{n=1}^N f_n. \quad (6)$$

Note that the localization radius R_L depends on the probability for Landau-Zener transitions, or impurity scattering. Two different criteria apply for the possibilities to observe resonant reflection and the exponential suppression of the averaged current, respectively. In the first case the rate ν of non-radiative inter-mode transitions should be smaller than the width of the discrete electron spectrum of trapped (non-propagating) modes in a widening: $\nu \ll r^2 t^2 \omega(d/L_W)$. Here L_W is the characteristic length of the widening and we have used the relation $v_F \sim \omega d$ between the Fermi velocity and channel width.

If we assume that ν is due to phonon emission we have $\nu \sim \gamma \omega^3 / \omega_D^2 - \omega_D$ is the Debye frequency and γ the electron-phonon coupling constant — and conclude that the inequality

$$\gamma (\omega/\omega_D)^2 \ll r^2 t^2 (d/L_W) \quad (7)$$

must be fulfilled for resonant reflection to be observable. This should be possible to achieve experimentally. For the exponential decay of the averaged conductance to be observable, it is necessary to maintain phase coherence along the entire channel (not only within one microwidening). Therefore the stronger inequality $\gamma(\omega/\omega_D)^2 \ll (d/L)^2$ must be fulfilled. Here L is the total length of the channel and we have assumed $r \sim t \sim 1$.

This work was supported by the Swedish Institute, the Swedish Engineering Science Research Council (TFR), and by Swedish Natural Science Research Council (NFR).

References

- [1] F. Hekking and Yu. V. Nazarov, Phys. Rev. B44, 11506 (1991).
- [2] L. Y. Gorelik, A. Grincwajg, V. Z. Kleiner, R. I. Shekhter, and M. Jonson, Phys. Rev. Lett. 73, 2260 (1994).
- [3] C. Zener, Proc. Roy. Soc. (London) A137, 696 (1932); L. D. Landau, Phys. Z. Sov. 2, 46 (1932).
- [4] See, e.g., D. J. Thouless, in *Physics in One Dimension*, Eds. J. Bernasconi and T. Schneider, Springer Series in Solid-State Science, vol. 23 (Springer, Berlin, 1981).

SURFACE ACOUSTIC WAVE STUDIES OF QUANTUM NANOSTRUCTURES

G. R. Nash, S. J. Bending, Y. Kershaw*, K. Eberl*, P. Grambow*, K. von Klitzing
 School of Physics, University of Bath, Claverton Down, Bath BA2 7AY, U.K.

* Max-Planck-Institut für Festkörperforschung, Heisenbergstr. 1, D-70569 Stuttgart, Germany

Surface acoustic wave (SAW) scattering has been used as a contactless probe of the electronic properties of quantum nanostructures. Interdigital transducers, operating at 70MHz, were deposited on the edges of samples containing large area arrays of quantum wires and dots. Due to the piezoelectric coupling between the SAWs and the electronic systems very small changes in the attenuation and velocity of a SAW pulse are measured with magnetic field, at low temperatures. With the transverse component of the SAW electric field parallel to the wires oscillations were observed due to the magnetic depopulation of 1D subbands. Using a simple model characteristic confinement potentials were calculated at different electron densities. With the transverse component of the SAW electric field perpendicular to the wires a monotonic decrease in amplitude is seen with increasing electron density. We speculate that structure superimposed on this background arises from acoustic collective modes. In quantum dots the transmitted SAW amplitude shows a broad asymmetric minimum as a function of magnetic field, with level crossings of single electron states reflected in a superimposed detailed fine structure.

INTRODUCTION

When it first became possible to fabricate high quality semiconductor nanostructures it was hoped that quantum wires and dots in particular would lead both to large improvements in the performance of existing electronic devices and to exciting new device possibilities [1], [2]. Power considerations require most applications to be based around nanostructure arrays and there is a pressing need for a better understanding of these. Drawing on pioneering work [3] in which SAWs were used to measure the conductivity of a homogeneous two dimensional electron gas (2DEG), we have used SAW scattering to probe for the first time the electronic properties of nanostructure arrays. This technique has several advantages over other characterisation techniques: The measurements are contactless and quasi-DC (70MHz), and many body effects do not directly modify the results. Large area arrays can easily be investigated, and as the SAW wavelength is large ($\lambda=40\mu m$) the measurements can be analysed in terms of a mean field approximation. SAW scattering allows us to investigate key issues such as sample homogeneity, ensemble averaging over a finite number of structures (approximately 36 million for dots and 6000 for wires), and collective effects in which many nanostructures are coherently excited.

EXPERIMENTAL DETAILS

Measurements were made on arrays of quantum wires and quantum dots which were fabricated from an AlGaAs/GaAs heterostructure, grown by MBE, on a semi-insulating (001) GaAs substrate, with a carrier concentration of $2.1 \times 10^{15} m^{-2}$ and a mobility of $60m^2/Vs$ at 4.2K. Holographic lithography and reactive ion etching with SiCl₄ were used to pattern the samples yielding arrays of wires or dots either 500nm or 250nm wide, with periods of 1000nm and 500nm respectively. The etch depth was less than the depth of the 2DEG below the surface. A final wet mesa etch left a square of nanostructures $3 \times 3 mm$ in the centre of each sample. Four interdigital transducers were realised by the evaporation of Cr/Au fingers onto the exposed edges of the substrate. The spacing of the fingers in each transducer was $10\mu m$ yielding a broad resonance about 70MHz (+/- 4MHz). Measurements were made by exciting $0.4\mu s$ SAW pulses, with a

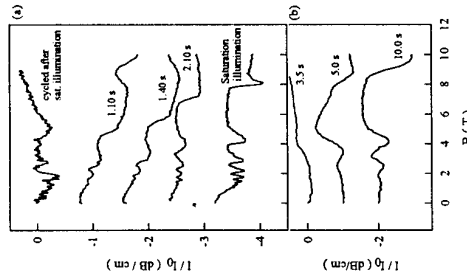


Fig.1: SAW attenuation for (a) 500nm and (b) 250nm quantum wires at various illumination levels. The transverse component of the SAW electric field is parallel to the wires.

Figs. 1a and 1b show measured SAW intensity (I_0 is the zero magnetic field intensity) as a function of illumination for 500nm and 250nm quantum wires, with the transverse component of the SAW electric field parallel to the wires. Velocity shift measurements in all cases confirm the amplitude data. Offsets of -0.8dB/cm and -1.0dB/cm were made to each trace on Figs. 1a and 1b respectively. To increase the electron concentration in the samples we pulsed an infrared LED, with pulse lengths of 100ms at 50mA. The oscillations in the intensity are attributed to the magnetic depopulation of 1D subbands; the minima corresponding to the point at which depopulation occurs. The interaction of SAWs with a 2DEG has been previously described using a classical relaxation model [3],[4] in which the effectiveness of the screening of the SAW electric field determines their attenuation. The attenuation coefficient ($\sigma_M \approx 3.3 \times 10^{-7} \Omega^{-1}$ [3]):

$$\Gamma = \frac{2\pi K_{eff}^2}{\lambda} \frac{\sigma_{xx}/\sigma_M}{2 + (\sigma_{xx}/\sigma_M)^2} \quad (1)$$

where K_{eff}^2 is an effective electromechanical coupling coefficient. The conductivity of the wires is greatly reduced, and the attenuation therefore increased, as each subband is depopulated. Surprisingly oscillations only occur when SAW propagation is perpendicular to the wires, suggesting that the transverse component of the electric field associated with the SAWs, in this case, is very much greater than the longitudinal component, contrary to conventional wisdom [4]. From here on we will refer to the transverse component as the SAW electric field. A simple analysis [5] assuming parabolic electrostatic confinement produces a non-linear relationship between the subband index j and magnetic field B :

$$N_e^{1D} = \frac{2}{\pi} \left(\frac{2m^*/\hbar}{n} \right)^{\frac{1}{2}} \left[\left(\frac{eB}{m^*} \right)^2 + \omega_0^2 \right]^{\frac{1}{4}} \left[\frac{n}{\omega_0} \sum_{j=1}^n \sqrt{j} \right] \quad (2)$$

where n^* is the effective mass, N_e^{1D} is the 1D electron concentration, ω_0 is a characteristic frequency defining the electrostatic confinement, n is the index of the subband that has just been

depopulated. Plots of B^2 versus $(\sum \sqrt{f})^{-1}$ were fitted successfully (regression coefficients were ≈ 0.999 in all cases), in the region $B=0$ to 5T, to this form and 1D electron concentrations and characteristic confinement energies $\chi/\hbar\omega_0$ were calculated and are plotted in Fig. 2. The characteristic confinement decreases with increasing carrier density as expected from self-consistent screening effects [6]. The effective electronic width of the wires, which is smaller than the geometrical width due to sidewall depletion [5] increases with increasing carrier concentrations for 500nm and 250nm wires, with calculated widths of 220nm and 75nm respectively at the greatest illumination levels. Inhomogeneous illumination is thought to have caused the non-linear background to the signal in Fig. 1a at intermediate illumination levels. After saturation illumination the sample appears very homogeneous and the minima are sharper. The top trace was obtained by thermally cycling a saturation illuminated sample and also appears to be very homogeneous. In Fig. 3a the amplitude of the transmitted SAW pulse is shown as a function of illumination for 500nm wires with the SAW electric field perpendicular to the wires. No offset has been added to the traces. A qualitative understanding of the decrease in amplitude with illumination may be obtained by considering the effect of the electric field of the SAWs on the confined wavefunctions of the electrons in the wires. High index wavefunctions (occupied at large electron densities) have electron densities that are weighted more towards the edges of the wires than low index ones. The electric field of the SAW will tilt the confinement potential and consequently the influence of the field will be greatest on high index wavefunctions, leading to an enhanced ‘‘screening’’ when more high index wavefunctions are occupied. The fine structure in the higher illumination traces does not correlate with the depopulation of 1D subbands and is also probably not due to edge magnetoplasmon excitation [7] as rough estimates of the resonant frequency for this absorption lie above 150MHz over our magnetic field range. We speculate that this structure may arise from acoustic collective modes in which many wires are coherently excited, and this is currently the topic of theoretical investigations.

Fig2: Characteristic confinement energies versus 1D carrier concentration. 250 nm wires 500 nm wires

Fig3: Transmitted SAW amplitude for (a) 250nm quantum wires, at various illumination levels. The SAW electric field is perpendicular to the wires. (b) 500nm quantum dots. The SAW electric field is perpendicular to the wires.

features. After 4s illumination there is no further decrease in amplitude, with the trace at 5s (which has been omitted for clarity) having almost the same amplitude as that at 4s and the trace at 7s having the pre-illumination amplitude. The deep asymmetric minimum in the traces appears to be characteristic of dots and is repeated in 250nm samples. Fine structure superimposed upon the broad background is clearly visible above the noise level (approximately +/- 10 units in the y-axis) and is interpreted in terms of energy level crossings at the Fermi energy. At these points the SAWs can excite transitions between two wavefunctions of very different symmetry leading to a strong ‘‘screening’’ effect. There is a trade-off between low and high level illumination levels; at low electron densities the crossings will occur at larger magnetic field intervals, but may be smeared out by strong sample inhomogeneities. At large densities the dots are probably more homogeneous, but the crossings will occur at magnetic field intervals that are too small to be resolved. At lowest and highest illumination levels we estimate that there might be ~100 and 500 electrons in the dots respectively, with level crossings at approximately every 0.1T and 0.02T. At low electron densities there is a clear coarsening of the fine structure, as expected, and the amplitude of these features is also greater. When many body effects (particularly magnetism) are included [8] large changes in electron configuration with magnetic field can occur that stand out above single particle confinement level crossings. A particularly homogeneous sample (Fig. 4b) shows strongly peaked structure that might correspond to those many body effects.

CONCLUSIONS/ACKNOWLEDGEMENTS

We have demonstrated that SAW scattering is a powerful probe of the electronic properties of nanostructures. Future work will concentrate on the realisation of more homogeneous arrays of nanostructures and the investigation of their associated properties. We acknowledge the support of the Royal Society (RSG 12607) and the help of Gordon Sowersby of Barman Electronic Instruments.

REFERENCES

- [1] J.N. Randall, M.A. Reed and G.A. Frazier, *J. Vac. Sci. Technol. B7* (1989) 1398
- [2] H. Sakaki, in: *Springer Series in Solid State Sciences Vol 97*, Eds. F. Kuchar, H. Heinrich and G. Bauer (Springer-Verlag, Berlin, 1990) p.2
- [3] A. Wixforth, J. Scriba, M. Wassermeyer, J.P. Kotthaus, G. Weimann and W. Schlapp, *Phys. Rev. B* **40** (1989) 7874
- [4] A.R. Hutson and D.L. White, *J. Appl. Phys.* **33** (1962) 40
- [5] K.-F. Berggren, G. Ross and H. van Houten, *Phys. Rev. B* **37** (1988) 10118
- [6] S.E. Laux, D.J. Frank and F. Stern, *Surf. Sci.* **196** (1988) 101
- [7] P. Hawker, P.F. Lencic, M. Tonouchi, V.W. Rampton, C.J. Mellor and M. Henini, *Physica B* **194** (1994) 419
- [8] S.-R. Eric Yang, A.H. MacDonald and M.D. Johnson, *Phys. Rev. Lett.* **71** (1993) 3194

Magnetotransport of electrons in arrays of wires in Si/Si_xGe_{1-x} heterostructures

M. Holzmann¹, D. Többen¹, P. Baumgartner¹, G. Abstreiter¹, A. Kriele², H. Lorenz², and F. Schäffler³

¹ Walter Schottky Institut, Technische Universität München, D-85748 Garching, Germany
² Sektion Physik der Ludwig-Maximilians-Universität München, Geschwister-Scholl-Platz 1,
 D-80539 München, Germany

³ Daimler-Benz AG, Forschungsinstitut Ulm, Wilhelm-Runge-Str. 11, D-89081 Ulm,
 Germany

Magnetotransport parallel to quantum wires in Si/SiGe heterostructures was conducted in the quasi-ballistic regime. We observe magnetoresistance oscillations due to the depopulation of quasi-one dimensional subbands and at low magnetic fields a well pronounced peak arising from diffuse scattering at the wire boundaries emerges. The analysis of these features yields a maximum subband spacing of 1meV at a corresponding wire width of 70nm. Electron transport perpendicular to shallow etched wires was investigated in lateral superlattices with a period of 350nm. At magnetic fields below 0.7T the magnetotransport measurements show commensurability oscillations corresponding up to 3 periods of the wire grating. However, the modulated lateral potential is not purely sinusoidal resulting in a splitting of the commensurability oscillations.

Because of the much higher electron mobility the Si/SiGe system seems to be more appropriate for the investigation of laterally nanostructured two-dimensional electron gases (2DEGs) in silicon than MOSFETs^(1,3). The fabrication of nanostructures, for instance via the field-effect by a modulated gate, by focused ion beam and focused laser beam writing or by reactive ion etching, is well established in transport experiments parallel to the wires have a period of $a=480$ nm, whereas a period of 350nm was chosen for magnetotransport perpendicular to wires. The wire grating was transferred into the SiGe heterostructure by reactive ion etching (RIE) using CF₄ as gas source. We achieved different etch depths by varying the etch time only. The profiles of the etched structures, i.e. their periods and etch depths, were measured by atomic force microscopy (AFM). In all samples with period $a=350$ nm the etch grooves were found to be very narrow and steep so that the AFM tip did not touch the bottoms of the trenches. Hence, the etch depth can only be estimated.

Photoresist stripes were fabricated by means of laser holography. All samples studied in transport experiments parallel to the wires have a period of $a=480$ nm, whereas a period of 350nm was chosen for magnetotransport perpendicular to wires. The wire grating was transferred into the SiGe heterostructure by reactive ion etching (RIE) using CF₄ as gas source. We achieved different etch depths by varying the etch time only. The profiles of the etched structures, i.e. their periods and etch depths, were measured by atomic force microscopy (AFM). In all samples with period $a=350$ nm the etch grooves were found to be very narrow and steep so that the AFM tip did not touch the bottoms of the trenches. Hence, the etch depth can only be estimated.

At first, magnetotransport parallel to wires will be discussed. The 2-terminal resistance of samples with increasing etch depth d is shown in figure 1. In the most shallow etched sample ($d=50$ nm) the doping layer has barely been cut. Its resistance shows well pronounced plateaus down to filling factor $v=36$ (fig. 1 a). The position of these plateaus agrees well with h/e^2 for magnetic fields above $2T$ ⁽⁴⁾ with v being the filling factor. The shape of the magnetotransport curves changes significantly if one etches deeper into the donor layer or into the 2DEG (fig. 1 b). Additionally, a low-field maximum arises which shifts to higher magnetic fields with increasing d (dashed line in fig. 1 b). For $d \geq 55$ nm, an oscillatory behavior in the magnetoresistance becomes clearly dominant. Furthermore, the number of resolvable oscillations decreases strongly with increasing etch depth. For $d=92$ nm, i.e. when the etched grooves cut through the 2DEG, only four minima are resolved up to 12T.

The specimen with 50nm deep etch grooves still shows typical two-dimensional transport characteristics. Etching deeper into the doped SiGe-layer results in the formation of quantum wires, indicated by the anomalous, low-field resistance maximum due to diffuse scattering at the wire boundaries⁽⁶⁾. The shift of this peak to higher magnetic fields for $d=60$ nm and 92nm is a consequence of the decreasing effective wire widths. The magnetoresistance oscillations result from the depopulation of quasi-one-dimensional subbands. As expected, the Landau-plots (fig. 1c) for successively deeper etched grooves display strong deviations from linear behavior⁽⁹⁾. The analysis of these features yields subband spacings between 0.3meV and 1meV at corresponding wire widths between 180nm and 70nm.

Figure 2 presents 4-point measurements

perpendicular to wires. The etch time and therefore the etch depth decreases from top to bottom. For all samples d is smaller than 50nm. The mesa geometry is schematically shown in the inset. The most deeply etched specimen (sample C) exhibits three additional oscillations below $B=0.7T$ whereas 5 low-field minima emerge for the other two samples. Above $B=0.6T$, Shubnikov de Haas (SdH) oscillations commence which shift slightly to lower magnetic fields for the deeper etched samples indicating a small reduction of the carrier density by the etching process. The deeper the specimens are etched the stronger the SdH

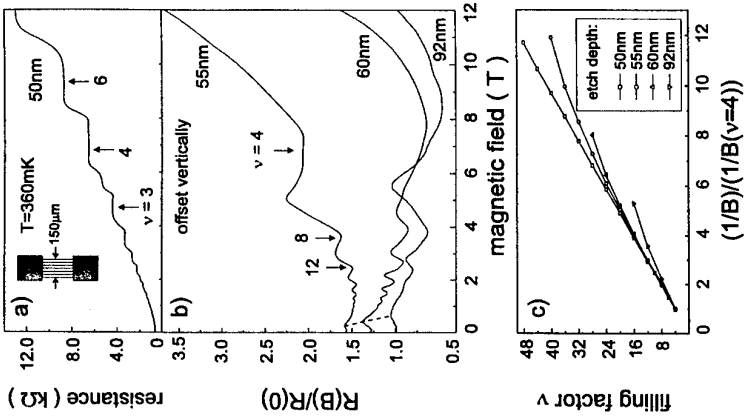


Fig. 1: (a) Two-terminal resistance of the sample with 50nm deep etch grooves. The inset schematically shows the sample geometry. (b) Magnetotransport of samples with successively increased etch depth normalized to the value at $B=0$. (c) Filling factors v versus $(1/B)/(1/B(v=4))$. The symbols refer to the measured minima in magnetoresistance.

oscillations are damped. The temperature dependence of these low field oscillations is displayed in figure 2b for sample C. At $T=1.45\text{K}$ a strong damping of the SdH can already be observed but the amplitude of the low field oscillations remains unchanged. At $T=4.52\text{K}$ the SdH oscillations are no longer resolvable in this magnetic field range whereas the low field oscillations can still be seen clearly.

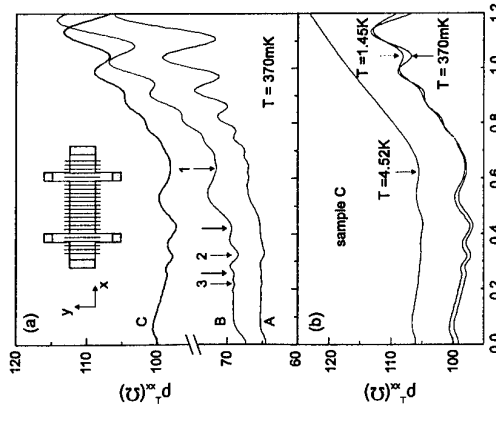


Fig. 2: (a) 4-terminal resistance perpendicular to wires. From top to bottom the etch time decreases. The inset shows the sample geometry. (b) Temperature dependence of the sample etched deepest.

The low field oscillations are periodic in $1/B$ but possess a different oscillation period compared to the SdH oscillations.

It is thus evident that the origin of the additional low-field structures is not Landau quantization of the 2DEG. Indeed the minima marked with filled arrowheads fit to commensurate orbits around 1, 2, and 3 periods of the wire grating. The magnetic field position of these minima can be explained

according to $2r_c=(n-\phi)a^{(10,11,12)}$, with r_c being the cyclotron radius. The value of the phase factor ϕ depends on the actual potential shape. However, the additional minima in between two successive commensurability oscillations (open arrowheads) cannot be described by this equation. They stem from higher Fourier components of the modulating potential⁽¹³⁾. As proposed by Beenakker and van Houten in a semiclassical approach⁽⁴⁾ the minima result from an $\mathbf{E} \times \mathbf{B}$ drift of the conducting electrons. The oscillatory behavior can be described by the following equation:

$$\frac{\rho_{xx}}{\rho_0} = 1 + \left(\frac{eV_0}{E_F} \right)^2 \left(\frac{1^2}{ar_c} \right) \times \left[V_1^2 \cos^2 \left(\frac{2\pi r_c}{a} - \frac{\pi}{4} \right) + 2V_1^2 \cos^2 \left(\frac{4\pi r_c}{a} - \frac{\pi}{4} \right) \right] \quad (1)$$

V_0 denotes the amplitude of the lateral, periodic potential $V(x)$ and E_F the Fermi energy. Equation 1 is deduced for a purely sinusoidal potential and yields $2r_c=(n-1/4)a$ for the magnetic field position of the minima. To explain the additional minima between two successive commensurability oscillations the second harmonic has to be taken into account.

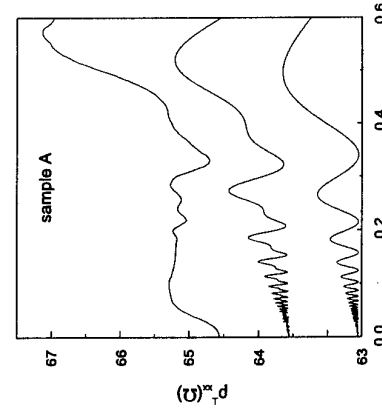


Fig. 3: Magnetotransport measurement of sample A (top) compared to calculations for a potential containing the second Fourier component and a purely sinusoidal potential (bottom). The calculated traces are vertically offset for clarity.

A potential of the form $V(x)=(V_1 \cos(x) + V_2 \cos(2x))$ leads to the following modification of equation 1:

$$\frac{\rho_{xx}}{\rho_0} = 1 + \left(\frac{e}{E_F} \right)^2 \left(\frac{1^2}{ar_c} \right) \times \left[V_1^2 \cos^2 \left(\frac{2\pi r_c}{a} - \frac{\pi}{4} \right) + 2V_1^2 \cos^2 \left(\frac{4\pi r_c}{a} - \frac{\pi}{4} \right) \right] \quad (2)$$

Figure 3 again shows the measured magnetoresistance of sample A (top) and calculated traces for the above potential and for a sinusoidal potential (bottom). Good agreement is found for $V_1=0.1\text{meV}$ and $V_2=0.25\text{V}_1$. The carrier density used for the calculation was determined from the SdH oscillations at higher magnetic fields.

Figure 4 shows the potential energy used for the calculation and a typical atomic force micrograph. The shape of the potential agrees well with the narrow and steep etch grooves. The high quality of the etching process is also proven by the fact that we can observe commensurable orbits around three periods of the superlattice.

In summary, we have observed quantum transport parallel to electron channels as well as commensurability oscillations in lateral superlattices, thereby demonstrating that RIE is very well suited for nanopatterning of Si/SiGe heterostructures.

Financial support by the *Bundesministerium für Bildung, Wissenschaft, Forschung und Technologie* (Germany) under grant NT 24137 and by the Siemens AG (*Siemens Mikrostrukturerte Bauelemente*) is gratefully acknowledged.

- (1) F. Schaffter, D. Többken, H.-J. Herzog, G. Abstreiter, and B. Holländer, *Semicond. Sci. Technol.* **7**, 260 (1992)
- (2) K. Ismail, F. K. LeGraes, K. L. Saenger, M. Arafa, J. O. Chu, P. M. Mooney, and B. S. Meyerson, *Phys. Rev. Lett.* **73**, 3447 (1994)
- (3) M. G. Gavrilov, Z. D. Kvon, I. V. Kulushkin and V. B. Timofeev, *Pis'ma Zh. Tekor. Fiz.* **39**, 420, (1984)
- (4) C.W.J. Beenakker and H. van Houten, in *Solid State Physics*, edited by H. Ehrenreich and D. Turnbull (Academic, San Diego, 1991), Vol. 44, p. 1
- (5) A. D. Wieck and K. Ploog, *Appl. Phys. Lett.* **56**, 928 (1990)
- (6) P. Baumgartner, K. Brunner, G. Abstreiter, G. Böhm, G. Tränkle, and G. Weimann, *Appl. Phys. Lett.* **64**, 592 (1994)
- (7) D. Többken, M. Holzmann, S. Kühn, H. Lorenz, G. Abstreiter, J. P. Kotthaus, and F. Schaffter, *Phys. Rev. B* **50**, 8853 (1994)
- (8) T. J. Thornton, M. L. Ronkes, and H. van Houten, *Phys. Rev. B* **37**, 10118 (1988)
- (9) K.-F. Berggren, G. Roos, and H. van Houten, *Phys. Rev. B* **37**, 6633 (1995)
- (10) D. Weiss, K. v. Klitzing, K. Ploog, and G. Weimann, *Europhys. Lett.* **8**, 179 (1989)
- (11) R. W. Winkler, J. P. Kotthaus, and K. Ploog, *Phys. Rev. Lett.* **62**, 1177 (1989)
- (12) C.W.J. Beenakker, *Phys. Rev. Lett.* **62**, 2020 (1989)
- (13) R. Cusco, M. C. Holland, J. H. Davies, I. A. Larkin, E. Skuras, A. R. Long, and S. P. Beaumont, *Surf. Sci.* **305**, 643 (1994)

modification of equation 1:

$$\frac{\rho_{xx}}{\rho_0} = 1 + \left(\frac{eV_0}{E_F} \right)^2 \left(\frac{1^2}{ar_c} \right) \times \left[V_1^2 \cos^2 \left(\frac{2\pi r_c}{a} - \frac{\pi}{4} \right) + 2V_1^2 \cos^2 \left(\frac{4\pi r_c}{a} - \frac{\pi}{4} \right) \right] \quad (2)$$

Figure 3 again shows the measured magnetoresistance of sample A (top) and calculated traces for the above potential and for a sinusoidal potential (bottom). Good agreement is found for $V_1=0.1\text{meV}$ and $V_2=0.25\text{V}_1$. The carrier density used for the calculation was determined from the SdH oscillations at higher magnetic fields.

Figure 4 shows the potential energy used for the calculation and a typical atomic force micrograph. The shape of the potential agrees well with the narrow and steep etch grooves. The high quality of the etching process is also proven by the fact that we can observe commensurable orbits around three periods of the superlattice.

- (1) F. Schaffter, D. Többken, H.-J. Herzog, G. Abstreiter, and B. Holländer, *Semicond. Sci. Technol.* **7**, 260 (1992)
- (2) K. Ismail, F. K. LeGraes, K. L. Saenger, M. Arafa, J. O. Chu, P. M. Mooney, and B. S. Meyerson, *Phys. Rev. Lett.* **73**, 3447 (1994)
- (3) M. G. Gavrilov, Z. D. Kvon, I. V. Kulushkin and V. B. Timofeev, *Pis'ma Zh. Tekor. Fiz.* **39**, 420, (1984)
- (4) C.W.J. Beenakker and H. van Houten, in *Solid State Physics*, edited by H. Ehrenreich and D. Turnbull (Academic, San Diego, 1991), Vol. 44, p. 1
- (5) A. D. Wieck and K. Ploog, *Appl. Phys. Lett.* **56**, 928 (1990)
- (6) P. Baumgartner, K. Brunner, G. Abstreiter, G. Böhm, G. Tränkle, and G. Weimann, *Appl. Phys. Lett.* **64**, 592 (1994)
- (7) D. Többken, M. Holzmann, S. Kühn, H. Lorenz, G. Abstreiter, J. P. Kotthaus, and F. Schaffter, *Phys. Rev. B* **50**, 8853 (1994)
- (8) T. J. Thornton, M. L. Ronkes, and H. van Houten, *Phys. Rev. B* **37**, 10118 (1988)
- (9) K.-F. Berggren, G. Roos, and H. van Houten, *Phys. Rev. B* **37**, 6633 (1995)
- (10) D. Weiss, K. v. Klitzing, K. Ploog, and G. Weimann, *Europhys. Lett.* **8**, 179 (1989)
- (11) R. W. Winkler, J. P. Kotthaus, and K. Ploog, *Phys. Rev. Lett.* **62**, 1177 (1989)
- (12) C.W.J. Beenakker, *Phys. Rev. Lett.* **62**, 2020 (1989)
- (13) R. Cusco, M. C. Holland, J. H. Davies, I. A. Larkin, E. Skuras, A. R. Long, and S. P. Beaumont, *Surf. Sci.* **305**, 643 (1994)

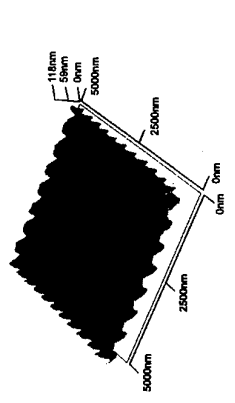
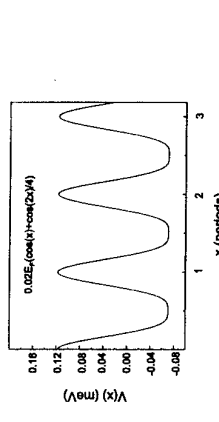


Fig. 4: Shape of the potential used for the simulation in comparison with an atomic force micrograph.

- (4) C.W.J. Beenakker and H. van Houten, in *Solid State Physics*, edited by H. Ehrenreich and D. Turnbull (Academic, San Diego, 1991), Vol. 44, p. 1
- (5) A. D. Wieck and K. Ploog, *Appl. Phys. Lett.* **56**, 928 (1990)
- (6) P. Baumgartner, K. Brunner, G. Abstreiter, G. Böhm, G. Tränkle, and G. Weimann, *Appl. Phys. Lett.* **64**, 592 (1994)
- (7) D. Többken, M. Holzmann, S. Kühn, H. Lorenz, G. Abstreiter, J. P. Kotthaus, and F. Schaffter, *Phys. Rev. B* **50**, 8853 (1994)
- (8) T. J. Thornton, M. L. Ronkes, and H. van Houten, *Phys. Rev. B* **37**, 10118 (1988)
- (9) K.-F. Berggren, G. Roos, and H. van Houten, *Phys. Rev. B* **37**, 6633 (1995)
- (10) D. Weiss, K. v. Klitzing, K. Ploog, and G. Weimann, *Europhys. Lett.* **8**, 179 (1989)
- (11) R. W. Winkler, J. P. Kotthaus, and K. Ploog, *Phys. Rev. Lett.* **62**, 1177 (1989)
- (12) C.W.J. Beenakker, *Phys. Rev. Lett.* **62**, 2020 (1989)
- (13) R. Cusco, M. C. Holland, J. H. Davies, I. A. Larkin, E. Skuras, A. R. Long, and S. P. Beaumont, *Surf. Sci.* **305**, 643 (1994)

THE FINE-STRUCTURE OF MAGNETOPLASMONS IN QUANTUM-WELL WIRES AND THEIR MAGNETOOPTICAL MANIFESTATION

L. Wendler, V.G. Grigoryan
Fachbereich Physik, Martin-Luther-Universität Halle, Friedemann-Bach-Platz 6,
D-06108 Halle, Germany

Abstract

The dispersion relation of magnetoplasmons in quantum-well wires is calculated using the random-phase approximation. It is shown that for certain values of the physical parameters additional intersubband modes exist which have the character of confined modes. With these modes it is possible to explain the recent experimental findings of resonance splitting and fine-structure effects in far-infrared transmission spectroscopy on quantum-well wires.

Far-infrared (FIR) optical transmission experiments on the quasi-one-dimensional electron gas (Q1DEG) synthesized in a quantum-well wire (QWW) show two unexpected effects when a magnetic field is applied: (i) a resonance splitting (anticrossing) of one Q1D magnetoplasmon mode at the line $2\omega_c$ ($\omega_c = eB/m_e$: cyclotron frequency, m_e : effective conduction-band-edge mass) [1] and (ii) for larger electron densities a very pronounced splitting of the lowest-frequency mode into several branches in a definite range of magnetic fields [1,2]. Unfortunately, the up to now developed theories [3–5] fail to explain these experiments. In a recent paper [6], we have presented a new method to calculate the dispersion relation of Q1D magnetoplasmons, valid for all physical parameters as long as the random-phase approximation (RPA) of the Q1D Fermi liquid model of the Q1DEG is valid.

In this article we focus on magnetoplasmons in QWW's with the goal to explain the two above mentioned effects detected in the FIR optical transmission experiments [1,2]. The electrons of the Q1DEG are assumed to be quantum-confined in a zero-thickness $x-y$ plane along the z -direction at $z=0$ and in y -direction the effective confining potential $V_{eff}(y) = m_e\Omega^2 y^2/2$ is assumed to be parabolic. Choosing the Landau gauge $\mathbf{A} = (-yB, 0, 0)$ for the vector potential \mathbf{A} of the external applied magnetic field $\mathbf{B} = (0, 0, B)$ and ignoring the Zeeman spin splitting, the eigenvalue problem of the single-particle Hamiltonian is exactly solvable with the single-particle wave function $\langle \mathbf{x}|N, k_x \rangle = \Psi_{Nk_x}(\mathbf{x}) = L_x^{-1/2} e^{ik_x x} \Phi_N(y - Y_k) [\delta(z)]^{1/2}$, where $\Phi_N(y - Y_k)$ is the displaced-center harmonic-oscillator wave function and $N = 0, 1, 2, \dots$ is the subband index. The center coordinate is $Y_{k_x} = \gamma \tilde{\beta}_0 k_x$ with $\gamma = \omega_c/\tilde{\omega}_c$, $\tilde{\omega}_c = (\omega_c^2 + \Omega^2)^{1/2}$ is the hybrid frequency, $\tilde{\beta}_0 = [\hbar/(m_e \tilde{\omega}_c)]^{1/2}$ and $\tilde{m}_e = m_e(\tilde{\omega}_c/\Omega)^2$ is the renormalized magnetic-field-dependent mass. The corresponding energy eigenvalues are $\mathcal{E}_N(k_x) = \mathcal{E}_N + \hbar^2 k_x^2/(2\tilde{m}_e)$, where $\mathcal{E}_N = \hbar\tilde{\omega}_c(N + 1/2)$. Representing the resulting single-particle wave function $\Phi_N(y - Y_k)$ of a shifted harmonic oscillator by the closure set of undisplaced wave functions $\{\Phi_L(y)\}$: $\Phi_N(y - Y_k) = \sum_{L=0}^{\infty} C_{LN}(Y_{k_x}) \Phi_L(y)$, the RPA dispersion relation of the Q1D magnetoplasmons reads [6]

$$\det[\delta_{LL_1}\delta_{L_1L_2} - \Xi_{L_1L_2LL_1}(q_x, \omega)] = 0, \quad (1)$$

$$\begin{aligned} \text{where } \Xi_{L_1L_2LL_1}(q_x, \omega) &= [\Lambda_{L_1L_2LL_1}(q_x, \omega) + \Lambda_{L_1L_2LL_1}(q_x, \omega)]/(1 + \delta_{LL_1}) \text{ and} \\ \Lambda_{L_1L_2LL_1}(q_x, \omega) &= \sum_{L_3, L_4} V_{L_1L_2L_3L_4}^s(q_x) \mathcal{P}_{L_3LL_4}^{(1)}(q_x, \omega) \end{aligned} \quad (2)$$

with

$$\mathcal{P}_{L_3LL_4}^{(1)}(q_x, \omega) = \sum_{N, N'} \sum_{k_z} P_{NN'}^{(1)}(q_x, k_z | \omega) C_{L_3N}(Y_{k_x + q_z}) C_{L_4N'}^*(Y_{k_x}) C_{L_4N'}^*(Y_{k_z}). \quad (3)$$

In Eq.(2), $V_{L_1L_2L_3L_4}^s(q_x)$ is the matrix element of the Coulomb potential and $P_{NN'}^{(1)}(q_x, k_z | \omega)$ is the RPA matrix polarization function, both explicitly given in Refs. [6,7].

Under the condition that $\xi k_F^{(0)} \ll 1$, where $\xi = \gamma \tilde{\beta}_0$ and $k_F^{(0)} = [2m_e(E_F - \mathcal{E}_0)/\hbar^2]^{1/2}$ is the Fermi vector, it is possible to restrict the representation of the shifted harmonic-oscillator wave function by the set of undisplaced wave functions on a small number of terms. Assuming three-subbands model, $N, N' = 0, 1, 2$, from which one occupied, in the calculation the dispersion relation gives in the long-wavelength limit up to the power $(q_x)^0$ the following analytical results

$$\omega_{mp}^{10j} = (1 + \alpha_{10j})^{1/2} \tilde{\omega}_c + \mathcal{O}[(\xi k_F^{(0)})^5], \quad (4)$$

$$\omega_{mp}^{20j} = (1 + \alpha_{20j})^{1/2} (2\tilde{\omega}_c) + \mathcal{O}[(\xi k_F^{(0)})^5], \quad (5)$$

with

$$\alpha_{101} = \frac{n_{1DEG} e^2}{2\pi\epsilon_0\tilde{\omega}_c} \left(1 - \frac{\pi^2 n_{1DEG}^2 \hbar \omega_c^2}{8m_e \tilde{\omega}_c^3} \right), \quad (6)$$

$$\alpha_{102} = \frac{n_{1DEG} e^2}{2\pi\epsilon_0\tilde{\omega}_c} \left(\frac{\pi^2 n_{1DEG}^2 \hbar \omega_c^2}{6m_e \tilde{\omega}_c^3} \right), \quad (7)$$

$$\alpha_{201} = \frac{n_{1DEG} e^2}{8\pi\epsilon_0\tilde{\omega}_c} \left(1 - \frac{\pi^2 n_{1DEG}^2 \hbar \omega_c^2}{3m_e \tilde{\omega}_c^3} \right), \quad (8)$$

$$\alpha_{202} = \frac{n_{1DEG} e^2}{8\pi\epsilon_0\tilde{\omega}_c} \left(\frac{\pi^2 n_{1DEG}^2 \hbar \omega_c^2}{12m_e \tilde{\omega}_c^3} \right) \quad (9)$$

for the (1–0) and (2–0) intersubband magnetoplasmons ω_{mp}^{10j} and ω_{mp}^{20j} , respectively. Herein, n_{1DEG} is the 1D electron density, ϵ_0 is the permittivity in vacuum and $\tilde{\omega}_c$ the static dielectric constant to account the dielectric screening of the background. As evident from Eqs. (4) to (9) only the intersubband magnetoplasmons with $j = 1$, ω_{mp}^{N0j} , have for vanishing magnetic field a non-vanishing depolarization shift, i.e., we have $\alpha_{N01} \neq 0$ but $\alpha_{N02} > 1 = 0$ at $B = 0$. An intersubband mode which has a vanishing depolarization shift is accompanied with a vanishing induced density. What follows is that the modes ω_{mp}^{10j} and ω_{mp}^{20j} disappear and only the plasmon branches $\omega_p^{10j} \equiv \omega_{mp}^{10j}$ and $\omega_p^{20j} \equiv \omega_{mp}^{20j}$ exist at $B = 0$. In the limit of large magnetic fields, i.e. for $B \rightarrow \infty$, the frequencies of the intersubband magnetoplasmons approach asymptotical multiples of the cyclotron frequency: $\omega_{mp}^{N0j}(B \rightarrow \infty) \rightarrow N\omega_c$, i.e. the modes become degenerated at multiples of ω_c . The (1–0) modes behave like the *principal magnetoplasmon* and the (2–0) modes like the *first Bernstein mode* of a Q2DEG. Hence, for large magnetic fields the 2D limit is realized.

In addition to the modes occurring at $B = 0$, which have the largest depolarization shifts and we call them *fundamental modes* (FM's), for $B \neq 0$ the intersubband modes ($N > 0$ and $\omega_{mp}^N, j > 1$ exist, which we call *additional modes* (AM's).

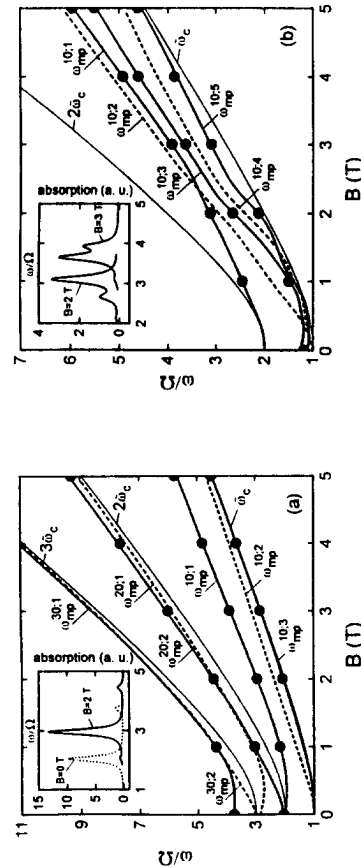


FIG. 1. Dispersion relation of the intersubband magnetoplasmons (collective intersubband transitions). The calculated full RPA dispersion relations are given by solid lines (antisymmetric modes) and dashed lines (symmetric modes). The symbols (●) represent the main peaks of the power absorption spectrum. Calculations are done numerically for a GaAs - $Ga_{1-x}Al_xAs$ QWW with $\hbar\Omega = 2$ meV, $\epsilon_r = 12.87$, and $m_e = 0.06324m_0$, (m_0 : bare electron mass); (a) for $n_{DDEG} = 3.7 \times 10^{18} \text{ cm}^{-2}$; (b) for $n_{DDEG} = 0.2 \text{ meV}$ is used. For the calculation of the power absorption a phenomenological relaxation time $\hbar/\tau = 0.2 \text{ meV}$ is used.

Now it is possible to understand the physical origin of the AM's. Without the lateral confining potential, i.e. in the 2D limit, we have one dispersion curve of the principal magnetoplasmon and one for each Bernstein mode. These modes propagate in the isotropic $x - y$ plane of the 2DEG, i.e. degeneracy according to the propagation direction arises. The lateral confining potential lifts this degeneracy and the modes become *confined modes*: the fine-structure ($j = 1, 2, 3, \dots$) of the intersubband-magnetoplasmon dispersion relations occurs. That means that all the magnetoplasmon oscillations, which exist at $B \rightarrow \infty$ become standing-wave like behaviour at finite magnetic fields. Hence, our theory gives a close picture of the Q1D magnetoplasmons with the correct $B = 0$ and $B \rightarrow \infty$ limits and for the first time the confined Bernstein modes results. These modes are caused by nonlocal effects in the magnetoplasma and are absent in earlier work [3] because the used semi-classical theory neglects nonlocality. Our nonlocal quantum-mechanical theory includes the confined Bernstein modes which hybridize with the principal ones to the Q1D magnetoplasmons. In Figure 1(a) the full RPA dispersion relations of the magnetoplasmons calculated numerically from Eq.(1), are plotted in dependence on the magnetic field. In addition to the dispersion relation we have calculated, using the current-response theory, the power absorption spectrum $\mathcal{P}_{abs}(\omega) = \frac{1}{2} \operatorname{Re} \left\{ \int d^3x \mathbf{j}(\mathbf{x}, \omega) \mathbf{E}^*(\mathbf{x}, \omega) \right\}$, where \mathbf{j} is the total current density and \mathbf{E} the total (or self-consistent) electric field. It is seen from Fig. 1(a) that for vanishing magnetic field the collective intersubband resonances ω_{mp}^{202} and ω_{mp}^{301} show the pronounced absorption peaks. The other modes should not be observable. For larger magnetic fields the mode ω_{mp}^{301}

have a vanishing oscillator strength. With increasing magnetic field the oscillator strength changes from ω_{mp}^{301} to ω_{mp}^{202} . Only one (2 - 0) and two (1 - 0) modes should be observable in this region. In the FIR experiment [1] it seems that the collective (3 - 0) intersubband resonance approaches at $2\omega_c$ for large magnetic fields. Hence, the observed splitting of the mode at $2\omega_c$ is in our opinion not an anticrossing of two Q1D magnetoplasmon modes, but simply an exchange of oscillator strength between two modes: for smaller magnetic fields one observes the FM ω_{mp}^{301} , but for larger magnetic fields the AM ω_{mp}^{202} is detected. Besides of these modes for smaller frequencies one observes in the experiment [1], one further branch, which is in our opinion an AM (here ω_{mp}^{103}). This mode is accompanied by an absorption peak of order than that of the mode ω_{mp}^{202} .

Now we come to explain the experimental detected splitting of the collective (1 - 0) intersubband resonance in several branches at larger electron densities and intermediate magnetic fields. From Eqs. (4), (5), (7) and (9) it becomes obvious that the depolarization shift of the AM's have the maximum at intermediate magnetic fields. Further, this maximum increases with increasing electron density and hence, AM's are only observable in a FIR transmission experiment for larger densities and in a definite range of magnetic fields. This results in the conclusion that the detected fine-structure of the mode spectrum for larger electron densities in Refs. [1,2] is nothing than the observation of the AM's. The full RPA calculations of the Q1D collective intersubband resonance frequencies for higher electron densities (three subbands are occupied for $B = 0$), plotted in Fig. 1(b), show significantly the fine-structure effects. With the increase of the magnetic field the FIR oscillator strengths of the FM and of the first antisymmetrical AM become comparable and e.g. for $B = 3$ T of Fig. 1(b) (see insert) the oscillator strength of the first (1 - 0) antisymmetrical AM is larger than that of the (1 - 0) FM. Such an effect on the transition of the oscillator strength from the upper to the lower mode was measured in Refs. [1,2]. Comparing our results with the experimental findings of Refs. [1,2] we come to the conclusion that in the experiment the observed splitting of the (1 - 0) mode in several branches is the first detection of the fine-structure of the intersubband magnetoplasmon dispersion of QWW's, i.e. the additional magnetoplasmons. In summary, it is shown that according to the size quantization additional modes exist which have the character of confined modes. The existence of the AM's is an intrinsic property of the Q1DEG in the presence of a magnetic field.

We gratefully acknowledge financial support of the Deutsche Forschungsgemeinschaft (DFG), Project We 1532/3-2.

References

- [1] H. Drexler, W. Hansen, J.P. Kotthaus, M. Holland and S.P. Beaumont, Phys. Rev. B 46 (1992) 12849.
- [2] G. Hertel, H. Drexler, W. Hansen, A. Schmeller, J.P. Kotthaus, M. Holland, and S.P. Beaumont, Solid State Electronics, 37 (1994) 1289.
- [3] G. Eliasson, Ji-Wei Wu, P. Hawrylak and J.J. Quinn, Solid State Commun. 60 (1986) 41.
- [4] Q.P. Li and S. Das Sarma, Phys. Rev. B 44 (1991) 6277.
- [5] S.-R. E. Yang and G.C. Aers, Phys. Rev. B 46 (1992) 12456.
- [6] L. Wendler and V.G. Grigoryan, Phys. Rev. B 49 (1994) 13607.
- [7] L. Wendler, R. Haupt and R. Pechstedt, Phys. Rev. B 43 (1991) 14669.

COHERENT PROPERTIES OF IN-PLANE GATED InGaAs/AlGaAs SUBMICRON RINGS

A.A.Bykov, L.V.Litvin, and S.P.Mostchenko
Institute of Semiconductor Physics, Russian Academy of Sciences,
Siberian Branch, Novosibirsk 630090, RUSSIA

Abstract

We have investigated the coherent properties of InGaAs/AlGaAs in-plane gated rings with diameters 0.7 μm and 0.4 μm at temperatures 4.2K and 1.6K. It was established that in smaller rings at T=1.6K the limiting factor for the increasing of the amplitude of magnetoresistance Aharonov-Bohm oscillations is not a short coherence length but rather the imperfection of interferometers operating in multimode regime. The investigation of the microwave mesoscopic e.m.f. in rings with diameter 0.7 μm has revealed a symmetry of interference processes in the rings with respect to both magnetic and electrostatic fields.

Beginning with the experimental work [1], attempts have been made to fabricate a solid state analog to the optical Mach-Zender interferometer - a so called interference transistor. Numerous investigation of the problem have shown that the main impediments to the development of an interference transistor are the scattering of carriers caused by random potential and the multimode operation of electron interferometers [1-4]. It is important to raise the operating temperature of interferometers which makes it necessary to decrease their dimensions.

In the present work we report the results of investigation of the coherent properties of InGaAs/AlGaAs rings in both magnetic and electrostatic fields. The preference of InGaAs/AlGaAs/GaAs heterostructures has been made because of a bigger energy discontinuity at the InGaAs/AlGaAs interface. To our opinion this feature might result in a higher 2D electron density and therefore give us certain advantages in making smaller rings. The experimental samples were fabricated on the basis of $\text{In}_{0.2}\text{Ga}_{0.8}\text{As}/\text{AlGaAs}$ MBE heterostructures by means of electron lithography and reactive ion etching. The 2D electron gas mobility at T=4.2K was $10^5 \text{ cm}^2/\text{Vs}$, the electron density - $(7\text{-}10)\times 10^{11} \text{ cm}^{-2}$. Schematic view of an interferometer with the inner and outer diameters $d_{in}=0.4 \mu\text{m}$ and $d_{out}=1 \mu\text{m}$ respectively is shown in Fig. 1a. Smaller rings had $d_{in}=0.1 \mu\text{m}$ and $d_{out}=0.7 \mu\text{m}$.

The measurements were carried out at T=4.2K and at T=1.6K in magnetic fields up to 1.5T. For magnetoresistance measurements we used the conventional four point ac scheme. The effect of gate bias voltage V_g on the coherent properties of the rings was studied with the use of microwave photovoltaic effect in the frequency range 9-80 GHz[5]. One of the two in-plane gates was biased. The other could be biased independently or grounded together with one of the ohmic contacts. The preference of microwave measurements to conductance one is explained by a higher sensitivity of the former to interference effects in the temperature range studied [4]. We have investigated in detail the properties of two rings with a diameter $d_{eff}=0.7 \mu\text{m}$ and two smaller rings with $d_{eff}=0.4 \mu\text{m}$. The effective diameter was determined from the period of Aharonov-Bohm oscillations in magnetic field. There was a hysteresis in $R(V_g)$ curves, as it is shown in figure 1b, explained by charge exchange of impurities in the vicinity of the 2D layer. The hysteresis was absent if the absolute value of V_g was held lower than 0.3V. Application of gate voltages in the

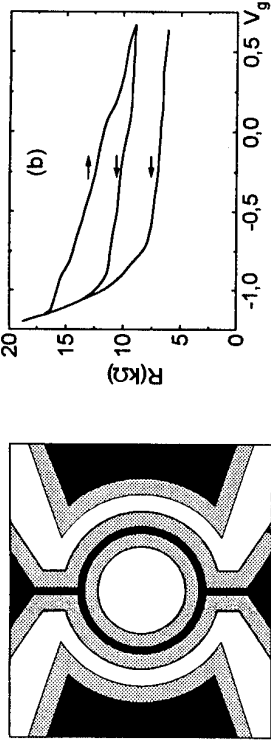


Figure 1 (a) - schematic top view of the sample, black is 2D gas regions, gray - depletion areas and white - etching grooves. (b) - resistance of the sample vs gate voltage, T=4.2K, $d_{eff}=0.7 \mu\text{m}$.
latter range produced no changes in the impurity potential configuration which is further supported by reproducibility of magnetic field dependencies of both conductance and e.m.f. It was found that by choosing the right gate voltages the rings with $d_{eff}=0.7 \mu\text{m}$ could be tuned into single mode regime[3]. However this method of varying V_g in order to obtain single mode regime proved ineffective in the case of the smaller rings which is probably due to their resistance in zero magnetic field, ΔR -the Aharonov-Bohm oscillations amplitude, d_{eff} - effective diameter of a ring.

Table 1 The parameters of InGaAs/AlGaAs rings, $L_T=(D/k_B T)$, L_Φ -the coherence length, R_0 - ring resistance in zero magnetic field, ΔR -the Aharonov-Bohm oscillations amplitude, d_{eff} - effective diameter of a ring.

T, K	$L_T, \mu\text{m}$	$L_\Phi, \mu\text{m}$	$R_0, \text{k}\Omega$	$\Delta R/R_0, \%, d_{eff}=0.7 \mu\text{m}$	$\Delta R/R_0, \%, d_{eff}=0.4 \mu\text{m}$
4.2	1.4	0.5±0.1	5-15	0.5-1	1.5-2.5
1.6	2.3	0.9±0.2	5-15	1.5-3	3-5

inferior quality. The relevant parameters of our rings are listed in table 1. To determine the coherence length L_Φ , we used the ratio of the amplitudes of Aharonov-Bohm (AB) oscillations (ΔR) measured in rings of different diameters and the expression $\Delta R = \exp(-\pi d_{eff}/2L_\Phi)$ [6].

Table 1 shows that for rings with $d_{eff}=0.4 \mu\text{m}$ the amplitude of AB oscillations at T=1.6K is not limited by L_T or L_Φ but rather by inherent imperfection of interferometers operating in a multimode regime. The highest amplitude we could produce in these rings varying V_g at T=1.6K turned out to be about 5% of R_0 , which is much less than the corresponding value observed in AlGaAs/GaAs rings of bigger diameter operating in a single mode regime in the mK range [3]. At the same time the ratio $\Delta R/R_0$ found in InGaAs/AlGaAs rings with $d_{eff}=0.7 \mu\text{m}$ at T=4.2K was comparable to that observed in AlGaAs/GaAs rings with approximately the same sizes and electron gas parameters, which showed $\Delta R/R_0 \sim 0.35$ at T 20mK [7]. We hope accordingly that it would be possible to obtain high amplitude AB oscillations in small diameter InGaAs/AlGaAs rings after their fabrication is optimized.

The effect of electrostatic field on the properties of submicron rings goes beyond mere changing the number of modes in conducting channels. In the same way as magnetic field does, it can produce phase shifts in the electron wave function components in either channel of a ring [2,3]. Fig. 2a shows a mesoscopic e.m.f. versus magnetic field dependence. Similar to AlGaAs/GaAs rings [4] this dependence has both a fluctuating and a periodical component, the latter with a period corresponding to a change of $\Phi_0=h/e$ in the magnetic flux through the

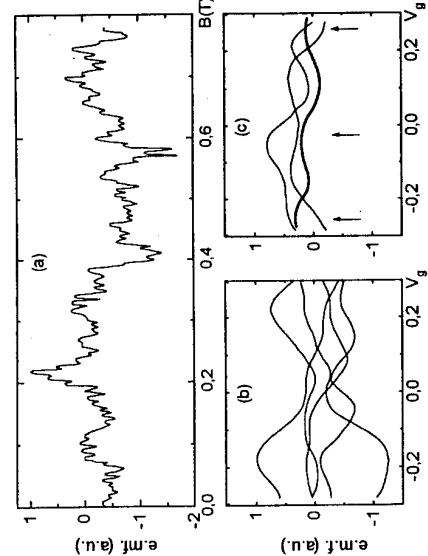


Figure 2 (a) Mesoscopic e.m.f. versus magnetic field dependence. (b) E.m.f. versus gate voltage for different magnetic field. (c) "Periodic" component of e.m.f. (thick line) obtained from $V(V_g)$ for magnetic flux $19\Phi_0$ and $19.5\Phi_0$ (two thin lines).

ring area. The amplitude of the fluctuating component is approximately three times larger than that of the periodical component. Since the characteristic magnetic field scales of these two components are sufficiently different they may be separated by means of Fourier analysis. Fig.2b shows $V(V_g)$ dependencies for several values of magnetic field. From Fig.2b one can see that the e.m.f. versus V_g dependence is irregular with an average amplitude of fluctuations approximately equal to the amplitude of the fluctuating component in magnetic field dependence of the e.m.f. Supposing there is a periodical component in a $V(V_g)$ dependence, it would be difficult to select it by Fourier filtering as it is possible to do in the case with $V(B)$ dependencies. The main difficulties are a too narrow V_g variation range and the fact that the correlation electric field of irregular fluctuations should be close in magnitude to the period of periodical component if such exists [4].

There is a possible solution however that follows from the fact that e.m.f. versus V_g oscillations resulting from direct electron interference should change their phase by π if the magnetic field flux Φ piercing the area of the ring is changed by $\Phi_0/2$ [8]. Hence, with an accuracy of the amount of the irregular component may change on the interval of magnetic field $\pi d_{\text{eff}}/\Phi_0/8$, the periodical e.m.f. component in V_g is given by the expressions $[V(V_g, \Phi) - V(V_g, \Phi + \Phi_0/2)]/2$.

This method is more accurate if the amplitudes of the two components are of the same order and its applicability depends also on the respective values of d_{eff} and W_{eff} . In our case we have $d_{\text{eff}} \gg W_{\text{eff}}$. Under these circumstances the described method is quite appropriate since the ap periodical component correlation magnetic field $\delta B > \pi d_{\text{eff}}^2/\Phi_0/8$ and this component changes but weakly in the interval of magnetic field corresponding to the magnetic flux change $h/2e$. To achieve a higher accuracy one has to look for a magnetic field region where the amplitudes of the two components are comparable and the ap periodical component changes weakly with V_g and B .

A periodical dependence determined in this way is shown in Fig.2b. The fact that for magnetic field fluxes differing by $\Phi_0/2$ the $V(V_g)$ dependencies in Fig.2b have a phase difference

of π indicates that we observe the effect of V_g on the direct interference of electron waves propagating in the two channels of the ring. The amplitudes of the ap periodical and periodical components in $V(B)$ dependencies are approximately equal to corresponding values in $V(V_g)$ dependencies. In order to qualitatively estimate the effect of V_g on the ring channels we have made a comparison between two correlation functions $F(B, \Delta V_g)$ and $F(B, \Delta f)$ of the ap periodical e.m.f. component; ΔV_g and Δf are variations of gate voltage and frequency. The results of this comparison together with the knowledge of the e.m.f. versus V_g oscillations "period" enabled us to come to the conclusion that in our ring geometry a variation of V_g results in a change of the Fermi energy E_F mainly in one of the ring channels, bringing about the e.m.f. oscillations "periodical" in V_g . One must not attach much significance to the term "periodical" as regards the e.m.f. oscillations in V_g . We call them periodical here in analogy with e.m.f. oscillations in magnetic field but actually their periodicity depends on where in the ring and how the E_F changes with the variation of V_g .

To conclude, we have experimentally established that InGaAs/AlGaAs heterostructure is a promising material for fabrication of electron interferometers with an operation temperature in the range 1.6–4.2 K. The study of microwave e.m.f. in InGaAs/AlGaAs rings with in-plane gates has shown that the coherent phenomena in an electron interferometer are symmetrical with respect to the effects of magnetic and electric fields as it was recently shown in a ballistic structure with two slits [8]. It was found that both the e.m.f. versus magnetic field and the e.m.f. versus gate voltage dependencies contain a periodical and an ap periodical components and the corresponding amplitudes are approximately equal.

We are grateful to Kvon Z.D. and O'l'shanetskii E.B. for fruitful discussions. The research described in this publication was made possible in part by grant No U84300 from the International Science Foundation and Russian Government and by Grant No 95-02-04409-a from RFFI.

References

- [1] S. Washburn, H. Schmid, D.P. Kern, and R.A. Webb, Phys. Rev. Lett. **59** (1987) 1791.
- [2] C.J.B. Ford, A.B. Fowler, J.M. Hong, C.M. Knoedler, S.E. Lau, J.I. Wainer, and S. Washburn, Symp. Sci. **229** (1990) 307.
- [3] J. Liu, W.X. Gao, K. Ismagil, K.Y. Lee, J.M. Hong, and S. Washburn, Phys. Rev. **B48** (1993) 15148.
- [4] A.A. Bykov, Z.D. Kvon, L.V. Litvin, S.P. Moshchenko, and Yu.V. Nastaushev, Pis'ma Zh. Eksp. Teor. Fiz. **60** (1994) 796.
- [5] V.I. Fal'ko and D.E. Khmel'nitsky, Zh. Eksp. Teor. Fiz. **95** (1989) 328.
- [6] W.X. Gao, K. Ismagil, K.Y. Lee, J.O. Chu, and S. Washburn, Appl. Phys. Lett. **65** (1994) 3114.
- [7] A.A. Bykov, Z.D. Kvon, E.B. O'l'shanetskii, L.V. Litvin, Yu.V. Nastaushev, V.G. Mansurov, V.P. Migal, S.P. Moshchenko, and V.G. Plyukhin, Pis'ma Zh. Eksp. Teor. Fiz. **57** (1993) 596.
- [8] A. Yacoby, M. Heiblum, V. Umansky, H. Shtrikman, and D. Mahalu, Phys. Rev. Lett. **73** (1994) 3149.

New h/e oscillations and electrostatic Aharonov-Bohm effect in a GaAs/AlGaAs-based mesoscopic ring

KyoungWan Park, Seongjae Lee, Mincheol Shin, and El-Hang Lee
Research Department, Electronics and Telecommunications Research Institute,
Yusong P.O.Box 106, Taejon 305 - 600, Korea

Hyuk Chan Kwon
Korea Research Institute of Standards and Science,
Yusong P.O.Box 102, Taejon 305-600, Korea

We have investigated the electrical properties of a GaAs/AlGaAs-based mesoscopic ring structure in the presence of magnetic flux and electrostatic potential. In a certain range of the electrostatic potential, new h/e magnetoresistance oscillations have been observed near zero magnetic field, where the new peaks of the oscillation are interspersed between the conventional ones. This phenomenon is attributed to the combined behavior of the magnetostatic and electrostatic Aharonov-Bohm effects simultaneously occurring in two different configurations of electron paths: one is the Mach-Zender type path and the other is a localization path which is composed of one turn of the ring. We have also observed that the magnetostatic Aharonov-Bohm oscillations are shifted by the electrostatic potential; the shift is not uni-directional but rather oscillating.

The phase of electrons in an electrical device can be controlled by the electrostatic potential and the magnetic vector potential that the traveling electrons experience in the conducting path. Changes in magnetic fluxes in a ring structure lead to the magnetostatic Aharonov-Bohm (AB) oscillations[1], whereas changes in gate potentials lead to the electrostatic quantum interference effects[2-4].

Recently, studies on one dimensional ring structures predicted two types of conductance minima in the electrostatic conductance spectra[5]. The primary minima are caused by the Mach-Zender type interference, and the other ones by the interference due to electron circulation around the ring, that is, "localization type interference". In addition, it has been demonstrated that the two types of the magnetostatic conductance minima are formed in the presence of small electrostatic potential, and that the positions of the minima do not change as the electrostatic potential varies[6].

On the other hand, some experiments have been performed in an attempt to realize electron interferometer devices[7-8]. Since the electrostatic potentials disturbs carrier densities, carrier trajectories[4], and number of the conduction model[3,7] as well as the electrostatic AB phase, the results are far from clear. In this paper, we present experimental results about the formation of new h/e oscillations in a small magnetic field range with the variation of the gate potential and the electrostatic AB effect demonstrated by a shift of the magnetic AB oscillations in the presence of the gate potential change in a corrugated gate AlGaAs/GaAs-based mesoscopic ring structure.

The conducting path of ring of two-dimensional electron gas(2DEG) has been fabricated by means of electron beam lithography and subsequent chemical etching on a modulation-doped AlGaAs/GaAs heterostructure grown by molecular-beam epitaxy; the average diameter is 1.9 μm , the width of the conducting path is 0.3 μm in the lithographic length, and distance between the measurement probes across the ring is 3.8 μm . The heterostructures were wet-etched down to 2DEG layer to form a well-shaped pathway. Lateral depatterning further reduces the conducting width. To form the gate, electron beam lithography and lift-off techniques were employed. The second step defined the corrugated AlNi gate; the metal gate length is 0.2 μm on the one conducting path of the ring and 1 μm on the other. Figure 1(a) shows the schematic diagram of the fabricated sample.

The carrier concentration and mobility in this substrate at 1.5K, as deduced from the measurement of Shubnikov-de Haas oscillation in two dimensional bar(50x150 μm), were found to be $n = 3.2 \times 10^{14} \text{ cm}^{-2}$ and $\mu = 5.5 \times 10^8 \text{ cm}^2 \text{ V}^{-1} \text{ s}^{-1}$, respectively. We measured longitudinal resistances in

the applied magnetic fields and gate voltages by using the lock-in technique and 10 nA driving current at 17 mK. We found the periodic magnetoresistance oscillations which are in direct correspondence with the penetration of the flux $\Phi_0 = h/e$ through the average area of the annulus. This result demonstrates that the mesoscopic ring was well fabricated.

When we apply the gate potential only at one conducting path of the ring as previously reported[7], uneven electrical properties between two conducting paths possibly occur and hinder from the measurement of the quantum interference effect. So we adopted a corrugated gate to induce only a path difference, thereby reducing the uneven properties[2]. In this structure the traveling distances of electrons under the gate potential are different in one arm of the ring from the other.

The measured resistances as a function of the gate voltage (V_g) are depicted in Fig. 1(b). The overall resistance increases as the gate voltage negatively increases. The resistance curve exhibits oscillatory behaviors, which possibly originate from both of the lateral quantum interference effect between two paths and the multiple reflection effect[2]. Since the electrons are quantized in the transverse direction in the narrow wires, the transverse mode depolarizations by the negative gate voltage are also apparent in the resistance curve (indicated by the horizontal bars in the figure). Finer measurements for observation of the electrostatic AB oscillations have been done in a range of low gate voltages without any mode depolarizations in between, as shown in the inset of Fig. 1(b).

In the inset of Fig. 1(b), two independent (almost) periodic oscillations (represented by dots and bars, respectively) are seen. The resistance curve with the electrostatic potential sweep alone cannot, however, identify the source of the two types of the oscillations, which leads us to turn to the magnetoresistance measurements at constant gate voltages.

The magnetic AB oscillations are observed to shift with the gate voltages, as expected, since the phase difference between electrons transmitted through the upper and the lower branches of the ring is dependent on the gate voltage. We found that the phase differences are π between two successive magnetic h/e AB oscillations at the selected gate voltages, which is shown in Fig. 2(a). A close examination of the phase shifts in the magnetic AB oscillations [Fig. 2(a)] and the electrostatic resistance spectrum [inset of Fig. 1(b)] indicates that the resistance minima represented by the dots are different in the interference characteristics from those represented by the bars.

In careful magnetoresistance measurements at different gate voltages from -195.3 mV to -242.3 mV, we have observed a striking feature [See Fig. 2(b)]. New set of oscillations with h/e period are clearly seen in the magnetoresistance measurement, (see the curve at $V_g = -206.2$ mV, for example), and they are shifted by π with respect to the background h/e AB oscillations. It is observed that the new h/e AB oscillations are formed only near zero magnetic field; approximately $40 \text{ G} < B < +40 \text{ G}$. In the magnetic field range, the peak positions of both of the h/e oscillations do not change as the gate voltage varies, but only their amplitudes alternate. Let us now start with the bottom curve of the figure, which is taken at -195.3 mV, where the newly formed oscillations begin to appear at the troughs of the background oscillations. As we negatively increase the gate voltage, the new peaks gradually grow while the background peaks shrink as much. At -206.2 mV, the two set of peaks are almost equal in magnitudes, so as to make the period of the resistance oscillations as a whole appear to be $h/2e$. If the gate voltage further increases, the new oscillations continue to grow and they take over the background oscillations at -230.3 mV. Therefore, while the gate voltage changes by 35 mV, we have half cycle with respect to the alternation between the new and the background oscillations. The estimated period of 35 mV is in good agreement with the period of the oscillations in the electrostatic measurements in inset of Fig. 1(b). We thus conclude that the electrostatic phase shift between the successive resistance minima in the electrostatic measurement is π .

In the ballistic transport of the mesoscopic ring structure, the reflection probability around the ring is so large at the junction of the source/drain side that we should consider the interference effect around localization path as well as the Mach-Zender type path. Takai and Ohta have investigated the influence of electrostatic potential on the magnetic AB effect in the one-dimensional ring structure[6]. At zero potential difference, the conventional AB oscillation is obtained. With larger voltages, the conductance minima grow shallower, while new minima appear between the original neighboring minima. These new minima grow, and the original minima fade away. The positions of the phase of these new minima differ by π from those of the original minima at zero voltage case. These oscillations can occur as a result of the competition between the two interference

conditions which are previously described[6]. The experimental behaviors of the h/e oscillations near zero magnetic field in the presence of electrostatic potential, as shown in Fig. 2(b), are qualitatively in good agreement with the calculation results of the magnetoresistance by Takai and Ohta. The discrepancy in the half period along the electrostatic potential, which is 6 mV from their calculation and 35 mV in the experimental results, may be attributed to the gate voltage drop effect in the conducting path.

Figure 3 shows the resistance curve versus the gate voltage at a fixed magnetic field, $B = 800$ G. We expect that the new h/e AB oscillations disappear in high magnetic field range. Compared with the resistance curve at $B = 0$, as shown in the inset of Fig. 1(b), some resistance minima represented by dots disappear or the intensities are much reduced (the overall resistance curve at $B = 800$ G is shifted by amount of -15 mV, which may be attributed to the interfacial charge built up at the metal gate/GaAs top layer interface). We believe that the AB effect of the Mach-Zender type is dominant in high magnetic fields. Thus, the resistance minima in Fig. 3 can be explained by the electrostatic AB interference with 2π phase difference (the multiple reflection effect induced by the gate potential should be included, but the intensity is small in the low gate bias voltage[2]). The gate voltage difference 86.5 mV between the two successive resistance minima, c. g., $V_g = -220.1$ mV and $V_g = -133.0$ mV, is in agreement with 2 times the half period 35 mV at $B = 0$.

Magnetoresistance curves taken at several gate voltages illustrating the shift of the magnetic h/e AB oscillations are displayed in Fig. 4. In order to avoid the other type of the electrostatic oscillations than the usual ones, we select a high magnetic field range, i. e., $750 \text{ G} < B < 850 \text{ G}$. We note that the magnetic AB oscillations at the gate voltages corresponding to the resistance minima of Fig. 3, c. g., $V_g = -17.4$, -48.4, -83.3, -133.6, -133.6, -220.1 and -264.9 mV, are nearly in phase. However the shift of the magnetic AB oscillations is not uni-directional, but rather oscillating with respect to the gate voltage. This behavior, which agrees with a previous report[3,4], may be attributed to the wave vector "pinning", which was proposed for two terminal measurements by Buttiker[9]. In our calculations that fully solve the Schrödinger equation for the quasi-one dimensional gated ring structure, we also find that the magnetic AB oscillations are unable to respond to the wave vector variation induced by the gate voltage, that is, amplitude modulation rather than an electrostatic phase shift should occur as the gate voltage changes. Although it is not clear in our four terminal measurements why the oscillations should be "pinned", we conjecture that this behavior may be due to the electrostatic AB effect in the multiple reflection effect at one arm of the ring between the source and drain junctions.

In conclusion, we have carefully investigated the electrical transport properties of a GaAs/AlGaAs-based mesoscopic ring structure in the presence of magnetic flux and electrostatic potential. New h/e AB oscillations near zero magnetic field and pinning of the AB oscillations in high magnetic fields have been observed. We find that these phenomena are well explained by the combined behavior of the magnetic and electrostatic Aharonov-Bohm effects simultaneously occurring in various configurations of electron paths.

References

- [1] Y. Aharonov and D. Bohm, Phys. Rev. 115 (1959) 485 ; R. A. Webb, S. Washburn, C. P. Umbach, and R. B. Laibowitz, Phys. Rev. Lett. 54 (1985) 2696; G. Timp, A. M. Chang, J. E. Cunningham, T. Y. Chang, P. Mankiewich, R. Behringer, and R. E. Howard, Phys. Rev. Lett. 58 (1987) 2814.
- [2] K. Park, S. Lee, M. Shin, E-H Lee, and H. C. Kwon, Phys. Rev. B 51 (1995) 13805.
- [3] C. J. B. Ford, A. B. Fowler, J. M. Hong, C. M. Knoedler, S. E. Laux, J. J. Wainer, and S. Washburn, Surf. Sci. 229 (1990) 307.
- [4] S. Washburn, H. Schmid, D. Kern, and R. A. Webb, Phys. Rev. Lett. 59 (1987) 1791.
- [5] M. Cahay, S. Banerjee, S. Bandyopadhyay, and H. L. Grubin, Phys. Rev. B 39 (1989) 12989.
- [6] D. Takai and K. Ohta, Phys. Rev. B 48 (1993) 1537.
- [7] P. G. N. de Vegaar, G. Timp, P. M. Mankiewich, R. Behringer, and J. Cunningham, Phys. Rev. B 40 (1989) 3491.
- [8] M. Okuda, S. Miyazawa, K. Fujii, and A. Shimizu, Phys. Rev. B 47 (1993) 4103.
- [9] M. Buttiker, Phys. Rev. Lett. 57 (1986) 1761.

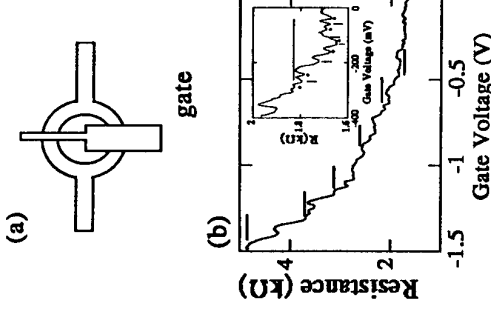


Fig. 1. (a) Schematic diagram of the sample geometry.
(b) The resistance as a function of gate voltage at $B = 0$. Finer measurement is shown in the inset.

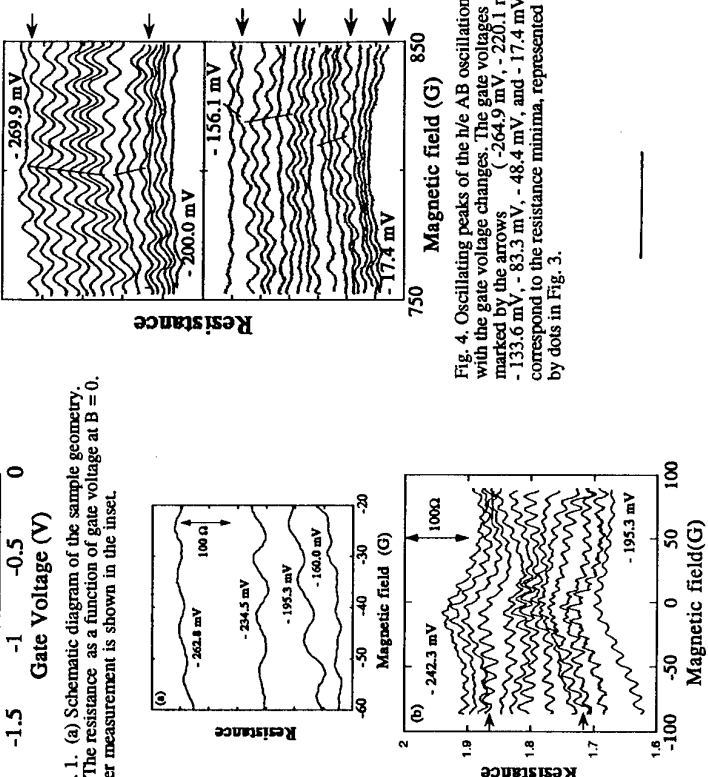


Fig. 3. The resistance as a function of gate voltage at $B = 800$ G. See text for details.

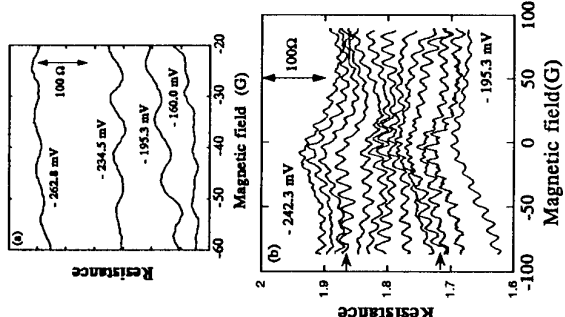


Fig. 4. Oscillating peaks of the sample geometry with the gate voltage changes. The gate voltages marked by the arrows (-264.9 mV, -220.1 mV, -133.0 mV, -83.3 mV, -48.4 mV, and -17.4 mV) correspond to the resistance minima, represented by dots in Fig. 3.

Fig. 2. (a) The phase shifts in the magnetic AB oscillations. (b) Generation of new set of h/e AB oscillations. Difference in the applied gate voltage between the successive curves is ~ 4 mV.

Magnetoresistance curves indicated by the upper and lower arrows are at $V_g = -230.3$ mV and $V_g = -206.2$ mV, respectively.

Spectroscopy of Quantum Dots in the Few Electron Limit

Z Borosfoldi, I A Larkin*, A R Long, M Rahman*, M C Holland*, J M R Weaver*,
I H Davies*, J G Williamson*

Department of Physics & Astronomy, University of Glasgow, Glasgow G12 8QQ

*Department of Electronics & Electrical Engineering, University of Glasgow, Glasgow.

Abstract

We have fabricated quantum dots with diameters of around 150 nm which contained less than 10 electrons. The conductance as a function of d.c. bias shows that the energy for adding successive electrons was around 3 meV, in good agreement with numerical modelling. We also present magnetic field data.

Introduction

We have studied the characteristics of small surface-gated quantum dots containing ten electrons or less to examine the relative contributions of single particle energies and Coulomb interactions to the level spacings. An account of related work on dots containing around 10 electrons has recently been published [1].

Techniques employed

The dots were formed on shallow GaAs/AlGaAs heterostructures with the electrons at an effective depth of 35 nm from the surface [2]. They were defined by 4 separate gates (Fig. 1), were between 100 and 150 nm in nominal diameter and were accessed through quantum point contacts around 100 nm wide. There are theoretical and experimental reasons for believing that this size is optimal for the electron depth. Approximating the dot by a single circular electrode and using the method of Davies, Larkin and Sukhorukov [3], the curvature of the electrostatic potential in the centre of the dot at complete depletion is a maximum for a ratio of dot radius to electron depth of $\sqrt{3}$, assuming a frozen semiconductor surface. For our layers this suggests an optimal diameter of approximately 120 nm .

Transport measurements through the dots were made at 1.3 K and above, as the spacing of conductance peaks is adequate for them to be resolved at this temperature (when the dots are almost fully depleted). The differential conductance between the regions either side of the dot (source and drain) was studied for different gate voltage combinations (defined with respect to the source), and for finite standing d.c. source drain voltages. Some measurements were also made in modest perpendicular magnetic fields ($< 3 \text{ T}$).

Experimental results

The parameters of two samples whose gate voltage characteristics contained only a few peaks are given in the Table. In Fig. 2 we show the gate voltage characteristics of sample 2. The electrostatic potential is swept by means of the "plunger" gate G2, and the whole characteristic is shifted in both cases by varying the voltages on the other 3 gates. The characteristics show 2 broad conductance peaks with some indication of a third. Sample 1, fabricated on a different layer, was broadly similar in its behaviour. At more negative values of the G2 voltage, little sign of any further peaks above the noise floor was found for either of the two samples. Hence, although it is not possible to exclude the possibility of further electrons remaining in the dot at large negative gate voltages, we believe that this is unlikely. From the voltage shift data, the voltage period between the major conductance peaks for applying bias to different combinations

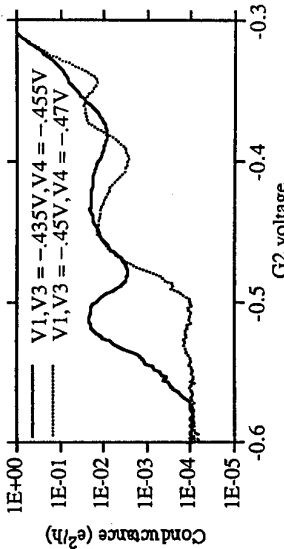
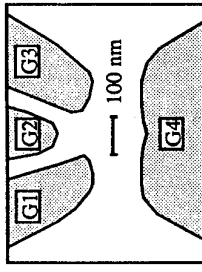


Fig. 1. Layout of a typical 150 nm 4 gate dot showing gates G1 to G4.

We have determined the values ΔV_g quoted in the Table are for varying bias being applied to all gates in the dot simultaneously. The energy parameters for the dots were determined [4] by applying a variable d.c. bias between source and drain and measuring the differential conductance characteristics. The d.c. bias causes peak shifts which may be used to determine the energy differences ΔE between energy levels in the dot. In all this biased data, the peaks corresponding to the electron energy level in the dot passing through the Fermi level in the drain are dominant, and the entry in the Table marked slope (s) gives the rate of change of this peak voltage with V_{ds} . For sample 2, two values, s_1 and s_2 , are given corresponding to the interchange of source and drain connections. Using these slopes, and assuming the capacitance model for the response of the

dots [5],

$$\Delta E = e\Delta V_g / (s_1 + s_2 - 1)$$

This gives the first ΔE value for sample 2 quoted in the Table.

In these two samples, the separation of the dot energy levels is large enough so that the weaker peaks associated with the coincidence of the energy level in the dot with Fermi level in the source, can also generally be seen even at 1.3 K. Hence the complete conductance "diamond" [4] and values for ΔE can be derived. Those in the Table correspond to the gap between the first two conductance peaks. For sample 2, the value obtained by this method, the second entry in the Table, is in good agreement with that derived by reversing source and drain. The calibrations of the energy scales derived from d.c. bias were checked by looking at the temperature dependences of the conductance minima and were found to be consistent in all cases.

The final entry in the Table is the ratio of energy separation to gate period (again for the first two major peaks). Two points may be noted about these values. Firstly they are similar for each of the samples (and for all the other 150 nm dots studied), as would be expected for dots of the same size near depletion. Secondly, the values are considerably less than 1. In the capacitance model for Coulomb blockade, such a low value would suggest that the capacitances of the dots dominate the gate capacitances.

A comparison of the data of Fig. 2 with the lineshapes expected for tunnelling through a single level [6] show that the observed lines are much wider than expected. We ascribe this tentatively to a number of resonant levels lying under a particular peak. Such sub-structure is apparent in Fig. 2, especially in the first peak. Lower temperature studies will be necessary to resolve the structure fully. One interesting feature of the substructure is that it varies with the

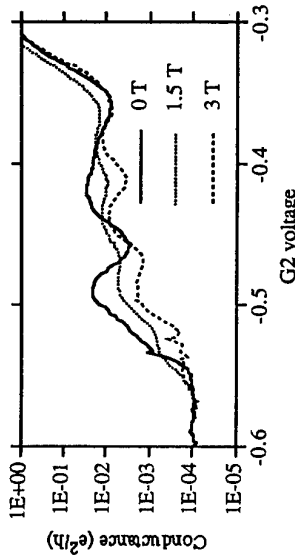


Fig. 3. Gate voltage characteristics of sample 2 at 1.3 K and various magnetic fields

voltages applied to the main gates 1, 3 and 4. The most likely reason for this lies in the observation, deduced from our simulations, that the dots change shape when the relative voltages on the gates are varied, becoming more or less elliptical. If the substructure is associated with excited states of the dot, then it is not surprising that their relative weight varies with the dot's shape.

We find that the exact energy spectra of these small dots depend critically on the local potential environment, and can change radically even during the course of a measurement in response to changes in the local environment due to trapped charge. The two dots reported here have particularly straightforward conductance peak structures with the largest energy separations observed in this type of dot. However we have studied other dots of the same nominal size and shape and have observed larger numbers of closer spaced conductance peaks. In addition to the potential imposed by the gates, we expect for dots containing few electrons that the local potential fluctuations generated by remote ionised donors [7] will have a significant effect on the energy spectrum. It is not yet clear whether fluctuations in gate shape due to irregularities in the lithography or potential fluctuations due to particular donor configurations have the dominant influence on the exact dot energy level spectrum.

Modelling

We have modelled this device self-consistently by solving numerically the three-dimensional Poisson equation and using the Thomas-Fermi approximation for the density of the 2DEG in the channel. The calculation shows that the cut-off voltage and number of electrons in the dot are strongly dependent on the boundary condition on the free surface [3]. The results for a frozen surface are in excellent agreement with experimental measurements of cut-off voltage and variation of numbers of electrons in a previous dot [1]. For sample 2 our calculated cutoff voltage is -0.55V , some 10% higher than experiment. The calculations also show that the shape of the dot is sensitive to the position of the 'plunger' gate, and the confining potential is almost circular for this dot. Independent variation of the Fermi level inside the dot permits the Coulomb blockade energy e^2/C to be evaluated. For 3 or 4 electrons in the dot $e^2/C = 2.8\text{ meV}$, in good agreement with experiment, and this decreases gradually with increasing N .

Discussion

In small dots there are two contributions to the energy spacings between levels, the Coulomb contribution due to interactions with the surrounding electrodes, dominant for larger

dots, and the "single-particle" terms, dependent on the size of the dot and the interaction between electrons within the dot. Which of these contributions is dominant is a crucial question for understanding of our data. Assuming that the dot is empty beyond the first peak, one may envisage two scenarios. Either the first peak involves the introduction of the first electron, with substructure due to single electron excited states, and the second peak corresponds to the second electron entering the dot. In this limit (1), the splitting is primarily Coulomb. Alternatively, the first peak involves two electrons of opposite spin entering the ground state, and its width reflects the Coulomb interactions. The gap between first and second peaks then reflects the energy spectrum of the dot (limit 2). At present we are not able to distinguish unambiguously between these two limits. However our semiclassical simulations suggest that the Coulomb spacing between the levels for the first few electrons is around 2.8 meV for this size of dot. This is much greater than the width of the first peak, and hence we consider that model 1 is more likely.

Evidence for the opposite limit (2) comes from the interesting effects of a perpendicular magnetic field on sample 2, shown in Fig. 3. Sample 1 behaves similarly. The first peak is strongly suppressed by the field, while the second splits into two. This behaviour is explained remarkably well by a single-electron model with a (roughly) parabolic potential, largely ignoring the electron-electron interaction. We find it hard to believe that this can be the case.

Several quantum mechanical calculations (e.g. [8]) of the energy spectra in small dots generally assume circular symmetry and ignore any ellipticity in the dot, (b) they use fixed parabolic confining potentials, and (c) they ignore any interaction with the surrounding gates and bulk 2DEG. Clarification of the exact model to apply to dots of this size in the few electron limit is only likely when further studies with samples of different geometries are performed. The magnetic field data may well assist in this problem of interpretation.

Conclusions

We have presented measurements on two fully gated 150 nm quantum dots which contain a very small number of electrons. The energy for adding successive electrons to the dots was around 3 meV in good agreement with our modelling.

This work was supported by EPSRC (UK) and by the University of Glasgow.

Table

Sample	2 / 4	Material	Carrier density	ΔV_g	Slope $s = \frac{dV_g}{dV_{ds}}$	$\Delta E/e\Delta V_g$
1	4	A866	4.3	150	1.7	3.2
3	4	A912	5.6	150	2.1/3.7	3.3/3.1
			$\times 10^{15}\text{m}^{-2}$	nm	mV	meV

References

- [1] Z. Borsosfoldi et al., Appl. Phys. Lett. **66** (June, 1995).
- [2] E. Skuras et al., Semicond. Sci Technol., to be published (1995).
- [3] J. H. Davies, I. A. Larkin and E. V. Sukorukov, J. Appl. Phys. **77** 4504 (1995).
- [4] E. B. Foxman et al., Phys. Rev. B **47** 10020 (1993).
- [5] N. S. Bakhvalov et al., Sov. Phys. JETP, **68** 581 (1989).
- [6] C. W. J. Beenakker, Phys. Rev. B **44** 1646 (1991).
- [7] J. A. Nixon, J. H. Davies and H. U. Baranger, Phys. Rev. B **43** 12638 (1991).
- [8] L. Wang, J. K. Zhang and A. R. Bishop, Phys. Rev. Lett. **73**, 585 (1994).

Far-infrared studies of induced superconductivity in quantum wells

E.L. Yuh¹, J.G.E. Harris¹, T. Eckhouse¹, K.C. Wong^{1,2,3}, E. Gwinn¹, H. Kroemer^{2,3}, and S.J. Allen¹

¹Department of Physics, UC Santa Barbara, Santa Barbara, CA 93106
²Electrical and Computer Engineering and Materials Departments, UCSB
³QUEST, the NSF Center for Quantized Electronic Structures, UCSB

Abstract

Recent work on periodic SNS microstructures, in which a superconductor grating periodically contacts the underlying InAs quantum well, has demonstrated that supercurrents can flow across the strips of quasi-two-dimensional electron gas between the superconductor grating lines. Here we show that the loss of d.c. resistance is accompanied by the emergence of striking features in the samples' excitation spectra, for energies below $\sim 2\Delta$. Although such series weak link structures should display a Josephson plasmon resonance, the changes in the samples' far-infrared transmission in an applied H field are inconsistent with the behavior expected for this mode. The transmission spectra also differ from the form expected if an energy gap were induced in the InAs quantum well strips between adjacent superconductor lines. We speculate that the observed absorption features instead arise from transitions between quasiparticle bands produced by Andreev reflections at the superconductor/InAs interfaces.

Advances in MBE growth and in selective etching of AlSb/InAs quantum wells recently have made possible the realization of supercurrent-carrying SNS structures in which the N channel is a high mobility, high carrier density quasi-2D electron gas (2DEG) confined in an InAs quantum well [1-4]. Due to the long elastic mean-free paths, ℓ , in the well, normal (N) channels with widths $w \ll \ell$ between superconducting (S) banks can be easily fabricated, providing access to the interesting, and relatively unexplored, limit in which transport across N is both phase-coherent and ballistic [5]. Here, we report studies of a *periodic* SNS structure, in which a superconductor grating contacts the underlying InAs. This lateral SNS superlattice provides an interesting analog to the intrinsically layered high T_c materials, which have recently been modelled as superlattices of alternating S and N slabs [6, 7].

D.c. transport studies of InAs-based periodic SNS structures have shown that at liquid He temperatures, supercurrents with J_c as large as ~ 20 A/m can flow perpendicular to the superconductor grating lines [4]. Below we show that the loss of d.c. resistance in the N strips between adjacent superconductor lines is accompanied by the emergence of striking features in the samples' excitation spectrum, at frequencies $\tilde{\nu}$ up to $\sim 2\Delta$, where Δ is the superconductor's gap. Since our samples may be regarded as series arrays of SNS junctions, they should display a resonance in the high-frequency dielectric function at the Josephson plasmon frequency. However, the magnetic field dependence of the resonance frequencies in the samples' far-infrared transmission spectra is inconsistent with the behavior expected for the Josephson plasmon. The spectra are also inconsistent with an interpretation in which the resonances are directly related to a gap in the 2DEG strips *between* Nb lines. We speculate that the observed absorption features instead arise from transitions between quasiparticle bands produced by Andreev reflections (AR) at the S/InAs interfaces, and thus provide information about the energy level structure in this periodic SNS system.

The left side of Fig. 1 shows the conduction band of the quantum well from which the

periodic SNS samples are fabricated. Te-doped, AlSb barriers fill the 150 Å InAs well to an

electron sheet density of 8×10^{12} cm⁻². The Hall mobility of the wafer is $\mu = 90,000$ cm²/V·sec

at 10 K, and corresponds to $\ell \sim 3\mu\text{m}$. A GaSb/AlSb superlattice lies above the well, and a layer of

GaSb caps the structure. The right side of Fig. 1 shows the geometry of the samples studied here. We fabricate the samples using holographic lithography, a multilayer resist, and dry etching processes to etch a 1 μm-period grating down to the top surface of the InAs well. A 2000 Å thick S layer (Nb or NbN) is sputter-deposited onto the surface, after cleaning the exposed InAs in an rf Ar plasma. Following lift-off, the sample appears as in Fig. 1; a w ~ 3000 Å-wide region of unmodified quantum well material separates adjacent, ~7000 Å-wide superconductor lines. Since $w \ll \ell$, transport normal to the grating is ballistic across w. For comparison, in our 1.4 K experiments, the clean-limit coherence length, $\xi = (\hbar/2\pi m^*k_B T)(2\pi N_S)^{1/2}$ [8], is $\sim 1.5\mu\text{m}$. Samples A and B have w = 3300 Å between edges of adjacent Nb lines, while sample C has w = 2700 Å between lines of NbN, which were deposited over 50 Å of Nb (to improve adhesion). Each sample has a 4 mm × 4 mm mesa that the far-infrared beam samples, and an adjacent 80 μm-wide Hall bar used for d.c. transport measurements. The small Hall bar avoids resistance arising from small flaws (holes) in the superconducting grating, which affect d.c. transport results but which we expect to have little effect on the transmission measurements.

For these samples, the measured differential sheet resistance for transport perpendicular to the grating lines, R, drops rapidly below 8–10 K, depending on the sample. We use the temperature of this initial, rapid fall in R to estimate the critical temperature, T_c, of the superconducting grating, and find T_c = 8.8 K and 7.5 K, respectively, for samples A and B, while sample C has T_c = 10 K [3,4]. Below T_c, R drops to below our measurement sensitivity of $\sim 10^{-3}$ Ω (roughly $10^{-5}xR(T>T_c)$), at temperatures of ~ 4.2 K, ~ 4.8 K, and ~ 5.5 K for samples A, B, and C, respectively.

To investigate how the dramatic reduction in R below T_c affects the high-frequency conductance of these lateral SNS superlattices, we compare the normal-incidence transmission spectrum, T_S, for the sample's resistanceless state, to the transmission T_N for its resistive state. For all spectra, the Nb or NbN grating remains superconducting. The ratioed spectra T_S/T_N would be one if the loss of d.c. resistance did not change the high-frequency conductivity, which determines the transmission. Deviations away from one in T_S/T_N indicate different electronic excitation spectra (and thus different high-frequency conductivity) in the superconducting and resistive states.

We use a Fourier transform spectrometer with a 3He-cooled bolometer detector to collect data between 5 cm⁻¹ and 100 cm⁻¹. A magnetic field, H_{perp}, normal to the sample plane, switches the 2DEG between superconducting and resistive states. H_{perp} is the sum of the earth's field and the field from a coil near the sample, and is constant to $\sim 3\%$ over the area sampled by the far-infrared beam. The H_{perp} that first produces measurable d.c. resistance in the quantum well, H*, is ~ 0.5 Gauss at 1.4 K. For all data shown below, the transmission T_N is taken at H_{perp} = 1 Gauss, which is well above H*. Because the grating reflects the component of the incident radiation polarized parallel to its lines, the high-frequency current in the quantum well flows perpendicular to the superconductor lines.

The spectra in Fig. 2 compare T_S(H_{perp}=0)/T_N for samples A, B, and C, at 1.4 K. All three samples show the same qualitative features: two distinct resonance dips appear (marked by arrows in Fig. 2), which indicate an enhancement in absorption in the samples' superconducting state. At higher frequencies, T_S/T_N rises smoothly to 1. For comparison, the arrow below Fig. 2 indicates $2\Delta_{Nb} = 22.5$ cm⁻¹ for clean Nb. Oscillations in T_S/T_N below ~ 9 cm⁻¹ are Fabry-Perot interference; and below 7 cm⁻¹, the signal becomes so weak that the data are unreliable, as indicated by the error bars shown at selected frequencies for sample A (Fig. 2). To verify that the observed structure in T_S/T_N arises from the 2DEG's interaction with the Nb, rather than directly from the grating itself, we have measured the transmission of a Nb grating with the same geometry as the sample gratings, but deposited onto a semi-insulating GaAs substrate. This isolated Nb grating has T(H_{perp}=0)/T(100 μJ/esta) = 1, independent of frequency.

Figure 2 indicates that the overall magnitude of T_S/T_N, and resonance frequencies, depend

both on the superconductor gap, and on the quality of the superconductor/Nb interface. For example, sample C has the highest T_c, and presumably the highest gap, Δ. However, its T_S/T_N

has resonances at roughly the same frequencies as in sample A, in which $T_S/T_N = 1$ for sample C are also a factor of 3.5 weaker than in the samples with Nb gratings, perhaps due to a lower interface transmittivity. Comparison of samples A and B, which were prepared under nominally identical conditions, with identical Nb gratings, also suggests that both interface transparency and superconductor gap determine the T_S/T_N spectra. Sample A has a higher T_S than sample B, and the absorption dips in A's spectra are higher in frequency than sample B's, but lower in magnitude, suggesting that the transmittivity has pronounced effects on the magnitude of T_S/T_N , but influences resonance frequencies less strongly than Δ .

Recent studies of high-T_c superconductors have shown that for fields polarized perpendicular to the layered structure of these materials, their low-frequency response can be modelled by a series array of weak links [6]. In particular, high-T_c materials display a Josephson plasmon resonance at ω , the resonant frequency of oscillations in the superconducting phase difference between adjacent S layers. Since our samples also have a series weak link structure, we expect that they should display this mode. However, the dependence of $T_S(H_{\text{perp}})/T_N$ on H_{perp} appears to be inconsistent with an interpretation of the observed resonances in terms of the samples' [6]. Figure 3 shows T_S/T_N from 5 cm⁻¹ - 25 cm⁻¹ for Sample A, for several values of H_{perp} (spectra were featureless from 25 cm⁻¹ - 100 cm⁻¹). As shown, all features in the spectrum weaken as H_{perp} approaches H^* , without shifting in frequency. For comparison, the inset shows that the sample's critical current I_c drops by a factor of ~4 from $H_{\text{perp}} = 0$ to $H_{\text{perp}} = 0.2$ G. Because I_c decays as $I_c/2$ [9], the frequencies of any features that arise from this resonance should drop by a factor of ~2 between the fields used for traces 1 and 2 in Fig. 3. In contrast, the frequencies of the spectral features in Fig. 3 do not depend on H_{perp} .

The observed resonances in T_S/T_N also cannot be attributed to an induced gap in the 2DEG strips between grating lines. These 2DEG strips, where we expect the absorption to occur, have width $w \ll \xi$, so that any induced gap, $\Delta_{2\text{DEG}}$, should be nearly constant across w . Since the superconductor gratings are opaque (and are unchanged by H_{perp}), T_S/T_N should be sensitive primarily to these 2DEG regions between superconductor lines. For these reasons, we expect that if there were a Δ 2DEG with a magnitude comparable to the observed resonance energies, T_S/T_N would be similar to that of a uniform BCS film, with gap Δ_{BCS} . However, the spectra in Fig. 3 differ qualitatively from the T_S/T_N for a uniform BCS film, with gap Δ_{BCS} , which would have a single peak near 2Δ , no local minima, and a peak height that greatly exceeds the observed maximum of T_S/T_N [4, 10].

Recent theoretical work on optical absorption in 3D periodic SNS multilayers has investigated how the modification of the electronic states by the S/N boundaries affects optical absorption [11]. The calculations show resonances in the absorption between filled levels at energies below the chemical potential, μ , and empty levels above μ , at the energies at which the densities of initial and final states peak. The peaks in the density of states lie at the edges of the bands of states that the SNS superlattice creates for motion perpendicular to the S/N boundaries (and are sensitive to the interface transmittivity). The geometry of our samples, which have a periodic array of S strips that sit on top of the continuous InAs layer, differs from that used in the calculations. Nonetheless, we expect the periodic S/N interfaces to create bands of allowed states within $\sim \Delta$ of μ , that are determined by AR and the S/N boundaries. If this is the case, then the same absorption mechanism should apply in our samples. The temperature-dependence of the transmission, to be reported elsewhere [41], is qualitatively consistent with this picture: T_S/T_N spectra measured between 1.4 K and 4.2 K show that the resonances weaken, and their frequencies fall, as T is increased. The variation of the resonance frequencies with T is well fit by the BCS form for a temperature-dependent gap. This is the expected behavior if the resonances are due to transitions between AR-created bands, since in this picture, the gap of the superconductor sets the overall energy scale.

This work was supported primarily by NSF DMR-9314899. Material growth was partly supported by QUEST, the NSF Center for Quantized Electronic Structures, and J.G.E. Harris by ONR N00014-92-J-1452.

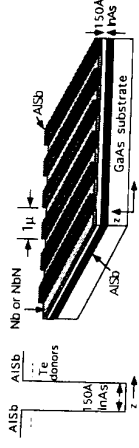


Figure 1. Left side: InAs quantum well structure. Right side: sample geometry.

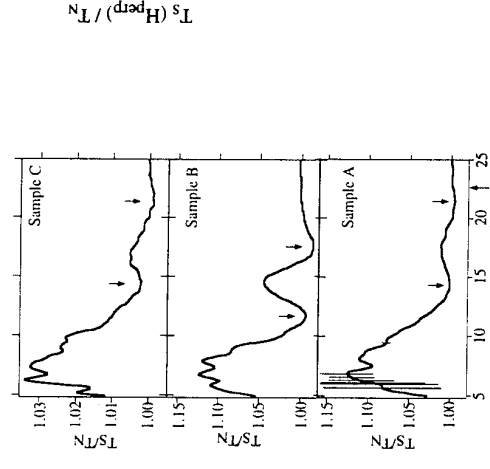


Figure 2. $T_S(H_{\text{perp}}=0)/T_N$ for samples A, B, and C.

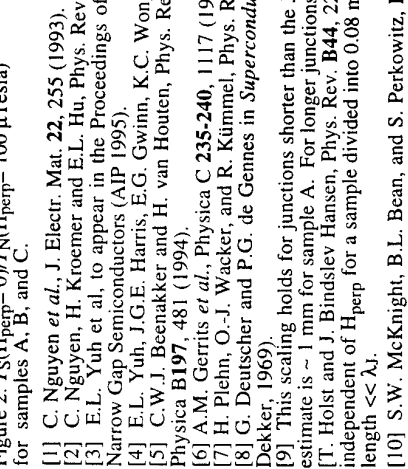


Figure 3. $T_S(H_{\text{perp}})/T_N(100 \mu\text{Tesla})$ for sample A. Traces 1-3; $H_{\text{perp}} = 0, 0.2$ G, and 0.4 G, respectively. Inset: $I_c(H_{\text{perp}})$ [sample width = $80 \mu\text{m}$].

[10] S.W. McKnight, B.L. Bean, and S. Perkowitz, Phys. Rev. B **19**, 1437 (1979).

[11] H. Pfehn and R. Kümmel, to appear in Phys. Rev. B.

Transport through a 2DEG channel with superconducting boundaries

J. Nitta*, B. J. van Wees, J. P. Heida, and T. M. Klapwijk
*Department of Applied Physics & Material Science Center, University of Groningen,
Nijenborgh 4, 9747 AG Groningen, The Netherlands*

A. Dimoulas
California Institute of Technology, Chemical Engineering, 210-41, Pasadena, CA 91125

W. van de Graaf, and G. Borghs
Interuniversity Micro Electronics Center, Kapeldreef 75, B-3030, Leuven, Belgium

Abstract

We have investigated transport through a channel with superconducting boundaries where electrons are confined by Andreev reflection. The superconducting phase sensitive transport is discussed using qualitative arguments. The resistances through the channel have been measured as a function of the phase difference ϕ between the superconducting boundaries. The oscillations exhibited resistance minima at $\phi = 2\pi n$ because of DC-SQUID oscillations. A DC bias was added in order to suppress the Josephson coupling. A shift in oscillation and reduction in amplitude were observed, and the resistance showed maxima at $\phi = 2\pi n$. An explanation for the phase shift is that the Josephson coupling dominates the experiments.

Introduction

Recently, much attention has been devoted to superconducting phase sensitive normal transport. The phase of the superconductor plays an important role in supercurrent flow in bulk superconductor as well as in Josephson junctions. An interference effect on the resistance which is influenced by the superconducting phase difference has been pointed out by Spivak et al. and Al'tshuler et al. [1]. Through the Andreev-reflection (AR) process at the interface between normal metal (N) and superconductor (S), the phase of quasiparticles is shifted by the phase of superconducting order parameter. The basic idea is that, if the superconducting phase difference is externally controlled, the resistance of the normal layer could be affected by constructive and destructive interference of quasiparticles. Several types of interferometers have been proposed [2]-[6], and such phase sensitive transport has been experimentally confirmed [7]-[10].

In this paper, we have studied transport through a two-dimensional-electron-gas (2DEG)

channel with superconducting boundaries. A decay length of incoming electrons in the channel is discussed. The operation principle and experimental results are shown in the following sections.

Principle of operation

First we discuss the operation principle of the superconducting phases sensitive transport in

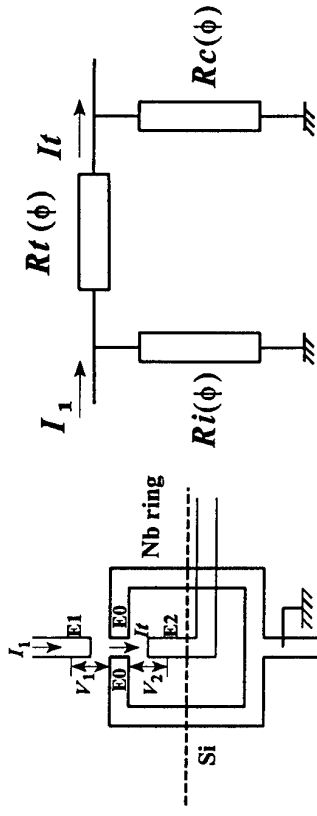


Fig. 1 (a) Schematic structure of channel

We consider the same structure as SNS junctions where N is the 2DEG. We consider the decay length ξ of the incoming electrons in the channel with parallel direction to the two superconducting boundaries.

The Andreev-reflections between two superconducting boundaries form discrete energy levels (bound state $E_n(\phi)$) which carries supercurrent. $E_n(\phi)$ depends on the phase difference ϕ between the superconducting boundaries. In the limit where a channel width is shorter than the coherence length, one gets the simple result $E_n(\phi) = \zeta(1 - \sin^2(\phi/2))^{1/2}$ [11], where T_p is the transmission coefficient.

Recently, it has been pointed out [12] that the bound state leads to an effective energy gap Δ_{eff} . The effective energy gap is approximately given by $\Delta_{\text{eff}} = (1/4)T_{\text{SN}}E_n(\phi)$ where T_{SN} is the transparency at the SN interface. In analogy to the the decay length of quasiparticle in a superconductor, this effective energy gap leads to the relation $\xi = \hbar v_F \Delta_{\text{eff}} = 4\hbar v_F T_{\text{SN}} E_n(\phi)$. Therefore, the bound state formed between two superconducting boundaries gives the decay length of the incoming electrons.

The bound state has maxima at $\phi = 2\pi n$, and minima at $\phi = (2n+1)\pi$ ($n=0, 1, 2, \dots$). By using the expression of ξ , the transmitted current I_I which is expected to be proportional to $\exp(-L/\xi)$ shows minima at $\phi = 2\pi n$, and maxima at $\phi = (2n+1)\pi$. Here L is the channel length. Therefore, we expect that we can modulate the transmission current through the channel by controlling ϕ .

Sample preparation

The schematic structure of the sample is shown in Fig. 1(a). A channel was made by surrounding an InAs 2DEG with two parallel superconducting Nb electrodes (E0). The channel length L was designed to be 0.5 μm which is of the order of the expected decay length ξ . The width W was about 0.2 μm . Electrons were injected from the 0.15 μm wide NH injector electrode (E1) to the channel. The transmitted electrons were detected by a receiver electrode (E2) which was placed inside the superconducting ring. To control the phase difference ϕ , a superconducting ring geometry was formed. The area S of the ring was about 60 μm^2 .

The 2DEG is formed in a 20 nm InAs layer of GaSb/InAs/GaSb heterostructures. The carrier concentration and the electron mobility of the 2DEG InAs were $N_s = 9.0 \times 10^{11} \text{ cm}^{-2}$ and $\mu = 48,000 \text{ cm}^2/\text{Vs}$. The carrier concentration gives a Fermi wavelength of 25 μm . The electron mean free path

The oscillations exhibit resistance minima at $BS = n\Phi_0$ ($\phi = 2\pi n$). This is because the Josephson coupling between E1 and the ring leads to a DC-SQUID oscillation [7]. A DC bias current $I_{dc} = 2 \mu\text{A}$ which is more than the critical current was added in order to suppress the Josephson coupling.

The shift in oscillation period and the reduction in amplitude were observed, and the resistance showed maxima at $\phi = 2\pi n$. The resistance maxima at $\phi = 2\pi n$ were also observed in $R = dV/dI$, by adding the DC bias as shown in Fig. 2(b). A simple explanation for the resistance maxima at $\phi = 2\pi n$ is that Josephson coupling still dominates these experiments.

In the previous section, we assumed a ballistic channel and a well-defined bound state. After

the fabrication process, it is observed that the carrier concentration of the InAs underneath the Nb electrodes is enhanced, and the electron mobility is much reduced [13]. This gives a mean free path of 10 nm. It is not so clear how the principle of operation will hold under such an interface condition.

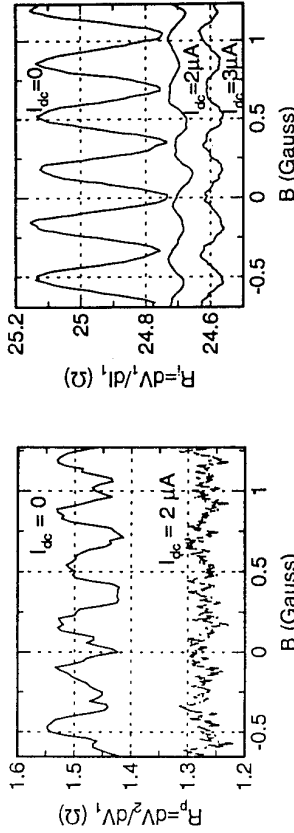


Fig. 2 (a) Differential resistance $R_p = dV/dI$,

Fig. 2 (b) Differential resistance $R = dV/dI$,

is estimated to be 0.75 μm from these values. The superconducting electrodes were fabricated by standard electron beam lithography and lift-off techniques. Prior to deposition of 60nm Nb, the 50 nm GaSb top layer was wet-etched and the free surface of InAs was Ar ion-cleaned. The top layer on the channel and the area from the injector to the receiver electrode was removed as well because of an over-etching. Si with 100nm thickness was used as an insulating layer between the superconducting ring and the lead for the receiver electrode.

Results and discussion

Both voltages V_I between E1 and E0 and $V_A(E2-E0)$ were measured by supplying currents $I_I(E1-E0)$ and $I_A(E2-E0)$, independently. E0 was always grounded to eliminate the leakage current through the 2DEG underneath Nb ring electrodes. The equivalent circuit of the sample is shown in Fig. 1(b). The resistance from the injector to the ring $R_I = dV/dI_I$ was 25 Ω , and the resistance from the receiver to the ring $R_C = dV/dI_C$ was 44 Ω . A sharp dip structure was observed in $dV/dI_I - I_I$ characteristics below $I_I = 800$ nA. This dip is attributed to the supercurrent. The dip structure was not observed in $dV/dI_A - I_A$, because the Josephson coupling between the Nb ring and receiver electrode was weak. The resistance through the channel was $R_p = dV/dI_A - I_A \sim R_I R_C / R_I$, where R_I is the effective channel resistance. The transmitted current I_I is approximately given by $(R_I/R_p) I_A$. From

these measurements, R_I was estimated to be 660 Ω . From the transmitted current I_I , it was also estimated that about 4% of the injected electrons could reach the receiver electrode E2 which was about 0.3 μm away from the channel. The transmitted current was reduced to 0.15% by putting the receiver electrode 1.0 μm away from the channel in the other sample. This result suggests that electrons through the channel do not ballistically reach the receiver electrode, and that the 2DEG became diffusive by the fabrication process.

The $R_p = dI_A/dI_I$, which is proportional to the transmitted current was measured at $T = 1.4$ K, as a function of the magnetic field B , for different DC current bias I_{dc} . The phase difference ϕ can be controlled by the relation $\phi = 2\pi(BS/\Phi_0)$, where Φ_0 is a flux quantum ($\hbar/2e$). The results are shown in Fig. 2 (a). For $I_{dc} = 0$, oscillations in the resistance R_p were observed with a period of about 0.35 G. This magnetic field corresponds to a flux quantum Φ_0 through the Nb ring area.

*Permanent address: NTT Basic Research Laboratories, 3-1, Morinosato-Wakamiya, Atsugi-Shi, Kanagawa 243-01 Japan

- [1] B. Z. Spivak and D. E. Khmel'nitskii, JETP Lett. **35** (1982) 412;
B. L. Al'tshuler and B. Z. Spivak, Sov. Phys. JETP **65** (1987) 343;
- [2] H. Nakano and H. Takayanagi, Solid State Commun. **80** (1991) 997;
Phys. Rev. B**47** (1993) 7986
- [3] F. W. J. Heikking and Yu. V. Nazarov, Phys. Rev. Lett. **71** (1992) 1625
- [4] C. J. Lambert, J. Phys.: Condens. Matter **5** (1993) 707
- [5] A. V. Zairov, JETP Lett. **61** (1995)
- [6] N. K. Allsopp, J. S. Cañizares, R. Raimondi and C. J. Lambert, (1995) preprint
- [7] A. Dimoulas, J. P. Heida, B. J. van Wees, T. M. Klapwijk, W. van de Graaf, and G. Borghs, Phys. Rev. Lett. **74** (1995) 602
- [8] P. G. N. de Vegvar, T. A. Fulton, W. H. Malmstrom, and R. E. Miller, Phys. Rev. Lett. **73** (1994) 1416
- [9] H. Pothier, S. Gueron, D. Esteve, and M. H. Devoret, Phys. Rev. Lett. **73** (1994) 2488
- [10] V. T. Petrushov, V. N. Antonov, P. Deising and T. Claeson, JETP Lett. **60** (1994) 606
- [11] C. W. J. Beenakker, Phys. Rev. Lett. **67** (1991) 3836
- [12] A. F. Volkov, P. H. C. Magnée, B. J. van Wees, and T. M. Klapwijk, Physica C **242** (1995) 261
- [13] P. H. C. Magnée, S. G. den Hartog, B. J. van Wees, T. M. Klapwijk, W. van de Graaf, and G. Borghs, to be submitted to Appl. Phys. Lett.

Transport Through Superconductor - Semiconductor Junctions in Different Scattering Limits

D.A. Williams*, A.M. Marsh and H. Ahmed.

Microelectronics Research Centre, University of Cambridge, Cavendish Laboratory, Madingley Road, Cambridge, CB3 0HE, U.K.
 * Hitachi Cambridge Laboratory, Cavendish Laboratory, Madingley Road, Cambridge, CB3 0HE, U.K.

Abstract

Electron transport in a two-dimensional electron gas between two superconducting regions has been studied under conditions where different scattering processes dominate in the two-dimensional gas, and there is significant Andreev reflection at the interfaces. If inelastic scattering dominates, so that transport is diffusive, then a smooth dip around zero-bias is seen in the differential resistance of the device. This corresponds to an 'excess current', characteristic of Andreev reflection. In the limit of ballistic transport a supercurrent is observed, and in the intermediate case, subharmonic gap structure is seen within the central dip.

Introduction

There have been many recent studies of electron transport in two-dimensional electron gases between two superconducting contacts [1]. The principal interest in this work is to obtain a significant probability of Andreev reflection, [2], at the interfaces between the superconductor and the electron gas, and so couple the superconductor pair state to the high-mobility electrons. Providing this criterion is observed, and the temperature is well below the critical temperature of the superconducting contacts (T_c), then the low frequency electron transport through such a device is found to fall into one of three distinct categories. In one extreme, where the two superconductors are phase-correlated, a supercurrent may flow between the two contacts, [3,4], and in the other limit where phase coherence is lost due to diffusive transport, there will be an 'excess current' and a smooth dip in the differential resistance around zero bias. In the intermediate case, steps or oscillations in the low-bias differential resistance are seen, which is known as subharmonic gap structure [5,6].

The GaAs:AlGaAs heterojunction is a particularly useful system for such studies, as a very large range of mobilities is accessible, and so the different scattering regimes can be studied. The use of a diffused granular superconductor with a relatively high critical temperature and critical field also assists in the exploration of these different regimes, as a wide range of temperatures and magnetic fields can be used whilst

keeping the contact superconducting. This also allows the demonstration of the relative insensitivity of disorder-enhanced Andreev reflection to magnetic field.

Experiments

The structures used for experiments were tin-chromium-gold or indium-chromium-gold multilayers on standard modulation-doped GaAs:AlGaAs heterostructures with mobilities ranging from 10^4 to 10^6 cm 2 V $^{-1}$ s $^{-1}$. The contact areas were defined by electron beam lithography, and then sintered by rapid electron-beam annealing. The electrical characteristics of the junctions were measured at temperatures from 20 mK to room temperature, in magnetic fields from 0-9T, and the device structure is shown in Figure 1.

Figure 2 shows the differential resistance characteristic of a device at 1.6K, and the smooth dip is characteristic of transport between two phase-decoupled superconductors with a high probability of Andreev reflection at the interfaces.

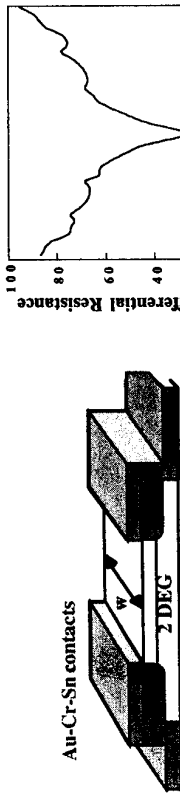


Figure 1: Schematic diagram of the device geometry. Typically the width w is very much greater than the contact separation d .

A high-mobility junction showed a supercurrent at low temperature, and a smooth dip at higher temperatures as the transition was seen from ballistic transport to inelastic scattering [4]. Junctions with lower intrinsic mobility showed subharmonic gap structure at lowest temperature, as shown in Figure 3, and a smooth dip at higher temperature; here the transition is from elastic to inelastic scattering. Subharmonic gap structure can also be seen at finite bias in structures which show a supercurrent near zero bias [7]. Here the bias destroys phase coherence across the device, and a treatment of the effects of elastic scattering can be found in [8].

In these devices, the probability of Andreev reflection has been found to be very high due to the presence of disorder around the superconductor-semiconductor interface. This enhancement has been predicted to be insensitive to magnetic field, and this insensitivity is clearly observed up to an applied field of 3T [6].

In the experiments, when a supercurrent was observed [4], the relative proportions estimated from the mobility, density and temperature of the electron gas were 0.42:0.49:0.09; when subharmonic gap structure was observed at 20mK as in Figure 3 they were 0.05:0.75:0.2; and for conditions where a smooth dip was seen as at 1.6K in Figure 2, the transport was estimated to be wholly diffusive, with $l_b l_e < d$.

The figure shows the case of $l_b > l_e$, which is often the case for the samples used at low temperature, but clearly this need not be true and the relationship between geometry and transport will be different in other systems. Also, the simple ratios need to be altered for narrower devices where edge effects are important, and the effects of scattering on the Andreev reflection probabilities should be taken into account. Nevertheless, the approximate limits do appear to match the experimental behaviour of the simple wide device geometries of the experiments reported here.

In conclusion, the coupling between two superconducting contacts to a two-dimensional electron gas is found to depend on the dominant scattering processes in the gas. If there is a high probability of Andreev reflection at the interfaces, and the transport in the 2DEG is ballistic, then a supercurrent may flow. If the transport is diffusive, then excess current is seen, with a smooth dip in the differential resistance. In the intermediate situation, where there is elastic but little inelastic scattering, subharmonic gap structure is seen. The rough estimates were found to be valid for large devices with simple geometry, but are not expected to hold for more complex devices. Under many conditions, there may be a mixture of the three transport mechanisms operating in parallel, leading to the wide range of device characteristics observed.

The authors acknowledge useful discussions with Dr T. Thornton and Dr B. Alphenaar

References

- [1] See papers in: *Proc. NATO ARW on Mesoscopic Superconductivity*, Physica B **203** (1994)
- [2] C.W.J. Beenakker in *Mesoscopic Quantum Physics*, Eds E. Akkermans, G. Montambaux and J.-L. Pichard. (North-Holland, Amsterdam, 1995)
- [3] H. Takayanagi and T. Kawakami, Phys.Rev.Lett. **54** (1985) 2449
- [4] A.M. Marsh, D.A. Williams and H. Ahmed, Phys.Rev. B, **50** (1994) 8118
- [5] T.M. Klapwijk, G.E. Blonder and M. Tinkham, Physica B **109** (1982) 1657
- [6] A.M. Marsh, D.A. Williams and H. Ahmed, Physica B, **203** (1994) 307
- [7] H. Takayanagi, T. Akazaki and J. Nitta, Phys.Rev. B, **51** (1995) 1374
- [8] N. van der Post, J. Nitta and H. Takayanagi, Appl.Phys.Lett., **63** (1993) 2555

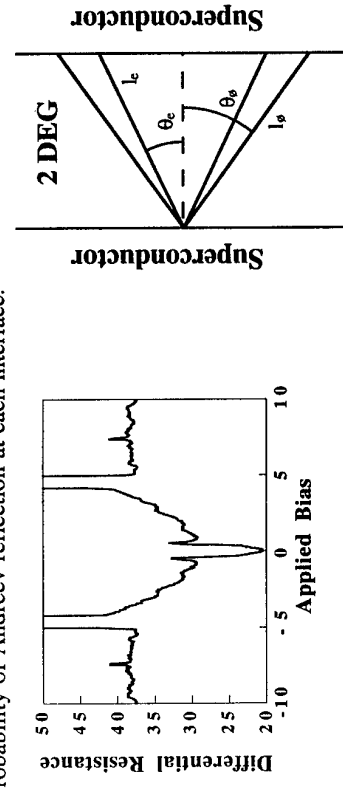


Figure 3: Differential resistance response of a device at 20mK, showing subharmonic gap structure in the low-bias range where a smooth dip is seen in Figure 2.

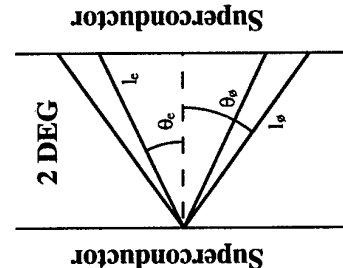


Figure 4: Schematic picture of the relationship between scattering mechanisms, trajectory and injection angle.

A very rough measure of the proportion of each scattering process in the current transfer through a device of this geometry may be obtained by matching the angular injection ratios to limits based on mean free paths. If we define the injection angle as that between the direction of current flow and the carrier trajectory, and if the separation of the contacts is d , and the width w , then the maximum possible injection angle that would send carriers ballistically from one contact to the other is $\tan^{-1}(d/w)$. In most devices studied the ballistic length is very much smaller than the width of the device. We can then place a limit on the angle of injection such that $\theta_e < \cos^{-1}(d/l_e)$, where l_e is the elastic mean free path of electrons in the 2D gas. The proportion of current carried ballistically is thus $2\theta_e/\pi$, assuming that all carriers entering the gas and reaching the second interface have approximately the same probability of Andreev reflection at the second interface. Clearly, this is multiplied by the appropriate transmission coefficient for a non-ideal interface, and will be modified by interference effects. The second limit is given by the crossover from elastic scattering to inelastic, where the angle θ_e is defined by the inelastic mean free path in the same manner. Thus the relative proportions of the various types of transport are roughly $2\theta_e/\pi$, $2(\theta_e - \theta_c)/\pi$ and $1 - (2\theta_e/\pi)$, for ballistic, elastic and diffusive transport respectively.

Two-Dimensional Electrons in a Lateral Magnetic Superlattice

H.A.Carmena, A.Nogaret, A.K.Geim, P.C.Main, T.J.Foster, M.Henini

Department of Physics, University of Nottingham, Nottingham NG7 2RD, UK

S.P.Beaumont, H.McLellan

Department of Electronics and Electrical engineering, University of Glasgow, G12 8QQ, UK

M.G.Blanire

Department of Materials Science and Metallurgy, University of Cambridge, CD2 3QZ, UK

Abstract

We have measured the magnetoresistance measurements of a 2D electron gas subjected to a periodic magnetic field created by the presence of type-II superconducting stripes on the surface of the heterostructure. We observe oscillatory behaviour due to a commensurability effect between the cyclotron radius and the period of the magnetic field. The results can be understood in terms of a simple semiclassical theory.

There have been several recent investigations of the motion of electrons in a two-dimensional-electron-gas (2DEG) subjected to an inhomogeneous magnetic field created by patterned superconductors on the surface of the heterostructure. For example the contribution of a single vortex to the quantum conductivity of a mesoscopic device and the motion of ballistic electrons in a random magnetic field have been reported[1]. In this work a periodic array of type-II superconducting stripes is patterned on top of a heterojunction to create a *periodic* magnetic field. It has been predicted [2] that the electron mobility undergoes resonant enhancements whenever the cyclotron diameter at the Fermi level is commensurate with the period of the magnetic potential within a constant phase factor. This effect can be understood in a semiclassical picture [3] analogous to the guiding-centre-drift resonance in the case of periodic electric potentials [4]. The effects of a modulated magnetic field acting on a 2DEG have been reported recently by two groups [5-6].

The structure used in the experiments is shown schematically in Fig. 1(a). A high mobility 2DEG is formed in a standard GaAs/(AlGa)As heterojunction 300 nm from the sample surface. The electron density is $\sim 1.5 \times 10^{15} \text{ m}^{-2}$ and the elastic mean free path $\sim 10 \text{ } \mu\text{m}$. A metallic gate of thickness 150 nm is deposited on the surface covering a standard Hall bar, followed by a 200 nm insulating Ge layer. An array of Pb or Nb stripes (200 nm thick) was fabricated on top of the insulator layer by electron beam lithography defining a grating of 1 μm or 2 μm period (Fig. 1(b)).

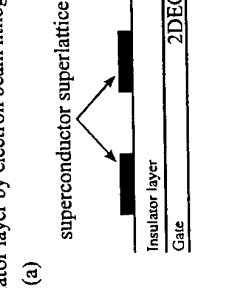


Fig. 1. (a) Schematic diagram of the devices. (b) Micrograph showing 2 μm period magnetic superlattice patterned on top of the 2DEG.

The magnetoresistance was measured sweeping the magnetic field from $B < 1 \text{ T}$ through zero to $B > 1 \text{ T}$ (sweep up) and vice versa (sweep down). Strong oscillations were observed, periodic in $1/B$ and which survive up to high temperature. These arise from a periodic electric potential at the 2DEG. We attribute this periodic electric potential to a strain effect caused by different thermal expansion coefficients of the superconductor stripes and the insulating Ge[7].

Figure 2(a) show the difference ΔR_{xx} between the sweep up and down traces at 0.3K for a device with a Pb grating of 2 μm period. The traces for sweep up and sweep down are identical at low magnetic fields and above some critical value B_C ($\Delta R_{xx} = 0$). However, at intermediate magnetic fields ΔR_{xx} exhibits an oscillatory behaviour reflecting a difference between the magnetoresistance oscillations for sweep up and sweep down traces. As we increase the temperature above the critical temperature of the superconductor ($\sim 7.2 \text{ K}$) ΔR_{xx} disappears indicating that the oscillations in ΔR_{xx} are caused by the superconducting stripes. Further proof can be produced by investigating the temperature dependence of the magnetoresistance [5]. By plotting the index of the peaks and valleys versus $1/B$ one can see in Fig 2(b) that the oscillations in ΔR_{xx} are periodic in $1/B$ with no phase shift.

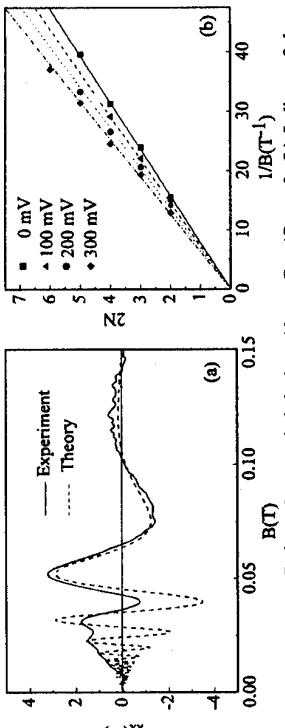


Fig. 2. (a) ΔR_{xx} vs. B for a 2 μm period device. Above B_C , $\Delta R_{xx} = 0$. (b) Indices of the maxima and minima of ΔR_{xx} vs. $1/B$ for various gate voltages and hence electron densities. For both diagrams theory lines have no adjustable parameters.

We now address the origin of the oscillations in ΔR_{xx} . Thin films of lead are type II superconductors[8] with a low-temperature upper critical field, $B_{c2} \sim 0.12 \text{ T}$. Below B_{c2} the flux penetrating the superconductor stripes is segregated into a distribution of vortices. The magnetoresistance hysteresis between sweep up and down is caused the pinning of these vortices. When the applied field is increased from 0 to $B > B_{c2}$ (sweep up) flux penetrates from the edges of the stripes whereas the magnetic field at the centre of the stripes remains close to zero. In this situation the modulation in magnetic field at the plane of the 2DEG is π out of phase with the electric potential modulation originating from strain [7]. When $|B|$ is above B_{c2} the superconductivity is destroyed leaving a homogeneous magnetic field at the plane of the 2DEG. When the applied field is decreased from a value larger the B_{c2} (sweep down) the pinning mechanism prevents the vortices from easily leaving the superconductor. The field inside the stripes in this situation becomes larger than in between them, so the magnetic field modulation is in phase with the electric modulation. This change by π in the phase between magnetic field modulation and electric potential explains the hysteretic behaviour in Fig. 2(a) although the situation is likely to be more complicated for $|B| < 10 \text{ mT}$ [1,5].

The low field magnetoresistance oscillations observed when the 2DEG is subjected to both periodic electric and magnetic fields can be understood within a semiclassical picture. Figure 3(a) shows computer simulations of electron trajectories at the Fermi energy for the cases where

only electric modulation (dashed line) and when only magnetic modulation (solid line) are present. In each case the magnetic field is chosen to correspond to a maximum in a magnetoresistance oscillation. For the calculations the electrostatic modulation is described by $V(x) = V_0 \sin(Kx)$ and the magnetic one by $\mathbf{B} = (B_x \pm B_0 \sin(Kx)) \hat{\mathbf{z}}$ ("+" in phase, and "-" π out of phase), where $K = 2\pi/a$ with a the period of the modulation. For the electrostatic case the resonance condition occurs when the $(1/B) \nabla V(x) \times \mathbf{B}$ drift velocity at the two extremes $x = x_0 \pm R_c$ (here x_0 is the orbit centre position and R_c is the cyclotron radius at the Fermi energy) has the same sign, i.e., when $2R_c = (n+1/4)a$ [3]. When only magnetic modulation is present the drift velocity is a maximum if the two extremes of the orbit lie at a maximum and minimum magnetic fields respectively. Because $R_c \propto 1/B$, the orbit size is slightly different on either side, leading to a finite drift velocity of the orbit centre in the direction of constant B (y direction). Following Beenaker [3], one can show that the resonance condition is $2R_c = (n-1/4)a$. By averaging the mean square drift velocities over all orbit centres we obtain the enhancement of the diffusion in the y direction and, therefore, a maximum in the resistivity in the x direction.

In considering both electric and magnetic modulations the drift velocities simply add together. In Fig. 3(b) electron trajectories at the Fermi energy are plotted both for electric and magnetic modulations *in phase* (full line) and *out of phase* (dashed line). The effect of adding a small magnetic modulation to the electric one is to change the phase angle of the resulting magnetoresistance oscillations. Resonance now occurs when $2R_c = (n-1/4 \pm \phi/\pi)a$ with

$$\tan \phi = 2\pi V_0 / (a k_F \hbar \omega_0), \quad (1)$$

where $\omega_0 = eB_0/m^*$, m^* is the electron effective mass and k_F is the Fermi wave vector.

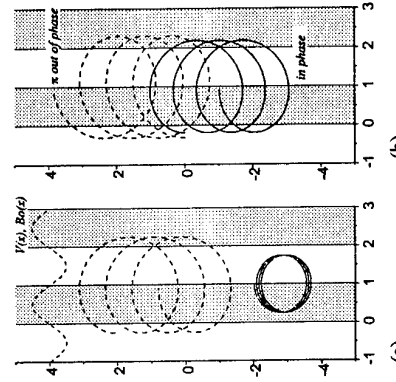


Fig. 3. (a) Semiclassical trajectories for electrons at the Fermi energy with an electric modulation (dashed curve) and with a spatially modulated magnetic field (solid curve). (b) Semiclassical trajectories for electrons at the Fermi energy in the presence of both electric and magnetic modulation. In each case B is chosen to correspond to the resonance condition. The shadowed regions correspond to the positions of the superconducting stripes.

It is possible to determine both V_0 and B_0 from the experimental data. To this end, we measure the phase difference 2ϕ between the magnetoresistance maxima and minima for sweep up and sweep down and use Eq. (1) to calculate values of V_0/B_0 . V_0 may be estimated using the cut-off magnetic field for the positive magnetoresistance at low B [9] and is about 1 meV. The maximum value for B_0 , *at the plane of the stripes*, in the $2\mu\text{m}$ period samples with Pb grating was about 20 mT for the external field 35 mT [5]. With these measured parameters we are able to generate the theoretical curve shown in Fig. 2(a).

We did not observe hysteresis in the magnetoresistance of samples with $1\mu\text{m}$ period. Assuming that the modulation amplitude decays exponentially [10] as $\exp(-2\pi z/a)$ at a distance z from the stripes a reduction of about an order of magnitude relative to the $2\mu\text{m}$ period device is expected, but that should still be measured within our experimental resolution. From the maximum B_0 obtained for the $2\mu\text{m}$ samples we can estimate the separation between 2 vortices in the Pb to be about 200 nm. When this distance is comparable to the size of the stripes there is no longer any macroscopic gradient in the vortex concentration due to pinning thus reducing the amplitude of the magnetic modulation in $1\mu\text{m}$ period samples smaller. Similarly, we observe no modulation effect in samples with Nb stripes. This might reflect the larger value of the penetration length λ in Nb [11] ($>0.12\mu\text{m}$) relative to Pb. Lead films are known to have one of the smallest penetration lengths that can be obtained for thin films [8]. In our structures we can estimate λ for Pb the stripes from the cut-off field B_C to be about $0.07\mu\text{m}$.

The low field magnetoresistance in our structures is dominated by the electric modulation. In order to have the magnetic modulation as the dominant effect in our samples we estimate that the amplitude of the electric modulation would have to be as low as 0.2 meV for the $2\mu\text{m}$ period sample. These values are difficult to achieve in a lithographed structure and will require careful sample design. A 2DEG closer to the surface may make the magnetic modulation relatively stronger since its amplitude is exponentially dependent on the distance from the surface but strain induced electrostatic modulation is not.

In summary, we have observed novel magnetoresistance oscillations resulting from the commensurability of R_c with the period of a lateral magnetic superlattice. Our results can be understood within semiclassical picture that takes into account both magnetic and electric modulations at the plane of the 2DEG .

Acknowledgement

This work is supported by EPSRC (UK), HAC wish to thank CNPq (Brazil) for financial support.

References

- [1] A.K. Geim *et al.*, Phys. Rev. B **46**, 324 (1992); A.K. Geim *et al.*, Phys. Rev. B **49**, 5749 (1994).
- [2] F.M. Peeters and P. Vasilopoulos, Phys. Rev. B **47**, 1466 (1993).
- [3] C.W.J. Beenakker, Phys. Rev. Lett. **62**, 2020 (1989).
- [4] D. Weiss *et al.*, Europhys. Lett. **8**, 179 (1989); R.R. Gerhardts, D. Weiss, and K. von Klitzing, Phys. Rev. Lett. **62**, 1173 (1989).
- [5] H.A. Campona *et al.*, Phys. Rev. Lett. **74**, 3009 (1995).
- [6] P.D. Ye *et al.*, Phys. Rev. Lett. **74**, 3013 (1995).
- [7] J.H. Davies and I.A. Larkin, Phys. Rev. B **49**, 4800 (1994).
- [8] R.P. Huebener, *Magnetic Flux Structures in Superconductors*, Springer Series in Solid State Physics Vol. 6 (Springer-Verlag, Berlin, 1979).
- [9] P.H. Beton *et al.*, Phys. Rev. B **42**, 9229 (1990).
- [10] J. Rammer and A.L. Shchekinov, Phys. Rev. B **36**, 3135 (1987).
- [11] C.E. Cunningham *et al.*, Appl. Phys. Lett. **62**, 2122 (1993).

Magnetoresistance Oscillation in a Two-dimensional Electron Gas under Periodic Modulation of Electric and Magnetic Fields

Akira Endo*, Shu-ichi Izawa, Shingo Katsumoto and Yasuhiro Iye

Institute for Solid State Physics,
University of Tokyo, Roppongi, Minato-ku, Tokyo 106, Japan

We have studied the oscillatory magnetoresistance (Weiss oscillation) in a two-dimensional electron gas (2DEG) subjected to a one-dimensional periodic modulation of both electric and magnetic fields. The relative amplitude of the two types of modulation can be controlled by applying a bias voltage to a gate consisting of a periodic array of ferromagnetic metal stripes. By letting the magnetic modulation dominate by applying +500 mV to the gate, we succeeded in observing *magnetic* Weiss oscillation characterized by peak/valley inversion in the magnetoresistance oscillation compared to the well-known *electric* counterpart. The oscillation curve shows continuous phase shift with smaller gate biases, until it reaches the peak/valley location of *electric* Weiss oscillation at about -250 mV.

A high mobility two-dimensional electron gas (2DEG) formed in a modulation doped GaAs/AlGaAs heterostructure, combined with modern lithography techniques, has made it possible to artificially introduce a potential variation in the lateral length scale comparable to or less than the electron mean free path. A one-dimensional periodic electrostatic potential modulation, thus introduced, are now well established to give rise to oscillatory magnetoresistance —so-called (*electric*) Weiss oscillation— periodic in $1/B$, with the minima of resistivity ρ_{xx} occurring at

$$2R_c = a(n - \frac{1}{4}) \quad (n = 1, 2, 3, \dots) \quad (1)$$

Here, x denotes the direction of the modulation, a the period, $R_c = \hbar k_F/eB = \sqrt{2m_e}l^2$ the cyclotron radius of an electron at the Fermi level, with k_F the Fermi wave number, n_e the electron density, and $l = \sqrt{\hbar/eB}$ the magnetic length [1-6]. The oscillation is well accounted for by the classical commensurability between a and $2R_c$.

A magnetic analogue of such periodic modulation is theoretically predicted to reproduce a similar oscillatory magnetoresistance but with peak/valley structure inverted [7-9]; the positions of ρ_{xx} minima obey the formula

$$2R_c = a(n + \frac{1}{4}) \quad (n = 1, 2, 3, \dots) \quad (2)$$

The structure of devices for our study are schematically drawn in the inset of Fig. 1. The devices were fabricated from MBE-grown GaAs/AlGaAs single heterojunction with electron density $n_e \sim 4 \times 10^{15} \text{ m}^{-2}$ and low temperature mobility $\mu \sim 60 \text{ m}^2/(\text{V}\cdot\text{s})$. A standard Hall-bar was formed by photolithography and wet etching, and nickel striped gates were deposited on the top defined by electron-beam lithography and lift-off process. It may be worth pointing out that this lift-off process, not completed in the previous work [8], seems to have contributed to reduce electrostatic potential modulation by eliminating elastic strain deriving from the differential contraction between GaAs and the electron-beam resist. The width and spacing of the stripes are designed to be equal for the devices used in the present paper. All the stripes are electrically connected with a thin line of nickel, not shown in Fig. 1, running parallel to the current direction.

Magnetotransport measurements were carried out at $T = 4.2 \text{ K}$, using a standard low-frequency ac technique. The main panel of Fig. 1 shows the magnetoresistance $\rho_{xx}(B)$ for a device with $a = 0.5 \mu\text{m}$ when the gate bias $V_g = +500 \text{ mV}$ is applied. The gate bias was chosen to suppress most efficiently the native electric modulation. Two traces, that of up-sweep and down-sweep of the magnetic field, are shown. Both traces show oscillatory behavior with the minima well explained by eq. 2. This means that we observed *magnetic* Weiss oscillation by making the magnetic modulation dominant in our device. The magnetoresistance displays hysteretic behavior; the down-sweep trace representing stronger magnetic modulation shows larger ρ_{xx} than the up-sweep one. The hysteresis loop closes at $B \sim 0.3 \text{ T}$, indicating that the magnetization of the nickel gates saturate around this field. To confirm the magnetic origin of the oscillation, we took the difference between up- and down-sweeps, $\Delta \rho_{xx}(B) = \rho_{xx}(B, \text{down}) - \rho_{xx}(B, \text{up})$, as plotted in Fig. 2, which obviously is associated only with magnetic modulation. The positions of ρ_{xx} minima expected from eq. 2 for $n = 1-5$ are marked with arrows in the figure, showing excellent agreement with those experimentally observed.

For smaller V_g , the compensation of the electric modulation is less complete. Then the situation is realized where both electric and magnetic modulations are simultaneously present in our device. In addition, the two modulations are likely to be spatially in phase, since both originate from the nickel stripes. In Fig. 3 are shown the magnetoresistance curves (normalized by zero field resistivity) of the same device as Fig. 1 for $V_g = +50, -50, -110, -125, -150, -175$, and -200 mV . The electron densities n_e determined by Hall measurements are $3.11, 3.19, 3.30, 3.37, 3.46, 3.62$, and $3.87 \times 10^{15} \text{ m}^{-2}$, and the zero field mobilities μ are $39.3, 41.4, 43.2, 45.3, 47.3, 51.5$, and $59.3 \text{ m}^2/(\text{V}\cdot\text{s})$ for each gate bias, respectively. The horizontal axis is taken as B/k_F , in order to scale the magnetoresistance traces of different electron densities. For clarity, only down-sweeps, which represent saturated magnetization of the nickel gates as mentioned, are shown in the figure. Expected locations of the resistivity minima for electric and magnetic positions (eqs. 1 and 2) are indicated by solid and dashed arrows for $n = 1-3$ and $n = 1-4$, respectively. It can be seen that with the decrease of V_g , the resistivity minima shifts continuously from magnetic toward electric Weiss minima.

Peters and Vasilopoulos [9] considered magnetoresistance in the case where both electric and magnetic modulations are simultaneously present. For the in-phase sinusoidal electrostatic-potential and magnetic-field modulations, $V(x) = V_0 \cos(\frac{2\pi}{a}x)$ and $B_z(x) = B_0 \cos(\frac{2\pi}{a}x)$, their calculation gives (for $\omega_c\tau \gg 1$)

$$\frac{\rho_{xx}(B) - \rho_{xx}(0)}{\rho_{xx}(0)} = \frac{ak_F \hbar \omega_0 \hbar \omega_c}{2\pi^2 \hbar \omega_c E_F} (\omega_c \tau)^2 (1 + \delta^2) [1 - A(T/T_a) + A(T/T_a) \sin^2(\frac{2\pi R_c}{a} - \frac{\pi}{4} + \phi)] \quad (3)$$

where $\omega_0 = eB_0/m^*$, $\omega_c = eB/m^*$ with m^* electron effective mass, E_F Fermi energy, $\tau = m^* \mu/e$ scattering time, $k_B T_a = \hbar \omega_c / 4\pi^2 \hbar k_F$, and $A(x) = x/\sinh x$.

$$\delta \equiv \frac{2\pi V_0}{ak_F \hbar \omega_0} = \tan \phi \quad (4)$$

*Contact Author. Fax: +81 3 3401 5169; E-mail: akendo@kodama.issp.u-tokyo.ac.jp

is a dimensionless parameter characterizing the relative amplitude of electric and magnetic modulations. δ can be deduced from the amplitude of the experimental oscillation traces using eq. 3. On the other hand, ϕ can be directly read from the same traces. The plot of δ versus ϕ for each V_g is shown in Fig. 4 for the traces shown in Fig. 3 and traces for $V_g = 0, -100, -250$ mV for a different run (not shown). The agreement of the plots with the relation $\delta = \tan \phi$ (dotted curve) is quite good, indicating that our experimental oscillation amplitude and phase shift is well explained by the formulation by Peeters and Vasilopoulos [9].

In summary, we have observed *magnetic* Weiss oscillation for 2DEG with a one-dimensional periodic array of nickel striped gates, suppressing stray electrostatic potential modulation by applying +500 mV to the gates. (We have learned that similar *magnetic* Weiss oscillation has been observed by H.A. Carmona et al. [12] and by P.D. Ye et al. [13] using superconducting lead stripes and dysprosium stripes for magnetic modulation, respectively.) The electric modulation can be restored by decreasing the gate bias. By changing the relative strength of the two modulation with the gate bias, we have observed continuous phase shift of the oscillatory magnetoresistance whose amplitude and the shift are in agreement with the theory by Peeters and Vasilopoulos [9].

Acknowledgements

We are grateful to Dr. R. Yagi for collaboration in the early stage of this work. This work was supported in part by Grant-in-Aid for Scientific Research on Priority Areas, "Quantum Coherent Electronics", from the Ministry on Education, Science and Culture.

References

- [1] D. Weiss, K.v. Klitzing, K. Ploog and G. Weimann, *Europhys. Lett.* **8** (1989) 179.
- [2] R.R. Gerhardts, D. Weiss and K.v. Klitzing, *Phys. Rev. Lett.* **62** (1989) 1173.
- [3] R.W. Winkler, J.P. Kotthaus and K. Ploog, *Phys. Rev. Lett.* **62** (1989) 1177.
- [4] C.W. Beenakker, *Phys. Rev. Lett.* **62** (1989) 2020.
- [5] C. Zhang and R.R. Gerhardts, *Phys. Rev.* **B41** (1990) 12850.
- [6] F.M. Peeters and P. Vasilopoulos, *Phys. Rev.* **B46** (1992) 4667.
- [7] D.P. Xue and G. Xiao, *Phys. Rev.* **B45** (1992) 5986.
- [8] R. Yagi and Y. Iye, *J. Phys. Soc. Jpn.* **62** (1993) 1279.
- [9] F.M. Peeters and P. Vasilopoulos, *Phys. Rev.* **B47** (1993) 1466.
- [10] S. Katsumoto, A. Endo and Y. Iye, *J. Phys. Soc. Jpn.* **64** (1995) 706.
- [11] S. Izawa, S. Katsumoto, A. Endo and Y. Iye, in preparation
- [12] H.A. Carmona, A.K. Geim, A. Nogaret, P.C. Main, T.J. Foster and M. Henini, *Phys. Rev. Lett.* **74** (1995) 3009.
- [13] P.D. Ye, D. Weiss, R.R. Gerhardts, M. Seeger, K. von Klitzing, K. Eberl and H. Nickel, *Phys. Rev. Lett.* **74** (1995) 3013.

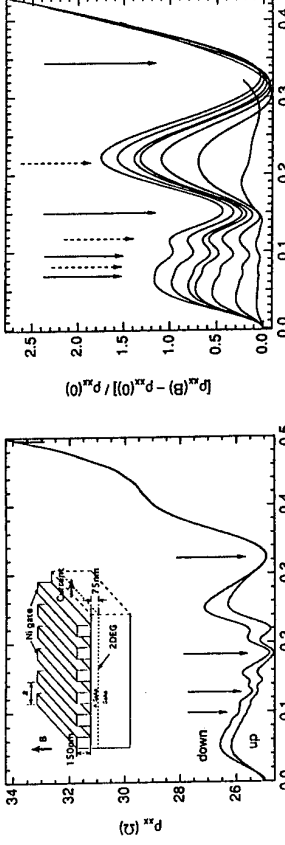


Fig. 1. Inset: Schematic drawing of the device structure. Main Panel: Magnetoresistance of a device with period $a = 0.5 \mu\text{m}$ at $T = 4.2$ K for different gate voltages; $V_g = +50$ (bottom), $-50, -110, -125, -150, -175, -200$ (top) mV. The expected positions of resistivity minima for electric and magnetic Weiss oscillation (eqs. 1 and 2) are marked with solid and dashed arrows, respectively.

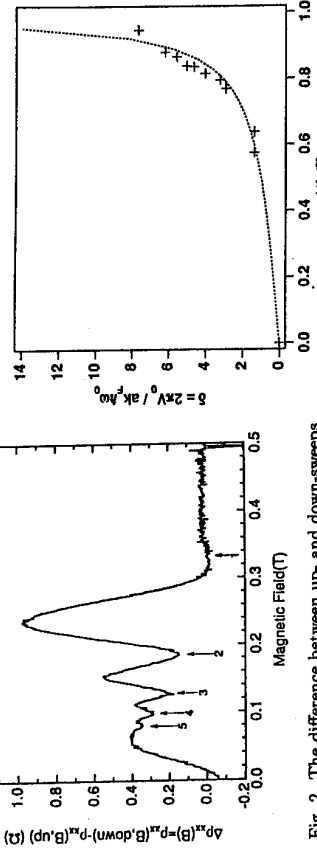


Fig. 2. The difference between up- and down-sweeps $\Delta\rho_{xx}(B) = \rho_{xx}(B, \text{down}) - \rho_{xx}(B, \text{up})$, shown in Fig. 1. The arrows indicated the expected positions of resistivity minima for *magnetic* Weiss oscillation (eqs. 1 and 2).

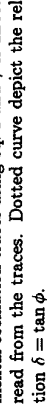


Fig. 3. Magnetoresistance of a device with $a = 0.5 \mu\text{m}$ at $T = 4.2$ K for different gate voltages; $V_g = +50$ (bottom), $-50, -110, -125, -150, -175, -200$ (top) mV. The expected positions of resistivity minima for electric and magnetic Weiss oscillation (eqs. 1 and 2) are marked with solid and dashed arrows, respectively.

Magnetotransport in Periodic Magnetic Fields

P. D. Weiss, R. R. Gerhardts, K. von Klitzing, K. Eberl, H. Nickel,*
Fach-Planck-Institut für Festkörperforschung, D-70569 Stuttgart, Germany

* *Forschungsinstitut der Deutschen Bundespost, D-64295 Darmstadt, Germany*

Abstract: By depositing an array of ferromagnetic dysprosium wires on top of a high mobility two-dimensional electron gas (2DEG), we generate a one-dimensional *periodic magnetic field* with periods between $a = 500$ nm and $1 \mu\text{m}$ giving rise to *magnetic commensurability oscillations* of the magnetoresistance ρ_{xx} . Here we study the commensurability oscillations as a function of the angle θ between the Dy-wires and the Hall-bar. For parallel orientation of the wires we find pronounced anomalies at intermediate magnetic fields which we ascribe to overlapping, modulation-broadened, Landau bands.

The resistance of a 2DEG subjected to a weak (modulation amplitude $B_m < B_0$) periodic magnetic field, which oscillates on a length scale small compared to the mean free path of the electrons, is expected to oscillate as a function of an externally applied field B_0 [1]. This effect, closely related to the commensurability oscillations observed in a 2DEG with superimposed *electrostatic* periodic potential [2 – 4], was recently verified experimentally by using either patterned ferromagnetic [5,6] or superconducting [7] gates placed on top of a 2DEG. In our experiment [5], we deposited an array of ferromagnetic dysprosium (Dy) wires on top of high-mobility GaAs-AlGaAs heterojunctions to generate a one-dimensional (1D) magnetic field modulation. By varying the maximum applied ‘conditioning’ field, the strength of the micromagnets and hence the amplitude of the periodic stray field was tuned. For a sufficiently high amplitude B_m (stray field component normal to the 2DEG), ρ_{xx} oscillates and minima appear at $2R_c = (\lambda + \frac{1}{4})a$ with $\lambda = 1, 2, \dots$, if the current flows perpendicular to the grating. This reflects the interplay of the two characteristic lengths of the system, the cyclotron radius R_c at the Fermi energy and the period a of the magnetic superlattice.

In the presence of a 1D periodic *electrostatic* field modulation, in contrast, minima appear whenever $2R_c = (\lambda - \frac{1}{4})a$ holds. Here, we study the dependence of the *magnetic* commensurability oscillations on the period a and on the angle of the Dy-wires with respect to the current flow (see inset of Fig.2).

Our samples were prepared from high-mobility GaAs-AlGaAs heterojunctions where the 2DEG was located approximately 100 nm underneath the sample surface. The carrier density n_s and electron mobility μ at 4.2 K were $\sim 2.2 \times 10^{11} \text{ cm}^{-2}$ and $1.3 \times 10^6 \text{ cm}^2/\text{Vs}$, respectively, corresponding to an elastic mean free path of $\sim 10 \mu\text{m}$ much longer than the period of the magnetic field modulation. $50 \mu\text{m}$ wide Hall bars with AuGe/Ni ohmic contacts were fabricated by standard techniques. A 10 nm thin NiCr film, evaporated on top of the devices, defines an equipotential plane to avoid electric modulation of the 2DEG. However, strain due to different thermal expansion coefficients of the ferromagnetic grating and the heterojunction always results in a weak electric periodic potential as the sample is cooled down to cryogenic temperatures [8]. The Dy gratings with period $a = 500$ nm and $1 \mu\text{m}$ were defined by electron beam lithography and lift-off technique on top of NiCr gates. Four

point resistance measurements were performed in a ^4He cryostat with superconducting coils using standard ac lock-in techniques. For all experiments, the external magnetic field B_0 was applied normal (z -direction) to the plane of the 2DEG.

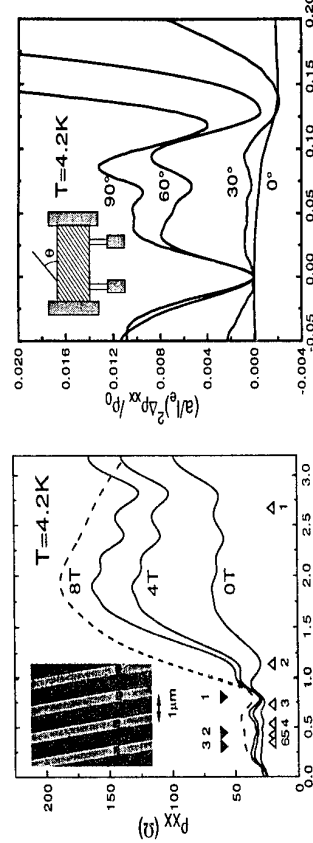


Fig.1: ρ_{xx} vs. $a/2R_c$ for different B^{\max} sweeps. Filled triangles with positions defined by Eq. (1) mark the flat-band condition in a periodic magnetic field. Open triangles mark the flat-band condition of the second harmonic of the strain induced electrostatic potential. Dashed curve: ρ_{xx} for $a = 1 \mu\text{m}$. Solid traces: ρ_{xx} for $a = 500$ nm. Inset: electron micrograph of the Dy strips evaporated across a mesa edge: $a = 1 \mu\text{m}$, height of a Dy strip: 200 nm.
 Fig.2: $(a/l_e)^2 \Delta \rho_{xx}/\rho_0$ as function of the external magnetic field B_0 for different angles θ . The amplitude of the oscillations decreases when the grating is tilted from 90° to 0° .

In Fig.1 we compare the magnetoresistance trace of 1D magnetic superlattices with period $a = 500$ nm (solid lines) and $1 \mu\text{m}$ (dashed line). The traces labeled 0T, 4T and 8T are taken after the initial cooldown and after the magnetic field was ramped up to a maximum field $B_{\max} = 4$ T and 8 T, respectively. By increasing B_{\max} to 4T and 8T, the magnetic polarization J of the Dy strips and hence the strength of the resulting stray field can be increased. Note that B_m also depends on B_0 (or a/R_c in Fig.1) reflecting the magnetization traces of Dy [5]. In Fig.1 a dramatically enhanced resistance peak can be found at $a/2R_c = 1.8$ for an increased strength of the micromagnets. The positions of the oscillation minima of the 4T and 8T ρ_{xx} traces closely follow the theoretical prediction, marked by filled triangles. On the normalized magnetic field scale the magnetic commensurability oscillations measured in the 500 nm and $1 \mu\text{m}$ gratings are in phase, reflecting the expected scaling behavior. The oscillations in the 0T trace are predominantly due to the electrostatic potential modulation caused by the strain. The open triangles mark the second harmonic of the grating induced potential which dominates here (see e.g. [8]). The evolution from *electric* commensurability oscillations to *magnetic* ones with increasing strength B_m was systematically investigated in [5]. From the amplitude of the maximum at $a/2R_c \approx 1.8$ we estimate, assuming a field modulation of the form $B_m \cos(\frac{2\pi}{a}x)$, the field amplitude B_m from [5].

$$\frac{\Delta\rho_{xx}}{\rho_0} = \frac{2e^2}{\pi h^2} \frac{a}{R_c n_e} l_e^2 P_m^2 \sin^2 \left[\frac{2\pi}{a} R_c - \frac{\pi}{4} \right], \quad (1)$$

where ρ_0 is the zero-field resistivity of the unmodulated 2DEG, n_e is the electron density and l_e is the mean free path. For the $B^{max} = 8$ T trace of the sample with $a = 500$ nm we estimate $B_m \approx 30$ mT, and for the 4T trace $B_m \approx 23$ mT.

The oscillations in ρ_{xx} , described above, are due to the formation of Landau bands whose widths oscillate as a function of the Landau index n and B_0 . For high quantum numbers n , we approximate the width W_m , given by Ref. [1], by

$$W_m = \hbar\omega_m \frac{ak_F}{2\pi} J_1 \left(\frac{2\pi}{a} R_c \right), \quad (2)$$

with $J_1(x)$ a Bessel function. The band formation and the resulting band conductivity contribution [3,4,9] dominate the commensurability oscillations if the current flows perpendicular to the magnetic grating (these bandconductivity oscillations can also be understood semiclassically for the case of 1D electric potentials [10]). *Minima* in ρ_{xx} appear when the bandwidth goes to zero and the bandconductivity vanishes. However, commensurability oscillations for electric 1D modulation were also observed for a current flow parallel to the grating [2,3]. These oscillations are due to the modified density of states (DOS) displaying *maxima* when the Landau bands become flat (DOS maxima at $W_m \approx 0$).

In Fig. 2 we investigate the commensurability oscillations for different angles of the Dy-grating with respect to the current flow (see inset). To account for different mobilities of the samples investigated we scaled ρ_{xx} by $(a/l_e)^2$ (see Eq.1). As the angle θ is changed from 90° to 0° , the amplitude of the oscillations decreases characteristically. In the simplest case we expect

$$\Delta\rho'_{xx} = \Delta\rho_{xx} \sin^2 \theta \quad (3)$$

to hold. This scaling, ignoring the positive magnetoresistance contributions in experiment, is roughly fulfilled by the traces in Fig.2. For the $\theta = 0^\circ$ case we do not observe the expected 'antiphase' oscillations. The reason could be that the grating is not exactly aligned along the Hall-bar so that bandconductivity contributions still dominate.

Effects of the modified DOS become pronounced, however, at higher magnetic field slightly beyond the commensurability regime. This is shown by the ρ_{xx} traces in Fig.3, where we changed the strength of the micromagnets by varying the maximum applied field B^{max} from 1T to 10T. Here, the Dy-wires are aligned parallel to the Hall-bar ($\theta = 0^\circ$). With increasing strength of the magnetic field modulation the amplitude of the Shubnikov-de Haas oscillations decays. This can be understood qualitatively as a consequence of the Landau band formation which reduces the maximum density of states of a Landau level by modulation broadening. Apart from the reduced amplitude of the SdH-oscillations we observe a characteristic shift of the SdH minima to higher magnetic fields and even additional oscillatory features (see trace 10T between 0.5T and 0.7T) for increasing magnetic modulation. This behavior we ascribe to overlapping modulation broadened Landau bands. This assumption is

supported by an estimate of the bandwidth W_m at $B_0 = 0.6$ T from previously published data (inset of Fig.3a, [5]). By extrapolation we obtain $B_m = 25$ mT (1T), 33 mT (2T), 45 mT (3T), 65 mT (10T) at $B_0 = 0.6$ T corresponding to $2W_m = 0.59$, 0.78, 1.06 and 1.53 meV derived from Eq.2. The latter two values are larger than the Landau gap $\hbar\omega_0 = 1.03$ meV at $B_0 = 0.6$ T. A shift of the SdH minima to higher magnetic field we expect when, while sweeping to higher B_0 , the next lower Landau band gets depopulated before the upper band is completely empty. However, more refined calculations are necessary to clarify this point.

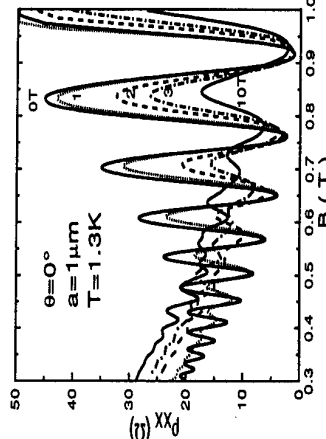


Fig.3: ρ_{xx} as function of the external magnetic field B_0 with the maximum applied field B^{max} varied between 0 and 10T. Here, the Dy-wires are aligned parallel to the Hall-bar.

We thank M. Rieck and U. Waizmann for technical support, and M. Tornow for valuable discussions. P. D. Ye acknowledges the Volkswagen Foundation for a fellowship.

- [1] F. M. Peeters and P. Vasilopoulos, Phys. Rev. B **47**, 1466 (1993).
- [2] D. Weiss, K. v. Klitzing, K. Ploog, and G. Weimann, Europhys. Lett. **8**, 179 (1989).
- [3] R. R. Gerhardt, D. Weiss, and K. v. Klitzing, Phys. Rev. Lett. **62**, 1173 (1989).
- [4] R. W. Winkler, J. P. Kotthaus, and K. Ploog, Phys. Rev. Lett. **62**, 1177 (1989).
- [5] P. D. Ye, D. Weiss, R. R. Gerhardt, M. Seeger, K. v. Klitzing, K. Eberl, and H. Nickel, Phys. Rev. Lett. **74**, 3013 (1995).
- [6] S. Izawa, S. Katsumoto, A. Endo, and Y. Iye, J. Phys. Soc. Jpn. **64**, 706 (1995).
- [7] H. A. Carmona, A. K. Geim, A. Nogaet, P. C. Main, T. J. Foster, M. Hennini, S. P. Beaumont and M. G. Blamire, Phys. Rev. Lett. **74**, 3009 (1995).
- [8] P. D. Ye, D. Weiss, R. R. Gerhardt, K. von Klitzing, K. Eberl, H. Nickel and C. T. Foxon, Semicond. Sci. Technol. **10**, 715 (1995).
- [9] D. Pfannkuche and R. R. Gerhardt, Phys. Rev. B **46**, 12 606 (1992).
- [10] C. W. J. Beenakker, Phys. Rev. Lett. **62**, 2020 (1989).

Electrons in a Periodic Magnetic Field

I.S. Ibrahim and F.M. Peeters
*Département de Physique, Université Antwerp (UIA),
 Universiteitsplein 1, B-2610 Antwerp, Belgium*

Abstract

The properties of a two-dimensional electron gas (2DEG) under the influence of a perpendicular magnetic field which is periodic in one direction are investigated. Two situations are considered: 1) a periodic array of magnetic field steps, and 2) a saw-tooth magnetic field profile. In contrast with the usual potential modulated case the present systems are not separable. We give the energy spectrum, the density of states and the diagonal components of the conductivity tensor.

1. Introduction

The wealth of information characterising the behavior of a two dimensional electron gas (2DEG) subjected to a perpendicular homogeneous magnetic field has provided the stimulus for exploring the nonhomogeneous field regime theoretically [1-4] and experimentally [5]. Recently, the problem of the motion of ballistic electrons in non-homogeneous magnetic fields has become important for the composite fermion picture of the fractional quantum Hall effect (FQHE). Normally, for a density modulated 2DEG in the FQHE regime, the problem can be mapped into one of ballistic motion of composite fermions moving in a periodic magnetic field [6,7].

In this paper we study the case in which we have a magnetic field of arbitrary strength which is periodic in one direction. The experimental system which we have in mind is one in which a ferromagnetic thin film is deposited on a heterostructure and patterned such that the magnetic domains consist of parallel strips with magnetization perpendicular to the thin film and which changes sign from one strip to the next. The magnetic field emerging from the patterned film will interact with the carriers in the underlying semiconductor structure. This physical system is sketched in Fig. 1(a) together with the corresponding magnetic field profiles (Fig. 1(b)) in the plane of the 2DEG.

2. Periodic Magnetic Fields

Consider a 2DEG in the (x, y) plane in the presence of a perpendicular magnetic field. The magnetic field is taken homogeneous along the y -axis and varies along the x -axis. Such a magnetic field is described, in the Landau gauge, by the vector potential $\mathbf{A} = (0, A(x), 0)$. The problem is translational invariant along the y -direction and the wave function can be written as $\Psi(x, y) = e^{ik_y y} \psi(x)$, where hk_y is the expectation value of p_y in the y -direction. We express all quantities in terms of the cyclotron frequency $\omega_c = eB_0/mc$ and the magnetic length $l_B = \sqrt{\hbar c/eB_0}$ where B_0 is some typical magnetic field strength in the problem. The wavefunction $\psi(x)$ satisfies the one-dimensional (1D) Schrödinger equation

$$\left\{ \frac{d^2}{dx^2} + 2E - 2V(x, k_y) \right\} \psi(x) = 0, \quad (1)$$

with the expression $V(x, k_y) = [k_y + A(x)]^2/2$, which can be interpreted as a k_y -dependent effective potential. In Ref. [1] the above problem was studied for $B(x)$ profiles of finite

extend in the x -direction. Here we will investigate $B(x)$ profiles which are periodic in x , but such that $< B(x) > = 0$. The resulting potential is therefore periodic $V(x, k_y) = V(x+n_l, k_y) = V(x+l, k_y)$ with period l and consequently it is sufficient to find the solution only in one period and use Bloch's theorem to propagate this solution throughout the lattice.

3. Periodic Step Magnetic Field

For the physical system of Fig. 1 we consider the limit of a small distance between the 2DEG and the ferromagnetic thin film. Then a periodic step magnetic field profile is obtained ($-z_0/l = 0.26$ in Fig. 1(b)) where in one period the vector potential is $A(x) = x - l/4$, ($0 \leq x \leq l/2$), $-x + 3l/4$ ($l/2 \leq x \leq l$). After making the following change of variable $X = \sqrt{2}(k_y + A(x))$ the Schrödinger equation (1) is cast into the following form

$$\left\{ \frac{d^2}{dX^2} + E - X^2/4 \right\} \psi(X) = 0, \quad (2)$$

which is the parabolic cylinder equation. This equation has two linearly independent solutions $\psi_1(X) = e^{-X^2/4} {}_{1F_1}(-E/2 + 1/4, 1/2, X^2/2)$ and $\psi_2(X) = X e^{-X^2/4} {}_{1F_1}(-E/2 + 3/4, 3/2, X^2/2)$ where ${}_1F_1(a, c; x)$ is the confluent hypergeometric function. Imposing the conditions of continuity and the Bloch periodicity on the wave function and its first derivative leads to a transcendental equation for the energy momentum relation which we solved numerically.

The energy dispersion relation, i.e. E versus k_y , is shown in Fig. 2 for $l = 8$. In order to understand the energy spectrum we refer to the expression for the effective potential $V(x, k_y)$ given above. First, note that $V(x, k_y) = V(x+1/2, -k_y)$ which results in spatially separated motions for the $+k_y$ and $-k_y$ electrons moving with $E < V_{max} = (|k_y| + l/4)^2/2$. For $k_y = 0$ the profile for $V(x, k_y)$ is a periodic array of harmonic oscillators with finite depth ($= l^2/32$) and period $l/2$. In this case, the first Brillouin zone (FBZ) edge is at $k = 2\pi/l$ and gaps in the spectrum appear at $k = 2n\pi/l$ where n is the band index. When k_y takes values different from zero the periodicity of $V(x, k_y)$ becomes twice as large and consequently the FBZ edge becomes $k = \pi/l$ and the number of energy bands and gaps doubles. For $0 < |k_y| < l/4$ the potential profile within one period consists of a double harmonic oscillator in which the middle barrier is smaller than the side barriers and decreases to zero at $|k_y| = l/4$ where $V(x, k_y)$ takes the shape of a single harmonic oscillator in one period with depth $= l^2/8$. The bands with energy below the barrier height (the dash-dotted curves in Fig. 2 indicate the bottom and top of the potential profile), i.e. $E < V_{max}$ correspond to open orbits traveling along the y -direction and oscillating around the boundary separating the two magnetic strips. Electrons at adjacent boundaries move in opposite y direction. For $|k_y| > l/4$, the profile $V(x, k_y)$ becomes increasingly V-shaped with minima at $V_{min} = (|k_y| - l/4)^2/2$ and maxima at $V_{max} = (|k_y| + l/4)^2/2$. The 1D states below V_{max} are similar to the so-called magneto-electric states (i.e. linear combinations of Airy functions). Notice that for $l \rightarrow \infty$ we recover the homogeneous field limit $E = (n + 1/2)\hbar\omega_c$ (see inset of Fig. 2).

The zero temperature density of states (DOS) for this system is depicted in Fig. 3. The structure can be understood in the light of Fig. 2 for E vs. k_y . The first singularity in $D(E)$ occurs at the onset of the allowed energy bands and corresponds to 1D states where motion is only possible along the y -direction. At higher energies the structure is gradually diminished due to the availability of 2D states above the barriers where the DOS approaches its limiting value for the free 2DEG. The components of the electric conductivity tensor are

also shown in Fig. 3. The σ_{yy} conductivity is obviously the least affected by the presence of the magnetic field modulations along x , since there are always states available for motion along the y direction regardless of the Fermi energy. In contrast the magnetic band structure has a pronounced effect on the σ_{xx} components due to the existence of the energy gaps for motion along the x direction [8]. Also the magnitude of σ_{xx} does not become appreciable until the Fermi energy is near or above the potential barrier at $k_y = 0$.

4. Saw-tooth Magnetic Field

The system considered in Ref.[2] is a 2DEG which is constrained by rigid walls in the x -direction $|x| = l/2$, but which is infinite along the y -axis. A nonhomogeneous magnetic field $B(x) = B_0 x$ directed perpendicular to the (x, y) plane was applied. Here we make a superlattice out of this system by removing the rigid wall condition and repeating the geometry indefinitely along the x -axis. Thus we consider a saw-tooth magnetic field profile. Because of Bloch's theorem, the Schrödinger equation (1) has only to be solved within one period, which reduces to the finite anharmonic oscillator problem

$$\left\{ \frac{d^2}{dx^2} + 2E - (k_y + x^2/2)^2 \right\} \psi(x) = 0. \quad (3)$$

The magnetic field profile is now no longer invariant under spatial inversion. As a consequence the effective potential $V(x, k_y)$ is asymmetric with respect to k_y . Therefore, the dispersion relation for E vs. k_y is no longer symmetric (see Fig. 4) for $k_y \rightarrow -k_y$, with other words: electrons moving in opposite y -directions no longer have the same energy. For large $|k_y|$ -values the effective potential for $k_y > 0$ consists of a periodic array of harmonic potentials while for $k_y < 0$ they are inverse parabolas. It is therefore not surprising that the electron motion in such two superlattices will be very different. Notice that the minibands are wider for $k_y < 0$. This is because the superlattice potential for $k_y < 0$ is shallower than for $k_y > 0$. The implication of wider minibands is that the corresponding electron states can more easily propagate in the x -direction, thus having a larger v_x . Also, for cases with large l -values (see inset of Fig. 4) the energy spectrum does not have a flat region near $k_y = 0$ as in previous case (see inset of Fig. 2). We notice that for $k_y < 0$ and for large l -values the energy bands become two-fold degenerate: symmetric and asymmetric states have the same energy for those k_y -values. This is a similar effect which was observed in the 1D-case with rigid walls [2]. For large values of the period l and not too large energy the system of Ref. 2 is a limiting case of the present system.

Acknowledgments: This work is supported by the Belgian National Science Foundation and the Interuniversity Microelectronics Center (IMEC, Leuven).

References

- [1] F.M. Peeters and A. Matulis, Phys. Rev. B **48**, 15166 (1993); A. Matulis, F.M. Peeters and P. Vasilopoulos, Phys. Rev. Lett. **72**, 1518 (1994).
- [2] J.E. Müller, Phys. Rev. Lett. **68**, 385 (1992).
- [3] F.M. Peeters and Vasilopoulos, Phys. Rev. B **47**, 1466 (1993). P. Vasilopoulos and F. M. Peeters, Superlatt. Microstrct. **7**, 393 (1990).
- [4] D.P. Xue and G. Xiao, Phys. Rev. B **45**, 5986 (1992); X. G. Wu and S. E. Ulloa, Solid Stat. Commun. **82**, 945 (1992).
- [5] H.A. Carmona, A.K. Geim, A. Nogaret, P.C. Main, T.J. Foster, M. Henini, S.P.

Beaumont, and M.G. Blamire, Phys. Rev. Lett. **74**, 3009 (1995); P.D. Ye, D. Weiss, R.R. Gerhardts, M. Seeger, K. von Klitzing, K. Eberl, and H. Nickel, Phys. Rev. Lett. **74**, 3013 (1995); S. Isawa, S. Katsumoto, A. Endo, and Y. Iye, J. Phys. Soc. Jpn. **64**, 3846 (1995).

[6] W. Kang, H.L. Störmer, L.N. Pfeiffer, K.J. Baldwin, and K.W. West, Phys. Rev. Lett. **71**, 3850 (1993); R.L. Willett, R.R. Ruel, K.W. West and L.N. Pfeiffer, Phys. Rev. Lett. **71**, 3846 (1993).

[7] A. Khaetskii and G.E. Bauer, Phys. Rev. B **51**, 7369 (1995); L. Brey and C. Tejedor, Phys. Rev. B **51**, (1995).

[8] R.B.S. Oakeshott and A. MacKinnon, J. Phys.: Condens. Matter **5**, 9355 (1993).

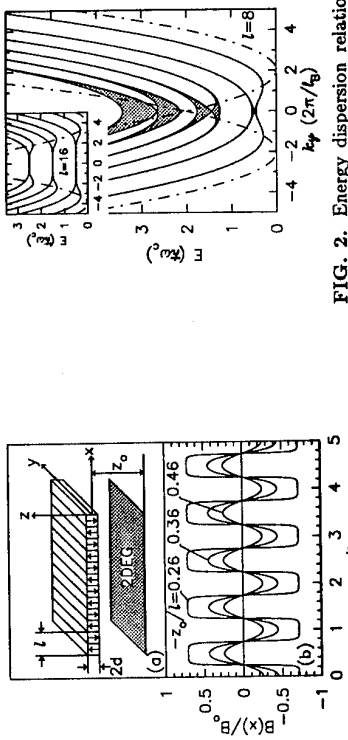


FIG. 1. The proposed physical system (a) and the resulting magnetic field profile in the plane of the 2DEG (b) for different setback distances of the 2DEG.

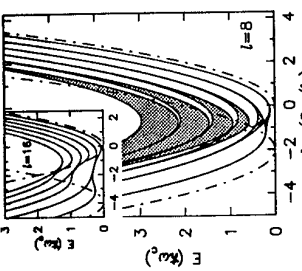


FIG. 2. Energy dispersion relation for the periodic step model with $l = 8$.

Only the lowest six bands are shown. the dash-dotted curves are the max. and min. of $V(x, k_y)$. Inset, the same with $l = 16$.

FIG. 3. The density of states and the diagonal components of the electric conductivity tensor for the periodic step model.

FIG. 4. The same as in Fig. 2 but now for the saw-tooth model.

2-DIMENSIONAL ELECTRON GAS IN A SPATIALLY VARYING MAGNETIC FIELD

E. Hofstetter, J.M.C. Taylor and A. MacKinnon

Blackett Laboratory, Imperial College, London SW7 2BZ, UK

Abstract

We have developed new methods to calculate dispersion curves (analytically in the simpler cases) from which we are able to derive expressions for various transport properties as well as the spatial distribution of electron and current densities. We investigate the case where the magnetic field varies linearly with position and the results provide useful insights into the properties of this and other field distributions. We consider spin and band structure effects as well as a confining electrostatic potential. An important objective of this work is to investigate possible applications, such as a device with a spin polarized current.

1 Introduction

A 2-dimensional electron gas (2DEG) in a magnetic field has proved to be an extremely rich subject for theoretical and experimental investigation [1]. For example, a lot of work has already been devoted to the study of the Integral and Fractional Quantum Hall Effects (I and FQHE), transport properties and edge states [2]. Except in a few cases [3, 4], however, the magnetic field considered was homogeneous. In this article we address the problem of a magnetic field varying linearly with position added to an underlying homogeneous field. This is of relevance because in real systems: (a) a constant magnetic field is not always attainable, and (b) an inhomogeneous field may be desired. Another interesting point is that in the Composite Fermion (CF) theory [5, 6] which is used to describe the FQHE, the electron-electron interaction, necessary for the appearance of the FQHE, is incorporated into an effective magnetic field via a singular gauge transformation. The result is a system of non-interacting quasi-particles carrying a fictitious magnetic flux in an inhomogeneous effective magnetic field. A better understanding of the properties of a simple non-interacting electron gas in an inhomogeneous field might therefore bring useful insights into CF theory.

2 Model

To investigate the electronic properties of a non-interacting electron gas in a linearly varying magnetic field we consider the Hamiltonian

$$H = \frac{1}{2m^*} (\mathbf{p} - e\mathbf{A})^2 - \frac{e\hbar s}{m_e} \mathbf{B} + V_c, \quad (1)$$

where $\mathbf{A} = (\frac{1}{2}B_1 y^2 + B_0 y, 0, 0)$, $\mathbf{B} = -(0, 0, B_1 y + B_0)$, the confining potential due to the wall $V_c(y) = \beta [\exp(\frac{\alpha}{y_e}(y - y_e)) + \exp(-\frac{\alpha}{y_e}(y + y_e))]$, and y_e is the position of the edge of the system. The parameters α and β allow the shape of the potential to change continuously from very sharp to very smooth, which can modify the properties of the system [6, 7]. The symmetry of the

Hamiltonian allows us to write the wave function as $\chi(x, y) = e^{ik_x x} \psi(y)$ and we then obtain the 1-dimensional Schrödinger equation

$$\left[\frac{p_y^2}{2m^*} + \frac{1}{2m^*} (\hbar k_x - eA_x)^2 - \frac{e\hbar s}{m_e} \mathbf{B} + V_c \right] \psi(y) = E\psi(y). \quad (2)$$

Solving Eq.(2) will enable us to derive the dispersion curves, $E_n(k_x)$, the electronic density, $\rho(y) = \sum_n \sum_{k_x} \psi^*(y) \psi(y)$, and the current density

$$j_x^{(n)}(x, y) = \frac{e}{m^*} \text{Re} [X_n^*(x, y) \Pi_x X_n(x, y)] + \frac{e\hbar s}{m_e} \nabla \times [X_n^*(x, y) n \chi_n(x, y)], \quad (3)$$

where n denotes the n^{th} state and the second term is due to the spin. As a result of our choice of \mathbf{A} and \mathbf{B} there is a current density only along the x axis.

3 Analytical Results

To illustrate the analytical approach we take the simplified case of Eq.(2) with $B_0 = 0$ and $V_c = 0$. We then have

$$\left[\frac{p_y^2}{2m^*} + \frac{\hbar^2}{2m^*} \left(\frac{e^2 B_1^2}{4\hbar^2} y^4 - \frac{eB_1}{\hbar} k_x y^2 + \frac{2eB_1 m^* s}{\hbar m_e} y + k_x^2 - E \right) \right] \psi(y) = 0 \quad (4)$$

We consider an ideal slab of GaAs/Al_xGa_{1-x}As heterostructure filled with an ideal 2DEG. The effective electron mass is $m^* = 0.067 \text{ m}_e$, the sample has width $2y_e = 2 \times 10^4 \text{ \AA}$ and infinite length along x , the magnetic field gradient is $B_1 = 1 \text{ G/\AA}$, and the spin eigenvalue is $s = \pm \frac{1}{2}$. We choose two regimes for which $B_1 \neq 0$: (1): $k_x < 0$, near $B = 0$, and (2): $k_x > 0$, near $B = \pm B_1 \sqrt{2\hbar s/eB_1}$. We expand parabolically around the minima of the effective potential and obtain harmonic oscillator equations which we solve analytically.

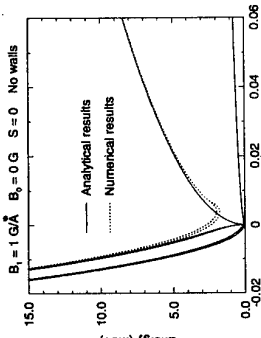


Fig.1. Dispersion curves obtained analytically compared with numerical results.

The energy E is

$$\{1\} : E = \frac{\hbar^2}{2m^*} \left[k_x^2 + \nu \gamma \sqrt{k_x} - \frac{\gamma^2 \eta^2}{k_x} \right] \quad \{2\} : E = \frac{\hbar^2}{2m^*} \left[k_x^2 + \nu \gamma \sqrt{k_x} - \frac{\gamma^2 \eta^2}{2k_x} \pm 2\gamma \eta \sqrt{2k_x} \right] \quad (5)$$

where $\gamma = \sqrt{eB_1/\hbar}$, $\eta = \frac{m^* s}{m_e}$, $\nu = (2n + 1)$, and all quantities to the right of the equal signs are positive, except η which may be positive and negative. A plot of the energy is shown in Fig.1. The group velocity may be calculated from the gradient of E with respect to k_x .

4 Numerical Results

Although it is possible to obtain useful information from analytical calculations they do not allow us to derive complete dispersion curves and hence the electronic or current densities. We therefore resort to numerical calculations. Eq.(2) can be solved by expanding ψ in terms of oscillator functions, $\phi_n(y) = H_n(y)e^{-y^2}$ where H_n is a Hermite polynomial, and then by numerically diagonalizing the corresponding secular equation. Using the properties of the Hermite polynomials all the matrix elements $\langle \phi_n | H | \phi_m \rangle$ can be calculated analytically which greatly improves the diagonalization method. The calculations were done for quite a sharp confining potential ($\alpha = 100$, $\beta = 50$) and the results for the dispersion curve with $B_1 = 10 \text{ G}\AA$, $B_0 = 0.5 \times 10^4 \text{ G}$ and $s = \frac{1}{2}$ are given in Fig.2. The degeneracy of the energy levels is completely removed and the new structure appearing in the dispersion curves is due to the breaking of the y symmetry in the Hamiltonian. It is interesting to note that some similar features were observed in the case of a curved 2DEG in a constant magnetic field [8]. From the dispersion curves we can now calculate $j_x^{(n)}$ and ρ , but to do this we need the Fermi energy E_F .

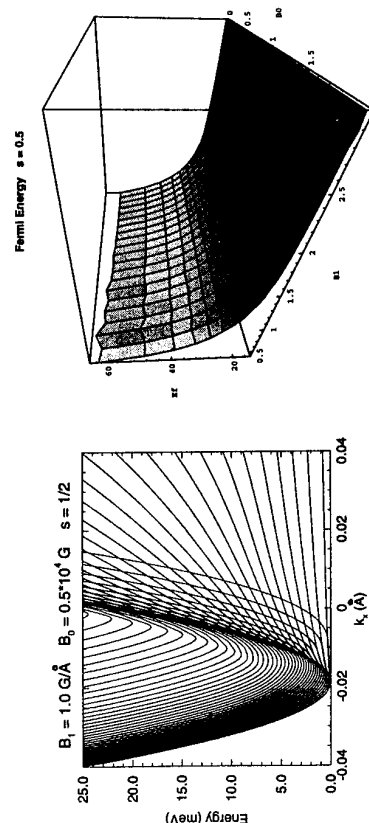


Fig.2. Dispersion curves.

This can be obtained by minimizing the total energy with the constraint that the number of electrons is constant. The results are given in Fig.3 and we see that in contrast to the assumption in [3], E_F is not independent of the magnetic field. This dependence is due to the walls, which can be seen by the fact that when B_1 increases, E_F becomes independent of the magnetic field. The electronic and current densities are plotted in Figs.4a,4b.

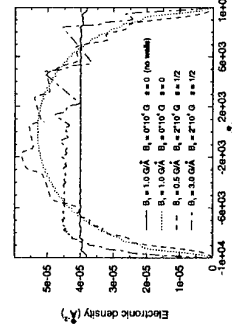


Fig.4a. Electronic densities for different magnetic fields.

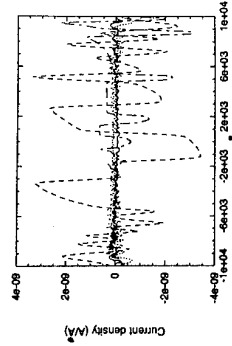


Fig.4b. Corresponding current densities.

We see that with an external confining potential ρ is not constant; it can have quite a rich structure with local charging effects. Moreover when $B_0 \neq 0$, ρ becomes asymmetric in y . Considering $j_x^{(n)}$ for $|k_x| \gg 0$, the movement of the electron can be described by its classical orbits (drifting orbits along the edges and snake orbits in the opposite direction along the line where $B \simeq 0$). For smaller k_x , however, the states tunnelling between the two wells as well as the ones of energy above the central maximum of the double well are very important and their contribution cannot be overlooked. In fact $j_x^{(n)}$, after summing over all n and k_x , turns out to be very small for the case where $B_0 = 0 \vee y$. When $B_0 \neq 0$ the current density increases with B_0 , flows in opposite directions on both sides of the sample, and is asymmetric. Also, $j_z^{(n)}$ becomes asymmetric.

5 Conclusions

In this work we derived the dispersion curves $E_n(k_x)$ as a function of magnetic field. Using them, we calculated the electronic and current densities. These show a very rich structure which could be worth further study. In particular, the fact that ρ is not constant could imply some interesting phenomena in relation to spin polarized currents.

References

- [1] For a review, see *The Quantum Hall Effect*, eds. E. Prange and S. M. Girvin, (Springer, New York, 1987).
- [2] For a review, see *Quantum Hall Effect*, ed. M. Stone, (World Scientific, Singapore, 1992).
- [3] J. E. Müller, Phys. Rev. Lett. **68** (1992) 385.
- [4] D. K. K. Lee, J. T. Chalker and D. Y. K. Ko, Phys. Rev. B **50** (1994) 5272.
- [5] I. K. Jain, Phys. Rev. Lett. **63** (1989) 199; Phys. Rev. B **41** (1990) 7653.
- [6] D. B. Chklovskii, preprint (cond-mat/9502014) (1995).
- [7] D. B. Chklovskii, B. I. Shklovskii and L. I. Glazman, Phys. Rev. B **46** (1992) 4026.
- [8] C. L. Foden, M. L. Leadbeater, J. H. Burroughes and M. Pepper, J. Phys.: Condens. Matter **6** (1994) L127.

MAGNETORESISTANCE OF A TWO-DIMENSIONAL ELECTRON GAS IN RANDOM MAGNETIC FIELDS

Luisa Theil Hansen, Rafiel Taboryski*, Anders Smith, Poul Erik Lindelof, and Per Hedegård
 The Niels Bohr Institute, University of Copenhagen, Universitetsparken 5,
 DK-2100 Copenhagen Ø, Denmark

Abstract

We report measurements on transport in a two-dimensional electron gas (2DEG) subject to an inhomogeneous magnetic field. To achieve the inhomogeneous magnetic field we randomly distributed superconducting lead (Pb) grains on the surface of the samples. In magnetic fields below the critical field for lead, the externally applied magnetic flux is either expelled from or trapped in the lead grains, and thus gives rise to inhomogeneities in the overall flux density penetrating the 2DEG. This inhomogeneous magnetic field causes a characteristic magnetoresistance with either one or two peaks and a pronounced hysteresis of the peak positions.

The response of a 2DEG to a spatially inhomogeneous magnetic field is a subject of considerable interest both theoretically and experimentally dating back to the predictions by Rammer and Shlankov of an enhanced weak localisation effect, when a random magnetic field is applied to an electron gas in the diffusive regime [1,2,3]. Recently a random magnetic field has been realised by utilising the randomly pinned flux in a superconducting (continuous) gate[4], and by Manoff et al. with a rough surface demagnetised NdFeB magnet attached to the surface of a high mobility AlGaAs heterostructure[5]. In a former publication [6] we reported on the outcome of a series of magnetoresistance measurements on a sample where the inhomogeneous magnetic field was produced by means of superconducting lead grains randomly distributed on the surface of a high mobility AlGaAs/GaAs heterostructure. In that experiment the Pb grains had a distribution in size with an average diameter of roughly $10\mu m$. For this sample we observed one peak in the magnetoresistance near $B=0$. The precise position in magnetic field of this peak exhibited a pronounced hysteresis effect. The width (and the height) of the peak was found to be limited by the temperature dependent critical field $B_c(T) = B_c(0)(1 - (T/T_c)^2)$ with $B_c(0) = 0.083T$ and $T_c = 7.2K$ for lead. This relation also provided the only temperature dependence of the effect. When cooled from above T_c in zero magnetic field, the first trace was fundamentally different from subsequent down and up sweeps in magnetic field. For the initial sweep up ("virgin trace") the magnetic field was completely expelled by the Meissner effect until the field reached $\approx 2/3B_c$, then the field began to penetrate the grains and the net flux density became less inhomogeneous. When the field reached the critical field, the superconductivity in the lead grains was killed and the flux density felt by the 2DEG completely homogenous. However, for the subsequent sweeps the pinned flux in the lead grains caused the observed hysteresis in the field dependence of the peak. In reference [6] and in the more recent paper by Hedegård and Smith [7] the observed magnetoresistance was explained in terms of semiclassical transport theory by solving the Boltzmann equation in the relaxation time approximation

assuming that the magnetic inhomogeneities average to zero throughout the 2DEG, and that the lead grains could be treated as diamagnetic or paramagnetic (depending on sweep direction) spheres of one particular size. This model gave a striking good agreement with the measurements. It turns out that the most important parameter in the theory is the ratio of mean free path to grain size $x = \lambda/\Lambda$. For $x \leq 2$, as clearly was the case in reference [6], only one maximum is expected in the magnetoresistance, while for $x > 2$ at least two maxima will appear. In order to test this very clear prediction we have manufactured another sample with smaller lead grains, and as we shall see, this indeed gives the predicted extra peak.

Samples were prepared from conventional MBE grown AlGaAs/GaAs modulation doped heterostructures with the 2DEG embedded some 100 nm below the surface of the samples. The samples used had mobilities in the range from 80 to $100m^2/Vs$ and carrier densities ranging from $3 \times 10^{11} m^{-2}$ to $4 \times 10^{15} m^{-2}$. The mean free path thus ranged from $7\mu m$ to about $10\mu m$. The wafers were mesa-etched to form standard $200\mu m$ wide Hall bars. In the present experiment lead powder with grain sizes of roughly $5\mu m$ was diluted in PMMA resist and spin-coated on the surface of the samples. The small lead grains however had the tendency to group together and form larger lead particles on the surface of the samples. This is clearly seen in fig. 1 which shows a SEM picture of the surface of one of our samples. It turned out that the mentioned asymmetry effect varied somewhat from sample to sample, and we ascribe this variation to the extend of which the lead grains were grouped together.

The magnetoresistance of the samples were measured below T_c in a four-probe configuration and normalised with respect to the length-width ratio of the probed mesa area. At each temperature we first measured the "virgin" sweep up curve and subsequently the corresponding sweep down and sweep up curves. Each time we swept the magnetic field to a numerical value larger than the critical field. In reference [6] we showed that the amplitude of the magnetoresistance anomalies are proportional to the squared amplitude of the modulation in the magnetic field. The amplitude of the peaks in magnetoresistance will thus depend on the amount of trapped flux. As seen in fig. 2 the trapped flux may either enhance or decrease the flux density variation produced by each lead particle. For the virgin sweep up curve no flux is trapped and the magnetic field inhomogeneities are produced exclusively by the Meissner effect. When the field has been above B_c and is swept down again, then, while $0 < B < B_c$, the frozen flux emerging under each lead grain will have the same direction as the externally applied flux, while the trapped flux outside the grain will oppose the external flux. As seen on the second schematic of fig. 2 the net effect will be a relatively smaller perturbation of the overall flux density, and thus a small peak in the corresponding magnetoresistance. However, when B reaches below 0 on the down sweep, the trapped flux will tend to increase the amplitude of the overall flux-density modulation, and thus give rise to a large peak in the magnetoresistance. Of course, the opposite situation occurs when B reaches below $-B_c$, and consecutively is swept up again. So, on the up sweep the peak for $-B_c < B < 0$ is small and the peak for $0 < B < B_c$ is large. This behaviour is clearly seen in the experimental traces in fig. 3.

The theory for the observed effect has been described in reference [6]. The starting point is the usual semiclassical Boltzmann equation in the relaxation time approximation, where the magnetic inhomogeneities are incorporated as a spatially varying magnetic field, composed of the inhomogeneities produced by the individual lead grain, to be inserted in the driving force term of the Boltzmann equation. All lead grains are assumed to have the same size. The random

distribution of the lead grains on the surface enters the theory via a correlation function. In the case of pure Meissner flux expulsion our theory is particularly simple, since here it is easy to model the flux density variation produced by each lead grain. The overall magnetic field modulation can then be expressed as a sum over all lead grains. The magnetic field modulation should then be averaged over different distributions of lead grains on the surface of the semiconductor. In the right panel of fig. 3 we show a comparison of the theoretical curve to the measured one for a virgin trace. The fit gives $\Lambda = 3.45 \mu\text{m}$ and $n_{\text{pg}} = 2.5 \times 10^9 \text{ m}^{-2}$ for the size and the density of the lead grains respectively. Both numbers are in excellent agreement with the known experimental parameters. The ratio of the mean free path to the average grain size thus turns out to be 2.6, and our theory predicts two peaks in the magnetoresistance for the following sweep up and sweep down traces[7], as indeed we observe for this particular sample.

References
 * Present address: Physics Dept., Technical Univ. of Denmark, Building 309, DK-2800 Lyngby, Denmark

- [1] J.Rammer and A.L.Shelankov, Phys.Rev. B 36, 3135 (87).
- [2] A.K.Geim, JETP Lett. 50, 389 (89).
- [3] S.J.Bending et al., Phys.Rev.Lett. 65, 1060 (90).
- [4] A.K.Geim et al. Phys.Rev. B 49, 5749 (1994).
- [5] F.B.Mancoff et al. preprint.
- [6] A.Smith, R.Taborowski, L.Theil Hansen, C.B.Sørensen, P.Hedegård, and P.E.Lindelof, Phys.Rev. B 50, 14726 (94).
- [7] P.Hedegård and A.Smith, Phys.Rev. B 51, 10869 (1995)

Figure Captions

Figure 1.

SEM micrograph of the one of our samples. The white bar in the lower left corner is 100 micron long, and defines the length scale. The mesa etch is faintly seen. The 5 micron lead grains tend to cluster on the surface and effectively producing somewhat larger particles. The magnetoresistance recorded for this sample however still showed a behaviour corresponding to a distribution of grains with an average size of roughly 5 micron.

Figure 2.

Various situations showing the magnetic field modulations (bottom curves) resulting from trapped flux and flux expulsion of an externally applied magnetic field. The shaded circles represent cross sections of the lead grains in a magnetic field (shown as flux lines). The first picture represents the first (virgin) sweep up, where no flux is trapped. The amplitude of the corresponding magnetoresistance peak is proportional to the square of the magnetic field modulation.

Figure 3.

A set of traces showing a large asymmetry in peak heights for different polarities and sweep directions of the magnetic field. The curves correspond to all the various situations in fig. 3. The right panel shows the virgin trace together with a theoretical curve as described in the text.



Fig.1

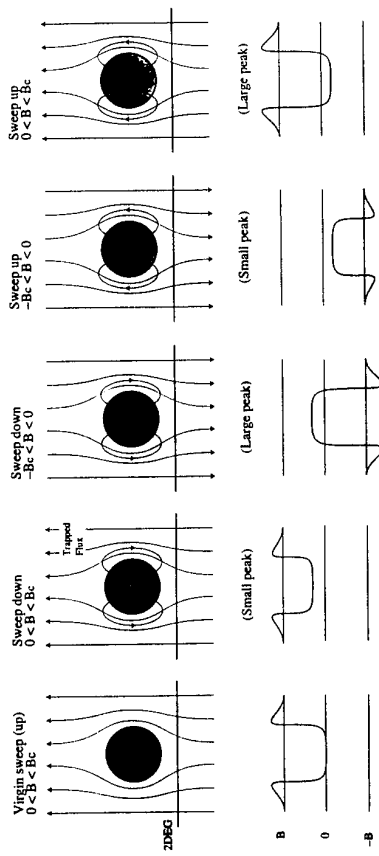


Fig.2

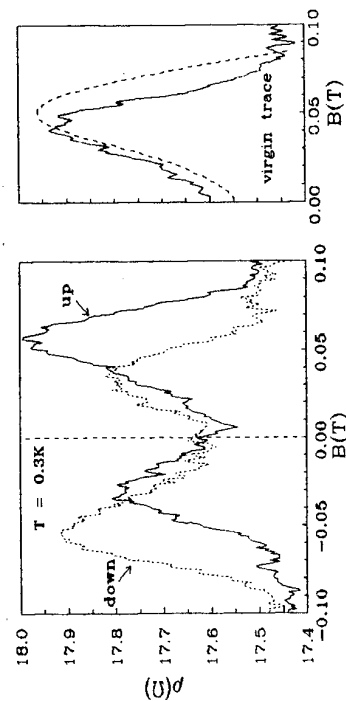


Fig.3

Microwave-Induced “Somersault Effect” in Flow of Josephson Current through a Quantum Constriction

L. Y. Gorelik*, V. S. Shumeiko*, R. I. Shekhter, G. Wendin, and M. Jonson
 Chalmers University of Technology and Göteborg University, Göteborg, Sweden, and
 *B. Verkin Institute for Low Temperature Physics and Engineering, Kharkov, Ukraine.

Abstract

We consider the supercurrent flow through a gated two-dimensional normal constriction confined between superconducting electrodes. Photon-assisted Landau-Zener transitions between Andreev bound states in the constriction are shown to give rise to a series of reversals in the direction of supercurrent flow.

The Josephson coupling between two superconductors is associated with charge transfer through the non-superconducting region that separates them. The coupling is therefore determined in a crucial way by the nature of the electron states in this region. Quantum mechanical tunneling through an insulating barrier (SIS junction), itinerant propagation of free electrons through a normal region (SNS), and propagation of plasma waves (boson modes) through a 1D-channel of strongly correlated electrons are examples of charge transfer mechanisms in different types of weak links.

The electron states carrying the supercurrent in the non-superconducting region can be influenced by an external time-dependent field. This possibility raises interesting questions on the nature of Josephson coupling due to nonequilibrium electron states. This is the problem addressed here.

Nonequilibrium effects can be expected to be particularly important in situations where the Josephson coupling is mediated by a normally conducting microconstriction, where only a few electron states — Andreev bound states — carry the current. Weak links through ballistic microconstrictions in the two-dimensional (2D) electron gas of gated semiconductor heterostructures have recently been observed experimentally [1]. An important feature of this structure is that the electron energy levels in the constriction can be easily influenced by applying a potential to the gate electrodes. In this way the electron concentration (and hence the Fermi wavevector, k_F) in the channel can be controlled. The potential due to induced charges on the gate electrodes furthermore provides a mechanism for coupling the 2D electrons to an external electromagnetic field.

The Josephson coupling between two superconductors can be expressed in terms of the phase difference ϕ between their respective order parameters. We will first consider this phase difference to be a fixed quantity, which in a SQUID geometry can be controlled entirely by the magnetic flux. Andreev reflection at the boundaries between superconducting and normal regions in a SNS configuration is known to lead to a discrete set of energy levels within the energy gap of the superconductors. Due to spatial quantization in the transverse y -direction, the energy spectrum of the Andreev bound states in a narrow and short constriction consists of a discrete set of pairs of levels labelled by the quantum number n [2],

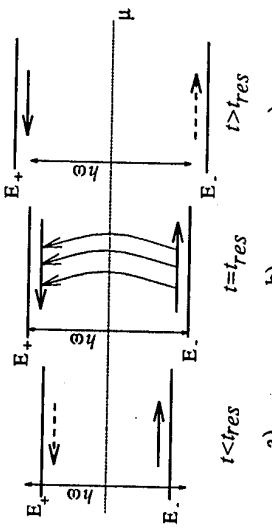
$$E_{n,\pm} = \pm \Delta \sqrt{1 - T_n(k_F)} \sin^2(\varphi/2). \quad (1)$$

Energy is measured from the Fermi level and the transmission eigenvalue $T_n(k_F)$ is related to the propagation of normal Fermi level electrons through the junction (along the x -direction).

For a short junction all of the Josephson current is carried by these Andreev states. It is important to note that states below ($E_{n,-}$) and above ($E_{n,+}$) the Fermi level carry current in different directions.

We shall consider a situation where a gate-induced time-dependent potential is a sum of one part $V_0(t)$, which varies slowly on a scale related to the interlevel spacing, and another rapidly oscillating part $V_\alpha \cos(\omega t)$, where ω is of the order of the interlevel spacing. The high-frequency component of the induced potential produces interlevel transitions, which result in a strong coupling of pairs of Andreev states at resonance. Due to the change in the interlevel distances resulting from a slow time variation of k_F the condition for resonance, $\omega = \omega_{\alpha\beta} \equiv (E_\alpha - E_\beta)/\hbar$ ($\alpha = n, \pm$), can be met for any pair of levels at some time $t = t_{\text{res}}$ even if they are out of resonance with the electromagnetic field at $t = 0$, when the potential is switched on.

Such a drift into and out of resonance is illustrated in the figure, where panel (a) shows a non-resonant configuration. The position of a pair of levels $E_{n,\pm}$ is indicated, and the directions of the corresponding partial currents are marked by arrows. The dashed arrow for the state $E_{n,+}$ above the Fermi energy illustrates that this state is unoccupied at zero temperature and hence does not contribute to the total current. When the two levels drift into resonance, as in panel (b), resonant interlevel mixing results in a finite population of the upper level and a corresponding contribution to the partial Josephson current in the reverse direction. If the Andreev levels pass slowly enough (see below) through the resonance, the result of the dynamic evolution is a complete depopulation of the lower level. Hence, as the levels drift out of resonance the Josephson current has been turned around and the current is flowing in the opposite direction (c). After some time out of resonance, the system relaxes back to its ground state and the Josephson current returns to the forward direction. The microwave-induced “Somersault” has been completed.



A problem of interlevel transitions due to adiabatic level drift was first discussed by Landau and Zener in connection with molecular pre-dissociation [3]. It follows from their theory that the probability $W_{\alpha\beta}$ for the system to be in a different state after passing through the resonance, $W_{\alpha\beta} = 1 - e^{-2\pi\gamma_{\alpha\beta}^2}$, $\gamma_{\alpha\beta} = |V_{\alpha\beta}/\hbar||\dot{\omega}_{\alpha\beta}(t_{\text{res}})|^{-1/2}$, is determined by the product of the interlevel transition frequency $|V_{\alpha\beta}|/\hbar$ and the characteristic time $\delta t_{\text{res}} = |\dot{\omega}_{\alpha\beta}t_{\text{res}}|^{-1/2}$ the system spends on resonance. If the characteristic time is long, $\gamma \gg 1$ ($\delta t_{\text{res}} \gg \hbar/|V_{\alpha\beta}|$), the transition between modes α and β is complete.

In the absence of relaxation, the Josephson current is solely determined by the dynamic evolution of the electron-hole wave function. Before the high frequency field is switched on, the Andreev levels are in equilibrium and the Josephson current has its equilibrium value I_0 . The deviation of the time averaged current, $\delta \bar{I} = \bar{I} - I_0$, is:

$$\delta \bar{I} = \sum_{\{\alpha,\beta\}_{\text{res}}} W_{\alpha\beta} (n_\alpha - n_\beta) (I_\beta - I_\alpha), \quad (2)$$

where $I_{\alpha\beta} = (2e/h)dE_{\alpha\beta}/d\phi$, and $n_{\alpha\beta} = n_F(E_{\alpha\beta})$. The summation in (2) is over pairs of levels, $\{\alpha, \beta\}_{\text{res}}$, which have passed through a resonance. As we can see from Eq. (2) only transitions between states with energies of opposite signs (the Fermi level is at zero) contribute to $\delta \bar{I}$. If the Josephson current through the channel is carried by a single pair of Andreev levels, the direction of the Josephson current is reversed for $W \geq 1/2$. Of course for $t \gg t_{\text{res}}$ there is no resonant coupling with the electromagnetic field to maintain the inverse population. Any inelastic relaxation mechanism will bring the system back to its equilibrium state and restore the original direction of Josephson current. This process of dynamically switching on the inverse population of Andreev states and the subsequent inelastic relaxation manifests itself as a ‘Somersault’ of the Josephson current.

Equation (2) is significantly simplified if the microconstriction joining the two superconductors is an adiabatically smooth ballistic channel with quantized energy levels (modes)

corresponding to the transverse electron motion. In this situation each propagating mode produces one pair of Andreev levels of the type (1) — one level above- and one below the Fermi energy — and the transmission eigenvalue T_n reduces to the normal electron transmission coefficient of the n -th mode,

$$T_n(k_F) = \left[1 + \frac{4R}{(1-R)^2} \sin^2(k_n L) \right]^{-1}, \quad (3)$$

where $k_n = \sqrt{k_F^2 - \pi^2 n^2/d^2}$, and R is the probability for electron backscattering at the Sm-S boundary. The electromagnetic field couples levels only within these pairs, i.e. if $\sigma = \pm$ one has $V_{\alpha\alpha'} = \delta_{n,n'}\delta_{\sigma,-\sigma'}V_n$ and consequently $\omega_{\alpha\alpha'} = \delta_{n,n'}\delta_{\sigma,-\sigma'}\omega_n$. The matrix element V_n has the form:

$$|V_n|^2 = V_\omega^2 \frac{L^2}{\xi_{\text{Sm}}^2} T_n^3 \frac{R}{(1-R)^2} \frac{\cos^2(k_n L) \sin^2 \phi}{1 - T_n \sin^2(\phi/2)}. \quad (4)$$

In the ballistic case the total current at zero temperature, taking into account Eq. (2), can be written in the form:

$$\bar{I} = \sum_n I_n (1 - 2W_n), \quad (5)$$

where the summation is formally done over all transverse modes and W_n is assumed to be zero for those Andreev levels which have not passed through a resonance.

As one can see from Eq. (4), the electromagnetic field can only mix Andreev states if the probability for electron backscattering at the Sm-S boundaries is finite. A ‘Somersault’ which changes the total momentum of the system can evidently only occur if backscattering is possible. It is interesting that if there is a geometric resonance, $k_n L = n\pi$, the Somersault

effect still takes place according to (2) even though the microconstriction is fully transparent for electrons in mode n , $T_n(k_F) = 1$. This fact provides an important possibility of distinguishing between resonant transmission through the double barrier structure and ballistic propagation in the absence of normal backscattering from Sm-S boundaries.

It is also interesting to consider the case when there is no drift with time of the Andreev levels, i.e. when $V_0(t) = 0$. A permanent resonant coupling of Andreev states is now possible and leads to an equalization of the average level population [4] and therefore to a complete blockade of the Josephson current. This phenomenon can be observed as a sequence of dips of the Josephson current is plotted as a function of the frequency of the electromagnetic field. The number of dips should equal the number of propagating modes in the ballistic constriction and the dip amplitude should equal the single mode contribution I_n to the stationary Josephson current.

In the discussion so far we have assumed that the phase difference between the two superconductors is constant in time. When the Josephson junction is connected to a current source, the Somersault effect causes phase slips at times when Andreev levels are resonantly coupled. The phase slips in turn manifest themselves as voltage spikes. The characteristic time scale of a phase slip Δt is determined by the Josephson plasma frequency ω_J , and in the case where the duration of the interlevel transition, δt_{res} , is shorter than Δt , i.e. if $1/\omega_J \gg \delta t_{\text{res}}$, the estimate for the amplitude and the duration of the voltage spike is $U = (\hbar/2e)\phi \sim (\hbar/e)\omega_J$ and $\Delta t \sim 1/\omega_J$ respectively.

The Somersault effect discussed above relies on the preservation of phase coherence during the dynamical evolution of the Andreev states and the redistribution of level populations at resonance. This implies that the phase breaking time τ associated with inelastic electron-phonon relaxation should be the largest time scale in the problem: $1/\omega_{\alpha\beta} \sim \hbar/\Delta \ll \hbar/V_{\alpha\beta} \ll \delta t_{\text{res}} \ll \tau$. According to Ref. [5] a typical estimate of the time τ in a superconductor is $\tau \Delta/\hbar > 10^2$. This value makes it possible to fulfil the above inequalities in a device with normal region length $L \approx \xi_{\text{Sm}}$ if the amplitude V_ω is of order of 10 mV. Meanwhile, an amplitude of the voltage spikes in a current biased junction is of order of 1-10 mV. Even though the considerable impedance mismatch between our device ($\approx 10 \text{ k}\Omega$) and a high frequency amplifier ($\approx 50 \Omega$) will reduce the signal by a factor of 100, the noise level of Low Noise Cooled Microwave Amplifiers available today is an order of magnitude lower.

References

- [1] A. Dimoulas, J.P. Heida, B.J. van Wees, T.M. Klapwijk, W. van der Graaf, and G. Borgnis, Phys. Rev. Lett., **74**, 602 (1994).
- [2] C.W.J Beenakker, Phys. Rev. Lett. **67**, 3836 (1991).
- [3] I.D. Landau, Phys. Z. Sowjet **1**, 88 (1932); C. Zener, Proc. R. Soc., Ser.A **137**, 696 (1922); **140**, 660 (1933).
- [4] V.S. Shumeiko, G. Wendin, and E.N. Bratus', Phys. Rev. B **48**, 13129 (1993).
- [5] S.B. Kaplan, C.C. Chi, D.N. Langenberg, J.J. Chang, S. Jafaney, and D.J. Scalapino, Phys. Rev. B **14**, 4854 (1976).

**COMPARATIVE TORQUE STUDIES OF α -(BEDT-TTF)₂MHg(SCN)₄
WITH M = K, Tl, NH₄**

P. Christ^a, W. Biberacher^a, A. G. M. Jansen^b, M. V. Kartsovnik^c, A. E. Kovalev^c,
N. D. Kushch^d, E. Steep^b, and K. Andress^a

^a Walther Meissner Institut, D-85748 Garching
^b High Magnetic Field Laboratory, F-38042 Grenoble
^c IISSP, Ru. Ac. Sci., Chernogolovka, 142432, Russian Federation
^d ICP, Ru. Ac. Sci., Chernogolovka, 142432, Russian Federation

Abstract

We report comparative studies of the oscillatory (de Haas - van Alphen effect) and the steady (anisotropy of the static susceptibility) torque in the quasi-two-dimensional organic metals α - (BEDT-TTF)₂MHg(SCN)₄ with M = K, Tl, NH₄. The measurements were carried out with a torque-magnetometer in magnetic fields up to 28T and temperatures between 0.4 and 4.2K. Up to the highest fields no anomalous behaviour of the steady or oscillatory torque is observed in the NH₄-salt. In contrary the K- and the Tl-salt undergo a phase transition at around 23T and 26T respectively, the so-called kink transition. These two compounds show very similar behaviour. For $\Theta \leq 60^\circ$, where Θ is the angle between the magnetic field and the normal to the conducting planes, the phase transition is characterized by a strong increase in the oscillation amplitude. For $\Theta > 60^\circ$ the kink transition can no longer be clearly seen, but up to the highest fields several anomalies appear together with strong hysteresis of the steady torque.

Introduction

The isostructural charge-transfer salts α - (BEDT-TTF)₂MHg(SCN)₄ with M = K, Tl, Rb and NH₄ are quasi-two-dimensional organic metals based on the donor-molecule bis(ethylenedithio)-tetraethialvalene (BEDT-TTF). All these compounds show metallic conductivity down to low temperatures [1,2]. Whereas the NH₄-salt becomes superconducting at ambient pressure and temperatures below 1K [1] the other three compounds undergo a phase transition around 10K, which is indicated by a small shoulder in the resistivity [2,3]. Susceptibility measurements show that this magnetic groundstate below 10K is characterized by an antiferromagnetic order, which is interpreted as a Spin-Density-Wave (SDW) [4]. The magnetoresistance in this groundstate increases strongly in low fields, going through a maximum at 10T and showing a kink at fields about 24T which is interpreted as a phase transition (the so called kink transition). Between 10 and 24T a hysteretic behaviour of the magnetoresistance is reported [5]. In fields below the kink transition both the de Haas-van Alphen (dHvA) and the Shubnikov-de Haas (SdH) oscillations are splitted below 2K [6,7,8]. High field torque measurements on the K-salt [8] show a complex angular and field dependence of the static susceptibility. In this compound strong hysteretic effects are observed up to 28T. The aim of this contribution is to compare the oscillatory and steady torque of (BEDT-TTF)₂KHg(SCN)₄ with measurements on the isostructural Tl- and NH₄- salts, where the Tl-compound has also a magnetic groundstate but the NH₄-salt becomes superconducting.

Experiment

The (BEDT-TTF)₂MHg(SCN)₄ single crystals (M = K, Tl and NH₄) were obtained by electrocrystallization as described in Ref. [9] (typical masses are between 50 and 200 µg). For the

magnetization measurements a capacitive cantilever torquemeter rotatable around one axis in situ [10] was used. Magnetic fields up to 28T were performed by the hybrid magnet at the high magnetic field laboratory in Grenoble and the temperatures down to 0.4K were produced utilizing a ³He cryostat.

Results and Discussion

Fig. 1 shows typical dHvA-oscillations of the K-, Tl-, and the NH₄-compound with the magnetic field between 20 and 28T and directed almost perpendicular to the crystal ac-plane. Θ is the angle between the perpendicular to the highly conducting ac-plane of the crystal and the direction of the magnetic field. The results for the Tl- and K-compound shown in Fig. 1 are typical for $\Theta < 25^\circ$. Up to this angle the low field state is characterized by a splitting of the oscillations. The phase transition is reflected in a strong increase of the dHvA-amplitude and disappearance of the splitting. Both, the waveform and the amplitude show hysteretic behaviour around this transition in the range of about 21T to 25T in the K-salt and 23T to 28T in the Tl-compound. On decreasing the field the large amplitude of the high field state is retained down to lower fields. In the K-compound a hysteresis of the torque between the up and the down sweep curves appears up to the highest field. The down sweep curve is shifted to higher torque values (note that this effect is completely absent in the NH₄-salt - Fig. 1c). We therefore conclude, that even at 28T the K-compound is not in a normal metallic state. In the case of the Tl-salt the hysteresis in the steady torque is not seen up to 28T likely because of the higher value of the transition field. The first appearance of this shift perhaps is seen at 28T (Fig. 1b).

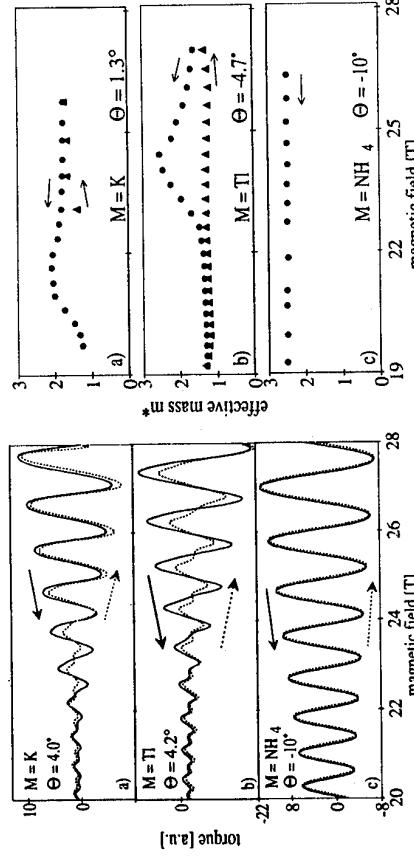


Fig. 1: dHvA-oscillations recorded at T = 0.4K of α - (BEDT-TTF)₂MHg(SCN)₄ with M = a) K, b) Tl, and c) NH₄.

Since the nature of the phase transition is not yet clear it is of interest to study the field dependence of the effective cyclotron mass $m^* = n/m_e$ in these compounds at the phase transition. We determined the field dependent dHvA-amplitude by fast Fourier transformation (FFT) of short oscillatory patterns. Data between 4.2K and 0.4K were used for the mass fits for the Tl- and K-salts whereas for the NH₄-compound the temperature interval was from 0.4 to 1.3K. In the NH₄-

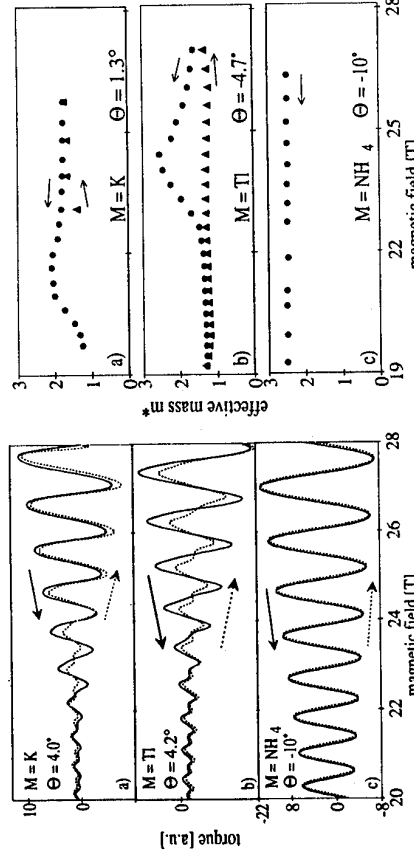


Fig. 2: The field dependence of the effective mass $m^* = n/m_e$ of α - (BEDT-TTF)₂MHg(SCN)₄ with M = a) K, b) Tl, and c) NH₄.

compound the effective mass determined at $\Theta = 10^\circ$ is field independent and amounts to $m^* = 2.6 \pm 0.1$ (Fig. 2c) in good agreement with the results of other groups [11]. No difference between increasing and decreasing the field is observed. In the K- and Tl-compounds there is a strong difference between the up and down sweep. Most striking are the humps in the curves obtained from data of decreasing the magnetic field: m^* increases roughly by a factor of two in the K- and Tl-salt (Fig. 2a,b). These humps are exactly in that field range of the hysteretic dHvA amplitude (Fig. 1). Very likely the origin of the mass peaks lies in the temperature dependence of the hysteresis magnitude. At 4.2K no hysteresis is seen within the experimental error. Upon cooling, the irreversibility arises and grows up rapidly. The dHvA amplitude recorded at the down-sweep increases faster than at the up-sweeps. Thus, the observed mass peaks are associated rather with the dynamics of the phase transition than with the intrinsic changes of the carrier characteristics. A clear increase from $m^*=1.4$ [3,10] to ~ 1.8 is observed. In this data set it was not possible to get reliable mass fits at lower fields because of the strong splitting in the low field regime at low temperatures ($T < 1\text{K}$). Very recently N. Harrison et al. [12] reported an increase of the effective mass up to 2.7. These data were taken from pulsed field experiments up to 55T. A possible explanation for the lower values found in this work could be that the phase transition is not yet completed at 28T even in the K-salt. In the Tl-compound no considerable difference between the low- and high-field masses is found (Fig. 2b). Higher fields are necessary here to determine the high-field state properties.

For $25^\circ < \Theta \leq 60^\circ$ the phase transition is still characterized by a strong increase of the dHvA-amplitude. Around $\Theta = 40^\circ$ for the K-salt and 44° for the Tl-salt a minimum in the amplitude of the high field state is observed, but a clear spin zero was not found in these experiments, in contrast to that reported in [7b].

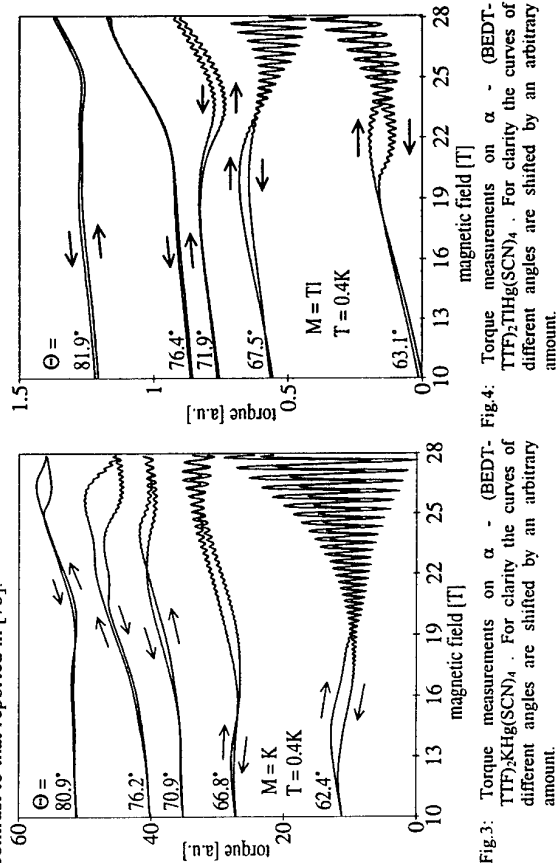


Fig. 3: Torque measurements on α - $(\text{BEDT-TTF})_2\text{KHg}(\text{SCN})_4$. For clarity the curves of different angles are shifted by an arbitrary amount.

Fig. 3 shows a selection of curves measured on the K-salt at angles $\Theta > 60^\circ$. In this angle range the kink transition can no longer be clearly seen but the steady torque becomes more complex, showing strong hysteresis effects at least up to 28T (a constant anisotropy of the static susceptibility causes a reversible torque signal which increases quadratically with the magnetic field [10]). The reproducibility of these anomalies can be seen in Fig. 3 of Ref. [8b], where measurements at similar angles on sample of a different batch are presented. In comparison to the K-salt an angular dependence of the torque at almost the same angles of the Tl-salt is shown in Fig. 4. Although it looks very similar to Fig. 3 the structure of the steady torque signal is not as pronounced as in the K-compound and the hysteresis occurs at higher fields. This can especially be seen at $\Theta \approx 81^\circ$ where the up and down sweep curves are reversible in the Tl-compound, whereas the K-salt shows a strong hysteresis above 22T. Obviously, these two compounds show nearly the same structure in the steady torque at high angles in high fields, where the features in the Tl-salt are shifted by approximately 6T to higher field values compared to the K-salt. This makes it very probable that both, the K- and the Tl-salt are in the same high field state above the kink transition. At least up to angles $\Theta > 60^\circ$ and fields up to 28T there are no structures or hysteretic effects observed in the isostructural NH₄-compound.

Summarizing our results, we conclude that the high-field state is the same in the K- and Tl-salts, in agreement with [7], the main difference being in the critical field value. The complicated behaviour of the high-field state implies that it differs from the usual metallic state which is believed to take place above the transition temperature.

The work was partially supported by the NATO Laboratory Linkage Grant HTECH.LG 930278.

References

- [1] H. Mori, S. Tanaka, K. Oshima, M. Oshima, G. Saito, T. Mori, Y. Maruyama, and H. Inokuchi, Solid State Commun. **74**, 1261 (1990)
- [2] N. D. Kushch, L. I. Buravov, M. V. Kartsovnik, V. N. Laukin, S. I. Pesotskii, R. P. Shibaeva, L. P. Rozenberg, E. B. Yagubskii, and A. V. Zvarikina, Synth. Met. **46**, 271 (1992)
- [3] T. Sasaki, N. Toyota, M. Tokumoto, N. Kinoshita, and H. Anzai, Solid State Commun. **75**, 93 and 97 (1990)
- [4] T. Sasaki, H. Sato, and N. Toyota, Synth. Met. **41**, 43, 2211 (1991)
- [5] T. Osada, R. Yagi, A. Kawasumi, S. Kagoshima, N. Miura, M. Oshima, and G. Saito, Phys. Rev. B **31**, 5428 (1990)
- [6] J. S. Brooks, C. C. Agosta, S. J. Klepper, M. Tokumoto, N. Kinoshita, H. Anzai, S. Uji, H. Aoki, A.S. Perel, G. J. Athas, and D. A. Howe, Phys. Rev. Lett. **69**, 156 (1992)
- [7] M. V. Kartsovnik, D. V. Mashovets, D. V. Smirnov, V. N. Laukin, A. Gilevskii, and N. D. Kushch, J. Phys. I France **4**, 159 (1994); M. V. Kartsovnik, A. E. Kovalev and N.D. Kushch, J. Phys. I France **3**, 1187 (1993)
- [8] P. Christ, W. Biberacher, H. Müller, K. Andres, E. Steep, and A. G. M. Jansen, Physica B **204**, 153 (1995); P. Christ, W. Biberacher, H. Müller, K. Andres, E. Steep, and A. G. M. Jansen, Synth. Met. **70**, 823 (1995)
- [9] W. Biberacher, C. P. Heidmann, H. Müller, W. Joss, Ch. Probst, and K. Andres, Synth. Met. **55**-57, 2241 (1993)
- [10] P. Christ, W. Biberacher, H. Müller, and K. Andres, Solid State Commun. **91**, 451 (1994)
- [11] J. Wosnitza, G. W. Crabtree, H. H. Wang, K. D. Carlson, M. D. Vashon, and J. M. Williams, Phys. Rev. Lett. **67**, 263 (1991); M. Doporto, F. L. Pratt, J. Singleton, M. Kurmo, and W. Hayes, Phys. Rev. Lett. **69**, 991 (1992)
- [12] N. Harrison, A. House, I. Duckers, J. Caulfield, J. Singleton, F. Herlach, W. Hayes, M. Kurmo, and P. Day, to be published

High-field Shubnikov-de Haas effect in the organic superconductor α -(BEDT-TTF)2NH4Hg(SCN)4

P. S. Sandhu, G. J. Athas, J. S. Brooks
Department of Physics, Boston University, Boston Massachusetts 02215

E. G. Hannappel, J. D. Goetsee, D. W. Rickel
Los Alamos National Laboratory, Los Alamos, New Mexico

M. Tokumoto, N. Kinoshita, T. Kinoshita, and Y. Tanaka
Electrotechnical Laboratory, Tsukuba, Ibaraki 305, Japan

Abstract

We have studied the Shubnikov-de Haas oscillation waveforms of the quasi-two dimensional organic superconductor α -(BEDT-TTF)2NH4Hg(SCN)4, in pulsed fields up to 50 T. Analysis of the field and temperature dependence of the oscillations reveals strong deviations from the standard Lifshitz-Kosevich formalism. This discrepancy manifests itself in the form of a field dependent effective mass parameter, non-linear Dingle plots and anomalously high harmonic content. It is argued that these deviations are a consequence of the highly two-dimensional nature of the material in the approach to the quantum limit.

Introduction

Organic conductors based on the molecular building block, BEDT-TTF (bis-ethylenedithio-tetrathiafulvalene), have been extensively studied in recent years owing to their numerous interesting properties [1]. These quasi-two dimensional charge transfer salts show unusually strong quantum oscillations [2], exhibit magnetic breakdown [3], and have been the source of a new technique for studying Fermi surface topology, namely angular dependent magnetoresistance oscillations [4].

Previous work in these materials has been carried out under the assumption that the quantum oscillations are well described by the Lifshitz-Kosevich (LK) formula [2,4,5]. And indeed at fields below 20 T, where most of the work has been concentrated, the LK formula seems to be a good approximation. We have recently studied the Shubnikov-de Haas effect in the material, α -(BEDT-TTF)2NH4Hg(SCN)4, in pulsed magnetic fields up to 50 T. The waveshape and harmonic content of the oscillations at the highest fields, are appreciably different from those observed in the low-field regime. Our results indicate strong deviations from the standard Lifshitz-Kosevich formalism and suggest field and temperature limitations to the applicability of the LK formula for these near two-dimensional systems.

Experimental

In this work, the sample resistances were measured using four terminal dc detection, with gold wire leads mounted so as to minimize appreciable closed loop pick up from the rapidly changing pulsed magnetic field. Samples were measured at 7 different temperatures ranging from 0.4 K to 4 K by controlling the pumping rate of the He3 and He4 reservoirs. The near instantaneous nature of the magnet pulses resulted in excellent temperature control. These measurements were done at the Los Alamos Pulsed Field Facility in Los Alamos, NM.

Figure 1 shows the magnetoresistance for this sample up to 50 tesla at 0.4 K. Below 1 K, this material undergoes a superconducting transition whose critical field is reached at < 0.1 T, and by 10 T the background MR saturates at about 200Ω with large superimposed SdH oscillations peaking at a maximum amplitude of 7 times the background MR. Plotting the indexed oscillation peaks vs. $1/H$ the lowest Landau level reached is determined to be 12. As the field increases, the lineshape of the SdH oscillations changes from sinusoidal to increasingly sharp "spikes" riding on

a very flat MR background (Fig. 1 a)). As the temperature is decreased the high field oscillations become more spiked in shape and highly asymmetric with respect to the horizontal axis.(Fig. 1 b).

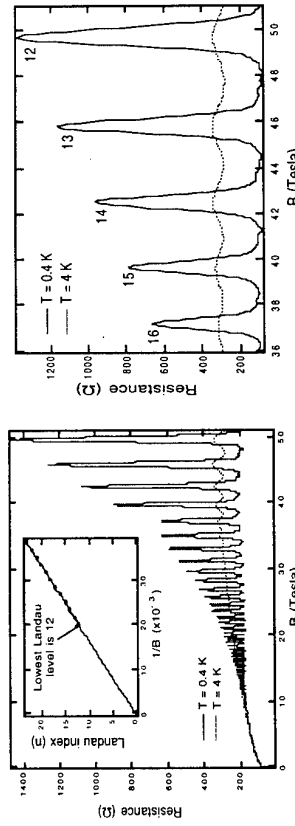


Fig. 1 a) Field sweeps for $M = NH_4$ showing the SdH oscillations, at the highest (4.2 K) and lowest (0.4 K) temperatures measured. Inset shows Landau level index vs inverse field. b) Temperature dependence of low index oscillation behavior.

Results and discussion

Analysis of the wave shapes is done by first dividing out the MR background and then Fast Fourier Transforming (FFT) over evenly-spaced windows in $1/H$ [6]. A FFT over the whole range of the sweep reveals strong spectral content at the highest fields - up to 9 harmonics of the fundamental frequency, $F = 589 \pm 7$ T, are discernible. Determination of the effective mass reveals what appears to be a strong field dependence (Fig. 2 a). From the first harmonic, $\mu_c = m_c/m_0 = 2.6$ at $H=16$ T, consistent with the values reported by other groups [7]. However, this value increases linearly with field, reaching 5.6 at the highest field window (centred at $B=40.4$ T). We interpret this result as an indication of the failure of the LK formalism to accurately describe this system. The apparent increase in effective mass is not a real effect, but rather a parameter, that indicates the deviation of this system from an ideal LK material. An increasing effective mass parameter indicates the amplitude of the oscillations at higher fields is suppressed relative to the LK predictions. This suppression of the oscillation amplitudes is further emphasized in plots to determine the Dingle temperature (Fig. 2 b). With increasing field, this curve deviates from the straight line fit expected from a standard Dingle plot. [8]. Only at low fields (< 20 T) can we get a reliable fit resulting in $T_D = 1$ K. The ratio of the fundamental to the first harmonic is also much greater than predicted by the LK formula, with the discrepancy increasing rapidly at higher fields.

The anomalous behaviour of the effective mass parameter and Dingle temperature as well as the unusually large harmonic content strongly suggest that the LK formula does not sufficiently explain the quantum oscillations in this system. The fact that the effective mass is sensitive to the value of the field at which the analysis is done, also accounts for the rather large discrepancies in the values of m^* reported in the literature [7]. The material used in this study is part of a family of four compounds with similar properties, which differ only by the substitution of the cation $M = NH_4$, K, Tl and Rb. The $M = NH_4$ salt is however particularly well suited for studying the deviations from the LK formalism, because the other three members show additional features associated with the formation of a density wave ground-state, which complicates the analysis. We have also made measurements on the $M = Tl$ and K salts, in both pulsed and steady fields [9] and obtained results which are qualitatively similar to those reported here. These results are also

consistent with the observation of a field dependent effective mass in these materials by other groups.[10,11].

Deviations from Lifshitz-Kosevich behaviour can occur due to magnetic interaction (M_1) when the field seen by the electrons is different from the applied magnetic field because of the magnetization of the sample [8]. M_1 becomes appreciable only when the parameter $a = 2\pi q_0 M/\Delta B$ (where $\Delta B = B^2/F$) is of the order of 1 or greater. For our sample, owing to the low value of F , a $\ll 1$. This suggests that M_1 is not a valid explanation for the non-LK behaviour in this material. Although the Lifshitz-Kosevich theory is derived under the assumption of independent particles, it is also unlikely that such a large increase in effective mass can arise as a consequence of many-body interactions alone. For most cases of experimental interest, the only effect of many-body interactions [8] is to modify the values of the LK parameters, leaving the analytic form unchanged [12,13,14].

Conclusion

We conclude that although the LK formula may be a good approximation for the quantum oscillations in these systems at relatively low fields ($B < 20$ T), it becomes increasingly invalid at higher fields at which their 2-D properties start to play a prominent role. Additional experiments in the 0-50 T field range, including the behaviour of the dHvA effect, are of special interest and are now being pursued. Further theoretical work on the modification of the LK formalism for realistic 2-D systems is required to adequately explain these experimental results.

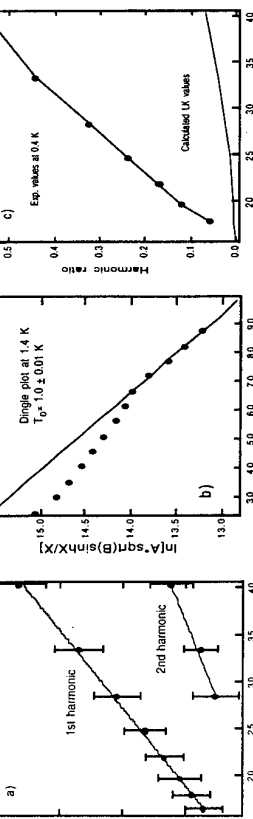


Fig. 2 a) Field-dependence of the first and second harmonic effective mass b) Dingle plot at $T = 1.4$ K. The straight line is the best fit to the low field points yielding a Dingle temperature, T_D of 1 K. The plot shows negative curvature at higher fields indicating that the amplitudes are suppressed relative to the values expected for a linear Dingle plot. c) Harmonic ratio of the fundamental to the first harmonic as function of field. Curve obtained from experimental values is compared to the theoretical curve predicted by the LK formula, for the values of effective mass (2.6) and T_D (1 K) obtained from the low field data.

The line shape of the high-field oscillations in this material is strikingly similar to the resistivity oscillations seen in 2-D semiconductor materials in the region close to the quantum limit [15]. This suggests that a proper explanation of these experimental results requires the 2-dimensionalality of the materials to be taken into account in an essential way. For quasi-two dimensional materials, both the Fermi surface and the Landau tubes are highly anisotropic in shape so that the LK formula needs to be appropriately modified [16,17]. The lowest Landau level reached in this material is as low as 12 (Fig.1), which is close enough to the quantum limit for the Landau levels to be sharply resolved. At such high fields, the spacing between the Landau levels is much larger than their broadening due to electron scattering and the density of states therefore approaches a set of evenly-spaced delta-functions. The peaks in the data correspond to the passage of the Fermi surface through one of the Landau levels. The sharpness of the Landau levels, makes the transition an abrupt one, leading to the spiky appearance of the resistivity peaks. In the regions between the peaks, the resistivity falls off sharply owing to the reduction in the density of states between the Landau levels.

We estimate that at the extreme conditions of field and temperature ($B = 50$ T, $T = 0.4$ K) the spacing of the Landau levels is $\hbar\omega_c = 2.3$ mev and their width, estimated as $\kappa(T + TD) = 0.13$ mev,

i.e. a factor of 18 smaller. In contrast at intermediate values of field and temperature ($B = 20$ T, $T = 1.5$ K), the ratio of the separation to the broadening reduces to about 5, a change large enough to explain the marked difference in the character of the oscillations under these conditions. In this sample, the latter value of field and temperature marks the limit up to which the oscillations are LK-like. For samples of poorer quality, i.e. with a higher Dingle temperature, a larger field and lower temperature would be required to see comparable effects.

Acknowledgements

We conclude that although the LK formula may be a good approximation for the quantum oscillations in these systems at relatively low fields ($B < 20$ T), it becomes increasingly invalid at higher fields at which their 2-D properties start to play a prominent role. Additional experiments in the 0-50 T field range, including the behaviour of the dHvA effect, are of special interest and are now being pursued. Further theoretical work on the modification of the LK formalism for realistic 2-D systems is required to adequately explain these experimental results.

References

1. T. Ishiguro and K. Yamaji, *Organic Superconductors* (Springer-Verlag, Berlin-Heidelberg, 1990)
2. J. S. Brooks, C. C. Agosta, S.J. Klepper, M. Tokumoto, N. Kinoshita, H. Anzai, S. Uji, H. Aoki, A. S. Perel, G. J. Athas and D. A. Howe, *Phys. Rev. Lett.* **69**, 156-159 (1992).
3. S. Uji, H. Aoki, J. S. Brooks, A. S. Perel, G. J. Athas, S. J. Klepper, C. C. Agosta, D. A. Howe, M. Tokumoto, N. Kinoshita, Y. Tanaka and H. Anzai, *Solid State Commun.* **88**, 683-686 (1993).
4. T. Osada, S. Kagoshima, N. Miura, *Phys. Rev. B* **46**, 1812 (1992).
5. F. L. Pratt, J. Singleton, M. Doporio, A. J. Fisher, T. J. B. M. Ianssen, J. A. A. J. Pinenboom, M. Kurmo and P. Day, *Phys. Rev. B* **45**, 13904-13912 (1992).
6. J. Caulfield, S. J. Blundell, M. S. L. d. C. d. Jongh, P. T. J. Hendriks, J. Singleton, M. Doporio, F. L. Pratt, A. House, J. A. A. J. Pinenboom, W. Hayes, M. Kurmo and P. Day, *Phys. Rev. B* **51**, 8325-8336 (1995).
7. J. Wosnitza, Int. Journal of Modern Phys. B **7**, 2707-2741 (1993).
8. D. Shoenberg, *Magnetic Oscillations in Metals* (Cambridge University Press, Cambridge, England, 1984).
9. P. S. Sandhu, G. J. Athas, J. S. Brooks, E. G. Hannappel, J. D. Goettee, D. W. Rickel, M. Tokumoto, N. Kinoshita, T. Kinoshita and Y. Tanaka, *Phys. Rev. B* (submitted)
10. V. N. Lautkin, N. D. Kusch, L. I. Buravov, A. G. Konenko, E. B. Yagubskii, H. Rakoto, J. M. Broto, L. Briassard, A. E. Kovalev, M. V. Kartsovnik, L. P. Rozenberg and R. P. Shibaeva, *Synth. Met.*, **69** (1995) in press
11. N. Harrison, A. House, I. Deckers, J. Caulfield, J. Singleton, F. Herlach, W. Hayes, M. Kurmo and P. Day, *Phys. Rev. B* (to be published)
12. M. Fowler and R. Prange, *Physics* **1**, 315 (1965).
13. D. Pines and P. Nozieres, *The Theory of Quantum Liquids* (Benjamin, New York, 1966).
14. J. Luttinger, *Physical Review* **119**, 1153 (1960).
15. G. Ebert, K. v. Klitzing, C. Probst, K. Ploog, *Solid State Commun.* **44**, 95 (1982).
16. D. Shoenberg, *Journal of Low Temp. Phys.* **56**, 417 (1984).
17. K. Jauregui, V. I. Marchenko, and I. D. Wagner, *Phys. Rev. B* **41**, 12922 (1990).

Millimetre Wave Magneto-Optical Studies of Low-Dimensional Organic Conductors

S.Hill¹, M.Boonman², S.Uji³, J.A.A.J.Perenboom², J.Singleton⁴, A.Widlin², J.S.Brooks¹, R.Kato⁵, H.Sawa⁵, S.Anoura⁵, M.Kurnoo^{4,6} and P.Day⁶

¹National High Magnetic Field Lab, 1800 E. Paul Dirac Dr., Tallahassee, FL 32310, USA

²High Field Magnet Lab, University of Nijmegen, Toernooiveld 1, 6525 ED, The Netherlands

³National Research Institute for Metals, Tsukuba, Ibaraki 305, Japan

⁴Clarendon Laboratory, University of Oxford, Parks Rd, Oxford, OX1 3PU, U.K.

⁵Institute for Solid State Physics, University of Tokyo, Roppongi, Minato-ku, Tokyo 106, Japan

⁶The Royal Institution, 21 Albemarle St., London WIX 4BS, U.K.

Abstract

We report millimetre-wave magneto-optical studies on a series of low dimensional organic conductors. In a previous work it was demonstrated that cyclotron resonance may be observed in BEDT-TTF salts. Considerable improvements in the experimental technique have given rise to more detailed information about the quasi-particle dynamics in these compounds. Furthermore, the previous measurements have been extend to another organic system, (DMe-DCNQI)₂Cu.

Keywords: Magnetic phenomena, Superconductivity, Many-body and quasi-particle theories, Reflection spectroscopy, Organic conductors (Chemical identity).

Introduction

In the same way that atoms may be brought together to make up 'conventional' solids, stable organic molecules may be used as fundamental building blocks for the design of new 'synthetic' compounds [1]. Stable crystalline salts, or charge transfer salts (CTS), result from electrochemical reactions in which organic molecules donate or accept charge from some other chemical entity. This process leads to electronic band formation and, by manipulating the shapes and sizes of the organic building blocks, chemists are able to engineer CTS with desired metallic, semiconducting and even superconducting properties [1]. The unique low temperature properties of these systems results from the unusual arrangements of the organic molecules in the solid state. Such arrangements tend to produce highly anisotropic electronic band structures and consequently the properties of most organic CTS are low-dimensional [1].

A large number of published works have demonstrated that magneto-oscillatory phenomena such as the Shubnikov-de Haas (SdH) and de Haas-van Alphen (dHvA) effects may be used to study the ground state properties of the BEDT-TTF (bis-ethylenedithio-tetrathiafulvalene or ET for short) salts [1, 2]; this has also been shown recently for the compound (DMe-DCNQI)₂Cu (DMe-DCNQI = 2,5-dimethyl-N,N'-dicyanquinone-dimine [3]). Although much controversy still surrounds the precise nature of the ground states in many of these compounds, the SdH and dHvA data are rarely questioned and form a sound basis upon which much of our current theoretical understanding of these systems is based [1, 2]. By contrast, there have been relatively few magneto-optical studies on organic charge transfer compounds [4 - 6].

Experimental

The measurements described here are concentrated in the frequency range 30 - 150 GHz (or 0.15 - 0.6 meV) using a variety of solid state microwave sources [4, 5, 7]. A detailed description of the experimental set-up may be found elsewhere [4, 5, 7]. To increase coupling between the radiation and the small metallic samples, mosaics containing up to 20 crystals were prepared and, in some cases, these mosaics were mounted inside resonant cavities [7]. In every case, it is

assumed, due to the high sample conductivities [1], that the detected signal gauges the sample reflectivity, i.e. no radiation penetrates the samples (see below). The samples were maintained at temperatures between 4.2 K and 1.2 K via low pressure exchange gas in contact with a liquid He bath. Magnetic fields of up to 25 T were provided by a superconducting solenoid ($B_{\max} = 17$ T) and the hybrid magnet at the University of Nijmegen in The Netherlands. All measurements were performed by illuminating the samples with a fixed radiation frequency while sweeping the field.

The α -phase BEDT-TTF salts

The quasi-two dimensional α -(ET)₂MHg(NCS)₄ salts ($M = \text{NH}_3, \text{K}, \text{Tl}, \text{Rb}$) show competing superconducting and density wave (DW) ground states [2, 5]. Bandstructure calculations predict a room temperature (300 K) Fermi surface (FS) comprising a single cylindrical hole pocket and a pair of open electron sheets [8]. The open FS sheets are prone to nesting, resulting in a DW transition ($T_{\text{DW}} \sim 10$ K) and a reconstruction of the 300 K FS [2]. Magnetotransport studies have confirmed that the α -phase salts undergo such a FS reconstruction at $T < T_{\text{DW}}$ with the exception of α -(ET)₂NH₄Hg(NCS)₄, which remains metallic down to ~ 1 K, when it becomes superconducting [2]; for this material, the measured FS is in good agreement with theory.

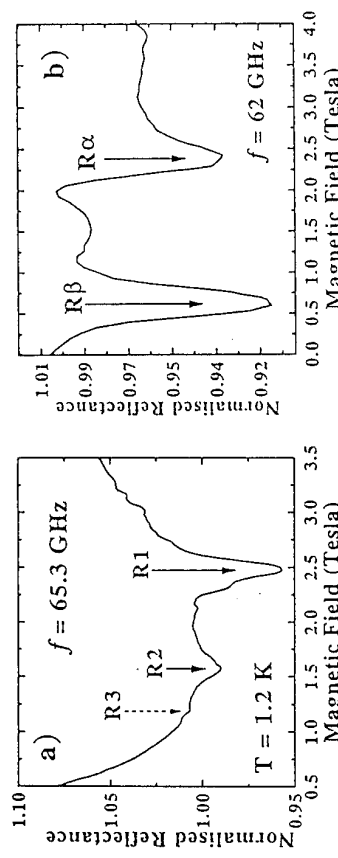


Figure 1. Normalised reflectance for a) α -(ET)₂NH₄Hg(NCS)₄ and b) α -(ET)₂KHg(NCS)₄. Figures 1a) and 1b) show, respectively, the normalised magneto-reflectance for α -(ET)₂NH₄Hg(NCS)₄ and α -(ET)₂KHg(NCS)₄. In both cases, the magnetic field was applied perpendicular to the 2D conducting planes. A series of resonant features are apparent which have been labelled in the figures in order to aid the following discussion. From these and previous measurements [4, 5], it is found that the field positions of the resonances labelled R1, R α and R β increase with increasing energy in a linear fashion characteristic of cyclotron resonance (CR).

It is apparent that the data in Figures 1a) and 1b), obtained for the two α -phase salts, is quite different. This is consistent with the fact that α -(ET)₂KHg(NCS)₄ undergoes a DW transition ($T_{\text{DW}} \sim 10$ K) whereas α -(ET)₂NH₄Hg(NCS)₄ remains metallic down to ~ 1 K. The existence of multiple resonances in Figures 1a) and 1b) is somewhat surprising, particularly in the case of α -(ET)₂NH₄Hg(NCS)₄ which is known to possess only a single cylindrical FS section. Several mechanisms have been proposed which could account for two different semi-classical k -space orbits, with different associated cyclotron mass values (for \mathbf{B}/c -axis), for the DW

material; the reader is referred to references [2, 5] for further details. In the case of $\alpha\text{-}(\text{ET})_2\text{NH}_4\text{Hg}(\text{NCS})_4$, it is proposed that the lower field resonances (R2 and R3 in Figure 1a) are harmonics of the fundamental resonance R1. It can be shown that 2D metals satisfying the 'anomalous skin effect' condition are ideal systems for observing Azbel'-Kaner resonances, particularly at low fields where the cyclotron radius becomes larger than the skin depth [5, 9]. This is due to the fact that the time averaged velocity of the 2D carriers vanishes in the plane perpendicular to the applied field; therefore, provided scattering rates are low, carriers return to the same place at the metal surface over many cyclotron orbits [5].

It has been suggested in a previous work that many-body effects are responsible for the large effective mass values deduced from ShH measurements in ET salts [4, 5]; values are typically factors of 2 - 5 times greater than the calculated band masses [8] and the CR masses deduced from the above data [4, 5]. In an analogous fashion to what is observed in a 2D *n*-channel inversion layer at the surface of Silicon [10], the cyclotron mass values deduced from successively higher harmonics increase, *i.e.* $m_{\text{eff}}/m_{\text{RI}} = 1.3$ and $m_{\text{eff}}/m_{\text{RI}} = 1.45$ (see Figure 1a). Ando ascribes this behaviour to many-body interactions which enhance all but the fundamental CR mass m_{RI} [10].

$(\text{DMe-DCNQI})_2\text{Cu}$

Although there have been many developments in the synthesis of organic conductors based on BEDT-TTF, their electronic structures remain low dimensional [1]. Recently, a molecular conductor containing Cu ions $(\text{DMe-DCNQI})_2\text{Cu}$ has been synthesised [11]. The planar DCNQI molecules are stacked in one dimensional (1D) columns along the tetragonal *c*-axis, interconnected by tetrahedrally co-ordinated Cu ions [11]. A 1D FS is formed by the overlapping $p\pi$ orbitals of the DCNQI molecules. The Cu ions, meanwhile, which form a seven fold diamond-like lattice, are found to be in a mixed valence state between Cu^+ and Cu^{2+} , indicating that the Cu 3*d* level lies close to the Fermi energy [11]. Consequently, a 3D energy band is expected in addition to the 1D $p\pi$ band [11]. Recent dHvA studies have confirmed the existence of a 3D FS [3]. The present study is motivated by speculation that the large carrier effective masses ($m > 2m_{\text{RI}}$) in this compound, as deduced from ShH measurements, result from strong many-body effects [3].

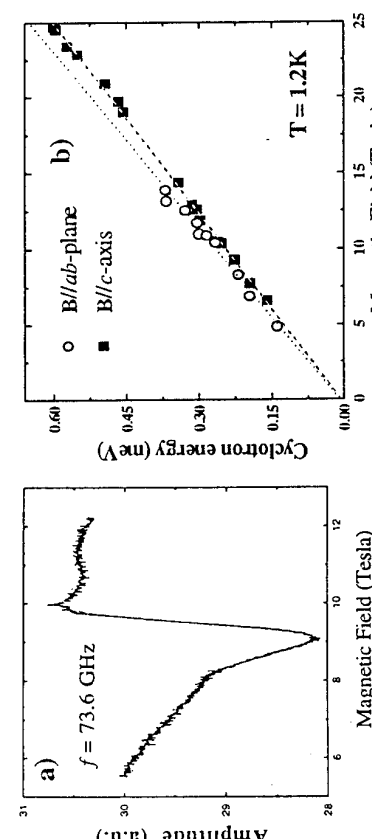


Figure 2. a) Reflectance of $(\text{DMe-DCNQI})_2\text{Cu}$ as a function of magnetic field and b) Cyclotron energies plotted against the resonance field positions.

Measurements were performed with the magnetic field applied parallel (*ll*) and perpendicular (\perp) to the 1D *c*-axis. Figure 2a) shows a typical result from a magnetic field swept measurement; the resonant features are once again attributed to CR. Figure 2b) shows the cyclotron energies plotted against magnetic field position for each sample orientation. From straight line fits to these plots, it is possible to extract cyclotron mass values for the two sample orientations, *i.e.* $m_{\text{eff}} = (4.92 \pm 0.07)m_{\text{RI}}$ and $m_{\text{eff}} = (4.5 \pm 0.2)m_{\text{RI}}$.

The similar cyclotron mass values obtained for the two sample orientations confirms the true 3D electronic nature of this material. The magnitude of the cyclotron mass values are somewhat large, however, to within $< 30\%$, they agree with the effective mass values deduced from ShH measurements [3] and from bandstructure calculations [3, 11], *i.e.* these measurements confirm that the large effective mass values are simply due to hybridisation between a flat Cu 3*d*-band and the DCNQI *p*-band, and are not a consequence of many-body effects (see also [4, 5]).

Acknowledgements

The Nijmegen Laboratory is supported by the Stichting voor Fundamenteel Onderzoek der Materie and by the European Community Large Installations Plan. The authors would also like to thank P. Goy of ABnIm for his advice and expertise.

References

1. *Organic Superconductors*, by T. Ishiguro and K. Yamaji, in *Springer Series in Solid State Sciences*, Vol. **88** (Springer-Verlag, Berlin 1991)
2. J. Caulfield, S. J. Blundell, M. S. L. du Croo de Jongh, P. T. J. Hendriks, J. Singleton, M. Doporrio, F. L. Pratt, A. House, J. A. A. J. Perenboom, W. Hayes, M. Kummo and P. Day, *Phys. Rev. B*, **51** (1995) 8325; M. V. Kartsovnik, H. Ito, T. Ishiguro, H. Mori, G. Saito and S. Tanaka, *J. Phys.: Condens. Matter* **6**, (1994) L479; S. Uji, T. Terashima, H. Aoki, J. S. Brooks, M. Tokumoto, N. Kinoshita, T. Kinoshita, Y. Tanaka and H. Anzai, *J. Phys.: Condens. Matter* **6**, (1994) L539.
3. S. Uji, T. Terashima, H. Aoki, J. S. Brooks, R. Kato, H. Sawa, S. Anuma, M. Tamura and M. Kinoshita, *Phys. Rev. B*, **50**, (1994) 15597.
4. S. Hill, J. Singleton, F. L. Pratt, M. Doporrio, W. Hayes, T. J. B. M. Janssen, J. A. A. J. Perenboom, M. Kummo and P. Day, *Synthetic Metals*, **55-57**, (1993) 2566.
5. S. Hill, D. Phil. Thesis, University of Oxford (1994).
6. T. J. B. M. Janssen, A. S. Perel, A. M. Gerits, W. Kang, J. S. Brooks, A. Witlin, J. A. A. J. Perenboom and P. J. M. van Bentum, *Phys. Rev. B*, **46** (1992) 8663.
7. S. Hill, M. Boonman, S. Uji, J. A. A. J. Perenboom, A. Witlin, J. S. Brooks, R. Kato, H. Sawa and S. Anuma, in *Proc. Physical Phenomena in High Magnetic Fields II*, Tallahassee, May 1995; also O. Klein, S. Donovan, M. Dressel and G. Grüner, in *International Journal of Infrared and Millimeter Waves*, Vol. **14** (1993) 2423-2517.
8. H. Mori, S. Tanaka, M. Oshima, G. Saito, T. Mori, Y. Maruyama and H. Inokuchi, *Bull. Chem. Soc. Japan*, **63** (1990) 2183
9. *Electricity and Magnetism*, B. I. Bleaney and B. Bleaney (Oxford University Press, 1976)
10. T. Ando, A. Fowler and F. Stern, *Rev. Mod. Phys.*, **54** (1982) 437-672.
11. H. Kobayashi, A. Miyamoto, R. Kato, F. Sakai, A. Kobayashi, Y. Yamakita, Y. Furukawa, M. Tasumi and T. Watanabe, *Phys. Rev. B*, **47** (1993) 3500.

Thermopower of Composite Fermions in a 2D Hole System

V. Bayot,^{1,2} E. Grivei,² X. Ying,¹ H.C. Manoharan,¹ and M. Shayegan,¹

¹Department of Electrical Engineering, Princeton University, Princeton, NJ 08544, USA

²Université Catholique de Louvain, Unité PCPM, Place Croix du Sud 1, 1348 LLN, Belgium

Abstract

We report thermopower measurements performed on a low-disorder two-dimensional hole system in GaAs/AlGaAs heterostructures in the integer and fractional quantum hall regimes. We focus on diffusion thermopower which probes the entropy of the current carrying particles, and dominates phonon-drag thermopower at low temperature. Data obtained in the fractional quantum Hall regime are analysed in the framework of the recently proposed composite Fermions (CFs) theory. The data are consistent with the presence of a Fermi surface for the CFs at low half-filling factors, and with the CFs exhibiting integral quantum Hall effect away from $v=1/2$.

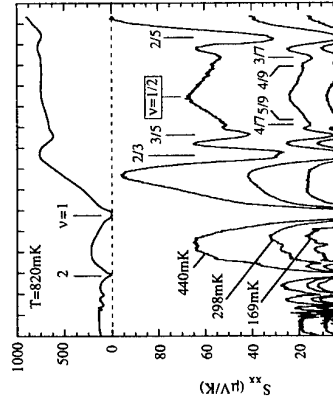
The striking similarities between the integral and fractional quantum Hall (IQH and FQH) effects [1] observed in two-dimensional (2D) systems have recently found an elegant explanation through a gauge transformation that attaches an even number of flux quanta ($2m\Phi$, where m is an integer and $\Phi=\hbar/e$) to each particle [2,3]. The new quasiparticles obey Fermi statistics and are termed composite fermions (CFs). They experience an effective magnetic field B^* which is zero at Landau level filling factors $v=1/(2m)$. Within this theoretical framework, the FQH effect corresponds to the Shubnikov-de Haas effect at low B^* and the IQH effect at higher B^* of the CFs. The effective filling factor for the CFs $v^*=|p|$ relates simply to that of the bare particles as $v=p/(2mp+1)$, and their effective mass is different from that of the bare particles at $B=0$ as it depends on the particle-particle Coulomb interaction.

The results of several recent experiments were found to be remarkably consistent with the predictions of the CF formalism. Among these are surface acoustic wave measurements [4] and geometrical resonances near $v=1/2$ [5,6] which demonstrated the existence of a CF Fermi surface, and transport measurements [7,8] which have provided information on the CF effective mass and scattering. Missing, however, are detailed and quantitative experimental results on the thermodynamic properties of the CFs.

Most parameters that are directly related to the thermodynamic properties of 2D electronic systems, such as the electronic specific heat, are hardly measurable because of the dominant lattice contribution [9,10]. An exception is the diffusion thermopower which is experimentally accessible at very low temperature (T) and can render valuable information as it probes the entropy of charge carriers [11–13].

Here we report thermopower measurements in a high-quality 2D hole system (2DHS), confined to a GaAs/AlGaAs (311)A interface, revealing strong FQH states in the filling range $1/3 \leq v \leq 2/3$. We show that both the temperature and magnetic field dependence of the FQH thermopower data can be explained by treating the FQH effect as the IQH effect of the CFs.

Figure 1 shows the B -dependence of the diagonal thermopower, S_{xx} , at different temperatures. Thermopower was measured in a dilution refrigerator using a AC technique described elsewhere [12,13]. The data exhibit strong S_{xx} oscillations characteristic of the IQH and FQH effects [12–17]. The developing high order FQH states up to $v=4/9$ and $5/9$ attest to the very high quality of the sample. At filling factors where S_{xx} shows maxima, we can distinguish between a low T regime where the magnitude of S_{xx} maxima varies approximately linearly with T , and a high- T regime where S_{xx} shows a faster ($\approx T^{-3}$) variation. The linear T -dependence of S_{xx} is a signature of a thermopower dominated by the diffusion mechanism, while phonon-drag, with a faster T -dependence, becomes predominant at higher T [12–17]. Here we mainly focus on the diffusion S_{xx} observed at very low T .



deduced $T=0.55\text{K}$ is in good agreement with $T=0.7\text{K}$ obtained from the onset of the magnetoresistance oscillations ($T/\hbar\omega_c \approx 1$) in the same sample. Third, for $9/2 \leq v \leq 15/2$, S_{xx} maxima increases approximately linearly with B .

The data of Fig. 2(a) at the lowest T reveal that the approximately linear dependence of S_{xx} maxima on B (dashed line) is observed only from $v=9/2$ up to $v=15/2$. At higher v , $T/\hbar\omega_c$ becomes comparable to unity and S_{xx} maxima deviate from the linear B -dependence [16,18]. For $v < 4$, the maxima are significantly smaller than expected from the intermediate- B linear dependence and FQH features appear in S_{xx} and in the magneto-resistance data. Here the system enters a new regime where the simple non-interacting picture is no longer valid.

The T -dependence of S_{xx} at $v=1/2$ and $3/2$ for the present sample can be fitted to a sum of linear and cubic terms representing the diffusion and phonon-drag contributions, respectively (Fig. 3). The linear T -dependence of the diffusion S_{xx} at these fillings can be interpreted to be consistent with the CF picture as it is similar to what is observed in a 2D metal. More importantly, as emphasized in Ref. 13, the ratio of the measured diffusion terms at $v=1/2$ and $3/2$ is ≈ 0.6 , in agreement with the ratio $1/\sqrt{3} \approx 0.58$ one may expect for CFs [13].

Since no theoretical predictions are yet available for the thermodynamic properties of CFs away from exactly half-filled LLs, we analyze our S_{xx} data assuming that CFs obey the entropy argument valid for bare holes in the IQH regime, and then check the consistency of this assumption with data available from other experiments. The FQH data between $v=1$ and $1/3$ are shown in more detail in Fig. 4.

We make the following observations in Fig. 4(a): (1) S_{xx} is symmetric with respect to $B=0$; (2) the field positions of the S_{xx} maxima match half-odd-integer v^* ; (3) the magnitude of S_{xx} maxima increases linearly with $|B^*|$ (dashed lines). We note that the behavior of CFs' thermopower as a function of B^* is qualitatively similar to that of bare holes as a function of B . Moreover, the symmetry of S_{xx} with respect to B^* is particularly noteworthy as it suggests that the CFs have similar thermodynamic properties on both sides of $v=1/2$. Fig. 4(b) presents the product v^*S_{xx} vs T for various values of p where $v^* = |p|$ and p takes the sign of B^* . The similarity of this plot to the one shown in Fig. 2(b) for the IQH effect is clear. In particular, the T -dependence of S_{xx} can be fitted in similar fashion using a T^3 phonon-drag term and a diffusion term based on the non-interacting theory of Ref. 16.

From the fitted curve we obtain a CF LL-broadening $\Gamma_{CF} \approx 1.5\text{K}$. This value is in agreement with $\Gamma_{CF} \approx 1.4\text{K}$ deduced in magneto-

transport measurements on a similar 2DHS sample from the analysis of the excitation energy gaps for the FQH states [8].

In summary, we have measured S_{xx} of a low-disorder 2DHS at very low temperatures and high magnetic fields, and find that the data support the CF formalism. The T and B dependences of the diffusion S_{xx} in the FQH regime $1/3 \leq v \leq 2/3$ are consistent with the prediction that CFs exhibit IQH effect away from filling factor $v=1/2$, and the values of Γ deduced from S_{xx} for both bare holes and CFs agree with magneto-transport data.

We thank S.M. Girvin for illuminating discussions. This work was supported by the National Science Foundation of the U.S.A. and the program "Action de Recherche Concertée" sponsored by D.G.E.S.R. de la Communauté Française de Belgique". V.B. is a Senior Research Assistant at the National Fund for Scientific Research (Belgium). H.C.M. acknowledges fellowship support from the Fannie and John Hertz Foundation.

References

- [1] For a review see for example: *The Quantum Hall Effect*, edited by R.E. Prange and S.M. Girvin (Springer-Verlag, New York, 1990).
- [2] J.K. Jain, Phys. Rev. Lett. **63**, 199 (1989).
- [3] B.I. Halperin, P.A. Lee, and N. Read, Phys. Rev. B **47**, 7312 (1993).
- [4] R.L. Willett, R.R. Ruel, M.A. Paalanen, K.W. West, and L.N. Pfeiffer, Phys. Rev. B **47**, 7344 (1993); R.L. Willett, R.R. Ruel, K.W. West, and L.N. Pfeiffer, Phys. Rev. Lett. **71**, 3846 (1993).
- [5] W. Kang, H.L. Stormer, L.N. Pfeiffer, K.W. Baldwin, and K.W. West, Phys. Rev. Lett. **71**, 3850 (1993).
- [6] V.J. Goldman, B. Su, and J.K. Jain, Phys. Rev. Lett. **72**, 2065 (1994).
- [7] R.R. Du, H.L. Stormer, D.C. Tsui, L.N. Pfeiffer, and K.W. West, Phys. Rev. Lett. **70**, 2944 (1993); Solid State Commun. **90**, 71 (1994); D.R. Leadley, R.J. Nicholas, C.T. Foxon, and J.I. Harris, Phys. Rev. Lett. **72**, 1906 (1994).
- [8] H.C. Manoharan, M. Shayegan, and S.J. Klepper, Phys. Rev. Lett. **73**, 3270 (1994).
- [9] E. Gornik *et al.*, Phys. Rev. Lett. **54**, 1820 (1985); J.K. Wang, D.C. Tsui, M. Santos, and W.A. Little (Plenum, New York, 1990), p. 101.
- [10] M. Shayegan, Phys. Rev. B **45**, 4384 (1992).
- [11] See, e.g., P.M. Chaikin, in *Organic Superconductivity*, edited by V.Z. Kresin and I.P. Eisenstein, L.N. Pfeiffer, and K.W. West, Phys. Rev. Lett. **68**, 674 (1992), also probe the thermodynamic properties of 2D systems.
- [12] V. Bayot, X. Ying, M.B. Santos, and M. Shayegan, Europhys. Lett. **25**, 613 (1994).
- [13] X. Ying, V. Bayot, M.B. Santos, and M. Shayegan, Phys. Rev. B **50**, 4969 (1994).
- [14] H. Obloho, K. von Klitzing, and K. Ploog, Surf. Sci. **170**, 292 (1986); R. Fletcher *et al.*, Phys. Rev. B **37**, 3137 (1988); C. Ruf, H. Obloho, B. Junge, E. Gimelin, K. Ploog, and G. Weimann, Phys. Rev. B **37**, 6377 (1988); U. Zeitler, J.C. Maan, P. Wyder, R. Fletcher, C.T. Foxon, J.J. Harris, Phys. Rev. B **47**, 16008 (1993).
- [15] M. Jonson and S.M. Girvin, Phys. Rev. B **29**, 1939 (1984); H. Oji, Phys. Rev. B **29**, 3148 (1984); P. Streda, Phys. Stat. Sol. B **125**, 849 (1984); S.K. Lyo, Phys. Rev. B **30**, 3257 (1984).
- [16] W. Zawadski and R. Lassing, Surf. Sci. **142**, 225 (1984).
- [17] For a recent review, see B.L. Gallagher and P.N. Butcher, in *Handbook on Semiconductors*, Vol. 1, edited by P.T. Landsberg (Elsevier, Amsterdam, 1992), p. 721.
- [18] We note that when $kBT < \Gamma$ the effect of a finite $T/\hbar\omega_c$ ratio is much less pronounced at half-filled LLs (S_{xx} maxima) than at integer v (S_{xx} minima); see, e.g., Fig. 7 of Ref. 16. We are therefore able to extract Γ from the S_{xx} maxima even though S_{xx} minima at the neighboring integer v do not go to zero. In our analysis, both in the IQH and FQH regimes, we made sure that $\hbar\omega_c$ is sufficiently large compared to the extracted value of Γ so that the error in the deduced Γ resulting from finite $T/\hbar\omega_c$ ratio is less than 10%.

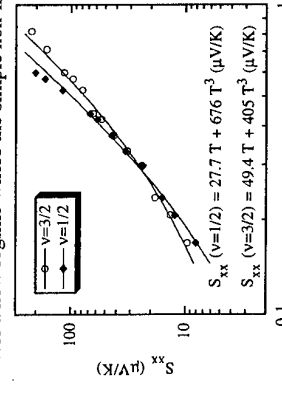


Figure 3: S_{xx} vs T at $v=1/2$ and $3/2$.

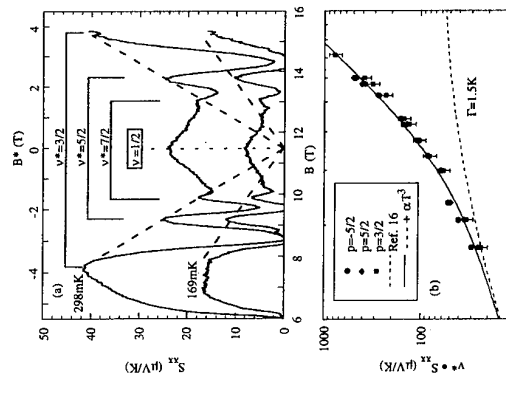


Figure 4: (a) S_{xx} vs B and B^* ; (b) v^*S_{xx} vs T in the FQH regime.

Evidence For Composite Fermions From The Magneto-thermopower of 2D Holes

P.A. Crump, B. Tieke*, R.J. Barracough, B.L. Gallacher, R. Fletcher†, J.C. Maan†,

T.M. Fromhold and M. Henini

Department of Physics, University of Nottingham, Nottingham NG7 2RD, UK.

* High Field magnet Laboratory, Nijmegen University, Nijmegen, The Netherlands.

† Physics Department, Queen's University, Kingston, Ontario, Canada.

Abstract

Magneto-thermopower measurements of high mobility 2D hole gases are shown to provide strong evidence for a composite fermion Fermi surface at Landau level filling factor $\nu = 1/2$. Novel behaviour at fractional filling factors 1/3 and 2/3 are also observed with thermopower minima evolving into *maxima* with increasing temperature. This is interpreted in terms of the strong screening of the high mass composite fermions.

Introduction

When a temperature gradient is applied to a conductor, thermoelectric voltages are generated. The measured longitudinal ($S_{xx} = \partial V_x / \partial T_x$) and transverse ($S_{xy} = \partial V_y / \partial T_x$) thermopowers can give detailed information about the strength of the carrier-phonon coupling as a function of magnetic field. In this study, we use measurements of S_{xx} to study the interaction of acoustic phonons with the composite fermions (CFs) formed in a 2D hole gas.

At a Landau Level filling factor of $\nu = 1/2$ the properties of 2D electrons or holes may be described in terms of composite Fermions (CFs), consisting of one carrier and two flux quanta. The CFs are predicted to form a new Fermi surface at $\nu = 1/2$ where they effectively experience zero field, with the region between $\nu = 1/3$ and $\nu = 1$ acting as the integer quantum hall regime for the new CFs. Using low field transport analysis, the CFs are found to have enhanced mass and reduced lifetime relative to the zero field values [1].

The thermopower in hole gases has recently been studied at both high temperatures ($T > 1K$) [3] and at very low temperatures ($T < 100mK$) [4]. In this paper we present thermopower measurements on high mobility $GeAs\text{-}(Ga,Al)As$ heterojunction 2D hole gases in the intermediate temperature range $260mK$ to $1.2K$. As we will show, this is the appropriate region to study the CF-phonon interaction. We observe similar behaviour in a number of samples but concentrate here on results for samples from wafer NU1155. The samples exhibited persistent photoconductivity after infra-red illumination, allowing control of the number density, p_s .

Results For $B = 0T$ And At $\nu = 1/2$

The measured thermopower is generally due to two effects, the diffusion thermopower, S_d , and the phonon-drag thermopower, S_g . S_d arises from the energy dependence of the conductivity of the carriers. S_g is due to scattering between the non-equilibrium phonons and the carriers [2]. When discussing the temperature dependence of the thermopower of degenerate carriers it is useful to consider the approximate expression [2]:

$$(1) \quad S = \alpha(p_s)T + \kappa(T)f(T,p_s)$$

Where $\alpha(p_s)$ is a constant giving the strength of the diffusion term, $\kappa(T)$ is the thermal conductivity, and $f(T,p_s)$ is the term giving the strength of the carrier-phonon interaction.

The influence of the two terms can be seen in figure 1a), which shows S_{xx} measured using DC techniques at zero field and at two number densities. S/κ is plotted as a function of temperature to reveal $f(T,p_s)$. In the low temperature limit we expect $\kappa \propto T^3$, as is observed (see fig 1a) inset). The diffusion term therefore gives $S_d/\kappa \propto T^{-2}$, a region clearly seen in fig 1a) at temperatures below $300mK$. This is the region studied by Bayot *et al.* [4]. Above $400mK$ the phonon drag term dominates, with $S/\kappa \simeq f(T,p_s)$. A maximum is seen in S/κ at $T \simeq 1K$ when $p_s = 0.93 \times 10^{11}cm^{-2}$. This corresponds to resonant phonon absorption across the Fermi circle, i.e. it is a form of Kohn Anomaly. The maximum will occur when the dominant phonon wavevector $q_D = 2k_F$, corresponding to a phonon back-scattering a carrier. $q_D \propto T$ so increasing number density will move the maximum to larger temperatures, as $k_F \propto \sqrt{p_s}$. Increasing p_s to $1.33 \times 10^{11}cm^{-2}$ moves the maximum out of the measurable range. Such features are well known at zero field and are a direct consequence of the existence of a Fermi circle [2, 7].

Figure 1b) shows the results at $\nu = 1/2$ for the same two number densities, again presented as S/κ . If a true Fermi surface forms then the functional form should be equivalent to the zero field case. This is observed, with both the low field diffusion limit and the resonant absorption maximum being present. The location of the maximum roughly scales with total number density as $\sqrt{p_s}$ as expected, although the shift is close to the resolvable limit. A Kohn anomaly in S/κ can only occur when a Fermi surface exists. This data therefore gives direct evidence for a Fermi surface at $\nu = 1/2$.

The expected positions of the Kohn Anomaly maxima estimated from the condition $q_D = 2k_F$ are marked on figures 1a) and 1b). For a given phonon velocity one would expect the peaks at $\nu = 1/2$ to be higher in temperature by a factor of $\sim \sqrt{2}$ than those at $B = 0T$. However the relative importance of the coupling for transverse and longitudinal phonons (the velocities of which differ by ~ 2) may have a major influence. Previous studies on n-type $GeAs\text{-}(Ga,Al)As$ heterostructures at zero field have found the transverse phonons to dominate [2]. However, recent work on hot carrier phonon emission in p-type $GeAs\text{-}(Ga,Al)As$ heterostructures has found strong coupling between holes and both longitudinal and transverse acoustic phonons at zero field [6]. Our results are consistent with this work, with the measured zero field Kohn Anomaly lying between the positions predicted for interaction with only transverse or only longitudinal phonons. This indicates that holes couple strongly to both types of acoustic phonon. However, as can be seen in figure 1b), the position at $\nu = 1/2$ agrees well with that expected if the CFs couple predominantly to the transverse phonons. The existence of these Kohn Anomaly peaks at $\nu = 1/2$ gives direct evidence for a CF Fermi surface. However, it is not immediately obvious why the CFs should couple much more strongly with transverse than with longitudinal acoustic phonons. These results indicate the need for theoretical work on the CF-phonon interaction.

Magneto-thermopower

The thermopower was measured using an a.c. pulsed heating technique as a function of field up to $20T$ in a Bitter magnet. Typical results for S_{xx} are shown in figure 2 for $T = 857mK$ and $T = 236mK$. As can be seen, at the highest temperatures S_{xx} *maxima* form at the $\nu = 1/3$ and $\nu = 2/3$ fractions. This is an effect unique to holes, fractional S_{xx} minima always being seen in electrons. The fractional size of the S_{xx} features at $\nu = 1/3$

and $2/3$ is plotted in figure 3 as a function of temperature. If the magnitude of this feature is determined by resonant phonon absorption across the energy gap E_g , the temperature dependence of the feature size should scale with both E_g and the energy at which the phonon number density is a maximum, $1.6k_B T$. As is seen in figure 3, the data at $\nu = 1/3$ and $2/3$ does indeed show such a scaling.

However, although resonant phonon absorption explains the temperature scaling of the data, it does not explain the functional form of the temperature dependence and should apply equally to electrons where no S_{xx} maximum is seen. In the low temperature limit the phonon drag term at the fractional states tends to zero since the probability of a phonon exciting a carrier across the energy gap tends to zero. S_{xx} zeroes form and the defined fractional feature size tends to -1. At the high temperature limit $T \gtrsim E_g/k_B$, the fractional state is unobservable in transport measurements, so the feature size tends to zero.

The striking observation is that in the intermediate temperature regime fractional maxima are observed. The unique feature of the CF holes is their large effective mass, larger than the electron CF mass. Previous theoretical work by Fromhold *et al.* [5, 2] on "normal" fermions showed that the relative phase of the resistivity and S_{xx} depended critically on the strength of the screening. In the phonon drag model, screening of the deformation potential controls the magnitude of the thermopower. Strong screening implies weak carrier-phonon coupling and small thermopower; conversely weak screening implies a large thermopower. If the density of states at the Fermi energy, $D(E_F)$ is large enough, the screening at the center of a Landau Level becomes so strong that a minimum forms in the thermopower, with maxima occurring between the Landau Levels. The resistivity follows the density of states, so anti-phase S_{xx} and ρ_{xx} arise. Strong Landau Level mixing in "normal" holes leads to an enhanced CF hole effective mass, producing an enhanced $D(E_F)$ for the CFs, which in principle can lead to an anti-phase S_{xx} . Preliminary calculations of the CF magnetothermopower using a reasonable CF mass are able to reproduce S_{xx} maxima at fractional filling but the results are very sensitive to the exact values chosen for both the mass and the CF scattering time.

Conclusion

Our results give strong support for the existence of a composite Fermi surface at $\nu = 1/2$ and indicate very strong screening of the CF-phonon interaction.

- H.C. Manoharan, M. Shayegan and S.J. Klepper, Phys. Rev. Lett. 73 (1994) 3270.
- B.I. Gallagher and P.N. Butcher, in: Handbook on Semiconductors. Vol.1, Eds. T.S. Moss and P.T. Landsberg (Elsevier Science Publs. B.V. 1992) p.721.
- R.J. Barraclough, T.M. Fromhold, P.J. Rodgers, B.L. Gallagher, P.A. Crump, A. Jezierski and M. Henini, in: Proc. 22nd Int. Conf. on Physics of Semicond. Vol.1, Ed. D.J. Lockwood (World Scientific 1994) p.819.
- V. Bayot, X. Ying, M.B. Santos and M. Shayegan, Europhys. Lett. 25 (1994) 613.
- T.M. Fromhold, P.N. Butcher, G. Qin, B.G. Mulvaney, J.P. Oxley and B.L. Gallagher, Phys. Rev. B 48 (1993) 5326 and references therein.
- R.E. George, K.R. Strickland and A.J. Kent, in: Proc. 22nd Int. Conf. on Physics of Semicond. Vol.1, Ed. D.J. Lockwood (World Scientific 1994) p.899.
- B.L. Gallagher, J.P. Oxley, T. Galloway, M.J. Smith and P.N. Butcher, J. Phys. Condens. Matter 2 (1990) 755.

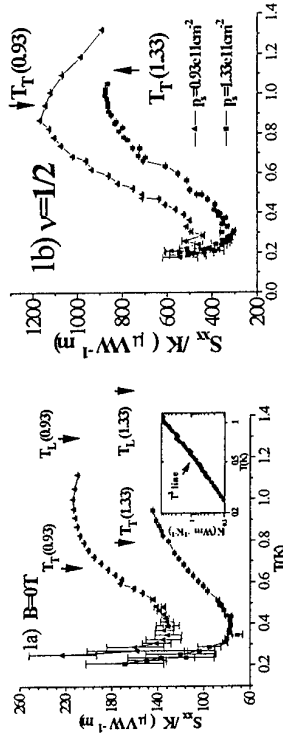


Figure 1a) Zero field thermopower scaled by measured thermal conductivity, K_s , at two values of p_s (shown in fig 1b). The expected positions for the Kohn Anomaly maxima are indicated for each p_s for transverse (T_T) and longitudinal (T_L) acoustic phonons. The measured maxima lie between the two expected positions. The inset shows K for sample A. As expected, $K \propto T^3$. **1b)** Results at $\nu=1/2$. The expected T_T are indicated, but not T_L , as they lie outside the range of the graph.

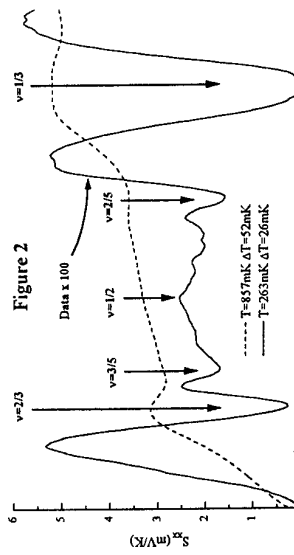


Figure 2

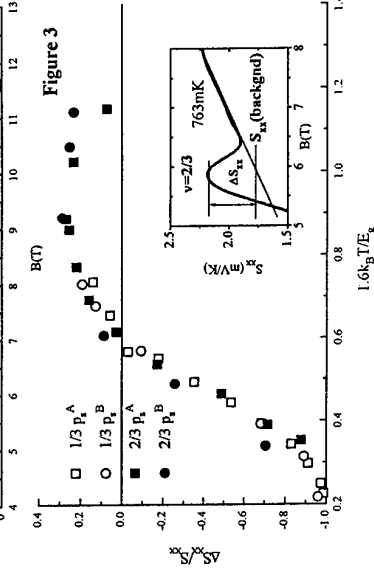


Figure 3) Magnetothermopower around $\nu=1/2$ at $T=263\text{mK}$ and $T=85\text{mK}$. The 263mK data is scaled by a factor of 100 for ease of comparison. The evolution from minimum to maximum at $\nu=1/3, 2/3$ with temperature is clear. Note also the striking symmetry in field around $\nu=1/2$ at lower T .

Electron Spin Resonance in AlGaAs/GaAs in the Regime of Fractional Filling

R. Meisels, I. Kulac, G. Sundaram, and F. Kuchar
Institut für Physik, Montanuniversität, A-8700 Leoben, Austria

B.D. McCombe
Department of Physics and Astronomy, SUNY at Buffalo, N.Y., USA

G. Weimann
Walter Schottky Institut, TU-München, D-85748 Garching, Germany

W. Schlapp
Deutsche Telekom Forschungsinstitut, D-64276 Darmstadt, Germany

Abstract

We have studied the electron spin resonance (ESR) at millimeterwave frequencies in high mobility AlGaAs/GaAs samples for the first time at filling factors $v < 1$ outside the $v=1$ resistance minimum. The magnetic field dependence of the ESR measured at $T=1.6K$ agrees with the calculations by Lommer et al. down to $v=0.5$. In this work no indication was found for the Overhauser shift reported previously by Dobers et al.

Introduction

In a two-dimensional electron system at low temperatures a magnetic field causes the splitting of the electronic states into Landau levels which are further split into two spin states each separated by the much smaller Zeeman splitting. These states are broadened in energy by disorder. States near the center of each level are delocalized and contribute to transport while states further out are localized. This energy level structure is responsible for the integer quantum Hall effect. At very low disorder many body effects cause additional plateaus and minima at fractional filling factors, e.g. $v=1/3$ or $2/3$. According to references 1 and 2, the fractional ground state for $v=1/3$ is spin polarized. On the contrary the $v=2/3$ state is unpolarized although the Zeeman splitting is larger than for $v=1$ [1,2].

Because of the importance of the spin properties in the regime of the fractional quantum Hall effect the investigation of the spin resonance appears to be particularly interesting. In this work we have studied electron spin resonance (ESR) in the range 40-60 GHz. These millimeterwave frequencies are appropriate in fulfilling the resonance condition $\hbar\omega = g\mu_B B$ at B values of about 7-10T because of the small g factor (0.44 in bulk GaAs).

Experimental Arrangement

The experiments were performed on a AlGaAs/GaAs heterostructure with a low concentration ($n_s = 1.4 \times 10^{11} \text{ cm}^{-2}$) high mobility ($\mu = 0.8 \times 10^6 \text{ cm}^2/\text{Vs}$) two dimensional electron system (2DES). Indium current and voltage contacts were placed at the edges of the sample, which was mounted inside a waveguide to apply millimeter wave radiation (40-60GHz) produced by a backward wave oscillator. The measurements were performed at 1.6K in pumped ^4He and

at 0.35K in a ^3He cryostat. Applied magnetic fields up to 10.7T correspond to filling factors down to 0.56. Because of the weak spin resonance oscillator strength and the small number of electrons, the detection of the resonance in a transmission experiment is not possible [3]. Therefore a sensitive millimeterwave-photoconductivity technique was employed. A double modulation method was used to detect the small resistance changes produced by the millimeterwave absorption. In this approach a small a.c. ($f_T=130\text{Hz}$) current ($I=1.5\mu\text{A}$ for the 1.6K measurements and down to 15nA at 0.35K) is applied to the sample, and one lock-in amplifier detects the drop across a pair of voltage contacts, which is proportional to ΔR_{xx} . R_{xx} is changed by the millimeter wave radiation by a small amount ΔR_{xx} . The millimeterwave power (microwatts to several milliwatts) is modulated at a rate of $f_{mod}=13\text{Hz}$, and the output of the first lock-in amplifier is fed into a second one, which detects the change of the output at f_{mod} and gives a signal proportional to ΔR_{xx} .

Experimental Results

Fig. 1 shows ΔR_{xx} vs. magnetic field B for $f=43\text{GHz}$ and $T=1.6\text{K}$. Broad non-resonant structures can be seen in ΔR_{xx} over the whole magnetic field range. Close to $v=1$, as well as close to $v=2$, there are two maxima in ΔR_{xx} and two minima further away. The ΔR_{xx} -maxima are due to the narrowing of the R_{xx} -minima by the radiation. The ΔR_{xx} -minima are due to the reduction in height of the maxima in R_{xx} . At the other integer filling factors and at $v=2/3$ the two ΔR_{xx} -maxima merge into one. On this non-resonant background appears a small sharp signal

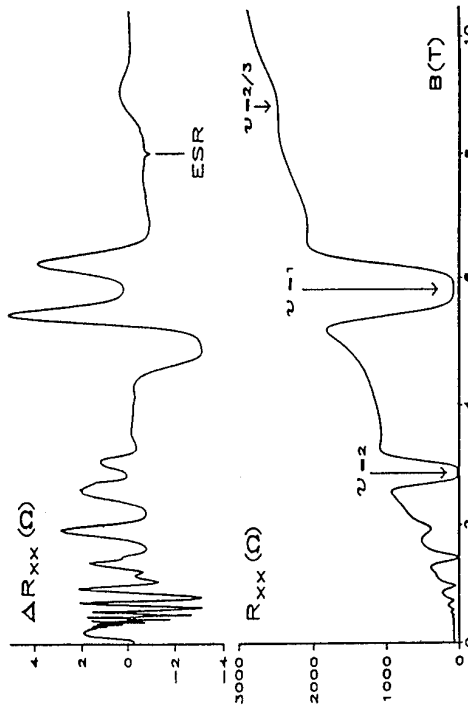


Fig. 1: Longitudinal resistance R_{xx} (upper curve) and its change due to millimeterwave radiation ΔR_{xx} (lower curve) vs. magnetic field B . $f=43\text{GHz}$. The spin resonance peak is indicated by "ESR". Arrows indicate integer and fractional filling factors 2, 1, and 2/3. $T=1.6\text{K}$.

which is attributed to the electron spin resonance (ESR). This signal is also observed over a broad range of millimeterwave frequencies with the resonance field increasing with frequency. The strength of the ESR signal is only about 10^{-4} of the R_{xx} value. Fig. 2 shows ΔR_{xx} for three frequencies with resonances at filling factors above, near, and below 2/3. The positions of the ESR peaks and their widths remain unchanged upon reversing the direction of the magnetic field sweep. The polarity of the ESR peak coincides with the polarity of the non-resonant background. Both are positive near $v=2/3$ and negative further away.

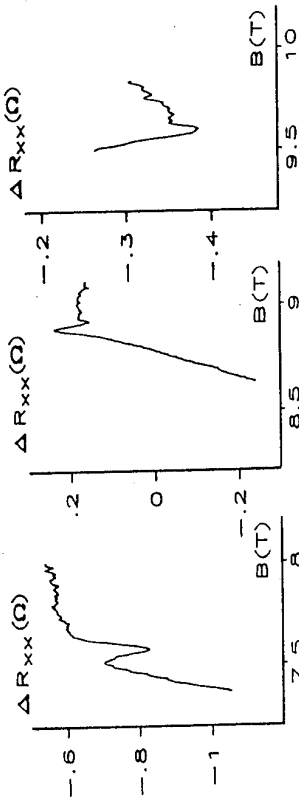


Fig. 2: ESR signal for three frequencies (41, 47, and 50 GHz), $T=1.6\text{K}$.

Discussion

From the results shown in Fig. 2 and additional data at a number of other frequencies we obtain the plot of resonance frequency f vs. magnetic field B shown in Fig. 3. The resonance positions are fitted by a quadratic polynomial which was predicted by Lommel et al [4] on the basis of bandstructure calculations. The quadratic fit corresponds to a linear dependence of the g-factor on field which extrapolates to the bulk value of $|g|=0.44$ for $B \rightarrow 0$, as also shown in Fig. 3. The sign of the ESR signal is the same as that of the non-resonant background signal and significantly depends on the deviation of the filling factor from 2/3. The negative sign further away from 2/3 is interpreted as a heating effect on the delocalized electrons by the millimeterwaves.

Apart from the change of the sign of the ESR signal no distinct anomalies were seen around the weak 2/3 resistance minimum at $T=1.6\text{K}$. Initial experiments at $T=0.35\text{K}$, however, have given indications of an interesting effect which accompanies the deepening of the 2/3 minimum. Instead of the ESR signal in ΔR_{xx} a sharp structure (width about 30 mT) is observed only in the derivative of R_{xx} vs. B in the presence of millimeterwave radiation. Its frequency vs. magnetic field dependence measured in the range 8.3 T to 8.7 T is stronger than that of the ESR signal at 1.6 K. We presently have no explanation for this observation, but its correlation with the deepening of the 2/3 minimum suggests that it is related to the FQHE many body state. In contrast to previous studies [5] the ESR position and width were found to be independent of the field sweep direction. In [5] a shift of the ESR position was explained by the Overhauser effect which involves a coupling of the electron spins to those of the nuclei.

Conclusions

The present study shows for the first time that ESR measurements can be performed in high mobility GaAs/AlGaAs heterostructures at fractional filling factors $v < 1$. This opens up the possibility of investigating the spin properties of the interacting electrons. We found that the theoretical results of [4] for the field position of the ESR are applicable down to $v \approx 0.5$ at $T=1.6\text{K}$. The present measurements also show that the Overhauser shift does not appear to be a general feature of the ESR of the two dimensional electron system in AlGaAs/GaAs.

References

- [1] P.A.Maksym, J. Phys. Condens. Matt. 1 (1989) 6299.
- [2] R.G.Clark, Springer Series in Solid-State Sciences 97 (1990) 168.
- [3] M.Dobers, K.v.Klitzing and G.Weimann, Phys.Rev. B38 (1988) 5453.
- [4] G.Lommel, F.Malcher and U.Röbler, Phys. Rev. B32 (1985) 6965.
- [5] M.Dobers et al., Phys.Rev.Lett. 61 (1988) 1650.

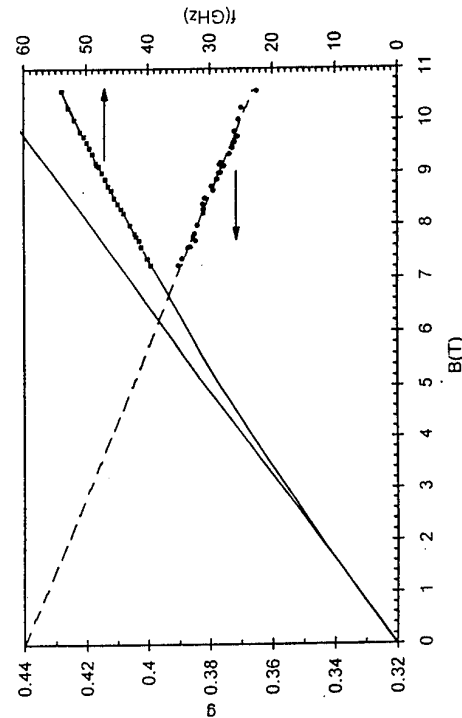


Fig. 3: ESR position, f vs. B (squares), and $g(B)$ (dots) at $T=1.6\text{K}$. The straight line shows the ESR positions for the bulk value $|g|=0.44$. The solid curve through the squares is a quadratic fit [4] and the dashed curve is a straight line extrapolation of the g-value data to zero field.

MESOSCOPIC TRANSPORT PROPERTIES OF COMPOSITE FERMIONS

**A S Sachrajda, Y Feng and P Coleridge, H A Carmona*, A K Geim*,
P C Main*, L Eaves* and C T Foxon***

Institute for Microstructural Sciences, NRC, Ottawa, Canada, K1A 0R6.

*Department of Physics, University of Nottingham, Nottingham, NG7 2RD, UK.

Abstract

We have measured the magnetoresistance of quantum wires, junctions and rings near Landau filling factor $\nu = 1/2$ to search for effects due to composite fermions (CF). We find evidence for semiclassical ballistic effects in the CF which are similar to those seen near zero magnetic field. However, we were not able to observe effects due to the phase-coherence of the CF, even where their analogues were apparent in the electron transport. We attribute this to sample inhomogeneity.

There has been a great deal of recent interest in the modelling of the fractional quantum Hall effect (FQHE) in terms of a novel "composite fermion" (CF) particle¹. The CF comprises an electron bound to an even number of flux quanta, $\phi_0 = h/e$. Since the bound flux quanta are part of the CF, the composite particle does not experience the magnetic field due to these flux lines. For the simplest CF, where an electron is bound to two flux quanta, this implies that the CF experience an effective magnetic field given by $B^* = B \mp 2\pi\phi_0$, where B is the applied magnetic field and n is the electron (and CF) density. It follows that $B^* = 0$ when the Landau filling factor, $\nu = n\phi_0/B$, is $1/2$. Experimental evidence for this model was provided by two demonstrations of semiclassical ballistic behaviour close to $\nu = 1/2$ in periodic potentials [2] and magnetic focusing [3]. However, these effects are by no means trivial to observe. For example, our attempts to repeat the focusing experiments in an equally high mobility device, which showed well developed "electron" magnetic focusing peaks, have proved unsuccessful.

Two possible explanations for this difficulty in observing semiclassical effects in CF are (i) a short CF mean free path and (ii) fluctuations in B^* resulting from inherent density fluctuations. In order to confirm the semiclassical behaviour at $\nu = 1/2$, it is clearly important to find other ballistic effects which are more easily observed. The two ballistic effects described above occur in open structures and, as a result, the density fluctuations are expected to be smaller than in more confined geometries in which ballistic effects have been studied, e.g. quantum wires and junctions. However, there are two properties of these latter geometries which make them suitable for establishing semiclassical CF behaviour. First, a small mean free path is sufficient, typically less than $1 \mu\text{m}$. Secondly, the ballistic effects are largely dependent on the randomization of trajectories, a process which is likely to be more resilient to fluctuations in B^* . In particular, the boundary scattering effect [4,5] observed in quantum wires is a result of non-specular reflection at the wire edges and the quenching of the Hall effect in quantum wires [6,7] relies largely upon scattering at the junction walls randomizing the electron trajectories. We

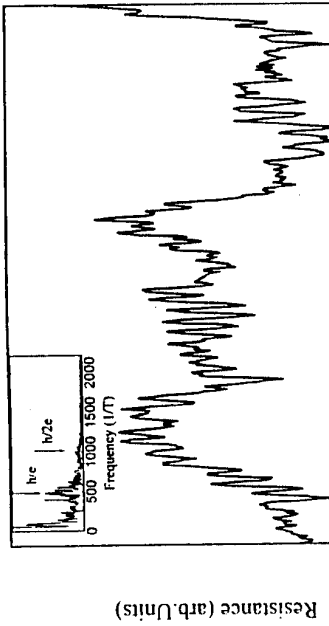


Figure 1.

Magnetoresistance oscillations for a $1.5\mu\text{m}$ diameter ring, wire width $0.7\mu\text{m}$. Before subtraction of the background, the relative amplitude of the oscillations was about 2%. The inset shows a Fourier transform of the oscillations.

$B = 0$ of a $1.5\mu\text{m}$ diameter ring. An unexpected observation in nearly all the devices was a slight curvature in the Hall slope, indicating an apparent increase of n (a few percent) with increasing B . This was accompanied by the equivalent shift in the minima of the longitudinal resistance. We have no explanation of this effect but we believe it is linked to inhomogeneities. Ballistic effects in wires and junctions have been studied experimentally and theoretically near $B = 0$ [4-7]. The quenching of the Hall effect is primarily due to the scrambling of trajectories [6] and the geometrical collimating properties of the junction [7]. The related effects in the longitudinal resistance are accompanied by an additional boundary scattering effect [4] due to diffuse scattering at the wire edges which is responsible for a reduction in the electron longitudinal momentum and hence an increase in the wire resistance. As B is increased the electron collides more frequently with the wire wall, decreasing the mean free path and creating a positive magnetoresistance. However as the field is raised still further and the cyclotron diameter $2R_c$ becomes smaller than the wire width w , the electrons are "guided" along the wire and the effective mean free path increases again leading to a negative magnetoresistance. In this way a resistance peak at low magnetic fields [4] ($w/R_c = 1.1$) is formed in addition to the peak caused by junction scattering. Examples of these effects near $B = 0$ for wires of width $0.5\mu\text{m}$ are shown in the insets of Figure 2 and Figure 3(b). A difference between our results and those described above [4,5] is that there is no dip in the broad magnetoresistance peak at $B=0$. We believe that this is due to an additional, narrow peak at $B=0$. The amplitude of this central peak decreased with increasing temperature at a much faster rate than the rest of the feature, for example the "bumps" labelled 2 and 3 in Figure 3(b), which we identify with the ballistic effects discussed above. This suggests that the central peak is not semiclassical in origin but is a phase coherent effect due to the interference of back-scattered trajectories, similar to weak localisation

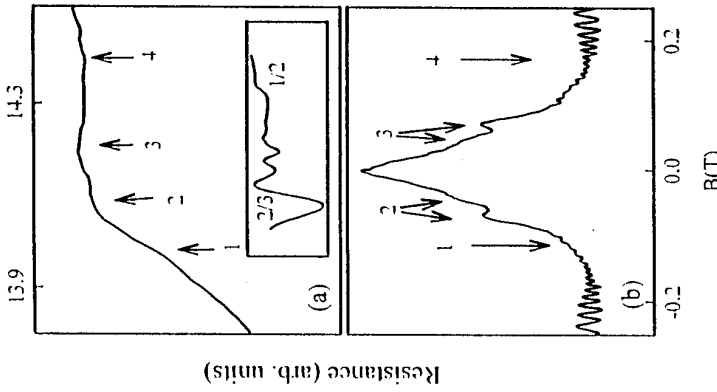


Figure 3.

R_{xx} of a wire of width 0.5 μm at 300 mK around (a) $\nu = 1/2$ and (b) $B = 0$. The numbered arrows indicate equivalent points in the two curves. The B-axes are scaled to allow direct comparison. Inset shows R_{xx} over a wider field range with $\nu = 2/3$ and $\nu = 1/2$ indicated.

References

- [1] B.I.Halperin, P.A.Lee and N.Read, Phys. Rev. **B47** 7312 (1993)
- [2] W.Kang et al., Phys. Rev. Lett. **71** 3850 (1993)
- [3] V.J.Goldman, B.Su and J.K.Jain , Phys. Rev. Lett. **72** 2065 (1994)
- [4] T.J.Thornon et al., Phys. Rev. Lett. **63** 2128 (1989) and proceedings of the "Quantum Coherence in Mesoscopic Systems" NATO ASI, Savoy, France 1990.
- [5] R.J.Blake et al.in "Quantum Effects: Devices and Applications" (ed K.Ishmail) Adam Hilger 1992.
- [6] M.L.Roukes et al., Phys. Rev. Lett., **59** 3011(1987)
- [7] C.W.J.Beenakker and H.van Houten, Phys. Rev. Lett. **63** 1857 (1989)
- [8] For an excellent review of weak localisation see G. Bergmann, Phys. Rep. **107** 1 (1984).

This work is supported by EPSRC (UK) and ECAMI and HAC wishes to thank CNPq (Brazil) for financial support.

Acknowledgements

[8]. We note that some of the original work also had an unexplained narrow central peak around zero magnetic field [4].

Figure 2 illustrates the Hall (R_{xy}) and longitudinal (R_{xx}) resistance of a quantum wire junction around $\nu = 1/2$ at 1K. At this high temperature the feature at $\nu = 1/2$ is readily distinguished. A clear peak can be seen in R_{xx} whereas the resistance of the bulk 2DEG has a dip at $\nu = 1/2$. The width of the feature is similar to that expected from scaling the width of the Hall effect is made difficult by the gentle curvature in R_{xy} of these devices as mentioned above. Nevertheless, an extremely weak "quenching" feature can be seen in the Hall resistance at $\nu = 1/2$. The width in magnetic field of this feature is slightly larger than that predicted from the equivalent zero-field effects. In some devices, the feature at $\nu = 1/2$ showed more complex structure which could be directly compared with the zero field feature. Figures 3(a) and 3(b) show a direct comparison of the low field and $\nu = 1/2$ features (i.e. the low field range has been stretched by 2^{2/3}). The features marked by 2 and 3, at the side of the central peak in Figure 3(b) can be related to those marked 2 and 3 in Figure 3(a). The overall width of the magnetoresistance peak in Figure 3(a) (between points 1 and 4) corresponds to the scaled width of the low field feature. The central peak, which we associate with coherent effects near $B = 0$, is absent in Figure 3(a) leaving a slight dip in R_{xx} as expected for the ballistic effect. The missing central peak is consistent with our lack of observation of any other CF coherent effects in these devices. For example, the ring which shows clear magnetoresistance oscillations in Figure 1, has no trace of equivalent oscillations near $\nu = 1/2$.

The absence of phase-coherent effects may be understood in terms of the device inhomogeneity. Weak localisation is caused by interference between time-reversed trajectories. The characteristic peak at $B = 0$ is due to the exact equivalence of the path lengths of the two trajectories regardless of the length of the interfering paths; the role of the magnetic field is to break the time-reversal symmetry. In the CF case, inhomogeneities mean that $B^* = 0$ occurs at slightly different magnetic fields in different parts of the device. To observe weak localisation, this variation in B^* must be less than the equivalent of one flux quantum threading the largest phase-coherent loop in the device. For a phase-coherence length of $\sim 1 \mu\text{m}$, this would require homogeneity of electron density considerably better than 0.1 %, better than is routinely achieved.

In conclusion, we have searched for both ballistic and coherent effects in quantum wires and rings. Although both universal conductance fluctuations and Aharonov-Bohm oscillations were present in the magnetoresistance of our devices near $B = 0$, no equivalent CF effects have been found. We attribute this absence to sample inhomogeneity. Similarly we have not been able to reproduce the observation of magnetic focusing of CF. However, weak features in both R_{xx} and R_{xy} were observed around $\nu = 1/2$. We attribute them to ballistic effects and relate them to the corresponding electron effects around $B = 0$. We argue that the apparent ease with which these effects can be observed in comparison with other ballistic effects is due both to the intrinsic nature of the effects and the short the mean free path required for their observation. These experiments provide further support for the CF description of the FQHE.

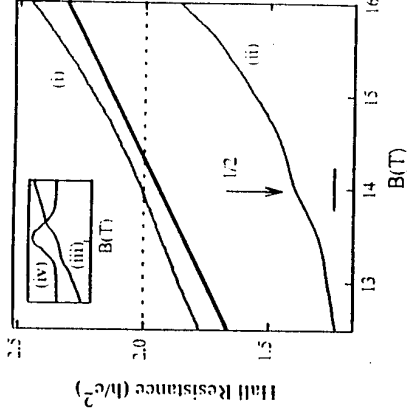


Figure 2.
Magnetoresistance at 1 K of a junction with wire width 0.5 μm . (i) R_{xy} indicating a weak quench at $\nu = 1/2$. The solid line is a guide to the eye. (ii) R_{xx} revealing a peak in the magnetoresistance at $\nu = 1/2$. The line underneath the peak is the predicted width of the feature based on the low field ballistic feature. Inset shows (iii) R_{xy} and (iv) R_{xx} around $B = 0$.

Transport properties of composite fermions in narrow cross junctions

J. Herfort^a, Y. Takagaki^a, R. Hey^a, K.-J. Friedland^a, K. Ploog^a, D.K. Maude^b, J.C. Porta^b, J. Takahara^c, K. Gamo^c

^a Paul-Drude-Institut für Festkörperelektronik, Hausvogteiplatz 5-7, D-10117 Berlin, Germany

^b High Magnetic Field Laboratory CNRS, 25 Avenue des Martyrs, F-38042 Grenoble, France

^c Department of Electrical Engineering, University of Osaka, Toyonaka, Osaka 560, Japan

Abstract

The bend resistance in narrow cross junctions is investigated in the fractional quantum Hall regime. Dips in the resistance due to the ballistic transmission of composite fermions have been observed near $v = 1/2$ and $1/4$. The temperature dependence of the dips is strong reflecting small Fermi energy of the composite fermions. The width of the dips in magnetic field is found to be much larger than the theoretical prediction.

The system of interacting electrons at filling factor $v = 1/2p$ can be replaced by a system of independent composite fermions (CF's), for which an even number $2p$ of magnetic flux quanta are attached to each electron, in zero effective magnetic field [1]. Consequently, metallic states with a well defined Fermi level are anticipated to appear in the fractional quantum Hall (FQH) regime near $v = 1/2p$ [1]. The replica of the transport phenomena which occurs near zero magnetic field is expected to take place in high magnetic fields near $v = 1/2p$ [1,2], where the CF plays the role of the electron. In this paper, we investigate the transport properties in narrow cross junctions at filling factors with even denominators. We have observed the negative bend resistance [3] due to the CF. It is noteworthy that the previous experiments [2] investigated the CF's in the vicinity of $v = 1/2$, whereas the negative bend resistance occurs exactly at $v = 1/2$, where the CF effective mass has been reported to diverge [4].

The samples were made from a GaAs/Al_xGa_{1-x}As heterostructure with the spacer layer thickness of 80 nm. After illumination, the mobility at $T = 0.3$ K is $\mu = 105 \text{ m}^2/\text{Vs}$ when the electron density is $n_s = 1.8 \times 10^{15} \text{ m}^{-2}$. The corresponding electron transport mean free path l_0^{el} is 7 μm . As shown in the inset of Fig. 1, the device consists of four narrow crossed-wire junctions fabricated using electron beam lithography. The resist pattern was transferred to the heterostructure by wet chemical etching with an etch depth of 160 nm to avoid process induced damages. The lithographic constriction width W_{lith} was varied between 0.8 and 4.0 μm .

Figure 1 shows the bend resistance $R_B = R_{12,43}$, where the four-terminal resistance $R_{L,\text{term}}$ is defined such that the current flows from lead k to lead l and the voltage difference is measured between leads m and n , as a function of the magnetic field B . The dip at $B = 0$ in the $W_{\text{lith}} = 0.8 \mu\text{m}$ sample arises from ballistic transport of the electrons. In a symmetric cross junction, R_B at $B = 0$ is described as [5]

$$R_B = -\left(\hbar/e^2\right)(T_F - T_S)/4T_S(T_F + T_S), \quad (1)$$

where T_F is the forward transmission probability and T_S is the transmission probability into each of the side probes. When the transport is ballistic, i.e., $T_F > T_S$, R_B becomes negative [3]. The negative R_B disappears when a strong magnetic field is applied as the electrons are deflected into the side probe favoured by the Lorentz force [6]. The classical transmission probabilities in a

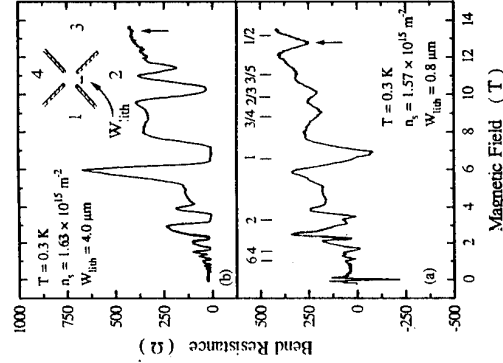


FIG. 1. Bend resistance R_B in (a) narrow and (b) wide cross junctions. The arrows indicate the dips near $v = 1/2$. The vertical bars indicate the positions of the fractions calculated from the electron density. The inset illustrates the schematic view of the cross junction.

cross junction of straight wires at $B = 0$ are $T_F/N = \sqrt{2} - 1$ and $T_S/N = 1 - 1/\sqrt{2}$,

leading to $R_B = -3.77 \text{ k}\Omega/N$. Here, $N = k_F W/\pi$ is the number of occupied subbands in the wire of the width W and k_F is the Fermi wavevector. The electron transport is expected to be almost entirely ballistic as $l_0^{\text{el}} \gg W$, and so N is roughly estimated to be ~ 12 from the amplitude of the dip near $B = 0$, giving rise to $W \sim 0.4 \mu\text{m}$. Since the subbands are defined by both magnetic and electrostatic confinement, the Landau plot is found to show a deviation from the linear behaviour. The effective conduction width estimated from the deviation is in reasonable agreement with the above estimated value of $0.4 \mu\text{m}$. A pronounced dip is observed near $v = 1/2$ in the narrow sample as indicated by an arrow in Fig. 1(a). The dip was observed in both of two $W_{\text{lith}} = 0.8 \mu\text{m}$ samples we measured. On the other hand, the large ($W_{\text{lith}} = 4.0 \mu\text{m}$) sample exhibits only a broad dip, which is always observed in the resistance of a two-dimensional electron gas [7].

In Fig. 2, we show R_B and the Hall resistance $R_H = R_{13,24}$ up to $B = 25 \text{ T}$. One finds minima in R_B near $v = 1/3$ and $2/5$ and a well developed plateau in R_H near $v = 1/3$ due to the FQH effect. In addition, we find a dip near $v = 1/4$, which we ascribe to ballistic transport of CF with $p = 2$. The dips associated with the $v = 1$ and $1/3$ quantum Hall states shift to higher B due to interedge scattering, while do those near $v = 1/2$ and $1/4$ to lower B , indicating their different origin. When the topmost edge state is nearly depleted, the electrons can be scattered into the states at opposite boundaries of the channel in the cross region. The appearance of the effect of the interedge scattering differs depending on the details of the potential around the cross junction. In our samples, the dips in R_B are enhanced (and become negative) at the higher magnetic field side of the quantum Hall states. Interedge scattering does not play a role near $v = 1/2$ and $1/4$ as there are no edge states. The dip at $B \sim 8.5 \text{ T}$ may be due to the metallic state at $v = 3/4$, which is the particle-hole conjugation of the $v = 1/4$ state. The observation of the dips at $v = 1/2$, $1/4$ and $3/4$ provides a strong evidence of ballistic transport of the CF. The amplitude of the dips near $v = 1/4$ and $3/4$ is smaller than that near $v = 1/2$, indicating stronger scattering for the CF with $p = 2$ from the Chern-Simons gauge field.

Figure 3 shows R_B at three different temperatures. The negative R_B at $B = 0$ is almost unchanged in the temperature range shown here and vanishes around $T \sim 40 \text{ K}$. In contrast, the temperature dependence is found to be strong for the dip near $v = 1/2$. As shown in the inset of

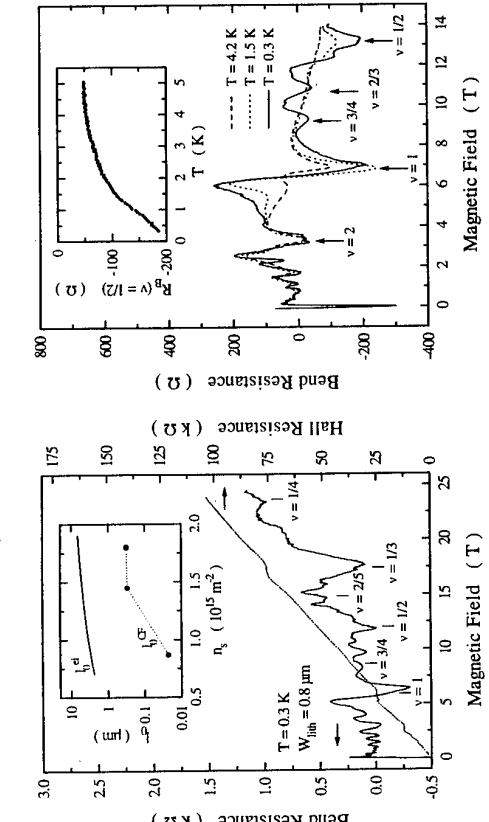


FIG. 2. Bend resistance and Hall resistance in a narrow cross junction. The vertical bars indicate the positions of the fractions. Inset: Transport mean free paths l_0 of the electrons and of the composite fermions in an unperturbed heterostructure as a function of carrier density n_s .

FIG. 3. Bend resistance in $W_{\text{bin}} = 0.8 \mu\text{m}$ sample for three different temperatures. The dip at $B = 0$ is nearly unchanged. Inset: Bend resistance at $v = 1/2$ as a function of temperature.

Fig. 3, the dip disappears above $T \sim 3 \text{ K}$, which is one order of magnitude lower than for the electrons. The negative R_B at $B = 0$ [6] and the metallic state of the CFs at $v = 1/2$ [7] are known to have weak temperature dependence. The strong temperature dependence is ascribed to the fact that the Fermi energy of the CF is smaller than that of the electrons. Because of the large CF effective mass [1,8], the density of states for the CF is larger than that for the electrons, resulting in the smaller Fermi energy of the CF. Therefore, the thermal energy $k_B T$ becomes appreciable at lower T for the CF.

Because of the large CF effective mass, the mean free path l_0^{CF} of the CF is considerably smaller than l_0^{el} . We show the mean free paths, l_0^{el} at $B = 0$ and l_0^{CF} at $v = 1/2$, as a function of n_s in the inset of Fig. 2. The CF density is identical to the electron density, and so l_0^{CF} is obtained from the resistance at $v = 1/2$. With increasing n_s , l_0^{el} increases linearly. The CF mean free path is less than or comparable to W , and so the transmission of the CF should be nearly diffusive [3]. However, the amplitude of the dip at $v = 1/2$ is suppressed only by a factor of $2 \sim 3$ compared to that at $B = 0$. It has been known that the *transport* mean free path of electrons in GaAs underestimates the effect of the elastic scattering as the long-range scattering does not influence the mobility very much while it does for most of the ballistic transport phenomena. On the contrary, the CF have been reported to experience short-range scatterers [8]. Therefore, the ratio of the *ballistic* mean free paths of the electrons and the CFs is smaller than $l_0^{\text{el}}/l_0^{\text{CF}}$. This will partly account for the discrepancy. Our result may indicate that the effective constriction width for the

CF is narrower than that for the electron. We will return to this point later. As reported by Du *et al.* [4], the CF mass diverges as $v \rightarrow 1/2$, implying that the scattering time becomes infinitely long to provide a finite resistance. Therefore, the mean free path may no longer be meaningful for the nonordinary Fermi liquid near $v = 1/2$.

The Fermi wavevector of the CF is given by $k_F^{\text{CF}} = (4\pi n_s)^{1/2}$ due to the spin polarisation. Thus, the magnetic field scale will be expanded by a factor of $\sqrt{2}$ for the structures in the magnetoresistance due to the CF [1]. However, the dip near $v = 1/2$ is much wider in B than the theoretical prediction. The broadening is enhanced for the dip near $v = 1/4$. This may suggest that the carrier density across the channel cannot be regarded as uniform in narrow wires. If the potential variation near the boundary of the channel is smooth compared to the magnetic length $l_B = (\hbar eB)^{1/2}$, the carrier density across the channel is not considered to be uniform [9]. This will result in a superposition of the magnetoresistance with shifted B for the CF, since zero effective magnetic field is realised at lower B for the CF away from the centre of the channel. This will explain the shift of the dips to lower B . The presence of the nonuniform magnetic field for the CF implies that the channel widths for the electrons and for the CF do not necessarily be the same. The electron feels zero effective magnetic field at $B = 0$ irrespective of the position in the transverse direction, whereas this is not the case for the CF at $v = 1/2$. The effective channel width for the CF will be narrower than for the electrons due to the finite effective magnetic field near the channel boundary.

In conclusion, we have investigated the negative bend resistance by composite fermions in narrow cross junction in the FQH regime. The broadening of the dip in magnetic field indicates that the nonuniform effective magnetic field for the CF is of significant importance in narrow channels.

The authors would like to thank H.L. Störmer for valuable discussions. This work was supported in part by the Bundesministerium für Forschung und Technologie of the Federal Republic of Germany and by the EU - "Access to research under high magnetic fields" program at Grenoble.

References

- [1] B.I. Halperin, P.A. Lee, and N. Read, Phys. Rev. B **47** (1993) 7312.
- [2] R.R. Willett, R.R. Ruel, K.W. West, and L.N. Pfeiffer, Phys. Rev. Lett. **71** (1993) 3846; W. Kang, H.L. Störmer, L.N. Pfeiffer, K.W. Baldwin, and K.W. West, Phys. Rev. Lett. **71** (1993) 3850; V.J. Goldman, B. Su, and J.K. Jain, Phys. Rev. Lett. **72** (1994) 2065.
- [3] Y. Takagaki, K. Gamo, S. Namba, S. Takaoka, K. Murase, K. Ishibashi and Y. Aoyagi, Solid State Commun. **68** (1988) 1051.
- [4] R.R. Du, H.L. Störmer, D.C. Tsui, A.S. Yeh, L.N. Pfeiffer, and K.W. West, Phys. Rev. Lett. **73** (1994) 3274.
- [5] M. Büttiker, Phys. Rev. Lett. **57** (1986) 1761.
- [6] Y. Takagaki, K. Gamo, S. Namba, S. Takaoka, K. Murase, and S. Ishida, Solid State Commun. **71** (1989) 809.
- [7] H.W. Jiang, H.L. Störmer, D.C. Tsui, L.N. Pfeiffer, and K.W. West, Phys. Rev. B **40** (1989) 12013.
- [8] R.R. Du, H.L. Störmer, D.C. Tsui, L.N. Pfeiffer, and K.W. West, Phys. Rev. Lett. **70** (1993) 2944; D.R. Leadley, R.J. Nicholas, C.T. Foxon, and I.J. Harris, Phys. Rev. Lett. **72** (1994) 1906.
- [9] L. Brey, Phys. Rev. B **50**, (1994) 11861; D.B. Chklovskii, Phys. Rev. B **51** (1995) 3895.

Ballistic conductance of composite fermions

A. Khaetskii^a, Yu.V. Nazarov and G.E.W. Bauer

Faculty of Applied Physics and DIMEES, Delft University of Technology,
2628 CJ Delft, The Netherlands,

^a Institute of Microelectronics Technology, Russian Academy of Sciences,
142432, Chernogolovka, Moscow District, Russia

Abstract

We consider ballistic transport of composite fermions in a realistic microconstriction. An unambiguous signature of such transport is revealed: the linear conductance increases with increasing magnetic field near filling factor 1/2 and then drops abruptly in a narrow magnetic field interval.

It was shown theoretically [1] that properties of two-dimensional (2D) electron gas in strong magnetic fields near filling factor $\nu = 1/2$ ($\nu = 2\pi\lambda^2 n$, $\lambda = \sqrt{\hbar c/eB}$ is the magnetic length and n the electron density) can be well described in terms of composite fermions. Within the mean field approach the average effective (external plus internal) magnetic field acting on the composite fermions is:

$$\Delta B = B - 2\Phi_0 n, \quad \Phi_0 = 2\pi\hbar c/e. \quad (1)$$

For filling factor $\nu = 1/2$ the average effective magnetic field vanishes.

Ballistic transport of *normal electrons* has been widely investigated using quantum point contacts (QPC). The conductance of these point contacts varies in a step-like manner as function of applied gate voltage if electrons transit the constriction region ballistically [2]. Applying a magnetic field, one can approach filling factor 1/2 where the transport through the constriction is expected to be due to *composite fermions*. In this work we reveal the characteristic properties of ballistic transport of these quasiparticles (the mean free path of c.f.'s is much larger than the width of the constriction).

We calculate the linear two-terminal conductance of a microconstriction of 2D electron gas near $\nu = 1/2$ (see Fig. 1). It should be noted that calculations of the ballistic conductance of a microconstriction in terms of uncorrelated electrons (we refer to these as normal

electrons) were given in Ref.[3]. The result is that the ballistic conductance in strong magnetic fields is determined by the filling factor at the saddle point of the electron-density distribution and is independent of the width of the constriction being always of the order of the conductance quantum for the magnetic fields under consideration. For ballistic transport of composite fermions we find completely different results. The magnetoconductance has a striking nonmonotonic and abrupt behaviour near filling factor 1/2 (see Fig.2). For a constriction much wider than the magnetic length the maximum conductance is much larger than the conductance quantum. Comparison of our results with experimental data should unambiguously identify the nature of transport through a constriction near $\nu = 1/2$ thus distinguishing between ballistic transport of electrons and composite fermions.

We concentrate on the case of small depletion, assuming that the depletion length $l_{dep} \ll d(0)$, being much larger than λ , is much smaller than the width $2d(0)$ of the constriction. This implies that the electron density is almost uniform everywhere except for the narrow regions near the boundaries. Similar to a normal-electron QPC [2], the ballistic conductance is determined by the number of propagating modes of c.f.'s through the constriction. The electron density varies in the constriction region giving rise to an inhomogeneous magnetic field according to Eq.(1). The conductance is determined mainly by the composite fermions that propagate near the lines of zero effective magnetic field (See also Ref.[4]). We will show below that the number of propagating modes is determined by the derivative of the electron density in the transverse direction at these lines. With increasing external magnetic field the lines of zero effective field move from the boundaries towards the middle of the constriction and the density derivative decreases thus increasing the middle of the constriction and, consequently, the conductance (Fig.2). When the filling factor in the center of the constriction becomes smaller than 1/2 ($n(0,0) > n(1/2,0)$, $n_{1/2} = 1/4\pi\lambda^2 \cdot n(0,0)$) is the electron density at the saddle point), the number of propagating modes drops abruptly, since the lines of zero effective magnetic field do not pass through the constriction but turn back to the same lead. This is reminiscent of the phenomenon predicted in Ref.[5].

Let us consider first an auxiliary problem of a straight channel where the electron density depends only on the transverse (y) coordinate. We approximate the effective magnetic field near the line $y=y_{1/2}$ where the effective magnetic field is zero as: $\Delta B = 2\Phi_0 n(y - y_{1/2})$, $n' = dn/dy|_{y=y_{1/2}}$. The Schrödinger equation for c.f.'s reads:

$$\frac{\hbar^2}{2} \frac{d^2 \chi(y)}{dy^2} + \left[E - \frac{\hbar^2}{2} (k - 2\pi n' y^2)^2 \right] \chi(y) = 0 \quad (2)$$

k being the wave vector along the x -axis. Eq.(2) has been discussed in Ref.[6] (see also Ref.[4]). It was revealed that there are two different types of states which cross the Fermi energy and have opposite velocities $dE/\hbar\partial k$ in the x -direction. The states of the first type ("snake" states) are localized near the line $y_{1/2}$ and have negative velocities. The others ("drift" states) having positive velocities are spatially separated from the line $y_{1/2}$ and drift due to the gradient of the magnetic field. They come in pairs corresponding to the possibilities to be on the left and on the right of $y = y_{1/2}$. In order to calculate the conductance of the system, we need to know the total number N_t of subbands below the Fermi energy. We have solved Eq. (2) semiclassically, obtaining this number with the help of the Bohr-Sommerfeld quantization rule. For a symmetric contact we have two identical lines of zero effective magnetic field, that doubles the conductance:

$$G = 2N_t \frac{e^2}{2\pi\hbar} \cdot N_t = \left[1.85 \frac{n_0^{3/4}}{(n')^{1/2}} + \frac{1}{2} \right], \quad (3)$$

where n_0 is the value of background density and brackets mean the integer part of the number. Since $N_t \gg 1$, in the following we will ignore term 1/2 in Eq. (3) compared to the

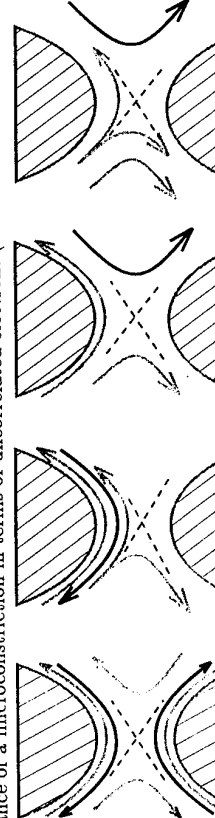


Fig.1 The geometry of the structure considered. Black and gray solid curves with arrows show respectively snake and drift trajectories of composite fermions for different values of external magnetic field (a-d) near filling factor 1/2. The rest of the curves in Figs. (b-d) can be obtained by inversion with respect to the saddle point. Dashed lines denote the $y(0,0)$ curves where the density has the saddle point value $n(0,0)$.

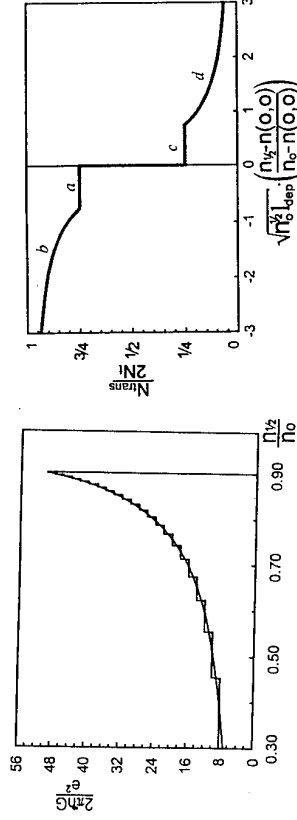


Fig. 2 Dependence of the conductance quantization vs. magnetic field described by Eq.(4) (smooth curve). Step-like curve describes the conductance quantization. The parameters are: $\lambda = 80 \text{ \AA}$, $d(0) = 1 \mu\text{m}$, $l_{dep} = 1000 \text{ \AA}$. The abrupt drop corresponds to the condition $n_{1/2} \equiv n(0,0)$.

Fig. 3. The number of transmitted modes through the constriction deviated by the total number of incoming c.f.'s modes as function of magnetic field near filling factor 1/2. Different parts of this dependence (a-d) correspond to the situations shown in Fig. 1.

The results obtained above can be immediately applied to a realistic constriction where the electron density depends on both coordinates (Fig. 1). Indeed, the value of the density derivative entering Eq.(3) far from the constriction (at infinity) is always larger than its value in the central section ($x = 0$). This means that the number of transverse modes of c.f.'s far from the saddle point is smaller than in the central section and the ballistic conductance of the system is determined by the number of modes at infinity. As a result, the conductance of a sufficiently smooth constriction does not depend on its shape. This situation is in sharp contrast to the common one [2]. We calculate now the density derivative entering Eq.(3) far from the saddle point (at infinity) where line $y_{1/2}$ lies much closer to one of the boundaries than to the other. Using the formula [7] for the electron density profile at large (compared to the depletion length) distance from the boundary, we find $n' = 2(n_0 - n_{1/2})^2/n_{0,dep}$ at the curve $y_{1/2}$. It determines the conductance of the system:

$$G(n_0 - n_{1/2}) = \left(\frac{e^2}{2\pi\hbar}\right)^2 \frac{2.62 n_0^{1/2} l_{dep}}{(n_0 - n_{1/2})}, \quad n_0 - n_{1/2} \ll n_0. \quad (4)$$

The conductance increases when the filling factor in the bulk approaches 1/2 (see Eq.(4)) since the line $y_{1/2}$ lies in the region of an increasingly flat density profile. This is only valid if $n_{1/2}$ is smaller than the density value at the saddle point $n(0,0)$. When the filling factor at the saddle point becomes smaller than 1/2, the line $y_{1/2}$ cannot pass the bottleneck of the constriction and the conductance should decrease. The magnetic field dependence of the conductance given by Eq.(4) is shown in Fig. 2. The maximum value of the conductance is equal to: $G_{max} \simeq (e^2/h)(d(0)/l_{dep})^{1/2} l_{dep} \gg e^2/h$.

The dependence of the conductance in the narrow interval near $n(0,0)$ actually has a rich additional structure due to the fact that c.f.'s trajectories of different types (drift and snake) behave differently in the bottleneck region. We notice that not all the modes of c.f.'s existing far from the saddle point can propagate through the constriction. Some of them will be reflected when $n_{1/2}$ approaches $n(0,0)$. This will first occur for drift trajectories which at infinity lie at the higher density side of the line $y_{1/2}$. When the drift trajectories move towards the bottleneck region their separation from the line $y_{1/2}$ increases since the density

derivative n' decreases. As a result, these trajectories have a small radius and drift along the lines of constant density in the bottleneck region. Those which lie on the higher density side of the line $y(0,0)$ will be reflected (see Fig. 1b) (their number is N_{refl}). Calculating the number of transmitted modes $2N_t - N_{refl}$, we obtain for the conductance:

$$G = \frac{e^2}{2\pi\hbar} \left\{ 2.62 \frac{n_0^{1/2} l_{dep}}{n_0 - n_{1/2}} - \frac{n_0}{2(n(0,0) - n_{1/2})} \right\}. \quad (5)$$

The dependence given by Eq.(5) holds if the number of reflected modes (the second term in brackets) is smaller than $N_t/2$ which is just the total number of the drift trajectories lying at infinity at the higher density side of the line $y_{1/2}$. The last drift trajectory coming from infinity is reflected at the magnetic field value determined by

$$n(0,0) - n_{1/2}^{(1)} = 0.76 \frac{n_0}{(n_0 l_{dep})^{1/2}}. \quad (6)$$

Since a fourth of the total number of modes coming from infinity has been already reflected (the corresponding situation is shown in Fig. 1a), starting from this magnetic field, the ratio of the number of transmitted modes to the total number of incoming modes remains equal to 3/4 in the finite interval of magnetic fields. This interval corresponds to the first plateau in Fig. 3. The width of the plateau is given by Eq.(6).

With further increase of the external magnetic field we reach a situation when $n_{1/2} = n(0,0)$. For larger values of magnetic field the snake trajectories coming from infinity cannot propagate through the constriction and give no contribution to the conductance. The number of snake states at infinity is a half of the total number of c.f.'s states. As a result, the conductance drops by the value $G_{max}/2$ in a narrow interval near $n_{1/2} = n(0,0)$ (see Fig. 3). As can be shown the width of this interval is much smaller than the plateau width Eq.(6). If $n_{1/2} > n(0,0)$ then only the drift trajectories which at infinity lie at the low density side of the $y_{1/2}$ curve will propagate through the constriction (see Fig. 1c). Again, in the finite interval of the magnetic fields the ratio of transmitted to incoming modes is constant ($1/4$) which corresponds to the second plateau in Fig. 3. For larger values of the magnetic field (when these propagating drift trajectories will also be reflected, Fig. 1d) we obtain for the conductance:

$$G = \left(\frac{e^2}{2\pi\hbar}\right) \frac{n_0}{2(n_{1/2} - n(0,0))} \quad (7)$$

Our results are formally valid in the limit of large values $n_0^{1/2} l_{dep}$. In this case, the decrease of conductance is abrupt, as it is shown in Fig. 2. In reality, this parameter takes only moderately large values, $n_0^{1/2} l_{dep} \simeq 3 - 5$. The conductance is still given by Eqs.(5,1) but the decreasing part of the curve is smooth and the maximum value is decreased.

Acknowledgements. We thank C.W.J. Beenakker and A.K. Geim for discussion of the results and D.B. Chklovskii who draw our attention to Ref.[4].

References

- [1] B.I. Halperin, P.A. Lee, N. Read, Phys. Rev. B **47**, 7312 (1993); V. Kalmeyer and S.C. Zhang, Phys. Rev. B **46**, 9889 (1992).
- [2] B.J. van Wees et al., Phys. Rev. Lett. **60**, 848 (1988); D.A. Wharam et al., J. Phys. C: Solid State Phys. **21**, L209 (1988); L.I. Glazman et al., JETP Lett. **48**, 238 (1988) [Zh. Eksp. Teor. Fiz. Pis'ma **48**, 218 (1988)].
- [3] D.B. Chklovskii, K.A. Matveev and B.I. Shklovskii, Phys. Rev. B **47**, 12605 (1993).
- [4] D.B. Chklovskii and P.A. Lee, Phys. Rev. B **48**, 18060 (1993).
- [5] A. Khaetskii and G.E.W. Bauer, Phys. Rev. B **51**, 71369 (1995); L. Brey and C. Tejedor, preprint.
- [6] J.E. Müller, Phys. Rev. Lett. **68**, 385 (1992).
- [7] D.B. Chklovskii, B.I. Shklovskii, and L.I. Glazman, Phys. Rev. B **46**, 4026 (1992).

Measurements on a Composite Fermion Split-gate

C.-T. Liang, C.G. Smith, D.R. Mace, J.T. Nicholls, J.E.F. Frost, M.Y. Simmons, A.R. Hamilton,
D.A. Ritchie, and M. Pepper
Cavendish Laboratory, Madingley Road, Cambridge CB3 0HE, United Kingdom

Abstract

Recent theoretical and experimental work demonstrates that at filling factor $\nu=1/2$ a two-dimensional electron gas can be described in terms of composite fermions (CFs) for which the effective magnetic field vanishes. We present low-temperature measurements on a wide split-gate (SG) device investigating CFs in the quantum point contact (QPC) defined by such a structure. Negative magnetoresistance due to suppression of backscattering in the QPC was observed both around zero magnetic field and $\nu=1/2$. We have also measured the resistance of a CF QPC at zero effective magnetic field as a function of gate voltage, with a compensating field to maintain $\nu=1/2$ in the QPC. Using a simple model, we determine the channel widths for CFs, which are narrower than those for electrons.

The fractional quantum Hall effect (FQHE) [1] can be observed in high-mobility two-dimensional (2D) electron systems in the low temperature and high magnetic field regime. It is believed that the FQHE arises from strong electron-electron interactions, causing the 2D electrons to condense into a fractional quantum Hall liquid. Jain [2] proposed a new approach to the FQHE in terms of 'composite fermions', consisting of electrons bound to an even number of magnetic flux quanta. The FQHE can then be understood as a manifestation of the integer quantum Hall effect of weakly interacting composite fermions. It has been shown [3] that at filling factor $\nu=1/2$, a 2D electron system can be transformed into a composite fermion (CF) system interacting with Chern-Simons gauge field. At $\nu=1/2$ the effective magnetic field B_{eff} acting on the CFs is zero, and a variety of experiments [4-6] support this picture.

Using the split-gate (SG) technique [7], a one-dimensional (1D) channel [8] (or a quantum point contact) [9] can be formed in the two-dimensional electron gas (2DEG). Subsequent investigation on such a channel reveals negative four-terminal magnetoresistance R_{xx} given by [10]

$$(1) \quad R_{xx} = (h/2e^2)(1/N_e(B)) - R_{xy},$$

where $N_e(B)$ is the number of occupied electric-magnetic subbands in the channel, R_{xy} is the Hall resistance of the bulk 2DEG region, and B is the magnetic field. Assuming spin degeneracy and ignoring the discreteness of $N_e(B), N_e(B)$ in a square well confinement is [10]

$$(2) \quad N_e(B) = \left(\frac{k_F l_c}{\pi} \right)^2 \left[\arcsin(\nu_e/2l_c) + (\nu_e/2l_c) \times \left[\sqrt{1 - (\nu_e/2l_c)^2} \right] \right], \text{ for } \nu_e < 2l_c,$$

where k_F is the Fermi wave vector in the channel, $l_c=\hbar k_F/eB$ is the cyclotron radius, and W_e is the channel width for electrons. Increasing the magnetic field causes electrons to start to execute skipping orbits towards the channel boundary, suppressing backscattering of electrons near the entrance of the channel, giving rise to such negative magnetoresistance (NMR) centred around $B=0$.

In this paper we present measurements on a wide SG device fabricated on a GaAs/AlGaAs

heterostructure. Over the measurement range, the channel defined by the SG is very wide (see later) and there are at least 12 1D subbands occupied. In this case the confining potential can be described as a square well therefore the carrier density is uniform across the channel. This ensures a uniform filling factor in the channel thus we are able to measure a composite fermion quantum point contact (QPC) at $B_{\text{eff}}=0$ as a function of gate voltage V_g with a compensating applied magnetic field to maintain $\nu=1/2$ in the channel. Recently, Khaetskii and Bauer [11] have considered CF transport in a bar-gated sample. In this case, applying a small negative gate voltage reduces the carrier density underneath the gate, inducing an effective magnetic field in those regions. Injected CFs approaching those areas can be bent back to the source contact by such an effective field. We shall show that our results qualitatively agree with this theory.

The SG device (0.3 μm long and 1.2 μm wide) was defined by electron beam lithography on the surface of a GaAs/AlGaAs heterostructure, 297 nm above the 2DEG. It has been demonstrated that clean 1D channels showing good ballistic conductance quantisation can be defined in such deep 2DEGs situated below the surface of a similar heterostructure [12]. After brief illumination with a red LED, the carrier concentration of the 2DEG was $1.385 \times 10^{15} \text{ m}^{-2}$ with a mobility of $550 \text{ m}^2 \text{V}^{-1} \text{s}^{-1}$. Experiments were performed in a 3 He cryostat at 0.3 K. The magnetoresistance was measured using a current of 10 nA with standard four-terminal ac phase-sensitive techniques. Similar results were obtained from experiments performed on seven devices fabricated on three different wafers. Measurements taken from one of the seven devices are presented in this paper.

When -0.7 V was applied to the SG, the channel was first defined and NMR was observed. It is noted that a background resistance $R_{xx}(V_g=0)$ due to the bulk 2DEG was measured in series with the resistance of the channel [10]. After subtracting the background resistance ($\approx 100 \Omega$) we have a good fit to Eq. (1) and obtain the width of the channel to be 0.39 to 0.88 μm over a range of $-3 \text{ V} \leq V_g \leq -0.7 \text{ V}$. In this range of V_g the channel width is very wide and we assume that carrier density n_s is uniform across the channel. $n_s(V_g)$ can be varied by changing V_g on the SG, whereas the carrier density of the bulk 2DEG remains unchanged. We can obtain $n_s(V_g)$ by two methods. Firstly taking the magnetic field value of the middle point of the $\nu=1$ two-terminal quantum Hall plateau, we determine $n_s(V_g)$ from $eB/h=n_s$. Secondly at $V_g \leq -2.1 \text{ V}$, we observed extra minima in R_{xx} around $B=8 \text{ T}$ corresponding to $\nu=2/3$ in the channel as shown in Fig. 1. $n_s(V_g)$ obtained from the two methods are very similar and the difference in the deduced positions of $\nu=1/2$ is within 0.06 T . For consistency we use $n_s(V_g)$ determined from the first method.

Figure 1 shows the high-field

positions of $\nu=1/2$ in the channel at various V_g are indicated by arrow heads.

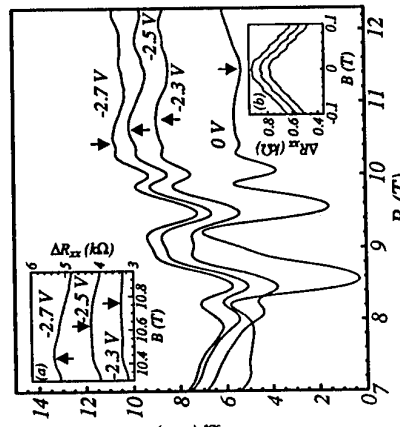


Fig. 1. $R_{xx}(B)$ at various V_g . For clarity the trace for $V_g=2.5 \text{ V}$ is vertically offset by $0.3 \text{ k}\Omega$. Inset (a) and (b) show the subtracted resistance ΔR_{xx} centred around $\nu=1/2$ and $B=0$, respectively. The positions of $\nu=1/2$ in the channel at various V_g are indicated by arrow heads.

magnetoresistance measurements at different gate voltages. The minima in R_{xx} around $B=8.6$, 9.5, and 10 T correspond to $\nu=2/3$, 3/5, and 4/7 in the bulk 2DEG measured in series with the QPC. When the channel is defined, NMR around $\nu=1/2$ is observed as indicated by arrow heads for $V_g=-2.3$, -2.5 and -2.7 V. After subtraction of the background resistance, the resistance $\Delta R_{xx} = R_{xx}(V_g) - R_{xx}(V_g=0)$ also shows NMR centred around $\nu=1/2$ and $B=0$, as displayed in the insets Fig. 1 (a) and (b), respectively. We believe the NMR in ΔR_{xx} around $\nu=1/2$ is evidence of suppression of backscattering of CFs in an effective magnetic field. However the fit to the modified form of Eq. (1) is very poor if we take different factors of the Fermi wave vector between electrons and CFs and no spin degeneracy for CFs into account. Thus we are not able to determine the channel width for CFs. This is probably due to the fact that when the filling factor is close to 1/2 in the channel, in the bulk 2DEG ν is greater than 1/2, leading to a negative B_{eff} in those regions. Therefore our case at $\nu=1/2$ is much more complicated than the case for $B=0$.

The inset to Fig. 2 shows the measured resistance when $\nu=1/2$ in the channel (\blacktriangledown) and the background resistance $R_{xx}(V_g=0)$ due to the bulk 2DEG at the corresponding magnetic field (\circ) as a function of V_g . Thus the deduced resistance of the CF QPC at $B_{eff}=0$ is given by $\bullet = \blacktriangledown - \circ$, as shown in Fig. 2. The resistance of the electron QPC at $B=0$ is displayed for comparison. Two features can be readily seen in Fig. 2: (i) At equal V_g , the resistance of the CF QPC is higher than that of the electron QPC. (ii) The definition voltage of the CF QPC is ≈ -0.3 V, larger than that of the electron QPC (-0.7 V). The latter can be explained by the recent theory [11]. At $\nu=1/2$, applying a small negative V_g induces a strong B_{eff} under the SG thus CFs cannot transverse those regions. In this case, after subtraction of a series resistance of 93.3 Ω due to the bulk 2DEG is plotted in a solid line.

Finally we use a simple model to calculate the channel widths for CFs. At $B=0$, the resistance of an electron QPC can be written as $R_e = \hbar/2e^2N_e$, where N_e is the number of 1D subbands occupied in the channel and the factor of 2 is due to spin degeneracy. Since $N_e = 2W_e/\lambda_e$ we have $R_e = \hbar\lambda_e/4e^2W_e$, where λ_e is the Fermi wavelength in the channel. Assuming 1D subbands also exist in a CF QPC, the resistance of such a device is $R_{CF} = \hbar\lambda_{CF}/e^2N_{CF}$ where N_{CF} is the number of occupied subbands, and there is no spin degeneracy. Following the same argument, we have $R_{CF} = \hbar\lambda_{CF}/2^{3/2}e^2W_{CF}$ where λ_{CF} is the Fermi wavelength of CFs and $2^{1/2}\lambda_{CF} = \lambda_e$ [3]. Thus the ratio of R_{CF} to R_e is given as

$$R_{CF}/R_e = \sqrt{2W_e/W_{CF}}, \quad (3)$$

at equal V_g . Using Eq. (1) to fit ΔR_{xx} centred around $B=0$, we determine $W_e(V_g)$, R_{CF}/R_e can be deduced from the data shown in Fig. 2. Thus we can obtain $W_{CF}(V_g)$ from Eq. (3). As shown in

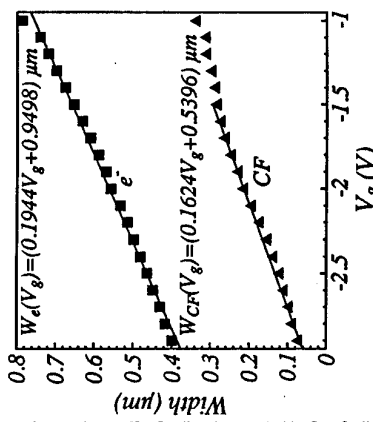


Fig. 3. $W_{CF}(V_g)$ is smaller than $W_e(V_g)$, agreeing with the recent experimental results [6]. This is due to lateral partial depletion from the SG. In this case, around $\nu=1/2$, a slight reduction in the carrier density near the boundary of the channel induces a strong B_{eff} , bending the CF trajectories back to the source contact. Thus CFs cannot go through those regions, consequently reducing the channel width. As shown in Fig. 3, we have a good linear fit of $W_e(V_g)$. This predicts a pinch-off voltage of -4.89 V, in good agreement with the measured value -5.18 V. The slope of the fit $W_{CF}(V_g)$ for $-2.9 \leq V_g \leq -1.5$ V is very close to that of $W_e(V_g)$. However for $-1.5 \leq V_g \leq -1$ V, $W_{CF}(V_g)$ only decreases slightly as V_g is made more negative. This is not fully understood at Fig. 3. The deduced channel widths for electrons $W_e(V_g)$ (marked by \blacksquare) and for CFs $W_{CF}(V_g)$ (marked by \blacktriangle) from Eq. (1) and of backscattering in a quantum point contact both (3). The straight line fits are also shown.

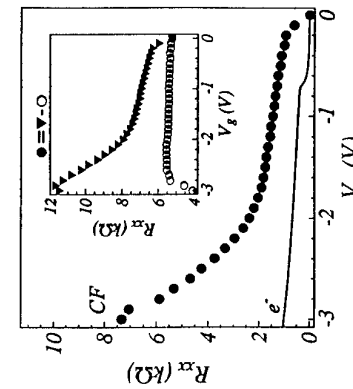


Fig. 2. Inset: The measured resistance (marked by \blacktriangledown) and the background resistance (marked by \circ) as a function of V_g . Main figure: Deduced resistance of the CF QPC given by $\bullet = \blacktriangledown - \circ$ as a function of V_g . The resistance of the electron QPC after subtraction of a series resistance of 93.3 Ω due to the bulk 2DEG is plotted in a solid line.

Finally we use a simple model to calculate the channel widths for CFs. At $B=0$, the resistance of an electron QPC can be written as $R_e = \hbar/2e^2N_e$, where N_e is the number of 1D subbands occupied in the channel and the factor of 2 is due to spin degeneracy. Since $N_e = 2W_e/\lambda_e$ we have $R_e = \hbar\lambda_e/4e^2W_e$, where λ_e is the Fermi wavelength in the channel. Assuming 1D subbands also exist in a CF QPC, the resistance of such a device is $R_{CF} = \hbar\lambda_{CF}/e^2N_{CF}$ where N_{CF} is the number of occupied subbands, and there is no spin degeneracy. Following the same argument, we have $R_{CF} = \hbar\lambda_{CF}/2^{3/2}e^2W_{CF}$ where λ_{CF} is the Fermi wavelength of CFs and $2^{1/2}\lambda_{CF} = \lambda_e$ [3]. Thus the ratio of R_{CF} to R_e is given as

$$R_{CF}/R_e = \sqrt{2W_e/W_{CF}}, \quad (3)$$

at equal V_g . Using Eq. (1) to fit ΔR_{xx} centred around $B=0$, we determine $W_e(V_g)$, R_{CF}/R_e can be deduced from the data shown in Fig. 2. Thus we can obtain $W_{CF}(V_g)$ from Eq. (3). As shown in

Fig. 3, we have observed suppression $W_{CF}(V_g)$ in a quantum point contact both (3). The straight line fits are also shown.

This work was funded by the Engineering and Physical Sciences Research Council. We thank C.J.B. Ford and G. Kirzenow for helpful discussions.

References:

- [1] D.C. Tsui, H.L. Störmer, and A.C. Gossard, Phys. Rev. Lett. 48 (1982) 1559.
- [2] J.K. Jain, Phys. Rev. Lett. 63 (1989) 19.
- [3] B.I. Halperin, P.A. Lee, and N. Read, Phys. Rev. B 47 (1993) 7312.
- [4] R.R. Du, H.L. Störmer, D.C. Tsui, L.N. Pfeiffer, and K.W. West, Phys. Rev. Lett. 70 (1993) 2724.
- [5] D.R. Leadley, R.J. Nicholas, C.T. Foxon, and J.J. Harris, Phys. Rev. Lett. 72 (1994) 1906.
- [6] V.J. Goldman, B. Su, and J.K. Jain, Phys. Rev. Lett. 72 (1994) 2065.
- [7] T.J. Thornton, M. Pepper, H. Ahmed, D. Andrew, and G.J. Davies, Phys. Rev. Lett. 56 (1986) 1198.
- [8] D.A. Wharam, T.J. Thornton, R. Newbury, M. Pepper, H. Ahmed, J.E.F. Frost, D.G. Hasko, D.C. Peacock, D.A. Ritchie, and G.A.C. Jones, J. Phys. C 21 (1988) L209.
- [9] B.J. van Wees, H. van Houten, C.W.J. Beenakker, J.G. Williamson, L.P. Kouwenhoven, D. van der Marel, and C.T. Foxon, Phys. Rev. Lett. 60 (1988) 848.
- [10] H. van Houten, C.W.J. Beenakker, P.H.M. van Loosdrecht, T.J. Thornton, H. Ahmed, M. Pepper, C.T. Foxon, and J.J. Harris, Phys. Rev. B 37 (1988) 8534.
- [11] A. Khaetskii and G.E.W. Bauer, Phys. Rev. B 51 (1995) 7369.
- [12] K.J. Thomas, M.Y. Simmons, J.T. Nicholls, D.R. Mace, M. Pepper, and D.A. Ritchie, to be published in Appl. Phys. Lett. (1995).

Critical behavior in the fractional quantum Hall effect

Bodo Huckestein*

Institut für Theoretische Physik, Universität zu Köln, D-50937 Köln, Germany

*ct

arged particles in a random magnetic field as a model of the fractional quantum Hall effect.

We consider the limit of weak fluctuations of the magnetic field on a strong background field. We show that in two limits the random magnetic field is equivalent to electrostatic disorder proving the universality of the critical behavior: in the lowest Landau level for arbitrary correlation length of the random magnetic field , and for correlation much longer than the magnetic length in any Landau level. For higher Landau levels and short-ranged correlations there is no strict equivalence but we argue that the differences are irrelevant for the critical behavior.

1 Introduction

The importance of disorder for the occurrence of the quantum Hall effect (QHE) was realized [1] soon after the discovery of the integer QHE (IQHE) [2]. The disorder potential localizes the electrons when the Landau level filling is not an integer. Only at a single energy in the center of the Landau levels are the states delocalized and the transition from one quantized Hall plateau to the next occurs. This transition is similar to a thermodynamic second order phase transition [3, 4]. Scaling behavior was observed close to this transition both experimentally [5, 4] and numerically [6, 4]. There is a remarkable agreement between the value of the localization length exponent ν_ζ obtained in finite-size scaling experiments in the IQHE regime, $\nu_\zeta = 2.3 \pm 0.1$ [7], and numerical calculations for non-interacting electrons $\nu_\zeta = 2.35 \pm 0.03$ [8].

For weaker disorder the Coulomb interaction between the electrons becomes dominant and new correlated ground states form that give rise to the fractional QHE (FQHE) [9]. It is believed that the plateau transition in the FQHE is due to the localization of the quasiparticles of these ground states. Experimentally the transitions between fractional QH plateaus are very similar to their integer quantized counterparts. In particular, the transitions between filling factors 1/3 and 2/5 and between 2/3 and 1 show scaling behavior with the same or similar critical exponents as the transitions in the IQHE [10]. The similarity between the fractional and integer QHE is the basis of Jain's construction of approximate ground states for FHQ states [11]. By attaching an even number p flux quanta to each electron Jain transforms a system of non-interacting electrons at filling factor ν' into an approximate ground state of the interacting electron system at filling factor $\nu = \nu'/(p'p \pm 1)$. The objects consisting of an electron and p flux quanta obey Fermi statistics and are called "composite fermions" (CFs). In this approach the most prominent FQH states are interpreted as filled Landau levels of the CFs ($\nu = \text{integer}$). Based on this approach Jain, Kivelson, and Trivedi argued that the transitions between FQH plateaus that correspond to successive Landau levels of the CFs should show the same scaling behavior as the IQHE [12]. The composite fermion picture of the FQHE has been further developed by introducing a fictitious Chern-Simons theory [13]. The attachment of flux quanta is achieved by introducing a vector potential $\mathbf{a}_0 = h/e$ is the quantum of flux. The argument of Jain, Kivelson, and Trivedi is equivalent to a mean-field approximation of the Chern-Simons theory.

This paper addresses the question whether fluctuations in the Chern-Simons vector potential change the critical behavior obtained in the mean-field approximation. A lot of work has been devoted to this question in the context of the half-filled Landau level. For $p = 2$ the CFs see no net magnetic field. In the absence of a magnetic field all electron states are known to be localized in two dimensions [14]. However, a number of numerical calculations claim to find evidence for a localization-delocalization transition due to static fluctuations in the magnetic field even if the mean value vanishes [15]. Other authors find a large increase in the localization length that could be mistaken for a divergence but fail to find a true transition [16]. We will show that in the limit relevant to the FQHE, where the mean value of the magnetic field is much larger than the fluctuations, static fluctuations in the magnetic field are irrelevant for the critical behavior. In this approximation the FQHE belongs to the same universality class as the IQHE.

The rest of this paper is organized as follows. We will first derive the central result of the paper. Next we compare the random magnetic field to an electrostatic disorder potential and discuss the universality of the critical behavior. Finally we summarize our findings.

2 Matrix elements of a random" magnetic field

We consider the Hamiltonian H of a single particle in a random magnetic field $\mathbf{B} = (B_0 + b(\mathbf{r}))\mathbf{e}_z$ with average strength B_0 . The vector potentials corresponding to the average and fluctuating magnetic fields are \mathbf{A} and \mathbf{a} , respectively. The Hamiltonian can be expressed as a sum of Hamiltonian $H_0 = (\mathbf{p} - e\mathbf{A})^2/2m^*$ of the system with constant magnetic field $B_0\mathbf{e}_z = \nabla \times \mathbf{A}$ and a part H' due to the fluctuating magnetic field $b(\mathbf{r})\mathbf{e}_z = \nabla \times \mathbf{a}$,

$$H = \frac{1}{2m^*} (\mathbf{p} - e\mathbf{A} - e\mathbf{a})^2 = H_0 + H', \quad (1)$$

$$H' = \frac{1}{2m^*} (-e((\mathbf{p} - e\mathbf{A})\mathbf{a} + \mathbf{a}(\mathbf{p} - e\mathbf{A})) + e^2\mathbf{a}^2). \quad (2)$$

We want to compare the effects of H' to those of a random electrostatic potential $V(\mathbf{r})$. The operators themselves are very different as the latter contains only a scalar random function while the former contains the random vector function \mathbf{a} as well as the momentum and the vector potential \mathbf{A} . The matrix elements of the two operators with eigenfunctions of H_0 , however, are remarkably similar in the limit that the fluctuations b are much smaller than the mean B . In order to calculate the matrix elements of H' we express it in terms of the Landau level ladder operators of H_0 ,

$$\hat{a}_0 = \frac{i_0}{\sqrt{2\hbar}} (\Pi_x^0 + i\Pi_y^0) \quad \text{and} \quad \hat{a}_0^\dagger = \frac{i_0}{\sqrt{2\hbar}} (\Pi_x^0 - i\Pi_y^0),$$

where $\Pi_j = p_j - eA_j$. Expressing the vector potential as a complex coordinate, $a = a_x + ia_y$, we get

$$H' = -\frac{e}{4m^*} \frac{\sqrt{2\hbar}}{i_0} (\hat{a}_0 \bar{a} + a \hat{a}_0^\dagger + \hat{a}_0^\dagger a + \bar{a} \hat{a}_0) + \frac{e^2}{4m^*} (a \bar{a} + \bar{a} a), \quad (3)$$

where \bar{a} denotes the complex conjugate of a . When choosing a Coulomb gauge for the Chern-Simons vector potential $\mathbf{a}, \nabla \cdot \mathbf{a} = 0$, the Hamiltonian H' becomes the sum of three terms, $H' = H_1 + H_2 + H_3$, with

$$H_1 = \frac{1}{2} \frac{e\hbar}{m^*}, \quad H_2 = -\frac{e\hbar}{\sqrt{2m}i_0} (\hat{a}_0^\dagger a + \bar{a} \hat{a}_0), \quad H_3 = \frac{e^2}{2m^*} a \bar{a}. \quad (4)$$

H_1 is already proportional to the fluctuating magnetic field b . The matrix elements of H_2 can be calculated by using the ladder operator properties of \hat{a}_0 , $\hat{a}_0|N, k\rangle = \sqrt{N}|N-1, k\rangle$. The inter-Landau level matrix elements of H_2 are then

$$\langle Nk | H_2 | Nk' \rangle = \frac{\hbar e}{m^*} \sum_{n=0}^{N-1} \langle nk | b | nk' \rangle. \quad (5)$$

The part H_3 is quadratic in the vector potential a and its matrix elements are hence smaller by a factor of b_0/B_0 than those of H_1 and H_2 where b_0 is a measure of the fluctuations of $b(\mathbf{r})$. In the limit $b_0 \ll B_0$ we can neglect its matrix elements as well as the couplings between different Landau levels and obtain for the intra-Landau level matrix elements of H' ,

$$\langle Nk | H' | Nk' \rangle = \frac{\hbar e}{m^*} \left(\frac{1}{2} \langle Nk | b(\mathbf{r}) | Nk' \rangle + \sum_{n=0}^{N-1} \langle nk | b(\mathbf{r}) | nk' \rangle \right). \quad (6)$$

3 Comparison with electrostatic disorder

It is obvious from eq. (6) that there are two limits in which the random magnetic potential is strictly equivalent to a random disorder potential. In the lowest Landau level, $N = 0$, a disorder potential $V(\mathbf{r}) = \hbar e b(\mathbf{r})/2m^*$ has the same matrix elements as the random magnetic field, i.e. the deviation of the local cyclotron energy from its mean value acts as an electrostatic potential. This holds irrespective of the distribution of $b(\mathbf{r})$. The second limit is that of slowly varying magnetic field in which case the matrix elements in eq. (6) become independent of the Landau level index and the equivalent potential is $V(\mathbf{r}) = (N+1/2)\hbar e b(\mathbf{r})/m^*$ as long as the magnetic field is smooth on the scale of the cyclotron radius in the N -th Landau level. In these two limits not only critical properties but all physical properties, such as the density of states, are identical to the equivalent random potential.

In general, no strict equivalence holds and a system with random magnetic fields will have different physical properties from systems with potential disorder. However, we will argue that the critical behavior of the systems is identical. For this we consider the matrices $\langle Nk | H' | Nk' \rangle$ and $\langle Nk | V | Nk' \rangle$ as random matrices. For potential disorder with gaussian correlations of range σ the matrix elements $\langle Nk | V | Nk' \rangle$ in the Landau gauge can be calculated from uncorrelated random numbers $u(x, k)$, [4]

$$\langle Nk_1 | V | Nk_2 \rangle = \frac{V_0 \beta l_0}{\sqrt{2L_y \pi \sigma}} \exp\left(-\frac{\kappa^2 l_0^2 \beta^2}{4}\right) \times \int dk_1 u_0(\beta\xi + K l_0, \kappa l_0) \exp(-\xi^2) F_N(\xi, \kappa; \sigma), \quad (7)$$

where $K = (k_1 + k_2)/2$, $\kappa = k_1 - k_2$, and

$$F_N(\xi, \kappa; \sigma) = (2^N N!)^{-1} \int dk_1 \exp\left(-\frac{l_0^2 + \sigma^2}{\sigma^2 - \eta}\right) H_N\left(\eta + \frac{\xi}{\beta} - \frac{\kappa l_0}{2}\right) H_N\left(\eta + \frac{\xi}{\beta} + \frac{\kappa l_0}{2}\right), \quad (8)$$

and L_y is the width of the system, l_0 is the magnetic length, and $\beta^2 = (\sigma^2 + l_0^2)/l_0^2$. Using this result for gaussian correlations of the magnetic field the matrix elements of H' are given by an identical expression with F_N replaced by a function

$$G_N(\xi, \kappa; \sigma) = \frac{1}{2} F_N(\xi, \kappa; \sigma) + \sum_{n=0}^{N-1} F_n(\xi, \kappa; \sigma), \quad (9)$$

and $V_0^2 = \hbar e b_0^2/m^* B_0$. The weight functions F_N and G_N are polynomials of order $2N$. Universality of the critical behavior in the IQHE implies that the particular form of F_N is irrelevant as long as it is given by eq. (8). We conjecture that universality holds for all polynomials in particular the G_N given by eq. (9).

4 Conclusions

We have studied the problem of a charged quantum particle in a random magnetic field in the limit that the average magnetic field is much stronger than the fluctuations of the field. In this limit the density of states splits into well separated Landau bands. These correspond in the ‘‘composite fermion’’ picture to the magical filling factors of the FQHE and the IQH transitions in the centers of these Landau bands correspond to the FQH plateau transitions. We have shown that in the two limits of the lowest Landau level and slowly varying magnetic field the random magnetic field is strictly equivalent to a random electrostatic potential. Analyzing the statistical properties of the random magnetic field projected onto the Landau levels we are led to the conjecture that the critical behavior of the present model and the IQHE are identical for arbitrary Landau level and distribution of the magnetic field.

References

- [*] This work was performed within the research program of the Sonderforschungsbereich 341.
- [1] R. B. Laughlin, Phys. Rev. B **23**, 5632 (1981); H. Aoki and T. Ando, Solid State Commun. **38**, 1079 (1981); B. I. Halperin, Phys. Rev. B **25**, 2185 (1982).
- [2] K. von Klitzing, G. Dorda, and M. Pepper, Phys. Rev. Lett. **45**, 494 (1980).
- [3] A. M. M. Pruisken, Phys. Rev. Lett. **61**, 1297 (1988).
- [4] For a review see: B. Huckestein, Rev. Mod. Phys. **67**, April (1995).
- [5] H. P. Wei, D. C. Tsui, M. A. Paalanen, and A. M. M. Pruisken, Phys. Rev. Lett. **61**, 1294 (1988).
- [6] B. Huckestein and B. Kramer, Phys. Rev. Lett. **64**, 1437 (1990).
- [7] S. Koch, R. Haug, K. v. Klitzing, and K. Ploog, Phys. Rev. Lett. **67**, 883 (1991).
- [8] B. Huckestein, Europhysics Lett. **20**, 451 (1992).
- [9] D. C. Tsui, H. L. Störmer, and A. C. Gossard, Phys. Rev. Lett. **48**, 1559 (1982); R. Laughlin, Phys. Rev. Lett. **50**, 1395 (1983).
- [10] L. W. Engel, H. P. Wei, D. C. Tsui, and M. Shayegan, Surf. Sci. **229**, 13 (1990); S. Koch, R. J. Haug, K. v. Klitzing, and K. Ploog, Phys. Rev. B **43**, 6828 (1991).
- [11] J. K. Jain, Phys. Rev. Lett. **63**, 199 (1989).
- [12] J. K. Jain, S. A. Kivelson, and N. Trivedi, Phys. Rev. Lett. **64**, 1297 (1990).
- [13] A. Lopez and E. Fradkin, Phys. Rev. B **47**, 7080 (1993); B. I. Halperin, P. A. Lee, and N. Read, Phys. Rev. B **47**, 7312 (1993).
- [14] E. Abrahams, P. W. Anderson, D. C. Liciardello, and V. Ramakrishnan, Phys. Rev. Lett. **42**, 673 (1979).
- [15] V. Kalmeyer and S. Zhang, Phys. Rev. B **46**, 9839 (1992); V. Kalmeyer, D. Wei, D. Arovas, and S. Zhang, Phys. Rev. B **48**, 11095 (1993); Y. Avishai, Y. Hatsugai, and M. Kohmoto, Phys. Rev. B **47**, 9561 (1993); T. Kawarabayashi and T. Ohtsuki, Phys. Rev. B **51**, 10897 (1995).
- [16] T. Sugiyama and N. Nagaosa, Phys. Rev. Lett. **70**, 1980 (1993); D. K. K. Lee and J. T. Chalker, Phys. Rev. Lett. **72**, 1510 (1994); A. Aronov, A. Mirin, and P. Wolfle, Phys. Rev. B **49**, 16609 (1994).

Understanding the dynamics of fractional edge states with composite fermions

Dmitri B. Chklovskii and Bertrand I. Halperin

Physics Department, Harvard University, Cambridge, MA 02138

Abstract

Fractional edge states can be viewed as integer edge states of composite fermions. We exploit this to discuss the conductance of the fractional states and the velocity of edge magnetoplasmons.

One of the most interesting developments in the physics of the quantized Hall effect was the introduction of the composite fermion approach [1, 2, 3, 4]. It is realized through an exact transformation of the initial electron system to the system of composite fermions by attaching two flux quanta to each particle. The mean-field approximation to the new system already contains much of the physics related to electron-electron correlations. In particular it allows one to understand fractional quantized Hall states as integer quantized Hall states of composite fermions. Because of the presence of an excitation gap in the bulk, edge states play an important role in these systems. It is natural then to apply composite fermions to study fractional edge states. This has been done using the Hartree approximation for composite fermions [5, 6], which yields ground state properties such as the density distribution and the number of edge channels for various filling factors. One has to go beyond the Hartree approximation in order to study the dynamics of the edge states, which involves excited states.

In this paper we use the RPA to study fractional edge states. We begin by reviewing “gauge argument” and applying it to the system of composite fermions. This leads us to the introduction of the composite fermion electrochemical potentials which are very useful in calculating conductance of the system.

Following Laughlin [7] and Halperin [8] we consider an idealized clean 2DEG sample of the annular shape at filling factor ν . As the magnetic flux threading the hole is increased adiabatically by one flux quantum (ϕ_0) ν electrons are transferred from the outer to the inner edge of the sample. This leads to the total energy change given by $\nu(\xi_o - \xi_i)$, where $\xi_o - \xi_i$ is the difference between electrochemical potentials on the two edges. Since the work done on the system is given by $I\phi_0/c$, where I is the current around the annulus,

$$I = \nu(e/h)(\xi_o - \xi_i). \quad (1)$$

Now we rederive this result by using composite fermions. The electron system at filling factor $\nu = p/(2p+1)$ is viewed as the system of composite fermions at integer filling factor p . Naively, increasing the magnetic flux threading the annulus by one flux quantum will transfer p composite fermions between the outer and the inner edge. However the change in the flux $\Delta\phi$ enclosed by the annulus median comes from the flux carried by composite fermions as well as from the external source. Thus $\Delta\phi = (1-2x)\phi_0$, where x is the net

number of composite fermions transferred between the edges. By relating the net transferred charge to the change in flux, using $x = p\Delta\phi/\phi_0$, we find that $x = p/(2p+1)$ in agreement with the electron result.

It is helpful to introduce the composite fermion electrochemical potential, ξ^f . We define it as a change in the total energy resulting from adiabatically adding a composite fermion to the edge. The difference from the electron potential becomes clear in view of the previous discussion. The addition of a composite fermion to the edge involves turning on of the Chern-Simons flux, which adds or removes electrons from the edge. We find the following relation between the two potentials:

$$\xi^f = \xi/(2p+1) \quad (2)$$

If the edges of the annulus are sufficiently well separated currents associated with each edge can be defined. These currents must depend only on the electrochemical potential of the corresponding edge. Since the total current is given by Eq.1 the edge current is

$$I = \nu(e/h)\xi. \quad (3)$$

Expressing this result in terms of the composite fermion potential

$$I = p(e/h)\xi^f. \quad (4)$$

For the case $|p| > 1$, there will be several states at each edge, and in the ideal case one can define separate chemical potentials ξ^f on each edge state. We have assumed that there is a sufficient amount of scattering due to impurities or phonons, so that the states at a given edge are equilibrated, and there is a single chemical potential at each edge.

Now we consider an electromagnetic response of a single edge at a finite wavevector along the edge. The single edge approximation is justified if the wavelength is smaller than the distance between the edges. For a given bulk filling factor there can be several magnetoplasmon modes at the edge if the impurity scattering is not too great. Here we restrict ourselves to the case of a sharp confinement potential. In this case there is only one mode present for simple fractions $\nu = 1/(2k+1)$. We focus on the $\nu = 1$ case where the composite fermion result can be easily compared against the electron calculation. We can use previously derived formulas setting $p = -1$. Our goal is to find a pole in the response function and identify it with the magnetoplasmon mode.

We start by deriving the electron result. For frequencies smaller than the cyclotron frequency and wavelengths larger than the magnetic length eq.3 can be written in terms of Fourier harmonics

$$I(k, \omega) = (e/h)\xi(k, \omega). \quad (5)$$

The electrochemical potential can be represented as a sum of the external potential and the induced potential

$$\xi(k, \omega) = \xi^e(k, \omega) + \xi^i(k, \omega) \quad (6)$$

The induced electrochemical potential is proportional to the electron density at the edge

$$\xi^i(k, \omega) = n(k, \omega)\partial\xi/\partial n. \quad (7)$$

The coefficient $\partial\xi/\partial n$ is independent of k in the limit $k \rightarrow 0$, if the electron-electron interaction is short ranged; for unscreened Coulomb interactions we have $\partial\xi/\partial n \sim |\ln k|$. For the wavelengths smaller than the length of the edge we invoke the continuity equation $n(k, \omega) = I(k, \omega)k/\omega$ to get

$$\xi'(k, \omega) = I(k, \omega)(k/\omega)\partial\xi/\partial n \quad (8)$$

By substituting $I(k, \omega)$ from the eq.5 and solving for $\xi(k, \omega)$ we find

$$\xi(k, \omega) = \frac{\xi^e(k, \omega)}{1 - (k/\omega)(e/h)\partial\xi/\partial n} \quad (9)$$

Substituting this expression in eq.5 we obtain the full response function

$$I(k, \omega) = \frac{(e/h)\xi^e(k, \omega)}{1 - (k/\omega)(e/h)\partial\xi/\partial n} \quad (10)$$

At finite k and ω there is a pole in the response function, which can be identified with the magnetoplasmon mode. Because of the stability considerations $\partial\xi/\partial n$ has to be positive. Then the direction of propagation is in agreement with the classical magnetoplasmon result.[9]

Attachment of two flux quanta transforms the $\nu = 1$ state into the $\nu = -1$ state with the effective magnetic field reversed. Therefore, on the mean field level one might expect that the composite fermion approach gives the reverse direction of propagation for the magnetoplasmon mode. In fact this is the result that comes out of the Hartree approximation, where the induced Chern-Simons field is neglected. Let us demonstrate that including properly the Chern-Simons electric field gives the expected direction of propagation in the composite fermion approach. Eq.4 can be written in terms of Fourier harmonics

$$I(k, \omega) = -(e/h)\xi'(k, \omega). \quad (11)$$

The composite fermion electrochemical potential ξ^f may be related to the electron potential ξ and the edge current I by

$$\xi(k, \omega) = \xi^f(k, \omega) + 2(h/e)I(k, \omega) \quad (12)$$

where the second term results from the Chern-Simons electric field produced by the current. [Eqs.11 and 12 imply Eq.2, as required] Substituting Eq. 12 in Eq. 6 we find

$$\xi^f(k, \omega) = \xi^e(k, \omega) - 2I(k, \omega)h/e + n(k, \omega)\partial\xi/\partial n \quad (13)$$

Using the continuity equation and expressing current in terms of the composite fermion electrochemical potential we get

$$\xi^f(k, \omega) = \xi^e(k, \omega) + 2\xi^f(k, \omega) + (k/\omega)\partial\xi/\partial n \xi^f \quad (14)$$

Solving this equation for ξ^f we find

$$\xi^f(k, \omega) = \frac{\xi^e(k, \omega)}{-1 - (k/\omega)(e/h)\partial\xi/\partial n} \quad (15)$$

Both of the terms in the denominator change signs here compared to Eq.9 thus giving the right direction of propagation for the magnetoplasmon mode. In Hartree approximation the Chern-Simons contribution to the electrochemical potential $2I(k, \omega)h/e$ is ignored thus yielding an incorrect direction of propagation.

For more complicated filling fractions ν , where there are two or more edge states at a single edge, it is necessary to take into account interactions between charge fluctuations associated with the different edge states. Similarly, if one considers wavelengths which are not large compared to the inverse magnetic length and/or the geometric width of the edge, it is necessary to take into account more details of the electron wavefunctions. A natural approximation to use in this case is the RPA (or time dependent Hartree approximation) where the composite fermions are treated as non-interacting particles, driven by the space and time-dependent scalar and vector potentials. For a single edge state, the integral equation which results from the RPA reduces properly to the above equations in the limit where k and ω are small, giving the correct direction of propagation as expected.

We are grateful to A. Stern for helpful discussions. This work has been supported by the Harvard Society of Fellows and by NSF Grant No. DMR94-16910.

References

- [1] J. K. Jain, Phys. Rev. Lett. **63**, 199 (1989).
- [2] A. Lopez and E. Fradkin, Phys. Rev. B, **44**, 5246 (1991).
- [3] V. Kalnins and S.-C. Zhang, Phys. Rev. B **46**, 9889 (1992).
- [4] B. I. Halperin, P. A. Lee, and N. Read, Phys. Rev. B **47**, 7312 (1993).
- [5] L. Brey, Phys. Rev. B **50**, 11861 (1994).
- [6] D. B. Chklovskii, Phys. Rev. B **51**, 9895 (1995).
- [7] R. B. Laughlin, Phys. Rev. B **23**, 5632 (1981).
- [8] B.I. Halperin, Phys. Rev. B **25**, 2185 (1982).
- [9] V.A. Volkov, S.A. Mikhailov, Sov. Phys. JETP **67**, 1639 (1988).

Liquid to Insulator Transition of Composite Particles

D. Shahar, L.W. Engel, D.C. Tsui, M. Shayegan and R.N. Bhatt
Dept. of Electrical Engineering, Princeton University, Princeton New Jersey, 08544.

J.E. Cunningham

AT&T Bell Laboratories, Holmdel, New Jersey 07733

Abstract

We present results of a systematic experimental study of the quantum Hall effect liquid to insulator transition. Our results provide evidence for the validity of the bosonic Chern-Simons transformation applied to two dimensional electron systems at high magnetic field.

There are two main theoretical approaches to the application of the Chern-Simons gauge transformation to two dimensional electron systems (2DES) at high B . In the “composite Fermions” approach¹, one attaches an even number of flux quanta to each electron and the resulting particles still obey Fermi statistics. This approach is particularly useful near even-denominator Landau filling fractions (ν) where the composite Fermions experience small or vanishing effective B .² In the other approach, composite Fermions are attached to each electron, and composite bosons are formed. For these bosons, zero effective B corresponds to odd denominator ν , where the incompressible fractional quantum Hall effect (FQHE) states are observed. The dissipationless FQHE states can then be interpreted as a bose-condensed liquid of the composite bosons.³

In a recent theoretical paper, Kivelson, Lee and Zhang (KLZ)⁴ utilized the bosonic transformation to formulate a global description of the various quantum phases of 2DES at high B . They developed a set of correspondence rules that relate the various quantum Hall effect (QHE) states, and the transitions between them. As part of this description, they predicted the existence of a novel insulator, termed the Hall insulator (HI), as the high B , high disorder limit of the QHE. The transitions from the QHE liquid states to this HI are also related by the same correspondence rules. Further, by utilizing this bosonic mapping, KLZ were able to draw an analogy between these transitions and the superconductor-insulator transitions in two dimensions.^{5,6}

In this paper we describe the results of a systematic study of the transitions from the $\nu = 1$ and $1/3$ QHE liquids to the HI.⁷ We studied a wide range of samples with mobilities from $\mu = 10 - 550 \cdot 10^3 \text{ cm}^2/\text{Vsec}$ and densities from $n = 0.1 - 2.26 \cdot 10^{11} \text{ cm}^{-2}$, at low temperatures ($T > 20 \text{ mK}$) and high magnetic fields ($B < 15.5 \text{ T}$). Our results demonstrate both the similarity of the QHE to HI transition with the superconductor-insulator transition observed in thin metal films and the correspondence between the transitions from the $\nu = 1$ and $\nu = 1/3$ QHE states to the HI. We also provide evidence for the existence of a universal ρ_{xx} value at the critical point of the transitions as suggested by KLZ.

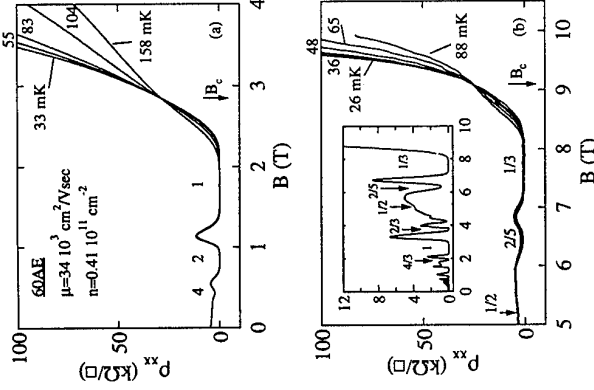


Figure 1. ρ_{xx} vs B traces at several T 's. Numbers denote the QHE state. The sample in (b) is M12412B, with $\mu = 5.5 \cdot 10^5 \text{ cm}^{-2}/\text{Vsec}$ and $n = 0.63 \cdot 10^{11} \text{ cm}^{-2}$.

In Fig. 1a, we plot ρ_{xx} vs B traces taken at various T 's for a typical low n , low μ sample. In addition to the usual integer quantum Hall minima observed at $\nu = 1, 2$ and 4 , the transition from the $\nu = 1$ state to the HI can be clearly identified with the crossing point of the ρ_{xx} traces at $B_c = 2.85 \text{ T}$. In Fig. 1b we plot similar ρ_{xx} traces, but for a sample with much higher μ . This sample exhibit a set of fractional quantum Hall liquid states including $4/3, 2/3, 2/5$ and $1/3$ (See inset of Fig 1b). Despite the large mobility difference between these samples, a striking similarity exists in the overall appearance of their ρ_{xx} traces (note the shifted B axis in Fig. 1b). In particular, the mapping referred to by KLZ between the transitions to the insulator is evident. This can be even more clearly seen in Fig. 2 where we plot ρ_{xx} vs T at several B values near the transition from the $\nu = 1$ and $1/3$ (Fig 2a and 2b, respectively) QHE states to the HI. In this figure, the role of B_c (solid symbols) is readily demonstrated: For all B values below B_c a QHE liquid like behavior is observed, with $\rho_{xx} \rightarrow 0$ as $T \rightarrow 0$, and for $B > B_c$ an insulating behavior with $\rho_{xx} \rightarrow \infty$ as $T \rightarrow 0$ is evident. The data presented in Fig. 2 is also reminiscent of the superconductor-insulator transition in thin metal films.⁶

$\nu=1/3$ to Insulator

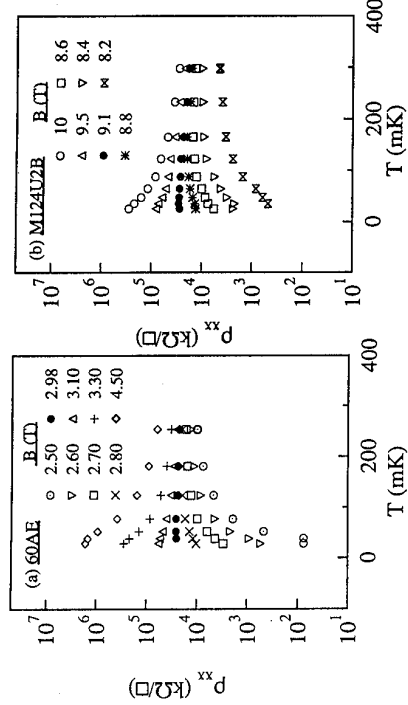


Figure 2. ρ_{xx} vs T at several B 's, for the samples in Fig. 1. Solid circles are data taken at B_c .

As suggested by Fisher⁵, near such phase transitions in two dimensions, universal behavior is a distinct possibility. For example, the value of ρ_{xx} at the transition point is expected to be independent of any sample parameter. In Fig. 3 we plot our values of ρ_{xx} obtained for several samples and runs. One can see that the data are scattered near h/e^2 , independent of sample parameters and, remarkably, of whether the transition is from the $\nu = 1$ IQHE or the $\nu = 1/3$ FQHE liquid states. This universal value is in agreement with the predictions of KLZ. We note that the existence of a universal value at the superconductor-insulator transition has not yet been convincingly demonstrated.⁸

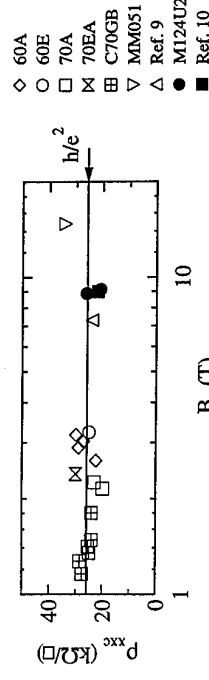


Figure 3. ρ_{xx} at the transition point for our samples, plotted against B_c .

To summarize, we have presented results of a comprehensive study of the QHE

liquid to insulator transition in a wide variety of samples. Our results are in support of the validity of the bosonic Chern-Simons mapping in the QHE regime.

1. J.K. Jain, Phys. Rev. Lett. **63**, 199 (1989); Phys. Rev. B **40**, 8079 (1989).
2. B.I. Halperin, P.A. Lee, and N. Read, Phys. Rev. B **47**, 7312 (1993).
3. S.C. Zhang, T.H. Hansson, and S.A. Kivelson, Phys. Rev. Lett. **62**, 82 (1989).
4. S. Kivelson, D.H. Lee, and S.C. Zhang, Phys. Rev. B **46**, 2223 (1992).
5. M.P.A. Fisher, G. Grinstein and S.M. Girvin, Phys. Rev. Lett. **64**, 587 (1990); M.P.A. Fisher, Phys. Rev. Lett. **65**, 923 (1990).
6. Y. Liu, D.B. Haviland, B. Nease, and A.M. Goldman, Phys. Rev. B **47**, (1993); and reference therein.
7. D. Shahar, D.C. Tsui, M. Shayegan, R.N. Bhatt and J.E. Cunningham, Phys. Rev. Lett. **74**, 4511 (1995).
8. A. Yazdani and A. Kapitulnik, Phys. Rev. Lett. **74**, 3037 (1995).
9. M.A. Paalanen, D.C. Tsui, A.C. Gossard and J.C.M. Hwang, Solid State Comm., **50**, 841 (1984).
10. A. Fukano, S. Kawaji, J. Wakabayashi, K. Hirakawa, H. Sakaki, T. Gotoh, Y. Koike, and T. Fukase, Proceedings of the 11th International Conference on High Magnetic Fields in Semiconductor Physics, Cambridge, (1994).

COMPOSITE-FERMION PICTURE FOR THE DOUBLE-LAYER FRACTIONAL QUANTUM HALL EFFECT

T. Nakajima¹ and H. Aoki²

¹Semiconductor Research Laboratory, Mitsubishi Electric Corporation, Amagasaki, Hyogo

661, Japan

²Department of Physics, University of Tokyo, Hongo, Tokyo 113, Japan

Abstract:

The composite-fermion picture is applied to the double-layer fractional quantum Hall system at the fractional total Landau level filling of $\nu = 1/m$ (m : odd integer) to study the collective pseudospin-wave excitation mode. The result indicates that the system may be regarded as a system of composite fermions with reduced inter-particle interactions and unchanged interlayer tunnelling, which makes the quantum-Hall regime, identified by a finite pseudospin-wave excitation gap, wider as ν becomes $1/3, 1/5, \dots$

1. Introduction

Recently much attention is focussed on what happens when two fractional quantum Hall (FQH) liquids are placed together [1,2]. The double-layer system is analogous to a single-layer system of spin 1/2 electrons if one mimics the layer degrees of freedom by a pseudospin, but an essential difference lies in two mechanisms that make the pseudospin polarised: (i) The interlayer tunnelling, which makes single-particle wavefunctions split into symmetric and antisymmetric ones with the energy gap Δ_{SAS} , tends to push the electrons into the symmetric band. (ii) The intra- and inter-layer electron correlations, which is controlled by the layer separation d , pushes the ground state towards Halperin's Ψ_{num} [3] [4]. The tunnelling degrades the symmetry $U(1)$, originally degraded from $SU(2)$ for finite d , and the double layer is analogous to an easy-plane ferronagnet for the (total) Landau level filling of $\nu = 1/m$ (m : odd integer) [5].

In a phase diagram against the layer separation normalised by the magnetic length, ℓ , and the strength of tunnelling, Δ_{SAS} , relative to the typical Coulomb-interaction energy, $e^2/\epsilon\ell$ (ϵ : dielectric constant), the nature of the quantum Hall (QH) state, for $\nu = 1$, evolves continuously [6,7] from correlation-dominated to tunnelling-dominated. The QH regime is identified from a finite charge excitation gap. The excitation spectra have been calculated for $\nu = 1$ with the single-mode approximation (SMA) [6,7] or RPA [8]. The low-lying excitation from the polarised ground state is a Nambu-Goldstone (pseudospin-wave) mode where the densities of two layers fluctuate in a correlated manner [6,7,8].

A natural question then is how we can extend the physics to the fractional case [9]. In view of the recent success in the composite-fermion picture or the Chern-Simons gauge field theory [10], for the ordinary (single-layer) FQH effect, it is intriguing to look into how the picture applies to the physics underlying the double-layer FQH effect.

A Chern-Simons (CS) approach, with the fluctuation around the mean CS gauge field treated with RPA, has been used to obtain the excitation spectra [1], but the effective mass of the particle remains a quantity difficult to fix. In fact the Chern-Simons RPA calculations for the double-layer system [12] are still some way from an accurate description. In an alternative approach by the present authors [13], the flux-attachment is plugged directly into the electron-electron interaction, which enables us to obtain a parameter-free, analytic formula for the Nambu-Goldstone mode for fractional cases for the first time, thickness of each layer for simplicity.

2. Formulation for the pseudospin wave

We first rewrite the theory of the pseudospin-wave excitation at $\nu = 1$ by MacDonald *et al* [6] in the spherical geometry to exploit the full rotational symmetry [7]. This makes the relevant quantum number the angular momentum, which in turn facilitates the flux-attachment. When the total magnetic flux going out of the sphere is $2S'$ (an integer) times the flux quantum, the relation to ν is $2S' = \nu^{-1}/N - \delta$ with N being the number of electrons and δ an integer. The inter-particle interaction may be projected onto the components $\{V_j^{\sigma\sigma'}\}$ (the Haldane pseudopotential) for the relative angular momentum $n = 2S' - J$, where $V_J^{11} = V_J^{22}$ and $V_J^{12} = V_J^{21}$ are the intra- and inter-layer pseudopotentials, respectively.

The effective Hamiltonian for the pseudospin ferronagnet at $\nu = 1$ in the SMA, now written for the spherical geometry, is diagonalised via a Bogoliubov transformation with the eigenenergy,

$$\begin{aligned}\omega_L &= \sqrt{\epsilon_L(\epsilon_L + 2\lambda_L)}, \\ c_L &= \Delta_{SAS} + \sum_{J=0}^{2S} (2J+1) (-1)^{2S-J} V_J^{12} \left[\frac{1}{2S+1} - (-1)^{2S-J} \left\{ \begin{array}{ccc} S & S & L \\ S & S & J \end{array} \right\} \right], \\ \lambda_L &= \sum_{J=0}^{2S-L-odd} (2J+1) (V_J^{11} - V_J^{12}) (-1)^{2S-J} \left\{ \begin{array}{ccc} S & S & L \\ S & S & J \end{array} \right\}. \end{aligned}\quad (1)$$

Here L the total angular momentum and $\{SS'\}$ is the $6j$ symbol.

Now we introduce the CF picture for $\nu = 1/m$ (m : odd integer), where we attach $(m-1)$ out of m flux quanta to each electron. The relative angular momentum n between electrons then translates into the relative angular momentum $n - (m-1)$ between composite fermions. Since B_{eff} is thereby reduced from the full field by a factor of $1/m$, the magnetic length ℓ and the number of single-particle states per unit area, $1/\pi\ell^2$, remain, in a mean-field sense, to have the values for $\nu = 1$. Therefore the correspondence between before ($\nu = 1/m$) and after ($\nu = 1$, tilde quantities) the CF transformation reads $2S = m(N-1) \rightarrow 2S' = N-1$, $V_{2S-n}^{\sigma\sigma'}/(\epsilon^2/\ell) \rightarrow \tilde{V}_{2S-[n-(m-1)]}^{\sigma\sigma'}/(\epsilon^2/\tilde{\ell})$, where the pseudopotentials are shifted to a higher side of the relative angular momentum (where the potential is weaker).

When we plug this transformation into the formula for $\nu = 1$, we arrive at the desired expression for $\nu = 1/m$, $\omega_L = \sqrt{\epsilon_L} (\tilde{\epsilon}_L + 2\tilde{\lambda}_L)$, where every quantity in ϵ_L and λ_L is replaced with tilde one. The range of the total angular momentum is now reduced to $0 \leq L \leq$

$2\hat{S}$. As for the tunnelling, we can regard that the flux attachment (or the singular gauge transformation) does not affect the interlayer tunnelling.

3. Results and discussions

The formulation above rests on the assumption that the QHE region is pseudospin-polarised throughout. We first check this for $\nu = 1$ by actually calculating the probability for the ground state, $|g\rangle$, to be pseudospin-polarised, given by $P = \sum_{N_1} (|\Psi_{111}^{N_1}|g\rangle)^2$, where $\Psi_{111}^{N_1}$ is Halperin's wavefunction for N_1 electrons in layer 1 [14]. The result (Fig.1) obtained numerically for an 8-electron system shows that the pseudospin-polarised region indeed agrees quite well with the QHE region identified by a finite pseudospin-wave gap in the SMA (Fig.2).

Thus the quantum Hall state for $\nu = 1$ does retain its pseudospin-polarisation and rotates its Bogoliubov angle continuously, with no intervening non-QHE region, from a tunnelling-dominated limit ($\Psi_{\text{sym}}^{\nu=1}$) to a correlation-dominated limit ($\Psi_{111}^{N=1/2}$). This is contrasted with a spurious dip seen when only the overlap with the extremes ($\Psi_{\text{sym}}^{\nu=1}$ or $\Psi_{111}^{N=1/2}$) are considered [15]. The continuity is consistent with an experimental result [1].

Now we turn to our original purpose of the composite-fermion SMA result with a numerical one for a 5-electron system at $\nu = 1/3$ in the inset of Fig.2. The result indeed indicates that the $\nu = 1/m$ double-layer FQH system may be regarded as a system of composite fermions, where we have reduced inter-particle interactions while the interlayer tunnelling is left unchanged.

The reduction of the inter-particle interaction increases the relative importance of Δ_{SAS} . Thus the persistence of the one-component character of the $\nu = 1/3$ FQH state observed in a wide single quantum well [2], where Δ_{SAS} is intrinsically large, can be explained naturally.

The increased relative importance of Δ_{SAS} can also be seen in the phase diagram for $\nu = 1/m$ (Fig.2), which is obtained by identifying the touching of the pseudospin-wave mode to the $E = 0$ axis as the disappearance of the QHE state. An enhanced role of Δ_{SAS} pushes the ground state towards the one-component FQH state and widens the QHE region as ν becomes $1/3, 1/5, \dots$

This work was in part supported by a Grant-in-Aid from the Ministry of Education, Science and Culture, Japan.

References

- [1] S.Q. Murphy *et al.*, Phys. Rev. Lett. **72** (1994) 728.
- [2] Y.W. Suen *et al.*, Phys. Rev. Lett. **72** (1994) 3405.
- [3] B.I. Halperin, Helv. Phys. Acta **56** (1983) 75.
- [4] D. Yoshioka, A.H. MacDonald and S.M. Girvin, Phys. Rev. B **39** (1989) 1932.
- [5] K. Moon *et al.*, Phys. Rev. B **51** (1995) 5138.
- [6] A.H. MacDonald, P.M. Platzman and G.S. Boebinger, Phys. Rev. Lett. **65** (1990) 776.
- [7] T. Nakajima and H. Aoki, Physica B **201** (1994) 327.
- [8] O. Narikiyo and D. Yoshioka, J. Phys. Soc. Jpn. **62** (1993) 1612.

[9] SMA calculations of the excitation spectra for fractional fillings have only been done in the absence of interlayer tunnelling for $\nu = 2/(m+n)$ by A.H. MacDonald and S.C. Zhang, Phys. Rev. B **49** (1994) 17208.

[10] J.K. Jain, Phys. Rev. Lett. **63** (1989) 199; A. Lopez and E. Fradkin, Phys. Rev. B **44** (1991) 5246; B.I. Halperin, P.A. Lee and N. Read, Phys. Rev. B **47** (1993) 7312.

[11] A. Lopez and E. Fradkin, Phys. Rev. B **47** (1993) 7050; S.H. Simon and B.I. Halperin, Phys. Rev. B **48** (1993) 17368.

[12] Z.F. Ezawa and A. Iwazaki, Phys. Rev. B **47** (1993) 7295; A. Lopez and E. Fradkin, Phys. Rev. B **51** (1995) 4347.

[13] T. Nakajima and H. Aoki, Phys. Rev. Lett. **73** (1994) 3568.

[14] X.G. Wen and A. Zee, Phys. Rev. Lett. **69** (1992) 1811.

[15] S. He, S. Das Sarma and X.C. Xie, Phys. Rev. B **47** (1993) 4394.

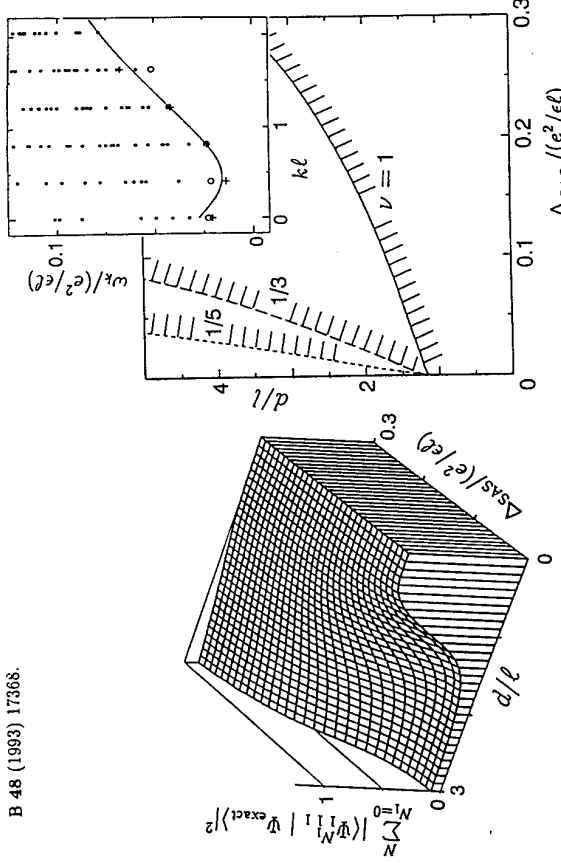


Fig.1. The probability of the ground state for $\nu = 1$ to be pseudospin-polarised, which is defined by $\sum_{N_1} (|\Psi_{111}^{N_1}|g\rangle)^2$ (g): the ground-state wavefunction, N_1 : the number of electrons in layer 1) and numerically obtained for an 8-electron system.

Fig.2. The composite-fermion SMA result for the phase diagram for the $\nu = 1/m$ pseudospin-polarised quantum-Hall state (the region below each line). The inset showing the pseudospin-wave excitation compares a numerical result for a 5-electron system (circles) with the composite-fermion SMA (for 5(crosses) or 5(solid line) electron systems) at $\nu = 1/3$ with $d/\ell = 1.0, \Delta_{\text{SAS}}/(\epsilon^2/\ell\ell) = 0.01$.

RESONANT RAMAN SCATTERING AND NUMERICAL STUDY IN
THE FRACTIONAL QUANTUM HALL REGIME

Song He & P. M. Platzman
AT&T Bell Laboratories
Murray Hill, NJ 07974, USA

We use finite size numerical method to address various issues related to resonant Raman scattering experiments in the fractional quantum Hall regime. We have calculated the excitation spectra and the multiple density correlation functions of such systems in the spherical geometry using the lowest Landau level approximation. We find, (1) In the excitation spectra of a system at filling factor $\nu = 1/3$, at small wave vectors, there are excited states at energies below that of the collective mode. The projected weights of these states into the double roton subspaces indicate that they are double roton bound states formed by two rotons with almost opposite momenta. We argue that these states could contribute significantly to Raman intensity in a resonant Raman scattering experiment. At wave vectors of about twice the roton wave vector, there are structures in the dynamic structural factor. Our numerical results indicate that they are resonant states formed by two rotons inside the continuum of excited states. We believe they are accessible in resonant Raman scattering by grating the sample. (2) If the filling factor moves away from the incompressible filling fractions, at momentum transfer comparable to $1/a$, where a is the inter particle spacing, there are broad peaks at energies comparable to Coulomb interaction energy in dynamic structural factor. We believe these structures describe excitations resulting from distorting the system locally on a length scale comparable to the inter particle spacing.

EFFECTIVE MASSES OF COMPOSITE FERMIONS

N. d'Ambrumenil¹ and R. Morf²

¹Department of Physics, University of Warwick, Coventry, CV4 7AL, UK
²Paul Scherrer Institut, Badenstrasse 569, CH 8048 Zurich, Switzerland

Abstract

The close correspondence we find between the ground state energy and that for free fermions as a function of system size in small systems allows us to make theoretical estimates of the CF effective mass, m^* , not based on the scaling of gap energies away from half-filling. The quasiparticle-quasihole excitations for systems with filled shells also yield an estimate of the effective mass of CF's. Both these estimates agree.

Much is already understood about the properties of a CF liquid once it has formed and once the effective mass parameter, m^* , is known [1]. Here we show how the results of finite size studies can give a good estimate of the effective mass parameter.

Rezayi and Read [2] showed that if a CF state is formed for a system of N particles on a sphere pierced by $2S = 2(N - 1)$ flux units, then the angular momentum should be the same as that expected on the basis of Hund's second rule for electrons in zero magnetic field (we are considering spin-polarized systems, so Hund's first rule is trivially satisfied). It has also been shown [4] that the ground state energy per particle follows closely that of weakly interacting quasi-particles in zero flux. The idea is that the dominant contribution to the ground state Coulomb energy comes from the CF 'kinetic' energy characterized by the effective mass parameter, m^* , with the residual CF-CF interactions playing a subsidiary role.

We now show how this correspondence in energies can be used to give estimates of the effective mass parameter at the filling fractions $\nu = 1/2$, $\nu = 1/4$ and $\nu = 9/4$. The ground state kinetic energy per particle of N non-interacting fermions on a sphere,

$$T(N) = (2\hbar^2/m a^2 N^2) \sum_i^N l_i(l_i + 1). \quad (1)$$

Here a is the ion disc radius, where $\pi a^2 = 1/\text{density}$, for the particles of mass m , and the l_i are the angular momenta of the N lowest energy single-particle states. For filled shells, $T_{f_s}(N) = (\hbar^2 m a^2)(1 - 1/N)$.

For the electrons in magnetic flux $2S = 2(N - 1)$, the ground state energy in the filled-shell configurations at $N = 4, 9, 16$ lie on a straight line when plotted against $1/N$ (Fig. 1a). We can check the extrapolation to the thermodynamic limit using the $L = 0$ states in the $2S = 2N - 3$ and $2N - 1$ families. All three families extrapolate to the same thermodynamic limit. We note in passing that the scaling with $1/N$ is a quite general phenomenon for electrons on a sphere which is associated with curvature effects and the

Figure 1(a) The ground state energy per particle plotted as a function of $1/N$ at $\nu_0 = 1/2$ for $2S = 2N - 2$ and for the $L = 0$ states in the sequences $2S = 2N$ and $2S = 2N - 1$. (For the sequence $2S = 2N$, the $N = 3$ result is off-scale but the dotted line passes through it.) Extrapolations linear in $1/N$ to the thermodynamic limit for all sequences yield -0.932 . The solid line defines the 'equivalent filled shell energy' (see text) at each N for the sequence $2S = 2N - 2$. Energies are quoted in units e^2/ea , where a is the ion disc radius.

(b) The ground state energy minus the respective 'filled shell' equivalent energies for non-interacting free fermions and for interacting electrons at $\nu_0 = 1/2$ and at $\nu_1 = 1/4$. The constant C in Eq 2 is taken as 0.2 at $\nu_0 = 1/2$ and 0.18 at $\nu = 9/4$.

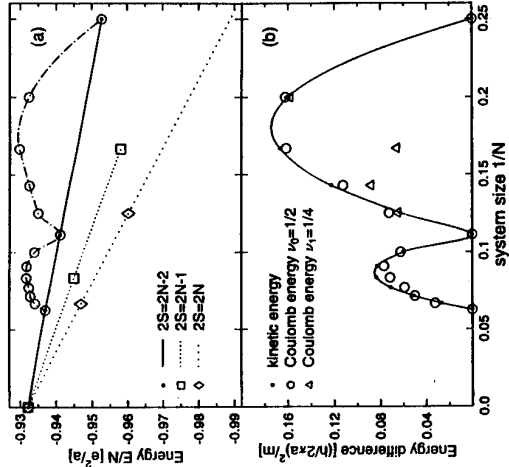
precise definition of the interparticle distance [3]. The linear extrapolation in $1/N$ for the family with $2S = 2(N - 1)$ defines an equivalent 'filled shell' energy for system with N particles given by the solid line in Fig 1a. We subtract this from the actual Coulomb energy to give a measure for the systematic variation of the energy with angular momentum and compare the result with the corresponding difference, $T(N) - T_{f_s}(N)$, for non-interacting CF's in zero field. The results are shown in Fig. 1b.

Fig. 1b is plotted with the effective mass parameter $C = 0.20$ for $\nu = 1/2$, where [1]

$$\frac{\hbar^2}{m^*} = \frac{C}{(4\pi\rho)^{1/2}} e^2, \quad (2)$$

We also show the corresponding result for $\nu = 9/4$ where we estimate $C = 0.18 \pm 0.02$. A similar analysis gives $C = 0.1 \pm 0.02$ for $\nu = 1/4$.

We should be able to improve on the estimates given for C , if we make the additional assumption that the results either side of the filled shell configurations are likely to give the most accurate estimates. This seems reasonable as the outer angular momentum shell is occupied by only one CF particle or hole so that the effects of the residual interaction between CF's should be small. With this assumption our estimates lie between $C = 0.22$ and 0.24 for $\nu = 1/2$. However, we also notice that C tends to increase slightly with system size ($C = 0.244$ for $N = 15$ against 0.232 at $N = 7$) which is, if anything, against expectation. There are expected to be logarithmic corrections to the effective mass as $\nu \rightarrow 1/2$ [1, 5]. These are associated with long wavelength fluctuations of the gauge field, which are cut-off



for $\nu \neq 1/2$ by the cyclotron orbit radius for CF's l_0^{CF} (or alternatively at energy scales less than the CF cyclotron energy). In finite systems on a sphere, this cut-off is provided by the diameter of the sphere and the energy level spacing. Increasing the system size should be somewhat akin to increasing l_0^{CF} in an infinite system. We would therefore expect m^* to increase (C to decrease) with increasing system size which, as we say above, is not what we find.

A complementary route to an estimate of the effective mass parameter involves analysis of the largest angular momentum one-particle one-hole excitation for CF's above the filled shell configurations at $N = 4, 9$ and 16 [6]. The excitation will involve one hole in the filled shell and a particle in the next angular momentum shell. By maximising the angular momentum the two excitations will be as far apart as possible on the sphere. The expectation is that the dominant contribution to the particle-hole excitation energy will be from the kinetic energy and that corrections resulting from any dipole moment and residual CF-CF interactions will be higher order in the inverse system size. The results of this analysis yields $C = 0.195$ for systems at $\nu = 1/2$.

To aid comparison with experiment we can translate the parameter C into a mass. For a sample with a number density of electrons $10^{15} m^{-2}$ and taking a relative permittivity $\epsilon = 13$ for GaAs, we obtain $m^* = .36m_e$ at $\nu = 1/2$, $m^* = .7m_e$ at $\nu = 1/4$ and $m^* = .13m_e$ at $\nu = 9/4$. For samples with number densities $n \times 10^{15} m^{-2}$ these results are multiplied by $n^{1/2}$. The estimates are based on a bare Coulomb interaction between electrons and do not take account of the extent of the wavefunction in the perpendicular direction.

Acknowledgement

We thank the ISI Foundation in Torino for their hospitality and the participants in the ISI workshop on the Quantum Hall Effect, June 1994, for many interesting seminars. We also thank B.I. Halperin and E. Rezayi for useful discussions.

References

- [1] B.I. Halperin, P.A. Lee and N. Read, Phys. Rev. B **47**, 7312 (1993).
- [2] E. Rezayi and N. Read, Phys. Rev. Lett. **72**, 900 (1994).
- [3] R. Morf and B.I. Halperin, Z. Phys. B **68** 391 (1987).
- [4] R. Morf and N. d'Ambrumenil, Phys. Rev. Lett. **74** 5115 (1995).
- [5] A. Stern and B.I. Halperin, preprint 1995, SISSA cond/mat 9502032.
- [6] E. Rezayi, N. Read, R. Morf, N. d'Ambrumenil and S.H. Simon, APS meeting March 1995, San Jose.

Breakdown Phenomena of Integer and Fractional Quantum Hall Effects under Pulsed Magnetic Fields

T. Takamatsu, H. Dodo, M. Ohno and N. Miura
Institute for Solid State Physics, University of Tokyo
7-22-1 Roppongi, Minato-ku, 106 Tokyo, Japan

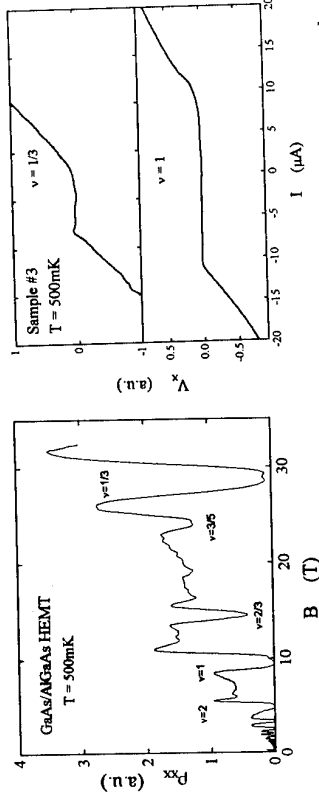
Current-driven breakdown of integer and fractional quantum Hall effects are studied in a wide range of magnetic fields up to 45T using a pulsed magnet and a ^3He refrigerator. Abrupt increase of magneto-resistance above a critical current was found at fractional filling in a similar manner to the breakdown phenomena at integer fillings. Magnetic field dependence of the critical electric fields of the breakdown is discussed in terms of the composite Fermion picture. Electron heating model of the breakdown was discussed in comparison with the breakdown of integer quantum Hall effect.

Recent theoretical studies have demonstrated that the fractional quantum Hall effect (FQHE) can be understood in terms of integer quantum Hall effect (IQHE) of a new type of Fermion which is composed from an electron and even number of flux quanta [1]. The existence of this new Fermion was also studied in experiments such as surface acoustic wave measurements [2] and geometrical resonance measurements [3] which revealed that the composite Fermion is real at least at low temperature. On the other hand, current driven breakdown of the integer quantum Hall effect is one of the most striking phenomena which characterize the non-dissipative current of quantum Hall effect. If the composite Fermion model is applicable even in the strong electric fields, similar phenomena are expected to occur in FQHE. In this paper, we studied the current dependence of diagonal and Hall conductivities in a wide range of magnetic fields using pulsed magnets up to 43T. We show the magnetic field dependence of the breakdown phenomena including FQHE.

Samples used are GaAs/AlGaAs heterostructures of three different carrier densities and mobilities as shown in Table 1. Measurements were performed at ^3He temperatures down to 0.5K using a single shot refrigerator. For the conductivity measurements, we used the active shielding method [4] to avoid the effect of stray and measurement circuit capacitances of the system [5]. Figure 1 shows a typical recorder trace of diagonal resistivity ρ_{xx} of sample # 3 at $T=0.5\text{K}$. Several minima of ρ_{xx} for fractional fillings of electrons were observed in addition to that of integer fillings. Current dependence of ρ_{xx} was measured in the interval of less than 1ms at the top of magnetic fields where derivative of magnetic field $d\mathbf{B}/dt$ was small and change of B is less than 1%. Figure 2 shows the current dependences of voltage drop along the sample V_x at $\nu=1/3$ of sample # 3. Similarly to those at integer fillings, the breakdown of V_x at $\nu=1/3$ of sample # 3 occurs with the same mechanism as IQHE.

Table 1: Mobility and carrier density of three samples used for measurements.

sample	mobility (cm^2/Vs)	carrier density (cm^{-2})
# 1	5×10^5	2×10^{11}
# 2	1.8×10^6	4×10^{11}
# 3	1.2×10^6	2.4×10^{11}



a smaller coefficient k than the experimental value by factor of 8-10 in the case of FQHE.

For the electron heating mechanism, E_{cr} is determined from the balance of the energy gain and the energy loss of the electron system. As discussed in reference [7], the energy gain of the system, in other words, the Joule heating is $\sigma_{xx} E_y^2$, where E_y is the Hall electric field. If we assume a constant energy relaxation time τ , the energy loss of the system should be proportional to $\Xi(T_e) - \Xi(T_L)$, where $\Xi(T_{e,L})$ is the total energy of the system at electron and lattice temperatures. Electron temperature and σ_{xx} at a given electric field E_y are determined by the balance of energy loss and gain of the system,

$$\{\Xi(T_e) - \Xi(T_L)\}/\tau_e = \sigma_{xx} E_y^2.$$

In fig. 4, we show the temperature dependence of the total energy calculated for integer and fractional fillings together with the all over feature of σ_{xx} . The shape of the σ_{xx} vs. T curves of integer and fractional fillings are referred from the data at $\nu=6$ ($B = 7.4$ T) in ref. [9] and from the value of the activation energy at $\nu=1/3$ ($B = 2.5$ T) in ref. [10], respectively. For the temperature dependence of Ξ at an integer filling, we used the same formalism as in ref. [7], i.e.,

$$\Xi = \int_{-\infty}^{\infty} D(\varepsilon) f(\varepsilon) \varepsilon d\varepsilon,$$

where $D(\varepsilon)$ and $f(\varepsilon)$ are the density of states and the Fermi distribution function, respectively. For estimating the temperature dependence of Ξ at fractional fillings, we do not have sufficient theoretical information of the energy spectra of the FQHE states. So, we calculated two kinds of energies: one is the energy of the electron system at $\nu = 1/3$ and $B = 7.4$ T and the other is that of composite Fermions at $\nu=1$ and $B = 7.4/3$ T. We used values of 0.067 m_0 and 0.6 m_0 for the effective masses of electrons and composite Fermions, respectively and $\Gamma=0.1$ meV. The energy balance is realized at the intersect points of two curves in the figure. Increase of electric field E_y results in the upward shift of the σ_{xx} curve. These two curves intersect at several points in a certain narrow range of E_y for the IQHE resulting in the S-shaped E_y dependence of σ_{xx} . Whichever energy loss curve is chosen, it is clear that the heating breakdown occurs. It is not so straightforward to estimate the value of E_{cr} correctly. However, E_{cr} for $\nu=1/3$ ($B = 7.4$ T) seems to have almost the same slope as that of corresponding integer filing ($\nu=6$ $B = 2.5$ T). E_{cr} of the heating breakdown, in general, is scaled by $\hbar\omega_e$ resulting in a small value for FQHE. However, the temperature dependence of σ_{xx} at fractional fillings has different scaling from that of IQHE, i.e., the activation behaviour of σ_{xx} can be written as $\sigma_{xx}(T) = \sigma_{xx}^c \exp(-\Delta/k_B T)$ with $\sigma_{xx}^c = h/e^2 q^2$ at $\nu=p/q$ [10,11]. Because of the small value of σ_{xx}^c , E_{cr} is enhanced to the same order of magnitude as IQHE even with a small value of $\hbar\omega_e$. This enhancement enables us to explain the breakdown of the FQHE states in terms of the heating model. For the scaling relation between E_{cr} 's of different denominators q , quantitative study of electron heating should be needed.

In summary, we have measured critical electric field of the integer and fractional quantum Hall effect and found the E_{cr} can be scaled by B_{rad} of the composite Fermion. The relation between E_{cr} and B_{rad} was discussed in terms of electron heating.
The authors are indebted to Dr. S. Tarucha of NTT, Dr. H. Noguchi and Prof. H. Sakaki of University of Tokyo and Dr. A. Endo and Prof. Y. Iye of University of Tokyo for supplying them with the samples.

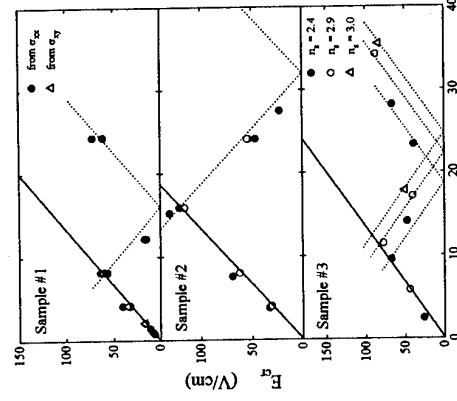


Fig. 3 Critical electric field E_{cr} of three samples determined from current dependence of σ_{xx} and from σ_{xy} (plateau width) as a function of magnetic field. Solid and dotted lines represent linear relation between E_{cr} and B and E_{cr} and B_{rad} , respectively.

References

- [1] J. K. Jain, Phys. Rev. Lett. **63**, 199 (1989).
- [2] R. L. Willett, R. R. Ruel, K. W. Baldwin and K. W. Pfeiffer, Phys. Rev. Lett. **71**, 3846 (1993).
- [3] W. Kang, H. L. Stormer, L. N. Pfeiffer, K. W. Baldwin and K. W. West, Phys. Rev. Lett. **71**, 3850 (1994).
- [4] G. Kido, N. Miura, H. Ohno and H. Sakaki, J. Phys. Soc. Japan **51**, 2168(1982).
- [5] T. Takamasu, H. Dodo and N. Miura, to be published in Solid State Commun.
- [6] S. Kawaji, K. Hirakawa, M. Nagata, T. Okamoto, T. Fukase and T. Goto, J. Phys. Soc. Japan **63**, 2303(1994).
- [7] S. Komiyama, T. Takamasu, S. Hiyamizu and S. Sasa, Solid State Commun. **54**, 47(1986).
- [8] R.R.Du, Phys. Rev. Lett. **70**, 2944 (1993).
- [9] D.R. Leadley, R.J. Nicholas, C.T. Foxon and J.J. Harris, Phys. Rev. Lett. **72**, 1906(1994).
- [10] Y. Kaayama, D. C. Tsui and M. Shavegan, Phys. Rev. **B49**, 7400 (1994).
- [11] R. G. Clark, S. R. Haynes, J. V. Branch, A. M. Suklja, P. A. Wright, P. M. W. Oswald, J. J. Harris and C. T. Foxon, Surface Science **229**, 25 (1990).

Bare and Composite Fermions in Anisotropic Two-dimensional Metals

M. Shayegan and H. C. Manoharan
 Department of Electrical Engineering, Princeton University, Princeton, NJ 08544, USA

Exploiting a gauge freedom unique to two dimensions, the theory of composite fermions^{1,2} (CFs) provides a simple mapping between the fractional quantum Hall effect at high fields and the Shubnikov-de Haas and integer quantum Hall effects at lower fields. Moreover, a full consideration of the “flux-attachment” gauge transformation yields several predictions about the compressible states at high field. For example, one may consider the 2D system near Landau level filling factor $\nu = 1/2$ as a state of weakly-interacting particle-flux composites under the influence of an effective magnetic field $B^* = B - B_{\nu=1/2}$, where B is the real magnetic field piercing the system. At exactly half filling, the resulting state is expected to be metallic with a well-defined Fermi surface, but with perhaps some important departures from a conventional Fermi liquid. Recently, this theoretical conjecture has received experimental support.^{3,4}

We have performed a series of experiments on a high-density ($n_p = 2.1 \times 10^{11} \text{ cm}^{-2}$), low-disorder 2D hole system confined in a 200 Å GaAs quantum well. This sample was grown on a (311)A substrate to incorporate Si atoms as acceptors; in such samples, the x-y planar symmetry of the 2D system is broken due to anisotropy in both scattering as well as in the Fermi surface. We have examined magnetotransport with current directed along the orthogonal directions [01̄] and [23̄] [Fig. 1(a)]. We confirm the remarkable finding³ that the mass of the hole-flux composite particles is very strongly enhanced in the neighborhood of $\nu = 1/2$ and appears to diverge close to the Fermi surface of this metal, i.e., as $B^* \rightarrow 0$ [Fig. 1(b)]. This renormalized mass, derived from a temperature-dependent Shubnikov-de Haas analysis, is larger than the previously measured mass of Ref. 3, consistent with the higher density of this sample.²

We make a comparison of the CF metal around $\nu = 1/2$ to the bare hole metal around zero field, where we observe significantly different low-field transport [Fig. 1(c)] in the two orthogonal directions. Notably, in each type of metal, the temperature dependence of the “zero-field” ($B = 0$ for bare holes, $B^* = 0$ for CFs) resistivity is opposite for each current direction [Fig. 2(a) and (b) separately]. Furthermore, the current directions for the CF metal must be rotated by 90° in order to match the temperature-dependent behavior at zero field [Fig. 2(a) compared to (b)]. We discuss these findings by comparing and contrasting the transport, temperature-dependence, deduced masses, and scattering processes in both types of anisotropic metal.

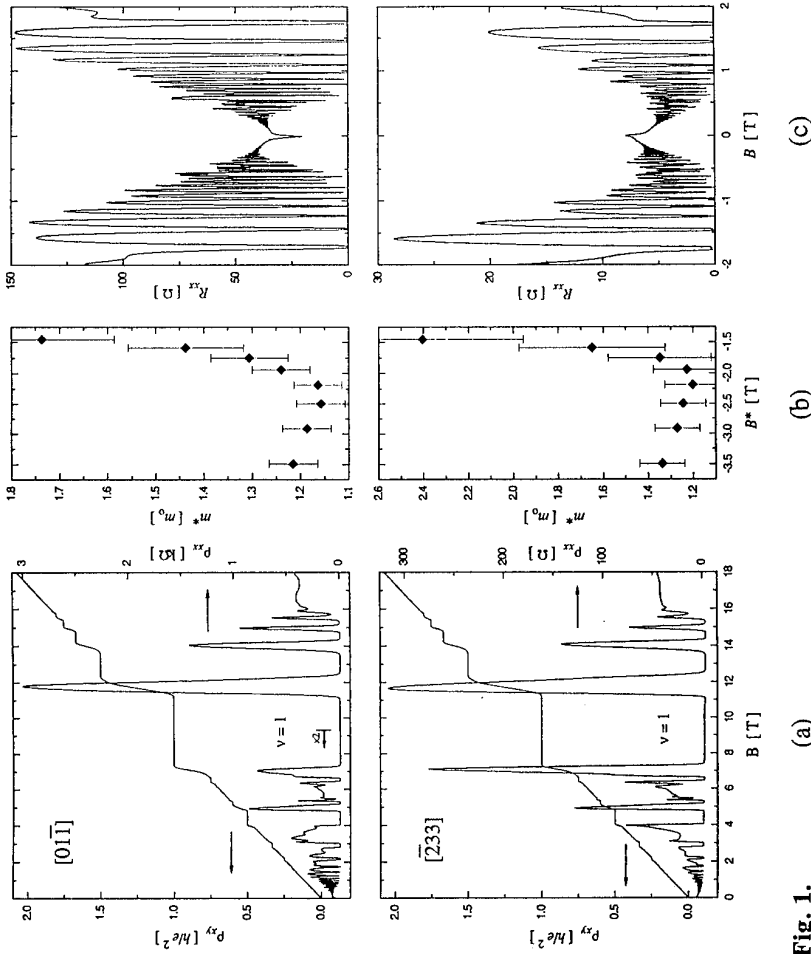
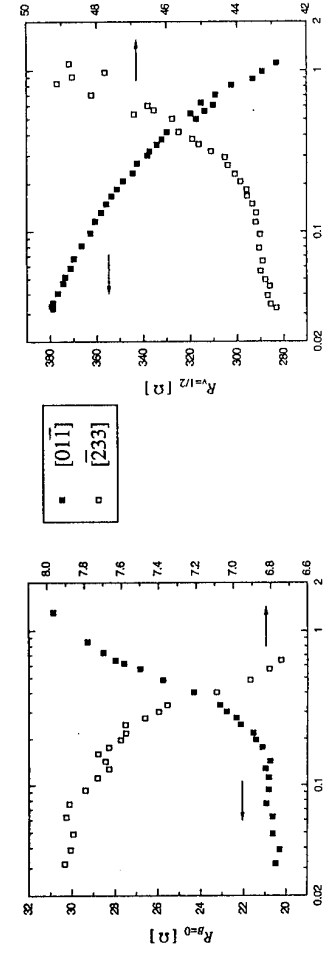


Fig. 1.



PC16 THURSDAY
 Fig. 2.
 (a)
 (b)
 (c)

- [1] J. K. Jain, Phys. Rev. Lett. **63**, 199 (1989).
- [2] B. I. Halperin, P. A. Lee, and N. Read, Phys. Rev. B **47** 7312 (1993).
- [3] H. C. Manoharan *et al.*, Phys. Rev. Lett. **73**, 3270 (1994).
- [4] R. R. Du *et al.*, Phys. Rev. Lett. **73**, 3274 (1994).

I.V. Kukushkin*, R.J. Haug, K.von Klitzing, K.Eberl

Max-Plank-Institut für Festkörperforschung,
Heisenbergstr.1, D-70569 Stuttgart, Germany

Abstract

Sweeping the magnetic field at low temperatures can result in metastable states of the system of two-dimensional electrons in GaAs/AlGaAs. These nonequilibrium states are stable in the range of filling factors $1/3 < \nu < 1$, but can be changed by an extremely small variation of magnetic field around $\nu=1$. We used this phenomenon to vary the disorder and to study its influence on the electronic properties of two-dimensional electrons in the vicinity of $\nu=1/2$. The temperature dependence of σ_{xx} at $\nu=1/2$ was analyzed logarithmic corrections to conductivity were found.

According to recent theories [1], the properties of two-dimensional electrons in perpendicular magnetic field at half filling of the Landau level ($\nu=1/2$) can be described in terms of a normal Fermi liquid of new quasiparticles (called composite fermions) with a well defined Fermi surface at zero effective magnetic field. These composite fermions consist of electrons to which an even number of flux quanta are attached due to electron-electron interaction. In this model a deviation of the magnetic field ΔB from $\nu=1/2$ corresponds to the appearance of an effective magnetic field ΔB , which results in quantization into Landau levels of composite fermions leading to the appearance of the Fractional Quantum Hall Effect (FQHE) [2]. There were several experimental tests of this model such as measurements of the mass of composite fermions from the dependence of the magnetic field [3, 4] and from the temperature dependence of the Shubnikov-de Haas oscillations of composite fermions [5, 6], acoustic wave geometrical resonance [7], magnetic focusing of composite fermions [8], and a study of the geometrical resonances in modulated 2D-system [9]. The results of these tests are controversial and therefore require additional investigations. The fundamental property of any two-dimensional conductor is its localization at low enough temperatures due to disorder which is always present in real systems. In this work we demonstrate that the sweeping of the magnetic field at low temperatures could result in metastable states of 2D-system with different and changeable disorder levels. This effect is used to test the model of composite fermions.

We studied five high quality GaAs/AlGaAs single heterojunctions 425 with different mobilities of 2D-electrons: $(0.5-3) \times 10^8 \text{ cm}^2/\text{V s}$.

All of these samples reach the highest concentration of about $2 \times 10^{11} \text{ cm}^{-2}$ after exposure to light. In Fig.1 we show two different realizations of 2D-electron system obtained in the same sample (a) by cooling the sample at $B=0\text{T}$ down to $T_s=70\text{mK}$ and sweeping the magnetic field from $B=0\text{T}$ to $B=16.4\text{T}$ ($\nu=1/2$) and (b) by sweeping at rather high temperature $T_s=1.4\text{K}$ with subsequent cooling to 70mK at $B=16.4\text{T}$ (the schemes of cooling and sweeping the magnetic field are shown in the insets). One can see that in the second realization (b) more FQHE states are observed at the lowest temperature, which illustrates the higher quality of the system. Note that such a state of electrons is absolutely stable and one can reproducibly sweep the magnetic field in the interval corresponding to $1 < \nu < 1/3$.

It is also seen from the Fig.1 that the better resolution of the FQHE states is accompanied by a reduction of resistivity ρ_{xx} at $\nu=1/2$. This value was previously attributed to the conductivity of composite fermions $\sigma_{xx}^F = 1/\rho_{xx}$ [1, 3] and reflects their transport mobility and, therefore, illustrates an enhancement of the CF transport mobility for the second realization. In the inset of Fig.1a we show typical dependencies of the ρ_{xx} measured at 70 mK for $\nu=1/2$ on the temperature T_s at which a sweep of the magnetic field till $\nu=1/2$ was performed. One can see that for different structures the properties of the 2D-electron system around $\nu=1/2$ depend on the temperature T_s at which the ultraquantum limit was reached. The amplitude of the variation of $\rho_{xx}(1/2)$ on T_s changes from sample to sample, but qualitatively such a behavior was typical for almost all studied samples.

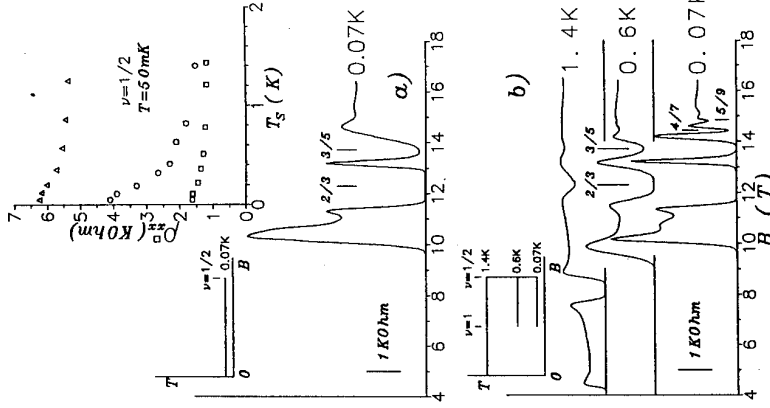


Fig.1

The high quality state of 2D-system, obtained by sweeping the magnetic field at high temperature, can be destroyed by a decrease of the magnetic field below the ultraquantum limit. One can see from Fig.2 that a sweep of the magnetic field within range $1/2 < \nu < 1$ is absolutely reproducible, whereas the crossing of the boundary at $\nu=1$ immediately results in a change of the state of 2D-system, which is accompanied by a change in the amplitudes of the FQHE oscillations and by an increase of ρ_{xx} ($1/2$). The perturbation of the 2D-system, associated with the crossing of $\nu=1$ depends on the number of the induced opposite spins of electrons, e.g. it depends on the value of the filling factor $\nu_s = 1 + \delta$ ($\delta > 0$) reached due to a decrease of the magnetic field to B_0 . The dependence of $\rho_{xx}(1/2)$ on B_0 is shown in the insert to Fig.2. A decrease of magnetic field corresponding to $\nu < 1$ means a population of the spin-up states of electrons, which could be realized, for example, through the edges. In the ultraquantum limit ($\nu < 1$) the spin-up electrons should relax to the ground spin-down state and the necessity to change the spin state during the relaxation process could drastically increase the relaxation time especially at low temperatures [10]. Due to the strong increase of the relaxation time for the usual phonon-assisted process an alternative mechanism of relaxation could be more effective at low temperatures. One possibility is that impurities in AlGaAs layer are involved in this relaxation and it results in perturbation of the impurities states and a change of disorder level [10].

We used this method to control the disorder level in 2D-system and to study its influence on the transport and quantum mobilities of composite fermions and on the FQHE activation energies [10]. We also investigated the temperature corrections to the conductivity of composite fermions. In Fig.3 we show the temperature dependence of ρ_{xx} (a) and of σ_{xx} (b), measured at $\nu=1/2$ for different realizations of disorder. One can see from this figure, that (a) the temperature corrections to the ρ_{xx} are stronger for the higher values of $\rho_{xx}(1/2)$ and (b) the

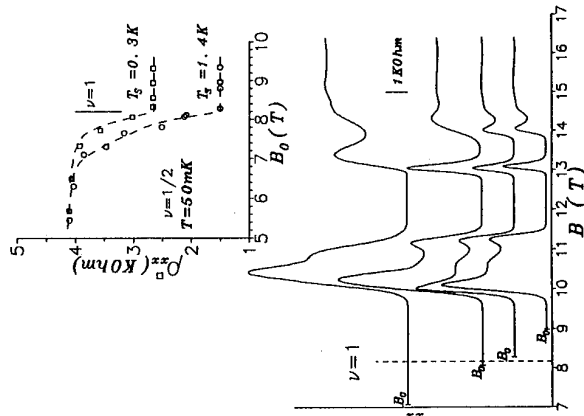


Fig.2

dependencies presented in terms of conductivity $\sigma_{xx} = 1/\rho_{xx}$ have more universal form and the same logarithmic corrections at low temperatures $\delta\sigma = \alpha \cdot e^2/h \cdot \ln(T)$ are found for all the studied samples (α is close to 0.15). The observed temperature dependence of conductivity at $\nu=1/2$ and its change with disorder are in agreement with the theory [1], which predicts the logarithmic corrections due to interaction effects in a presence of disorder.

FIGURES CAPTIONS:

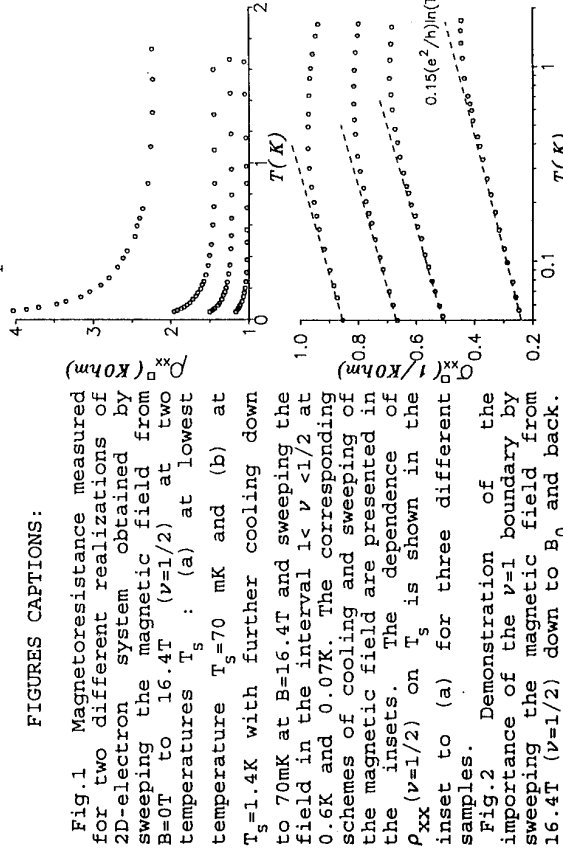


Fig.1 Magnetoresistance measured in two different realizations of the 2D-electron system obtained by Kondo effect, sweeping the magnetic field from $B=0$ to 16.4 T ($\nu=1/2$) at two temperatures T_s : (a) at lowest temperature $T_s=70$ mK and (b) at $T_s=1.4$ K with further cooling down to 70 mK at $B=16.4$ T and sweeping the field in the interval $1 < \nu < 1/2$ at 0.6 K and 0.07 K. The corresponding schemes of cooling and sweeping of the magnetic field are presented in the insets. The dependence of $\rho_{xx}(1/2)$ on T_s is shown in the inset to (a) for three different samples. The dependence of $\rho_{xx}(1/2)$ on B_0 is shown in the inset to (b).

REFERENCES:

- [1] B.I. Halperin, P.A. Lee, N. Read, Phys. Rev. **B47**, 7312 (1993).
- [2] J.K. Jain, Phys. Rev. Lett., **63**, 199 (1989).
- [3] R.R. Du, et al., Phys. Rev. Lett., **70**, 2944 (1993).
- [4] I.V. Kukushkin, et al., Phys. Rev. Lett., **72**, 736 (1994).
- [5] D.R. Leadley, et al., Phys. Rev. Lett., **72**, 1906 (1994).
- [6] R.R. Du, et al., Solid State Commun., **90**, 71 (1994).
- [7] R.L. Willett, et al., Phys. Rev. Lett., **71**, 3846 (1993).
- [8] V.J. Goldman, et al., Phys. Rev. Lett., **72**, 2065 (1994).
- [9] W. Kang, et al., Phys. Rev. Lett., **71**, 3850 (1993).
- [10] I.V. Kukushkin, et al., Phys. Rev., **B51**, (1995).

Pulse propagation in spin-polarized edge channels and at fractional filling factors

G. Ernst, N. B. Zhitenev, R. J. Haug, K. von Klitzing and K. Eberl
Max-Planck-Institut für Festkörperforschung, Heisenbergstr. 1, 70569 Stuttgart, Germany

We have studied time-resolved transport in a two-dimensional electron gas in high magnetic fields. At filling factor $\nu = 3$ two edge magneto-plasmon modes appear which contribute to the transmission of negative pulses, whereas for positive pulses the signal is transmitted by only one collective mode. While the spreading of the potential just above $\nu = 1$ is not restricted to edge channels alone, a fast propagating signal in an edge mode was observed at filling factor $\nu = 4/3$.

PACS numbers: 72.30.+q, 72.20.-i, 73.40.-c

Time-resolved transport measurements have recently become an important tool to study the electronic structure near the boundary of a two-dimensional electron gas (2DEG) in high magnetic fields [1,2]. The interplay between the electrostatic confining potential, the Landau quantization, and the electron-electron interaction leads to the formation of compressible and incompressible regions near the edge of the sample. The dependence of their local distribution on the applied magnetic field has been calculated self-consistently for a smooth confining potential [3]. The coupling between adjacent compressible strips or edge channels (EC's) as well as the coupling between EC's and the bulk of the 2DEG may be weak enough for a non-equilibrium potential distribution to be established on a macroscopic length scale. This has been observed in many DC magnetotransport experiments (for a review see, for example, [4]). In AC measurements, the propagation of edge magnetoplasmon (EMP) modes [5] studied both in the frequency [6] and the time domain [1] has also been discussed within the framework of the EC model. However, the edge structure for odd [7] and fractional filling [8] factors, where the bulk energy gap is mainly determined by correlation effects, is still under discussion.

Here, we report on time-resolved measurements of non-equilibrium transport, focusing on odd and fractional filling factors. For these measurements, standard Hall-bar geometries were used, made from $\text{Al}_x\text{Ga}_{1-x}\text{As}/\text{GaAs}$ heterostructures. The 2DEG has a carrier concentration $n = 2.3 \cdot 10^{15} \text{ m}^{-2}$, a mobility $\mu = 50 \text{ m}^2/\text{Vs}$, and is located 90 nm below the surface. In Fig. 1, the sample geometry is shown together with a sketch of the experimental set-up for time-resolved transport measurements. In order to slow down the dynamic processes in the sample by screening long-range Coulomb interactions, we covered the largest part of the sample with a metallic top gate. A narrow top gate across each arm of the potential probes can be used to couple and decouple the probes from the rest of the 2DEG. A long voltage pulse with a rise time of 350 ps and an amplitude V_{in} reaches contact 1 at time t_0 with contact 3 being grounded. A large negative bias is applied to the gate G2, and additionally, positive strobe pulses supplied from the same pulse generator (HP8131A dual channel pulse generator) arrive at G2 at a time $t_0 + \Delta t$. During these short time intervals, the 2DEG underneath G2 becomes conducting and the integrating capacitance is charged up to the potential existing at the edge of the sample near contact 2 at this time. By varying the time delay, Δt , the transient potential, V_t , at this contact is sampled. The achieved time

resolution of about 150 ps, together with a sensitivity of $5\mu\text{V}$ results from the non-linearity of the gate characteristics and a reduction of the effective capacitance by EC transport [9]. All measurements were made in a $^3\text{He}/^4\text{He}$ dilution refrigerator at a temperature of 70 mK with magnetic fields up to 12 T, the direction of the field being chosen such that the EMP's for electrons propagate along the shortest, $160 \mu\text{m}$ long, connection between the injection (1) and the detection (2) contact.

Typical data for different filling factors with $V_{in} = \pm 5 \text{ mV}$ are shown in Fig. 2. The time $t = 0$ where the applied pulse reaches the injection contact is determined from the residual capacitive signal present at very low magnetic fields. The delay of the leading edge of the pulse appearing at contact 2 depends on the filling factor and increases with applied magnetic field. The general shape of the signal is characterized by a fast rise up to a value V_0 , followed by a slower increase until saturation. The small oscillations before and after $t = 0$ are presumably caused by reflections of the pulses in the sample and the external circuit. Pulses with negative polarity exhibit a steeper front and usually a larger V_0 than their positive counterparts. Around the odd integer filling factors $\nu = 3$ and $\nu = 5$ however, an additional feature appears in the transient signal: the amplitude of the first step is smaller compared to the signal with positive polarity, which is compensated by a second step marked by an arrow in the waveform for $\nu = 3$. For $\nu = 5$ even a third step seems to be distinguishable for negative polarity.

The difference between applied and transmitted voltage is not only influenced by the polarity but also by the amplitude of the incoming pulse as one can see from Fig. 3. The transmission T , defined here as the time-dependent output voltage normalized with the injected pulse amplitude $T = V_t/V_{in}$, is shown for different (negative) values of V_{in} and for the same filling factors as in Fig. 2. For small values of V_{in} , complete transmission ($T = 1$) is reached at all filling factors shown except for $\nu = 1/1$. The largest value of V_{in} for which $T = 1$ is reached depends on filling factor and is significantly lower for odd and fractional filling factors compared with the neighboring even integers. The observed transmission for signals with positive polarity is lower or equal compared with pulses of negative polarity.

An overview of the features appearing at different filling factors is provided by Fig. 4, where the step height V_0 is plotted as a function of ν for $V_{in} = \pm 5 \text{ mV}$. V_0 reaches a maximum above each integer filling factor, evidently not only for even but also for odd integers and for the fractional value $\nu = 4/3$. For the amplitude V_{in} chosen in this plot, the maximum values above $\nu = 1/2$ and $4/3$ do not depend on polarity (regime I). Here the above mentioned difference favoring pulses of negative polarity develops only at larger amplitudes. Since for $\nu = 1$ the transmission T saturates at $T < 1$ this regime is marked by I'. At the fractional filling factor $\nu = 4/3$ negative pulses are transmitted better than positive ones (regime II). Around $\nu = 3$ and $\nu = 5$ (regime III) different edge modes manifest themselves for positive and negative polarities.

In the following, we will treat the effects reported above in terms of signals transferred by magnetoplasmon excitations. Restricting these excitations to a strip of finite width near the boundary of a 2DEG changes their dispersion relation and leads to the appearance of EMP's [5]. The experimental observation of such fast propagating edge modes was interpreted within the concept of non-equilibrium transport as a consequence of the decoupling between edge and bulk excitations [1]. The width of the confining incompressible strip which is a measure of its decoupling strength was found to be well described by

$$a = a_0 \sqrt{(E_g - eU_{eb})/E_g} \quad (1)$$

where $U_{eb} = 0$ is the potential difference between edge and bulk, a_0 the equilibrium width (for $E_g = \hbar\omega_c$) the energy gap for even integer filling factors [9]. Eq. (1) implies that negative excitations are better transmitted along the boundary than positive ones due to the wider incompressible strip, which fits well to the observed behavior in the regimes I and II. In regime III, on the other hand, the enhanced decoupling due to an incompressible strip with a negative potential difference across it, together with the screening by the metallic top gate, make the observation of several edge modes with different group velocity possible, whereas, for positive polarity, the potential is transmitted by one edge mode only. As a consequence V_0 is larger for positive pulses than for negative ones. At the present stage, we can not fully answer the question whether the two experimentally distinguishable modes for $\nu = 3$ in the negative signals result simply from transmission in decoupled edge channels or from more complex modes in EC's. However, the fact that the propagation velocity of the slower mode at $\nu = 3$ is nearly the same as the velocity of the signal at $\nu = 1 + \delta$ supports the former interpretation.

Astonishingly, the transmission properties around $\nu = 4/3$ look similar to those observed for even integers. Even the asymmetry of the maxima in the $V_0(\nu)$ -plot, visible at even integers, is reproduced for $\nu = 4/3$, the only difference being the smaller amplitudes of V_{in} at which the breakdown of non-equilibrium transport occurs. The fact that full transmission ($T = 1$) is reached in the first step for small V_{in} is clear evidence for the existence of a fast propagating edge mode at this fractional filling factor.

In conclusion, we have studied non-equilibrium transport in a 2DEG focusing on odd and fractional filling factors by measuring the transient potential at the edge of the 2DEG after the application of a voltage pulse with a sharp leading edge.

We would like to thank V. Fal'ko and Y. Kershaw for a critical reading of the manuscript.

- [1] N. B. Zhitenev, R. J. Haug, K. v. Klitzing, and K. Eberl, Phys. Rev. Lett. **71**, 2292 (1993).
- [2] R. C. Ashoori, H. L. Stormer, L. N. Pfeiffer, K. W. Baldwin and K. Eberl, Phys. Rev. B **45**, 3894 (1992).
- [3] D. B. Chklovskii, B. I. Shklovskii and L. I. Glazman, Phys. Rev. B **46**, 4026 (1992); K. Lier and R. R. Gerhards, Phys. Rev. B **50**, 7757 (1994).
- [4] R. J. Haug, Semicond. Sci. Technol. **8**, 131 (1993).
- [5] V. A. Volkov and S. A. Michailov in *Modern Problems in Condensed Matter Sciences*, edited by V. M. Agranovich and A. A. Maradudin (North-Holland, Amsterdam, 1991), Vol. 27.2.
- [6] V. I. Talyanski, M. Y. Simmons, J. E. Frost, M. Pepper, D. A. Ritchie, A. C. Churchill, and G. A. C. Jones, Phys. Rev. B **50**, 1582 (1994).
- [7] J. Dempsey, B. Y. Gelfand and B. I. Halperin, Phys. Rev. Lett. **70**, 3639 (1993).
- [8] C. W. J. Beenakker, Phys. Rev. Lett. **64**, 2116 (1990); A. M. Chang, Solid State Commun. **74**, 871 (1990).
- [9] N. B. Zhitenev, R. J. Haug, K. v. Klitzing, and K. Eberl, Europhys. Lett. **28**, 121 (1994); N. B. Zhitenev, R. J. Haug, K. v. Klitzing, and K. Eberl, to be published.
- [10] N. B. Zhitenev, R. J. Haug, K. v. Klitzing, and K. Eberl, Phys. Rev. B **51**, (1995) in print.

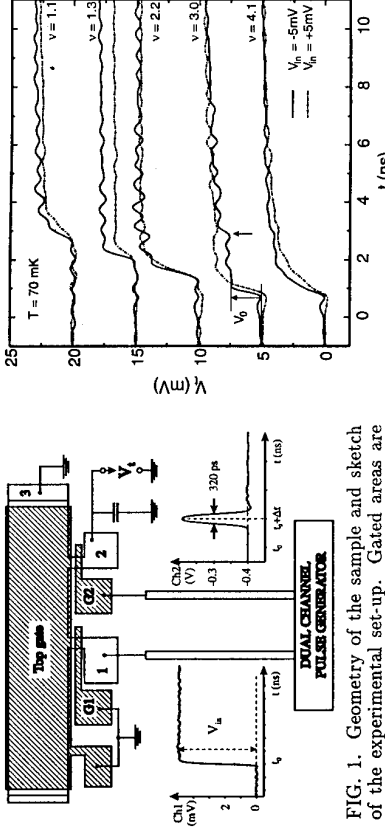


FIG. 1. Geometry of the sample and sketch of the experimental set-up. Gated areas are shaded. A voltage pulse from channel 1 of the pulse generator is applied to contact 1. The wave packet runs along the shorter boundary to contact 3. The transient potential at the intermediate contact 2 is detected using gate G2 as a sampling switch which is opened and closed by means of a strobe pulse supplied from channel 2 of the pulse generator.

We thank V. Fal'ko and Y. Kershaw for a critical reading of the manuscript.

In conclusion, we have studied non-equilibrium transport in a 2DEG focusing on odd and fractional filling factors by measuring the transient potential at the edge of the 2DEG after the application of a voltage pulse with a sharp leading edge.

We would like to thank V. Fal'ko and Y. Kershaw for a critical reading of the manuscript.

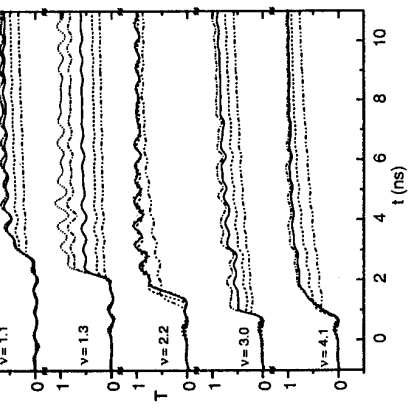


FIG. 2. The transient potential V_t measured at contact 2 for filling factors $\nu = 4.1, 3.0, 2.2, 1.3$ and 1.1 . Waveforms belonging to different filling factors are offset by 5 mV. The measured signals with $V_{in} < 0$ are inverted for a better comparison between the two polarities. $t = 0$ corresponds to the arrival of the voltage pulse on contact 1. The stepheight V_0 of the first sharp rise is shown for $\nu = 3.0$ and $V_{in} = -5$ mV. The arrow at $t \approx 5$ ns marks the onset of the second step-like increase.

We thank V. Fal'ko and Y. Kershaw for a critical reading of the manuscript.

In conclusion, we have studied non-equilibrium transport in a 2DEG focusing on odd and

fractional filling factors by measuring the transient potential at the edge of the 2DEG after the application of a voltage pulse with a sharp leading edge.

We would like to thank V. Fal'ko and Y. Kershaw for a critical reading of the manuscript.

FIG. 3. Transient transmission for filling factors $\nu = 4.1, 3.0, 2.2, 1.3$ and 1.1 and for $V_{in} = -2$ mV, -3 mV, -5 mV, -10 mV and -20 mV.

X_z - X_{xy} CROSSOVER IN A TWO DIMENSIONAL ELECTRON GAS IN AlAs.

A.F.W. van de Stadt*, P.M. Koenraad*, J.A.A.J. Perenboom**, J.H. Wolter*.

* COBRA, Inter University Research Institute, Eindhoven University of Technology, PO 513 5600 MB
Eindhoven, The Netherlands.
** High Field Magnetic Laboratory and Research Institute for Materials, University of Nijmegen,
Toernooiveld 6525 ED Nijmegen, The Netherlands.

Abstract

We have performed magnetoresistance measurements up to 20T on high mobility two dimensional electron gasses in single AlAs quantum wells with well widths ranging from 40-80Å. We observe a sharp transition from a two-fold valley degenerate X_{xy} occupied state in a 60Å well to a non-degenerate X_z occupied state in a 40Å well. These two states are distinguished by their different effective masses, which have been determined using the temperature dependence of the Shubnikov-de Haas effect. By using self-consistent calculations we can explain this transition in relative occupation assuming an X-splitting energy of 24meV. Furthermore for the X_{xy} electrons the effect of the large ratio of spin to Landau splitting is shown by the occurrence of strong magnetoresistance minima at filling factors 2.6 and 10 in the Hall-effect.

Although AlAs is commonly used in e.g. super lattices (SL) and as a barrier material in heterostructures, its electrical parameters are hardly studied. This is mainly due to the fact that AlAs is an indirect semiconductor, having the X-minimum as the lowest conduction band minimum, and that confining these X-electrons to a 2DEG is difficult. The equi-energy surfaces at this X-minimum are strongly non-isotropic in k-space and are described by different longitudinal and transverse effective masses m_l and m_t . The minimum has a threefold degeneracy, denoted by X_x , X_y and X_z . In a two dimensional system the X_x and X_y valleys remain degenerate, whereas the degeneracy with the X_z -minimum is lifted.

The band structure parameters of AlAs become apparent in short period type-II GaAs_n/AlAs_m SL's. In optically detected magnetic resonance measurements it is found that in those SL's, the lowest X-state changes from X_{xy} character to X_z character if the AlAs thickness becomes smaller than 55Å [1]. Cyclotron resonance measurements and recently Shubnikov-de-Haas measurements [2,3,4] revealed the density-of-states (DOS) effective

masses of these states, $m_{X_{xy}} = \sqrt{m_l m_t} = 0.5$ -0.6m₀ and $m_{X_z} = m = 0.3m_0$. Apparently for wide wells the energy position of the X_{xy} and X_z states is reversed with respect to what is expected from the binding masses m_l and m_t ($\sim 1.0m_0$). It is commonly accepted that this level reversal is caused by the small but finite strain in the AlAs layer induced by the lattice mismatch between GaAs and AlAs [5]. The strain induced energy splitting ranges from 19-23meV [1,6]. Up to now the DOS effective masses of the X-minimum have only been determined in quasi two dimensional in low mobility electron gases (2DEG) in multiple quantum well (QW) structures, where the barrier material itself is indirect (e.g. Al_xGa_{1-x}As with $x > 0.37$) [4,7]. The disadvantage of a multiple QW system is the unknown number of active wells and the non-uniformity of the 2DEG. The use of AlGaAs as a barrier material, makes comparison with optical measurements on the GaAs/AlAs SL's more difficult. Lay [8] used a single AlAs/AlGaAs QW, but determined only the cyclotron mass of the X_{xy} state and its two-fold degeneracy.

In this paper we present a different structure, in which we overcome the aforementioned problems. We have designed a single AlAs QW embedded between 5 periods of a 22Å/11Å GaAs/AlAs SL. Two buffer layers of Al_{0.37}Ga_{0.63}As (0.1μm) terminate the SL's. The structure is capped by a thick GaAs layer (0.5μm) to provide the acceptor background charges to accommodate for the surface band bending, and to make the structure symmetrical. The X-band structure is sketched in fig. 1. The thickness of the GaAs and AlAs layers in the SL is chosen such that the bound Γ and X-states are much higher in energy (-100meV) than the bottom of the AlAs well. Free carriers are provided by δ -doping one of the GaAs layers in the SL on each side of the well. By doping the GaAs we avoid trapping of electrons by the DX-centre. Due to the band bending the Fermi-level in the SL is lifted with respect to the centre of the AlAs well and may therefore reach the Γ and X-levels in the SL if the total doping density is too high or the distance from the δ -layer to the well is too large. By fine tuning the design of our structures we were able to obtain a 2DEG with a single occupied subband populated up to $1.5 \cdot 10^{12}$ cm⁻².

Using MBE we have grown structures at 600°C with well widths of 40, 60 and 80Å, and a total Si doping concentration of $2 \cdot 10^{12}$ cm⁻². The growth temperature was deliberately lower than the optimum growth temperature of a GaAs/AlAs SL to suppress diffusion of Si.

Electrical measurements were performed on Hall-bar etched samples with Sn diffused contacts. The characterisation data is given in table 1. The 40Å well with an X_z-like 2DEG has the highest mobility reported so far and demonstrates the high quality of our samples.

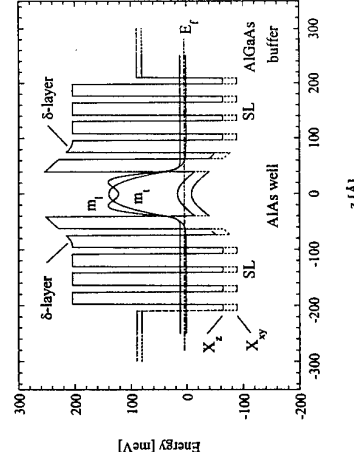


Fig. 1. Diagram showing the potential energy at the X-minimum of our modulation doped AlAs QW structure. The wavefunctions and potential are shown for a 2DEG with an electron density of $1.5 \cdot 10^{12}$ cm⁻². The splitting of the X-band has been indicated for the SL and the AlAs well. The energy is measured with respect to the energy at the centre of the well, when no strain is included.

Sample	AlAs well width [Å]	Distance δ-layer - centre well [Å]	n_{well} [10^{12} cm ⁻²]	n_{well} [cm ⁻² /Å ²]	DOS effective mass [m ₀]
S40	40	65	1.26	1.19	3700
S60	60	75	1.25	0.63	4100
S80	80	85	0.94	0.32	1700
S80P	80	120	1.06	0.54	7100

Tab. 1. Sample parameters for our single AlAs QW structures. Sample S80 has been grown with the δ-layer either in the second (a) or in the third (b) GaAs layer of the SL.

Magnetoresistance measurements up to 20T were performed and effective masses have been determined from the temperature dependence of the SdH-oscillations [9]. By pumping a ^4He bath cryostat the temperature was varied between 4.2K and 1.5K. Additional temperature reduction to 0.5K could be obtained in a ^3He cryostat. The relative amplitude variation of a SdH-maximum (minimum) has been measured with respect to a line tangent to the adjacent SdH-minima (maxima). This method eliminates the effect of a background in the magnetoresistance. Effective masses were determined in this way for magnetic fields up to ~6T. Beyond this magnetic field, the oscillation amplitudes become too large and the spin and valley splitting can not be neglected. This results in absurd values for the effective mass. The DOS effective masses and their degeneracy have been determined for all well thicknesses and are presented in table 1.

The striking difference between samples S40 and S80° is shown in fig. 2. In both wells only one subband is occupied, which simplifies the interpretation of the measurements. The effective mass measurements indicate that S40 is occupied by X_z electrons and S80 by X_{xy} electrons. Sample S60 shows a similar behaviour as sample S80°. The degeneracy follows from the ratio of the density obtained from the SdH-periods at low magnetic fields and the density obtained from the Hall-resistance. The degeneracy, excluding spin degeneracy, is 1 for the X_z and 2 for the X_{xy} electrons. The twofold degeneracy of the X_{xy} state is supported by the successive strong magnetoresistance minima at filling factors $v=2, 6$ and 10. This sequence is explained by a large ratio of the spin to Landau splitting, $\alpha = g^* \mu_B / \hbar \omega_c = \frac{1}{2} g^* m^*/m_0$, where g^* is the effective g-factor (~3 in this system [7]). Thus for these type of electrons the spin and Landau splitting are of comparable size ($\alpha \sim 0.9$). This causes the valley degenerate spin states of two adjacent Landau levels to join each other resulting in an effective fourfold degeneracy. At high magnetic fields the degeneracy of such a set of levels is lifted and magnetoresistance minima at filling factors $v=2, 4$, and 5 are resolved.

The samples S60 and S80°, with the δ-layer in respectively the second and third GaAs layer of the SL have a comparable effective mass of ~0.63 m_0 . Sample S80° however gives a much lower value of 0.48 m_0 . These values cover the range of values determined by temperature dependent SdH-measurements in literature [4,7]. We note that we have indications that the sample quality of S80° is much poorer than S80°. The effective mass measured for the X_z -electrons, 0.27 m_0 , is identical to the one found by Yamada et al. [4].

Our measurements indicate that the transition region of crossover from an X_z to an X_{xy} populated state is very sharp and occurs between 40 and 60Å. We have modelled our structures by solving the

Schrödinger and Poisson equation in a selfconsistent way. The model incorporates the conservation of probability flux at the GaAs/AlAs interfaces (e.g. $I/m_{GaAs} \cdot \partial \varphi_{GaAs} / \partial z = I/m_{AlAs} \cdot \partial \varphi_{AlAs} / \partial z = 1/m_{AlAs}$). Commonly accepted material parameters have been used for GaAs and AlAs. The transition region of the relative occupation change from X_z to X_{xy} can best be described by taking an X-splitting energy of 24±2meV, which is comparable with the value of van Kesteren et al. [1] (fig. 3a). The crossover in relative occupation of the X_z and X_{xy} states occurs at ~48Å and does not coincide with the crossover of the confinement energies in the well (E_x , E_y) as is shown in fig. 3b. If we compare this crossover of E_x and E_y for doped and undoped wells, we have to conclude that the shift towards lower well widths of the crossover in relative occupation depends largely upon the different DOS in the X_z and X_{xy} levels.

To summarise, we have demonstrated the X_z - X_{xy} crossover in a high quality 2DEG in a single AlAs QW and determined the effective masses and their degeneracy. A longitudinal effective mass of 1.5 m_0 and a transverse effective mass of 0.3 m_0 have been found, which compare to the values in literature. In addition the effect of a large ratio of spin to Landau splitting has been shown. Still there's a discrepancy between the effective masses of different samples with the same well width, which is not yet understood.

References

- [1] H.W. van Kesteren, E.C. Cosman, P. Dawson, K.J. Moore, and C.T. Foxon, Phys. Rev. B 39 (1989) p13426.
- [2] N. Miura, H. Yokoi, J. Kono and S. Sasaki, Solid State Commun. 79 (1991) p1039.
- [3] M. Goiran, J.L. Martin, J. Lefebvre, R. Pernal and S. Askenazy, Physica B 177 (1992) p465.
- [4] S. Yamada, K. Maezawa, W.T. Yuen and R.A. Stradling, Phys. Rev. B 49 (1994) p2189.
- [5] T.J. Drummond, E.D. Jones, H.P. Hjalmarson and B.L. Doyle, SPIE vol. 796 Growth of Compound Semiconductors 1987 p2.
- [6] P. Lefebvre, B. Gil, H. Mathieu and R. Pernal, Phys. Rev. B 39 (1989) p5550.
- [7] T.P. Smith III, W.I. Wang, F.F. Fang and L.L. Chang, Phys. Rev. B 35 (1987) p9349.
- [8] T.S. Lay, J.J. Heremans, Y.W. Suen, M.B. Santos, K. Hirakawa, M. Shayegan and A. Zrenner, Appl. Phys. Lett. 62 (1993) p120.
- [9] K. Maezawa, T. Mizutani and S. Yamada, J. Appl. Phys. 71 (1992) p296.

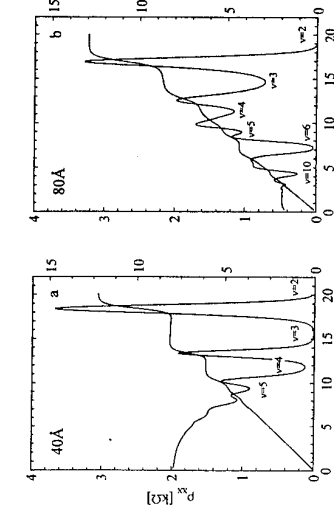


Fig. 2. Magnetoresistance and Hall-resistance of samples (a) S40 and (b) S80° at 0.7K. The filling factors at the magnetoresistance minima are indicated.

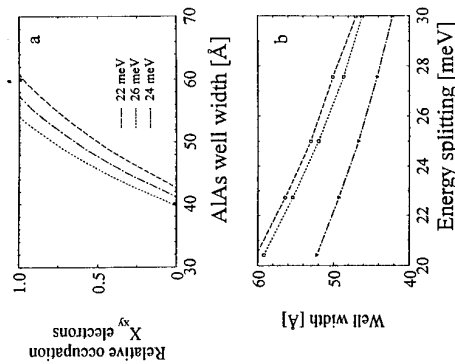


Fig. 3. (a) The relative occupation of the X_{xy} electrons as a function of well width for various strain induced energy splittings of the X_z and X_{xy} levels at a doping concentration of $1.25 \cdot 10^{11} \text{ cm}^{-3}$. Our measurements are indicated by the dots. (b) The crossover in energy position for undoped (○) and doped (●) structures, and the relative occupation (v) as a function of the strain induced energy splitting.

Magnetotransport in wide parabolic PbTe quantum wells

J. Oswald, G. Heigl, M. Pippan, G. Span, T. Stellberger
Institut für Physik, Montanuniversität Leoben, Franz Josef Str. 18, A-8700 Leoben, Austria

D.K. Maude, J.C. Portal
High Magnetic Field Laboratory, CNRS, 25 Avenue des Martyrs, BP 166 Grenoble, France

Abstract

The 3D- and 2D- behaviour of wide parabolic PbTe single quantum wells, which consist of PbTe p-n-p-structures, are studied theoretically and experimentally. A simple model combines the 2D- subband levels and the 3D-Landau levels in order to calculate the density of states in a magnetic field perpendicular to the 2D plane. It is shown that at a channel width of about 300nm one can expect to observe 3D- and 2D-behaviour at the same time. Magnetotransport experiments in selectively contacted Hall bar samples are performed at temperatures down to $T = 50$ mK and at magnetic fields up to $B = 17$ T.

Introduction

Wide parabolic quantum wells (WPQW) are of particular interest because of the intermediate dimensionality of two- (2D) and three-dimensional (3D) physics. During the past few years much effort in fabricating, investigating and modelling [1,2,3] of $\text{Al}_x\text{Ga}_{1-x}\text{As}$ - WPQW's have been made. The realization of wide quantum wells with a flat potential in the electron channel requires a parabolic bare potential which is difficult to obtain by MBE growth in quantum well systems. WPQW's can be made much easier by using the nipi-concept [4].

PbTe is a narrow gap semiconductor with both the conduction and the valence band extrema located at the L points of the Brillouin zone. The effective mass ellipsoids are oriented along the four $\langle 111 \rangle$ directions and have a mass anisotropy of about a factor of 10. With respect to the growth direction there are two different effective masses for both the subband quantization and the Landau level splitting. Therefore there are two sets of subbands and two sets of Landau levels for a magnetic field perpendicular to the 2D-plane.

The PbTe layer systems are grown on $\langle 111 \rangle$ BaF_2 substrates by HWE (Hot Wall Epitaxy). The p-layers of the p-n-p structures are designed to be non-depleted in order to screen the embedded n-channel from any influence from surface and interface states [4]. Selective contacts to the embedded n-channel are realised [5] in order to perform magneto transport experiments. The mobility in this selectively conducted structures is in the order of $1 \times 10^5 \dots 1 \times 10^6 \text{ cm}^2 \text{V}^{-1} \text{s}^{-1}$ at lowest temperatures. The extreme high dielectric constant ($\epsilon = 500 - 1000$) leads to wide quasi parabolic potential wells with a typical subband separation ranging from 1-3 meV.

Model

The subband energies are calculated self consistently by a numerical solution of the Schrödinger equation within the effective mass approximation at zero magnetic field. The LL's are obtained from a 3D-calculation according to [6,7]. The energy level system $E_{ij}(B)$ consists of

all Landau levels (LL's) $E_{ij}(B)$ sitting on all subband levels E_i , according to a "rigid potential model". Since in wide quantum wells the Landau level separation is much higher than the subband splitting, the LL's can be considered to be split by the subband quantization. The calculation of the density of states (DOS) is done by a superposition of the individual Landau peaks with a broadening factor b . The broadening function in this approximation is assumed to be Gaussian. The DOS as a function of energy E and magnetic field B then reads as follows [8]:

$$\text{DOS}(E, B) = \frac{q_e \cdot B}{h} \sum_{i,j} \frac{1}{b \cdot \sqrt{\pi}} \cdot \left(e^{-\frac{(E-E'_j(B))^2}{b^2}} + 3 \cdot e^{-\frac{(E-E''_j(B))^2}{b^2}} \right)$$

i denotes the longitudinal and o the oblique valleys, j denotes the subband level index and j the Landau level index. The numerical factor 3 in the second term in brackets accounts for the threefold degeneracy of the oblique valleys.

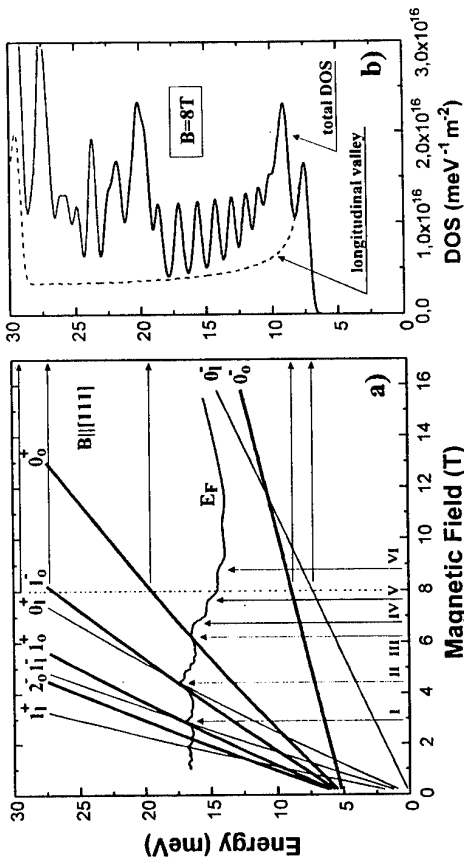


Fig. 1a) Landau levels of the subband ground states and Fermi energy versus magnetic field. b) density of states at $B = 8$ Tesla. Dashed line in b): contribution of the longitudinal valley to the total DOS.

Fig. 1 shows the result of the model calculation of a WPQW with parameters according to the sample used in the experiment. For this sample the carrier sheet density is $n^2_D = 9.8 \times 10^{12} \text{ cm}^{-2}$ and the background doping level in the electron channel is $N_D = 3 \times 10^{17} \text{ cm}^{-3}$ resulting in an effective electron channel width of $d_n = 330$ nm. The shape of the screened potential is a mixture of a square potential (flat region in the middle of the channel) and a parabolic potential. Therefore the subband splitting is very small for the lower subbands and it increases with the subband index. Finally at high subband energies it approaches a constant subband spacing according to the parabolic bare potential. Consequently the associated Landau levels (of same Landau index) of the lower subbands cause an overall enhancement of the density

of states near the subband ground state. The energy of the subband ground state is nearly identical to the position of the associated 3D - LL (LL of a three dimensional sample). At higher subband energies the subband levels are separated more and more and therefore a modulation of the DOS by the subband structure is more and more pronounced. For magneto transport experiments the 2D-model predicts an overall enhancement of the DOS at the energy position of the 3D-LL's and therefore also bulk like Shubnikov - de Haas (SdH) oscillations of the magneto resistance can be expected. At higher subband energies, which means the energy range between the 3D-LL's, a modulation of the DOS due to the subband structure of the oblique valleys can be expected. The LL's of the subband ground states are plotted in Fig. 1a. The LL-energies at $B = 8$ T is plotted. The contribution of the longitudinal valley to the DOS is a uniform background because of the much smaller subband separation. The contribution of the longitudinal valley is plotted by a dashed line. Due to the lattice mismatch between BaF₂ and PbTe a strain induced energy shift between the longitudinal and the oblique valleys of 5 meV is included in the calculation. The energy shift depends strongly on the sample history and is consistent with the value of Ref. [9].

Experiments

The sample parameters in the experiment are those used for the model calculation in the previous section. The shape of the sample is a conventional Hall bar of $w = 90 \mu\text{m}$ width. The experiments where performed in an 11 Tesla super conducting magnet at pumped He⁴ and in a 17 Tesla super conducting magnet with a dilution refrigerator. A conventional lock-in technique using an ac-current of $I = 10 \text{nA}$ at $T = 50 \text{ mK}$ and $I = 100 \text{nA}$ at $T = 2.2 \text{ K}$ was used.

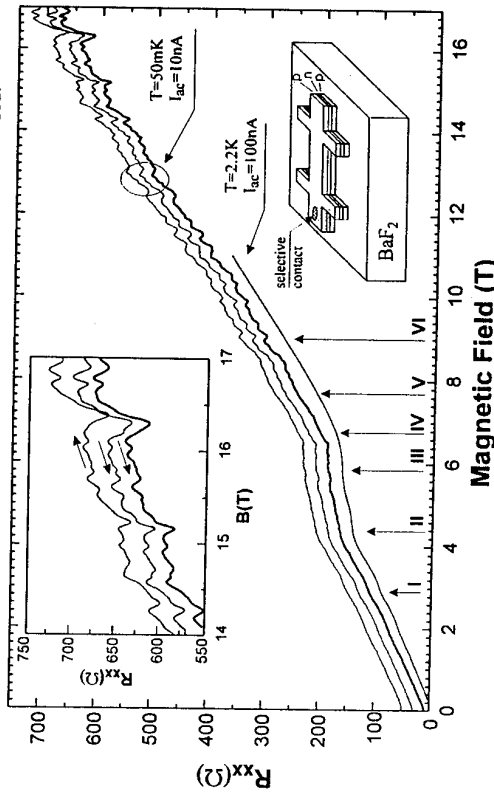


Fig. 2: Magneto resistance data. The labelled arrows indicate the position of the main features which have to be compared with Fig. 1. Upper insert: magnification of the higher field range. The arrows indicate the sweep direction. Lower insert: Scheme of the sample configuration with one representative selective contact.

Shubnikov - de Haas oscillations according to the 3D parameters of the sample dominate the magnetotransport experiments (Fig.2) and no additional structure in the data at $T = 2.2 \text{ K}$ is found. At lower temperatures structures in addition to that found at $T = 2.2 \text{ K}$ appear in the upper field range. This smooth structures are covered by strong fluctuations which are perfectly reproducible. The position of the main features are labelled I, II, III, IV, V, VI and have to be compared with the calculation in Fig.1. Three different sweeps at 50mK are shown in order to demonstrate the reproducibility of the data. For better visibility all plots apart from the thick solid trace are shifted vertically by a small amount.

Discussion and conclusive remarks

The modulation of the DOS at the Fermi level results from changes of the individual filling factors of the different subband systems involved. The carrier distribution between the different subband systems changes with the magnetic field. Since only the total filling factor is periodic in $1/B$ a plot of the data over $1/B$ cannot be used to check the periodicity. At 2.2 K only a structure at I, II and III is visible while structures at IV, V and VI appear at lowest temperatures only. From the comparison with the calculation I, II and III can be attributed to 3D-SdH oscillations and IV, V, VI can be attributed to the 2D subband quantization. The appearance of strong fluctuations in parallel to the appearance of the 2D-features can be an indication of the formation of edge states by the oblique valleys while at the same time the longitudinal valley still enables bulk conduction. An intermediate regime between quantum edge conduction and bulk transport was investigated e.g. by Geim et. al. in n⁺-GaAs layers [10] and it was shown that the edge states play an important role in carrying the current to classically inaccessible regions. The observed fluctuations are the subject of further investigations and will be published elsewhere.

Acknowledgements

Financial support by Fonds zur Förderung der wissenschaftlichen Forschung (FWF), Vienna (Project No. P10510-NAW) and by Steiermärkischer Wissenschafts- und Forschungslandesfonds.

References

- [1] A.J. Rimberg and R.M. Westervelt, Phys. Rev. B **40**, 3970 (1989)
- [2] C.E. Hembre, B.A. Mason, J.T. Kwiatkowski and J.E. Furneaux, Phys. Rev. B **50**, 15197 (1994)
- [3] M. Shayegan, T. Sajoto, M. Santos and C. Silvestre, Appl. Phys. Lett. **53**, 791 (1988)
- [4] J. Oswald, B. Trantta, M. Pippan and G. Bauer, J. Opt. Quantum Electron. **22**, 243 (1990)
- [5] J. Oswald and M. Pippan, Semicond. Sci. Technol. **8**, 435 (1993)
- [6] H. Burkhardt, G. Bauer and W. Zawadzki, Phys. Rev. B **19**, 5149 (1979)
- [7] J. Oswald, P. Pichler, B.B. Goldberg and G. Bauer, Phys. Rev. B **49**, 17029 (1994)
- [8] J. Oswald, M. Pippan, G. Heiss, G. Span, T. Stellberger, Proc. 7th Int. Conf. on Narrow Gap Semiconductors, Santa Fe, New Mexico 1995, in print
- [9] J. Oswald, B.B. Goldberg, G. Bauer and P.J. Stiles , Phys. Rev. B **40**, 3032 (1989)
- [10] A.K. Geim, P.C. Main, P.H. Beton, P. Streda and L. Eaves, Phys. Rev. Lett. **67**, 3014 (1991)

Magneto-Oscillations of the Gate Current in a Laterally Modulated Two-Dimensional Electron Gas

¹Cobra Interuniversity Research Institute, Eindhoven University of Technology, Department of Physics, P.O. Box 513, 5600 MB Eindhoven, The Netherlands

²University of Antwerp (UIA), B-2610 Wilrijk-Antwerpen, Belgium
³IMEC, B-3001 Leuven, Belgium

Abstract

By using a low-field magnetic field modulation technique we are able to detect gate current oscillations in a 1D-laterally modulated two-dimensional electron gas in the magnetic field range where Weiss oscillations occur. The experimental results can be qualitatively well explained by a simple analytical expression for the density-of-states at the Fermi energy.

Introduction

In recent years the transport properties of a two-dimensional electron gas (2DEG) subjected simultaneously to a perpendicular magnetic field and a laterally periodic electric potential have attracted much attention. In addition to the Shubnikov-de Haas (SdH) effect, low-field magnetoresistance oscillations periodic in the reciprocal magnetic field occur in 2DEG-systems containing a one-dimensional (1D) or a two-dimensional (2D) potential, or a lattice of antidots. These oscillations, most clearly seen in the magnetoresistance of a 2DEG with a 1D modulation potential (Weiss oscillations [1-4]), are a consequence of the commensurability between the period of the imposed modulation and the cyclotron radius. Quantum mechanically the oscillations are explained as a result of the lifting of the degeneracy of the Landau levels [2,3,5,6]. The linewidth of the modulation-broadened Landau levels becomes an oscillatory function of the level index, giving rise to oscillations of the peak values of the density-of-states (DOS). Direct experimental verification of the theoretical models for the DOS have only been obtained from magnetocapacitance measurements [7,8]. These measurements show a pronounced modulation in the envelope of the magnetocapacitance oscillations in the magnetic field region where SdH- and Weiss-type oscillations interfere. In this paper we present investigations of oscillations in the gate current of a 1D modulated 2DEG in the Weiss regime itself. The experimentally observed oscillations are compared with those expected from an analytical expression for the DOS.

Sample and experimental set-up

The modulation-doped MBE-grown GaAs/AlGaAs heterostructure used in

this study consists of a semi-insulating GaAs substrate, followed by a 4 μm thick undoped GaAs layer, an undoped Al_{0.3}Ga_{0.7}As spacer (40 nm), a Si-doped Al_{0.3}Ga_{0.7}As layer (38 nm), and a cap layer of GaAs (17 nm). Using holographic lithography we fabricated a patterned gate of Ti/Au on top of the sample, giving a 1D laterally modulated potential with a period of 450 nm. The electron concentration and mobility under the patterned gate are $n_s = 2.7 \times 10^{11} \text{ cm}^2$ and $\mu = 45 \times 10^4 \text{ cm}^2/\text{Vs}$, respectively. The sample ($3 \times 3 \text{ mm}^2$) is placed in a cryostat with a superconducting magnet and a small modulation coil; the experiments are carried out at 4.2 K. In stead of measuring the gate current by means of a quasi-dc-technique [9] ($\text{dB}/\text{dt} = 1\text{T}/\text{min}$) we used an a.c. magnetic field modulation technique, where a small oscillating field $B_m \cos(\omega t)$ is superimposed on the main field B_0 ($\text{dB}/\text{dt} \sim \omega B_m \sim 1\text{T/sec}$). The signals detected with a lock-in amplifier can be written as the sum of harmonics of the modulation frequency weighted by Bessel functions [10]. This technique strongly enhances the sensitivity, particularly at low magnetic fields; we are able to detect gate current oscillations in magnetic fields as low as 0.15 T, whereas oscillations in the capacitance are seen at fields above 0.5 T [7].

Results and discussion

In Figs. 1a and 1b we present measurements of the gate current detected at the first and second harmonic of the modulation frequency F , respectively. These signals are similar to the first and second derivative of the gate current with respect to the magnetic field; in fact the amplitude is multiplied by the Bessel functions $J_1(\alpha)$ and $J_2(\alpha)$ with $\alpha = 2\pi B_m/PB_0^2$, where P is the period of the oscillation in the reciprocal magnetic field. The two different periods corresponding to the Weiss and SdH oscillations are clearly visible. Fig. 2 shows the second harmonic of the gate current in the Weiss regime in detail. The oscillations in the gate current are connected to the DOS at the Fermi level via the selfconsistent rearrangement of the chemical potential, the electron density, the differential capacitance, and the DOS as the magnetic field is varied while the gate voltage V_g is kept constant (in our case $V_g = 0$) [11]. In a recent paper by Raikh and Shahbazyan [8] an analytical expression was presented for the DOS of a 2DEG in the presence of a weak lateral 1D modulation. We have used this result to calculate the magnetic field dependence of the gate current. However, we found that the expression of Ref. [8] is unable to reproduce the experimentally observed oscillations. Therefore we have followed the approach of Ref. [6] where the Fermi energy was calculated numerically using Gaussian broadening for the DOS but in which the energy of the electron was calculated using first order perturbation theory. In the case of zero temperature and in the absence of any broadening we were able to find an analytical expression for the magnetic field dependence of the DOS at the Fermi level E_F .

$$\frac{\text{DOS}(E_F)}{D_o} - 1 = \frac{1}{2} \frac{1}{4\pi} \left(\frac{V_o}{E_F} \right)^2 \sin \left(2KR_c - \frac{\pi}{2} \right) - \frac{1}{4\pi} \left(\frac{V_o}{E_F} \right)^2 KR_c \cos \left(2KR_c - \frac{\pi}{2} \right)$$

$$+ 2 \cos \left(\frac{2\pi E_F}{K\omega} \right) \left[1 - \left(\frac{V_o}{K\omega} \right)^2 \right] \frac{2\pi}{KR} \cos^2 \left(KR_c - \frac{\pi}{4} \right)$$

Here V_o is the strength of the modulation potential, $K = 2\pi/a$, a is the geometrical period, $R_c = (2\pi m)^2/(eC)$, and $D_o = m\tau/\pi\hbar^2$. The first two terms of the right-hand side of this equation gives the pure Weiss contribution to the DOS, while the third term represents the interference of the Weiss and SdH oscillations. This third term is a simplified form of the expression given in Ref. [8]. If we take only the leading term ($P = 1$), neglect any broadening, substitute $E = E_F$, and expand the Bessel function asymptotically for $KR_c \gg 1$ (low magnetic field), the expression of Ref. [8] reduces exactly to the one given above. In the low-field regime where the pure Weiss oscillations are observed, the DOS can be described by the first two terms of our equation only. Since in low fields $KR_c \gg 1$ the first term can be neglected. The amplitude $(V_o/E_F)^2 KR_c$ of the second term in the DOS gives the correct order of magnitude for the gate current oscillations using the following values of the parameter: $V_o = 1$ meV, $E_F = 10$ meV, $n_s = 2.66 \times 10^{11}$ cm⁻², and $a = 450$ nm. The above result predicts however Weiss oscillations in the gate current whose amplitude is only weakly dependent on the magnetic field, which is clearly not seen experimentally. Therefore we have relaxed some of the approximations we have used. We first included temperature which resulted only in a weak magnetic field dependence of the amplitude. We also included a Gaussian broadening of the DOS (and checked that the same conclusion holds for a Lorentzian broadening) resulting in a damping factor $\exp(-KR_c\Gamma/E_F)$. If we use an experimental value for Γ of 1.3 meV, determined from the magnetic field dependence of the SdH oscillations, the shape of the oscillations in Fig. 2 is practically reproduced. Full agreement could only be obtained if we include fluctuations in the Weiss period, either caused by fluctuations in the geometrical period or in the electron concentration. Using a fluctuation in the range of 5-10% we find that the Weiss oscillations in the gate current decreases sufficiently fast at small magnetic fields in order to agree quantitatively with experimental findings.

In conclusion we showed that the low-magnetic field modulation technique is a powerful tool to detect oscillations in the gate current at very small magnetic fields, so that the DOS can be resolved directly in the Weiss regime itself.

References

- [1] D. Weiss, K. von Klitzing, K. Ploog, and G. Weimann, *Europhys. Lett.* **8**, 179 (1989).
- [2] R.R. Gerhardts, D. Weiss, and K. von Klitzing, *Phys. Rev. Lett.* **62**, 1173 (1989).
- [3] R.W. Winkler, J.P. Kotthaus, and K. Ploog, *Phys. Rev. Lett.* **62**, 1177 (1989).

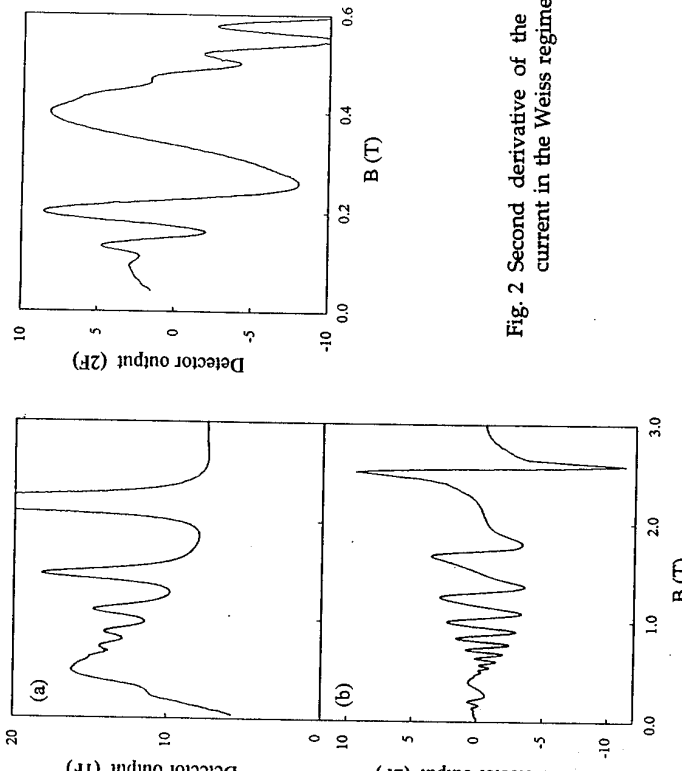


Fig. 1 First (a) and second derivative-like (b) signals of the gate current, showing both Weiss and SdH-oscillations.

Fig. 2 Second derivative of the gate current in the Weiss regime

Metal-Non-Metal Transition at the Crossover from Antidots to Quantum Dots

G. Lütjering¹, D. Weiss¹, R. Tank¹, K. v. Klitzing¹, A. Hülsmann², T. Jakobus², and K. Köhler²

¹ Max-Planck-Institut für Festkörperforschung, 70569 Stuttgart, Germany
² Fraunhofer Institut IAF, 79108 Freiburg i. B., Germany

Abstract. A three-dimensionally structured gate resembling a pillared hall allows the exertion of a strong potential modulation on a two dimensional electron gas in a GaAs/AlGaAs heterostructure. The system can be tuned over a wide range, from an metallic, open antidot lattice to an insulating system of disconnected dots, by a negative gate voltage. At threshold each dot typically contains 50 electrons. The conductance near threshold shows strongly activated behaviour at liquid helium temperatures, which can be modelled by considering tunnelling through a barrier between two dots.

It is well established that patterned gates provide a way to impose a periodic potential on a two dimensional electron gas (2DEG). Lorke et al. have shown that it is possible to tune such a system from a connected electron gas with periodically spaced voids (antidots) to an array of weakly coupled dots [1]. In the antidot case, where the Fermi energy is well above the potential barriers at the constrictions between the antidots, the system shows metallic behaviour. It becomes insulating if the Fermi energy is shifted below these barriers by a sufficiently negative bias. In this paper we introduce a novel gate design which allows to fully deplete the electrons beneath periodically arranged metal posts in the immediate vicinity of the 2DEG while maintaining a high electron density in between the posts. Here results on the temperature dependence of the conductivity for such a system are presented.

Our devices consist of three-dimensionally shaped gates in the form of a miniature pillared hall patterned on top of a shallow delta-doped GaAs/AlGaAs heterostructure grown by molecular beam epitaxy (MBE). The circular pillars of the gate, each with a typical diameter of 100 nm, are arranged in a square lattice with periods, a , between 200 and 300 nm and support the "roof" that serves as a connector. The height of the pillars (≈ 200 nm) is large compared to the distance of the 2DEG to the surface which equals 50 nm. The spacing between the bottom of the pillars and the 2DEG is further reduced to 30 nm in a second type of structure by sinking the pillars into the GaAs cap-layer. A schematic cross-section of such a recessed gate is shown drawn to scale in fig. 1a, and in detail with respect to the layer composition of the heterostructure in fig. 1b. The structure is similar to a normal high-mobility heterojunction but contains additional layers in the cap used as etch stops for the gate recess and is also covered with a SiON protection layer. At 4.2K the heterostructure has a electron density of $6 \times 10^{11} \text{ cm}^{-2}$ and a mobility of $10^5 \text{ cm}^2/\text{Vs}$.

The fabrication of the devices is based on a technology developed for T-gate MODFETs which is described in detail in reference [2]. A three-layer PMMA-resist is patterned in a single e-beam exposure for use both as an etch-mask for the gate recess as well as a mask for evaporation of the metal gate (Ti/Pt/Au 50/50/350 nm) with subsequent lift-off. In the last step of the gate recess, a wet chemical etchant selectively removes the 3 nm AlGaAs layer, resulting in a very smooth interface of the gate-pillars to the GaAs and good control of their distance to the 2DEG. The SEM-micrograph depicted in fig. 1c shows a recessed gate in cross-section after cleaving the sample and completely removing the GaAs/AlGaAs heterostructure. The sample is slightly tilted so that the bottom of the gate, i.e. the side representing the interface to the heterostructure, is visible in the lower part of the micrograph extending to the back. The SiON pro-

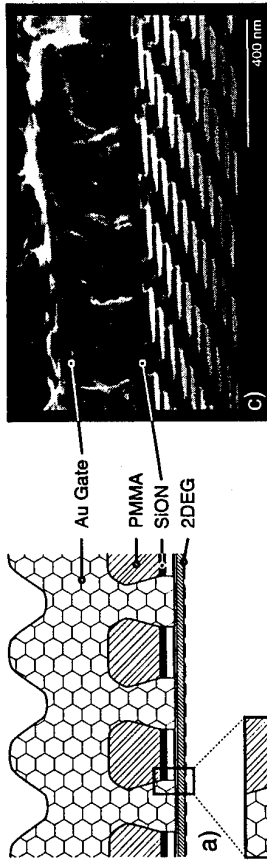


Figure 1: (a) Schematic cross-section of a sample with a recessed gate. (b) Partial blow up of (a) focusing on the layer structure. (c) SEM-micrograph of a recessed gate after cleaving of the sample and complete removal of the GaAs/AlGaAs heterostructure. The sample is slightly tilted so that the underside of the gate (i.e. the interface to the heterostructure) is visible in the lower half of the micrograph, extending to the back.

tection layer - the only part remaining from the wafer - is clearly visible, confirming that the gate-pillars indeed extended into the GaAs cap of the heterostructure.

The gates were patterned on a Hall-bar of 170 μm length and 100 μm width that had been defined by oxygen implantation at 80keV. Ohmic contacts to the 2DEG were provided by alloyed Au/GeNi pads. The measurements were performed by using standard low-frequency techniques at T = 4.2 K in two or four terminal geometry. The conductivity near threshold was obtained in a voltage biased two terminal set-up. All data was taken in the limit of low electric field (E < 1 V/m). We limit our presentation to data from one recessed and one non-recessed structure with a = 300 nm and approximately equal diameter of the gate-pillars. For comparison we also discuss a reference sample with an unpatterned gate on top of the SiON protection-layer.

Four-point measurements of the magnetoresistance at zero gate bias (not shown) exhibit the well-known anomalies of antidot-systems, i.e. commensurability peaks around one and four antidots [3]. In the Hall-voltage we find additional plateaux and also quenching that can be suppressed by increasing the gate voltage. Figure 2 shows the conductivity measured in two-terminal geometry as a function of applied gate voltage for the three samples. The corresponding carrier density also plotted was obtained from Shubnikov-de-Haas oscillations of the four-terminal magnetoresistance. In all samples the conductivity is suppressed by a sufficiently negative gate bias. The shift in bias

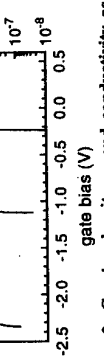
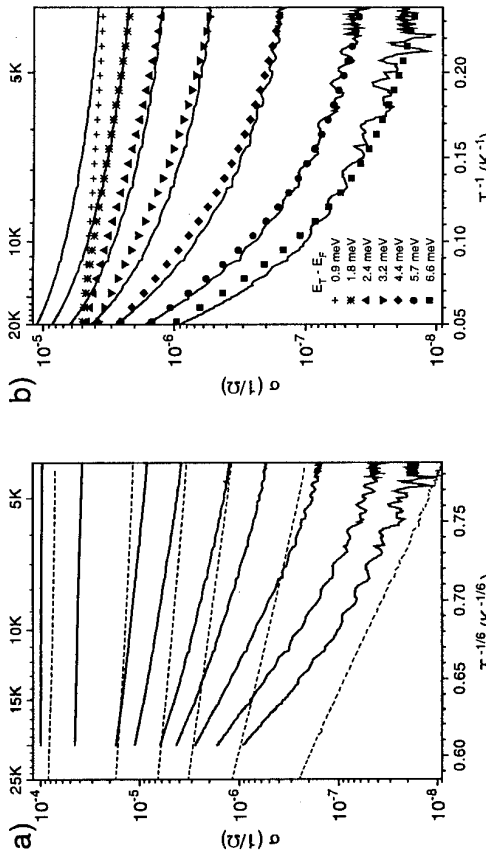


Figure 2: Carrier density n_s and conductivity as a function of gate bias for three samples: the reference with unpatterned gate (squares, left trace), the top gate (triangles, middle), and the recessed gate (circles, right). Arrows show the threshold densities obtained by linear extrapolation.



voltage is consistent with the change in the spacing between the gate and the 2DEG for the different samples. The threshold density n_r of the unpatterned sample of $1.4 \times 10^{11} \text{ cm}^2$ is relatively high compared to other high-mobility heterostructures [4], indicating a larger amount of density fluctuations [5]. Still, the threshold densities of the patterned structures ($3.8 \times 10^{11} \text{ cm}^2$ for the recessed / top gate) are clearly higher than that for the unpatterned reference. The values for n_r (marked by arrows in fig. 2) were determined by linear extrapolation to the bias voltage where the conductivity had fallen below $10^{-8} \Omega^{-1}$. Taking the effective size of the dots to be 22% of the unit-cell we estimate each dot to contain 50 (70) electrons at threshold for the surface (recessed) structure. This is in good qualitative agreement with self-consistent classical and quantum mechanical calculations performed for the geometry of the recessed gate [6]. This demonstrates that we have indeed realised a system of dots separated by potential barriers at the constrictions between two pillars. The cut-off of the conduction is also considerably sharper in the patterned gates: the necessary change in density for a decrease of the mobility by one order of magnitude near threshold is only 4.9% (9.3%) for the recessed (top) gate compared to 20% for the unpatterned gate. Thus the suppression of the conductance is due to the confinement of the electrons in artificially generated potential wells in contrast to localisation in the random potential of the unpatterned device. Fig. 3 shows the dependence of the conductivity for the recessed sample on an applied perpendicular magnetic field for different gate voltages. Due to the two-terminal measurement the value is a mixture of σ_{xx} and σ_{yy} , and also contains parts from the ungated 2DEG which complicates direct interpretation. The minimum in σ at low fields is associated with the basic commensurability of the cyclotron radius R_c with the antidot period ($2R_c = a$) which remains present even at the onset of the metal-non-metal-transition. Here the conductance is suppressed by a strong magnetic field which leads to an effective increase in confinement energy.

The temperature dependence of the conductivity is shown in figure 4a for the recessed sample and the flat reference gate for different applied gate voltages. For both samples this becomes increasingly strong below $\sigma_{xx} \approx 10^{-7} \Omega^{-1}$ as the negative gate voltage is increased, suggesting that a transition from diffusive to activated transport occurs around this value of conductivity. We find that the unpatterned reference can be described by an equation of the form

$$\sigma = \sigma_0 \exp(-T_0 / T)^\kappa \quad (1)$$

Best fits are obtained for $\kappa \approx 1/6$. In comparison, the recessed sample shows a much stronger temperature dependence near threshold and cannot be well described by equation (1), suggesting a different mechanism for the temperature dependence involved. Particularly the experimental data rule out a constant activation energy ($\kappa = 1$, see fig. 4b) that one might expect for such a system.

Figure 4b shows calculated conductivities which are in good agreement with experiment obtained by modelling a system of two dots connected by a tunnelling barrier. In this model we assume that the conductance is due to tunnelling from occupied to unoccupied single electron states on

Figure 4: (a) Temperature dependence of the two-point conductivity as a function of gate bias for the recessed sample (solid line) and the reference sample (dotted line). From top to bottom, $U_c = 0 \text{ V}$, -0.150 V , -0.200 V , -0.220 V , -0.225 V , -0.230 V , -0.235 V , and -0.240 V for the recessed sample and -1.70 V , -1.90 V , -2.00 V , -2.10 V , -2.15 V , and -2.20 V for the reference sample. (b) Calculated temperature dependence of the conductivity for the recessed system (symbols) in comparison to the experimental data (solid lines). The gate voltage was varied from -0.21 V to $-0.24V$ in 5 mV steps. The model used is discussed in the text.

$$\sigma = \frac{e^2}{h} \sum_{i \in \text{active}} f_i (1 - f_i) e^{-\alpha(E_r - E_i)} \quad (2)$$

The number of active states is small compared to the number of electrons per dot, and their level spacing depends only on the geometry [7]. The temperature dependence arises from the $f(1 - f)$ Fermi factor. We assume a simple but realistic exponential decay of the tunnelling rate with respect to the energy of the state below the barrier top ($E_r - E_i$). The parameter α depends on the geometry and the electron density [7]. The remaining free parameter is the Fermi energy in respect to the barrier ($E_r - E_p$). This depends on gate voltage and is thus fitted (see legend of fig. 4b).

In conclusion we have presented a novel model system enabling the study of the metal-non-metal transition. The temperature dependence can be modelled by considering two dots between two dots allowing the estimation of the height of the potential barriers. We gratefully acknowledge F. Stern for valuable discussions and U. Waizmann for technical support.

- [1] A. Lorke, J. P. Koithaus, and K. Ploog, Superlatt. and Microstruc. **9**, 103 (1991).
- [2] A. Hultmann, W. Brönnier, K. Kühler, B. Raynor, J. Schneider, J. Braunstein, M. Schlechtweg, P. Tasker, A. Thiede, and T. Jakobus, Proc. GaAs & Related Compounds 1993, Freiburg
- [3] D. Weiss, M. L. Roukes, A. Menuschig, P. Grambow, K. v. Klitzing, and G. Weimann, Phys. Rev. Lett. **66**, 2190 (1991)
- [4] C. Liang, D. C. Tsui, and G. Weimann, Appl. Phys. Lett. **53**, 1533 (1988)
- [5] We ascribe these potential fluctuations as well as the nonlinear bias dependence of n_s and the strong dependence of the mobility on n_s for the reference sample to the presence of the SiON layer (e. g. to inhomogeneities in the layer thickness).
- [6] A. Kumar, S. Lax, and F. Stern, unpublished
- [7] R. W. Tank and R. B. Stinchcombe, J. Phys.: Condens. Matter **7**, 849 (1995)

Semimetal–Semiconductor Transition in InAs–GaSb Heterostructures

Jennifer J. Quinn^{a,c}, John J. Quinn^{b,c}

^a Occidental College, Los Angeles, CA 90041, USA

^b University of Tennessee, Knoxville, TN 37996, USA

^c Naval Research Laboratory, Washington D.C. 20375, USA

Abstract

In a heterostructure consisting of neighboring layers of InAs and GaSb in a large band gap host like AlSb, the bottom of the InAs conduction band lies about 150 meV below the top of the GaSb valence band. However, because the electron and hole subbands are weakly coupled for nonzero values of the wavevector k_{\parallel} along the layer, an anticrossing of the levels occurs at $k_{\parallel} = k_c$, where $\lambda_c^2 = (2\mu/\hbar^2)(\Delta - \varepsilon_0^v - \varepsilon_0^c)$. Here Δ is the band overlap, ε_0^c and ε_0^v are the lowest electron and hole subband energies, and μ is the reduced mass. The splitting is of the order 5 to 10 meV. For an intrinsic material, the Fermi level lies in this gap, so that no semimetallic state occurs. If the InAs layers are sufficiently wide, or if an electric field can be applied across the heterostructure (by fabricating front and back gates) it is possible to have the first excited electron subband ε_1^c realize an anticrossing with ε_0^v as well. Then a true semimetallic state can occur with a circle of electrons in the ε_1^c subband near $k_{\parallel} = 0$ and a ring of holes near the anticrossing in the hybridized valence subband. A semimetal to semiconductor transition driven by shifting the single particle subband energies with applied electric or magnetic field should occur.

Introduction

The electronic and optical properties of InAs–GaSb heterostructures[1] are of special interest because the top of the GaSb valence band is higher than the bottom of the InAs conduction band by an energy $\Delta \approx 150$ meV. It is possible for GaSb valence electrons to transfer into the conduction band of the neighboring InAs layer giving rise to a semimetallic state containing equilibrium concentrations of spatially separated electrons and holes even in the absence of any dopants. The semimetallic state is expected to occur when the InAs conduction subband is lower in energy than the GaSb valence subband. Increasing the subband energies by decreasing the quantum well widths or by applying a large dc magnetic field could give rise to a semimetal to semiconductor transition when the subband energies cross.

Altarelli and his coworkers[2] pointed out that the conduction and valence subbands are coupled at k_{\parallel} different from zero. Because of this coupling an anticrossing of the subbands occurs near $k_{\parallel} = k_c$, the point at which the uncoupled subbands cross. The splitting is of the order of 5 to 10 meV. For an intrinsic material, the Fermi level always lies in the gap between the new hybridized valence and conduction subbands. Thus no semimetallic phase

¹Corresponding author

occurs. Many of the magneto-transport and magneto-optical measurements on InAs–GaSb heterostructures can be understood by assuming that the Fermi level is pinned in such a way as to give an excess of electrons[3]. Then the new W-shaped conduction band will contain occupied states near the minimum at $k_{\parallel} \approx k_c$. However, the interesting many body effects associated with electron-hole correlations, e.g. exciton condensation and the excitonic insulator transition, can be investigated only with samples in which the number of electrons, n_e , is approximately equal to the number of holes, n_h .

The object of this note is to point out that for a sufficiently wide InAs quantum well it is possible to have two conduction subbands that lie lower in energy than the valence subband at $k_{\parallel} = 0$. Both of the conduction subbands will couple to the valence subband for $k_{\parallel} \neq 0$, resulting in anticrossings at $k_c^{(0)}$ and $k_c^{(1)}$, where the lowest and first excited conduction subbands respectively cross the valence subband. Because $m_c \ll m_v$, the bottom of the original first excited subband can lie lower in energy than the top of the new hybridized valence band at $k_{\parallel} \approx k_c^{(0)}$. Then, electrons will transfer from the new hybridized valence subband into the lower of the new hybridized conduction subbands, and the desired semimetallic state will occur.

The Hartree field associated with the charge transferred from GaSb to InAs reduces the separation between the valence and conduction subbands, and one might suppose that, even for a very wide InAs quantum well, it would be impossible to achieve occupancy of the first excited conduction subband when the self-consistent Hartree field is included. However, Naveh and Laikhtman[4] have recently noted that if an InAs–GaSb bilayer in a large band gap host like AlSb can be fabricated with front and back gate electrodes, then the applied gate field can overcome the Hartree field and allow the effective band overlap to be changed at will. This should allow realization of the semimetallic state, and the systematic study of the effect of the electron–hole correlations.

Simple Model

We shall consider a very simple model to illustrate qualitatively the physics of the system. A GaSb layer of width a_1 is separated from an InAs layer of width a_2 by a very thin AlSb barrier of width $h \lesssim 10$ Å. The entire structure is embedded in an AlSb host in which front and back gate electrodes have been fabricated at a large distance from the quantum wells. We start by assuming that there is no coupling between the InAs conduction subbands and the GaSb valence subbands. Their energies are given by

$$\varepsilon_0^v(k_{\parallel}) = -\varepsilon_0^v - \frac{\hbar^2 k_{\parallel}^2}{2m_v},$$

and

$$\varepsilon_i^c(k_{\parallel}) = -\Delta + \varepsilon_i^c + \frac{\hbar^2 k_{\parallel}^2}{2m_c}.$$

Here Δ is the band overlap, ε_0^v is the energy of the lowest hole subband, and ε_i^c (for $i = 0$ or 1) are the energies of the lowest and first excited electron subbands.

The heavy, light and split-off band structure of the valence band of bulk GaSb is being ignored. Only a single heavy hole subband is included in the simple model. The actual energy spectrum in the presence of band coupling and the Hartree field associated with the

transfer of electrons from GaSb to InAs should be calculated by self-consistently solving the Schrödinger equation and Poisson's equation in a multiband model[4],[5]. We will mimic the results of such a self-consistent multiband calculation by simply assuming that the InAs conduction subbands and the GaSb valence subband are coupled by an interaction $V(k)$. We choose $V(k)$ to give a splitting of the order of 5 meV. Figure 1 is a plot of subband energy as a function of k_{\parallel} . It is assumed that the well widths and applied gate voltage can be chosen such that the valence subband is roughly 60 meV above the conduction subband at $k_{\parallel} = 0$. If we take $m_v = 0.37m$ and $m_c = 0.023m$, where m is the free electron mass, and take a_1 and a_2 equal to 100 fm and 150 Å respectively, this would occur when the applied gate voltage produces a field of the order of and opposite to the Hartree field. The coupling between bands results in new hybridized conduction and valence subbands separated by a gap of roughly 5 meV. For an intrinsic material the Fermi level lies in this gap (as shown by the dashed line in Figure 1) and the sample is semiconducting. The top of the new valence band occurs near $k_{\parallel} = k_c$. For $k_{\parallel} \gg k_c$ this subband is essentially identical to the GaSb, but for $k_{\parallel} \ll k_c$ it is very close to the ε_0^v InAs conduction subband. Near $k_{\parallel} = k_c$ there is a strong mixing of the two subbands. The opposite behavior is reflected in the hybridized conduction subband. It is InAs-like for $k_{\parallel} \gg k_c$ and GaSb-like for $k_{\parallel} \ll k_c$.

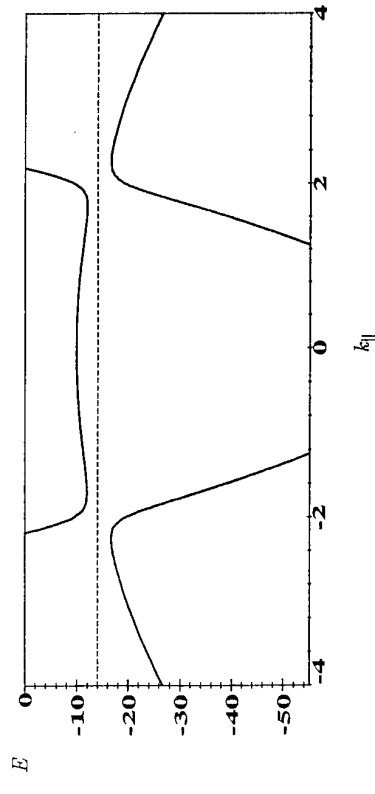


Figure 1. A sketch of the subband energies E as a function of k_{\parallel} . The interband coupling results in new hybridized conduction and valence subbands separated by a small gap. The Fermi level is indicated by the dashed line. E is in units of meV and k_{\parallel} in units of 10^{-6}cm^{-1} .

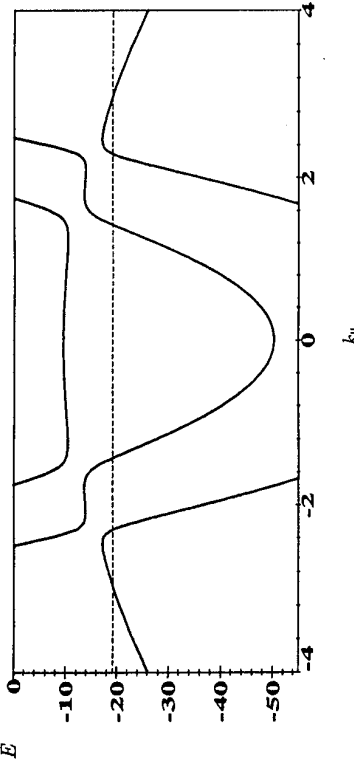


Figure 2. Same as Figure 1, but for the case in which both the ε_0^v and ε_1^c subbands are lower in energy than the ε_0^v subband.

Conclusion

We have shown that a semimetallic state can occur in the InAs-GaSb system if the well widths and applied gate voltage are chosen appropriately. By varying the gate voltage, the number of electrons and holes can be increased or decreased (all the way to zero). Our simple model has neglected some one particle effects (realistic valence band structure of GaSb) and some many body effects (exchange-correlation effects among electrons and among holes, and electron-hole correlations). The many body effects should give rise to exciton formation at low electron-hole concentrations. The ability to vary the electron-hole concentration with gate voltage could be a useful tool for studying excitonic instabilities in this system.

The authors would like to acknowledge stimulating discussions with Drs. B. Shanabrook and R. Wagner of the Naval Research Laboratory.

References

- [1] See, e.g. L.L. Chang in: Heterojunctions and Semiconductors Superlattices, Eds. G. Allan, G. Bastard, N. Boccara, M. Lannoo, and M. Voos (Springer, Berlin, 1986), p. 152, and references therein.
- [2] M. Altarelli, Phys. Rev. B **28** (1983) 842; A. Fassolino and M. Altarelli, Surf. Sci. **142** (1984) 322.
- [3] M. Altarelli, J.C. Maan, L.L. Chang, and L. Esaki, Phys. Rev. B **35** (1987) 9867.
- [4] Y. Naveh and B. Laikhtman, Applied Phys. Letters **66** (1995) 1980.
- [5] Y.C. Chang, Phys. Rev. B **37** (1988) 8215.

Oscillations in the low-field diffusion thermopower of a 2D electron gas

R. Fletcher
Physics Department, Queen's University, Kingston, Ontario K7L 3N6 Canada

P.T. Coleridge and Y. Feng
Microstructural Sciences, National Research Council, Ottawa, Ontario K1A 0R6 Canada

II. THEORY

can be calculated with no unknowns (except for Γ which can be obtained from an analysis of resistivity oscillations) and has a unique thermal damping factor. This is the main reason we have chosen to work at low fields. A full account of the low-field theory and experimental details will be published elsewhere [4].

Abstract

Oscillations in the diffusion thermopower of a GaAs/Ga_{1-x}Al_xAs heterojunction have been clearly observed for the first time. Phonon drag has been strongly reduced by growing the 2DEG on a heavily-doped conducting substrate and by working below 1K. The low-field oscillations in the Nernst-Ettingshausen coefficient have been investigated and are found to show the unique thermal damping factor of diffusion.

I. INTRODUCTION

Quantum oscillations in the diffusion thermopower of 2DEGs at high magnetic fields were theoretically investigated soon after the discovery of the quantum Hall effect. A number of experimental groups published results which were interpreted in terms of these theories and there appeared to be reasonable agreement, at least initially. Reference [1] has a comprehensive review of the early work on the thermopower of 2DEGs and many references may be found there. A theoretical study [2] of the low-field diffusion case also used then-current experimental data to compare with predictions.

However, it was later shown, both experimentally and theoretically, that phonon drag overwhelms the diffusion component over the range of temperatures where the experiments were made, usually the ⁴He range. Meanwhile the mobility of samples had steadily increased and there remained some uncertainty as to the extent that the mobility of the 2DEG affects phonon drag. It seemed possible that the early low mobility samples might have a much smaller phonon drag component than later high mobility samples, but recent work [3] has shown that phonon drag is essentially independent of mobility down to at least 0.1m²/Vs. There remains little doubt that the early experiments actually observed oscillations in phonon drag not diffusion. The aim of the present work was to reduce phonon drag to a level where diffusion dominates and to look for the diffusion oscillations.

Under high-field conditions diffusion and phonon drag oscillations are expected to be rather similar in form and difficult to reliably separate. High-field conditions correspond to $\hbar\omega_c \gg \Gamma$ where ω_c is the cyclotron frequency and Γ is the half-width of the Landau levels. In the opposite extreme of low-field conditions the amplitude of diffusion oscillations

The thermopower S is defined by $\mathbf{E} = S\nabla T$ where \mathbf{E} is the electric field developed in the sample under the applied temperature gradient ∇T . If we take the magnetic field \mathbf{B} to be perpendicular to the plane of the 2DEG and along \hat{z} , and the temperature gradient to be along \hat{x} , then the transverse thermopower (often called the Nernst-Ettingshausen coefficient) is defined by $S_{yx} = E_y/\nabla T_x$. The oscillatory diffusion component, \tilde{S}_{yx} , for elastic scattering of the electrons at low fields is found to be given by [4,2]

$$\tilde{S}_{yx} = \frac{4\omega_c\tau_l}{1 + \omega_c^2\tau_l^2} \left(\frac{\pi k_B}{e} \right) D'(X) \exp \left(-\frac{\pi}{\omega_c\tau_q} \right) \sin \left(\frac{2\pi\epsilon_F}{\hbar\omega_c} - \pi \right). \quad (1)$$

In this equation ϵ_F is the Fermi energy and τ_l and τ_q are the transport and quantum lifetimes, the latter being related to Γ by $\Gamma = \hbar/2\tau_q$. The quantity $D'(X)$ is the thermal damping factor and is the derivative of $D(X)$ with respect to X , where $D(X) = X/\sinh X$ and $X = 2\pi^2 k_B T/\hbar\omega_c$. The oscillations in the longitudinal component S_{xx} are predicted to be very similar but smaller by a factor $1/2\omega_c\tau_l$. It is noted that there is a phase difference of $\pi/2$ between the oscillations in ρ_{xx} and S_{yx} predicted by Eq. 1. We also expect oscillations to occur in the phonon drag thermopower but no theory yet exists for the low-field case. Experimentally it is known [5] that phonon drag oscillations in S_{xx} behave roughly like those in the resistivity and increase monotonically with field, though the amplitude is much more rapidly reduced at low fields, i.e. the effective impurity damping factor is much stronger; this presumably arises because of the thermal energy $k_B T$ involved in each scattering event. What happens with S_{yx} at low fields is unclear but the fact that the monotonic phonon drag contribution is quite small, and in fact is zero as a first approximation [6], is perhaps an advantage.

III. RESULTS AND ANALYSIS

The sample has an electron density of $\sim 1.9 \times 10^{15} \text{ m}^{-2}$ and mobility of $\sim 40 \text{ m}^2/\text{V}\cdot\text{s}$. By growing the sample on a strongly doped substrate the lattice thermal conductivity has been reduced; this in turn decreases the flux of phonon momentum in the applied temperature gradient so there is less phonon momentum available to transfer to the electrons as compared to the undoped case, thereby reducing phonon drag. Substrate doping has no effect on the diffusion component which at low temperatures depends only on the scattering of electrons by impurities close to the 2DEG. To further accentuate diffusion it is an advantage to reduce the temperature below 1K where phonon drag decreases much more rapidly with temperature than diffusion.

Fig. 1 gives experimental data on \tilde{S}_{yx} at a temperature of 0.55K. The two experimental traces are from two different pairs of transverse probes on the sample, and the upper data

are continued up to 8T. These traces are derived from data taken with $\pm B$ by eliminating the part even in field, which is about 20% of the total. Near 1T there is a clear change in the appearance of the oscillations. At high fields the oscillations are found to resemble the derivative of ρ_{xx} with respect to field. This is the form expected for high-field diffusion oscillations [7], but phonon drag seems to have a similar form so the origin of these oscillations is not yet unambiguous.

The lowest trace is calculated according to Eq. 1 using parameters appropriate to the sample and $m^* = 0.07m$, but is multiplied by a factor of two. There is substantial agreement between experiment and theory, especially in the appearance of a maximum in the amplitude near 0.5T. This maximum is basically due to $D'(X)$ in Eq. 1, though modified by the term in τ_t , and is believed to be unique to diffusion thermopower. It has previously been seen in bulk metal systems (e.g. see [8]). In comparison, the amplitude of $\tilde{\rho}_{xx}$ monotonically increases with B in this range. Observation of the predicted phase difference between the oscillations in ρ_{xx} and S_{yx} would provide a further test. However, as can be seen in Fig. 1 the experimental data on \tilde{S}_{yx} from two independent pairs of sample probes show relative phase shifts. This might be due to inhomogeneities in the sample.

As a final test, we use both $\tilde{\rho}_{xx}$ and \tilde{S}_{yx} to extract τ_q which should be the same for both coefficients. The amplitude data for \tilde{S}_{yx} are plotted in Fig. 2 in the form $\log[\tilde{S}_{yx}(1 + \omega_c^2 \tau_q^2)/\omega_c \tau_q D(X)]$ as a function of $1/B$ over the temperature range 0.35–0.72K for two pairs of sample probes. The scaled data follow a straight line within experimental error and the line through the data has a slope corresponding to $\tau_q = 1.8ps$ which is identical to that obtained from a similar analysis [9] of ρ_{xx} oscillations. If phonon drag was important, and if the phonon drag oscillations in \tilde{S}_{yx} behave similarly to those in S_{xx} , then we would expect a much smaller effective τ_q [5]. The intercept at $1/B = 0$ is $2.3 \pm 1.0mV/K$ which is about a factor of two larger than the expected value of $4\pi k_B/e = 1.08mV/K$; this factor of two was also indicated from the comparison of theory with experiment in Fig. 1.

IV. CONCLUSIONS

The observed thermopower oscillations exhibit the expected thermal damping factor for diffusion. They also yield the same impurity damping term as the resistivity oscillations as is expected because both are determined by the same impurity scattering of electrons. In contrast previous experiments have shown that phonon drag oscillations behave as if they have a much stronger effective impurity damping term. The only significant discrepancy with calculation is that the absolute amplitude of the thermoelectric oscillations is about a factor of 2 higher than predicted.

V. ACKNOWLEDGEMENT

The work was partially supported by the Natural Sciences and Engineering Research Council of Canada.

REFERENCES

- [1] B. L. Gallagher and P. N. Butcher, in *Handbook on Semiconductors* ed. P. T. Landsberg (Elsevier, Amsterdam, 1992) Vol. 1, p. 817.
- [2] H. Havlová and L. Snrká, Phys. Stat. Solidi, (b) **137**, 331 (1988).
- [3] R. Fletcher, J. J. Harris and C. T. Foxon, M. Tsatsoulis and P. N. Butcher, Phys. Rev. **B50**, 14991 (1994).
- [4] R. Fletcher, P.T. Coleridge and Y. Peng, Phys. Rev. (to be published).
- [5] M. D'Uorio, R. Stoner and R. Fletcher, Solid State Comm. **65**, 697 (1988).
- [6] X. Ziamni, P. N. Butcher and M. J. Kearney, Phys. Rev. **B49** 7520 (1994).
- [7] H. Oji, J. Phys. C: Solid State Phys., **17** 3059 (1984).
- [8] R. Fletcher, Phys. Rev. **28** 6670 (1983); Phys. Rev. **28** 1721 (1983); Phys. Rev. **B39**, 1120 (1989).
- [9] P. T. Coleridge, R. Stoner and R. Fletcher, Phys. Rev. **B39**, 1120 (1989).

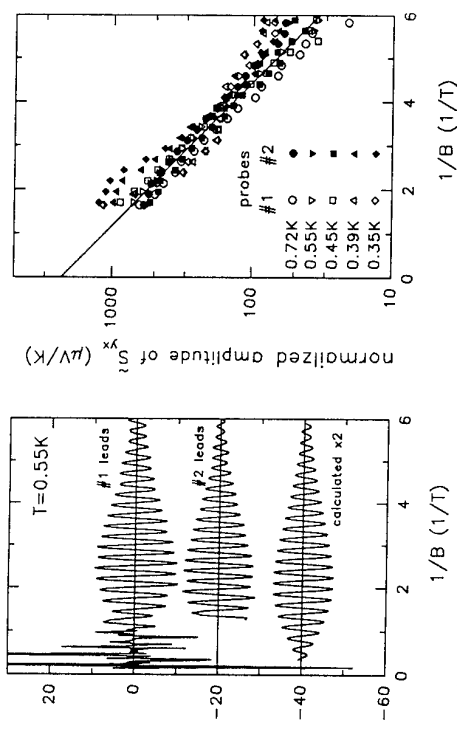


Fig. 1. The oscillations in S_{yx} as a function of inverse magnetic field $1/B$. The upper two curves are experimental data from different voltage probes, the lowest curve is calculated using parameters appropriate to the present sample but the magnitude is multiplied by a factor of 2. The bottom two traces are offset by 20 and $40 \mu V/K$. (The calculated curve contains the monotonic component but this is essentially negligible in this range of field).

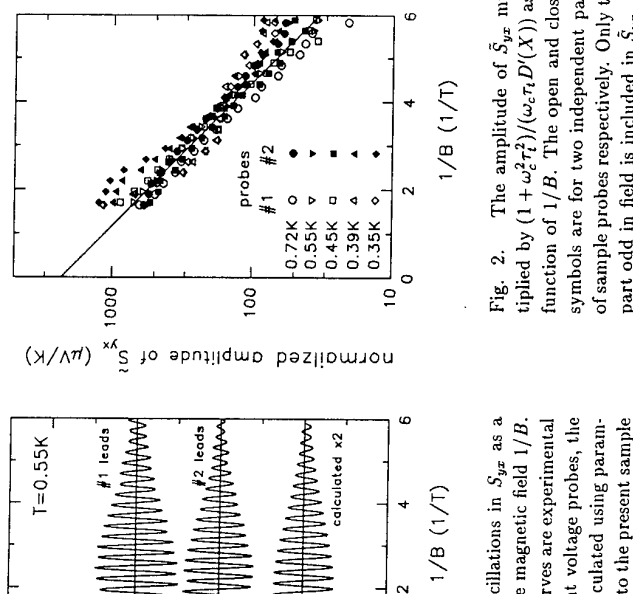


Fig. 2. The amplitude of \tilde{S}_{yx} multiplied by $(1 + \omega_c^2 \tau_q^2)/(\omega_c \tau_q D(X))$ as a function of $1/B$. The open and closed symbols are for two independent pairs of sample probes respectively. Only the part odd in field is included in \tilde{S}_{yx} .

Magnetoresistance Anomaly of a Two-dimensional Electron Gas in Tilted Magnetic Fields

P.Středa, P.Vášek and M.Cukr
Institute of Physics, Academy of Sciences of Czech Republic,
Cukrovarnická 10, CZ-162 00 Praha.

Abstract

The magnetoresistance of a two-dimensional electron gas in the presence of magnetic fields applied parallel to or slightly tilted from the plane of the confined electron gas is described. It is argued that the magnetoresistance dependences are strongly influenced by a *Hall field* across electron gas plane, which is controlled by the in-plane component of the magnetic field.

Introduction

In 1990 Leadley et al [1] have reported positive magnetoresistance with rising the angle between the two-dimensional electron gas and the magnetic field direction in the range of few degrees for a fixed magnetic field strength. It has been suggested that this effect is due to the pear-like shaped Fermi surface of electron gas which arises due to the break of the time reversal symmetry in strong in-plane fields when the confining potential has an asymmetric, about triangular, shape [2]. However, the self-consistent calculations of electron energy spectra [3] show that the asymmetry in real two-dimensional systems is rather weak even in the case of strong in-plane magnetic fields, B_{\parallel} . Also, the fact that the positive magnetoresistance observed for the current J applied parallel to B_{\parallel} is of the same order as that for $J \perp B_{\parallel}$ is difficult to explain by the Fermi surface asymmetry only.

The in-plane magnetic field does not only influence electron energy spectra but it also shifts electron mass centra (guiding centra) in the direction perpendicular to the electron gas plane. The electrons of the unlike velocity directions are shifted towards opposite sides of the confinement. The resulting electron charge distribution is modified in order to minimize the energy of the Coulomb interaction with the fixed positive background of ionized impurities [3]. The velocity redistribution induced by an applied current necessarily leads to the redistribution of the electronic charge as well. Although it takes part on the microscopic distances of the order of 100 Å a *Hall field* has to appear. To estimate its value we will assume that it just has to return the electron charge distribution back into the equilibrium one in order to minimize the Coulomb energy. Making use of this idea we have found qualitative agreement with the observed magnetoresistance dependences.

Experimental results

The magnetoresistance has been studied on standard $\text{Al}_x\text{Ga}_{1-x}\text{As}-\text{GaAs}$ heterostructures grown by the molecular beam epitaxy. The typical layer structure consists of a 2 μm GaAs buffer, 100 Å spacer, 1000 Å of Si-doped $\text{Al}_x\text{Ga}_{1-x}\text{As}$ ($x \sim 0.32$) and 200 Å cap layer of GaAs. The Hall-bar samples of 400 μm conducting channel width have been used for the

measurement. At helium temperature 4.2 K their carrier density and mobility are typically in the range of $n_s = 3.05 \times 10^{15} \text{ m}^{-2}$ and $20.41 \text{ m}^2/\text{Vs}$, respectively. The relatively small carrier density ensures the existence of the two-dimensional electron gas with only the lowest subband occupied in the whole range of the used magnetic field strength.

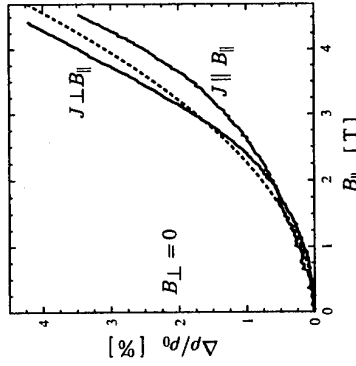


Fig. 1 : Magnetoresistances $\Delta\rho_{xx}/\rho_0$ ($J \perp B_{\parallel}$) and $\Delta\rho_{yy}/\rho_0$ ($J \parallel B_{\parallel}$) as functions of the in-plane magnetic field B_{\parallel} for $B_{\perp} = 0$, $\rho_0 = 1/\sigma_0$ denotes the zero field resistivity. The dashed line represents the model calculation for harmonic confinement frequency $\Omega = eB_{conf}/m$ with $B_{conf} = 16 \text{ T}$.

Typical magnetoresistance traces presented in Fig. 1 and Fig. 2 were taken at 4.2 K for the sample with $n_s = 5.2 \times 10^{15} \text{ m}^{-2}$ and the mobility $35 \text{ m}^2/\text{Vs}$. The effects of in-plane magnetic fields and those slightly tilted by an angle θ from the direction parallel to the two-dimensional electron gas plane have been studied in two different configurations. The resistivity component ρ_{xx} corresponds to the current applied perpendicularly to the magnetic field direction ($J \perp B_{\parallel}$) while ρ_{yy} has been measured with the current applied along the in-plane component of the magnetic field ($J \parallel B_{\parallel}$).

Model calculation

Let us first briefly summarize the effect of the in-plane magnetic field, $B_y \equiv B_{\parallel}$, on a free electron gas confined in \hat{z} direction. Assuming for the sake of the simplicity the harmonic confinement represented by a frequency Ω and using the Landau gauge for the

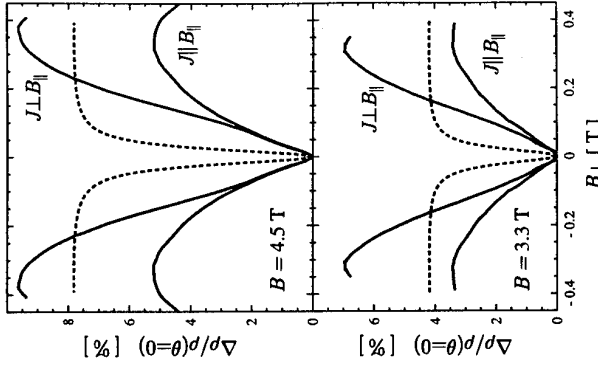


Fig. 2 : Angle dependences of the magneto resistance shown as functions of $B_{\perp} = B \sin \theta$ for two fixed values of the magnetic field strength B , $\rho(\theta = 0)$ denotes the resistivity for the in-plane field orientation. Dashed lines represent the model calculation with $B_{conf} \equiv m\Omega/e = 16 \text{ T}$.

vector potential, $\vec{A} \equiv (B_{\parallel} z, 0, 0)$, the single electron Hamiltonian has the following form

$$H = \frac{1}{2}m \left(\frac{p_x}{m} + \omega_{\parallel} z \right)^2 + \frac{p_{\perp}^2}{2m} + \frac{p_z^2}{2m} + \frac{1}{2}m\Omega^2 z^2 + e\mathcal{E}_z z , \quad (1)$$

where $\omega_{\parallel} = eB_{\parallel}/m$ is the cyclotron frequency, m and e are an effective electron mass and the absolute value of the electron charge, respectively. We have incorporated a slave field \mathcal{E}_z in \hat{z} direction for later use. The energy dispersion $E(\vec{k})$ of the lowest subband representing the two-dimensional electron gas is given as follows

$$E(\vec{k}) = \frac{\hbar^2 k_y^2}{2m} + \frac{\hbar^2 k_x^2}{2m_z^*} - v_d k_x + \frac{1}{2}mv_d^2 , \quad (2)$$

where $v_d = \mathcal{E}_z/B_{\parallel}$ is the drift velocity and $m_z^* = (1 + \omega_{\parallel}^2/\Omega^2)m$ represents the increase of the effective mass induced by the magnetic field component B_{\parallel} . The expectation values of the z coordinate, determining guiding center locations $Z(k_x)$, yield

$$Z(\vec{k}) = -\frac{1}{\omega_{\parallel}} \left[\frac{\hbar k_x}{m} - \frac{1}{\hbar} \frac{\partial E(\vec{k})}{\partial k_x} \right] = -\frac{1}{\omega_{\parallel}} \left[(1 - \frac{m}{m_z^*}) \frac{\hbar k_x}{m} + v_d \right] . \quad (3)$$

Tilting the magnetic field by an angle θ from the in-plane direction gives the non-zero perpendicular component $B_z \equiv B_{\perp} = B \sin \theta$. For small enough angles the effect of B_{\perp} may be included through the electron dynamics in \vec{k} -space which is governed by the semiclassical equation of the motion

$$\hbar \frac{\partial \vec{k}}{\partial t} = -e\vec{\mathcal{E}} - e\vec{v}(\vec{k}) \times B_{\perp}\hat{z} - \frac{\vec{k} - \vec{k}_0}{\tau} , \quad \vec{v}(\vec{k}) = \frac{1}{\hbar} \nabla_{\vec{k}} E(\vec{k}) , \quad (4)$$

where $\vec{\mathcal{E}} \equiv (\mathcal{E}_x, \mathcal{E}_y)$ is an applied external electric field and $\vec{v}(\vec{k})$ denotes the velocity expectation value. The relaxation processes forcing electrons to return back into an initial state \vec{k}_0 are supposed to be represented by an uniform relaxation time τ . Making use of the dispersion relation, Eq.(2), the equation of motion leads to Drude-Zener-like expressions for the current densities

$$J_x = en_s v_d + \frac{\sigma_0}{1 + \omega_c^2 \tau^2} \frac{m}{m_z^*} \mathcal{E}_x - \frac{\sigma_0 \omega_c \tau}{1 + \omega_c^2 \tau^2} \sqrt{\frac{m}{m_z^*}} \mathcal{E}_y , \quad (5)$$

$$J_y = \frac{\sigma_0}{1 + \omega_c^2 \tau^2} \mathcal{E}_y + \frac{\sigma_0 \omega_c \tau}{1 + \omega_c^2 \tau^2} \sqrt{\frac{m}{m_z^*}} \mathcal{E}_x , \quad \sigma_0 = \frac{e^2 n_s \tau}{m} , \quad (6)$$

where $\omega_c = eB_{\perp}/\sqrt{mm_z^*}$ is the cyclotron frequency.

The equation of motion, Eq.(4), defines \vec{k} -space trajectory along which electron is moving and the probability to find the electron in the particular state $\vec{k}(t)$ during its life time. The corresponding guiding centre moves in time as well and the time average $\langle Z(\vec{k}) \rangle$ taken over all electrons having the same initial expectation value $Z(\vec{k}_0)$, may be used to determine the drift velocity v_d . To preserve the equilibrium charge distribution the change of $\langle Z(\vec{k}) \rangle$

due to the applied electric field $\vec{\mathcal{E}}$ has to be just compensated by the corresponding shift due to the Hall field \mathcal{E}_z and we get

$$en_s v_d = \left(1 - \frac{m}{m_z^*} \right) \frac{\sigma_0}{1 + \omega_c^2 \tau^2} \mathcal{E}_x . \quad (7)$$

The relaxation time is generally dependent on B_{\parallel} . We will use the simplest possible approach for which it is inversely proportional to the density of states which equals to $\sqrt{m_z^* n_s}/(\pi \hbar^2)$ for the considered harmonic confinement. The dependence of the resistivity on the magnetic field components, B_{\perp} and B_{\parallel} , is thus controlled by the following expressions

$$\rho \equiv \rho_{xx} = \rho_{yy} = \frac{m}{e^2 \tau n_s} \frac{1 + \omega_c^2 \tau^2}{1 + \frac{m}{m_z^*} \omega_c^2 \tau^2} , \quad \tau = \sqrt{\frac{m}{m_z^*} \tau_0} , \quad \frac{m_z^*}{m} = 1 + \frac{\omega_{\parallel}^2}{\Omega^2} . \quad (8)$$

where τ_0 is the zero field relaxation time.

Conclusions

The harmonic confinement, Eq.(1), and the uniform relaxation time we have used are not too realistic assumptions. Nevertheless the resistivity given by Eq.(8), with the confinement frequency Ω being the single fitting parameter, qualitatively describes the main features of the experimental magnetoresistance traces as shown in Fig. 1 and Fig. 2. The fact that instead of the magnetoresistance saturation predicted for $\omega_c \tau > 1$ the negative magnetoresistance is observed at $B_{\perp} > 0.3$ T (see Fig. 2) we ascribe to the localization effects that were excluded from our consideration by using the semiclassical description of the electronic transport.

Nevertheless, despite of the used simplified model, the presented analysis allows us to conclude that any more-realistic treatment has to take into account the *Hall field* across the electron gas layer which, under particular conditions, might have the dominant effect on the magnetoresistance.

This work was supported by the Grant Agency of the Czech Republic under the Grant No. 202/94/1278 and by the ASCR Grant No. 110423.

References

- [1] D.R.Leadley, R.J.Nicholas, J.J.Harris and C.T.Foxon, in: 20th International Conference on Physics of Semiconductors, Eds. E.M.Anastassakis and J.D.Joannopoulos (World Scientific Publishing Co., Singapore, 1990) p. 1609.
- [2] W.Zawadzki, S.Klahn and U.Merkel, Phys.Rev. **B 33** (1986) 6916.
- [3] L.Smrká and T.Jungwirth, J.Phys.:Condens. Matter **6** (1994) 55.

Electron-Phonon Scattering Rates in GaAs/AlGaAs 2DEG Samples Below 0.5K

A. Mittal^a, R. G. Wheeler, and D. E. Prober
Dep. of Applied Physics and Physics, Yale University, New Haven, CT 06520-8284, USA

R. N. Sacks^b
United Technologies Research Center, East Hartford, CT 06108, USA

Abstract

We have studied electron heating in a 2DEG in GaAs/AlGaAs heterojunctions below 0.5K. The electron temperature was raised above the lattice temperature using Joule heating. Weak localization and the temperature dependent sample resistance were used as thermometers for the electrons. The electron-phonon energy relaxation rate was found to be proportional to T_3 . We find that the relaxation rate increases with disorder in the system.

Introduction

Electron-phonon scattering is one of the fundamental processes in solids. Although well characterized in clean bulk metals, the understanding in lower-dimensional and in disordered systems is limited. Studies in metal films are complicated by issues of film purity, film thickness and effects of substrate coupling [1]. A two dimensional electron gas (2DEG) formed at the interface of a lattice matched heterostructure from electrons in the lowest quantized subband offers a cleaner system to study this interaction, because the issues of phonon dimensionality and non-sphericity of the Fermi surface do not pose a problem. One can then study just the effect of disorder on electron-phonon scattering.

We present an experimental study of electron-phonon interaction time, $\tau_{e\text{-ph}}$, below 0.5K, in a 2D electron gas in GaAs/AlGaAs heterostructures. Aside from being a fundamental quantity in itself, the energy relaxation rate is also relevant to studies of novel phenomena which occur only at low temperatures.

Most investigations of $\tau_{e\text{-ph}}$ are based on one of the following two kinds of experiments. The first relies on weak localization to extract the phase-breaking rate [2]. At high temperatures, the phase-breaking rate is approximately the electron-phonon scattering rate [3]. However, at low

measurements that only the first subband is occupied.

Thermometry

We employ two techniques to determine the electron temperature, T_e . These give results which are consistent with each other. The first method uses weak localization. The magnetoresistance can be fit to a well established theory [4] to find the electron phase coherence length, L_Φ . A temperature dependence of $L_\Phi \propto T_e^{-1/2}$ is expected to hold down to mK temperatures. The details have been discussed previously [5].

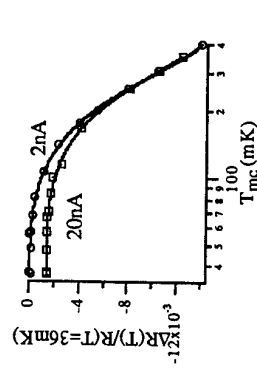


Fig. 1 Change in the normalized resistance of the sample as a function of the mixing chamber temperature for two different input currents.

Sample Description

The 2DEG devices in a standard Hall configuration were fabricated from modulation doped, MBE grown Al_{0.3}Ga_{0.7}As/GaAs heterojunctions. The results presented here were obtained from three different samples fabricated from two wafers, A and B. Table 1 summarizes the sample parameters and geometries. The relevant length scales in the experiment, such as the mean free path and the phase coherence length are much less than the sample dimensions and the distance between measuring probes. Thus we have a 2D diffusive system and even in the presence of uniform heating, one has a well defined local electron temperature. For both the samples, it was confirmed using Shulinikov de-Haas

heat flows out of the electrons to the phonons. There are two different mechanisms for electrons to lose this energy via phonon emission. We estimate the power flowing out by this mechanism by a theory put forward by Price [6], which predicts $P_{e\text{-ph}} = 3.3 \times 10^6 T_e^{-1/2} A_{device} (T_e^5 - T_{ph}^5)$. The numerical factors are valid specifically for a single-subband Al_{0.3}Ga_{0.7}As/GaAs heterojunction. The temperature dependence in (1) stems from piezoelectric coupling of acoustic phonons to electrons. The electron-phonon coupling due to deformation potential instead has a T^7 temperature dependence. Below 1K, the power flowing out via this mechanism can be neglected. It is to be noted that the existing theories [6,7] do not take into account the effects of impurities on the electron-phonon interaction.

The second mechanism of energy escape is via electron diffusion. Hot electrons can diffuse out to the cold ohmic contacts to be replaced by cold electrons. Using the Wiedemann-Franz law, we calculate the heat flow out through the electron gas for our sample geometry to be

$$P_{e\text{-diff}} = \frac{10^{-7}}{R} (T_e^2 - T_{ph}^2) \quad (2)$$

Numerical estimates of the thermal conduction path between the sample and the mixing chamber show that the sample lattice and the ohmic contacts are at most 1mK above the mixing chamber temperature [5].

We also use the temperature dependent resistance of the sample, due primarily to electron-electron interaction, as a secondary thermometer. This is done at a magnetic field large enough to destroy the weak localization. Fig. 1 shows the change in the normalized sample resistance as a function of the mixing chamber temperature for two different measuring currents 2nA and 20nA. (the solid lines are an aid to the eye). The two curves are identical in the high temperature region, while at lower temperatures the curve for 20nA saturates at a lower resistance value. The curve for 2nA can thus be used as a thermometer to obtain the temperature of the electron gas when larger currents are used.

	Sample parameters		
	A	B1	B2
$n_s (10^{15}/\text{m}^2)$	1.6	8.3	8.3
$\mu (\text{m}^2/\text{V}\cdot\text{s})$	12.4	2.3	2.3
# of squares	20	15	15
A (mm ²)	0.2	0.5	0.05

Table 1.

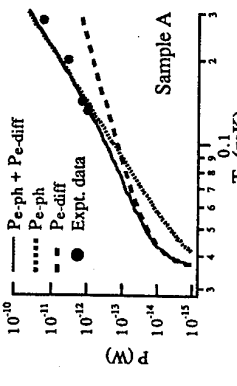


Fig. 2 The power flowing out of the electron gas as a function of the electron temperature at a mixing chamber temperature of 36mK. The lines are the theory curves and the dots experimental data.

Theory

At low temperatures, even small power levels can raise the electron temperature above that of the phonons. This temperature difference is determined by the rate at which

^a Corresponding author.
 Electronic mail : mittana@minerva.cis.yale.edu
 Phone : 203 432 4286 ; Fax : 203 432 4283
^b Present address : Dept. of Electrical Engineering,
 Ohio State University, USA.

Fig. 2 depicts the relative importance of the two mechanisms for typical sample parameters. As can be seen, 100mK represents a rough crossover between the two mechanisms, with electron-phonon coupling dominating at higher temperatures. The dark solid line is the sum of the two contributions and represents the total power flowing out of the electron gas at that temperature.

When heat flows out mainly via electron diffusion, the electrons in the center of the Hall bar are hotter than those near the ohmic contacts. We have simulated the temperature profile along the sample length including both mechanisms of heat conduction (Fig. 3). As the input current increases, more heat is carried out by phonon emission and the electrons start attaining a uniform temperature along the sample length. Even when the dominant mechanism of heat flow is electron out-diffusion, the temperature profile is flat near the center. Hence, we measure the central region of our sample which corresponds to the temperature T_e in our formulas.

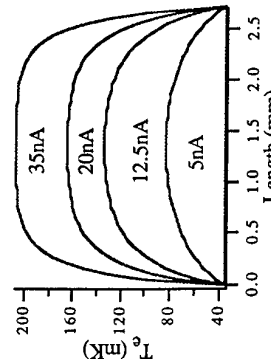


Fig. 3 Simulations of temperature profile along the length of the sample for typical parameters.

Results and Discussion

Using Joule heating from the measuring current we dissipate known amounts of power, such that in the operating regime phonon emission is the dominant energy relaxation mechanism. We then determine the electron levels used to exceed any extraneous power in the device. Fig. 2 shows the results for Sample A. The experimental data is in fair agreement with

the theory confirming that the power flowing out via phonon emission is proportional to T_e^5 . We can now extract the electron-phonon scattering rate using

$$\tau_{e-ph}^{-1} = \left(\frac{d P_{e-ph}}{dT_e} \right) / C_e \quad (3)$$

where dP_{e-ph}/dT is the thermal conductance due to phonon emission, and C_e the electronic heat capacity for the 2DEG at T_e . Hence we extract for sample A,

$$\tau_{e-ph}^{-1} \approx 2.4 \times 10^8 T_e^3 \text{ s}^{-1} \text{K}^{-3}$$

This value along with the Price prediction is listed in Table 2. We note that Wennberg et al. [8] used a multiple quantum well heterostructure and found the scattering rate to be two orders of magnitude lower than that predicted by Price.

In order to understand the role of impurities, we fabricated two devices B1 and B2 from a wafer with lower mobility. They were designed to have the same number of squares and a sheet resistance close to that of sample A ($\sim 315\Omega$), ensuring that the thermal conductance due to electron diffusion is similar for all three samples. Samples B1 and B2 are on the same chip and were measured simultaneously, ensuring a comparison based solely on the geometrical difference between the two. Fig. 4 shows the results for samples B1 and B2. The power scales with the device area, implying that phonon emission is the operative energy relaxation mechanism (the power flowing out via electron diffusion is independent of area). We find for both the B devices that the power flowing out per unit area via phonon emission at a given electron temperature is about six times higher than that predicted by Price. Using (3), we extract an average value for samples B as

$$\tau_{e-ph}^{-1} \approx 1 \times 10^9 T_e^3 \text{ s}^{-1} \text{K}^{-3}$$

Thus it appears that the electron-phonon scattering rate increases with disorder.

To our knowledge, there does not exist any prediction for the dependence of the scattering rate on disorder for a 2DEG. A few theories [9-12] do examine this effect in thin metallic films, but do not reach consensus. Takayama [9] predicts that the inelastic scattering of electrons by vibrating impurities leads to $\tau_{eph}^{-1} \propto 1^{-1}$, where 1 is the electron

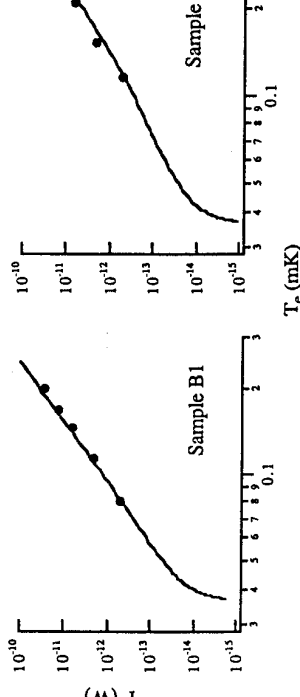


Fig. 2. Fig. The total power flowing out of the electron gas vs its peak temperature at $T_{mc}=36\text{mK}$. The solid lines represent the sum of the heat carried by the Price mechanism multiplied by a factor of six, plus the WF contribution.

References

- [1] G. Bergmann, W. Wei, Y. Zhou, and R.M. Mueller, Phys. Rev. B 41 (1990) 7386.
- [2] G. Bergmann, Physics Reports, 107 (1984) 1.
- [3] P. Santhanam, S. Wind, and D.E. Prober, Phys. Rev. B 35 (1987) 3188.
- [4] S. Hikami, A. I. Larkin, and Y. Nagaoka, Prog. Theor. Phys. 63 (1980) 707.
- [5] A. Mitai, M. W. Keller, R. G. Wheeler, D. E. Prober, and R. N. Sacks, Physica B 194 (1994) 167. This paper considered only cooling by electron out-diffusion, and thus does not give a complete picture of the heat flow.
- [6] P.J. Price, J. Appl. Phys. 53 (1982) 6863.
- [7] V. Karpus, Sov. Phys. Semicond. 22 (1988) 268.
- [8] A. K. M. Wennberg, S. N. Yterboe, C. M. Gould, H. M. Bozler, J. Klein, and H. Morkoc, Phys. Rev. B. 34 (1986) 4409.
- [9] H. Takayama, Z. Phys. 259 (1973) 421.
- [10] J. Rammer, and A.Schmid, Phys. Rev. B 4 (1986) 1352.
- [11] M.Y. Reizer, and A.V. Sergeyev, Sov. Phys. JETP 63 (1986) 616.
- [12] D. Belitz, and S. Das Sarma, Phys. Rev. B 36 (1987) 7701.

Electronic mail of principal investigator:
daniel.prober@yale.edu

Tilted magnetic field studies of spin- and valley-splittings in Si/Si_{1-x}Ge_x Heterostructures

P. Weitz, R. J. Haug, K. v. Klitzing
Max-Planck-Institut für Festkörperforschung, Heisenbergstr. 1, 70569 Stuttgart, Germany

F. Schäffler

Daimler-Benz-Forschungszentrum, Wilhelm-Raabe-Straße 11, 89081 Ulm, Germany

Magnetotransport measurements on the 2DEG of a Si/Si_{1-x}Ge_x heterostructure with an electron mobility of $32 \text{ m}^2/\text{Vs}$ are presented. The coincidence method in a tilted magnetic field is used to determine the effective g-factor. In the filling factor range $16 \leq \nu \leq 28$ an almost constant effective g-factor of $g^* = 3.39$ is found. For lower filling factors g^* increases. Activation energy experiments at different tilting angles show that the size of the valley splitting depends only on the normal component of the magnetic field. Around filling factor $\nu = 3$ in a tilted field, an overshoot occurs in the Hall resistance, which is attributed to level crossings as a consequence of the exchange enhancement effects of spin- and valley-splitting.

In the last decade strong interest arose in the study of Si/SiGe heterostructures [1], [2], [3]. In many cases the motivation was to improve the crystal growth for a higher performance of heterobiopolar transistors [4] and an increased mobility of the 2DEG at the interface. The achieved mobilities [5] are about an order of magnitude larger than found in silicon MOSFETs so that the peculiarities of the spin- and valley-splitting of the Landau levels for the 2DEG in silicon [6], [7] can be studied in much more detail than before.

Magnetotransport measurements have been performed on Si/Si_{1-x}Ge_x heterostructures grown by MBE. The lower part of the structure consists of a Si substrate and a graded Si_{1-x}Ge_x buffer layer with a final Ge concentration of about 25 %. On top of this buffer, a strained Si channel has been grown with a thickness of 24 nm. The channel is separated from the doped layer (doping concentration = $1.8 \times 10^{18} \text{ cm}^{-3}$) by a 16 nm thick spacer. A silicon cap layer protects the surface [8]. Hall-bars with alloyed Sh/Au contacts were processed. The samples were mounted in a dilution refrigerator to perform magneto-transport measurements at temperatures down to 50 mK. At this temperature the samples show an electron mobility as high as $\mu_e = 32 \text{ m}^2/\text{Vs}$ with a carrier concentration of $n_e = 3.75 \times 10^{15} \text{ m}^{-2}$. The corresponding transport relaxation time τ_s has a value of 34 ps and the single-particle relaxation time τ_d is 2.6 ps as calculated from the amplitudes of the Shubnikov-de Haas (SdH) oscillations (the effective mass in Si/SiGe heterostructures has a value of $m^* = 0.19m_0$).

In Fig. 1 SdH and Hall measurements are shown. The large plateau visible around $B = 15 \text{ T}$ corresponds to a filling factor of $\nu = 1$, indicating the valley splitting of the lowest spin level. Between $B = 10 \text{ T}$ and 12 T , ρ_{xx} shows two minima. The minimum at $B = 12 \text{ T}$ corresponds to the fractional filling factor $\nu = 4/3$, whereas the other one is not at $\nu = 5/3$ but at $\nu = 1.51$. The plateau in ρ_{xy} between 9.5 and 6.5 T and the simultaneous vanishing of ρ_{xx} corresponds to the spin splitting of the lowest Landau level, i.e. the first spin level, consisting of two valley levels, is filled. At $B = 5.2 \text{ T}$ the second valley splitting at $\nu = 3$ can be seen. The plateau around $B = 4 \text{ T}$ ($\nu = 4$) indicates that the first Landau band is filled. In decreasing the magnetic field, the minima corresponding to valley splittings slowly begin to vanish. The largest observable valley filling factor is $\nu = 13$ ($B = 1.25 \text{ T}$). The spin splitting starts to be observable at $B = 0.6 \text{ T}$, with the SdH oscillations themselves beginning at $B = 0.4 \text{ T}$. The single-particle relaxation time τ_s , calculated from this starting point, has a value of 2.7 ps, which is in good agreement with the value, calculated from the amplitude of the SdH

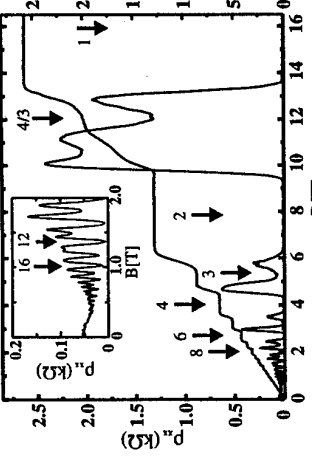


Fig. 1. Longitudinal and Hall resistance versus magnetic field B ($T=50 \text{ mK}$). The inset shows the lower magnetic field range. Different filling factors are indicated with arrows and numbers.

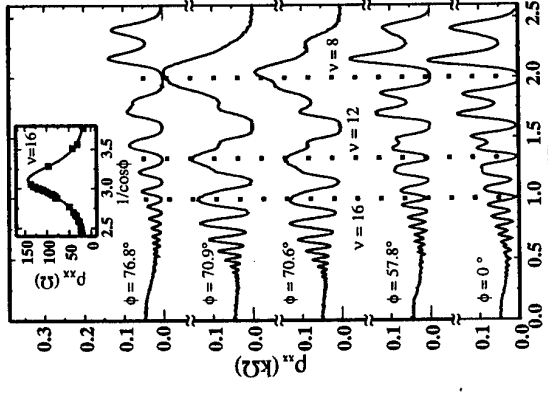


Fig. 2. ρ_{xx} for different angles versus B_\perp . The position of some integer filling factors ($\nu = 16$) plotted versus integer filling factor ($\nu = 16$) plotted versus $1/\cos \phi$. The measured data can be nicely fitted by a Lorentzian profile. As described above, ρ_{xx} rises, until the coincidence is reached at

oscillations. Further on we will focus on extracting absolute sizes of spin- and valley splittings. The size of the spin splitting is given by $g^* \mu_B B$, with μ_B the Bohr magneton and g^* the effective g-factor. g^* depends on the population difference between the different spin levels due to the exchange enhancement. In case of equal population, the effective g-factor has a value of approximately $g^* = 2$, given by the band structure, otherwise g^* is larger. One possibility of measuring the spin splitting consists of doing measurements in tilted magnetic field. The size of the Landau splitting is given by the normal component of the magnetic field B_\perp , however the spin splitting depends on the total magnetic field B . Therefore in tilted magnetic fields, the spin splitting can be enlarged in comparison with the Landau splitting, and can be determined with respect to the size of the Landau splitting.

In Fig. 2 ρ_{xx} is plotted versus B_\perp for different tilt angles ϕ . The angle ϕ is measured with respect to the normal of the surface (2DEG) and was extracted from the slope of ρ_{xy} in the linear regime ($\Delta\phi < 0.1^\circ$). We will first concentrate on the magnetic field range below 1.0 T ($\nu \geq 16$). In this range, the valley splitting is small and can be neglected. At an angle of $\phi = 57.8^\circ$, the spin splitting has approximately half the size of the Landau splitting. Therefore, spin- and Landau-splitting form an equidistant energy ladder with equally resolved SdH oscillations. For the traces at $\phi = 70.6^\circ$ and 70.9° the minima corresponding to the Landau splitting disappear, instead maxima are observable at filling factors $\nu = 16, 20, 24, \dots$ due to the coincidence of spin levels of adjacent Landau levels. For an angle of $\phi = 76.8^\circ$, the spin splitting has approximately 1.5 times the size of the Landau splitting.

The inset of Fig. 2 shows ρ_{xx} at a constant integer filling factor ($\nu = 16$) plotted versus $1/\cos \phi$. The measured data can be nicely fitted by dotted lines. The inset shows ρ_{xx} at constant integer filling factor of $\nu = 16$ versus $1/\cos \phi$.

$1/\cos \phi = 3.1$. Since spin- and Landau-splitting have the same size at this angle ($g^* \mu_B B = \hbar \omega_c = \hbar e B \cos \phi / m^*$, ω_c = cyclotron frequency), it is possible to extract the effective g-factor ($g^* = \hbar e \cos \phi / \mu_B m^*$). For $28 \geq \nu \geq 16$ g^* is almost constant and has a value of 3.39 ± 0.01 . The above determined value is not the maximum possible effective g-factor. During the coincidence, two levels overlap completely with the Fermi energy located in the middle of these levels. Both levels are half filled with electrons, therefore the population difference is half as large as the maximal possible. This leads to medium values of the effective g-factor. By analyzing ρ_{xx} (Fig. 2, inset) at the angle range around the coincidence, it is possible to deduce effective g-factors for angles larger and smaller than the angle of coincidence. The analysis of these profiles for filling factors of the first and the second coincidence will be published elsewhere [9]. For $\nu = 16$ we obtain an effective g-factor of 3 at $1/\cos \phi = 2.6$ and a value of 3.8 at $1/\cos \phi = 3.6$.

In the following we will discuss the magnetic field range from 1.0 to 2.5 T. Analyzing the angle at which ρ_{xx} reaches a maximal value, we obtain an effective g-factor of $g^* = 3.41$ for $\nu = 12$ and $g^* = 3.44$ for $\nu = 8$. These values indicate a slight rise of g^* with magnetic field. Note that the valley splitting can not be neglected in this magnetic field range and may influence the above values. The influence of the valley splitting can clearly be seen in the third and fourth trace in Fig. 2 (70.6° and 70.9°). The longitudinal resistance at $\nu = 8$ almost reaches a maximal value, but $\nu = 9$ is still resolved in both traces and $\nu = 7$ can be observed in the third trace.

Since the valley splitting can not be neglected, one can not obtain an effective g-factor from a study of the angular dependence of ρ_{xx} near coincidence in this magnetic field range. Moreover, it is unclear, whether the valley splitting depends on the total or normal component of the magnetic field. The best way to obtain this is the direct measurements of this gap energy, by performing activation energy measurements at different tilt angles.

In Fig. 3 the extracted activation energies E_a for four different valley filling factors are plotted versus the total magnetic field. The activation energy was obtained from a fit to the usual activation energy formula $\rho_{xx} \propto \rho_{xx}^{\max} \exp(-E_a/2k_B T)$, as presented in the inset of this figure. The deduced energies for the filling factors $\nu = 3, 5, 7$ and 9 are almost independent of the tilting angle. For $\nu = 7$ the activation energies even decrease slightly with the tilting angle. This clearly shows that the valley splitting, Σ , is not proportional to the total magnetic field but more likely proportional to the normal component of the magnetic field.

It is interesting to note that the activation energies for $\nu = 5$ are approximately twice as large as the energies for $\nu = 3$. Since the valley splitting depends linearly on the magnetic field, one would expect a much larger value for $\nu = 3$ than for $\nu = 5$. Unusual behavior near $\nu = 3$ can also be seen in the SdH oscillations of Fig. 1. The longitudinal resistance at $\nu = 3$ is larger than at $\nu = 5$. Moreover, a number of phenomena in the range of filling factor $\nu = 3$ occur at angles near the coincidence. In Fig. 4, the longitudinal and Hall resistances for different tilting angles are plotted versus B_1 . As described earlier, for

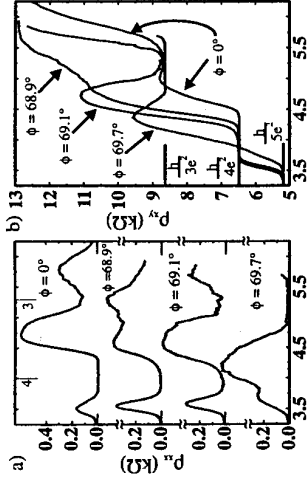


Fig. 3. Longitudinal (a) and Hall resistance (b) for different tilting angles plotted versus B_1 . The short solid lines with numbers indicate the different filling factors. $\nu = 4$ with the peak between $\nu = 4$ and $\nu = 3$. At $\nu = 3$ a strong minimum is visible and ρ_{xy} shows a strong overshoot. For higher magnetic fields, ρ_{xy} rises up to a value of $h/2.3e^2$ and then drops down almost to the value $h/3e^2$. In the last trace ($\phi = 69.7^\circ$), ρ_{xx} at $\nu = 4$ rises, indicating that a coincidence takes place. In addition, the plateau of ρ_{xy} at $\nu = 4$ has vanished. The overshoot is still clearly resolved, ρ_{xy} reaches a value of $h/2.7e^2$ at $B=4.3$ T and drops down to the value of $h/3e^2$ between $B=4.8$ T and $B=5.6$ T.

Under the assumption that a change of the magnetic field induces level crossings as a consequence of exchange enhancement, these phenomena can be understood. The overshoot at an angle of $\phi = 69.1^\circ$ for example is induced by the crossing of the third valley level of the first Landau band and the first valley level of the second Landau band. The maximum Hall resistance ($B=4.8$ T) is reached at the complete overlap of these two levels with the Fermi energy located within the extended states in the middle of the levels. By increasing the magnetic field the levels cross each other and electrons from localized states of one level populate extended states of the other one, leading to a drop of the Hall resistance.

In conclusion, we have performed magnetotransport experiments on high quality Si/Si_{1-x}-Ge_x heterostructures in tilted magnetic field. Temperature dependent measurements show that the valley splitting depends only on the normal component of the magnetic field.

The effective g-factor for higher filling factors is constant ($\nu \geq 16$, $g^* = 3.39$) and increases for lower filling factors. For tilted field measurements in the range of $\nu = 3$, the Hall resistance shows an overshoot as a consequence of exchange enhancement effects.

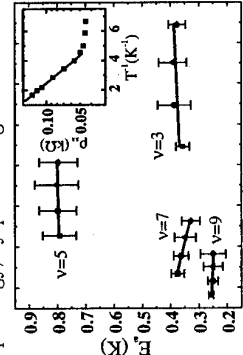


Fig. 3. Activation energy E_a for different filling-factors and angles versus total magnetic field B . The squares indicate measurements at $\phi=0^\circ$, the circles at $\phi=32.5^\circ$, the up-triangles at $\phi=43.5^\circ$ and the diamonds at $\phi=49.8^\circ$. The solid lines are guides to the eye. The inset shows as an example ρ_{xx} for $\nu = 5$, $\phi = 0^\circ$ versus $1/T$. By fitting an exponential behavior, the activation energies were deduced.

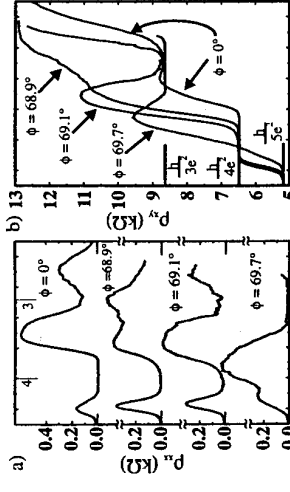


Fig. 3. Longitudinal (a) and Hall resistance (b) for different filling factors plotted versus B_1 . The short solid lines with numbers indicate the different filling factors. $\nu = 4$ with the peak between $\nu = 4$ and $\nu = 3$. At $\nu = 3$ a strong minimum is visible and ρ_{xy} shows a strong overshoot. For higher magnetic fields, ρ_{xy} rises up to a value of $h/2.3e^2$ and then drops down almost to the value $h/3e^2$. In the last trace ($\phi = 69.7^\circ$), ρ_{xx} at $\nu = 4$ rises, indicating that a coincidence takes place. In addition, the plateau of ρ_{xy} at $\nu = 4$ has vanished. The overshoot is still clearly resolved, ρ_{xy} reaches a value of $h/2.7e^2$ at $B=4.3$ T and drops down to the value of $h/3e^2$ between $B=4.8$ T and $B=5.6$ T.

Under the assumption that a change of the magnetic field induces level crossings as a consequence of exchange enhancement, these phenomena can be understood. The overshoot at an angle of $\phi = 69.1^\circ$ for example is induced by the crossing of the third valley level of the first Landau band and the first valley level of the second Landau band. The maximum Hall resistance ($B=4.8$ T) is reached at the complete overlap of these two levels with the Fermi energy located within the extended states in the middle of the levels. By increasing the magnetic field the levels cross each other and electrons from localized states of one level populate extended states of the other one, leading to a drop of the Hall resistance.

In conclusion, we have performed magnetotransport experiments on high quality Si/Si_{1-x}-Ge_x heterostructures in tilted magnetic field. Temperature dependent measurements show that the valley splitting depends only on the normal component of the magnetic field.

The effective g-factor for higher filling factors is constant ($\nu \geq 16$, $g^* = 3.39$) and increases for lower filling factors. For tilted field measurements in the range of $\nu = 3$, the Hall resistance shows an overshoot as a consequence of exchange enhancement effects.

- [1] D. Többken, F. Schäffler, A. Zrenner and G. Abstreiter, Phys. Rev. B **46**, 4344 (1992).
- [2] Don Monroe, Y. H. Xie, E. A. Fitzgerald and P. J. Silverman Phys. Rev. B **46**, 7935 (1992).
- [3] F. F. Fang, Surface Science **305**, 301 (1994).
- [4] F. Schäffler, Solid-State Electronics **37**, 765 (1994).
- [5] K. Ismail, F. K. LeGoues, K. L. Saenger, M. Arafa, J. O. Chu, P. M. Mooney and B. S. Meyerson, Phys. Rev. Lett. **73**, 3447 (1994).
- [6] F. F. Fang and P. J. Stiles, Phys. Rev. Lett. **174**, 823 (1968).
- [7] T. Ando, A. B. Fowler, F. Stern, Rev. Mod. Phys., **54**, 437 (1982).
- [8] F. Schäffler, D. Többken, H.-J. Herzog, G. Abstreiter and B. Holländer, Semicond. Sci. Technol. **7**, 280 (1992).
- [9] P. Weitz, R. J. Haug, K. v. Klitzing and F. Schäffler, to be published.

NEGATIVE MAGNETORESISTANCE AND ELECTRON-ELECTRON INTERACTION IN Si:SiGe QUANTUM WELLS

T J Thornton ^{a)}, A Matsumura ^{a), b)} and J Fernández ^{b)}

^{a)} Dept. of Electrical and Electronic Engineering, Imperial College of Science, Technology and Medicine, Exhibition Road, London SW7 2BT

^{b)} ICR for Semiconductor Materials, Imperial College of Science, Technology and Medicine, Prince Consort Road, London SW7 2BZ

Abstract

We have measured the magnetoresistance of n-channel Si:SiGe quantum wells in the temperature range 0.4 to 6.6 K. For magnetic fields less than 1 Tesla and before the onset of Shubnikov de Haas oscillations there is a broad negative magnetoresistance. The change in resistance follows a B^2 dependence and can be explained in terms of the 2D electron-electron interaction.

Introduction

It is well known that an ideal metal shows no magnetoresistance (MR). However, in a disordered system quantum corrections such as weak localisation [1] and electron-electron interaction [2] can lead to an observable MR at low temperatures. Weak localisation is a manifestation of the quantum interference between electron waves and gives rise to a negative MR which is quenched for fields above a maximum value given by $B_C = \hbar^2 l_e^2 / [2e^2]$ [3] where l_e is the electron mean free path. The electron-electron interaction modifies the diffusion coefficient [4] and leads to a positive MR for fields large enough to cause Zeeman splitting ie $B > B_Z = kT/g^* \mu_B$ where μ_B is the Bohr magneton and g^* is the effective electron g-factor. Between these two limits (ie $B_C < B < B_Z$) there is a regime where the magnetic field has no effect on the conductance and for a 2DEG the conductivity correction can be written as [5]

$$\Delta\sigma_{2D} = (e^2 / 2\pi^2 \hbar) N_v F^* [\Psi(0.5 + \hbar/kT_e) - \Psi(0.5)] \quad (1)$$

Here, Ψ is the digamma function, τ_e is the transport time and F^* is the effective screening factor given by

$$F^* = [4 - 3 \{ (2 + F) / F \} \ln(1 + F/2)] \quad (2)$$

where F can take values between 0 and 1 depending upon whether the 2DEG is poorly screened or well screened [5]. The valley degeneracy, N_v , is equal to 2 in tensile strained silicon quantum wells. In a transport measurement we are usually concerned with the resistance which can be found by inverting the conductivity tensor. For magnetic fields in the range $B_C < B < B_Z$ the result is a negative MR given by [6]

$$\Delta R_{xx} = (1/N_s e)^2 (\tau_s / \tau_e)^2 B^2 \Delta\sigma_{2D} \quad (3)$$

where N_s is the sheet density and τ_s is the single particle relaxation time. We have measured the low temperature MR of the 2DEG formed in modulation doped Si:SiGe quantum wells. By fitting the data to equation (3) it is possible to extract values for the screening factor, F , as described below.

Experimental Results

The Si:SiGe quantum wells are grown by gas source molecular beam epitaxy and details of their growth and characterisation have been given elsewhere [7]. The data presented here were taken from samples from a wafer which consisted of a $Si_{0.7}Ge_{0.3}$ virtual substrate, a 110 \AA tensile strained Si well a 150 \AA undoped SiGe buffer layer, a 560 \AA heavily doped SiGe supply layer and a 20 \AA Si cap. The quantum wells were patterned into Hall bars and the low temperature MR of a typical sample with a mobility of $90,000 \text{ cm}^2/\text{Vs}$ and a sheet density of $7.2 \times 10^{11} \text{ cm}^{-2}$ is shown in Figure 1. The mean free path in these samples is approximately $0.9 \mu\text{m}$ and the lower critical field $B_C = 0.4 \text{ mT}$ is therefore well below the range of magnetic field that we are interested in here.

The magnetoresistivity, R_{xx} , has clear Shubnikov-de Haas (SdH) oscillations and the lifting of the spin degeneracy occurs for fields in excess of $2.5T$. The Hall resistance, R_{xy} , shows well developed quantum Hall plateaus and from the low field gradient we obtain a Hall density of $7.3 \times 10^{11} \text{ cm}^{-2}$ very similar to that obtained from periodicity of the SdH oscillations suggesting that there is little parallel transport in the SiGe supply layer.

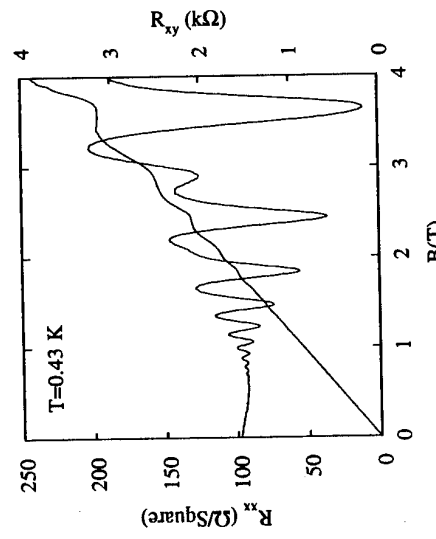


Figure 1: The magnetoresistivity, R_{xx} , and Hall resistance, R_{xy} , of a modulation doped Si:SiGe quantum well

Before the onset of the SdH oscillations at fields $B \geq 0.8 \text{ T}$ there is a distinct negative MR with a quadratic dependence on B [6]. Results for two different temperatures are shown in Figure 2

where the dashed lines are the best fits to equation (3). We have fitted similar data over a range of temperatures from 0.4 to 6.6 K and have calculated the parameter, $\Delta R_{xx} \pi^2 \hbar N_s / B^2$. The results plotted against the corresponding value of $\Psi(0.5 + \hbar/kT\tau_e) - \Psi(0.5)$ are shown in Figure 3. The data follows a fairly linear behaviour passing through the origin as expected from equation (3). The gradient of the linear fit gives an estimate of the value for $(\tau_S/\tau_e)^2 F^*$ as 0.69 from which we can obtain a value for the screening factor, F .

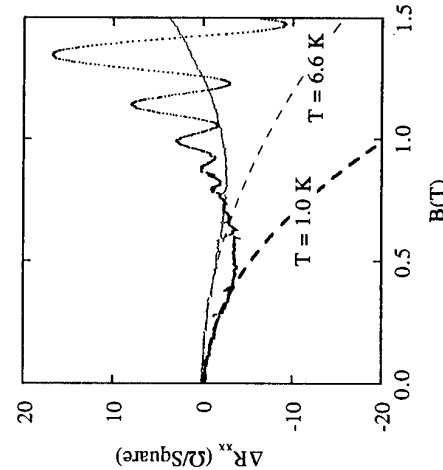


Figure 2: The low field magnetoresistance change measured at two different temperatures. The dashed curves are the fit to equation (3).

Analysis and Conclusions

Before we can calculate a value for F we need to know the ratio of the single particle time to the transport time, τ_S/τ_e , and a convenient way to obtain this is by means of a Dingle plot [8]. The very strong damping of the SdH oscillations, ΔR_{SdH} (see figure 2) is well described by the formula $\Delta R_{SdH} = 4R_0 X(T) \exp(-\pi c \omega_c \tau_S)$ where $X(T) = (2\pi^2 kT/\hbar\omega_c)^2 / \sinh(2\pi^2 kT/\hbar\omega_c)$ is a thermal damping factor, R_0 is the zero field resistance and ω_c is the cyclotron frequency. By plotting $\ln(\Delta R_{SdH}/X(T))$ against $1/B$ it is possible to extract values of τ_S and using the transport time extracted from the mobility $\tau_e = \mu n/e$ we obtain a ratio $\tau_S/\tau_e \sim 0.1$. Unfortunately this result implies that $F^* = 69$ for which it is impossible to extract a real root to equation (2). However, making the assumption that $\tau_S/\tau_e = 1$ gives $F=0.44$ as a solution to equation (2), a result which lies within the theoretical range and is similar to results obtained from GaAs/AlGaAs heterojunctions [6].

To understand the apparent discrepancy we should consider how the two scattering times determine the resistivity in the regimes of high and low magnetic field. For high magnetic fields such that $\mu B > 1$ the electrons are confined to Landau orbits. The condition $\mu B > 1$ corresponds to an electron being able to complete at least one Landau orbit without being scattered. The Landau orbits are susceptible to small angle scattering events which will deflect the electron from its circular trajectory. The single particle relaxation time that determines the amplitude of

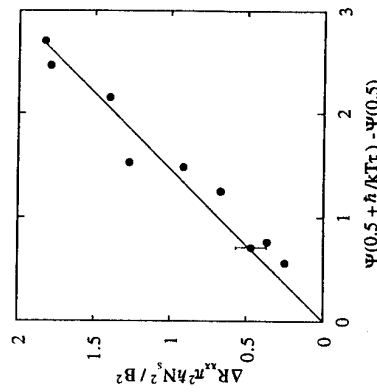


Figure 3: Plot of $\Delta R_{xx} \pi^2 \hbar N_s / B^2$ versus $\Psi(0.5 + \hbar/kT\tau_e) - \Psi(0.5)$. The error bar indicates the variation in the results obtained for two nominally identical samples from the same wafer.

In conclusion we have shown that modulation doped Si:SiGe quantum wells display a pronounced negative magnetoresistance at low temperatures. The negative MR is well explained by the 2D electron-electron interaction theory and assuming that $\tau_S/\tau_e = 1$ we estimate the screening factor to be given by $F=0.44$. This work was supported, in part, by the EPSRC.

- * Permanent address: Advanced Semiconductor Technology Laboratory, Electronics Research Laboratories, Nippon Steel Corporation, 5-10-1 Fuchinobe, Sagamihara-shi, Kanagawa 229, Japan
- [1] G Bergmann, Phys. Rev. B²⁸, 2914 (1983)
- [2] B L Alsthaler, A G Aronov and P A Lee, Phys. Rev. Lett. 44, 1288 (1980)
- [3] K K Choi, Phys. Rev. B²⁸, 5774 (1983)
- [4] A M Finkel'stein, Sov. Phys. JETP 59, 212 (1984)
- [5] H Fukuyama, J. Phys. Soc. Jpn. 50, 3407 (1981)
- [6] K K Choi, D C Tsui and S C Palmateer, Phys. Rev. B³³, 8216 (1986)
- [7] J M Fernandez et al accepted for publication in J. Materials Science (June 1995); see also A Matsumura et al accepted for publication in Semicond. Sci. and Technol.
- [8] P T Coleridge, Phys. Rev. B⁴⁴, 3793 (1991)

Low temperature magneto-transport of 2D electron and hole systems in high mobility Si-Si_xGe heterostructures

R.B. Dunford¹, R. Newbury¹, V.A. Stadnik¹, F.F. Fang², R.G. Clark¹, R.H. McKenzie¹, R.P. Starrett¹, E.E. Mitchell¹, P.J. Wang², J.O. Chu², K.E. Ismail² and B.S. Meyerson²

¹ National Pulsed Magnet Laboratory, University of New South Wales, Sydney 2052, Australia
² IBM T.J. Watson Research Center, Yorktown Heights, NY 10598, USA

Abstract Low temperature magneto-transport measurements of 2D electron and hole systems (2DES, 2DHS) in high quality n- and p-type modulation-doped Si-Si_xGe heterostructures (respectively) have been extended to high magnetic fields (50T) and low temperatures (30mK). For the high mobility 2DES in n-Si, a two valley system, signatures of the fractional quantum Hall effect (FQHE) in the region $v < 1$ (one valley occupied, lowest spin state) usually observed in GaAs-AlGaAs are replicated out to $v=2/5$ at $B=48T$. For $1 < v < 2$ however (both valleys occupied, lowest spin state), prominent FQHE states such as $v=5/3$ are absent, indicative of the importance of valley occupation. For the 2DHS in p-Si_xGe_x, in addition to the QHE two low temperature insulating phases (IP) are identified at $v=1.5$ and $v \geq 0.5$ ($B=30T$), with re-entrance to the QHE regime at $v=1$ ($B=15T$). The IP centred at $v=1.5$ has the characteristics of a Hall insulator but is unanticipated by the global phase diagram for 2D systems. The important physics associated with the IP is related to an energy degeneracy of adjacent Landau levels of opposite spin.

1. Introduction

Recent advances in preparing Si_xGe layers on (100)Si substrates by MBE or UHV-CVD [1-4] exploit pseudomorphically-strained layers on strain-relieved substrates or intermediate layers. For our n-type samples [5,6], the 2D electron system is formed in a biaxially tensile stressed silicon layer (~10nm thick) clad between strain-relieved Si_xGe_x layers. The 2D electrons are transferred from phosphorus doping in the top-clad Si_xGe_x alloy, with an undoped spacer extending 15nm from the Si-Si_xGe_x interface. For our p-type samples [7], holes are confined to 2D in a Si_xGe_x layer under compressive biaxial stress (~40nm thick) clad between the Si substrate and a top Si cap layer, which is modulation-doped with boron (6nm spacer).

In this paper, we extend previous magneto-transport results for electrons [6,8,9] and holes [10] to focus on the low temperature properties of these strained layers in strong magnetic fields. Measurements in 20ms duration (~200mV) which suppresses intersubband scattering. For the lowest subband, the energy of the two valleys corresponding to momenta along $\pm\hat{z}$ (where \hat{z} is the growth direction) are lowered while the other four are raised in a magnetic field there is consequently a fourfold degeneracy for each Landau level, two for spin and two for valley.

Transport data for a sample with $n=4.6 \times 10^{11} \text{ cm}^{-2}$ and $\mu=1.5 \times 10^7 \text{ cm}^2/\text{Vs}$ are shown in Fig. 1. Parallel conduction observed in this sample has been subtracted from the ρ_{xx} data in Fig. 1 ab; error in the simple B2 background subtraction at highest field leads to the minimum in ρ_{xx} at $v=2/5$ lying below zero. The important observation is that for $v < 1$ (Fig. 1b), where only one valley (lowest spin state) is occupied, FQHE structure normally observed in GaAs-AlGaAs heterostructures is replicated, namely ρ_{xx} minima at $v=2/3$, $3/5$ and $2/5$. In contrast, for the interesting region $1 < v < 2$ which corresponds to the lowest spin state but with two valleys occupied, a deep ρ_{xx} minimum is observed at $v=5/3$ (Fig. 1a) but there is no structure at $v=2/3$, normally a strong FQHE state in GaAs. Unlike the situation in GaAs in the low magnetic field regime where the spin configuration of FQHE states can lead to magneto-transport anomalies, this anomaly in Si-Si_xGe_x is observed at high magnetic fields for the fully spin polarised $v=5/3$ state, ruling out explanations in terms of spin effects. Whilst it is tempting to speculate that odd-numerator states are absent (with a view that $v=5/3$ corresponds to $2/3$ filling in both valley 1

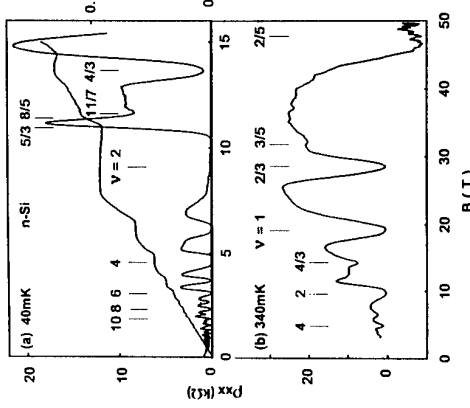


FIG. 1 Transport data for the 2DES in n-type Si-Si_x-Ge_x (n=4.6×10¹¹cm⁻²) taken (a) in steady fields at 40mK and (b) pulsed fields at 340mK.

Figs. 2 (traces a and e) and 3 show magnetoresistance data for single-side doped p-type Si-Si_xGe_x samples ($x=0.10-0.12$) with dark hole density $n_d = 3 \cdot 8 \times 10^{11} \text{ cm}^{-2}$ and mobility $\mu = 8000 \text{ cm}^2/\text{Vs}$ [10], amongst the highest reported for 2D holes in a Si-based system. Both strain and confinement act to lift the doubly-degenerate valence bands; the $m_F=\pm 1/2$ heavy hole band has the lowest energy for holes. The energy level scheme for these samples in a magnetic field is unusual. From a detailed study of the temperature dependence (not shown) of the low-field Shubnikov-de Haas oscillations in Fig. 2 (trace a), we obtain $m^*=0.24 \text{ me}$. In these samples $g_{LLB} \sim 6-8$ [10]. Consequently, the spin splittings $g_{LLB}B$ is comparable to the cyclotron energy $\hbar v_F B/eB^2$.

Considering the ratio of the Landau level (LL) width to the cyclotron energy, given by $(3/(2\pi e\hbar c)^{1/2}$ (where the lifetime $\tau = m^*\mu/e$), indicates that the LL broadening at 10T, for example, is ~25% of the cyclotron splitting. The net result is that spin-up and spin-down energies associated with extended states of adjacent LLs overlap (except for $v=2$ in Fig. 2 (trace a)).

For $v > 1$ there are three features of note in Fig. 2 (traces a and e) which result from this unusual energy level degeneracy: (i) A weak ρ_{xx} minimum develops close to $v=8/3$ (and also close to $v=7/3$ in a second sample, not shown). Whilst the ρ_{xx} minimum lines up in field with a p_x plateau-like structure, this plateau is not at the correct position. (ii) At $v \geq 2$ a ρ_{xx} minimum forms at $v=2$, with no plateau at $h/2e^2$. The position of the ρ_{xx} minimum slightly above 8T in Fig. 2 (trace a) is 0.6T higher in field than the $v=2$ position determined from the odd-integer sequence to lower field; in Fig. 3 we denote the filling factor at this ρ_{xx} minimum as $v=2'$. At higher field the Hall resistance reappears towards the classical value (blue) shown in Fig. 2 (trace e); the details depend on the polarity of the magnetic field (+B, -B) with the average ρ_{xy} (which removes ρ_{xx} admixture effects)

reasonably close to the classical line. (iii) An anomalously large ρ_{xx} peak is observed in the region $2v > 1$ centred at $v=1.5$ which increases from $\rho_{xx} \sim 5KQ$ at $T=1.75K$ to $\sim 40KQ$ below 100mK, as shown in Fig. 3a. The detailed temperature dependence of ρ_{xx} at $v=1.5$ is contrasted with that at $v=2'$ (ρ_{xx} minimum) and $v=2.1$ (next largest ρ_{xx} peak to lower field) in Fig. 3b depicting insulating, activated QHE and metallic character respectively. The IP centred at $v=1.5$ was reproduced in two samples and on several cool-downs.

The p_{xy} jump to $h/2$ at $v=2'$, and the ρ_{xx} minimum at a field value slightly higher than the expected $v=2$ position can be understood from the unusual energy level degeneracy. At exactly $v=2$ filling, with unresolved spin states of adjacent Landau levels, the Fermi energy E_F will be in overlapping extended states of the 0, 1' levels and ρ_{xx} will be finite. If extended states are sufficiently narrow, a small increase in magnetic field will move E_F into localised states with only the lowest Landau level (0') extended states below E_F resulting in $\rho_{xx} \rightarrow 0$ and $\rho_{xy} \rightarrow h/e^2$. Any magnetic field dependence of the g*-factor in this system adds to the complexity and ρ_{xx} , ρ_{xy} structure between the v=2 and 3 QHE is likely to arise from similar mechanisms, as opposed to the fractional QHE. If this energy level degeneracy persists at higher fields, a very broad $v=1$ p_x plateau would be expected, which is not the case in our data due to the observed onset of an IP centred at $v=1.5$, for which the single particle density of states picture above is unlikely to be appropriate. The IP requires separate explanation.

The unusual energy level degeneracy in p-type Si-Si_x-Ge_x described above is central to the formation of the

IP at $v=1.5$. This is demonstrated in Fig. 2 (traces b, d, f), where the sample is systematically illuminated using a Ti:Sapphire laser operating at $\lambda = 785\text{nm}$ and low power levels ($<1\text{W}$). Illumination lifts the energy degeneracy by reducing the difference in population of \uparrow and \downarrow spins, which in turn reduces the exchange enhancement of the g-factor. There is also an effect due to narrowing of the Landau level width with increased density and mobility of the 2DHS, however this is expected to be small since the zero-field mobility is only observed to increase by less than 5%. This lifted degeneracy is clearly evidenced by comparison of p_{xx}, p_{xy} data at $v=2$ for fully illuminated density n_2 (Fig. 2 traces c, e) with the situation at dark density n_1 (Fig. 2 traces a, e). At density n_2 the $v=2, p_{xx}$ minimum becomes broad, is accurately zero and is at its correct position in magnetic field and, most importantly, is now accompanied by a corresponding p_{xy} plateau quantised at h/e^2 , in striking contrast to the p_{xx}, p_{xy} anomalies at dark density. The activation energy Δ at $v=2$ derived from $p_{xx} = C \exp(-\Delta/2kT)$ increases from a dark value of 0.4K to 9K after illumination. There is also evidence for resolution of the $v=4$ QHE in p_{xx}, p_{xy} structure at illuminated density n_2 . The important observation is that in lifting the energy level degeneracy in this way, the IP resistance at $v=1.5$ collapses to $\sim 10\%$ of its dark value. The sharp rise of p_{xy} beyond $v=2$ and the $v=2, p_{xx}$ minimum just beyond $v=2$ and the observation of a substantially reduced but nonetheless remnant IP at illuminated densities are all associated with a rapidly changing g-factor. Also shown in Fig. 2 (trace d) are p_{xx} data for a double-sided sample with $n = 4.4 \times 10^{11}\text{cm}^{-2}$ in each

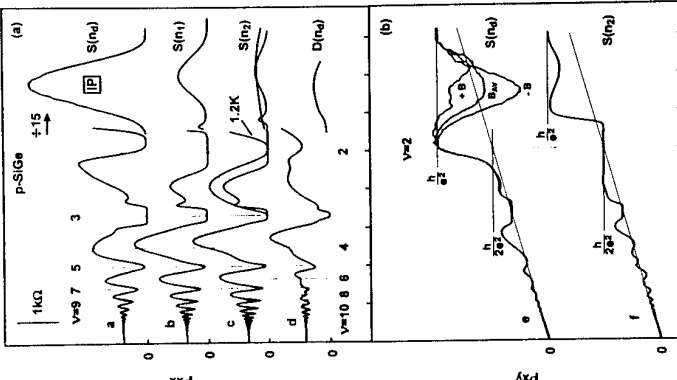


FIG. 2 (a) Longitudinal resistivity ρ_{xx} for the region $V > 1$ with increasing sample illumination (and density) for a single-side (S) doped sample; **a** - dark density $n_d = 3.8 \times 10^{11} \text{ cm}^{-3}$ (at 30mK); **b** - illuminated densities $n_1, n_2 = 4, 2.6 \times 10^{11} \text{ cm}^{-3}$ (at 30mK); **c** - double-side (D) doped sample at dark density $n_d = 4.4 \times 10^{11} \text{ cm}^{-3}$ (at 30mK); **d** - double-side (D) doped sample at dark density $n_d = 4 \times 10^{11} \text{ cm}^{-3}$ (at 40mK). (b) Corresponding Hall ρ_{xy} resistivities for e - dark density $n_d = 4 \times 10^{11} \text{ cm}^{-3}$ (at 30mK) and f - illuminated density n_2 (at 130mK). The classical Hall slope is shown.

However the global phase diagram for 2D systems that situates the onset of this insulating phase on a plot of sample disorder versus inverse filling factor excludes such a phase being observed in a transition between $v=1$ and 2 QHE states; in particular the IP observed here is inconsistent with an explanation in terms of disorder. I-V measurements carried out in the IP region between $v=1$ and 2 are shown in Fig. 4. Non-linear effects are observed which are characterised by a threshold voltage V_T , defined as shown in trace (e) of Fig. 4c. Fig. 4a shows the V_T variation as a function of v at 40mK derived from the measurements shown in Fig. 4c. V_T has a peak value of $2.7mV$ at $v=1.5$. A temperature-dependent study of the $I-V$ measurements at $v=1.5$ (Fig. 4b,d) indicates that this peak threshold value falls to zero around $300mK$.

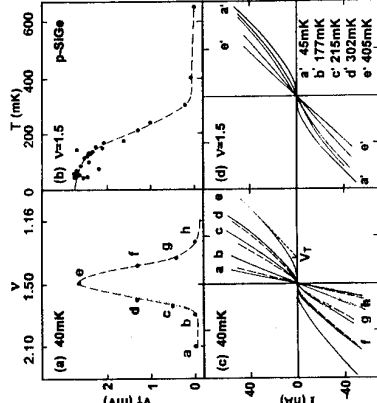


FIG. 3 T-dependence of P_{xx} in the IP region (30mK-1.75K) and for a second, dominant region $V < 340\text{mK}$ and 1.3K, pulsed fields) which around 30T ($V=0.5$) (note P_{xx} scale change). The V=1 OHE state is shown at 340mK. (b) Dependence of P_{xx} at $V=1.5$, 2 and 2.1 illustrating in activated QHE and metallic behaviour, respectively.

$v=0.5$ (at low temperature) is expected from the global phase diagram, the field-dependence of the high field IP data in Fig. 3a is somewhat different than that expected from the topology of this diagram.

The observation of an IP at $v=1.5$ characterised by a melting temperature $\sim 300\text{mK}$ and a low threshold voltage for non-linear $I\text{-}V$ ($\sim 3\text{meV}$) raises the possibility of correlation effects. Wigner crystallisation is clearly not expected at this filling factor in a conventional spin polarised model; using $m^*=0.24m_e$ and $\varepsilon=12.6$ (for $\text{Si}-x\text{Ge}$) r_s is only ~ 3 (too small) and additionally the cyclotron radius at $-11T$ ($v=1.5$) is $\sim 70\text{\AA}$ which is too large compared to the inter-particle separation $\sim 90\text{\AA}$ for $n=3.8 \times 10^{11}\text{cm}^{-2}$. The relatively low mobility for holes compared to the situation in p-type GaAs and the absence of transport structure at fractional filling factor that can be clearly attributed to the FQHE should also be noted. However whilst disorder is always a consideration in relatively low mobility samples, the important link between the IP and the degeneracy of energy levels of adjacent Landau level indices $n, n+1$ (for which holes have a different orbit radius) and opposite spin, together with violation of the 2D global phase diagram, provides a basis for consideration of an intrinsic many-body effect.

consideration of an inelastic, nearly- δ origin.

References

- [1] B.S. Meyerson, K.J. Uram and F.K. LeGoues, Appl. Phys. Lett. 50 (1987) 113; 53 (1988) 2555.

References

- FIG. 4** Threshold voltages V_T for the IP centred at $v=1.5$ are shown (a) as a function of v at $T=40mK$ and (b) as a function of T at $v=1.5$, derived from selected I-V data shown in (c). (d) V_T is estimated by linear extrapolation as shown by the short-dashed line from trace e.

Panel	Parameter	Value
(a)	v	1.5
(a)	T (mK)	40
(b)	v	1.5
(c)	v	1.5
(d)	v	1.5
(d)	T (mK)	40

[10] J.P. Fang, P.J. Wang, B.S. Meyerson, J.J. Nocera and K.E. Ismail, *Surf. Sci.* **263** (1992) 175.
 [11] S. Kivelson, D.H. Lee and S.C. Zhang, *Phys. Rev. B* **46** (1992) 2223.

Magnetotransport Anomalies in Dilute Two-dimensional Electron Systems: an Experiment and a Model

S.I. Dorožkin

Institute of Solid State Physics RAS, Chernogolovka, Moscow district, 142432, Russia

C.J. Emeleus, O.A. Mironov and T.E. Whall

Department of Physics, University of Warwick, Coventry CV4 7AL, United Kingdom

G. Landwehr
Physikalisches Institut der Universität Würzburg, Am Hubland, 97074 Würzburg, Germany

Abstract

Magnetotransport characteristics of dilute two-dimensional hole gases (2DHGs) in Si/SiGe heterostructures are shown to have two types of anomalous behaviour. (1) With increasing magnetic field, the normal sequence of quantum Hall effect states is interrupted by the appearance of the insulating state in the region of filling factor two, which in turn is replaced by the $i = 1$ quantum Hall effect state. Tilting the sample plane relative to the magnetic field direction increases dramatically the degree of insulating behaviour. (2) In a similar heterostructure, but one with a higher areal density of holes, the insulating state is not observed. However the measured, almost quantised, value of the Hall conductivity turns out to be different from that expected from the Shubnikov-de Haas oscillation periodicity. A new model [1], which describes quantum transport in terms of percolation phenomena, predicting a non-monotonic dependence of Hall conductivity on magnetic field, is shown to be capable of explaining the data.

Oscillations in the magnetoresistance of two-dimensional electron systems (2DES) in quantising magnetic fields ($\omega_c\tau > 1$) may be understood in terms of the formation of integer quantum Hall effect states (IQHESSs) (ω_c is the cyclotron frequency and τ a relaxation time). In each IQHES, the magnetocconductivity σ_{xx} tends to zero, while the Hall conductivity takes a quantised value, $\sigma_{xy} = ie^2/h$, where i is an integer which decreases with increasing magnetic field. The conventional viewpoint is that i denotes the number of bands of delocalised states below the Fermi level which coincides with the number of completely occupied magnetic levels, each of which produces a peak in the density of states (DOS) [2].

Various contradictions with this picture have been reported, however. Firstly, the standard sequence of IQHES formation in sweeping magnetic field may be modified, with the appearance between states with non-zero values of i of an insulating phase ($\sigma_{xx} \rightarrow 0$, $\sigma_{xy} \rightarrow 0$, such that $i \rightarrow 0$), the implication being that all extended states lie above the Fermi energy. This has been seen for 2DES in various material systems, as the following sequences of σ_{xy} in increasing magnetic field (units of e^2/h): (i) (6.0, 2.0, 1.0) for a two-dimensional electron gas (2DEG) in Si MOSFETs [3]; (ii) (0, 2.0) for a 2DEG at a GaAs/AlGaAs heterojunction [4]; and (iii) (1.0, 1) or (2.0, 1) for a 2DHG at a Si/SiGe heterojunction [5, 6]. Secondly, a discrepancy between the number of filled magnetic levels deduced from the value of σ_{xy} , i , and from the positions of minima in the Shubnikov-de Haas oscillations of R_{xx} , ν , has been noted for 2DHGs in Si/SiGe heterostructures [5, 7]. The experimental observation of both

these anomalies in Si/SiGe 2DHGs is reported here together with a possible explanation based on the effect of long-range potential modulation [1].

The two samples used for the study were grown by solid source molecular beam epitaxy. The following layers were defined on top of a n^- Si substrate: first, a 300 nm Si buffer layer; next, a $\text{Si}_{0.8}\text{Ge}_{0.2}$ quantum well for holes; then, a thin undoped spacer layer; and finally, a Si:B doping supply region (50 nm thick, with $N_A = 2 \times 10^{18} \text{ cm}^{-3}$). The 2DHG in each sample has a mobility of $\sim 2,000 \text{ cm}^2\text{V}^{-1}\text{s}^{-1}$. The hole densities differ by a factor of two (see below), due only to the particular spacer layer thicknesses. Hall bar devices were used for the experiments, with the sample current set low enough to avoid any non-ohmic effects.

Resistance data for sample A are shown in Fig. 1. A value of n_s defined from the low-field R_{xx} oscillation periodicity is $n_{sA} = 2.5 \times 10^{11} \text{ cm}^{-2}$, and positions of the associated filling factors ν are marked on the figures. The main feature of the data for discussion is that an insulating state is formed in between $\nu = 1$ and $\nu = 3$ ($\sigma_{xx} \approx 0$, $\sigma_{xy} \approx 0$). The degree of insulating behaviour increases markedly with tilting of the sample plane away from an orientation perpendicular to the magnetic field, a feature described and discussed in more detail elsewhere [6]. The inset to Fig. 1(a) shows a form of thermoactivation-like behaviour for R_{xx} in the insulating phase.

The evolution of R_{xx} and R_{xy} with temperature for sample B is shown in Fig. 2(a). Oscillations in R_{xx} at higher temperatures are used to define filling factors, with $n_{sB} = 5.3 \times 10^{11} \text{ cm}^{-2}$. The Hall conductivity for the lowest temperature (30 mK), calculated from the data in Fig. 2(a), is shown in Fig. 2(b). For this higher carrier density, there is no evidence of an insulating state in the filling factor range $\nu = 1 \div 3$. However, the observations that (i) $\sigma_{xy} = 2e^2/h$ for $\nu \approx 2 \div 3.5$ and (ii) σ_{xy} changes from $2e^2/h$ to e^2/h in the vicinity of $\nu = 2$ are both in contradiction with the standard model of IQHES formation.

We now use a recently proposed model [1] of a sample with a regular, long-range potential modulation, to describe these observations. The applicability of this model to real samples will be discussed later. The potential has values $V = 0$ and $V = 2V_0$ on the white and black squares respectively of a chess board [see inset to Fig. 3(a)]. The width δ of the transition between regions of high and low potential is much less than the square size a , but large compared with the magnetic length $l_c = (\hbar c/eH)^{1/2}$. We choose to define an asymmetric form of the potential in the transition region, which is included in the following:

$$V(\mathbf{r}) = \begin{cases} 0 & 0 \leq x \leq a/2 - \delta/2 \\ 2V_0(x - a/2 + \delta/2)^2/\delta^2 & a/2 - \delta/2 \leq x \leq a/2 + \delta/2 \\ 2V_0 & a/2 + \delta/2 \leq x \leq a \end{cases}$$

The potential, as given by the equations for the region in the (x, y) plane $0 \leq x \leq a$, $0 \leq y \leq \min\{x, a-x\}$ [see Fig. 3(a)] can be easily extended to cover all the plane by the symmetry transformations characteristic for the chosen potential. It can be shown that an extended equipotential line exists in this potential only at an energy $E_p = eV_0/2$. In such a potential, the magnetic levels $E_n^\pm(\mathbf{r}) = (n + 1/2)\hbar\omega_c \pm E_z/2 + eV(\mathbf{r})$ are inhomogeneously broadened, with the extended states located at energies $E_{pn}^\pm = (n + 1/2)\hbar\omega_c \pm E_z/2 + eV_0/2$. Here n is an integer and E_z is the Zeeman splitting energy. The total area of transition region is relatively small ($\delta \ll a$), so that the DOS for a given magnetic level may be considered to consist of two peaks, located at $E_{in}^\pm = (n + 1/2)\hbar\omega_c \pm E_z/2$ and $E_{un}^\pm = E_{in}^\pm + 2eV_0$, each with degeneracy $eH_z/2\hbar c$. (Below, these peaks are referred to as magnetic sublevels.) Given that

n_s is fixed, the Fermi level E_f will oscillate with magnetic field due to changing magnetic sublevel DOS and may cross the energies of extended states: this is shown for two values of n_s in Fig. 3(a). Setting σ_{xy} equal to e^2/h times the number of delocalized bands under the Fermi level [2], we obtain the magnetic field dependences of σ_{xy} shown in Fig. 3(b) for the two carrier densities. Positions of integer filling factors ν shown in Fig. 3(b) correspond to the positions of the Fermi energy discontinuities of Fig. 3(a), with values equal to the number of occupied sublevels.

The results of these calculations give a good description of the non-standard dependence of σ_{xy} on magnetic field present in the data. In particular, the result that increasing carrier density causes the disappearance of the re-entrant insulating state is quite apparent. In fact, if the percolation energy is much less than the Fermi energy, the model predicts a conventional picture for the quantum oscillations. The effect of magnetic field tilting on the re-entrant insulating state can be also accounted for by the model [6]. This model may in principle be used to describe the related anomalies mentioned for other materials systems [3,4].

It is clear that a regular potential modulation is not crucial for obtaining this behaviour: what is necessary is for at least one peak in the DOS of a magnetic level to be separated from the delocalised state of that level by an energy greater than the magnetic level separation. This might arise in a non-periodic potential, and possibly also as a result of the non-linear screening of long-range potential fluctuations [8]. The exact physical origin of a long-range potential modulation is not known for these samples, but three-dimensional growth or dopant and alloy atom self-organisation processes are both possibilities [9]. A random distribution of remote donors has been shown to give rise to long range potential fluctuations [8].

We consider that the model provides a good framework with which to understand these anomalies in the magnetotransport, but exact quantitative agreement is not obtained. More accurate calculations should consider the self-consistent variation of a real potential with magnetic field, as well as short range disorder effects. Further experiments on 2DEGs and 2DHGs of appropriate carrier density in Si/SiGe heterostructures would be very useful.

We thank R.A. Kubiak for the crystal growth and V.T. Dolgopolov, A.A. Shashkin and G.V. Kravchenko for assistance with measurements in the dilution fridge. The work was supported by the Deutsche Forschungsgemeinschaft (grant La 179/54-1), INTAS (grants 2010-CT-93-0051 and -93-1403) and the Royal Society. O.A.M. is on leave from the Institute of Radiophysics and Electronics, Kharkov, Ukraine.

References

- [1] S.I. Dorozhkin, JETP Lett. **60**, 555 (1994).
- [2] see, for example, B.I. Halperin, Phys. Rev. B **25**, 2185 (1982).
- [3] M. DiIorio, V.M. Pudalov, and S.G. Semenchinsky, Phys. Rev. B **46**, 15992 (1992).
- [4] H.W. Jiang *et al.*, Phys. Rev. Lett. **71**, 1439 (1993).
- [5] F.F. Fang *et al.*, Workbook of the SEMI MAG 94 conference, p. 680.
- [6] S.I. Dorozhkin *et al.*, submitted to Phys. Rev. B (1995).
- [7] S.I. Dorozhkin *et al.*, to be submitted for publication (1995).
- [8] A.L. Efros, Solid State Commun. **70**, 253 (1989).
- [9] Ordering phenomena in SiGe alloy thin films have been reported, for example, by J.Z. Tischler *et al.*, Phys. Rev. B **51**, 10947 (1995).

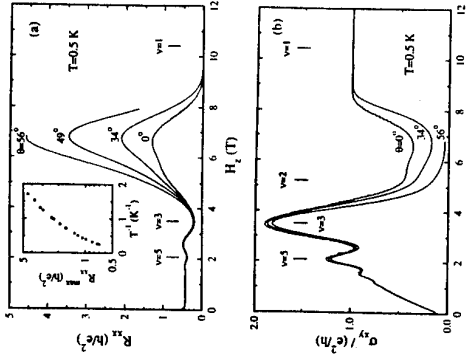


Fig. 1. Sample A: (a) Magnetoresistance R_{xx} at different tilt angles θ between the field and direction normal to the 2D-plane. (b) Hall conductivity σ_{xy} for the same sample ($T=30$ mK), calculated from the data in fig. 2(a).

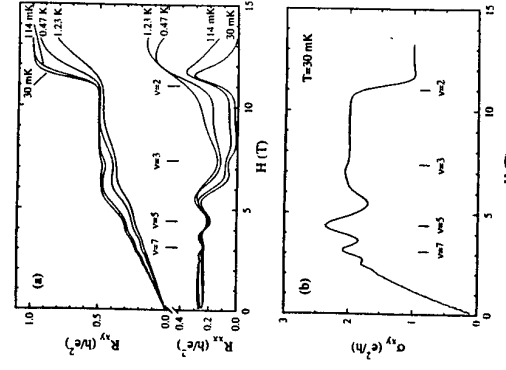


Fig. 2. Sample B: (a) Magnetoresistances R_{xx} and R_{xy} for various temperatures. Filling factors ν are defined from the 1.23 K data. (b) Hall conductivity σ_{xy} for the same sample ($T=30$ mK), calculated from the data in fig. 2(a).

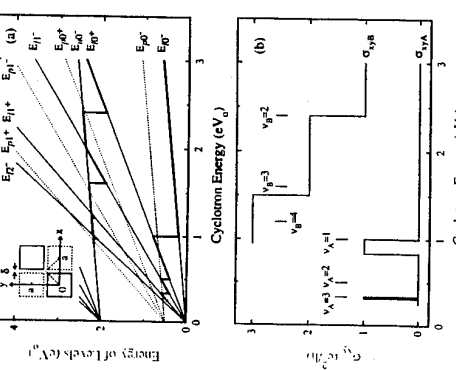


Fig. 3. The model: (a) Cyclotron energy dependence of the Fermi energies (broad solid lines), E_{FA} and E_{FB} , for two carrier densities (zero-magnetic field values are $E_{FA}^0 = 0.5eV_0$ and $E_{FB}^0 = 0.6eV_0$). $E_z = 0.6eV_0$, $E_{\perp} = 2.2eV_0$. $E_{\parallel} = 0.5eV_0$. Labeling of magnetic sublevels and extended states is as in the text. Inset: plan view of model potential. (b) Calculated Hall conductivity σ_{xy} versus cyclotron energy.

Re-entrant metal-insulator transitions Si-SiGe-Si heterostructures

M. D'orio, D. Stewart, S. Débilois, D. Brown and J.-P. Noël

National Research Council Canada, IMS, Ottawa, ON, Canada K1A 0R6

Abstract

We have studied the low-temperature transport properties of p-type Si/Si_{0.97}Ge_{0.03}/Si modulation-doped heterostructures as a function of SiGe well width. We have observed re-entrant metal-insulator transitions in the quantum Hall effect regime at half-filled Landau levels. We report on the non-linear current-voltage characteristics and the thermal activation of the diagonal resistivity associated with these transitions. We have also studied the temperature dependence of the resistivity at zero magnetic field as a function of well width and present evidence for a metal-insulator transition.

1. Introduction

In the last decade, the Si_{1-x}Ge_x strained layer heterostructure has been developed for its compatibility with existing Si technology and its ability to provide better device performance than conventional Si-based structures. The valence band structure in SiGe heterostructures is particularly rich, as revealed by transport studies of the quasi two-dimensional hole gas occupying the ground heavy hole subband in pseudomorphically grown Si/Si_{1-x}Ge_x/Si quantum well structures [1-4]. Simple estimates suggest that the richness of the SiGe system might cast further light on the metal-insulator transition in appropriate SiGe quantum well structures. Indeed, there has been a revival of interest in the scaling of metal-insulator transitions at zero magnetic field in a variety of semiconductor heterostructures from disordered AlGaAs/GaAs [5] to very high mobility Si-MOSFETs [6]. The onset of a re-entrant metal-insulator transition as a signature of Wigner crystallisation in both quantum (Si-MOSFETs) and extreme quantum limits (GaAs-AlGaAs) has also led to a reexamination of the nature of the insulating state and the fate of extended states during this process [7].

2. Experimental

The Si/Si_{0.97}Ge_{0.03}/Si heterostructures were grown on a n+ Si (100) substrate by molecular beam epitaxy. The symmetrically-doped samples were grown on a 500 Å i-Si buffer and consisted of a 500 Å Si layer modulation-doped with boron acceptors at 10¹⁸ cm⁻³ and a 300 Å i-Si setback on each side of a Si_{0.97}Ge_{0.03} quantum well of thickness d where 45 Å < d < 115 Å. The cap layer consisted of 400 Å of B-doped Si. The samples were patterned as Hall bar structures 10mm long and 2 mm wide with intercontact distance of 2 mm; ohmic contacts were made using Al evaporation and annealing below the eutectic point. The sample temperature was varied from 20 mK to 4.2 K using an Oxford top-loading dilution refrigerator. Detailed sample characterisation have been presented elsewhere [4]. The mobility and carrier density were highest in the 115 Å quantum well with $\mu = 4300 \text{ cm}^2/\text{Vs}$ and $n = 3.1 \times 10^{11} \text{ cm}^{-2}$ decreasing to $\mu = 1500 \text{ cm}^2/\text{Vs}$

and $n = 1.8 \times 10^{11} \text{ cm}^{-2}$ in the 45 Å well. The DC-transport measurements were carried out using a four-terminal technique with a high impedance ($10^{14} \Omega$) differential electrometer.

3. Results and Discussion

The samples show well-defined Shubnikov-de Haas oscillations in the longitudinal resistance and quantum Hall plateaux in the Hall resistance above 1 Tesla at 25 mK. The carrier density was fixed by the growth parameters at $\sim 2 \times 10^{11} \text{ cm}^{-2}$. The obvious admixture of two carrier densities seen in the 115 Å well in Figure 1 is attributed to the proximity of the light hole ground subband as seen from $\mathbf{k} \cdot \mathbf{p}$ Luttinger Hamiltonian calculations for these heterostructures [8]. More striking is the large peak in the longitudinal resistance at filling factor 3/2 followed by a deep minimum at ν=1. For the narrower wells, these peaks shift to lower magnetic fields and appear at ν=3/2, and 5/2 re-entrant with deep minima at ν=1 and 2. The Shubnikov-de Haas oscillations are superimposed on a parabolically increasing background which is attributed to hole-hole coupling [9]. The Hall resistance is not anomalous in the regime where the longitudinal resistance is large. The temperature dependence of the current-voltage characteristics taken at ν=3/2 reveal that the onset of the large resistance maxima ($> h/e^2$) occurs around 500 mK. This is illustrated in Figure 2 for the 65 Å well. The typical threshold field is 140 mV/cm and no evidence of significant carrier heating effects was observed under our experimental conditions. Similar results are shown in Figure 3 for the 90 Å well with the subthreshold differential resistance at ν=3/2 increasing by two orders of magnitude below 500 mK. The inset shows the thermal activation of the differential resistance where $dV/dI \propto \exp(\Delta/T)$ with $\Delta \approx 0.47 \text{ K}$ in the temperature range above 100 mK.

Although taken at a fixed density $\sim 2 \times 10^{11} \text{ cm}^{-2}$, these results are reminiscent of those obtained in high mobility Si-MOSFETs where a collective metal-insulator transition occurs at half-filled Landau levels below a given critical density and temperature. The re-entrant metal-insulator transition in Si-MOSFETs has been attributed to the formation of a pinned Wigner solid in the quantum regime [7]. It is interesting to note that, at $2 \times 10^{11} \text{ cm}^{-2}$, the Wigner Seitz radius in Si/SiGe, i.e. the ratio of the interhole spacing to the Bohr radius, is identical to the one in Si-MOSFETs at the critical density $9.6 \times 10^{10} \text{ cm}^{-2}$. In addition, the critical density for quantum cold melting is twice as large in Si/SiGe as in Si/SiO₂ assuming a heavy hole effective mass of 0.44 m₀ [10-11]. A detailed study of the carrier density dependence of the transition is required to determine whether the transition is driven by percolation, heating, collective solidification or some other process.

In light of the trends observed in the onset of the metal-insulator transition at half filled Landau levels, we have studied the temperature dependence of the diagonal resistivity in a vanishing magnetic field, for different quantum well widths. As shown in Figure 4, there is a transition from an insulating state where ρ_{xx} increases with decreasing temperature for the 45 Å and 65 Å wells to a metallic state where ρ_{xx} decreases with temperature for the 90 Å and 115 Å wells. The curves appear to converge near a critical resistivity of $h/2e^2$. These features are similar to those observed in superconducting thin films of Bi as a function of thickness [12], Si MOSFETs [6] and GaAs/AlGaAs

heterostructures [5] as a function of carrier density. Further study of scaling parameters will require the variation of the density in the Si/SiGe/Si heterostructures.

Conclusion

In this paper we report on the magneto-transport properties of the 2D hole gas confined in p-type modulation-doped $\text{Si}/\text{Si}_{0.7}\text{Ge}_{0.3}/\text{Si}$ heterostructures with the SiGe quantum well width varying between 45 Å to 115 Å. We show how, with decreasing well width, the diagonal resistivity becomes anomalously large at half-filled Landau level (3/2 and 5/2) while filled Landau levels exhibit the quantum Hall effect with deep minima in the diagonal resistivity and well developed plateaux in the off-diagonal resistivity. The current-voltage characteristics at half-filled Landau levels become non-linear below ≈ 500 mK and the increase of the differential resistance with decreasing temperature is thermally activated below threshold. We show how the temperature dependence of the longitudinal resistance at zero magnetic field follows a typical progression from an insulating to a metallic behaviour as $T \rightarrow 0$ with increasing well widths. This adds to the growing number of physical systems in two-dimensions which deviate from the conventional scaling theory for which there is no true metal-insulator transition in an infinite 2D sample.

References

1. P.J. Wang, F.F. Fang, B.S. Meyerson, J. Nocera, and B. Parker, *Appl. Phys. Lett.* **54** (1989) 2701.
2. Y. Guldner, J.M. Berroir, J.P. Vieren, M. Voos, I. Sagnes, P.A. Badoz, P. Warren and D. Dutarte, *Phys. Rev. B* **48** (1993) 12312.
3. T.E. Whall, N.L. Matthey, A.D. Plews, P.J. Phillips, O.A. Mironov, R.J. Nicholas and M.J. Kearney, *Appl. Phys. Lett.* **64** (1994) 357.
4. M. D'Inorio, D. Stewart, D. Brown, J.-P. Noel and J. Scott-Thomas, *Proc. of the 22nd Int. Conf. on the Physics of Semiconductors*, ed. D.J. Lockwood, World Scientific (1995) 1544.
5. H.W. Jiang, C.E. Johnson, K.L. Wang, and S.T. Hannahs, *Phys. Rev. Lett.* **71** (1993) 1439.
6. S.V. Kravchenko, G.V. Kravchenko, J.E. Furneaux, V.M. Pudalov, and M. D'Inorio, *Phys. Rev. B* **50** (1994) 8039; S.V. Kravchenko, W.E. Mason, G.E. Bowker, J.E. Furneaux, V.M. Pudalov, and M. D'Inorio, *Phys. Rev. B* **51** (1995) 7038.
7. For a review see "Physics of the electron solid" ed. S.-T. Chui, World Scientific (1995).
8. P. Hawrylak, private communication.
9. A. Houghton, J.R. Senna, and S.C. Ying, *Phys. Rev. B* **25** (1982) 2196.
10. J.-P. Cheng, V.P. Kesan, D.A. Grutzmacher, T.O. Sedgwick, and J.A. Ott, *Appl. Phys. Lett.* **62** (1993) 1522.
11. P.J. Wang, F.F. Fang, B.S. Meyerson, J. Nocera, and B. Parker, *Appl. Phys. Lett.* **54** (1989) 2701.
12. Y. Liu, K.A. McGreer, B. Nease, D.B. Haviland, G. Martinez, J.W. Halley, and A.M. Goldman, *Phys. Rev. Lett.* **67** (1991) 2068.

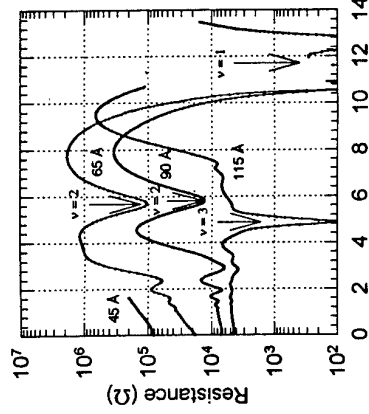


Figure 1: Longitudinal resistance as a function of magnetic field for different SiGe quantum well widths at $T \sim 25$ mK.

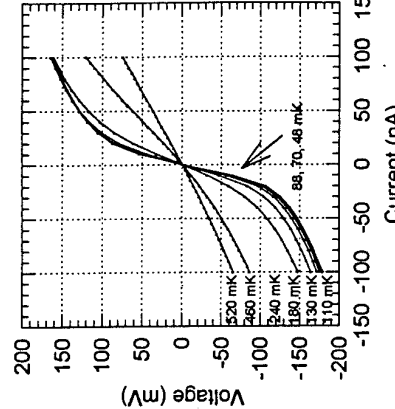


Figure 2: I - V characteristics as a function of temperature for $v = 3/2$ at $B = 7.75$ T for the 65 Å well.

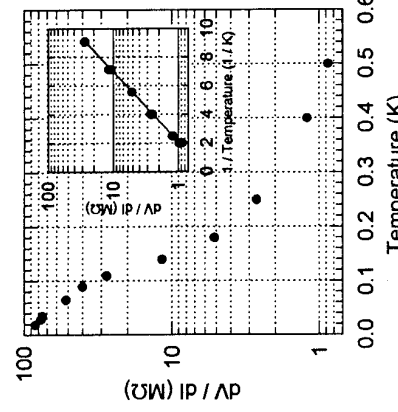


Figure 3: Temperature dependence of the differential resistance for the 90 Å well at $v = 3/2$, $B = 7.95$ T. Inset shows the activated behavior in the higher temperature range.

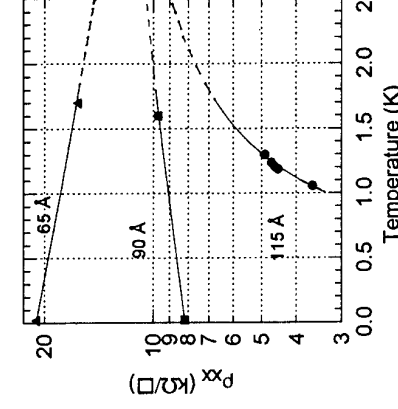


Figure 4: Temperature dependence of the diagonal resistivity in a vanishing magnetic field for different SiGe quantum well widths.

Electric Field Induced Non-Ohmic Conduction in the 2D Insulating Phase

V.M. Pudalov^(a), M.D'Iorio^(b), and J.W. Campbell^(c)

^(a)Institute for High Pressure Physics, Troitsk, Moscow District, 142092, Russia

^(b)National Research Council Canada, M23A, Montreal Rd. Ottawa, Ont., K1A 0R6 Canada

^(c)University of Ottawa, Ottawa, Ontario, K1N 6N5, Canada

Abstract

A threshold conduction was studied in Si MOSFET samples with mobility ranging from 5,000 to 55,000 cm²/Vs, and in the wide temperature range, 20 mK to 4K. We found that the non-ohmic conduction is qualitatively different in low and high mobility samples near and away from the critical density. In the high mobility samples we observed the novel feature, where the differential resistance changes sign slightly above the threshold.

The insulating (I) state in high-mobility Si-MOSFETs and GaAs-Al(Ga)As heterojunctions has recently become the focus of experimental interest [1-5]. At mK temperatures, conduction in the I phase sets in sharply as the electric field exceeds a threshold E_r . The transport features of the I state have been considered as evidence for either collective solidification [1-5], true M-I transition [6], Joule heating [7], and a percolating transition [8]. There have also been reports of universality of non-ohmic conduction in the quantum Hall effect regime and in the IS in the high field-low density limit [8]. In order to assess the relevance of these various mechanisms and to clarify the role of disorder, we have analyzed the non-ohmic conduction in a number of Si MOSFET samples with different mobility. Our main findings are:

(1) The non-ohmic conduction is qualitatively different in low and high- μ samples, near and away from the critical density. For the high- μ samples, the exponent $p \approx 1.5$ in the power law dependence $E_i \propto \delta\mu^p$, crosses over to $p \approx 2$ as density decreases away from $n_{c,0}^{(1)}$. In the low mobility sample, the nonohmic conduction depends on current as $dI/dE \propto I^{-0.3(1)}$ and does not display a threshold. This agrees with the theoretically predicted exponent 0.3 for the electric field assisted quantum percolation.

(2) A novel feature was observed where the differential resistance dV/dI changes sign close to but slightly above the threshold field. This is a characteristic of high mobility samples only ($\mu > 30,000$ cm²/Vs) and sets in at $\rho_{xx} > 4 \times 10^6 \Omega/\square$.

The Si MOSFET samples for this study were selected to provide a wide range of peak mobilities $\mu_{peak} = 5,000$ to 55,000 cm²/Vs. For the most disordered sample, Si-39, we expected the single-particle effects to govern the metal-insulator (M-I) transition. Three other samples, Si-5, Si-11, and Si-15 have mobility exceeding the critical value [5], $\mu_{peak} > 10,000$ cm²/Vs, and the M-I transition was expected to develop as a collective effect. All samples were patterned as a Hall bars with a source to drain length 5mm, a width $w=0.8$ mm and an intercontact distance $l=2.5$ mm. The carrier density could be varied from 4×10^{10} to 10^{12} cm⁻² by the top gate. We now describe our results.

- (1) In the high-mobility samples, at $E < E_c$, both current and the subthreshold conduction increase exponentially with electric field: $I \propto \exp(E)$, as shown in Fig. 1(a). The temperature dependence of the subthreshold conduction, both at $H=0$ and $H \neq 0$ is indicative of variable range hopping and the presence of a Coulomb gap, $\sigma(T) \propto \exp(T_0/T)^{1/2}$. The threshold in $V-I$ curves is extremely sharp, resembling an exponential-to-linear transition at $E=E_r$. Further growth of the voltage at $I > 2$ nA is presumably due to Joule heating effect.
- (2) For the low- μ sample, the $V-I$ characteristics in the insulating phase are nonlinear at mK temperatures as well, as seen in Fig. 1(b). However, V grows smoothly, sublinearly, $V \propto I^{0.6(0.9)}$, without a threshold [9].

(3) Fig. 2 shows $E_i(\mu)$ dependence, typical for the high- μ samples. At small deviation from the critical density, $\delta\mu < 10^9$ cm⁻², the threshold field saturates due to the step like onset at the transition [10]. In the intermediate range, $\delta\mu = 1-10 \times 10^9$ cm⁻², $E_i \propto \delta\mu^{1.5}$ both at $H=0$ and $H \neq 0$. Far away from the critical density, at $\delta\mu > 2 \times 10^{10}$ cm⁻², the threshold field crosses over to a $p \geq 2$ power law consistent with [8]. This crossover agrees with the “disorder-critical density” phase diagram proposed in Ref. [5].

(4) We focus on the novel feature where the differential resistance changes sign close to but slightly above the threshold field. Fig. 3 shows, that as the current increases, the electric field first rises at the threshold, then falls by about 10% and remains almost constant. The field drop is a characteristic of high mobility samples, $\mu_{peak} > 30,000$ cm²/Vs, and sets in at $\rho_{xx} > 4 \times 10^6 \Omega/\square$ and at electric fields $E > 10$ mV/cm. The field drop is observed in a narrow density range, $\delta\mu < 10^{10}$ cm⁻² in the vicinity of the M-I transition, in the magnetic field range 0 to 3T. As the temperature increases, the field drop decreases, and, finally, disappears at $T > 100$ mK. It is not seen in low- μ samples at similar or higher values of E and ρ_{xx} . The effect is reproducible and does not display a nonstationary and hysteresis features. The lineshape, however, seemed to depend slightly on the direction of the current sweep. The field drop is not characteristic of a percolation transition, but rather is indicative of other transitions such as one associated with depinning, breakdown, or tunneling in the presence of an energy gap. As we have found, the temperature dependence of ρ_{xx} in the “quasilinear” regime is reminiscent of the Coulomb gap hopping, thus the Coulomb gap may contribute also to the field drop at the threshold.

The experimental data including the total set of $\sigma_{xx}(E,T)$ are quantitatively modeled by the depinning of a charge density wave state in 2D [11] with the phase slippage involved. The inset in Fig. 3 illustrates how the field drop also fits this picture. As seen, the field drop is similar to the “yield drop” effect in *strain-stress curves in mechanics of solids corresponding to the creation of glide dislocations* [12]. In this analogy the electric field corresponds to the stress, the current to the strain (or elongation) and the glide dislocation to the depinning. This simple analogy points to the importance of the dislocation motion mechanism in the transport processes in the insulating state in high mobility samples at mK temperatures.

In general, the weak electric field E assists the nonohmic conduction, while the stronger field can brake the localized states. For the weak electric field range, the nonohmic hopping

conduction was calculated by Shklovskii [13]:

$$dI/dE \propto \sigma(T, E=0) \exp(eEL_0/kT)^{1/(1+\nu)}$$

Here ν is the critical index for the correlation length, $\nu=4/3$ or $7/3$, in the classical or quantum percolation models [14,15], correspondingly. L_0 is the characteristic size of the percolation network, $L_0=d_{\text{oxide}}$ in our gated system. From the $V-I$ curves for the low-mobility samples shown in Fig. 1(b), we find $V \propto I^{0.6-0.9}$, and hence, $dI/dE \propto I^{0.4-0.1}$. This agrees with the predicted exponent $p=1/(1+\nu)=0.3$ for the quantum percolation [15]. The above model does not evidently fit conduction for the high-mobility samples.

In the tunneling, or "low- T " regime, and in the high-mobility samples, there is an energy barrier Δ for tunneling between two neighboring states. Associated with this barrier there is a decay length $d_d \sim (\hbar^2/2m^* \Delta)^{1/2}$. At further increase of E , when the energy gained from electric field within the decay length becomes equal to Δ , the conduction will sharply rises. This provides for an estimate [10] of the threshold field $E_t = \Delta/e d_d$. Taking into account that $\Delta \propto (\delta n)$ [4,5], we get:

$$E_t \propto (\delta n)^{3/2}.$$

This power law is in agreement with the experimental data, Fig. 2, for the high- μ samples. In summary, the subthreshold transport in the insulating state in high- μ samples is in agreement with electric field assisted tunneling, and the CDW model involved. As mobility and/or density decreases, a crossover to the percolation mechanism occurs.

This work has been supported in part by the Russian Foundation for Basic Research, the International Science Foundation and by the Ministry for Science and Technical Policy.

References

- [1] M. D'Iorio, V.M. Pudalov, and S.G. Semenchinsky, Phys. Letters A **150** (1990) 422.
- [2] V.J. Goldman, M. Santos, M. Shayegan, and J.E. Cunningham, Phys. Rev. Lett. **65** (1990) 2189.
- [3] H.W. Jiang, R.L. Willett, H.L. Stormer, D.C. Tsui, L.N. Pfeiffer, and K. West, Phys. Rev. Lett. **65** (1990) 633.
- [4] M. D'Iorio, V.M. Pudalov, and S.G. Semenchinsky, Phys. Rev. B **46** (1992) 15992.
- [5] V.M. Pudalov, M. D'Iorio, S.V. Kravchenko, and J.W. Campbell, Phys. Rev. Lett. **70** (1993) 1866.
- [6] S.V. Kravchenko, W.E. Mason, G.E. Bowker, J.E. Furneaux, V.M. Pudalov, and M. D'Iorio, Phys. Rev. B **51** (1995) 7038.
- [7] H.W. Jiang, H.L. Stormer, D.C. Tsui, L.N. Pfeiffer and K.W. West, Phys. Rev. B **44** (1991) 8107.
- [8] A.A. Shashkin, V.T. Dolgopolov, and G.V. Krachenko, Phys. Rev. B **49** (1994) 14486.
- [9] V.M. Pudalov and M. D'Iorio, in Proc: 22nd Int. Conf. on the Physics of Semiconductors, Vancouver, 1994, Ed. D.J. Lockwood, World Scient. (1995) 851.
- [10] V.M. Pudalov and S.-T. Chui, Phys. Rev. B **49** (1994) 14062.
- [11] J.W. Campbell, M. D'Iorio, and V.M. Pudalov, Physica B **194-196** (1994) 1241.
- [12] A.M. Cottrell, in the *Mechanical Properties of Matter*, John Wiley and Sons Inc, New York (1964).
- [13] B.I. Shklovskii, Fiz. i Techn. Poluprov. **10** (1976) 1440.
- [14] B.I. Shklovskii, A.L. Efros, *Electronic properties of Doped Semiconductors*, M. Cordona, ed., Springer, Berlin (1984).
- [15] G.Y. Mil'nikov and I.M. Sokolov, Sov. Phys.: JETP Lett. **48** (1988) 536.

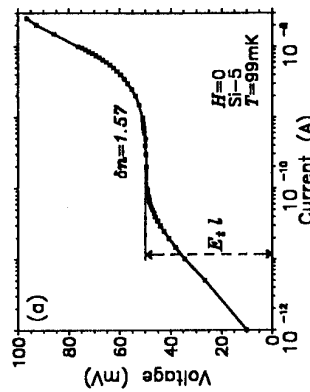


Fig. 1. Typical voltage-current characteristics for high-mobility (a) and low-mobility (b) samples. δn is indicated in units of 10^{10} cm^{-2} .

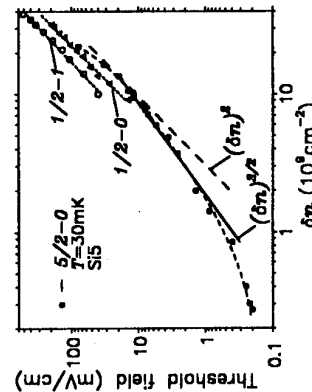


Fig. 2. E_t vs δn for the high- μ sample. Full circles show the data for the transition between the M state with 5/2 Landau levels filled and the insulator. Empty triangles and circles show the data from Ref. [8] for the transitions from the half-filled Li to insulator and to fully filled level, correspondingly. The dashed lines show two power laws. The inset shows the stress-strain curve for a whisker crystal from Ref. [12].

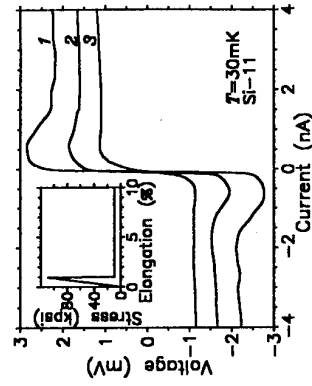


Fig. 3. The set of $V-I$ curves for the high- μ sample, showing the emerging negative differential resistance with lowering density in the insulating state. $\delta n = 1.247, 1.026, 0.803 \times 10^{10} \text{ cm}^{-2}$ for the curves 1, 2, and 3, correspondingly. The inset shows, for comparison, the stress-strain curve for a whisker crystal from Ref. [12].

Conduction band spin splitting and negative magnetoresistance in A_3B_5 heterostructures.

G. E. Pikus
A. F. Ioffe Physico-Technical Institute, 194021, St. Petersburg, Russia.

F. G. Pikus
Department of Physics, University of California at Santa Barbara, Santa Barbara, CA 93106
(June 12, 1995)

The quantum interference corrections to the conductivity are calculated for an electron gas in asymmetric quantum wells in a magnetic field. The theory takes into account two different types of the spin splitting of the conduction band: the Dresselhaus terms, both linear and cubic in the wave vector, and the Rashba term linear in wave vector. While the contributions of all terms of the conduction band splitting into the Dyakonov–Perel' spin relaxation rate are additive, in the conductivity the two linear terms cancel each other. The theory agrees very well with experimental results and enables one to determine experimentally parameters of the spin-orbit splitting of the conduction band.

It is well known that in the quantum wells in cubic crystals with symmetry T_d there is a spin splitting of the conduction band, which is described by the Hamiltonian [1–5]:

$$H = \frac{k^2}{2m^*} + (\sigma \Omega), \quad (1)$$

where $\sigma = (\sigma_x, \sigma_y)$, σ_i are the Pauli matrices, and $\Omega = (\Omega_x, \Omega_y)$ are two-dimensional vectors with components in the plane of the quantum well. Here the spin splitting coefficients Ω are proportional to the bulk coefficient γ . According to Ref. [6],

$$\begin{aligned} \Omega_x &= -\Omega_1^{(1)} \cos \varphi - \Omega_3 \cos 3\varphi, \\ \Omega_y &= \Omega_1^{(1)} \sin \varphi - \Omega_3 \sin 3\varphi, \\ \Omega_1^{(1)} &= \gamma k \left(\langle k_z^2 \rangle - \frac{1}{4} k^2 \right), \quad \Omega_3 = \gamma \frac{k^3}{4}, \end{aligned} \quad (2)$$

where $k^2 = k_x^2 + k_y^2$, $\tan \varphi = k_x/k_y$, and $\langle k^2 \rangle$ is the average wave vector in the direction z , normal to the quantum well.

In asymmetric quantum wells, or in the presence of a deformation ϵ_{xy} , the Hamiltonian H includes another, so-called Rashba term [3], which can be included in the Hamiltonian Eq. (1) if one includes additional terms into Ω :

$$\Omega_x = \Omega_1^{(2)} \sin \varphi, \quad \Omega_y = -\Omega_1^{(2)} \cos \varphi, \quad \Omega_1^{(2)} = \alpha k. \quad (3)$$

If the linear in k spin splitting is given by only one of the terms Eq. (2) or Eq. (3), and $\Omega_3 = 0$, all observable effects are identical, because these two Hamiltonians can be converted one into the other by a unitary transformation. In both cases the conduction band minimum is shaped like a ring around $k = 0$. However, if both terms are present, the electron spectrum changes qualitatively: the energy minima now occur at finite k along the axes (110) or (111), depending on the signs of $\Omega_1^{(1)}$ and $\Omega_1^{(2)}$.

Both terms Eq. (2) and Eq. (3) give additive contributions into the Dyakonov–Perel' spin-relaxation rate [4]:

$$\frac{1}{\tau_{zz*}} = \frac{2}{\tau_{zz*}} = 2(\Omega_1^2 \tau_1 + \Omega_3^2 \tau_3), \quad (4)$$

where $\Omega_1^2 = \Omega_1^{(1)2} + \Omega_1^{(2)2}$ and τ_n , $n = 1, 3$, is the relaxation time of the respective component of the distribution function:

$$\frac{1}{\tau_n} = \int W(\vartheta) (1 - \cos n\vartheta) d\vartheta. \quad (5)$$

Here $W(\vartheta)$ is the probability of scattering by an angle ϑ . In this paper we show that such additivity does not exist, for weak localization effects, which are responsible for the negative magnetoresistance (NMR). In the theory of the NMR the spin splitting of the conduction band was first taken into account in Ref. [2]. In this paper it was supposed that the magnetic conductivity $\Delta\sigma(B)$ depends only on the spin relaxation times, by analogy with the Larkin–Filatini–Nagaoka theory [7], which considered the Elliott–Yafet spin-relaxation mechanism. In Ref. [6] it was shown that for Dyakonov–Perel' spin relaxation this approach is valid when Hamiltonian Eq. (1) contains only cubic in k terms, the ones with Ω_3 (note also that the spin relaxation rates, given in Ref. [2], should be increased two times [6]). The formulas derived in Ref. [6] can be used if only one of the terms Eq. (2) or Eq. (3) is present in the Hamiltonian Eq. (1).

When both terms Eq. (2) and Eq. (3) coexist in the conduction band Hamiltonian, one can reduce the equation for the Cooperon propagation $C_0(q)$, as described in Ref. [6], using the iteration in the parameters $\Omega_1 \tau_0$ and $q \tau_0^{-1}$, where $\tau_0^{-1} = \int W(\vartheta) d\vartheta$ is the elastic lifetime and v is the Fermi velocity, to the following form:

$$\mathcal{H} C_0 = \frac{1}{2v^2 \tau_0^2}, \quad (6)$$

where ν_0 is the density of states at the Fermi level. \mathcal{H} is the Hamiltonian in a magnetic field:

$$\begin{aligned} \mathcal{H} &= \delta(a a^\dagger) + \frac{1}{\tau_\varphi} + 2(\Omega_1^2 \tau_1 + \Omega_3^2 \tau_3)(2 - J_z^2) - \\ &4i\Omega_1^{(1)}\Omega_1^{(2)}\tau_1(J_+^2 - J_-^2) + 2(\delta\tau_1) \\ &\left[-\Omega_1^{(1)}(J_+ a - J_- a^\dagger) + i\Omega_1^{(2)}(J_+ a^\dagger - J_- a) \right]. \end{aligned} \quad (7)$$

where $\delta = \frac{4\pi D}{\hbar c}$ is a dimensionless magnetic field, D is the diffusion coefficient, τ_φ is the phase-breaking time, J_+ , J_y , and J_- are the matrices of the angular momentum operator with total momentum $L = 1$, $J_\pm = (J_x \pm iJ_y)/\sqrt{2}$, and the creation and annihilation operators a^\dagger and a increase and decrease the Landau level number n [6].

The magnetic field dependent correction to the conductivity is

$$\Delta\sigma = -\frac{e^2 \delta}{4\pi^2 \hbar} \sum_{n=0}^{n_{\max}} \left(-\frac{1}{E_{0n}} + \sum_{m=-1}^1 \frac{1}{E_{mn}} \right), \quad (8)$$

where $n_{\max} = 1/\delta\tau_1$ and

$$\mathcal{E}_{0n} = \delta \left(n + \frac{1}{2} \right) + \frac{1}{\tau_\varphi}, \quad (9)$$

and E_{mn} are the eigenvalues of the operator \mathcal{H} .

In a particular case, when $\Omega_1^{(1)} = \Omega_1^{(2)}$ and $\Omega_3 = 0$, an analytical solution can be obtained. It shows that while the contributions of the terms with $\Omega_1^{(1)}$ and $\Omega_1^{(2)}$ into the spin relaxation rate are additive, they exactly cancel each other in the magnetoresistivity, as if there were no spin splitting at all. In the general case the conductivity can be found only numerically. The computations have shown that the cancellation of the two terms in linear splitting exists also for $\Omega_1^{(1)} \neq \Omega_1^{(2)}$, though it is not exact any more.

We now present the results of the numerical computations. Let us introduce the following characteristic magnetic fields [6]:

$$\begin{aligned} H_\varphi &= \frac{c\hbar}{4eD\tau_\varphi}, \quad \frac{B}{H_\varphi} = \delta\tau_\varphi, \\ H_{SO} &= \frac{c\hbar}{4eD}(2\Omega_1^2 \tau_1 + 2\Omega_3^2 \tau_3), \quad H'_{SO} = \frac{c\hbar}{4eD}2\Omega_1^2 \tau_1, \\ H_{SO}^{(1)} &= \frac{c\hbar}{4eD}2\Omega_1^{(1)2} \tau_1, \quad H_{SO}^{(2)} = \frac{c\hbar}{4eD}2\Omega_1^{(2)2} \tau_1. \end{aligned} \quad (10)$$

Note that the field H_{SO} is proportional to the spin relaxation rate. We also use dimensionless units for the conductivity and magnetic field:

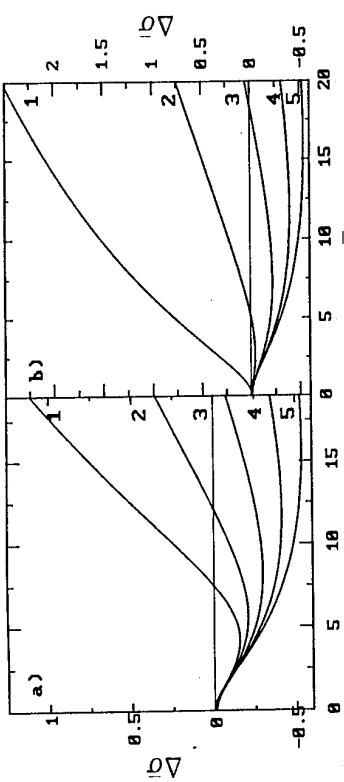


FIG. 1. Dimensionless magnetoconductivity $\Delta\sigma$ vs dimensionless magnetic field δ (Eq. (11)) for $H'_{SO}/H_φ = 4$ and $Ω_1^{(2)} = 0$ (a) and $Ω_1^{(2)} = Ω_1^{(1)}$ (b). For both plots (a) and (b) the curves 1 through 5 show dependencies at different $E'_{SO}/H_{SO} = 1, 3/4, 1/2, 1/4$, and 0, respectively.

$$\delta \equiv \frac{B}{H_φ} = \delta\tau_φ, \quad \Delta\bar{\sigma} = \frac{4\pi^2\hbar}{e^2} \left(\Delta\sigma - \lim_{\delta \rightarrow 0} \Delta\sigma \right). \quad (11)$$

We demonstrate now the effect of the coexistence of both terms $Ω_1^{(1)}$ and $Ω_1^{(2)}$ in the spin splitting. In Fig. 1a we reproduce the results of Ref. [6] for magnetoconductivity at $H'_{SO}/H_φ = 4$ and different H'_{SO}/H_{SO} . Note that the lowest curve, with $H'_{SO} = 0$, gives the result of the Larkin-Hikami-Nagaoka theory [7]. In Fig. 1b we show the curves for same values of $H'_{SO}/H_φ$ and H'_{SO}/H_{SO} , but now $Ω_1^{(1)} = Ω_1^{(2)}$. The effect of the spin splitting between $Ω_1^{(1)}$ and $Ω_1^{(2)}$ is, naturally, more pronounced for large H'_{SO}/H_{SO} , when the linear in k term dominates the spin relaxation. One can see that for $H'_{SO}/H_{SO} > 0.5$ the results in Fig. 1a and b are qualitatively different: the magnetoresistance minimum shifts closer to $B = 0$ and eventually disappears, and $\Delta\sigma$ becomes monotonic.

As far as comparison of theory and experiment is concerned, no good agreement had been achieved for quantum wells (unlike the NMR in metal films, where the theory provides very accurate description of experimental results). The source of this problem lied in the incorrect assumption that linear and cubic terms give additive contributions to the magnetoresistance [6, 8]. In Fig. 2 we show the comparison of the experimental results from Ref. [9] with the theory presented in this paper. The main difficulty in obtaining a well-defined fit arises from the cancellation of the two terms in the linear splitting, discussed above. Indeed, the best fit, shown in Fig. 2 by the solid line, is obtained for $Ω_1^{(1)}\tau_1\tau_φ = 13$, $Ω_1^{(2)}\tau_1\tau_φ = 1.25$, and $Ω_3^2\tau_3\tau_φ = 1.25$. If one wants to find the best fit with only one term in the linear splitting of the conduction band, the fitting parameters are $Ω_1^{(1)}\tau_1\tau_φ = 11.75$, $Ω_1^{(2)} = 0$, and $Ω_3^2\tau_3\tau_φ = 1.25$, and the agreement is also very good. Comparison of the two sets of fitting parameters above shows that the addition of the second term in linear splittings, with $Ω_1^{(2)}$, almost cancels a part of the first term, with $Ω_1^{(1)}$. The effect is that the main dependence of the magnetoconductivity on the linear splitting can be described by the parameter $(Ω_1^{(1)} - Ω_1^{(2)})\tau_1\tau_φ$, and an equal increase of both $Ω_1^{(1)}$ and $Ω_1^{(2)}$ makes only a small difference. On the other hand, an attempt to fit the experiment with the formula of Ref. [2], which can be used for $Ω_1 = 0$, fails: one can see in Fig. 2 that it is possible to fit the magnetoconductivity either on the right of the minimum or on the left, but not in the whole range of the magnetic field.

Using values of the characteristic magnetic fields Eq. (10), determined from the fit, we can estimate the coefficient $γ ≈ 25 \text{ eV Å}^3$. In conclusion, we have presented a new, improved theory for quantum interference corrections to the conductivity of an electron gas in a semiconductor quantum well in a magnetic field. The theory is valid for D'yakonov-Perel' spin relaxation and when the phase relaxation time $τ_φ$ is much longer than the momentum

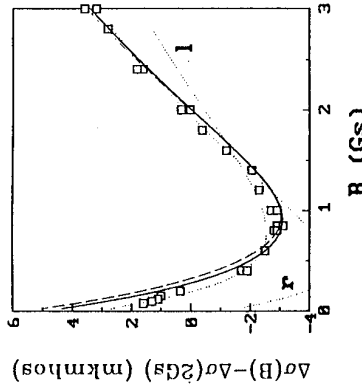


FIG. 2. Comparison of theoretical and experimental results for the magnetoconductivity. Squares show the experimental results of Ref. 9. Solid line shows the best fit obtained from our theory, fitting parameters are $H_φ = 0.028 \text{ Gs}$, $H'_{SO}/H_φ = 31$, $H'_{SO}/H_{SO} = 28.5$, and $H'_{SO}/H_φ = 26$. The best fit with only one term in linear splitting is shown by the dashed line, fitting parameters are $H'_{SO}/H_φ = 26$ and $H'_{SO}/H_φ = 23.5$. The fits for $Ω_1 = 0$ are shown by dotted lines. It is not possible to fit the experiment in the whole range of magnetic fields in this case. The fit which works best to the left of the magnetoresistivity minimum (marked by l) has $H'_{SO}/H_φ = 6.7$ (this is the value found in Ref. 18), the fit to the right side of the minimum (marked by r) has $H'_{SO}/H_φ = 4$. (this is the value found in Ref. 18).

relaxation time $τ_1$, so that the diffusion approximation can be used. Our theory correctly takes into account the contributions of different terms in spin splitting of the conduction band. We have shown that while the spin relaxation rate depends only on the total magnitude of the spin splitting, the different parts of the latter give non-additive contributions to the magnetoresistance. Furthermore, the two terms in the linear in wave vector part of the spin splitting, known as Rashba and Dresselhaus terms, actually cancel each other when their magnitudes are comparable. Using the new theory we were able to fit the experimental data for the magnetoconductivity in a wider range of magnetic fields. The spin-orbit splitting coefficient for the conduction band, obtained from the fit, is in very good agreement with the one measured in optical orientation experiments.

We are grateful to J. Allen and D. Hone for helpful comments. The authors acknowledge support by the San Diego Supercomputer Center, where part of the calculations were performed. The research was supported in part by the Soros Foundation (G. E. P.) and by the Center for Quantized Electronic Structures (QUEST) of UCSB (F. G. S.).

¹ G. Dresselhaus, Phys. Rev. 100, 580 (1955).

² B. L. Altshuler, A. G. Aronov, A. I. Larkin, and D. E. Khmel'nitskii, JETP 54, 411 (1981).

³ Yu. L. Bychkov and E. I. Rashba, J. Phys. C 17, 6093 (1984).

⁴ M. I. D'yakonov, V. Yu. Kachorovskii, Sov. Phys. Semicond. 20, 110 (1986).

⁵ E. L. Ivchenko and G. E. Pikus, "Superlattices and other heterostructures: symmetry and optical phenomena", Springer series in solid state sciences, 110, Springer-Verlag, Berlin, Heidelberg, 1994.

⁶ S. V. Jordan斯基, Yu. B. Lyanda-Geller, G. E. Pikus, JETP Letters 60, 206 (1994).

⁷ S. Hikami, A. Larkin, Y. Nagaoka, Prog. Theor. Phys. 63, 707 (1980).

⁸ F. G. Pikus and G. E. Pikus, Phys. Rev. B, in press.

⁹ D. P. Dresselhaus, C. C. Papavassiliou, R. Wheeler, and R. Sacks, Phys. Rev. Lett. 68, 106 (1992);

Effective Masses in High Mobility 2D Electron Gas Structures

P.T. Coleridge, M. Hayne[†], P. Zawadzki and A.S. Sachrajda

*Institute for Microstructural Sciences, National Research Council
Ottawa, Ontario K1A OR6, Canada
Physics Department, Exeter University, Stocker Road, Exeter EX4 4QL, UK*

Abstract

Effective masses derived from the low field Shubnikov-de Haas oscillations in high mobility GaAs/AlGaAs samples are found to decrease systematically with density. Measurements in a low density sample show the temperature dependence does not conform to standard theory. This, it is argued, is to be expected when there is extra structure, in addition to the Landau levels, in the density of states. This may be important in interpreting measurements of composite fermion effective masses.

For many years effective masses have been determined from the temperature dependence of oscillatory magnetic phenomena [1]. The technique exploits the expression, shown for example for the conductivity σ ,

$$\sigma(T) = \int \sigma(E) (-\partial f / \partial E) dE, \quad (1)$$

where f is the Fermi function. In a magnetic field, because the density of states splits into Landau levels, σ is usually written as a harmonic expansion

$$\sigma(E) = \sum_k s_k \cos(2\pi k [E/\hbar\omega_c - 1/2]), \quad (2)$$

and the thermal damping of each harmonic is then given by a factor

$$D_n(kX_r) = kX_r / \sinh(kX_r). \quad (3)$$

Here $X_r = 2\pi^2 k_B T / \hbar\omega_c$ the Landau level spacing $\hbar\omega_c = eB/m^*$ and m^* is the effective mass. We note, however, that this assumes the coefficients s_k have no energy dependence or equivalently that the Landau levels all have the same shape. Deviations from equation 3 would certainly be expected if there is additional structure in the density of states around the Fermi energy with an energy scale of order $k_B T$.

We have used this method to determine values of m^* from the low field Shubnikov-de Haas (SdH) oscillations in a series of high mobility, low density GaAs/AlGaAs heterostructures; a typical experimental plot is shown in figure 1. The results, summarised in figure 2, show a systematic decrease of m^* with decreasing density. Similar results have also been reported in another set of samples using a somewhat different analysis procedure [2]. This suppression of m^* was tentatively attributed to many-

body corrections but a quantitative comparison of theory [3] with experiment (see figure 2) does not seem consistent with this picture. We have therefore undertaken a detailed investigation of this phenomenon in a low-density ($1.27 \times 10^{11}/\text{cm}^2$), high mobility ($3.5 \times 10^8 \text{ cm}^2/\text{Vs}$) sample, where the effects seemed most pronounced.

The sample, grown at NRC, was a conventional 2DEG with a spacer layer of 1200\AA . Measurements were made in a dilution refrigerator using low frequency AC techniques and a Hall geometry (sample width $300\mu\text{m}$). Temperatures were controlled using a calibrated Ge thermometer in a magnetic field compensated region. Following the usual analysis procedure (cf figure 1) equation 3 has been fitted (see figure 3) to the higher temperature data ($T \geq 0.18\text{K}$), where the strong exponential decay of the amplitude is sensitive to the value of m^* . The value of $m^* = (0.58, \pm .001)m_0$ is independent of B within experimental error and significantly smaller than $.067m_0$ which is consistent with the general trend seen in figure 2. Below 0.18K , however, and particularly for lower magnetic fields, there are large deviations from this fit. Conversely, if a fit is made to the low temperature data, even smaller values of m^* are obtained but the high temperature data then deviates from the fit. It is impossible to fit the temperature dependence of the oscillations, between 50mK and 0.28K , to equation 3 using a single parameter m^* . This behaviour is not confined to this sample (see eg ref [2]) and it seems to be generally true, that for high mobility, low density 2DEGs not only are the values of m^* anomalously low, but also equation 3 is unable to explain the observed thermal damping over the whole temperature range. It might perhaps be argued that the low temperature deviations in figure 2 are an experimental artefact associated with electron heating effects. We believe this not to be the case: other experimental features, such as the onset of spin-splitting at 0.2T , show a large sensitivity to temperature between 50 and 120mK .

More insight into this phenomena can be obtained by looking at the magnetic field dependence of the oscillations. It has been shown in a variety of samples [4] that the amplitude of the oscillations (ΔR) is given, in a "Dingle Plot", by

$$\Delta R/R_0 = 4 \exp(-\pi/\mu_q B) D_n(X_r) \quad (4)$$

where R_0 is the zero field resistance and μ_q the quantum mobility. The prefactor is 4 because the conductivity is proportional to the square of the density of states [4,5]. Figure 4 shows a Dingle plot at $T = 50\text{mK}$. This uses $m^* = .067m_0$ in D_n but at these temperatures and fields D_n is very insensitive to the precise value of m^* . Equation 4 provides a good description of the data and the ratio $\mu_{\text{eff}}/\mu_q (= 13.7)$ agrees satisfactorily with the expected value [4,6]. If the same procedure is used, however, at higher temperatures, with measured values of m^* , the intercept deviates increasingly from $4R_0$ and is approximately $2R_0$ at 1.3K . The value of μ_q also increases; this analysis procedure actually gives negative values of μ_q in some samples.

We interpret these results as showing that while the very low temperature SdH oscillations behave normally the thermal damping is anomalous. The deviation from conventional theory is largest around about 0.15K and at higher temperatures persists as apparent values of m^* lower than would normally be expected. In both this sample, where

the Dingle temperature ($T_D = h/2\pi k_B \tau_q$) is 0.12K and in figure 4 of ref 2, where it is 0.38K, the characteristic temperature of the anomaly is approximately equal to T_D .

We have no quantitative theoretical explanation for this behaviour. It might, perhaps be produced by the temperature dependence of oscillations in the Fermi-level but a quite detailed modelling of equation 1, including this effect, shows deviations at least an order of magnitude smaller than those seen experimentally. Another possible explanation might be weak localisation but in these very high mobility samples there is little evidence of this, and certainly not of the magnitude needed to explain the incorrect intercepts in the higher temperature Dingle plots.

If, as explained above, there is structure in the density of states, in the region of the Fermi level, over and above the Landau level structure, then deviations from equation 3 are to be expected. This suggests an explanation for the experimental results. Structure confined to a single Landau level will extend over an energy range of about $k_B T_D$; if it is tied to the Fermi level, as would be the case if it were many-body in origin, then it would not be visible in the field dependence of the oscillations. Both of these features are observed experimentally. To explain a suppression of the normal thermal damping, as is observed, requires a dip or local broadening of the Landau level at the Fermi energy compared with adjacent Landau levels. Although we have no detailed theoretical explanation for the source of such structure it seems, in principle, to be able to explain satisfactorily the anomalous temperature dependence observed in these samples.

The experimental confirmation of the limited applicability of equation 3 has implications for recent determinations of composite Fermion effective masses using this approach [7]. Rough estimates, for the best samples, suggest that for composite Fermions $k_B T_D \approx 3K$ and $\hbar \omega_c \approx 1.5K$ with $T \leq 1.5K$. It is just in this regime, ie $k_B T_D \approx \hbar \omega_c \approx k_B T$, that large deviations from equation 3 are observed. If all the structure in the density of states is due only to the basic Landau levels there is no problem, but given the unconventional and incompletely understood nature of this system, it is probably best to be cautious when interpreting these experimental results.

Acknowledgement: MH would like to acknowledge support from SERC and from the British Council for travel expenses.

References

- [1] D. Shoenberg, Magnetic Oscillations in Metals, (Cambridge University Press, 1984)
- [2] M. Hayne et al, Phys. Rev. B **46**, 9515 (1992)
- [3] A.P. Smith, A.H. MacDonald and G. Gumbs, Phys. Rev. B **45**, 8829 (1992)
- [4] P.T. Coleridge, R. Stoner and R. Fletcher, Phys. Rev. B **39**, 1120 (1989); P.T. Coleridge, Phys. Rev. B **44**, 3793 (1991)
- [5] P.T. Coleridge, P. Zawadzki and A.S. Sachrajda, Phys. Rev. B **49** 10798 (1994)
- [6] S. Das Sarma and F. Stern, Phys. Rev. B **32**, 8442 (1985)
- [7] R.R. Du et al, Phys. Rev. Lett. **70**, 2944 (1993); D.R. Leadley et al, Phys. Rev. Lett. **72**, 1296 (1994); H.C. Manoharan et al, Phys. Rev. Lett. **73**, 3270 (1994)

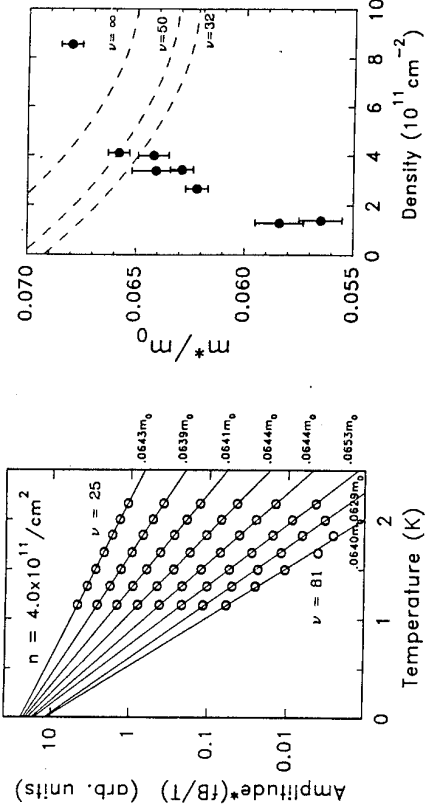


Figure 1. An example of an effective mass plot using equation 3 to extract the values of m^* shown. If A is the amplitude of the SdH oscillations and $f = 1 - \exp(-2X_0)$, then the function $A f B/T$ decays exponentially with a slope proportional to m^* . The factor f depends on m^* but is approximately equal to 1 and can be evaluated reiteratively. [3].

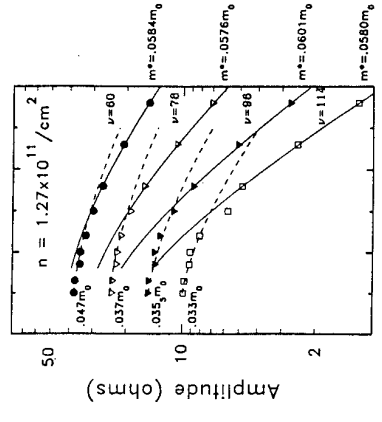


Figure 2. Effective masses obtained from a variety of samples using the procedure illustrated in figure 1. The errors bars show the RMS deviations for fits at various magnetic fields including any field dependence. The dashed lines show theoretical values taken from Smith, MacDonald and Gumbs [3].

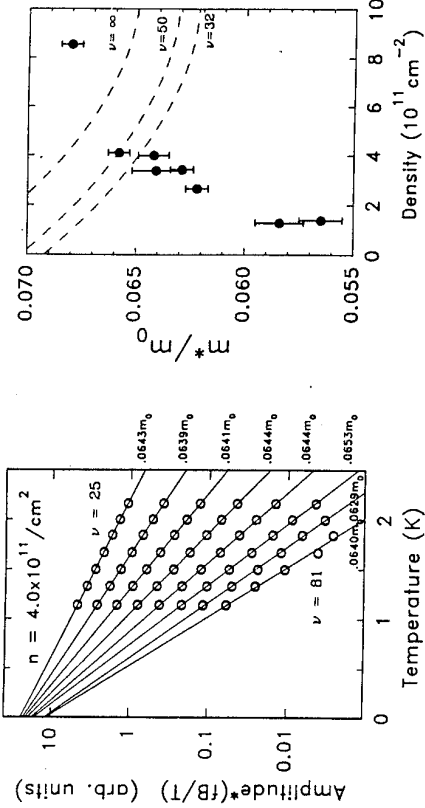


Figure 3. Temperature dependence of the SdH amplitude measurements in a low density sample. The solid lines represent fits to equation 3 using the data with $T \geq 0.18K$, the dashed lines for data with $T \leq 0.12K$.

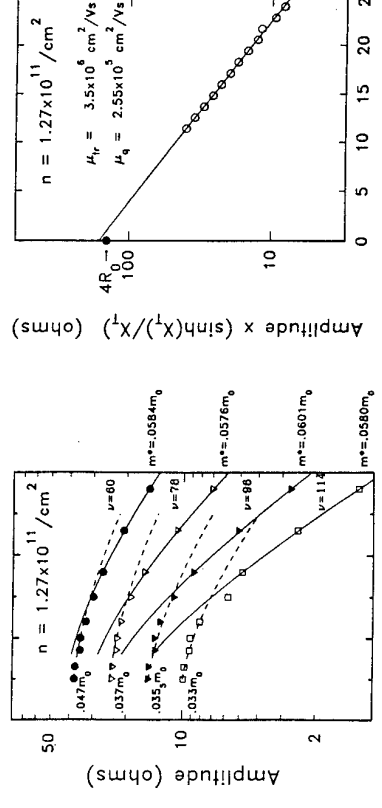


Figure 4. Dingle Plot (equation 4) at 30mK for the amplitude of the SdH oscillations. The slope corresponding to a quantum mobility (μ_q) of $2.55 \times 10^5 \text{ cm}^2/\text{Vs}$ and the intercept is 12% larger than the theoretical value of $4R_0$.

THE COULOMB GAP AND THE TRANSITION TO MOTT HOPPING

F.W. Van Keuls, X.L. Hu, A.J. Dahm

Department of Physics, Case Western Reserve University, Cleveland, OH 44118

and

H.W. Jiang

Department of Physics, University of California at Los Angeles, Los Angeles, CA 90024

Resistivity data are presented which confirm a Coulomb gap in the single particle density of states in two-dimensional variable-range hopping. For large hopping lengths the Coulomb interaction is screened by a metallic gate. A universal crossover to Mott hopping is observed at low temperatures. Excellent agreement with theory is achieved with a single parameter fit.

The Coulomb gap in the density of states in electron systems is well-established in three dimensions [1]. Formulas for the resistivity in the presence [2], and absence of [3], a Coulomb gap are given, respectively, as

$$\rho_{xx}(T) = \rho_0(T) \exp(r_m/\xi) = \rho_0(T) \exp((T/T^*)^{1/2}); \quad \text{Coulomb Gap} \quad (1)$$

$$\rho_{xx}(T) = \rho_0(T) \exp(r_m/\xi) = \rho_0(T) \exp((T_0/T)^{1/3}); \quad \text{Mott Hopping} \quad (2)$$

where r_m is the hopping length and ξ is the localization length. In two dimensions, (2D), evidence for the Coulomb gap from resistance data has been unconvincing [4]. Mott hopping is more commonly cited to explain the data. At high magnetic fields, where data [5,6] fit Eq. (1), an alternate theory [7], which does not involve a Coulomb gap, yields the same expression for the resistivity, and these data cannot unambiguously prove the existence of a Coulomb gap. Tunneling experiments suggest a depletion of states in the vicinity of the Fermi level [8].

In an attempt to answer the question of the existence of the Coulomb gap in 2D, we have conducted experiments on gated samples, where the electron density can be varied across a predicted transition between Coulomb gap and Mott hopping behaviors. Screening of the 2D electrons by a metallic gate causes this transition by bridging the Coulomb gap very close to the Fermi energy. The assumed form of the density of states, $g(E)$, is shown in Fig. 1. The distance, d , separating the 2D electron layer and the gate, determines the height of the bridge. At very low temperatures, the flat, screened $g_s(E_F)$ governs the electron behavior, producing a Mott hopping regime. At higher temperatures, the electrons probe the slopes of $g(E)$, resulting in a Coulomb gap regime. Aleiner and Shklovskii [9] have developed a theory for this crossover. They find that the hopping distance, r_m , can be interpolated in the following universal form:

$$r_m/d = [C f(T/T^*)(TT^*)^{1/2}]^{1/2} \rightarrow \begin{cases} (\xi/d)(T_0/T)^{1/2} & \text{for } T \gg T^* \\ (\xi/d)(T_0/T)^{1/3} & \text{for } T \ll T^* \end{cases} \quad (3)$$

where the characteristic temperature $T^* = e\xi/\epsilon k_B d^2$, ϵ is the dielectric constant, and $f(x)$ is a dimensionless function with the correct asymptotes given numerically in Ref. [9]. Several numerical coefficients enter the equations through the definitions of ξ in each regime:

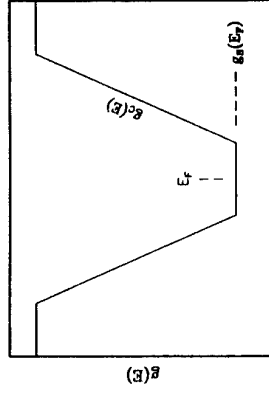


Fig. 1. The electronic density of states $g(E)$ with a soft Coulomb gap and screening by a gate. The value of $g(E)$ in the screened region is $g_s(E_F) = \alpha \epsilon / e^2 d$. In the soft gap region, $g_c(E) = 2e^2 |E - E_F| / \pi e^4$.

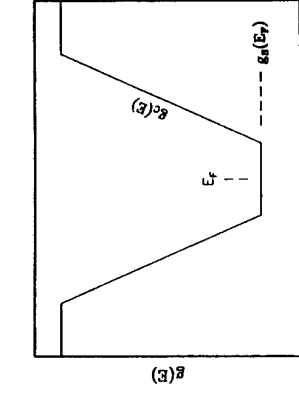


Fig. 2. The ratio $\rho_{xx}/T^{0.8}$ versus $T^{-1/2}$. The numbered curves in increasing order correspond to densities of $[0.61, 0.83, 0.94, 1.05, 1.27, 1.33, 1.38, 1.44, 1.49] \times 10^{15} \text{ m}^{-2}$ for sample A. Solid lines are fits to Eq. (1). Lettered curves correspond to densities of $[0.70, 0.85, 0.95, 1.06, 1.13, 1.21, 1.31] \times 10^{15} \text{ m}^{-2}$ for sample B.

$$\xi = C e^2 / \epsilon k_B T_1; \quad (4)$$

$$\xi = (\beta/g_s(E_F)k_B T_0)^{1/2} = (\beta e^2 d / \alpha \epsilon k_B T_0)^{1/2}; \quad (5)$$

Calculations have found the various coefficients to be $\alpha \approx 0.1$, $\beta = 13.8$ and $C = 6.2$. We found good agreement with the universal curve, Eq. (3), in an extensive study of two samples with different gate to electron separations. We found both Coulomb gap and screened Mott hopping behavior in their predicted regions of phase space. These equations were fit over large ranges of the parameters; 7 orders of magnitude for ρ_{xx} , 2 orders of magnitude for T , 2 orders of magnitude for ξ , and electron densities between $0.6 \times 10^{15} \text{ m}^{-2}$ and $1.5 \times 10^{15} \text{ m}^{-2}$.

We studied two gated GaAs/Al₃Ga₇As heterostructures fabricated by molecular beam epitaxy. Samples A and B are from different wafers with d values of 320 nm and 90 nm, respectively. The donor potentials at the electron layer are enhanced by omitting the conventional undoped Al₃Ga₇As spacer between the 2D electron layer and the doped layer. The low temperature mobilities at $V_g = 0$ of samples A and B are 1.1 and $2.3 \text{ m}^2/\text{Vs}$, respectively. The electron densities at zero gate voltage were $n_A = 5.56 \times 10^{15} \text{ m}^{-2}$ and $n_B = 8.87 \times 10^{15} \text{ m}^{-2}$. The resistance was measured by two-terminal methods. The temperature independent resistance of the contacts was measured at $V_g = 0$ as a function of magnetic field, and this resistance is subtracted from measurements of the sample resistance. The contact resistance is small compared to the sample resistance except in the conducting state where data are not presented. Chopped dc measurements were used above about 10^8 ohms, while faster 2 Hz lock-in techniques were used at lower resistances. All data are taken in the ohmic regime and in the insulating phase. The measuring current varied from 20 fA at the highest resistances to 15 nA at the lowest.

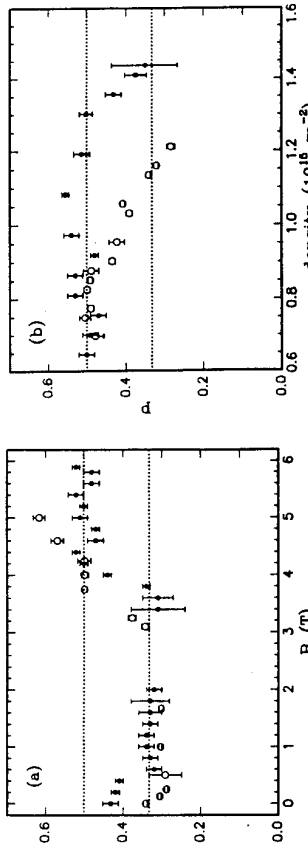


Fig. 3. The exponent p : a) p versus B : open symbols; $d = 100$ nm, $n = 1.13 \times 10^{15} \text{ m}^{-2}$; closed symbols: $d = 300$ nm, $n = 1.33 \times 10^{15} \text{ m}^{-2}$. b) p versus density for $B = 0$: open symbols; $d = 100$ nm; closed symbols: $d = 300$ nm. Dotted lines are drawn at $p = 1/3$ and $1/2$.

To distinguish Coulomb gap from Mott hopping behavior, one must divide $\rho_{xx}(T)$ by $\rho_0(T)$. Figure 2 illustrates some of our data at zero magnetic field from both samples in this form. The lower electron density curves have a exponential dependence of $T^{-1/2}$ while the higher densities are close to an $T^{-1/3}$ dependence. The frequently overlooked temperature dependence of the pre-factor, ρ_0 , is critical to determining the exponential dependence. If resistance measurements consist of a set of data points of limited number and accuracy which vary over two orders of magnitude, then $\rho_{xx} \sim T^m \exp(T_1/T)^{1/2}$, with m in the range 0.5 to 1, will fit the data equally well as $\rho_{xx} \sim \exp((T_0/T)^{1/2})$. Calculations of the prefactor have proven difficult, leaving the temperature dependence of the prefactor an open question theoretically.

To determine $\rho_0(T)$, we fit $\rho_{xx}(T)$ to $A T^m \exp((T/T_0)^{1/2})$ for all data from the insulating phase. The fitted values of p fall into two categories. The larger values of p at higher temperatures and lower electron densities are set to $1/2$. The average value of m is then determined to be $m = 0.8 \pm 0.2$. Using this value of m , the two regimes coincide well with $p = 1/2$ and $p = 1/3$.

Figure 3 shows the values of p obtained from setting $m = 0.8$ for both samples. Figure 3a reveals a wide Mott hopping region in data taken at a fixed density while the magnetic field was varied. Between 2 and 3 T the localization lengths are very long, and ρ_{xx} is not described well by the hopping formulas in this cut of phase space. Figure 3b shows the variation of p with density at zero magnetic field. The Coulomb gap region is clear at low densities, but the Mott hopping region is narrow since p drops further as the one nears the conducting phase at large densities.

All of the resistance measurements on both samples can be fit to the universal function for r_w/d given in Eq. (3) by adjusting a single parameter, η . This parameter is the following combination of constants that enter the models of both temperature dependencies, $\eta = \epsilon\beta/\alpha C^2$.

Figure 4 shows data taken at eleven densities at zero magnetic field plotted with a line denoting Eq. (3). The adjustment of η is necessary to cause data from all densities to bend at the same values of T/T^* . This condition is equivalent to requiring that the values of ξ calculated in both regimes for a given density be identical. For the data set shown in Fig. 4, we find the optimal value of $\eta = 5.3 \eta_0$, where the expected value, η_0 , contains the lattice dielectric constant, and the other constants given after Eq. (5). Analysis of data from both samples taken at a variety of

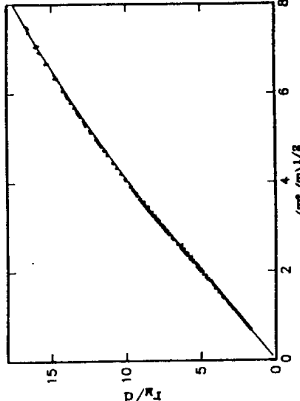


Fig. 4. The ratio r_w/d versus $(T^*/T)^{1/2}$. The solid line is given by Eq. (3) with $\eta = 5.3 \eta_0$. Symbols represent eleven densities from 0.7 to $1.2 \times 10^{15} \text{ m}^{-2}$ for sample B.

magnetic fields up to 4 T show that η is consistent between samples has little or no field dependence with an average value of $\eta = (6.4 \pm 1.3) \eta_0$. This analysis shows that the dielectric constant ϵ is constant while the localization length changes by two orders of magnitude. Our resistivity measurements over wide ranges of resistance, temperature, density and localization length exhibit Coulomb gap behavior at small hopping lengths and Mott hopping behavior for large hops. The data agree with Aleiner and Shklovskii's theory of a universal screening transition between these two regimes. We find a prefactor temperature dependence of approximately $T^{0.8}$ and an adjustment parameter $\eta = 6.4 \eta_0$. We believe these data provide the most convincing evidence for the existence of the Coulomb gap in 2D.

The authors are indebted to I.L. Aleiner, M.E. Raikh and B.I. Shklovskii for many stimulating conversations. This work was supported in part by NSF grants DMR-93-13786 and DMR-94-02647.

REFERENCES

1. B.I. Shklovskii and A.L. Efros, Electronic Properties of Doped Semiconductors (Springer, Berlin, 1984).
2. A.L. Efros and B.I. Shklovskii, J. Phys. C8 (1975) L49.
3. N.F. Mott, J. Non-Crystalline Solids 1 (1968) 1.
4. For a review, see M. Pollak, Phil. Mag. B 65 (1992) 657.
5. G. Ebert et al., Solid State Comm. 45 (1983) 625.
6. A. Briggs et al., Phys. Rev. B 27 (1983) 6549.
7. Y. Ono, J. Phys. Soc. Jpn. 51 (1982) 237.
8. R.C. Ashoori, et al., Phys. Rev. B 48 (1993) 4616.
9. I.L. Aleiner and B.I. Shklovskii, Phys. Rev. B 49 (1994) 13721.

Scaling of a metal/insulator transition in a 2D system at $B = 0$.

S. V. Kravchenko¹, Whitney Mason¹, G. E. Bowker¹, J. E. Furneaux¹, V. M. Pudalov², and M. D'Uorio³

¹Laboratory for Electronic Properties of Materials and Department of Physics and Astronomy, University of Oklahoma, Norman, OK 73019, U.S.A.

²Institute for High Pressure Physics, Troitsk, 142092 Moscow District, Russia

³National Research Council of Canada, IMS, Ottawa, Ontario, Canada K1A 0R6

Abstract

The resistivity of a two-dimensional electron system in silicon at low electron densities was empirically found to scale with a single parameter, T_0 , which approaches zero at some critical electron density, n_c , and increases as a power $T_0 \propto |n_s - n_c|^\nu$ with $\nu = 1.6 \pm 0.1$ both in metallic ($n_s > n_c$) and insulating ($n_s < n_c$) regions. This behavior suggests a true metal/insulator transition in the two-dimensional electron system in silicon at $B = 0$, in contrast with the well-known scaling theory.

For a number of years it has been generally believed that at zero magnetic field, all the states are localized in the two dimensional electron system (2DES) in the limit of infinite sample size [1]. Early experiments on relatively low mobility samples [2,3] confirmed this behavior. Thus, conventional wisdom has been that there is no metal/insulator (M/I) phase transition in an infinite 2D sample. However, recently there were several theoretical indications [4,5] that true M/I phase transition can exist in 2DES even in zero magnetic field. Here we report experimental results showing evidence for such a transition.

We have studied several silicon MOSFET samples from four wafers. Below we show results obtained with three samples: Si-12a with maximum mobility, μ_{max} , of 3.5×10^4 cm²/Vs, Si-12b with $\mu_{max} = 3.0 \times 10^4$ cm²/Vs, and Si-15 with $\mu_{max} = 7.1 \times 10^4$ cm²/Vs. Other samples from other wafers showed similar results. The samples are rectangular Hall bars with a source to drain length of 5 mm, a width of 0.8 mm, and an intercontact distance of 1.25 mm. The thickness of the oxide separating the 2DES and the gate was close to 2000 Å for all samples. The resistance was measured using a four-terminal dc technique with cold amplifiers (input resistances $> 10^{14}$ Ω) installed on the 1 K pot of a dilution refrigerator.

Figure 1 (a) shows the zero-magnetic-field resistivity (ρ) in units of h/e^2 as a function of temperature for 30 different electron densities. A striking feature of the $\rho(T)$ dependencies for different n_s is that they can be made to overlap by scaling them along the T -axis.

Mathematically this means that the resistivity can be written in the form

$$\rho(T, n_s) = \rho[T/T_0(n_s)]. \quad (1)$$

This was possible for quite a wide range of electron densities (typically $n_c - 2.5 \times 10^{10} < n_s < n_c + 2.5 \times 10^{10}$ cm⁻²) and in the temperature interval 0.2 to 3 K. The results of this scaling are shown in Fig. 1 (b) where ρ is represented as a function of T/T_0 . One can see that the data dramatically collapse into two separate curves, the upper one with open symbols for the insulating side of the transition and the lower one with filled symbols for the metallic side. The procedure used to bring about the collapse and determine T_0 for each n_s has been reported elsewhere [6]. It is worth noting that qualitatively the same scaling picture was obtained in Ref. [7] for insulator/superconductor transition in thin Bi films.

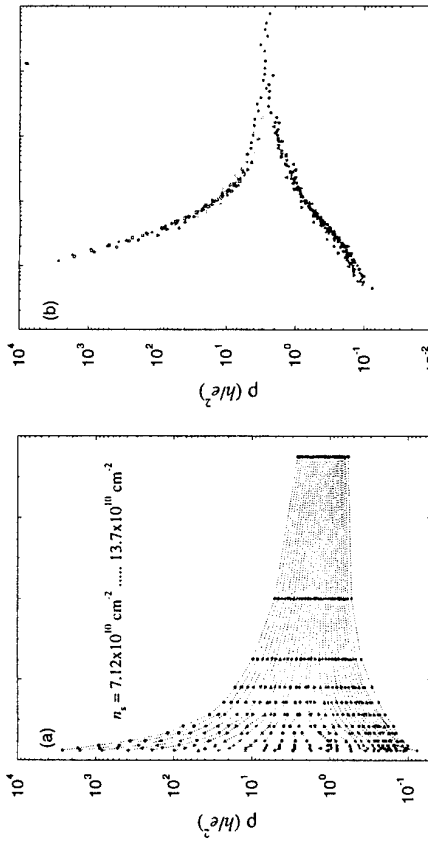


FIG. 1. Resistivity vs T (a) and vs T/T_0 (b). Open symbols correspond to the insulating side of the transition, closed — to the metallic one.

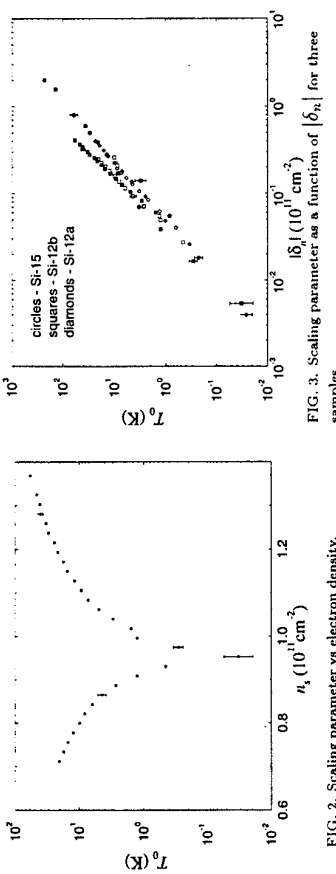


FIG. 2. Scaling parameter as a function of n_s for three samples.

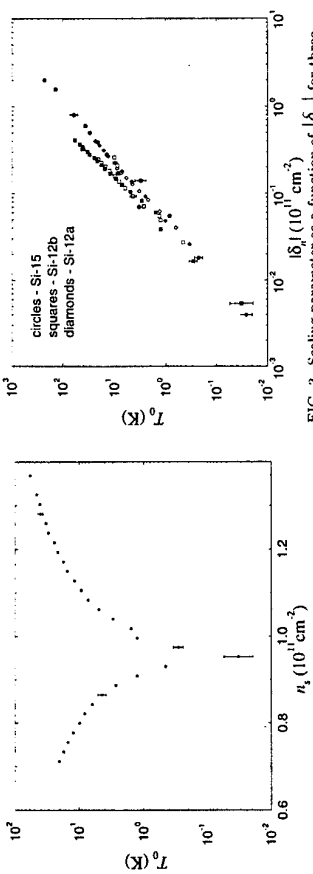


FIG. 3. Scaling parameter as a function of T/T_0 (K).

We should mention that the similar power law with an exponent 1.5 ± 0.2 was observed for scaling of the superconductor/insulator transition in thin Bi films [7,8] though we believe the physical mechanism driving the transition is different in the two systems. Our data allow us to derive the scaling function (see, e.g., Ref. [9]),

$$\beta(g) = \frac{d(\log g(L_c))}{d(\log L_c)}, \quad (2)$$

where g is a dimensionless conductance in units of e^2/h , and L_c is the inelastic scattering length, the latter being a function of temperature. Assuming $L_c \propto T^{0.5}$ [10], we get the $\beta(\log g)$ dependence shown in Fig. 4. The principal difference between this scaling function and the traditional one for 2DES [1,9] is that the curve does cross the $\beta = 0$ axis showing the metal/insulator transition. We were unable to produce a scaling function for $\log g > 1.2$ because our data does not scale here; however, it is clear that $\beta(\log g)$ should asymptotically approach zero as $g \rightarrow \infty$ because the conductance of 2DES is equal to conductivity at $\beta(\log g)$ and is therefore independent of L_c .

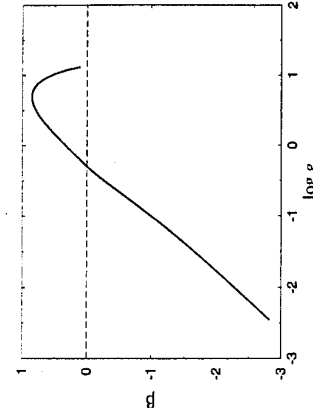


FIG. 4. Scaling function derived from our experimental data by fitting the scaled data to an analytic function and then finding the appropriate derivatives.

We acknowledge useful discussions with B. Shklovskii, A. M. Goldman, L. Zhang, B. Manson, K. Mullen, S. Simon, X. C. Xie and experimental assistance from K. Schneider. This work was supported by grants DMR 89-22222 and Oklahoma EPSCoR via LEPM from the National Science Foundation, grant 94-0204941 from the Russian Fundamental Science Foundation, and a Natural Sciences and Engineering Research Council of Canada (NSERC) operating grant.

References

- 1 E. Abrahams, P. W. Anderson, D. C. Licciardello, and T. V. Ramakrishnan, Phys. Rev. Lett. 42 (1979) 673.
- 2 D. J. Bishop, D. C. Tsui, and R. C. Dynes, Phys. Rev. Lett. 44 (1990) 1153.
- 3 M. J. Uren, R. A. Davies, M. Kaveh, and M. Pepper, J. Phys. C: Solid State Phys. 14 (1981) 5737.
- 4 A. Gold, Phys. Rev. B 44 (1991) 8818.
- 5 M. Ya. Azbel', Phys. Rev. B 45 (1992) 4208.
- 6 S. V. Kravchenko, W. E. Mason, G. E. Bowker, J. E. Furneaux, V. M. Pudalov, and M. D'Iorio, Phys. Rev. B 51 (1995) 7038.
- 7 Y. Liu, K. A. McGreer, B. Nease, D. B. Haviland, G. Martínez, J. W. Halley, and A. M. Goldman, Phys. Rev. Lett. 67 (1991) 2068.
- 8 A. M. Goldman, private communication.
- 9 H. Kamimura and H. Aoki, *The physics of interacting electrons in disordered systems* (Clarendon Press, Oxford, 1989).
- 10 H. P. Wei, L. W. Engel, and D. C. Tsui, Phys. Rev. B 50 (1994) 14 609.
- 11 S. V. Kravchenko, G. V. Kravchenko, J. E. Furneaux, V. M. Pudalov, and M. D'Iorio, Phys. Rev. B 50 (1994) 8039.
- 12 F. Stern, Phys. Rev. Lett. 44 (1980) 1469.
- 13 A. Gold and V. T. Dolgopolov, Phys. Rev. B 33 (1986) 1076.

Scaling of an appropriate physical variable is one of the hallmarks of a phase transition. We see the scaling behavior for the resistivity of the high-quality 2DES in Si MOS-FET's with the scaling parameter approaching zero as the density of electrons approaches the critical value. This behavior strongly suggests a true metal/insulator transition in the two-dimensional system in silicon at zero magnetic field, in apparent contradiction to the theoretical arguments of Abrahams and coworkers [1]. We must note however that the temperature behavior of resistivity on the metallic side of the transition with ρ dropping by an order of magnitude at temperatures below 1-2 K is not what one would expect for an ordinary metal where resistivity saturates when the frequency of phonons $\Theta = k_B T/h$ becomes less than τ^{-1} , the inverse elastic scattering time, i.e., at temperatures $T < T_\Theta = h/k_B \tau$ (in the regime of interest, $T_\Theta > 10$ K). We have discussed in detail the precipitous drop of resistivity at $T < 1 - 2$ K in Ref. [11]. In particular, we showed that this drop can be explained neither by electron-phonon scattering nor by the temperature-dependent screening considered in Refs. [12,13].

Experimental evidence of the Coulomb gap in high-mobility 2D electron system in silicon

Whitney Mason, S. V. Kravchenko, G. E. Bowker, and J. E. Furneaux
Laboratory for Electronic Properties of Materials and Department of Physics and Astronomy, University of Oklahoma, Norman, Oklahoma 73019, U.S.A.

Abstract

In some intermediate temperature range, for low electron densities and zero magnetic field, the resistivity of a two-dimensional electron system in silicon was found to follow the form, $\rho = \rho_0 \exp[(T_0/T)^{\frac{1}{2}}$] for at least four orders of magnitude. It is believed that this is evidence of a gap in the 2D density of states. We see no evidence of a temperature-dependent prefactor. A comparison with the theory shows that there exists a specific set of conditions which are necessary in order to observe this Coulomb gap.

For many years, it was believed that as the temperature was lowered, the resistivity would change from activated behavior to hopping behavior, following the form, $\rho = \rho_0 \exp[(T_1/T)^{\frac{1}{2}}$], where T_1 is some characteristic temperature. This relation was derived by Mott [1] by assuming a constant density of states at the Fermi level. This is a single-particle picture which ignores the Coulomb interaction. Efros and Shklovskii [2] have argued that the Coulomb interaction cannot be ignored for some intermediate temperature range; this Coulomb interaction creates a gap in the density of states near the Fermi level. The Coulomb gap is manifested by a resistivity of the form

$$\rho = \rho_0 \exp[(T_0/T)^{\frac{1}{2}}] \quad (1)$$

for 2D systems, where T_0 is some other characteristic temperature. Here we present evidence for the existence of the Coulomb gap.

The samples used for the studies reported here were 2D electron systems (2DES) in silicon MOSFET's with maximum mobility, μ , of $3.0 \times 10^4 \text{ cm}^2/\text{Vs}$ (sample Si-1) and $3.5 \times 10^4 \text{ cm}^2/\text{Vs}$ (Si-2). The gate oxide thickness is 200 nm. Electron density was changed by changing the voltage, V_g , between the 2DES and the gate. The resistance was measured with a four-terminal dc technique using cold amplifiers with a very high input impedance. The data discussed here is for electron densities where the samples exhibited strongly insulating behavior. In this case, the current-voltage ($I - V$) characteristics are strongly nonlinear [3]. To get a "true" resistivity, we measured $V(I)$ for each n_s and T ; then the values of resistivity corresponding to $I \rightarrow 0$ were obtained as $(dV/dI)|_{I=0}$ divided by the number of squares. The measurements were taken at temperatures ranging from 200 mK to 10K at $B = 0$.

Figure 1 shows ρ in units of h/e^2 versus $T^{-\frac{1}{2}}$ for various electron densities¹ for sample Si-1.² To analyze our data, we fit the resistivity to $\exp(T^*)$ where x is the parameter to be

¹The values of n_s in the low-density limit were obtained by extrapolation of the linear $n_s(V_g)$ dependence, obtained by the Shubnikov-de Haas oscillations at higher n_s , to the low- n_s region.

²A more detailed presentation will be published elsewhere.

determined, while assuming a temperature-independent prefactor. For $T > 400\text{mK}$, we found that the value of x is very close to 0.5. For actual values, see Table I. The linear behavior in Fig. 1 extends for four orders in magnitude in resistivity for lower electron densities. At lower temperatures, weaker temperature dependence is evident, particularly for higher electron densities. However, as Coulomb gap behavior is an intermediate temperature effect [5], this is exactly what one would expect. Note that the data are consistent with a *temperature-independent prefactor*, unlike Ref. [4]. The prefactor, however, is density-dependent, as it can be seen that the lower the electron density, the lower the prefactor.

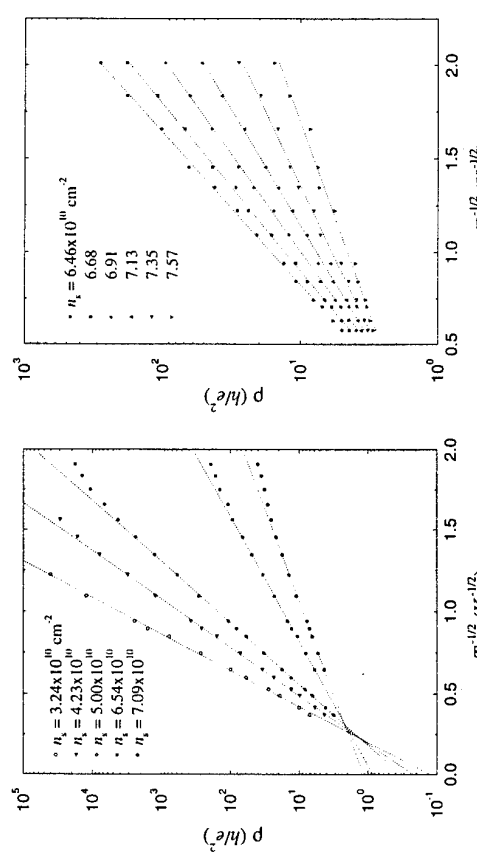


FIG. 1. Resistivity vs $T^{-\frac{1}{2}}$ for sample Si-1 in the insulating regime for various electron densities.



FIG. 2. Resistivity vs $T^{-\frac{1}{2}}$ for sample Si-2 for a narrow interval of n_s near the metal/insulator transition.

Figure 2 again shows ρ versus $T^{-\frac{1}{2}}$ for sample Si-2 with slightly higher mobility for a somewhat higher electron densities in a narrow interval, close to the metal-insulator transition.³ These curves show Coulomb gap behavior for about two orders of magnitude. Perhaps the most impressive part of the data is that all curves shown in Fig. 2 can be made to collapse onto one curve by scaling along the T axis. The resulting curve is shown in Fig. 3. Notice that the curve extrapolates to the value h/e^2 , the quantum of resistivity, as T becomes large. In addition, the data even scale when there are deviations at high temperature; again, these deviations are expected for $T \sim T_0$.

³A two-dimensional electron gas at $B = 0$ is supposed to be in an insulating state at zero temperature regardless of the electron density. However, there is a recent evidence for a true metal/insulator phase transition in $B = 0$ [S. V. Kravchenko et al., Phys. Rev. B 50, 8039 (1994); 51, 7038 (1995)].

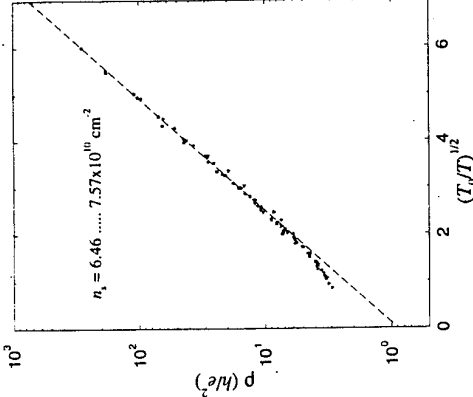


FIG. 3. Resistivity as a function of $(T_0/T)^{1/2}$ for Si-2.

$n_s (10^{10} \text{ cm}^{-2})$	x	$T_0 (\text{K})$	$\xi (\text{nm})$
3.24	0.494±0.007	108	120
4.23	0.493±0.005	61	200
5.00	0.500±0.002	38	330
6.54	0.500±0.004	9.1	1400
7.09	0.493±0.006	4.1	3000

Table 1. Values of the best fit for x in Eq. (1) for sample Si-1 and the parameters discussed in the text for various electron densities.

Eq. 3, corresponds to $r_h \approx 2400$ nm, i.e., 6 times larger than $2d$. Two possible reasons for this disagreement are the values of the constant C or the value of the dielectric constant. In conclusion, the data presented here is consistent with the existence of the Coulomb gap in two dimensions. The resistivity was found to follow the Coulomb gap law (Eq. 1), with a temperature-independent prefactor for up to four orders of magnitude. In some range of electron density, the prefactor is close to h/e^2 , and resistivity scales with temperature. For lower n_s , the prefactor decreases as n_s decreases.

We acknowledge useful discussions with B. I. Shklovskii. This work was supported by grants DMR 89-22222 and Oklahoma EPSCoR via LEPM from the National Science Foundation.

When the Coulomb interaction is included [5], T_0 in Eq. 1 is equal to

$$T_0 = \frac{Ce^2}{k_B \epsilon \xi}. \quad (2)$$

Here e is the electron charge, ϵ is the dielectric constant, here given an average value of 8, ξ is the localization length, and C is a constant which has been found [6] to be about 6.2. Using this, it is possible to determine the value of the localization length from the slope of $\log \rho$ vs. $T^{-1/2}$. Table 1 gives values of the localization length for various electron densities. Because the gate is a good metal, the effective distance to the gate, d , plays the role of a screening radius [5]. In other words, the Coulomb interaction calculated by Mott should exist only when the hopping length,

$$r_h \sim \frac{1}{4} \xi (T_0/T)^{1/2}, \quad (3)$$

is shorter than $2d$, while in the opposite case, when r_h is a few times d , temperature dependence of resistivity should obey the Mott's law, $\rho(T) \propto \exp(T_0/T)^{1/3}$. If $\xi \ll d$, the crossover between the two regimes should happen at the temperature calculated by Aleiner and Shklovskii [5] to be

$$T \sim 0.013 \frac{e^2 \xi}{k_B \epsilon d^2}. \quad (4)$$

The net effect of the condition for Coulomb gap formation that $2d > \xi$ is to place an upper bound on the n_s where the Coulomb gap can form. However, for the lowest curve in Fig. 1 ($T_0 = 4.1$ K), we see a Coulomb gap behavior down to $T \approx 400$ mK which, according to

References

- 1 N. F. Mott, J. Non-Crystalline Solids 1 (1968) 1.
- 2 A. L. Efros and B. I. Shklovskii, J. Phys. C 8 (1975) L49.
- 3 V. M. Pudalov, M. D'orio, S. V. Kravchenko, and J. W. Campbell, Phys. Rev. Lett. 70 (1993) 1866.
- 4 X. L. Hu, Y. Carmi, A. J. Dahm, and H. W. Jiang, in: Proceedings of 11th International Conference on High Magnetic Fields in Semiconductor Physics (Cambridge, 1994), edited by D. Heiman, to be published; A. J. Dahm, Bull. Am. Phys. Soc. 40 (1995) 86.
- 5 I. L. Aleiner and B. I. Shklovskii, Phys. Rev. B 49 (1994) 13721.
- 6 Nguyen Van Lien, Fiz. Tekh. Poluprovodn. 18 (1984) 335 [Sov. Phys. Semicond. 18 (1984) 207].

MAGNETORESISTANCE OSCILLATIONS IN A DIMPLED TWO-DIMENSIONAL ELECTRON GAS.

G.M. Gusev,^{1*} U. Gemser,^{1†} Y.X. Kleber,^{1,2} D.K. Maude,¹ J.C. Portal,^{1,2}

D.I. Lubyshov,³ P. Basnaji,³ M. de P.A. Silva,³ J.C. Rossi,⁴ and Yu.V. Nastaushev.⁵

¹CNRS-LCMI, F-38042, Grenoble, France

²TNSA-Toulouse, 31077, France

³Instituto de Física de São Carlos, 13560-970, Universidade de São Paulo, SP, Brazil

⁴Universidade Federal de São Carlos, Brazil

⁵Institute of Semiconductor Physics, Russian Academy of Sciences, Novosibirsk, Russia

Abstract

We report on magnetoresistance measurements of a two-dimensional electron gas (2DEG) grown on dimpled substrates. As the 2DEG is sensitive only to the normal component of B_{\perp} , electrons will experience an inhomogeneous (B perpendicular to the substrate) or sign-alternating "tilted" magnetic field (when B is parallel to the substrate). In a tilted magnetic field Shubnikov - de Haas oscillations change the phase at high field because the introduction to the system of "magnetic barriers"-regions with large normal component of B . In a "tilted" magnetic field magnetoresistance oscillations are found, which may be due to snake-states traversing the sample, when the cyclotron radius is commensurable with the spatial periodicity of the magnetic field.

The problem of electrons moving in a two-dimensional static random magnetic field has recently attracted considerable interest. The most important physical system, where this model can be employed, is the fractional quantum Hall effect. Within the framework for the composite fermion theory, the quasi-particles move in a random, or non-uniform magnetic field near the electron filling factor $1/2$ [1]. Novel electron states have been predicted for two-dimensional systems in magnetic fields that changes sign [2]. These so-called snake states traverse the sample along lines of zero magnetic field. Experimentally, non-uniform and weakly periodically modulated magnetic fields have been realised by depositing patterned ferromagnetic or superconducting films on the top of samples containing a two-dimensional electron gas [3]. However, these methods allow only for a limited magnetic field modulation, and cannot produce a system with alternating signs of the magnetic field. Here, we demonstrate a novel experimental method to overcome these limitations, and show that, in a uniform external magnetic field, B_{ext} , electrons confined to a non-planar GaAs/AlGaAs heterojunction experience a modulated effective magnetic field B . We exploit the idea, that 2D electrons are sensitive only to the normal component of B_{ext} (neglecting the spin degree of freedom). Thus electrons will move in an strongly modulated (B_{ext} perpendicular to the substrate (B_{\perp})) or "tilted" magnetic field (with changing signs, when B_{ext} is parallel to the substrate (B_{\parallel})).

Samples were fabricated employing overgrowth of GaAs and AlGaAs materials by molecular beam epitaxy (MBE) on pre-patterned 100-GaAs substrates. The patterning consisted of lattices (periodicity $d = 0.3$ and $1 \mu\text{m}$) of holes (depth $1 \mu\text{m}$, diameter $0.1\text{--}0.3 \mu\text{m}$), made by electron beam lithography and wet etching. A thick ($1 \mu\text{m}$) GaAs buffer layer was grown to smooth out any steps in the crystal planes, and a rapid planarisation of the initial surface is indeed seen in scanning electron microscope picture of the structure surface. Instead, a "dimpled" surface is obtained with a modulation of the surface of $0.1 \mu\text{m}$. This agrees with studies of MBE overgrowth on corrugated (100) GaAs substrates [4], which have demonstrated that growth on $[00\bar{1}]$ oriented grooves leads to the existence of $\{111\}\bar{A}$ crystal planes at the bottom of the grooves and $\{111\}A$ on the slopes. Growth on $[01\bar{1}]$ grooves, on the other hand, is characterised by the formation of $[100]$ facets with smooth slopes forming on the edges of grooves. Thus the region of etched holes is non-planar and has a smooth slope on all edges. This shape of a "dimpled" surface is shown schematically in fig. 1. It consists of unetched planes (marked by filled square), surrounding non-planar valleys with planes tilted towards the centre of the valley by 10° with respect to the normal of the substrate (triangles), and slopes with tilt-angles 45° - 60° between the valleys

and the unetched surfaces (circles). An AlGaAs/GaAs heterojunction was grown, with a doping setback of 100 \AA and a spacer of 100 \AA , to obtain a "dimpled" two-dimensional electron gas (dimpled 2DEG). The patterned area was $400 \times 400 \mu\text{m}^2$. The mobility of the 2DEG is $25\text{--}70 \times 10^3 \text{ cm}^2/\text{Vs}$, and the density $5.5 \times 10^{11} \text{ cm}^{-2}$. In the following magnetotransport measurement, the current was directed along x -axis, always perpendicular to the applied magnetic field (fig. 1).

The magnetoresistance at $T = 1.5 \text{ K}$ has been measured in external magnetic fields up to 28 T , for different angles θ between the field and the normal of the substrate plane. The field normal to the dimpled 2DEG changes with the slopes of the different planes. As the external field is tilted away from the normal with respect to the substrate, several "conventional" 2DEG Shubnikov - de Haas (SdH) oscillations are shifted towards higher total field, following as expected a $(\cos\theta)^{-1}$ - law. Fig. 2 shows the magnetoresistance of a dimpled 2DEG (with the substrate lattice parameter $d = 0.3 \mu\text{m}$) as a function of the magnetic field component perpendicular to the substrate, for different angles θ . For angles close to zero most of the peaks correspond to SdH oscillations from the 2DEG planes parallel to the substrate (filled square and triangles in fig. 1). However, the behaviour of the magnetoresistance is distinct from that of a 'conventional', planar 2DEG, with comparable electron densities. There is a large, positive magnetoresistance at low fields, and non-vanishing magnetoresistance minima are found between the peaks at strong field. At $B_{\perp} = 9, 21$ and 25 T additional structures are seen, that does not belong to the same SdH-series as the oscillations observed for lower magnetic fields. As B_{ext} is tilted away from B_{\perp} , up to angles $\theta \approx 45^\circ$, no continuous shift of the low-fields oscillations, as well as the peak at 11 T (and, for the relative small range of angles possible to explore, the peak at 22 T) do not shift for a fairly large θ is changed, supporting the suggestion, that they originate from electron trajectories at the unetched planes. When increasing the tilting angle, the oscillations at higher field changes: new minima start to appear around $B_{\perp} = 12 \cdot 13 \text{ T}, 8.5\text{--}9 \text{ T}$ and 5.5 T for the corresponding angles $\theta \sim 37^\circ, 46^\circ$, and 64° , respectively. At higher angles these minima gets deeper. By following all the oscillations as a function of both B_{\perp} and B_{\parallel} , it is in fact seen, that these new minima correspond to a phase shift of the oscillations, where the maxima turns into minima, and vice-versa, with respect to the oscillations from 2DEG on the unetched planes. The positions of the shifted oscillations still follow a $(\cos\theta)^{-1}$ - law. This phase-shift can be followed to B_{\perp} as low as 3.5 T , and occurs at angles $40^\circ \sim 65^\circ$ (or $B_{\parallel} \sim 7 \text{--} 9 \text{ T}$). At even high angles ($\theta > 73^\circ$) the magnetoresistance changes completely, with the disappearance of the SdH oscillations in near-parallel fields.

With the exception of the unetched planes, where the normal component of the magnetic field is constant, a magnetic field is strongly inhomogeneous. Since, for most of the field range explored, the magnetic length is much smaller than the width of the steps on the dimpled surface, the Landau levels from the modulated surface can be expected to be determined by the local magnetic field. As discussed earlier, oscillations are seen in fig. 2, that follows a $(\cos\theta)^{-1}$ - law, and which stem from the contributions to the SdH oscillations from electrons at the unetched area. However, the new oscillations, that occur when tilting the external magnetic field, have a θ -dependence that cannot be explained by SdH oscillations connected to the tilted planes, nor to possible inhomogeneities in the 2DEG electron density. As indicated by the SEM picture of the dimpled surface, these areas appear isolated from each other, and therefore the electrons have to pass through the regions with inhomogeneous magnetic field. These regions may constitute magnetic barriers to the electron transport, and may explain the observed phase shift of the oscillations at high parallel magnetic fields. Since the current in these experiments is perpendicular to the tilt-plane of the magnetic field, the change in the barriers will affect the Hall conductance. At small tilt-angles, the field at the slopes between the plateaux is lower than at the plateaux, but the electrons may be able to overcome the ensuing energy gaps, due to the large broadening of the Landau levels, and the smaller spacing between the levels, enabling scattering to take place between them. At higher θ , the additional B_{\parallel} component can lift all or almost all Landau levels above the Fermi energy in the inhomogeneous field regions, preventing the

electrons to traverse these tilted planes. As a consequence, the Hall voltage (which are perpendicular to the current (fig. 1)) starts to increase, and secondly, the electron trajectories become strongly anisotropic. In a 2DEG the resistivity ρ_{IIK} and the conductivity σ_{IIK} tensors defined by: $E_i = \rho_{\text{IIK}} j_i$, $j_i = \sigma_{\text{IIK}} E_i$, where E and j are the electric field and current density respectively. For a conventional 2DEG at strong magnetic field $\sigma_{xx} = \sigma_{yy}$ and $\rho_{xy} > \rho_{xx}$, and thus $\rho_{xx} \sim \sigma_{xx}$. Hence, a maximum in resistivity is consistent with a maximum in the conductivity. However, in the case of a strongly anisotropic conductivity, $\sigma_{xx} \gg \sigma_{yy}$, so that for $\sigma_{xx} > \sigma_{yy}/2/\sigma_{yy}$, one finds that $\rho_{xx} \sim 1/\sigma_{xx}$, so that instead of maxima in the resistivity when the conductivity have maxima, there appear minima. We suggest, that the phase shift observed in the SdH oscillations for $\theta = 40^\circ - 65^\circ$ are connected with this effective "magnetic barrier" for the electrons. For lower fields, the magnetic field has to be tilted more, in order to for the barrier to be sufficiently large to be effective. At $\theta = 73^\circ$ all SdH oscillations are quasi-phase inverted, so that $\rho_{xx} \sim 1/\sigma_{xx}$. Thus, by tilting the external magnetic field it is possible to introduce an effective magnetic barrier in the y -direction. This barrier is responsible for the dramatic change of the behaviour of the SdH oscillations, which appears at high tilt-angles. It is possible to obtain an estimate of the slope of the planes between the valleys and the plateaux of the dimples samples, where the barriers occur. Around $B_\perp = 15$ T there is only one Landau level populated. Assuming that this field is sufficient to avoid intra-level scattering, and the observed onset-angles of the phase-shift for the different oscillations indicate a plane at 55° inclination to the substrate-plane, where the magnetic barriers occur.

As mentioned earlier, in near-parallel fields the SdH oscillations disappears. However, in an interval of 10° of the parallel-field orientation, oscillations are observed, that do not shift with θ . In fig. 3 the magnetoresistance as a function of B_{ext} is shown for a sample with a pre-patterned lattice parameter $d = 1 \mu\text{m}$, in a magnetic field oriented quasi-parallel to the substrate. Oscillations are seen, with a periodicity of 1.5 T. For a sample with $d = 0.3 \mu\text{m}$ only two oscillations are found, separated by 5.5 T. In an in-plane external magnetic field, the component normal to the surface of the dimpled 2DEG is positive, negative or zero in different regions of the dimpled sample. A schematic illustration of the resulting "tilted" effective magnetic field is shown in fig. 4. Along the line dividing the regions with different sign of B_\perp electronic snake states can be formed. Because of the "tilted" periodical structure of the effective magnetic field these snake states run along the lattice axis only if the cyclotron diameter $2R_L$ is commensurable with the periodicity of the lattice: $2R_L = d/2n$, where $n = 1, 2, \dots$. The situation is similar to that of an antidot lattice in a 2DEG [5], where magnetoresistance oscillations can be observed due to skipping orbits along a row of antidots [6]. These snake-states can be divided into two parts: with an odd or an even number of semicircles of the region with + and - signs of B inside a lattice cell. "Odd" snake states can only move in a direction perpendicular to the applied magnetic field, whereas "even" snake states can move in both directions, as indicated in fig. 4. In the present experiment the current was kept normal to the magnetic field, so that commensurable snake states should increase the conductivity. The oscillations shown in fig. 3 can then be related to commensurable snake-states. For a quantitative comparison, we assume that B_\perp is constant within each tile (i.e., the slope of the surface in the valley regions is constant). For the first oscillation at $B_{\text{ext}} = 1.5$ T ($n = 1$) of the sample with $d = 1 \mu\text{m}$, the commensurability conditions gives $B_\perp = 0.13$ T, i.e. the electron is moving on a plane tilted by 5° with respect to the substrate plane. Comparing it with the $d = 0.3 \mu\text{m}$ sample, where the $n = 1$ peak occurs at $B = 5.4$ T, a calculated ratio between the lattice periodicities of the two samples of 3.6 is obtained, close to the actual value of 3.3 . The angle of the tilted planes is probably somewhat larger, than what this simple calculation gives, since the cyclotron diameter should be commensurable with the size of the tilted cell, which is probably somewhat less than half of the periodicity. We should note, that linear dependence of the minima position with B (insert in fig. 3), indicating that the shape of the surface in the overgrown region is closer to the simple tilted plane shape, than to the shape with gradual increase in the slopes.

This work is supported by CNRS (France), FAPESP, CNPq (Brazil) and COFECUB.

G.M.G was supported by NATO, and U.G. by NFR through the HCM program.

* Permanent address- Institute of Semiconductor Physics, Novosibirsk, Russia

REFERENCES

- [1] B.I.Halperin, P.A.Lee, N.Read, Phys. Rev. B, 47 (1993), 7312.
- [2] J.E.Muller, Phys. Rev. Lett., 68 (1992), 385.
- [3] A.Gem, S.J.Bending, I.V.Grigorieva, Phys. Rev. Lett., 69 (1992), 2252; H.A.Carmona, A.K.Geim, A.Nogaret, P.C.Main, T.J.Foster, M.Helmi, S.P.Beaumont, M.G.Blanion, Phys. Rev. Lett., 74 (1995), 3009; P.D.Ye, D.Weiss, R.R.Gerhardt, M.Seger, K.von Klitzing, K.Ebert, H.Nickel, Phys. Rev. Lett., 74 (1995), 3013.
- [4] E.Kapon, in: Epitaxial microstructures, Semiconductors and Semimetals v.40, ed. A.C.Gossard (Academic Press, New York, 1994), p.259.
- [5] D.Weiss, M.I.Roukes, A.Menschig, P.Grambow, K.von Klitzing, G.Welmann, Phys. Rev. Lett., 66 (1991), 2790.
- [6] E.M.Baskin, G.M.Gusev, Z.D.Kvon, A.G.Pogosov, M.V.Entin, JETP Lett., 55 (1992), 678.

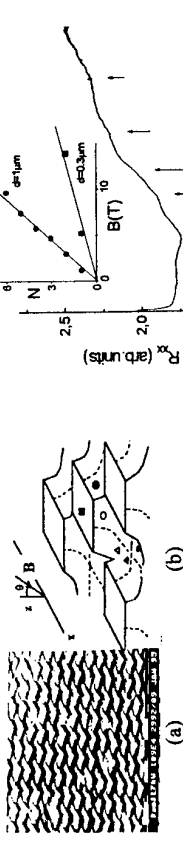


Fig. 1(a) Sideview micrograph of a dimpled GaAs

surface of AlGaAs/GaAs heterostructure.
(b) Schematic illustration of the "dimpled" surface containing the 2DEG. Square, circles, and triangles - planes with 2DEG tilted by different angles with respect to the substrate plane.

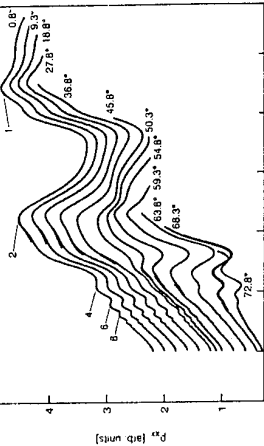


Fig. 1 Magnetoresistance as a function of parallel magnetic field for sample with periodicity $1 \mu\text{m}$, $T = 50$ mK. Oscillations, due to the damped nature of some, are indicated with an arrow. Insert- position of the minima as a function of B for samples with different lattice periodicity.

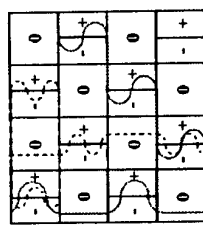


Fig. 2. Magnetoresistance as a function of the magnetic field component perpendicular to the substrate, for different angles between the applied magnetic field and the normal to the substrate. The peaks marked by numbers in the figure correspond to Shubnikov-de Haas oscillations from the 2DEG planes parallel to the substrate, $T = 1.5$ K, $d = 0.3 \mu\text{m}$.

Fig. 3. Schematic illustration of the "tilted" effective magnetic field, when a field is applied parallel to the substrate. Each tile is marked with its effective magnetic field perpendicular to the 2DEG (+, - or 0). Some "odd" (dashed lines) and "even" (full lines) snake states are indicated in the figure.

Magnetoresistance Oscillations due to Intersubband Scattering in a Two-Dimensional Electron System

T.H. Sander^a, S.N. Holmes^{a†}, J.J. Harris^a, D.K. Maude^b, J.C. Portal^b
 a IRC Semiconductor Materials, Imperial College, London, SW7 2BZ, UK
 b CNRS, Laboratoire des Champs Magnétiques Intenses, BP 166, 38042 Grenoble and INSA-CNRS, 31077 Toulouse, France

Abstract

We show that at intermediate temperatures the oscillatory magnetoresistance of the quasi-two dimensional electron system can be dominated by Magnetointersubband Scattering (MIS). The longitudinal resistance in high carrier concentration Al_{0.3}Ga_{0.7}As/GaAs heterojunctions and pseudomorphic Al_{0.3}Ga_{0.7}As/In_{0.1}Ga_{0.9}As/GaAs quantum wells exhibits magnetoresistance oscillations with fundamental fields significantly different from the Shubnikov-de Haas and Magnetophonon resonance fundamental fields. The subband spacing can be calculated from the measured MIS fundamental field and good agreement is found between measured and calculated subband spacings.

Introduction

The majority of recent work on magnetotransport properties of two dimensional electronic systems (2DES) has concentrated on systems where only the lowest quantized electronic subband was populated. The best known manifestation of several occupied subbands is the observation of different simultaneous Shubnikov-de Haas (SdH) oscillation periods [1].

Mobility measurements as a function of carrier concentration at the onset of second subband occupancy have established the importance of intersubband scattering processes [2]. At low temperatures intersubband scattering leads to an additional weak oscillatory component in the SdH oscillations of two subbands [3]. We have found experimental evidence that this oscillatory component can dominate the magnetoresistance at higher temperatures.

Theory

In a two subband, 2DES with an external magnetic field applied perpendicular to the layer the Landau levels from the lowest subband crossover the Landau levels from the next higher subband at well defined magnetic fields, i.e. the Landau levels of different subbands are degenerate when:

$$B = (E_{01} m^*) / (h e (l_0 - l_1)) \quad (1),$$

where $E_{01} = E_1 - E_0$ is the subband spacing and l_0, l_1 are the Landau level quantum numbers of the first and second subband. The inverse of the field values given by (1) form a harmonic series for increasing $l_0 - l_1$ and the periodicity of this series is directly related to Eq.1. A variety of elastic scattering mechanisms have been suggested [3,4] that lead to elastic intersubband scattering at the fields given by (1) and magnetoresistance oscillations with a periodicity proportional to the subband spacing should occur.

It was recently predicted [5] that the oscillatory magnetoresistivity should be dominated by MIS oscillations at elevated temperatures, where SdH oscillations are strongly temperature damped and where the LO-phonon population is too low to cause Magnetophonon resonances. A simplification of the expression given in [5] for the MIS conductivity oscillations yields

$$\frac{\Delta\sigma_{xx}}{\sigma_0} \approx - \left(1 - \frac{2 \mu_1^2 B_f^2}{1 + \mu_1^2 B_f^2} \right) \exp \left(- \frac{\pi}{\mu_2 B_f} \right) \cos \left(\frac{2\pi B_f}{B} \right) \quad (2),$$

where the fundamental field B_f is given by the rhs of (1) when $l_0 - l_1 = 1$, and μ_1, μ_2 are mobilities related to different combinations of inter- and intra-subband scattering times. For the full expressions and further details we refer to [5].

This prediction is now confirmed experimentally. These MIS oscillations have an amplitude much weaker than SdH oscillations and have a smaller field and temperature damping term. Therefore their direct observation is possible only at temperatures and magnetic fields, where SdH oscillations have essentially vanished due to their strong temperature damping factor $X/\sinh X$ (where $X = 2\pi^2 K T / \hbar \ell_{\text{loc}}$). As the Fermi-Dirac function broadens with temperature, carriers within an increasing energy range around the Fermi energy participate in conduction and the average density of states approaches a constant value leading to the strong damping of SdH oscillations. In contrast the additional elastic scattering giving rise to MIS oscillations is caused by a change in the density of states simultaneously for nearly all electronic states.

Results and discussion

We have studied a range of samples but report here only two. Sample A was a modulation-doped Al_{0.3}Ga_{0.7}As/GaAs heterojunction with a spacer width of 25 Å, sample B was a modulation-doped pseudomorphic Al_{0.3}Ga_{0.7}As/In_{0.1}Ga_{0.9}As/GaAs heterojunction with a well width of 150 Å. Their carrier concentrations (n_s) and mobilities (μ_s) are given in table 1.

Typical magnetoresistance data are shown in fig. 1 for sample A. This sample was measured in the dark (DARK) and in the dark after illumination (DAL) with a red LED at 4.2 K. To eliminate any non-oscillating background resistance the numerically second derivative of the magnetoresistance is shown and the individual curves are vertically shifted for clarity. At 40 K in the dark weak SdH peaks are still visible at high fields, but at low fields a second series of oscillations have appeared with a strength comparable to the SdH oscillations. The scaling information in fig. 1 shows that the amplitude of the low field oscillations at 40 K is about 300 times weaker than the SdH oscillation amplitude at 4 K. The combined temperature and field damping factor $X/\sinh X$ for SdH oscillations has a value of around 1×10^{-6} at 3 T and 40 K. This suggests that a mechanism different from the SdH effect is producing the low field oscillations. Illuminating the sample increased the carrier concentration due to the persistent photoconductivity effect and the second subband is populated at 4.2 K. The envelope of the measured data at 20 K is changed dramatically by illumination, but at 50 K the data are qualitatively very similar, before and after illumination.

We determine the fundamental field of the oscillations by plotting an appropriate index ($= 2^*(l_0 - l_1)$) associated with each extremum against the inverse field value of the extremum position. Figure 2 shows the resulting linear behaviour and for clarity we have shifted individual data sets along the ordinate. The following values result for B_f from the linear fits in fig. 2: DARK 14.9 T at 4.2 K, 17.1 T at 50 K; DAL 23.3 T at 4.2 K, 22.5 T at 50 K. Assuming that the new oscillations are due to the MIS effect we calculated the subband spacings E_{01} from B_f at 50 K using (1) and (2). Before illumination only the lowest subband is occupied at 4.2 K and we find in table 1 that $E_F < E_{01}$ (measured), after illumination the second subband is occupied and the reverse is true. This is a requirement of the theory and it confirms that a thermal population of the second subband is sufficient to observe MIS oscillations.

To test the validity of (2) in describing MIS oscillations, the second derivative of (2) together with a cubic polynomial background was fitted numerically to data at 50 K as shown in fig. 3. All parameters of (2) were freely variable during the fit. The approximation of the measured data in the fit range by the fit function is very good with the following parameters: $\mu_1 = 2200 \text{ cm}^2/\text{Vs}$, $\mu_2 = 2100 \text{ cm}^2/\text{Vs}$, $B_f = 17.2 \text{ T}$ (17.1 from fig. 2). At $\approx 50 \text{ K}$ the transport

mobility in sample A is $> 10^4 \text{ cm}^2/\text{Vs}$. The fit results suggest that μ_1 and μ_2 reflect the total scattering rate (quantum mobility) and not the direction weighted scattering rate appropriate in calculating the transport mobility [6].

Figure 4 a) shows the data measured with sample B at lower fields, where the MIS oscillations are resolved. The oscillation amplitude of sample B shows a decrease with temperature above 4 K, but increases again above 40 K. A maximum is reached around 80 K and oscillations can be observed up to 140 K. B_f changes from 19.0 T at 4.2 K to 25.4 T at 60 K. Remarkably, oscillations corresponding to approximately the 10th harmonic are present at low fields (2-3 T) and high temperatures (80 K), suggesting a very low field damping factor $\pi\mu_2$.

A comparison is shown in fig. 4 b) between E_{01} measured from the oscillations above 40 K in fig. 4 a) using the MIS equations (1,2) and E_{01} calculated self-consistently solving the coupled Poisson-Schrödinger equations. The agreement between the measured E_{01} and the theoretical value is within 5%. This is very good considering measurement errors and deviations in the self-consistent calculation due to compositional uncertainties. The value for E_F for this sample is well below the second subband as shown. The agreement within E_{01} is not as good for sample A, we found that E_{01} has a much stronger temperature dependence in the Al_{0.3}Ga_{0.7}As/GaAs heterojunction than in the pseudomorphic Al_{0.3}Ga_{0.7}As/In_{0.1}Ga_{0.9}As/GaAs heterojunction. Experimental evidence for this is the constant change in the low field peak positions with increasing temperature for sample A in the dark (fig. 1).

Summary

This work is a conclusive observation of recent theoretical predictions [5] for magnetoresistance oscillations at intermediate temperatures due to Magnetointer-subband scattering in 2 DESSs. The magnetoresistance oscillations can be approximated very well by equation (2). The MIS oscillation period is directly related to the subband spacing of the 2 DESS, but the accuracy of the proportionality is different for asymmetric quantum wells and simple heterojunctions. A striking feature of MIS oscillations is their low field damping factor leading to oscillation peaks at low magnetic fields and higher temperatures. The detailed physical interpretation of the field damping behaviour is not clear yet.

References

- [1] J.J. Harris, D.E. Lackison, C.T. Foxon, F.M. Seltzer, A.M. Suckling, R.J. Nicholas, and K.W.J. Barnham, Semicond. Sci. Technol. 2 (1987) 783
- [2] H.L. Störmer, A.C. Gossard, and W. Wiegmann, Sol. Stat. Comm. 41 (1982) 707
- [3] D.R. Leadley, R. Fletcher, R.J. Nicholas, F. Tao, C.T. Foxon, and J.J. Harris, Phys. Rev. B 46 (1992) 12439
- [4] P.T. Coleridge, Semicond. Sci. Technol. 5 (1990) 961
- [5] M.E. Raikh and T.V. Shahbazyan, Phys. Rev. B 49 (1994) 5531
- [6] P.T. Coleridge, R. Stoner, and R. Fletcher, Phys. Rev. B 39 (1989) 1120

Table 1: Carrier concentration and mobility together with results for E_{01} .

Sample	n_s (10^{11} cm^{-2})	μ ($\text{cm}^2\text{V}^{-1}\text{s}^{-1}$)	E_{01} (measured) (meV)	E_{01} (theoretical) (meV)
A	DARK: 7.2	4.2 K: 160000	DARK: 25.8	50 K, DARK: 29.6
	DAL: 11.3	DAL: 40.3	DAL: 38.9	50 K, DAL: 35.8
B	9.2	77 K: 69000	33.8	60 K: 45.2
				60 K: 47.4

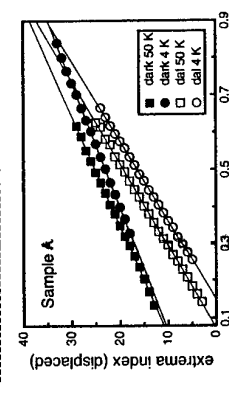
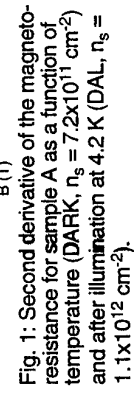
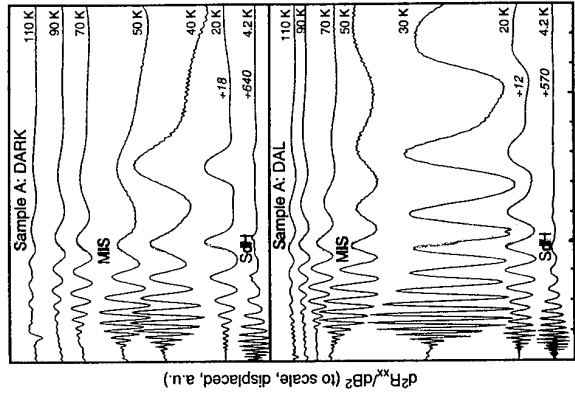


Fig. 4: a) Second derivative of the magnetoresistance for sample A = 9.2 $\times 10^{11} \text{ cm}^{-2}$, b) comparison between measured and self-consistently calculated subband spacing.

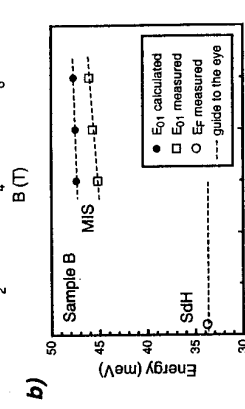
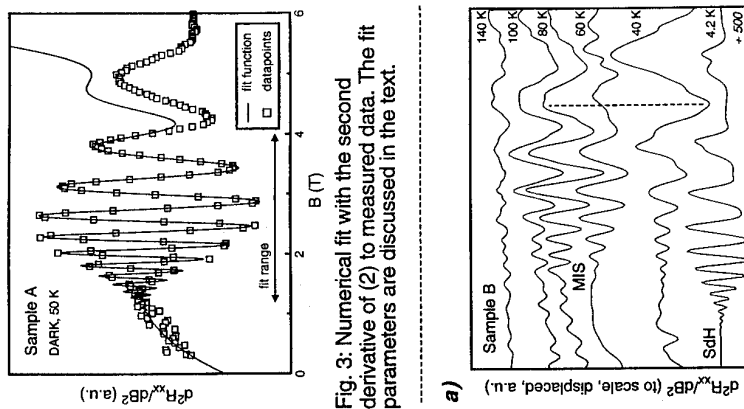


Fig. 3: Numerical fit with the second derivative of (2) to measured data. The fit parameters are discussed in the text.

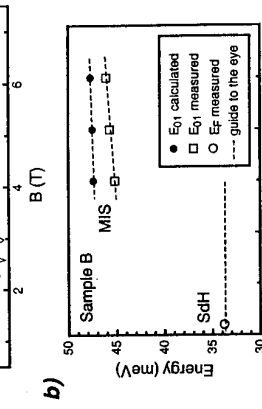


Fig. 3: Numerical fit with the second derivative of (2) to measured data. The fit parameters are discussed in the text.

Fig. 4: a) Second derivative of the magnetoresistance for sample B = 9.2 $\times 10^{11} \text{ cm}^{-2}$, b) comparison between measured and self-consistently calculated subband spacing.

Fig. 3: Numerical fit with the second derivative of (2) to measured data. The fit parameters are discussed in the text.

RESONANT TUNNELLING THROUGH TWO IMPURITIES IN DISORDERED BARRIERS

A.K.Savchenko, V.V.Kuznetsov
Department of Physics, Exeter University, Stocker Road, Exeter EX4 4QL, UK
 A.Woolfe, D.R.Mace, M.Pepper, D.A.Ritchie, G.A.C.Jones
Cavendish Laboratory, Madingley Road, Cambridge CB3 0HE, UK

We have studied the conductance through localised states in a lateral barrier produced by a short ($\sim 0.2\mu\text{m}$) gate in GaAs MESFETs. Distinctive peaks in the ohmic conductance as a function of the gate voltage have been associated with hopping and resonant tunneling (RT). In addition to RT through one impurity a new effect has been observed: RT through two and more impurities. We distinguish between the three mechanisms by the temperature dependence of the conductance, its variation with dc bias along the barrier and the I-V characteristics of the samples.

The conduction of mesoscopic structures with localised states in the potential barrier reveals elementary acts of electron hopping and tunneling [1-5]. In hopping an electron is transferred with phonon assistance between two localised states with different energies, hence the conductance increases with increasing temperature. In resonant tunneling (RT) an electron tunnels between the contacts and the transmission probability strongly increases in the presence of an impurity placed in the middle of the barrier. One-impurity RT is seen in the ohmic conductance-gate voltage dependence as a peak with an amplitude which is either temperature independent or decreases with increasing temperature [1].

Hopping peaks are seen in larger samples, e.g. in Si MOSFETs [2] and GaAs MESFETs [3]. In [3] the barrier length was about $2\mu\text{m}$ and the experiments were performed at temperatures above 1.5K . Now we have studied structures similar to those in [3] but with smaller gates ($\sim 0.2\mu\text{m}$) and at lower temperatures (50mK). Both hopping through a pair of states and RT through one state has been seen, as well as RT through several impurities which has been discussed in theory [6] but has not been observed before. All three processes give similar peak-like structure in the $G(V_g)$ -dependence. The hopping and RT have been distinguished by the temperature dependence of the conductance and the difference between RT through one and several impurities has been established by measurements in the presence of a dc bias, V_{sd} , Fig.1. For one-impurity RT the current-voltage characteristic has a step-like form. The current is switched on with increasing V_{sd} when the resonant level passes through the Fermi level in the left contact. With a further increase of V_{sd} it does not change significantly as other electrons below the Fermi level can tunnel through the same impurity. The step-like feature for one-impurity RT, although modified at the current threshold due to Coulomb interaction [7], has been observed experimentally in [5]. On the contrary, two-impurity RT should produce a peak in the current corresponding to alignment of the two localised states at a particular source-drain voltage. The further increase of V_{sd} moves the levels out of resonance giving rise to the negative differential conductance.

Our samples are MESFET's made on the basis of a MBE grown uniformly doped GaAs layer with $N_d=1\text{-}2\text{\times}10^{17}\text{cm}^{-3}$. The barrier between the source and drain is formed by a gate of

length $0.2\mu\text{m}$ and of ten to a hundred times larger size in the direction perpendicular to the current ($2\text{-}20\mu\text{m}$). Measurements of the ohmic conductance G and dI/dV_{sd} at some applied bias V_{sd} have been performed at $T=50\text{mK}$ - 4.2K by a lock-in technique with an ac voltage of $1\text{-}10\mu\text{V}$ on the sample. In addition, the dc source-drain current was measured as a function of V_{sd} . Fig.2 shows an example of the peaks in the $G(V_g)$ -dependence near the conductance threshold at different temperatures. The peak amplitude increases with increasing temperature for the hopping peaks and decreases for the RT peaks. We cannot distinguish between one- and many-impurity RT on this graph as we expect that the temperature dependence for many impurity RT is similar to the one-impurity case [8]. We know that the role of many impurities in RT increases with increasing density of localised states $g(E_F)$ and with increasing the barrier length [6]. The density of states in the tail of the conduction band changes exponentially, and if we take $g\sim 10^9\text{cm}^{-3}\text{meV}^{-1}$ which is about ten times less than the two dimensional density of states, the estimation based on [6] for the gate length of $0.2\mu\text{m}$ shows that in our structures two- and three-impurity RT can give a significant contribution to the conduction.

Indeed, in the I-V characteristics we have observed both step- and peak-like structures, as is seen in Fig.3. As the contribution of many-impurity RT channels decreases with increasing the number of impurities in them [6] we will connect the peaks in the current primarily with two impurities.

The difference between one- and two-impurity RT is also seen in the evolution of the differential conductance $dI/dV_{sd}(V_g)$ with applied V_{sd} [9]. In the one-impurity case, Fig.3(a), the conductance peak is split into two as the resonance level passes through two Fermi levels in the left/right contact. The separation between the peaks in the V_g -scale increases with V_{sd} with a factor $\alpha=\Delta V_{sd}/\Delta V_g=\Delta E/\Delta Vg<1$ which characterises the rate of the energy level movement with V_g . By the asymmetry of the cross-feature a conclusion can be drawn about the position of the impurity along the channel. In the two-impurity case, Fig.3(b), a similar splitting of the conductance peak is also seen due to the left (right) impurity level passing through the Fermi level in the left (right) contact when the tunneling conductance becomes zero. In addition, a region of negative differential conductance appears with increasing V_{sd} .

We have analysed the suppression of the current peaks by a perpendicular magnetic field to estimate the distance r between the impurities and the contacts. The peak amplitude decreases by ten times at a magnetic field of about 5T as the result of squeezing the wave functions in a way similar to the magnetic field's effect on the one-impurity RT peak in the conductance [4]. Suppose that the wave function in a small magnetic field varies as $\Psi(r)=\Psi(H=0)\exp(-ar^3/24\lambda^4)$, where $\lambda=(\hbar/eB)^{1/2}$ is the magnetic length [9]. Taking into account that the amplitude of the current is determined by the leak rate from an impurity to the nearest contact $\Gamma_{\min}\propto\Psi^2$, we have $a^3r^3/12\lambda^4=1$ at $B=3\text{T}$ when the peak amplitude decreases by e times. With $a=2\mu\text{m}$ this gives the value of the separation $r=40\text{\AA}$.

We can estimate the value of Γ_{\min} from the peak amplitude at zero field, $I=(4e^2/h)\Gamma_{\min}$, which gives $\Gamma_{\min}\sim 1\mu\text{eV}$. This agrees with an estimation $\Gamma_{\min}\approx\varepsilon_0\exp(-2r/a)\sim 1.5\mu\text{eV}$, where $\varepsilon_0=\hbar^2/2ma^2$ -eV is the height of the barrier. The width of the two-impurity resonance, Γ_{\max} , can be estimated from the width of the resonance in Fig.3(b) as $\Gamma_{\max}\approx\Delta V_g\alpha\sim 200\mu\text{eV}$ for $\alpha\sim 0.1$ [3]. For one-impurity RT the ratio of $\Gamma_{\min}^{(1)}/\Gamma_{\max}^{(1)}\sim 0.01$ is obtained from the amplitude of the ohmic conductance peak $G\approx$

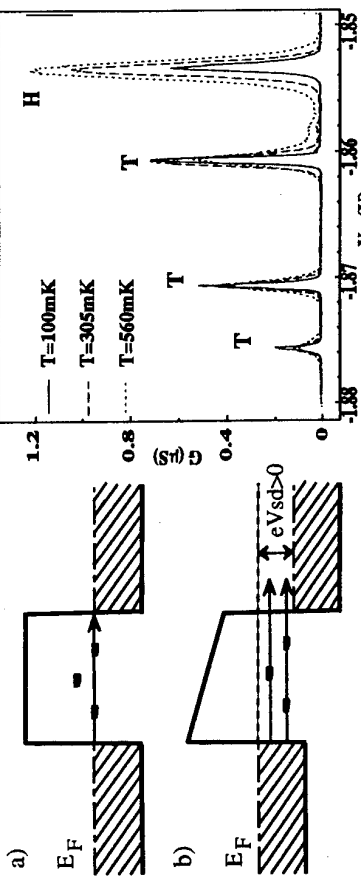


Fig. 1: Energy diagram of the barrier in the direction of current flow. The arrows show resonant tunneling through one and two localized states. a) Ohmic conduction regime. b) Positive source-drain bias applied.

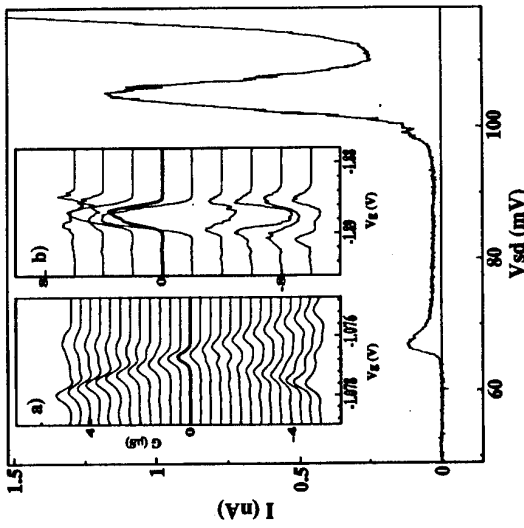


Fig. 2: Ohmic conductance as a function of gate voltage at different temperatures. Labels: T=tunneling H=hopping.

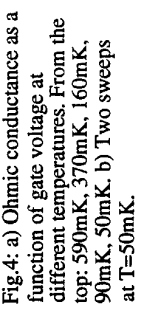


Fig. 3: Current as a function of V_{sd} at $V_g = -2.1\text{V}$ and $T = 50\text{mK}$. Insets: differential conductance as a function of gate voltage for different values of V_{sd} . Highlighted curves correspond to $V_{sd}=0$. Curves are offset for clarity: a) $\Delta V_{sd}=40\mu\text{V}$, b) $\Delta V_{sd}=220\mu\text{V}$.

a)

b)

DIRECT MEASUREMENTS OF ENERGY RELAXATION TIME OF ELECTRONS IN AlGaAs/GaAs HETEROSTRUCTURES UNDER QUASI-EQUILIBRIUM CONDITIONS

A.A. Verevkin, N.G.Pritsina, G.M.Chulcova, G.N.Golitsman
and E.M.Gershenson
Physics Department, Moscow State Pedagogical University,
Moscow, 119435, Russia.

Department of Electrical and Computer Engineering,
University of Massachusetts, Amherst, MA 01003, USA
K.S.Yngvesson

Abstract

For the first time, results are presented of a direct measurement of 2D electrons energy relaxation time τ_e in AlGaAs/GaAs heterojunction at $T=1.5\text{-}20\text{ K}$. A weak temperature dependence of τ_e for the $T>4\text{ K}$ range and a linear temperature dependence of the reciprocal of τ_e for $T<4\text{ K}$ have been observed. The linear dependence $\tau_e^{-1} \sim T$ in the Bloch-Gruneisen regime is a direct evidence of the predominance of the piezo-electric mechanism of electron-phonon interaction in nonelastic electron scattering processes. The values of τ_e in this regime are in very good agreement with the results of the Karpus theory. At higher temperatures, where the deformation-potential scattering becomes noticeable, a substantial disagreement between the experimental data and the theoretical results is observed.

Over the last decade, intensive research into the electron-phonon interaction in 2D electron gas (2DEG) in AlGaAs/GaAs heterostructures has been going on. At low temperatures, measurements of the energy loss rate of heating electrons have been widely used. So far, measurements of the energy loss rate per electron Q_e as a function of the electron temperature T_e have remained the only technique to be used in the studies of electron energy relaxation. Since such measurements are usually taken in conditions of a significant electron gas heating [1, 2, 3], it is not easy to extract information on the kinetic relaxation times of the energy and the momentum in the equilibrium conditions. For the first time, we have measured the energy relaxation time of 2D electrons by a direct method under quasiequilibrium conditions over the $T=1.5\text{-}20\text{ K}$ temperature range in AlGaAs/GaAs heterojunctions. The measurements were taken in the submillimeter wavrange with a high temporal resolution. In this technique, which had previously been effectively used in the studies of superconducting thin film structures [4], the electromagnetic radiation from two BWOs (backward wave oscillators) shifted in frequency by a value of Δf is applied to the sample to be studied. The absorption of the electromagnetic radiation by free carriers leads to electron gas heating. The sample responds to the increased electron temperature T_e by changing its resistance. The change of the sample resistance ΔR at frequency $f=\Delta f$ is measured through a voltage response ΔU on the sample biased with DC current source. The submillimeter photoconductive relaxation time is equal to the energy relaxation time of free carriers in the absence of the bolometric effect. This time is defined through the frequency dependence of ΔU :

$$\Delta U(f) = \frac{\Delta U_{(f=0)}}{\sqrt{1 + \omega^2 \tau_e^2}} \quad (1)$$

In order to determine τ_e in the quasiequilibrium conditions, highly sensitive equipment should be used. This strict requirement arises from the weak temperature dependence of $\Delta U(f)$ dependences for various P_e at a fixed temperature T (see Fig. 1b). Therefore, quasi-

the total mobility $\mu(T)$, which can be attributed to the fact that at low temperature the contribution of the electron-phonon interaction is quite negligible. At the same time, the main factor contributing to the mobility at low temperatures is the temperature independent scattering by ionized impurities. Additional requirements to the sensitivity arise from a strict limitation on the total absorbed power per electron of DC P_e and of AC $P_{e\sim}$. It is accounted for by the quasiequilibrium conditions. Moreover, the maximally acceptable limit of the total absorbed power ($P_e+P_{e\sim}$) is diminished with the temperature decrease due to growing τ_e . The sensitivity of our equipment allows to operate at minimum power levels of $P_{e\min} = 5 \times 10^{-17}\text{ W/el}$ and $P_{e\sim\min} = 10^{-17}\text{ W/el}$. The experimental samples, grown by:

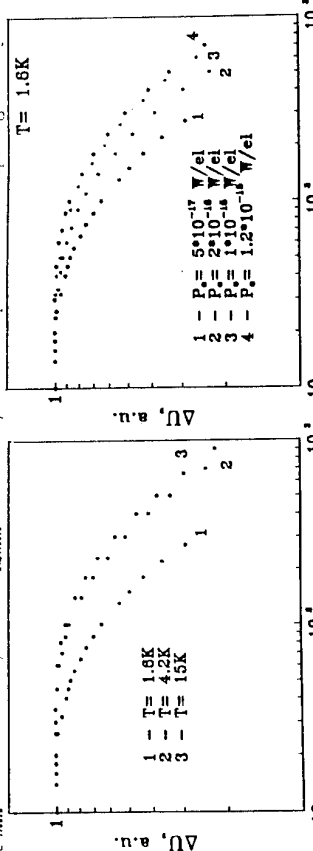


Fig.1a. $\Delta U(f)$ at various temperatures T

for the minimum total power ($P_e+P_{e\sim}$).
molecular beam epitaxy (MBE), have had a sheet charge density of $n_s=4.2 \times 10^{11}\text{ cm}^{-2}$, while their mobility at 4.2 K has been $7.9 \times 10^5\text{ cm}^2/\text{Vs}$. The active 2DEG area was $200\text{ }\mu\text{m}$ long by $50\text{ }\mu\text{m}$ wide. The measurements were performed using a 2-mm wave band spectrometer with f varying from 10^7 to 10^9 Hz in the $T=1.6\text{-}20\text{ K}$ range. Frequency dependencies of $\Delta U(f)$ for several temperatures at the minimum P_e and $P_{e\sim}$ are shown in Fig. 1a. The maximums of ΔU for $f=0$ are attached to the unit value. The figure allows to conclude that the shapes of all the dependences of $\Delta U(f)$ are well represented by expression (1). Fig. 1a also shows that the values of f , which correspond to $\Delta U(f)/\Delta U(0)=0.7$ grow together with the increase of the temperature. These data testify to the fact that the photoconductive relaxation process is adequately described by the time value alone. The measurements of $\tau_e(P_e)$ at different lattice temperatures have revealed that the quasiequilibrium conditions are only fulfilled within the $T>3\text{ K}$ temperature range. For lower T , the electron temperature is higher than the lattice temperature. Nevertheless, the real changes in the electron temperature ΔT_e caused by radiation are in good agreement with the requirement $\Delta T_e \ll T_e$. Owing to this fact, in such a case the energy relaxation process, which determines the photoreponse relaxation, is also described by the relaxation time $\tau_e(P_e)$ alone, in the same way as under the quasiequilibrium conditions. These results are confirmed by the shapes of $\Delta U(f)$ dependences for various P_e at a fixed temperature T (see Fig. 1b). Therefore, quasi-

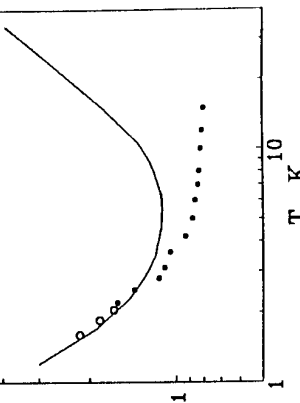


Fig.1b. $\Delta U(f)$ for various DC power values per electron P_e .

equilibrium values τ_e at the lowest temperatures could be extrapolated from the $\tau_e(T_e)$ data for $P_e \rightarrow 0$. Fig. 2 shows how the energy relaxation time depends on the temperature $\tau_e(T)$. The values of τ_e , extrapolated in the way described above, are marked in Fig. 2. It can be observed that τ_e is almost independent of T in the high temperature region $T > 4$ K. One can also note that for the low temperatures $T < 4$ K τ_e is growing with the decreasing T close to the T^{-1} law. The $\tau_e(T_e)$ dependences have also been obtained for the conditions of strong electron heating by DC field for various lattice temperatures. To determine the electron temperature, the standard Schubnikov-de Haas technique of measuring the oscillation amplitude damping has been used. We compared the oscillation amplitudes in the magnetic fields < 1 T for two procedures: varying P_e at fixed lattice temperatures and varying the lattice temperature at a negligibly small fixed DC power ($P_e \sim 10^{-17}$ W/el.). The collective data of $\tau_e(1)$ and $\tau_e(P_e)$ measurements and Schubnikov-de Haas oscillations demonstrate that the time of energy relaxation for sufficiently low values of T ($T < 5$ K) is determined by the electron temperature alone (i.e. $\tau_e(T) = \tau_e(T_e)$ for the same T and T_e values). Theoretical papers on electron-phonon interaction in 2DEG structures [1, 5, 7] normally either discuss the temperature dependence of the mobility or the energy loss rate dependencies of DA contributions into the total scattering prove to be of the same order of magnitude in the temperature range we are concerned with. At higher temperatures, the prevalence of DA scattering is observed, whereas the lower temperatures reveal the prevalence of PA scattering. In this connection the papers usually give numerical calculations of $Q_e(T_e)$ given for the conditions of strong heating can be used to obtain the following τ_e values:

$$\tau_e(T_e) = \frac{dE}{dQ(T_e)}, \quad (2)$$

where ΔE is the change of the average carrier energy caused by the variation of electron-absorbed power ΔQ . According to [1], for the two-dimensional degenerate electron gas the following expression holds true:

$$dE = \frac{\pi^2 k^2 T_e dT_e}{3\epsilon_F}, \quad (3)$$

where ϵ_F is the Fermi energy level and k is the Boltzmann constant. Exactly this situation is realized in our experiment in the conditions of strong DC field heating condition ($T_e \gg T$), where the absorbed power of the electromagnetic radiation is small. An exhaustive theoretical analysis of electron-phonon scattering in 2D structures, including the most popular electron system of a 2DEG channel in GaAs[001] (which is also used by us), has been offered by Karpus [5]. As is apparent from his papers, for $T < 6$ K the τ_e values must be determined by the electron temperature alone, the reason being that the main mechanism which underlies the electron energy relaxation processes in the relevant temperature range ($T < (\hbar k_F s)/(k)$, where k_F is the electron wave vector on the Fermi surface and s is the speed of sound) is a spontaneous emission of acoustic phonons. This conclusion has been supported by our experimental evidence, which shows that $\tau_e(T_e) = \tau_e(T)$ for the same T_e and T .

The theoretical curve of the $\tau_e(T)$ dependence, obtained in paper [6], is shown in Fig. 2 by a solid line. It can be seen that the experimental results practically coincide with the theoretical estimations in the lowest temperature region $T < 4$ K. The linear dependence $\tau_e \sim T^{-1} \sim T$ is an unambiguous evidence of the PA scattering predominance in these conditions. This is also confirmed by precise measurements for $Q_e(T_e)$ [2]. In paper [2], a correlation $Q_e \sim T_e^3$ proper for specific PA scattering has been obtained at $T_e = 1.6$ K. At $T > 4$ K, our experimental data for $\tau_e(T)$ and Karpus numerical calculations in the conditions of strong heating reveal a noticeable difference. On the one hand, it can be explained by the strengthened induced character of the electron-phonon scattering, which leads to decreasing quasi-equilibrium τ_e values as compared to strong heating conditions for the same electron temperatures within

this transition temperature range where $T > (\hbar k_F s)/(k)$. On the other hand, there is a pronounced discrepancy between the theoretical prediction and the experimental results under strong heating: the square law $Q_e(T_e)$, obtained in this temperature range by Sakaki [1], disagrees with the theoretical results of Karpus at $T > 8$ K [6]. It can be calculated from the results by Sakaki that τ_e must be about 0.7 ns for the sheet density $n = 4.2 \times 10^{11} \text{ cm}^{-2}$ at 4.2 K. This value is close to our data for $T > 6$ K region. It must be emphasized that the accuracy of $Q_e(T_e)$ measurements is usually insufficient to obtain $\tau_e(T_e)$ dependence from the experimental data.

A good agreement of our experimental data with the theory [5, 6] at low temperatures allows to assume that the accuracy of numerical calculation of the acoustic limited mobility temperature dependence [5] is also sufficiently high in this temperature region. An attempt can also be made to use the best experimental results for 2DEG in AlGaAs/GaAs heterostructures (e.g. [8]) at low temperatures in order to obtain the ultimate limit of the mobility which is set by the scattering due to acoustic phonons in conditions where nonequality of τ_e and the momentum relaxation time occur. For this purpose one needs to exclude the contribution of the impurity scattering, which sets a real limitation on μ at low temperatures, from the total measured mobility. Although the accuracy of such estimates procedure is not too good, the results of Karpus [5] show no contradictions with these estimations at low temperatures.

Thus, our experimental data on energy relaxation time for 2DEG in AlGaAs/GaAs heterostructures show the predominance of PA scattering with $\tau_e \sim T$ in the Bloch-Gruneisen temperature region ($T < 4$ K). The law underlying this correlation is $\tau_e \sim T^{-1} \sim T$. The values of τ_e in this regime are in a good agreement with the Karpus numerical calculations [5, 6]. There is a significant disagreement between the experimental data and theoretical results at higher temperatures (in the transition area), where DA scattering is significant.

This work was jointly supported by the International Science Foundation (grant M7K000), FRSF and the Russian Government (grant M7K300), and the Russian Fundamental Research Foundation (grant 95-02-06409).

References

- [1] H.Sakaki, K.Hirakawa, J.Yoshino, S.P.Svensson, Y.Sekiguchi, T.Hotta, Surf.Sci. 142 (1984) 386; K.Hirakawa, H.Sakaki, Appl.Phys.Lett. 49 (1986) 889.
- [2] M.G.Bliumina, A.G.Denisov, T.A.Polianetskaya, I.G.Savel'ev, A.P.Senichkin, Yu.V. Shmar'tsev, JETP Letters, 44 (1986) 257 (in Russian); A.M.Kreschuk, M.Yu.Martisov, T.A.Polyanskiy, I.G.Savel'ev, I.I.Saidashhev, A.Ya.Slik, Yu.V.Shmar'tsev, Solid State Commun., 65 (1988) 1189.
- [3] P.Hawker, A.J.Kent, O.H.Hughes, L.J.Challis, Semicond.Sci.Technol., 7 (1992) B29.
- [4] Yu.Gousev, G.N.Gol'tsman, A.D.Semenov, E.M.Gershenson, R.S.Nebosis, M.A.Heusinger, K.F.Renk, J.Appl.Phys., 75 (1994) 3695.
- [5] V.Karpus, Sov.Phys.Semicond., 20 (1986) 126 (in Russian); Sov.Phys.Semicond., 21 (1987) 1949 (in Russian); V.Karpus, Semicond.Sci.Technol., 5 (1990) 691.
- [6] V.Karpus, Sov.Phys.Semicond., 22 (1988) 43 (in Russian).
- [7] P.J.Price, Ann.Phys.(N.Y.), 133 (1981) 217; J.Vac.Sci.Technol., 19 (1981) 599; Surf.Sci., 113, (1982) 199; Surf.Sci. 143 (1984) 145.
- [8] C.T.Foxon, J.J.Harris, D.Hilton, J.Hewett, C.Roberts, Semicond.Sci.Technol., 4 (1989) 582.

An Elegant Verification of the Negative Charge-State of the DX-Centre from Mobility Measurements of 2D Electrons

M. Hayne^(a), A. Usher^(a), J. J. Harris^(b) and C. T. Foxon^(c)

^(a)Department of Physics, University of Exeter, Stocker Road, Exeter EX4 4QL, UK.

^(b)IRC for Semiconductor Materials, Department of Electronic and Electrical Engineering, University College, London WC1E 7JE, UK.

^(c)Department of Physics, University of Nottingham, University Park, Nottingham NG7 2RD, UK.

Abstract

We have measured the persistent changes in the mobility and density of the two-dimensional electron system in two modulation-doped GaAs/Al_xGa_{1-x}As single-heterojunctions at 0.3K following illumination with an infra-red light-emitting diode. One sample behaves conventionally with an immediate increase in both density and mobility when illuminated. However, the second sample shows remarkably different behaviour, with no change in density for more than 20% of the total time taken to reach the maximum density, and an increase in mobility of more than 10% in this initial illumination period. We demonstrate that these results provide very simple and convincing evidence for the negative-charge state of the DX-centre.

Introduction

It has been known for more than fifteen years [1] that donors in some semiconductor alloys produce a deep level known as a DX-centre with the unusual property that an energy barrier must be overcome to occupy the level. At low temperatures this leads to the persistent photoconductivity (PPC) effect [1,2] in which the level may be ionised optically but does not become re-occupied. Given the technological importance of doping in semiconductors, and the widespread use of PPC in studies of low-dimensional systems [3], it is not surprising that a considerable amount of effort has gone into attempting to understand the properties of the DX-centre and the process of PPC [2,4]. In particular, Chadi and Chang [5] have proposed an atomic configuration in which the level has negative effective Hubbard correlation energy (negative U), i.e. it captures two electrons via the 'reaction'



where d is a substitutional donor. As a result of this there has been much interest in experimentally determining the charge of the DX-centre in order to distinguish this from any positive-U model in which the level is singly occupied and therefore neutral. There is now a large body of evidence which supports the negative-U model, though transport studies have been surprisingly inconclusive [4,6]. Here we present the results of standard transport experiments which are readily explained by the negative-U model and inconsistent with the positive-U model. Our experiments therefore provide an elegant verification of the negative-charge state of the DX-centre.

Experimental Details

We have studied the changes in density (n) and mobility (μ) of the two-dimensional electron system (2DES) formed at the interface of two conventional GaAs/Al_xGa_{1-x}As single-heterojunction samples, with $x=0.33$, grown by molecular beam epitaxy. Both samples were modulation doped with Si in the Al_xGa_{1-x}As at a density of $1.33 \times 10^{18} \text{ cm}^{-3}$ for 380Å, and differed only in the thickness of the spacer layer between the dopants and the 2DES which was 200Å for

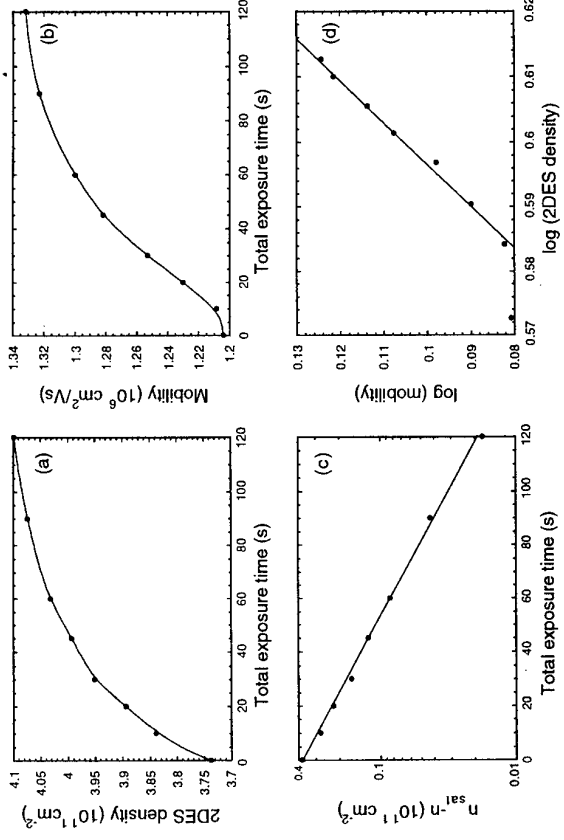


Figure 1: (a) n and (b) μ versus illumination time for sample A. The solid lines are guides to the eye. This conventional behaviour is characterised by the exponential decrease in $n_{\text{sat}} \cdot n$ ($n_{\text{sat}} = 4.12 \times 10^{11} \text{ cm}^{-2}$) with time (c). For this sample $\mu \ll 1.54$ (d).
 sample A and 400Å for sample B. The samples were cooled in a 3He cryostat to 0.3K, and magneto-transport measurements were made using a standard low-frequency lock-in technique, with Hall bar geometry, in order to determine n and μ . PPC was induced by exposure to an infrared light-emitting diode with spectral emission below the GaAs bandgap for a given time, after which the sample was left for five minutes before the measurements were made. This light source was chosen to ensure that the observed effects were entirely due to ionisation of the DX-centres. The diode current was 1μA in all cases. The 2DES density was determined from the slope of low-field Hall measurements and confirmed using the positions of the quantum Hall plateaux.

Results

Figure 1(a) shows n versus total illumination time for sample A. The increase of n under illumination is immediate, and tends to a saturated value, n_{sat} , with an exponential decay of $n_{\text{sat}} \cdot n$ with time (figure 1(c)). The rise in mobility of the electrons, and the consequent increase in the momentum relaxation time has an approximate $n^{3/2}$ dependence (figure 1(d)) [3,7]. The reason for the anomalous first point in figures 1(b) and (d) is not understood.

The equivalent results for sample B are very different: there is no change in n for more than 60s of illumination time, which is approximately 20% of the total time taken for n to reach its maximum value (figure 2(a)). Furthermore, despite the fact that there is no change in n at low illumination there is a 10% improvement in μ (figure 2(b)). We note that in this sample parallel conduction in the Al_xGa_{1-x}As set in at 300s, accounting for the abrupt levelling off of n at this point, but this has no effect on our conclusions.

Discussion

The 'anomalous' behaviour of sample B may be used to demonstrate the negative- U nature of the DX-centre. Under illumination a DX-centre with negative- U releases two electrons, and changes from being negatively charged to being positively charged, with no resultant change in its ability to scatter electrons in the 2DES. However, each of the two electrons which are released by this process can either find their way to the 2DES at the interface, or neutralise an ionised shallow donor in the Al_xGa_{1-x}As. If the latter is the case for both of the electrons then there will be a drop of two in the total number of ionised impurities, and an increase in mobility with no change in the density. Confirmation of this behaviour is given by the following argument. For independent scattering mechanisms the total inverse mobility is given by Matthiessen's rule,

$$\frac{1}{\mu} = \frac{1}{\mu_1} + \frac{1}{\mu_2} + \dots \quad (2)$$

While the density remains constant, the inverse mobility due to ionised impurity scattering is simply proportional to the density of ionised impurities, N_{ii} (neglecting correlation effects). Furthermore, since the exponential behaviour of n_{sat} seen in figure 1(c) is itself a consequence of the reduction in the density of occupied DX-centres with illumination, the rate at which ionised impurities are neutralised should also decay exponentially with time. This means that the total inverse mobility in the constant density regime should consist of a constant and an exponentially decaying term. As can be seen from figure 3, this is indeed the case.

In contrast, the equivalent process for positive- U DX-centres cannot explain the data. In this case PPC releases just one electron and the DX-centre changes from being neutral to being positively charged. If the electron neutralises a shallow donor then although the 2DES density will not change, there will also be no change in the total number of ionised impurities, and hence no change in the mobility. In fact, because optical ionisation of the DX-centres is a random process one would expect a decrease in mobility as a result of a reduction in the correlated distribution of ionised impurities achieved in the initial cool-down [6].

We now discuss the difference in behaviour of the two samples, which is characterised by an immediate increase in density in sample A, but not in sample B. Electrons photo-ionised from the DX-centres rapidly relax to the bottom of the conduction band, where they may find their way to the 2DES by two different mechanisms, either by tunnelling through the barrier in the Al_xGa_{1-x}As or via the contacts. It is the strong dependence of the former mechanism on the spacer width [8] that accounts for the difference between the two samples. For sample A, which has a 200Å spacer width, the characteristic tunnelling time estimated from a simple model [8] is 13ms, and this explains the rapid increase in density. In contrast, the same process for the 400Å spacer sample is very slow; an estimate of the tunnelling time gives about 35 hours. In this case all the photo-ionised electrons will remain in the conduction band of the Al_xGa_{1-x}As and diffuse along the Hall bar towards the contacts, where they enter the 2DES. However, if they come across an ionised

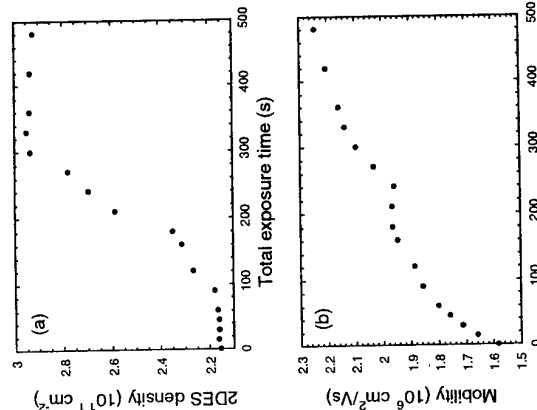


Figure 2: (a) n and (b) μ versus illumination for sample B. As discussed in the text this behaviour demonstrates the negative-charge state of DX-centres.

DX-centres are neutralised should also decay exponentially with time. This means that the total inverse mobility in the constant density regime should consist of a constant and an exponentially decaying term. As can be seen from figure 3, this is indeed the case.

In contrast, the equivalent process for positive- U DX-centres cannot explain the data. In this case PPC releases just one electron and the DX-centre changes from being neutral to being positively charged. If the electron neutralises a shallow donor then although the 2DES density will not change, there will also be no change in the total number of ionised impurities, and hence no change in the mobility. In fact, because optical ionisation of the DX-centres is a random process one would expect a decrease in mobility as a result of a reduction in the correlated distribution of ionised impurities achieved in the initial cool-down [6].

We now discuss the difference in behaviour of the two samples, which is characterised by an immediate increase in density in sample A, but not in sample B. Electrons photo-ionised from the DX-centres rapidly relax to the bottom of the conduction band, where they may find their way to the 2DES by two different mechanisms, either by tunnelling through the barrier in the Al_xGa_{1-x}As or via the contacts. It is the strong dependence of the former mechanism on the spacer width [8] that accounts for the difference between the two samples. For sample A, which has a 200Å spacer width, the characteristic tunnelling time estimated from a simple model [8] is 13ms, and this explains the rapid increase in density. In contrast, the same process for the 400Å spacer sample is very slow; an estimate of the tunnelling time gives about 35 hours. In this case all the photo-ionised electrons will remain in the conduction band of the Al_xGa_{1-x}As and diffuse along the Hall bar towards the contacts, where they enter the 2DES. However, if they come across an ionised

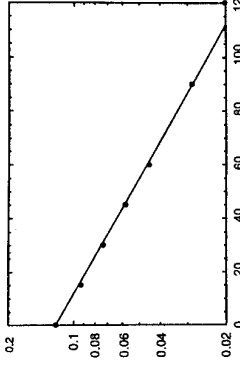


Figure 3 : The exponential decrease of $1/\mu_1 = 1/\mu - 1/\mu_2$, where $\mu_2 = 1.96 \times 10^6 \text{ cm}^2/\text{Vs}$, in the constant density regime for sample B confirms the explanation given in the text.

Finally, it is noteworthy that since $\mu \sim n^{-3/2}/N_{ii}$ [3,7], the μ dependence on n for sample A implies that there is no change in the number of scattering centres as n is increased, and is therefore indicative of negative- U . In contrast, a positive- U model in which $N_{ii} \propto n$ would give an $n^{1/2}$ dependence.

Conclusions

We have used measurements of the density and mobility of two-dimensional electrons in two modulation-doped GaAs/Al_xGa_{1-x}As single-heterojunction samples to study the persistent photoconductivity effect induced by the ionisation of DX-centres using an infra-red light emitting diode. The sample with a 200Å spacer width has been shown to behave conventionally, with an increase in both the density and mobility of the two-dimensional electron system at the interface. In contrast, the 400Å spacer sample showed an increase of more than 10% in the mobility of the two-dimensional electrons with no corresponding change in the density. The behaviour of both these samples is readily explained by the negative- U model for the DX-centre and is inconsistent with the positive- U model, and thus provides unambiguous verification of the negative-charge state of the DX-centre.

Acknowledgements

MH and AU would like to acknowledge the financial support of the EPSRC.

References

- [1] D.V. Lang, R.A. Logan and M. Jaros, Phys. Rev. B **19**, 1015 (1979).
- [2] D.E. Lackison, J.I. Harris, C.T. Foxon, J. Hewett, D. Hilton and C. Roberts, Semicond. Sci. Technol. **3**, 633 (1988).
- [3] I.I. Harris, J.A. Pals and R. Wolter, Rep. Prog. Phys. **52**, 1217 (1989).
- [4] P.M. Mooney, Semicond. Sci. Technol. **6**, B1 (1991).
- [5] D.J. Chadi and K.J. Chang, Phys. Rev. Lett. **61**, 873 (1988).
- [6] P.L. Coz, C. Ghezzi and A. Parisini, Semicond. Sci. Technol. **8**, 13 (1993).
- [7] K. Lee and M.S. Shur, J. Appl. Phys. **54**, 6432 (1983).
- [8] M. Hayne, A. Usher, A.S. Plaut and K. Ploog, Phys. Rev. B **50**, 17208 (1994).

Mobility and Quantum Lifetime in GaAs/AlGaAs Heterostructure. Tuning of The Remote-Charge Correlations

P. Wisniewski¹, T. Suski¹, E. Litwin-Staszewska¹,

G. Brunthaler², and K. Köhler³

¹Unipress, Polish Academy of Sciences, 01-142 Warsaw, Poland

²Institut für Halbleiterphysik, Johannes Kepler Universität, A-4040 Linz, Austria

³Franhofer-Institut für Angewandte Festkörperphysik, D-79108 Freiburg, Germany

Abstract

We demonstrate that depending on the method used for modification of the spatial correlations among remote impurity charges in the GaAs/AlGaAs quantum well different values of i) the transport-, ii) the single-particle-relaxation time and iii) the width of the Integer Quantum Hall plateaus could be achieved. These findings supply a qualitatively new information about the important contribution of the nonrandom arrangement of remote charges to the properties of semiconductor heterostructures.

Very high mobilities of a two-dimensional electron gas (2 DEG) achieved in modulation doped heterostructures of GaAs/AlGaAs result mainly from the separation of remote Si-donors and the conducting channel. The above idea of a reduction in the ionized impurity scattering seems to be well understood and commonly accepted [1]. There is however, also another factor leading to the considerable enhancement of the low temperature mobility. It has been proposed very recently that electrons localized by the remote donors can populate them in a spatially correlated manner [2-4]. As a consequence, fluctuations of the potential originating from the nonhomogeneous distribution of the remote donors, are significantly reduced. In samples doped above the Mott transition (about 10^{18} cm^{-3}) the formation of shallow, neutral donor states in the doping region is suppressed. The Si-donor can exist only in two charged states. The ionized donor represents a substitutional impurity with a positive charge, d^+ . Trapping of two electrons by d^+ state results in appearance of negatively charged DX center. It is a consequence of the negative-U nature of the localized state of Si-donor [5]. DX center has a metastable character consisting in thermally activated barriers for electron emission and capture (relevant at temperatures below about 100 K). It turns out, that partially occupied Si-donors tend to form dipole-like objects composed of close pairs of d^+ -DX states (see e.g.[6] and references there). These pairs appear as counterparts of spatially closed donors with the same charge. Since the electron scattering by ionized impurities is inversely proportional to the square of the effective charge, it is natural to expect an enhancement of electron mobility related to the introduced spatial correlation of charges.

The corresponding effect has been observed in heavily doped three-dimensional samples

of GaAs and AlGaAs [6]. Enhancement of 2 DEG mobility, μ_s , due to the correlations has

been identified at low temperatures in modulation doped heterostructures GaAs/AlGaAs [4,7]

and in pseudomorphic AlGaAs/InGaAs/GaAs structures [8]. The above findings were based on

the observation that depending on the manner electrons are distributed among Si-donors

centers located close one to the other [4]. As a result a high degree of correlations in the d^+ -DX- system can be achieved. Open circles on Figure 1a correspond to a variation of τ_i with decreasing of n_{2D} by means of HPFO procedure. The observed increase of τ_i before reaching a maximum is due to the reduced contribution related to the intersubband scattering of 2 DEG (for $n_s > 1.1 \times 10^{12} \text{ cm}^{-2}$). The drop of τ_i at the lowest values of n_{2D} corresponds to the less efficient screening (less dense 2 DEG) of the potential fluctuations related to RDC. As it can be deduced from the work of Sobkowicz et al. [12] for the examined sample and for the range of the achieved n_{2D} variation the enhancement of τ_i due to the spatial correlations of RDC remains constant.

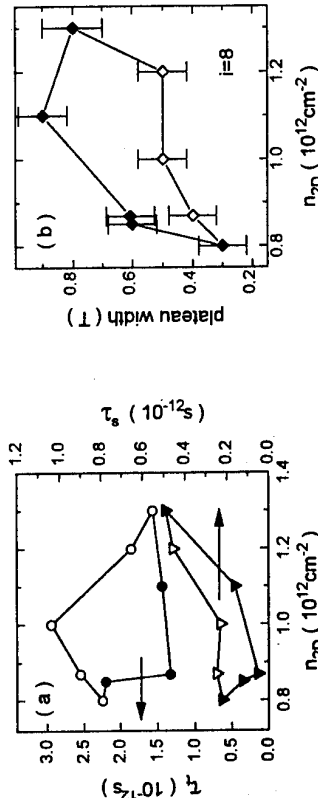


Figure 1. (a) Transport relaxation time (τ_s) and single particle relaxation time (τ_i) variations with electron concentration measured at $T=4.2\text{K}$ and at ambient pressure. (b) integer quantum Hall plateau width (for $i=8$) versus 2 DEG concentration. Open symbols represent strong correlation paths (HPFO), filled symbols correspond to weak correlation paths (annealing).

The method leading to the reduction of the correlation degree consists in a thermal ionization of DX centers. This treatment of the sample was employed after the reservoir of metastable electrons captured on DX centers was "prepared" by HPFO procedure. We have employed cycles of the sample annealing at temperatures exceeding roughly 110K. Every annealing cycle consisted of temperature increase from 4.2K, at which all measurements of τ_i vs. n_{2D} were performed. Higher annealing temperature causes more effective emission of electrons to the channel due to emptying of DX centers as they tend to their thermal equilibrium. The electron emission induced by annealing cycles occurs from randomly chosen DX state and therefore leads to the destruction of correlations in the distribution of charges among the remote-impurity sites [4]. Closed circles on Figure 1a show changes of τ_i versus n_{2D} . The different behavior of τ_i in comparison with that related to HPFO is due to a decrease in the degree of correlations among RDC.

Qualitatively similar behavior can be observed for the dependence of τ_s versus n_{2D} .

Open triangles on Figure 1a represent values of τ_s obtained after the sample preparation by HPFO procedure. Solid triangles correspond to the arrangement of RDC randomized by means of the annealing procedure. One can notice that relative changes of τ_s due to the spatial

different values of μ_i are achieved for the same 2 DEG concentration, n_{2D} . Changes of 2 DEG concentration have been induced either by the high pressure freezeout (HPFO) of electrons on the Si-DX states of remote donors or by a consecutive annealing of this reservoir of the localized electrons [4]. The former procedure corresponds to a higher correlation degree in the remote donor system and thus to the higher values of mobility. The annealing produces the opposite effect.

There are obviously other parameters which should be sensitive to the potential fluctuation caused by the remote-donor charges (RDC). The natural candidates are a single-particle relaxation time (or quantum lifetime), τ_s , and a width of the Integer Quantum Hall Effect (IQHE) plateaus. In this paper we will demonstrate how changes in the arrangement of RDC influence a behavior of these parameters. With the same purpose a contribution of the spatial correlations to the transport scattering time $\tau_t = \frac{1}{4} \epsilon m^*$ (m^* is the electron effective mass and ϵ is the electronic charge) will be also studied.

τ_s characterizes the total scattering probability and can be extracted from the amplitude of the Shubnikov-de Haas oscillations (see e.g. [3]). At low temperatures the diagonal magnetoresistivity, ρ_{xx} , is related to a density of states at the Fermi level. Due to disorder, the Landau levels are broadened with localized states in the tails of the levels [9]. Thus, ρ_{xx} contains detailed information about electronic scattering including a contribution arising from potential fluctuations caused by RDC. There has been no direct experimental demonstration of the τ_s modification caused by spatial correlations of RDC [3-7]. Width of the IQHE plateaus depends strongly on the impurity concentration [9-11]. Much less is known about the influence of impurity charges distribution on a density of states of 2 DEG and on the width of the QHE plateaus.

The used sample was grown by molecular beam epitaxy (MBE) on semi-insulating (100) GaAs substrates. The sample consists of the following sequence of layers: a 300 nm GaAs buffer, a GaAs/AlGaAs super-lattice, 200 nm thick undoped $\text{Al}_{0.3}\text{Ga}_{0.7}\text{As}$, a nominal $3 \times 10^{12} \text{ cm}^{-2}$ Si δ-doping layer, 6 nm $\text{Al}_{0.3}\text{Ga}_{0.7}\text{As}$ spacer, a 15 nm GaAs quantum well, another 6 nm $\text{Al}_{0.3}\text{Ga}_{0.7}\text{As}$ spacer, a nominal $4 \times 10^{12} \text{ cm}^{-2}$ Si δ-doping layer, 20 nm $\text{Al}_{0.3}\text{Ga}_{0.7}\text{As}$ undoped and 20 nm GaAs cap layer. Except for the first 100 nm of the buffer, grown at 650 °C, the rest of the structure was grown at 500 °C. To characterize the sample measurements of Shubnikov-de Haas effect were performed. Presence of two frequencies in the oscillations of ρ_{xx} was found. In the sample cooled to T=4.2K at ambient pressure about 5 percent of the conducting electrons populate the second subband of the GaAs well.

From Hall effect and longitudinal resistivity ρ_{xx} the transport scattering time was estimated. From a fit of the SDH oscillations the Dingle temperature T_D and equivalently τ_s have been determined [3]. All measurements were performed at T=4.2K and at ambient pressure. Hydrostatic pressure was used as a tool to obtain various nonequilibrium occupation of DX centers by means of high pressure freezeout (HPFO) procedure. HPFO procedure consists of applying pressure at room temperature, resulting in an enhanced occupation of DX centers which are in thermal equilibrium with the n_{2D} at this temperature. Then, cooling of the sample at constant pressure occurs and this is followed by releasing of the pressure at 77K. The whole procedure results in a persistent lowering of n_s and its value decreases with increasing of a freezeout pressure. Such pressure-induced capture of electrons onto DX centers favors high values of mobility corresponding to a given n_{2D} . Electrons populate likely d⁺

correlations among RDC are much higher than that observed for τ_s . Moreover, an increase of τ_s for n_{2D} higher than about $1.10^{12} \text{ cm}^{-2}$ reflects a screening contribution appearing above the onset of the second subband occupation [13].

Measurements of ρ_{xy} evolution with magnetic field (taken simultaneously with ρ_{xx}) were employed for determination of a width of the IQHE plateaus. The quantized Hall resistance is given by $\rho_{xy} = h/i e^2$, where h is the Planck constant and the quantum number i is the number of completely filled Landau levels. Width of the plateaus increases significantly for the annealing path (closed symbols) with respect to HPFO path (open symbols). Figure 1b illustrates this behavior for i=8. As it could be expected, processes leading to a randomization in the distribution of d⁺ and DX⁻ states of remote donors (i.e. an enhancement of the related potential fluctuations) induce an appearance (in tails of the Landau levels) of much wider regions occupied by the localized states.

In summary, we demonstrated the role played by the spatial correlations among remote impurity charges in determination of the important transport properties of low dimensional semiconductor structures. Employing the HPFO procedure, which privileges a high degree of the spatial correlations, resulted in the strong enhancement of the transport and single particle relaxation times as well as in the decrease of the width of the Quantum Hall plateaus. The opposite behavior of these three parameters accompanies the sample sequential annealing which leads to a randomization in the distribution of remote charges.
Acknowledgments- This work was supported by the KBN(Poland), Grant 3 P407 028 07 and G.B. got a financial support from the FWF Austria, Project P8833.

References:

- [1] S. Das Sarma and F. Stern, Phys. Rev. B32, 8442 (1985).
- [2] A.L. Efros, F.G. Pikus, and G.G. Samsonidze, Phys. Rev B41, 8295 (1990).
- [3] P.T. Coleridge, Phys. Rev. B44, 3793 (1991).
- [4] T. Suski, P. Wisniewski, I. Gorecza, L.H. Dmowski, R. Piotrkowski, P. Sobkowicz, J. Smoliner, E. Gornik, G. Bohm, and G. Weimann, Solid-St. Electron., 37, 677 (1994), Phys. Rev. B50, 2723 (1994).
- [5] D.J. Chadi and K.J. Chang, Phys. Rev. Lett. 61, 873 (1988).
- [6] T. Suski, Materials Science Forum, 143-147, 1439 (1994).
- [7] E. Buks, M. Heiblum and H. Shtrikman, Phys. Rev. B49, 14790 (1994), Semicond. Sci. Technol., 9, 2031 (1994).
- [8] E. Litwin-Staszewska, T. Suski, C. Skierbiszewska, F. Kobbi, J.L. Robert, and V. Mosser, J. Appl. Phys., 77, 405 (1995).
- [9] A.M. Chang, in The Quantum Hall Effect, edited by R.E. Prange and S.M. Girvin (Springer Verlag, New York, 1987) p. 175.
- [10] J.E. Furneaux and T.L. Reinecke, Phys. Rev. B29, 4792 (1984).
- [11] R.J. Haug, R.R. Gerhardts, K.v. Klitzing, and K. Ploog, Phys. Rev. Lett. 59, 1349 (1987).
- [12] P. Sobkowicz, Z. Wilamowski, and J. Kossut, Semicond. Sci. Technol. 7, 1155 (1992).
- [13] R. Fletcher, E. Zaremba, M. D'Iorio, C.T. Foxon, and J.J. Harris, Phys. Rev. B41, 10649 (1990).

Anisotropy of the Conductivity in δ -Doped Multilayers

Th. Ihn¹, C. Gauer^{*}, F. Koch and J.P. Kotthaus^{*}
 Physik Department E16, Technische Universität München, James-Franck-Str.,
 D-85748 Garching, FRG

* Sektion Physik, Ludwig-Maximilians Universität, D-80539 München, FRG

Abstract

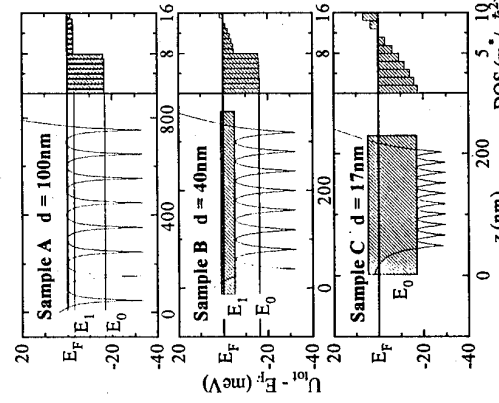
We have investigated three Si δ -doped multilayer structures with sheet-doping concentrations around $N_d = 5 \times 10^{11} \text{ cm}^{-2}$ and sheet distances of 17 nm, 40 nm and 100 nm. Cyclotron resonance measurements and far-infrared spectroscopy in a multiple reflection geometry allow the determination of the effective masses and the scattering times normal and parallel to the doping planes. While the scattering time was found to be isotropic, the effective mass exhibited a strong anisotropy with $m_{\perp} < m_{||}$. The measurements are supported by a self-consistent calculation of the subband structure of the samples.

A number of evenly spaced δ -doped planes in a MBE-grown GaAs matrix can be considered to be a periodical doping structure in the growth direction. Many authors have reported measurements of the electronic properties of such multilayers which probed the motion of carriers parallel to the doping planes [1-4]. The usual description of a single metallic δ -doped layer considers it as translationally invariant within the doping plane. In multilayers an additional translation symmetry in the third dimension is introduced. A displacement by a multiple of the sheet distance d leaves the system unchanged (ignoring boundaries). In the limit of $d \approx N_d^{-1/2}$ (N_d is the sheet-doping concentration) we have a three dimensional system, whereas the case of $d \gg N_d^{-1/2}$ represents a system with fully decoupled parallel two-dimensional electron gases. The conductivity measured in the growth direction is expected to be different from that measured in the plane. The conductivity is determined by the number density of the charge carriers contributing to the transport, their effective masses and the scattering times. We measured the anisotropy of the two latter quantities by comparing the in-plane cyclotron resonance with the plasmonic excitations normal to the δ -layers. All measurements were performed with a Fourier-transform spectrometer at $T=4.2\text{K}$.

The samples investigated typically contained 10 Silicon δ -doped layers with a sheet-doping concentration of about $N_d = 5 \times 10^{11} \text{ cm}^{-2}$ embedded in a GaAs matrix. The main difference between the three samples is the separation of the doped planes, which is $d=100\text{nm}$ (sample A), 40nm (sample B) or 17nm (sample C). Details about the sample growth can be found in reference [3].

Fig. 1 shows the calculated self-consistent potential, the energy levels and the density of states (DOS) in the three samples. Resonant subband-states of neighbouring sheets interact more

Figure 1: Self-consistent potential and electron density at $T=1.3\text{K}$ for the three samples.
 (a) Sample A with $d=100\text{nm}$ and $N_d=5.6 \times 10^{11} \text{ cm}^{-2}$. (b) Sample B with $d=40\text{nm}$ and $N_d=5.4 \times 10^{11} \text{ cm}^{-2}$. (c) Sample C with $d=17\text{nm}$ and $N_d=4.3 \times 10^{11} \text{ cm}^{-2}$.



strongly for smaller d and when the states are higher in energy and, hence, more extended. This interaction leads to the splitting of the subbands labelled E_0 and E_1 which is indicated by the hatched areas in Fig. 1. In sample A this interaction is not strong enough to split the levels significantly, whereas in sample C the splitting is so strong, that the subband character of individual wells is completely destroyed and the energy dispersion in the z -direction is given by $E(k)=\hbar^2 k^2 / 2m_{\perp}$ with $m_{\perp} = m^*$, the GaAs effective mass. Sample B with a sheet spacing between that of samples A and C has two occupied subbands like sample A. While the E_0 -subband states are hardly split, the E_1 -subband states can be described by a parabolic dispersion in the z -direction similar to the states in sample C. The effective mass $m_{\perp}=0.45m^*$ is, however, significantly smaller than the GaAs conduction band mass m^* . This important result, which can be understood as a consequence of the electrons in a weak periodic potential situation, raises the question, whether this effective mass of the electrons in the E_1 -subband can be measured in an experiment.

We have employed both cyclotron resonance and magnetotransport measurements in order to obtain information about the in-plane transport properties of the three samples. The results of the self-consistent calculation are in excellent agreement with the magnetotransport data [3]. In the cyclotron resonance measurements we observe two modes of different linewidths in both sample A and sample B, in accordance with the two occupied subbands of different mobilities. In sample C, however, only one very broad resonance is identified similar to a three-dimensional sample. The in-plane cyclotron effective mass of the E_1 -subbands extracted from the data according to $m_{\text{CR}}=\epsilon B/E_{\text{res}}$, where B is the magnetic field and E_{res} the resonance energy, is about $0.062m_0$, e.g. lower than the expected value of $0.067m_0$. This decreased effective mass due to a resonance energy increased relative to $\hbar\omega_c$ is a result of the strong potential fluctuations in the δ -doping planes [5,6].

In order to obtain information about transport properties normal to the doping planes we measured the transmission of the samples in the multiple reflection geometry shown in the inset of Fig. 2. The metal film evaporated on top of the multilayer leads to a parallel component of the electric field vector which is small compared to the normal component in the near-field. This geometry therefore allows an optimal excitation of electrons in the growth direction of the crystal. We used a magnetic field parallel to the doping planes (see Fig. 2) in order to obtain the reference

^{*}present address: Department of Physics, Univ. of Nottingham, University Park, Nottingham NG7 2RD, England

measurements necessary in Fourier transform spectroscopy. The diamagnetic shift of the subbands, which in first order perturbation theory is given by $\Delta E_{\text{dia}} = e^2 B^2 \cdot z^2 / (2m^*)$, leads to the depopulation of the E_1 -subband at sufficiently high magnetic fields enabling us to switch the excitations in this subband on and off. With this arrangement we can explore plasmonic excitations in the E_1 -subband normal to the doping planes of the multilayer structure.

Fig. 2 shows the results of the measurements for sample A. The resonance at about 6meV is attributed to the $E_1 \rightarrow E_2$ intersubband transition. The self-consistent calculation gives a separation of 3meV between the E_1 - and the E_2 -subbands (The E_2 -subband is not shown in Fig. 1.). The discrepancy to the measured value is caused by a strong depolarisation shift of the transition. To confirm this interpretation we performed a calculation of the $E_1 \rightarrow E_2$ resonance in the random phase approximation (RPA) using the wave functions and energy-spectrum from the self-consistent calculation [7]. The solid line in Fig. 2 shows the result for a calculation in which a broadening of the resonance was achieved by introducing a scattering time which is not too far from the experimental value of 0.45ps. There is an excellent agreement between the measured and the calculated resonance energy confirming that the individual δ -layers are decoupled, as expected for $d \gg N_D^{-1/2}$, and that it is actually the depolarisation-shifted $E_1 \rightarrow E_2$ transition that is observed.

In sample B, however, the splitting of the E_1 -subband is about 5meV (see Fig. 1). In contrast to the observed *intersubband* plasmon in sample A it should therefore be possible to detect an *intrasubband* plasmon in this E_1 -subband. The participating one-electron states are above the barriers which separate neighbouring layers and thus the electron motion is mainly confined by the potential barriers at the top and bottom of the multilayer rather than by the inter-layer barriers. Quantum mechanically, a simplified picture of the electronic potential for electrons in the E_1 -subband would be a large well (with extension over all layers) with a weakly modulated pseudo-potential accounting for the orthogonality of the states. The total density of states of all the levels constituting this 'miniband' sums up to a shape that is well described by a $E^{1/2}$ -behaviour as for a three-dimensional density of states (see Fig. 1), containing the 'miniband-mass' m_L . We therefore expect to find an intrasubband plasmon with energy close to the three dimensional plasma energy

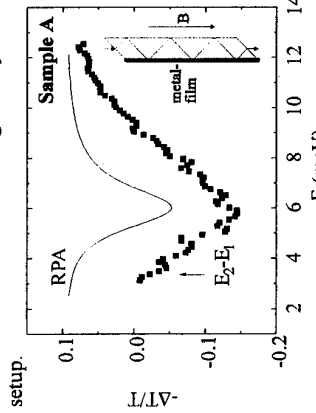


Figure 2: Intersubband resonance in sample A. The result of an RPA-calculation is shown as solid line. The inset shows the geometry of the setup.

where $E_{\text{Ry}}^* = 5.8 \text{meV}$ denotes the Rydberg-energy in GaAs, m^* is the GaAs conduction-band mass and m_L is the effective mass relevant for the motion normal to the doping planes. The Fermi energy in this sample is determined to be $E_F = 5 \text{meV}$ from the calculation and from Shubnikov-de Haas measurements parallel to the doping planes [3]. The plasmon frequency is thus estimated with Eq. (1) to be $E_p = 8 \text{meV}$. Fig. 3 shows the measured resonance. The resonance position is in excellent agreement with the estimated value, confirming the value of the calculated effective mass m_L .

The width of the plasmon resonance is determined by the momentum decay of the plasmon. It is caused by scattering of the electrons which constitute the plasmon at the potential fluctuations of the δ -layers. This allows us to determine a scattering time τ_L normal to the doping planes from the linewidth of the plasma resonance. The Lorentz-fit of the resonance [see Fig. (3)] gives a plasmon life-time of $\tau_L = 0.45 \text{ps}$, which agrees with the in-plane value determined from Hall-measurements [3] and cyclotron resonance measurements. Similar agreement was found for sample C.

In conclusion, we have measured the transport properties normal to the doping planes of δ -doped multilayers in a far-infrared experiment. The samples exhibit no significant anisotropy in the scattering times parallel and perpendicular to the doped layers. However, a strong anisotropy in the E_1 -subband effective masses relevant for the motion in the two directions was calculated and proven experimentally for sample B, where we found $m_L = 0.45 m^*$ for the E_1 -subband.

References

- [1] F. Koch, Physica B 184 (1993), 298 and references therein.
- [2] X. Zheng, T.K. Cams, K.L. Wang, and B. Wu, Appl. Phys. Lett. 62 (1993), 504.
- [3] T. Ihn, F. Koch, K.J. Friedland, and R. Hey, accepted for publication in Phys. Rev. B.
- [4] H. Kostial *et al.*, Phys. Rev. B 47 (1993), 4485.
- [5] J.P. Kotthaus, G. Abstreiter and J.F. Koch, Phys. Rev. Lett. 34 (1975), 151.
- [6] H.-J. Mikeska and H. Schmidt, Z. Physik B 20 (1975), 43.
- [7] T. Ando, Z. Physik B 26 (1977), 263.

$$\left(\frac{E_p}{E_{\text{Ry}}^*} \right)^2 = \frac{16}{3\pi} \left(\frac{E_F}{E_{\text{Ry}}^*} \right)^{3/2} \cdot \left(\frac{m^*}{m_L} \right)^{1/2}, \quad (1)$$

ASYMMETRIC MAGNETORESISTANCE IN GaAs/AlGaAs MESOSCOPIC HETEROSTRUCTURES

A. R. Alves, J. S. Cruz, P.S.S. Guimarães, A. S. Chaves, R.P. Diniz, A. G. de Oliveira
Departamento de Física - ICEx, Universidade Federal de Minas Gerais, Cx Postal 702, 30161-970 Belo Horizonte MG Brazil

and

M. Henini
Department of Physics, University of Nottingham, Nottingham NG7 2RD, UK

Abstract

We report an asymmetry in the magnetoresistance with respect to the direction of the magnetic field, that is, $R(B) \neq R(-B)$, for high mobility GaAs/AlGaAs heterojunctions at low temperatures with the magnetic field applied parallel to the interface. This magnetic field-induced asymmetry is due to the deformation of the quasi-two dimensional conduction band of the potential well in the presence of the planar field, and to the shift of the electron wavefunction relative to the interface. The asymmetry in $R(B)$ increases as the distance between the voltage contacts in the sample is decreased, showing that, under the experimental conditions, the system is not Markovian and therefore the observed effect does not violate Onsager's reciprocity relations.

Introduction

There are many interesting effects associated with the application of a strong magnetic field in the plane of the quasi-two dimensional electron gas (2DEG) formed at semiconductor quantum wells and interface accumulation layers. The applied field significantly changes the structure of the electronic subbands of the confining potential [1,2], altering the energy dispersion $\epsilon(k)$ of both electrons and holes in the in-plane direction, x , perpendicular to $B = B\hat{y}$. Previous calculations [2] have shown that for an asymmetric quantum well the energy dispersion becomes asymmetric, i.e., $\epsilon(-k_x) \neq \epsilon(k_x)$, in the presence of the planar magnetic field. Hence, electrons with a given k_x have a different effective mass than electrons with $-k_x$. To investigate the effect of this asymmetry in the energy dispersion on the electric transport properties, we measured the magnetoresistance of several GaAs/AlGaAs:Si heterojunctions with the magnetic field applied in the plane of the 2DEG, perpendicular to the current. We find an asymmetry in the magnetoresistance with respect to the direction of the magnetic field. The effect is strongly sample dependent and is clearly seen only in the highest mobility samples at temperatures around or below 1 K. The magnitude of the asymmetry also depends on the distance between the voltage-probe contacts, being larger for smaller distances, showing that this is a mesoscopic effect and as such does not imply in a violation of Onsager's [3] reciprocity relations. Instead, we find that electrical conduction in this system follows Büttiker's relation [4]. We attribute the effect to the deformation of the quasi-two dimensional conduction band of the asymmetric potential well in the presence of the magnetic field [2,5], and to the change in interface scattering associated with the

shift of the electron wavefunction by the magnetic field, in a conduction regime where the electrons coherent mean free path is comparable to the distance between the electrical contacts.

Experimental

The GaAs/AlGaAs:Si heterojunctions studied in this work are conventional modulation-doped structures grown by Molecular Beam Epitaxy (MBE). A GaAs/AlGaAs multiquantum well structure with 7 periods is grown on top of a semi-insulating GaAs (100) substrate followed by an undoped GaAs buffer layer with thickness 1 and 2 μm , then an undoped $\text{Al}_{0.3}\text{Ga}_{0.7}\text{As}$ spacer layer, 40 to 200 nm of n-doped $\text{Al}_{0.3}\text{Ga}_{0.7}\text{As}$ and, finally, a GaAs cap layer of around 20 nm thickness. In all cases the n-dopant is Si. For the magnetotransport measurements, Hall bars were fabricated using standard photolithographic and AuGeNi contact fabrication techniques. The sample structure and Hall bar geometry are shown schematically in Figure 1. The width of the Hall bar is 250 μm and the distance between the voltage probe contacts is $d_{ab} = d_{bc} = 800 \mu\text{m}$.

The experiments were performed at temperatures between 0.3 K and 4 K employing conventional superconductor magnets and galvanomagnetic measurement techniques.

We measured the 2DEG electrical resistance as a function of the magnetic field, up to 15 T, for several modulation-doped GaAs/AlGaAs heterojunctions. The measurement geometry is shown in Figure 1. The magnetic field is in the plane of the heterojunction interface, perpendicular to the current. As defined in Fig. 1, B_+ corresponds to the direction of the magnetic field that shifts the electronic wavefunctions away from the interface and B_- is the opposite direction. The voltage is probed between contacts a and b or between a and c.

Figure 1 - Sample structure and measurement geometry.

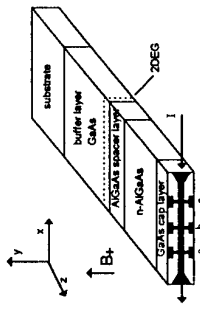


Figure 2 shows the variation of the electric resistance with the in-plane magnetic field for the sample with the highest mobility ($\mu = 230 \text{ m}^2/\text{V}\cdot\text{s}$). The magnetic field direction is as defined in Fig. 1, with B_+ being $B > 0$ and B_- as $B < 0$. The solid curves shows the resistance $R(B)$ measured with the voltage probed between the nearest pair of contacts (a and b). For the dashed curves the voltage probe contacts are a and c. In both cases the current is kept constant at a value low enough to prevent heating or non-ohmic effects. It is seen clearly in Fig. 2 that $R(B) \neq R(-B)$ and that this asymmetry is larger when the sample is probed between the nearest contacts. The asymmetry in the magnetoresistance also increases as the temperature T is lowered. Some oscillations which appear in the curves probably come from the Shubnikov-de Haas effect resulting from a small misalignment of the sample. The anomalous asymmetry shown in Fig. 2 is not seen for samples with lower mobility ($\mu \leq 50 \text{ m}^2/\text{V}\cdot\text{s}$).

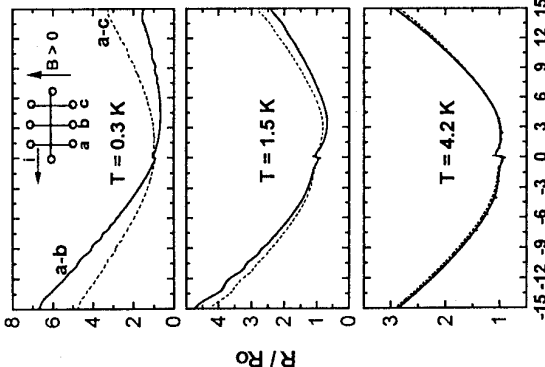


Figure 2. Magnetoconductance for a high-mobility sample at 0.3, 1.5 and 4.2 K. The voltage is probed between the nearest contacts a-b (solid curves) and between contacts a-c (dashed curves).

reciprocity relations [3] because the system is not Markovian and one cannot speak about local properties like the electric conductivity σ . For the limit when the electron inelastic scattering is completely absent and the carriers can traverse the sample maintaining phase coherence, Büttiker [4] obtained symmetry relations for the resistance. These relations state that the resistance should stay the same when one interchanges current leads and voltage leads and reverses the magnetic field, i.e., $R_{deac}(B) = R_{ac,dc}(-B)$. Figure 3 shows the effect of such an interchange in the role of the electrical contacts. At $T = 4$ K the Büttiker's relation is clearly violated while Onsager's relation is verified, as shown in Fig. 2. At $T = 1.5$ K there is a much smaller deviation from the symmetry established by Büttiker's relation. At $T = 0.3$ K (not shown) this symmetry is perfect. This temperature dependence is as expected since as $T \rightarrow 0$ K one approaches the condition of complete phase coherence, for which Büttiker relations are valid. These experimental results indicate that the coherent mean free path in our high mobility sample is comparable to the distance between the voltage contacts, i.e., of the order of 1 mm. The low mobility samples, which have a much lower free electron mean path, do not show any asymmetry in their magnetoconductance curves.

There are two mechanisms which combine to generate the asymmetry in the resistance observed in Fig. 2. The most important one comes from the magnetic field-induced asymmetry in

the electronic energy dispersion curve. A preliminary calculation by Chaves et al [5] shows that this asymmetry leads to a diode effect, that is, the resistance depends on the direction of the electric field, $R(E_x) \neq R(-E_x)$. An inversion in the direction of the magnetic field reverses the asymmetry in the energy dispersion curve and therefore one should also obtain $R(B) \neq R(-B)$. In the results shown in Fig. 2, the direction of the magnetic field that gives rise to higher resistance, B_+ , is that for which the electronic wavefunctions are pushed towards the interface, where the electronic density of states is low. This behavior is in accordance with Chaves calculations.

The second mechanism which contributes to the asymmetry seen in Fig. 2 comes from the negative magnetoresistance which appears for the B_+ direction of the magnetic field. In this geometry the electronic wavefunctions are shifted away from the interface. This shift leads to a decrease of interface scattering and therefore to a higher conductance, i.e., the resistance decreases with magnetic field. For the direction B_- the electronic wavefunctions are shifted towards the interface and there is a corresponding increase in interface scattering. This phenomenon is more pronounced when the voltage is probed between the nearest contacts, as shown in Fig. 2, which indicates that this is also a mesoscopic effect.

Conclusion

We showed that the transverse resistance of a quasi-two dimensional electron gas formed in an asymmetric quantum well depends on the direction of the magnetic field applied in the plane of the 2DEG. The effect occurs for samples in which the electron coherent mean free path is comparable to or larger than the distance between the contacts. In this case the Onsager reciprocity relations do not mean that the magnetoresistance is symmetric. The asymmetry in the resistance is due to the deformation of the quasi-two dimensional conduction band by the planar B-field and to the change in interface scattering caused by the shift of the electronic wavefunctions by the magnetic field.

Acknowledgments

This work is supported by FAPEMIG. One of us, A.R.Alves, is on leave from UFV, Viçosa, MG, supported by CAPES.

References

- [1] T. Ando, Journal of the Physical Society of Japan **39**, 411 (1975) & **44**, 475 (1978).
- [2] G.M.G. Oliveira, V.M.S. Gomes, A.S. Chaves, J.R. Leite and J.M. Worlock, Physical Review B **35**, 2896 (1987).
- [3] L. Onsager, Physical Review B **38**, 2265 (1931).
- [4] M. Büttiker, Physical Review Letters **57**, 1761 (1986).
- [5] A.S. Chaves, G.M.G. Oliveira, V.M.S. Gomes and J.R. Leite, unpublished.

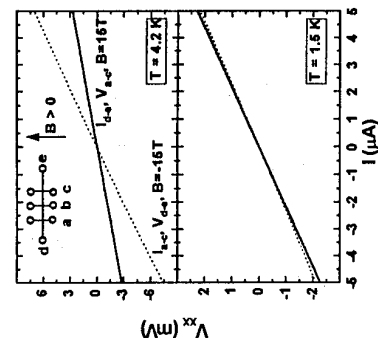


Figure 3. Current - Voltage curves for the same sample of Fig. 2, interchanging current and voltage leads and the B-field to verify Büttiker's relations.

The asymmetry in the conductance of the 2DEG is a mesoscopic effect which appears when the coherent mean free path of the electrons is comparable or larger than the distance between the contacts. Under these conditions, the observed asymmetry does not mean a violation of the Onsager

reciprocity relations [3] because the system is not Markovian and one cannot speak about local properties like the electric conductivity σ . For the limit when the electron inelastic scattering is completely absent and the carriers can traverse the sample maintaining phase coherence, Büttiker [4] obtained symmetry relations for the resistance. These relations state that the resistance should stay the same when one interchanges current leads and voltage leads and reverses the magnetic field, i.e., $R_{deac}(B) = R_{ac,dc}(-B)$. Figure 3 shows the effect of such an interchange in the role of the electrical contacts. At $T = 4$ K the Büttiker's relation is clearly violated while Onsager's relation is verified, as shown in Fig. 2. At $T = 1.5$ K there is a much smaller deviation from the symmetry established by Büttiker's relation. At $T = 0.3$ K (not shown) this symmetry is perfect. This temperature dependence is as expected since as $T \rightarrow 0$ K one approaches the condition of complete phase coherence, for which Büttiker relations are valid. These experimental results indicate that the coherent mean free path in our high mobility sample is comparable to the distance between the voltage contacts, i.e., of the order of 1 mm. The low mobility samples, which have a much lower free electron mean path, do not show any asymmetry in their magnetoconductance curves.

There are two mechanisms which combine to generate the asymmetry in the resistance observed in Fig. 2. The most important one comes from the magnetic field-induced asymmetry in

ROOM TEMPERATURE MANIPULATION OF C₆₀ MOLECULES ON A Si SURFACE

P.H. Beton, A. Dunn and P. Moriarty
Department of Physics, University of Nottingham, Nottingham NG7 2RD, UK

Abstract

The tip of a scanning tunnelling microscope is used to position individual C₆₀ molecules on a Si(111) - 7×7 surface. The molecules may be manipulated into simple patterns and we describe in addition how a molecule may be moved over a bilayer step between two terraces. We also discuss C₆₀ manipulation on a Si(111) surface with a sub-monolayer coverage of Ag.

The manipulation of individual atoms and molecules on solid surfaces is now established as a new area of research following the work of Eigler et al. [1] and Crommie et al. [2]. So far most experiments have been performed using a metal substrate and a scanning tunnelling microscope (STM) operating in a low temperature environment. Recently we demonstrated that it is possible to manipulate C₆₀ molecules into simple patterns using an STM [3]. This work was performed using a semiconductor substrate and the STM was operated at room temperature. We have continued this work and now describe further examples of C₆₀ manipulation.

Our work is performed using an STM [4] housed in an ultra-high vacuum system (base pressure $P < 10^{-10}$ Torr). As a substrate we use 7mm × 3mm pieces of a p-type Si(111) wafer (resistivity $> 1\Omega$ cm). These are heated to 1200°C and then cooled to room temperature whilst maintaining low pressure ($< 10^{-9}$ Torr) so that the Si surface undergoes a 7×7 reconstruction. C₆₀ molecules are sublimed onto the Si surface from a Knudsen cell operated at 320°C.

Controlled deposition of coverages down to 10⁻³ monolayers is possible. We use electrochemically etched tungsten tips which are cleaned in vacuum by electron beam heating.

A typical STM image of C₆₀ on Si(111)-7×7 is shown in Figure 1a. The C₆₀ molecules appear as the bright features in the image and their arrangement on the surface is found to be stable at room temperature. The unit cell of the underlying 7×7 reconstruction may be resolved in Fig. 1a and is made up of two equilateral triangles. Within each of these triangles there are six Si atoms (referred to as adatoms [5]). These are resolved in Fig. 1c. At the corner of each triangle there is a dark topographic feature referred to as a corner hole [5]. The interaction of C₆₀ molecules with Si(111)-7×7 has been investigated previously using STM by a number of groups [6,7]. The majority of molecules are adsorbed onto the adatom sites of the 7×7 reconstruction with only a small proportion (~5%) sitting at corner holes. Note that charge is transferred from the Si adatoms to C₆₀ so the nature of the bonding is not van der Waals [8]. STM tip induced movement of C₆₀ on Si(111) has been previously reported with the feedback loop either off [9] or on [3]. In Figure 2 we illustrate schematically how a C₆₀ molecule may be moved while maintaining feedback control. We refer to this movement as

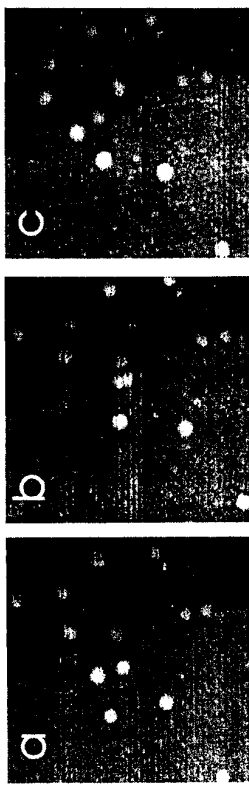
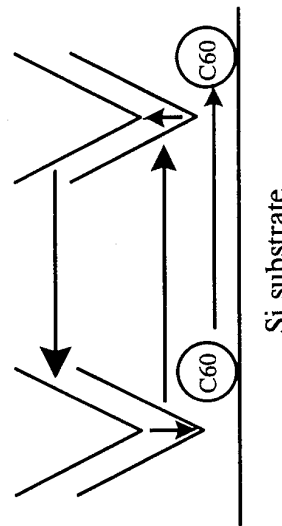


Figure 1. Topographic STM images (28nm × 28nm) illustrating the manipulation of an individual C₆₀ molecule over a terrace step edge. The images were taken with a sample bias -2.0V and tunnel current -0.5nA and have had a plane subtracted to emphasise the height difference between the two terraces (0.31 nm). The 7×7 reconstruction may be observed in the background and the C₆₀ molecules appear as bright circular features approximately 1.5nm in diameter. The two molecules nearest the step edge on the upper terrace are first moved towards the step by applying the sweeping procedure described in the text (compare a and b). Further application of the sweeping procedure forces one of the molecules on to the lower terrace.

'sweeping'. First the tip is moved closer to the surface by adjusting the sample bias and tunnel current from V_{sc} ~ -2.0V, I_{sc} ~ -0.5nA (appropriate for imaging) to V_{sc} ~ -0.4V, I_{scw} ~ -4nA (appropriate for sweeping). The tip is swept across the surface, moved away from the surface (by returning the tunnel current and bias voltage to their original values) and then moved back



Si substrate

Figure 2. Schematic illustration of the sweeping procedure. The tip is first moved towards the surface by increasing the tunnel current and reducing the absolute value of the sample bias and then moved across the surface. It is then retracted by adjusting the tunnel current and voltage back to their original value. The tip is then moved back across the surface to its starting position.

to its original position. In order to move a C₆₀ molecule the tip is first positioned close to the molecule and then a number of parallel lines are swept out. Typically the tip is swept 6 nm across the surface and we sweep out 10 parallel lines separated by 0.6 nm so that the total swept area is 6 nm × 6 nm. By applying this procedure we have been able to move C₆₀ molecules in preferred directions. Repeated application may be used to form predetermined patterns of C₆₀ molecules on Si(111) [3] which are stable at room temperature.

A mechanism for manipulation on this surface has been proposed by Li et al. [6] and is based on a strong interaction between tip and C₆₀ at voltages for which the local density of states associated with the C₆₀ is small. From previous imaging data [6] it is known that this condition is satisfied for molecules at some adsorption sites for a sample bias ~ 0.4 V. This corresponds to the sample bias we normally use for sweeping. However, we have recently been able to move molecules using a positive sweeping voltage and it is not clear that this result can be explained in terms of the model of Li et al.[6].

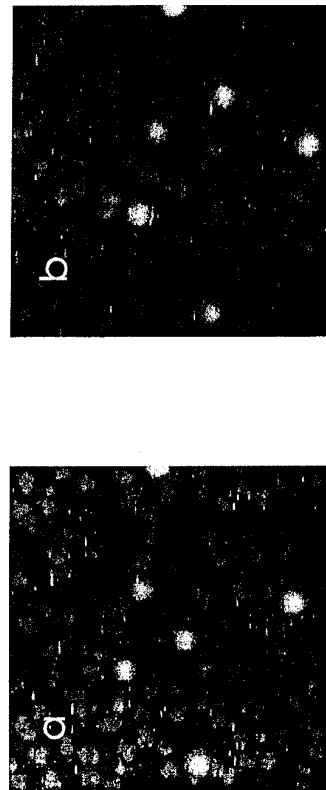


Figure 3. Manipulation of C₆₀ on a Ag terminated Si(111) surface. A comparison of (a) and (b). shows that the molecule close to the centre of image (a) has been moved using the sweeping procedure. The sweeping direction was the x axis and the sweeping parameters were $V_{sw} = -0.4$ V, $I_{sw} = -4$ nA. The imaging parameters were -2.0 V, -0.5 nA and the image size is 20 nm × 20 nm.

We have applied the sweeping procedure repeatedly to an area in Fig. 1a which covers the 3 C₆₀ molecules on the upper (brighter) terrace which are closest to the step edge. The sweeping procedure is then applied resulting in the re-positioning of these 3 molecules which is apparent from a comparison of Figs. 1a and 1b (there were 4 individual movements between Figs. 1a and 1b). The sweeping direction is parallel to the horizontal (x) axis of the image and it is clear that the molecules are also displaced perpendicular to the x-axis as we have previously observed [5]. It is apparent from Fig. 1b that 2 of the molecules have been moved to the top of the step edge. To investigate whether it is possible to move C₆₀ over the step the sweeping procedure is then repeated over an area which covers the two molecules near the step edge and also the molecule on the lower terrace which is closest to the step. After further

applications of the procedure we find that it is indeed possible to move a C₆₀ from the upper to the lower terrace. Note that in doing this (compare Figs 1b and 1c); (i) the C₆₀ which remains on the upper terrace has moved in the opposite direction; (ii) the C₆₀ on the lower terrace has also been moved. Nevertheless it is clear the one of the C₆₀ molecules has moved across the step edge.

We have also investigated C₆₀ manipulation on Si(111) which has a sub-monolayer coverage of Ag. This is prepared by evaporating 0.3 monolayers of Ag on a surface which has a 0.005 monolayer coverage of C₆₀. The sample is held at room temperature during deposition. For this experiment Ag is evaporated at an angle of 16° to the surface to determine whether the C₆₀ molecules have a masking effect. Figure 3a shows an STM image of the surface following Ag deposition and shows no evidence for such masking. The Ag is chemisorbed at the reactive adatom sites and forms small islands as has been previously reported [10]. It is likely that the Ag diffuses on the surface to the adatom sites displacing the C₆₀ molecules from these sites and eliminating any masking effects.

A comparison of Figs. 3a and 3b shows the effect of applying the sweeping procedure to the area which covers the C₆₀ molecule at the centre of Fig. 3a. With a sweeping range of 6 nm this molecule is moved to a new site. Inspection of Figs. 3a and 3b shows that the C₆₀ molecule was initially positioned above a Si adatom but is displaced to a site where it sits above a Ag island. This result implies that manipulation of C₆₀ is not restricted to the clean Si(111)-7x7 surface.

Our work has shown that it is possible to move C₆₀ molecules on a semiconductor surface using the tip of an STM. As an extension of our previous work we have shown that C₆₀ may be moved across step edges and may also be manipulated on the Ag/Si(111) surface. We have been able to move C₆₀ on Si(111) during 5 separate experimental runs over the course of nearly nine months and our work demonstrates that this is a new and extremely interesting combination of materials for the study of molecular manipulation.

This work was supported by the UK Engineering and Physical Sciences Research Council

References

- [1] D.M. Eigler and L.K. Schweizer, *Nature* **344** 524 (1990).
- [2] M.F. Crommie, C.P. Lutz and D. Eigler, *Science* **262** 218 (1993).
- [3] P.H. Beton, A.W. Dunn and P. Moriarty, *Appl.Phys.Lett.* to be published
- [4] The STM, electronics and software were purchased from W.A Technology, U.K.
- [5] K. Takayangai, Y. Tanishiro, M. Takahashi and S. Takahashi, *J.Vac.Sci.Technol.* **A3** 1502 (1985)
- [6] Y.Z. Li, M. Chander, J.C. Patrin, J.H. Weaver, L.P.F. Chibante and R.E. Smalley, *Phys. Rev. B* **45** 13837 (1992).
- [7] D. Chen, J. Chen and D. Sarid, *Phys. Rev. B* **50** 10905 (1994).
- [8] S. Soto, A. Kasuya, O. Ikeno, C.-W. Hu, A. Wawro, R. Nishitani, T. Goto and Y. Nishina, *Jpn. J. Appl. Phys.* **33** L1489 (1994).
- [9] S. Maruno, K. Inanaga and T. Isu, *Appl. Phys. Lett.* **63** 1339 (1993).
- [10] St. Tosch and H. Neddermeyer, *Phys.Rev.Lett.* **61** 349 (1988).

COULOMB BLOCKADE AND DOT SIZE IN SPLIT-GATE WIRE WITH A SMALL MESA OR A HOLE MADE BY SCANNING TUNNELING MICROSCOPY

Syoji Yamada
Japan Advanced Institute of Science and Technology (JAIST) - Hokuriku
15 Asahidai, Tatsunokuchi, Ishikawa, 923-12 Japan

Masafumi Yamamoto
NTT LSI Laboratories
3-1, Morinosato Wakamiya, Atsugi-shi, Kanagawa, 243-01 Japan

Abstract

Coulomb blockade effects and related dot sizes of two-dimensional electron gas (2DEG) are investigated in split-gate quantum wires with a mesa or a hole made by scanning tunneling microscopy (STM). From the dependencies on front (split)- and back-gate voltages, the smallest size of the 2DEG dot under the mesa is found to be limited by the mesa size itself giving stable Coulomb gaps. In a wire with a hole, Coulomb oscillations modulated by random telegraph signal (RTS) oscillation were observed. This suggests the coexistence of a "dot" and electron traps both probably created via STM fabrication. The "dot" was found to be larger than in the mesa case and to be unstable due to the interaction between the "dot" and traps.

1. Introduction

As a new alternative for creating semiconductor nanostructures, we recently proposed a split-gate quantum wire with a small mesa or a hole later fabricated by STM[1]. By analogy with a shallow etched structure, the formation of a 2DEG dot just below the mesa and of a 2DEG anti-dot around the hole would be expected. More precisely, in a split-gate wire with a mesa, the appearance of a series barrier (*constriction*)-dot-barrier (*constriction*) structure could be formed under an almost pinch-off condition. This was essentially verified by the observation of clear Coulomb blockades in such samples[1,2]. In a split-gate wire with the hole, however, the dominant quantum transport phenomenon was found to differ greatly depending on the size of the hole[3]: When the hole was relatively small (typically a 200 nm upper diameter and 100 nm deep), conductance quantization in units of $2e^2/h$ was observed, which suggests the hole simply acts as an anti-dot forming a constriction in the split-gate wire. In contrast, when the hole size was relatively large (a 300 nm upper diameter and 150 nm deep), RTS phenomenon[4] often associated with Coulomb oscillation was observed.

In this paper, after a short description of sample preparation, we report various Coulomb blockade effects observed in split-gate quantum wires with a mesa or a hole. We then deduce the size of the 2DEG dots and discuss their origins and stability. This is important, since the unique feature of our proposed approach is the easy and controllable fabrication of 2DEG dots (or anti-dots) of various sizes in the desired (quantum wire surface) position by STM.

2. Sample preparation

A basic split-gate wire (2.5 μm long and 0.8 μm wide) was fabricated by standard electron-beam lithography and a lift-off method on the surface of a 2DEG wafer using a p⁺-substrate. Each sample thus has also a back-gate in addition to front (split)-gates. Before the processes, the sheet electron density, n_s , and mobility, μ , of the 2DEG were respectively $5.0 \times 10^{11}/\text{cm}^2$ and $1.8 \times 10^5 \text{ cm}^2/\text{V}\cdot\text{sec}$ at 4.2 K. Figure 1 schematically shows mesa and hole fabrication

procedures[3]. When the Tungsten (W) tip is positioned over the center of the wire (left two panels), a small mesa is created just beneath the tip. But if the tip is positioned off center i.e. closer to one split-gate electrode (right two panels), the hole is made near the electrode. The small mesa in the measured specimen was only about 70 nm in diameter and 15 nm tall. The hole, with which modulated Coulomb oscillations were observed, had about a 300 nm upper diameter and was 150 nm deep.

3. Coulomb blockade effects in a split-gate wire with a mesa

Figure 2 shows I-V characteristics measured at 0.3 K when (a) back-gate voltage V_{bg} was varied for a fixed front (split)-gate voltage V_{fg} of -1.80 V and when (b) V_{fg} was varied for V_{bg} of 0 V. From those results, dot diameter dependencies on V_{fg} and V_{bg} were obtained and are shown in Fig. 3. Here, the dot diameter L was estimated by the relations of $C_{self}=4\pi\epsilon_0 L$ and $C_{self} \sim C_{total} = e/2 V_{th}$, where C_{self} and C_{total} are the self and total capacitance of the dot, respectively, and V_{th} is the Coulomb gap. In both cases, saturation behavior is apparent, when gate voltages become deeper, that is, when the split-gate wire is squeezed. The saturation occurred at just about the mesa diameter (70 nm), which is indicated by the bold horizontal dashed line. This result clearly suggests that the 2DEG dot size is essentially determined and hence can be controlled by the diameter of the mesa, fabricated by STM. Note here that Coulomb oscillations were also observed in the two-terminal conductance (G_{2e}) as a function of V_{fg} for $V_{bg}=0$ V (not shown). They have given almost the same dot sizes as those mentioned above. The reason for the difference of the saturation between the two curves in Fig. 3 is considered as follows: The relatively slow saturation for V_{fg} is probably due to the fact that the mesa diameter is almost the same as that of the minimum wire width attained by V_{fg} when $V_{bg}=0$ V. The rapid saturation for V_{bg} is mainly due to using a p⁺-substrate wafer. For $V_{bg} \sim 3.0$ V, n_s becomes 2/3 of that with $V_{bg}=0$ V when $V_{fg}=0$ V. However, within this V_{bg} range (from -2.75 to -2.85 V), the number of electrons in the dot could change drastically due to the almost pinch-off condition of $V_{fg}=-1.80$ V. There seem to be electron traps related to defects made during hole formation[3]. The above results, however, exclude electron traps as a possible origin of the Coulomb blockade effects observed here. They rather show the simple and controllable fabrication of small 2DEG dots by STM.

4. Coulomb oscillation in a split-gate wire with a hole

As already reported elsewhere[3], the typical transport phenomenon observed in a wire with a relatively large hole was RTS, suggesting the damage-related formation of some kind of electron traps near the hole by the STM electrical evaporation. However, among those samples, there were several that showed twofold oscillatory conductances when V_{fg} was swept. A typical example of such oscillations is shown in Fig. 4. As shown in this trace, the short-period oscillation was "modulated" by a long one, which is indicated explicitly by thin dashed lines as envelopes. The long-period oscillation was found to be RTS phenomenon, since it was not reproducible against up and down sweeps of V_{fg} and the period changed depending on the V_{fg} sweep rate[3]. The short-period one was thought to be a Coulomb oscillation, since the oscillation peaks were fairly reproducible against the different sweep directions of V_{fg} . In addition, there was a Coulomb gap in I-V characteristics (not shown), although it was not so obvious due to the modulation by the RTS oscillation. These results indicate the formation of not only electron traps but also a "dot" near the hole by the STM electrical evaporation.

An interesting feature in Fig. 4 is that the period of the Coulomb oscillation itself, ΔV_{fg} , is also modulated by the RTS phenomenon. (Short vertical bars indicate the peaks of the oscillation.) This feature clearly contrasts to previous reports where Fabry-Perot resonance or discrete energy levels were pointed out as origins of the amplitude modulation in the Coulomb blockade oscillations[5]. This means that the dot capacitance, C_{total} , and hence the effective dot size are modulated by the RTS phenomenon. If we use an approximate relation of $\Delta V_{fg} = e/C_{total}$, the dot diameter L is found to vary within the range of 120 - 400 nm in Fig. 4. Moreover, L takes a minimum and a maximum value when the RTS oscillation amplitude is maximum and minimum, respectively, in one V_{fg} range between the knots of the envelope. The accurate mechanism is not known at present, but there seems to be a strong correlation between the electron traps and the "dot". Another possibility is that a defect may possibly change its role from an electron trap to a "dot" and vice versa depending on V_{fg} .

Summary

We have investigated the Coulomb blockade effects and the related dot sizes of 2DEG in split-gate quantum wires with a mesa or a hole made by STM. From the analysis of the size dependence on front (split)- and back-gate voltages, the smallest size of the 2DEG dot (~ 80 nm) in a wire with a mesa is found to be determined by the mesa size itself, giving stable and controllable Coulomb gaps. In a wire with a hole, Coulomb oscillations modulated by RTS oscillation was observed. This suggests the coexistence of "dot" and electron traps both simultaneously created via STM fabrication. From the period of the Coulomb oscillation, the "dot" was found to have a larger size, 120 - 400 nm, than that in the mesa case and to be unstable due to interaction with the traps.

References

- [1] S.Yamada, Proc.22nd Int.Conf.Phys.of Semicon., 1975(1994).
- [2] S.Yamada and M.Yamamoto, Appl.Phys.Lett., 65, 2000(1994).
- [3] S.Yamada and M.Yamamoto, submitted to J. Appl.Phys.
- [4] Most recently reported in GaAs/AlGaAs system is: D.H.Cobden, N.K.Patel, M.Pepper, D.A.Ritchie, J.E.Frost, and G.A.C.Jones, Phys. Rev. B44, 1938(1991).
- [5] For example, T.Heinzel, F.Hofmann, D.A.Wharam, J.P.Kotthaus, G.Bohm, W.Klein, G.Trankle, and G.Weimann, Proc.22nd Int.Conf.Phys.Semicon., 1871(1994).

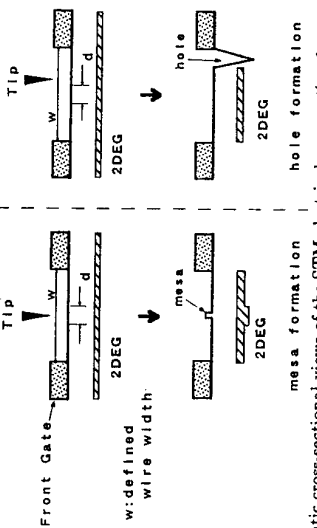
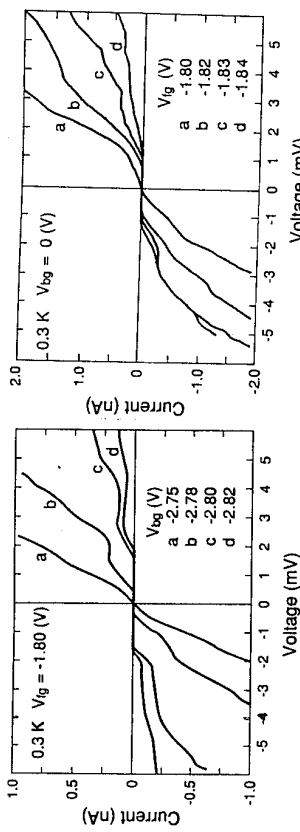
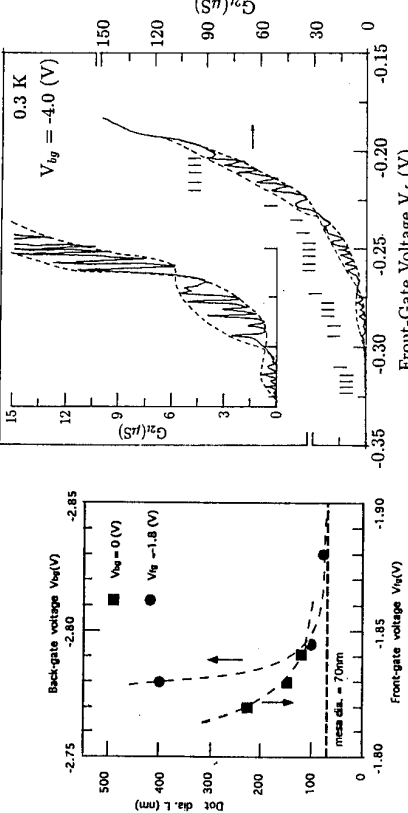


Fig. 1. Schematic cross-sectional views of the STM electrical evaporation for producing a small round mesa and a cone-shaped hole. The desired structure can be produced by changing the relative distance between the tip and the (one) split-gate.



(a)

Fig. 2. Low temperature I - V characteristics in the split-gate wire with a mesa when (a) back-gate voltage V_{bg} was varied for fixed $V_{fg} = -1.8$ V and (b) front-gate voltage V_{fg} was varied for $V_{bg} = 0$ V measured at 0.3 K.



(b)

Fig. 4. Two terminal conductance G_{21} as a function of V_{fg} in the split-gate wire with a relatively large hole. There seem to be two kinds of oscillation as indicated by the thin solid line (Coulomb oscillation close to the value of the mesa diameter (70 nm)) and by thin dashed lines (RTS) as an envelope. Short vertical bars indicate the peaks of the Coulomb oscillation.

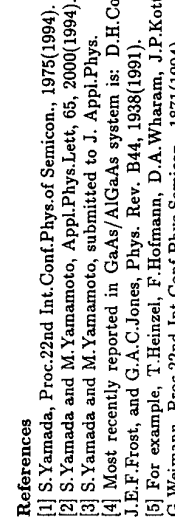


Fig. 3. 2DEG dot size dependences on V_{bg} and V_{fg} , the minimum value of which is showing the saturation close to the value of the mesa diameter (70 nm).

mesa formation
hole formation

Fig. 4. Two terminal conductance G_{21} as a function of V_{fg} in the split-gate wire with a relatively large hole. There seem to be two kinds of oscillation as indicated by the thin solid line (Coulomb oscillation close to the value of the mesa diameter (70 nm)) and by thin dashed lines (RTS) as an envelope. Short vertical bars indicate the peaks of the Coulomb oscillation.

ELECTRON TRANSPORT IN A NON-PLANAR 2DEG

M. L. Leadbeater*, C. L. Foden*, J. H. Burroughes*, T. M. Burke†, L. L. Wang†, M. P. Grimshaw†,
D. A. Ritchie† and M. Pepper*†

* Toshiba Cambridge Research Centre, 260 Cambridge Science Park, Milton Road, Cambridge
CB4 4WE UK.

† Cavendish Laboratory, Madingley Road, Cambridge, CB3 0HE UK.

Abstract

We investigate electron transport in a spatially varying magnetic field generated by applying a uniform field to a non planar 2DEG grown by MBE on a substrate patterned with etched facets. When a magnetic field is applied in the plane of the substrate, the resistance measured across a facet is quantised. Magneto-oscillations with the same periodicity are measured between probes on the planar region adjacent to the facet even though there is no perpendicular component of magnetic field in that region. By rotating the direction of the magnetic field we produce a normal component of field on the facet which is of opposite sign to that on the planar regions. We observe plateaux in the resistance across the facet at values determined by the sum of the inverse filling factors.

The development of regrowth technology means that we can investigate the effects of varying the *topography* of a two-dimensional electron gas (2DEG). We etch a series of facets on a wafer and then grow a heterojunction. The resulting electron gas is confined to a sheet at the GaAs/AlGaAs interface but this is no longer flat. If we apply a uniform magnetic field to a non-planar 2DEG, the perpendicular field component field varies with position depending on the angle between the field and the local facet [1]. This is a flexible technique to investigate the physics of electron motion in a non-uniform field which has attracted considerable attention [2-8].

A (100) GaAs wafer was etched to produce a 3 μm long facet at an angle of $\phi=20^\circ$ to the substrate. Following an *in-situ* clean with a hydrogen radical flux the wafer was transferred to the MBE growth chamber where a modulation-doped heterostructure was grown 2000 Å from the original interface. Details of the growth are given elsewhere [9]. Hall bars with width 40 or 5 μm apart for the 40 μm mesas (4 μm apart for the 5 μm mesas). Other pairs of voltage probes either side of the facet were used to measure the 2DEG in the planar regions alone. A schematic diagram of the Hall bar is inset in figure 1. Four terminal ac resistance measurements were made at 1.4 K with a constant current in the range 10 to 500 nA.

Figure 1 plots the resistance measured across the facet for a 40 μm mesa at angles in the range $0^\circ > \phi > 90^\circ$. At $\theta=0^\circ$ there are well-defined zeroes in the resistance at integer filling factors but as the sample is rotated a pronounced positive magnetoresistance is apparent. At most angles two frequencies of magneto-oscillations are observed, one from the facet and one from the planar regions. The results of a Fourier analysis of the data are plotted in figure 2. By fitting the period of the magneto-oscillations to $\Delta(I/B)=2e \cos(\theta\phi)/nh$ we find the number density, n , on the plane to be $5.5 \times 10^{11} \text{ cm}^{-2}$, that on the facet to be $5.25 \times 10^{11} \text{ cm}^{-2}$ and the facet angle $\phi = 19 \pm 1^\circ$. This

relatively small variation in number density demonstrates that by using *in situ* cleaning techniques we can produce a uniform 2DEG on the different facets.

With the magnetic field applied in the plane of the substrate ($\theta = \pm 90^\circ$) there is a perpendicular component of field only on the facet. Figure 3 shows the longitudinal magnetoresistance measured across the facet for a 5 μm wide mesa for gate voltages between 0.3 and 0.7 V. Plateaux appear at resistances approximately given by $R=h/v^2$, where v is an even integer. The planar regions of the sample act as high mobility contacts to the facet and we are in effect performing a two-terminal resistance measurement on a short wide Hall bar with the dimensions of the etched facet with a magnetic field of $B_{\text{H}}n\theta$. For a planar Hall bar, a two terminal measurement shows quantised plateaux at integer filling factor [10]. We see clearer plateaux in the narrow mesas due to the higher aspect ratio of the facet (0.6 compared to 0.075).

The resistance between voltage probes on the planar regions directly adjacent to the facet shows a strong magnetoresistance which depends on the direction of the applied magnetic field even when $\theta=90^\circ$ and there is no perpendicular field in these regions, as shown in figure 4. We observe magneto-oscillations with the same periodicity as those measured across the facet and which therefore must be associated with the field on the facet. We again consider the facet as a Hall bar and the planar regions as the leads. Current enters a small area at one corner of a Hall bar and exits through the diagonally opposite corner. Electrons injected from the facet into the planar region travel a considerable distance before equilibrating i.e. contact to the facet is made a characteristic scattering length away from the facet. If the distance between a voltage probe and the facet is less than this length, the potential is influenced by the magnetic field on the facet. When the magnetic field direction is reversed, current flows from the opposite pair of corners explaining the asymmetry of the magnetoresistance.

When the magnetic field is rotated out of the plane, there are different numbers of occupied edge channels on the facet and on the planar regions. We observe plateaux in the resistance measured across the facet for angles where both regions are at integer filling factor [9]. This situation is similar to that in Hall bars with a small electrostatic gate region where it is found that the resistance across the gated region is given by the difference in the inverse of the filling factors [11,12]. With magnetically modulated samples we can have opposite signs of field component in the different regions. In this case the edge states propagate in opposite directions on the facet and on the plane. The four terminal resistance across the facet calculated from the Landauer-Büttiker formula [13] is $R_{1,8;4,5} = h/e^2(I/\nu_2 + I/\nu_1)$. This assumes perfect equilibration between states on the facet and on the plane. We directly determine the filling factor on the facet from the diagonal resistance $R_{1,8;5,12} = -(I/\nu_2)/h/e^2$. In the region where the field changes sign we have the trochooidal states discussed by Müller [3]. These have a large spatial extent compared to states at the boundary so it is reasonable to expect strong coupling between them. Figure 5 plots the longitudinal, diagonal and the Hall resistances for $\theta = -36^\circ$ where $\nu = 2\nu_2$. The longitudinal resistance is given by the sum of the inverse filling factors as calculated.

In conclusion we have shown that by varying the topography of a 2DEG we have been able to produce a spatially non-uniform magnetic field. By rotating the sample we generate a wide variety of field profiles and achieve the novel situation of reversing the sign of the perpendicular field component on neighbouring facets. MBE regrowth on a patterned substrate produces a much greater field variation than alternative techniques [5-8] and the use of an *in situ* cleaning process allows us to produce a uniform electron density throughout the structure avoiding electrostatic and strain variations which are present in patterned gate samples. This technique offers a flexible route for exploring electron transport in a spatially varying magnetic field.

- [1] C. L. Foden, M. L. Leadbeater, J. H. Burroughes, and M. Pepper, *J. Phys.: Condens. Matt.* **6** (1994) L127.
 [2] D. Yoshioka and Y. Iye, *J. Phys. Soc. Jpn.* **56** (1987) 448.
 [3] J. E. Müller, *Phys. Rev. Lett.* **68** (1992) 385.
 [4] F. M. Peeters and A. Matulis, *Phys. Rev. B* **48** (1993) 15166.
 [5] A. K. Geim, S. V. Dubonos, and A. K. Khaetskii, *JETP Lett.* **51** (1990) 121.
 [6] S. J. Bending, K. von Klitzing, and K. Ploog, *Phys. Rev. Lett.* **65** (1990) 1060.
 [7] H. A. Carmona, A. K. Geim, A. Nogaret, P. C. Main, T. J. Foster, M. Henini, S. P. Beaumont, and M. G. Blamire, *Phys. Rev. Lett.* **74** (1995) 3009.
 [8] P. D. Ye, D. Weiss, R. R. Gerhardts, M. Seeger, K. von Klitzing, K. Eberl, and H. Nickel, *Phys. Rev. Lett.* **74** (1995) 3013.
 [9] M. L. Leadbeater, C. L. Foden, T. M. Burke, J. H. Burroughes, M. P. Grimshaw, D. A. Ritchie, L. L. Wang, and M. Pepper, *J. Phys.: Condens. Matt.* **7** (1995) L307.
 [10] F. F. Fang and P. J. Stiles, *Phys. Rev. B* **27** (1983) 6487.
 [11] R. J. Haug, A. H. MacDonald, P. Streda, and K. von Klitzing, *Phys. Rev. Lett.* **61** (1988) 797.
 [12] S. Washburn, A. B. Fowler, H. Schmid, and D. Kern, *Phys. Rev. Lett.* **61** (1988) 2801.
 [13] M. Büttiker, *Phys. Rev. B* **38** (1988) 9375.

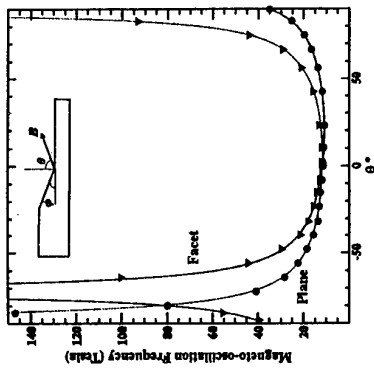


Fig. 2. Frequency of the magnetooscillations for the facet (\blacktriangle) and a planar region (\bullet) as a function of magnetic field direction.

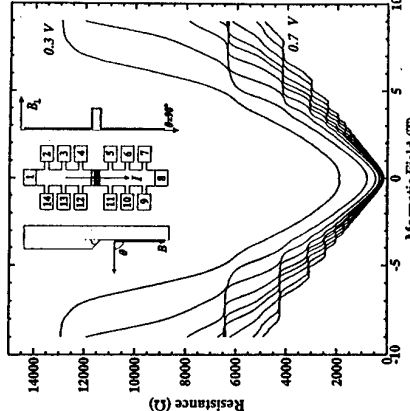


Fig. 3. Magnetoresistance measured across the facet (probes 4 and 5) for a 5 μm mesa for gate voltages between 0.3 V (top) and 0.7 V (bottom). The magnetic field is in the plane of the substrate ($\theta=90^\circ$).

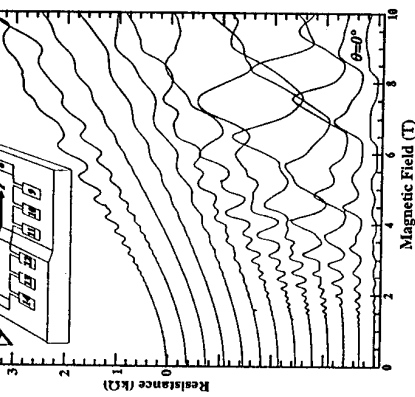


Fig. 1. Magnetoresistance at 1.4 K measured across a facet for a 40 μm mesa at angles between $\theta=0^\circ$ and $\theta=-90^\circ$. The curves are offset for clarity. The current is passed between probes 1 and 8 and the voltage measured at probes 4 and 5. The inset sketches the layout of the Hall bar.

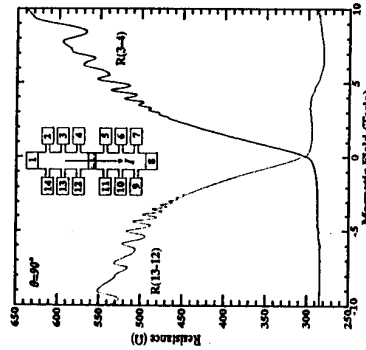


Fig. 4. Resistance measured between pairs of voltage probes on the planar region of the sample adjacent to the facet with the Hall resistance on the plane for a 5 μm mesa as a function of applied magnetic field at $\theta=-86^\circ$.

Fig. 5. The longitudinal and diagonal resistance measured across the facet and the Hall resistance on the plane for a 5 μm mesa as a function of applied magnetic field at $\theta=90^\circ$.

From Low to High Field : Magneto-Transport Properties of Electron Gases in Lateral Superlattices Grown on GaAs Vicinal Surfaces

L. Sfaxi, F. Petit, F. Lelarge, A. Cavanna and B. Etienne
Laboratoire de Microstructures et de Microélectronique (L2M)
C.N.R.S., B.P. 107, 92225 Bagneux Cedex, France

Abstract

Arrays of coupled quantum wires are obtained by growing a lateral superlattice in the channel of selectively doped heterojunctions. Before and beyond the magnetic quantum limit, new phenomena are observed. Our analysis of the low field magnetoresistance and of the quantum transport in the Landau bands gives a consistent value of the lateral potential amplitude.

Introduction

Intensive efforts are being made, which aim at fabricating electron gases, with a significant 1D or 2D lateral potential modulation [1,2,3,4], but with low enough disorder to allow the observation of quantum transport properties truly determined by phase coherency and by in-plane periodicity (i.e. revealing lateral minibands and band gap opening, singularities in the density of states,...).

A 1D potential modulation of the order of the Fermi energy, $E_F = (3.6 \text{ meV}) (n_s / 10^{11} \text{ cm}^{-2})$ in GaAs, at a lateral scale comparable to the Fermi wavelength, $\lambda_F = (79 \text{ nm}) (n_s / 10^{11} \text{ cm}^{-2})^{1/2}$, can be obtained by heteroepitaxy, making use of the lateral organization of group III species, such as Ga and Al, by the array of atomic steps on a misoriented substrate[5].

Accurate optical measurements of the linear polarization ratio and of the organization induced spectral shift in lateral superlattices (LSSL's) with a mean Al content $\bar{x} \sim 0.10$ and with a period between 8 and 32 nm indicate that a periodic lateral Al composition modulation of magnitude $\sim \bar{x}/2$ can be achieved[6]. This

results in a conduction band potential amplitude $V_{pp} \sim 500\bar{x} \text{ meV}$. We have grown 200 to 300 Å thick FLS's with $\bar{x} \sim 0.05$ before the barrier of selectively doped heterojunctions. With a Ga_{0.67}Al_{0.33} spacer thickness of 90, 100 or 200 Å, we get a 2D mean charge density n_s of 4.5, 4.3 or $1.8 \times 10^{11} \text{ cm}^{-2}$ respectively for samples A, B and C. The lateral periodicity, defined by the misorientation angle, being $L = 32 \pm 2 \text{ nm}$, the Fermi level lies in the second lateral miniband because $\pi/2L^2 < n_s < 2\pi/L^2$. The quantum wires are coupled because $L \sim \lambda_F$ and also $E_F \sim V_{pp}$ as we shall see. The resistivity tensor is strongly anisotropic[7], but V_{pp} cannot be easily determined from these transport measurements because of the wave vector dependence on the collision time. The electron elastic mean free path l_e , which is deduced from the resistivity component along the wires, ranges from 1.8 to 2.3 μm.

We present here magneto-transport

measurements which are analyzed in terms of

semi-classical open orbits and magnetic

breakdown at low field ($B < 0.5 \text{ T}$) and of 1D

Landau bands, unpolarized at medium field

($0.5 < B < 5 \text{ T}$) and strongly spin-polarized at high field.

At low field : magnetoresistance from open orbits and new resonances

The diagonal magneto-resistance (MR) is very anisotropic. When the current flows along the wires, it is either negligible (A and B) or strongly negative (C). This is explained by a weak boundary roughness scattering (which would give a positive MR) and by the values of λ_F and L (see ref.[7] for more detail). When the current flows across the wires, the MR is always positive at the beginning (weakly in A and B, very strongly in C) and reaches peak for $B_m = 0.3 \text{--} 0.5 \text{ T}$. It decreases (weakly in A and C, strongly in B), before the onset of the quantum oscillations. We try to ascribe the positive MR to the electron open orbits resulting from a band gap opening due to the periodic modulation and its decrease beyond B_m to magnetic breakdown [8]. With the value of V_{pp} estimated from the Shubnikov-de Haas oscillations (see below), we obtain the bandgap (4.8 to 5.3 meV) with a 2D self-consistent calculation of the band structure. A satisfying agreement for the MR amplitude and for the peak field B_m is obtained using a simple model [8,9] with the collision time (which is shorter than the transport time) as the only fitting parameter. The results are presented on Fig. 1 for sample C. Note that we compare the calculated MR with the experimental anisotropy ratio $R(B)$ (once the weak localization correction is subtracted) because the model does not take into account any anisotropy at $B = 0$. We get a correct prediction for the MR dependence with n_s . But we have no evidence for double or more complicated orbits beyond B_m [10].

In sample B, two sharp resonances at

0.15 and 0.30 T are observed below 0.5K and 0.2K respectively (fig.2). They look similar to those observed in antidot arrays [11] but cannot be the same effect because of the different type of modulation and of the different temperature range. We have no clear idea of their origin.

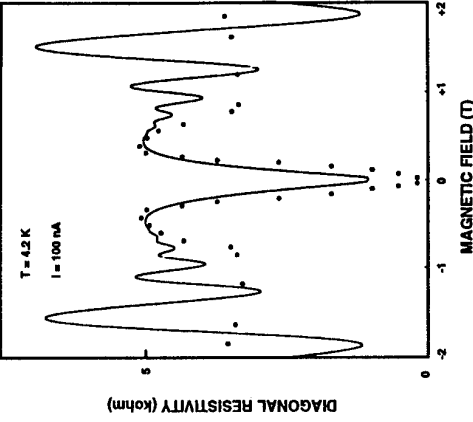


Fig.1 : Observation of the magnetoresistance in sample C (current perpendicular to the steps). The dots are the result of the calculation with a collision time equal to 3/4 of the transport time.

At high field : critical enhancement of the spin polarization

We restrict ourselves here to the analysis of the measurements on samples A and B which are similar, except at low field (see above) and around the Landau level filling factor $v=3$. Shubnikov-de Haas oscillations are resolved up to v larger than 30. Because 2 lateral minibands are partially filled at $B=0$, this indicates that the phase coherence extends at least over a diameter of 15 lateral periods ($\sim 0.5 \mu\text{m}$). As shown on Fig.2 for sample B, the remarkable fact is that no spin splitting is conspicuous below 5T, in spite of the low

temperature (60 mK) and the collision time which allows the oscillations to start below 0.5T. At higher field, the Landau levels are spin-split as usual (vanishing diagonal resistance, quantized Hall resistance). In sample A, the $v=3$ state is hardly resolved in the same conditions, but the data are just the same at larger and lower v . Increasing the temperature of sample B, we observe a decrease of the $v=3$ splitting (with an activation energy of 0.03 meV). While it weakens, some well defined structures (3 main sub-peaks) develop on the adjacent resistivity maxima. In sample A, only two sub-peaks are seen.

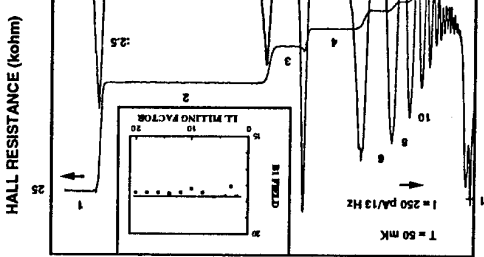


Fig. 2 : Shubnikov-de Haas oscillations and quantum Hall effect in sample B. The insert shows the variation of $B_1 = VB_v$ versus v .

Although it could seem paradoxical at first sight, the non-observation of any spin-splitting at medium field is in our eyes an indication that the samples are good, i.e. have strong potential modulation. It is known that

the observation of spin-splitting results from the strong exchange enhancement of the g factor Zeeman splitting [12]. It has been calculated recently [13] that potential gradients are able to destroy this enhancement because the energy dispersion of the partially filled Landau band prevents spin polarization. In addition we can note that the onset of spin-splitting occurs here approximately when the condition of having the cyclotron radius R_C equal to $L/2$ is fulfilled, i.e. for $B = (h/e)(2n_s/\pi L)^{1/2}$. This formula, which neglects the anisotropy of R_C , gives $B = 6.4T$, a value very close to $B_{v=3} = 5.85T$. The differences in spin-splitting between both samples indicates that the effect is not only determined by a geometrical condition but also that the strength of the modulation potential (stronger in A than in B) is a key parameter.

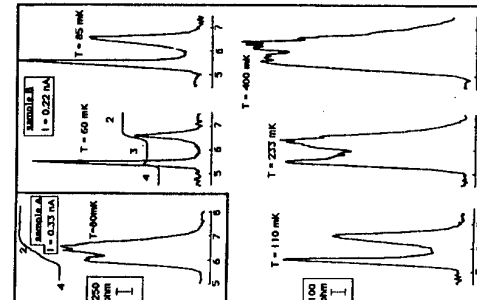


Fig. 3 : Shubnikov-de Haas measurements between 5 and 7 T in the insert at different temperatures around $v=3$. The Hall curves, if any, are shown off scale but the plateaus have the expected quantized resistance.

So far, we cannot explain this effect in details because we have calculated the Landau bands in a single electron model (in-plane screening and exchange are ignored). Assuming that the lateral potential is independent of the z coordinate (along the growth axis), we have done an exact 1D calculation [14] which takes fully into account the Landau level mixing (which cannot be neglected here because we have $V_{pp} > K_{0c}$). We have to explain altogether that : i) the position of the minima (which is well aligned with the center of the Quantum Hall plateaus) varies linearly as a function of B-1 with a variation smaller than 20% (see insert of Fig.x), ii) we do not see any modulation of the peak amplitude. This absence of Weiss oscillations [11] determines a lower limit to V_{pp} while the existence of Landau gaps determines an upper one [14]. A good compromise is obtained for $V_{pp} \sim 15$ meV (i.e. $\sim 300\bar{x}$). In addition, we get then a correct field value for the resistivity maxima and we are able to explain their asymmetrical shape.

This calculation of the Landau bands, although it neglects exchange, can be applied to understand the sub-peak structure which is observed when the spin-splitting around $v=3$ is weak. It obviously predicts only 2 van Hove singularities, which agrees well with sample A (probed area $20 \times 20 \mu\text{m}^2$). In B (probed area $50 \times 50 \mu\text{m}^2$), the 3 sub-peaks could be assigned to some lateral inhomogeneity and a superposition of 2 groups of 2. For both samples, a closer look at the data reveals the existence of several other faint structures which might be related to these inhomogeneities.

Conclusion

We have observed several new features in the transport properties of electron systems

laterally modulated at the scale of the Fermi wavelength. They demonstrate the high quality of low dimensional structures obtained by organized epitaxy. More experimental and theoretical work is needed to get an accurate measurement of the modulation and to assess the importance of disorder.

We thank F. Laruelle for discussions and F.I.B. Williams (Saclay) for the use of his dilution refrigerator. Partial support by DRET and by EEC (HCM network GOODSS) is acknowledged.

References

- W. Wegscheider, W. Kang, L.N. Pfeiffer, K.W. West, H.L. Stormer and K.W. Baldwin, Solid-St. Electron. 37, 547 (1994).
- Y. Nakamura, M. Tsuchiya, S. Koshiba, H. Noge and H. Sakaki, Appl. Phys. Lett. 64, 2552 (1994).
- G. Müller, P. Streda, D. Weiss, K. von Klitzing and G. Weimann, Phys. Rev. B50, 8938 (1994).
- T. Schliösser, K. Ensslin, J.P. Kotthaus and M. Holland (to be published).
- B. Etienne, F. Laruelle, J. Bloch, L. Sifxi, F. Lelarge, J. Cryst. Growth 150, 336 (1995).
- J. Bloch, U. Bockelmann and F. Laruelle, Europhys. Lett. 28, 501 (1994).
- L. Sifxi, F. Lelarge, F. Petit, A. Cavanna and B. Etienne, presented at MSS-VII, Madrid (1995).
- L.M. Falicov and P.R. Sievert, Phys. Rev. 138, A88 (1965).
- P. Streda and A.H. MacDonald, Phys. Rev. B41, 11892 (1990).
- T. Ebelbauer, A. Wixforth and J.P. Kotthaus, Z. Phys. B - Condensed Matter 64, 69 (1986).
- D. Weiss, Elektronen in künstlichen "Kristallen", Verlag H. Deutscher, Frankfurt a. Main (1994).
- T. Ando and Y. Uemura, J. Phys. Soc. Japan 37, 1044 (1974).
- A. Manolescu, R.R. Gerhardts, Phys. Rev. B51, 1703 (1995).
- L. Sifxi et al., unpublished.

Quantum Size Effects in the Optical Conductivity of Ultrathin Metal Films

L.A.Kuzik, V.A.Yakovlev
Institute of Spectroscopy, Russian Academy of Sciences,
Troitsk, Moscow reg. 142092 Russia

F.A.Pudonin
Lebedev Physical Institute, Russian Academy of Sciences,
Moscow, 117924, Russia

G.Mattei

Istituto di Metodologie Avanzate Inorganiche, CNR
Area della Ricerca di Roma, C.P. 10, Monterotondo Scalo (Roma), 00016, Italy

Abstract

Optical and electrical properties of ultrathin (0.15-7 nm) metal films (Nb, Cu, Mo, W, Ni and Ti) deposited by radio-frequency sputtering have been studied. Infrared (IR) reflectivity, transmittance as well as direct current (DC) conductivity measurements have been used to characterize these films. The periodic thickness dependence of the optical and DC conductivity was found. The periods of oscillations for different metals are of the order of the electron Fermi wavelength. Thus it was proposed that these oscillations are due to quantum size effects.

Low-dimensional objects are attracting increasing attention. Such objects exhibit unusual properties that are different from bulk properties of the original material. Ultrathin continuous metal films can be considered as such objects. Manufacturing of continuous metal films has become possible using radio-frequency sputtering for film deposition. Films obtained in this way are continuous and appear a metal behavior already when being of the order of several tenths of nm [1,2].

Sample Preparation

The samples were made by a high-frequency sputtering technique in set-up SPUTRON II. Layer deposition was fulfilled in a following way: a discharge was switched on, its parameters were chosen beforehand and were stabilized, then a sputtering of the targets carried out by applying a high-frequency power to one of the targets in a required sequence.

The deposition rate is defined by the power applied to the target, and its constancy was provided by high stability of the discharge parameters. The sputtering was carried out in Ar atmosphere (the Ar pressure $P = 10^{-3}$ Torr) in the vacuum chamber, previously evacuated to pressure better than 10^{-7} Torr. The temperature during the layers' deposition on substrates was not more than 80°C.

For determination of film deposition rate a layer was deposited for fixed time. The thickness of deposited layer was measured by interference microscope MII-4. We have checked an independence of deposition rate on layer thickness by comparison of thicknesses of film made using layer by layer deposition and of film deposited continuously. The deposition duration was the same in both processes. Then we have determined deposition rates for both processes. They have coincided within 2% precision.

The films were deposited onto crystalline quartz or silicon substrates. The film thicknesses were controlled by sputtering time. The metal film thicknesses are in the range 0.15-7 nm. The steps of thickness changing are 0.05-0.15 nm but through one set are constant. The rate of the film deposition depends on the step of changing. It was 0.02-0.05 nm/s. So the thickness determination accuracy was 0.02-0.03 nm. Immediately after metal deposition each film was covered by protective 4-5 nm thick Si film to prevent metal oxidation and film contamination.

Measurements

To characterize the thin metal (niobium, copper, nickel, molybdenum, tungsten, titanium) films we have used the reflectivity, transmittance, surface electromagnetic waves (SEW) infrared spectroscopic techniques as well as DC conductivity measurements. The optical and DC conductivity was found from these measurements.

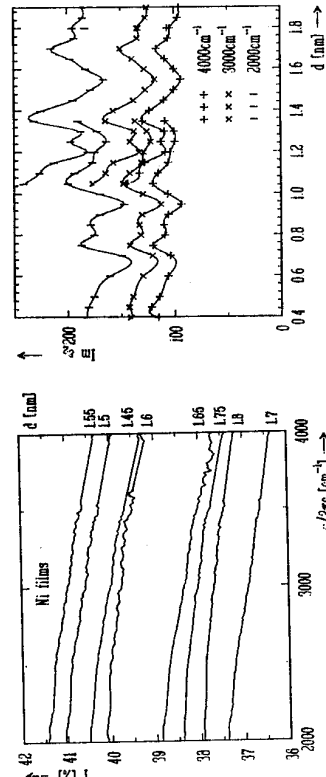


Fig. 1. Transmittance spectra of several nickel films of different thickness d on silicon substrates.

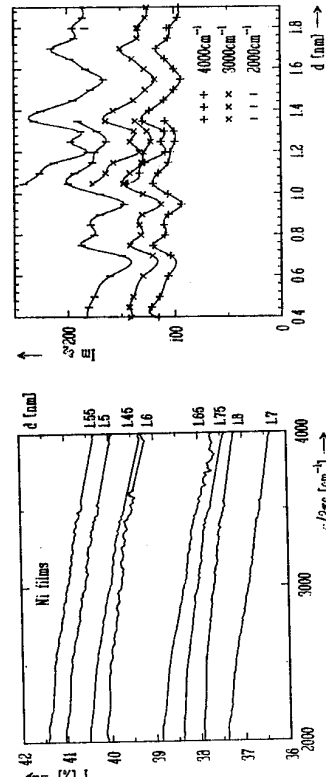


Fig. 2. Thickness dependences of $\text{Im } \epsilon_2$ for two overlapping sets of nickel films at three frequencies.

The film transmittance and reflectivity spectra were obtained using Fourier-transform spectrometers MICHELSON-110 (BOMEM) and FTS-40 (BIORAD) in the range 2500-5000 cm⁻¹ for quartz substrates and 500-5000 cm⁻¹ for silicon substrates. The transmittance spectra of some nickel film samples on silicon substrates are shown in Fig. 1. In this figure one can see that the uniform change of film thickness results in nonuniform change of spectra as a thickness function. This is a characteristic feature of transmittance and reflectivity spectra of all metal film sets.

The optical constants of such thin films can not be determined directly from transmittance and reflectivity spectra [3]. These spectra are not sensitive to the real part of the film dielectric function. The imaginary part of thin film dielectric function can be estimated using approximate formulas. For normal incidence on a film with dielectric function ϵ_2 and thickness d such that $4\pi\epsilon_2 d \ll 1$ on a substrate with dielectric function ϵ_3 in the transparency range of the substrate we can write [1]:

$$\text{Im } \epsilon_2 \approx \frac{R - R_0}{4 \pi d R_0} \left\{ \frac{1 + 2 R_J}{(\epsilon_3 - 1)(1 + 2 R_J)} - \frac{1 - R_J}{\sqrt{\epsilon_3 + 1}} \right\}^{-1} \approx \frac{T - T_0}{4 \pi d T_0} \left\{ \frac{2 R^2}{(\epsilon_3 - 1)(1 - R^2)} - \frac{1}{\sqrt{\epsilon_3 + 1}} \right\}^{-1} \quad (1)$$

where R_0 and R are reflectivity of substrate without and with the film, respectively, T_0 and T are the transmittance of substrate without and with the film, respectively, $R_S = R_0 / (2 - R_0)$.

The values of imaginary part $\text{Im } \epsilon_2$ for each sample were calculated from transmittance spectrum and then from reflectivity spectrum. The difference between these values was less than 5%. We have studied two different sets of nickel films on silicon substrates, which have common thickness range 1.0-1.4 nm. The thickness dependencies of $\text{Im } \epsilon_2$ for nickel films are placed in Fig. 2. The dependence character of both sets is the same. The main feature is their oscillating shape with period ~ 0.35 nm. The thickness dependencies of imaginary part for other metal films have similar oscillating character with period, depending on metal and independent on substrate. Lines are drawn through experimental points.

Fig. 3. $\text{Im } \epsilon_2$ thickness dependencies for four niobium films' sets made on quartz (Q1, Q2 and Q3) and silicon (Si) substrates. DC conductivity thickness dependence is given for Q1 quartz substrate. Lines are drawn through experimental points.

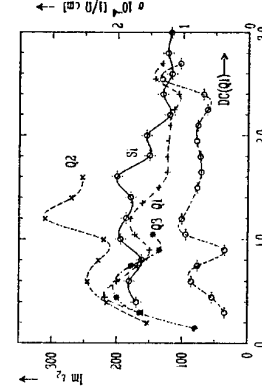


Fig. 3. $\text{Im } \epsilon_2$ thickness dependencies for four niobium films' sets made on quartz (Q1, Q2 and Q3) and silicon (Si) substrates. DC conductivity thickness dependence is given for Q1 quartz substrate. Lines are drawn through experimental points.

shape. The oscillation periods for all investigated metals are of order of some tenths of nm: for Nb - 0.6 nm, for Cu, Mo, W - 0.2 nm, for Ti - 0.15 nm.

For niobium films on quartz the DC conductivity measurements were performed using four points' technique [1]. The thickness dependence of DC conductivity for one of sets is shown in Fig. 3. Its character is similar to thickness dependence of $\text{Im } \epsilon_2$ of the same films.

Discussion

The periods of oscillations for film optical and electrical properties are of the order of electron Fermi wavelength in these metals. So we suggest that the oscillations concern with quantum size effects in metal film. The theory of quantum size effect in electric conductivity for semimetals was given by Sandomirskii [5]. According to this theory the free carrier momentum perpendicular to film surface is quantized, this results in oscillating thickness dependence of film electrical properties with period equal to a half of Fermi wavelength of free carriers. The quantum size theory for metals was developed in [6, 7, 8]. In these papers it had been shown that free electron density changes periodically with film thickness, the period equals to a half of electron Fermi wavelength. We suppose that this is the reason of oscillating thickness dependence of thin metal film optical properties. The temperature measurements of niobium films [4] confirm our suggestion.

Thus in the present paper we have given evidence of quantum size effect in thin metal film optics. It seems to be the common feature of thin perfect continuous metal films.

Acknowledgments

It is a pleasure for authors to acknowledge Professor G.N.Zhizhin for the fruitful discussions. The research described in this publication was made possible in part by grant from Russian Foundation for Fundamental Research.

References

- [1] L.A.Kuzik, Yu.Ye.Petrov, V.A.Yakovlev, G.N.Zhizhin and F.A.Pudonin, Physics Letters, A 171 (1992) 418
- [2] E.A.Alieva, L.A.Kuzik, F.A.Pudonin and V.A.Yakovlev, Sov.Phys.Solid State, 34 (1992) 1730.
- [3] H.Walter, Z.fur Phys., 105 (1937) 269
- [4] L.A.Kuzik, Yu.Ye.Petrov, V.A.Yakovlev and F.A.Pudonin, JETP 78(1994)114.
- [5] V.B.Sandomirskii, Sov.Pays.-JETP 25 (1967) 101
- [6] F.K.Seuttle, Surf.Si. 55 (1976) 427.
- [7] G.Govindaraj and V.Devanathan, Phys.Rev.B 34 (1986) 5904.
- [8] N.Thirivedi and N.W.Ashcroft, Phys.Rev.B 38 (1988) 12298.

Novel technique for fabrication of one- and two-dimensional systems.

V.Ya.Prinz, V.A.Seleznev, A.K.Gutakovskiy
Institute of Semiconductor Physics, pr. Lavrenteva, 13,
Novosibirsk 630090, Russia

A new technique for fabrication of nano- and atomic-scale device elements and quantum systems which cannot be obtained by any other technology is proposed. The technique is based on experimentally established possibility to create atomically sharp-edged cracks of desired length and direction in a given layer of heterostructure. Ultra-narrow (1 nm) and perfectly straight windows-slits in the GaAs layer-mask of semiconductor structures and ultra-thin (2 nm) semiconductor membranes have been fabricated for the first time.

1. Introduction

In recent years much attention was devoted to development of nanometer-scale fabrication technology. Conventional methods of nanolithography, though have been in progress for several years, have had a little success in breaking 5-10 nm linewidth barrier. For obtaining ultrasmall elements with atomic sizes, one needs an instrument permitting rupture of atomic bonds of substance at prescribed places without affecting neighbouring adjacent areas.

In this work as in our previous ones [1,2], a controllable crack formation was chosen as such an instrument. Crack-tips are known to serve as concentrators of elastic stresses arising in the bulk of substance upon its deformation. The stresses concentrated can exceed those in the bulk by million times and attain values sufficient for both breaking atomic bonds and providing successive propagation of brittle crack along a desired trajectory.

This work proposes a new concept and technique for fabrication of one- and two-dimensional systems and atomic-scale device elements which cannot be achieved by any other known technology. The concept is based on the experimentally established possibility to create atomically-sharp-edged cracks of a desired length, width and direction at a predetermined place in a given layer of structure.

The technology of controllable crack formation in the cap epitaxial layer-mask of A_3B_5 heterostructures has been developed and applied for the case when a GaAs/AlAs double-layer system grown in a single process on the main structure was served as a mask. The crack formation only in the cap GaAs layer was performed after local AlAs underlayer removing without affecting the main structure [3].

2. Fabrication process

Figure 1 shows schematically the technology for obtaining ultra-narrow windows-slits in the cap GaAs layer-mask of structure (Fig.1-a-e) and ultra-thin membranes (Fig.1-f-i). The stages of the windows-slits fabrication process are: b) fabrication of initial windows in the mask layer. It is possible to use here nanolithography or point indentation which induces an initial microcrack; c) selective removal of built-in underlying AlAs layer in the region located under the window. The HF-acid etchant which does not affect GaAs [3] was used for removing AlAs layer; d) lateral crack formation exclusively in the area of GaAs layer, free of any bonding with substrate. Due to the presence of initial microcracks in the GaAs layer, or stress concentrators in it, the tensile stresses needed to produce cracks in GaAs are so low that they can be provided by the pressure generated by gas bubbles arising upon the AlAs etching. After creating windows-slits in the mask, one can produce, for example, quantum wires by either evaporating a metal through the slits, or performing ion implantation, or etching; e) removal of the mask layer by dissolution of remaining AlAs coating. The process steps for fabri-

cating membranes are the following: f) fabrication of initial holes without any concentrator in the cap layer; g) selective removal of the supporting AlAs layer under the holes. Triangle topology produced by etching of AlAs (Fig.1,g) is typical for structures grown on faceted 311A surfaces of GaAs substrates; h) creation of an excessive pressure in the etched-out region, resulting in the formation of a crack in GaAs layer propagating along the boundary of the region. The lift-out process of the forming membranes occurs just after the crack development as depicted in Fig.1, g by arrow; i) the epitaxial film is being additionally undercut and lifted off the substrate. The obtained membranes appear in the form of a semiconductor wire with atomically-sharp edges.

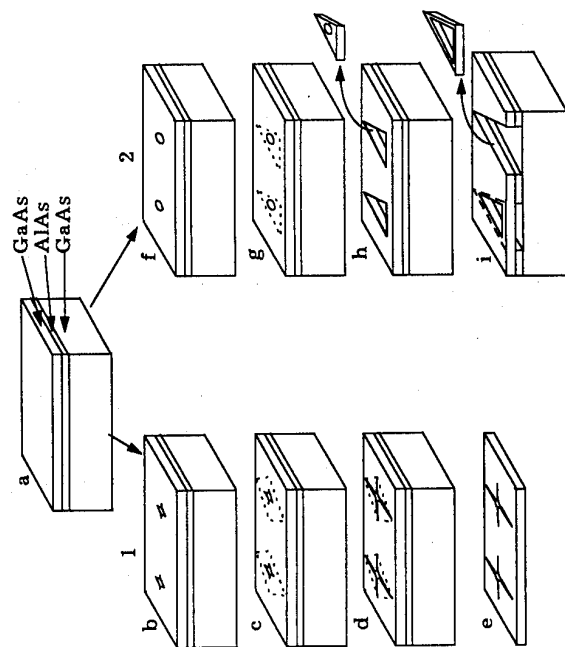


Fig. 1. Scheme of main stages of forming windows-slits in the cap GaAs layer-mask of the structure (a, b-e) and ultra-thin membranes (f-i).

3. Results

The above technological processes have been realized using epitaxially-grown A_3B_5 structures with AlAs layers of 1 to 50 nm thickness. The resulting GaAs masks with ultrathin windows-slits were lifted off the main structures and studied by high resolution transmission electron microscopy (HRTEM). Figure 2(a,b) presents photographs of a cap GaAs layer-mask with cracks of 2 and 8 nm width remaining practically constant over entire 250 μm crack length. It was found that windows-slits of 1nm width with atomically-sharp edges in the 0.1 μm thick GaAs cap layer could be obtained. To the best of our knowledge, such properties of the obtained windows as i) ultra-narrow width, ii)atomically-sharp edges, iii) practically constant width over the windows, iii) perfectly straight boundaries free of roughness cannot be obtained by any other technologies.

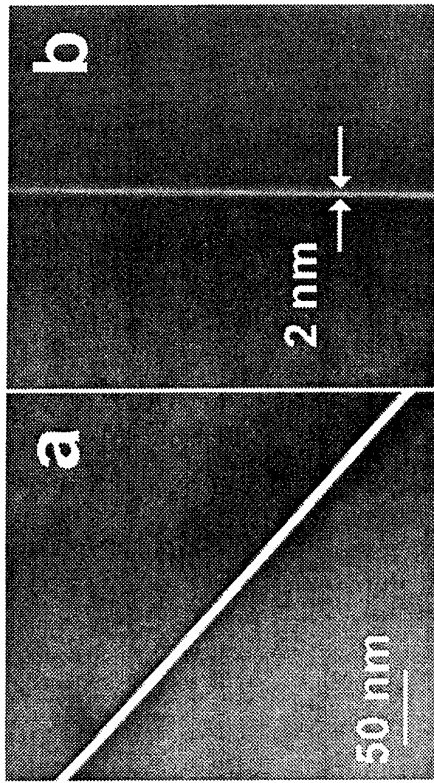


Fig. 2. HRTEM image of cap-GaAs layer-mask with controllable introduced cracks a) thickness of GaAs $0.25\mu\text{m}$; b) thickness of GaAs $0.1\mu\text{m}$

On decreasing the mask thickness (down to 20 nm), an possibility arises to reach an atomic-size windows.

Using these properties of cracks, we fabricated lateral tunnel diodes by cutting InAs, InSb, GaAs semiconductors layers and a layer containing GaAs quantum wires which were grown on 311A surfaces [4]. Figure 3 shows the measured tunnel current as a function of voltage applied to InAs and GaAs layers broken with an ultra-narrow crack ($<3\text{ nm}$). The upper inset shows a general view of a sample having a tunnel-junction length of $200\text{ }\mu\text{m}$. The obtained experimental results are indicative of the voltage at which sharp increase of tunnel current occurs. This voltage is different for different semiconductors and it equals 0.4 V for InAs, 1.4 V for GaAs (see dependencies 2 and 3 in Fig.3) and 0.2 V for InSb. These characteristic voltage are those at which it becomes possible for electrons to tunnel from the valence band into the conduction one (see the lower inset). The most remarkable properties of such lateral tunnel junctions are: stability of their I-V characteristics and possibility to vary, by using special mechanical influences, the slit width up to full connecting together of crack edges. A possibility is established experimentally to realize periodical transition from ohmic dependence 1 to dependence 2 (Fig.3) of InAs junction with accumulation of charge carriers at the InAs surface.

By using the above-described technology and possibility to grow by MBE layer with monolayer thickness control, ultra-thin 2 nm GaAs membranes were fabricated. A possibility was shown to lift-off these membranes and put them onto wide-band gap or metal substrates. In such a manner GaAs, InAs membranes and membranes containing a GaAs quantum wires were produced with areas $<10 \times 10\text{ }\mu\text{m}^2$. A possibility was shown of obtaining membranes with thicknesses ranging from 2 to 300 nm . It is important that the windows formed after removing of membranes as well as the membranes themselves had the atomically-sharp edges.

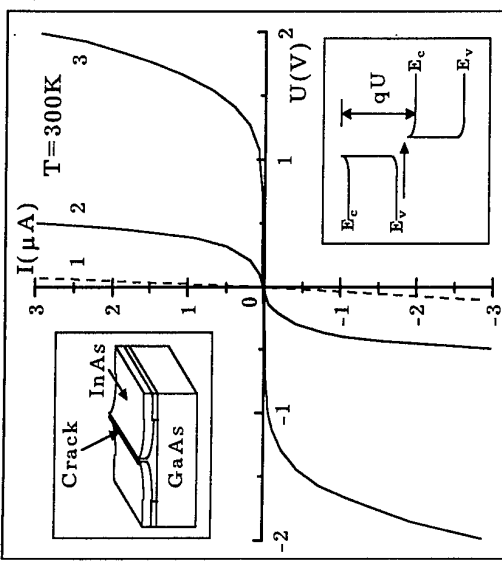


Fig.3. Current-voltage characteristics of lateral tunnel junctions. The upper inset shows a general view of a sample. The lower inset shows energy band diagram of tunnel junction under bias.

New maskless fabrication techniques for atomic-scale elements are also described. A tunnel diode was created by breaking with an ultra-thin crack a thin metal wire sputtered onto a AlB_5 heterostructure. The width of crack could be controlled by varying the external conditions.

The technology of controllable atomically-sharp-edged crack formation makes it possible to obtain device elements with super-low sizes, especially by using self-alignment technique.

It is shown that the proposed technique can be easily coupled with the ordinary submicron lithography, thus permitting grouped fabrication of atomic-scale objects.

Conclusion

The proposed technique opens up new possibilities for the production of device element and quantum systems with super-low sizes ($<1\text{ nm}$). This work was supported by the Russian Foundation for Fundamental Researches (Project N 95-02-04386)

References

- [1] V.Ya.Prinz, V.A.Selznev, A.K.Gutakovskiy in: Heterostructure in Science and Technology, International Symposium (Germany, Wuzburg, 1995) 112.
- [2] E.B.Gorokhov, A.G.Noskov, V.Ya.Prinz, Material Science Forum: in press
- [3] E.Yablomovitch, T.Gmutter, J.P.Harbison, and R.Bhat, Appl. Phys. Lett. 51 (1987) 2222.
- [4] V.Ya.Prinz, I.A.Panaev, V.V.Preobrazhenskii, and B.R.Simyagin, JETP Lett. 60 (1994) 217.

Coulomb Staircase with Negative Differential Resistance at Room Temperature for a Metal Tip/Metal Dot/Semiconductor Double Junction

P. Radojkovic, E. Hartmann, M. Schwartzkopff, E. Stefanov, and F. Koch
 Physics Department E16, Technical University of Munich
 D-85747 Garching, Germany

Abstract

Nanometer-sized Au dots have been fabricated on *p*-type Si(111) substrates by field-induced transfer of tip material in a scanning tunnelling microscope (STM). Positioning the STM tip on a very tiny dot (10–15 nm in diameter), equidistant steps with a spacing of several 100 mV and regions with negative differential resistance (NDR) are observed in the current-voltage characteristic. Numerical simulations confirm that the capacitance between tip and Au dot falls in the 10^{-19} F range. The occurrence of NDR might be explained by a leaking of excess carriers from the dot to the immediate surroundings.

1. Introduction

Extremely small-capacitance double-barrier tunnel junctions can be fabricated by a very tiny metallic island connected via a set of two resistances and capacitances R_1 , R_2 and C_1 , C_2 , respectively, to its leads. The tunneling process is no longer purely random in nature, but is governed by the fundamental macroscopic charging energy $e^2/2C$, where $C = C_1 + C_2$ is the total capacitance of the island to its environment. To limit the tunnel rate across each junction (determined by a RC product) the resistances R_1 and R_2 have to exceed the resistance quantum \hbar/e^2 ($\sim 25.8 \text{ k}\Omega$). For double-barrier junctions that accomplish these conditions, the time-averaged tunnel probability will be markedly reduced for voltages smaller than $V_C = e/2C$, a phenomenon referred to as “Coulomb blockade” [1]. In the case of strongly asymmetric junctions, a sequence of equidistant steps at voltages differing by e/C_1 (assuming $R_1 > R_2$) will appear in current-voltage (*I*-*V*) characteristics (Coulomb staircase or incremental charging effect) [1].

Recently, using a scanning tunneling microscope (STM), single-electron effects have been studied at temperatures ranging from approximately 1 K up to 300 K. Working in a liquid-helium bath, incremental charging effects have been observed at single nanometer-sized Al particles covering a thick oxidized Al layer [2] as well as at two serially coupled tunnel junctions consisting of an Au STM tip positioned on an In droplet which was deposited on a thin Al-oxide layer [3]. Coulomb staircase behavior in *I*-*V* curves have also been detected on single-crystal high- T_c superconducting layers [2,4]. For room-temperature observations of single-electron phenomena, ultrasmall double-barrier tunnel junctions have been realized by employing tiny isolated Au particles fabricated by electron-beam evaporation onto a 1-nm-thick ZrO_2 layer [5,6]. The tunnel oxide layer has successfully been replaced by coating Au particles with a thin organic film [7]. The evidence for incremental charging of a single molecule at room temperature has been documented by Nejoh [8].

In this article we demonstrate the observation of Coulomb staircase in conjunction with the occurrence of regions with negative differential resistance (NDR) at 300 K for an

STM tip/Au dot/Si substrate arrangement which forms a double-barrier junction. One junction is given by the gap between tip and Au dot (R_1 , C_1) and the second junction arises from the space charge region within the semiconductor surrounding the dot (R_2 , C_2). The latter is not a usual tunnel junction but represents a nanometer Schottky diode with a variable capacitance. In addition, the dot/substrate system is affected by the electric field exerted by the tip. Taking the respective geometrical and material properties into account, numerical simulations confirm our interpretations and provide quantitative explanation. The origin of the NDR might be explained by carrier leakage from the dot to the immediate surroundings as the metal/semiconductor structure is not a well-insulating system.

2. Experimental

Boron-doped (*p*-type) [111]-oriented Si wafers are employed with a resistivity of approximately 1 $\Omega \text{ cm}$ (doping concentration $\sim 10^{16} \text{ cm}^{-3}$). For preparing atomically flat and H-terminated Si(111)1x1:H surfaces, the samples are chemically treated in buffered HF (40% NH_4F). Au tips are prepared by electrochemical etching of a 0.25-mm-diam. wire in a 3:1 mixture of H_2O and concentrated HCl. From scanning electron microscopy micrographs, the typical tip radii are estimated to be $\sim 20 \text{ nm}$.

3. Results and Discussion

For the creation of a Au dot, the STM tip is positioned above the Si substrate and the distance to the sample surface is controlled by choosing appropriate values for tunnel current and tunnel voltage. Subsequently, a short voltage pulse is applied resulting in a field-induced transfer of tip material to the Si surface.

Fig. 1 displays an STM image with a tiny Au deposit in the central part which is fabricated by employing a single voltage pulse with an amplitude of +9 V for 100 ns. The dimensions of the Au dot are $\sim 13 \text{ nm}$ in width and $\sim 3 \text{ nm}$ in height. Actually, as a result of the finite tip size, the expansion of the imaged particle is less than the value determined from the STM topograph. The step-terrace structure of the Si wafer is resolved which results from its natural misalignment of 0.25° with respect to the exact [111] orientation (step height: 0.314 nm; average terrace width $\sim 70 \text{ nm}$).

Immediately after the deposition process, an *I*-*V* curve between -4 V and +4 V is recorded to ensure that the tip is located directly above the Au dot (fig. 2a). The overall *I*-*V* characteristic resembles a usual metal/*p*-type semiconductor Schottky diode with a positive voltage applied to the sample corresponds to the forward bias regime). In the case of nanometer-sized Au particles, a series of equidistant steps is superimposed with a step width of $\Delta V \sim 350 \text{ mV}$, which exceeds by far the thermal voltage of 26 mV at 300 K. This value is closely associated with a capacitance $C_1 \sim 5 \times 10^{19} \text{ F}$ ($C_1 \sim e/\Delta V$) – a magnitude which is also confirmed by our numerical simulations (see below).

To observe incremental charging effects, a further relation has to be accomplished that can be determined experimentally, namely $R_1 > R_2$. By establishing a point contact between tip

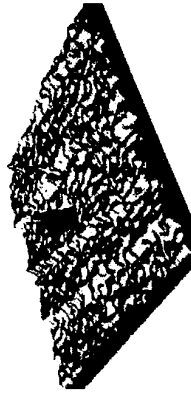


Fig. 1. Single Au dot fabricated by field-induced transfer of tip material. The dimensions of the Au deposit are $\sim 13 \text{ nm}$ in width and $\sim 3 \text{ nm}$ in height (scan area: $300 \text{ nm} \times 300 \text{ nm}$).

and Au dot, the I - V behavior is mainly dominated by the Au dot/semiconductor junction. At a voltage of +3 V, the resistance R_2 is $\sim 20 \text{ M}\Omega$. On the other hand, from Fig. 2, a voltage-dependent resistance R_1 can be estimated; at +3 V, R_1 is $\sim 300 \text{ M}\Omega$ which is considerably larger than R_2 and, consequently, represents the tunnel gap resistance.

At voltages larger than +3 V, regions with distinct negative differential resistance appear. We interpret this behavior to arise from a leakage of excess carriers which are stored on the dot either via states located at the Si surface or to the Si bulk material - an effect which is forced by the room-temperature conditions. As a result, the center of the time-averaged excess charge is displaced apart from the tip, leading to a decrease of the capacitance C_1 and, thus, to an enhancement of the charging energy. Although the applied voltage increases linearly with time, the current decreases. This behavior becomes more pronounced when the total amount of the excess charge on the dot is increased, according to higher voltage values. In addition, the appearance of the steps and the NDR depends on the ramping time (in the present case 1/400 s) and on the dot size. For Au deposits wider than $\sim 30 \text{ nm}$, recorded I - V curves show the overall Schottky behavior, but exhibit no particular structures. By varying the distance between tip and Au dot, characteristic changes in the I - V curves have been observed. This topic, however, is beyond the scope of this article. In fig. 2b, we depict the normalized numerical derivation of the upper I - V curve. The equidistant steps appear as periodic oscillations, and the regions with NDR are characterized by peak-crossing with the zero-level (circle). This effect is more often observed in the positive than in the negative voltage range. In the latter case, holes are transferred from the dot to the Si substrate. Possibly due to the lower mobility of holes in Si compared with electrons, the occurrence of NDR is suppressed. In further experiments, this phenomenon has yet to be studied in more detail.

Numerical simulations have been carried out by solving the 3D Poisson's equation with cylindrical symmetry. The rough tip shape is taken from scanning electron micrographs and the

dot profile from STM images. Owing to the convolution of the finite tip geometry, the lateral dimensions of the Au particle are overestimated. Hence, we used a reduced dot diameter of 10 nm compared with 13 nm as determined from fig. 1. For a doping concentration of 10^{16} cm^{-3} , the resulting barrier height for the Au/p-type Si "quantum" Schottky junction amounts to 0.35 eV. At a voltage of +3.5 V applied to the sample, C_1 is calculated to be $4.4 \times 10^{-19} \text{ F}$, in excellent accordance with the respective value derived from the I - V characteristic portrayed in fig. 2a. Under the same forward bias conditions, the resulting capacitance between dot and Si substrate is $2.7 \times 10^{-18} \text{ F}$. Consequently, the total capacitance amounts to roughly $C \sim 3.14 \times 10^{-18} \text{ F}$, which is somewhat beyond the maximum capacitance value allowed to observing single-electron effects at room temperature. Additionally, the tunneling component for the metal/semiconductor junction is negligible compared to the prevailing current contributions (thermionic emission, diffusion-drift). Thus, in this case, Coulomb blockade cannot be detected.

4. Summary

Using an STM tip/tiny Au dot/ p-type Si substrate arrangement, Coulomb staircase and regions with negative differential resistance have been observed in I - V characteristics at 300 K. The occurrence of equidistant steps of $\sim 350 \text{ mV}$ is associated with a capacitance between tip and the nanometer-sized Au dot of approximately $5 \times 10^{-19} \text{ F}$. This value is in excellent accordance with numerical simulations. The origin of regions with distinct negative differential resistance might be interpreted to arise from a leakage of excess carriers from the dot to the immediate surroundings.

References

- [1] H. Grabert and M. H. Devoret, *Single Charge Tunneling*, NATO ASI Series B, Vol. 294 (Plenum, New York, 1992).
- [2] P. J. M. van Bentum, H. van Kempen, L. E. C. van de Leemput, and P. A. A. Teunissen, Phys. Rev. Lett. **60** (1988) 369; P. J. M. van Bentum, R. T. M. Smokers, and H. Van Kempen, Phys. Rev. Lett. **60** (1988) 2543.
- [3] R. Wilkins, E. Ben-Jacob, and R. C. Jaklevic, Phys. Rev. Lett. **63** (1989) 801.
- [4] T. G. Miller, R. Reifenberger, M. W. McElfresh, D. W. Face, and W. L. Holstein, J. Low Temp. Phys. **94** (1994) 239; T. G. Miller and R. Reifenberger, Phys. Rev. B **50** (1994) 3342.
- [5] C. Schönenberger, H. van Houten, and H. C. Donkersloot, Europhys. Lett. **20** (1992) 249.
- [6] C. Schönenberger, H. van Houten, J. M. Kerkhof, and H. C. Donkersloot, Appl. Surf. Sci. **67** (1993) 222; C. Schönenberger, H. van Houten, and C. W. J. Beenakker, Physica B **189** (1993) 218.
- [7] C. Schönenberger, H. van Houten, H. C. Donkersloot, A. M. T. van der Putten, and L. G. J. Fokkink, Phys. Scr. T **45** (1992) 289; D. Anselmetti, T. Richmond, A. Baratoff, G. Borer, M. Dreier, M. Bernasconi, and H.-J. Güntherodt, Europhys. Lett. **25** (1994) 297; M. Dorogi, J. Gomez, J. Henderson, C. P. Kubik, R. P. Andres, R. Reifenberger, APS March Meeting, March 20-24, 1995, San Jose, California, USA.
- [8] H. Nejoh, Nature **353** (1991) 640.

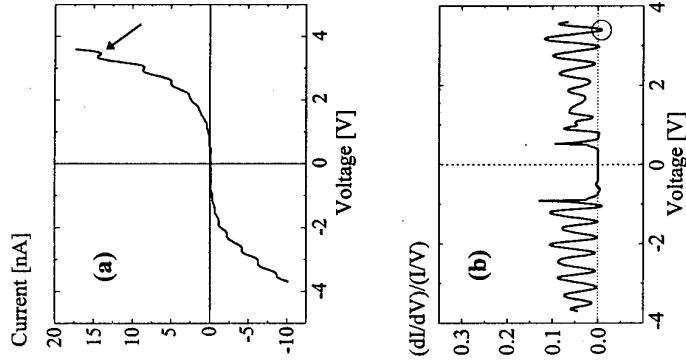


Fig. 2. (a) Current-voltage characteristic obtained on the Au dot shown in fig. 1, unveiling equidistant steps of $\sim 350 \text{ mV}$ and the occurrence of regions with negative differential resistance (NDR) (arrow). (b) Normalized numerical derivation of (a) showing periodical oscillations and the NDR regions where peaks intersect the zero-level (circle).

SUBMITTED FOR POSTER PRESENTATION

Semiconductor band-switching induced by single-electrons on a metal island

J.W.G. Wildoer^{1,2}, A.J.A. van Roy², C. Harmans¹ and H. van Kempen²

¹*Department of Applied Physics and DMEES, Delft University of Technology, POB 5046, 2600GA Delft, Netherlands*

²*Research Institute for Materials, University of Nijmegen, Toernooiveld, 6525ED Nijmegen, Netherlands*

Scanning tunneling spectroscopy allows the study of the local surface electronic density-of-states (DOS) with sub-atomic lateral resolution. In common metallic systems the electron density and the DOS at the Fermi energy are large. This leads to a negligible effect of an external electrostatic field on the surface electronic band structure. In contrast, in low density materials like (degenerate) semiconductors such a field affects the surface band-bending. STM at low temperatures allows the study of this band-bending employing the electrostatic field emerging from the STM tip.

We have studied the band-bending induced by the direct field from an STM tip and the field resulting from the (tip controlled) addition of single electrons onto a nearby small metallic island. This island is weakly coupled to the semiconductor and capacitively coupled to the tip, leading to strong charging effects which regulate the exchange of charge to the island in single electron units. The intricate interplay between the tip and the island leads to a *continuous* bending of the conduction band edge induced by the tip and a *stepwise* bending resulting from the addition of one electron to the island.

The experiment is performed on an in-situ cleaved n-InAs (110) surface in vacuum at 4K, with a metallic grain of ~ 3 nm size at the surface. STM topographic images at constant (positive) tip voltages clearly show the atomic lattice. In addition however these reveal a remarkably *sharp change in the local DOS*, visible as a circularly shaped area around the island. The diameter of the circle depends on the tip voltage. This band switching is attributed to the stepwise change of the charge residing on the small island, induced by the capacitive coupling of the tip to the island.

The experiments provide a unique direct way to study the effect of electrostatic fields on the band structure, in particular allowing the study of screening in low density electron systems and its associated length scales.

This work is supported by the Dutch Foundation of Fundamental Physics (FOM).

Magneto-optical spectra in a doped 2-dimensional system with periodic lateral modulation

Marcos S. Tavares^{1,2} and C. Tejedor²

¹ Departamento de Física, Universidad Federal de São Carlos, São Carlos, SP 13565-905, Brazil.
² Departamento de Física de la Materia Condensada, Universidad Autónoma de Madrid, Cantoblanco, Madrid 28049, Spain.

ABSTRACT

In this work we have adapted the Mahan-Nozières-De Dominicis formalism to study the characteristics of both emission and absorption spectra of a doped two-dimensional system at zero temperature and under both a perpendicular magnetic field and a periodic lateral modulation. Since the electron-hole interaction depends on the hole coordinates, we have analysed how the hole position modifies both emission and absorption spectrum for filling factor $\nu = 1$ and $\nu = 1/2$. *****

I. INTRODUCTION

Two dimensional (2D) doped system under both perpendicular magnetic field and a weak periodic lateral modulation potential has been the subject of great interest from both experimental and theoretical point of view [1]. The lateral modulation potential introduces a perturbation on the Landau level energies which can be treated by first order perturbation theory provided the amplitude of the modulation is small compared with typical energies of the system [2]. In particular, such systems have shown an interesting variation of the optical spectra with respect to the applied magnetic field intensity [3]. This reference is the motivation of the present paper. There, experiments performed under condition in which only the first Landau level is occupied, are reported. When the magnetic field increases new peaks, connected with the first Landau band, appear in both photoluminescence (PL) and photoluminescence excitation (PLE) spectrum. The energy difference between first Landau peak intensities is of the order of a few tenths of meV. Non-occupied states in the first perturbed Landau band exist ($\nu < 1$) and, therefore, transitions to such states are allowed. On the other hand, the Fermi edge singularity (FES) intensity in the PL spectrum decreases and a new

peak appears. It has been associated by the authors, with hot electrons at the top of the first perturbed Landau level. Temperature effects on the PL optical spectra have also shown a broadening and an increasing of the high energy peak when temperature increases, supporting the interpretation of the existence of hot electrons.

This paper is devoted to investigate the many-body effects, within the Mahan-Nozières-De Dominicis (MND) theory, in such systems. Particular attention will be devoted to the effect of the hole position on the optical spectrum. Such a theory has already been used to study the optical properties of 2D doped system at zero temperature [4]. The use of a complete finite temperature theory of such systems is beyond the scope of this paper. Our results show that the change of the hole position, with the electron-hole interaction approximated by a separable potential, allows the observation of the FES at zero temperature.

In Section 2 we present our theoretical scheme.

Section 3 is devoted to the results and conclusions.

II. THEORETICAL SCHEME

The single particle Hamiltonian of the problem is given by:

$$\hat{H}_0 = \frac{1}{2m^*} (\vec{p} - \frac{e}{c} \vec{A})^2 + V(\vec{y}). \quad (1)$$

\vec{p} is the 2D momentum operator and \vec{A} the vector potential that we take in the Landau gauge, $\vec{A} = (-B_0 \vec{y}, 0)$, $V(\vec{y}) = V_m \cos(G\vec{y})$, where $G = 2\pi/a$. V_m is the amplitude of the periodic potential with period a . As mentioned above $V(\vec{y})$ is treated as a first order perturbation so that the eigenvalues of the Hamiltonian are given by:

$$\epsilon_{n\vec{k}} = \epsilon_f + (n + \frac{1}{2}) \hbar w_c + \langle n\vec{k}|V(\vec{y})|n\vec{k} \rangle, \quad (2)$$

where ϵ_f is the 2D subband energy, w_c is the cyclotron frequency, and $\langle n\vec{k}|V(\vec{y})|n\vec{k} \rangle$ are the diagonal matrix elements of the periodic potential obtained from wavefunction:

$$\psi_{n\vec{k}}(\vec{x}, \vec{y}) = \frac{1}{\sqrt{L_x}} e^{i\vec{k}\cdot\vec{x}} \chi_{n\vec{k}}(\vec{y}), \quad (3)$$

where L_x is the size of the system in the x-direction, and the wavefunction in the y-direction given by:

$$\chi_{n\vec{k}}(\vec{y}) = \frac{1}{\sqrt{2^n \pi^{\frac{n}{2}} l_b n!}} \exp\left(-\frac{(\vec{y} - y_0)^2}{2l_b^2}\right) H_n\left(\frac{y - y_0}{l_b}\right). \quad (4)$$

l_b is the magnetic length, H_n a Hermite polynomial and y_0 is the classical orbit center coordinate which is related with x-direction wave vector \vec{k} by the relation: $y_0 = -l_b^2 \vec{k}$.

MND theory, within the determinantal approach [5], can be extended to finite temperature in order to study many-body effects in such systems. The absorption time-dependent response function is given by the current-current correlation function:

$$A(\tau) = Z_G^{-1} \text{Tr} \left\{ e^{-\beta \vec{K}} j_{\vec{K}}(\tau) \vec{j}_{\vec{K}}(0) \right\}. \quad (5)$$

Z_G is the grand-canonical partition function. The trace is taken over the configuration states of the abstract Hilbert space: $|n_1, \dots, n_\infty\rangle$, where $n_i = 0$ or 1 (fermions). $\beta = (k_B T)^{-1}$. \vec{K} is the grand-canonical Hamiltonian. The subindex \vec{K} in the current operators means that such operators are in the Heisenberg picture. Following the steps of the determinantal approach algebra, one can write eq.(5) as follows:

$$A(\tau) = Z_G^{-1} e^{(\tau+\beta)N_p} \sum_{n_{\vec{k}}, n'_{\vec{k}'}} M_{n\vec{k}} M_{n'\vec{k}'} \times \left\{ \sum_I e^{(\tau-\beta)E_I} F_{n\vec{k}, n'\vec{k}'}^I(\tau) \right\} \quad (6)$$

where:

$$F_{n\vec{k}, n'\vec{k}'}^I(\tau) = \det \left\{ \phi_{p_1, p'_1}(\tau) \right\} \times \left\{ \phi_{n\vec{k}, n'\vec{k}'}(\tau) - \sum_{p_1, p'_1} \phi_{n\vec{k}, p_1}(\tau) \phi_{p'_1, n'\vec{k}'}^{-1}(\tau) \right\}.$$

We must point out that in the MND theory the only perturbation is from the conduction electrons interacting with the transient potential of the valence hole. This transient is assumed to be switched on infinitely fast. The theory studies how the non-interacting electron system responds to the potential suddenly switched on in the valence

band. In principle, this non-interacting electron system approach does not describes everything in the real system. However, in the presence of magnetic field, exchange and Coulomb-hole contributions to electron self-energies in 2D gases, cancel out to each other, apart from a constant factor [9]. This suggests that a description of the system in terms of free-particle wavefunctions, could be adequate because the constant factor should not affect essentially to the wavefunction shape.

III. RESULTS

We have used the above theory with the two lowest Landau levels. All the energies are given in units of $\hbar\omega_c$. In order to clarify the discussion on the spectra, we show in figure 1 the Landau bands perturbed by the periodic potential.

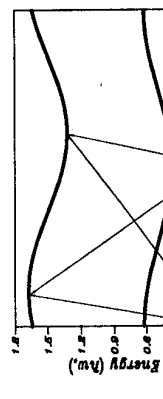


FIG. 1. Dispersion relation of Landau levels perturbed by a periodic potential. For the periodic potential we take: $V_n = 15 \text{ h}\omega_c$ and $a = 1000 \text{ \AA}$, and for the magnetic field $B = 3.5 T$.

Fig. 2A shows the PLE calculated spectra for two values of the hole Y-coordinate: $y_h = 0$ (solid line) and $y_h = a/2$ (dashed line). When $y_h = 0$, the hole is closer to the states at the top of the second perturbed Landau level than to the states at the bottom. Since the filling factor is $\nu = 1$, there is only one asymmetric peak. This asymmetry appears because two peaks, coming from transitions to the bottom and the top of the second Landau bands, become together. Transition to states at the top of the second band is favoured by the hole position. On the other hand, when $y_h = a/2$ the hole is closer to states at the bottom of the second Landau level and then, the lowest energy peak intensity domi-

nates. In the same figure there is also a blue-shift when the hole position is changed. This is due to hole self-energy effects. Single particle transitions involving the second perturbed Landau level extremes are shown in FIG. 1 by arrows.

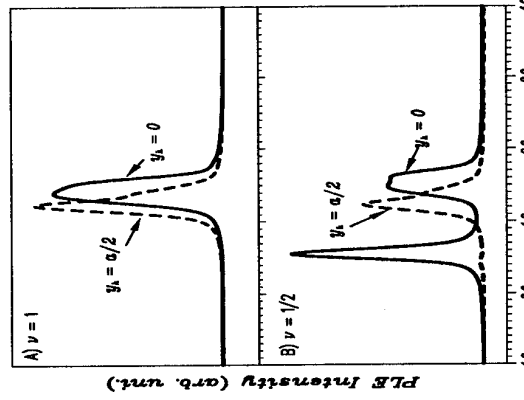


FIG. 2. PLE spectra for filling factor $\nu_h = -0.03 \hbar\omega_c$. The other parameters are the same than in FIG. 1. Hole coordinates are $y_h = 0$ for the solid line, and $y_h = a/2$ for the dashed line.

FIG. 2B shows the PLE spectrum for filling factor $\nu = 1/2$. Solid line shows the PLE spectrum for $y_h = 0$. Now, an extra peak appears since there are empty states at the first perturbed Landau level. At such position the hole is just at the maximum of the first perturbed Landau level. Then, this hole position implies a maximum peak intensity. On the other hand, when $y_h = a/2$, a small transition probability to states at the maximum of the first Landau level, occurs. The peaks corresponding to the second Landau level, present the same characteristics discussed in the $\nu = 1$ case. However,

more pronounced. This suggests that both the hole coordinate and the filling factor variation have the same effects on the hole self-energy. A more detailed hole self-energy study will be clarified in a future publication.

FIG. 3 shows the PL spectrum for $\nu = 1$ (fig. 3A) and for $\nu = 1/2$ (fig. 3B). The position $y_h = 0$ is just at the maximum of the first perturbed Landau level and, $y_h = a/2$ is at the minimum of such band (see fig. 1). The two FES intensities in FIG. 3A are the same, because the density of states have peaks with the same intensity at the extremes of the first Landau level.

both a small blue-shift and a strong intensity decrease at the high energy peak. The blue-shift occurs because Fermi energy shifts down when the filling factor decreases so that the FES energy position changes. On the other hand, the decrease of the FES intensity appears because there are no occupied states at the top of the first Landau band so that the recombination of electrons from the Fermi level with hole at $y_h = 0$ is an indirect one.

In conclusion, we have analyzed, within MND theory, how the hole coordinate can modify the magneto-optical spectrum when the electron-hole potential is approximated by a separable form. Our zero temperature results show that direct and indirect transitions in the k-space are allowed both in the PLE and PL spectra. The finite temperature formalism is the subject of future studies.

This work has been supported in part by the CICYT of Spain under contract MAT-94-0982-C02-01 and by the European Community under contract CIPX-CT92-0062. M.S.Tavares would like to thank CAPES-Brazil for the financial support.

- [1] U. Wulf, V. Gudmundsen and R. R. Gerhardt, *Phys. Rev. B* **38**, 4218 (1988), and references therein.
- [2] R. R. Gerhardt, D. Weiss, and K. v. Klitzing, *Phys. Rev. Lett.* **62**, 1173 (1989).
- [3] J.M.Calleja, A.R. Goñi, A.Pinczuk, B.S.Dennis, J.S.Winer, L.N. Pfeiffer and K.W.West, *Phys. Rev. B* **51**, 4285 (1995).
- [4] Pascale Hawrylak, *Phys. Rev. B* **44**, 3821 (1991); *Phys. Rev. B* **44**, 6262 (1991) and *Phys. Rev. B* **44**, 11296 (1991).
- [5] M. Combescot and P. Nozières, *J. Physique (Paris)* **32**, 913 (1971).
- [6] G. D. Mahan, *Many-Particle Physics* (Plenum, New York, 1981), Third edition, p. 754.
- [7] G.D. Mahan, *Phys. Rev. B* **21**, 1421 (1980).
- [8] These integrals are done following reference 4.
- [9] S. Katayama and T. Ando, *Solid State Communications* **70**, 97-101, (1989); and T. Uenoyma and L.J. Sham, *Phys. Rev. Lett.* **65**, 1048, (1990).

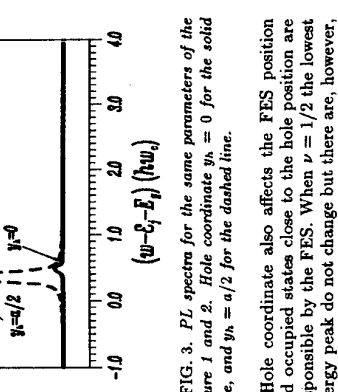


FIG. 3. PL spectra for the same parameters of the figure 1 and 2. Hole coordinate $y_h = 0$ for the solid line, and $y_h = a/2$ for the dashed line.

Hole coordinate also affects the FES position and occupied states close to the hole position are responsible by the FES. When $\nu = 1/2$ the lowest energy peak do not change but there are, however,

MAGNETO-OPTICAL STUDIES OF LATERALLY MODULATED NANOSTRUCTURES GROWN ON GaAs VICINAL SUBSTRATES

S. Huant¹ and B. Etienne²

¹High Magnetic Field Laboratory, MPI/PKf and CNRS
BP 166, 38042 Grenoble Cédex 9, France

²Laboratoire de Microstructures et Microélectronique (L2M), CNRS
92225 Bagneux Cédex, France

We report on cyclotron resonance measurements of laterally modulated two-dimensional electron systems grown on GaAs vicinal substrates. In a heterojunction modulated by a fractional AlAs layer, an anomalous cyclotron-intersubband coupling is observed which is due to the lateral potential modulation. In lateral-surface superlattices, oscillations in the position and in the linewidth of the cyclotron resonance are observed. It is shown that this is the result of the lifting of Landau degeneracy in the superlattice potential, i.e., the formation of Landau bands. The magnitude of this potential is determined from our experiments. Additional absorption features are observed above the cyclotron resonance which we tentatively ascribe to magnetoplasmons at $q = \frac{2\pi}{a}$ (a = lateral periodicity).

Nanostructures grown on GaAs vicinal substrates are promising self-organised low-dimensional electronic systems. Vicinal substrates which are slightly misoriented with respect to the (001) crystallographic direction exhibit atomic steps at the surface with a lateral periodicity depending on the vicinal angle (160 Å for 1°). This allows to grow various types of nanostructures such as fractional lateral-surface superlattices. Recently, the structural quality of these vicinal structures has been significantly improved as evidenced from atomic-force-microscopy studies of the structures grown at L2M.

Here, we discuss some of the far-infrared (FIR) magneto-optical properties of modulation doped vicinal structures. The main goal of our work is to understand how the lateral potential modulation will change the one-particle magneto-optical response of the 2D electron system as compared to an unmodulated system. The optical properties in the visible range [1] and the magneto-transport properties [2] of some of the structures studied here are discussed elsewhere in this conference.

Two samples representative from different types of lateral structures have been studied by means of FIR Fourier-transform spectroscopy in a magnetic field up to 13 T (T = 2 K). Sample 1 is formed by a GaAs/GaAlAs heterojunction with a fractional $(GaAs)_{7/8}/(AlAs)_{1/8}$ monolayer placed at the maximum of the ground-state wavefunction z_0 . The AlAs fractional layer covers $\frac{1}{8}$ of the period, the remaining $\frac{7}{8}$ are covered by pure GaAs. In sample 1, the carrier concentration is $1.9 \times 10^{11} \text{ cm}^{-2}$ and the vicinal angle is 0.5° (lateral periodicity $a = 320 \text{ \AA}$). Although expected to be organized along the atomic steps, the fractional pattern has been shown to be weakly ordered by the step array in this type of samples. It is rather made of anisotropic islands [3]. Sample 2 is a lateral-surface superlattice (LSS) obtained at the interface of a classic heterojunction by repeating a fractional $(Ga_{1-x}Al_xAs)_{1/2}/(Ga_{1-y}Al_yAs)_{1/2}$ pattern over 300 Å. In sample 2, the electron concentration is $1.8 \times 10^{11} \text{ cm}^{-2}$, the vicinal angle is 0.5°; the average Al content of the LSS is 5 %; both the Al-poor ($x \approx 0.04$) and Al-rich ($y \approx 0.06$) regions cover 1/2 of the lateral period. In contrast to sample 1, the fractional pattern is here periodic [4].

In sample 1, FIR spectra reveal a sharp cyclotron resonance (CR) with a typical full line width at half maximum of 0.7 cm^{-1} (the substrate was wedged to avoid interference effects). Apart from the cyclotron-intersubband coupling described below, the cyclotron resonance presents no anomalous behaviour. The effective mass extrapolated to zero field is found to be $m^* = 0.0712 m_e$. This agrees with our expectation from the average Al content $<Al>$ probed by the electron gas and

from the correction due to band-nonparabolicity. Indeed, within the triangular-well approximation (with an averaged electric field), we estimate $<Al> > 3.5 \%$ which gives a band-edge effective mass of $m_b^* = 0.0694 m_e$ [5]. There is a further mass enhancement due to confinement (band non-parabolicity) which we can estimate from Ekenberg's model [6]: $m_b^* = m_b^*[1 + (2\alpha + \beta)E_{av}]$, where $\alpha = 0.652 \text{ eV}^{-1}$ and $\beta = 0.731 \text{ eV}^{-1}$ are band and anisotropy parameters of the $Ga_{0.965}Al_{0.035}As$ alloy. With $E_{av} = E_o/3$ in the triangular well and $E_o = 31 \text{ meV}$ for the ground electric subband (see below), we obtain $m_b^* = 0.0709 m_e$, in very good agreement with the experiment.

At field strengths around 10 T, the CR peak broadens and splits in sample 1. This is due to the cyclotron-intersubband coupling [7] as confirmed by intentionally tilting the sample in the magnetic field by 13°. In contrast to regular heterojunctions, this coupling is already strong in a perpendicular magnetic field. This is due to the lateral modulation of potential $V(y, z)$ which depends on both the lateral coordinate y (steps are supposed to be aligned in the x direction) and the vertical coordinate z . This potential can be idealized as $V(y, z) = V_0 \delta(z - z_0) f(y)$, where $f(y)$ is one in AlAs and zero in GaAs, V_0 is the conduction-band offset between GaAs and AlAs. This potential couples the z -electric motion and the in-plane magnetic motion, even in a perpendicular field, thus producing a splitting of the CR peak at the intersubband energy E_{01} . E_{01} deduced from this experiment is $\approx 23.5 \text{ meV}$ as compared to 23.5 meV expected from the triangular-well approximation (we assume a background acceptor concentration of 10^{14} cm^{-2}). Even with an overestimate of $\approx 15\%$ of E_{01} due to the triangular-well approximation [8], E_{01} is $\approx 25\%$ lower than expected. Again, this is a manifestation of the potential modulation. The latter pushes up E_0 more than E_1 because the fractional monolayer is placed at the maximum of the ground-state wavefunction z_0 where the first-excited state is close to having a nodal plane. This suggests that an actual lateral potential height \tilde{V}_0 can be inferred from our experiment. For instance, treating $V(y, z)$ as a first-order perturbation, we obtain a decrease of E_{01} of $2.85\% \tilde{V}_0$ from which we estimate a lateral Al height of 18%. This could indicate a partial lateral demixing and/or a partial vertical segregation of the fractional monolayer in sample 1.

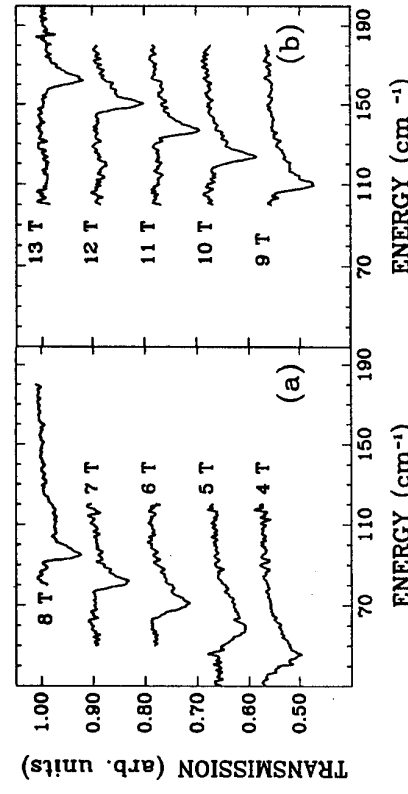


Figure 1. Magneto-transmission spectra of sample 2 for different magnetic field strengths indicated on the curves. Spectra have been normalized to the zero-field spectrum. T = 2 K.

We turn now to the CR in the LSS sample 2. Figure 1 shows typical CR traces of sample 2. It can be seen that the CR trace narrows considerably above 5 T, its linewidth at half maximum going from 21 cm^{-1} at 5 T to $\approx 7 \text{ cm}^{-1}$ above 7 T. A high-energy broad band is also clearly visible at 8 T and 9 T and, to a lesser extent, at some other field strengths (e.g. 12 T). Figure 2 gives the CR energy as a function of magnetic field which we compare with three predictions. The high-energy line has been computed with the band-edge mass of the $\text{Ga}_{0.95}\text{Al}_{0.05}\text{As}$ alloy: $m_b^* = 0.0712 m_e$; the medium line corresponds to a zero-field mass of $m_b^*/l = 0.0726 m_e$ corrected for nonparabolicity [6], and the low-energy line has been drawn with a field-dependent cyclotron mass (see Eq. (39) of [6]). It is clear from Fig. 2 that the CR energy in sample 2 deviates considerably from its classic behaviour in an unmodulated 2D electron gas in which a slight sublinear increase with field is observed due to band nonparabolicity (the dotted line would hold). While the experimental value agrees well at high field, the CR energy is well below the predicted value over a wide field range from 4 T to 9 T.

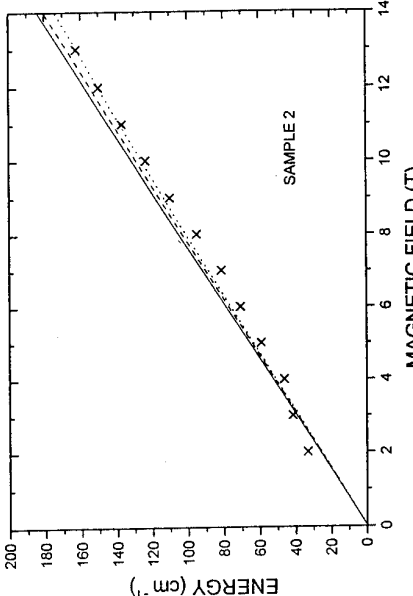


Figure 2. Field position of the cyclotron resonance in sample 2. The full, dashed and dotted lines have been computed with $m_b^* = 0.0712 m_e$, $m_b^*/l = 0.0726 m_e$ and a field-dependent cyclotron mass, respectively (see text).

This behaviour is linked to the formation of Landau bands (LB) in the conduction band of the LSS sample 2 (see e.g. Ref. 9 and references therein). In a uniform system subjected to a uniform magnetic field B , Landau states are degenerate with the centre of the cyclotron orbit. This gives rise to sharp Landau levels with a high degeneracy of eB/h per spin. An additional potential modulation in a plane perpendicular to the magnetic field lifts this degeneracy into LB. In the limit of weak lateral confinement $V_0 \ll E_F$, this Landau level broadening leads to the so-called low-field Weiss oscillations in the magneto-resistance which reflect the commensurability between the classical cyclotron orbit and the lateral period [10]. It is worth noting that similar oscillations have been predicted in the CR position and linewidth of such weakly modulated 2D systems [11] which, however, are by far too weak to be observed experimentally. In a strong magnetic field, a two-peak structure of the CR line has even been predicted due to the singular nature of the DOS in LB [12].

A detailed interpretation of the field dependence and linewidth of the CR in LSS is left for a future publication. Here, we wish to substantiate our interpretation in terms of LB formation by carrying out partial LB calculations for sample 2 (see Ref. 2 for details). We have assumed a lateral potential $V(y) = V_0[1 + \lambda \cos(2\pi y)]$, with $V_0 = 48 \text{ meV}$ for an average Al content of 5% in the LSS. Spin splitting and band non-parabolicity are neglected (we took m_b^* as effective mass). Three LB have been calculated for several λ at 7.5 T (LB filling factor $\nu = 1$) at which E_F is located low in the $N = 0$ LB. From the calculated LB, we estimate a CR energy which we find in excellent agreement with the experimental value for $\lambda = 0.14$. In fact, the CR energy at 7.5 T is quite sensitive to the modulation parameter λ . Choosing $\lambda = 0.2$ pushes the CR energy to 16 cm^{-1} above the experiment while choosing $\lambda = 0.125$ brings it to 5 cm^{-1} below the experiment. Thus, the potential modulation is accurately characterised from our measurements.

Finally, we comment on the high-energy broad band seen in Fig. 1 at $\approx 20 \text{ cm}^{-1}$ above the CR at 8 T. This additional feature is not expected from our LB calculations. A tempting explanation for it is the excitation of magnetoplasmon modes at $q = \frac{2\pi}{a}$ as was previously observed in a related quasi three-dimensional system, namely wide parabolic wells perturbed with periodic arrays of planar δ -like potentials [13]. Such an excitation is not allowed in a uniform system due to Kohn's theorem [14] which, however, is broken in a controlled way in the system of Ref. 13 and in our LSS sample. Our interpretation finds some support by looking at the dispersion curve of 2D magnetoplasmons at a filling factor $\nu = 1$ [15]. This dispersion curve has a roton-like minimum at $q \approx \frac{2}{l_c}$ (with correspondingly high DOS) with an energy $E \approx 0.15 \frac{l_c^2}{\epsilon}$ above the cyclotron energy (l_c is the cyclotron radius and ϵ is the dielectric constant). In our case at 8 T, we have $\frac{2\pi}{a} \approx \frac{l_c}{2}$ and $E \approx 15 \text{ cm}^{-1}$, in a reasonable agreement with the experiment. However, more measurements, in particular with other samples, are needed to reach any definitive conclusion.

References

- [1] Th. Melin and F. Laruelle, this conference.
- [2] F. Petit, L. Sizzi and B. Etienne, this conference.
- [3] J. Bloch, U. Bockelmann and F. Laruelle, Solid State Elec. 37 (1994) 529.
- [4] J. Bloch, U. Bockelmann and F. Laruelle, Europhys. Lett. 28 (1994) 501.
- [5] M. Zachau, F. Koch, G. Weinmann, and W. Schlapp, Phys. Rev. B33 (1986) 8564.
- [6] U. Eikenberg, Phys. Rev. B40 (1989) 7714; S. Huant, A. Mandray and B. Etienne, Phys. Rev. B46 (1992) 2613.
- [7] Z. Schlesinger, J.C.M. Hwang and S.J. Allen Jr, Phys. Rev. Lett. 50 (1983) 2098.
- [8] F. Stern and S. Das Sarma, Phys. Rev. B30 (1984) 840.
- [9] A. Manolescu and R.R. Gerhardt, Phys. Rev. B51 (1995) 1703.
- [10] D. Weiss, K. von Klitzing, K. Ploog and G. Weinmann, Europhys. Lett. 8 (1989) 179; R.R. Gerhardt, D. Weiss, and K. von Klitzing, Phys. Rev. Lett. 62 (1989) 1173; R.W. Winkler, J.P. Kotthaus and K. Ploog, Phys. Rev. Lett. 62 (1989) 1177.
- [11] P. Vasilopoulos and F.M. Peeters, Phys. Rev. Lett. 63 (1989) 2120.
- [12] A.V. Chaplik, Solid State Commun. 53 (1985) 539.
- [13] K. Karrai et al., Phys. Rev. Lett. 67 (1991) 3428.
- [14] W. Kohn, Phys. Rev. 123 (1961) 1242; Q.P. Li et al., Phys. Rev. B 43 (1991) 5151.
- [15] C. Kallin and B.I. Halperin, Phys. Rev. B 31 (1985) 3635.

Combined 1D–2D Intersubband Excitations and 1D Single-Particle Spectrum in Narrow Quantum Wires

G. Biese, C. Schüller, T. Kurth, and D. Heitmann
Institut für Angewandte Physik und Zentrum für Mikrostrukturforschung
der Universität Hamburg, Jungiusstraße 11, 20355 Hamburg, Germany.

P. Grambow and K. Eberl
Max-Planck-Institut für Festkörperforschung, Heisenbergstraße 1,
70569 Stuttgart, Germany.

Abstract

Electronic excitations in AlGaAs–GaAs quantum wires have been investigated by means of resonant inelastic light scattering. Besides a rich spectrum of 1D electronic excitations at low frequencies we find at higher frequencies transitions in the regime of the original 2D intersubband excitations. Interestingly we observe not only the original 2D intersubband excitations but additional modes ω_k in polarized scattering geometry. The experimental observation is that the frequencies of these modes obey the relation $\omega_k^2 = \omega_{2D}^2 + \omega_D^2$, where ω_{2D} is the vertical intersubband plasmon frequency and ω_D the lateral confined plasmon frequency. This relation suggests that the additional modes are combined 2D–1D intersubband excitations of collective charge–density type.

Introduction

In recent years electronic excitations in quasi-one-dimensional semiconductor heterostructures have been extensively investigated by various spectroscopy methods. Resonant inelastic light scattering allows the investigation of the wave vector dispersion of the measured excitations as well as the distinction between charge density (CDE), spin density (SDE), and single-particle excitations (SPE) by means of polarization selection rules.[1] Intersubband excitations in systems with many occupied subbands have been observed first by Weiner et al.[2] Engeler et al. found an anisotropic plasmon dispersion in multilayered systems where also many subbands are occupied.[3] Goriî et al. [4] and Schmeller et al. [5] investigated one-dimensional intrasubband and intersubband SDE, SPE and CDE in samples with only two occupied subbands. Very recently Strenz et al. have investigated the wave vector dispersion of SPE in quasi-one-dimensional systems with several occupied subbands.[6] Furthermore they reported for the first time the inelastic light scattering by electronic excitations in zero-dimensional systems. It has been found that in systems with many occupied subbands generally plasmons and SPE should dominate the excitation spectrum because exchange–correlation contributions to the electron–electron interaction are

expected to be very small [7, 8]. This is in contrast to systems in the extreme quantum limit where exchange–correlation interactions contribute significantly to collective CDE and SDE [5].

Starting from single-layered modulation-doped AlGaAs–GaAs quantum wells we have prepared quantum wires by deep mesa etching. It was possible to fabricate wires with very narrow widths down to 170 nm which still contain highly mobile electrons. This leads to the unique situation that, in contrast to earlier experiments [2–5], we have (a) a huge 1D quantization and (b) the 1D quantization occurs both in the lowest and first excited originally 2D subband. In such samples we observe not only 1D electronic excitations but at higher excitation energies we also find transitions in the regime of the original 2D intersubband excitations. Interestingly we find in this regime new additional modes in polarized spectra which do not exist in the unstructured sample and which we attribute to combined 1D–2D intersubband excitations of collective charge–density type.

Experiments and Results

We present results from quantum wire samples with 500 nm (800 nm) lateral period and 170 nm (270 nm) geometrical wire width. The samples were prepared by holographic lithography and reactive ion etching. The electron density and mobility of the unstructured 25 nm wide one-sided modulation-doped SQW at $T = 2$ K after illumination are about $8 \times 10^{11} \text{ cm}^{-2}$ and $3.5 \times 10^5 \text{ cm}^2/\text{Vs}$, respectively. The Raman experiments were performed at $T = 12$ K using a closed cycle cryostat. The energy of the exciting Ti:Sapphire laser was in the range of the effective E_0 bandgap of the unstructured SQW and the power densities were below 10 W cm^{-2} . The spectra were analyzed using a triple Raman spectrometer with a multi-channel diode array.

In Fig. 1 Raman spectra of the 170 nm wires are shown for different laser energies. Several modes can be observed. The modes labeled $\Delta n=0,1,2,\dots$ can be identified as 1D SPE since they occur in depolarized as well as in polarized scattering geometry. The notation p (s) means that the polarization direction was parallel (perpendicular) to the wires. Due to the observation of several 1D SPE in both samples we are able to characterize the lateral confining potential. If this potential is ideally parabolic, the energies of intersubband transitions with $\Delta n = 1, 2, 3$ should behave as $1 : 2 : 3$. Our experiments yield transition energies of about 25 cm^{-1} , 55 cm^{-1} , 87 cm^{-1} , 15 cm^{-1} , 32 cm^{-1} , 54 cm^{-1} for the 170 nm (270 nm) quantum wires. Thus the lateral potential is indeed nearly parabolic. Moreover, we have also performed microwave magnetic-depopulation experiments and find nearly the same confining energy (28 cm^{-1}). From these measurements we can also determine the linear density $N_L = 7.5 \times 10^6 \text{ cm}^{-1}$ and the Fermi energy $E_F = 210 \text{ cm}^{-1}$ assuming a parabolic lateral confinement. We find from the Fermi energy that 8 (12) 1D subbands are occupied. The measured wave vector dispersions of the observed 1D SPE are displayed in Fig. 2. The shaded areas mark the calculated single particle continua for 1D intersubband transitions using the parameters above. An additional mode is observed only in polarized spectra (lower part of Fig. 1). The dispersion of this mode is shown in Fig. 2 (filled triangles). This excitation can be identified as an 1D plasmon which is confined perpendicular to the wires and propagates freely along the wire.

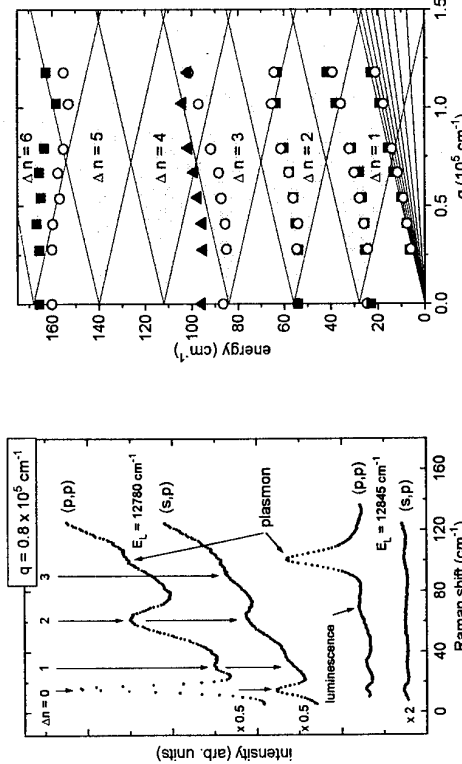


Fig. 1: Polarized and depolarized Raman spectra of the 170 nm wires for different energies E_L . The wave vector q is transferred parallel to the wire. In the upper part 1D intersubband excitations with different changes Δn of the 1D subband quantum number dominate the spectrum. The increasing background at higher energies is due to luminescence. In the lower part the 1D confined plasmon is most pronounced.

At higher frequencies we observe the originally 2D intersubband excitations which result from transitions from states $m = 0$ to $m = 1$ with change in the 1D subband quantum number $\Delta n = 0$ (Fig. 3). m is the vertical quantum number. The positions of the '2D' intersubband SPE (at about 215 cm^{-1}), CDE (at about 237 cm^{-1} in Fig. 3), and SDE (not displayed here) differ only slightly from those in the unstructured sample. But there is an additional mode at about 244 (254) cm^{-1} in the 170 (270) nm quantum wire sample (Fig. 3) which can only be excited in polarized geometry and which does not exist in the unstructured sample. The frequencies of these modes obey the relation $\omega_k^2 = \omega_{2D}^2 + \omega_{1D}^2$ where ω_{2D} is the frequency of the 2D intersubband CDE and ω_{1D} the lateral confined plasmon frequency. This relation suggests that the additional modes are combined 1D-2D intersubband excitations of collective charge-density type. If both the vertical and lateral confining potential would be parabolic, the frequency of the coupled mode should exactly follow this quadratic relation. In spite of the fact that at least the vertical potential is definitely not parabolic this relation is surprisingly well fulfilled. The combined excitations can only be observed in polarized spectra. The polarizations of incident and scattered light can either be parallel (p,p) or perpendicular (s,s) to the wires (Fig. 3).

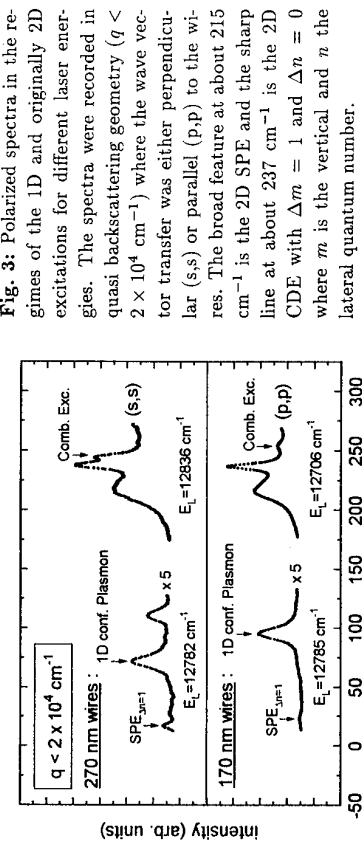


Fig. 3: Polarized spectra in the regimes of the 1D and originally 2D excitations for different laser energies. The spectra were recorded in quasi backscattering geometry ($q < 2 \times 10^4 \text{ cm}^{-1}$) where the wave vector transfer was either perpendicular (s,s) or parallel (p,p) to the wires. The broad feature at about 215 cm^{-1} is the 2D SPE and the sharp line at about 237 cm^{-1} is the 2D CDE with $\Delta m = 1$ and $\Delta n = 0$ where m is the vertical and n the lateral quantum number.

References

- [1] For an overview see: A. Pinczuk, and G. Abstreiter in: *Light Scattering in Solids V*, Topics in Applied Physics. Vol. 66, Eds. M. Cardona, and G. Güntherodt (Springer Berlin Heidelberg New York London Paris Tokyo, 1988) p. 153.
- [2] J. S. Weiner, G. Danan, A. Pinczuk, J. Valladares, L. N. Pfeiffer, and K. W. West, Phys. Rev. Lett. **63** (1989) 1611.
- [3] T. Egeler, G. Abstreiter, G. Weimann, T. Demel, D. Heitmann, P. Grambow, and W. Schlapp, Phys. Rev. Lett. **65** (1990) 1804.
- [4] A. R. Goni, A. Pinczuk, J. S. Weiner, J. S. Calleja, B. S. Dennis, L. N. Pfeiffer, and K. W. West, Phys. Rev. Lett. **67** (1991) 3298.
- [5] A. Schmeller, A. R. Goni, A. Pinczuk, J. S. Weiner, J. S. Calleja, B. S. Dennis, L. N. Pfeiffer, and K. W. West, Phys. Rev. Lett. **73** (1994) 3022.
- [6] R. Strenz, U. Bockelmann, F. Hirler, G. Böhm, and G. Weimann, Phys. Rev. Lett. **72** (1994) 1506.
- [7] R. Decca, A. Pinczuk, S. Das Sarma, B. S. Dennis, L. N. Pfeiffer, and K. West, Phys. Rev. Lett. **72** (1994) 16821.
- [8] P. I. Tamborenea, and S. Das Sarma, Phys. Rev. B **49** (1994) 16821.

Excitons in Complex Quantum Nanostructures

Garnett W. Bryant^{a,*}, Paul S. Julienne^a, Yehuda B. Band^b

^aNational Institute of Standards and Technology, Gaithersburg, MD 20899, USA

^bDepartment of Chemistry and Physics, Ben-Gurion University, Beer Sheva, ISRAEL

Abstract

A theory for excitons in complex quantum nanostructures with complicated geometries and strong coupling between nanostructures is presented. Effective mass models with screened Coulomb interaction give reasonable ground state energies for excitons in T-shaped quantum wires, coupled T-shaped quantum wires, and quantum dot quantum wells provided the effects of complex geometry are included. A sizable shift between excitation states in quantum wells and T-shaped wires occurs due to a forty percent enhancement in binding energy, confinement in the wire, and significant interwire coupling.

Introduction

As nanotechnology develops, nanostructures become more complex, with complicated geometries and strong coupling between nanostructures. For example, T-shaped quantum wires [1-3] are created at the intersections between orthogonal quantum wells that are made by growing a quantum well on the cleaved edge of a multiple quantum well system (see Fig. 1). Uniform, nmsize wires are formed by this all-growth nanofabrication. Experiments suggest that the exciton binding energy is enhanced by seventy percent when an exciton is localized to a T-shaped wire. As a result, these nanostructures are the first to lase from the exciton state [1]. Strongly coupled nanostructures will be easy to make because the coupling between T-shaped wires is determined by the separation, S_d , between the multiple wells and the width, L_c , of the overgrown well that couples the multiple wells. Complex multilayer quantum dots, called quantum dot quantum wells (QDQW) (see Fig. 1), can now be fabricated by chemically controlling the composition of each layer as the dot is grown layer-by-layer [4-7]. Inclusion of a well in the quantum dot band profile provides additional flexibility to tailor energy levels, charge distributions, and oscillator strengths.

An accurate theory for the optical properties of complex nanostructures must account for quantum confinement, valence-band mixing, and pair correlation in complicated spatial potentials, coupling between nanostructures, and different length scales for electron confinement, hole confinement, and correlation due to the different electron and hole masses. Our aim in this paper is to understand how the complicated geometry and strong coupling affect quantum confinement and pair correlation. We first find the single-particle states in the complex geometry of the nanostructure. For T-shaped wires, we find single-particle states in a discrete variable representation on a grid that covers the cross section of the wires. For QDQWs, we solve the single-particle radial Schrödinger equation for a radial quantum well potential using a transfer matrix approach. We then use these single-particle states to define electron-hole pair states for large-scale configuration-interaction (CI) calculations to account for correlation in these complicated geometries. For wires, we include correlation along the wire axis by representing the pair wavefunction for relative separation along the wire as a sum of Gaussian functions. A different sum is used for each lateral configuration included in the CI calculation. We use an isotropic-effective-mass model for the single-particle Hamiltonian and an electron-hole interaction screened by an average dielectric constant to simplify the calculations.

T-shaped quantum wires

We determine the excitation states of isolated T-shaped wires and coupled T-shaped wires to model experiments on wires formed by cleaved edge overgrowth. For the wires grown by

Wegscheider et al [1,2], the GaAs multiple wells and the GaAs coupling well are the same ($L_w = L_c = 7$ nm) and the barriers are Al0.35Ga0.65As. We consider structures (see Fig. 1) with up to five coupled wires to study interwire coupling. Fig. 2 compares the energy for a heavy-hole exciton in a 7 nm well with the energies for a heavy-hole exciton in an isolated wire and in coupled wires. The error bars show the expected exciton energy in a wire relative to the exciton energy in a well determined from the experimental energy difference between photoluminescence peaks of excitons in wires and wells. For widely spaced wires ($S_d = 38$ nm), the energy for a single wire is just above the experimental energy while the energy for coupled wires lies within the uncertainty. The energy of the coupled wires is lower because charge can sit in the overgrown well between the wires even when the wires are widely spaced. This energy reduction is larger for structures with an even number of wires since more charge can localize in the one central bond of a system with an even number of wires. Fig. 3 compares the exciton binding energy (difference between the exciton energy and the noninteracting pair energy) in an isolated wire and in coupled wires. The binding energy initially increases as the wire separation decreases because charge localization in the coupling well increases. For closely spaced wires ($S_d = 7$ nm), the exciton energy in coupled wires is further reduced because the exciton delocalizes across the coupled structure. When the exciton delocalizes, pair correlation is maintained with only a slight decrease in binding energy (see Fig. 3). Calculations for the single-particle states of a superlattice of T-shaped wires made from a superlattice of wells indicate that the exciton lowers its energy more from delocalization in a wire superlattice than in few-wire systems when the wires are closely spaced. This could account for the remaining discrepancy between the calculated energies and the experimental results for $S_d = 7$ nm obtained for systems with 22 wires [1,2]. Wegscheider et al. [1,2] estimated a 17 meV exciton binding energy in widely spaced wires. This is a seventy percent enhancement of the 10 meV exciton binding energy in a 7 nm well. We find less enhancement of the binding energy, not more than forty percent, depending on the number of wires and their separation. Recently, Sonnay et al. [3] investigated four T-wire nanowires, one made from wells larger than the structures studied by Wegscheider et al., one made from wells of comparable size, and two made from smaller wells. For the first two structures, we get reasonable agreement between our calculated energies and the measured energies. The agreement is worse for the smaller structures, where valence-band mixing not in our calculations should be more important.

Quantum dot quantum wells

We calculate the excitation states of the CdS/HgS QDQW studied by Mews et al. [4,5] to understand how the internal well affects pair correlation and charge localization. The inner CdS core radius is 2.35 nm, the outer CdS cladding layer is 0.8 nm wide. Fig. 4 compares the energies of the eight lowest optically active excitation states (angular momentum $L_{ex} = 0$) of QDQWs with a HgS internal well to the energies of uniform CdS QDs with the same dimensions. The calculated and experimental energies for the QDQW excitation ground state agree well even though a simple effective-mass model is used for QDQWs with internal wells that are only a few monolayers wide. The excitation energies redshift significantly, providing flexibility to tailor levels by an eV, when the lower bandgap HgS internal well is in the QDQW. The binding energy of the QDQW exciton ground state is less than the QD ground state binding energy and is also less than the binding energy of the first QDQW excited state. Strong confinement of the QDQW pair ground state (but not the first QDQW excited state) to the internal well inhibits correlation and lowers the QDQW ground state binding energy. In a small CdS QD, the heavy hole, is localized in the center of the electron cloud by the electron-hole interaction while the electron distribution is determined by quantum confinement. This strong hole localization reduces the electron-hole overlap, so the oscillator strength in a small QD is less for a correlated pair than for a noninteracting pair. The ground state oscillator strength is enhanced when the internal well is added to the QD because the electron and hole are localized to the same region, interaction-induced hole localization is suppressed, and the pair overlap increases toward the overlap for a noninteracting pair.

Conclusions

Effective mass models with screened pair interaction give reasonable ground state energies for excitons in GaAs/AlGaAs T-shaped quantum wires and CdS/HgS quantum dot quantum wells provided that the effects of the complex geometry on the quantum confinement and the pair correlation are accounted for. A sizable shift between exciton states in quantum wells and T-shaped quantum wires arises due to a forty percent enhancement in binding energy, confinement in the wire, and significant interwire coupling. Interwire coupling through the overgrown well is important even when the multiple wells are separated by more than 30 nm. In a multiple well system with no overgrown well, interwell coupling is insignificant for these large separations. In small CdS quantum dots the hole is strongly localized to the center of the electron distribution. Inclusion of a HgS well into a CdS quantum dot localizes the electron and hole to the same region of the dot. Pair correlation is suppressed by strong confinement to the internal well, but exciton oscillator strength is enhanced because the pair is localized to the same region. The amount of internal localization will depend critically on the composition of the quantum dot quantum well.

* Corresponding author. Tel: +1 301 975 2595, Fax: +1 301 975 3038, E-mail: garnettb@molphys.nist.gov

References

- [1] W. Wegscheider, L. N. Pfeiffer, M. M. Dignam, A. Pinczuk, K. W. West, S. L. McCall and R. Hull, Phys. Rev. Lett. **71** (1993) 4701.
- [2] W. Wegscheider, L. Pfeiffer, M. Dignam, A. Pinczuk, K. West and R. Hull, Semicond. Sci. Technol. **9** (1994) 1933.
- [3] T. Someya, H. Akiyama and H. Sakaki, Phys. Rev. Lett. **74** (1995) 3664.
- [4] A. Mews, A. Eychmuller, M. Giersig, D. Schooss and H. Weller, J. Phys. Chem. **98** (1994) 934.
- [5] D. Schooss, A. Mews, A. Eychmuller and H. Weller, Phys. Rev. B **49** (1994) 17072.
- [6] H. S. Zhou, I. Honma, H. Komiyama and J. W. Haus, J. Phys. Chem. **97** (1993) 895.
- [7] A. R. Kortan, R. Hull, R. L. Opila, M. G. Bawendi, M. L. Steigerwald, P. J. Carroll and L. E. Brus, J. Am. Chem. Soc. **112** (1990) 1327.

Figures

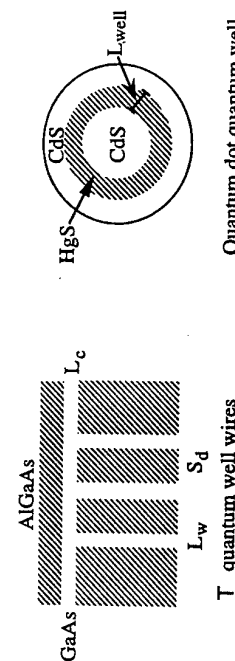


Fig. 1. Cross sectional view of coupled T-shaped wires and of a quantum dot quantum well.

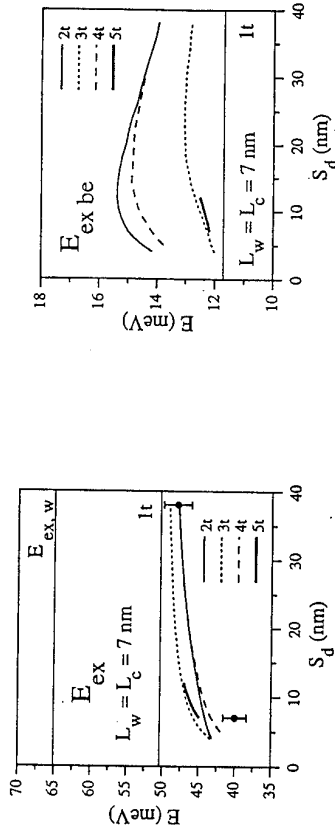


Fig. 2. Exciton energy in a 7 nm well, in an isolated wire, and in coupled wires. The error bars are experimentally determined energies for wires. Energies are relative to the GaAs bandgap.

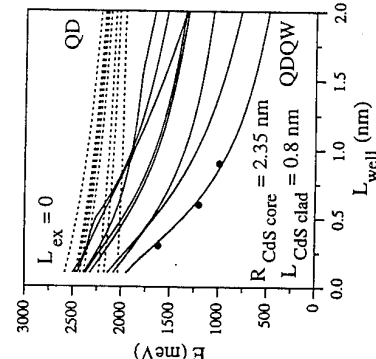


Fig. 3. Exciton binding energy in an isolated wire and in coupled wires. The error bars are experimentally determined energies for wires. Energies are relative to the GaAs bandgap.

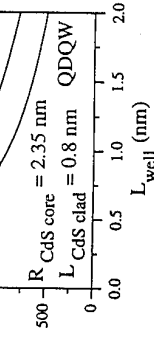


Fig. 4. Energies for the eight lowest optically active exciton states ($L_{ex} = 0$) in a CdS/HgS quantum dot quantum well (solid curves) and in a CdS quantum dot with the same dimensions (dotted curves). Energies are relative to the HgS bandgap. The points are experimental data for QDQW with 1, 2, and 3 monolayer HgS internal wells.

Exciton interaction effects in the Emission Spectra of Single Free-Standing InGaAs/GaAs Quantum Dots

R. Steffen, Th. Koch, J. Ostiniwo, F. Fallier, A. Forchel
Technische Physik, Universität Würzburg, Am Hubland, 97074 Würzburg, Germany

Abstract

We report on highly spatially resolved photoluminescence studies on individual free-standing InGaAs/GaAs quantum dots with diameters between 100 nm and 40 nm. Single dots with spacings of 20 μm between adjacent structures have been developed by low-voltage electron beam lithography and wet chemical etching. Photoluminescence spectra taken at low excitation densities systematically shift to higher energies with decreasing dot diameter. With increasing excitation power the emission includes additional peaks at higher energies due to transitions between the second and third quantized levels. Simultaneously a renormalization of the transition energies by up to 2 meV and a significant broadening of the spectra are observed. The energy renormalization and the spectral broadening are discussed on the basis of coulomb interaction between excitons inside the dot and carrier pairs in the surrounding GaAs barriers.

1. Introduction

Quantum wires and quantum dots have attracted growing interest during the last years because of the possibility to study fundamental physical effects which depend on the dimensionality of the confined electronic system. Furthermore, controlling the electronic properties by varying the lateral extensions of such systems makes quantum dots and wires very attractive for possible new device applications [1,2].

Usually, optical experiments on low-dimensional structures are carried out on large ensembles with inherent fabrication-induced size fluctuations and structural imperfections [3]. This leads to an inhomogeneous broadening of the spectra that masks basic effects like the observation of excitonic transitions between higher sublevels or the direct spectroscopic study of the δ -shaped electronic density of states in quantum dots. A challenging solution to this problem is the spectroscopic study of a reduced number of objects or even of an isolated quantum dot. One recent approach to achieve this deals with spatially resolved photoluminescence (PL) studies of island-like interface defects in GaAs/AlGaAs structures [4]. Other groups have studied strain-induced InAs islands grown on a GaAs substrate [5]. In those experiments dense series of sharp luminescence lines due to ground state transitions in several simultaneously detected quantum dots of slightly varying size have been observed. Yet, there are no reports in the literature so far on systematic studies of free-standing individual single dots of different sizes. In this paper we present results of PL experiments on individual free-standing InGaAs/GaAs single quantum dots with diameters between 100 nm and 40 nm which were defined by low-voltage electron beam lithography and wet chemical etching.

2. Experimental

The patterns were defined on MBE-grown $\text{In}_{0.14}\text{Ga}_{0.86}\text{As}/\text{GaAs}$ single quantum well layers (quantum well thickness 5 nm, 20 nm GaAs cap layer). This quantum well thickness was chosen in order to allow only one two-dimensional confined electron level, resulting in a single optical transition for the unpatterned sample. The dot patterns with dot diameters between 100

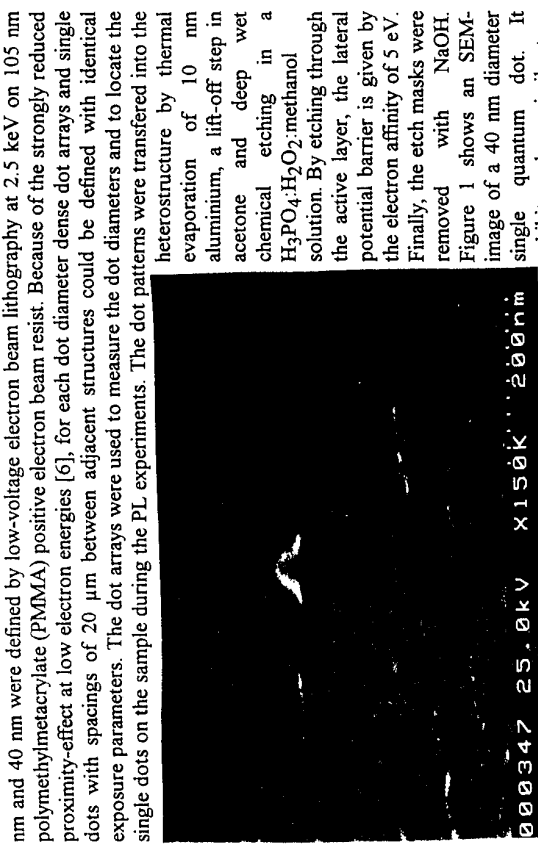


Fig. 1: SEM-micrograph of a deep etched 40 nm diameter InGaAs/GaAs single quantum dot.

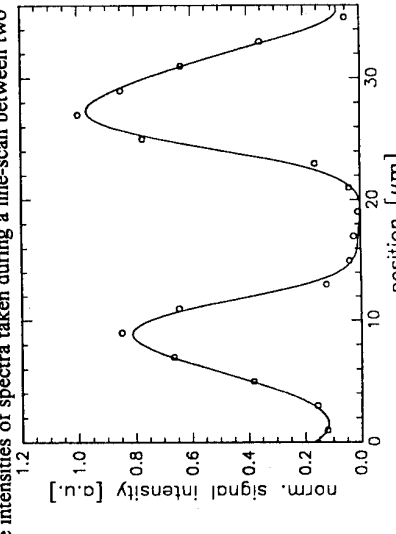
nm and 40 nm were defined by low-voltage electron beam lithography at 2.5 keV on 105 nm polymethylmethacrylate (PMMA) positive electron beam resist. Because of the strongly reduced proximity-effect at low electron energies [6], for each dot diameter dense dot arrays and single dots with spacings of 20 μm between adjacent structures could be defined with identical exposure parameters. The dot arrays were used to measure the dot diameters and to locate the single dots on the sample during the PL experiments. The dot patterns were transferred into the heterostructure by thermal evaporation of 10 nm aluminium, a lift-off step in acetone and deep wet chemical etching in a $\text{H}_3\text{PO}_4\text{-H}_2\text{O}_2\text{-methanol}$ solution. By etching through the active layer, the lateral potential barrier is given by the electron affinity of 5 eV. Finally, the etch masks were removed with NaOH. Figure 1 shows an SEM-image of a 40 nm diameter single quantum dot. It exhibits a shape similar to a bell. The etch depth is 50 nm.

For PL experiments with high spatial resolution, the samples were mounted in a cold-finger cryostate ($T=35$ K). An Ar-ion laser beam ($\lambda=514$ nm) was focused with a microscope lens to about 3 μm diameter on the samples. The luminescence signal was dispersed in a 0.25 m monochromator and detected with a liquid-nitrogen cooled CCD camera.

3. Results and Discussion

With this setup it was possible to detect luminescence from individual quantum dots. Figure 2 shows the normalized luminescence intensities of spectra taken during a line-scan between two 80 nm diameter single dots. Two maxima of the PL intensity can be observed with a spacing of 20 μm which is identical to the designed distance between two dots. The spectral intensity in the wide gap decreases to a few percent of the maximum value.

Fig. 2: Integrated spectral intensities at various positions along a linescan over two single dots



By varying the excitation density the dependence of the dot transitions on the electron-hole pair interaction can be studied. Figure 3 shows emission spectra for a 65 nm diameter dot for different excitation densities ($T=35$ K). In the low excitation case (200 nW for the lowest trace in the figure) the emission is due to individual excitons with different diameters in the dot ground state which sequentially recombine in the structures. When the laser power is increased a second dot level starts to be populated. In this case the emission is due to up to four electron-hole pairs (including spin). Simultaneously with the population of the second level the transition energy of the ground state and of the first excited state shift to lower energy. At the same time the emission spectra broaden significantly. This energy renormalization between about 1 meV for 100 nm diameter dots and 2 meV for 60 nm diameter dots as well as the dependence of the broadening on the excitation density are observed for all dots investigated.

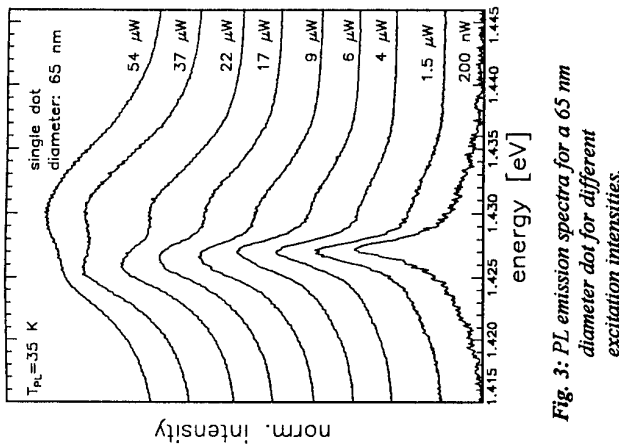


Fig. 3: PL emission spectra for a 65 nm diameter dot for different excitation intensities.

recombination is also responsible for the fact that no second dot level could be populated for small dots.

We attribute the observed red-shift of the luminescence lines to the Coulomb-interaction between excitons inside the active section of the quantum dot. In the literature biexciton correlation energies observed for quantum wells are reported around 1 meV [7], and because of the strong localization of excitons in quantum dots larger biexciton binding energies up to 5 meV are expected for zero-dimensional systems [8] of only a few Bohr radii extension. The energy renormalization observed in our spectra of about 1 meV for 100 nm diameter dots and about 2 meV for dots with 60 nm diameter are of the same order as those values. Taking into account the dependence of the biexcitonic transition intensity on the excitation power squared and the large inherent linewidth of our spectra, it is reasonable to assume biexciton formation with increasing correlation energy for decreasing dot diameters to be responsible for the excitation power dependent red shift of the emission lines. The origin of the large linewidth observed in our spectra may be due to an coulomb interaction of excitons in the dots with carrier pairs in the bottom GaAs barrier. The laser excitation takes place above the GaAs band gap. Because of the large difference of the dielectric constant between the vacuum surrounding the free-standing dot and the semiconductor ($\epsilon=12$) the exciting laser field is strongly repelled out of the dot [9]. This leads to a strong difference of the photogenerated carrier density between the free-standing dot and the homogenous GaAs bottom barrier with its high laser absorption, causing high electric fields across the active dot area. The broadening of the spectra is then naturally explained by temporal fluctuations of the electron-hole concentration surrounding the quantum dot.

References

- [1] Y. Arakawa, H. Sakaki, Appl. Phys. Lett. **40**, j939 (1982)
- [2] P. Ils, A. Forchel, K.H. Wang, Phys. Rev. **B50**, 11746 (1994)
- [3] M. Bayer, A. Schmidt, A. Forchel, F. Faller, T.L. Reinecke, P.A. Knipp, A.A. Dremlin, V.D. Kulakovskii, Phys. Rev. Lett. **74**, 3439 (1995)
- [4] K. Brunner, G. Abstreiter, G. Böhm, G. Tränkle, G. Weimann, Phys. Rev. Lett. **73**, 1138 (1994)
- [5] J.-Y. Marzin, J.-M. Gérard, A. Izraël, D. Barrier, G. Bastard, Phys. Rev. Lett. **73**, 716 (1994)
- [6] R. Steffen, F. Faller, A. Forchel, J. Vac. Sci. Technol. **B12**, 3653 (1994)
- [7] R.C. Müller, D.A. Kleinmann, A.C. Gossard, O. Munteanu, Phys. Rev. **B25**, 6545 (1982)
- [8] Y.Z. Hu, S.W. Koch, M. Lindberg, N. Peyghambarian, E.L. Pollock, Farid F. Abraham, Phys. Rev. Lett. **64**, 1805 (1990)
- [9] P. Ils, Ch. Gréus, A. Forchel, V.D. Kulakovskii, N.A. Gippius, G.G. Tikhodeev, Phys. Rev. Lett. **51**, 4272 (1985)

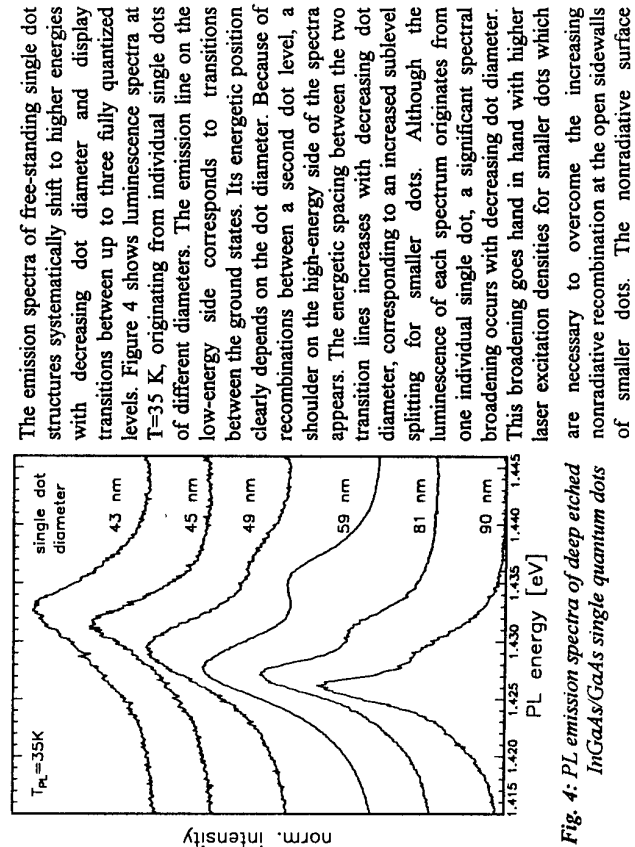


Fig. 4: PL emission spectra of deep etched InGaAs/GaAs single quantum dots

The emission spectra of free-standing single dot structures systematically shift to higher energies with decreasing dot diameter and display transitions between up to three fully quantized levels. Figure 4 shows luminescence spectra at $T=35$ K, originating from individual single dots of different diameters. The emission line on the low-energy side corresponds to transitions between the ground states. Its energetic position clearly depends on the dot diameter. Because of recombinations between a second dot level, a shoulder on the high-energy side of the spectra appears. The energetic spacing between the two transition lines increases with decreasing dot diameter, corresponding to an increased sublevel splitting for smaller dots. Although the luminescence of each spectrum originates from one individual single dot, a significant spectral broadening occurs with decreasing dot diameter. This broadening goes hand in hand with higher laser excitation densities for smaller dots which are necessary to overcome the increasing nonradiative recombination at the open sidewalls of smaller dots. The nonradiative surface

Radiative and Non-Radiative Recombination Times in a Single Quantum Well with Self-Assembled Islands

M.V.Marquezini¹, M.J.S.P.Brasil¹, J.A.Brun¹, P.Pool², S.Charbonneau²
M.C.Tamargo³

¹Instituto de Física, UNICAMP, Campinas, Brazil

²Institute for Microstructural Sciences, NRC, Ottawa, Canada
³Chemistry Dept., City College-CUNY, New York, USA

We present an investigation of the exciton dynamics in a single quantum well with self-assembled islands. We combine continuous-wave and time-resolved luminescence measurements as a function of the temperature to obtain quantitative information on the recombination processes in the well. The obtained radiative recombination times indicate that excitons are localized at low temperatures. We also discuss the evidences of inter-island transferring of excitons.

The understanding of the exciton dynamics in quantum wells (QWs) involves special effects as compared to the bulk analysis. The presence of interfaces breaks the translation symmetry along the growth direction and alters the exciton behavior. Besides, interface roughness affects the excitonic states. It is usual to divide the interface roughness in two scales as compared to the exciton diameter. Macroroughness features, usually called islands, are larger than the exciton diameter and originate multiple emission lines. Microroughness, interface fluctuations smaller than the exciton diameter, breaks the symmetry of translation along the QW plane. The in-plane dispersion is then replaced by a myriad of states with a variable degree of spatial localization and randomly distributed for each island. This gives rise to a broad emission band, where the lower energy states correspond to strongly localized excitons with relatively low mobility.

The InAs single QW investigated in this work was grown by Chemical Beam Epitaxy on a (100) InP substrate. The nominal integrated InAs thickness is 1.5 monolayers. However, macroroughness gives rise to as many as five well-resolved emission bands, labeled **a** to **e** in increasing order of energy, as shown in fig. 1. The observed energies correspond to InAs islands with thickness varying from 2 to 6 monolayers [1]. Continuous-wave (cw) photoluminescence (PL) measurements have been performed using a Ti:sapphire laser tuned at 920 nm, bellow de barrier bandgap energy. The inset on fig. 1 shows the temperature dependence of the integrated cw PL intensity for the four main bands. All bands show a thermal quenching, whose quenching edge shifts to higher temperatures as the island thickness increases. We also observe that the emission intensity slightly increases with temperature before its quenching. This effect is stronger for lower energy bands.

Time-resolved PL measurements were performed using the up-conversion technique [2]. We have used two synchronously pumped mode-locked dye lasers with 5 ps pulselwidth. A 920 nm dye-laser was used to excite the sample. The resulting luminescence was then mixed in a nonlinear crystal with a 620 nm dye-laser. The time resolution of our system is approximately 60 ps. We have measured the luminescence decay for the three main PL bands as a function of the temperature. We present in fig. 2 the time constants (τ_{PL}) obtained for each band assuming a single monoexponential decay. The interpretation of this time constant will be discussed below.

We analyze our results using a system of rate equations based on the following assumptions. The exciton formation time is neglected, since it is expected to be much shorter than the decay times obtained here [3]. We only consider excitonic transfer from thinner to thicker islands, given that the energy separation of around 70 meV between two bands makes the thermal occupation relatively small. We assume that the photogeneration of carriers by the bellow-bandgap excitation is independent of the island width and the temperature. The number of photogenerated excitons in a given island is then proportional to its areal density, f_i . The areal density of each island is estimated by the integrated luminescence intensity over the PL band immediately after the excitation pulse. Assuming that the radiative recombination time has approximately the same value for all islands at low temperature, this intensity gives the following proportionality ratios for the areal densities: $d:c:b:a = 10:7:3:1$. Island **e** is neglected because its areal density is more than one order of magnitude smaller than the others.

In our model, excitons created at island **d** can then be transferred to all possible neighbors islands with a characteristic transferring time, τ_{td} . On the other side, no neighbor island can transfer excitons to island **d**. For a constant photogeneration rate G , we thus obtain a cw steady density of carriers at island **d**:

$$N_d = r_d G \tau_{td} \quad (1)$$

and a transient solution $N_d(t)$, considering a delta-function-like generation rate:

$$N_d(t) = N_d(0) \exp\left(\frac{-t}{\tau_{td}}\right) \quad (2)$$

Fig. 1: PL spectrum at 2 K from the InAs/InP QW. The inset shows the integrated PL intensities as a function of temperature for the main four PL bands.

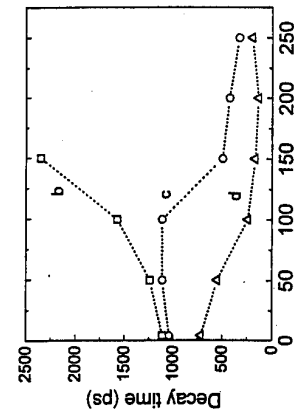
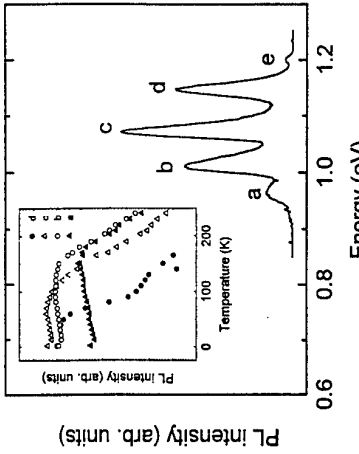


Fig. 2: Time constant obtained from the luminescence decays as a function of temperature. Labels **b**, **c** and **d** correspond to the emission bands in the PL spectrum.

where $\frac{1}{\tau_{td}} = \frac{1}{\tau_{rd}} + \frac{1}{\tau_{md}} + \frac{1}{\tau_{ad}}$, τ_{rd} and τ_{md} corresponding, respectively, to radiative and nonradiative times for island **d**. We remark that using this model, the PL decay for band **d** is expressed as a single exponential. Therefore, the time constant presented on fig. 2 for this band can be directly interpreted as τ_{ad} .

Since the cw PL intensity, I_{PL} , is proportional to N_d/τ_{td} , we can write the radiative recombination time as the ratio of two experimental results as:

$$\tau_{rd}(T) = I_0 \frac{\tau_a(T)}{I_{PL}(T)} \quad (4)$$

where the proportionality constant I_0 can be expressed as a function of $\eta(T=4K)$, the radiative efficiency at 4 K, as $I_0 = I_{PL}(T=4K)/\eta(T=4K)$. The results obtained for $\tau_{rd}(T)$ using different values of $\eta(T=4K)$ are presented in fig. 3. Since $\eta(4K)$ only acts as a multiplier factor, it does not change the temperature behavior of $\tau_{rd}(T)$. The radiative recombination time is almost constant up to 50 K, increasing with the temperature for higher temperatures. The low temperature behavior probably reflects a dominance of localized excitons, which are expected to have a radiative time nearly independent on the temperature. At higher temperatures thermal activation increases the ratio of free/localized excitons, that should result in an increase of τ_{rd} with temperature [4-6], as observed.

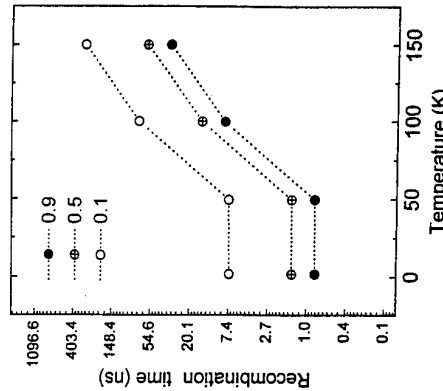


Fig. 3: Radial recombination time considering different values for the radiative efficiency at 4 K.

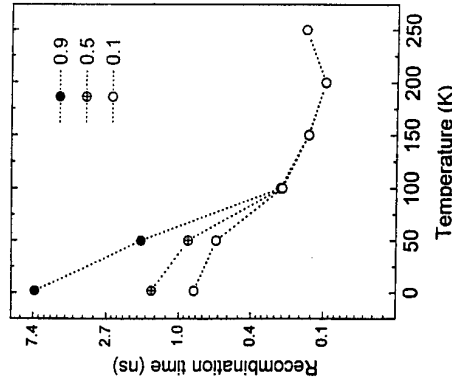


Fig. 4: Characteristic recombination time (τ_{loss}) for different values of the radiative efficiency at 4K.

where the rates R_1 and R_2 are constants. Fitting the data presented in fig. 4 using Eq. 5 gives E_a of the order of 17 meV. E_a does not vary significantly for different values of $\eta(4K)$, even so $\eta(4K)$ is not a simple multiplier factor for τ_{loss} . We can interpret E_a as the effective energy that localized excitons have to overcome to recover its usual mobility restrained by microroughness. As long as the exciton becomes free, it can reach the interface between neighbor islands and either be transferred or recombine non-radiatively at the foreseen centers at these interfaces. This means that the temperature activated loss, i.e. the second term on Eq. 5, may also comprise non-radiative and transferring losses of excitons.

The rate equation for the exciton density at island **c** is analogous to that of island **d**, but it has an additional term corresponding to excitonic transfer from island **d** weighted by the relative areal density of island **c** as compared to **a** and **b**. The additional term results in an extra negative exponential for the PL decay and a generation-like term in the cw solution. In order to make any quantitative analysis, we have to express the fraction of detrapped excitons from island **d** that will actually undergo transferring to neighbor islands. Since this information can not be obtained directly from our analysis, we will use it as an open parameter. We have obtained fairly good fits for the PL decay of band **c** considering a transferred fraction ranging from 0 to 30% of the total detrapped excitons. The radiative recombination time shows a temperature behavior qualitatively similar to that obtained for island **d**. The fitting procedure for the corresponding values of $\tau_{loss}(T)$ gave an activation energy that depends on the excitonic transferred fraction, going from approximately 50 meV for 0%, to 23 meV for 30%. The fact that the PL linewidths from all bands are similar suggests that the detrapping mechanism should not be very different from island to island. Besides, as we will discuss below, cw PL measurements gives further evidence of excitonic transfer. Therefore the lower energy activation cited above is more physically reasonable.

Quantitative analysis of the subsequent PL bands becomes unfeasible due to the large number of unknown parameters and the induced uncertainty related to parameters obtained from analysis of the higher energy bands. We however would like to remark that the slightly increase of the PL intensity just before its quenching, as observed in the inset of fig. 1, can only be explained by the generation-like term originated from the transfer of excitons from higher to lower energy bands. This effect then represents an evidence of excitonic transfer between islands.

In conclusion, our results show that the dynamics is dominated by localized excitons at low temperatures. As the temperature increases, detrapping of excitons takes place with an activation energy that can be estimated from our modeling. Our analysis suggests that a fraction of detrapped excitons actually undergoes inter-islands transferring.

- [1] M.J.S.P Brasil, R.E.Nahory, M.C.Tamargo and S.A.Schwarz, Appl. Phys. Lett. **63** , 2688 (1993).
- [2] J. Shah, IEEE J. of Q. E. **24**, 276 (1988).
- [3] B. Deveaud, T. C. Damen, J. Shah, C. W. Tu, Appl. Phys. Lett. **51**, 828 (1987).
- [4] J. Feldmann, G. Peter, E. O. Göbel, P. Dawson, K. Moore, C. Foxon, R. J. Elliott, Phys. Rev. Lett. **59**, 2337 (1987).
- [5] M. Gurioli, A. Vinattieri, M. Colocci, C. Deparis, J. Massies, G. Neu, A. Bosacchi, S. Franchi, Phys. Rev. B **44**, 3115 (1991).
- [6] R. Klann, H. T. Grahn, K. Fujiiwara, Phys. Rev. B **51**, 10232 (1995).

$$\frac{1}{\tau_{loss}(T)} = R_1 + R_2 \exp(-E_a / KT) \quad (5)$$

Since the mechanisms related to both, τ_{rad} and τ_{td} , result in the same effect, i.e. losses of photogenerated carriers from the island **d** with no radiative emission, we can not resolve their relative contributions. We then define the characteristic time, $\tau_{loss}(T)$, as $\tau_{loss}^{-1}(T) = \tau_{rd}^{-1}(T) + \tau_{md}^{-1}(T)$. $\tau_{loss}(T)$ can also be determined from our experimental results and is presented on fig. 4 considering different values of $\eta(4K)$. To achieve a quantitative analysis of this result, we consider that τ_{loss} may be constituted of two components, one term temperature independent and another comprehending a thermal activation E_a .

SPECTROSCOPY OF SINGLE NATURALLY-FORMED GaAs QUANTUM DOTS

D. Gammon, E.S. Snow and D.S. Katzer
Naval Research Laboratory
Washington DC 20375-5347

A photoluminescence study of the excitons localized in the quantum dots naturally formed by interface roughness in narrow GaAs quantum wells is presented. By reducing the number of dots probed in a resonant excitation measurement we study the spectra of single quantum dots. Extremely narrow linewidths for both the ground and excited states are measured. With such narrow lines it is possible to measure the thermal broadening due to acoustic phonons.

Interface roughness in narrow GaAs quantum wells tends to localize the excitons at low temperatures. In certain cases the system is then best thought of as a collection of quantum dots. These dots are defined by the large monolayer-high islands formed at the quantum well interfaces and may be expected to have lateral dimensions of $\sim 10^2\text{--}10^4 \text{ \AA}$, depending on growth conditions. The lateral potential discontinuities arise from the difference in well width of one monolayer and are about 20 meV for our samples. Recently the ability to optically probe single quantum dots which are naturally formed in narrow GaAs quantum wells through micron- and submicron-sized laser beams has been demonstrated.^{1,2,3} This development is exciting because it provides a method of removing the inhomogeneous distribution and studying directly the homogeneous properties of a single quantum dot. Furthermore, this can be done on very high quality samples without the damage associated with processing.

We have used a new, though similar, approach which allows us to probe systematically with spatial resolutions varying almost continuously from the macroscopic to the optical near-field. We excite and detect through a hole in an aluminum mask which is lithographically defined directly on the sample. We have measured photoluminescence (PL) and PL excitation spectra through holes which vary in size from 25 down to 0.5 μm in diameter (Fig. 1). With small enough hole size (depending on the dot dimensions and densities in a given sample) and with resonant excitation we are able to measure the excited state spectra of a single exciton in individual quantum dots.

The results from two MBE samples which were grown with growth-interrupts at the interfaces are discussed. The first has three GaAs

single quantum wells with differing well widths and 5 nm AlAs barriers. The spectra discussed here came from the quantum well closest to the surface (5 nm AlAs barrier and 14 nm GaAs cap). The second sample has five GaAs single quantum wells with differing well widths and 25 nm Al_xGa_{1-x}As barriers with a 50 nm GaAs cap. More growth details can be found in Ref. 4 and references therein. Electron-beam lithography and metal liftoff were used to open a series of small holes in a 100 nm-thick Al film which was deposited on the surface. The holes, ranging in diameter from 25 to 0.5 μm , were spaced sufficiently far apart to allow optical probing of a single hole. The PL was excited at 7 K through a given hole with either an Argon laser or a Ti:Sapphire laser, and the PL was detected from the same hole with a Dilor triple spectrometer and a CCD detector. The resolution of the PL measurements was determined by the spectrometer which has a limit of 30 μeV . The resolution of the PL excitation spectroscopy was determined by the laser linewidth which was 8 μeV . The exciting and detected light were linearly polarized along the (011) axes of the sample.

When the growth is interrupted at the interfaces of a quantum well the cations are able to migrate to the edges of monolayer-high islands. Under appropriate growth conditions these islands grow larger than the exciton Bohr diameter (20 nm) and the spectral lines in the PL spectrum split into doublets due to the resulting monolayer differences in well width. This splitting is clearly seen in the bottom spectrum of Fig. 1 which was taken with a large hole aperture of 25 μm . In this spectrum the two peaks arise from first heavy-hole excitons recombining in regions of the quantum well which have well widths of 15 or 16 monolayers (1 monolayer = 2.83 \AA). As the hole aperture is reduced the broad PL lines split into a decreasing number of much sharper lines. These lines arise from the quantum dots. Dots of different lateral size have different lateral confinement contributions to the energies. As the area of the sample which is probed is reduced the number of dots is also reduced and the inhomogeneous distribution breaks up into individual quantum dots. This happens primarily in the lower energy monolayer (16 mono.) for the following reason. The intensity of the lower energy monolayer is larger than the higher one because the excitons efficiently thermalize. In fact, the actual area or number of dots represented in this lower monolayer is an order of magnitude smaller (from excitation spectroscopy) than that in the higher energy monolayer. The excitation spectrum has been measured for each of the lines in one 1.5 μm aperture. An example for one quantum dot is shown in Fig. 2. We find that for the majority of lines the excitation spectra are unique. From this we deduce that the lower energy monolayer is best thought of as a dilute system of independent quantum dots.

In Fig. 2 is shown the excitation spectrum of a single quantum dot. Also shown is the PL spectrum with the laser energy in resonance with the second excited state. In addition to the ground state the first excited state is also seen to luminescence. The energy spectrum of the quantum dot shown in Fig. 2 can be understood in

Fig. 2 PL and PLE spectra of a single quantum dot from the GaAs/AlAs quantum well sample.

terms of the quantum states of a rectangular box confined by the monolayer steps at the interface. In the growth direction the quantum dot is strongly confined by the AlAs barrier with a quantum well width of 17 monolayers. This vertical confinement gives rise to large intersubband energies and we consider only the effect of lateral confinement on the first electron and heavy hole states. The lateral confinement arises from monolayer steps at the quantum well interfaces and the lateral dimensions are determined by the size of the island. The depth of the lateral potential well is given by the energy splitting between 17 and 16 monolayers and is 16 meV. To provide a rough estimate of the lateral dimensions of the quantum dot we perform a finite square well potential calculation in a separable approximation assuming a rectangular-shaped box and neglecting the Coulomb interaction. We assign the first excited state (E_1) to the second single particle electron and hole states in the long dimension of the rectangle and the first electron and hole states in the short dimension. The second excited state (E_2) is assigned to the first excited single particle states in the short dimension. From this assignment we calculate an approximate size of 750 Å by 550 Å for the quantum dot by fitting the first (E_1-E_0) and second (E_2-E_0) transition energies. We tentatively assign the higher transitions (E_3 and E_4) to the next allowed transitions which are the third single particle states derived from each of the two lateral dimensions.

Because we are measuring a single quantum dot the lines are homogeneously broadened. Because the linewidths are not sensitive to laser power under our experimental conditions the linewidth cannot arise from broadening due to other photoexcited excitations. However, we find that the linewidths of both excited and ground states of all the quantum dots in this quantum well close to the surface (160 µeV) are at least a factor of two larger than those derived from deeper quantum wells. This result is consistent with recent results on tunneling from near-surface quantum wells into surface states,^{5,6,7} and we assign the linewidths we measure for these quantum dots to lifetime broadening due to nonradiative recombination with states associated with the surface.

We have also studied a second sample with quantum wells deeper beneath the surface and with AlGaAs barriers. The ground state PL of one particular quantum dot as well as its corresponding excitation spectra are shown in Fig. 3. This sample was found to have much narrower linewidths. With such narrow lines it now becomes possible to measure the thermal broadening. The full-width-half-maximum (FWHM) of the ground state as a function of temperature is plotted in the inset to Fig. 3 as solid circles. With a spectrometer resolution of 30 µeV the ground state linewidth is not completely resolved and we have deconvoluted the line with the spectrometer response to obtain the open circles. This procedure leaves considerable uncertainty below 20K but has little effect at higher temperatures.

The thermal broadening of a zero-dimensional quantum dot at low temperatures arises

from absorption of acoustic phonons accompanied by the transition of the exciton into excited states. Because the lowest energy excited states are discrete the only phonons which can contribute are those with energies equal to the exciton transition energies. Therefore, the temperature-dependence of the ground state linewidth should go as the scattering rate into a given excited state (γ_1) times the number of phonons with that transition energy (E_{01}),

$$\Gamma(T) = \Gamma_0 + \sum_i \gamma_i n(E_{0i}, T), \quad (1)$$

where the sum is over all excited states of the exciton and $n(E_{0i}, T)$ is the Bose-Einstein factor. We also note that the low temperature linewidth of the first excited state is determined at least in part by the phonon emission rate into the ground state γ_1 : $[n(E_{01}, T) + 1] \approx \gamma_1$. Therefore, the measured linewidth of the first excited state of 35 µeV (inset to Fig. 3) gives an upper bound to γ_1 . This is true for each of the excited states. Taking these measured values for the γ_i as well as the measured E_{0i} we can calculate $\Gamma(T)$ from Eqn. (1). This is done and the results are shown in the inset to Fig. 3 using only one excited state, then two, and so on up to six at which point good agreement is reached with the data. Note that the only adjustable parameter is Γ_0 . The higher energy states become progressively less important. In particular, the "2D-continuum" starting at 11 meV above E_0 is not expected to contribute strongly at low temperature. Such good agreement implies that the excited state linewidths are dominated by relaxation into the ground state.

In conclusion, the spectra of single GaAs quantum dots naturally formed by the interface roughness in narrow quantum wells have been studied. With extremely narrow linewidths it has been possible to measure the temperature dependence of the linewidth which is shown to be consistent with a model using measured excited state energies and linewidths.

REFERENCES

1. A. Zrenner, L.V. Butov, M. Hagn, G. Abstreiter, G. Bohm and G. Weimann, Phys. Rev. Lett. **72**, 3382 (1994).
2. K. Brunner, G. Abstreiter, G. Bohm, G. Frankle and G. Weimann, Appl. Phys. Lett. **64**, 3320 (1994); Phys. Rev. Lett. **73**, 1138 (1994).
3. H.F. Hess, E. Betzig, T.D. Harris, L.N. Pfeiffer and K.W. West, Science **264**, 1740 (1994).
4. D. Gammie, B.V. Shanabrook, and D.S. Katzer, Appl. Phys. Lett. **57**, 2710 (1990); Phys. Rev. Lett. **67**, 1547 (1991).
5. Y.L. Chang, I.H. Tan, Y.H. Zhang, D. Bimberg, J. Merz and E. Hu, J. Appl. Phys. **74**, 5144 (1993).
6. V. Emiliani, B. Bonanni, C. Capizzi, M. Presilla, A. Frova, Y.L. Chang, I.H. Tan, J.L. Merz, M. Coloccia and M. Guaroli, J. Appl. Phys. **75**, 5114 (1994).
7. J. Dreybrodt, F. Daiminger, J.P. Reithmaier and A. Forchel, Phys. Rev. B **51**, 4657 (1995).

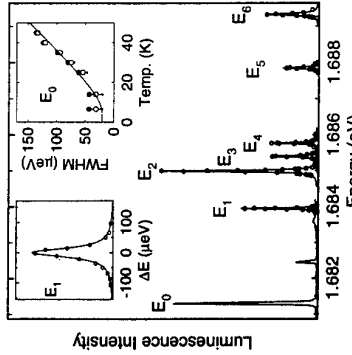


Fig. 3 PL and PLE spectra from the GaAs/AlGaAs sample. The left inset shows an expanded plot of the lineshape of the first excited state (E_1) from PLE. The right inset shows the temperature dependence of the ground state linewidth.

Effects of collective modes on single particle electronic excitations of semiconductor quantum wells and quantum dots

P. A. Knipp

Department of Physics and Computer Science, Christopher Newport University, Newport News, VA 23606-2998

Stephen W. Pierson, T. L. Reinecke*

Naval Research Laboratory, Washington, DC 20375-5347

(June 13, 1995)

We have studied the interaction of collective excitations with single-particle electronic excitations in semiconductor quantum wells and quantum dots. It is found that "hybrids" of these excitations are formed, and we calculate their energies. In the case of the quantum wells, one of them is a coupled intersubband plasmon-LO phonon mode localized at a neutral donor, and the other is a donor electronic excitation which is "dressed" by coupled intersubband plasmon-LO phonon modes. For quantum dots, these excitations are hybrids of LO phonon modes and a transition between different states of an electron confined to the dot. For dots we include both confined and interface phonons. We comment on the comparison of these results with experimental data.

I. Introduction: The possibility of an LO phonon hybridizing with a low-lying electronic excitation of a neutral donor in bulk semiconductors has been studied extensively theoretically [1] and experimentally [2]. These excitations have been interpreted as phonons bound in the vicinity of the donor and as donor excitations "dressed" by phonons. As the methods for growing samples and for producing semiconducting nanostructures has improved, the interest in neutral donor-bound phonons (or other collective excitations such as plasmons) has extended to lower dimensions. In Raman studies of quantum wells, Gammon *et al.* [3] have observed well-width dependent and carrier density dependent excitations which they attributed to coupled phonon-intersubband plasmon modes bound at neutral donors. Recently we have made a fully quantum mechanical treatment of the binding of collective excitations at neutral donors [4] and have showed that the results account for the well-width and carrier density dependence of these data.

As one moves to confinement in three dimensions, i.e. quantum dots, such hybrid excitations can involve dot-confined electronic transitions. This is because the quantum dots behave like artificial atoms thereby allowing the phonons to interact with electrons in them just as they do with the electrons in neutral donors in quantum well or bulk systems. Recent photoluminescence (PL) experiments [5] on CuCl nanocrystals suggest that the optical transitions involve such hybrid excitations.

Here, we briefly describe how the hybridization of the phonon (or collective excitation) with the electronic transition is modified as one goes to the quantum well and to the quantum dot. Note that in the former case, the electronic excitation involves low-lying states of a

donor, and in a quantum dot it involves electronic states confined to the dot. Nevertheless, the mechanism for the hybridization is the same in both cases.

II. Hybrid Energies: In this section we give results of calculations of the energies of hybrids of (A) coupled intersubband plasmon-LO phonon modes and neutral donors in quantum wells, and of (B) confined and interface LO phonons and electrons in quantum dots. We use the Fröhlich interaction and almost-degenerate Brillouin-Wigner perturbation theory [6] to couple the collective excitations with the single-particle excitations.

Quantum Well: Based on the methods of Ref. [6], one can derive the following equation for the hybrid energy E :

$$E - E_{\text{exc}} - I \left(\frac{1}{E - \Delta E} + \frac{2}{E - \Delta E - 2E_{\text{exc}}} \right) = 0, \quad (1)$$

where E_{exc} is the energy of the collective excitation [$\equiv \hbar\omega_{\pm}$, the upper (+) and lower (-) branches of the coupled intersubband plasmon-LO phonon modes], ΔE is the splitting of the ground- and first-excited state of the neutral donor, and I is given by [4]

$$I = \left(\frac{\alpha_{1s}\alpha_{2p_z}}{\alpha_{1s} + \alpha_{2p_z}} \right)^2 \frac{\Omega_0^3 \alpha_{1s}^2}{2\pi n_{2D} \hbar \omega_{\pm} (\omega_+^2 - \omega_-^2)(\omega_{\pm}^2 - \omega_{\text{LO}}^2)}, \quad (2)$$

where n_{2D} is the two-dimensional carrier density, Ω_0 is the bare intersubband transition energy between the ground and first excited state, $\omega_{\text{LO}}(\text{TO})$ is the LO (TO) phonon frequency, and $\alpha_{11} = 80L^3 n_{2D}a_0/27\pi^3 a_B\epsilon_{\infty}$. α_{1s} (α_{2p_z}) is the exponential coefficient for the the 1s ($2p_z$) state wave function, L is the quantum well width, a_B is the Bohr radius of the hydrogenic donor electron, and to (ϵ_{∞}) is the low- (high-) frequency dielectric constant. The frequencies of the coupled LO phonon-plasmon modes are given by

$$\omega_{\pm}^2 = (\omega_{\text{LO}}^2 + \omega_{\text{pl}}^2)/2 \pm \sqrt{(\omega_{\text{LO}}^2 + \omega_{\text{pl}}^2)^2 - 4\Omega_0^2(\omega_0^2 + \alpha_{11}\omega_{\text{LO}}^2)/\hbar^2}, \quad (3)$$

where $\omega_{\text{pl}} = \Omega_0(1 + \alpha_{11})^{1/2}/\hbar$ is the intersubband plasmon frequency, which is assumed to be dispersionless here, as are the phonon frequencies.

Equation (1) is essentially a cubic equation having three real solutions for E . In the present work we have gone beyond the treatment of Ref. [4] by finding exactly all three solutions rather than approximating the denominators in Eq. (1) with $E = \hbar\omega_{\pm}$ and hence only finding the energy of the collective-excitation-like hybrid. Because I is sufficiently small, one of these solutions is near E_{exc} , one solution is near ΔE , and one is near $\Delta E + 2E_{\text{exc}}$. The first solution is interpreted as a collective excitation which is bound to the donor, and the second as an electronic excitation of the donor which is dressed by the collective excitation.

Our results for the binding energies ($E_{\text{b}\pm} \equiv E - \hbar\omega_{\pm}$) corresponding to collective-excitation-like solutions are shown in Fig. 1 along with the data from Ref. [3]. The general trend of the experimental data and of our results agree reasonably well. The differences in magnitude may be accounted for by the approximations made in the calculations or by experimental uncertainties [8]. One can see from these calculations that the well-width dependence of the binding energies is richer than suggested by the experimental data, which was obtained for a limited range of well widths.

Quantum Dot: We consider the coupling of LO phonons with an electronic transition of a spherical quantum dot of GaAs of diameter d embedded in a nonpolar material having ϵ_{∞}

the same as that of GaAs. Here we are interested in the hybridization of this electronic transition with both “interface” (IF) phonon modes as well as “confined” phonon modes of the dot. Previous workers [5] have considered such hybridization with the confined modes alone, but electron-phonon interactions are in fact dominated by interface phonons for nanoscale sizes small enough [typically $d < O(10 \text{ nm})$] that the energetic splitting between the electronic states exceeds the phonon energy [7].

For the spherical dots studied here, the optical phonons and the electronic states can be classified by angular quantum numbers (l, m) . We consider virtual transitions of an electron from its ground state $[(l, m) = (0, 0)]$ to one of its threefold-degenerate first-excited states $[(l, m) = (1, 0) \text{ or } (1, \pm 1)]$. Conservation of angular momentum dictates that the phonons participating in these transitions are those for which $(l, m) = (1, 0) \text{ or } (1, \pm 1)$. This condition is satisfied by an infinite number of confined phonon modes (having different radial “confinement numbers”) and by three IF phonon modes (“Mie resonances”). The energies of the three (degenerate) IF phonons are smaller than that of the confined phonons, which we take to be the dispersionless $\hbar\omega_{\text{LO}}$ of the bulk. We generalize the ansatz of Ref. [6] to obtain the following extension of Eq. (1) to find that the determinant of the following matrix must equal zero:

$$\begin{bmatrix} E - E_{\text{IF}} - \left(\frac{I_{\text{IF}}}{\Gamma} + \frac{4I_{\text{conf}}}{\Gamma - 2E_{\text{IF}}} + \frac{3I_{\text{conf}}}{\Gamma - 2E_{\text{LO}}}\right) & -\sqrt{I_{\text{IF}}I_{\text{conf}}}\left(\frac{1}{\Gamma} + \frac{1}{\Gamma - E_{\text{IF}} - E_{\text{LO}}}\right) \\ -\sqrt{I_{\text{IF}}}\left(\frac{1}{\Gamma} + \frac{1}{\Gamma - E_{\text{IF}} - E_{\text{LO}}}\right) & E - E_{\text{LO}} - \left(\frac{I_{\text{conf}}}{\Gamma} + \frac{4I_{\text{conf}}}{\Gamma - 2E_{\text{LO}}} + \frac{3I_{\text{conf}}}{\Gamma - 2E_{\text{IF}}}\right) \end{bmatrix}, \quad (4)$$

where I_{IF} and I_{conf} are the quantum dot analogs of Eq. (2), $\Gamma = E - \Delta E$, $\Delta E = 20.6h^2/(m_{\text{eff}}d^2)$, and m_{eff} is the effective mass of the electron.

Equation (4) is essentially a ninth degree polynomial in E , having nine real roots. These energies correspond to hybrids of the electronic excitations, IF phonon modes, and confined phonon modes of the quantum dot system. Because I_{IF} and I_{conf} are small, one of the solutions for E lies near E_{IF} , one near E_{LO} , and one near ΔE , for most values of ΔE . The first (second) solution is an IF (confined) phonon mode whose energy is shifted owing to its hybridization with the electronic excitation. The third solution is an electronic excitation of the dot which is dressed by a combination of IF phonons and confined phonons. The remaining six solutions form three nearly-degenerate doublets which are energetically near the sum of ΔE and respectively either $2E_{\text{IF}}$, $2E_{\text{LO}}$, or $E_{\text{IF}} + E_{\text{LO}}$, and they are not the main interest of the present work.

We have calculated these energies E for varying values of the dot diameter d , and the results are plotted in Fig. 2. For dot diameters d such that ΔE lies either considerably above or considerably below E_{LO} and E_{IF} , the hybrid energies lie very close to either E_{IF} , E_{LO} , ΔE , or a simple sum of these. However for ΔE sufficiently near E_{LO} or E_{IF} we see avoided crossings, indicating that for quantum dot systems of this size the collective excitations can hybridize strongly with the single-particle electronic excitations.

In their recent PL studies of CuCl dots Itoh *et al.* have seen Stokes shifts whose energies lie close to the bulk LO phonon energy of CuCl. Additionally they see features which they attribute to TO phonons of CuCl. However, from our results here we suggest that these features may not be TO phonons, which couple only weakly to charge carriers, but instead may be IF phonons, which couple more strongly (i.e., via the Fröhlich mechanism) to charge carriers, and whose energy lies only slightly above the bulk TO energy. Detailed calculations of the optical intensities of these transitions should clarify this identification.

III. Summary: The effects of confinement on the energies of hybrid excitations formed from collective modes and localized electronic transitions in quantum wells and quantum dots are studied. In quantum wells, the collective excitations are coupled intersubband plasmon-LO phonon modes, and the electrons are in hydrogenic states of neutral donors. In quantum dots, the collective excitations are confined and interface LO phonons, and the electrons are confined to the quantum dot, an artificial atom.

This work was supported in part by contract of the U. S. Office of Naval Research and by a National Research Council Research Associateship.

* Present address: Max-Planck Institut für Festkörperforschung, Heisenbergstrasse 1, D-7056 Stuttgart, Germany.
[1] Sh. M. Kogan *et al.*, *Zh. Eksp. Teor. Fiz.* **50**, 1279 (1966) [*Sov. Phys. JETP* **23**, 850 (1966)].

[2] P. J. Dean *et al.*, *Phys. Rev. Lett.* **25**, 1027 (1970).

[3] D. Gammie, B. V. Shanabrook, and D. Muzz, *Phys. Rev. B* **39**, 1415 (1989).

[4] S. W. Pierson, T. L. Reinecke, and S. Rudin, *Phys. Rev. B* **51**, 10817 (1995).

[5] T. Itoh *et al.*, *Phys. Rev. Lett.* **74**, 1645 (1995).

[6] J. Moncke *et al.*, *Phys. Stat. Sol. (b)* **138**, 685 (1986).

[7] P. A. Knipp and T. L. Reinecke, *Phys. Rev. B* **48**, 5700 (1993).

[8] D. Gammie, private communication.

FIG. 1. The binding energy of the hybridized mode which is associated with the upper (lower) collective excitation is plotted as a dashed (solid) line as a function of the quantum well width. Also included are experimental data from Ref. [3]. The diamonds (squares) represent the binding energy of the upper (lower) mode. In the absence of coupling to the donor transition these binding energies would vanish.

FIG. 2. Energies of a spherical GaAs dot as a function of the dot diameter d . Solid lines represent the energies of the hybrid excitations, short-dashed lines represent the bare IF- and confined-phonon energies, and the long-dashed line represent the bare electronic excitation.

Fig. 2

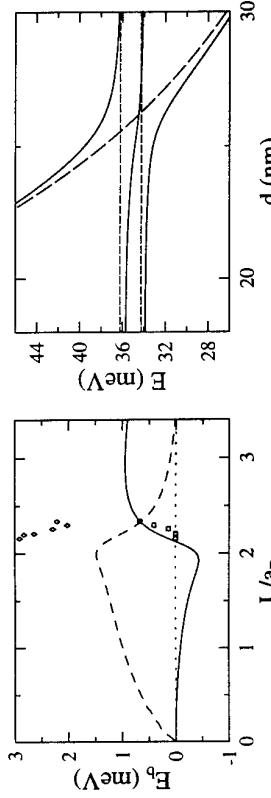


Fig. 1

Magnetic Field Effects on the Vacuum Rabi Coupling in Semiconductor Quantum Microcavity Structures

¹T A Fisher, ¹A M Afshar, ¹D M Whittaker, ²M S Skolnick, ²J S Roberts, ²G Hill, ²M A Pate

¹ Department of Physics, University of Sheffield, Sheffield, S3 7RH, UK

² Department of Electronics Electrical Engineering, University of Sheffield, Sheffield, S1 3TN, UK

We investigate the effect of magnetic field on the vacuum Rabi coupling strength (Ω_{HH}) in very high quality semiconductor quantum microcavity structures. Keeping the exciton and photon on-resonance at each magnetic field (B) by varying the temperature we observe an increase in Ω_{HH} by a factor of 1.4 when B is increased from 0 to 14T. By using Transfer Matrix Reflectivity simulations we deduce an increase in exciton oscillator strength of 2.2, in very reasonable agreement with predictions of quantum well exciton calculations. An additional weaker splitting, attributed to exciton Zeeman splitting (Δ_2) is also seen. We make a comparison of on and off-resonance spectra, at $B = 12T$.

Semiconductor quantum microcavity (QMC) structures are ideal structures for the investigation of exciton-photon vacuum Rabi coupling. The photon properties are controlled by the Fabry-Perot mode of the cavity whilst the excitons are controlled by quantum wells (QWs) placed at the anti-node of the photon-field. The vacuum Rabi coupling on-resonance is observed in reflectivity as two peaks of equal intensity with splitting, Ω_{HH} . The coupling strength, Ω_{HH} , has an approximately square root dependence on the exciton oscillator strength. The first observation and study of the vacuum Rabi splitting in semiconductor structures was by Weisbuch et al [1], followed by further studies by Houdré, Stanley and co-workers [2,3]. In our previous work we have used both temperature [4] and electric field [5] for tuning the exciton through the cavity mode. By using temperature to keep the exciton and photon on-resonance we have shown how the reduction in exciton oscillator strength, due to the electric field, reduces the vacuum Rabi coupling strength (Ω_{HH}) [4,5].

In the present paper we study the effect of magnetic field on very high quality QMC structures. In this case the exciton oscillator strength increases with field. At each magnetic field, temperature is used to keep the exciton and cavity mode on-resonance. An increase in magnetic field from 0 to 14T leads to an observed increase in the vacuum Rabi splitting of 1.4. By simulating the observed spectra with a Transfer Matrix Reflectivity (TMR) model [6,4,5], we deduce that this corresponds to an increase in exciton oscillator strength (f_{osc}) of a factor of 2.2, in very good agreement with quantum well exciton calculations.

Interestingly, for fields, $B \geq 6.6T$, clearly resolved splitting of the low energy coupled peak is seen, interpreted as arising from exciton Zeeman splitting. The observed behaviour can be simulated reasonably well by the TMR model if it is assumed each spin component of the exciton interacts independently with the confined photon.

The QMC structure consists of a λ GaAs cavity sandwiched between two Bragg mirrors, each composed of 20 periods of quarter wavelength AlAs (high refractive index) and $\text{Al}_{0.3}\text{Ga}_{0.7}\text{As}$ (low refractive index). Three $\text{In}_{0.13}\text{Ga}_{0.87}\text{As}$ QWs of nominal width 100Å are placed centrally in the cavity at the antinode of cavity photon mode. Since the QW is strained only the lowest energy heavy-hole exciton (HH_x) is expected to be observed [7].

The exciton is affected by magnetic field in the following way. On increasing the field the exciton undergoes a diamagnetic shift to higher energy and in addition the exciton oscillator strength increases due to wavefunction shrinkage [8]. Increasing temperature, on the other hand, decreases the exciton energy with no change in the exciton oscillator strength [4]. Therefore to study the effect of magnetic field on the vacuum Rabi coupling strength (Ω_{HH}), the temperature is increased to keep the exciton and photon on-resonance.

The reflectivity spectra on-resonance are shown at selected magnetic fields in Fig. 1 (Resonance is defined as the magnetic field and temperature for which the coupled peaks have equal intensity (area under the curve)). At $B = 0T$ the structure is on-resonance at 27K, and at 14T resonance is observed at 95K. There are several interesting features to note. At $B = 0T$ (Fig. 1(a)) two coupled peaks are observed with a splitting $\Omega_{\text{HH}} = 5.1$ meV and linewidths (FWHM) 0.95 meV and 1.25 meV. The high energy peak is broader, interpreted as being due to coupling of the photon with higher discrete and continuum excitation states[2]. The very small linewidths attest to the high sample quality.

The splitting on-resonance of the two main features shows a strong increase with increasing magnetic field. In addition, at 6.6T a second weak feature is seen only on the low energy peak. As the field increases this feature becomes more resolved, with an increase in the splitting from 0.4 meV at 6.6T to 0.8 meV at 14T. This additional splitting arises from the exciton Zeeman splitting. The vacuum Rabi splitting is found to increase from 5.1 meV at 0T to an average of 7.2 meV at 14T.

In order to deduce the change in exciton oscillator strength and Zeeman splitting with magnetic field the results are simulated using the TMR model. Agreement between the observed spectra and the simulated spectra is only achieved if it is assumed that each of the spin components of the exciton interacts independently with each circularly polarised spin component of the photon mode [9].

From 0 to 14T an increase in exciton oscillator strength (f_{osc}) by a factor of 2.2 is deduced from the simulations (plotted as circles in Fig. 2), corresponding to the observed increase in Ω_{HH} of 1.4. QW exciton calculations were performed, which use a numerical solution of Schrödinger's equation for a finite QW with decoupled heavy and light-hole bands. The predicted changes in oscillator strength are shown in Fig. 2 for the nominal well width of 100Å (dashed line) and a well width of 120Å (solid line). Very reasonable agreement is found between the deduced change in f_{osc} and the calculated values for 120Å [10].

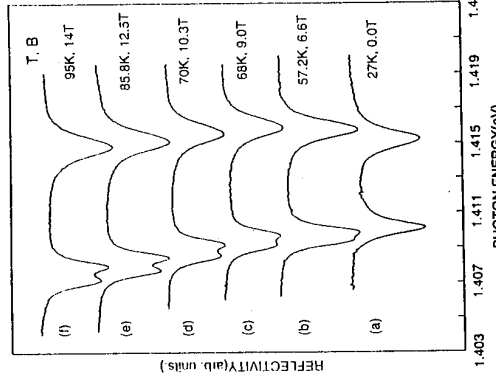


Figure 1 On-resonance reflectivity spectra, shown from B= a) 0T to f) 14T. The spectra are kept on-resonance by increasing the temperature with magnetic field.

The exciton Zeeman splittings, deduced from the simulations at fields where the observed splitting is well-resolved, are plotted in Fig. 3. The Zeeman splitting increases from 1.05 meV at 6.6T to 1.72 meV at 14T. Note, that these values are approximately twice those of the observed splittings, as expected from simple perturbation theory arguments[11]. Our splitting at 11T of 1.4 meV compares with the value of 2.27 meV at 11T for 100Å QW, reported by Wimbauer et al [12], but for Indium composition $x=0.18$. However Traynor et al[13] have reported strong dependence of the Zeeman splitting on x (and well-width), with an approximately factor of 2 increase between $x=0.075$ and $x=0.11$. In view of this strong dependence on x we regard our deduced value of spin-splitting as being in reasonable agreement with the result of Ref.[12].

Temperature tuning at a high field of 12T was also performed. Fig. 4(a) shows the on-resonance spectra at $T = 85\text{K}$ where the two coupled features are of equal intensity. The splitting of the low energy peak (0.65 meV) is clearly resolved, corresponding to a Zeeman splitting of 1.48 meV. Fig. 4(b) shows the off-resonance spectra at $T = 32\text{K}$ where the exciton, labelled X, is significantly weaker than the cavity. However, the only evidence of a splitting of the exciton is a weak shoulder at 1.421 eV (indicated by the arrow). Simulated spectra for comparison to the 32K and 85K spectra at 11T, are shown in Figs. 4(c) and (d) respectively. The overall agreement between the experiment and the simulations is good. In particular the lower energy peak at 85K, which exhibits the clear Zeeman splitting, is simulated well. The predicted Zeeman splitting (Fig. 4(c)) is not observed on the high energy feature in the experimental spectra (Fig. 4(a)), as noted earlier. This arises in part due to the greater broadening (also observed at $B=0\text{T}$ (Fig. 1(a))), and also due to an apparent reduction of the splitting (by $\sim 30\%$) for the high energy feature. Such a reduction of splitting for the high energy feature, which may arise from coupling between the two exciton components, is not however

understood at present.

In summary we have investigated the effect of magnetic field on the exciton-photon coupling in quantum microcavity structures. An increase in magnetic field from 0 to 14T gives an observed increase in the vacuum Rabi splitting by a factor of 1.4. Using TMR simulations we deduce an increase in exciton oscillator strength of a factor of 2.2, in very reasonable agreement with QW exciton calculations for a 120Å QW which show an increase of 2.1. An additional weaker splitting is observed and attributed to Zeeman splitting.

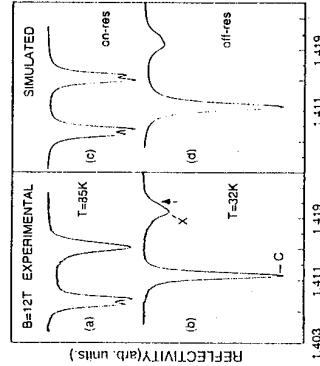


Figure 2 Exciton oscillator strengths deduced from the experimental reflectivity spectra, using the Transfer Matrix Reflectivity model (solid circles). These are compared with predicted oscillator strengths for 100Å (dashed line) and 120Å QW (solid line).

Temperature tuning at a high field of 12T was also performed. Fig. 4(a) shows the on-resonance spectra at $T = 85\text{K}$ where the two coupled features are of equal intensity. The splitting of the low energy peak (0.65 meV) is clearly resolved, corresponding to a Zeeman splitting of 1.48 meV. Fig. 4(b) shows the off-resonance spectra at $T = 32\text{K}$ where the exciton, labelled X, is significantly weaker than the cavity. However, the only evidence of a splitting of the exciton is a weak shoulder at 1.421 eV (indicated by the arrow). Simulated spectra for comparison to the 32K and 85K spectra at 11T, are shown in Figs. 4(c) and (d) respectively. The overall agreement between the experiment and the simulations is good. In particular the lower energy peak at 85K, which exhibits the clear Zeeman splitting, is simulated well. The predicted Zeeman splitting (Fig. 4(c)) is not observed on the high energy feature in the experimental spectra (Fig. 4(a)), as noted earlier. This arises in part due to the greater broadening (also observed at $B=0\text{T}$ (Fig. 1(a))), and also due to an apparent reduction of the splitting (by $\sim 30\%$) for the high energy feature. Such a reduction of splitting for the high energy feature, which may arise from coupling between the two exciton components, is not however

References

- C. Weisbuch, M. Nishioka, A. Ishikawa and Y. Arakawa, Phys. Rev. Letts, **69**, 3314 (1992)
- R. Houdré, R. P. Stanley, U. Oesterle, M. Illegems, C. Weisbuch, Phys. Rev. B, **42**, 16761 (1994)
- R. P. Stanley et al, Appl. Phys. Letts, **65**, 1833 (1994); ibid. **65** (2003) 1994; Phys. Rev. Letts, **73**, 2043 (1994)
- T. A. Fisher, A. M. Afshar, D. M. Whittaker, M. S. Skolnick, J. S. Roberts, G. Hill and M. A. Pate, Phys. Rev. B**57**, 2600 (1995)
- T. A. Fisher, A. M. Afshar, M. S. Skolnick, D. M. Whittaker, J. S. Roberts, G. Hill and M. A. Pate, Proceedings of 7th Int. Conf. on Modulated Semiconductor Structures, Madrid, July 1995.
- See M. Born and E. Wolf, Principles of Optics (Pergamon, Oxford, 1986), 6th Ed.
- M. K. Saker, D. M. Whittaker, M. S. Skolnick, M. T. Emery and C. R. Whitehouse, Phys. Rev. B**43**, 4945 (1991)
- H Q Hou, W Stagni, S Takeyama, N Miura, Y Segawa, Y Aoyagi and S Namba, Phys Rev B**43**, 4152 (1991); R L Green and K K Bajaj, Phys Rev B**31**, 6498 (1985)
- If the two unperturbed excitons are of equal strength and are assumed to be completely coupled through the photon mode, the simulations show two strong reflectivity features, split by Ω_{RHHX} , and a very weak third feature.
- In the electro-optic tuning experiments of the same sample [5], a well-width of 120Å was required to reproduce the unperturbed exciton shift rate with electric field.
- The exciton is split into two components by the magnetic field. At resonance each component is repelled by the cavity mode by approximately half the value of the Zeeman splitting, as can be shown by simple perturbation theory arguments.
- Th. Wimbauer, K. Oettinger, A. L. Efros, B. K. Meyer and M. Brugger, Phys. Rev. B**50**, 889 (1994)
- N. J. Traynor, R T Harley and R J Warburton, Phys. Rev. B**51**, 7361 (1995)

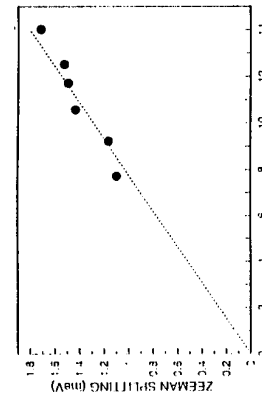
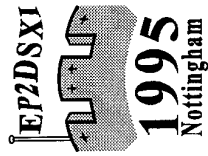


Figure 3 Deduced Zeeman splitting as a function of magnetic field (solid circles). The dashed line is a guide to the eye.



Correspondence Address

All communication relating to this conference should be sent to:

EP2DS XI
Department of Physics
University of Nottingham
Nottingham NG7 2RD
United Kingdom

Fax +44 115 951 5180
(note new area code)
or 0115 951 5180 from inside the UK
e-mail: ppzpcm@ppnl.nott.ac.uk

Conference Office
(7-11 August 1995 *only*)
Phone +44 155 951 5023

Tourist Information

Further tourist information about Nottingham can be obtained from:

The Nottingham Information Centre
1-4 Smithy Row
Nottingham NG1 2BY
United Kingdom

Tel. +44 115 9470661 or
0115 947 0661 from within the UK.
Fax 0115 935 0883